The international journal of science / 2 January 2020

nature

KEEPING TRACK

Ways to quantify progress towards Sustainable Development Goals

Hot tickets 2020
The must-see plays, exhibitions and films for the year ahead

Galactic archaeology
Mature galaxy cluster offers insight into cosmic dark ages

Medical imaging
Could breast cancer screening benefit from artificial intelligence?

The international journal of science / 2 January 2020

nature

Get the Sustainable Development Goals back on track

Most of the goals will be missed. Here's how to put them back on the right path.

In 2015, world leaders met in New York at a landmark conference of the United Nations. Their aim: to end poverty, stop environmental destruction and boost well-being. In the world of multilateral diplomacy, such meetings are not uncommon, but they tend to focus on individual areas, such as climate change or food security. The 2015 summit was different because heads of state and governments pledged concrete action across an integrated set of economic, environmental and social issues. They signed up to the Sustainable Development Goals (SDGs), a package of 17 goals and associated targets for ending hunger, eliminating extreme poverty, reducing inequality, tackling climate change and halting the loss of biodiversity and ecosystems — all by 2030.

With that deadline now a decade away, the world is set to miss most of the SDGs. Just two of them — eliminating preventable deaths among newborns and under-fives, and getting children into primary schools — are closest among all the goals to being achieved. By contrast, the goal to eliminate extreme poverty will not be met because some 430 million people are expected still to be living in such conditions in 2030.

Targets to end hunger and to protect climate and biodiversity are completely off track. Whereas some of the richer countries are making a degree of progress in the SDGs overall, two-thirds of poorer ones are not expected to meet those that relate even to their most basic needs.

The SDGs are extremely valuable, and five years is too short a time to see real progress towards economic transformation, which must happen if the goals are to be achieved in full. But at the same time, the SDGs have had a considerable positive impact — including in research and higher education. Institutions globally are signing up to supporting the SDGs, and staff and students are taking on responsibilities, from eliminating single-use plastic, to switching to renewable energy. The goals' cross-cutting nature has fuelled research, too, providing scientists with opportunities in the fields of the environment, engineering, health policy, development economics and beyond.

But these bright spots cannot mask what is still a bleak trend. The UN secretary-general, António Guterres, puts the halting progress down to a lack of funding — especially from the governments of developed countries. The goals come with a price tag of between US$5 trillion and $7 trillion per year, and the shortfall has been put at $2.5 trillion.

But there's a larger obstacle. The goals are still a voluntary effort, although monitoring of progress is extensive. A UN-affiliated organization called the Sustainable Development Solutions Network produces an annual report that shows how well countries are performing on the SDGs, and on page 74 of this issue, researchers from the United States and China describe how progress can be more accurately recorded (Z. Xu *et al. Nature* **577**, 74–78; 2020) (see also page 8). But it's not compulsory for countries to report how they are doing.

> **"Time is short, and there's a lot to do when a decade is all we have."**

To be achieved, the SDGs need to become mandatory — not necessarily in the legal sense, but in the sense that nations have to know that there's no alternative but to make them happen. One analogy is the way in which countries report their economic data. There's no international law that says every country must report data, such as on consumer spending, that go into calculating its gross domestic product (GDP). But for more than 50 years, these data have been collected at a granular level and are now reported every quarter by national statistics offices. Every agency of government understands that a nation's economy must always be seen to be growing, and so the data underlying the GDP must also always be increasing. That's why there's a massive national effort to make sure that everyone works towards what could be called the 'GDP goals'. The SDGs are unlikely to be achieved unless they, too, sit at the apex of a similar national effort.

At the same time — and as is often pointed out — some GDP goals are in opposition to sustainability efforts such as the SDGs. Take new sources of fossil-fuel energy. They provide much-needed power for communities lacking basic needs and contribute positively to economic growth. But they also have a negative impact on the environment and on human health. Yet it's only the positive economic impact that counts in official data, and that is one reason — although not the only one, by far — why it's proving so difficult to shift power to renewable-energy platforms. One solution might be to factor the cost of degrading the environment into national accounting — although there is as yet little consensus on how this would be done.

Tighter focus

One research-led effort where there is more consensus is the Global Sustainable Development Report (GSDR). Due to be published every four years, it is commissioned by the UN secretary-general and written by a team of 15 authors nominated by UN member states, but working independently with the wider scientific community. The first report was published last September, and the UN will appoint authors for the second one, due in 2023, later this month.

The first report's authors are aware that the SDGs lack a mandatory reporting mechanism, and that in some cases the goals are competing with GDP goals. And they have come up with an innovative solution. They recommend that nations consider redistributing the 17 SDGs into 6 'entry points'. These are: human well-being (including eliminating poverty and improving health and education); sustainable economies (including reducing inequality); access to food and nutrition; access to — and decarbonizing — energy; urban development; and the global commons (combining

nature

biodiversity and climate change).

This is a sensible recommendation. A focus on a smaller, more integrated set of goals could help to reduce instances in which implementing one of the SDGs has the potential to hinder another. Take the case of wind energy. This has a part to play in meeting the climate action SDG, but if wind farms are sited in the wrong places, or if the turbines are the wrong height, they can potentially harm bird populations, which would affect the SDG on protecting biodiversity and ecosystems. Under the GSDR proposals, climate and biodiversity would sit under one category for action. If properly implemented, this would mean that decisions on new energy sources would need to consider the implications for biodiversity – reducing the numbers of wind power plants that end up in inappropriate locations.

So how could the GSDR's recommendations be implemented? So far, it's not clear that they have reached the ministries of finance and economics, and the central banks, where they need to be heard. Last month, Guterres appointed the departing Bank of England governor Mark Carney as UN climate envoy. That is a positive move because Carney's office has the potential to expand the report's footprint by creating a formal link between the GSDR team and economic policymakers.

As the 15 scientists tasked with preparing the next report take their posts, they must also urge Guterres to give them the resources to raise the profile of their work further, so that it becomes as well known and influential as the UN reports on climate and biodiversity.

The SDGs were launched in a 2015 UN report called *Transforming our World*. That's because a world without hunger and disease, with meaningful jobs and a clean environment, requires transformational change. But, on present trends, there are few signs that such change will be achieved by 2030. That's a reason to redouble policy efforts guided by evidence. Real change won't come until the research–policy interface is strengthened. Time is short, and there's a lot to do when a decade is all we have.

Index of improvement

A US–Chinese team shows how sustainability metrics can be improved.

How can a country tell that it's making progress on sustainability? How can it work out, from year to year, whether its environment is improving, along with the economy and well-being?

This is incredibly difficult. A successful measure must have at least three characteristics: it needs to be based on a comprehensive set of reliable data; it must be accessible to non-specialists; and it has to be updated regularly and presented so that progress (or lack of it) can be seen easily.

For decades, researchers and policymakers have been searching for a measure that everyone can agree on. But most efforts, from the Human Development Index to the Genuine Progress Indicator, end up lacking some aspect of those three characteristics.

The need is becoming more urgent now that the international community is set on its 2030 deadline to meet the United Nations' 17 Sustainable Development Goals (SDGs), which aim to end poverty and hunger, tackle climate change and more.

The UN publishes an annual report that ranks countries on their progress towards each goal, with a score out of 100. It shows how nations are doing relative to each other and whether they're on track to meeting the goals (most are not – see page 7). But the report doesn't record local-level data, and inter-year comparisons are hard.

For example, Denmark – the top-ranked country in the 2019 report, with an impressive aggregate score of 85.2 – still has some way to go in reaching Goal 14, which measures the health of the marine environment ('life below water'). But those who want to know whether Denmark's score has improved over time are forced to comb through PDFs of the previous years' reports, and these include nothing comparing different parts of the country.

> **"It's possible to measure progress towards the Sustainable Development Goals, and to reveal where countries fall short."**

But help could be at hand. In *Nature* this week, a team led by researchers from Michigan State University in East Lansing and China Agricultural University in Beijing show how it's possible to use the SDG reporting framework to construct an index that allows progress to be compared across regions and over periods of time (Z. Xu *et al. Nature* **577**, 74–78; 2020).

The team chose China as its case study, and the results show that the country's overall SDG score increased from 45.5 in 2000 to 55.4 in 2015. Each of its 31 provinces also increased its score. Nationally, the trend is in the right direction, although the rate of progress so far is not enough to meet the 2030 target. Moreover, China's scores have fallen in four goals – life below water, responsible production and consumption, gender equality, and climate action.

Can such an approach to data gathering be scaled up? Yes, but it needs a large literature base to draw on, and public authorities must be willing to recognize the value of such an effort – and must know how to use it.

China's government is aware of the environmental and social risks of rapid industrialization, and the country has an active community of researchers and policymakers working on sustainability measures. The authors of the paper went to national data sources such as the National Bureau of Statistics of China, as well as specialized sources that hold data on health, energy and population – all of which are accessible for research. But that is expensive on a global scale. In many low- and middle-income countries, especially, the infrastructure to collect such data still needs to be built.

This work is a milestone, nonetheless, because it shows how it's possible to measure detailed progress towards the SDGs, and to reveal where countries fall short. With 17 goals and just 10 years in which to achieve them, the world needs better measures to see both how far we have come, and how far we have to go.

World view

GEOFF MACDONALD

By Simine Vazire

A toast to the error detectors

Let 2020 be the year in which we value those who ensure that science is self-correcting.

Last month, I got a private Twitter message from a postdoc bruised by the clash between science as it is and how it should be. He had published a commentary in which he pointed out errors in a famous researcher's paper. The critique was accurate, important and measured — a service to his field. But it caused him problems: his adviser told him that publishing the criticism had crossed a line, and he should never do it again.

Scientists are very quick to say that science is self-correcting, but those who do the work behind this correction often get accused of damaging their field, or worse. My impression is that many error detectors are early-career researchers who stumble on mistakes made by eminent scientists, and naively think that they are helping by pointing out those problems — but, after doing so, are treated badly by the community.

Stories of scientists showing unwarranted hostility to error detectors are all too common. Yes, criticism, like science, should be done carefully, with due diligence and a sharp awareness of personal fallibility. Error detectors need to keep conversations focused on concrete facts, and should be open to benign explanations for apparent problems.

Even when criticism is done well, error detectors are often subjected to personal attacks. Junior scientists are accused of bullying their seniors. In one case, early-career researchers who showed that a famous scientist had engaged in extensive self-citation and recycled his own publications were accused of being vigilantes and mounting a witch hunt. Scientists who found flaws in high-profile nutrition research that required retractions were accused of cyberbullying and, bizarrely, of holding a grudge against school-lunch programmes. And those are just a few incidents that became public.

Researchers are often warned against pointing out errors — and sometimes kindness is used as justification. They are told to focus on improving their own research, or to state only the positive aspects of that done by others. If you don't have anything nice to say, don't say anything at all.

There are several problems with these arguments. First, we scientists present ourselves as a community of individuals committed to scrutinizing each other. Historian of science Naomi Oreskes, in urging non-scientists to trust science, argues that "scientists have a kind of culture of collective distrust". We cannot tell people to trust us because we monitor each other, and then appeal to kindness to halt that scrutiny.

Second, when we suggest that those working on error detection and correction are being unkind, we are the ones being unkind. Imagine that you are a trainee. You feel that science values self-correction, and that it's not about any one person's ego, but the collective motivation to find new knowledge, to check everything thrice or more, to discard false hypotheses and so to move ever closer to truth. Thus, when you find an error, you trust that it's okay to point it out. And then you find yourself accused of being a destructive, sanctimonious second-stringer — all for applying the 'scientific values' that you'd been taught.

> **"Scientific criticism must not be conflated with bullying."**

Yes, error detectors can make research less comfortable — but that discomfort is healthy. We should feel responsible for minimizing errors in our work, and worried that we might have missed some.

Scientific criticism must not be conflated with bullying. It's not fair to victims of actual bullying to use the term so loosely and inappropriately. Instead, we need mechanisms to protect those who engage in scientific criticism. These mechanisms would make science fairer and more inclusive. Advisers can get away with awful behaviour — bullying, harassment and other abuses of power — because their trainees are so dependent on them for funding, recommendations and other opportunities. Universities need to hold themselves and senior faculty members accountable for preventing abuse, including intimidation and bullying of error detectors.

We should do more to make criticism an established part of science. Universities need policies that assess inappropriate responses to criticism. Responsible research training should include sessions on how to assess whether apparent anomalies could be substantive problems, how to communicate concerns and how to respond when issues arise. Funders and research-evaluation committees should find ways to support and recognize all the work that error detection requires.

Furthermore, journals need to make clearer and firmer commitments to self-correction. In my opinion, they have a responsibility to share replication attempts for the work that they publish, including creating explicit criteria to enable publication of high-quality replications. Consider the Social Science Replication Project (C. F. Camerer *et al. Nature Hum. Behav.* **2**, 637–644; 2018), which focused on systematically repeating 21 experiments published in *Science* and *Nature*. It was an author, not either journal, who said that both journals had rejected the submission and shared the reasons given for doing so. As a former editor-in-chief of *Social Psychological and Personality Science*, I was shocked at how easy it would be to reject or hide criticism of the editorial process. There should be greater transparency and other measures of accountability over editors, senior authors and reviewers.

It's time to be kinder to those doing the criticizing, and to demand more accountability and humility from those in power. Instead of punishing people who flag errors, we should scramble to hire them, give them prizes and award them grants so they can keep improving science. The least we can do is provide a space for fact-based criticism that is safe from intimidation and retaliation. It's only thanks to error detectors that we can proclaim that science is self-correcting.

Simine Vazire is a professor of psychology at the University of California, Davis.
e-mail: simine@gmail.com

News in focus

JAMIE KIDSTON/ANU

Ross Mandi Wunungmurra helped to negotiate the return of blood samples to his community.

AUSTRALIAN BIOBANK REPATRIATES HUNDREDS OF INDIGENOUS BLOOD SAMPLES

The return is part of a groundbreaking approach that could inspire other institutions grappling with how to use historical samples ethically in research.

By Dyani Lewis

Late last year, the Galiwin'ku community of Elcho Island off the coast of northern Australia celebrated the return of more than 200 vials of blood that were collected from their ancestors half a century ago, before modern research principles on informed consent existed. Unbeknownst to the Galiwin'ku community, the blood vials had been in freezers at the Australian National University in Canberra ever since.

Many Indigenous Australian communities believe that the remains of their people, including blood and hair, must return to their ancestral home, or Country, to be at peace. Having the vials returned "meant a lot to us", says Ross Mandi Wunungmurra, chair of the Yalu Aboriginal Corporation, the community organization that helped negotiate the return. Mandi is one of several hundred living members of the community whose blood was also collected after a typhoid outbreak in 1968.

Before the samples from deceased people were repatriated, their relatives gave permission for DNA to be extracted from the blood. People who are still alive offered fresh samples. The genetic information will be stored in the biobank of the National Centre for Indigenous Genomics (NCIG), which the Australian National University (ANU) established specifically to manage its historical samples.

The return was part of a groundbreaking attempt by the NCIG to right the research wrongs of the past. It comes against a backdrop of global uncertainty about what institutions should do with such historical samples, which might contain genetic or other information that is valuable to science, but which were gathered before the establishment of modern research principles governing the ethical collection and storage of such samples. When the Galiwin'ku samples were collected, Australia's government had only recently recognized Indigenous people as citizens, and racist

attitudes that denied them the same rights as white Australians were rife.

Scientists say that the approach is laudable, and could be adopted by other institutions with similar legacy collections. But some researchers warn that it may be challenging to find a data-access policy that satisfies both Indigenous communities and the researchers who want use the data.

Governed by a majority-Indigenous board, the NCIG has a mandate to approach communities whose historical samples are in the ANU's store and ask whether the samples should be kept for future research, returned or destroyed. So far, the team has contacted four out of several dozen communities.

"The basic principle here is we just do what the community wants us to do," says NCIG director Simon Easteal.

Innovative approach

Researchers say the scale of the NCIG's endeavour is impressive. Visiting communities, many remote, to ask them what to do about historical samples is resource-intensive and beyond the budget of many institutions, so many just leave such samples in their freezers, says Easteal.

Sometimes researchers will ask communities for permission to collect specimens for an individual research project, but that doesn't solve the problem of what to do with the specimens once that project is over, he adds.

Negotiations between the Galiwin'ku community and the NCIG took two years, and involved people from both groups travelling between Canberra and Elcho Island many times, says Azure Hermes, a Gimuy Walubara Yidinji woman from far north Queensland who runs community engagement for the centre.

The centre will attempt to follow the wishes of every Indigenous person whose samples are in its collection, which includes specimens and records from 7,000 Indigenous people. If the person from whom a sample was collected has died, the centre will consult their relatives.

Of the roughly 2,000 people from 4 communities whom the NCIG has contacted, about 90% have given permission for their DNA or the DNA of their deceased relatives to be extracted and data added to the NCIG biobank, says Hermes.

"Australia is definitely leading the way with legacy samples or orphan samples, and figuring out how to deal with them," says Ripan Malhi, an anthropologist at the University of Illinois at Urbana–Champaign, who has worked with Native American communities.

The NCIG is giving communities control over their genomic data, as well as their samples.

Data in the centre's biobank will eventually be available for other researchers, but participants are able to withdraw consent for their DNA to be used in specific projects — or the biobank as a whole — at any time using an online portal, an approach known as dynamic consent. Annual visits to communities provide further opportunities for people to make decisions about how their data are used, and learn about research outcomes, says Hermes.

Dealing with the genomic data appropriately is just as important as handling the samples themselves sensitively, says Māui Hudson, a Maori man who is a research ethicist at the University of Waikato in New Zealand.

But he says that the dynamic-consent model is at odds with the move towards open data in research. Communities "need to be involved in the process of decisions about what appropriate uses look like, and that's not possible in a truly open-data environment", he says.

UNITED STATES TO FUND GUN-VIOLENCE RESEARCH AFTER 20-YEAR FREEZE

Government spending deal includes $25 million for studies of firearms safety.

By Nidhi Subbaraman

Lawmakers in the United States have reached an agreement that would fund gun-violence research for the first time in more than 20 years.

A wide-ranging spending bill introduced on 16 December includes US$25 million for studies on the issue, split evenly between the Centers for Disease Control and Prevention (CDC) and the National Institutes of Health (NIH). President Donald Trump signed the bill into law on 20 December, after it was approved by the House of Representatives and the Senate.

"It's a good start," says Garen Wintemute, director of the Violence Prevention Research Program at the University of California, Davis, who has been studying gun violence for decades. "Violence-prevention policy should be guided by solid scientific evidence."

"We've lost several generations of researchers in this field."

"Is it adequate? Absolutely not. But is it meaningful and is it important? Absolutely yes," says Mark Rosenberg, president emeritus of the non-profit Task Force for Global Health in Atlanta, Georgia, and the founding director of the CDC's National Center for Injury Prevention and Control (NCIPC), also in Atlanta.

The CDC says that 39,773 people died of gun-related injuries in 2017, the last year for which it has released a full analysis.

The federal government stopped funding gun-violence research after Congress passed a rule called the "Dickey Amendment" in 1996. It barred the CDC from using funds "to advocate or promote gun control". That was widely interpreted as prohibiting the funding of research into gun violence.

Jay Dickey, the Republican congressman from Arkansas who wrote the amendment, reversed his position on gun-violence research in the years before his death. "Both of us now believe strongly that federal funding for research into gun-violence prevention should be dramatically increased," Dickey wrote in *The Washington Post* in 2015, along with former NCIPC chief Rosenberg.

Slow thaw

Last year, Congress clarified that the ban on federal dollars for "advocacy" or the promotion of gun control did not extend to a ban on research. But lawmakers did not immediately set aside money for such research. The new law will require that the CDC and NIH directors report back to Congress to ensure that any grants they award "support ideologically and politically unbiased research projects".

David Studdert, who studies health law at Stanford Law School in California, says that the push to fund gun-violence work at the NIH and CDC is encouraging, but that meaningful research would require sustained support.

"We've lost several generations of researchers in this field, and it's going to take a while to build that back up," Studdert says.

The federal government is best positioned to undertake such an immense financial commitment, says Andrew Morral, a senior behavioural scientist at the RAND Corporation in Arlington, Virginia, and director of the National Collaborative on Gun Violence Research, a philanthropic organization that funds research on the topic. "Where are illegal guns coming from? Are different state laws effective? Are the programmes that are being developed to counter firearm suicide effective? There are so many questions that we don't have answers for."

MATTHIAS BALK/DPA

Flying to conferences creates a large carbon footprint.

VIRTUAL SCIENCE CONFERENCE TRIES TO RECREATE SOCIAL BUZZ

Psychologists assessed interaction at a meeting broadcast in 32 nations to cut its carbon footprint.

By Alison Abbott

Hundreds of attendees watched circadian biologist Paolo Sassone-Corsi give his keynote talk at a scientific meeting last month. But barely one-fifth of them were sitting in the lecture hall in Munich, Germany. The others were viewing from virtual hubs across 18 time zones.

The five-hour 'pop-up' conference on 18 November was an experiment to test the feasibility of making scientific meetings virtual, in a bid to cut the large carbon footprints created by attendees' air travel.

Organizers of academic and other international meetings have begun experimenting with ways to offset or cut down on carbon emissions, but the November meeting of the European Biological Rhythms Society (EBRS) is one of the first to take a systematic approach to retaining a key benefit of conventional meetings: networking and face-to-face contact. Its organizers invited psychologists to evaluate whether technology and organizational techniques can aid interaction and networking, for example by enabling seamless discussion across different locations, and encouraging participants at all sites to hold social events.

"We are now busy analysing the outcome, but at first glance it seems to have been more successful than I had dared hope," says Martha Merrow, a circadian biologist at the Ludwig Maximilian University (LMU) in Munich, who organized the mostly virtual meeting. Participants, who joined from 32 countries, said there were advantages beyond cutting carbon – for instance, parents who might find it difficult to arrange travel could attend. The EBRS says it will continue experimenting with the approach.

Virtual movement

The experiment comes in a year of worldwide activism on climate change, and as scientists in many fields have started to think about the carbon footprints of their globetrotting activities. "Our work tends to be dominated by international meetings and flights," says Corinne Le Quéré, a climate scientist at the Tyndall Centre for Climate Change Research in Norwich, UK. "We need to have a plan to reduce emissions by carrying out our work differently."

In 2015, Le Quéré co-authored one of the first carbon-reduction strategies created for a research institute. It recommended that scientists monitor the carbon output of their professional activities, avoid travelling to meetings unnecessarily and prioritize events with only small carbon footprints.

Le Quéré says that the Tyndall Centre has since tested ways to reduce travel, such as using video-conferencing, and many meetings are trying similar online approaches.

Fluent discussions

The EBRS meeting is a more advanced experiment, says Le Quéré, because of the inclusion of psychologists.

For Merrow, who was inspired by the climate-strike movement, the pop-up conference was a way to test the waters. She chose a topic – the influence of the circadian rhythm on metabolism – for which there was lots of expertise near Munich, where all the talks were given.

Sasonne-Corsi, who is based at the University of California, Irvine, was in Europe anyway when he gave the plenary lecture. Six short talks were repeated before and after his speech to ensure that participants in all the time zones could listen to them, whether in the morning or late evening. Three of the speakers travelled to Munich by train or car, and Merrow bought carbon offsets to compensate for the drive.

Invited speakers were enthusiastic, she says. Sassone-Corsi says, "The scientific endeavour has become too big – we all travel to too many meetings, and I get very tired." He travels intercontinentally around ten times a year.

The meeting was broadcast to five virtual hubs through high-quality, two-way video systems at universities in Tel Aviv, Israel; Zurich, Switzerland; Boston, Massachusetts; Tokyo; and Porto Alegre in Brazil. Another 69 hubs were set up for small groups of researchers to watch one-way video broadcasts and send questions or comments through Twitter.

"It was possible to have fluent scientific discussions," says Merrow, and some satellite groups organized local social events. In total, at least 450 people attended the conference and nearly 60% joined in through the interactive hubs on Twitter. About 10% more people attended the virtual meeting than went to the EBRS's annual conference in August in Lyon, France.

Psychological needs

Merrow invited LMU psychologist Anne Frenzel to assess the success of the approach, and the two are analysing feedback collected at the virtual conference and the Lyon meeting.

Aside from cutting emissions, participants mentioned advantages of the virtual meeting, including not losing time and energy to travel, and students being able to attend for free. Scientists in Brazil and Israel mentioned that it released them from the bureaucracy involved in booking flights to overseas conferences.

"This is not only about carbon footprints – it also offers a huge opportunity to think innovatively about how scientific discussions take place," says Merrow.

Q&A

FACEBOOK

Joelle Pineau

Joelle Pineau doesn't want science's reproducibility crisis to come to artificial intelligence (AI). So the machine-learning scientist at McGill University and Facebook in Montreal, Canada, is spearheading a movement to get AI researchers to open their methods and code to scrutiny. She holds a role dedicated to reproducibility on the organizing committee for the Conference on Neural Information Processing Systems (NeurIPS), a major AI meeting. At last month's gathering in Vancouver, Canada, Pineau told *Nature* about the measures the committee put in place.

Why are some algorithms irreproducible?
It's true that with code, you press start and, for the most part, it should do the same thing every time. The challenge can be trying to reproduce a precise set of instructions in machine code from a paper. And then there's the issue that papers don't always give all the detail, or give misleading detail. That's a big issue.

What got you interested in reproducibility?
I fell into it by accident. My students would say 'I can't get these results', or to get the results, they had to do things that I thought were methodologically wrong. It's important to stop it before it becomes the norm.

What reproducibility measures were enacted at NeurIPS this year?
We encouraged people to submit their code; we're running a reproducibility challenge; and we introduced a checklist for papers. The checklist asks, for example, whether you clearly labelled the type of metrics and measures you're using, what the details of your model are and how you set certain aspects of the model that can change the results a lot.

What has the reception been like?
Very good. Code submission is one of the elements I'm most impressed with. A year ago, 50% of accepted NeurIPS papers contained a link to code; this year, it's 75%.

Interview by Elizabeth Gibney
This interview has been edited for length and clarity.

RUSSIA JOINS RACE TO MAKE QUANTUM DREAMS REAL

National initiative aims to build a quantum computer and develop practical technologies.

By Quirin Schiermeier

Russia has launched an effort to build a working quantum computer, in a bid to catch up with other countries in the race to develop practical quantum technologies.

The government will inject about 50 billion roubles (US$790 million) over the next 5 years into basic and applied quantum research at leading Russian laboratories, the country's deputy prime minister, Maxim Akimov, announced on 6 December.

"This is a real boost," says Aleksey Fedorov, a quantum physicist at the Russian Quantum Center (RQC), a private research facility in Skolkovo near Moscow. "If things work out as planned, this initiative will be a major step towards bringing Russian quantum science to a world-class standard."

Quantum computers use elementary particles, which can exist in multiple quantum states at once, to carry out calculations. Quantum bits, or qubits, can in theory process information exponentially faster than the binary one–zero bits used in classical computing. Powerful quantum computers could be used to predict the outcomes of chemical reactions, search huge databases or factor large numbers, such as those used in encryption.

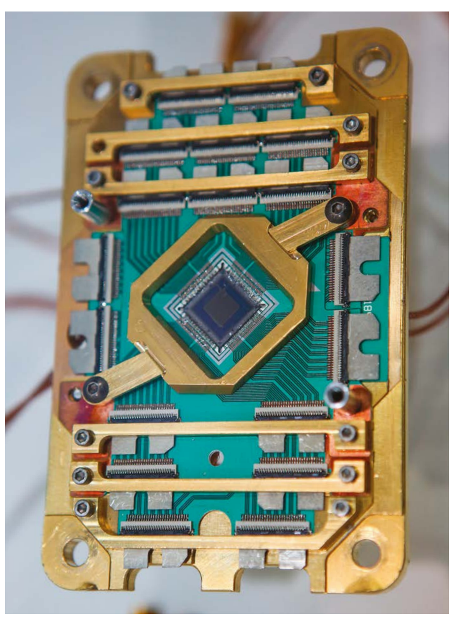

CHRISTIAN LADEMANN/ALAMY

A quantum processor with a 2,048-qubit chip.

Quantum technology already receives massive governmental support in a number of countries, including China, the United States and Germany. The European Union's €1-billion (US$1.1-billion) Quantum Flagship programme, first announced in 2016, is expected to produce technology-demonstration projects, such as a quantum processor on a silicon chip, within a few years.

US technology companies are also racing to create quantum computers that outperform classical machines in specific tasks. Prototypes developed by Google and IBM, for example, are becoming as capable as classical computers. In October, scientists at Google announced that a quantum processor working on a specific calculation had achieved such a quantum advantage. Russia is "five to ten years behind" other countries, says Fedorov. "But there's a lot of potential here."

Poor funding has excluded Russian quantum scientists from competing with Google, says Ilya Besedin, an engineer at the National University of Science and Technology in Moscow. The national quantum initiative might help to turn this around, he says.

"No one is close to the quantum-computing capacity that would be required for practical applications," says Besedin. "We're all looking for new avenues to explore. With serious government support, this is going to become a very interesting research opportunity."

Home-grown qubits

The initiative comes as quantum science in Russia begins to recover from the departure, in the 1990s and 2000s, of top researchers who left for better salaries and funding opportunities. Several Russian quantum physicists working abroad are on the RQC's international advisory board. Others, including Alexey Ustinov, a condensed-matter physicist at the Karlsruhe Institute of Technology in Germany, have received grants from the Russian government to set up research groups in Russia.

And scientists in Russia are already developing their own approaches to building large-scale quantum computers, says Ustinov. "The initiative is a promising start to increase the level of quantum research in Russia," he says. "We will see where this will lead."

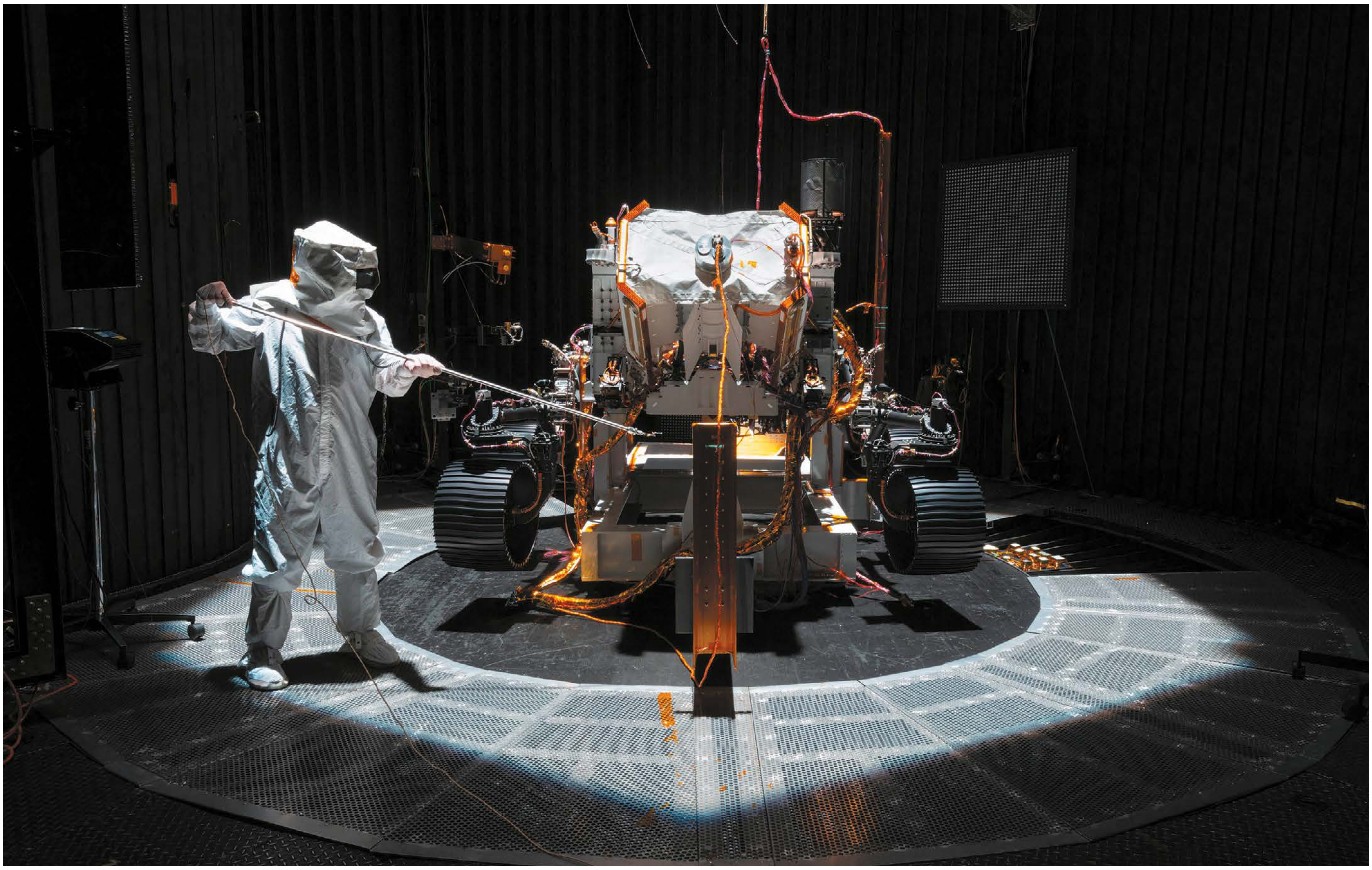

NASA/JPL-CALTECH

NASA's Mars 2020 mission will feature a detachable helicopter drone, and is just one of several missions to the red planet in the coming year.

THE SCIENCE EVENTS TO WATCH FOR IN 2020

A Mars invasion, a climate meeting and human–animal hybrids are set to shape the research agenda.

Compiled by Davide Castelvecchi

Mars attack

2020 will see a veritable Mars invasion as several spacecraft, including three landers, head to the red planet. NASA will launch its Mars 2020 rover, which will stash rock samples that will be returned to Earth in a future mission and will also feature a small, detachable helicopter drone. China will send its first lander to Mars, Huoxing-1, which will deploy a small rover. A Russian spacecraft will deliver a European Space Agency (ESA) rover to the red planet – if issues with the landing parachute can be resolved. And the United Arab Emirates will send an orbiter, in the first Mars mission by an Arab country.

Closer to home, China is planning to send the Chang'e-5 sample-return mission to the Moon. And elsewhere in the Solar System, Japan's Hayabusa2 mission is due to return samples of the asteroid Ryugu to Earth, and NASA's OSIRIS-REx will bite off a chunk of its own asteroid, Bennu.

Big sky, big data

Following the media splash made by its image of supermassive black hole at the centre of the galaxy Messier 87 in 2019, the Event Horizon Telescope collaboration expects to release new results, this time about the black hole at the Milky Way's centre. This could include multiple images and perhaps even a movie of gas swirling around the behemoth, which is called Sagittarius A*.

Later in the year, ESA's Gaia mission will update its 3D map of the Milky Way, which has markedly changed how scientists understand the Galaxy's structure and evolution. And gravitational-wave astronomers will unveil the troves of cosmic collisions they observed in 2019 that created ripples in space-time. These include many mergers of black holes but also previously unseen collisions of a black hole and a star.

Mega-collider dreams

CERN hopes to secure funding for a future mega-collider this year. The European particle-physics laboratory near Geneva, Switzerland, will hold a special meeting of its council in Budapest in May, where a committee will decide on the plans as part of an update to the lab's European Strategy for Particle Physics. CERN's proposal includes a menu of options for a future collider. The lab hopes to build a 100-kilometre machine that could be up to six times as powerful as the Large Hadron Collider and cost up to €21 billion (US$23.4 billion).

In the United States, the Fermi National Accelerator Laboratory near Chicago, Illinois, should unveil long-awaited results from Muon g–2, a high-precision measurement of how muons – more-massive siblings of electrons – behave in a magnetic field. Physicists hope that slight anomalies could reveal previously unknown elementary particles.

Climate homework due

In August, the United Nations Environment Programme will release a major report on the scientific and technical aspects of geo-engineering – approaches that could be used to fight climate change. These include

Mosquitoes are being infected with bacteria that prevent them from spreading diseases.

APU GOMES/AFP/GETTY

pulling carbon dioxide out of the atmosphere and blocking sunlight. Also in 2020, the International Seabed Authority is due to issue long-awaited regulations that will enable mining of the bottom of the sea. Scientists worry that not enough is known about how the practice could damage marine ecosystems, with potentially disastrous impacts on already stressed environments.

But the big event on climate will come in November, when the COP26 climate conference — a moment of truth for the Paris agreement — kicks off in Glasgow, UK. Under the 2015 accord, countries must come forward with updated targets for reducing their greenhouse-gas emissions to help limit global warming to no more than 2 °C. But most countries have been slow to act on their promises. And the future of the treaty itself hangs in the balance: the United States is expected to formally drop out that month.

US election climax

The White House and the US Congress are up for grabs in November, and the outcome could have big implications for science, in particular the climate. A second term in office would allow President Donald Trump to continue unravelling his predecessor's climate policies — and all but ensure the United States' formal exit from the Paris agreement a day after the election. Democrats could stymie those efforts by winning the White House or gaining a majority in both houses of Congress. All 435 seats in the House of Representatives and 35 of the Senate's 100 seats are being contested.

'Humice' are coming

The dream of growing replacement organs for humans in other animals could get closer as researchers make strides in the ethically fraught technique. Stem-cell scientist Hiromitsu Nakauchi at the University of Tokyo plans to grow tissue made of human cells in mouse and rat embryos. He will then transplant those hybrid embryos into surrogate animals, a step that wasn't allowed until a new law in Japan came into effect last March. Nakauchi and collaborators have also applied to do a similar experiment using pig embryos. The ultimate goal of such research is to produce animals with organs that can, eventually, be transplanted into people. But some researchers think it will be safer and more effective to grow 'organoids' in the lab.

Pressure to perform

Physicists hope to achieve their dream of creating a material that conducts electricity with no resistance at room temperature — although, for now, such superconducting materials work only at pressures of millions of kilopascals. Following the success of compounds known as lanthanum 'superhydrides', which in 2018 broke all temperature records for superconductivity, researchers hope to synthesize yttrium superhydrides that could be superconducting at temperatures of up to 53 °C.

Mozzie counter-attack

In the Indonesian city of Yogyakarta, a major test of a technique that could halt the spread of dengue fever will reach its conclusion. Researchers have released mosquitoes carrying *Wolbachia* bacteria — which inhibit the replication of mosquito-borne viruses that cause dengue, chikungunya and Zika — and let the infection spread in the wild population. Smaller tests in Indonesia, Vietnam and Brazil have shown tantalizing promise.

Also promising is a malaria vaccine that is due to be trialled on Equatorial Guinea's island of Bioko. And in 2020, the World Health Organization hopes to eliminate sleeping sickness, or African trypanosomiasis, as a public health problem. This notorious disease is carried by tsetse flies (*Glossina* spp.).

Solid energy

Companies large and small plan to start selling solar cells that use perovskites, promising materials that could be cheaper and easier to produce than the silicon crystals used in conventional solar panels. When paired with silicon in 'tandem' cells, perovskites could yield the most efficient solar panels on the market.

The energy sector could achieve another milestone during the Tokyo Olympic Games in July, when Toyota is expected to unveil the first prototype of a car powered by 'solid-state' lithium-ion batteries. These replace the liquid that separates the electrodes inside the battery with a solid material, increasing the amount of energy that can be stored. Solid-electrolyte batteries last longer, but they tend to charge more slowly.

Synthetic yeast

An ambitious effort by synthetic biologists to rebuild baker's yeast (*Saccharomyces cerevisiae*) is due to reach completion in 2020. Researchers have entirely replaced the genetic code of much simpler organisms before — for example, the bacterium *Mycoplasma mycoides* — but doing this in yeast cells is much more challenging because of their complexity. The effort, called Synthetic Yeast 2.0, is a collaboration between 15 laboratories on 4 continents. Teams have replaced the DNA in each of the 16 chromosomes of *S. cerevisiae* piecemeal with synthetic versions. They have also experimented with reorganizing and editing the genome — or deleting chunks of it — to understand how the organism evolved and how it copes with mutations. Researchers hope that engineered yeast cells will unleash more-efficient and -flexible ways to manufacture a host of products, from biofuels to medicines.

Scientists are brewing up synthetic yeast.

EYE OF SCIENCE/SPL

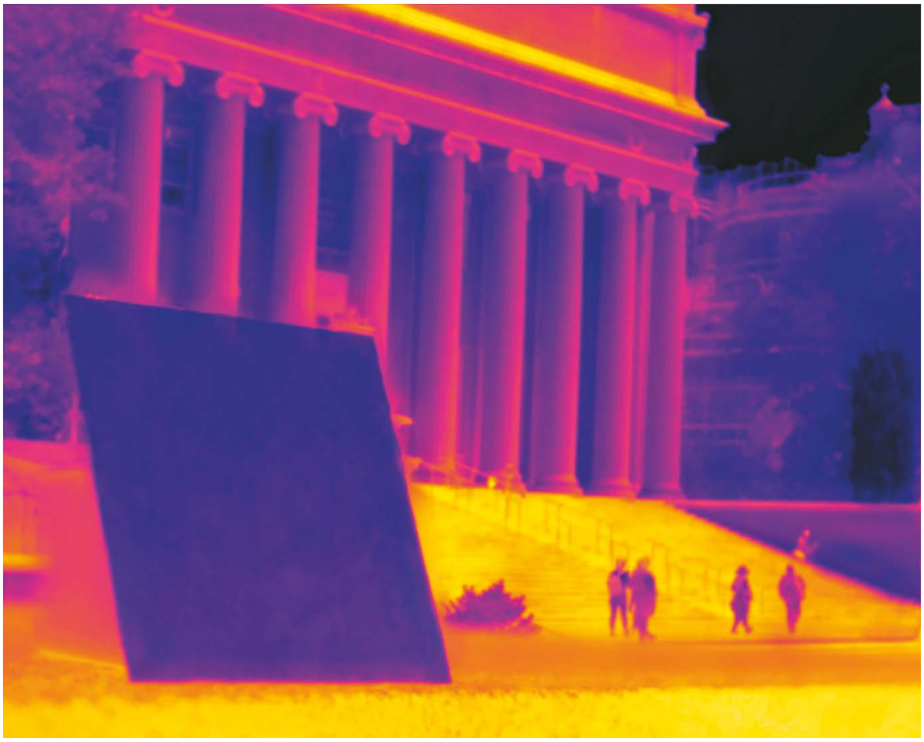

A thermal image of a panel with a 'super-cool' coating outside Columbia University in New York City.

JYOTIRMOY MANDAL

THE SUPER-COOL MATERIALS THAT SEND HEAT TO SPACE

Paints, plastics and even wood can be engineered to stay cool in direct sunlight – but their role in displacing power-hungry air conditioners remains unclear. **By XiaoZhi Lim**

When businessman Howard Bisla was tasked with saving a local shop from financial ruin, one of his first concerns was energy efficiency. In June 2018, he approached his local electricity provider in Sacramento, California, about upgrading the lights. The provider had another idea. It offered to install an experimental cooling system: panels that could stay colder than their surroundings, even under the blazing hot sun, without consuming energy.

The aluminium-backed panels now sit on the shop's roof, their mirrored surfaces coated with a thin cooling film and angled to the sky. They cool liquid in pipes underneath that run into the shop, and, together with new lights, have reduced electricity bills by around 15%. "Even on a hot day, they're not hot," Bisla says.

The panels emerged from a discovery at Stanford University in California. In 2014, researchers there announced that they had created a material that stayed colder than its surroundings in direct sunlight[1]. Two members of the team, Shanhui Fan and Aaswath Raman, with colleague Eli Goldstein, founded a start-up firm, SkyCool Systems, and supplied Bisla's panels. Since then, they and other researchers have made a host of materials, including films, spray paints and treated wood, that stay cool in the heat.

These materials all rely on enhancing a natural heat-shedding effect known as passive radiative cooling. Every person, building and object on Earth radiates heat, but the planet's blanket-like atmosphere absorbs most of it and radiates it back. Infrared rays between 8 and 13 micrometres in wavelength, however, are not captured by the atmosphere and leave Earth, escaping into cold outer space. As far back as the 1960s, scientists sought to harness this phenomenon for practical use. But passive radiative cooling is noticeable only at night: in the daytime, sunlight bathes us in much more heat energy than we can send into space.

The new materials reflect a broad spectrum of light, in much the same way as mirrors or white paint do. In the crucial 8–13-μm part of the infrared spectrum, however, they strongly absorb and then emit radiation. When the materials point at the sky, the infrared rays can pass straight through the atmosphere and into space. That effectively links the materials to an inexhaustible heat sink, into which they can keep dumping heat without it coming back. As a result, they can radiate away enough heat to consistently stay a few degrees cooler than surrounding air; research suggests that temperature differences could exceed 10 °C in hot, dry places[2,3]. David Sailor, who leads the Urban Climate Research Center at Arizona State University in Tempe, has termed them super-cool materials.

These materials might not only save on electricity bills, say enthusiasts, but also reduce a surge in demand for power-hungry refrigeration and air conditioning as the world warms. "My belief is that in four to five years, daytime radiative cooling systems will be the number one technology for buildings," says Mattheos Santamouris at the University of New South Wales in Sydney, Australia, who himself is working to improve such materials. "It is the air conditioner of the future."

A few researchers have even suggested that the materials might be considered as part of a geoengineering strategy, to help Earth shed heat to counteract global rising temperatures. "Rather than try to block the incoming heat from the Sun, can we just make Earth emit more?" asks Jeremy Munday, a physicist at the University of California, Davis.

But many scientists are cautious about these ideas. So far, theoretical estimates of how much electrical power can be saved have been based on data from small samples tested over short times. There are also doubts about the materials' ability to work in a wide variety of climates and places. The cooling effect works best in dry climates and with clear skies; when it's cloudy or humid, water vapour traps the infrared radiation. And the super-cool materials might not last in all weathers or fit easily to all buildings.

Another unknown is whether consumers will embrace the idea. Even the simple measure of replacing worn-out roofs with reflective

white ones to cool houses has not been widely adopted by homeowners, says Sailor. His modelling work, however, suggests that use of a super-cool paint might double the energy savings compared with a white roof. "It's a bit of a game-changer — potentially," he says.

Overcoming the Sun

In 2012, Raman — who was completing his PhD with Fan on materials for harvesting solar energy — stumbled on old studies about passive radiative cooling, an effect he'd not heard of. Realizing that no one had worked out how to use it under direct sunlight, he examined the optical properties a material would need to overcome the Sun's heat. It must reflect the solar spectrum in wavelengths from 200 nanometres to 2.5 µm even more effectively than white paint, which is already up to 94% reflective. And it must absorb and emit as close as possible to 100% of the wavelengths in the crucial 8–13-µm range (see 'Keeping their cool').

All this could be done by engineering materials at the nanoscale, Raman and Fan thought. Creating structures smaller than the wavelengths of light that will pass through them should enhance the absorption and emission of some wavelengths and suppress that of others.

The group came up with the idea to etch patterns into surfaces[4] and published it in 2013. Then the team submitted a proposal to the US Advanced Research Projects Agency–Energy (ARPA-E) for funding to make it.

"I immediately thought, 'Wow, I'd really like to see somebody actually do this,'" recalls Howard Branz, then a programme director at ARPA-E in Washington DC, and now a technology consultant in Boulder, Colorado. "There'd been a lot of night-time radiative-cooling work, but to do it under broad, full sunlight is quite startling."

Branz gave the researchers US$400,000 and a year. With so little time, the Stanford team decided to simplify the design and try layering materials in more familiar ways. To create something highly reflective, the researchers alternated four thin layers of materials that refract light strongly (hafnium dioxide) and weakly (silicon dioxide, or glass), a commonly used motif in optical engineering that works because of how light waves interfere as they pass through different layers. They used the same principle to amplify infrared emissions, depositing three thicker layers of the same materials on top.

When they tested their material outdoors[1], it stayed almost 5 °C cooler than the ambient temperature, even under direct sunlight of around 850 watts per square metre. (On a bright, clear day at sea level, the intensity of sunlight directly overhead reaches around 1,000 Wm^{-2}).

After that success, ARPA-E funded other proposals for super-cool materials. Among these was an idea from Xiaobo Yin and Ronggui

KEEPING THEIR COOL

'Super-cool' materials stay colder than their surroundings even in direct sunlight, by emitting heat that can pass through the atmosphere and into space.

Transparent atmosphere

Earth's blanket-like atmosphere absorbs most infrared wavelengths but is transparent to those between 8 and 13 micrometres.

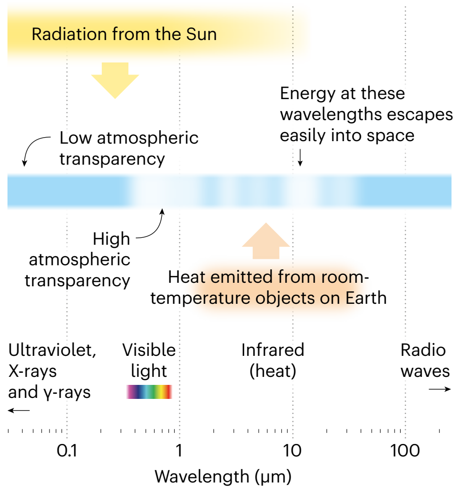

Reflect and emit

Super-cool materials are extremely reflective (even more so than white paint), so they are relatively unaffected by sunlight. They also absorb wavelengths between 8 and 13 µm, then emit them into space.

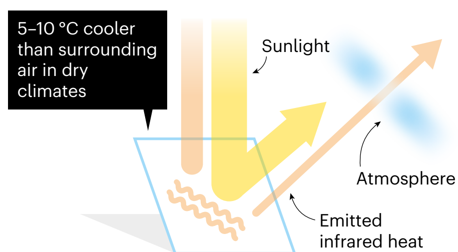

Yang at the University of Colorado Boulder, who wanted to make materials at large scale. They chose to work with cheap plastic and glass. Glass spheres of the right size — a few micrometres across — emit strongly in the 8–13-µm range. Embedding these in a 50-µm-thick film of transparent polymethylpentene — a plastic used in some lab equipment and cookware — and backing this with reflective silver was sufficient to create a super-cool material[5]. More importantly, the researchers could make the film with roll-to-roll technology that churns out 5 metres per minute.

It turned out that many materials exhibit super-cooling if structured in the right way — not just exotic or speciality ones. In 2018, researchers at Columbia University in New York City and Argonne National Laboratory in Lemont, Illinois, reported a super-cool paint, based on a sprayable polymer coating[6]. Many polymers naturally emit in the infrared 8–13-µm range because their chemical bonds, such as those between carbon atoms or between carbon and fluorine, eject packets of infrared light when they stretch and relax, explains team member Yuan Yang. The key was to strengthen the polymers' ability to reflect sunlight.

Yang's student Jyotirmoy Mandal — who is now a postdoctoral researcher in Raman's lab at the University of California, Los Angeles — dissolved fluorinated polymer precursors in acetone with a small amount of water. This mixture can be sprayed onto a surface to create an even polymer coating with tiny water droplets dispersed through it. The volatile acetone dries first, followed by the water droplets, leaving behind pores that fill with air. The overall result is a white coating with pores inside that reflect the sunlight, Yang says.

Last May, the Colorado team reported another material: a cooling wood, created with Liangbing Hu and Tian Li at the University of Maryland, College Park. Just like polymers, wood contains chemical bonds that emit the right kind of infrared radiation, says Li. A net cooling effect can be achieved by chemically removing a rigid component called lignin to make the wood reflective and compressing the product to align its cellulose fibres and amplify infrared emissions[7].

Scientists have also made super-cool thin films from polydimethylsiloxane (PDMS), a silicone material found in products such as lubricants, hair conditioners and Silly Putty, by spraying it onto a reflective backing. As recently as last August, Zongfu Yu at the University of Wisconsin–Madison and Qiaoqiang Gan at the State University of New York at Buffalo found that an aluminium film spray-coated with a 100-µm layer of PDMS stayed 11 °C cooler than ambient air when placed in a campus car park in the middle of the day[2].

Staying cool

Almost all the research teams have patented their inventions and are now trying to market them. Gan is working with industry partners, which he declined to name, to commercialize the PDMS–aluminium film. Columbia University has licensed its super-cool paint to New York start-up MetaRE, founded by Mandal and Yang's Columbia collaborator Nanfang Yu, for development. MetaRE is also working with industry to develop the paint for roofing, refrigerated transportation, storage and textile applications, says chief executive April Tian. The product is "highly competitive" with conventional paints, she says.

Other start-ups have highlighted how much electricity their products could save. Fan and Raman have developed a proprietary system for SkyCool Systems' panels. In 2017, they predicted that the system could reduce the amount of electricity a building uses for cooling by 21% during the summer in hot, dry Las Vegas, Nevada[8]. Raman says the panels will pay for themselves in three to five years. Yin and Ronggui Yang have started a company in Boulder called Radi-Cool, to commercialize the glass-embedded plastic. Last January, they reported that the material could reduce

ELECTRICITY AT NIGHT, WATER IN THE DAY

Super-cool materials have added benefits.

Materials that dump heat from Earth into space could have unexpected applications. They could, for instance, make it easier to harvest water from the atmosphere in the daytime. At night, water vapour condenses into dew on surfaces that lose heat to the clear night sky, an effect harnessed for centuries to capture water. Zongfu Yu at the University of Wisconsin–Madison and Qiaoqiang Gan at the State University of New York at Buffalo found that an aluminium film coated in polydimethylsiloxane could not only stay cool, but also enhance water condensation during the day[12]. The pair started a company in Buffalo called Sunny Clean Water to commercialize the device.

The temperature difference between a super-cool material and its surroundings could also be used to generate electricity at night — unlike solar panels, which work only in the day. Last September, Aaswath Raman, Shanhui Fan and Wei Li at Stanford University in California managed to produce a trickle of electricity — milliwatts per square metre — from such a nocturnal device[13]. That shows it's possible to make at least enough electricity at night to power a small LED. That's an exciting proof of concept, says Howard Branz, a technology consultant in Boulder, Colorado. But electricity from solar panels can be stored in batteries to generate much larger flows of electricity, so it's not yet clear whether the idea will be useful.

AASWATH PATTABHI RAMAN

Super-cool panels on the roof of a shop in Sacramento, California.

electricity consumption for cooling in the summer by 32–45% if it were integrated with water chillers in commercial buildings in Phoenix, Arizona; Miami, Florida; and Houston, Texas[9]. Hu, meanwhile, has licensed the super-cool wood material to a Maryland-based firm he co-founded called InventWood. He predicts that it could save 20–35% of cooling energy across 16 US cities[7].

But these estimates are based on experiments and models that are too limited to be extrapolated to whole buildings in cities, cautions Diana Ürge-Vorsatz, an environmental scientist at the Central European University in Budapest who specializes in climate-change mitigation. Actual energy savings and how quickly a super-cool material will pay for itself will depend on a building's structure, location and weather conditions, adds Yin.

Location is the biggest obstacle. "There are certain geographical regions where it just won't work because the atmosphere isn't dry enough," says James Klausner, a mechanical engineer at Michigan State University in East Lansing who served as an ARPA-E programme director after Branz and has funded some proposals in the field. But that's not too off-putting, he says, because the regions where the effect works well are arid areas such as the southwestern United States or the Middle East, which have high demands for air conditioning.

Another challenge is that radiative-cooling systems might increase heating costs in winter. To address this problem, Santamouris is trying to introduce a liquid layer on top of the super-cool materials that would freeze when the temperature drops low enough. Once the liquid solidifies, radiation can no longer escape to space, so the cooling effect is cut off. And last October, Mandal and Yang reported another way to stop overcooling[10]. If they fill the pores of their polymer coating with isopropanol, the coating starts to trap heat rather than shed it. This can be reversed by blowing air through the pores to dry them out.

There's another issue: the materials achieve super-cooling only if they can send their radiation directly to the cold heat sink of outer space. In an urban setting, buildings, people and other objects can get in the way, absorbing the heat and re-emitting it. The best-performing materials currently remove heat at a rate of around 100 $\mathrm{W\,m^{-2}}$. Gan and Yu hope to double that by positioning their films perpendicular to the roof so that emissions can escape from both surfaces. But this will require adding materials around the films that can reflect the emissions up into the sky.

Researchers are looking at other ways to increase the materials' cooling ability. Last October, Evelyn Wang at the Massachusetts Institute of Technology in Cambridge and her colleagues reported that covering a radiative-cooling film with a light, insulating aerogel kept the structure 13 °C cooler than its surroundings at noon in the dry Atacama Desert in Chile, compared with just 1.7 °C without the aerogel[3]. The aerogel concept could be used with other super-cool materials, she says.

Dreams of using the super-cool materials for geoengineering to mitigate global warming seem further off, and unlikely from a practical perspective. Last September, Munday used "back-of-the-envelope calculations" to suggest that current rising temperatures could be balanced by covering 1–2% of Earth's surface with existing materials that generate around 100 $\mathrm{W\,m^{-2}}$ of cooling power in the daytime[11]. But because solar panels still don't reach that level of cover after decades of development, it seems impossible that this nascent technology could do so in time to be useful, says Mark Lawrence, a climate scientist at the Institute for Advanced Sustainability Studies in Potsdam, Germany. As with any geoengineering proposal, Munday acknowledges the possible unintended consequences of disturbing precipitation patterns and local climates – which Ürge-Vorsatz agrees are likely to be a problem.

Still, passive radiative cooling might have many benefits, says Raman (see 'Electricity at night, water in the day'). It could, for instance help to stop solar panels losing efficiency as the temperature rises. And all electricity generation and conversion processes produce waste heat, says Yin, even if they use renewable energy rather than fossil fuels. "This is the only technology that harnesses all this wasted heat and dumps it back to space," he says.

XiaoZhi Lim is a freelance writer in Natick, Massachusetts.

1. Raman, A. P., Anoma, M. A., Zhu, L., Rephaeli, E. & Fan, S. *Nature* **515**, 540–544 (2014).
2. Zhou, L. *et al. Nature Sustain.* **2**, 718–724 (2019).
3. Leroy, A. *et al. Sci. Adv.* **5**, eaat9480 (2019).
4. Rephaeli, E., Raman, A. & Fan, S. *Nano Lett.* **13**, 1457–1461 (2013).
5. Zhai, Y. *et al. Science* **355**, 1062–1066 (2017).
6. Mandal, J. *et al. Science* **362**, 315–319 (2018).
7. Li, T. *et al. Science* **364**, 760–763 (2019).
8. Goldstein, E. A., Raman, A. P. & Fan, S. *Nature Energy* **2**, 17143 (2017).
9. Zhao, D. *et al. Joule* **3**, 111–123 (2019).
10. Mandal, J. *et al. Joule* https://doi.org/10.1016/j.joule.2019.09.016 (2019).
11. Munday, J. N. *Joule* **3**, 2057–2060 (2019).
12. Zhou, M. *et al.* Preprint at https://arxiv.org/abs/1804.10736 (2018).
13. Raman, A. P., Li, W. & Fan, S. *Joule* **3**, 2679–2686 (2019).

2020 in science & culture

The new uncanny valley, climate on film, imperilled elephants and Earth Day at 50: what's coming this year. **By Nicola Jones**

Ecovisionaries
Royal Academy of Arts, London.
Until 23 February.

Sustainability demands creative thinking. At the Royal Academy, architects, artists and designers are collectively reimagining our relationship with nature amid challenges ranging from climate change to species extinction. New commissioned works include *The Substitute* by Alexandra Daisy Ginsberg. This life-size digital reproduction of the critically endangered northern white rhinoceros (*Ceratotherium simum cottoni*) was made using film footage enhanced by data from artificial-intelligence company DeepMind. Older works explore endangered fish in Africa's Lake Victoria (Tue Greenfort's 2017 *Tilapia*) and mining lithium for batteries in the Atacama Desert (research studio Unknown Fields' *In The Breast Milk of the Volcano*, 2016–18; **pictured**).

Troy: Myth and Reality
British Museum, London.
Until 8 March.

The ancient city of Troy has many faces. There is the legendary, war-torn Troy of Homer's epic *Iliad* and *Odyssey*. And there are the Troys uncovered by archaeology in modern-day Turkey: a 'layer cake' of sites spanning 3000 BC to AD 500. This blockbuster exhibition covers both, and includes artefacts stretching back three millennia, from Athenian pottery (detail **pictured**) to Roman sculpture. Evidence suggests that a battle between the Hittite empire and Greece (which they called Ahhiyawa) might have been the real Trojan War.

Origins: Fossils from the Cradle of Humankind
Perot Museum of Nature and Science, Dallas, Texas.
Until 22 March.

Hominin fossils rarely leave their countries of origin. Now, two South African skeletons from recently discovered branches of the hominin family tree are on display in the United States: Karabo (*Australopithecus sediba*) and Neo (*Homo naledi*). Both are from digs led by palaeoanthropologist Lee Berger. Researchers will attempt to 3D-print missing parts of Karabo's skeleton, using scans of rocks from the discovery site.

People keen to learn more about hominin history can look to the Iziko South African Museum in Cape Town, where the Origins of Early Sapiens Behaviour Exhibition has been expanded.

Sahel: Art and Empires on the Shores of the Sahara
The Metropolitan Museum of Art, New York City.
30 January – 10 May.

Africa's Sahel (Arabic for 'shore') is a vast semi-arid band spanning Senegal, Mali, Mauretania and Niger. This culturally rich region, now plagued by war and desertification, has a

Earth Day 50th Anniversary
22 April

L TO R: UNKNOWN FIELDS; THE TRUSTEES OF THE BRITISH MUSEUM; MARIO TAMA/GETTY; FINE ARTS MUSEUMS OF SAN FRANCISCO

nature.com For the latest reviews of books and art events published by *Nature*, visit: go.nature.com/2se869n

In 1970, some 20 million people across the United States joined the first Earth Day to protest against the constellation of problems plaguing the planet, from toxic dumping to extinctions. This year, the Earth Day Network is launching a series of events to kick anniversary protests into high gear, including a citizen-science mobile app and a registry of Earth-inspired art, theatre, dance and film. See go.nature.com/36xxi1e for more.

fascinating history. A succession of influential kingdoms held sway here, from the empire of Ghana (AD 300–1200) to that of Segu (1640–1861). This show is the culmination of a four-year partnership with academics from Yale University in New Haven, Connecticut, Dakar's Fundamental Institute of Black Africa and elsewhere. Featured are manuscripts, textiles and sculptures ranging from a 3-tonne eighth-century Senegalese megalith in the form of a lyre to a 7-centimetre statue of a female torso more than 4,000 years old.

As the Met celebrates its 150th birthday in 2020, look out for other shows, from Making Marvels: Science and Splendor at the Courts of Europe (until 1 March) to Cubism and the Trompe l'Oeil Tradition (24 November 2020 to 28 February 2021).

Countryside: Future of the World

Guggenheim Museum, New York City.
20 February – Summer.

Cities house more than half of humanity, but cover less than 3% of Earth's non-icy lands. Here, architect and urbanist Rem Koolhaas turns to the rural. The show will examine artificial intelligence and automation, the effects of genetic experiments, political radicalization, migration, large-scale territorial management, human–animal ecosystems and the impact of the digital.

Neri Oxman: Material Ecology

Museum of Modern Art,
New York City.
22 February – 25 May.

Can useful structures be grown rather than built? So asks Neri Oxman, a medically trained architect who directs the Mediated Matter group at the Massachusetts Institute of Technology (MIT) Media Lab in Cambridge — a facility renowned for fomenting academic creativity at the intersection of art and science. This show will feature 8 major projects from Oxman's 20-year career in 'material ecology': the realm of biologically inspired or created products. *Silk Pavilion* (2013) used thousands of silkworms to spin a dome in an MIT building; *Ocean Pavilion* (2014) built structures out of chitosan, a polymer found in crustacean shells.

Uncanny Valley: Being Human in the Age of AI

de Young Museum,
San Francisco, California.
22 February – 25 October.

In 1970, Japanese engineer Masahiro Mori noted that lifelike androids occupy an 'uncanny valley' — a realm between non-human and fully human that evokes discomfort, even revulsion. This exhibition, a few dozen kilometres from Silicon Valley, explores modern denizens of this uncanny realm. A statue in the museum garden has an active beehive for a head (an allusion to the complex workings of a neural network; **pictured**); termite mounds symbolize the minions of the crowdsourced marketplace; abandoned patents are 3D-printed to bring them to life. The biases and pitfalls of artificial-intelligence algorithms are thrown into stark relief by a host of art and film projects.

CLIMATE CHANGE ON SHOW

Stage and screen events highlighting a climate crisis.

Climate Speaks 2020
Climate Museum, New York City.
January — June.
The first US museum dedicated to the climate emergency is hosting its second spoken-word programme for teenagers. Successful applicants will spend six months exploring links between climate change, social justice and the arts, leading to a May performance (**pictured**, one of last year's participants).

Last Catastrophist
Boston Center for the Arts, Massachusetts.
24 January – 8 February.
In this dystopian science-fiction play by David Valdes, climatologists Marina and Lucia are holed up in Iceland, hiding from the threats of anti-climate-science cabal Eternal Sunshine.

The Flight of the Hummingbird
Touring schools in British Columbia, Canada.
January – May.
Based on a graphic novel by Indigenous Haida artist Michael Nicoll Yahgulanaas, this opera brings issues of climate change, social justice and personal responsibility to an audience aged 5 to 15.

Billie Eilish Eco-Village
March – July.
Alternative singer-songwriter Billie Eilish has partnered with sustainability-focused non-profit organization Reverb to 'green' her 2020 world tour. Venues from Miami to London will host 'eco-villages' where fans can learn about climate change.

Greta vs Climate
Director Nathan Grossman is planning a documentary on pioneering teenage activist Greta Thunberg — who founded the Friday student climate strikes that have swept the globe.

Serpentine Galleries 50th Anniversary

The Serpentine Gallery, London.
4 March – 17 May.

The Serpentine Galleries will celebrate its 50th anniversary with events on issues from sustainability to new technologies, guided by curator of ecology Lucia Pietroiusti. Two shows will spearhead the year. Cao Fei: Blueprints will feature virtual reality and installations alongside the artist's film *Nova* (2019), all examining the urbanization of Beijing's Jiuxianqiao district. And Amsterdam-based Studio Formafantasma presents Cambio, a project on the ecological legacy of forestry and wood products. A summer exhibition will kick off the multiyear programme Back to Earth, with works to spur action against the climate crisis (see also 'Climate change on show').

Janet Echelman's *1.8*

Renwick Gallery of the Smithsonian American Art Museum, Washington DC.
3 April 2020 – 14 August 2022.

The initial inspiration for Janet Echelman's ephemeral installations were fishing nets on Indian beaches and Lithuanian lace. She scales them up with high-tech materials to create building-sized works that reflect the global impacts of seismicity. Her 2010 work *1.26* – a fibre sculpture sparked by computer simulations of that year's earthquake and tsunami in Chile, which shortened the day by 1.26 microseconds – has been hung between buildings, from Colorado to Singapore. *1.8*, another installation of knotted fibres, was sparked by the catastrophic 2011 earthquake and tsunami in Tohoku, Japan, which cut off 1.8 microseconds.

Hiroshima: 75th Anniversary

6 August.

The Summer Olympic Games in Tokyo will be threaded with memories of the Second World War nuclear attack on Hiroshima

L TO R: SARI GOODFRIEND/THE CLIMATE MUSEUM; JAZZ EDITIONS/GAMMA-RAPHO VIA GETTY; MARK ROGERS/UNIVERSAL PICTURES

75 years earlier (**pictured**, the 9 August Nagasaki attack). The Hiroshima Peace Memorial, for example, will be on the Olympic opening ceremony's torch-relay route. Memorial events will also be held around the world. The Japanese American National Museum in Los Angeles, California, in partnership with Hiroshima and Nagasaki, will display artefacts belonging to victims of the attacks (Under a Mushroom Cloud: Hiroshima, Nagasaki, and the Atomic Bomb, will show until 7 June). And in Hiroshima itself, the annual 6 August Peace Memorial Ceremony will mark the moment with silence, and a procession of thousands of lanterns floating down the Motoyasu River.

Elephants and Us: Considering Extinction

National Museum of American History, Washington DC.
Until 13 September.

From the nineteenth to the mid-twentieth centuries, ivory was a luxury commodity used to produce piano keys, billiard balls, buttons and hair combs. African elephant populations plummeted from more than ten million to fewer than one million. This exhibition tracks US work to stem the trade, starting with the enactment of the African Elephant Conservation Act in 1989. Yet a poaching surge that began in 2006 threatens the bush and forest elephants of Africa: a 2015 count was the first in 25 years to report a decline in elephant numbers.

Turner and the Modern World

Tate Britain, London.
28 October 2020 – 7 March 2021.

Artist J. M. W. Turner was a technophile, famously capturing the Industrial Revolution in paint. Tate Britain celebrates his fascination with machine power in this major exhibition. The show – featuring works from the 1790s to the steam boats and railways of the 1840s – coincides with the showing of finalists for the year's Turner Prize.

SCIENCE FICTION ON FILM

Apocalypses and AIs.

BIOS
US opening 2 October.
Tom Hanks is back. Playing a sickly inventor and the last human left on a post-apocalyptic Earth, he creates a robot to keep him and his dog company, and to protect the dog after he dies. Director Miguel Sapochnik boasts an epic CV, including the *Game of Thrones* episode 'Battle of the Bastards'.

Dune
US opening 18 December.
David Lynch's 1984 adaptation of Frank Herbert's sprawling 1965 cult-classic novel (featuring giant sand worms and battles over a mind-altering drug called the spice) was a box-office failure. Fans are hoping that Denis Villeneuve's version — the first of a planned two-parter — will prove more satisfying.

The Division
Rumoured Netflix release.
On Black Friday, bioterrorists in New York City seed banknotes with a modified strain of smallpox called the Green Poison. Jake Gyllenhaal and Jessica Chastain star in this video-game adaptation directed by David Leitch.

Robocalypse
Rumoured cinematic release.
In the 2011 novel of the same name, artificial intelligence Archos R-14 sets out to preserve life on Earth — by wiping out human civilization. Produced by Steven Spielberg, this long-delayed project might finally come to fruition in 2020 under the direction of Michael Bay.

The Invisible Man
US opening 28 February.
Loosely based on the 1897 novel of the same name by H. G. Wells, this psychological thriller — directed by Leigh Whannell and starring Elisabeth Moss (of *The Handmaid's Tale*) — follows the tribulations of a woman stalked by an invisible ex-boyfriend.

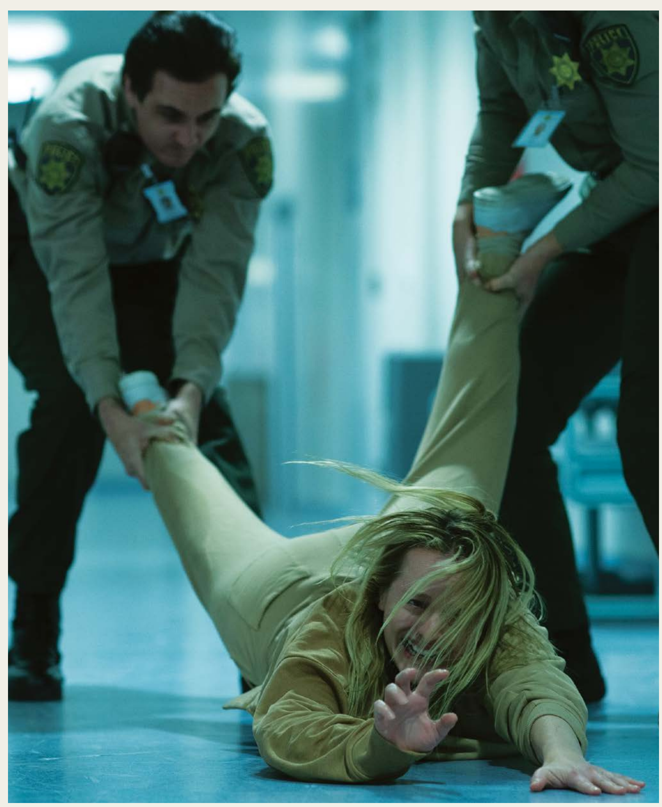

Elisabeth Moss plays Cecilia Kass in *The Invisible Man*.

Comment

ROSLAN RAHMAN/AFP/GETTY

One of five water-reuse plants in Singapore, which together supply about 40% of the nation's water for drinking and other uses.

Drink more recycled wastewater

Cecilia Tortajada and Pierre van Rensburg

There is no room for squeamishness in the face of the world's growing water shortage — three steps could vastly improve the image of reused water for drinking.

Drinkable water is becoming increasingly scarce. Population growth, pollution and climate change mean that more cities are being forced to search for unconventional water sources[1]. In a growing number of places, drinking highly treated municipal wastewater, called 'reused water', has become the best option — and, in some cases, the only one (see 'What is reused water?').

But anxieties about reused water, often heightened by sensational media coverage, have prevented several projects from going ahead. Some people are concerned that reused water will contain more pathogens and chemicals than drinking water sourced from lakes or rivers. Others are simply disgusted by the idea of consuming water that has passed through toilets and drains before being treated.

Around two billion people now live in countries with 'high water scarcity' — mainly in northern Africa and western, central and southern Asia[2]. With the global population predicted to increase from 7.7 billion today to 10 billion in 2050 — an estimated 70% of whom will live in urban areas — the demand for safe drinking water is set to rise drastically.

WHAT IS REUSED WATER?

'Reused' water comes from highly treated wastewater.

In middle- and high-income countries, domestic (municipal) wastewater — from houses, shops and businesses, but not from industries — is generally collected, treated in sewage plants and discharged into rivers, lakes and other natural water bodies. The 'raw water' is then collected, treated again and used by towns and cities downstream for drinking, agriculture, landscape irrigation or industrial processes.

An alternative strategy is to treat municipal wastewater more rigorously so that it can be used for drinking. After it goes through the sewage plant, it is treated in a second plant (and sometimes a third) using advanced chemical, biological and physical treatments. The water is then fed directly into the drinking supply system or into the natural system (rivers, lakes, aquifers or reservoirs). In the latter scenario, water is subsequently extracted from the natural system, treated again and then supplied to people for drinking or other uses. In both cases, the resulting water is termed reused[8].

In many places, discharges of wastewater treated in the usual way (so just once) are making up an increasing proportion of river flow[15]. Yet authorities still consider such rivers 'natural sources of freshwater'. Because downstream treatment methods might not be adapted to the actual quality of the raw water, this is increasingly posing a health risk. Thus, treating wastewater to higher standards in a controlled environment and reusing it for specific purposes can make more sense, for both economic and health reasons. **C.T. & P.v.R.**

According to a 2019 United Nations assessment, water demand in general is likely to increase by 20% to 30% between now and 2050 (ref. 3).

Thus, conserving water is paramount. Supply infrastructure needs to be improved and better managed, including through the use of smart sensors and other technologies. Economic instruments, such as appropriate pricing, can boost efficient usage. Legislation needs to be implemented to lessen pollution. And all sectors – public and private – need to be educated about the importance of saving water, as does society more broadly.

High on the list should be efforts to investigate the benefits and risks of drinking reused water, including ways to make it more acceptable to consumers.

Public perception

Opposition from citizens has stalled several projects aimed at providing people with reused drinking water over the past two decades.

In 2000, the *Los Angeles Daily News* ran an article titled 'Tapping toilet water' about the East Valley Water Recycling project that had begun in the San Fernando Valley in Los Angeles, California, in 1995. People in the region were worried that the water, which they thought would be supplied only to those living in low-income areas, would be unsafe. The project was politicized by mayoral candidates, and the Los Angeles Department of Water and Power, which had proposed the project, eventually decided not to implement it. Since then, the reused water has been used only in irrigation and industry[4].

In Queensland in Australia, residents successfully opposed a reuse project in Toowoomba in 2006 and the Western Corridor Recycled Water Scheme in southeastern Queensland in 2009, even while the country was experiencing the most severe drought since records began.

> **"Reused drinking water is actually subject to stricter regulations, monitoring, assessments and auditing."**

In Toowoomba, 62% of around 95,000 people voted against the project, largely because of safety concerns and fears that it would harm industries including tourism, food processing and property sales[5]. The Western Corridor Recycled Water Scheme cost Aus$2.4 billion (US$1.6 billion) to construct and aimed to produce up to 230,000 cubic metres of water per day to cover around 30% of southeastern Queensland's water supply needs. But in 2009, following political pressure and a break in the drought, it was decided that the scheme would produce drinkable reused water only when the levels of the reservoir (where the reused water would be stored) fell below 40% of full capacity[6].

Public scepticism over water safety is not completely unwarranted. In the United States and Canada, for example, there are still communities that lack access to safe drinking water – predominantly among low-income and minority ethnic populations[7]. In several cases, drinking water has been shown to be unsafe for the population, such as in Flint, Michigan, in 2014, and in several cities in Canada this year. In all of these instances, the water was found to contain higher concentrations of lead than those deemed safe by the regulatory authorities. In October last year, testing revealed that nearly 300 drinking-water wells and other water sources in California contain traces of chemicals known as PFASs (per- and poly-fluoroalkyl substances) that have been linked to certain cancers and other health problems.

Currently, however, reused drinking water is actually subject to stricter regulations, monitoring, assessments and auditing than standard drinking water.

Image enhancement

Three steps would improve the image of reused water.

Do more research. Wastewater contains hundreds of known chemical and pathogenic contaminants that, if not treated properly, can cause serious acute and chronic diseases, such as cholera or typhoid. Also, new chemicals are continually being introduced to the market, and new strains of bacteria and viruses discovered. Investigators at universities and those working for water-utility companies must study, quantify and effectively mitigate any emerging risks, and must keep appraising the overall benefits and costs of reused water on both human and environmental health.

Especially as technologies for detection become more sensitive, more affordable and widely available, the presence of pathogens and chemicals must be continuously monitored (by daily or even more frequent testing[8]) to protect the public from problems that might emerge[9]. Chronic risks from long-term exposure to low levels of toxic chemical substances are just as important to track as acute risks resulting from a one-off exposure[10].

In middle- and high-income countries, drinking water, whether or not it is reused water, must meet national, regional and local health standards (or whichever apply) for pathogens, chemicals and any other types of contaminant[8]. So far, water agencies in cities using reused water have been able to meet these standards – through the use of multiple barrier-treatment steps from chemical to

THREE SUCCESSES

People in Windhoek in Namibia, Orange County in California and Singapore had to start drinking reused water.

Located in an arid to semi-arid environment with little access to surface water sources, Windhoek was the first city to create a drinking-water supply from reused water in 1968. The Goreangab Water Reclamation Plant currently produces around 24% of Windhoek's drinking water (21,000 cubic metres per day)[16]. During the 2014–16 drought, supplies from nearby reservoirs could meet only 10% of demand, instead of the expected 75%. Reused water from Goreangab then contributed up to 30% of the city's total water supply.

Operational since 2008, the Orange County Groundwater Replenishment System has become the largest reuse facility in the world. It produces 379,000 m^3 of drinkable water per day. The project is widely accepted in part because the utility company, the Orange County Water District, prioritized public information and engagement from the start.

Singapore spent decades planning a water reuse scheme now called NEWater. By the time the project was launched in 2003, comprehensive communication and education efforts on long-term safety and reliability issues, involving the government and other decision-makers, had already been established. Today, NEWater supplies about 40% of Singapore's drinkable and non-drinkable water. If all goes to plan, by 2060, it will meet 55% of the city's water demands[17]. Most people in Singapore are aware that their island city state is short of water, being too small to store the rainfall it receives. And they appreciate the importance of NEWater. On each Singapore National Day (9 August), thousands of people who attend the celebrations are given bottles of NEWater, which they drink without qualms. **C.T. & P.v.R.**

microbial, through real-time monitoring of microbes and chemicals, and by using various risk-management strategies throughout treatment and distribution[11,12].

Improve public outreach. Water-utility companies must develop more comprehensive strategies on information dissemination, public consultation, education and engagement.

Community engagement is not – and must never be perceived to be – a means to convince the public that certain projects should go ahead. Rather, it should be about setting up platforms, so that people's concerns can be heard and addressed early on, even if that means modifying plans.

Some successful projects can offer a model. In the 1990s, for instance, the city of San Diego in California planned a water reuse project to reduce its dependence on water transfers from the Colorado River and other sources. The project was initially supported by the public. But that support fell away for various reasons, including inconsistencies in the information provided by expert panels on the safety of recycled wastewater. Following the use of terms in the media such as 'toilet to tap' and 'sewerage beverage', and claims that the reused water would be supplied only to low-income communities, resistance was such that the city council converted the project to a non-drinkable scheme in 1999 (ref. 13).

Yet San Diego still needed more drinking water. So in 2004, the company Public Utilities decided to develop more-comprehensive strategies for public outreach and education. Among the suite of approaches deployed were an online and telephone survey, research involving focus groups, opportunities for city staff to discuss the project with San Diego voluntary service organizations and others, and a dedicated website providing information.

These efforts paid off. In 2004, only 26% of those surveyed approved of water reuse. By 2012, 73% did. The city approved the 'Pure Water San Diego' project in 2013 (ref. 14). It is expected to produce some 114,000 m^3 of drinking water per day by 2023 and to supply one-third of the city's water needs by 2035.

> **"Water-utility companies should start implementing reuse projects in places where the need is greatest."**

Implement projects where need is great. Competent water-utility companies should start implementing reuse projects in places where the need is greatest. They will need to have sufficient knowledge, technical know-how, staffing levels and financial capacity, and be operating in cities where there are strict water-quality regulations. Once such schemes have been proved safe and effective in places where the stakes are high, others will be more likely to support similar projects in their own communities.

Keys to success

The key to these strategies working is the continuous involvement of all stakeholders – from city mayors to national governments, from businesses and local health and medical boards to community and environmental groups, religious leaders and the media.

At least three important economic centres – Singapore, Windhoek in Namibia and Orange County in California – would not have progressed to where they are today without reused drinking water (see 'Three successes'). In fact, without these reuse projects, the strict water rations that were likely to result could have had severe impacts on socio-economic development. Moreover, reused water can benefit streams, rivers, lakes, wetlands and aquifers, in part because the excess water from such projects that is returned to natural systems is of better quality than standard treated wastewater[8].

The authors

Cecilia Tortajada is a senior research fellow at the Institute of Water Policy, Lee Kuan Yew School of Public Policy, National University of Singapore, Singapore. **Pierre van Rensburg** is strategic executive for urban and transport planning at the Department of Urban and Transport Planning, City of Windhoek, Namibia.
e-mails: cecilia.tortajada@nus.edu.sg; pierre.vanrensburg@windhoekcc.org.na

1. World Health Organization. *Potable Reuse: Guidance for Producing Safe Drinking-Water* (WHO, 2017).
2. United Nations. *Sustainable Development Goal 6: Synthesis Report 2018 on Water and Sanitation* (United Nations, 2018).
3. UNESCO. *Leaving No One Behind: The United Nations World Water Development Report 2019* (UNESCO, 2019).
4. US Bureau of Reclamation. *Recycled Water Project Implementation Strategies. Technical Memorandum* (US Department of the Interior & CH2MHILL, 2004).
5. Hurlimann, A. & Dolnicar, S. *Water Res.* **44**, 287–297 (2010).
6. Australian Academy of Technological Sciences and Engineering. *Drinking Water Through Recycling: The Benefits and Costs of Supplying Direct to the Distribution System* (ATSE, 2013).
7. Patel, A. I. & Schmidt, L. A. *Am. J. Public Health* **107**, 1354–1356 (2017).
8. US Environmental Protection Agency & CDM Smith. *2017 Potable Reuse Compendium* [EPA-CDM CRADA 844-15] (EPA, 2017).
9. US Environmental Protection Agency Office of Water. *Draft Framework for a Water Reuse Action Plan* (EPA, 2019).
10. US National Research Council. *Water Reuse: Potential for Expanding the Nation's Water Supply through Reuse of Municipal Wastewater* (National Academy of Sciences, 2012).
11. Water Research Foundation. *Assessment of Techniques to Evaluate and Demonstrate the Safety of Water from Direct Potable Reuse Treatment Facilities* [Web Report #4508] (Water Research Foundation, 2016).
12. WateReuse Research Foundation. *Framework for Direct Potable Reuse* (WateReuse Research Foundation, 2015).
13. Brouwer, S., Maas, T., Smith, H. & Frinjs, J. *D5.2 Trust in Water Reuse: Review Report on International Experiences in Public Involvement and Stakeholder Collaboration* [DEMOWARE Project D5.2] (KWR Watercycle Research Institute, 2015).
14. The City of San Diego. *Report to the City Council* (City of San Diego, 2013).
15. Rice, J., Wutich, A. & Westerhoff, P. *Environ. Sci. Technol.* **47**, 11099–11105 (2013).
16. van Rensburg, P. *Int. J. Water Resour. D.* **32**, 622–636 (2016).
17. Tortajada, C. & Nambiar, S. *Water* **11**, 251 (2019).

Correspondence

Equality drives can silence women

Gender-equality initiatives in academia can have unintended drawbacks (see C. Tzanakou *Nature* **570**, 277; 2019). Counter-intuitively, they can result in the serious under-reporting of sexual harassment in academia, according to the 2019 European Gender Summit at which I chaired a session (see gender-summit.com).

Universities recruiting women academics through gender-equality initiatives search for top-tier talent. Those that receive extra funding for such initiatives do not necessarily look kindly on staff who speak out about harassment or unequal treatment. There are reports of leaders exposing whistle-blowers to retaliation tactics such as intimidation, exclusion and silencing (D. Fernando and A. Prasad *Hum. Relat.* **72**, 1565–1594; 2019).

The research output of whistle-blowers can plunge under such harrowing circumstances. They lose trust in the institutions they worked so hard to become a part of. Moreover, witnesses to such retaliatory practices become reluctant to report harassment.

Universities must embrace complaints if they are to achieve diversity and inclusivity. Otherwise, recruiting top women academics through gender-equality initiatives could become an unintentional search-and-destroy mission.

Susanne Täuber Groningen, the Netherlands.
s.tauber@rug.nl

China's shades of greening

Your view that China's re-vegetation of its deserts could exacerbate water shortages risks oversimplifying an incredibly complex eco-restoration problem (*Nature* **573**, 474–475; 2019).

Far from just planting trees in arid areas, China's re-vegetation codes vary for different regions and greening programmes. The nationwide Grain-to-Green programme, for example, aims to restore unstable and low-productivity farmlands to forest or natural vegetation. In humid areas, research optimizes greening programmes for plant selection and socio-economic benefits. And China's re-vegetation projects are confined to a range that local water resources can sustain.

Re-vegetation, like any eco-restoration strategy, is not a catch-all solution to carbon sequestration, soil erosion and flooding. But, rather than worrying mainly about water consumption, Chinese and other scientists are investigating the nexus of vegetation, soil, water, ecosystems and human society.

Lele Shu University of California at Davis, USA.
llshu@ucdavis.edu

Zexuan Xu Lawrence Berkeley National Laboratory, Berkeley, California, USA.

Earthquakes: heed shocks and patterns

Being able to distinguish foreshocks and aftershocks of earthquakes in real time could be useful for earthquake prediction (see L. Gulia and S. Wiemer *Nature* **574**, 193–199; 2019). For example, the authors claim that — in retrospect — their method could have predicted the biggest such event in the 2016–17 cluster of earthquakes that occurred in the Apennines in central Italy: the magnitude-6.6 earthquake that hit the town of Norcia in October 2016. There were no casualties, yet the death toll from a similar event in the region — the Avezzano earthquake of magnitude 6.7 in January 1915 — was 30,000.

How could this difference be explained? It could be because Italy's Major Risk Committee, of which we were members at the time, found that a large event had a higher probability of occurring than usual, based on the persistence of the earthquake sequence in the region, and recommended putting the entire area under official alert. The committee issued a warning 40 hours ahead of the earthquake to the public, the press and the Civil Protection organization (see go.nature.com/2ecmvwk). As a result, prefects and mayors enforced mass evacuation.

Sergio Bertolucci, Francesco Mulargia University of Bologna, Italy.
francesco.mulargia@unibo.it

Domenico Giardini ETH Zurich, Switzerland.

Testosterone's role in ovulation

As authors of the book reviewed by Randi Epstein (*Testosterone: An Unauthorized Biography*, *Nature* **574**, 474–476; 2019), we wish to clarify two issues.

The first concerns Epstein's assertion that testosterone and its precursor, DHEA, have a role in the maturation of ovarian cells. She suggests that "DHEA might boost fertility directly or as a mediator of oestrogen production". But our reading of the evidence indicates that DHEA's positive effect on fertility is not because it mediates oestrogen production but because it is converted to testosterone. In our book, we describe studies in animal models showing that blocking the conversion of DHEA to oestrogen doesn't reduce DHEA's effects, whereas knocking out androgen receptors creates major fertility problems in females, including premature ovarian failure.

The second issue concerns Epstein's implication that our case for testosterone's role in ovulation rests on interviews with a single clinician. In fact, our conclusions are based on more than a dozen studies in non-human animals, and on a comprehensive analysis of original research and review articles on the use of DHEA or other androgens to boost the response to fertility treatment in women. The interview with the clinician simply served as a 'hook' for the story.

Rebecca Jordan-Young Barnard College, New York, New York, USA.

Katrina Karkazis Yale University, Connecticut, USA.
katrina.karkazis@yale.edu

News & views

Medical research

Tuberculosis vaccine finds an improved route

Samuel M. Behar & Chris Sassetti

A widely used vaccine against tuberculosis has now been shown to provide almost complete protection when injected intravenously. This is a striking improvement over vaccination through the typical intradermal route. **See p.95**

Tuberculosis is the deadliest human infection, killing 1.5 million people in 2018 alone (go.nature.com/2kbuiq). It is widely accepted that an effective vaccine against the bacterium responsible, *Mycobacterium tuberculosis*, would be the most practical way to control the disease. However, the pathogen is often able to resist the immune responses elicited by vaccination. This has raised the question of whether it is possible for a conventional vaccine to confer sterilizing immunity against TB — a gold-standard immune status for vaccines, under which disease is prevented and the pathogen completely eliminated, often before it can even establish a productive infection. On page 95, Darrah *et al.*[1] provide a resounding answer to this question by showing that near-complete protection from TB infection can be conferred using a century-old vaccine, simply by changing its route of administration.

The only currently licensed vaccine against TB is a live strain of the related pathogen *Mycobacterium bovis*, the virulence of which was attenuated in the laboratory between 1908 and 1921. The strain, known as bacille Calmette–Guérin (BCG), has been administered to more than one billion people (go.nature.com/2cxwew6) since then (Fig. 1).

The BCG vaccine is effective against some deadly early-childhood forms of TB. However, its ability to prevent the transmissible pulmonary form, which is the dominant form in adults, has been patchy[2]: it confers protection for some groups of people in some countries, but is generally insufficient to reduce the number of active TB cases in countries where the infection is endemic. Despite these limitations, BCG remains the only TB vaccine to confer protection in large-scale trials[3]. The mechanisms that determine its efficacy are a topic of much interest.

BCG is typically given as an injection into the dermal tissue that lies just beneath the outer layer of the skin. This injection site is convenient and contains specialized cells that stimulate immune responses. However, vaccines that activate immune cells at the site of potential infection can be more effective at destroying invading pathogens. Thus, current immunological thinking suggests that vaccines administered directly into the lung or the upper airways would be better at preventing pulmonary infections, including influenza and TB. Darrah and colleagues therefore investigated whether a different route of BCG administration could improve protection against pulmonary TB.

Darrah *et al.* performed their analysis using rhesus macaques, because TB infection in these monkeys closely mirrors the human disease. They evaluated five vaccination strategies. Animals were given the BCG vaccine in one of the following ways: at the standard dose through the conventional intradermal (i.d.) route; at a higher-than-normal dose intradermally; by means of an aerosol to inoculate the lung; through a combination of the high dose i.d. and inoculation by aerosol; or through an intravenous (i.v.) injection. The authors exposed the macaques to *M. tuberculosis* six months after vaccination, and tracked disease progression to determine how the administration route and dose of the vaccine affected protection against the infection.

Vaccinations given intradermally or by aerosol conferred, at best, modest protection from pulmonary TB. By contrast,

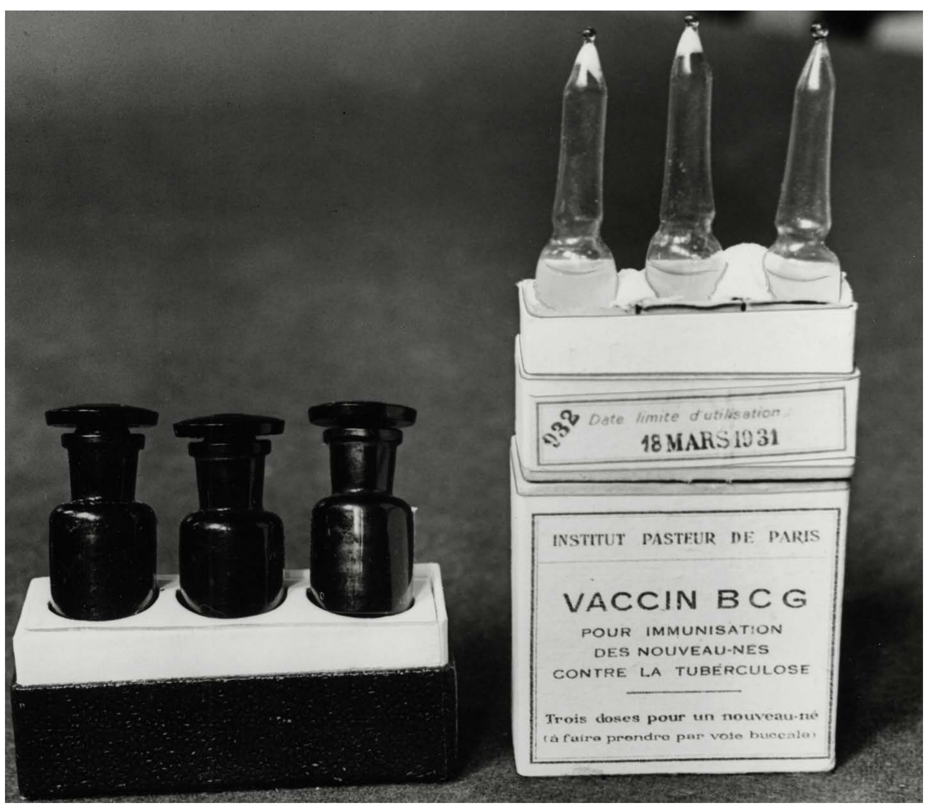

Figure 1 | Ampoules of the BCG vaccine against tuberculosis. This vaccine has been used for almost a century, typically given as an injection just under the skin. Darrah *et al.*[1] now provide evidence in monkeys that the vaccine's efficacy can be greatly improved using intravenous injection.

PALFRED EISENSTAEDT/AP/SHUTTERSTOCK

i.v. vaccination afforded nearly complete protection from the disease. Strikingly, the researchers could not detect any trace of the pathogen in six out of ten animals that received the i.v. vaccination, indicating that the infection had been either prevented or cleared. Three of the other monkeys also showed high levels of protection. Thus, the route of BCG inoculation clearly affects immunity, and the i.v. route confers by far the strongest protection against TB.

What makes i.v. BCG vaccination so effective? Clear immunological correlates of protection (characteristics indicative of immunity against a disease) proved difficult to identify in the current study, because only one of the ten animals that received i.v. BCG was not protected against the infection, making it hard to properly compare protected and unprotected animals. To gain an understanding of the potential underlying mechanism, Darrah and colleagues therefore compared the immune responses of animals vaccinated by the different routes.

Compared with i.d. and aerosol vaccination, i.v. BCG led to a massive influx of immune cells called T cells into the lungs. The increased number of T cells was still apparent six months later, when the animals were exposed to *M. tuberculosis*. It is likely that this expansion occurs because i.v. injection leads to the delivery of a high dose of BCG to the lung – a hypothesis consistent with a recent study[4] showing that direct intrabronchial inoculation of BCG can also protect against *M. tuberculosis*.

The authors next showed that the T cells recognized protein fragments called antigens produced by BCG. Because BCG and *M. tuberculosis* are closely related bacteria, these T cells also recognize *M. tuberculosis* antigens. The T cells that were recruited to the lung were classified as differentiated 'memory' T cells on the basis of their gene-expression profiles, the proteins on their surfaces and their function. These T cells survive long after vaccination, and, because they recognize the antigens produced by *M. tuberculosis*, they can be rapidly activated on infection, producing many 'effector' T cells, which combat the invading pathogen.

Although this circumstantial evidence implicates T cells in immunity against *M. tuberculosis*, the surprising efficacy of i.v. BCG relative to the other vaccine routes (which also elicit T-cell responses) suggests that other mechanisms of immunity are also involved. As Darrah *et al.* propose, these might involve: antibody responses against *M. tuberculosis*; innate immune cells, which are activated indirectly by infection (and do not require specific recognition of *M. tuberculosis* antigens); or innate training, a process by which immune cells such as macrophages gain an enhanced ability to protect, often nonspecifically, against microbes.

Darrah and co-workers' findings raise the obvious possibility of controlling TB by giving people BCG by i.v. injection. In support of this idea, the intervention proved to be safe in the small cohort of rhesus macaques studied. But there is currently a drive to simplify vaccine deployment by eliminating the need for vaccines to be kept cold or for experts to administer them[5] – both of which are crucial for i.v. injection.

Whether or not i.v. BCG is developed for clinical use, research that builds on Darrah and colleagues' work could lead to an improved understanding of what protection against TB looks like – that is, to define correlates of protection. In addition, future work must delineate the mechanisms that lead to sterilizing immunity after i.v. BCG. If successful, it might be possible to develop a vaccine designed to activate the same protective immune mechanisms as those triggered by i.v. BCG, but that could be administered in a way that is safe and adaptable to mass vaccination programmes.

Samuel M. Behar and **Chris Sassetti** are in the Department of Microbiology and Physiological Systems, University of Massachusetts Medical School, Worcester, Massachusetts 01605, USA.
e-mails: samuel.behar@umassmed.edu; christopher.sassetti@umassmed.edu

1. Darrah, P. A. *et al. Nature* **577**, 95–102 (2020).
2. Mangtani, P. *et al. Clin. Infect. Dis.* **58**, 470–480 (2014).
3. Colditz, G. A. *et al. J. Am. Med. Assoc.* **271**, 698–702 (1994).
4. Dijkman, K. *et al. Nature Med.* **25**, 255–262 (2019).
5. Preiss, S., Garçon, N., Cunningham, A. L., Strugnell, R. & Friedland, L. R. *Vaccine* **34**, 6665–6671 (2016).

Microbiology

Food for thought about manipulating gut bacteria

Nathalie M. Delzenne & Laure B. Bindels

Knowing how dietary fibre nourishes gut microorganisms might suggest ways to boost health-promoting bacteria. A method developed to pinpoint bacteria that consume particular types of dietary fibre could advance such efforts.

Certain gut microorganisms can boost human health, but it is unclear how diet could be harnessed to easily manipulate the composition of gut microbes to boost the levels of desired bacteria. Writing in *Cell*, Patnode *et al.*[1] present a useful approach for assessing interactions between human gut microbes and the dietary fibre that sustains their existence.

Dietary fibre is promoted as part of a healthy diet worldwide. Many people, however, do not achieve their recommended fibre intake because they consume insufficient fruit, vegetables and cereals. Inadequate fibre intake is associated with common conditions including obesity, diabetes and cancer[2]. Yet understanding the mechanisms that link fibre-rich food to good health is challenging. Dietary fibre encompasses a wide range of complex molecules, most of which are present in plant cells; among them are carbohydrate molecules called glycans, which are resistant to digestion by human enzymes. As a consequence, some ingested fibre is excreted unchanged in faeces, whereas most is metabolized by gut microbes.

These microbes have a diverse and extremely complex metabolic capacity. Bacteria that express different enzymes for metabolizing fibre can survive and grow using a range of foods. Some bacterial species might compete with each other for the same food source, which could lower the abundance of species that compete less successfully. How might gut microbes be manipulated through human dietary intervention? For example, the concept of using prebiotics – compounds that affect gut microbes, thereby benefiting the human host – has been proposed. One such idea is to use particular fibre sources that provide food for the desired gut microbes[3,4]. However, determining whether dietary fibre can promote health in this way requires a sophisticated understanding of the interactions that occur when the complex community of gut microbes encounters a source of fibre.

Previous work[5] had indicated that transferring the gut microbes of human twins who have contrasting body masses (obese and lean) into mice induced a corresponding difference in the animals' body masses. However, when some of the obese mice were housed with the lean mice, they had less adipose fat than did obese animals that were not co-housed with lean mice – and this weight-loss effect correlated with the transfer of *Bacteroides* bacterial species from the lean mice to the obese mice[5]. High consumption of fibre-rich plant foods was required for this adipose-fat reduction to occur[5]. However, the types of fibre responsible for this effect, and how these interact with specific gut microorganisms, was

https://doi.org/10.1038/d41586-019-03704-z

News & views

Microbiology

Food for thought about manipulating gut bacteria

Nathalie M. Delzenne & Laure B. Bindels

Knowing how dietary fibre nourishes gut microorganisms might suggest ways to boost health-promoting bacteria. A method developed to pinpoint bacteria that consume particular types of dietary fibre could advance such efforts.

Certain gut microorganisms can boost human health, but it is unclear how diet could be harnessed to easily manipulate the composition of gut microbes to boost the levels of desired bacteria. Writing in *Cell*, Patnode *et al.*[1] present a useful approach for assessing interactions between human gut microbes and the dietary fibre that sustains their existence.

Dietary fibre is promoted as part of a healthy diet worldwide. Many people, however, do not achieve their recommended fibre intake because they consume insufficient fruit, vegetables and cereals. Inadequate fibre intake is associated with common conditions including obesity, diabetes and cancer[2]. Yet understanding the mechanisms that link fibre-rich food to good health is challenging. Dietary fibre encompasses a wide range of complex molecules, most of which are present in plant cells; among them are carbohydrate molecules called glycans, which are resistant to digestion by human enzymes. As a consequence, some ingested fibre is excreted unchanged in faeces, whereas most is metabolized by gut microbes.

These microbes have a diverse and extremely complex metabolic capacity. Bacteria that express different enzymes for metabolizing fibre can survive and grow using a range of foods. Some bacterial species might compete with each other for the same food source, which could lower the abundance of species that compete less successfully. How might gut microbes be manipulated through human dietary intervention? For example, the concept of using prebiotics – compounds that affect gut microbes, thereby benefiting the human host – has been proposed. One such idea is to use particular fibre sources that provide food for the desired gut microbes[3,4]. However, determining whether dietary fibre can promote health in this way requires a sophisticated understanding of the interactions that occur when the complex community of gut microbes encounters a source of fibre.

Previous work[5] had indicated that transferring the gut microbes of human twins who have contrasting body masses (obese and lean) into mice induced a corresponding difference in the animals' body masses. However, when some of the obese mice were housed with the lean mice, they had less adipose fat than did obese animals that were not co-housed with lean mice – and this weight-loss effect correlated with the transfer of *Bacteroides* bacterial species from the lean mice to the obese mice[5]. High consumption of fibre-rich plant foods was required for this adipose-fat reduction to occur[5]. However, the types of fibre responsible for this effect, and how these interact with specific gut microorganisms, was unknown. Patnode and colleagues now reveal how particular types of glycan can drive competition between different *Bacteroides* species resident in the human gut.

Patnode *et al.* studied mice that lacked their normal microbes, and instead harboured 15 strains of gut-dwelling bacteria from a lean human who had an obese twin. The authors fed the mice different combinations of fibre sources as part of their diet. Analysing faecal samples enabled the researchers to track how the diets affected the relative abundance of each bacterial species in the animals' gut. This approach pinpointed, for example, a dose–response effect of pea fibre on the relative abundance of *Bacteroides thetaiotaomicron* in the bacterial population, as well as a pronounced effect of certain

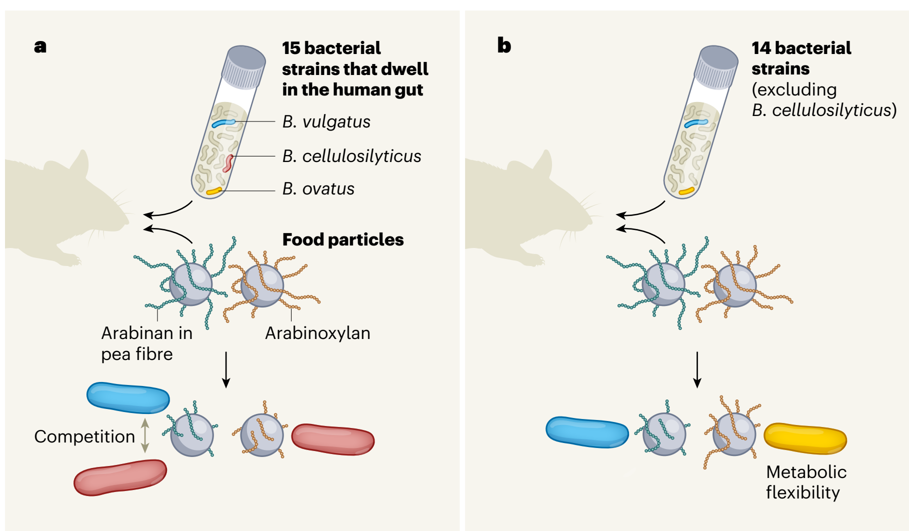

Figure 1 | Investigating how human gut-dwelling bacteria metabolize dietary fibre. a, Patnode *et al.*[1] gave mice that lacked their natural gut microbes a set of 15 bacterial strains that dwell in the human gut, including the species *Bacteroides cellulosilyticus*, *Bacteroides ovatus* and *Bacteroides vulgatus*. The authors developed a method for tracking fibre digestion. They generated magnetic beads coated with a fibre of interest, and fed these beads (termed food particles) to the animals. Applying a magnetic field enabled the recovery of food particles and assessment of the extent of fibre degradation. The animals received food particles that included some coated with pea fibre that is rich in the molecule arabinan, and some coated with the molecule arabinoxylan. *B. vulgatus* and *B. cellulosilyticus* competed to degrade the arabinan, *B. cellulosilyticus* degraded arabinoxylan, and *B. ovatus* degraded other molecules (not shown). **b,** When the experiment was repeated without *B. cellulosilyticus, B. ovatus* demonstrated metabolic flexibility, by switching to degrade arabinoxylan. *B. ovatus* degraded less arabinoxylan than did *B. cellulosilyticus*.

types of barley fibre (β-glucan and bran) on the relative abundance of *Bacteroides ovatus*. These results reveal the specificity of the effects that different forms of dietary fibre can have on bacterial populations.

To identify the genes required for a specific bacterium of interest to metabolize fibre, the authors gave mice bacterial strains that were engineered to contain mutations at random sites across their genome, and fed the animals different kinds of dietary fibre. By analysing the proteins in mouse faecal samples, the authors identified a set of bacterial proteins that allow certain microbes to grow successfully in particular feeding regimes. For example, when mice received dietary fibre from fruit peelings (citrus pectin) that are rich in a type of molecule called methylated homogalacturonan, this led to a rise in the expression of proteins that degrade such molecules in the bacterium *Bacteroides cellulosilyticus*. And when mice received pea fibre, which is rich in a polymer molecule called arabinan (which contains the sugar arabinose), the expression of proteins involved in arabinan degradation rose in the bacterium *B. thetaiotaomicron*.

Perhaps the most original part of this research is the development of artificial 'food particles' consisting of glycan-coated magnetic beads (Fig. 1) that can be administered orally to mice and recovered by applying a magnetic field. Patnode *et al.* used this strategy to investigate how bacterial species respond to different food sources by assessing the extent of glycan degradation in the recovered beads. When mice that had been colonized only with *B. cellulosilyticus* or *Bacteroides vulgatus* were given food particles coated with pea fibre, the levels of arabinose in the recovered beads were lower than the original levels, demonstrating that both of these bacterial species had metabolized this molecule *in vivo*.

In a parallel experiment, mice were colonized either with all 15 bacterial strains from the lean twin, or with 14 of the strains (*B. cellulosilyticus* excluded), before being given food particles containing pea fibre (Fig. 1). The level of degradation of arabinose in the arabinan-rich pea-fibre beads was then compared, and was found to be the same in both cases. This suggests that some change occurs in the bacterial community, in the absence of *B. cellulosilyticus*, that enables arabinose from pea fibre to be degraded as much as it would be if all 15 bacterial strains were present. The story might be different for other forms of dietary fibre.

Along with the food particles coated with pea fibre, the animals received some coated with molecules of arabinoxylan (a polymer of the sugars arabinose and xylose). However, in the case of arabinoxylan, the bacterial strains were less able to process this molecule when *B. cellulosilyticus* was absent than when it was present, and the arabinoxylan-metabolizing activity was attributed to *B. ovatus*. In the absence of *B. cellulosilyticus*, *B. ovatus* undergoes a metabolic shift that boosts its ability to use arabinoxylan. When both *B. ovatus* and *B. cellulosilyticus* were absent from the bacterial populations, arabinoxylan-coated beads retained their original levels of arabinose, revealing that none of the remaining 13 bacterial strains took advantage of arabinoxylan availability.

This study reveals the flexibility and adaptability of gut microbes in response to their nutritional environment. It provides a useful focus on specific forms of dietary fibre and bacterial species known to be linked to diet-associated resistance to a rise in adipose tissue[5]. This 'simplification' of the context suggests a way forward in understanding the key genes and proteins of *Bacteroides* that are crucial for the degradation of dietary fibre, and that might affect the abundance of particular gut bacteria. The findings also reveal how *B. cellulosilyticus* can have a dominant role in its interactions with certain bacteria with which it can compete for the same food source. The work also uncovers hidden metabolic flexibility, such as the ability of *B. ovatus* to adapt its metabolic strategy.

When assessing this study, it is worth bearing in mind that *Bacteroides* is not the only type of bacterium that commonly uses dietary fibre for food, and that the fibre-containing foods tested by the authors are not the major sources of dietary fibre in a typical human diet. Moreover, the abundance of *Bacteroides* varies enormously between people[6], and the hypothesis that key *Bacteroides* species might affect the success of dieting efforts to control obesity requires further investigation.

Although it concentrates on *Bacteroides* only, Patnode and colleagues' work represents useful progress towards developing personalized nutrition strategies for tailoring gut microbes in the future. The study also complements other research[7–9] that explores how bacteria in the human gut might contribute to the body's response to a particular diet. Thanks to Patnode *et al.*, we have fresh insights into how specific types of bacterium use and compete for dietary fibre. Future research will undoubtedly continue to refine the link between fibre-rich food and health, by taking into account the role of the gut microbial community.

Nathalie M. Delzenne and **Laure B. Bindels** are at the Louvain Drug Research Institute, Metabolism and Nutrition Research Group, Catholic University of Louvain, 1200 Brussels, Belgium.
e-mail: nathalie.delzenne@uclouvain.be

1. Patnode, M. L. *et al. Cell* **179**, 59–73 (2019).
2. Delzenne, N. M. *et al. Clin. Nutr.* https://doi.org/10.1016/j.clnu.2019.03.002 (2019).
3. Bindels, L. B., Delzenne, N. M., Cani, P. D. & Walter, J. *Nature Rev. Gastroenterol. Hepatol.* **12**, 303–310 (2015).
4. Gibson, G. R. *et al. Nature Rev. Gastroenterol. Hepatol.* **14**, 491–502 (2017).
5. Ridaura, V. K. *et al. Science* **341**, 1241214 (2013).
6. The Human Microbiome Project Consortium. *Nature* **486**, 207–214 (2012).
7. Salonen, A. *et al. ISME J.* **8**, 2218–2230 (2014).
8. Bindels, L. B. *et al. Microbiome* **5**, 12 (2017).
9. Zhao, L. *et al. Science* **359**, 1151–1156 (2018).

personalized nutrition strategies for tailoring gut microbes in the future. The study also complements other research[7–9] that explores how bacteria in the human gut might contribute to the body's response to a particular diet. Thanks to Patnode *et al.*, we have fresh insights into how specific types of bacterium use and compete for dietary fibre. Future research will undoubtedly continue to refine the link between fibre-rich food and health, by taking into account the role of the gut microbial community.

Nathalie M. Delzenne and **Laure B. Bindels** are at the Louvain Drug Research Institute, Metabolism and Nutrition Research Group, Catholic University of Louvain, 1200 Brussels, Belgium.
e-mail: nathalie.delzenne@uclouvain.be

1. Patnode, M. L. *et al. Cell* **179**, 59–73 (2019).
2. Delzenne, N. M. *et al. Clin. Nutr.* https://doi.org/10.1016/j.clnu.2019.03.002 (2019).
3. Bindels, L. B., Delzenne, N. M., Cani, P. D. & Walter, J. *Nature Rev. Gastroenterol. Hepatol.* **12**, 303–310 (2015).
4. Gibson, G. R. *et al. Nature Rev. Gastroenterol. Hepatol.* **14**, 491–502 (2017).
5. Ridaura, V. K. *et al. Science* **341**, 1241214 (2013).
6. The Human Microbiome Project Consortium. *Nature* **486**, 207–214 (2012).
7. Salonen, A. *et al. ISME J.* **8**, 2218–2230 (2014).
8. Bindels, L. B. *et al. Microbiome* **5**, 12 (2017).
9. Zhao, L. *et al. Science* **359**, 1151–1156 (2018).

This article was published online on 4 December 2019.

Analytical chemistry

Infrared spectroscopy finally sees the light

Andreas Barth

The reliance of infrared spectroscopy on light transmission limits the sensitivity of many analytical applications. An approach that depends on the emission of infrared radiation from molecules promises to solve this problem. **See p.52**

Atoms in molecules oscillate when irradiated by infrared light. The particular light frequencies that drive these vibrations are absorbed by molecules, and depend on the molecules' chemical structure and environment. The infrared absorption spectrum of a sample can therefore be used as a molecular fingerprint by which to characterize its chemical composition. This has made infrared spectroscopy a widespread analytical technique. However, infrared spectra are difficult to measure for low concentrations of analytes and for samples in water. On page 52, Pupeza *et al.*[1] present a concept for infrared spectroscopy that promises to alleviate these limitations.

Infrared light was discovered[2] as a result of the problem it caused William Herschel while he was making astronomical observations of the Sun — it created a disturbing heating sensation in his eye that he wanted to filter out. Today, however, the benefits of infrared radiation for a multitude of analytical purposes are widely appreciated. Its applications range from the detection of molecules in outer space[3,4], including that of water on Mars[5], to deciphering the molecular mechanisms of proteins in living organisms[6,7]. In the everyday world, it is used in food analysis[6,8] and in forensic police investigations[6,9], for example. Much research is being done to bring infrared spectroscopy to the clinic, because the analysis of biological tissue and body fluids can be used to detect and diagnose disease[6,7,10].

One of the main obstacles to the infrared analysis of biological samples is the strong absorption of infrared radiation by water — a problem that limits the sample thickness to less than 10 micrometres for most purposes. This issue also makes it difficult to add aqueous solutions of reagents (such as acids or salts) to samples to manipulate the state of molecules in the sample. Such manipulations are desirable, for example, for studying the binding of small molecules to proteins, and are standard practice when using ultraviolet or visible spectroscopy. Furthermore, because infrared radiation is absorbed by water, samples must often be concentrated or dried.

Pupeza and colleagues report a solution to this problem. They irradiate samples with an ultrashort pulse (on the scale of femtoseconds; 1 fs is 10^{-15} seconds) of mid-infrared light. Specific frequencies of the light are absorbed by sample molecules, generating vibrations. These vibrations continue after the pulse has ended, and last until the vibrational energy is dissipated to the environment (which takes a few picoseconds; 1 ps is 10^{-12} s). Because the vibrating atoms carry partial electrical charges, their oscillations generate electromagnetic radiation, similar to the way in which oscillating electrons produce electromagnetic radiation in an antenna. The generated radiation has the same frequency as that of the molecular vibrations, and so carries information about all of the sample molecules — the authors therefore call it a global molecular fingerprint. It is measured using a second ultrashort pulse of light, this time in the near-infrared spectral range, through a method called electro-optic sampling[11].

The authors' approach is conceptually different from conventional absorption

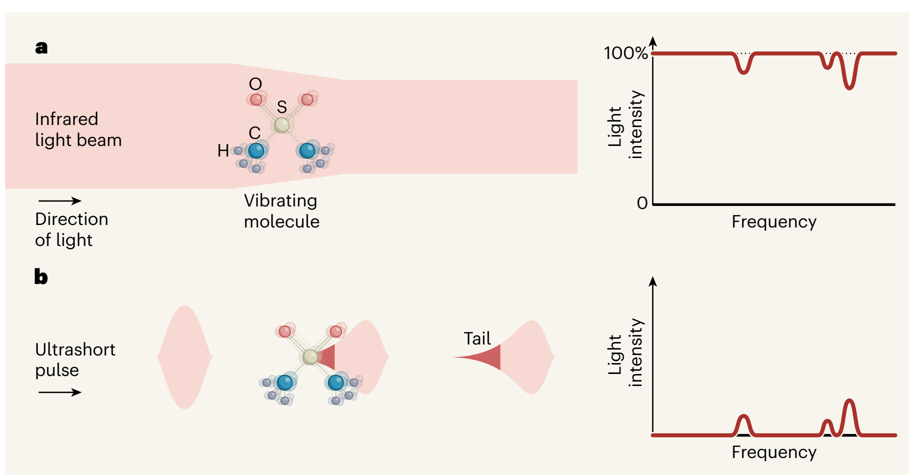

Figure 1 | A fresh approach for obtaining infrared spectra. a, In conventional infrared spectroscopy, molecules are irradiated with infrared light. They absorb certain frequencies of the light, which causes them to vibrate. The signals of interest are the absorption 'troughs' in the transmitted light spectrum, but these change the overall intensity of the transmitted light only marginally when the samples are highly diluted, limiting the sensitivity of this technique. **b**, Pupeza *et al.*[1] irradiate analytical samples with ultrashort bursts of infrared light, again causing molecules in the sample to vibrate. These vibrations continue after the pulse has ended, and generate infrared radiation, shown here as a 'tail' that trails after the pulse. This tail is analysed to determine the infrared spectrum of the molecules. Because the experimental signal is emitted light and is detected directly, this method can be more sensitive than absorption infrared spectroscopy.

measurements. In absorption spectroscopy, the signal is sensed only indirectly, from the light that does not interact with the sample (Fig. 1a). Weak absorption is therefore very difficult to detect, because it changes the intensity of the transmitted light only marginally. Theoretically, the detection of weak absorbers could be improved by increasing the intensity of the incident light, but commonly used infrared detectors become less sensitive at higher light intensities[12], imposing a practical limit on the maximum light intensity that can be used. By contrast, Pupeza *et al*. detect the signal of interest — the radiation emitted from the vibrating molecules — directly (Fig. 1b). This is analogous to the difference between absorbance and fluorescence measurements in the visible spectral range: fluorescence measurements are the more sensitive because they detect a signal directly from the sample, and can even detect it from a single molecule.

Pupeza and colleagues demonstrate the high sensitivity of their approach in various ways. For example, they were able to detect 40-fold lower concentrations of a compound in solution, and to better distinguish between two similar compounds, than when using absorption spectroscopy. They also obtained spectra of biological samples that block nearly all of the incoming light (in one case, at least 99.999%). Thus, the new approach senses light where currently used methods see only darkness. This is an impressive achievement, and might alleviate both of the main problems of conventional infrared spectroscopy: sensitivity and strong infrared absorption by water. It will simplify sample preparation in many cases by removing the need for sample concentration or drying, and will open up new applications — particularly those involving aqueous biological samples.

The authors suggest several ideas for taking the method further, such as by increasing the power of the laser used to irradiate the sample. It is to be hoped that such measures will further narrow the technological gap that at present prevents the method from achieving the ultimate goal of single-molecule sensitivity in bulk water. Other challenges will be to increase the spectral range of the measurements to include the shorter wavelengths at which prominent and diagnostically useful signals are found for proteins, lipids and nucleotides, and to develop a spectrometer suitable for commercialization at a competitive price.

Andreas Barth is in the Department of Biochemistry and Biophysics, Stockholm University, Stockholm 106 91, Sweden.
e-mail: barth@dbb.su.se

1. Pupeza, I. *et al. Nature* **577**, 52–59 (2020).
2. Herschel, W. *Phil. Trans. R. Soc. Lond.* **90**, 284–292 (1800).
3. van Dishoeck, E. F. *Annu. Rev. Astron. Astrophys.* **42**, 119–167 (2004).
4. Ehrenfreund, P. & Charnley, S. B. *Annu. Rev. Astron. Astrophys.* **38**, 427–483 (2000).
5. Bibring, J.-P. *et al. Nature* **428**, 627–630 (2004).
6. Chalmers, J. M. & Griffiths, P. R. (eds) *Handbook of Vibrational Spectroscopy* Vols 4 & 5 (Wiley, 2001).
7. Barth, A. & Haris, P. I. (eds) *Biological and Biomedical Infrared Spectroscopy* (IOS, 2009).
8. Sun, D.-W. (ed.) *Infrared Spectroscopy for Food Quality Analysis and Control* (Academic, 2008).
9. Chalmers, J. M., Edwards, H. G. M. & Hargreaves, M. D. (eds) *Infrared and Raman Spectroscopy in Forensic Science* (Wiley, 2012).
10. Bunaciu, A. A., Fleschin, Ş., Hoang, V. D. & Aboul-Enein, H. Y. *Crit. Rev. Anal. Chem.* **47**, 67–75 (2017).
11. Wu, Q. & Zhang, X.-C. *Appl. Phys. Lett.* **67**, 3523–3525 (1995).
12. Theocharous, E., Ishii, J. & Fox, P. N. *Appl. Opt.* **43**, 4182–4188 (2004).

Medical research

AI shows promise for breast cancer screening

Etta D. Pisano

Could artificial intelligence improve the accuracy of screening for breast cancer? A comparison of the diagnostic performance of expert physicians and computers suggests so, but the clinical implications are as yet uncertain. **See p.89**

Screening is used to detect breast cancer early in women who have no obvious signs of the disease. This image-analysis task is challenging because cancer is often hidden or masked in mammograms by overlapping 'dense' breast tissue. The problem has stimulated efforts to develop computer-based artificial-intelligence (AI) systems to improve diagnostic performance. On page 89, McKinney *et al.*[1] report the development of an AI system that outperforms expert radiologists in accurately interpreting mammograms from screening programmes. The work is part of a wave of studies investigating the use of AI in a range of medical-imaging contexts[2].

Despite some limitations, McKinney and colleagues' study is impressive. Its strengths include the large scale of the data sets used for training and subsequently validating the AI algorithm. Mammograms for 25,856 women in the United Kingdom and 3,097 women in the United States were used to train the AI system. The system was then used to identify the presence of breast cancer in mammograms of women who were known to have had either biopsy-proven breast cancer or normal follow-up imaging results at least 365 days later. These outcomes are the widely accepted gold standard for confirming breast cancer status in people undergoing screening for the disease. The authors report that the AI system outperformed both the historical decisions made by the radiologists who initially assessed the mammograms, and the decisions of 6 expert radiologists who interpreted 500 randomly selected cases in a controlled study.

McKinney and colleagues' results suggest that AI might some day have a role in aiding the early detection of breast cancer, but the authors rightly note that clinical trials will be needed to further assess the utility of this tool in medical practice. The real world is more complicated and potentially more diverse than the type of controlled research environment reported in this study. For example, the study did not include all the different mammography technologies currently in use, and most images were obtained using a mammography system from a single manufacturer. The study included examples of two types of mammogram: tomosynthesis (also known as 3D mammography) and conventional digital (2D) mammography. It would be useful to know how the system performed individually for each technology.

"Clinical trials will be needed to further assess the utility of this tool in medical practice."

The demographics of the population studied by the authors is not well defined, apart from by age. The performance of AI algorithms can be highly dependent on the population used in the training sets. It is therefore important that a representative sample of the general population be used in the development of this technology, to ensure that the results are broadly applicable.

Another reason to temper excitement about this and similar AI studies is the lessons learnt from computer-aided detection (CAD) of breast cancer. CAD, an earlier computer system aimed at improving mammography interpretation in the clinic, showed great promise in experimental testing, but fell short in real-world settings[3]. CAD marks

mammograms to draw the interpreter's attention to areas that might be abnormal. However, analysis of a large sample of clinical mammography interpretations from the US Breast Cancer Surveillance Consortium registry demonstrated that there was no improvement in diagnostic accuracy with CAD[3]. Moreover, that study revealed that the addition of CAD worsened sensitivity (the performance of radiologists in determining that cancer was present), thus increasing the likelihood of a false negative test. CAD did not result in a significant change in specificity (the performance of radiologists in determining that cancer was not present) and the likelihood of a false positive test[3].

It has been speculated that CAD was not as useful in the clinic as experimental data suggested it might be because radiologists ignored or misused its input owing to the high frequency of marks on the images that were not findings suggestive of cancer. This outcome was attributed by some to the limited processing power available for CAD, which meant that comparisons with previous imaging studies of the same person were not possible[4]. Thus, CAD might mark regions that were not changing over time and that could be easily dismissed by expert readers. Another factor that limited CAD is that it was developed using the performance of human-based diagnosis. It was trained using mammograms in which humans had found signs of cancer and others that were false negatives — cases in which humans could not see signs of cancer although the disease was indeed present[4]. Similar pitfalls could be encountered with AI-based decision aids, too.

A system by which AI finds abnormalities that humans miss will require radiologists to adapt to the use of these types of tool. Imagine a system in which an algorithm marks a dense breast area on a screening mammogram and the human radiologist cannot see anything that looks potentially malignant. With CAD, radiologists scrutinize the areas marked, and if they decide the mark is probably not cancer, they assign the mammogram as being negative for malignancy. However, if AI algorithms are to make a bigger difference than CAD in detecting cancers that are currently missed, an abnormality detected by the AI system, but not perceived as such by the radiologist, would probably require extra investigation. This might result in a rise in the number of people who receive callbacks for further evaluation. A clinical trial would show the effect of the AI system on the detection of cancer and the rate of false positive diagnoses, while also allowing the development of effective clinical practice in response to mammograms flagged as abnormal by AI but not by the radiologist.

In addition, it would be essential to develop a mechanism for monitoring the performance of the AI system as it learns from cases it encounters, as occurs in machine-learning algorithms. Such performance metrics would need to be available to those using these tools, in case performance deteriorates over time.

It is sobering to consider the sheer volume of data needed to develop and test AI algorithms for clinical tasks. Breast cancer screening is perhaps an ideal application for AI in medical imaging because large curated data sets suitable for algorithm training and testing are already available, and information for validating straightforward clinical end points is readily obtainable. Breast cancer screening programmes routinely measure their diagnostic performance — whether cancer is correctly detected (a true positive) or missed (a false negative). Some areas found on mammograms might be identified as abnormal but turn out on further testing not to be cancerous (false positives). For most women, screening identifies no abnormalities, and when there is still no evidence of cancer one year later, this is classified as a true negative.

Most other medical tasks have more-complicated clinical outcomes, however, in which the clinician's decision is not a binary one (between the presence or absence of cancer), and thus further signs and symptoms must also be considered. In addition, most diseases lack readily accessible, validated data sets in which the 'truth' is defined relatively easily. Obtaining validated data sets for more-complex clinical problems will require greater effort by readers and the development of tools that can interrogate electronic health records to identify and annotate cases representing specific diagnoses.

To achieve the promise of AI in health care that is implied by McKinney and colleagues' study, anonymized data in health records might thus have to be treated as precious resources of potential benefit to human health, in much the same way as public utilities such as drinking water are currently treated. Clearly, however, if such AI systems are to be developed and used widely, attention must be paid to patient privacy, and to how data are stored and used, by whom, and with what type of oversight.

Etta D. Pisano is at the American College of Radiology, Philadelphia, Pennsylvania 19103, USA, and at Beth Israel Lahey Medical Center, Harvard Medical School, Boston, Massachusetts.
e-mail: episano@bidmc.harvard.edu

1. McKinney, S. M. *et al. Nature* **577**, 89–94 (2020).
2. Neri, E. *et al. Insights Imaging* **10**, 44 (2019).
3. Lehman, C. D. *et al. JAMA Intern. Med.* **175**, 1828–1837 (2015).
4. Kohli, A. & Jha, S. *J. Am. Coll. Radiol.* **15**, 535–537 (2018).

Astronomy

Galaxy cluster illuminates the cosmic dark ages

Nina A. Hatch

Observations of a distant cluster of galaxies suggest that star formation began there only 370 million years after the Big Bang. The results provide key details about where and when the first stars and galaxies emerged in the Universe. See p.39

Shortly after the Big Bang, the Universe was completely dark. Stars and galaxies, which provide the Universe with light, had not yet formed, and the Universe consisted of a primordial soup of neutral hydrogen and helium atoms and invisible 'dark matter'. During these cosmic dark ages, which lasted for several hundred million years, the first stars and galaxies emerged. Unfortunately, observations of this era are challenging because dark-age galaxies are exceptionally faint[1]. On page 39, Willis *et al.*[2] provide a glimpse of what happened during the dark ages by doing some galactic archaeology. By measuring the ages of stars in one of the most distant clusters of galaxies known, the authors located galaxies that formed stars in the dark ages, close to the earliest possible time that stars could emerge.

A galaxy cluster is a group of thousands of galaxies that orbit each other at speeds[3] of about 1,000 kilometres per second. They are prevented from flying apart by the gravitational pull of the accompanying dark matter, which has the equivalent total mass of about one hundred trillion Suns[4]. Astronomers use these clusters as laboratories for many experiments in astrophysics, such as measuring the composition of the Universe, testing theories of gravity and determining how galaxies form. Willis *et al.* used one of the

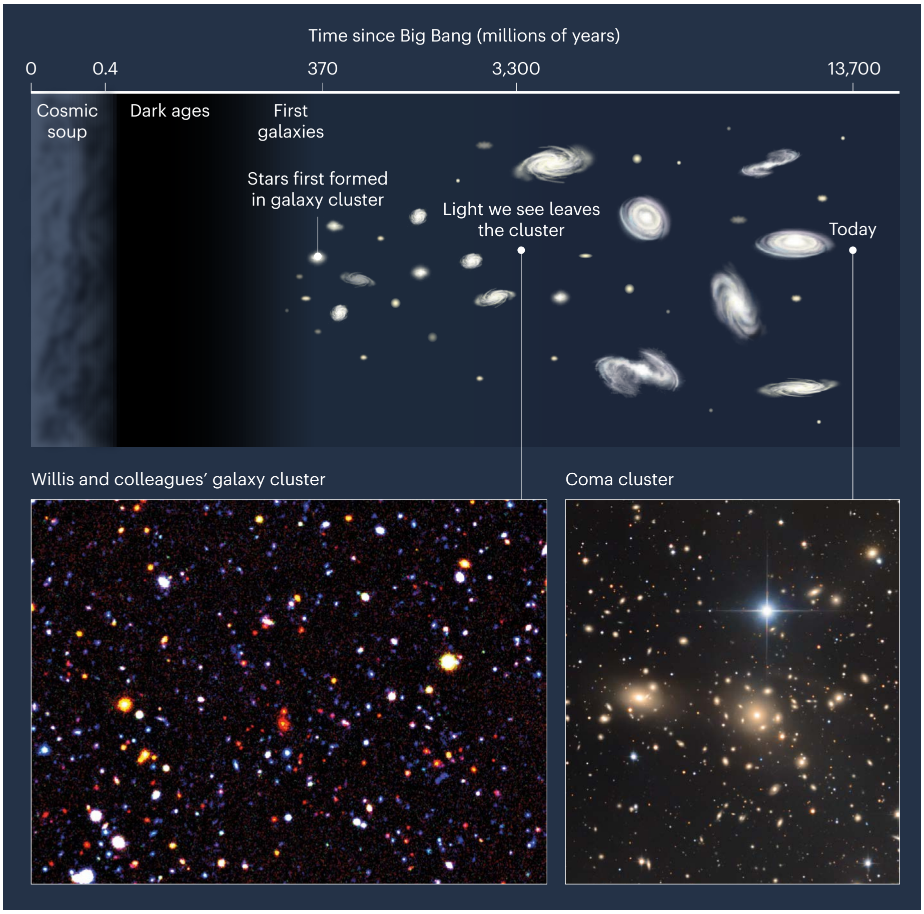

Figure 1 | Chronology of the Universe. After the Big Bang, the Universe consisted of a cosmic soup of radiation and matter. About 400,000 years later, it entered an era known as the cosmic dark ages in which it was devoid of light. The first stars and galaxies began to emerge a few hundred million years later, and gradually provided the Universe with light. Willis *et al.*[2] report that star formation in a distant cluster of galaxies began roughly 370 million years after the Big Bang. The light that we see from this galaxy cluster was emitted when the Universe was about 3.3 billion years old. The cluster is likely to have become one of the largest structures in the present-day Universe, comparable in mass to the Coma cluster. (Image credits: Willis and colleagues' galaxy cluster: N. A. Hatch; Coma cluster: Russ Carroll, Rob Gendler, Bob Franke/Dan Zowada Memorial Observatory, Wayne State Univ.)

most distant clusters known to study when the most massive galaxies in the Universe began to produce stars.

Although nearby clusters, such as the Coma cluster, are easier to observe than those farther away, we cannot measure their ages precisely because the galaxies are extremely old. It is difficult to differentiate between, for example, a galaxy that is 7 billion years old and one that is 13 billion years old[5]. Therefore, to obtain a precise date for when clusters first formed their stars, Willis and colleagues used NASA's Hubble Space Telescope to look at one of the most distant clusters they could find.

Because light travels at a finite speed, the most distant clusters we can see are also those in the earliest stages of the Universe that we can see. The light from the cluster examined by Willis *et al.* has been travelling for 10.4 billion years before it reaches Earth, which means that we are looking at a cluster as it was just 3.3 billion years after the Big Bang. Consequently, this cluster acts as a keyhole through which we can peer into the early Universe (Fig. 1).

Willis and colleagues found that the cluster contains several galaxies that have similar red colours. The colour of a galaxy can be used to estimate its age because younger stars are bluer than their older, redder counterparts. As a result, galaxies that have red colours formed their stars a long time ago[5]. By comparing the colours of the cluster galaxies with those of models, the authors estimated that the stars of these galaxies started to emerge when the Universe was only 370 million years old. This epoch is when we expect the first stars to have formed in the cosmic dark ages[6].

"The galaxy cluster acts as a keyhole through which we can peer into the early Universe."

One particularly intriguing point is that Willis *et al.* identified at least 19 galaxies in the cluster that have similar colours, which means that the galaxies have similar ages. At the time when these galaxies formed their stars, they would have been well spread out, so it is a conundrum as to why they all began producing stars at approximately the same time. Were they influenced by their environment? Alternatively, did the star formation in one galaxy somehow trigger a chain reaction, leading to star formation in nearby gas clouds? We do not currently have the answer, but what is clear from the authors' work is that these distant clusters are full of the oldest galaxies in the Universe.

In my opinion, Willis and colleagues' age estimates are the best ones possible, given the limited data that the authors have from the Hubble telescope. However, determining ages from the colours of galaxies is a relatively crude method that is subject to large uncertainties. For example, a young galaxy that contains a lot of astronomical dust can have the same colour as an old galaxy containing little dust. Therefore, although the authors' results are tantalizing, they should be treated with caution until NASA's James Webb Space Telescope (JWST) is launched in the next few years.

The JWST will measure spectra of the light emitted by these galaxies. A comparison of the spectra with models will be a much more accurate way to determine the ages of the stars than using the colours of galaxies. Furthermore, because it is easier to measure the ages of earlier galaxies than those of more recent ones[5], it makes sense to target galaxies in the progenitors of these galaxy clusters in the early Universe. Willis and colleagues' results make a strong case for these distant clusters being some of the first targets that the JWST should observe.

Nina A. Hatch is in the School of Physics and Astronomy, University of Nottingham, Nottingham NG7 2RD, UK.
e-mail: nina.hatch@nottingham.ac.uk

1. Stark, D. P. *Annu. Rev. Astron. Astrophys.* **54**, 761–803 (2016).
2. Willis, J. P. *et al. Nature* **577**, 39–41 (2020).
3. Struble, M. F. & Rood, H. J. *Astrophys. J. Suppl. Ser.* **125**, 35–71 (1999).
4. Bahcall, N. A. *Annu. Rev. Astron. Astrophys.* **15**, 505–540 (1977).
5. Bruzual, G. & Charlot, S. *Mon. Not. R. Astron. Soc.* **344**, 1000–1028 (2003).
6. Planck Collaboration. *Astron. Astrophys.* **596**, A108 (2016).

Article

Spectroscopic confirmation of a mature galaxy cluster at a redshift of 2

https://doi.org/10.1038/s41586-019-1829-4

Received: 14 August 2019

Accepted: 4 November 2019

Published online: 1 January 2020

J. P. Willis[1*], R. E. A. Canning[2], E. S. Noordeh[2,3], S. W. Allen[2], A. L. King[2], A. Mantz[2,3], R. G. Morris[2,4], S. A. Stanford[5] & G. Brammer[6]

Galaxy clusters are the most massive virialized structures in the Universe and are formed through the gravitational accretion of matter over cosmic time[1]. The discovery[2] of an evolved galaxy cluster at redshift $z = 2$, corresponding to a look-back time of 10.4 billion years, provides an opportunity to study its properties. The galaxy cluster XLSSC 122 was originally detected as a faint, extended X-ray source in the XMM Large Scale Structure survey and was revealed to be coincident with a compact overdensity of galaxies[2] with photometric redshifts of 1.9 ± 0.2. Subsequent observations[3] at millimetre wavelengths detected a Sunyaev–Zel'dovich decrement along the line of sight to XLSSC 122, thus confirming the existence of hot intracluster gas, while deep imaging spectroscopy from the European Space Agency's X-ray Multi-Mirror Mission (XMM-Newton) revealed[4] an extended, X-ray-bright gaseous atmosphere with a virial temperature of 60 million Kelvin, enriched with metals to the same extent as are local clusters. Here we report optical spectroscopic observations of XLSSC 122 and identify 37 member galaxies at a mean redshift of 1.98, corresponding to a look-back time of 10.4 billion years. We use photometry to determine a mean, dust-free stellar age of 2.98 billion years, indicating that star formation commenced in these galaxies at a mean redshift of 12, when the Universe was only 370 million years old. The full range of inferred formation redshifts, including the effects of dust, covers the interval from 7 to 13. These observations confirm that XLSSC 122 is a remarkably mature galaxy cluster with both evolved stellar populations in the member galaxies and a hot, metal-rich gas composing the intracluster medium.

To further our understanding of this galaxy cluster, particularly the properties of its member galaxies, we undertook a series of observations of XLSSC 122 with the Hubble Space telescope (HST) Wide Field Camera 3 (WFC3). We obtained images of the cluster in two wavebands, F105W and F140W, and performed low-spectral-resolution slitless spectroscopy using the G141 grism (see Methods). These observations cover the observed frame wavelength interval 1.0–1.7 μm, corresponding to an interval of 0.33 μm to 0.57 μm in the rest frame of a galaxy at redshift $z = 2$. Figure 1 displays the F140W image of XLSSC 122 and shows a compact cluster of galaxies associated with the extended X-ray-emitting region.

We extracted one-dimensional spectra of all galaxies identified within the dispersed G141 grism image of the field (see Methods) and computed redshifts using a galaxy template-fitting algorithm with redshift as a free parameter. Figure 2 displays the histogram of galaxy redshifts in the field of XLSSC 122 over the restricted interval $1.9 < z < 2.05$. Inspection of this interval reveals a primary peak at $z = 1.98$ associated with the central, red galaxies closest to the X-ray peak, and a secondary redshift peak at $z = 1.93$ associated with a mixture of red and blue galaxies, located at larger projected cluster-centric distances (see Fig. 1). The line-of-sight separation between $z = 1.93$ and $z = 1.98$ is 76 co-moving megaparsecs, far larger than the size of the XLSSC 122 cluster, and the two structures are therefore physically distinct. As outlined in the Methods, we identify 37 galaxies as being members of the cluster and a further 13 galaxies identified as members of the foreground structure.

We performed photometry of all galaxies within the HST field of view in both the F105W and F140W images (see Methods) and summarize this information in Fig. 3. The galaxies identified at $1.9 < z < 2.05$ form a clear bimodal distribution in colour with a well populated sequence of red galaxies (corresponding to larger values of F105W − F140W) clearly separated from a broader distribution of blue galaxies.

Interpreting this red sequence as representing a restricted locus of star-formation histories, Bower, Lucey and Ellis[5] employed B − V (the astronomical magnitude difference between a blue and a visual filter) photometry of red-sequence galaxies in the Virgo and Coma clusters to constrain the dispersion of stellar ages in their member galaxies. The F105W and F140W photometry obtained for XLSSC 122 at $z = 2$ spans almost exactly the age-sensitive break feature at wavelength 4,000 Å in the member galaxy rest-frame spectral energy distributions (SEDs) and permits a similar analysis.

[1]Department of Physics and Astronomy, University of Victoria, Victoria, Canada. [2]Kavli Institute for Particle Astrophysics and Cosmology, Stanford University, Stanford, CA, USA. [3]Department of Physics, Stanford University, Stanford, CA, USA. [4]SLAC National Accelerator Laboratory, Menlo Park, CA, USA. [5]Department of Physics, University of California, Davis, CA, USA. [6]Cosmic Dawn Centre, Niels Bohr Institute, University of Copenhagen, Copenhagen, Denmark. *e-mail: jwillis@uvic.ca

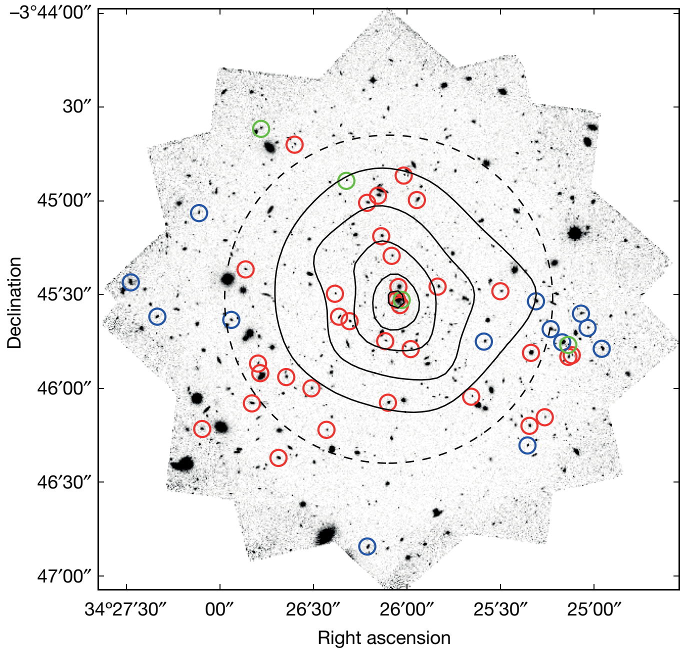

Fig. 1 | HST image of the galaxy cluster XLSSC 122. The greyscale is the F140W image. Contours display X-ray emission corresponding to the 100-ks XMM-Newton image presented in ref. [4]. The dashed circle is drawn with a radius equal to the measured value of r_{500} (the radius within which the average matter density is 500 times the critical density of the Universe). Spectroscopic 'gold' and 'silver' members (see Methods) of the $z = 1.98$ cluster are indicated by red and green circles, respectively. Members of the $z = 1.93$ foreground structure are indicated by blue circles. See text for further details.

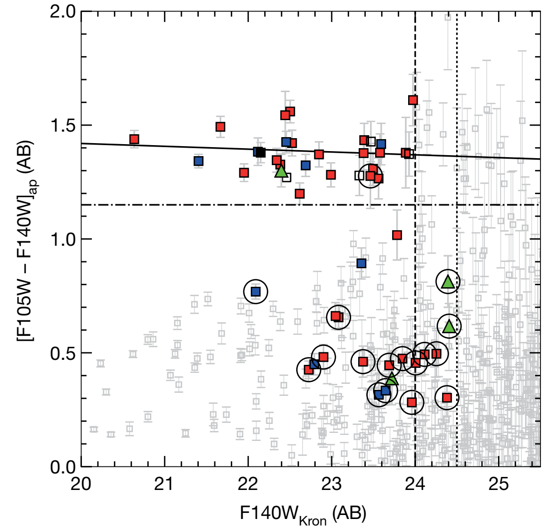

Fig. 3 | Colour–magnitude diagram of all galaxies within the HST/WFC3 field of view. Spectroscopically confirmed $z = 1.98$ 'gold' and 'silver' cluster members are indicated as red squares and green triangles, respectively. Members of the $z = 1.93$ structure are indicated as blue squares. Galaxies at $z \approx 2$ yet which are not formal cluster members are shown as solid black squares, whereas potentially contaminated or confused spectroscopic sources are shown as open black squares. Galaxies with visually classified emission lines are marked using black circles (only $z = 1.98$ and $z = 1.93$ are marked in this manner). All other galaxies in the field are indicated by grey squares. Error bars indicate the 1-sigma measurement uncertainty. The spectroscopic completeness limits of $F140W_{Kron} = 24$ and 24.5 are indicated by the vertical dashed and dotted lines, respectively. The horizontal dot-dashed line shows the lower colour limit for a source to be considered on the cluster's red sequence. The angled solid line indicates a simple least-squares fit to the colour–magnitude relation for red-sequence cluster members. Subscript 'ap' indicates that the magnitudes of these objects are measured within an aperture of fixed angular size as opposed to a flexible aperture, indicated by subscript 'Kron'.

We therefore employed the F105W and F140W photometry of red-sequence galaxies to constrain the posterior distributions of luminosity-weighted stellar age and stellar mass for a set of synthetic stellar population models (see Methods). Computing the product of these posterior distributions generates a mean posterior on the luminosity-weighted stellar age of the red-sequence cluster members (Fig. 4), the details of which are presented in Table 1.

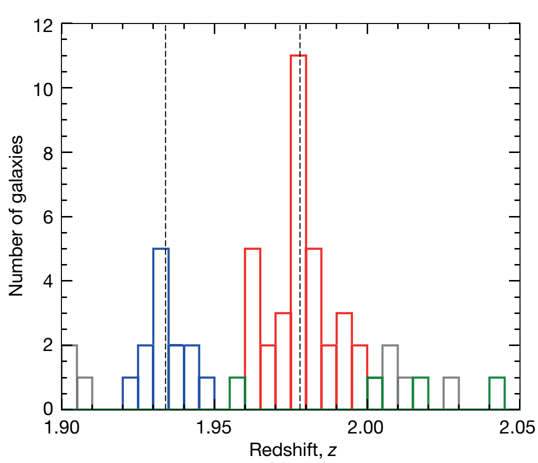

Fig. 2 | Redshift histogram of all galaxies along the line of sight to XLSSC 122. The histogram considers galaxies satisfying the magnitude measurement $F140W_{Kron} < 24$. Galaxies classified as 'gold' members of the $z = 1.98$ cluster are shown in red, 'silver' members are shown in green and members of the $z = 1.93$ structure are shown in blue. Galaxies not classified as a member of either the $z = 1.98$ cluster or the $z = 1.93$ structure are shown in grey. The vertical dashed lines show the unweighted mean redshift of both the cluster and the foreground structure (see text for further details).

Our analysis assumes that the tight correlation of colour on the red sequence arises from scatter in age at fixed metallicity and internal dust absorption. Assuming no dust absorption ($A_V = 0.0$) we determine a mean red-sequence luminosity-weighted stellar age of 2.98 billion years (Gyr), corresponding to a redshift marking the onset of star formation of 12. This value is consistent with the inferred formation redshifts of the earliest observations of star formation in the Universe[6]. We also consider dust absorption characterized by $A_V = 0.3$ and $A_V = 0.5$, which generate lower mean stellar ages and greater dispersion of the mean age. Despite the uncertainties that govern a number of the assumptions in such stellar population analyses, the main conclusion of this analysis is that red-sequence galaxies in XLSSC 122 are composed of stars of uniformly old age. When combined with the already large look-back time to this cluster, it is clear that star formation occurred in these galaxies in a coordinated manner at early times.

Table 1 | The mean luminosity-weighted stellar ages of red-sequence cluster galaxies

SED model A_V	Mean t_w (Gyr)	Mean formation redshift (spread)
0.0	2.98 ± 0.05	12.0 (10.9–13.3)
0.3	2.77 ± 0.13	8.7 (8.3–10.4)
0.5	2.63 ± 0.11	7.4 (6.6–8.3)

The table lists the mean and standard deviation of the computed luminosity-weighted stellar age t_w for SED models of specified A_V. Corresponding values of the mean formation redshift and spread (from standard deviation) are computed for the assumed cosmological model.

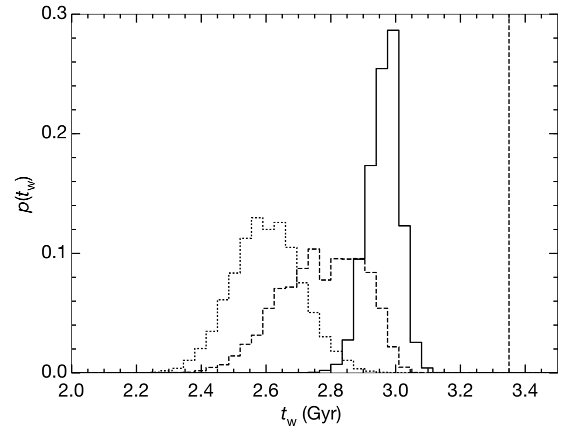

Fig. 4 | The luminosity-weighted age distribution of stars within red-sequence cluster galaxies. The lines depict mean t_w posteriors for 19 'gold' $z = 1.98$ cluster red-sequence members for each of the three SED models characterized by $A_V = 0.0$ (solid), $A_V = 0.3$ (dashed) and $A_V = 0.5$ (dotted). The vertical dashed line indicates the age of the Universe at $z = 1.98$ for the assumed cosmological model.

Analysis of the X-ray-emitting gas in XLSSC 122 provides an alternative perspective on the formation history of the galaxy cluster as a whole. Using standard theory[7], one may combine the X-ray gas temperature ($k_B T = 5$ keV, where k_B is the Boltzmann constant) and an estimate of the virial radius of the cluster ($r_{200} = 440$ kpc, ref. [4]) to obtain a sound-crossing time for XLCCS 122 of 3.3×10^8 yr. Hydrodynamical simulations of the gas physics in a forming cluster indicate that structures typically achieve virial equilibrium following a minimum of 2 to 3 sound-crossing timescales[8]. This indicates that XLSSC 122 is unlikely to have assembled earlier than 1 Gyr before the epoch of observation, equivalent to a redshift of 2.8. Although this argument does not place an upper limit on the elapsed time between assembly and virialization, the assembly of a cluster of mass equal to XLSSC 122 at redshifts greater than 3 appears unlikely[9,10]. It is clear, therefore, even allowing for the uncertainty present in these estimates, that coordinated star formation in the member galaxies located in XLSSC 122 preceded the assembly of the cluster environment.

Computer simulations of the accretion history of massive, gravitationally bound halos in an expanding Universe indicate that it is likely that XLSSC 122 will evolve with time into a present-day galaxy cluster comparable in mass to that of Coma, that is, about 1×10^{15} solar masses[9–11]. Although caution is required in both the interpretation of the scatter in the accretion histories of halos of fixed total mass and the more subtle point of whether XLSSC 122 represents a typical galaxy cluster at $z = 2$ or is perhaps an extreme case, the conclusion remains robust that this system will continue to grow in mass until it becomes a massive galaxy cluster in the present-day Universe.

The recent discovery of SPT2349-56, a massive proto-cluster of galaxies at a redshift of 4.3 (ref. [12]), provides a further, tantalising, glimpse of the kind of structure from which XLSSC 122 may have evolved. The same structure growth simulations that predict the future evolution of massive halos can also be used to infer their likely past accretion histories. Even taking into account the caveats expressed above, such simulations indicate that structures such as SPT2349, XLSSC 122 and Coma may represent similar clusters viewed at very different cosmic epochs. From such studies we are beginning to achieve a coherent view of the formation and evolution of the largest gravitationally bound structures in the Universe.

Online content

Any methods, additional references, Nature Research reporting summaries, source data, extended data, supplementary information, acknowledgements, peer review information; details of author contributions and competing interests; and statements of data and code availability are available at https://doi.org/10.1038/s41586-019-1829-4.

1. Kravtsov, A. V. & Borgani, S. Formation of galaxy clusters. *Annu. Rev. Astron. Astrophys.* **50**, 353–409 (2012).
2. Willis, J. P. et al. Distant galaxy clusters in the XMM Large Scale Structure survey. *Mon. Not. R. Astron. Soc.* **430**, 134–156 (2013).
3. Mantz, A. B. et al. The XXL survey. V. Detection of the Sunyaev–Zel'dovich effect of the redshift 1.9 galaxy cluster XLSSU J021744.1–034536 with CARMA. *Astrophys. J.* **794**, 157 (2014).
4. Mantz, A. B. et al. The XXL survey. XVII. X-ray and Sunyaev–Zel'dovich properties of the redshift 2.0 galaxy cluster XLSSC 122. *Astron. Astrophys.* **620**, A2 (2018).
5. Bower, R. G., Lucey, J. R. & Ellis, R. S. Precision photometry of early-type galaxies in the Coma and Virgo clusters: a test of the universality of the colour–magnitude relation. II. Analysis. *Mon. Not. R. Astron. Soc.* **254**, 601–613 (1992).
6. Hashimoto, T. et al. The onset of star formation 250 million years after the Big Bang. *Nature* **557**, 392–395 (2018).
7. Sarazin, C. L. *X-Ray Emission From Galaxy Clusters* (Cambridge Univ. Press, 1988).
8. Roettiger, K., Stone, J. M. & Mushotzky, R. F. Anatomy of a merger: a numerical model of A754. *Astrophys. J.* **493**, 62–72 (1998).
9. Chiang, Y.-K., Overzier, R. A. & Gebhardt, K. Ancient light from young cosmic cities: physical and observational signatures of galaxy proto-clusters. *Astrophys. J.* **779**, 127 (2013).
10. Harrison, I. & Hotchkiss, S. A consistent approach to falsifying ΛCDM with rare galaxy clusters. *J. Cosmol. Astropart. Phys.* **7**, 022 (2013).
11. Gavazzi, R. et al. A weak lensing study of the Coma cluster. *Astron. Astrophys.* **498**, L33–L36 (2009).
12. Miller, T. B. et al. A massive core for a cluster of galaxies at a redshift of 4.3. *Nature* **556**, 469–472 (2018).

Methods

We assume a Lambda cold dark matter (CDM) cosmological model described by the parameters $\Omega_M = 0.286$, $\Omega_\Lambda = 0.714$, $H_0 = 69.6\ \mathrm{km\,s^{-1}\,Mpc^{-1}}$ (ref. [13]). The present-day age of the Universe in this model is 13.72 Gyr. All magnitude information is presented using the AB system.

The HST observations were obtained between 4 November 2017 and 13 January 2018 and comprised one orbit in F105W and 12 orbits in the F140W+G141 filter and grism combination. The 12 F140W+G141 orbits were split into three orbits at each of four orientations using an ABB BBA pattern for exposures in each orbit. The total exposure times in F105W, F140W and G141 were, respectively, 2,612 s, 5,171 s and 26,541 s.

The imaging and spectroscopic observations were reduced with Grizli version 0.3.0 (ref. [14]). Raw HST data products were processed by applying standard image-calibration techniques with additional corrections applied for variable backgrounds (the HST reduction pipeline calwf3 assumes a constant background not appropriate for WFC3 infrared observations) and to mask artefacts such as satellite trail features[15,16]. Relative and absolute astrometric registration was achieved by aligning to reference sources in the Sloan Digital Sky Survey. The final steps included flat fielding and master background subtraction for both the direct and grism images, and drizzling of the individual data frames to produce stacked images.

Reduced data were processed with SExtractor (version 2.5.0; www.astromatic.net/software/sextractor) to generate photometric catalogues. The F140W image was processed using standard WFC3 zero point information with the gain parameter set to the image exposure time. Source detection used a pixel-based inverse variance weighting (pipeline IVM file in SExtractor), whereas source photometry employed a root mean square (pipeline RMS file in SExtractor) variation per pixel weight. The F105W image was processed employing the SExtractor two-image mode with the F140W image used as the detection image. Source fluxes and AB magnitudes were computed within two apertures: a 0.8-arcsecond circular aperture[17,18] and an elliptical aperture based upon the Kron radius (a statistical moment computed from the surface brightness distribution in each object) with the Kron factor set to $k = 0.8$ to avoid excessive source blending in the central cluster regions. Sources with a half-light radius of <0.22 arcseconds were classified as stellar. In the following analysis we consider sources brighter than F140W = 25.5, corresponding to an image signal-to-noise ratio (SNR) >10.

Spectral extraction from the G141 images employed the F140W segmentation map produced by SExtractor (see above) to identify undispersed source positions. These source positions were then employed to construct a full field contamination model of each G141 image. The contamination model initially assumes a spectrally flat continuum for all sources brighter than 25th magnitude in F140W. This provides a first-pass estimate of those pixels contaminated by spectra from more than one source. Spectral traces, represented by 2nd-order polynomial functions, were fitted to all of the above bright sources in each exposure at each orientation. Extracted spectra for these sources were then employed to compute a second-pass contamination model. The model was further refined for 26 bright objects, which were identified as contaminating the spectra of bright red-sequence galaxies. In these cases synthetic stellar population models were fitted to the contaminating spectra and these updated spectral models were propagated to the global contamination model. Employing the above procedures, and with the G141 observations split into four orientations, we were able to obtain a satisfactory contamination model for most sources even in such a densely packed field.

Two-dimensional spectra were extracted separately for each G141 exposure and resulted in a maximum of 48 spectral extractions per source. These spectra were optimally extracted[19] and simultaneously fitted with a suite of galaxy templates[20]. The templates were stepped in redshift over a coarse ($\Delta z = 0.01$) grid from $z = 0.2$–4.0 and subsequently refitted over a fine grid ($\Delta z = 0.0004$) in redshift around peaks in the probability distribution function.

We define the SNR of each spectrum as the average spectral flux per pixel divided by the pipeline-computed noise per pixel integrated over the wavelength interval 1.3–1.55 μm. A galaxy of brightness $\mathrm{F140W_{Kron}} = 24$ typically generates a spectrum of SNR = 5 with a scatter consistent with random noise. We inspected visually all spectra displaying a spectral SNR >2 to assess the reliability of the fitted redshift and template model. We concluded that all spectra displaying SNR ≥ 5 possess a visually reliable redshift measurement and consequently we employ $\mathrm{F140W_{Kron}} = 24$ as the galaxy brightness corresponding to our spectroscopic completeness limit. Furthermore, we determined that sources with visually identified emission lines possess a reliable redshift to a limit of SNR ≥ 3, corresponding to a brightness $\mathrm{F140W_{Kron}} = 24.5$, which we adopt for our spectroscopic completeness limit for emission line sources. Extended Data Fig. 1 shows two examples of extracted grism spectra.

Galaxy membership of the $z = 1.98$ cluster was defined according to a number of criteria that we describe below. We define 'gold' members as those displaying $\mathrm{F140W_{Kron}} = 24$ (24.5 for emission line sources) and $P_{\mathrm{mem}} > 0.5$ where P_{mem} is defined as the integral of the redshift probability distribution function for each galaxy over the interval $1.96 < z < 2.00$. This interval corresponds to $z_{\mathrm{cluster}} \pm 3\sigma_z$ where σ_z is the observed frame velocity dispersion of a 5-keV galaxy cluster expressed in redshift space[21]. There are 33 galaxies in this class (of which four are emission line sources with $24 < \mathrm{F140W_{Kron}} \leq 24.5$). We compute the redshift of XLSSC 122 as the unweighted mean of the 'gold' cluster member redshifts. The redshift is $z = 1.978 \pm 0.010$. We define 'silver' members as those displaying $0.1 < P_{\mathrm{mem}} < 0.5$—a change that adds four new members (one of which is on the red sequence)—for a total of 37. Finally, we create an additional class to identify members of the z = 1.93 foreground structure as those displaying $P'_{\mathrm{mem}} > 0.5$, where P'_{mem} is defined as the integral of the redshift probability distribution function for each galaxy over the interval $1.91 < z < 1.95$ with the same brightness limits as before. There are 13 galaxies in this class. We compute the redshift of this structure as the unweighted mean redshift of these 13 galaxies. The resulting structure redshift is $z = 1.934 \pm 0.007$. This analysis therefore identifies a total of 50 galaxies that are members of either XLSSC 122 or the $z = 1.93$ structure (see Extended Data Table 1 and Fig. 1 for these members plotted on the greyscale HST/WFC3 image).

Figure 3 shows the colour–magnitude diagram for all galaxies identified within the HST field. We identify a total of 30 red-sequence members according to $1.15 < \mathrm{F105W_{ap}} - \mathrm{F140W_{ap}} < 1.65$ and $\mathrm{F140W_{Kron}} < 24$. Of these, 19 are defined as 'gold' cluster members as described above. Of the remaining 11 galaxies, one is a silver cluster member, one is located at $z \approx 2$ with a relatively broad redshift probability distribution function, five are located within the $z = 1.93$ structure and four are located at $z > 2$ yet display spectra affected by source confusion and contamination. We restrict our subsequent red-sequence analysis to the 19 'gold' cluster members. An unweighted, linear, least-squares fit to the red-sequence members generates the angled dotted line shown in Fig. 3. The root-mean-square deviation in colour about this line normalized by the photometric error is 1.72, that is, the observed scatter is 72% larger than expected from the computed colour errors.

At redshifts $z < 1$, the dominant populations of evolved, red galaxies are interpreted to be the result of the prompt suppression of star formation within galaxies accreting into the cluster environment[22]. The details of this process, euphemistically referred to as 'quenching', remain uncertain, with likely physical scenarios including the ram pressure stripping of gas from galaxies falling through the hot, X-ray-emitting, intra-cluster medium[23,24]. The exact mass scale at

which quenching occurs is also debatable, with uncertainty as to whether the suppression of star formation occurs as galaxies are accreted into less massive groups before encountering more massive clusters[25]. With a quenched fraction of 0.51 ± 0.14 at a look-back time of 10.4 Gyr for XLSSC 122, it is clear that the physical processes involved in quenching were established at an even earlier cosmic epoch.

We employ the F105W and F140W photometry of red-sequence galaxies to constrain the stellar age, star formation rate and stellar mass of a set of synthetic stellar population models. The analysis presented in this paper intentionally follows that performed by Andreon et al.[26] and Newman et al.[27] of galaxies within the cluster JKCS 041 at $z = 1.8$. This was done in order to allow as direct a comparison as possible between galaxy populations in two high redshift clusters, albeit observed in different photometric filters.

We employ a grid of simple stellar population models[28] to generate synthetic F105W and F140W photometry. The likelihood of the model photometry given the data is expressed as $L = \exp(-\chi^2/2)$, where:

$$\chi^2 = \sum_i \left(\frac{D_i - M_i}{\sigma_i}\right)^2$$

and D_i represents the measured apparent magnitude in the ith filter, M_i is the apparent magnitude computed from the stellar population model and σ_i is the uncertainty in the measured magnitude. The stellar population models are characterized by an exponentially declining burst of star formation where the star formation rate SFR $\propto \exp(-t/\tau)$. The variable t denotes the time since the burst commenced and τ is the e-folding time. Models are further characterized by a Salpeter[29] initial mass function and solar metallicity. Gas lost during stellar evolution is not recycled and the effects of dust are included by applying a Calzetti attenuation law[30] parameterized by the extinction parameter A_V at 5,500 Å. The stellar population model photometry is normalized per unit stellar mass and is scaled by a total stellar mass variable, M_{star}.

The stellar population model grid spans $8 < \log[t\,(yr)] < 9.7$ and $8 < \log[\tau\,(yr)] < 9.7$. We compute posterior distributions in $\log t$, $\log\tau$ and $\log M_{star}$, employing a Markov chain Monte Carlo algorithm and assuming flat priors. We do not explore the A_V posterior explicitly at this stage. Instead we compute the posterior distributions of the above variables at three explicit values of A_V (0.0, 0.3 and 0.5). Finally, we compute the average luminosity-weighted stellar population age, following refs. [26,31], as:

$$t_w = \frac{t}{1 - e^{-t/\tau}} - \tau$$

The posterior distributions of t_w and M_{star} are displayed in Extended Data Fig. 2 for the 19 'gold' cluster members. Extended Data Fig. 3 displays the one-dimensional posterior distribution in t_w for each cluster member having marginalized over M_{star}. In addition, Fig. 4 compares the average t_w posterior for all cluster members, computed as the product of individual posteriors, for each of the three dust models, $A_V = 0.0$, 0.3 and 0.5. Values of mean luminosity-weighted stellar age and standard deviation are listed in Table 1. For the canonical model employing zero dust absorption the mean stellar age of 2.98 Gyr at $z = 1.98$ corresponds to a mean star formation redshift of $z = 12.0$.

The spread of stellar age values in XLSSC 122 overlaps with those determined for the galaxy cluster JKCS 041 at $z = 1.803$ (ref. [26]), yet the mean stellar age in XLSSC 122 is older, even though the Universe is 0.32 Gyr younger at $z = 1.98$ compared to $z = 1.8$. Although this comparison employs the same analysis methodology, the two clusters are observed using different photometric filters, while the clusters themselves may represent very different structures. It is instructive therefore to further compare our results to the study of Strazzullo et al.[32] who also analysed HST WFC3 F105W and F140W photometry for the $z = 2$ cluster CL1449+0856[33]. Applying a stellar population model characterized by a short (0.25 Gyr) burst of metal-rich (150% the solar value) star formation, they obtain a typical formation redshift of 3 to 5 for galaxies of similar colour and redshift to those analysed in XLSSC 122. Applying a similar model to the data for XLSSC 122, we obtain a typical stellar population age of 1.4 Gyr, corresponding to formation redshift of 3.3, in agreement with ref. [32]. Ultimately, we consider the assumption of a short, metal-rich burst of star formation to be unnecessarily restrictive given the considerable uncertainty regarding the exact physical state of these high-redshift stellar populations and adopt a more flexible approach as outlined in this paper. Overall however, the comparison is instructive because it highlights the key influence of the assumptions governing the stellar population model upon the inferred formation redshift of the luminosity weighted stellar content of the cluster member galaxies. The acquisition of further data, in particular concerning the dust and metal content of the member galaxies of these high-redshift clusters provides a clear observational route to resolving such issues. We therefore emphasize in conclusion that the results of such stellar population modelling, when based upon broad-band photometry, are most conservatively interpreted as indicating the range of physically reasonable input parameters and not as indicating a definitive physical state of the stellar population.

Data availability

All HST data presented in this paper are publicly available at the Hubble Legacy Archive (https://hla.stsci.edu/). The programme number is 15267.

13. Bennett, C. L., Larson, D., Weiland, J. L. & Hinshaw, G. The 1% concordance Hubble constant. *Astrophys. J.* **794**, 135 (2014).
14. Brammer, G. GRIZLI: grism redshift and line analysis software. *Astrophys. Source Code Library record ascl*:**1905**.001 (2019).
15. Brammer, G., Pirzkal, N., McCullough, P. & MacKenty, J. *Time-Varying Excess Earth-Glow Backgrounds In The WFC3/IR Channel*. Instrument Science Report WFC3 2014-03 (Space Telescope Science Institute, 2014).
16. Brammer, G. *Reprocessing WFC3/IR Exposures Affected by Time-Variable Backgrounds*. Instrument Science Report WFC3 2016-16 (Space Telescope Science Institute, 2016).
17. Stanford, S. A. et al. IDCS J1426.5+3508: discovery of a massive, infrared-selected galaxy cluster at $z = 1.75$. *Astrophys. J.* **753**, 164 (2012).
18. Kron, R. G. Photometry of a complete sample of faint galaxies. *Astrophys. J. Suppl. Ser.* **43**, 305–325 (1980).
19. Horne, K. An optimal extraction algorithm for CCD spectroscopy. *Publ. Astron. Soc. Pacif.* **98**, 609–617 (1986).
20. Brammer, G. B., van Dokkum, P. G. & Coppi, P. EAZY: A fast, public photometric redshift code. *Astrophys. J.* **686**, 1503–1513 (2008).
21. Ruel, J. et al. Optical spectroscopy and velocity dispersions of galaxy clusters from the SPT-SZ Survey. *Astrophys. J.* **792**, 45 (2014).
22. Stanford, S. A., Eisenhardt, P. R. & Dickinson, M. The evolution of early-type galaxies in distant clusters. *Astrophys. J.* **492**, 461–479 (1998).
23. Gunn, J. E. & Gott, J. R. III On the infall of matter into clusters of galaxies and some effects on their evolution. *Astrophys. J.* **176**, 1–19 (1972).
24. Butcher, H. & Oemler, A. Jr The evolution of galaxies in clusters. II. The galaxy content of nearby clusters. *Astrophys. J.* **226**, 559–565 (1978).
25. Jung, S. et al. On the origin of gas-poor galaxies in galaxy clusters using cosmological hydrodynamic simulations. *Astrophys. J.* **865**, 156 (2018).
26. Andreon, S. et al. JKCS 041: a Coma cluster progenitor at $z = 1.803$. *Astron. Astrophys.* **565**, A120 (2014).
27. Newman, A. B. et al. Spectroscopic confirmation of the rich $z = 1.80$ galaxy cluster JKCS 041 using the WFC3 grism: environmental trends in the ages and structure of quiescent galaxies. *Astrophys. J.* **788**, 51 (2014).
28. Bruzual, G. & Charlot, S. Stellar population synthesis at the resolution of 2003. *Mon. Not. R. Astron. Soc.* **344**, 1000–1028 (2003).
29. Salpeter, E. E. The luminosity function and stellar evolution. *Astrophys. J.* **121**, 161–167 (1955).
30. Calzetti, D. et al. The dust content and opacity of actively star-forming galaxies. *Astrophys. J.* **533**, 682–695 (2000).
31. Longhetti, M. et al. Dating the stellar population in massive early-type galaxies at $z \sim 1.5$. *Mon. Not. R. Astron. Soc.* **361**, 897–906 (2005).
32. Strazzullo, V. et al. The red sequence at birth in the galaxy cluster Cl J1449+0856 at $z = 2$. *Astrophys. J.* **833**, L20 (2016).
33. Gobat, R. et al. WFC3 grism confirmation of the distant cluster Cl J1449+0856 at $\langle z \rangle = 2.00$: quiescent and star-forming galaxy populations. *Astrophys. J.* **776**, 9 (2013).

Acknowledgements We acknowledge the builders of the XMM-LSS and XXL surveys, on whose work this paper is based. This work is based on observations made with the NASA/ESA Hubble Space Telescope, obtained at the Space Telescope Science Institute, which is operated by the Association of Universities for Research in Astronomy, Inc., under NASA contract NAS5-26555. These observations are associated with programme number 15267. J.P.W. and E.S.N. acknowledge support from NSERC. R.E.A.C., E.S.N., S.W.A., A.L.K., A.M. and R.G.M. acknowledge support from NASA grant number HST-GO-15267.002-A. The Cosmic Dawn Center is funded by the Danish National Research Foundation.

Author contributions J.P.W., R.E.A.C. and E.S.N. analysed the data and wrote the paper. S.W.A., A.L.K., A.M., R.G.M., S.A.S. and G.B. provided guidance on the analysis and commented on the paper.

Competing interests The authors declare no competing interests.

Additional information

Correspondence and requests for materials should be addressed to J.P.W.

Peer review information *Nature* thanks Florence Durret and the other, anonymous, reviewer(s) for their contribution to the peer review of this work.

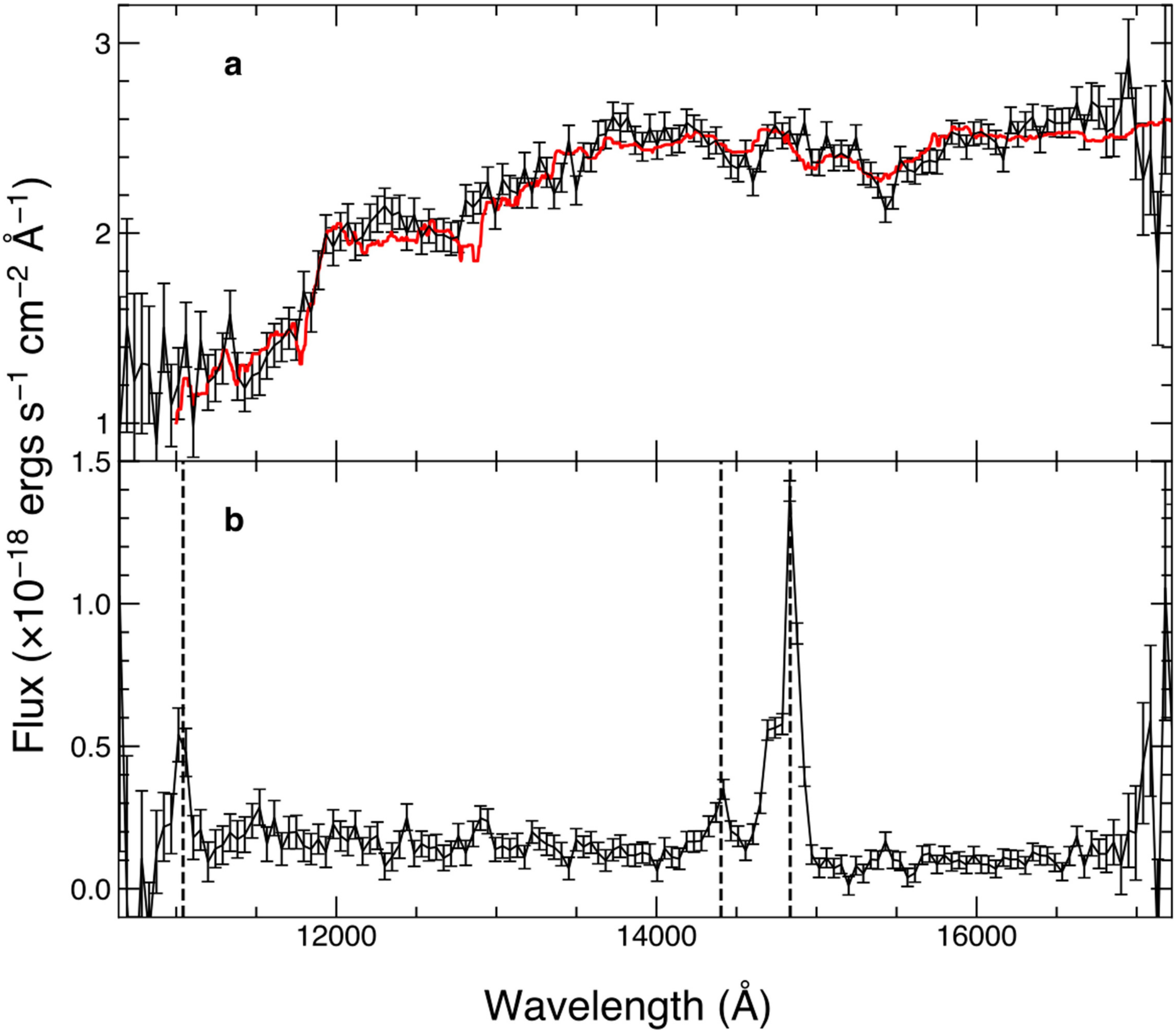

Extended Data Fig. 1 | Example spectra of two member galaxies of XLSSC 122. **a**, The brightest cluster galaxy (ID 526) as the black line with error bars with the best-fitting, redshifted galaxy template shown in red (see Methods). **b**, A fainter cluster member with strong emission lines (ID 1141) as the black line with error bars. Error bars indicate the 1-sigma measurement uncertainty. The vertical dashed lines show the observed frame location of [O II] 3,727 Å, Hβ 4,861 Å and [O III] 5,007 Å at a redshift of 1.963.

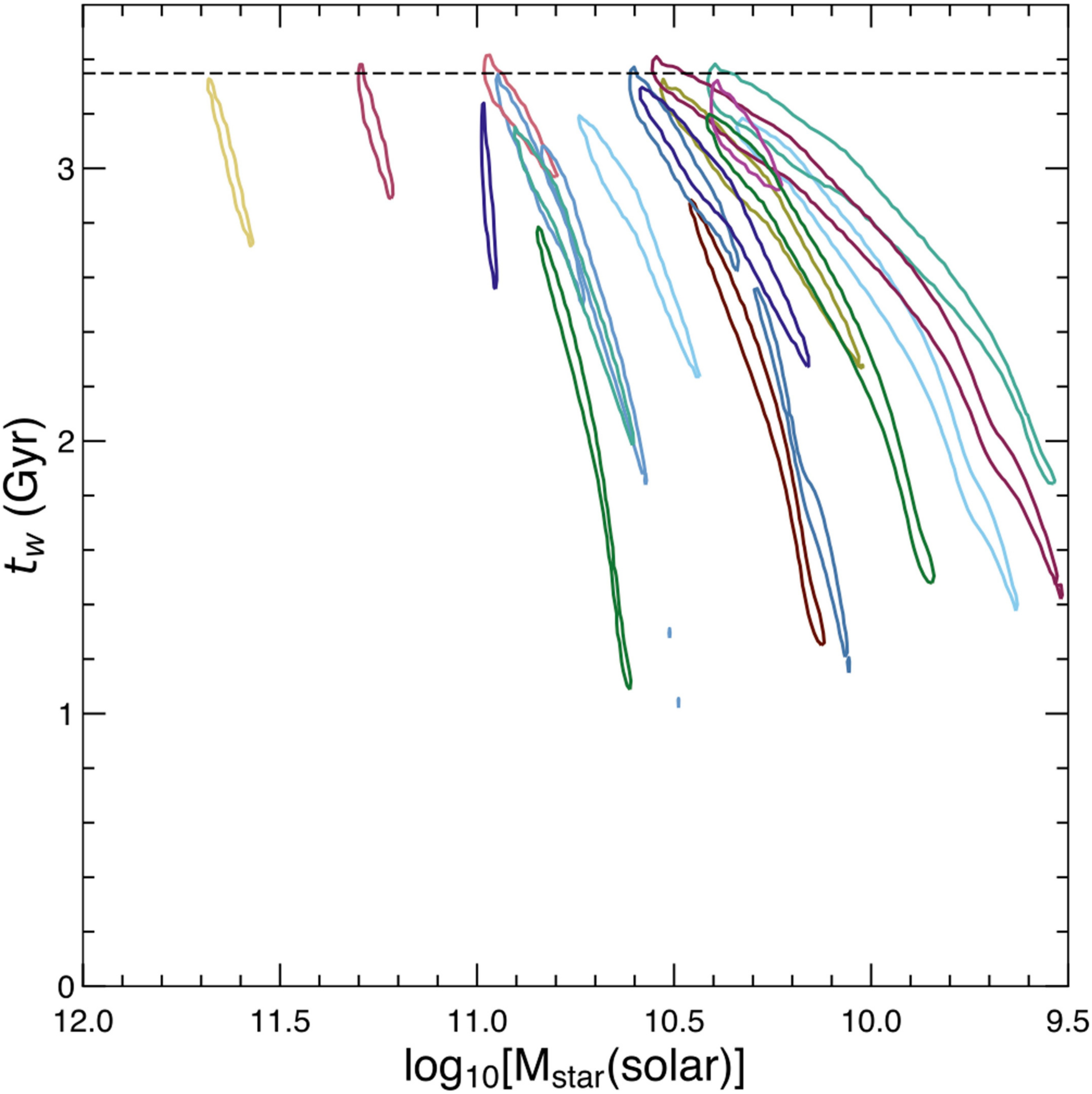

Extended Data Fig. 2 | The luminosity-weighted stellar age versus the mass of red sequence cluster member galaxies. Posterior distributions in mean stellar age (t_w) and log stellar mass for the 19 'gold' members of the cluster red sequence. Only SED models assuming $A_V = 0.0$ are shown. Contours enclose 67% of the posterior probability for each galaxy. The horizontal dashed line indicates an age of 3.35 Gyr, that is, the age of the Universe at a redshift $z = 1.98$ in the assumed cosmological model.

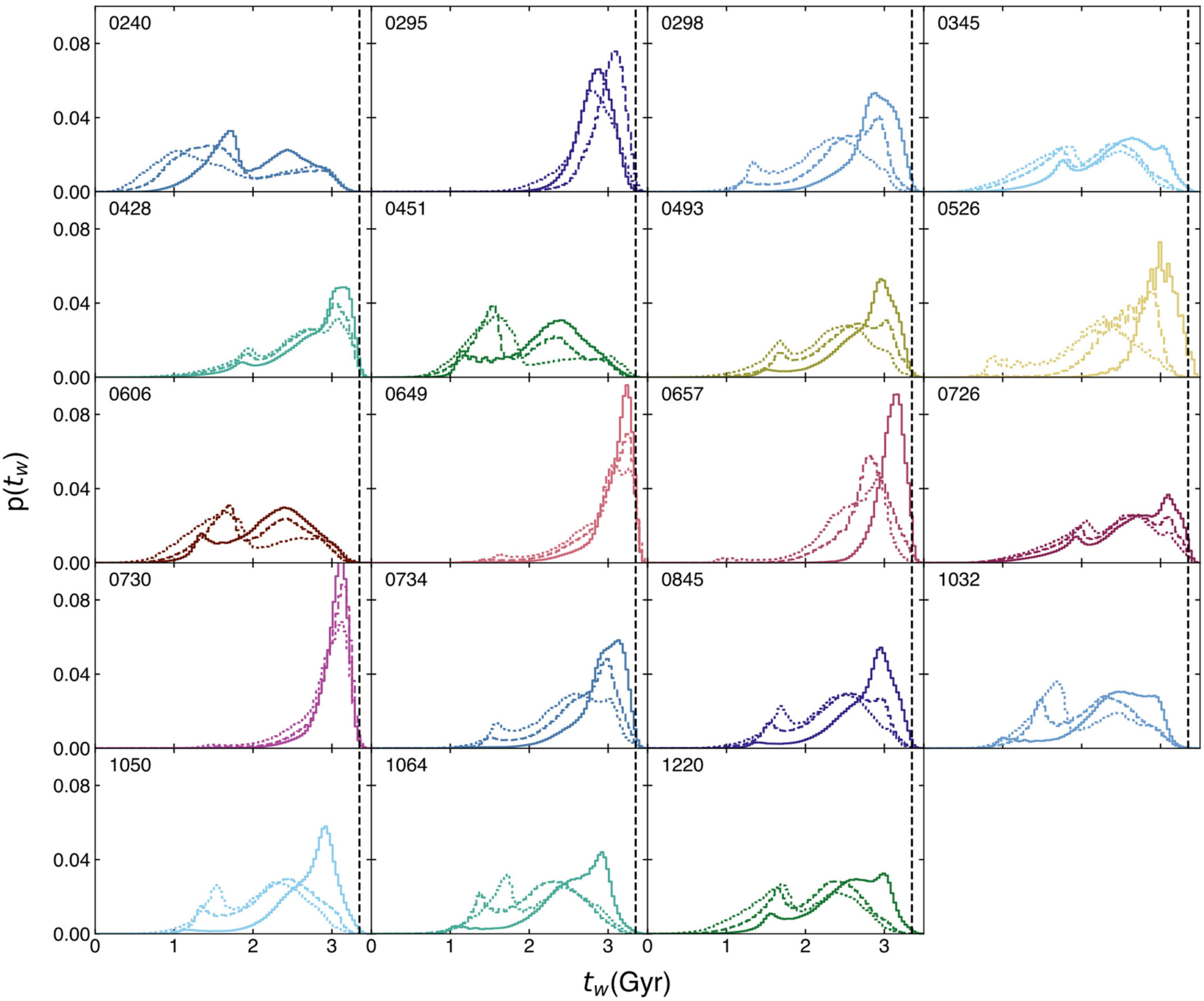

Extended Data Fig. 3 | The luminosity-weighted stellar age distributions for red-sequence cluster member galaxies. Panels show posterior distributions in t_w for each 'gold' member galaxy of XLSSC 122, having marginalized over M_{star}. For convenience, the same colour scheme is employed as in Extended Data Fig. 2. In each panel the solid, dashed and dotted curves display, respectively, SED models characterized by $A_V = 0.0$, 0.3 and 0.5. The vertical dashed line in each panel indicates the age of the Universe at $z = 1.98$.

Extended Data Table 1 | Measured properties of confirmed members of XLSSC 122 and $z = 1.93$ structure

ID	Right Ascension (deg.)	Decl. (deg.)	Magnitude	Colour	Redshift	Notes
526	34.43422	-3.75880	20.64	1.44	1.980	G
451	34.42228	-3.76351	21.95	1.29	1.981	G
657	34.43410	-3.75766	21.67	1.49	1.983	G
1032	34.43245	-3.74992	22.38	1.33	1.982	G
295	34.43503	-3.76795	22.50	1.56	1.987	G
917	34.43563	-3.75314	22.73	0.43	1.963	G
298	34.44715	-3.76801	22.52	1.42	1.993	G
1050	34.43689	-3.75017	22.85	1.37	1.977	G
1064	34.43592	-3.74954	22.34	1.35	1.988	G
606	34.43845	-3.76070	22.99	1.28	1.966	G
240	34.42242	-3.77000	22.62	1.20	1.977	G
845	34.43470	-3.75489	23.38	1.38	1.979	G
372	34.44410	-3.76567	23.08	0.66	1.963	G
734	34.42501	-3.75803	23.39	1.43	1.996	G
1220	34.44335	-3.74500	23.49	1.31	1.976	G
345	34.44185	-3.76667	23.56	1.27	1.991	G
145	34.44478	-3.77286	22.90	0.48	1.981	G
493	34.43300	-3.76318	23.58	1.38	1.962	G
603	34.43939	-3.76030	23.38	0.46	1.979	G
1141	34.43362	-3.74775	23.85	0.47	1.963	G
402	34.44641	-3.76532	23.05	0.66	1.972	G
730	34.43975	-3.75826	23.97	1.61	1.993	G
649	34.43396	-3.75927	22.44	1.54	1.997	G
726	34.43060	-3.75762	23.46	1.28	1.969	G
452	34.41895	-3.76387	23.69	0.45	1.971	G
806	34.44771	-3.75609	23.78	1.02	1.981	G
236	34.45158	-3.77029	23.02	N/A	1.977	G
547	34.43527	-3.76248	23.96	0.28	1.963	G
428	34.44661	-3.76447	23.89	1.38	1.977	G
466	34.41865	-3.76372	24.11	0.49	1.979	GE
229	34.44051	-3.77036	24.01	0.46	1.978	GE
329	34.42761	-3.76741	24.38	0.30	1.972	GE
263	34.42106	-3.76924	24.25	0.50	1.976	GE
642	34.43380	-3.75881	22.40	1.30	2.041	S
1253	34.44633	-3.74360	23.72	0.39	2.018	S
1125	34.43874	-3.74822	24.41	0.62	2.000	SE
522	34.41896	-3.76281	24.39	0.81	1.959	SE
462	34.41950	-3.76258	21.41	1.34	1.930	F
662	34.42184	-3.75893	22.09	0.77	1.943	F
574	34.42053	-3.76141	22.46	1.43	1.931	F
514	34.42648	-3.76251	22.69	1.32	1.935	F
483	34.41598	-3.76315	22.12	1.38	1.930	F
631	34.41783	-3.76003	22.79	0.45	1.933	F
607	34.44899	-3.76058	23.36	0.89	1.941	F
598	34.41724	-3.76130	23.59	1.42	1.939	F
623	34.45558	-3.76030	22.96	N/A	1.948	F
5	34.43687	-3.78074	22.74	N/A	1.931	F
954	34.45186	-3.75109	23.57	0.32	1.927	F
181	34.42259	-3.77175	23.65	0.33	1.936	F
750	34.45794	-3.75725	22.29	N/A	1.923	F

Magnitudes are measured using the F140W filter and employ a Kron-type aperture. Colours are expressed as F105W – F140W magnitudes and are measured in 0.8-arcsecond circular apertures. The notes refer to gold (G) and silver (S) cluster members in addition to galaxies located in the foreground (F) structure; E refers to an emission line galaxy. Decl., declination. ID numbers are output from SExtractor.

Article

Localization and delocalization of light in photonic moiré lattices

https://doi.org/10.1038/s41586-019-1851-6

Received: 9 January 2019

Accepted: 12 September 2019

Published online: 18 December 2019

Peng Wang[1,2,8], Yuanlin Zheng[1,2,8], Xianfeng Chen[1,2], Changming Huang[3], Yaroslav V. Kartashov[4,5], Lluis Torner[4,6], Vladimir V. Konotop[7] & Fangwei Ye[1,2*]

Moiré lattices consist of two superimposed identical periodic structures with a relative rotation angle. Moiré lattices have several applications in everyday life, including artistic design, the textile industry, architecture, image processing, metrology and interferometry. For scientific studies, they have been produced using coupled graphene–hexagonal boron nitride monolayers[1,2], graphene–graphene layers[3,4] and graphene quasicrystals on a silicon carbide surface[5]. The recent surge of interest in moiré lattices arises from the possibility of exploring many salient physical phenomena in such systems; examples include commensurable–incommensurable transitions and topological defects[2], the emergence of insulating states owing to band flattening[3,6], unconventional superconductivity[4] controlled by the rotation angle[7,8], the quantum Hall effect[9], the realization of non-Abelian gauge potentials[10] and the appearance of quasicrystals at special rotation angles[11]. A fundamental question that remains unexplored concerns the evolution of waves in the potentials defined by moiré lattices. Here we experimentally create two-dimensional photonic moiré lattices, which—unlike their material counterparts—have readily controllable parameters and symmetry, allowing us to explore transitions between structures with fundamentally different geometries (periodic, general aperiodic and quasicrystal). We observe localization of light in deterministic linear lattices that is based on flat-band physics[6], in contrast to previous schemes based on light diffusion in optical quasicrystals[12], where disorder is required[13] for the onset of Anderson localization[14] (that is, wave localization in random media). Using commensurable and incommensurable moiré patterns, we experimentally demonstrate the two-dimensional localization–delocalization transition of light. Moiré lattices may feature an almost arbitrary geometry that is consistent with the crystallographic symmetry groups of the sublattices, and therefore afford a powerful tool for controlling the properties of light patterns and exploring the physics of periodic–aperiodic phase transitions and two-dimensional wavepacket phenomena relevant to several areas of science, including optics, acoustics, condensed matter and atomic physics.

One of the most salient properties of an engineered optical system is its capability to affect a light beam in a prescribed manner, such as to control its diffraction pattern or to localize it. The importance of wavepacket localization extends far beyond optics and impacts all branches of science dealing with wave phenomena. Homogeneous or strictly periodic linear systems cannot result in wave localization, and the latter require the presence of structure defects or nonlinearity. Anderson localization[15] is a hallmark discovery in condensed-matter physics. All electronic states in one- and two-dimensional potentials with uncorrelated disorder are localized. Three-dimensional systems with disordered potentials are known to have both localized and delocalized eigenstates[14], separated by an energy known as the mobility edge[16]. Coexistence of localized and delocalized eigenstates has been predicted also in regular quasiperiodic one-dimensional systems, first in the discrete Aubry–André[17] model and later in continuous optical and matter-wave systems[18–20]. Quasiperiodic (or aperiodic) structures, even those that possess long-range order, fundamentally differ both from periodic systems, where all eigenmodes are delocalized Bloch waves, and from disordered media, where all states are localized (in one or two dimensions). Upon variation of the parameters of a quasiperiodic system, it is possible to observe the transition between localized and delocalized states. Such a localization–delocalization transition (LDT)

[1]School of Physics and Astronomy, Shanghai Jiao Tong University, Shanghai, China. [2]State Key Laboratory of Advanced Optical Communication Systems and Networks, Shanghai Jiao Tong University, Shanghai, China. [3]Department of Electronic Information and Physics, Changzhi University, Shanxi, China. [4]ICFO-Institut de Ciencies Fotoniques, The Barcelona Institute of Science and Technology, Castelldefels, Spain. [5]Institute of Spectroscopy, Russian Academy of Sciences, Troitsk, Russia. [6]Universitat Politecnica de Catalunya, Barcelona, Spain. [7]Departamento de Física and Centro de Física Teórica e Computacional, Faculdade de Ciências, Universidade de Lisboa, Lisbon, Portugal. [8]These authors contributed equally: Peng Wang, Yuanlin Zheng. *e-mail: fangweiye@sjtu.edu.cn

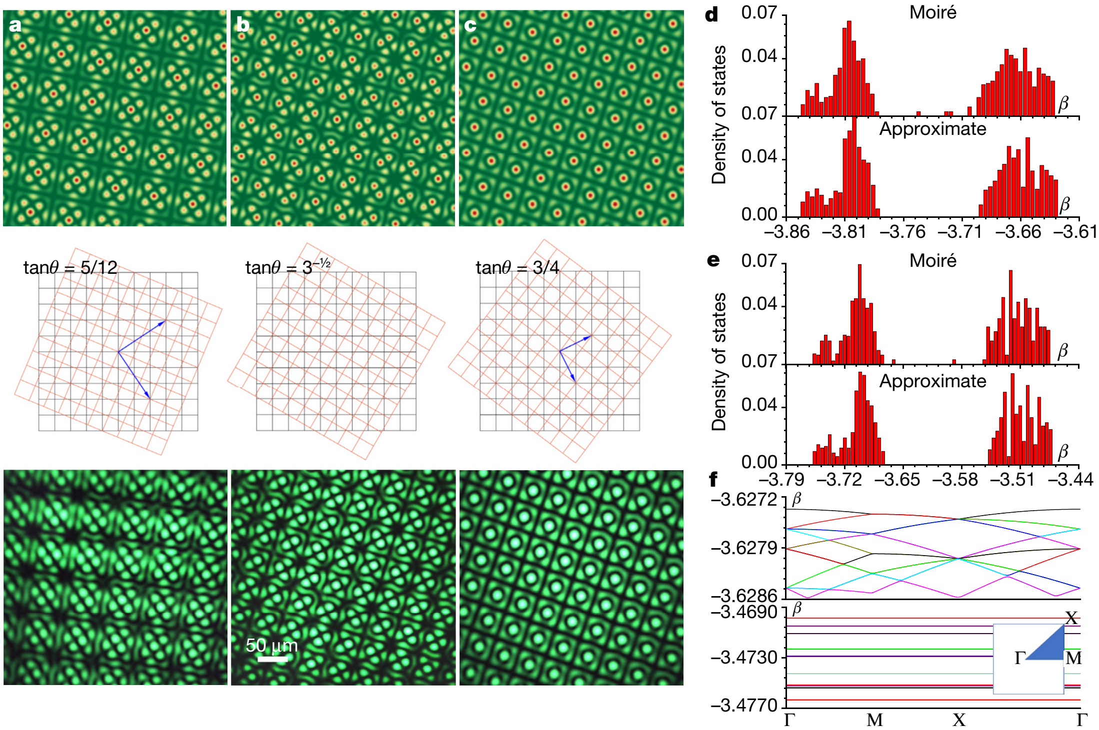

Fig. 1 | Moiré lattices, density of states and band structures. a–c, Moiré lattices with lattice intensity $I(\mathbf{r})$, generated by two interfering square sublattices with $p_1 = p_2$ and axes mutually rotated by the angle indicated in each panel. Top row, calculated patterns. Middle row, schematic discrete representation of two rotated sublattices. Bottom row, experimental patterns at the output face of the crystal. The scale is the same for all images. **d**, **e**, Comparison of the density of states calculated for a moiré lattice (top) and its periodic approximation (bottom) at $p_2 = 0.1$ (**d**) and $p_2 = 0.2$ (**e**). The approximate Pythagorean lattice has period $b_1 = \sqrt{3361}\,\pi$ (see Supplementary Information). **f**, Band structures for a periodic lattice approximating a moiré lattice at $p_2 = 0.1$ (top; 15 upper bands are shown) and $p_2 = 0.2$ (bottom; 68 upper bands are shown). In all cases $p_1 = 1$.

has been observed in one-dimensional quasiperiodic optical[21] and in atomic systems[22,23].

Wave localization is sensitive to the dimensionality of the physical setting. Anderson localization and a mobility edge in two-dimensional systems were first reported in experiments with bending waves[24] and later in optically induced disordered lattices[25]. In quasicrystals, localization has been observed only under the action of nonlinearity[12] and in the presence of strong disorder[13]. Although localization and delocalization of light in two-dimensional systems without any type of disorder and nonlinearity have been predicted theoretically for moiré lattices[26] and very recently for Vogel spirals[27], the phenomenon has never been observed experimentally.

Here we report the first, to our knowledge, experimental realization of reconfigurable photonic moiré lattices with controllable parameters and symmetry. The lattices are induced by two superimposed periodic patterns[28] (sublattices) with either square or hexagonal primitive cells, and have tunable amplitudes and twist angle. Depending on the twist angle, a photonic moiré lattice may have different periodic (commensurable) structure or aperiodic (incommensurable) structure without translational periodicity, but it always features the rotational symmetry of the sublattices. Moiré lattices can also transform into quasicrystals with higher rotational symmetry[11]. The angles at which a commensurable phase (periodicity) of a moiré lattice is achieved are determined by Pythagorean triples in the case of square sublattices[26], or by another Diophantine equation when the primitive cell of the sublattices is not a square (see Methods). For all other rotation angles, the structure is aperiodic albeit regular (that is, it is not disordered). Changing the relative amplitudes of the sublattices allows us to smoothly tune the shape of the lattice without affecting its rotational symmetry.

In contrast to crystalline moiré lattices[1–5], optical patterns are monolayer structures; that is, both sublattices interfere in one plane. As a consequence, light propagating in such media is described by a one-component field. In the paraxial approximation, the propagation of an extraordinarily polarized beam in a photorefractive medium with an optically induced refractive index is governed by the Schrödinger equation for the dimensionless field amplitude[29] $\psi(\mathbf{r}, z)$:

$$\mathrm{i}\frac{\partial\psi}{\partial z} = -\frac{1}{2}\nabla^2\psi + \frac{E_0}{1 + I(\mathbf{r})}\psi \tag{1}$$

Here $\nabla = (\partial/\partial x, \partial/\partial y)$; $\mathbf{r} = (x, y)$ is the radius vector in the transverse plane, scaled to the wavelength $\lambda = 632.8$ nm of the beam used in the experiments; z is the propagation distance, scaled to the diffraction length $2\pi n_e\lambda$; n_e is the refractive index of the homogeneous crystal for extraordinarily polarized light; $E_0 > 0$ is the dimensionless applied d.c. field; $I(\mathbf{r}) \equiv |p_1V(\mathbf{r}) + p_2V(S\mathbf{r})|^2$ is the intensity of the moiré lattice induced by two ordinarily polarized mutually coherent periodic sublattices, $V(\mathbf{r})$ and $V(S\mathbf{r})$, interfering in the (x, y) plane and rotated by angle θ with respect to each other (see Methods); $S = S(\theta)$ is the operator of the two-dimensional rotation; and p_1 and p_2 are the amplitudes of the first and second sublattices, respectively. The number of laser beams creating each sublattice $V(\mathbf{r})$ depends on the desired lattice geometry. The form in which the lattice intensity $I(\mathbf{r})$ enters equation (1) is determined by the mechanism of the photorefractive response.

To visualize the formation of moiré lattices, it is convenient to associate a continuous sublattice $V(\mathbf{r})$ with a discrete one that has lattice vectors determined by the locations of the absolute maxima of $V(\mathbf{r})$. The resulting moiré pattern inherits the rotational symmetry of $V(\mathbf{r})$. At specific angles some nodes of different sublattices may coincide, thereby leading to translational symmetry of the moiré pattern in the commensurable phase; see the primitive translation vectors illustrated by blue arrows in Fig. 1a, c for the case of square sublattices. The rotation

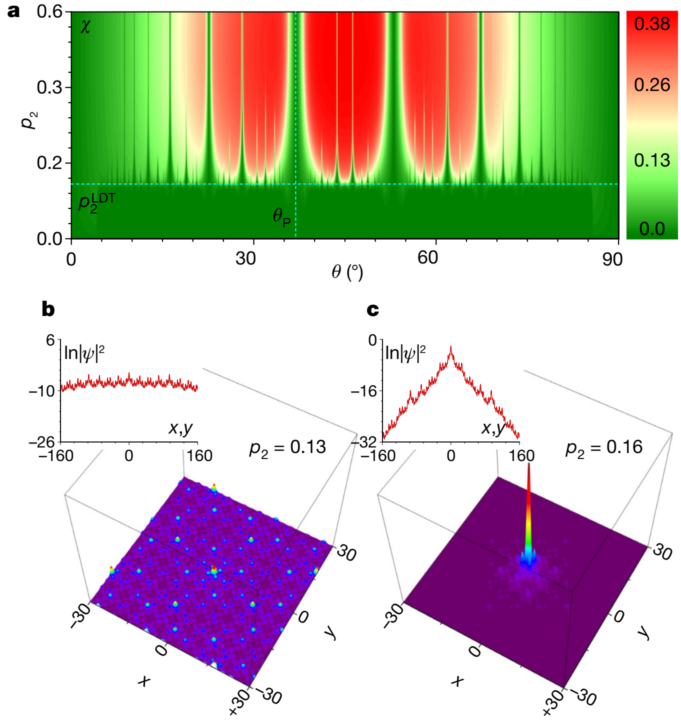

Fig. 2 | Form factor and moiré states. a, Form factor (inverse width) of the eigenmodes with largest β versus rotation angle θ and versus the amplitude of the second sublattice, p_2, at $p_1 = 1$. The horizontal dashed line indicates the sublattice depth p_2^{LDT} at which LDT occurs. The vertical dashed line shows one of the Pythagorean angles $\theta_{\mathrm{P}} = \arctan(3/4)$. **b**, **c**, Examples of mode profiles with the largest β for $p_2 < p_2^{\mathrm{LDT}}$ (**b**) and $p_2 > p_2^{\mathrm{LDT}}$ (**c**). The insets show cuts of the $\ln|\psi|^2$ distribution along the x and y axes.

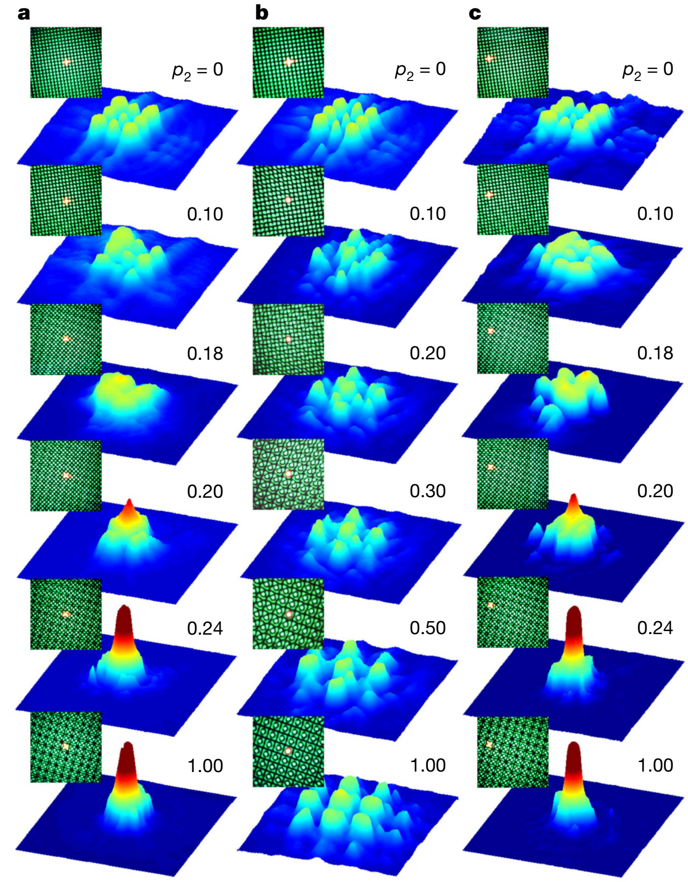

Fig. 3 | Output patterns of light propagating through moiré lattices. a–c, Observed output intensity distributions, illustrating LDT with increasing amplitude p_2 of the second sublattice for rotation angle $\theta = \arctan 3^{-1/2} = \pi/6$ (**a**, **c**) and absence of LDT for the Pythagorean angle $\theta = \arctan(3/4)$ (**b**). The insets show the location of the excitation: central (**a**, **b**) and off-centre (**c**).

angles at which the periodicity of $I(\mathbf{r})$ is achieved are determined by triples of positive integers $(a, b, c) \in \mathbb{N}$ related by a Diophantine equation characteristic for a given sublattice[26] (see Extended Data Table 1).

First, we consider a Pythagorean lattice created by two square sublattices. For rotation angles θ such that $\cos\theta = a/c$ and $\sin\theta = b/c$, where (a, b, c) is a Pythagorean triple (that is, $a^2 + b^2 = c^2$), $I(\mathbf{r})$ is a periodic moiré lattice. Such angles are hitherto referred to as Pythagorean. For all other, non-Pythagorean, rotation angles θ, the lattice $I(\mathbf{r})$ is aperiodic. Figure 1a–c compares calculated $I(\mathbf{r})$ patterns (first row) with lattices created experimentally[29] in a biased SBN:61 photorefractive crystal with dimensions $5 \times 5 \times 20$ mm^3 (third row) for different rotation angles. The second row shows the respective discrete moiré lattices. Figure 1a, c shows periodic lattices, whereas Fig. 1b gives an example of an aperiodic lattice. All results were obtained for $E_0 = 7$, which corresponds to a d.c. electric field of 8×10^4 V m^{-1} applied to the crystal. The amplitude of the first sublattice was set to $p_1 = 1$ in all cases, which corresponds to an average intensity of $I_{\mathrm{av}} \approx 3.8$ mW cm^{-2}. For such parameters, the refractive index modulation depth in the moiré lattice is of the order of $\delta n \approx 10^{-4}$.

Mathematically, incommensurable lattices are almost periodic functions[30]. Any non-Pythagorean twist angle can be approached by a Pythagorean one with any prescribed accuracy (see Supplementary Information). Thus, any finite area of an incommensurable moiré lattice can be approached by a primitive effective cell of some periodic Pythagorean lattice, whereas a more accurate approximation requires a larger primitive cell of the Pythagorean lattice. This property is illustrated in Fig. 1d, e by the quantitative similarities between the densities of states calculated for an incommensurable lattice and its effective-cell approximation. A remarkable property of Pythagorean lattices is the extreme flattening of the higher bands that occurs when the ratio p_2/p_1 exceeds a certain threshold (Fig. 1f). The number of flat bands grows with the size of the area of the primitive cell of the Pythagorean lattice approximation. Thus, an incommensurable moiré lattice can be viewed as the large-area limit of a periodic Pythagorean lattice with extremely flat higher bands. We note that the existence of flat bands for twisted bilayer graphene was discussed in refs. [7,8,31]. Because flat bands support quasi-nondiffracting localized modes, an initially localized beam launched into such a moiré lattice will remain localized. This flat-band physics of moiré lattices, which is fundamentally different from that of Anderson localization in random media, allows us to predict light localization above a threshold value of the ratio p_2/p_1. Furthermore, flat bands support states that are exponentially localized in the primitive cell and that can be well approximated by exponentially localized two-dimensional Wannier functions[32] (see Fig. 2c and Supplementary Information).

To elucidate the impact of the sublattice amplitudes and rotation angle θ on the light localization, we calculated the linear eigenmodes $\psi(\mathbf{r}, z) = w(\mathbf{r})e^{i\beta z}$ (where β is the propagation constant and $w(\mathbf{r})$ is the mode profile) supported by the moiré lattices. To characterize their localization we use the integral form factor $\chi = \left(U^{-2}\iint|\psi|^4 d^2\mathbf{r}\right)^{1/2}$, where $U = \iint|\psi|^2 d^2\mathbf{r}$ is the energy flow (the integration is over the transverse area of the crystal). The form factor is inversely proportional to the mode width: the larger the value of χ, the stronger the localization. The dependence of the form factor of the most localized mode (the mode with largest β) on θ and p_2 is shown in Fig. 2a (for modes with lower values of β, the dependencies are qualitatively similar). One observes a sharp LDT above a certain threshold depth p_2^{LDT} of the second sublattice, at the amplitude of the first sublattice, $p_1 = 1$. Below p_2^{LDT} all modes are extended (Fig. 2b), and above the threshold some modes are

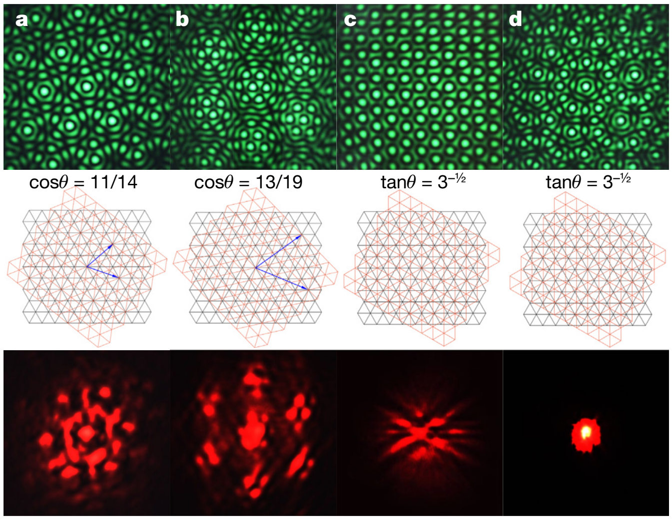

Fig. 4 | Moiré lattices created by superposition of two rotated hexagonal lattices. a–d, Top row, moiré lattices produced by the interference of two hexagonal patterns rotated by angle θ with $p_2 = 1$ (**a**, **b**, **d**) and $p_2 = 0.18$ (**c**). Middle row, schematic discrete representation of two rotated hexagonal sublattices. Bottom row, measured output-intensity distributions for the signal beam at the output face of the crystal. In all cases $p_1 = 1$. Blue arrows in the middle panels of **a** and **b** indicate the primitive translation vectors of the corresponding discrete lattice.

localized (Fig. 2c). This is consistent with the extreme band flattening of the approximate Pythagorean lattice at $p_2 > p_2^{\mathrm{LDT}}$ (Fig. 1f). The inset in Fig. 2c reveals exponential tails for $p_2 > p_2^{\mathrm{LDT}}$, from which the localization length for the most localized mode can be extracted.

Figure 2a shows delocalization for angles θ set by the Pythagorean triples when all modes are extended, regardless of the value of p_2. It also reveals that p_2^{LDT} is practically independent of the non-Pythagorean rotation angle. This is explained by the fact that a large fraction of the power in a localized mode resides in the vicinity of a lattice maximum (that is, at $\mathbf{r} = 0$). In an incommensurable phase, when $I(\mathbf{r}) < I(0)$, for all $\mathbf{r} \neq 0$ the optical potential can be approximated by the Taylor expansion of $E_0/[1 + I(\mathbf{r})]$ with respect to $\mathbf{r}$ near the origin. Such expansion includes the rotation angle θ only in the fourth order (see Supplementary Information) and therefore locally can be viewed as almost isotropic.

To study the guiding properties of the Pythagorean moiré lattices experimentally, we measured the diffraction outputs for beams propagating in lattices corresponding to different rotation angles θ for a fixed input position of the beam, centred or off-centre. The diameter of the Gaussian beam focused on the input face of the crystal was about 23 μm, covering approximately one bright spot (channel) of the lattice profile. The intensity of the input beam was about 10 times lower than the intensity of the lattice-creating beam, I_{av}, to guarantee that the beam did not distort the induced refractive index and that it propagated in the linear regime.

Experimental evidence of LDT in the two-dimensional lattice is presented in Fig. 3, where we compare output patterns for the low-power light beam in the incommensurable ($\tan\theta = 3^{-1/2}$; Fig. 3a and Fig. 3c for central and off-centre excitations, respectively) and commensurable ($\tan\theta = 3/4$, Fig. 3b) moiré lattices, tuning in parallel the amplitude p_2 of the second sublattice. When $p_2 < p_2^{\mathrm{LDT}}$ (in Fig. 3 $p_2^{\mathrm{LDT}} \approx 0.15$), the light beam in the incommensurable lattice notably diffracts upon propagation and expands across multiple local maxima of $I(\mathbf{r})$ in the vicinity of the excitation point. However, when p_2 exceeds the LDT threshold, it is readily visible that diffraction is arrested for both central (Fig. 3a) and off-centre (Fig. 3c) excitations and a localized spot is observed at the output over a large range of p_2 values. In clear contrast, localization is absent for any p_2 value in the periodic lattice associated with the Pythagorean triple (Fig. 3b). Additional proof of the LDT is reported in Extended Data Fig. 1. We compare experimental and theoretical results for propagation at $p_1 = 1$. In an incommensurable lattice, at $p_2 < p_2^{\mathrm{LDT}}$ one observes beam broadening (top row). Localization takes place at $p_2 > p_2^{\mathrm{LDT}}$ (middle row). At a Pythagorean twist angle, localization does not occur even for $p_2 = p_1 = 1$ (bottom row). Simulations of the propagation to much larger distances beyond the available sample length (Extended Data Fig. 2) confirm localization of the beam in the incommensurable lattice at any distance at $p_2 > p_2^{\mathrm{LDT}}$ and its expansion at $p_2 < p_2^{\mathrm{LDT}}$.

The mutual rotation of two identical sublattices allows the generation of commensurable and incommensurable moiré patterns with sublattices of any allowed symmetry. To illustrate the universality of LDT, we created hexagonal moiré lattices using an induction technique similar to that used for single honeycomb photonic lattices[33]. For such lattices, the rotation angles producing commensurable patterns are given by the relation $\tan\theta = b\sqrt{3}/(2a + b)$, where the integers a, b and c solve the Diophantine equation $a^2 + b^2 + ab = c^2$. Two examples are presented in Fig. 4a, b. In such periodic structures, the light beam experiences considerable diffraction for any amplitude of the sublattices, as shown in the bottom row. To observe LDT, one has to induce aperiodic structures. To this end, we set the rotation angle to 30°. In this incommensurable case, we did observe LDT by increasing the amplitude of the second sublattice, keeping the amplitude p_1 fixed. Delocalized and localized output beams are shown in the lower panels of Fig. 4c, d. In Fig. 4c the ideal six-fold rotation symmetry of the output pattern is slightly distorted, presumably owing to the intrinsic anisotropy of the photorefractive response. At $p_2 = p_1$ the moiré pattern acquires a 12-fold rotational symmetry (shown in Fig. 4d), as proposed in ref. [11] as a model of a quasicrystal, and similar to the twisted bilayer graphene quasicrystal reported in ref. [5].

Moiré lattices can be created in practically any arbitrary configuration consistent with two-dimensional symmetry groups, thus allowing the creation of potentials that may not be easily produced in tunable form using material structures. In addition to their direct application to the control of light patterns, the availability of photonic moiré patterns allows the study of phenomena relevant to other areas of physics, particularly to condensed matter, which are harder to explore directly. An outstanding example is the relation between conductivity/transport and the symmetry of incommensurable patterns with long-range order. The concept can be also extended to atomic physics and in particular to Bose–Einstein condensates, where potentials are created using similar geometries (and where Anderson localization has been observed[34]). Finally, we note that whereas most previous studies of moiré lattices were focused on graphene and quasicrystals, our results suggest that the photonic counterpart affords a powerful platform for the creation of synthetic settings to investigate wavepacket localization and flat-band phenomena in two-dimensional systems at large.

Online content

Any methods, additional references, Nature Research reporting summaries, source data, extended data, supplementary information, acknowledgements, peer review information; details of author contributions and competing interests; and statements of data and code availability are available at https://doi.org/10.1038/s41586-019-1851-6.

1. Decker, R. et al. Local electronic properties of graphene on a BN substrate via scanning tunneling microscopy. *Nano Lett*. **11**, 2291–2295 (2011).
2. Woods, C. R. et al. Commensurate–incommensurate transition in graphene on hexagonal boron nitride. *Nat. Phys*. **10**, 451–456 (2014).
3. Cao, Y. et al. Correlated insulator behaviour at half-filling in magic-angle graphene superlattices. *Nature* **556**, 80–84 (2018).
4. Cao, Y. et al. Unconventional superconductivity in magic-angle graphene superlattices. *Nature* **556**, 43 (2018).
5. Ahn, S. J. et al. Dirac electrons in a dodecagonal graphene quasicrystal. *Science* **361**, 782–786 (2018).

6. MacDonald, A. H. Bilayer graphene's wicked, twisted road. *Physics* **12**, 12 (2019).
7. Bistritzer, R. & MacDonald, A. H. Moiré bands in twisted double-layer graphene. *Proc. Natl Acad. Sci. USA* **108**, 12233–12237 (2011).
8. Tarnopolsky, G., Kruchkov, A. J. & Vishwanath, A. Origin of magic angles in twisted bilayer graphene. *Phys. Rev. Lett*. **122**, 106405 (2019).
9. Dean, C. R. et al. Hofstadter's butterfly and the fractal quantum Hall effect in moiré superlattices. *Nature* **497**, 598–602 (2013).
10. San-Jose, P., González, J. & Guinea, F. Non-Abelian gauge potentials in graphene bilayers. *Phys. Rev. Lett*. **108**, 216802 (2012).
11. Stampfli, P. A dodecagonal quasiperiodic lattice in two dimensional. *Helv. Phys. Acta* **59**, 1260–1263 (1986).
12. Freedman, B. et al. Wave and defect dynamics in nonlinear photonic quasicrystals. *Nature* **440**, 1166–1169 (2006).
13. Levi, L. et al. Disorder-enhanced transport in photonic quasicrystals. *Science* **332**, 1541 (2011).
14. Abrahams, E., Anderson, P. W., Licciardello, D. C. & Ramakrishnan, T. V. Scaling theory of localization: absence of quantum diffusion in two dimensions. *Phys. Rev. Lett*. **42**, 673–676 (1979).
15. Brandes, T. & Kettemann, S. *The Anderson Transition and its Ramifications: Localization, Quantum Interference, and Interactions* (Springer, 2003).
16. Mott, N. The mobility edge since 1967. *J. Phys. C* **20**, 3075–3102 (1987).
17. Aubry, S. & André, G. Analyticity breaking and Anderson localization in incommensurate lattices. *Ann. Isr. Phys. Soc*. **3**, 133 (1980).
18. Boers, D. J., Goedeke, B., Hinrichs, D. & Holthaus, M. Mobility edges in bichromatic optical lattices. *Phys. Rev. A* **75**, 063404 (2007).
19. Modugno, M. Exponential localization in one-dimensional quasi-periodic optical lattices. *New J. Phys*. **11**, 033023 (2009).
20. Li, C., Ye, F., Kartashov, Y. V., Konotop, V. V. & Chen, X. Localization–delocalization transition in spin–orbit-coupled Bose–Einstein condensate. *Sci. Rep*. **6**, 31700 (2016).
21. Lahini, Y. et al. Observation of a localization transition in quasiperiodic photonic lattices. *Phys. Rev. Lett*. **103**, 013901 (2009).
22. Roati, G. et al. Anderson localization of a non-interacting Bose–Einstein condensate. *Nature* **453**, 895–898 (2008).
23. Lüschen, H. P. et al. Single-particle mobility edge in a one-dimensional quasiperiodic optical lattice. *Phys. Rev. Lett*. **120**, 160404 (2018).
24. Ye, L., Cody, G., Zhou, M., Sheng, P. & Norris, A. N. Observation of bending wave localization and quasi mobility edge in two dimensions. *Phys. Rev. Lett*. **69**, 3080–3083 (1992).
25. Schwartz, T., Bartal, G., Fishman, S. & Segev, M. Transport and Anderson localization in disordered two-dimensional photonic lattices. *Nature* **446**, 52–55 (2007).
26. Huang, C. et al. Localization delocalization wavepacket transition in Pythagorean aperiodic potentials. *Sci. Rep*. **6**, 32546 (2016).
27. Sgrignuoli, F., Wang, R., Pinheiro, F. & Dal Negro, L. Localization of scattering resonances in aperiodic Vogel spirals. *Phys. Rev. B* **99**, 104202 (2019).
28. Fleischer, J., Segev, M., Efremidis, N. & Christodoulides, D. Observation of two-dimensional discrete solitons in optically induced nonlinear photonic lattices. *Nature* **422**, 147–150 (2003).
29. Efremidis, N. K., Sears, S., Christodoulides, D. N., Fleischer, J. W. & Segev, M. Discrete solitons in photorefractive optically induced photonic lattices. *Phys. Rev. E* **66**, 046602 (2002).
30. Franklin, P. The elementary theory of almost periodic functions of two variables. *J. Math. Phys*. **5**, 40–54 (1926).
31. Suárez Morell, E., Correa, J. D., Vargas, P., Pacheco, M. & Barticevic, Z. Flat bands in slightly twisted bilayer graphene: tight-binding calculations. *Phys. Rev. B* **82**, 121407 (2010).
32. Brouder, C., Panati, G., Calandra, M., Mourougane, C. & Marzar, N. Exponential localization of Wannier functions in insulators. *Phys. Rev. Lett*. **98**, 046402 (2007).
33. Peleg, O. et al. Conical diffraction and gap solitons in honeycomb photonic lattices. *Phys. Rev. Lett*. **98**, 103901 (2007).
34. Billy, J., Sanchez-Palencia, L., Bouyer, P. & Aspect, A. Direct observation of Anderson localization of matter waves in a controlled disorder. *Nature* **453**, 891–894 (2008).

Publisher's note Springer Nature remains neutral with regard to jurisdictional claims in published maps and institutional affiliations.

Methods

Experimental setup

The experimental setup is illustrated in Extended Data Fig. 3. The lattice is created using optical induction, as described in ref. [29] and was first realized experimentally in ref. [28]. A continuous-wave frequency-doubled Nd:YAG laser at a wavelength of $\lambda = 532$ nm is divided by a polarizing beam splitter into two polarization components, which are sent to path a and path b separately. Light in path a is extraordinarily polarized and it is used to image the induced potential in the photorefractive crystal (bottom row of Fig. 1). Light in path b is ordinarily polarized and it is used to write the desirable potential landscape in a photorefractive SBN:61 crystal with dimensions $5 \times 5 \times 20$ mm^3 and extraordinary refractive index $n_e = 2.2817$. Before entering the crystal, the ordinarily polarized light beam in path b is modulated by masks 1 and 2 and is transformed into a superposition of two rotated periodic patterns. Their relative strength p_2/p_1—more precisely, the strength of the second lattice—as well as the twist angle θ are controlled by the polarizer-based mask 1 and the amplitude mask 2. A He–Ne laser with wavelength $\lambda = 633$ nm shown in path c provides an extraordinarily polarized beam focused onto the front facet of the crystal, which serves as a probe beam for studying light propagation in the induced potential. We record the output light intensity pattern using a charge-coupled device (CCD) at the exit facet of the crystal after a propagation distance of 20 mm.

Characteristics of moiré lattices used in experiment

Two types of moiré lattices were used in the experiments, and their characteristics are summarized in Extended Data Table 1. In all cases the centre of rotation in the (x, y) plane was chosen to be coincident with a node of one of the sublattices.

Data availability

The data that support the findings of this study are available from the corresponding author upon reasonable request.

Code availability

The codes that support the findings of this study are available from the corresponding author upon reasonable request.

Acknowledgements P.W. and F.Y. acknowledge support from the NSFC (grant numbers 91950120, 11690033 and 61475101). Y.V.K. and L.T. acknowledge support from the Severo Ochoa Excellence Programme (SEV-2015-0522), Fundacio Privada Cellex, Fundacio Privada Mir-Puig and CERCA/Generalitat de Catalunya. F.Y. thanks Z. Chen, Y. Hu and D. Song for technical discussions on the experiment with the SBN crystals.

Author contributions All authors contributed significantly to the study.

Competing interests The authors declare no competing interests.

Additional information

Supplementary information is available for this paper at https://doi.org/10.1038/s41586-019-1851-6.

Correspondence and requests for materials should be addressed to F.Y.

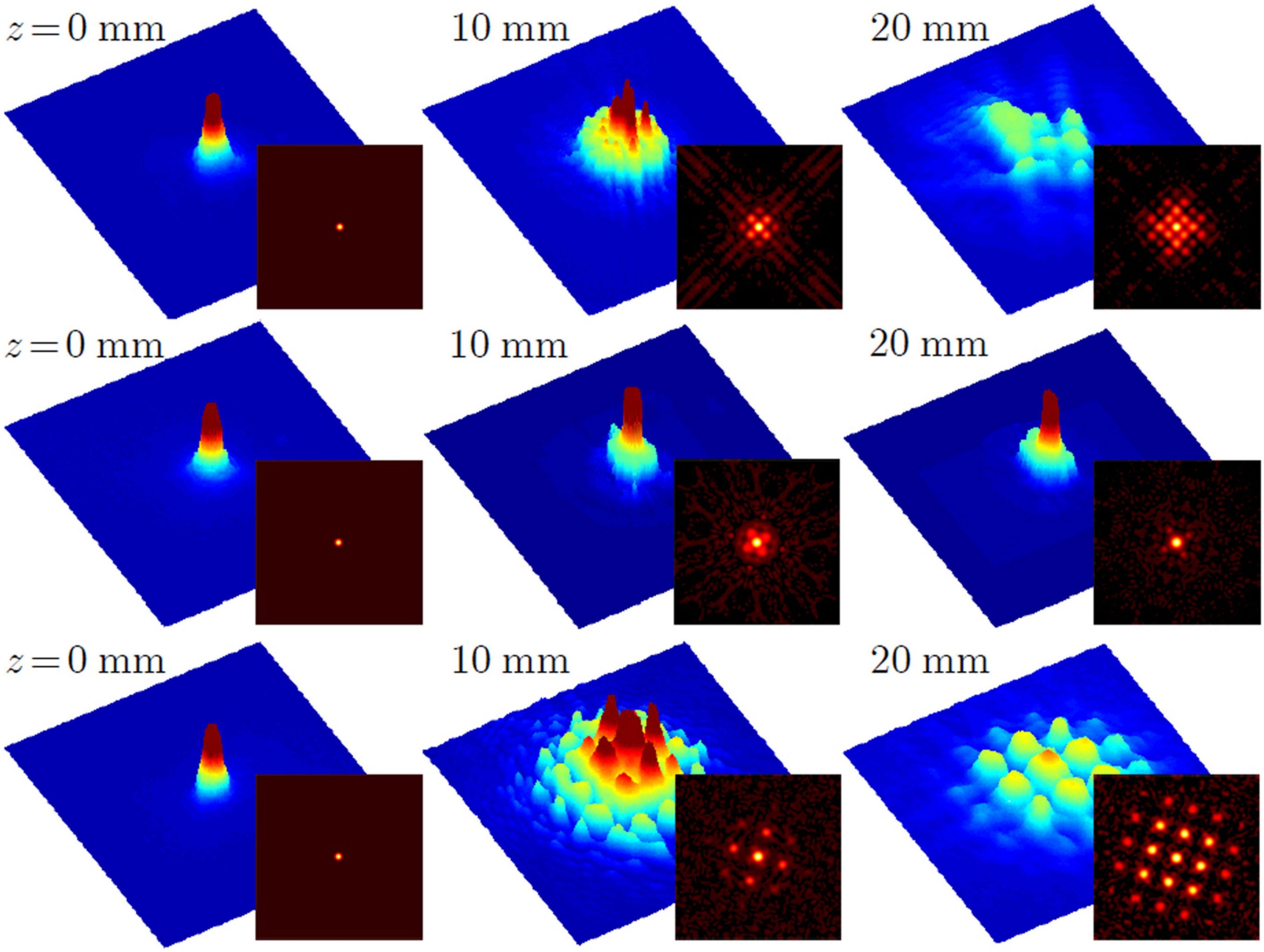

Extended Data Fig. 1 | Evolution of light in moiré lattices. Experimentally observed intensity distributions of the probe beam (colour-surface plots) and corresponding theoretically calculated distributions (insets) at different propagation distances z, for $\tan\theta = 3^{-1/2}$ and $p_2 = 0.1$ (below the LDT point; top row), $\tan\theta = 3^{-1/2}$ and $p_2 = 1$ (above the LDT point; middle row) and $\tan\theta = 3/4$ and $p_2 = 1$ (bottom row). The two top rows correspond to the incommensurable Pythagorean lattice shown in Fig. 1b. The third row corresponds to the commensurable lattice shown in Fig. 1c.

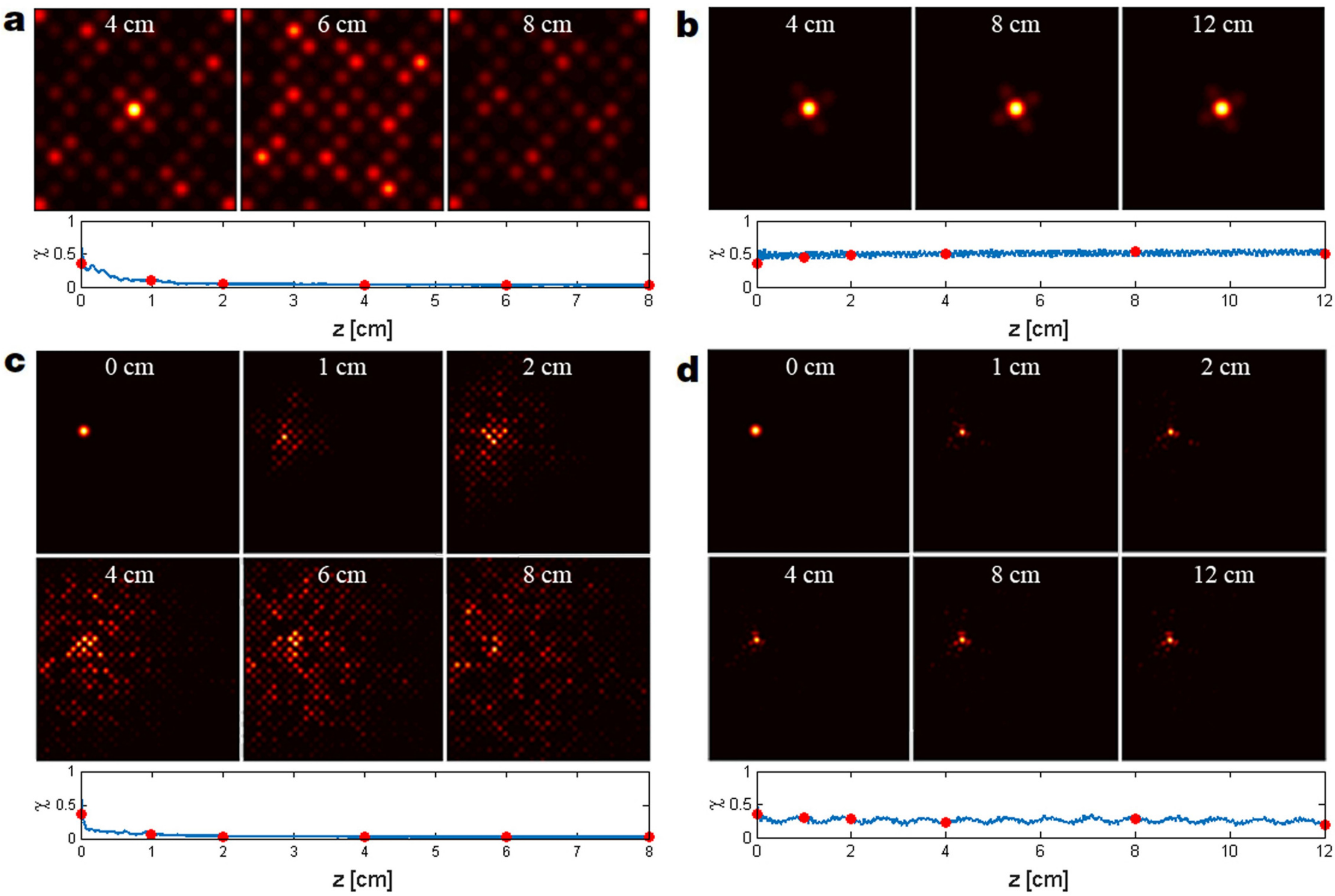

Extended Data Fig. 2 | Numerical simulation of light propagation to distances beyond the crystal length. a, **b**, Numerical simulations of the light-beam propagation in the incommensurable moiré lattice for central excitation, corresponding to the top and middle rows of Extended Data Fig. 1, but for larger distances, exceeding the sample length. **c**, **d**, Similar numerical results, but for an off-centre excitation position in the moiré lattice. $p_2 = 0.1$ (**a**, **c**), $p_2 = 1.0$ (**b**, **d**), $\theta = \pi/6$. In all cases, a Gaussian beam exciting a single site of the potential is assumed.

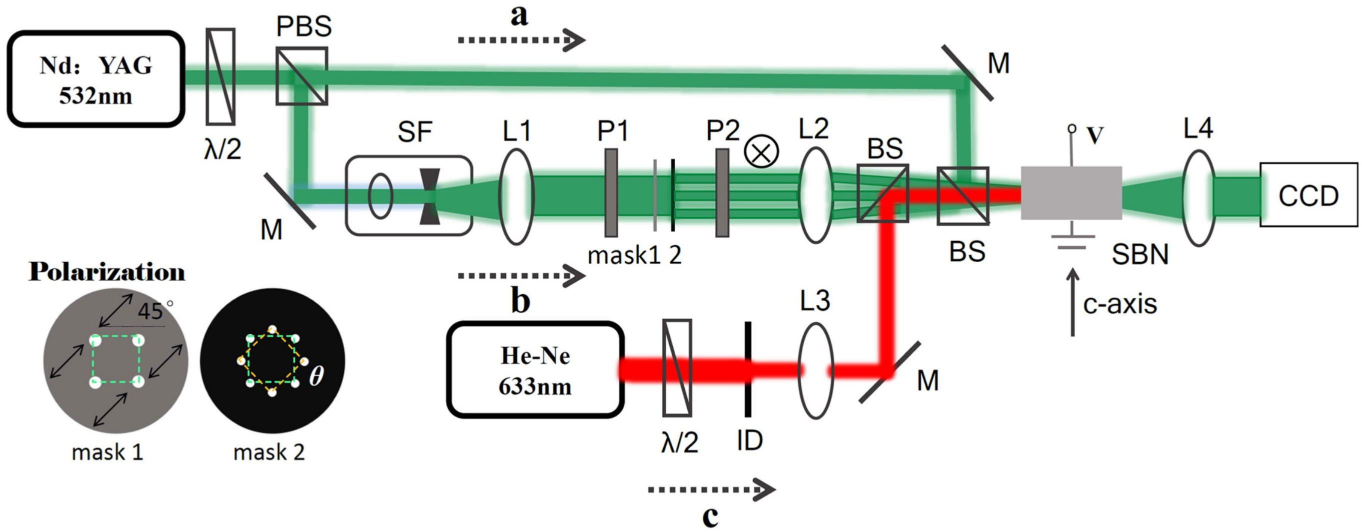

Extended Data Fig. 3 | Experimental setup. $\lambda/2$, half-wave plate; PBS, polarizing beam splitter; SF, spatial filter; L, lens; BS, beam splitter; ID, iris diaphragm; M, mirror; P, polarizer; SBN, strontium barium niobate crystal; CCD, charged-coupled device. Mask 2 is an amplitude mask used to produce two group of sub-lattices with rotation angle θ, and mask 1 is made of a polarizer film.

Extended Data Table 1 | Characteristics of the moiré lattices used in the experiments

Moiré lattice $I(\boldsymbol{r})$	Sublattice $V(\boldsymbol{r})$	Diophantine equation	$\tan\theta$
Pythagorean	$\cos(2x)+\cos(2y)$	$a^2+b^2=c^2$	b/a
hexagonal	$\sum_{n=1}^{3}\cos\left[2(x\cos\theta_n+y\sin\theta_n)\right]$	$a^2+b^2+ab=c^2$	$\sqrt{3}b/(2a+b)$

For hexagonal lattices $\theta_1 = 0$, $\theta_2 = 2\pi/3$ and $\theta_3 = 4\pi/3$.

Article

Inverse transition of labyrinthine domain patterns in ferroelectric thin films

https://doi.org/10.1038/s41586-019-1845-4

Received: 9 May 2018

Accepted: 10 September 2019

Published online: 1 January 2020

Y. Nahas[1]*, S. Prokhorenko[1], J. Fischer[2], B. Xu[3], C. Carrétéro[2], S. Prosandeev[1,4], M. Bibes[2], S. Fusil[2,5], B. Dkhil[6], V. Garcia[2] & L. Bellaiche[1]

Phase separation is a cooperative process, the kinetics of which underpin the orderly morphogenesis of domain patterns on mesoscopic scales[1,2]. Systems of highly degenerate frozen states may exhibit the rare and counterintuitive inverse-symmetry-breaking phenomenon[3]. Proposed a century ago[4], inverse transitions have been found experimentally in disparate materials, ranging from polymeric and colloidal compounds to high-transition-temperature superconductors, proteins, ultrathin magnetic films, liquid crystals and metallic alloys[5,6], with the notable exception of ferroelectric oxides, despite extensive theoretical and experimental work on the latter. Here we show that following a subcritical quench, the non-equilibrium self-assembly of ferroelectric domains in ultrathin films of $Pb(Zr_{0.4}Ti_{0.6})O_3$ results in a maze, or labyrinthine pattern, featuring meandering stripe domains. Furthermore, upon increasing the temperature, this highly degenerate labyrinthine phase undergoes an inverse transition whereby it transforms into the less-symmetric parallel-stripe domain structure, before the onset of paraelectricity at higher temperatures. We find that this phase sequence can be ascribed to an enhanced entropic contribution of domain walls, and that domain straightening and coarsening is predominantly driven by the relaxation and diffusion of topological defects. Computational modelling and experimental observation of the inverse dipolar transition in $BiFeO_3$ suggest the universality of the phenomenon in ferroelectric oxides. The multitude of self-patterned states and the various topological defects that they embody may be used beyond current domain and domain-wall-based[7] technologies by enabling fundamentally new design principles and topologically enhanced functionalities within ferroelectric films.

To investigate polarization self-patterning, we use an ab initio-based effective Hamiltonian approach[8] and examine ultrathin films of $Pb(Zr_{0.4}Ti_{0.6})O_3$ (see Methods), as these widely used quasi-two-dimensional ferroelectric systems are known to exhibit various modulated phases depending on the interplay between strain and the amount of screening of surface charges[8–13].

It is worth noting that two underlying nested symmetry-breaking processes are at play in these systems and involve two distinct dynamical length scales. Whereas compressive strain introduces crystalline anisotropy and favours dipoles with orientation perpendicular to the film plane[1,8] (cubic symmetry is reduced to a quasi-Z_2 symmetry), the depolarizing field arising from incomplete screening of surface charges essentially imposes zero net polarization, and instead favours the formation of multiple mesoscopic domains as a result of the spontaneous breaking of the residual discrete symmetry. These domains of opposite polarization alternate along in-plane directions, and each consists of ferroelectrically ordered ensembles of dipoles. More precisely, while an individual dipole retains the freedom to flip between the [001] and [00$\bar{1}$] out-of-plane directions, an individual domain, as an emergent mesoscopic degree of freedom, has the propensity to align along either the [100] (horizontal) or the [010] (vertical) in-plane tetragonal directions, owing to the underlying square lattice geometry[1]. Naturally, the dynamics pertaining to the motion and relaxation of domains is slower than that of individual dipole fluctuations, and this very fact poses important questions as to what extent domain dynamics and their morphology will be kinetically constrained.

One manifestation of this kinetic constraint resides in the possibility of obtaining two distinct modulated phases at low temperatures depending on the cooling rate. While the well known parallel-stripe domain pattern (Fig. 1a) emerges as the ground state upon adiabatically cooling (annealing) the system[8,11], the labyrinthine domain polarization pattern (Fig. 1b) onsets upon abruptly cooling (subcritical quenching) the system. The latter pattern consists of convoluted stripes and meandering domains and has a very close internal energy that is only 0.6% higher than that of the ground state. Interestingly, inquiring into the stability of the labyrinthine state at $T \to 0$ K, we find that the eigenvalues of the Hessian matrix of the Hamiltonian are closely distributed around zero, with 75% of them being negative, indicating that the labyrinthine

[1]Physics Department and Institute for Nanoscience and Engineering, University of Arkansas, Fayetteville, AR, USA. [2]Unité Mixte de Physique, CNRS, Thales, Univ. Paris Sud, Université Paris-Saclay, Palaiseau, France. [3]School of Physical Science and Technology, Soochow University, Suzhou, China. [4]Institute of Physics and Physics Department, Southern Federal University, Rostov-na-Donu, Russia. [5]Université d'Evry, Université Paris-Saclay, Evry, France. [6]Laboratoire Structures, Propriétés et Modélisation des Solides, CentraleSupélec, UMR CNRS 8580, Université Paris-Saclay, Gif-sur-Yvette, France. *e-mail: yousra.nahas@gmail.com

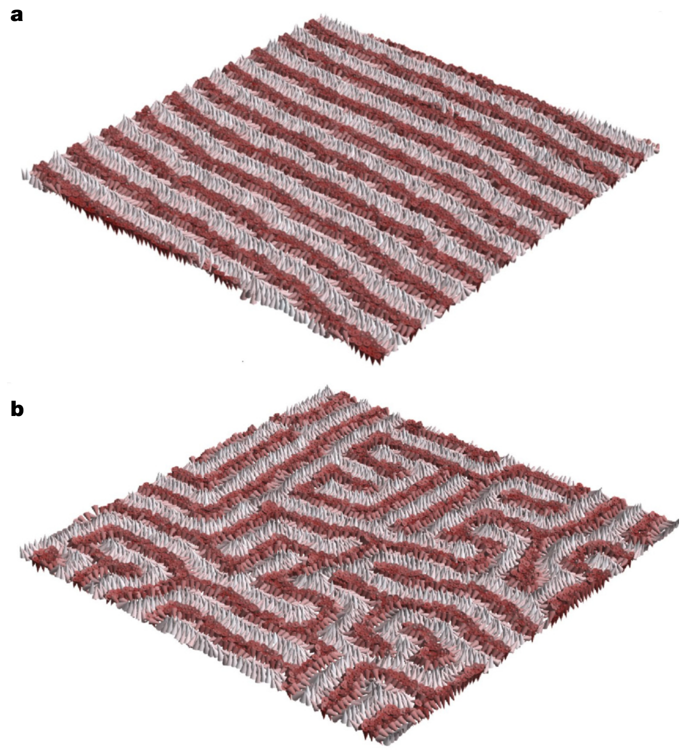

Fig. 1 | Stripes versus maze at low temperature. a, Ground-state dipolar configuration (parallel stripes) in the middle layer of an 80 × 80 × 5 unit-cell film of $Pb(Zr_{0.4}Ti_{0.6})O_3$ as obtained upon slowly decreasing the temperature from 650 K to 10 K. **b**, Dipolar configuration of the maze or labyrinthine pattern as obtained upon abruptly cooling the system from 650 K to 10 K. Grey (red) dipoles are oriented along the [001] ([00$\bar{1}$]) pseudo-cubic direction.

state is weakly unstable[14]. Furthermore, we find that at 10 K, the labyrinthine state has a quasi-vanishing relaxation rate without evidence of a growing static cooperative length, similarly to a glass-like kinetically arrested state[15,16]. The slightly off-equilibrium labyrinthine structure only asymptotically departs from the state in which it initially vitrified, hence being effectively stationary at $T \to 0$ K in the thermodynamic limit. The frozen labyrinthine state retains some of the properties of the high-temperature paraelectric state (similarly to the common local structure exhibited by glasses and their liquid phases), such as the overall absence of long-range orientational order at the mesoscale mirrored by its structure factor, which has a ring-shaped spectral weight (inset of Fig. 2b). However, the spectral weight distribution is deformed by the underlying four-fold square lattice anisotropy (four-peaked crown), signalling that the labyrinthine domain pattern is only weakly disjoint from the square symmetry of the lattice geometry. In fact, upon subcritical quenching of the system, we discern a local tendency of adjacent domains to order by adopting one of the two lower equilibrium states of the Hamiltonian (either horizontal [100] or vertical [010] periodicity of parallel stripes is associated with the two-fold-degenerate ground state). This local ordering process ensures a local minimization of the energy and can extend only up to a certain finite length scale, beyond which collective mismatch and surface tension effects hinder further ordering[17,18]. In this regard, the low-temperature labyrinthine state can be apprehended as a mosaic pattern consisting of a spatial mixture of tiles with different realization of local order. This labyrinthine state inherently features frustration due to the unresolvable competition between local interactions and the long-ranged dipolar interaction[1,16,19].

Upon heating the labyrinthine state, thermal activation effects come into play, and the resulting kinetic unfreezing elicits the phenomenon of inverse transition, whereby a state with higher symmetry transforms into a lower-symmetry one. This is shown in Fig. 2b–g, where upon increasing the temperature, the more symmetric labyrinthine phase obtained by quenching the system from 650 K to 10 K experiences a lessening of its junctions, resulting in a transient reordering and the occurrence of the less-symmetric parallel-stripe state at higher temperatures. This inverse transition onsets at a temperature of $T_{inv} \approx 200$ K, before transitioning to the paraelectric state at a transition temperature of $T_c \approx 380$ K (Extended Data Figs. 1, 2). As the temperature increases, the distribution of the spectral weight of the structure factor gradually yields two primary spots along the direction of the Brillouin zone, perpendicular to the direction of the stripes in real space, mirroring the acquired long-range orientational order. This inverse symmetry breaking can be quantified using the order parameter $O_{hv} = (n_h - n_v)/n$, where n is the total number of first nearest-neighbour pairs of dipoles having the opposite sign to their z component, and n_h (n_v) is the number of horizontal (vertical) bonds among such dipoles[1,20]. The average of this quantity over 100 labyrinthine realizations is shown in Fig. 2a and its evolution with temperature captures the sequential onset of three distinct phases: a low-temperature labyrinthine phase with no net orientation, which bears the symmetry of the underlying lattice; a mid-temperature broken-symmetry phase with distinguishable orientation of domains that are all oriented as stripes along a common axis; and a high-temperature disordered paraelectric phase characterized by the dissolution of domains and domain walls.

As a general energetic feature of domain walls within modulated phases[1], we find that the gain realized by short-range interactions is counterbalanced by the cost of the dipolar interaction, which plays an important—if not dominant—role (Extended Data Figs. 3, 4). The excess length of domain walls within the labyrinthine state therefore yields an excess in the dipolar cost when compared with the parallel-stripe domain structure. We find that this excess gradually reduces with increasing temperature as a result of the straightening of meandering stripes, and vanishes at T_{inv} (Extended Data Fig. 5a).

We experimentally observed such an inverse-transition phenomenon in $BiFeO_3$ thin films (Fig. 3a), in agreement with our first-principles computations (Fig. 3c). The 95-nm-thick $BiFeO_3$ layer was grown by pulsed-laser deposition on a (110)-oriented orthorhombic $DyScO_3$ substrate at 933 K (Extended Data Figs. 9, 10) and, after having been cooled to room temperature, exhibited a labyrinthine domain structure (Fig. 3a; as-grown). We then performed series of experiments in which the as-grown sample was first annealed for 1 h at an elevated target temperature and then cooled to room temperature with an effective cooling rate of 2 K min^{-1}. The ferroelectric domain landscape observed at room temperature after annealing at 773 K, 1,023 K and 1,073 K is shown in Fig. 3a. As can be readily seen, for target temperatures up to 1,023 K the labyrinthine morphology is retained, while following the 1,073 K annealing, a profound modification to a perfect stripe domain pattern onsets. The increased ordering of the ferroelectric array was confirmed macroscopically by X-ray diffraction (XRD) measurements (Extended Data Fig. 12) following the pioneering work of Streiffer et al.[12]. These experiments indicate an inverse transition (T_{inv}) between 1,023 K and 1,073 K, while no transition to the paraelectric state could be detected by XRD up to 1,160 K (Extended Data Fig. 11). Using conducting atomic force microscopy measurements, we also found that elementary point defects (Fig. 3b) are characterized by enhanced conduction that can be up to 50 times larger than the conduction at straight segments of domain walls. Indeed, we found that the typical current level is 0.2 pA in domains, 0.5–1.0 pA at domain walls, 15 pA at end-point defects and 50 pA at three-fold junctions. The inverse transition in $BiFeO_3$ is also seen in our first-principles effective Hamiltonian simulations[21–23], which yield $T_{inv} \approx 1,100$ K and $T_c \approx 1,300$ K for $BiFeO_3$ films (Fig. 3c). Interestingly, the antiferrodistortive (AFD) degrees of freedom in $BiFeO_3$, albeit coupled to the ferroelectric order parameter[24], do not hamper the onset of the inverse transition (Extended Data Figs. 6, 7). These first-principles-obtained numerical results, along with our experimental

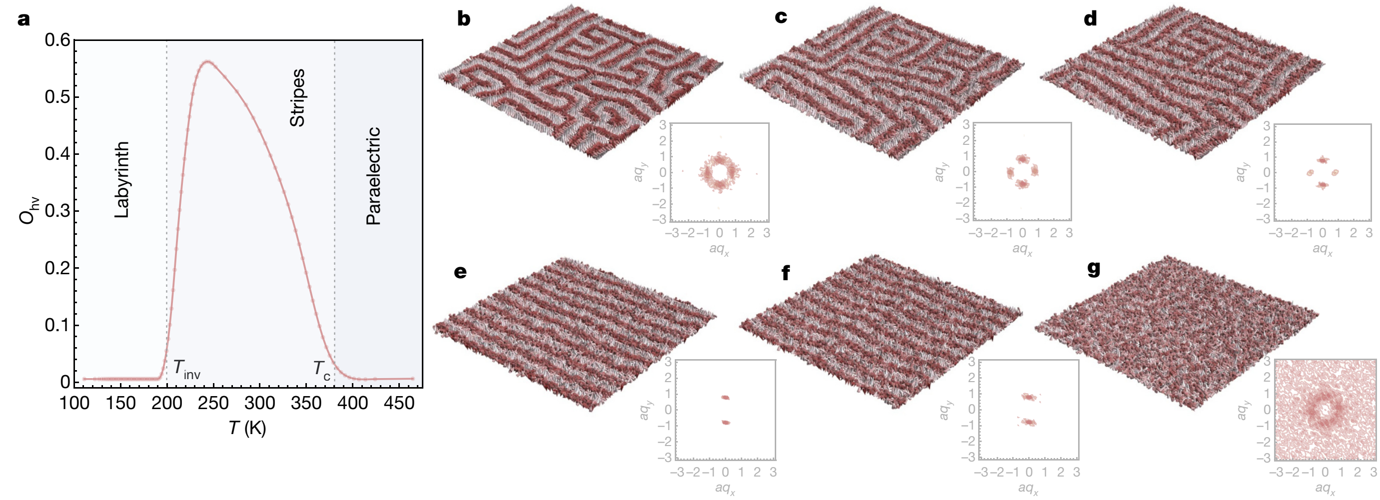

Fig. 2 | Inverse transition simulations. a, Temperature dependence of the orientational order parameter O_{hv} upon slowly heating the labyrinthine state of an 80 × 80 × 5 film of $Pb(Zr_{0.4}Ti_{0.6})O_3$. **b**–**g**, The evolution of the labyrinthine domain pattern in the middle layer of the film with increasing temperature: 10 K (**b**), 110 K (**c**), 185 K (**d**), 260 K (**e**), 335 K (**f**) and 410 K (**g**). Grey (red) dipoles are oriented along the [001] ([00$\bar{1}$]) pseudo-cubic direction. The structure factor plots obtained by Fourier transformation of the *z* component of the corresponding dipolar field are also provided, where aq_x and aq_y are the *x* and *y* components of the dimensionless wave vector, which take values within the interval from −π to +π (*a* is the in-plane lattice constant). The colouring corresponds to the value of the structure factor, with white (pink) indicating the lowest (highest) value. The colour scale is the same for all plots.

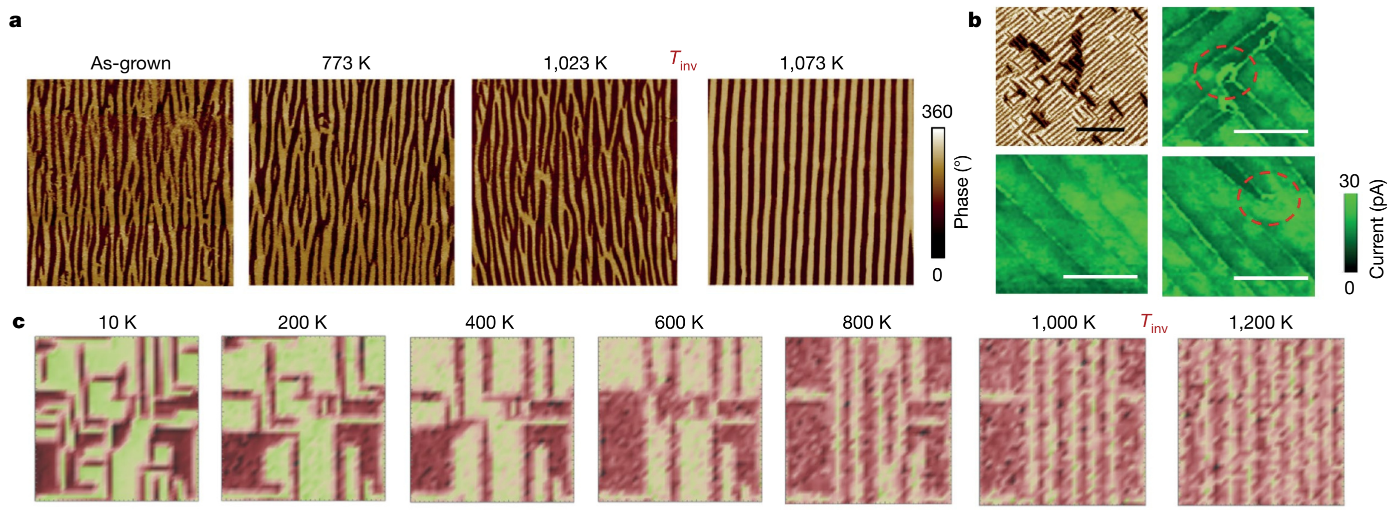

Fig. 3 | Experimental observation and simulations of the inverse transition in $BiFeO_3$ films. a, In-plane piezoresponse force microscopy phase images of a 95-nm-thick $BiFeO_3$ film grown on a (110)-oriented orthorhombic $DyScO_3$ substrate, for the as-grown sample, and the same sample after annealing at 773 K, 1,023 K and 1,073 K. The images are 5 × 5 μm². **b**, In-plane piezoresponse force microscopy image of a 30-nm-thick $BiFeO_3$ film grown on $SrRuO_3$ (10 nm)/$DyScO_3$(110) (top left). Scale bar, 2 μm. Conducting atomic force microscopy (current mapping) images acquired with $V_{d.c.}$ = 1.7 V applied on a $SrRuO_3$ bottom electrode in periodic stripy areas (bottom left) and defected areas (red dashed lines) with high-conduction spots at three-fold junctions (top right) and end-point (bottom right) topological defects. Scale bars, 500 nm. **c**, Distribution of the *z* component of polarization (red to green indicate negative to positive values) in a middle layer of $BiFeO_3$ film at different temperatures, as obtained from 36 × 36 × 10 supercell effective-Hamiltonian-based Monte Carlo simulations under periodic boundary conditions with ideal short-circuit screening and isotropic misfit strain of −0.16%. The system was abruptly quenched from 2,000 K to 10 K and consequently progressively heated up with 40,000 relaxation sweeps at each temperature. In the simulations, we find that below T_{inv}, the system exhibits mixed 109° and 71° domain walls, while above T_{inv}, only 109° domain walls are observed.

findings and other computations given in Methods, demonstrate that the inverse-transition phenomenon is robust against intrinsic and extrinsic parameters such as boundary conditions, film thickness, as well as screening conditions and misfit strain. Naturally, varying the conditions in the studied systems ($Pb(Zr_{0.4}Ti_{0.6})O_3$ and $BiFeO_3$) yields different transition temperatures, as well as different types of domain walls (for example, 180° in $Pb(Zr_{0.4}Ti_{0.6})O_3$ versus 109° and 71° domain walls in $BiFeO_3$) and labyrinthine morphologies, with no incidence on the occurrence of the inverse transition.

Figure 4a provides the evolution with temperature of the free-energy-like potential associated with the transverse component of dipoles at the domain walls. Each curve is obtained by averaging over the distributions of 100 labyrinthine realizations. Results are gathered at 10 K, 110 K and 210 K upon heating the labyrinthine states and the transverse component is taken to be the projection of dipoles onto the domain-wall normal at each point. At 10 K, the potential features three minima, the leftmost and rightmost ones being associated with the Néel nature of the domain walls. The minimum at zero is associated with dipoles

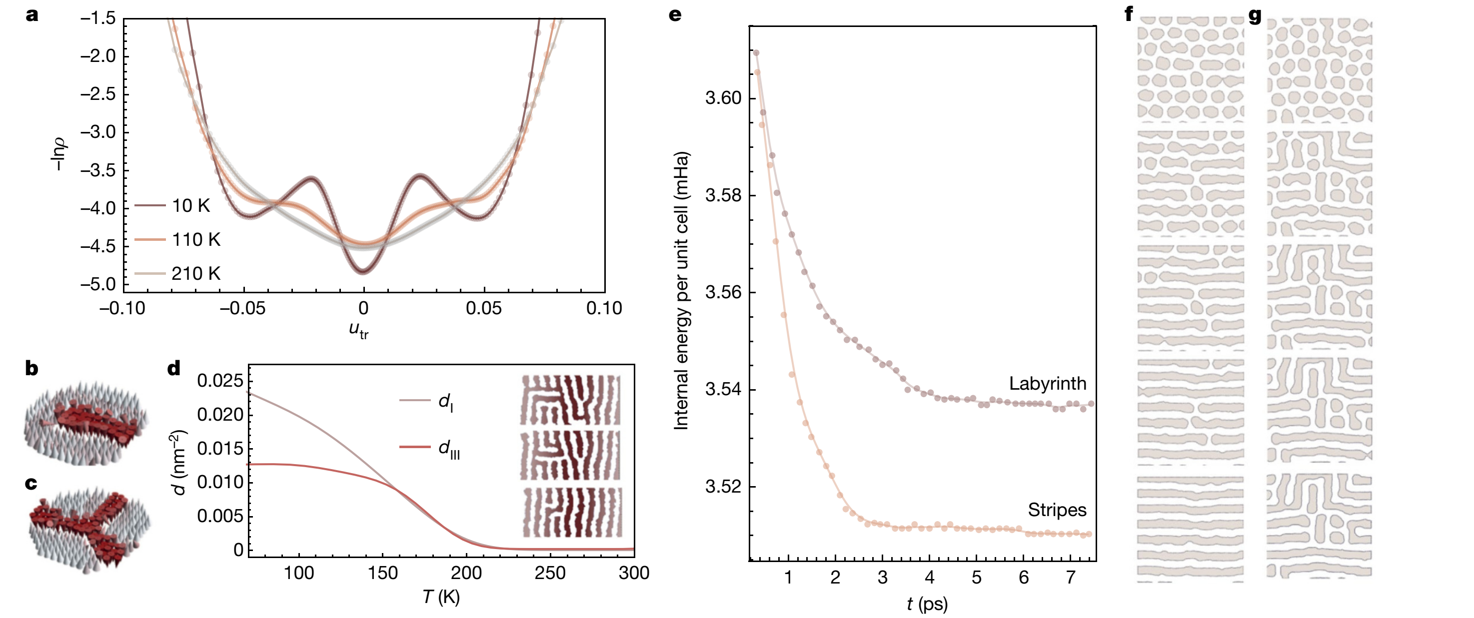

Fig. 4 | Energy, topological defects and memory effects. a, Free-energy-like potentials of the labyrinthine domain pattern at 10 K, 110 K and 210 K. Curves are obtained by calculating the logarithm of the probability distribution functions ρ (averaged over the distributions of 100 labyrinthine realizations) of the transverse to the domain wall component of the local modes, u_{tr}, within an $80 \times 80 \times 5$ $Pb(Zr_{0.4}Ti_{0.6})O_3$ supercell. Note that the local mode u is a vector proportional to the electric dipole moment. **b**, **c**, Stripe end-points (**b**) and three-fold junctions (**c**). **d**, Evolution with temperature of the densities d (per square nanometre) of stripe end-points d_{I} and three-fold junctions d_{III}. The insets show the evolution with increasing temperature (from top to bottom) of the labyrinthine stripe morphology within a portion of the middle layer of the simulated $80 \times 80 \times 5$ $Pb(Zr_{0.4}Ti_{0.6})O_3$ film. The dark area highlights a local straightening process of neighbouring stripes upon increasing the temperature. **e**, Temporal evolution at 10 K of the internal energy per unit cell of a $56 \times 56 \times 5$ supercell of $Pb(Zr_{0.4}Ti_{0.6})O_3$ during the relaxation of the two bubble states upon removal of the external electric field. The dark (bright) curve corresponds to the relaxation of the bubble state obtained from electric field treatment of the labyrinthine (parallel-stripe) pattern. **f**, **g**, Consecutive snapshots of such temporal evolutions (from top to bottom) of the two bubble states just after removal of the field for the parallel-stripe (**f**) and labyrinthine (**g**) initial patterns. Snapshots correspond to the middle layer of the supercell, where dark and white regions represent the [00$\bar{1}$] and [001] dipole orientations.

residing at the boundaries of the domain walls, the orientation of which is along the [001] and [00$\bar{1}$] directions. Increasing the temperature leads to a gradual flattening of the minima, ultimately resulting in a single minimum potential at $u_{tr} = 0$ for $T \geq T_{inv}$. The gradual lessening of barrier heights is associated with increased thermal fluctuations of dipoles, which not only lead to more corrugated walls but also enable the reorientation of the meandering stripes. In this regard, the barrier softening of the transverse components of the domain-wall dipoles undermines surface tension effects and enhances wall fluidity. The loss of configurational entropy subtending the parallel reorientation of the labyrinthine stripes (greater mesoscopic order) is offset by the increase of the vibrational entropy of dipoles (greater microscopic disorder). Frozen in the 'disordered' high-symmetry labyrinthine phase, the transverse components of the dipoles melt in the 'ordered' low-symmetry parallel-stripe state. In this sense, the inverse-transition phenomenon, although seemingly counterintuitive, is only inverse from the mesoscopic symmetry standpoint, as it can be fathomed without violating the laws of thermodynamics or relying on a paradoxical inverse entropic scenario[3,16,18].

This configurational entropy reduction can be rationalized by regarding the labyrinthine domain pattern as a fragmented, mosaic state composed of tiles with a ground-state morphology of a local parallel-stripe arrangement of domains. Such local realization of mesoscopic order within each tile is favoured by the dipolar interaction that stabilizes parallel adjacent stripes. Within the mosaic ansatz, an estimate of the degeneracy of the labyrinthine phase yields $2^{L^2/\xi^2}$ (where ξ is the typical lateral length of a tile and L is the lateral size of the supercell), because each of the L^2/ξ^2 tiles can locally harbour a parallel-stripe alignment along either the [100] or the [010] direction. These exponentially many labyrinthine states are statistically equivalent while being morphologically incongruent[18]. As expected, ξ is a temperature-dependent quantity, as can be seen in Extended Data Fig. 5b. Approaching T_{inv} from low temperatures, ξ becomes comparable to the lateral size of supercell L, indicating the onset of a global symmetry-breaking and long-range parallel arrangement of stripes. We find that the coarsening of structures is conveyed by the diffusion and relaxation of topological defects localized at the junction of different tiles and reconciling discrepancies in their prevailing local orientations and/or wavelengths[25]. The examination of elementary point topological defects indeed shows that the densities d_{I} and d_{III} of stripe end-points (or convex disclinations of +1/2 Pontryagin charge[26,27]) and three-fold junctions (or concave disclinations of −1/2 Pontryagin charge[26]), respectively (Fig. 4b, c), feature a gradual lessening upon approaching T_{inv} from low temperatures (Fig. 4d). We find that domain coalescence is driven by the recombination/annihilation of defects[28,29], whereby, for instance, a pair of concave–convex disclinations rebinds into a diffusing dislocation (inset of Fig. 4d) yielding a straightening of the labyrinthine pattern[3,30].

Rather unexpectedly, we find that these modulated phases (stripe and labyrinthine domain arrangements) are endowed with memory. Upon applying an electric field perpendicular to the film plane, the ground state of the stripe domains transforms into a nanobubble phase before yielding a monodomain state at high enough electric field values[11]. We find that the labyrinthine state exhibits an equivalent sequence of electric-field-induced morphological transitions, that is, from labyrinthine to bubble to monodomain states, with increasing magnitude of the external field. The two bubble states obtained from either the stripe domains or the labyrinthine ones are energetically equivalent. Notably, upon releasing the stabilizing external field, each of the two bubble states relaxes back to its parent state morphology, obtained before any electric field treatment. This can be seen in Fig. 4e–g, which provides the temporal relaxation as obtained from molecular dynamics

simulations of each of the bubble states upon removal of the field. This history-dependent behaviour is rooted in a complex energy landscape and attests of an original intrinsic memory effect, the seed of which lies in the arrangement of the bubble array (Extended Data Fig. 8).

In summary, we report an inverse phase sequence in ferroelectric films, whereby a high-symmetry kinetically arrested labyrinthine phase transforms into a less-symmetric parallel-stripe domain structure upon increasing the temperature. Such an inverse transition involves pattern straightening and coarsening and is predominantly driven by the relaxation and diffusion of point topological defects. We also experimentally show that these nanometric defects encompass up to 50 times larger conductivity when compared with straight domain wall segments and numerically demonstrate that the self-assembled dipolar configurations are endowed with an original memory effect. These findings will allow the development of novel applications of ferroelectric films in logic and storage devices, as well as in memristors[31–34] for neuromorphic computing.

Online content

Any methods, additional references, Nature Research reporting summaries, source data, extended data, supplementary information, acknowledgements, peer review information; details of author contributions and competing interests; and statements of data and code availability are available at https://doi.org/10.1038/s41586-019-1845-4.

1. De'Bell, K., MacIsaac, A. B. & Whitehead, J. P. Dipolar effects in magnetic thin films and quasi-two-dimensional systems. *Rev. Mod. Phys*. **72**, 225–257 (2000).
2. Seul, M. & Andelman, D. Domain shapes and patterns: the phenomenology of modulated phases. *Science* **267**, 476–483 (1995).
3. Schupper, N. & Shnerb, N. M. Inverse melting and inverse freezing: a spin model. *Phys. Rev. E* **72**, 046107 (2005).
4. Tammann, G. *Kristallisieren und Schmelzen* (Johann Ambrosius Barth, 1903).
5. Greer, A. L. Too hot to melt. *Nature* **404**, 134–135 (2000).
6. Portmann, O., Vaterlaus, A. & Pescia, D. An inverse transition of magnetic domain patterns in ultrathin films. *Nature* **422**, 701–704 (2003).
7. Gu, Z. et al. Resonant domain-wall-enhanced tunable microwave ferroelectrics. *Nature* **560**, 622–627 (2018).
8. Kornev, I. I. A., Fu, H. & Bellaiche, L. Ultrathin films of ferroelectric solid solutions under a residual depolarizing field. *Phys. Rev. Lett*. **93**, 196104 (2004).
9. Feigl, L. et al. Controlled stripes of ultrafine ferroelectric domains. *Nat. Commun*. **5**, 4677 (2014).
10. Peters, J. J. P., Apachitei, G., Beanland, R., Alexe, M. & Sanchez, A. M. Polarization curling and flux closures in multiferroic tunnel junctions. *Nat. Commun*. **7**, 13484 (2016).
11. Lai, B.-K., Ponomareva, I., Kornev, I. A., Bellaiche, L. & Salamo, G. J. Electric-field-induced domain evolution in ferroelectric ultrathin films. *Phys. Rev. Lett*. **96**, 137602 (2006).
12. Streiffer, S. K. et al. Observation of nanoscale 180 degrees stripe domains in ferroelectric $PbTiO_3$ thin films. *Phys. Rev. Lett*. **89**, 067601 (2002).
13. Zhang, Q. et al. Nanoscale bubble domains in ultrathin ferroelectric films. *Adv. Mater*. **29**, 1702375 (2017).
14. Solokhin, M. A., Solokhin, A. V. & Timofeev, V. S. Phase-equilibrium stability criterion in terms of the eigenvalues of the Hessian matrix of the Gibbs potential. *Theor. Found. Chem. Eng*. **36**, 444–446 (2002).
15. Ritort, F. & Sollich, P. Glassy dynamics of kinetically constrained models. *Adv. Phys*. **52**, 219–342 (2003).
16. Crisanti, A. & Leuzzi, L. Stable solution of the simplest spin model for inverse freezing. *Phys. Rev. Lett*. **95**, 087201 (2005).
17. Parisi, G. Spin glasses and fragile glasses: statics, dynamics, and complexity. *Proc. Natl Acad. Sci. USA* **103**, 7948–7955 (2006).
18. Leuzzi, L. & Nieuwenhuizen, T. M. *Thermodynamics of the Glassy State* (Taylor and Francis, 2007).
19. Bouchaud, J. P. Weak ergodicity breaking and aging in disordered systems. *J. Phys. I* **2**, 1705–1713 (1992).
20. Booth, I., MacIsaac, A. B., Whitehead, J. P. & De'Bell, K. Domain structures in ultrathin magnetic films. *Phys. Rev. Lett*. **75**, 950–953 (1995).
21. Prosandeev, S., Lisenkov, S. & Bellaiche, L. Kittel law in $BiFeO_3$ ultrathin films: a first-principles-based study. *Phys. Rev. Lett*. **105**, 147603 (2010).
22. Prosandeev, S., Wang, D., Ren, W., Iniguez, J. & Bellaiche, L. Novel nanoscale twinned phases in perovskite oxides. *Adv. Funct. Mater*. **23**, 234–240 (2013).
23. Kornev, I. A., Lisenkov, S., Haumont, R., Dkhil, B. & Bellaiche, L. Finite-temperature properties of multiferroic $BiFeO_3$. *Phys. Rev. Lett*. **99**, 227602 (2007).
24. Eliseev, E. A., Morozovska, A. N., Nelson, C. T. & Kalinin, S. V. Intrinsic structural instabilities of domain walls driven by gradient couplings: meandering anferrodistortive-ferroelectric domain walls in $BiFeO_3$. *Phys. Rev. B* **99**, 014112 (2019).
25. Pismen, L. M. *Patterns and Interfaces in Dissipative Dynamics* (Springer, 2006).
26. Nagaosa, N. & Tokura, Y. Topological properties and dynamics of magnetic skyrmions. *Nat. Nanotechnol*. **8**, 899–911 (2013).
27. Lu, L. et al. Topological defects with distinct dipole configurations in $PbTiO_3/SrTiO_3$ multilayer films. *Phys. Rev. Lett*. **120**, 177601 (2018).
28. Newell, A. C., Passot, T., Ercolani, N. & Indik, R. Elementary and composite defects of striped patterns. *J. Phys. II* **5**, 1863–1882 (1995).
29. Prokhorenko, S., Nahas, Y. & Bellaiche, L. Fluctuations and topological defects in proper ferroelectric crystals. *Phys. Rev. Lett*. **118**, 147601 (2017).
30. Harrison, C. et al. Mechanisms of ordering in striped patterns. *Science* **290**, 1558–1560 (2000).
31. Boyn, S. et al. Learning through ferroelectric domain dynamics in solid-state synapses. *Nat. Commun*. **8**, 14736 (2017).
32. Chua, L. Memristor-the missing circuit element. *IEEE Trans. Circuit Theory* **18**, 507–519 (1971).
33. Yang, S. Y. et al. Above-bandgap voltages from ferroelectric photovoltaic devices. *Nat. Nanotechnol*. **5**, 143–147 (2010).
34. Yang, J. J., Strukov, D. B. & Stewart, D. R. Memristive devices for computing. *Nat. Nanotechnol*. **8**, 13–24 (2013).

Methods

Computational details

We mimic $Pb(Zr_{0.4}Ti_{0.6})O_3$ ferroelectric ultrathin films that are grown along the (001) direction (which is chosen to be the z axis) and are Pb–O terminated at all surfaces/interfaces. The studied films typically have a thickness of 2.0 nm (that is, of five unit cells), and are subjected to a compressive strain of −2.65% to ensure that dipoles have a preferential direction along the out-of-plane direction. Such a value would approximately account for the mismatch of lattice constants of the cubic phases of strontium titanate and $Pb(Zr_{0.4}Ti_{0.6})O_3$. They are interposed between (realistic) electrodes that can screen only 80% of the polarization-induced surface charges, and modelled by various $L \times L \times 5$ supercells that are all periodic along the [100] and [010] directions while finite along the z axis. Technically, a first-principles-based effective Hamiltonian[11] is used within Monte Carlo simulations to determine the energetics and local electric dipoles in each perovskite five-atom cell of these supercells. The validity of this approach was demonstrated by previous theoretical studies of ultrathin $Pb(Zr_{0.4}Ti_{0.6})O_3$ films under compressive strains that (1) yield 180° up and down stripe domains that periodically alternate along [100] (or along [010]) for their ground state[8,11], in agreement with experimental observation[12] (note that 'up' (respectively, 'down') domains refer to domains in which the z component of the dipole is parallel (respectively, antiparallel) to the z axis, respectively); (2) predict a linear dependency between the width of these periodic stripes and the square root of the film's thickness[35], as consistent with recent measurements[36]; and (3) have also led to the prediction of various topological defects such as vortices[37], dipolar waves[38], bubbles[11] and merons (or convex disclinations)[27] in ferroelectrics, which have been experimentally confirmed[13,27,39]. Note that the predicted temperature has to be rescaled by a factor of ~1.6 with respect to measurements[40]. It is also worthwhile clarifying the role of thickness in the observed inverse transition. The phenomenon is expected to survive as long as the thickness of the film allows the stripe domain arrangement, where the morphological alteration as the thickness of the film increases should mainly affect the width of the domains[41].

Additional insights from the computations

Extended Data Fig. 1a–f shows the evolution of the parallel-stripe ground state upon slowly increasing temperature. In refs. [42,43], the authors studied the morphology of equilibrium domain patterns depending on the magnitude of gradient terms within the classical Landau–Ginzburg–Devonshire theory, and found that the labyrinthine-like ground state can be stabilized if the gradient energy is sufficiently reduced. Therefore, we can conclude that in our case, the effective gradient energy is above the critical value of the gradient that grants the parallel-stripe ground state upon slowly annealing the system. In Extended Data Fig. 1g, we provide the temperature variation of the scaled structure factor $\widetilde{S}(aq_s, T)$, where $\widetilde{S}(aq_s, T)$ is taken as the ratio of $S(aq_s, T)$ to $S(aq_s, 10\,\mathrm{K})$, a is the lattice parameter and q_s is the q point corresponding to the wavelength of the striped phase modulation. $S(aq, T)$ is calculated as the thermodynamic average of the squared norm of the three-dimensional discrete Fourier transform of the z component of local dipoles u_z. Looking into the behaviour of $\widetilde{S}(aq_s, T)$, it can be readily seen that paraelectricity onsets at $T_c \approx 380$ K. In Extended Data Fig. 2, we show the evolution with temperature of the specific heat C upon (1) heating the parallel-stripe ground state and upon (2) heating the low-temperature labyrinthine kinetically arrested state. While the first curve exhibits only one peak around T_c, the second curve features two peaks, one at the inverse transition temperature (T_{inv}) and one at T_c. C is extracted from the supercell energy fluctuations $C = (1/k_B T^2)(\langle E^2\rangle - \langle E\rangle^2)$, where $\langle E\rangle$ corresponds to the average over Monte Carlo sweeps of the internal energy E and $\langle E^2\rangle$ to that of its square, and where k_B is the Boltzmann constant.

Extended Data Figs. 3, 4 provide the probability density functions of the cell-by-cell energies calculated for the labyrinthine domain structure at 10 K for $Pb(Zr_{0.4}Ti_{0.6})O_3$ within a $64 \times 64 \times 5$ supercell. Extended Data Fig. 3a–d refers to the on-site energy, first nearest neighbours (1NN) interaction energy, second nearest neighbours (2NN) interaction energy, and dipole–dipole interaction energy, respectively. Extended Data Fig. 4a–c pertains to the third nearest neighbours (3NN) interaction energy, elastic energy and electrostrictive energy, respectively. The mappings of each contribution to the energy onto the middle layer of the film are also provided in these figures. It is therein seen that while the on-site energy, the second and third nearest neighbours interaction energy, as well as the electrostrictive energy feature energy gain at the domain walls, the dipole–dipole interaction is the main counterbalancing cost.

In Extended Data Fig. 5a, we show the dependence on temperature of the dipole–dipole energy density upon heating each of the ground-state parallel-stripe domain pattern and the kinetically arrested labyrinthine state. It can be seen that before the onset of the inverse transition (around 200 K), the excess dipolar energy in the labyrinthine state gradually reduces with increasing temperature as a result of the straightening of meandering stripes. Also provided in this figure is the estimate of the evolution with temperature of the dipolar energy density of a fictive labyrinthine state whose serpentine stripe domains are artificially precluded from straightening. The mismatch between the curves associated with each of the fictive and real evolution of labyrinthine state establishes that the labyrinthine domain pattern effectively reduces its energy upon increasing temperature by adopting a parallel reordering of its stripes. In Extended Data Fig. 5b, we show the growth with temperature of the tile typical lateral length ξ. Upon approaching T_{inv} from low temperatures, ξ becomes comparable to the lateral size of the supercell L, indicating the onset of a global symmetry-breaking and long-range parallel arrangement of stripes.

We performed additional first-principles-based effective Hamiltonian simulations[21–23] for $BiFeO_3$ films of different geometries. Specifically, we simulated thick (with respect to the lattice constant) $BiFeO_3$ films where local modes (proportional to dipoles) are centred on the A-sites of the perovskite structure. The supercell size was $36 \times 36 \times 10$ and subjected to compressive strain of −0.16% (Extended Data Fig. 6). We have also examined ultrathin $BiFeO_3$ films using the film effective Hamiltonian model where local modes (proportional to dipoles) are centred on the B-sites of the perovskite structure. In this second case, the film thickness was taken to be five unit cells (as in the simulations on $Pb(Zr_{0.4}Ti_{0.6})O_3$ ultrathin film), and misfit strain was set to −0.5%. Partial screening electric boundary conditions at film interfaces were used (Extended Data Fig. 7). Both numerical approaches listed above include AFD degrees of freedom in addition to variables describing inhomogeneous and homogeneous strain as well as local mode vectors. The employed Hamiltonians incorporate, among other terms, the coupling of AFD and ferroelectric degrees of freedom, as well as short range interactions of each of the two order parameters. Both Extended Data Figs. 6 and 7 show that upon heating the deep-quench-obtained low-temperature configurations, the domain pattern gradually transforms into parallel-stripe domains. Interestingly, the AFD vectors feature similar behaviour with increasing temperature for both investigated $BiFeO_3$ film geometries. These first-principles-obtained numerical results, along with their experimental realizations, demonstrate that the inverse-transition phenomenon is robust against boundary conditions, film thickness, as well as screening conditions and misfit strain.

We also provide additional details regarding the discovered memory effect. We found that bubbles emerge from either the labyrinthine or the parallel-stripe states starting from an applied external field value of 32×10^7 V m^{-1}. Beyond the threshold field of 42×10^7 V m^{-1}, the system forgets its history and does not relax back to the original state. This value is below the field value of 52×10^7 V m^{-1} that induces the transition to the monodomain state. Note that typically, theoretical electric fields

are about 20 times larger than the experimental ones[44]. We found that the seed underlying this memory effect is rooted in the arrangement of bubbles. The array of bubbles obtained from the parallel-stripe phase shows two additional peaks in its structure factor plot, at the position of the wave vectors that define the periodicity of the parent stripe state. Such peaks are absent in the structure factor characterizing the array of bubbles obtained from the labyrinthine state (Extended Data Fig. 8).

Experimental details

The $BiFeO_3$ thin film was grown by pulsed laser deposition on a (110)-oriented $DyScO_3$ substrate using an excimer laser. First, a 5-nm-thick electrode of $SrRuO_3$ was deposited at 933 K under 0.2 mbar of oxygen with a laser frequency of 5 Hz. The 95-nm-thick $BiFeO_3$ film was grown at 933 K under 0.36 mbar of oxygen with a laser frequency of 1 Hz. The bilayer was then cooled down to room temperature under 300 mbar of oxygen. The XRD pattern shows the monoclinic (001) orientation of $BiFeO_3$ with Laue fringes attesting the high quality of the epilayer. Piezoresponse force microscopy (PFM) indicates a homogeneous out-of-plane polarization direction towards the $SrRuO_3$ electrode. The in-plane PFM contrast shows two alternating variants with 71° domain walls (Fig. 3a). We conducted successive ex situ annealing experiments under oxygen flow on this sample increasing the maximum temperature from 773 K to 1,073 K, ramping at 20 K min^{-1} from room temperature and keeping the maximum temperature constant for 1 h. The cool down process was limited by the inertia of the oven and we estimate the cooling rate to be around 2 K min^{-1}. The resulting PFM domain structure evolution is shown in Fig. 3a for annealing temperatures of 773 K, 1,023 K and 1,073 K. No substantial change was reported in the maze-like pattern up to 1,023 K, while a profound modification to perfectly straight lines is observed after the 1,073 K annealing. Note that the PFM images were taken on random zones of the 5 × 5 mm^2 sample. While the surface topography shows surface desorption in addition to the preserved step and terrace structure (Extended Data Fig. 9), XRD does not reveal any structural changes induced by the successive annealing (Extended Data Fig. 10).

We additionally conducted PFM experiments with an atomic force microscope (Nanoscope V multimode, Bruker) and external SR830 lock-in detectors (Stanford Research) for simultaneous acquisition of in-plane and out-of-plane responses. A DS360 external source (Stanford Research) was used to apply the a.c. excitation to the $SrRuO_3$ bottom electrode at a frequency of 35 kHz while the conducting platinum-coated tip was grounded. The out-of-plane response is homogeneous in accordance with the homogeneous pristine downward polarization all over the $BiFeO_3$ thin film. Current maps were acquired with the same tip connected to a transimpedance amplifier (TUNA, Bruker) with $V_{\mathrm{d.c.}}$ = 1.7 V applied on the $SrRuO_3$ bottom electrode. The data show enhanced conduction for labyrinthine defects as reported in Fig. 3b.

XRD measurements as a function of temperature were performed using a high-resolution two-axis diffractometer equipped with a rotating anode generator of 18 kW (Rigaku), with a Bragg–Brentano geometry and a 50-cm-diameter focalization circle allowing an accuracy as high as 0.0002 A in 2Θ. The (002) out-of-plane pseudo-cubic Bragg peak of $BiFeO_3$ thin film grown on $SrRuO_3/DyScO_3$ is measured between 300 K and 1,160 K (precision better than 1 K) and a step of 20 K. Above 1,160 K, the film decomposes. From the measured Bragg peak position, the out-of-plane unit cell parameter is extracted and reported in Extended Data Fig. 11 and shows a quasi-linear variation of the film parameter with temperature, which indicates that there is no phase transition up to 1,160 K.

As visible from Extended Data Fig. 12, we observe the same features as Yang et al.[33] in the reciprocal space mappings measured in our $BiFeO_3$ thin films and the relative intensity of the 'superlattice' peaks is increased after annealing. From the in-plane PFM image after annealing (Extended Data Fig. 12b), we estimate the width of the domains (or the periodicity of the domain walls) to be 90 ± 5 nm. Consistently, the satellites around the (002) $BiFeO_3$ film peak (Extended Data Fig. 12d) correspond to a periodicity of 95 ± 5 nm. We checked that these features disappear when aligning the X-ray beam parallel to the ferroelectric stripes (Φ = 0°), and doing the same reciprocal space mappings around (002).

Data availability

The data that support the findings of this study are available from the corresponding author upon reasonable request.

Code availability

The codes that are used in this study are available from the corresponding author upon reasonable request.

35. Thickness dependency of 180 degree stripe domains in ferroelectric ultrathin films: a first-principles study. *Appl. Phys. Lett.* **91**, 152909 (2007).
36. Schilling, A. et al. Scaling of domain periodicity with thickness measured in $BaTiO_3$ single crystal lamellae and comparison with other ferroics. *Phys. Rev. B* **74**, 024115 (2006).
37. Naumov, I. I., Bellaiche, L. & Fu, H. Unusual phase transitions in ferroelectric nanodisks and nanorods. *Nature* **432**, 737–740 (2004).
38. Sichuga, D. & Bellaiche, L. Epitaxial $Pb(Zr,Ti)O_3$ ultrathin films under open-circuit electrical boundary conditions. *Phys. Rev. Lett.* **106**, 196102 (2011).
39. Yadav, A. K. et al. Observation of polar vortices in oxide superlattices. *Nature* **530**, 198–201 (2016); corrigendum 534, 138 (2016).
40. Bellaiche, L., Garcia, A. & Vanderbilt, D. Finite-temperature properties of $Pb(Zr_{1-x}Ti_x)O_3$ alloys from first principles. *Phys. Rev. Lett.* **84**, 5427–5430 (2000).
41. Kittel, C. Theory of the structure of ferromagnetic domains in films and small particles. *Phys. Rev.* **70**, 965–971 (1946).
42. Eliseev, E. A. et al. Labyrinthine domains in ferroelectric nanoparticles: manifestation of a gradient-induced morphological transition. *Phys. Rev. B* **98**, 054101 (2018).
43. Morozovska, A. N., Fomichov, Y. M., Maksymovych, P., Vysochanskii, Y. M. & Eliseev, E. A. Analytical description of domain morphology and phase diagrams of ferroelectric nanoparticles. *Acta Mater.* **160**, 109–120 (2018).
44. Xu, B., Iniguez, J. & Bellaiche, L. Designing lead-free antiferroelectrics for energy storage. *Nat. Commun.* **8**, 15682 (2017).

Acknowledgements We acknowledge DARPA grant number HR0011727183-D18AP00010 (TEE programme), ARO grant number W911NF16-1-0227 and DARPA grant number HR0011-15-2-0038 (MATRIX programme). Computations were made using the Arkansas High Performance Computing Center and the Arkansas Economic Development Commission. B.X. acknowledges the startup fund from Soochow University and support from Priority Academic Program Development (PAPD) of Jiangsu Higher Education Institutions. S. Prosandeev appreciates the support of RMES grant number 3.1649.2017/4.6 and RFBR grant number 18-52-00029_Bel_a. V.G., S.F. and B.D. acknowledge a public grant overseen by the French National Research Agency (ANR) as part of the Investissements d'Avenir programme (reference: ANR-10-LABX-0035, Labex NanoSaclay) and the project EXPAND through ANR-17-CE24-0032, as well as through the PIAF project.

Author contributions Y.N. conceived the study of the inverse-transition phenomenon as part of a research project about labyrinthine structures initiated by L.B. Y.N. and S. Prokhorenko carried out the simulations and analysed the data. J.F. fabricated the thin films by pulsed-laser deposition, carried out the annealing experiments with the help of C.C., and performed the PFM measurements. B.X. and S. Prosandeev performed additional $BiFeO_3$ simulations. S.F. performed the conducting atomic force microscopy experiments. This experimental work was done under the guidance of V.G. B.D. performed XRD measurements. After a first draft written by Y.N., all authors discussed the results and contributed to the final manuscript.

Competing interests The authors declare no competing interests.

Additional information
Correspondence and requests for materials should be addressed to Y.N.
Peer review information *Nature* thanks Anna Morozovska and the other, anonymous, reviewer(s) for their contribution to the peer review of this work.

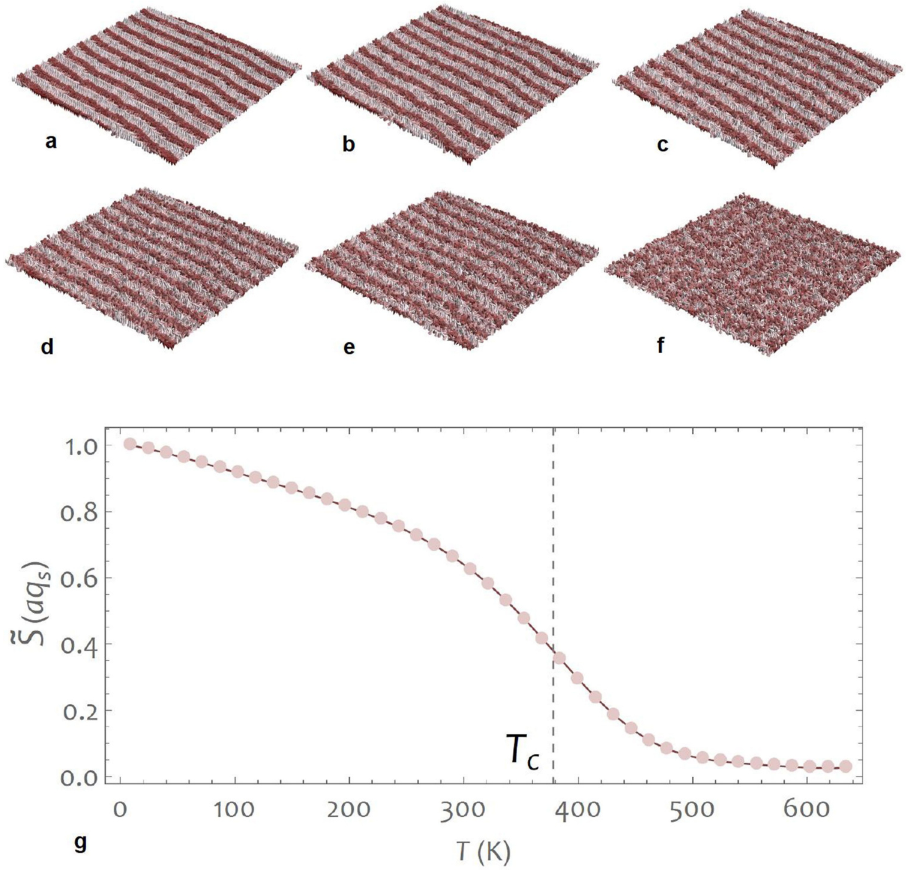

Extended Data Fig. 1 | Temperature evolution of the parallel-stripe ground state. a–f, The evolution with temperature of the ground-state dipolar configuration (parallel stripes) in the middle layer of an 80 × 80 × 5 film of $Pb(Zr_{0.4}Ti_{0.6})O_3$ upon increasing temperature (10 K (**a**), 110 K (**b**), 185 K (**c**), 260 K (**d**), 335 K (**e**) and 410 K (**f**)), where grey (red) dipoles are oriented along the [001] ([00$\bar{1}$]) pseudo-cubic direction). **g**, The temperature variation of the scaled structure factor $\tilde{S}\,(aq_s, T)$. Vertical dashed line indicates the inflection point of $\tilde{S}\,(aq_s, T)$ and is taken as the locus of T_c.

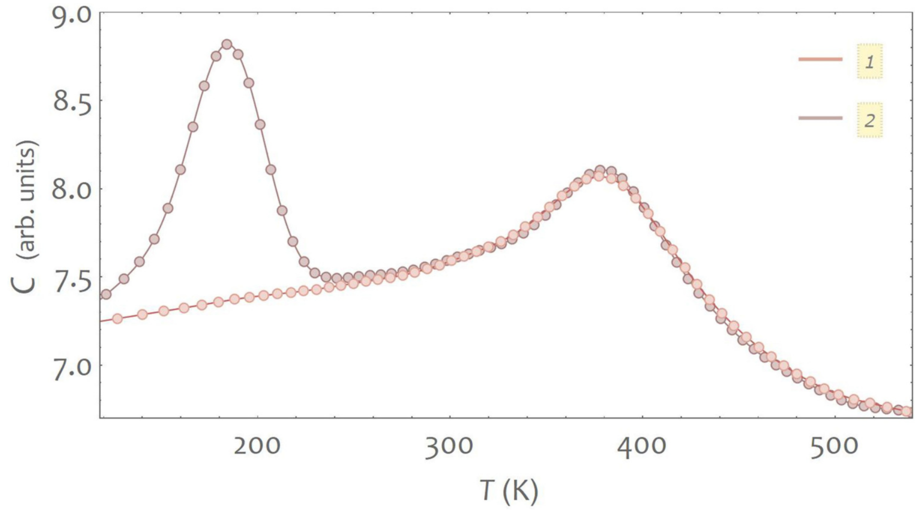

Extended Data Fig. 2 | Specific heat of the parallel-stripe and labyrinthine states. Specific heat C as a function of temperature (in arbitrary units). Data were gathered upon slowly heating the ground-state parallel-stripe domain pattern (1) and the labyrinthine domain pattern (2).

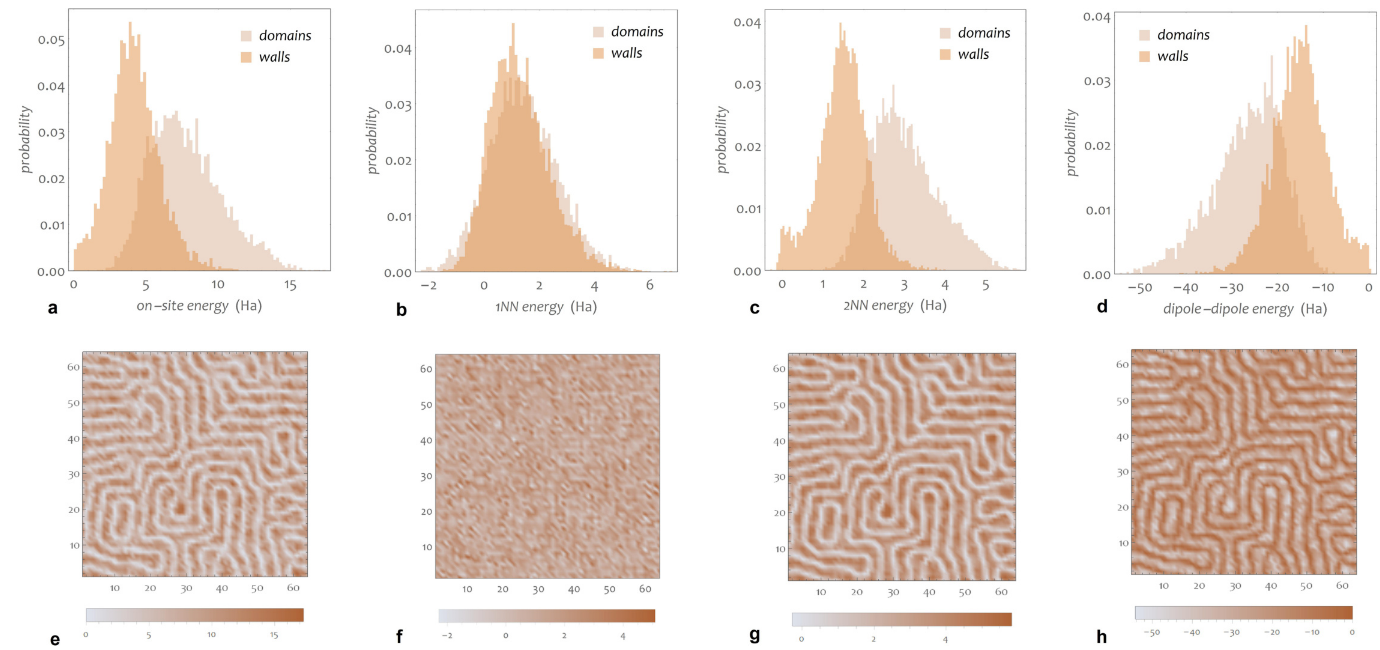

Extended Data Fig. 3 | Spatial distribution of on-site, first and second nearest neighbours and dipole–dipole interaction energies. a–**d**, The probability density functions of the cell-by-cell energies (on-site energy (**a**), first nearest neighbours (1NN) interaction energy (**b**), second nearest neighbours (2NN) interaction energy (**c**) and dipole–dipole interaction energy (**d**)) calculated for the labyrinthine domain structure at 10 K for $Pb(Zr_{0.4}Ti_{0.6})O_3$ within a 64 × 64 × 5 supercell. Each panel provides the contributions stemming from the domains and domain walls, separately. **e**–**h**, The corresponding mappings of energies onto the middle layer of the film. Blue to red colour gradient shows increasing values of unit-cell energies.

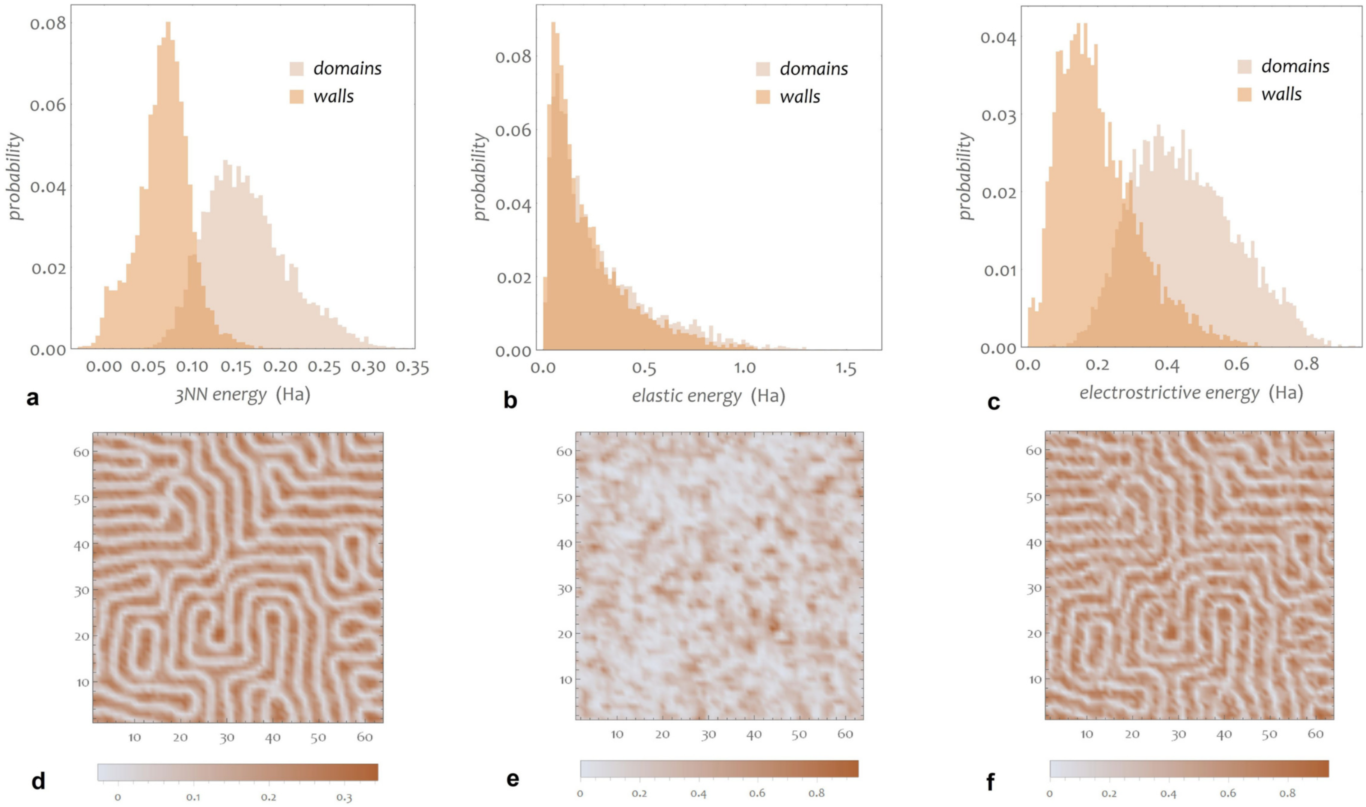

Extended Data Fig. 4 | Spatial distribution of third nearest neighbours, elastic and electrostrictive energies. a–c, The probability density functions of the cell-by-cell energies (third nearest neighbours (3NN) interaction energy (**a**), elastic energy (**b**) and electrostrictive energy (**c**)) calculated for the labyrinthine domain structure at 10 K for $Pb(Zr_{0.4}Ti_{0.6})O_3$ within a 64 × 64 × 5 supercell. Each panel provides the contributions stemming from the domains and domain walls, separately. **d–f**, The corresponding mappings of energies onto the middle layer of the film. Blue to red colour gradient shows increasing values of unit-cell energies.

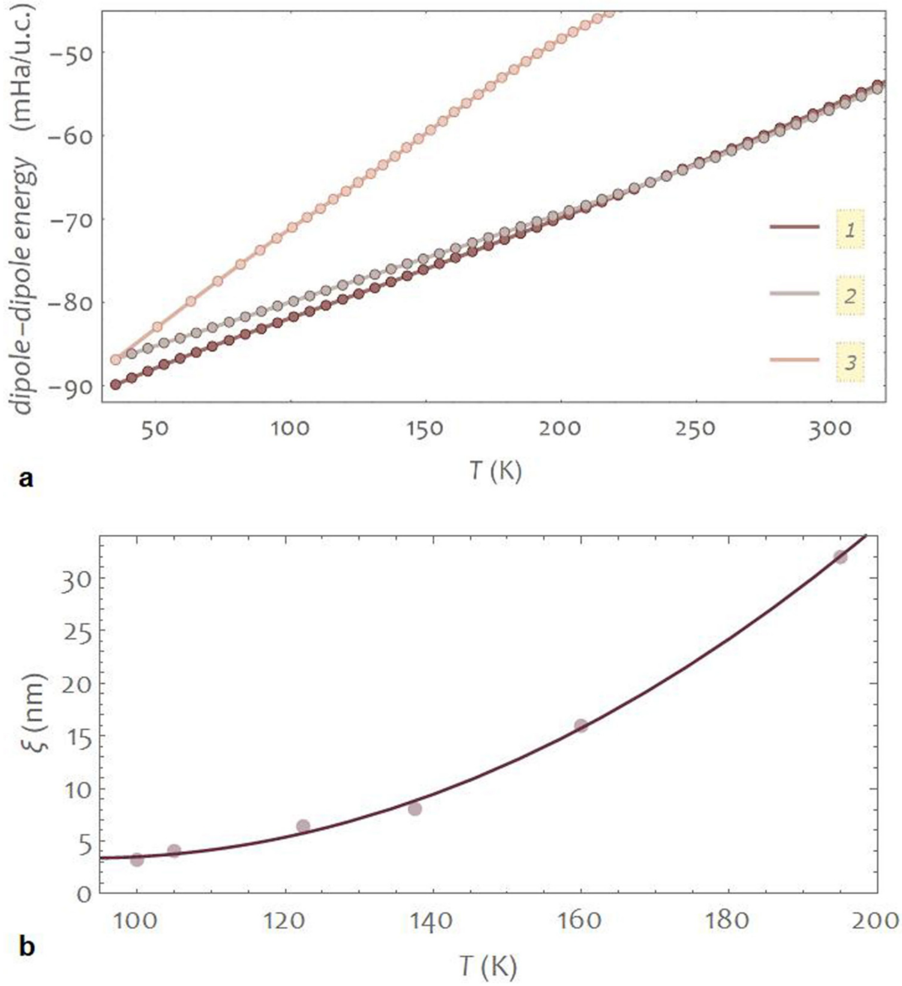

Extended Data Fig. 5 | Energetics and spatial correlations at play in the inverse transition. **a**, Evolution with temperature of dipole–dipole energy density upon heating the ground-state parallel-stripe domain pattern (1) and the labyrinthine domain pattern (2). These two curves meet above 200 K, the temperature at which the inverse transition occurs. The third curve (3) corresponds to what would have been the dipole–dipole energy of domain walls if the labyrinthine domain walls would have gradually wiggled with no reordering of the stripes (fictive labyrinthine evolution). **b**, Evolution with temperature of the typical size of locally ordered ground-state tiles composing the labyrinthine domain pattern. Data were obtained via the analysis of structure factors of square patches of varying size at each temperature. Specifically, at each temperature, ξ corresponds to the maximal patch size featuring two-peaked structure factor. Solid line is a guide for the eyes.

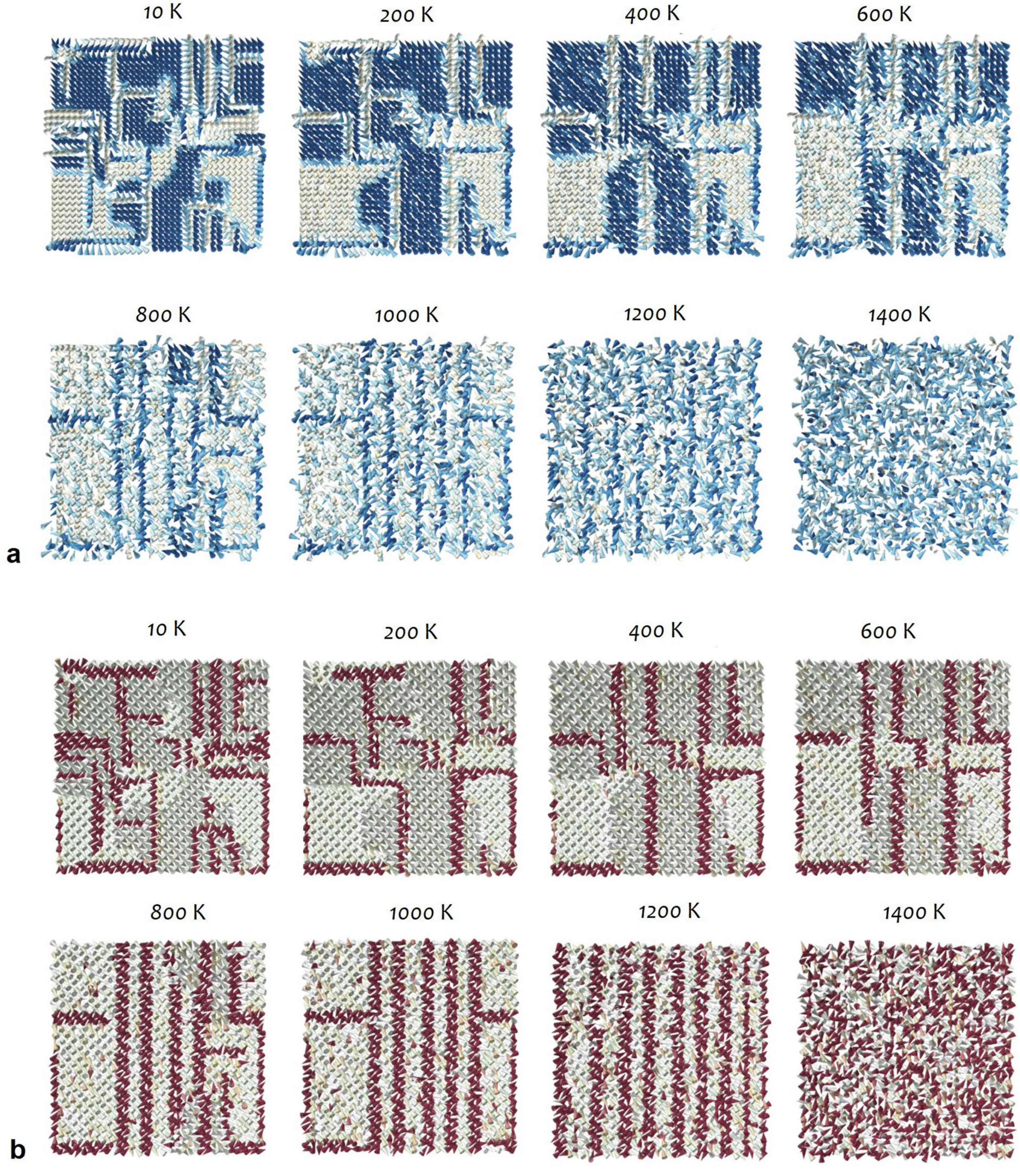

Extended Data Fig. 6 | Simulations of the inverse transition in thick $BiFeO_3$ films. a, **b**, The evolution with temperature of the domain pattern in $BiFeO_3$ in terms of the distribution of the ferroelectric (**a**) and AFD (**b**) order parameters. Results were obtained through Monte Carlo simulations using the effective Hamiltonian scheme of a 36 × 36 × 10 film subjected to a −0.16% misfit strain, with periodic boundary conditions. The system was abruptly quenched from 2,000 K down to 10 K and consequently progressively heated up with 40,000 relaxation sweeps at each temperature. It can be seen that the distributions of both ferroelectric and AFD order parameters exhibit the inverse transition with $T_{inv} \approx 1{,}100$ K and $T_c \approx 1{,}300$ K (these numerically predicted temperatures are in good agreement with our experimental findings). We find that below T_{inv}, the system exhibits mixed 109° and 71° domain walls, while above T_{inv}, only 109° domain walls are observed. In **a**, dipoles are coloured according to their z component. In **b**, AFD vectors are coloured according to the arctan(W_y/W_x), where W_y and W_x denote the y and x components of the AFD local vectors.

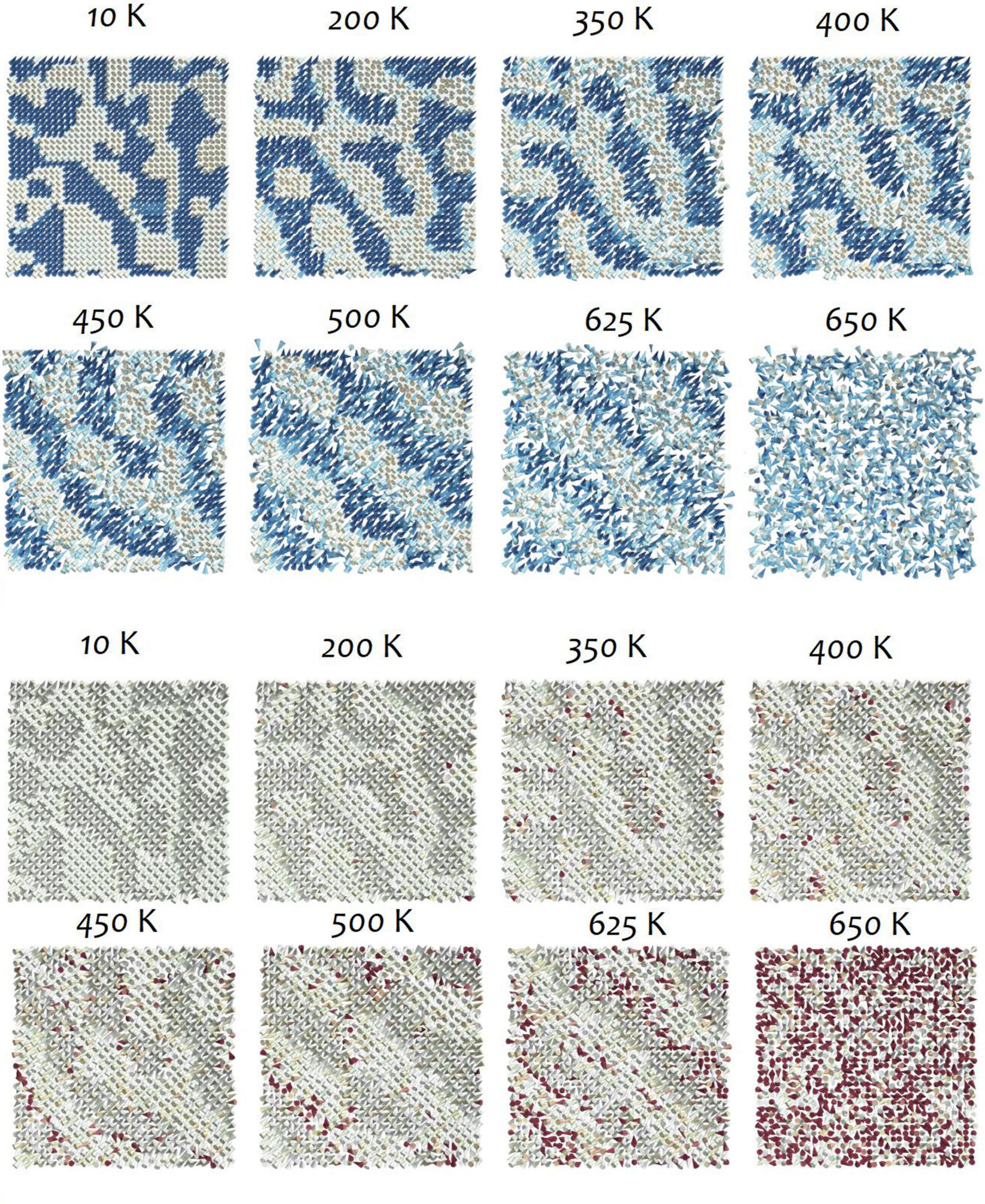

Extended Data Fig. 7 | Simulations of the inverse transition in thin $BiFeO_3$ films. a, **b**, The evolution with temperature of the domain pattern in $BiFeO_3$ in terms of the distribution of the dipolar (**a**) and AFD (**b**) order parameters. Results were obtained through Monte Carlo simulations using the effective Hamiltonian scheme of a 36 × 36 × 5 film subjected to a −0.5% misfit strain with open boundary conditions, a partial screening at film interfaces (effective screening parameter $\beta = 0.5$). The system was abruptly quenched from 2,000 K down to 10 K and consequently progressively heated up with 40,000 relaxation sweeps at each temperature. It can be seen that the distributions of both ferroelectric and AFD order parameters exhibit the inverse transition with $T_{inv} \approx 525$ K and $T_c \approx 650$ K. We find that the system exhibits 71° domain walls. In **a**, dipoles are coloured according to their z component. In **b**, AFD vectors are coloured according to the $\arctan(W_y/W_x)$, where W_y and W_x denote the y and x components of the AFD local vectors.

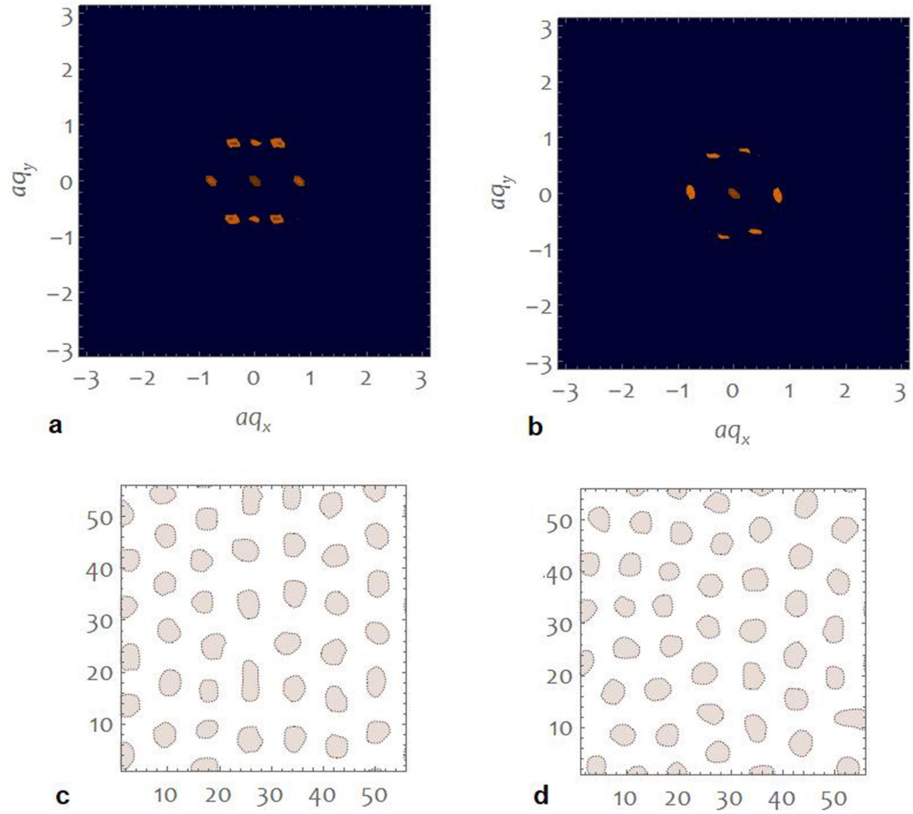

Extended Data Fig. 8 | Origin of the memory effect. a–d, Structure factor plots (**a**, **b**) and bubble configurations (**c**, **d**). Panels **a** and **c** correspond to the bubble state at 10 K, as obtained upon applying a field of 40×10^7 V m^{-1} to the parallel-stripe configuration. Panels **b** and **d** correspond to the bubble state at 10 K, as obtained upon applying a field of 40×10^7 V m^{-1} to the labyrinthine configuration.

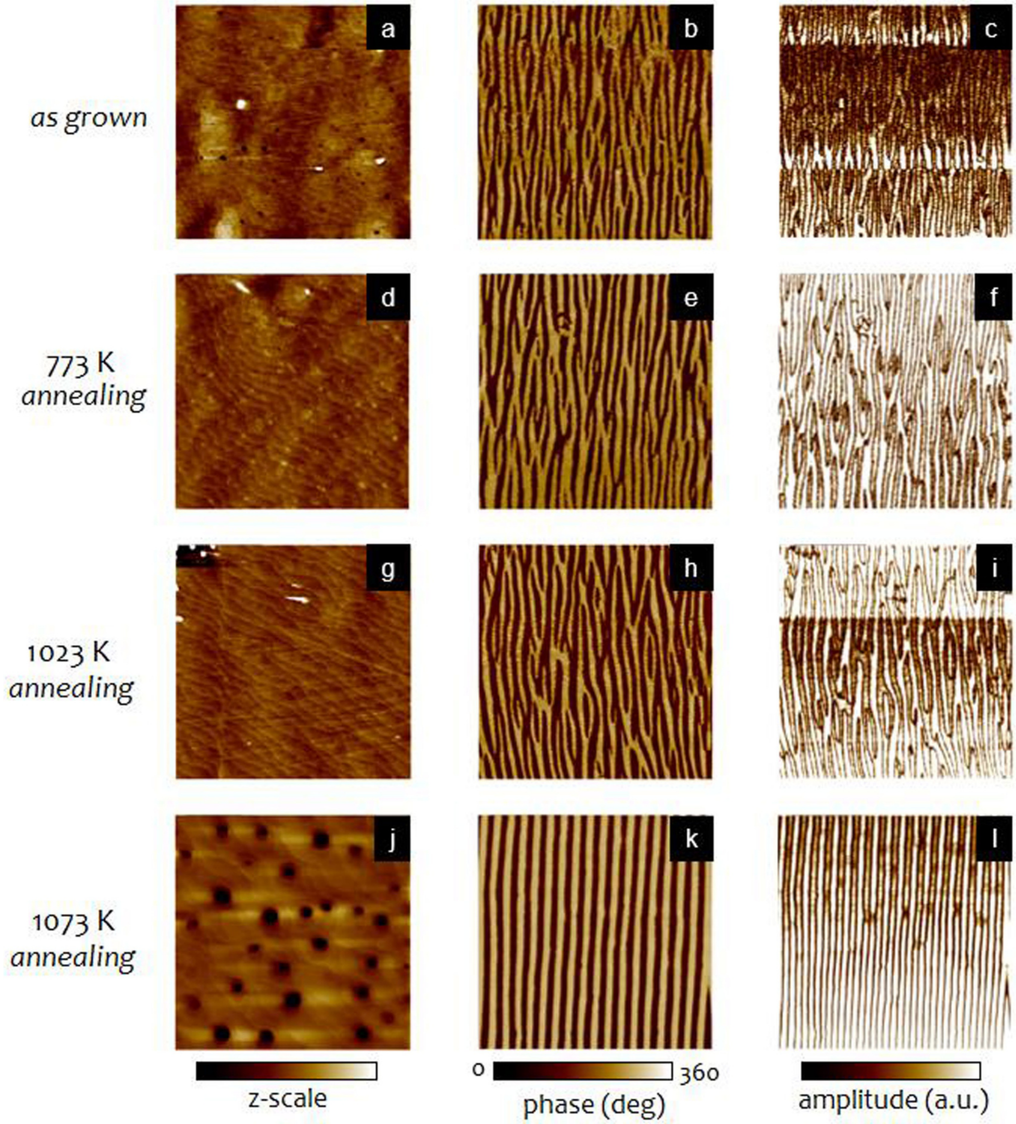

Extended Data Fig. 9 | Imaging of the domain structure evolution with temperature in the $BiFeO_3$ sample. a–l, Topography, in-plane PFM phase and amplitude of the as-grown sample (**a**–**c**), and the same sample after annealing at 773 K (**d**–**f**), 1,023 K (**g**–**i**) and 1,073 K (**j**–**l**). Each annealing step was 1 h long. 'z-scale' corresponds to 4 nm (**a**, **d**, **g**) and 10 nm (**j**).

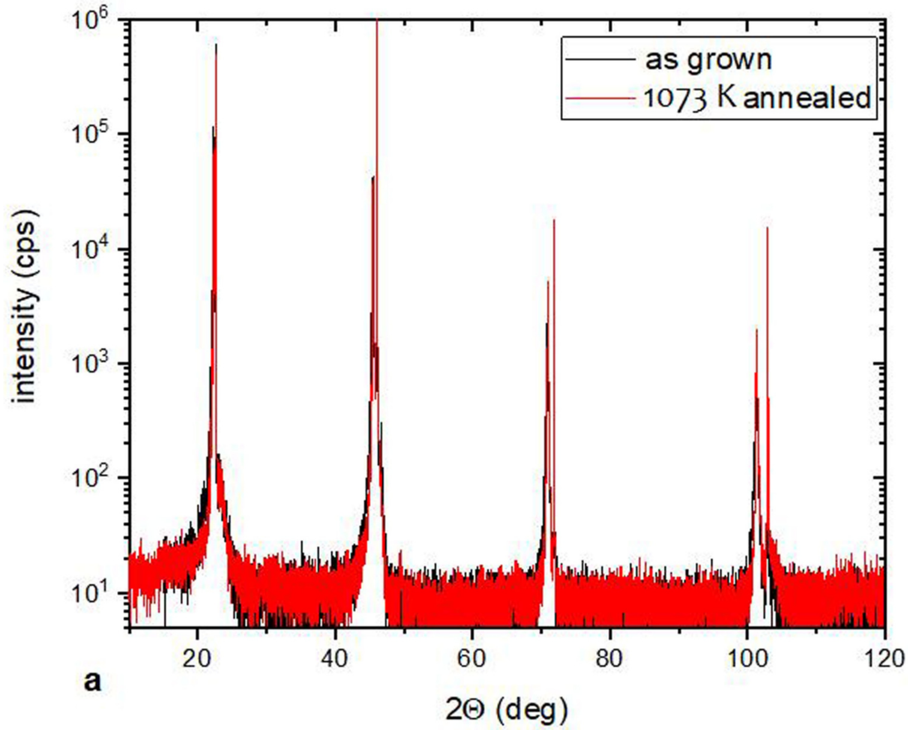

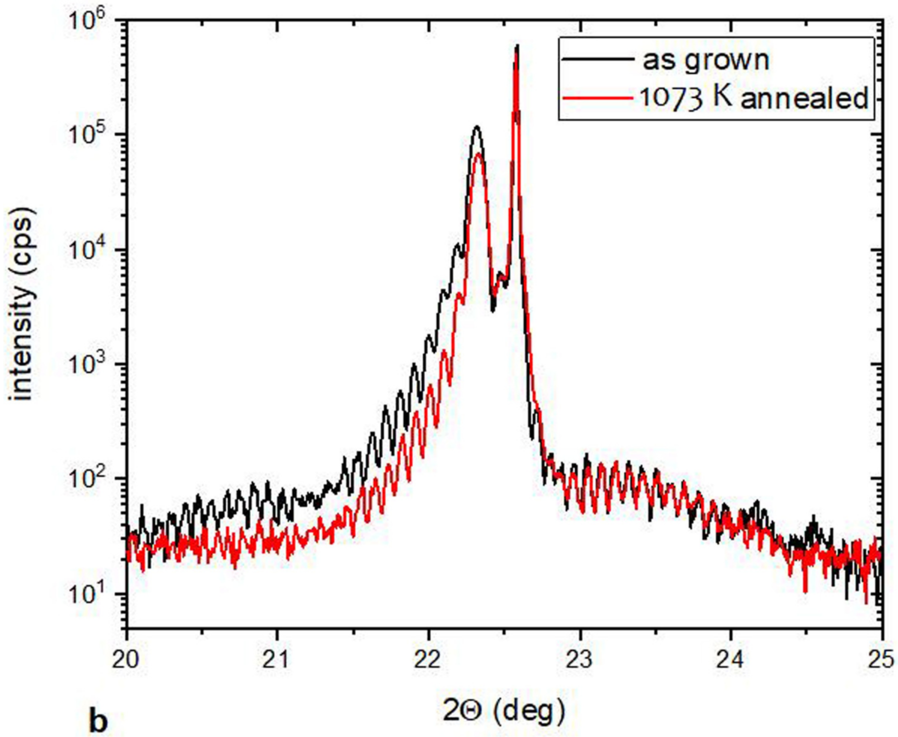

Extended Data Fig. 10 | Structural properties of the $BiFeO_3$ sample before and after annealing. $2\theta-\omega$ XRD patterns of the as-grown $BiFeO_3$ sample and the same sample after the successive annealing up to 1,073 K. **a**, Full scale. **b**, Zoom around the (001) peak.

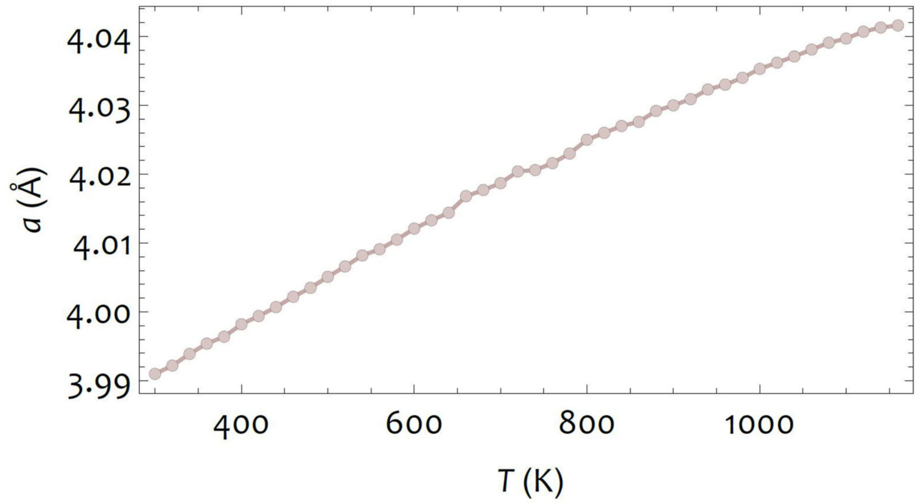

Extended Data Fig. 11 | Evolution with temperature of the lattice parameter of the $BiFeO_3$ sample. Evolution of the out-of-plane parameter upon heating the parallel-stripe phase of the $BiFeO_3$ sample. Values were obtained by fitting the XRD data and do not reveal any phase transition up to 1,160 K.

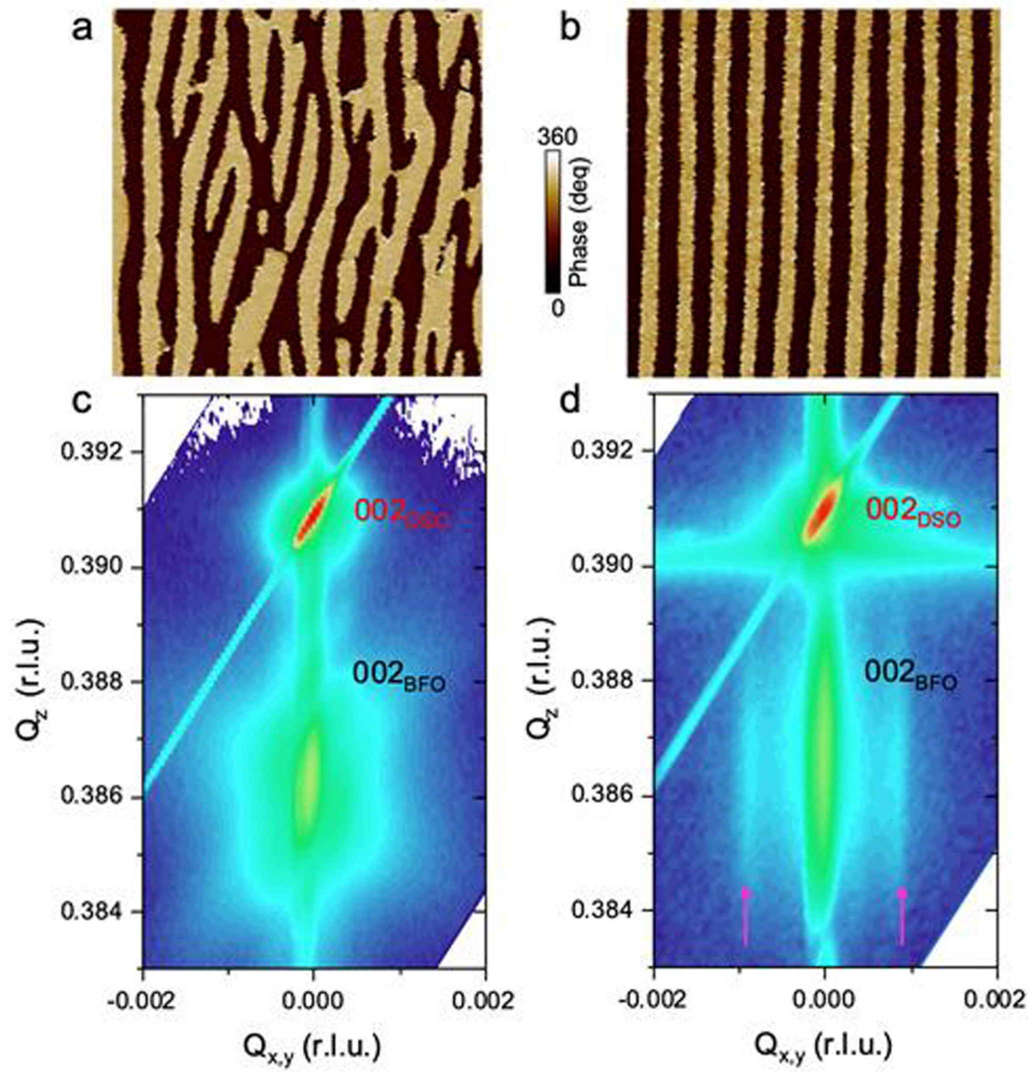

Extended Data Fig. 12 | Ferroelectric and elastic domains in the $BiFeO_3$ sample. Ferroelectric and elastic domain structures in a $BiFeO_3$ thin film grown on a (110)-oriented $DyScO_3$ substrate before and after annealing. **a**, **b**, In-plane PFM phase images of a $BiFeO_3$ thin film for an as-grown sample (**a**) and a sample after annealing at 1,073 K for 1 h (**b**). Images are $2 \times 2\ \mu m^2$. **c**, **d**, Reciprocal space mappings around (002) reflections for the same $BiFeO_3$ thin film for the as-grown sample (**c**) and the sample after annealing at 1,073 K for 1 h (**d**). The pink arrows indicate the satellite positions to the left and right of the (002) film peak. The X-ray beam is aligned at $\Phi = 90°$, that is, perpendicular to the stripes. The indices of $DyScO_3$ and $BiFeO_3$ are written in the monoclinic cells. $Q_{x,y}$ and Q_z indicate the in-plane and out-of-plane reciprocal space units, respectively.

Field-resolved infrared spectroscopy of biological systems

https://doi.org/10.1038/s41586-019-1850-7

Received: 1 February 2019

Accepted: 29 October 2019

Published online: 1 January 2020

Ioachim Pupeza[1,2,5*], Marinus Huber[1,2,5], Michael Trubetskov[2], Wolfgang Schweinberger[1,3], Syed A. Hussain[1,2], Christina Hofer[1,2], Kilian Fritsch[1], Markus Poetzlberger[2], Lenard Vamos[2], Ernst Fill[1], Tatiana Amotchkina[1], Kosmas V. Kepesidis[1], Alexander Apolonski[1], Nicholas Karpowicz[2], Vladimir Pervak[1,2], Oleg Pronin[1,2], Frank Fleischmann[2,4], Abdallah Azzeer[3], Mihaela Žigman[1,2,4] & Ferenc Krausz[1,2,4*]

The proper functioning of living systems and physiological phenotypes depends on molecular composition. Yet simultaneous quantitative detection of a wide variety of molecules remains a challenge[1–8]. Here we show how broadband optical coherence opens up opportunities for fingerprinting complex molecular ensembles in their natural environment. Vibrationally excited molecules emit a coherent electric field following few-cycle infrared laser excitation[9–12], and this field is specific to the sample's molecular composition. Employing electro-optic sampling[10,12–15], we directly measure this global molecular fingerprint down to field strengths 10^7 times weaker than that of the excitation. This enables transillumination of intact living systems with thicknesses of the order of 0.1 millimetres, permitting broadband infrared spectroscopic probing of human cells and plant leaves. In a proof-of-concept analysis of human blood serum, temporal isolation of the infrared electric-field fingerprint from its excitation along with its sampling with attosecond timing precision results in detection sensitivity of submicrograms per millilitre of blood serum and a detectable dynamic range of molecular concentration exceeding 10^5. This technique promises improved molecular sensitivity and molecular coverage for probing complex, real-world biological and medical settings.

The molecular composition of living organisms is a sensitive indicator of their physiological states. Even apparently simple physiological transitions are often connected to highly multivariate concurrent molecular changes. Therefore, the capability to simultaneously observe changes in concentrations of a variety of molecules embedded in complex organic consortia is likely to be instrumental in advancing biology and medical diagnostics systems.

Many biologically relevant changes occur at concentration levels that are often not detectable in system-wide molecular milieus owing to the vast dynamic range of molecular concentrations[1]. Simultaneous quantitative probing of multiple molecules within a complex consortium relies on either biochemical separation of certain types of molecules or depletion of highly abundant ones[16]. Such approaches are time-consuming or expensive or suffer from poor reproducibility, impeding robust, high-throughput implementations. Here we harness broadband optical coherence to address this challenge directly.

Optical spectroscopy of biological samples interrogates the chemical substructures of intact molecules (molecular fragments[17]) rather than molecules as a whole[18,19] by detecting their resonant vibrational response to infrared or Raman excitation. Occurrence of the same or similar fragments in different biomolecules and rapid dephasing results in overlapping temporal and spectral responses and hampers the identification of individual molecules[2–4] in complex samples. However, the detected superposition of the responses of all fragments is characteristic of molecular composition, representing what may be referred to as the global molecular fingerprint (GMF) of the sample.

Higher excitation power increases the GMF signal, making smaller changes in the sample's molecular composition detectable. In spectroscopies that capture time-integrated fields[11,20–23]—that is, frequency-resolved spectroscopy—the GMF signal hits the detector along with the (much stronger) excitation transmitted through the sample. This has far-reaching implications. First, in the limit of strong excitation, the weakest molecular signal detectable tends to be limited by the technical noise of the excitation source[22,24]. Second, and more fundamentally, even in the absence of technical noise, saturation of the detector (elements) places a limit on the sensitivity[11,22,24]. These limitations are schematically illustrated in Fig. 1a, see 'Frequency-resolved spectroscopy'.

In this work, we show how time-resolved sampling of the electric-field emitted by impulsively excited molecular vibrations allows us to overcome these limitations by isolating the retarded molecular signal from any excitation background. We term the technique field-resolved spectroscopy (FRS). Sensitive sampling of the isolated molecular signal generated by a powerful, ultrashort-pulsed infrared source enables broadband transmission spectroscopy of biological systems in their

[1]Ludwig Maximilians University München, Garching, Germany. [2]Max Planck Institute of Quantum Optics, Garching, Germany. [3]King Saud University, Department of Physics and Astronomy, Riyadh, Saudi Arabia. [4]Center for Molecular Fingerprinting, Budapest, Hungary. [5]These authors contributed equally: Ioachim Pupeza, Marinus Huber. *e-mail: ioachim.pupeza@mpq.mpg.de; krausz@lmu.de

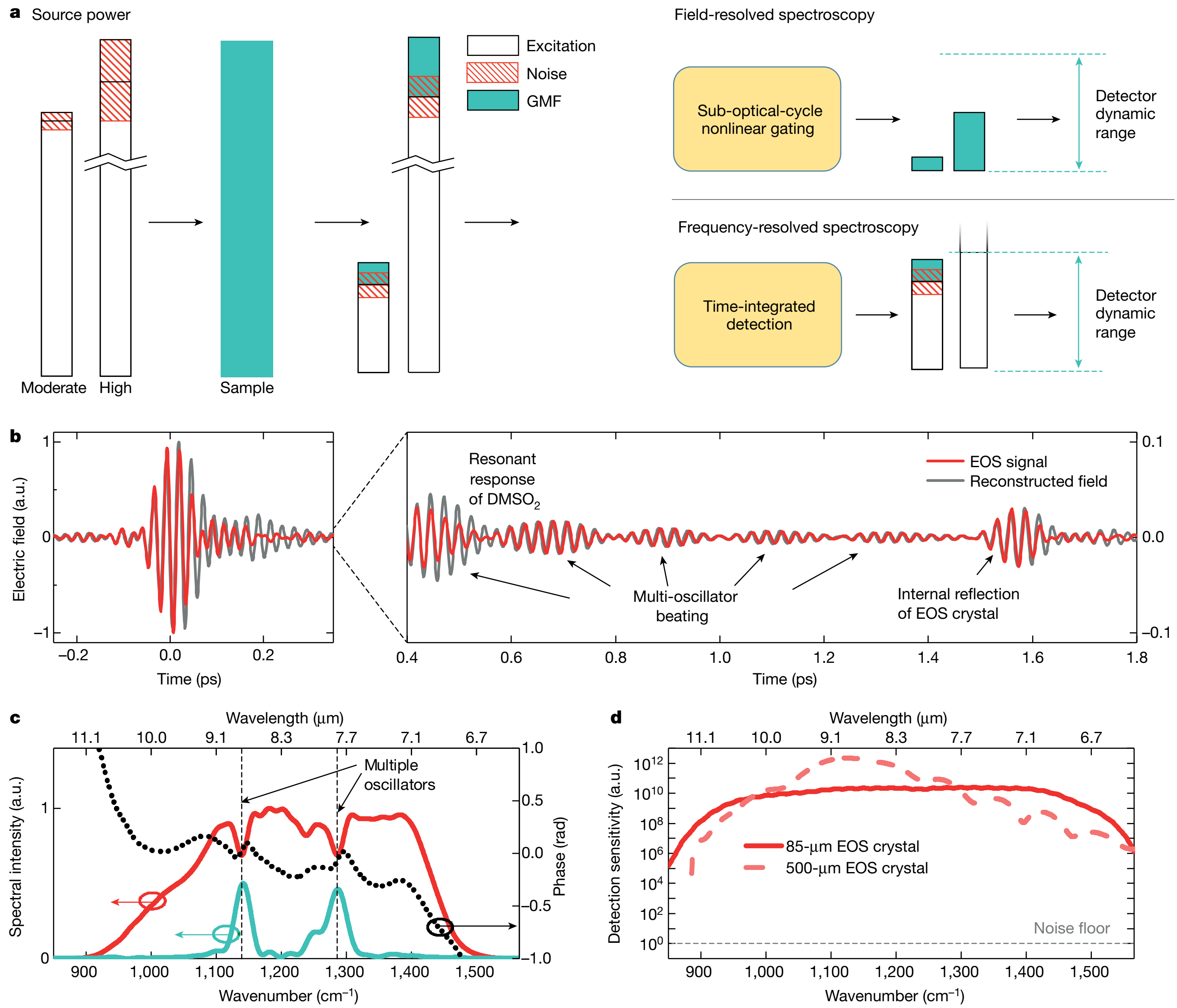

Fig. 1 | Infrared FRS. a, Schematic comparison of spectroscopic techniques. Infrared light (white bar length indicates source power) with intensity noise (technical noise, red hatching) is transmitted through a sample, acquiring GMF information (cyan shading). For frequency-resolved spectroscopy, the GMF signal is detected 'on top' of the excitation signal transmitted through the sample. As a consequence, (1) the GMF signal needs to surpass the excitation noise (surviving balanced detection) and (2) enhancing the GMF signal by increasing the excitation power is limited by the detector's dynamic range. For FRS, following a few-cycle excitation, sub-optical-cycle nonlinear gating isolates ultrabrief fractions of the GMF from any infrared background, avoiding both requirement (1) and limit (2); see Methods. **b**, Infrared electric field as reconstructed from the measured electro-optic sampling (EOS) trace using an 85-μm-thick GaSe EOS crystal (Supplementary Information section I) after transmission through a solution of 10 mg ml^{-1} $DMSO_2$ in water. The reconstructed electric field strongly resembles the EOS signal, owing to the broadband instrument response function. The resonant sample response is temporally well separated from the non-resonant response (incorporating the excitation) and exhibits 'beating' of several oscillation frequencies. **c**, Fourier transform of the EOS trace shown in **b**, truncated at 1.5 ps to exclude spectral modulations caused by the echo in the EOS crystal. The solid red line shows the spectral intensity, revealing absorption dips associated with vibrational modes of $DMSO_2$ molecules; the black dashed line shows the spectral phase; the cyan line shows the spectral intensity of the signal in the time window 380–1,500 fs, showing time-filtered GMF information. **d**, Spectral detection sensitivity above the detection noise floor (3-ps time window, 25-s measurement time, transmission through cuvette filled with water). The solid and dashed lines are the bandwidth-optimized versus quantum-efficiency-maximized EOS (Supplementary Information section I), respectively.

natural, aqueous environment (see 'Field-resolved spectroscopy' in Fig. 1a).

Field-resolved molecular spectroscopy

Fourier-transform infrared (FTIR) spectrometers employing thermal radiation sources[20] are the gold standard for broadband vibrational spectroscopy[2–4,7,8,19,24–33]. In liquid samples, they have detected concentration levels down to several micrograms per millilitre[3,25,27,30,33,34]. This limitation has so far been overcome only by sample drying[33] or targeted detection with functionalized optical biosensors[34,35].

Recently, tunable quantum cascade lasers[23,24,27,36,37] and femtosecond laser sources[15,38–40] have dramatically enhanced the excitation brilliance. For the reasons sketched in Fig. 1a and explained in the Methods, frequency-resolved spectroscopies have not been able to fully capitalize on this to achieve improved sensitivity and specificity in molecular

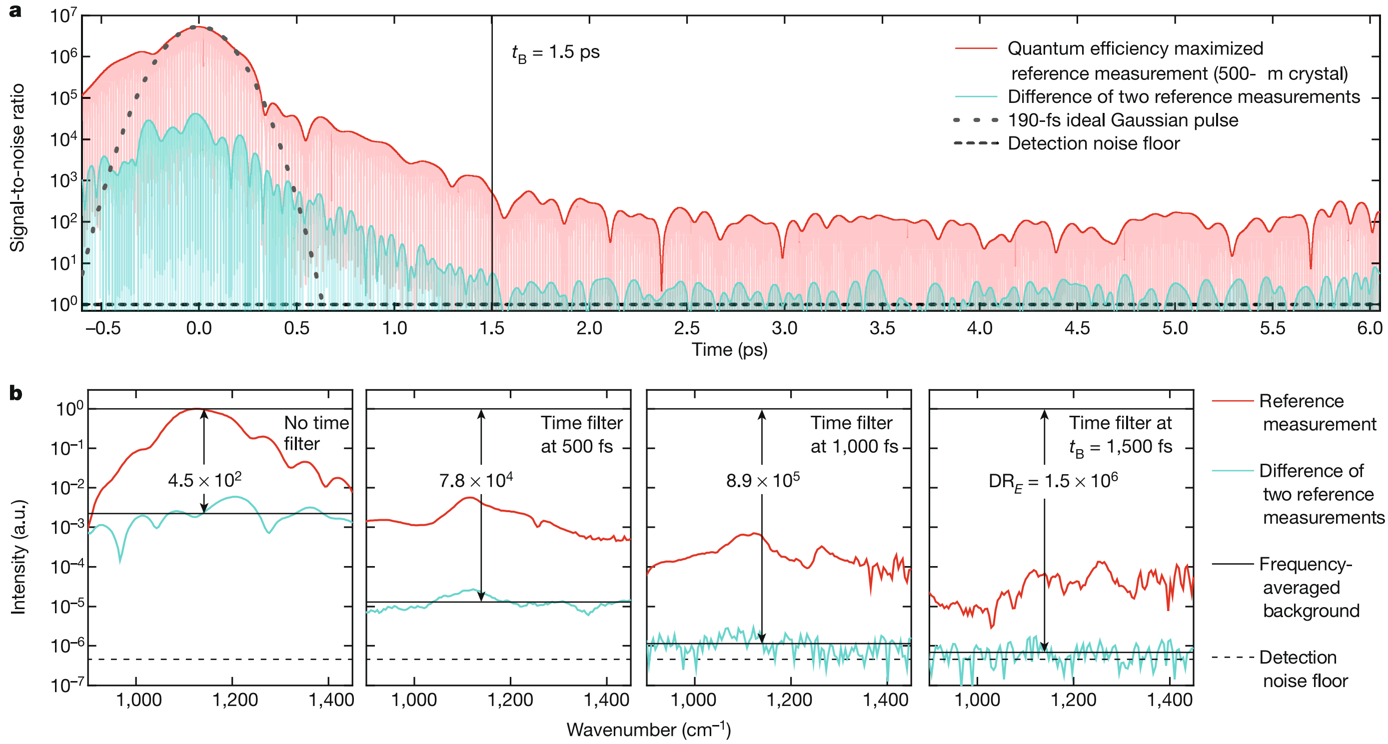

Fig. 2 | Background quantification for detection of resonant molecular responses. a, The red line is the time-resolved magnitude of the EOS signal (revealing field oscillations) related to the detection noise floor (signal-to-noise ratio), for a reference measurement of pure water (quantum-efficiency-maximized detection setting, 37-s effective measurement time). Following the excitation, the molecular signal from residual atmospheric background in the beam path is observed. The cyan line is the numerical difference of two independent reference measurements. The recorded traces were frequency-filtered by a 20th-order super-Gaussian filter suppressing any noise outside the spectral window 900–1,450 cm^{-1}. The grey dotted line is the 190-fs (full-intensity-width-at-half-maximum duration) ideal Gaussian pulse, for comparison. **b**, Frequency-domain definition of DR_E and t_B. The magnitudes of the Fourier transforms of the traces in **a** are shown for different numerical high-pass time filter values. Setting the filter at t_B (the beginning of the background-free time-domain measurement, rightmost panel) yields an electric-field peak dynamic range of $DR_E = 1.5 \times 10^6$ around 1,140 cm^{-1}.

detection[24,27]. Here, we show how FRS of few-cycle infrared-laser-excited molecular vibrations enables us to take advantage of the temporal structure and power of laser-driven few-cycle infrared sources.

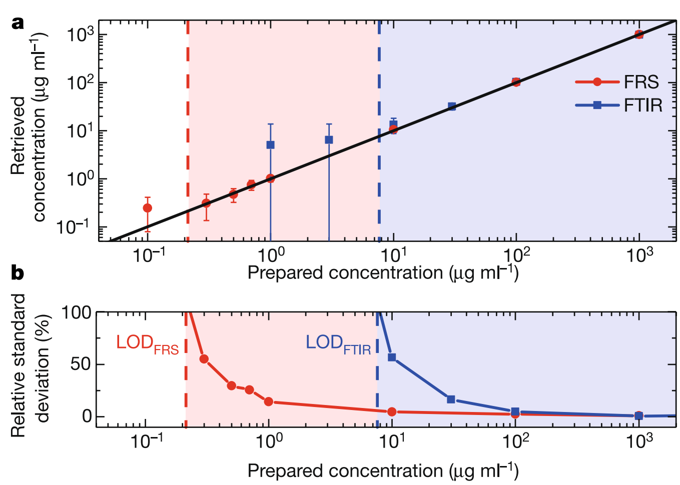

Fig. 3 | Limit of detection of DMSO2 molecules dissolved in water. a, Results of the concentration retrieval (see Supplementary Information section IV) with quantum-efficiency-optimized FRS (red data points) and FTIR (blue data points). The dots indicate the mean values obtained from at least five measurements per concentration and the error bars show the absolute standard deviation. **b**, Relative standard deviation for the retrieved values. LOD, limit of detection. The coloured shading indicates the range of concentrations exceeding the LOD of each instrument.

The experimental setup is described in the Methods and in Supplementary Information section I (see also Extended Data Figs. 3, 4). In short, waveform-stable, few-cycle mid-infrared (MIR) pulses abruptly excite molecular vibrations by resonant absorption. The sample-specific electric field (previously referred to as GMF) emitted in the wake of the excitation pulse (Supplementary Video 1 and Methods) is detected via EOS[10,13–15] (Fig. 1b, c). The thickness of the electro-optic crystal controls a trade-off between the bandwidth and the sensitivity of detection (Fig. 1d).

The nonlinear frequency conversion underlying EOS sequentially isolates ultrabrief fractions of the GMF from any infrared background—including the excitation pulse transmitted through the sample, and the thermal background (see Fig. 1a and Methods). Drawing on preliminary experiments[41,42], here we report a direct measurement of MIR molecular electric fields emanating from biological samples.

Detection of time-gated molecular signals

In any scheme measuring time-integrated fields, the minimum detectable absorbance, MDA_{FD}, defining the minimum detectable depth of the dips in the red line in Fig. 1c, is given by (Supplementary Information section II):

$$MDA_{FD} \approx \sigma \quad (1)$$

where σ represents the relative fluctuations of the measured signal in the considered spectral element. Here, σ incorporates contributions from excitation and detection noise, as well as from the limited detector dynamic range[22].

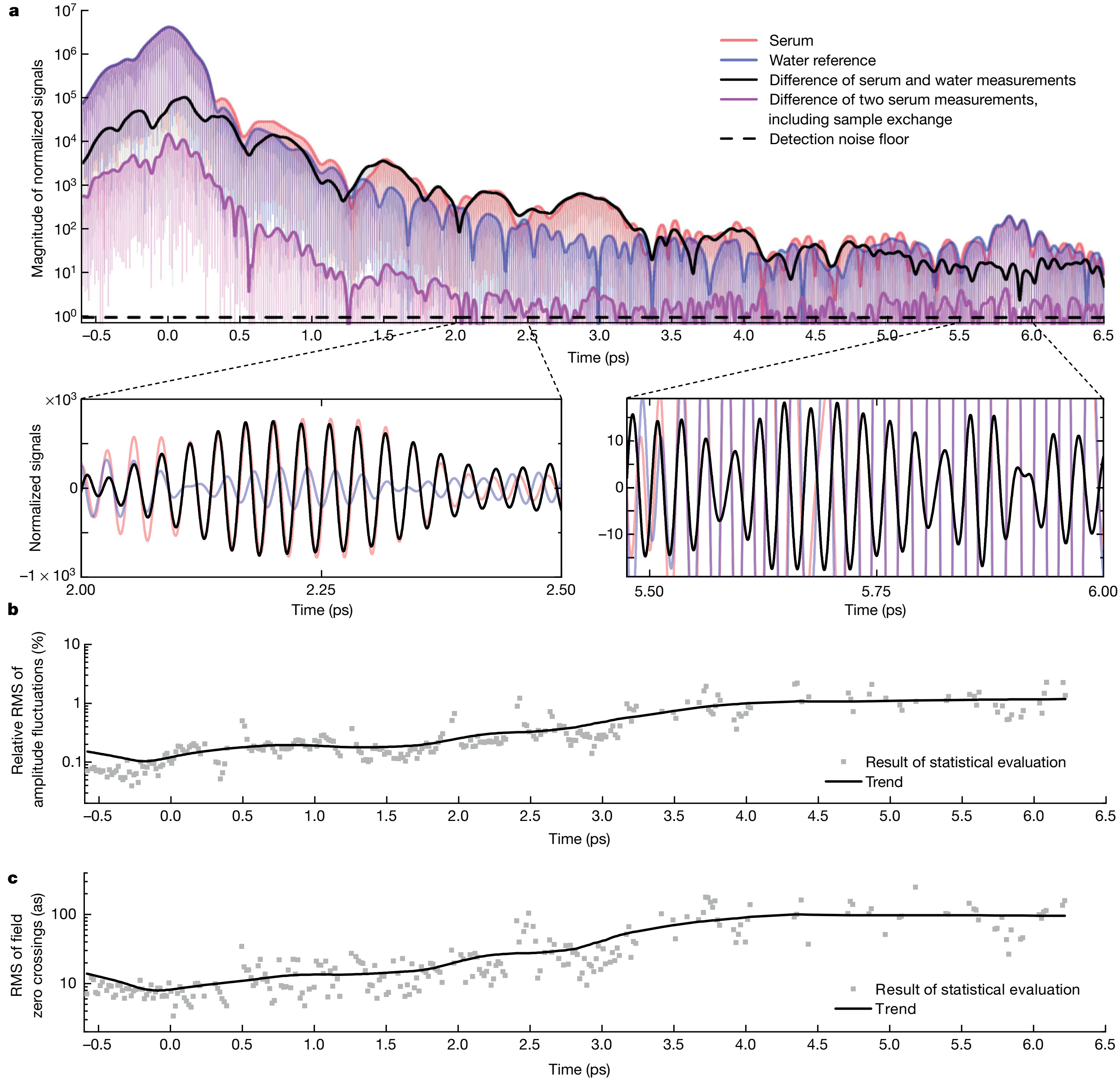

Fig. 4 | GMFs of human blood serum and their reproducibility. a, Magnitude of the EOS signals, recorded with quantum-efficiency-optimized FRS (see key). The insets show linear-scale representations of the signals depicted in the main panel in two different time windows. **b**, **c**, Relative (**b**) and absolute (**c**) root-mean-square (RMS) of oscillation amplitude and zero crossings of five hundred measurements of the GMF of a serum sample (without sample exchange) (see Supplementary Information section V).

In FRS, temporal isolation of (wave-cycle-scale) fractions of the GMF renders the weakest detectable molecular response largely immune against the noise of excitation intensity, as is apparent from the cyan line in Fig. 1c. This is indicated by the expression for the MDA obtained by time-domain modelling of the molecular system with an isolated Lorentzian oscillator of dephasing time T_L (Supplementary Information section II):

$$\mathrm{MDA_{FRS}} = \frac{2}{\mathrm{DR}_E}\exp\left(\frac{t_B}{T_L}\right) \quad (2)$$

Here, the dynamic range DR_E is defined as the ratio of the spectral amplitude of the electric field of the overall signal reaching the detector at the centre frequency of the Lorentzian oscillator to that of the weakest signal detectable after passage through a temporal filter opening at t_B. The parameter t_B is defined as the instant when the temporal window for an infrared-background-free measurement begins.

This is the case when the numerical difference between two subsequent measurements (in this case, of liquid water) reaches the detection noise floor (Fig. 2a). In our proof-of-principle measurement with the quantum-efficiency-maximized FRS setting, this occurs at about $t_B = 1{,}500$ fs, yielding a value of DR_E in excess of 10^6 for absorptions with centre frequencies between 1,080 cm^{-1} and 1,190 cm^{-1} (for a 7-ps time window and 37-s effective measurement time, see right panel of Fig. 2b). For a dephasing time of the order of a picosecond, typical for an aqueous environment[9], equation (2) predicts a minimum detectable absorbance of the order of 10^{-6}.

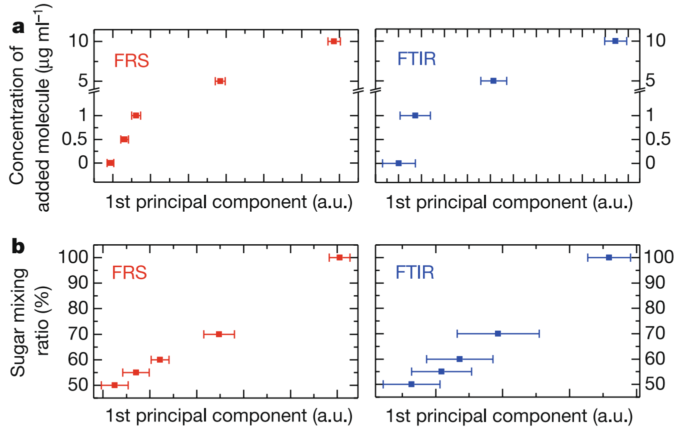

Fig. 5 | Sensitivity and specificity of FRS of complex fluids performed with bandwidth-optimized sampling. a, Principal component analysis results (separation along the 1st principal component) for a human blood serum sample containing an added aqueous solution of decreasing $DMSO_2$ concentration, and fingerprinted with FRS using quantum-efficiency-optimized detection (left panel) and with FTIR (right panel). The plots show the mean and relative standard deviation of the values of the 1st principal component for data classes obtained by repeated measurements of samples with nominally identical added $DMSO_2$ concentration. **b**, Principal component analysis results for a mixture of two sugars dissolved in water with constant total concentration and varying relative concentration (see text), and fingerprinted with FRS using bandwidth-optimized detection (left panel) and with FTIR (right panel).

For experimental verification, we investigated methylsulfonylmethane ($DMSO_2$) dissolved in deionized water. FRS was benchmarked against a state-of-the-art FTIR spectrometer equipped with a thermal infrared source (MIRA Analyzer, Micro Biolytics; see Supplementary Information section III). With both instruments, at least five aliquots of concentrations ranging from 1 mg ml^{-1} to 100 ng ml^{-1} were measured over a duration of T = 45 s each, with a spectral resolution of 4 cm^{-1} (realized in FRS by setting the duration of the temporal window of measurement equal to 8.3 ps). Reference measurements of solvent only (deionized water) were performed in alternating order. The concentration values retrieved from the measured data (see Supplementary Information section IV) are summarized in Fig. 3. The limit of detection is defined as the concentration retrieved with a relative standard deviation of 100%. Our study yields an FRS limit of detection of 200 ng ml^{-1}, by a factor of 40 lower than that obtained with the FTIR spectrometer (8 μg ml^{-1}). This is in agreement with the prediction of equation (2); see Supplementary Information section IV and Extended Data Fig. 7. We estimate a limit of detection of approximately 7 μg ml^{-1} for Fourier-transform spectroscopy (FTS)[22] performed with our coherent infrared source and state-of-the-art infrared photodetectors (see Methods).

The exponential dependence of the detection limit on t_B in equation (2) emphasizes how FRS is fundamentally different from any frequency-domain spectroscopy, where t_B is irrelevant (see also Methods). To investigate this dependence—and thereby this hitherto unexplored advantage—we repeated the $DMSO_2$ dilution series measurement with shorter, sub-60-fs infrared excitation pulses (Supplementary Information section I) and the bandwidth-optimized detection setting of the FRS instrument (Fig. 1d, continuous line). This combination substantially improved the opening time for background-free detection to t_B = 450 fs (Supplementary Information section IV). The improvement came at the expense of a factor-of-ten reduction of DR_E (Fig. 1d). This reduction would, in its own right, result in a factor-of-ten increase of the minimum detectable concentration, according to equation (2). By contrast, we observe an increase from 200 ng ml^{-1} to 450 ng ml^{-1} only, mainly due to shortening t_B from 1.5 ps to 0.45 ps (Supplementary Information section IV). This corroborates the predicted sensitivity of MDA_{FRS} to t_B.

A more powerful broadband few-cycle infrared source[40] will improve DR_E while preserving the full bandwidth along with the reduced t_B. This holds promise for a detection limit below 50-ng ml^{-1} in combination with super-octave spectral coverage.

Attosecond-timed molecular signals

For the investigation of complex molecular consortia, the sensitivity and specificity of FRS-based molecular fingerprinting depends critically on the temporal coherence of the GMF signal and its reproducibility over extended measurement time. In gas-phase samples, vibrational dephasing occurs on the nanosecond scale and the required long acquisition delays are advantageously realized with two asynchronous femtosecond oscillators[12,21,43,44], harnessing optical frequency-comb techniques[45,46]. By contrast, in the liquid phase the coherent molecular signal survives only for several picoseconds[9]. To efficiently use measurement time and ensure attosecond delay precision, we implemented waveform sampling with a mechanical delay line equipped with interferometric delay tracking[47]. Figure 4a shows the field-resolved GMF of a human blood serum sample, as representative of a cell-free bioliquid routinely used in biomedical profiling. The insets in Fig. 4a, b show the differential GMF of the biomolecular ensemble in the sample, as a result of subtracting the signal obtained from pure water from the one of the sample. This 'pure' biomolecular signal decays by a few orders of magnitude within 5 ps (compare the left and right panels in Fig. 4b), revealing a dephasing time of collective biomolecular vibrations in human blood serum far below 1 ps.

Five hundred consecutive measurements of the same serum sample yield a relative root-mean-square deviation of the field oscillation amplitude from its mean value of around 0.2% and an absolute root-mean-square of the zero crossings of the infrared GMF field in the range of 20 as, within the first two picoseconds following the excitation (Fig. 4c, d). It is this reproducibility that enables suppression of the electric field background by up to three orders of magnitude via comparison with a reference field (Figs. 2a and 4a), opening the window for background-free measurement less than 2 ps after the excitation pulse peak, even in a highly complex sample such as blood serum (Fig. 4a, magenta line).

Sensitivity and specificity of FRS

In real-world applications[2–4,26,27], molecular fingerprinting of complex biofluids will need to probe miniscule changes in the sample's chemical composition, often caused by low-abundance molecules. The method's utility for biological or medical applications will be greatly dependent on the smallest changes in molecular concentration that can cause a detectable distortion of the field-resolved GMF. To assess this concentration level, we added controlled amounts of $DMSO_2$ to the serum sample fingerprinted in Fig. 4a. The results of a principal component analysis of the infrared fingerprints of these samples, measured with our FRS and FTIR devices (Supplementary Information section VI and Extended Data Fig. 8) are shown in Fig. 5a. The plots show the mean and the spread of the data classes of repeated measurements of samples with different concentrations of the added molecule, along the first principal component. FRS appears to clearly separate the sample containing additional $DMSO_2$ molecules at a concentration of 500 ng ml^{-1} from the reference sample. Moreover, the error bars suggest that FRS is capable of detecting changes in molecular concentration down to the 200 ng ml^{-1} level in human blood serum, an improvement of nearly an order of magnitude compared to state-of-the-art FTIR spectrometry.

Hence, the smallest changes currently detectable are more than five orders of magnitude below the concentration of the most highly

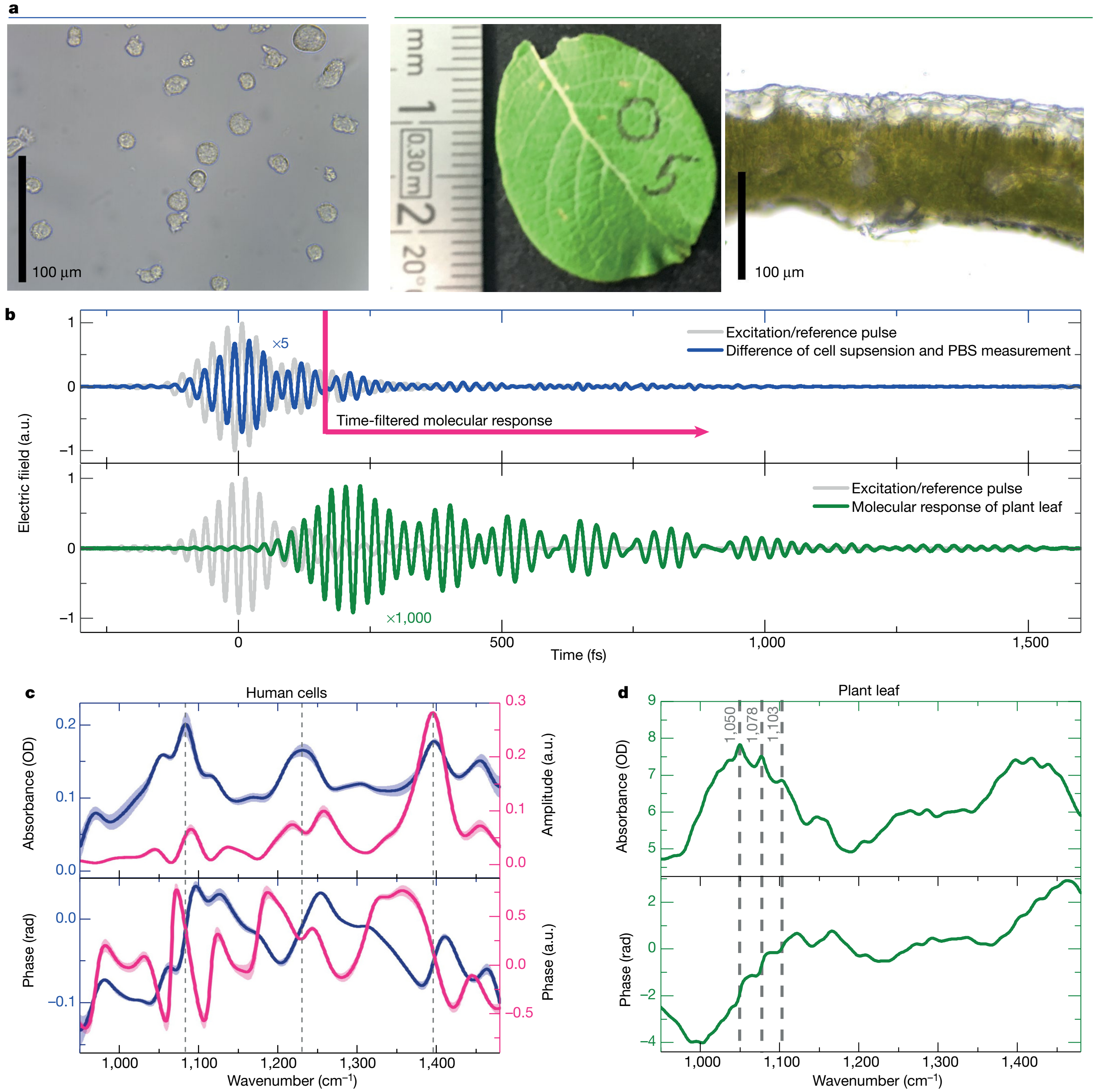

Fig. 6 | FRS of strongly absorbing living systems. a, The blue-outlined (left) panel is an optical microscope image of cultured human THP-1 cells. The green-outlined panel (right) shows the top and lateral views of a leaf from *Salix caprea*. The measurement of the intact hydrated leaf was performed 5 min after collection, within the marked area. **b**, The upper panel shows GMF of THP-1 cells in suspension, contained in a 100-μm-thick cuvette (blue line) referenced by numerical subtraction to the signal of the suspension medium (phosphate-buffered saline, PBS; grey line). The lower panel shows the molecular response obtained after transmission through a 120-μm-thick leaf of *Salix caprea* (green line) with air reference (grey line). **c**, Absorption (top panel) and phase (lower panel) spectra of five measurements of human THP-1 cells (blue lines) along with the amplitude and phase of temporally-filtered GMFs (magenta lines). Absorption and phase spectra of the plant leaf are shown in **a**. The standard deviations of multiple measurements in **c** and **d** are indicated by the shaded areas (see Supplementary Information section VII for data processing). We note that the error corridor of the measurement in **d** is smaller than the line thickness and therefore not visible. The grey dotted lines in **c** and **d** indicate prominent absorption peaks.

abundant molecules of blood serum, albumin[1]. This implies a detectable concentration dynamic range in excess of 10^5.

Although the relative intensity noise of the excitation does not affect the FRS limit of molecular detection with a spectrally isolated feature, the lowest detectable concentration of the same molecule in a complex environment is limited by the relative intensity noise of the overall GMF signal. This, in turn, is likely to be dominated by the noise of the excitation source. As an important consequence, the current FRS concentration dynamic range of 10^5 offers substantial room for further improvement by suppressing the noise of the GMF signal. An efficient measure to this end may be 'freezing' the excitation source noise by scanning faster than the characteristic time of low-frequency intensity fluctuations[22,48].

To test the specificity of the measured fingerprints, that is, the sensitivity to small changes in relative concentrations, we prepared aqueous solutions of two different sugar molecules of constant total concentration and varying relative concentrations (Supplementary Information section VI). The total concentration of 100 μg ml^{-1} was chosen to be well above the limit of detection of both instruments. To challenge the method, we used two molecules, maltose and melibiose, which have very similar absorption characteristics (Supplementary Information Section VI and Extended Data Fig. 9). The data in Fig. 5b reveal that FRS outperforms FTIR spectrometry in sensing not only small absolute changes but is also sensitive to relative changes in concentration of molecules of a complex ensemble.

Probing of intact biological systems

Non-invasive, quantitative probing of intact biological systems would benefit a diversity of biological, biomedical, pharmaceutical and ecological applications. To circumvent sensitivity limitations caused by the strong absorption of infrared radiation in liquid water, so far the majority of studies of biological matter have drawn on sample preparations[7,8,28,29] that substantially alter the state of the sample (such as drying, fixation, slicing, chemical extraction, homogenization and so on). Direct interrogation of intact living systems with infrared spectroscopy has been limited to interaction lengths of the order of 10 μm (or less), either in attenuated-total-reflection geometry[28] or by using extremely thin microfluidic cuvettes[31,32]. Both implementations prevent the majority of living cells from being studied in vivo (for example, human cells are on average larger than 10 μm in diameter). More recently, quantum-cascade lasers have enabled infrared transmission measurements of living systems with path lengths of several tens of micrometres, albeit with restrictions on the bandwidth and with modest signal-to-noise ratios[36,37].

The unparalleled dynamic range of FRS implemented with a powerful few-cycle infrared source enables these restrictions to be overcome. Here we present the feasibility of infrared fingerprinting of living human cells (THP-1 leukaemic-monocyte-like cell line) cultured and measured directly in suspension (Fig. 6a, left panel) by transillumination of a 0.1-mm-thick flow-through cuvette (see also Supplementary Information section VII). In spite of the order-of-magnitude increase in interaction length as compared to previous broadband measurements of cells from the same cell line[49], the differential signal originating from the molecules of the cells (blue line in Fig. 6b) is acquired with a high signal-to-noise ratio (Supplementary Information section VII). The corresponding absorption and phase spectra are depicted in Fig. 6c (blue lines), with the former reflecting well the spectral signatures featured by THP-1 cells when squeezed into a 7-μm-thick cuvette[49]. Temporal gating of the molecular signal (magenta lines in Fig. 6c) uncovers the splitting of the absorption lines at approximately 1,080 cm^{-1} and 1,230 cm^{-1}, along with relevant phase oscillations—features that are not apparent in the time-integrated spectra (blue lines). This underlines the power of isolating the molecular signal from an (inherently) noisy excitation, offered by FRS.

We have further tested the ability of FRS to acquire transmission spectra of strongly absorbing samples by transilluminating intact plant leaves from the goat willow (*Salix caprea*), a common deciduous tree, with a thickness of approximately 120 μm (Fig. 6a, right panel). The spectra in Fig. 6d feature clearly discernible absorption bands at 1,050 cm^{-1}, 1,078 cm^{-1} and 1,103 cm^{-1}, corresponding to the C–O stretching motion characteristic of carbohydrates[7,50] widespread in cell walls and cellular compartments of plant leaves. The spectrally resolved attenuation ranges from 5 to 8 orders of magnitude, which is orders of magnitude higher than previously demonstrated in a broadband infrared transmission measurement. In addition, it shows the instrument's ability to resolve absorption over several orders of magnitude in strength without the need to adjust the light power reaching the detector[24].

Conclusions and outlook

We have measured infrared-electric-field molecular fingerprints of organic molecules in aqueous solution and in human blood sera. In both settings, the limit of detecting changes in concentration of individual molecules lies in the range of hundreds of nanograms per millilitre for less than one minute of data acquisition time. The amplitude of the coherent emission carrying the GMF of human blood serum was observed to decay by a few orders of magnitude within a few picoseconds. The reproducibility of electric-field oscillations was found to be in the range of tens of attoseconds over a temporal span exceeding six picoseconds following the excitation.

These findings emphasize the performance of FRS of impulsively excited molecular vibrations for GMF of complex biofluids and uncover potential for its further improvement. First, the extremely fast (much less than a picosecond) decay of vibrational coherence in human blood serum suggests an exponential improvement of the detection limit with further steepening of the temporal decay of the excitation transmitted through the sample. Second, the coherence of the recorded molecular signal over spans of several picoseconds along with reduced source-noise-induced GMF noise, by rapid scanning[48], for example, will increase the detectable range of concentrations in biofluids. The capability of simultaneous probing of multi-molecular changes over a dynamic range of detectable concentration changes in excess of 10^5 holds promise for applications in the life sciences and medical diagnostics.

Last, broadband infrared fingerprinting of physiologically relevant living human cells is now feasible in transmission, opening the door for combining infrared fingerprinting with standard flow cytometry. The unparalleled dynamic range of FRS implemented with powerful few-cycle light promises a new regime of transmission-mode vibrational spectroscopy and spectro-microscopy of intact living systems: individual biological cells, bulk-cell and tissue cultures, organs such as plant leaves—all settings in which excessive water absorption has so far constituted a major obstacle.

Online content

Any methods, additional references, Nature Research reporting summaries, source data, extended data, supplementary information, acknowledgements, peer review information; details of author contributions and competing interests; and statements of data and code availability are available at https://doi.org/10.1038/s41586-019-1850-7.

1. Geyer, P. E., Holdt, L. M., Teupser, D. & Mann, M. Revisiting biomarker discovery by plasma proteomics. *Mol. Syst. Biol*. **13**, 942 (2017).
2. Barth, A. & Haris, P. I. *Biological and Biomedical Infrared Spectroscopy* (IOS Press, 2009).
3. Lasch, P. & Kneipp, J. *Biomedical Vibrational Spectroscopy* (Wiley, 2010).
4. Baker, M. J. et al. Developing and understanding biofluid vibrational spectroscopy: a critical review. *Chem. Soc. Rev*. **45**, 1803–1818 (2016).
5. Hasin, Y., Seldin, M. & Lusis, A. Multi-omics approaches to disease. *Genome Biol*. **18**, 83 (2017).
6. Chen, R. et al. Personal omics profiling reveals dynamic molecular and medical phenotypes. *Cell* **148**, 1293–1307 (2012).
7. Türker-Kaya, S. & Huck, C. A review of mid-infrared and near-infrared imaging: principles, concepts and applications in plant tissue analysis. *Molecules* **22**, 168 (2017).
8. Doherty, J., Cinque, G. & Gardner, P. Single-cell analysis using Fourier transform infrared microspectroscopy. *Appl. Spectrosc. Rev*. **52**, 560–587 (2017).
9. Laubereau, A. & Kaiser, W. Vibrational dynamics of liquids and solids investigated by picosecond light pulses. *Rev. Mod. Phys*. **50**, 607–665 (1978).
10. Sell, A., Scheu, R., Leitenstorfer, A. & Huber, R. Field-resolved detection of phase-locked infrared transients from a compact Er:fiber system tunable between 55 and 107 THz. *Appl. Phys. Lett*. **93**, 251107 (2008).
11. Coddington, I., Swann, W. C. & Newbury, N. R. Time-domain spectroscopy of molecular free-induction decay in the infrared. *Opt. Lett*. **35**, 1395–1397 (2010).
12. Kowligy, A. S. et al. Infrared electric field sampled frequency comb spectroscopy. *Sci. Adv*. **5**, eaaw8794 (2019).
13. Wu, Q. & Zhang, X.-C. Free-space electro-optic sampling of terahertz beams. *Appl. Phys. Lett*. **67**, 3523–3525 (1995).
14. Nahata, A., Weling, A. S. & Heinz, T. F. A wideband coherent terahertz spectroscopy system using optical rectification and electro-optic sampling. *Appl. Phys. Lett*. **69**, 2321–2323 (1996).

15. Pupeza, I. et al. High-power sub-two-cycle mid-infrared pulses at 100 MHz repetition rate. *Nat. Photon*. **9**, 721–724 (2015).
16. Gianazza, E., Miller, I., Palazzolo, L., Parravicini, C. & Eberini, I. With or without you—proteomics with or without major plasma/serum proteins. *J. Proteomics* **140**, 62–80 (2016).
17. Dębska, B. & Guzowska-Świder, B. Fuzzy definition of molecular fragments in chemical structures. *J. Chem. Inf. Comput. Sci*. **40**, 325–329 (2000).
18. Demtröder, W. *Molecular Physics* (Wiley, 2005).
19. Movasaghi, Z., Rehman, S. & ur Rehman, Dr. I. Fourier transform infrared (FTIR) spectroscopy of biological tissues. *Appl. Spectrosc. Rev*. **43**, 134–179 (2008).
20. Griffiths, P. R. & De Haseth, J. A. *Fourier Transform Infrared Spectrometry* (Wiley, 2007).
21. Keilmann, F., Gohle, C. & Holzwarth, R. Time-domain mid-infrared frequency-comb spectrometer. *Opt. Lett*. **29**, 1542–1544 (2004).
22. Newbury, N. R., Coddington, I. & Swann, W. Sensitivity of coherent dual-comb spectroscopy. *Opt. Express* **18**, 7929–7945 (2010).
23. Villares, G., Hugi, A., Blaser, S. & Faist, J. Dual-comb spectroscopy based on quantum-cascade-laser frequency combs. *Nat. Commun*. **5**, 5192 (2014).
24. Schwaighofer, A. et al. Beyond Fourier transform infrared spectroscopy: external cavity quantum cascade laser-based mid-infrared transmission spectroscopy of proteins in the amide I and amide II region. *Anal. Chem*. **90**, 7072–7079 (2018).
25. Haas, J., Catalán, E. V., Piron, P., Karlsson, M. & Mizaikoff, B. Infrared spectroscopy based on broadly tunable quantum cascade lasers and polycrystalline diamond waveguides. *Analyst* **143**, 5112–5119 (2018).
26. Ollesch, J. et al. An infrared spectroscopic blood test for non-small cell lung carcinoma and subtyping into pulmonary squamous cell carcinoma or adenocarcinoma. *Biomed. Spectrosc. Imaging* **5**, 129–144 (2016).
27. Brandstetter, M., Volgger, L., Genner, A., Jungbauer, C. & Lendl, B. Direct determination of glucose, lactate and triglycerides in blood serum by a tunable quantum cascade laser-based mid-IR sensor. *Appl. Phys. B* **110**, 233–239 (2013).
28. Baker, M. J. et al. Using Fourier transform IR spectroscopy to analyze biological materials. *Nat. Protocols* **9**, 1771–1791 (2014).
29. Martin, M. C. et al. 3D spectral imaging with synchrotron Fourier transform infrared spectro-microtomography. *Nat. Methods* **10**, 861–864 (2013).
30. Rohleder, D. et al. Comparison of mid-infrared and Raman spectroscopy in the quantitative analysis of serum. *J. Biomed. Opt*. **10**, 031108 (2005).
31. Bhargava, R. Infrared spectroscopic imaging: the next generation. *Appl. Spectrosc*. **66**, 1091–1120 (2012).
32. Quaroni, L., Zlateva, T., Wehbe, K. & Cinque, G. Infrared imaging of small molecules in living cells: from *in vitro* metabolic analysis to cytopathology. *Faraday Discuss*. **187**, 259–271 (2016).
33. Bonnier, F. et al. Ultra-filtration of human serum for improved quantitative analysis of low molecular weight biomarkers using ATR-IR spectroscopy. *Analyst* **142**, 1285–1298 (2017).
34. Haas, J. & Mizaikoff, B. Advances in mid-infrared spectroscopy for chemical analysis. *Annu. Rev. Anal. Chem*. **9**, 45–68 (2016).
35. Lu, R. et al. High-sensitivity infrared attenuated total reflectance sensors for in situ multicomponent detection of volatile organic compounds in water. *Nat. Protocols* **11**, 377–386 (2016).
36. Haase, K., Kröger-Lui, N., Pucci, A., Schönhals, A. & Petrich, W. Advancements in quantum cascade laser-based infrared microscopy of aqueous media. *Faraday Discuss*. **187**, 119–134 (2016).
37. Haase, K., Kröger-Lui, N., Pucci, A., Schönhals, A. & Petrich, W. Real-time mid-infrared imaging of living microorganisms. *J. Biophoton*. **9**, 61–66 (2016).
38. Gaida, C. et al. Watt-scale super-octave mid-infrared intrapulse difference frequency generation. *Light Sci. Appl*. **7**, 94 (2018).
39. Seidel, M. et al. Multi-watt, multi-octave, mid-infrared femtosecond source. *Science Advances* **4**, eaaq1526 (2018).
40. Butler, T. P. et al. Watt-scale 50-MHz source of single-cycle waveform-stable pulses in the molecular fingerprint region. *Opt. Lett*. **44**, 1730–1733 (2019).
41. Pupeza, I. et al. Field-resolved spectroscopy in the molecular fingerprint region. In *Lasers and Electro-Optics Europe & European Quantum Electronics Conf. (CLEO/Europe-EQEC)* https://doi.org/10.1109/CLEOE-EQEC.2017.8086859 (IEEE, 2017).
42. Huber, M. et al. Detection sensitivity of field-resolved spectroscopy in the molecular fingerprint region. In *Lasers and Electro-Optics Europe & European Quantum Electronics Conference (CLEO/Europe-EQEC)* https://doi.org/10.1109/CLEOE-EQEC.2017.8086921 (IEEE, 2017).
43. Timmers, H. et al. Molecular fingerprinting with bright, broadband infrared frequency combs. *Optica* **5**, 727–732 (2018).
44. Muraviev, A. V., Smolski, V. O., Loparo, Z. E. & Vodopyanov, K. L. Massively parallel sensing of trace molecules and their isotopologues with broadband subharmonic mid-infrared frequency combs. *Nat. Photon*. **12**, 209–214 (2018).
45. Udem, T., Holzwarth, R. & Hänsch, T. W. Optical frequency metrology. *Nature* **416**, 233–237 (2002).
46. Ye, J. & Cundiff, S. T. *Femtosecond Optical Frequency Comb: Principle, Operation, And Applications* (Springer, 2005).
47. Schweinberger, W. et al. Interferometric delay tracking for low-noise Mach-Zehnder-type scanning measurements. *Opt. Express* **27**, 4789–4798 (2019).
48. Schubert, O. et al. Rapid-scan acousto-optical delay line with 34 kHz scan rate and 15 as precision. *Opt. Lett*. **38**, 2907–2910 (2013).
49. Birarda, G. et al. IR-Live: fabrication of a low-cost plastic microfluidic device for infrared spectromicroscopy of living cells. *Lab Chip* **16**, 1644–1651 (2016).
50. Max, J.-J. & Chapados, C. Glucose and fructose hydrates in aqueous solution by IR spectroscopy. *J. Phys. Chem. A* **111**, 2679–2689 (2007).

Publisher's note Springer Nature remains neutral with regard to jurisdictional claims in published maps and institutional affiliations.

Methods

Nonlinear time-domain gating in FRS

Here, we elucidate the qualitative differences between FRS and traditional, frequency-resolved spectroscopy. For the latter, we choose FTS as the perhaps most advanced form of frequency-resolved infrared spectroscopy, in particular in the dual-frequency-comb implementation[11,21,22]. Furthermore, the interferograms obtained by FTS performed either with ultrashort pulses[11,21,22] or with broadband, incoherent light[51] resemble the electric field emerging from a sample after resonant excitation with a few-cycle infrared pulse, which FRS samples with sub-optical-cycle resolution by means of nonlinear optics (see Fig. 1b). To understand the important performance differences between the two techniques, it is essential to recognize the conceptual differences in the acquisition of these time-domain signals. First, using simple formalisms for the signals acquired in FTS and FRS, we reveal two major advantages introduced by the time-domain, nonlinear-conversion-based gating of the sampled electric field in FRS over FTS: the robustness of detection sensitivity against technical noise of the MIR excitation transmitted through the sample, and the mitigation or circumvention of the detector-dynamic-range limitation of sensitivity inherent to FTS[22]. Then, we evaluate the performance of FTS achievable with our coherent infrared source and state-of-the-art infrared detection (both described in Supplementary Information section I), employing a well established frequency-domain formalism[22]. Contrasting the results with those of FRS presented in this work, we observe detection sensitivities higher by more than a factor of 30 for FRS of impulsively excited molecular signals decaying with a time constant on the order of 1 ps, as is typical for liquid-phase samples—owing to the above-mentioned advantages.

Extended Data Fig. 1a illustrates the working principle of FTS. Here, we consider an ultrashort-pulsed MIR excitation source. Its broadband pulses are sent along two arms of an interferometer, one of which contains the sample and one of which acts as a 'local oscillator' for homodyne (or heterodyne) detection. The field transmitted through the sample is the convolution of the sample response with the incident excitation field[22] $E_{ex}(t)$. It can be written as the sum of (1) a non-resonant response representing an attenuated (and temporally altered) version of $E_{ex}(t)$, which for simplicity we approximate here as $aE_{ex}(t)$, with a scalar $a < 1$, and (2) the response $E_{GMF}(t)$ of the resonantly excited molecules (a more rigorous treatment of the sample response is given in Supplementary Information section II). The field $R_{LO}(t-\tau)$ in the local oscillator arm is a copy of $E_{ex}(t)$, delayed by a variable time τ. FRS implemented with EOS (Extended Data Fig. 1b) employs a near-infrared (NIR) gate pulse $E_g(t-\tau)$ fulfilling two functions[52] (see also Supplementary Information section I). First, this pulse 'carves out' an ultrashort portion of the sample response, for instance via a second-order nonlinear upconversion process. Second, it acts as a local oscillator in the homodyne/heterodyne detection of this upconverted signal.

In both schemes, at each delay τ, the superposition of the sample response (time-gated and upconverted in the case of FRS) and local oscillator fields is sent to (usually two) t-integrating intensity detectors placed at each of the sum and difference ports of the beam combiner. In the wake of the excitation, where the strength of $aE_{ex}(t)$ can be neglected against that of $E_{GMF}(t)$, the resulting signals recorded by the two respective detectors read:

$$I_{\mathrm{FTS},1,2}(\tau) \propto \int [aE_{\mathrm{ex}}(t) + E_{\mathrm{GMF}}(t)]^2 \mathrm{d}t + \int E_{\mathrm{LO}}^2(t-\tau)\mathrm{d}t \pm 2\int E_{\mathrm{GMF}}(t)E_{\mathrm{LO}}(t-\tau)\mathrm{d}t \quad (1a)$$

$$I_{\mathrm{FRS},1,2}(\tau) \propto \int [\chi E_{\mathrm{g}}(t-\tau)E_{\mathrm{GMF}}(t)]^2 \mathrm{d}t + \int E_{\mathrm{g}}^2(t-\tau)\mathrm{d}t \pm 2\int \chi E_{\mathrm{GMF}}(t)E_{\mathrm{g}}^2(t-\tau)\mathrm{d}t \quad (1b)$$

where $\chi E_g(t-\tau)E_{GMF}(t)$ is a qualitative expression for the time-gated, upconverted sample response in FRS, neglecting effects such as phase matching or depletion/saturation. The first two right-hand-side terms of equation (1a, b) represent a background (direct-current baseline) around which the third term, containing the spectroscopic information, oscillates. A major difference stems from the first background term in the two equations and immediately becomes apparent after two approximations. In equation (1a), this term can be approximated by $\int [aE_{ex}(t)]^2 \mathrm{d}t$, which is typically orders of magnitude larger than the (time-integrated) GMF signal. In equation (1b), owing to temporal gating, the first right-hand-side term is orders of magnitude smaller than the other two terms (see Extended Data Fig. 1c), and can be neglected. With these two approximations, equation (1a, b) becomes:

$$I_{\mathrm{FTS},1,2}(\tau) \propto \int [aE_{\mathrm{ex}}(t)]^2 \mathrm{d}t + \int E_{\mathrm{LO}}^2(t-\tau)\mathrm{d}t \pm 2\int E_{\mathrm{GMF}}(t)E_{\mathrm{LO}}(t-\tau)\mathrm{d}t \quad (2a)$$

$$I_{\mathrm{FRS},1,2}(\tau) \propto \int E_{\mathrm{g}}^2(t-\tau)\mathrm{d}t \pm 2\int \chi E_{\mathrm{GMF}}(t)E_{\mathrm{g}}^2(t-\tau)\mathrm{d}t \quad (2b)$$

The fact that in FTS the time-integrated excitation transmitted through the sample always impinges on the detector(s), whereas in FRS this background term is negligible in the wake of an impulsive excitation, illustrated by equation (2a, b), has two far-reaching implications, described as follows.

Robustness of FRS against excitation noise. Although for both schemes the contribution of the local-oscillator term to the background can be readily reduced to the shot-noise/detector-noise level, for example, via lock-in detection (see Supplementary Information section I), in FTS the minimum detectable molecular signal is directly affected by the technical noise of the MIR excitation, whose contribution to the recorded signal is constant along the entire delay range. This requires its suppression by sophisticated fast scanning methods[22] and/or balancing techniques[53,54]. In spite of all these efforts, photon quantum-noise-limited sensitivity[54] has not been experimentally demonstrated for broadband measurements for wavenumbers shorter than 2,000 cm^{-1}, to the best of our knowledge. In FRS, by contrast, excitation-background-free detection of the molecular signal in the wake of an impulsive excitation implies a sensitivity that is ultimately limited by the quantum noise of the NIR gating field but largely immune to the noise of the MIR excitation.

Circumvention or mitigation of detector-dynamic-range-induced sensitivity limitation. In FTS, the usable input power is restricted by the excitation, transmitted through the sample, saturating the detector(s); see the first right-hand-side term of equation (2a). This implies a severe detector-dynamic-range-induced sensitivity limit[11,22] that can only be circumvented/mitigated by techniques such as spectral multiplexing[22] or building the difference between a sample and a reference response to the same excitation interferometrically, before detection[55,56]. This adds substantial complexity to any detection scheme and has not been widely used so far. In FRS, for a fixed local-oscillator power (set to be below the detector saturation level), the signal-to-noise ratio can readily be increased by increasing the excitation field, which linearly increases the sought-for molecular signal $E_{GMF}(t)$ in the third right-hand-side term in equation (2b). Because the excitation signal transmitted through the sample is eliminated by the femtosecond temporal gate, the molecular signal can, in principle, be increased up to levels at which $aE_{ex}(t)$ vastly exceeds the saturation level of any available detector.

Sensitivity estimation of FTS implemented with our infrared source

Here, we calculate the expected sensitivity for an FTS implementation employing our infrared radiation source and state-of-the-art MIR

detectors. Because of the delay-independent contribution of excitation noise to the recorded signal (see above), time-domain filtering of the recorded signal does not have such a dramatic effect as in FRS, and well established frequency-domain models for FTS lend themselves for a sensitivity estimation. Here we use the model of Newbury et al.[22] who derived an expression for the frequency-domain signal-to-noise ratio in dependence of detector noise, shot noise, excess laser relative intensity noise (RIN) and detector dynamic range. Although the formula was derived for dual-comb spectroscopy, it can be readily applied to FTS with (slow) mechanical scan, with our experimental parameters (see Supplementary Information section I, Extended Data Fig. 5 and summary in Extended Data Table 1). In addition, we assume no limitations due to digitization, no sequential or parallel multiplexed acquisition and a duty cycle of 1. The power level in both the signal and the local oscillator arms was set to 0.45 mW, limited by detector saturation and well within the range of our source.

For direct comparison with our FRS results, we consider the absorption of $DMSO_2$ solved in water, spectrally centred at 1,139 cm^{-1} (see Extended Data Fig. 6 and parameters in Extended Data Table 1). According to equation (4) of ref. [22], for these parameters we obtain a limit of detection of 7 μg ml^{-1} of $DMSO_2$ dissolved in water for FTS, which is a factor of 35 above what is demonstrated here with FRS.

Experimental setup

The instrument (see also Supplementary Information section I for a detailed description) is based on a Kerr-lens mode-locked thin-disk Yb:YAG oscillator[57] emitting a 28-MHz repetition-rate train of 220-fs pulses, spectrally centred at 1,030 nm. After temporal compression via nonlinear spectral broadening based on multi-pass self-phase modulation in bulk fused silica followed by chirped-mirror compressors[58], the resulting NIR pulses are 16 fs long, with an average power of 60 W. These pulses drive intrapulse difference-frequency generation (optical rectification) in a 1-mm-thick $LiGaS_2$ crystal. The emerging MIR radiation with an average power of the order of 100 mW is spectrally tunable with a coverage of nearly one octave around a central frequency of 1,200 cm^{-1}. After the crystal, the NIR pulse is recycled and used for gating in the EOS detection of the MIR waveforms. Balanced detection in EOS is optimized close to the NIR shot-noise limit, with an impinging NIR power on the GaSe EOS crystal of 420 mW. In order to reduce phase artefacts introduced by variations of the mutual delay between the MIR sampled wave and the NIR sampling pulse, we track this delay interferometrically, with an additional continuous-wave laser[47]. In this manner, data can be recorded with few-nanometre delay precision and a temporal duty cycle close to 100% during forward as well as backward scans. Starting with the last NIR pulse compression stage, all the beams are enclosed in vacuum chambers at a background pressure in the 1-mbar range. Further measures of stabilization include an acousto-optical-modulator-based active noise eater[59] and lock-in detection employing mechanical chopping of the MIR beam.

Dynamic range of FRS

The 500-μm-thick GaSe electro-optic crystal constitutes a trade-off between a high quantum efficiency and broad bandwidth (Fig. 1d). In addition, it avoids internal reflections within the measurement time window. This quantum-efficiency-optimized apparatus resulted in a linearity of the instrument response over more than seven orders of magnitude of electric-field strength and, moreover, the intensity dynamic range scales linearly with measurement time (Extended Data Fig. 2). Thus, sampling of the oscillating electric field rather than its cycle-averaged intensity[60] results in an unprecedented linear-response intensity dynamic range of $>10^{14}$, vastly exceeding that of infrared spectroscopy so far, to our knowledge[2]. This enables transillumination of aqueous samples of several tens of micrometres in thickness while maintaining a high signal-to-noise ratio.

Measurement principle and the nature of the signal

FRS molecular fingerprinting relies on the generation of ultrashort infrared pulses with identically repeating electric-field waveforms (in our setup, 28 million such pulses per second). These pulses are transmitted through the sample under investigation, and the waveforms emerging from this interaction are recorded with EOS (see Supplementary Information section I). The spatial distribution of microscopic electric charges (that is, electrons and nuclei) in organic molecules is (1) inhomogeneous and (2) characteristic of the molecular species. Because of (1), when the electric field of the above-mentioned infrared pulses interacts with the molecules, it induces microscopic spatial charge separations (due to the existence of electric dipole moments). These charge separations evolve in time, driven by the oscillating electric field. Because of (2), these microscopic charge oscillations occur with characteristic magnitudes and frequencies—albeit having a fixed mutual timing, set by the common excitation field. In particular, resonant vibrations oscillate long after the excitation by the few-cycle infrared waveform, emanating a GMF. This resonant response is the coherent superposition of the fields of all sample-specific oscillations, thus containing most of the sample-specific information. Importantly, at the centre frequency of any such oscillation, the emission of light as a consequence of the resonant excitation by a light field occurs with opposing phase to the latter[9]. Consequently, the coherent superposition of the GMF and the excitation transmitted through the sample results in a destructive interference at these frequencies, leading to the typical 'absorption dips' observed in frequency-domain spectroscopy; see Fig. 1c.

Data availability

The data that support the findings of this study are available from the corresponding author upon reasonable request.

51. Tsurumachi, N., Fuji, T., Kawato, S., Hattori, T. & Nakatsuka, H. Interferometric observation of femtosecond free induction decay. *Opt. Lett.* **19**, 1867–1869 (1994).
52. Gallot, G. & Grischkowsky, D. Electro-optic detection of terahertz radiation. *J. Opt. Soc. Am. B* **16**, 1204–1212 (1999).
53. Hobbs, P. C. D. Ultrasensitive laser measurements without tears. *Appl. Opt.* **36**, 903–920 (1997).
54. Foltynowicz, A., Ban, T., Masłowski, P., Adler, F. & Ye, J. Quantum-noise-limited optical frequency comb spectroscopy. *Phys. Rev. Lett.* **107**, 233002 (2011).
55. Buberl, T. Broadband interferometric subtraction of optical fields. *Opt. Express* **27**, 2432–2443 (2019).
56. Tomberg, T., Muraviev, A., Ru, Q. & Vodopyanov, K. L. Background-free broadband absorption spectroscopy based on interferometric suppression with a sign-inverted waveform. *Optica* **6**, 147–151 (2019).
57. Fritsch, K., Poetzlberger, M., Pervak, V., Brons, J. & Pronin, O. All-solid-state multipass spectral broadening to sub-20 fs. *Opt. Lett.* **43**, 4643–4646 (2018).
58. Schulte, J., Sartorius, T., Weitenberg, J., Vernaleken, A. & Russbueldt, P. Nonlinear pulse compression in a multi-pass cell. *Opt. Lett.* **41**, 4511–4514 (2016).
59. Huber, M. et al. Active intensity noise suppression for a broadband mid-infrared laser source. *Opt. Express* **25**, 22499–22509 (2017).
60. Lanin, A. A., Voronin, A. A., Fedotov, A. B. & Zheltikov, A. M. Time-domain spectroscopy in the mid-infrared. *Sci. Rep.* **4**, 1–8 (2014).

Acknowledgements We thank D. Gerz, A. Zigman Kohlmaier, L. Fuerst and I. Kosse for their contributions and help with the measurements. We acknowledge the support of the Max Planck Society, the Center for Advanced Laser Applications of the Ludwig-Maximilians University and the King Saud University via the Researchers Supporting Project (NSRSP-2019/1).

Author contributions I.P., M.H., M.T., W.S., S.A.H., C.H., E.F., A. Apolonski, A. Azzeer, M.Z. and F.K. conceived the experiments. I.P., M.H., M.T., W.S., S.A.H., C.H., K.F., M.P., L.V., T.A, K.V.K., N.K., V.P., O.P., M.Z. and F.K. designed the experiments and analysed the experimental data. M.H., F.F. and M.Z. prepared the living systems. S.A.H., K.F., M.P. and O.P. designed and built the few-cycle near-infrared femtosecond laser source. I.P., M.H., W.S., S.A.H., C.H., L.V., V. P. and N.K. developed the optical system for the generation and electro-optic detection of waveform-stable MIR radiation. All authors contributed to evaluating the results and writing the manuscript.

Competing interests The authors declare no competing interests.

Additional information

Supplementary information is available for this paper at https://doi.org/10.1038/s41586-019-1850-7.

Correspondence and requests for materials should be addressed to I.P. or F.K.

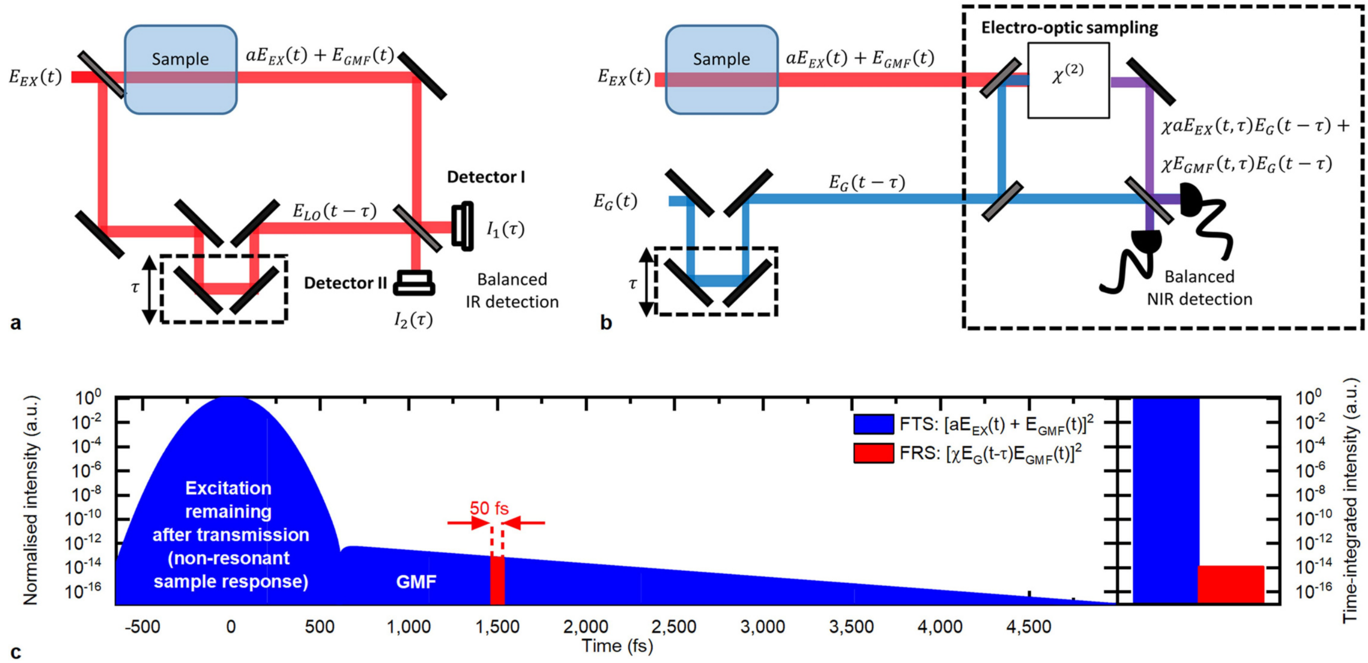

Extended Data Fig. 1 | Comparison of FTS with FRS. a, Schematic of FTS. **b**, Schematic of FRS. **c**, Portions of the background signal contributed by the sample response to the FTS (blue, first right-hand-side term of equation (1a)) and to the FRS (red, first right-hand-side term of equation (1b)) signals at a fixed delay (τ = 1,500 fs). For illustration purposes, the nonlinear upconversion efficiency was set to 1 and the 'carved out' effective window time length to 50 fs (without loss of generality). Example parameters: 190-fs Gaussian excitation pulse and 1,139-cm^{-1} $DMSO_2$ absorption (see Extended Data Table 1).

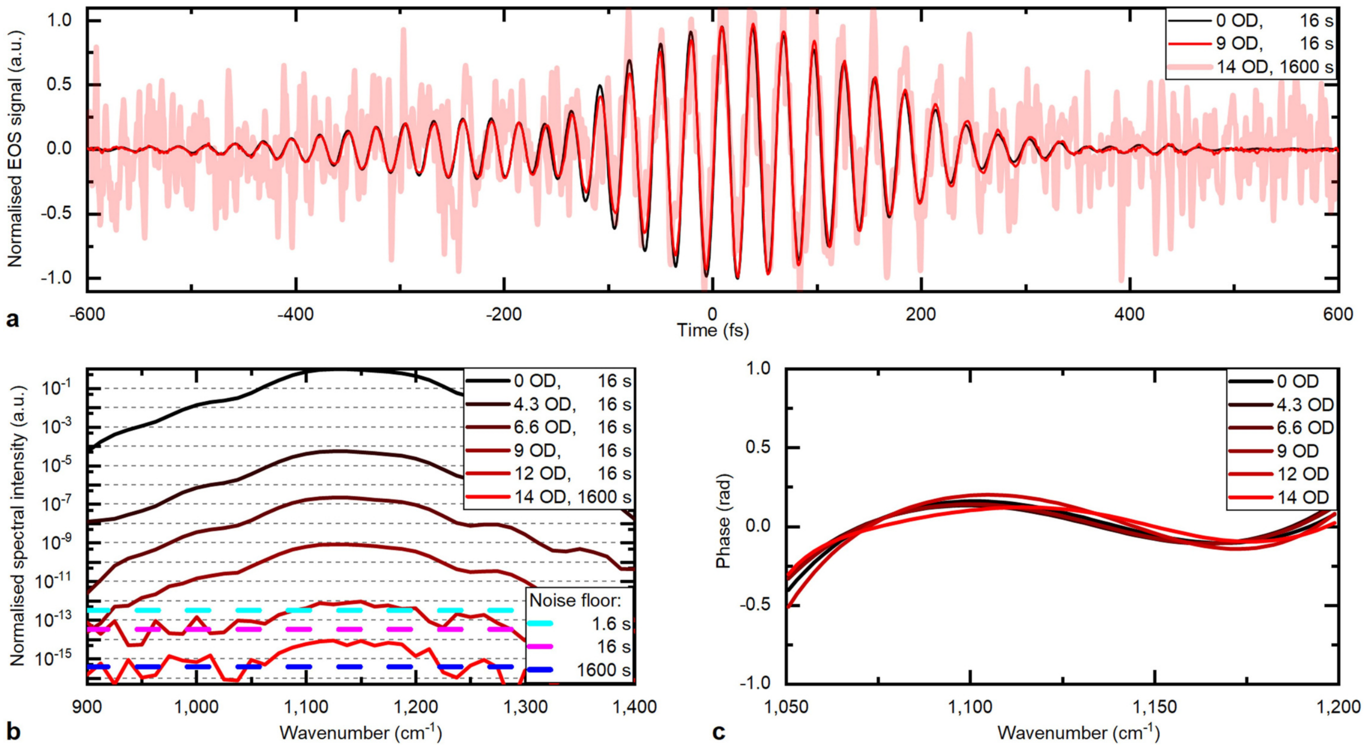

Extended Data Fig. 2 | Detection dynamic range and linearity of the instrument response. **a**, Infrared excitation pulse (normalized to maximum), recorded with attenuating optical density (OD) filters instead of the cuvette in the beam path, for increasing attenuation and measurement time *T*. A 1,200-fs scan range and $T = 16$ s and $T = 1{,}600$ s were considered. Small variations of the pulse shape for different attenuations are attributed to slight dispersion variations among the OD filters. The attenuation-independent pulse shape confirms the instrument linearity over the entire parameter range considered. **b**, **c**, Spectral intensity (normalized to the maximum of the attenuation-free measurement) and phase of the signals in **a**, respectively. The detection noise floors in **b** were obtained by blocking the MIR signal and evaluating the mean of the (white) noise in the considered spectral range, and confirm the linear decrease of the noise floor with *T*. For the data in **c**, for all time-domain waveforms a super-Gaussian filter (width 700 fs, order 20) was applied.

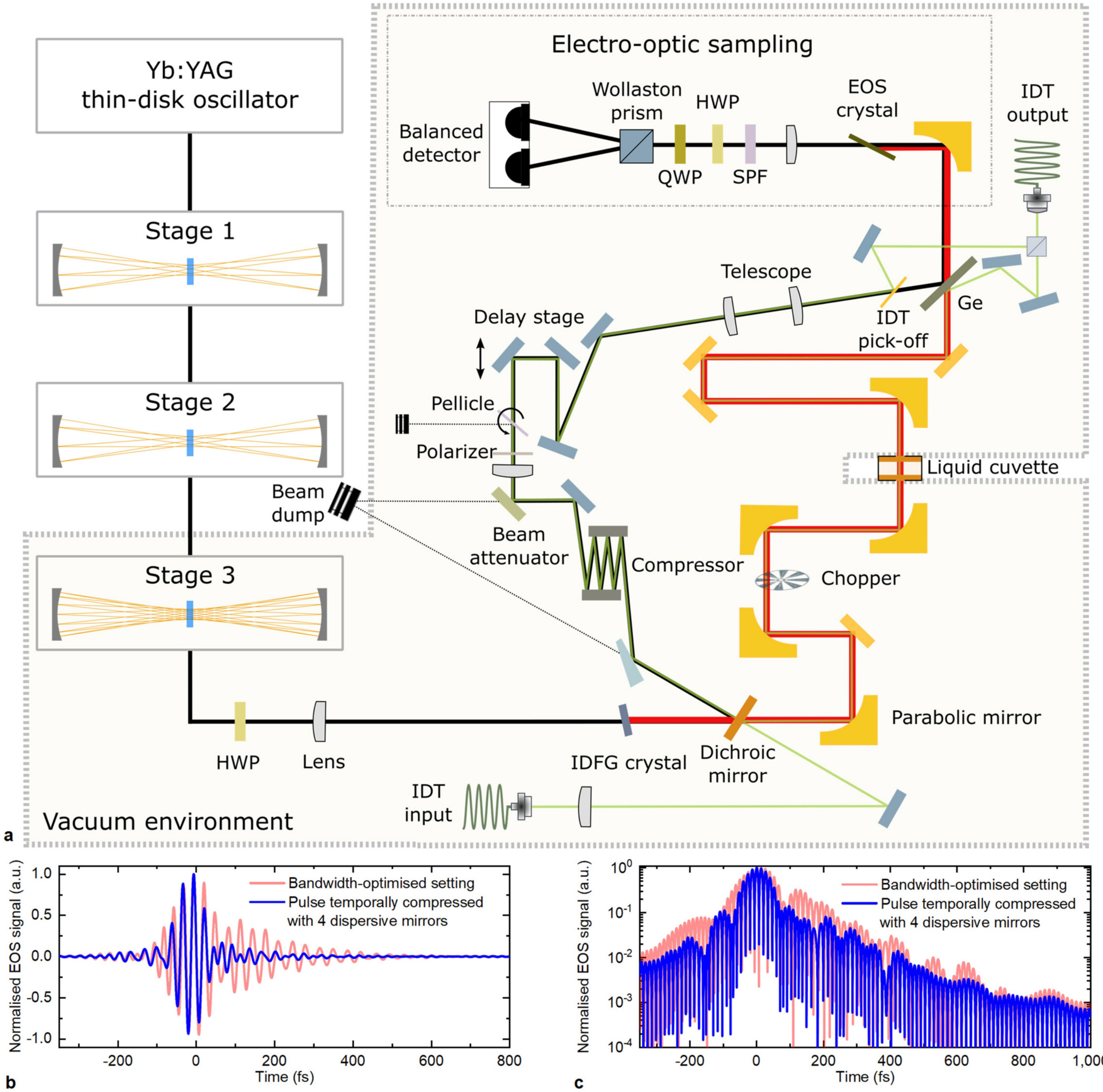

Extended Data Fig. 3 | Experimental setup. See subsection 'High-power femtosecond oscillator and generation of waveform-stable MIR Pulses' in Supplementary Information section I for details. **a**, HWP, half-wave plate; QWP, quarter-wave plate; IDFG, intra-pulse difference frequency generation; IDT, interferometric delay tracking; Ge, germanium beam combiner. All steering mirrors for the MIR beam were gold-coated. In the bandwidth-optimized instrument setting, four custom dispersive mirrors were added to the MIR beam path (see text). The pulse was temporally compressed with customized dispersive optics. Pulse compression. EOS traces of the excitation pulse transmitted through water in the bandwidth-optimized instrument setting, with (blue) and without (red) four dispersive mirrors in the MIR beam path. **c**, As in **b** but on a logarithmic scale, visualizing the improved roll-off of the signal achieved with the dispersive optics.

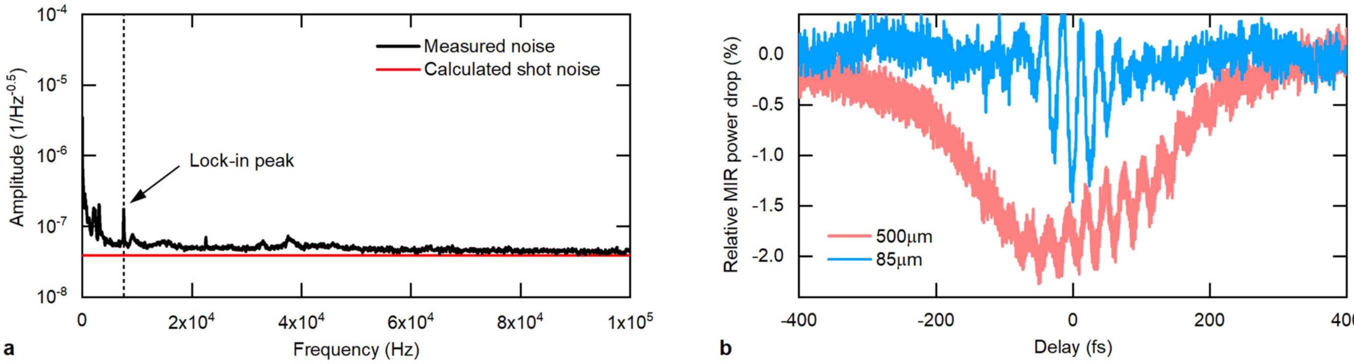

Extended Data Fig. 4 | Contributions to quantum efficiency in electro-optic sampling. a, Frequency-resolved measurement of the noise of the balanced detection (black), and calculated shot noise (red). The dashed line indicates the lock-in frequency, and its peak stems from the chopper. **b**, Comparison of MIR power depletion after EOS crystal for the two different crystal thicknesses. The oscillations originate from interferences of the MIR pulse incident to the EOS crystal and MIR radiation generated therein (these oscillations do not affect the performance of EOS detection).

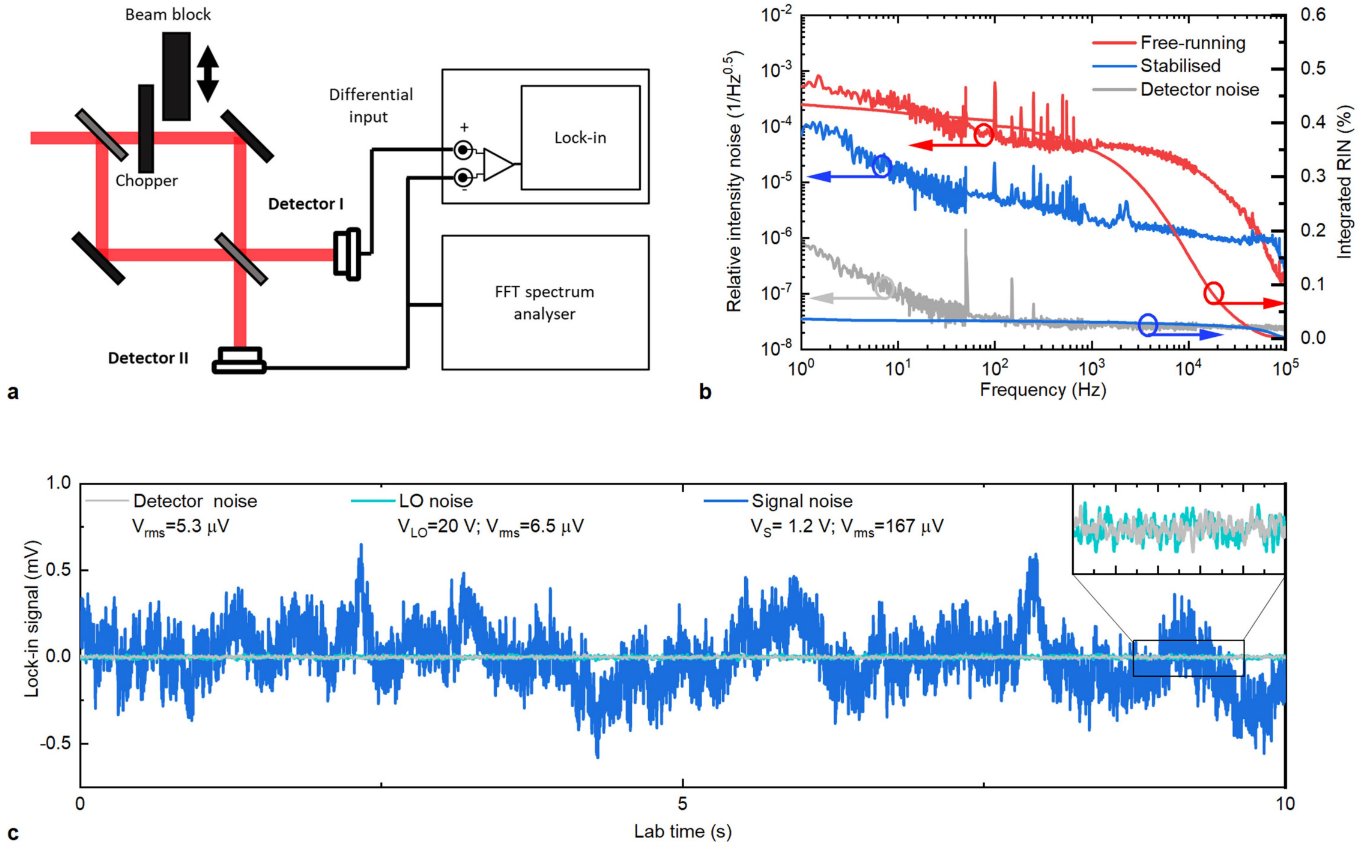

Extended Data Fig. 5 | Measurement of noise contributions for the estimation of the performance of FTS with our femtosecond-laser-based source, our mechanical scan, and state-of-the-art infrared detection. a, The setup mimics a FTS setup in the Mach–Zehnder configuration, with balanced lock-in detection. For lock-in frequency modulation, a mechanical chopper is placed in the 'sample arm'. The two arms are recombined with a 50:50 beam splitter. The two outputs are detected with two independent MIR detectors (see text for details). The power impinging on each detector was limited to 450 mW, corresponding to a detector output voltage of 20 V. The relative intensity noise (RIN) spectrum of the source is recorded with an FFT-Analyzer in the range 0.1–100 kHz (before balanced detection). Balanced lock-in detection is performed with a lock-in amplifier with differential input. The beam block was used in the measurements shown in **c**. **b**, RIN spectrum of the free-running (red curve) and intensity-stabilized (blue curve) MIR beam (before the interferometer). The integrated RIN of the stabilized source from 1 Hz and 100 kHz is as low as 0.04%. **c**, Demodulated (after lock-in detection with a time constant of 1.6 ms and 4th-order filter) time-domain trace of detector noise (grey), local-oscillator signal with sample arm blocked (turquoise) and of the combination of both interferometer arms impinging on the balanced detection (blue). The inset shows a 1-second section of the signals, for a detailed comparison of the local-oscillator noise and the detector noise.

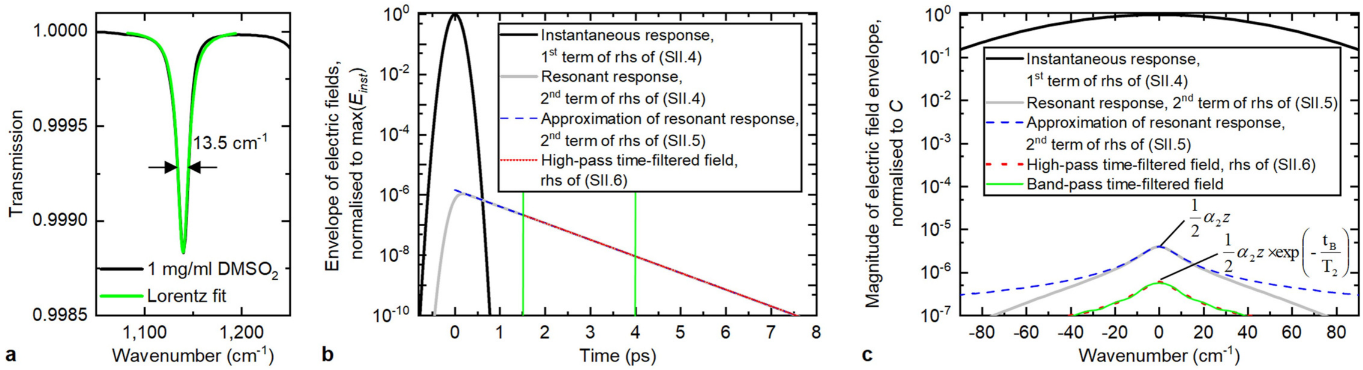

Extended Data Fig. 6 | Simulations of time-domain decay of a molecular Lorentzian oscillator. **a**, Fit of a Lorentzian oscillator to the 1,139 cm^{-1} absorption of (low-concentration) $DMSO_2$. Black line, intensity transmission through pure, molecular $DMSO_2$, determined by referencing the transmission spectrum of a 1 mg ml^{-1} solution to that of water, measured via FTIR, and normalizing to a 1-µm path. Green line, least-squares fit (1,080–1,190 cm^{-1}) of a Lorentzian oscillator to the 1,139 cm^{-1} absorption, yielding a full width at half depth of 13.47 cm^{-1} and an absorption coefficient $\alpha = 11.96$ cm^{-1}. The numerical example shows the instantaneous and resonant parts of the electric field as described by equations (1) to (4) in Supplementary Information section II. The initial pulse is a Gaussian pulse with an intensity envelope (full width at half maximum) of 190 fs. The Lorentzian absorption band has a peak of $\alpha_2 z$ with $\alpha_2 = 0.0024$ cm^{-1}, corresponding to a 200 ng ml^{-1} solution of $DMSO_2$ in water, and a width $\delta\upsilon = 13.47$ cm^{-1}. These values were obtained from fitting a Lorentzian absorber to the 1,139 cm^{-1} band of the transmission spectrum of a 1 mg ml^{-1} solution obtained with FTIR and linear extrapolation to a concentration 5,000 times lower. **b**, Time-domain representation of the normalized envelope functions of the electric fields described (see key). A value of $t_B = 1.5$ ps is chosen. The green vertical bars indicate the boundaries of the band-pass-filtered resonant response shown in green: 1.5 ps and 4 ps. **c**, Magnitudes of the Fourier transforms of the envelopes shown in **a**, normalized to C. At the absorption maximum, the discrepancy between the resonant response as in Supplementary Information section 2 and its approximation as in Supplementary Information section 3 is 1%, justifying this convenient approximation. The error introduced by band-pass filtering the resonant response between 1.5 ps and 4 ps compared to the high-pass time-filtered signal is 4%.

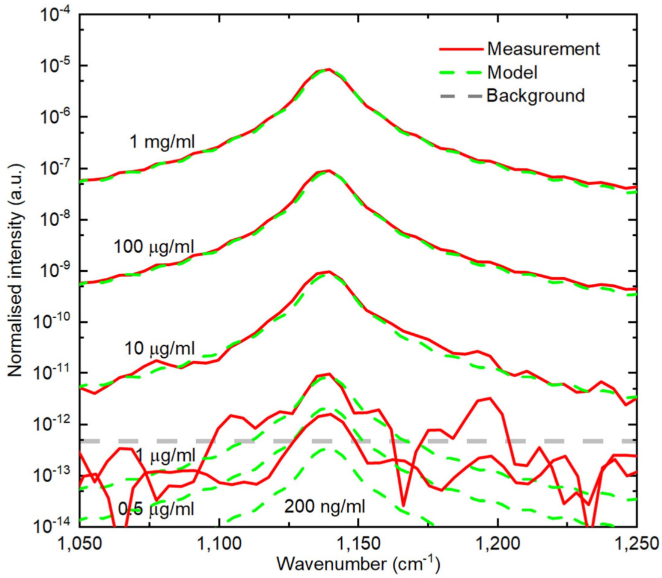

Extended Data Fig. 7 | Spectral intensity of the Fourier-transformed temporal fingerprints of $DMSO_2$. Spectral intensity is shown for different concentrations, after high-pass-time-filtering at t_B = 1,500 fs and subtraction of pure water reference, normalized to the spectral intensity of the reference pulse. Green dashed lines, modelled Lorentzian oscillator with the parameters derived from the fit in Extended Data Fig. 6. This model agrees excellently with the measured fingerprints, and confirms the minimum detectable absorbance predicted by equation (2) as well as the linear response of the instrument.

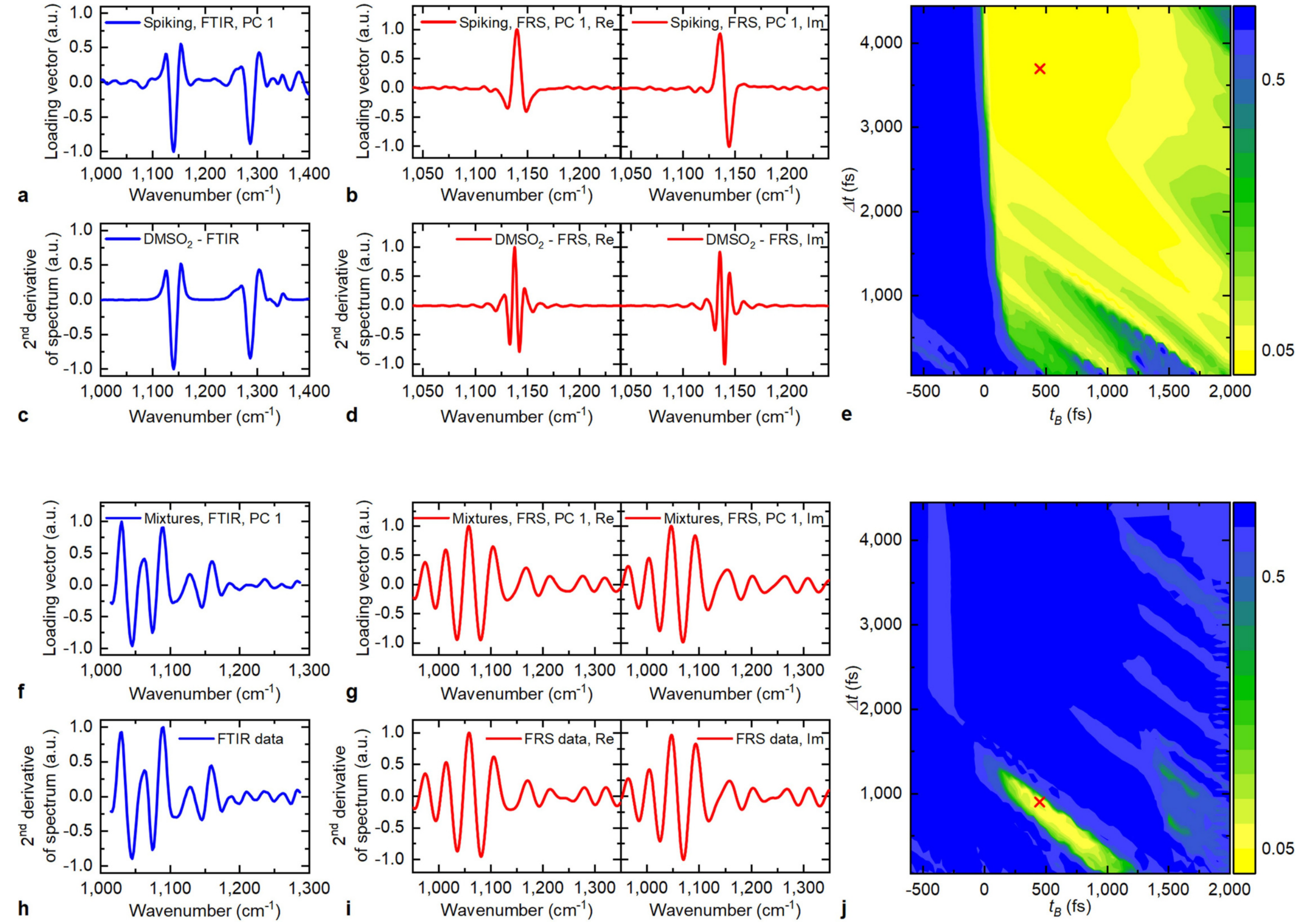

Extended Data Fig. 8 | Principal component analysis. a–d, Comparison of the loading vectors for the first principal component for the FTIR data (**a**) and the FRS data (**b**) from the serum spiking experiment, with the pre-processed GMF data (see text) of the FTIR (**c**) and FRS (**d**) measurements of a 1 mg ml^{-1} $DMSO_2$ solution. We note that the FRS spectra are complex, so the real and imaginary parts were considered separately (and stitched to single vectors). **e**, Figure of merit (FOM) (colour scale in arbitrary units; see Supplementary Information section VI) quantifying the separation of classes according to the first principal component (the lower the FOM, the better the separation), evaluated for a large range of the beginning time t_B and time window length Δt. The cross indicates parameters yielding optimum separation. **f**–**i**, Comparison of the loading vectors for the first principal component for the FTIR data (**f**) and the FRS data (**g**) from the sugar mixture experiment, with the pre-processed GMF data of the FTIR (**h**) and FRS (**i**). For the latter, the difference of the spectra of the 50/50 mixture and the pure maltose solution is shown. The real and imaginary parts were considered separately. **j**, FOM quantifying the separation of classes according to the first principal component, in analogy to **e**.

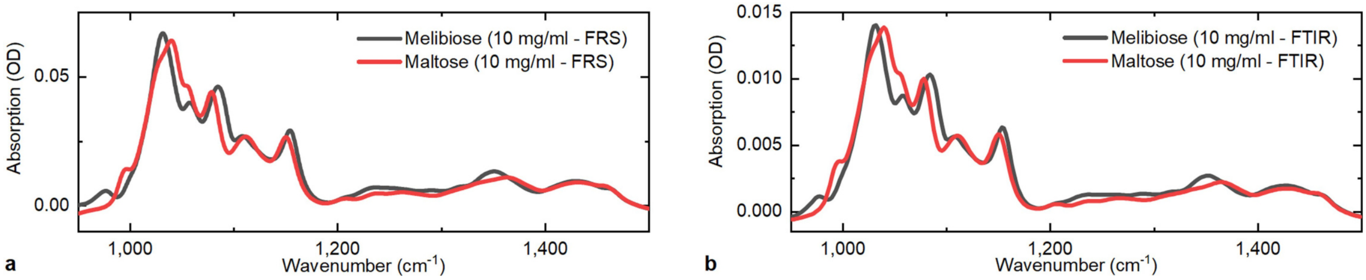

Extended Data Fig. 9 | Absorption spectra of 10 mg ml^{-1} aqueous solutions of maltose and melibiose, measured by FRS and FTIR. The difference in total absorption is due to the differing cuvette thickness. **a**, FRS; **b**, FTIR. OD, optical density.

Extended Data Table 1 | Parameters for numerical estimation of the sensitivity of FTS implemented with our infrared source

Parameter	Quantity	Comment
Central wavelength	$\lambda_C = 8.5\ \mu m$	
Spectral width	$\Delta\nu_{FWHM} = 180\ cm^{-1}$	
MIR power (FTS)	$P_{LO} = P_S = 0.45\ mW$	Maximum incident power limited by detector saturation
MIR detector noise	$NEP_{MCT} = 2.5\ pW/Hz^{0.5}$	e.g.: InfraRed Associates; MCT-13-1.00
Relative intensity noise	$RIN = 2.7 \times 10^{5}\ 1/Hz^{0.5}$	
FTS detector efficiency	$\eta_{FTS} = 1$	Quantum efficiency is not stated in the detector datasheet
Measurement time	$T = 37\ s$	Measurement time for sample and reference measurement
Spectral resolution	$\nu_{res} = 4.7\ cm^{-1}$	This corresponds to a scan time window of 7 ps
$DMSO_2$ absorption line at $\nu_{DMSO_2} = 1139\ cm^{-1}$		
Absorptivity	$\alpha_{DMSO_2} = 12.92\ cm^{-1}$	For 1 mg/ml $DMSO_2$ solution
Line width	$\nu_{FWHM} = 13.47\ cm^{-1}$	This corresponds to a dephasing time T_2 of ~770 fs

Article

Atomic imaging of the edge structure and growth of a two-dimensional hexagonal ice

https://doi.org/10.1038/s41586-019-1853-4

Received: 3 March 2019

Accepted: 19 September 2019

Published online: 1 January 2020

Runze Ma[1,2,14], Duanyun Cao[1,14], Chongqin Zhu[3,4,14], Ye Tian[1,14], Jinbo Peng[1], Jing Guo[1], Ji Chen[5], Xin-Zheng Li[5,6], Joseph S. Francisco[3], Xiao Cheng Zeng[4,7,8,9,10]*, Li-Mei Xu[1,6]*, En-Ge Wang[1,11,12]* & Ying Jiang[1,6,13]*

The formation and growth of water-ice layers on surfaces and of low-dimensional ice under confinement are frequent occurrences[1–4]. This is exemplified by the extensive reporting of two-dimensional (2D) ice on metals[5–11], insulating surfaces[12–16], graphite and graphene[17,18] and under strong confinement[14,19–22]. Although structured water adlayers and 2D ice have been imaged, capturing the metastable or intermediate edge structures involved in the 2D ice growth, which could reveal the underlying growth mechanisms, is extremely challenging, owing to the fragility and short lifetime of those edge structures. Here we show that noncontact atomic-force microscopy with a CO-terminated tip (used previously to image interfacial water with minimal perturbation)[12], enables real-space imaging of the edge structures of 2D bilayer hexagonal ice grown on a Au(111) surface. We find that armchair-type edges coexist with the zigzag edges usually observed in 2D hexagonal crystals, and freeze these samples during growth to identify the intermediate edge structures. Combined with simulations, these experiments enable us to reconstruct the growth processes that, in the case of the zigzag edge, involve the addition of water molecules to the existing edge and a collective bridging mechanism. Armchair edge growth, by contrast, involves local seeding and edge reconstruction and thus contrasts with conventional views regarding the growth of bilayer hexagonal ices and 2D hexagonal matter in general.

Scanning tunnelling microscopy (STM) has been widely used to study 2D ices at surfaces[7,9,10], but resolving edge structures is difficult because STM is not sensitive to the position of nuclei and its tip can induce disturbances. Although transmission electron microscopy (TEM) can resolve atomic lattice edges[23], high-resolution TEM usually requires high-energy electrons that can change or even completely decompose the edge structure of covalently bonded 2D materials[23] and are expected to damage more weakly bonded ice edges. By contrast, noncontact atomic-force microscopy (AFM) based on a qPlus sensor[24,25] can probe interfacial water with excellent resolution[12,26,27], with use of a CO-terminated tip ensuring that water molecules are only minimally disturbed thanks to the ultrahigh flexibility of the tip apex and the weak higher-order electrostatic force[12]. Here we use this method to image various metastable edge structures of a 2D bilayer hexagonal ice grown on a Au(111) surface (Fig. 1a) and resolve the growth mechanisms with atomic detail.

The 2D ice was grown on a Au(111) surface at about 120 K with a thickness of around 2.5 Å (see Methods, Fig. 1a), corresponding to two water overlayers (Extended Data Fig. 1a–f). The STM image of the 2D ice (Fig. 1c) and the corresponding fast Fourier transform (FFT) image (inset of Fig. 1a) both show a well ordered hexagonal structure, with periodicity[6] Au(111)-$\sqrt{3} \times \sqrt{3}$-30° (Wood's notation; Extended Data Fig. 1g). Although the honeycomb H-bonding network of the 2D ice is visible in the STM image, the detailed topology of the edge structures is difficult to resolve. The AFM frequency-shift (Δf) image of the same island exhibits much higher resolution (Fig. 1d), such that the atomic structures of the zigzag and armchair edges can be easily identified. The total length of the zigzag and the armchair edges are comparable, but the average length of the former is statistically somewhat larger (two-sided t-test, $P = 1 \times 10^{-7}$; Fig. 1b). Zigzag edges can grow perfectly up to lengths of 60 Å, but armchair edges are always interrupted by step kinks or defects that result in shorter lengths, predominantly around 10–30 Å (Extended Data Fig. 2).

We then performed systematic AFM imaging at different tip heights (see Methods and Fig. 2a). At a large tip height, where the AFM signals are dominated by the higher-order electrostatic force[12], we can distinguish two sets of $\sqrt{3} \times \sqrt{3}$ sub-lattices in the 2D bilayer ice, one of which

[1]International Center for Quantum Materials, School of Physics, Peking University, Beijing, China. [2]Physical Science Laboratory, Huairou National Comprehensive Science Centre, Beijing, China. [3]Department of Earth and Environmental Science, University of Pennsylvania, Philadelphia, PA, USA. [4]Department of Chemistry, University of Nebraska–Lincoln, Lincoln, NE, USA. [5]School of Physics, Peking University, Beijing, China. [6]Collaborative Innovation Center of Quantum Matter, Beijing, China. [7]Department of Chemical and Biomolecular Engineering, University of Nebraska–Lincoln, Lincoln, NE, USA. [8]Department of Mechanical & Materials Engineering, University of Nebraska–Lincoln, Lincoln, NE, USA. [9]Department of Physics, University of Nebraska–Lincoln, Lincoln, NE, USA. [10]Nebraska Center for Materials and Nanoscience, University of Nebraska–Lincoln, Lincoln, NE, USA. [11]Ceramics Division, Songshan Lake Materials Lab, Institute of Physics, Chinese Academy of Sciences, Guangdong, China. [12]School of Physics, Liaoning University, Shenyang, China. [13]CAS Center for Excellence in Topological Quantum Computation, University of Chinese Academy of Sciences, Beijing, China. [14]These authors contributed equally: Runze Ma, Duanyun Cao, Chongqin Zhu, Ye Tian. *e-mail: xzeng1@unl.edu; limei.xu@pku.edu.cn; egwang@pku.edu.cn; yjiang@pku.edu.cn

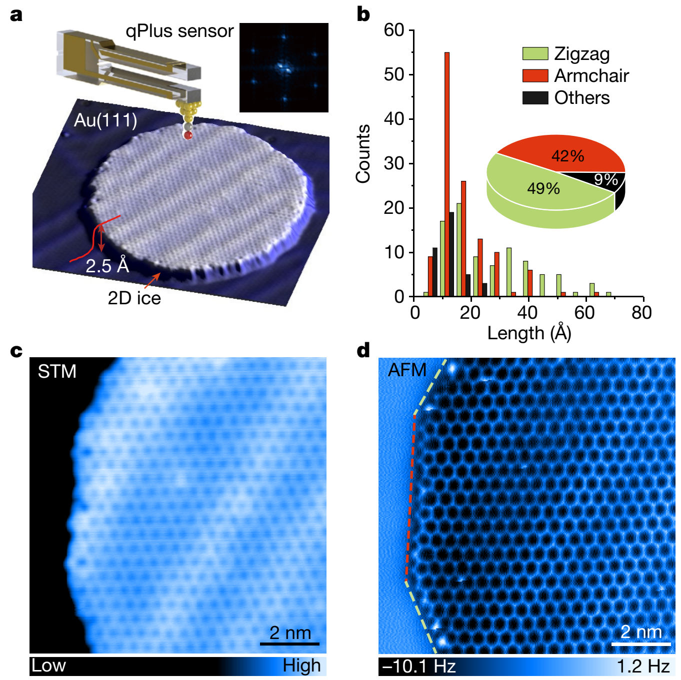

Fig. 1 | Experimental setup and STM and AFM images of 2D bilayer ice. **a**, Schematic of STM and AFM imaging of a 2D bilayer ice island on Au(111) using qPlus-based non-contact AFM with a CO-terminated tip. Inset, 2D FFT image inside the 2D ice island. The line profile across the step edge shows the height of the island (about 2.5 Å). **b**, Length distribution diagram of the zigzag and armchair edges for ten ice islands ($n = 249$). Inset, statistics on the length of the zigzag and armchair edges as a fraction of the total length of all counted edges. **c**, Constant-current STM image acquired at the set point, 100 mV and 10 pA. **d**, Constant-height AFM (Δf) image of the same area as in **c**, recorded at a tip height of 10 pm. The zigzag and armchair edges are denoted by green and red dashed lines, respectively. The tip height is referenced to the STM set point on the bilayer ice (100 mV, 50 pA), and the oscillation amplitude is 100 pm.

is highlighted in Fig. 2a (left panel). At a smaller tip height, the bright features of this sub-lattice start to show directionality, and the other sub-lattice resolves into a V-shaped feature (see the red lines in Fig. 2a, middle panel). When the tip height is further decreased to enter into the Pauli repulsion-force region, the AFM image shows a honeycomb structure with sharp lines connecting the two sub-lattices, resembling the H bonds (Fig. 2a, right panel).

Density functional theory (DFT) calculations reveal that the 2D ice grown on the Au(111) surface corresponds to an interlocked bilayer ice structure (Fig. 2c) consisting of two flat hexagonal water layers (see Methods). The hexagons of the two sheets are in registry and the angle between water molecules in the plane is 120°. In each water layer, half of the water molecules are lying flat (parallel to the substrate), and the other half are vertical (perpendicular to the substrate), with one O–H either upward or downward. The vertical water in one layer donates a H bond to the flat water in the other layer, leading to a fully saturated H-bonding structure. Although evidence for such a flat bilayer of hexagonal ice has been observed previously on hydrophobic surfaces and under hydrophobic confinements[17–19], its atomic structure has not been directly imaged.

The AFM simulation using a quadrupole (d_{z^2}) tip (Fig. 2b, Methods) based on the above model agrees well with the experimental results (Fig. 2a, Extended Data Fig. 3). The very similar height of the flat and vertical water molecules makes it very difficult to distinguish them in STM images. However, the flat and vertical water molecules show distinctly different contrast in AFM images (Fig. 2a, b, left panel) because the higher-order electrostatic force is very sensitive to the orientation of the water molecules[12,26]. We can additionally discern the O–H directionality of the flat and vertical water via the interplay between the higher-order electrostatic forces and Pauli repulsion forces (Extended Data Fig. 3), as highlighted by the red lines in Fig. 2a, b (middle panel). At small tip heights, where the Pauli repulsion force is dominant, the sharp bond-like features represent ridges of the potential-energy landscape experienced by the functionalized probe, mainly arising from the lateral relaxation of the CO tip induced by the Pauli repulsion force[28] (Fig. 2a, b, right panel).

Figure 3a, b (step 1) displays magnified AFM images of the zigzag and armchair edges, respectively, revealing that the zigzag edge grows

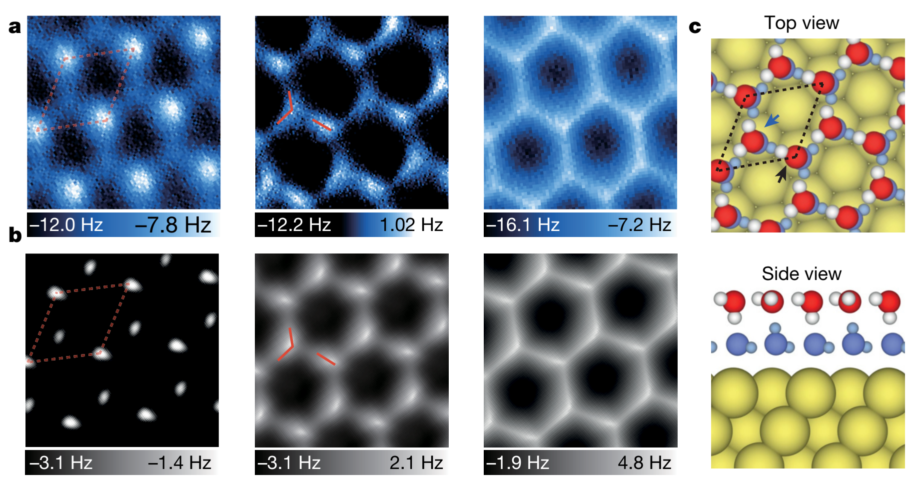

Fig. 2 | Detailed AFM characterization of the 2D bilayer ice and the corresponding structural model. **a**, Constant-height AFM (Δf) imaging at tip heights of 20 pm (left), 0 pm (middle) and −10 pm (right). **b**, Simulated AFM images at tip heights of 14 Å (left), 13.7 Å (middle) and 13.5 Å (right). The $\sqrt{3} \times \sqrt{3}$ unit cell is indicated by the dashed red rhombus. The O–H directionality of the water molecules is highlighted by the solid red lines. **c**, Top and side views of the bilayer ice structure on the Au(111) surface. Au, H and O atoms in the top water layer are denoted as yellow, white and red spheres, respectively. H and O atoms in the bottom water layer are shown by blue spheres (with a smaller size for clarity). The flat and vertical water molecules in the top layer are denoted by the blue and black arrows, respectively. In the side view, only the water molecules along one zigzag direction are shown for a clearer view of the top–bottom water pairs. The tip heights in **a** are referenced to the STM set point on the bilayer ice (100 mV, 50 pA). The tip heights in **b** are defined as the vertical distance between the apex atom of the metal tip and the outermost atom of the Au substrate. All the oscillation amplitudes of the experimental and simulated images are 100 pm and the image sizes are 1.25 nm × 1.25 nm.

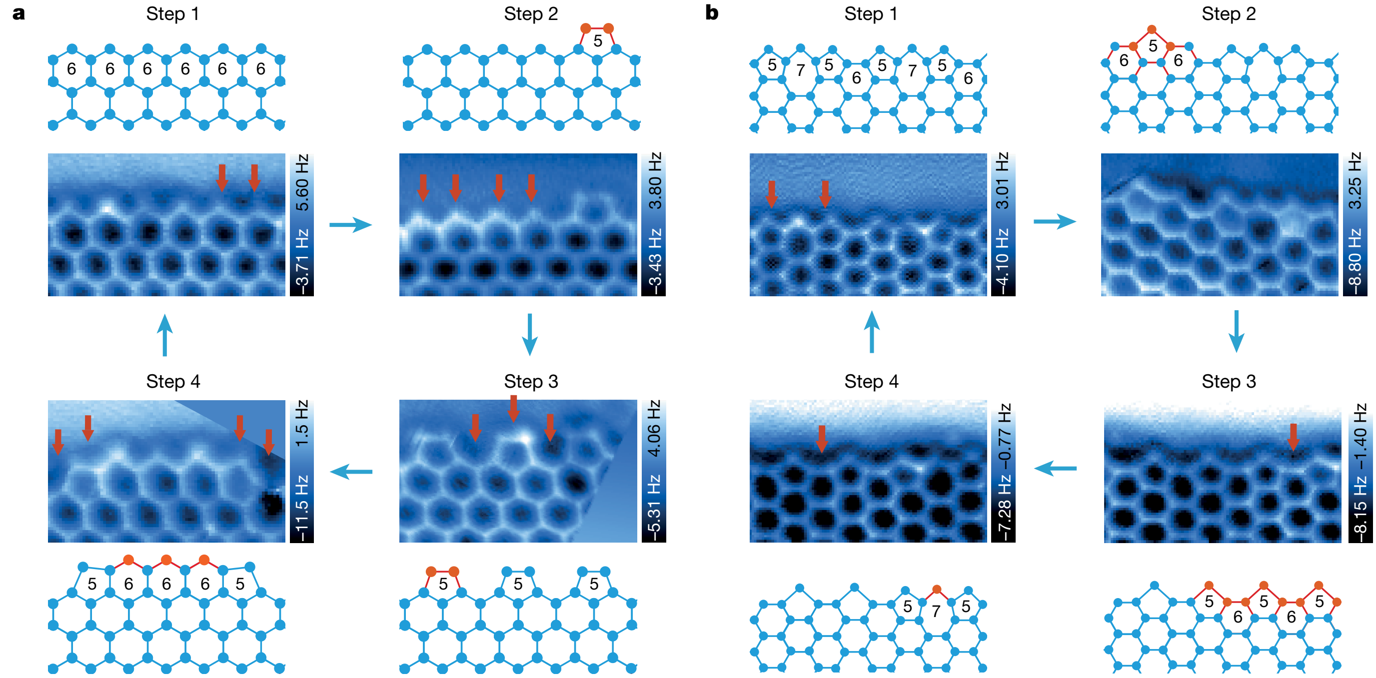

Fig. 3 | Proposed growing process for zigzag and armchair edges. **a**, **b**, Constant-height AFM images and the corresponding ball-and-stick models of the most stable (1) and metastable structures (2–4) of zigzag (**a**) and armchair (**b**) edges. The proposed growing process cycles through steps 1 to 4. In the AFM images, each red arrow indicates the addition of one bilayer water pair, leading to the structure in the subsequent image. In the ball-and-stick models, the red balls and sticks represent the newly added bilayer water pairs, and those in blue represent the existing structures. The size of the images is 3.2 nm × 1.9 nm (**a**) and 3.7 nm × 2.2 nm (**b**).

under preservation of its original structure, but the armchair-edge growth involves edge reconstruction into a periodic structure of 5756-type member rings—that is, where the edge structure periodically repeats the sequence pentagon–heptagon–pentagon–hexagon. DFT calculations indicate that the unreconstructed zigzag edge and the 5756-type armchair edge are the most stable edges (Extended Data Fig. 4). The 5756-type armchair edge forms as a result of combined effects that minimize the number of unsaturated H bonds and reduce the strain energy (Extended Data Fig. 5). It is well known that the basal planes of hexagonal ice are usually terminated with zigzag edges and that armchair edges are absent because of the higher density of unsaturated H bonds. However, in lower-dimensional systems or under confinement, the armchair edge can lower its energy by proper reconstruction.

After ice growth was stopped at 120 K, the sample was immediately cooled down to 5 K (see Methods) in an attempt to freeze metastable or intermediate edge structures and ensure relatively long lifetimes to allow STM and AFM imaging. Owing to the weakly perturbative character of the CO-functionalized tip[12], we were able to identify metastable and intermediate structures and reconstruct the 2D ice-growing process (Fig. 3).

For zigzag edges, we occasionally find individual pentagons attached to the straight edges and that these can line up to form an array with a periodicity of $2 \times a_{ice}$ (where a_{ice} is the lattice constant of the 2D ice). We interpret this as indicating that the growth of the zigzag edges is initiated by the formation of a periodic array of pentagons (Fig. 3a, steps 1–3), which involves the addition of two water pairs for a pentagon (see red arrows). The pentagon array is then bridged to form a 56665-type structure (Fig. 3a, step 4) and eventually recovers the original zigzag edge by adding more water pairs. Interestingly, we can even capture the tip-induced growth of an individual pentagon (Extended Data Fig. 6).

By contrast, the armchair edges do not exhibit this pentagon array structure and we instead frequently observe short 5656-type steps at the edge (Extended Data Fig. 2). The length of the 5656-type edges is considerably shorter than that of the 5756-type edges, presumably

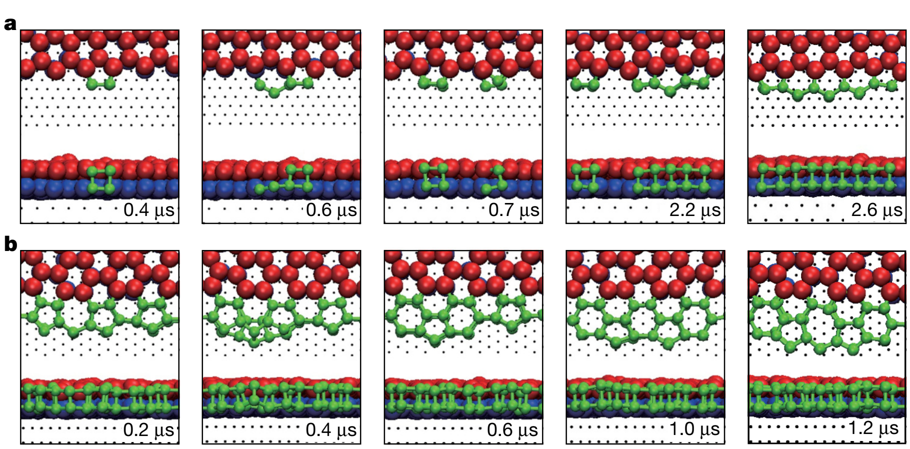

Fig. 4 | Molecular-dynamics simulation of the growth of the zigzag and armchair edges. **a**, **b**, Time-lapse snapshots of molecular-dynamics simulations during the growth of the zigzag (**a**) and armchair (**b**) edges. The simulation times are indicated in the bottom right of each snapshot. In all snapshots (upper panel, top view; lower panel, side view), the red and blue spheres represent the top-layer and bottom-layer water molecules of a pre-existing bilayer ice grain, respectively. The green spheres represent newly deposited water molecules and formed structures during the simulated growth process.

because the 5656-type edge is heavily stressed and is less stable than the 5756-type edge (Extended Data Fig. 5). Starting from the 5756-type armchair edge, the 575-type member rings are locally converted to 656-type member rings by the addition of two water pairs (Fig. 3b, step 2). The 656-type member rings then grow laterally to form a 5656-type edge (Fig. 3b, step 3) but with limited length, owing to the accumulation of strain energy. The strain can be partially relaxed by inserting one water pair into the hexagon of the 5656-type edge, leading again to the formation of a 5756-type edge (Fig. 3b, step 4). Kinetically, such a growth mechanism prohibits the formation of armchair edges as long as the zigzag edges (Fig. 1b).

To further corroborate this proposed growth mechanism, molecular-dynamics simulations of water vapour on a Au(111) surface were carried out (see Methods). We found that 2D bilayer ice islands form on the surface, in agreement with our experimental observations (Extended Data Figs. 7, 8). The collective bridging mechanism at the zigzag edge is perfectly reproduced in Fig. 4a. It is worth noting that the single pentagon attached to the zigzag edge cannot act as a local nucleation centre to promote the growth ($t = 0.6–0.7$ μs in Fig. 4a, Supplementary Video 1). Instead, a periodic but unconnected array of pentagons is initially formed at the zigzag edge, and subsequent incoming water molecules collectively attempt to connect these pentagons, resulting in a 565-chain structure ($t = 2.2$ μs in Fig. 4a, Supplementary Video 2). Such a structure was not observed experimentally, owing to its short lifetime (Extended Data Fig. 9). The addition of one water pair further bridges the 565-type structure and the nearby pentagon, leading to the formation of a 5666-type structure ($t = 2.4$ μs; see Supplementary Videos 3, 4). The 5666-type structure grows laterally to form a 56665-type structure ($t = 2.6$ μs) and eventually turns into a fully connected hexagon array.

As for the armchair edges, the local seeding growth can be clearly seen in Fig. 4b, agreeing nicely with the proposed mechanism from our experiments (Fig. 3b). The conversion from 575- to 656-type member rings starts from the bottom layer, forming a composite 575/656 structure ($t = 0.4$ μs in Fig. 4b, Supplementary Videos 5, 6), which is indistinguishable from the 5756-type edge in the experiments, because only the top layer of the 2D bilayer ice can be imaged. The resulting 656 step then serves as the nucleation centre to grow the 5656-type edge ($t = 0.6–1$ μs, Supplementary Video 7). The addition of one water molecule into the 5656-type edge results in a highly mobile unpaired-molecule structure (Supplementary Video 8). Two of those unpaired water molecules can subsequently coalesce into a more stable heptagon structure, completing the 5656-to-5756 conversion ($t = 1.2$ μs, Supplementary Video 9).

We believe that the observed growth behaviour is a generic phenomenon for 2D ice, given that the relative stability of the different edge structures shows negligible dependence on the water spacing and the commensurability with the substrate (Extended Data Fig. 10). Indeed, bilayer hexagonal ice forms on different hydrophobic surfaces[6,17,18] and under hydrophobic confinement[19,22], and can be viewed as a stand-alone 2D crystal (2D ice I), the formation of which is insensitive to the underlying structure of the substrate[29]. Although it would be exceedingly difficult to extend our imaging method to observe three-dimensional (3D) ice growth[8,30], the growth mechanism that we have uncovered might also occur at the surface of bilayer hexagonal ice, because it lacks dangling H bonds on its surface and might therefore support bilayer-on-bilayer ice growth and ultimately a 2D-to-3D ice transformation.

Online content

Any methods, additional references, Nature Research reporting summaries, source data, extended data, supplementary information, acknowledgements, peer review information; details of author contributions and competing interests; and statements of data and code availability are available at https://doi.org/10.1038/s41586-019-1853-4.

1. Cao, L. L. et al. Anti-icing superhydrophobic coatings. *Langmuir* **25**, 12444–12448 (2009).
2. Weber, B. et al. Molecular insight into the slipperiness of ice. *J. Phys. Chem. Lett*. **9**, 2838–2842 (2018).
3. Graether, S. P. et al. β-helix structure and ice-binding properties of a hyperactive antifreeze protein from an insect. *Nature* **406**, 325–328 (2000).
4. Kiselev, A. et al. Active sites in heterogeneous ice nucleation—the example of K-rich feldspars. *Science* **355**, 367–371 (2017).
5. Hodgson, A. & Haq, S. Water adsorption and the wetting of metal surfaces. *Surf. Sci. Rep*. **64**, 381–451 (2009).
6. Corem, G. et al. Ordered H_2O structures on a weakly interacting surface: a helium diffraction study of H_2O/Au(111). *J. Phys. Chem. C* **117**, 23657–23663 (2013).
7. Nie, S., Feibelman, P. J., Bartelt, N. C. & Thurmer, K. Pentagons and heptagons in the first water layer on Pt(111). *Phys. Rev. Lett*. **105**, 026102 (2010).
8. Thurmer, K. & Nie, S. Formation of hexagonal and cubic ice during low-temperature growth. *Proc. Natl Acad. Sci. USA* **110**, 11757–11762 (2013).
9. Maier, S., Lechner, B. A., Somorjai, G. A. & Salmeron, M. Growth and structure of the first layers of ice on Ru(0001) and Pt(111). *J. Am. Chem. Soc*. **138**, 3145–3151 (2016).
10. Lin, C. et al. Two-dimensional wetting of a stepped copper surface. *Phys. Rev. Lett*. **120**, 076101 (2018).
11. Mehlhorn, M. & Morgenstern, K. Faceting during the transformation of amorphous to crystalline ice. *Phys. Rev. Lett*. **99**, 246101 (2007).
12. Peng, J. B. et al. Weakly perturbative imaging of interfacial water with submolecular resolution by atomic force microscopy. *Nat. Commun*. **9**, 122 (2018).
13. Hu, J., Xiao, X. D., Ogletree, D. F. & Salmeron, M. Imaging the condensation and evaporation of molecularly thin-films of water with nanometer resolution. *Science* **268**, 267–269 (1995).
14. Xu, K., Cao, P. G. & Heath, J. R. Graphene visualizes the first water adlayers on mica at ambient conditions. *Science* **329**, 1188–1191 (2010).
15. Odelius, M., Bernasconi, M. & Parrinello, M. Two dimensional ice adsorbed on mica surface. *Phys. Rev. Lett*. **78**, 2855–2858 (1997).
16. Meier, M. et al. Water agglomerates on Fe_3O_4(001). *Proc. Natl Acad. Sci. USA* **115**, E5642–E5650 (2018).
17. Lupi, L., Kastelowitz, N. & Molinero, V. Vapor deposition of water on graphitic surfaces: formation of amorphous ice, bilayer ice, ice I, and liquid water. *J. Chem. Phys*. **141**, 18C508 (2014).
18. Kimmel, G. A. et al. No confinement needed: observation of a metastable hydrophobic wetting two-layer ice on graphene. *J. Am. Chem. Soc*. **131**, 12838–12844 (2009).
19. Koga, K., Zeng, X. C. & Tanaka, H. Freezing of confined water: a bilayer ice phase in hydrophobic nanopores. *Phys. Rev. Lett*. **79**, 5262–5265 (1997).
20. Algara-Siller, G. et al. Square ice in graphene nanocapillaries. *Nature* **519**, 443–445 (2015).
21. Chen, J. et al. Two-dimensional ice from first principles: structures and phase transitions. *Phys. Rev. Lett*. **116**, 025501 (2016).
22. Bampoulis, P. et al. Hydrophobic ice confined between graphene and MoS_2. *J. Phys. Chem. C* **120**, 27079–27084 (2016).
23. Girit, C. O. et al. Graphene at the edge: stability and dynamics. *Science* **323**, 1705–1708 (2009).
24. Giessibl, F. J. Advances in atomic force microscopy. *Rev. Mod. Phys*. **75**, 949–983 (2003).
25. Gross, L. et al. The chemical structure of a molecule resolved by atomic force microscopy. *Science* **325**, 1110–1114 (2009).
26. Peng, J. B. et al. The effect of hydration number on the interfacial transport of sodium ions. *Nature* **557**, 701–705 (2018).
27. Shiotari, A. & Sugimoto, Y. Ultrahigh-resolution imaging of water networks by atomic force microscopy. *Nat. Commun*. **8**, 14313 (2017).
28. Hapala, P. et al. Mechanism of high-resolution STM/AFM imaging with functionalized tips. *Phys. Rev. B* **90**, 085421 (2014).
29. Zhu, C. et al. Direct observation of two-dimensional ices on different surfaces near room temperature without confinement. *Proc. Natl Acad. Sci. USA* **116**, 16723–16728 (2019).
30. Gerrard, N. et al. Strain relief during ice growth on a hexagonal template. *J. Am. Chem. Soc*. **141**, 8599–8607 (2019).

Methods

STM and AFM experiments

All the experiments were performed with a combined noncontact AFM/STM system (Createc) at 5 K using a qPlus sensor equipped with a tungsten tip (parameters: spring constant, $k_0 \approx 1{,}800\ \mathrm{N\,m^{-1}}$; resonance frequency, $f_0 = 26.7$ kHz; quality factor, $Q \approx 45{,}000$). Ultrapure H_2O (deuterium-depleted, ≤1 ppm; Sigma Aldrich) was used and further purified under vacuum by 3–5 freeze-and-pump cycles to remove remaining gas impurities. Then H_2O molecules were dosed in situ onto a clean Au(111) surface held at 120 K through a dosing tube. The as-grown sample was first checked by STM at 77 K, and then quickly cooled down to 5 K for further STM and AFM measurements. Throughout the experiments, bias voltage refers to the sample voltage with respect to the tip. The STM topographic images and AFM frequency-shift (Δf) images were obtained with the CO-terminated tips in constant-current and constant-height modes, respectively. The CO tip was obtained by positioning the tip over a CO molecule on the Au(111) surface at a set point of 100 mV and 30 pA, followed by increasing the bias voltage to 300 mV. The oscillation amplitude of experimental AFM imaging is 100 pm if not specifically mentioned.

DFT calculations

DFT calculations were performed using the Vienna Ab initio Simulation Package (VASP version 5.3)[31,32]. Projector-augmented wave pseudopotentials were used with a cutoff energy of 550 eV for the expansion of the electronic wave functions[33]. Van der Waals corrections for dispersion forces were considered using the 'optB86b-vdW' functional[34,35]. In the DFT calculations, the system consisted of the hexagonal 2D bilayer ice on top of a Au(111) substrate modelled by a four-layer slab. The lattice constant for Au was set to be 4.078 Å and the bottom three-layer Au substrate was fixed in the DFT calculations. Monkhorst–Pack k-point meshes of spacing denser than $2\pi \times 0.058\ \text{Å}^{-1}$ were used and the thickness of the vacuum slab was larger than 13 Å. The geometry optimizations were performed with a force criterion of $0.01\ \mathrm{eV}\ \text{Å}^{-1}$.

Simulations of AFM images

The Δf images were simulated with a molecular-mechanics model based on methods described previously[28,36]. We used the following parameters for the probe-particle–tip model: effective lateral stiffness, $k = 0.75\ \mathrm{N\,m^{-1}}$; atomic radius, $R_c = 1.661$ Å. A quadrupole-like (d_{z^2}) charge distribution at the tip apex was used to simulate the CO tip[12] with $q = -0.25e$. d_{z^2} represents the atomic-orbital function used to simulate the spatial distribution of charge density at the tip apex, d is the atomic orbit, z is the orientation of the orbit, e is the elementary charge and q is the magnitude of the quadrupole charge at the tip apex. The electrostatic potentials of the ice on Au(111) used in the AFM simulations were obtained from DFT calculations. The Lennard-Jones parameters for O and H atoms in the AFM simulation were: $r_H = 1.487$ Å, $\varepsilon_H = 0.680$ meV, $r_O = 1.661$ Å and $\varepsilon_O = 9.106$ meV.

Molecular-dynamics simulations

We performed large-scale molecular-dynamics simulations and used the monoatomic model for water–water interactions[37], which consists of short-ranged two-body and three-body non-bonding potentials without explicitly including hydrogen atoms[37,38]. The 12-6 Lennard-Jones potential was used for the interaction between water and the Au atoms of the Au(111) surface. The Lennard-Jones parameters were determined to be $\varepsilon_{\text{Au–wat}} = 1.553\ \mathrm{kJ\,mol^{-1}}$ and $\sigma_{\text{Au–wat}} = 3.2$ Å to match the experimentally measured contact angles for a water droplet on the Au(111) surface[39]. A cutoff of 10 Å was used for the Lennard-Jones potential. The velocity Verlet algorithm was used to integrate the equations of the motion with a time step of 2 fs. Periodic boundary conditions were applied in all three directions of the simulation box. All molecular-dynamics simulations were carried out using the Large-scale Atomic/Molecular Massively Parallel Simulator (LAMMPS) package[40].

We performed deposition simulations of water vapour on the Au(111) surface at 120 K. The deposition was initiated on a bare Au sheet with an area of 155.72 Å × 159.832 Å consisting of three atomic layers. The simulations were performed in a constant-volume and constant-temperature (NVT) ensemble. The temperature was controlled by a Langevin thermostat with a relaxation time of 1 ps. The Au sheet was kept rigid during the molecular-dynamics simulations, and the water molecules—initially located 20–25 Å above the Au surface—were given initial velocities with a random magnitude from 5.0 to 10.0 $\text{Å}\,\mathrm{ps^{-1}}$ in the direction towards the Au surface. First, we introduced one water molecule to the simulation cell every 0.3 ns. Next, more detailed molecular-dynamics simulations were performed to explore the growth behaviour of the bilayer ice at the zigzag and armchair edges, after the larger-sized bilayer ice grains were formed. For these more detailed simulations, one water molecule was introduced to the simulation cell every 100 ns at either the zigzag edge or the armchair edge. The water molecules were placed at a random initial location with a distance of 3 Å from the nearest water molecule at the edge.

The mechanism of submolecular-resolution AFM imaging

In refs. [7,27], the electrostatic forces of the individual water clusters give rise to dark features at the position of H atoms at large tip heights. However, for 2D bilayer ice at large tip heights, the long-range attractive van der Waals background of the extended water network (Extended Data Fig. 3c, green line) smears out the dark contrast of the H atoms (Extended Data Fig. 3a, z_1 in Extended Data Fig. 3c). Instead, we found that the O–H directionality imaging of the 2D ice can be achieved at smaller tip heights (z_2 in Extended Data Fig. 3c), where the Pauli repulsive forces start to set in, such that the total force signals of the water molecules are separated out from the van der Waals background (Extended Data Fig. 3b). Such an imaging mechanism relies on the delicate interplay between the higher-order electrostatic forces and Pauli repulsion forces. The contribution from the electrostatic force of H and O atoms (Extended Data Fig. 3g) can spatially modulate the Δf contrast of the Pauli repulsions, leading to the apparent O–H directionality.

To confirm the role of the higher-order electrostatic force in the AFM images, we performed systematic AFM image simulations for the 2D bilayer ice using quadrupole (d_{z^2}) (Extended Data Fig. 3d) and neutral (Extended Data Fig. 3e) tip apexes at different tip heights. The O atoms of the flat water molecules are about 1–2 pm higher than those of the vertical water molecules. At a large tip height, the vertical water molecules exhibit brighter contrast than the flat water molecules with the d_{z^2} tip (Extended Data Fig. 3d, left), and the brighter features correspond to the flat molecules for neutral tip (Extended Data Fig. 3e, left).

When the tip height was set to an intermediate value at which the higher-order electrostatic and Pauli repulsion forces are comparable, the O–H directionality of the water molecule is evident in the simulated AFM images with the d_{z^2} tip (Extended Data Fig. 3d, middle). However, such submolecular features are much less obvious when using the neutral tip (Extended Data Fig. 3e, middle). Therefore, the inclusion of the higher-order electrostatic force (d_{z^2} tip) is essential to reproduce the experimental AFM contrasts (Extended Data Fig. 3b). At a smaller tip height, where the AFM signals are dominated by the Pauli repulsion[12], the simulated AFM images show the same honeycomb structure of the 2D ice for both the neutral and d_{z^2} tips (Extended Data Fig. 3d, e, right).

To further justify the importance of the d_{z^2} tip in reproducing the experimental results, we compare the experimental and simulated force curves in Extended Data Fig. 3i–k. We note that the dip in the experimental force curve (F_z) of the flat water molecules is deeper than that of the vertical water molecules (Extended Data Fig. 3i), which cannot be explained by the simple picture based on the height difference of the flat and vertical water molecules. Instead, such a difference can be attributed to the fact that the negatively charged tip apex gains a

larger (or smaller) attractive (or repulsive) electrostatic force above the flat water molecules than that above the vertical molecules (see Extended Data Fig. 3g, j). By contrast, the neutral tip yields negligible difference in F_z curve at the dip position (Extended Data Fig. 3k). In addition, we found a crossover behaviour at small tip heights where the Pauli repulsion force is dominant (black ellipse in Extended Data Fig. 3i), which is also reproduced nicely by the d_{z^2} tip (black ellipse in Extended Data Fig. 3j) but is absent when the neutral tip is used (Extended Data Fig. 3k). This crossover behaviour results from the strong deflection of the CO tip by the Pauli repulsion force (see the red and blue arrows in Extended Data Fig. 3l). The relaxation of the CO molecule occurs earlier at the vertical water molecules than at the flat molecules, primarily arising from the different shapes of the potential surface (Extended Data Fig. 3h), where the potential distribution above the vertical water molecules appears to be more anisotropic than above the flat water molecules.

DFT-calculated formation energies of different edges of the 2D ice

To compare the relative stability of the zigzag and armchair edges, edge-formation energies (E_f) were calculated using DFT, which revealed that the unreconstructed zigzag edge and reconstructed 5756-type armchair edge are the most stable edges. The edge-formation energy[41] is defined as

$$E_f = (n_e \times E'_{ad,i} - E_{ad,e})/l$$

where n_e is the number of the water molecules in edged bilayer ice, l (in nanometres) is the length along the ice edge, and $E'_{ad,i}$ and $E_{ad,e}$, defined in Eqs. (1a) and (1b) below, are the adsorption energy (per water molecule) of the infinite 2D bilayer ice on the Au substrate and the adsorption energy of the edged 2D bilayer ice on the Au substrate, respectively.

$$E'_{ad,i} = (E[\mathrm{Au}] + n_i \times E[(\mathrm{H_2O})_g] - E[\mathrm{ice_i/Au}])/n_i \quad (1a)$$

$$E_{ad,e} = E[\mathrm{Au}] + n_e \times E[(\mathrm{H_2O})_g] - E[\mathrm{ice_e/Au}] \quad (1b)$$

where n_i is the number of the water molecules in the infinite ice, E[Au] is the energy of the bare Au substrate, $E[(H_2O)_g]$ is the energy of the isolated water molecule in the gas phase, and $E[\mathrm{ice_i/Au}]$ and $E[\mathrm{ice_e/Au}]$ are the total energies of the Au-supported infinite and edged 2D ices, respectively.

There are three different orientations for zigzag edges (ZZ1, ZZ2 and ZZ3) and armchair edges (AC1, AC2, and AC3), given a specific type of proton ordering (Extended Data Fig. 4a). ZZ1 and ZZ3 are equivalent, as are AC1 and AC3. Each orientation can produce two types of proton order along the edge. Experimentally, it is difficult to discern the O–H directionality at the edges because the vertical relaxation of the water molecules at the edges can easily smear out the weak-force contrasts arising from the O–H directionality. However, we could determine that the dangling OH is disfavoured at the edge of the top water layer.

We thus only performed calculations of the non-equivalent orientations for zigzag edges (Extended Data Fig. 4b, c) and armchair edges (Extended Data Fig. 4d, e) without or with fewer dangling OHs. In our calculations, one edge of the bilayer ice (orange O atoms in Extended Data Fig. 4b–e), was fixed at the same position of the infinite bilayer ice. Therefore, the relative formation energies of the other edge, ΔE_f, can be calculated after structural relaxation. Extended Data Fig. 4f shows ΔE_f with respect to the corresponding unreconstructed 6666-type zigzag and armchair edges, where the unreconstructed zigzag edge and 5756-type armchair edge are the most stable edges no matter which type of edge is considered. We note that the 6666-type armchair edge cannot be seen in the experiment, although the energy of the 6666-type edge is smaller than that of the 5656-type edge. This is due to the existence of a stable composite 575/656 structure (t = 0.4 μs in Fig. 4b), which considerably lowers the 5756-to-5656 conversion barrier (see Extended Data Fig. 9). Therefore, the growth of armchair edges is governed by the interplay between the thermodynamics and kinetics, leading to the 5756-to-5656 conversion in the absence of a 6666-type edge.

Insight into the stability of the zigzag and armchair edges

To gain further insight into the formation energies of different edges, we decomposed the DFT-calculated formation energy E_f into three parts: the energy difference between the edged state and infinite state of the Au(111) substrate, $E_{f,Au}$, the ice, $E_{f,ice}$, and the interaction between the Au(111) substrate and the ice, $E_{f,Au-ice}$. We found that $E_{f,Au}$ is negligible, and thus the only noticeable contributions to E_f are from $E_{f,ice}$ and $E_{f,Au-ice}$. The detailed relative energies (ΔE) with respect to the energy of the corresponding unreconstructed 6666-type edge are shown in Extended Data Fig. 5a, b, where the cyan, blue and red bars represent $\Delta E_{f,Au-ice}$, $\Delta E_{f,ice}$ and ΔE_f, respectively. In particular, we found that $\Delta E_{f,ice}$ is the dominant component of ΔE_f, which largely determines the relative stability of different ice edges.

The three parts of the formation energy E_f are defined as

$$E_{f,Au} = (E[\mathrm{Au_e}] - E[\mathrm{Au_i}])/l \quad (2)$$

$$E_{f,ice} = (E[\mathrm{ice_e}] - n_e \times E[\mathrm{ice_i}]/n_i)/l \quad (3)$$

$$E_{f,Au-ice} = (E[\mathrm{ice_e/Au}] - E[\mathrm{ice_e}] - E[\mathrm{Au_e}] - n_e \times E'_{Au-ice})/l \quad (4)$$

The E'_{Au-ice} is the binding energy (per water molecule) between the Au(111) substrate and the infinite 2D ice, defined in Eq. (5)

$$E'_{Au-ice} = (E[\mathrm{ice_i/Au}] - E[\mathrm{ice_i}] - E[\mathrm{Au_i}])/n_i \quad (5)$$

where $E[\mathrm{Au_e}]$ and $E[\mathrm{ice_e}]$ are the energies of the Au substrate and the ice separated from the Au-supported edged ice, respectively; $E[\mathrm{Au_i}]$ and $E[\mathrm{ice_i}]$ are the energies of the Au substrate and the ice separated from the Au-supported infinite ice, respectively.

To explore the reason why the armchair edge is reconstructed to the 5756-type edge, we analysed some details of H bonds at different armchair edges in DFT calculation. $\Delta E_{f,ice}$ is mainly related to the H-bonding interaction between the water molecules at the ice edge. We note on one hand that the density of unsaturated H bonds at the 5756-type armchair edge is reduced from that of the unreconstructed 6666-type ($1.15/a_{ice}$) to $0.87/a_{ice}$, which can greatly lower the formation energy of the armchair edge. On the other hand, the formation of the 5756-type armchair edge introduces only a very small strain on the H bonds, as suggested by the small deviation of H-bonding length and angles from the unreconstructed 6666-type (Extended Data Fig. 5c). Therefore, the 5756-type armchair edge should be energetically favoured over the unreconstructed 6666-type.

Although the 5656-type edge has an even smaller density of unsaturated H bonds ($0.58/a_{ice}$) than does the 5756-type edge, it is much more stressed (Extended Data Fig. 5c) and becomes less stable than the 5756-type edge. Indeed, we found by experiment that the length of the 5656-type edges is primarily below 10 Å, which is considerably shorter than that of the 5756-type edges (Extended Data Fig. 5d). Such a difference can be explained by considering that the 5656-type edge cannot grow too long, owing to the accumulation of strain energy. Therefore, the stabilization of the 5756-type armchair edge results from the combined effects of minimizing the unsaturated H bonds and reducing the strain energy.

Stability of various intermediate structures at the edges obtained by molecular-dynamics simulations

We note that some intermediate structures in molecular-dynamics simulations shown in Fig. 4 cannot be observed in experiments (Fig. 3).

This is related to the relative stability and lifetime of the various intermediate structures. Owing to computational limitations, it is very difficult to obtain the accurate lifetimes for the intermediate structures, which are relatively long compared to the simulation time. Instead, we have calculated the interacting energy (ΔE_b) between a water molecule at the edge and the remaining water molecules together with the Au substrate after optimization for various intermediate structures by classical force field. The maximum interacting energy corresponds to that needed to decompose the existing structure during the growth, thus providing an estimation for the lifetime.

As shown in Extended Data Fig. 9, our calculations show that the maximum interacting energy between a water molecule at the zigzag edge and the remaining water molecules follows ZZ3 > ZZ2 > ZZ4 > ZZ5 > ZZ6 > ZZ1. Such a trend suggests that individual pentagon structures attached at the zigzag edge (ZZ1) are the most stable. By contrast, zigzag-565 (ZZ4) should have the shortest lifetime among the intermediate structures with paired water, which explains why such a structure cannot be observed experimentally. In addition, we note that the lifetime of the 5(6···6)5 structure at the zigzag edge increases with the number of the hexagons.

For armchair edge structures, the maximum interacting energy follows AC4 > AC3 > AC2 > AC1. Interestingly, it was revealed that the composite 575/656 structure (AC1) is very stable. However, we cannot distinguish between the 575/656 structure and the 5756-type edge in experiment, because only the top layer of the 2D bilayer ice can be imaged by STM and AFM. Such a composite 575/656 structure would greatly facilitate the 5756-to-5656 conversion during the growth of the armchair edge structure. Furthermore, the lifetime of the 5656-type edge decreases rapidly as its length increases, which is consistent with experimental results that indicate that the observed 5656-type edges are mostly short.

Data availability

The source data are available from the corresponding authors upon reasonable request.

Code availability

The custom code and mathematical algorithms that support the findings of this study are available from the corresponding authors upon reasonable request.

31. Kresse, G. & Hafner, J. Ab initio molecular dynamics for liquid metals. *Phys. Rev. B* **47**, 558–561 (1993).
32. Kresse, G. & Furthmuller, J. Efficient iterative schemes for ab initio total-energy calculations using a plane-wave basis set. *Phys. Rev. B* **54**, 11169–11186 (1996).
33. Kresse, G. & Joubert, D. From ultrasoft pseudopotentials to the projector augmented-wave method. *Phys. Rev. B* **59**, 1758–1775 (1999).
34. Klimeš, J., Bowler, D. R. & Michaelides, A. Chemical accuracy for the van der Waals density functional. *J. Phys. Condens. Matter* **22**, 022201 (2010).
35. Klimeš, J., Bowler, D. R. & Michaelides, A. van der Waals density functionals applied to solids. *Phys. Rev. B* **83**, 195131 (2011).
36. Hapala, P., Temirov, R., Tautz, F. S. & Jelinek, P. Origin of high-resolution IETS-STM images of organic molecules with functionalized tips. *Phys. Rev. Lett*. **113**, 226101 (2014).
37. Molinero, V. & Moore, E. B. Water modeled as an intermediate element between carbon and silicon. *J. Phys. Chem. B* **113**, 4008–4016 (2009).
38. Lupi, L. et al. Role of stacking disorder in ice nucleation. *Nature* **551**, 218–222 (2017).
39. Erb, R. A. Wettability of gold. *J. Phys. Chem*. **72**, 2412–2417 (1968).
40. Plimpton, S. Fast parallel algorithms for short-range molecular dynamics. *J. Comput. Phys*. **117**, 1–19 (1995).
41. Gao, J. F., Zhao, J. J. & Ding, F. Transition metal surface passivation induced graphene edge reconstruction. *J. Am. Chem. Soc*. **134**, 6204–6209 (2012).
42. Sader, J. E. & Jarvis, S. P. Accurate formulas for interaction force and energy in frequency modulation force spectroscopy. *Appl. Phys. Lett*. **84**, 1801–1803 (2004).
43. Li, X. Z., Walker, B. & Michaelides, A. Quantum nature of the hydrogen bond. *Proc. Natl Acad. Sci. USA* **108**, 6369–6373 (2011).

Acknowledgements We thank J.-J. Wang for discussions. This work was supported by the National Key R&D Program under grant numbers 2016YFA0300901, 2017YFA0205003 and 2015CB856801, the National Natural Science Foundation of China under grant numbers 11888101, 11634001, 21725302 and 11525520, the Strategic Priority Research Program of the Chinese Academy of Sciences under grant number XDB28000000, and the Beijing Municipal Science & Technology Commission. J.S.F. and X.C.Z were supported by US National Science Foundation (CHE-1665324). We are grateful for the computational resources provided by the TianHe-1A and TianHe II supercomputers, by the High-performance Computing Platform of Peking University supercomputing facility, and by the UNL Holland Computing Center.

Author contributions Y.J. and E.-G.W. designed and supervised the project. R.M. and Y.T. performed the STM/AFM measurements with J.G. and J.P.; D.C., J.C., X.-Z.L. and L.-M.X. performed ab initio DFT calculations. C.Z., J.S.F. and X.C.Z. carried out the classical molecular-dynamics simulations. D.C. carried out the theoretical simulations of the AFM images. R.M., D.C., C.Z., Y.T., J.C., X.-Z.L., X.C.Z., L.-M.X., E.-G.W., and Y.J. analysed the data. Y.J., R.M., D.C., L.-M.X., C.Z. and X.C.Z. wrote the manuscript with the input of all other authors. The manuscript reflects the contributions of all authors.

Competing interests The authors declare no competing interests.

Additional information

Supplementary information is available for this paper at https://doi.org/10.1038/s41586-019-1853-4.

Correspondence and requests for materials should be addressed to X.C.Z., L.-M.X., E.-G.W. or Y.J.

Peer review information *Nature* thanks Miquel Salmeron and Yoshiaki Sugimoto for their contribution to the peer review of this work.

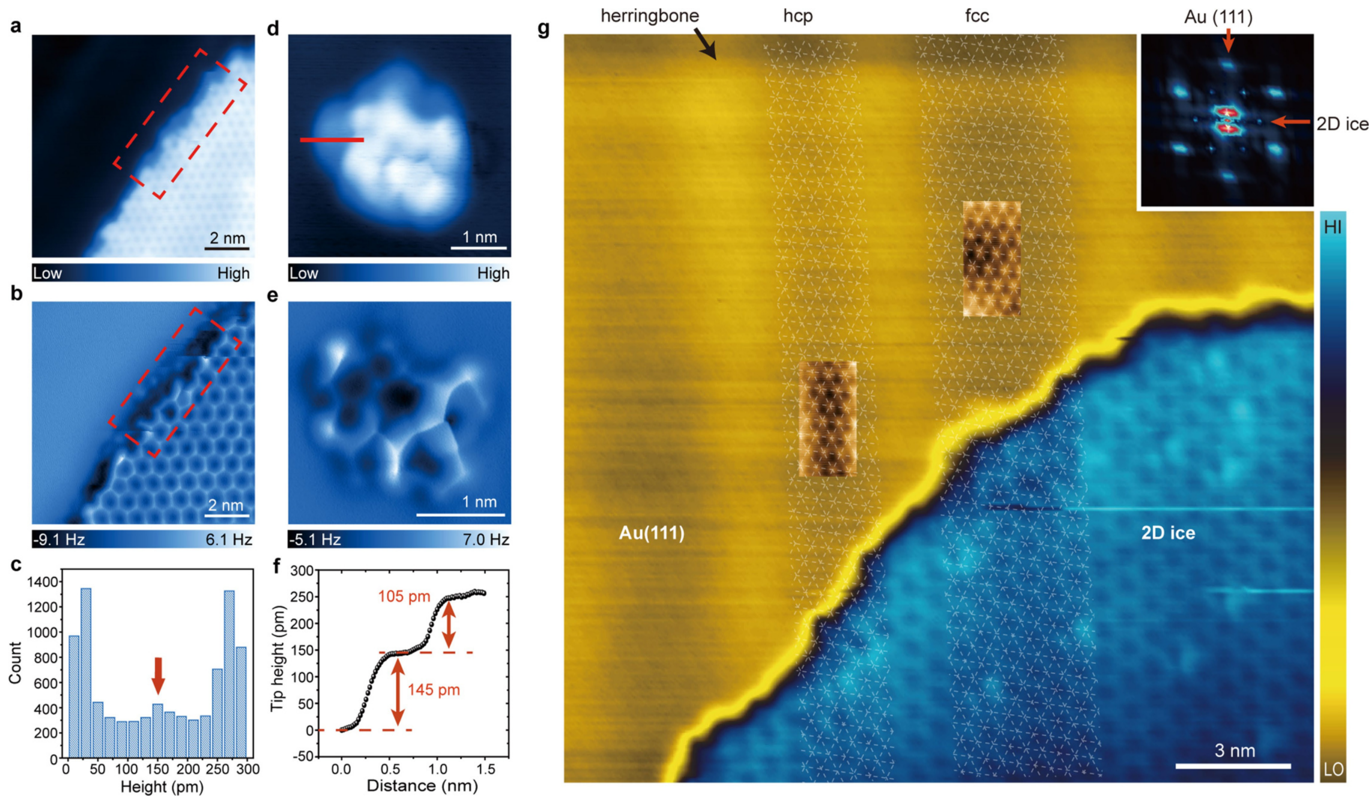

Extended Data Fig. 1 | Experimental evidence for the bilayer nature of 2D ice. **a**, **d**, STM images of a bilayer ice island (**a**) and cluster (**b**). Set point, 100 mV and 10 pA. **b**, **e**, AFM images of the same ice island (**b**) and cluster (**e**). **b** was acquired at the constant-current mode with set point 100 mV and 50 pA. **e** was recorded at a constant height of 280 pm, referenced to the set point of 100 mV and 50 pA on the Au(111) substrate. **c**, Height-distribution diagram within the red dashed rectangular area in **a**. The red arrow denotes the bottom layer of the bilayer ice, proving the bilayer nature of the 2D ice. **f**, Height profile across the red line shown in **d**, giving two different steps with heights of about 150 pm and about 250 pm, consistent with the results of the 2D ice island. **g**, False-colour STM image of a 2D ice island grown on a Au(111) surface, where the honeycomb structure of the 2D ice and the herringbone reconstruction of the Au(111) surface are distinguishable. The atomically resolved STM images of the Au(111) lattice are superimposed within the face-centred cubic (fcc) and hexagonal close-packed (hcp) regions, showing good registry between the 2D ice and the Au substrate. The set points are 100 mV and 10 pA and 5 mV and 6 nA for the ice island and the Au(111) lattice, respectively. The white dashed grids correspond to the 1×1 lattice of Au(111) within the fcc and hcp regions. The inset at the upper-right corner is a composite 2D-FFT image of the Au(111) and 2D-ice lattice, and shows the corresponding 1×1 and $\sqrt{3} \times \sqrt{3}$ periodicities.

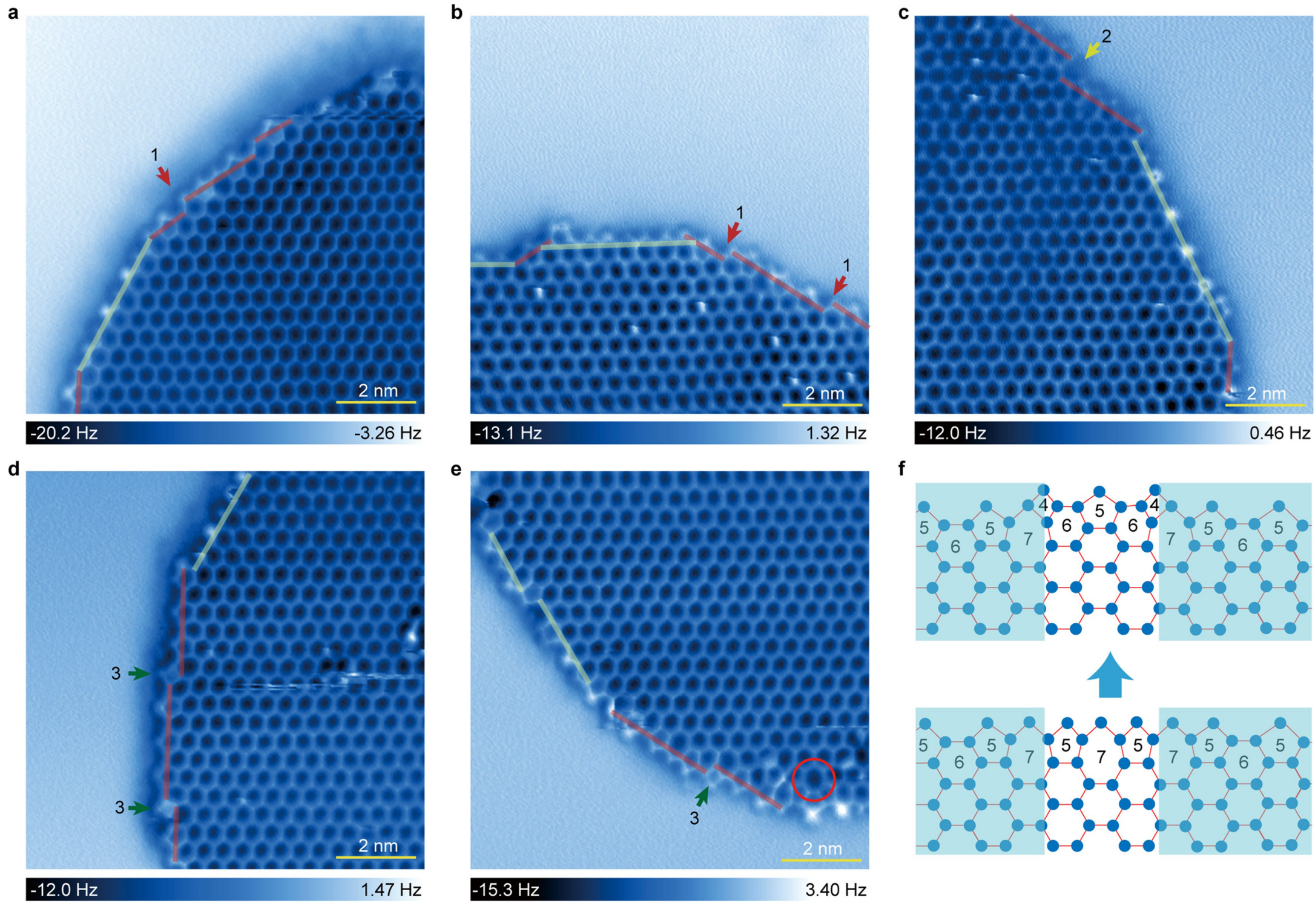

Extended Data Fig. 2 | Interruption of the armchair edges by defects and kinks. a–**e**, Constant-height AFM images of edge areas that contain short reconstructed armchair edges. The tip height is $z_{\text{offset}} = -10$ pm, referenced to the STM set point 100 mV and 50 pA on the water molecules of the second layer of bilayer ice. The red and green lines represent the armchair and zigzag edges, respectively. The red, green and yellow arrows point to three types of kinks at the armchair edges. Type-1 (red) and type-2 (yellow) kinks correspond to the cases where the armchair edges are terminated at the hexagons and pentagons, respectively. The local seeding growth model requires individual nucleation centres to facilitate the growth of the armchair edges, naturally leading to these step-like structures. **f**, Schematic showing the formation of type-3 (green arrows) kink defects, consisting of 647-type member rings. These defects are formed owing to the position of the heptagons at the armchair edges, which leads to two different structure series. The green shaded areas represent 5657-member-ring series, and the unshaded areas represent the 5756-type member ring series. The joint of the two different series results in a type-3 defect, which could further develop into a trapped 7-type member ring in the second-outermost layer, as indicated by a red circle in **e**.

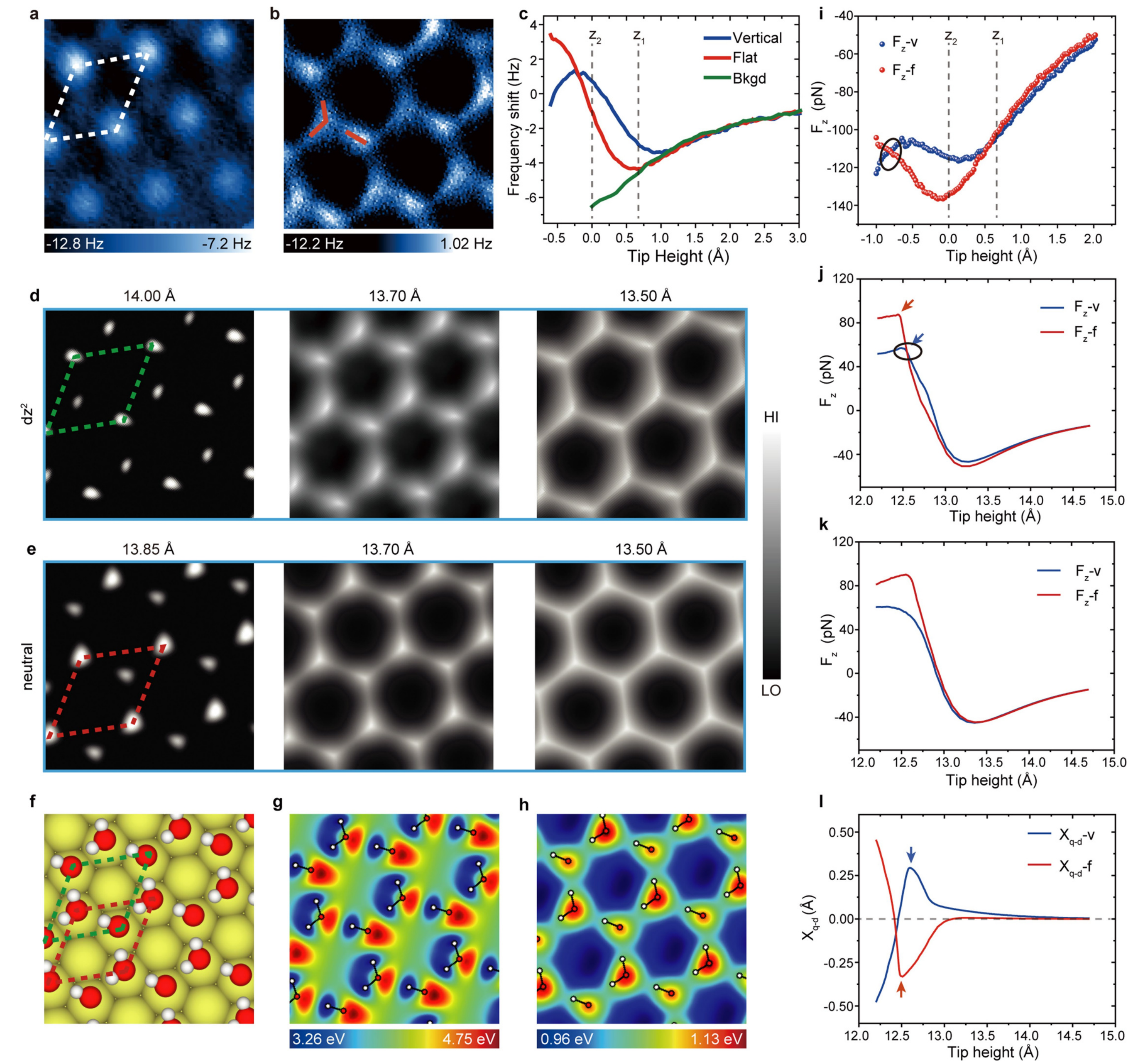

Extended Data Fig. 3 | The mechanism of submolecular-resolution AFM imaging. a, **b**, Experimental AFM frequency-shift (Δf) images obtained at tip heights and oscillation amplitudes of 70 pm and 40 pm (**a**) and 0 pm and 100 pm (**b**). **c**, Δf curves (oscillation amplitude, 40 pm) above a vertical water molecule (vertical), a flat molecule (flat) and the hollow site of hexagonal ice lattice (denoted as background, bkgd) as a function of the tip height. z_1 and z_2 denote the tip heights of the two Δf images in **a** and **b**, respectively. **d**, **e**, Simulated Δf images at different tip heights z (given above each image) obtained with quadrupole (d_{z^2}, $q = -0.25e$; **d**) and neutral ($q = 0$; **e**) tips. **f**, Top view of the 2D bilayer ice structure (top layer) on the Au(111) substrate. The bottom ice layer is hidden to highlight the structure of the top layer. The green and red dashed parallelograms in **d**–**f** denote the sub-lattices of the vertical and flat water molecules, respectively. **g**, Calculated electrostatic potential map of the bilayer ice on the Au(111) in a plane 7.24 Å above the highest atom in the Au substrate. **h**, Simulated total potential map of the bilayer ice on Au(111) in a plane, corresponding to the position of the CO-tip apex at a tip height of 12.5 Å. **i**–**k**, Vertical force above the flat ($F_{z\text{-f}}$) and vertical ($F_{z\text{-v}}$) water molecule as a function of tip height. **i**, Experimental F_z obtained by integrating the experimental $\Delta f(z)$ in **c** according to ref. [42]. Before the integration, $\Delta f(z)$ was smoothed using a moving average filter with a span of 5. **j**, **k**, Simulated F_z computed with d_{z^2} (**j**) and neutral (**k**) tips. **l**, Simulated lateral deflection of the quadrupole probe particle in the x direction ($X_{q\text{-d}}$) as a function of the tip height. $X_{q\text{-d-v}}$ and $X_{q\text{-d-f}}$ correspond to $X_{q\text{-d}}$ above the vertical water molecule and the flat water molecule, respectively. Tip-height references are the same as those in Fig. 2. In **g** and **h**, H and O atoms in the top-layer ice are denoted as white and red spheres, respectively. The image sizes in **a**, **b** and **d**–**h** are 1.25 nm × 1.25 nm. See Methods for details.

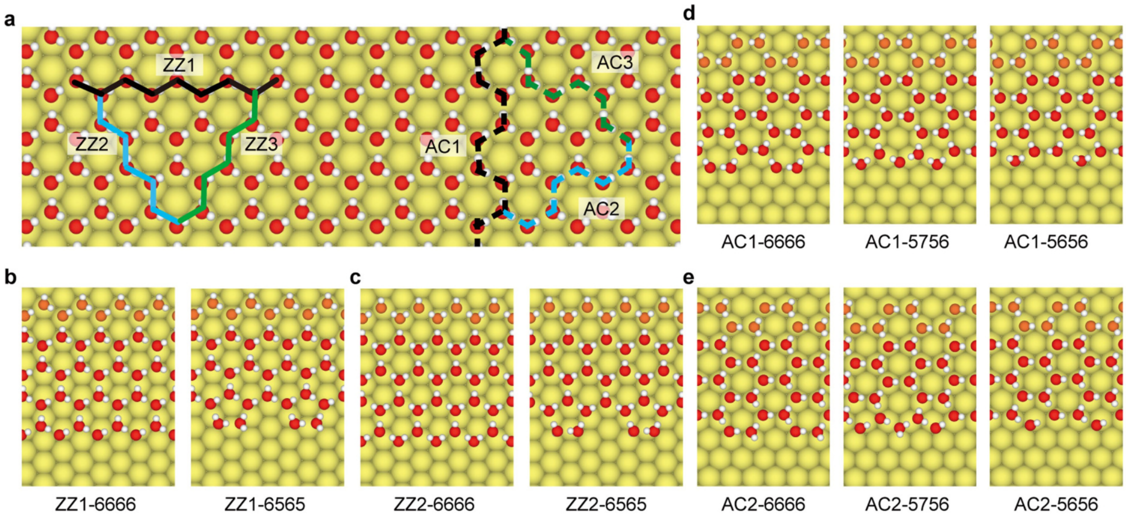

f

ΔE_f (meV/nm)	Zigzag edge (ZZ)		Armchair edge (AC)		
	6666	6565	6666	5756	5656
Type 1	0	127	0	-105	109
Type 2	0	75	0	-28	179

Extended Data Fig. 4 | DFT-calculated formation energies of different edges of the 2D ice. a–**e**, Top view of the top layer of bulk (**a**), zigzag (ZZ)-edged (**b**, **c**), and armchair (AC)-edged (**d**, **e**) 2D ices on a Au(111) substrate. The three different zigzag and armchair edge type are denoted in **a** by solid and dashed poly lines, respectively. The fixed edges during the structural relaxation are marked in orange. The bottom ice layer is hidden, to highlight the structure of the top layer. Image sizes: 6.52 nm × 2.17 nm (**a**), 2.00 nm × 2.61 nm (**b**, **c**), and 1.73 nm × 2.61 nm (**d**, **e**). Lateral size of the supercell used in the DFT calculations: 2.00 nm × 3.46 nm (**b**, **c**) and 1.73 nm × 3.50 nm (**d**, **e**). **f**, The relative formation energy (ΔE_f) of the different edge types. See Methods for details.

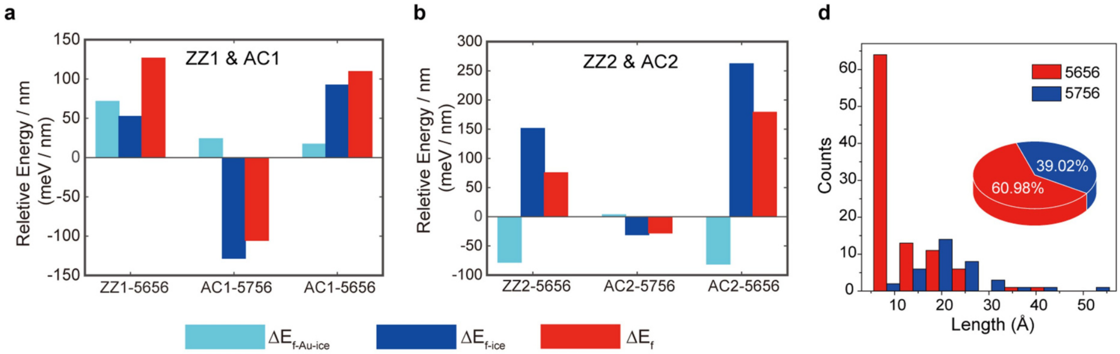

c

Armchair edge	d_{OO} (Å)			O-H…O angel (°)		
	6666	5756	5656	6666	5756	5656
AC1	2.756	2.781	2.945	165.489	165.860	162.311
AC2	2.761	2.771	2.934	165.960	165.326	163.081

Extended Data Fig. 5 | Insight into the stability of the zigzag and armchair edges. a, **b**, Decomposed DFT-calculated relative formation energies of the 2D bilayer ice with different edge types (ZZ1 and AC1, **a**; ZZ2 and AC2, **b**). The relative formation energies of different edges are referenced to that of the corresponding unreconstructed 6666-type edge. The cyan, blue and red bars represent the relative energy of the interaction between the Au(111) substrate and the bilayer ice, the isolated bilayer ice, and the Au-supported bilayer ice, respectively. **c**, The average O–O distance[43] (d_{OO}) and H-bonding angle[43] (O–H…O angle) of the outermost rings of different armchair edges. **d**, Experimental length distribution diagram of 5656- and 5756-type armchair edges for ten ice islands, n = 122. Inset, Statistics on the total length of corresponding edges. See Methods for details.

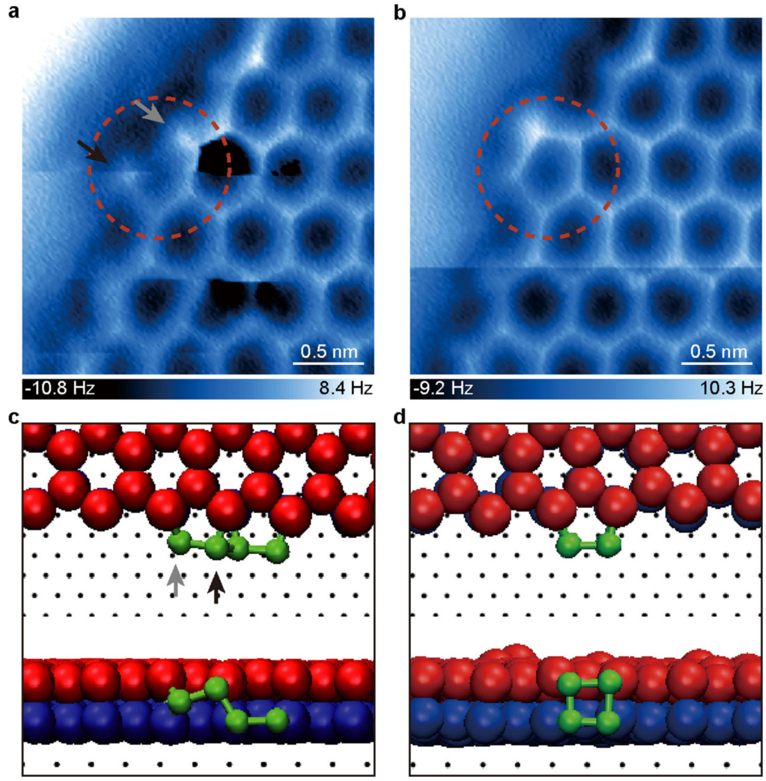

Extended Data Fig. 6 | Tip-induced growth of the pentagon structure at the zigzag edge. a, **b**, AFM images of the same area during the consecutive scanning showing the formation of the pentagon structure. Tip height, $z_{offset} = -10$ pm, referenced to the STM set point of 100 mV and 50 pA on the water molecule of the bilayer ice. **c**, **d**, The corresponding snapshots in the molecular-dynamics simulations. The dangling-like water molecule corresponds to the molecule attached to the top layer (see the black arrows in **a** and **c**), and the water molecule located at the middle of the bilayer ice has an apparently shorter bond (grey arrows in **a** and **c**). As highlighted by the red dashed circles in **a** and **b**, during close imaging at a very small tip height, a complete pentagon structure at the zigzag edge can be formed, induced by the perturbation of the tip.

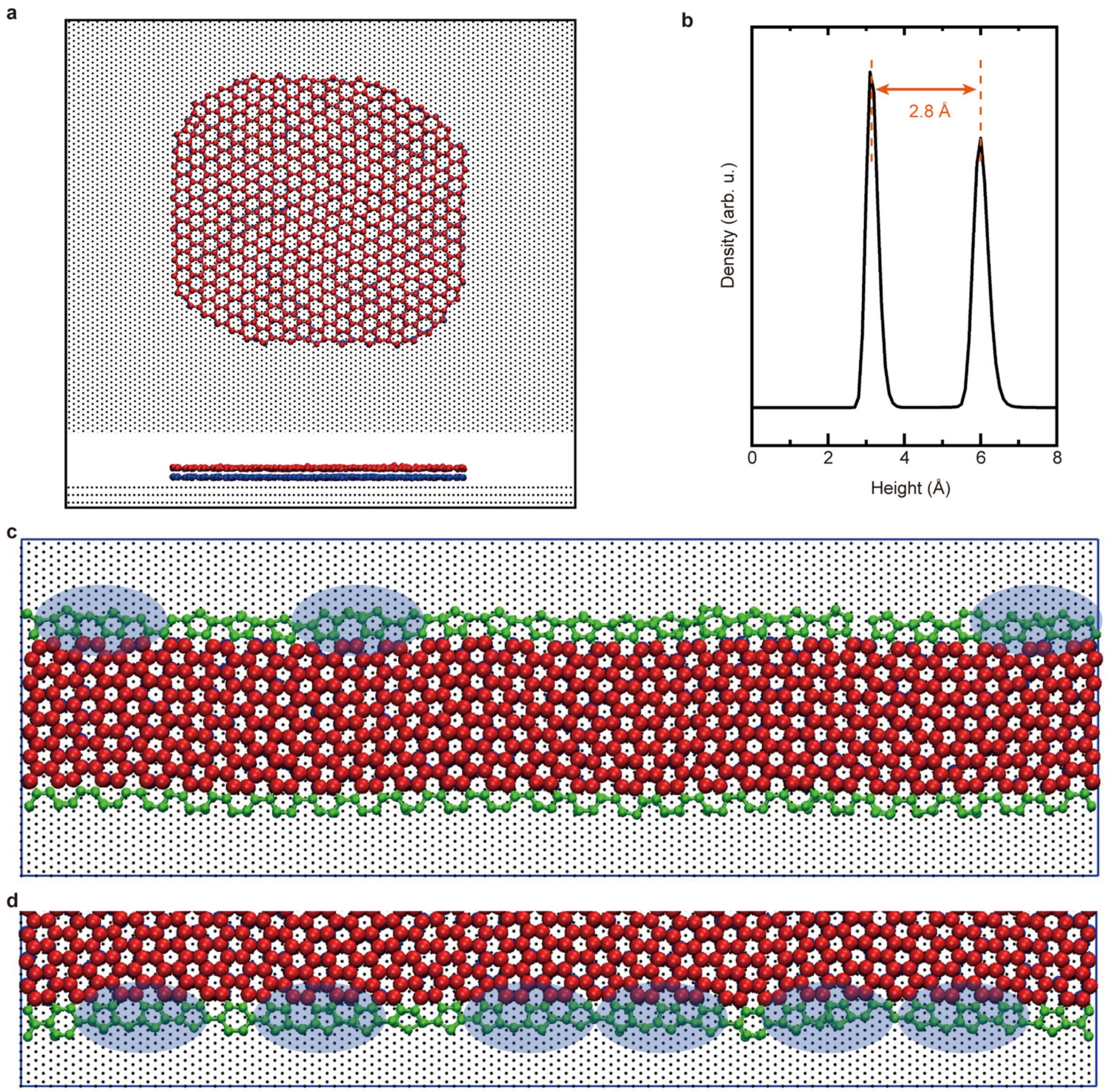

Extended Data Fig. 7 | Molecular-dynamics simulation of 2D ice formation and armchair edge stability. a, Top (upper) and side views (lower) of a snapshot show 1,394 water molecules deposited on a Au(111) surface at 120 K. The bottom layer of water molecules is shown in blue and the top layer in red. Au atoms of the Au surface are shown in black. No good registry between the 2D ice and the Au substrate is found, probably due to the weak interaction between them. Although 5656-type armchair edges appear, the 5756-type and 6666-type armchair edges are absent, because of the coincident number of the water molecules added and the limited length of the edges. **b**, Transverse density profile of the 2D bilayer ice. The intensity of the lower peak is slightly larger than that of the higher one, indicating that the growth of bilayer ice starts from the bottom layer. **c**, Snapshot of a bilayer ice ribbon (20.76 nm in length) on a Au(111) surface after relaxation for 20 ns, originally with two armchair edges of 5656-type (upper) and 6666-type (lower). Some 5656-type structures spontaneously convert to 5756-type structures (highlighted by blue ellipses) during the simulation, indicating that the 5756-type edge should be thermodynamically more stable than the 5656-type edge. **d**, Snapshot at $t = 1$ μs after 63 water molecules were introduced to 6666-type armchair edges. Most of 6666-type structures change to 5756-type or 5656-type structures, suggesting that the growth of armchair edges is governed by the 5756-to-5656 conversion in the absence of a 6666-type edge.

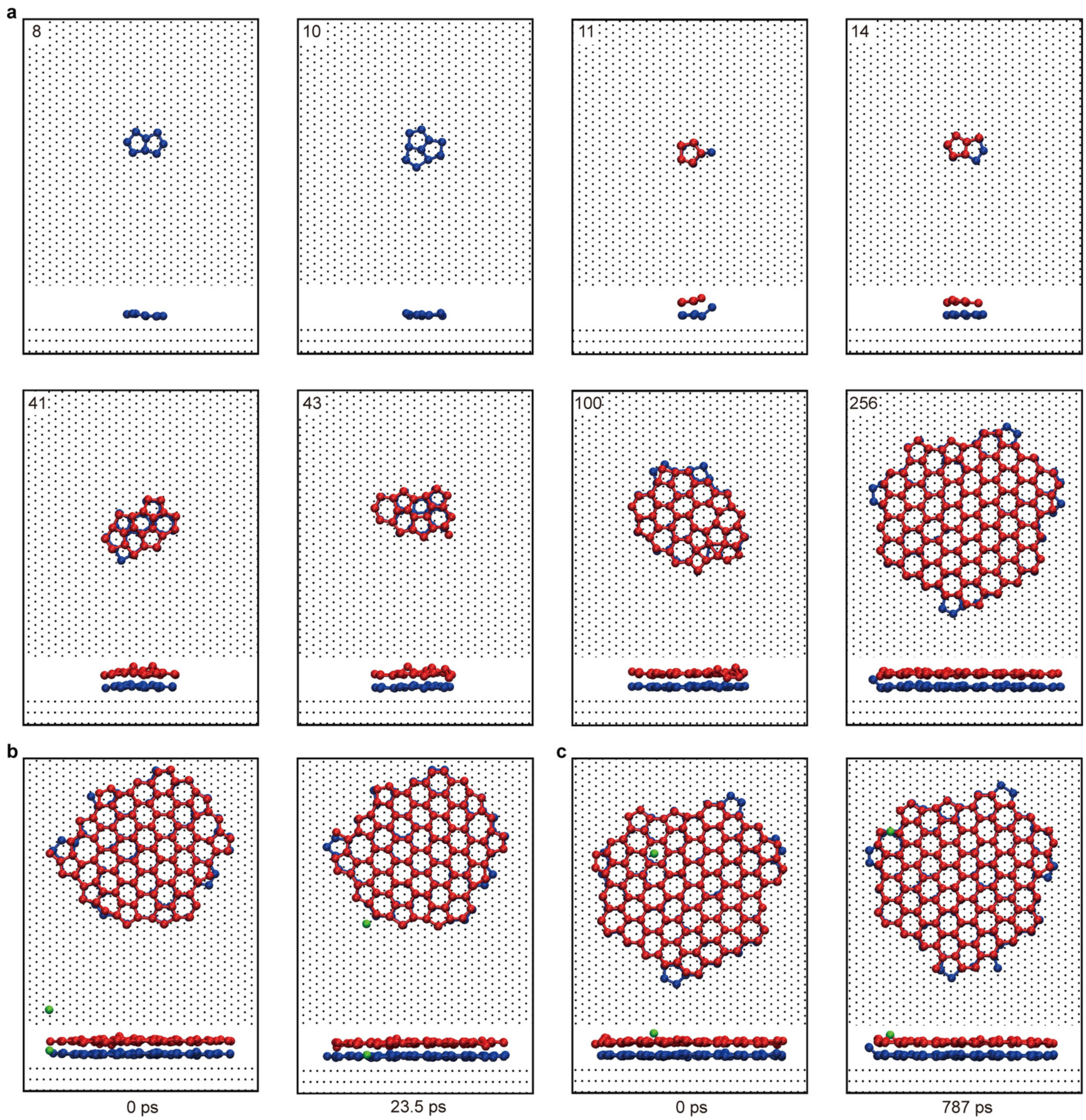

Extended Data Fig. 8 | Nucleation of the 2D ice on the Au surface. a, Top (upper) and side views (lower) of consecutive snapshots show 8, 10, 11, 14, 41, 43, 100 and 256 water molecules deposited on a Au(111) surface at 120 K. The 2D bilayer ice structure was gradually formed through single-layer and double-layer liquid clusters. **b**, Top (upper) and side views (lower) of snapshots at times $t = 0$ and 23.5 ps after the deposited water molecule (green ball) arrived at the Au surface. **c**, Top (upper) and side views (lower) of snapshots at times $t = 0$ and 787 ps after the deposited water molecule (green ball) arrived on the surface of bilayer ice. The bottom layer of water molecules is shown in blue and the top layer in red, and the Au atoms of the Au surface are shown in black. The water molecule landing on the Au or ice-island surface moves around until it finds its way to attach to the edge of the ice, without creating any new nucleation centres.

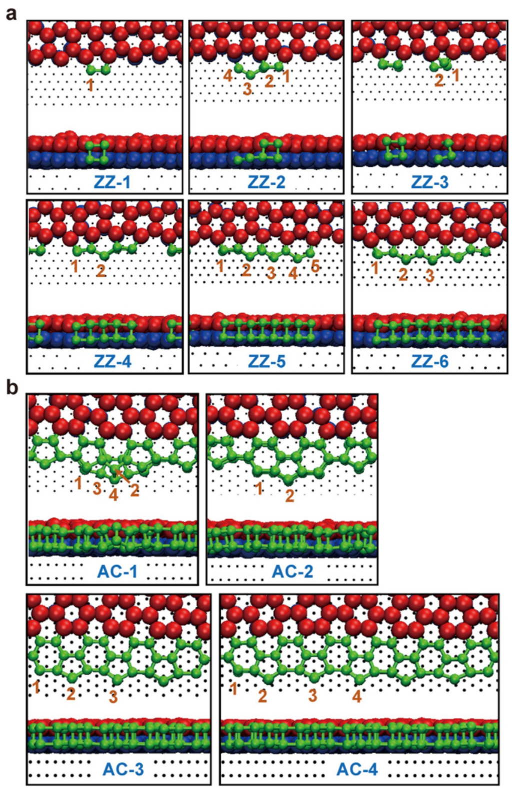

c

Zigzag edge (ZZ)					
	ZZ-1	ZZ-2			
ΔE$_b$ (meV)	water-1	water-1	water-2	water-3	water-4
	-693.4	-686.4	-687.9	-589.1	-604.3
	ZZ-3			ZZ-4	
ΔE$_b$ (meV)	water-1		water-2	water-1	water-2
	-530.0		-714.2	-641.5	-633.6
	ZZ-5				
ΔE$_b$ (meV)	water-1	water-2	water-3	water-4	water-5
	-646.0	-665.0	-689.7	-694.7	-694.0
	ZZ-6				
ΔE$_b$ (meV)	water-1		water-2		water-3
	-648.7		-660.7		-681.8
Armchair edge (AC)					
	AC-1				
ΔE$_b$ (meV)	water-1		water-2	water-3	water-4
	-709.0		-714.0	-759.1	-725.5
	AC-2		AC-3		
ΔE$_b$ (meV)	water-1	water-2	water-1	water-2	water-3
	-662.7	-650.7	-629.3	-651.9	-634.8
	AC-4				
ΔE$_b$ (meV)	water-1		water-2	water-3	water-4
	-652.3		-634.4	-621.7	-599.9

Extended Data Fig. 9 | Stability of various intermediate structures at the zigzag and armchair edges obtained by molecular-dynamics simulations. **a**, **b**, Molecular-dynamics simulations snapshots of various intermediate structures during the growth of the zigzag (**a**) and armchair (**b**) edges. One water molecule was introduced to the simulation cell every 100 ns. The representative water molecules with low coordination at the edges are marked by numbers. **c**, The calculated interacting energy (ΔE_b) for the different intermediate structures shown in **a** and **b**. ΔE_b is defined as the interacting energy between a specific water molecule and the remaining water molecules together with the Au atoms in substrate after optimization. The maximum energy values are indicated in red. See Methods for details.

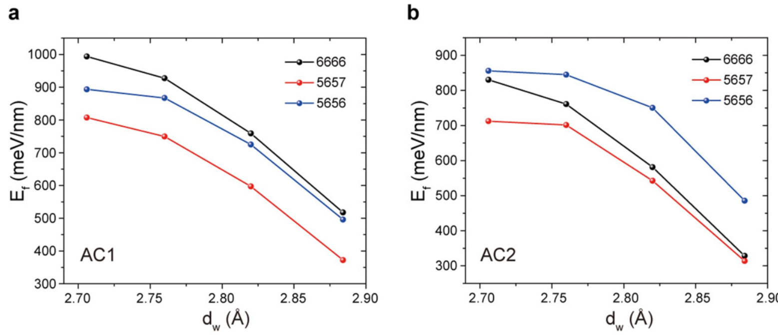

c

d(Au-Au) = 2.884 Å,d(water-water) = 2.884 Å					
ΔE_f (meV/nm)	zigzag edge		armchair edge		
	6666	6565	6666	5756	5656
	0	99.2	0	-159.5	144.2
d(Au-Au) = 2.884 Å, d(water-water) = 2.768 Å (no lattice registry)					
ΔE_f (meV/nm)	zigzag edge		armchair edge		
	6666	6565	6666	5756	5656
	0	63.8	0	-22.6	51.0
free-standing ice, d(water-water) = 2.74 Å					
ΔE_f (meV/nm)	zigzag edge		armchair edge		
	6666	6565	6666	5756	5656
	0	62.7	0	-35.4	29.1
d(Au-Au) = 2.74 Å, d(water-water) = 2.74 Å					
ΔE_f (meV/nm)	zigzag edge		armchair edge		
	6666	6565	6666	5756	5656
	0	83.6	0	-5.0	100.0

Extended Data Fig. 10 | The influence of water spacing on the stability of different edges. a, **b**, The DFT-calculated edge-formation energies as a function of water spacing (d_w) for free-standing 2D ice with different proton ordering (AC1 and AC2, see Extended Data Fig. 4a for detailed definitions). The 2D ice with minimum energy has a water spacing of 2.706 Å. The relative stability of the different armchair edges remains unchanged with water spacing from 2.706 Å to 2.884 Å; the 5756-type armchair edge is the most stable edge. The abscissa reflects the cell size in the direction parallel to the edge, which is crucial, owing to the periodic boundary conditions in the calculation. d_w corresponds to the nearest water–water spacing along the direction parallel to the edge. E_f represents the edge formation energy, similar to that defined in Methods section 'DFT-calculated formation energies of different edges of the 2D ice'. All atoms in the ice edge were fully relaxed and the structures of the different ice edges are similar as those in Extended Data Fig. 4. **c**, The relative formation energy (ΔE_f) of different edges calculated by classical force field, which follows 5656 > 6666 > 5756 for all cases, regardless of the water spacing and the commensurability with the substrate.

Confinement of atomically defined metal halide sheets in a metal–organic framework

https://doi.org/10.1038/s41586-019-1776-0

Received: 18 June 2019

Accepted: 26 September 2019

Published online: 18 November 2019

Miguel I. Gonzalez[1,6], Ari B. Turkiewicz[1,6], Lucy E. Darago[1], Julia Oktawiec[1], Karen Bustillo[2], Fernande Grandjean[3], Gary J. Long[3] & Jeffrey R. Long[1,4,5]*

The size-dependent and shape-dependent characteristics that distinguish nanoscale materials from bulk solids arise from constraining the dimensionality of an inorganic structure[1–3]. As a consequence, many studies have focused on rationally shaping these materials to influence and enhance their optical, electronic, magnetic and catalytic properties[4–6]. Although a select number of stable clusters can typically be synthesized within the nanoscale regime for a specific composition, isolating clusters of a predetermined size and shape remains a challenge, especially for those derived from two-dimensional materials. Here we realize a multidentate coordination environment in a metal–organic framework to stabilize discrete inorganic clusters within a porous crystalline support. We show confined growth of atomically defined nickel(II) bromide, nickel(II) chloride, cobalt(II) chloride and iron(II) chloride sheets through the peripheral coordination of six chelating bipyridine linkers. Notably, confinement within the framework defines the structure and composition of these sheets and facilitates their precise characterization by crystallography. Each metal(II) halide sheet represents a fragment excised from a single layer of the bulk solid structure, and structures obtained at different precursor loadings enable observation of successive stages of sheet assembly. Finally, the isolated sheets exhibit magnetic behaviours distinct from those of the bulk metal halides, including the isolation of ferromagnetically coupled large-spin ground states through the elimination of long-range, interlayer magnetic ordering. Overall, these results demonstrate that the pore environment of a metal–organic framework can be designed to afford precise control over the size, structure and spatial arrangement of inorganic clusters.

Several reports have demonstrated the uniform incorporation of nanoparticles or clusters in metal–organic frameworks through encapsulation of preformed particles or serendipitous self-assembly during framework synthesis[7–10]. Constraining cluster formation within framework pores has proven to be more difficult, as the absence of sufficiently stabilizing interactions in most metal–organic frameworks leads to nonselective agglomeration and unrestricted growth[7,8]. Nonetheless, frameworks bearing coordinating groups have, in a few cases, been shown to encourage site-specific nucleation of clusters or nanoparticles[11–15]. Although these methods afford some control over cluster size and distribution, correlating the properties of the resulting species to their atomic structure remains challenging.

We proposed that pre-organization of the coordinating groups in a metal–organic framework could enable the templated growth of discrete inorganic clusters. Thus, we selected the framework $Zr_6O_4(OH)_4(bpydc)_6$ (**1**) (Fig. 1a; where $bpydc^{2-}$ = 2,2′-bipyridine-5,5′-dicarboxylate), which features roughly 1.3-nm-wide octahedral cages lined with chelating sites that readily bind a variety of metal sources as isolated, mononuclear complexes, including metal(II) halides[12–14,16,17]. Notably, metallation of the bipyridine linkers of this framework induces a single-crystal-to-single-crystal transformation that results in crystallographic ordering of the metal–linker complexes[16,17], thereby enabling their structure determination by crystallography. Once metallated, six bipyridine linkers point towards the centre of each octahedral cavity, providing nucleation sites and creating a multidentate scaffold for cluster growth.

Reaction of **1** with $Ni(DME)Br_2$ (where DME = 1,2-dimethoxyethane) in bis(2-methoxyethyl) ether (diglyme) at 120 °C afforded **1**$(NiBr_2)_{9.9}$, and characterization of single crystals by X-ray diffraction at 100 K revealed the growth of isolated nickel(II) bromide sheets within the octahedral cages of the framework (Fig. 1b and Supplementary Fig. 1). Coordination of six bipyridine linkers to edge nickel sites constrains the diameter of each sheet to about 1.5 nm, with the octahedral cage distorting slightly to accommodate the sheet dimensions. At full occupancy, each cluster represents a monolayer of 19 edge-sharing nickel octahedra that closely resembles a portion of a single layer within the structure of bulk $NiBr_2$[18]. Each cluster contains four crystallographically distinct nickel(II) sites. Two of these sites correspond to twelve nickel centres that define the

[1]Department of Chemistry, University of California, Berkeley, CA, USA. [2]National Center for Electron Microscopy, Molecular Foundry, Lawrence Berkeley National Laboratory, Berkeley, CA, USA. [3]Department of Chemistry, Missouri University of Science and Technology, University of Missouri, Rolla, MO, USA. [4]Department of Chemical and Biomolecular Engineering, University of California, Berkeley, CA, USA. [5]Materials Sciences Division, Lawrence Berkeley National Laboratory, Berkeley, CA, USA. [6]These authors contributed equally: Miguel I. Gonzalez, Ari B. Turkiewicz. *e-mail: jrlong@berkeley.edu

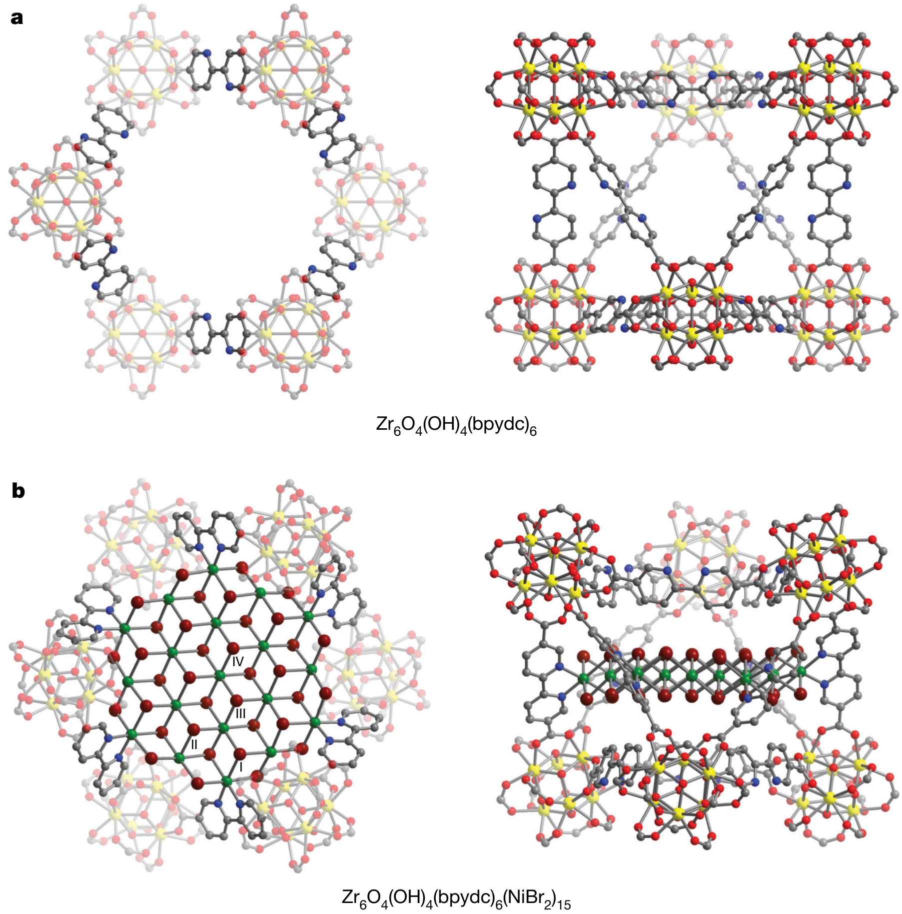

Fig. 1 | Solid-state structures. a, **b**, Portions of the structures of **1** (**a**) and **1**$(NiBr_2)_{15}$ (**b**) at 100 K as determined by single-crystal X-ray diffraction. The four crystallographically distinct Ni(II) sites in the structure of **1**$(NiBr_2)_{15}$ are labelled with Roman numerals at the upper right of each site. Yellow, green, dark red, red, blue and grey spheres represent Zr, Ni, Br, O, N and C atoms, respectively; H atoms are omitted for clarity.

sheet edges, alternating between nickel centres bound by bipyridine (site I) and sites facing the tetrahedral cages of the framework (site II). The third and fourth sites form the sheet interior, comprising six symmetry-equivalent nickel octahedra (site III) surrounding a central nickel site (site IV). Nickel site occupancies in the **1**$(NiBr_2)_{9.9}$ structure decrease from 78.4(1)% for site I and 43.2(9)% for site II at the sheet edges to 39.9(9)% for site III and 23.3(17)% for site IV at the centre (values in parentheses correspond to standard uncertainties calculated from the crystallographic refinement). Overall, these occupancies amount to 52.2(5)% of the expected loading for a $Ni_{19}Br_{38}$ cluster and suggest that complete sheets fill 23% of the framework cages and partial sheets take up 20%, and a combination of mononuclear bipyridine–$NiBr_2$ complexes and unmetallated linkers probably occupy the remaining cages. Optimizing the reaction conditions by lowering the concentration of coordinating solvent (as further discussed below) led to a higher overall Ni occupancy of 80.5(3)% in the structure of **1**$(NiBr_2)_{15}$. The average nearest Ni···Ni separation (3.723(18) Å) in this structure closely matches the separation in bulk $NiBr_2$ (3.723(10) Å), further corroborating the similarity of these sheets to those in the bulk structure[18].

Bulk $NiCl_2$ adopts the same layered structure type as $NiBr_2$, but exhibits contracted lattice dimensions as a result of having shorter nickel–halide bonds[19]. To probe whether **1** could also stabilize nickel(II) chloride sheets, the framework was treated with a solution of Ni(DME)Cl_2 in diglyme at 120 °C. The structure of the resulting framework **1**$(NiCl_2)_{13}$ at 100 K (Fig. 2a and Supplementary Fig. 2) confirmed the formation of analogous nickel(II) chloride sheets. Notably, the flexibility of the framework allows the bipyridine linkers to conform to the more compact nickel(II) chloride lattice. Consistent with its greater lattice stabilization energy[20], nickel(II) chloride affords a higher crystallographic Ni loading (69.9(4)%) compared with nickel(II) bromide under similar reaction conditions. Moreover, the nickel site occupancies were found to be 78.4(7)%, 67.1(7)%, 64.5(7)% and 68.4(16)% for sites I, II, III and IV, respectively, implying that 65% of the octahedral cages contain full sheets, whereas only 3% contain partial sheets. These results suggest that nickel(II) chloride preferentially forms complete clusters. Unlike the nickel(II) bromide structure, **1**$(NiCl_2)_{13}$ features a slightly expanded average Ni···Ni separation of 3.578(17) Å in **1**$(NiCl_2)_{13}$ compared with 3.483(6) Å in the bulk structure[19], which probably reflects a subtle interplay between the stabilization gained from forming an ideal $NiCl_2$ lattice and the strain incurred upon contraction of the bipyridine linkers of the framework around the cluster.

Encouraged by the stabilization of nickel(II) halide clusters in **1**, we pursued the extension of this chemistry to cobalt(II) chloride and iron(II) chloride; however, attempts under similar reaction conditions resulted in metallation of only the bipyridine sites. Recognizing that an equilibrium between the metal(II) halide clusters and solvated metal species governs sheet assembly, we conducted reactions under reduced concentrations of coordinating solvent to drive the equilibrium towards sheet formation. Specifically, performing the reaction of single crystals of **1** with either $CoCl_2$ or $FeCl_2$ in a 10% (v/v) solvent mixture of DME and 1,2-difluorobenzene (DFB) at 120 °C facilitates the growth of cobalt(II) and iron(II) chloride sheets in the framework to yield **1**$(CoCl_2)_{14}$ (Fig. 2b and Supplementary Fig. 3) and **1**$(FeCl_2)_{17}$ (Fig. 2c and Supplementary Fig. 4), respectively. Close inspection of the cobalt

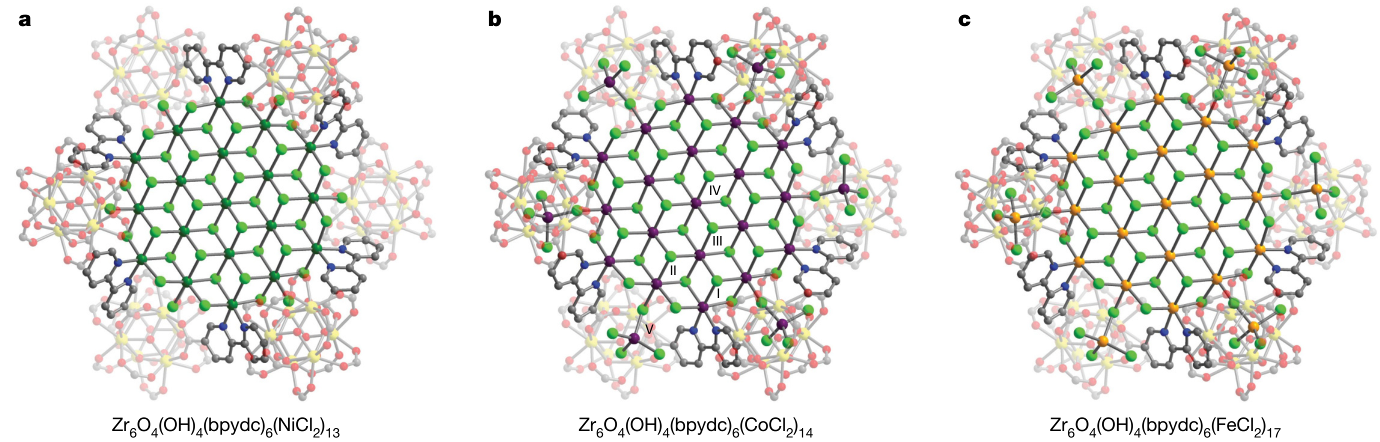

Fig. 2 | Solid-state structures. a–c, Portions of the structures of **1**$(NiCl_2)_{13}$ (**a**), **1**$(CoCl_2)_{14}$ (**b**), and **1**$(FeCl_2)_{17}$ (**c**) at 100 K as determined by single-crystal X-ray diffraction. The five crystallographically distinct metal sites in the structure of **1**$(CoCl_2)_{14}$ are labelled with Roman numerals at the upper right of each site. Yellow, green, purple, orange, light green, red, blue and grey spheres represent Zr, Ni, Co, Fe, Cl, O, N and C atoms, respectively; H atoms are omitted for clarity.

and iron structures revealed a fifth metal site (site V) in addition to the four distinct octahedral sites present in the nickel(II) halide clusters. Complexes at site V cap the edges of each sheet at site II and probably represent a mixture of $[MCl_4]^{2-}$ and $M(DME)_nCl_2$ (n = 1 or 2) complexes; however, disorder of these species precluded unambiguous assignment of their identity. Site occupancies for the four octahedral sites in the cobalt and iron clusters were found to range from 60.5(12)% to 81.4(6)% for Co and from 74.6(10)% to 88.5(5)% for Fe (Supplementary Table 1), and the tetrahedral sites were generally found to be only one-third occupied. Both structures display relatively high metal loadings (74.7(4)% for Co and 91.6(3)% for Fe relative to a $M_{19}Cl_{38}$ sheet), indicating that minimizing the amount of coordinating solvent strongly promotes sheet formation. As with the nickel(II) chloride structure, the two frameworks contain sheets with slightly longer average M···M separations between octahedral centres (Co···Co = 3.65(2) Å and Fe···Fe = 3.680(12) Å) compared to those in the bulk (Co···Co = 3.553 Å and Fe···Fe = 3.603 Å)[21].

Considering that sheet formation close to the crystal exterior may hinder further diffusion of metal(II) halide (MX_2) units into the crystal, microcrystalline samples were analysed by scanning transmission electron microscopy energy-dispersive X-ray spectroscopy (STEM-EDS) to

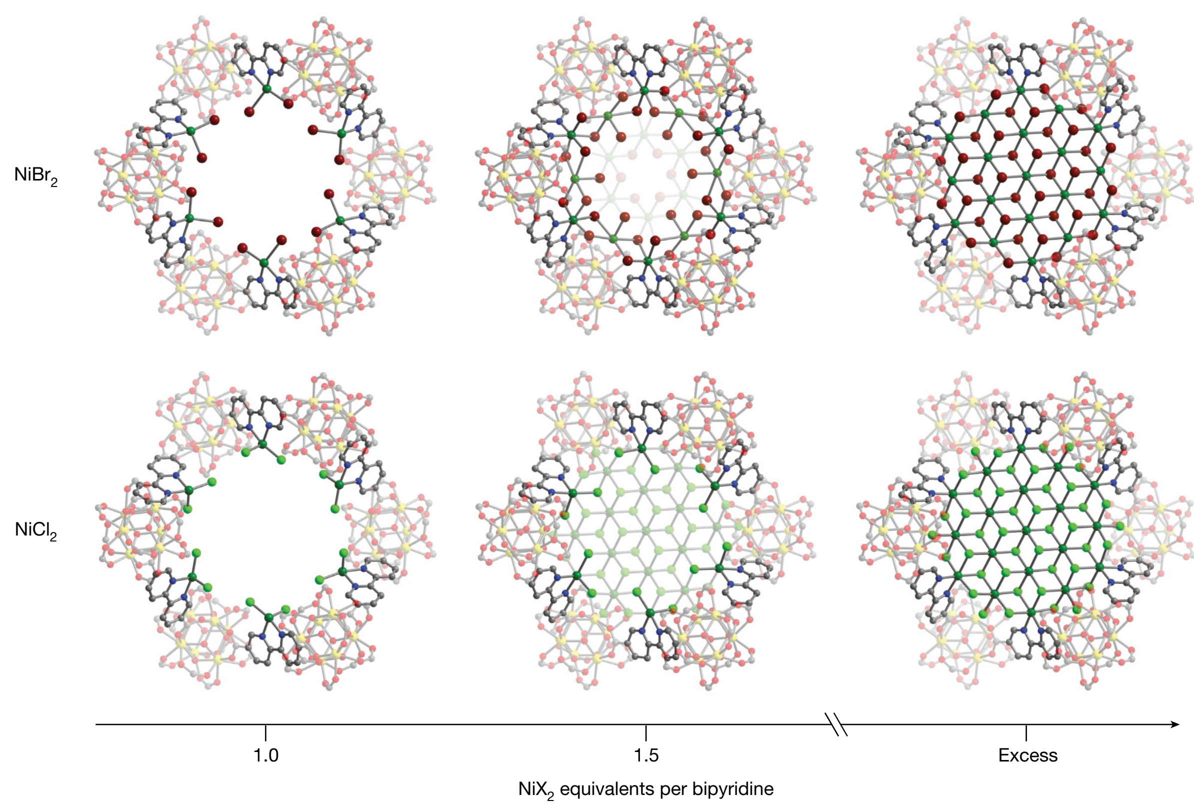

Fig. 3 | Solid-state structures monitoring the growth of nickel(II) halide sheets. Stages of nickel(II) halide cluster growth based on 100 K single-crystal structures of **1** after reaction with 1.0, 1.5 and excess equivalents of $NiBr_2$ (top row) and $NiCl_2$ (bottom row) (Supplementary Tables 1 and 2). In the structures obtained from the reactions with 1.5 equiv NiX_2, sections of the clusters are faded to illustrate their lower occupancies. Yellow, green, dark red, light green, red, blue and grey spheres represent Zr, Ni, Br, Cl, O, N and C atoms, respectively; H atoms are omitted for clarity.

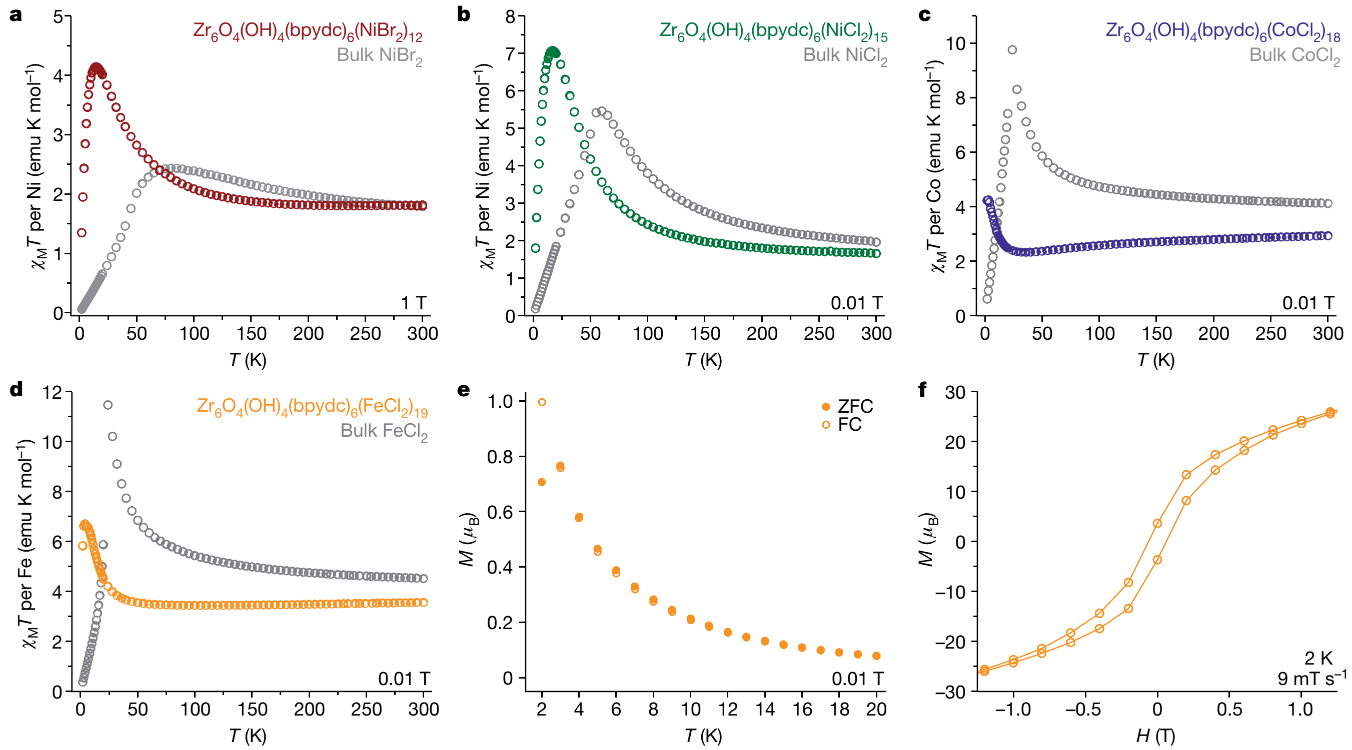

Fig. 4 | Magnetic data. a–d, d.c. magnetic susceptibility data collected for $\mathbf{1}(NiBr_2)_{12}$ (**a**, red symbols), $\mathbf{1}(NiCl_2)_{15}$ (**b**, green symbols), $\mathbf{1}(CoCl_2)_{18}$ (**c**, purple symbols), $\mathbf{1}(FeCl_2)_{19}$ (**d**, orange symbols), and their corresponding bulk metal(II) halides (grey symbols) under a 1 T or 0.01 T applied field. emu, electromagnetic unit. **e**, Zero-field-cooled (filled orange circles) and field-cooled (empty orange circles) magnetization per mole of $\mathbf{1}(FeCl_2)_{19}$ (M) versus temperature (T) data taken under a 0.01 T applied field for $\mathbf{1}(FeCl_2)_{19}$. **f**, Magnetization per mole of $\mathbf{1}(FeCl_2)_{19}$ (M) versus applied d.c. magnetic field (H) data for $\mathbf{1}(FeCl_2)_{19}$ (empty orange circles) collected at 2 K using a sweep rate of 9 mT s^{-1}. Solid lines are guides for the eye. μ_B, Bohr magneton.

obtain elemental maps and determine the extent of MX_2 penetration. These experiments reveal that the M and X spatial distributions of each variant match well with that of Zr (Extended Data Figs. 1–4), suggesting uniform dispersion of sheets throughout the crystal, rather than their accumulation at regions near the crystal surface. Importantly, these results also indicate that an equilibrium exists between the clusters and dissolved metal species under the reaction conditions, enabling migration of MX_2 species to the crystal interior and reversible sheet formation.

The formation of partially filled sheet fragments in $\mathbf{1}(NiBr_2)_{9.9}$ suggested that snapshots of sheet growth could be monitored as a function of metal halide loading, and towards this end single-crystal structures were determined at 100 K for samples of **1** treated with increasing equivalents of $NiBr_2$ or $Ni(DME)Cl_2$ relative to bipyridine (Fig. 3). Reaction with one equivalent of either metal source exclusively resulted in metallation of the bipyridine linkers[17], confirming that cluster nucleation occurs at these sites. For nickel(II) bromide, additional equivalents populate the rest of the sites, preferring edge sites over those at the interior (Extended Data Fig. 5a). This trend implies that nickel(II) bromide sheet formation initiates at the bipyridine sites, followed by a progressive inward growth towards the centre. In contrast, the remaining sites in the nickel(II) chloride sheets fill uniformly with increasing $NiCl_2$ loading (Extended Data Fig. 5b), further indicating the tendency of nickel(II) chloride to form completely filled sheets.

Because the sheets represent fragments of the corresponding metal halide monolayers, we anticipated that their magnetic behaviour might be related to that of the bulk material. In the latter, ferromagnetic coupling is dominant within monolayers, and antiferromagnetic coupling occurs between adjacent layers[21,22]. Accordingly, the product of the molar magnetic susceptibility times temperature ($\chi_M T$) for each bulk material initially increases with decreasing temperature as the spins within each monolayer align ferromagnetically. Below the Néel temperature (T_N) for each solid, a sharp decrease in $\chi_M T$ is then observed as alternating monolayers adopt opposite spin orientations to form an antiferromagnetic ground state[21,22]. Notably, the isolation of individual layer fragments within **1** presents an opportunity to eliminate the antiferromagnetic interlayer interactions and simultaneously confine the magnetic domains to the nanoscale.

To compare the magnetic properties of the framework-confined clusters to those of the bulk solids, d.c. magnetic susceptibility data were collected on microcrystalline powder samples of $\mathbf{1}(NiCl_2)_{15}$, $\mathbf{1}(NiBr_2)_{12}$, $\mathbf{1}(FeCl_2)_{19}$ and $\mathbf{1}(CoCl_2)_{18}$ between 300 and 2 K under applied fields of 0.01, 0.1 and 1 T. For each framework, the per-metal susceptibilities measured at room temperature are slightly lower than those observed in the corresponding bulk material, with the exception of $\mathbf{1}(NiBr_2)_{12}$, which exhibits a large temperature-independent paramagnetic contribution (Fig. 4a–d). In the case of $\mathbf{1}(FeCl_2)_{19}$ and $\mathbf{1}(CoCl_2)_{18}$, it is likely that the tetrahedral metal sites contribute a lower magnetic moment than do the octahedral sites, thereby suppressing the per-metal susceptibility. Analogous to the bulk metal halides, $\chi_M T$ increases for all cluster-containing materials upon cooling below 300 K, indicative of ferromagnetic coupling of individual spins within each sheet fragment to form a total spin S. Notably, $\chi_M T$ continues to increase well below the Néel temperature for each corresponding bulk material, consistent with the behaviour expected for isolated monolayers. A steep decrease in $\chi_M T$ is eventually observed below 10 K for all confined sheets, which we attribute primarily to Zeeman splitting of the high-spin ground state, and, in the case of $\mathbf{1}(FeCl_2)_{19}$, to magnetic blocking (as discussed below).

To characterize further the static magnetic behaviour of the framework-confined sheets, we collected zero-field-cooled (ZFC) and field-cooled (FC) magnetization data for temperatures ranging from 2 to 300 K. Whereas these data are completely superimposable for the cobalt(II) and nickel(II) materials and are indicative of simple paramagnetism at low temperatures, a divergence is observed for $\mathbf{1}(FeCl_2)_{19}$ at around 3 K (Fig. 4e), suggesting the immobilization of the total spin

S along a magnetic easy direction and the onset of superparamagnetism. In support of this observation, variable-field magnetization data collected for **1**$(FeCl_2)_{19}$ with a sweep rate of 9 mT s^{-1} revealed magnetic hysteresis at 2 K with a coercive field of H_c = 70 mT (Fig. 4f).

To determine the magnitude of the barrier to spin reversal for the confined sheets in **1**$(FeCl_2)_{19}$, we collected temperature-dependent a.c. magnetic susceptibility data under zero d.c. field and at discrete frequency values ranging from 1 to 1,000 Hz (Extended Data Fig. 6). A maximum was observed in both the in-phase (χ') and out-of-phase (χ'') magnetic susceptibility data, with the peak shifting only 1.3 K over the measured frequency range. The frequency dependence in χ'' precludes the existence of long-range magnetic ordering, and this low-temperature behaviour can instead be attributed to either superparamagnetism or a glassy magnetic phase transition. The magnitude of the frequency shift can be quantified using the Mydosh parameter (γ), which adopts characteristic values for different magnetic behaviours[23]. We find a Mydosh parameter of 0.14 for the $FeCl_2$ clusters, which is most consistent with superparamagnetism. An Arrhenius fitting of the a.c. susceptibility data affords physically meaningful values for the spin reversal barrier of U_{eff} = 16 cm^{-1} and a relaxation attempt time of $\tau_0 = 10^{-10}$ s. Notably, these values are competitive with iron(II) cluster-based single-molecule magnets[24].

As an additional probe of the magnetic behaviour of **1**$(FeCl_2)_{19}$, Mössbauer spectra were collected on a microcrystalline sample at temperatures ranging from 5 to 295 K (Extended Data Fig. 7 and Supplementary Fig. 24). At all temperatures, the spectra exhibit iron(II) quadrupole doublets, consistent with the crystallographic environments in **1**$(FeCl_2)_{17}$ (Supplementary Fig. 25 and Supplementary Tables 4 and 5), and the spectral fits between 10 and 295 K indicate that **1**$(FeCl_2)_{19}$ behaves as a paramagnet at these temperatures. Upon cooling from 8 to 5 K, a substantial broadening is observed concomitant with the gradual appearance of a superparamagnetic sextet with an average iron(II) hyperfine field of 9.8(2) T. In conjunction with the a.c. magnetic susceptibility data, these results support the observation that the framework-confined iron(II) chloride sheet fragments exhibit superparamagnetism below 8 K.

As research into the electronic and magnetic properties of two-dimensional materials intensifies[25,26], increased attention is being paid towards lateral confinement of monolayers to yield two-dimensional clusters or quantum dots[27,28]. Analogous to the confinement of three-dimensional materials, confinement of two-dimensional materials is anticipated to reveal distinct or enhanced physical and chemical properties, including those associated with edge states[29,30]. Understanding and exploiting the structural influences on the properties of these two-dimensional clusters will therefore require chemical syntheses that yield monodisperse and well defined materials.

Online content

Any methods, additional references, Nature Research reporting summaries, source data, extended data, supplementary information, acknowledgements, peer review information; details of author contributions and competing interests; and statements of data and code availability are available at https://doi.org/10.1038/s41586-019-1776-0.

1. Bawendi, M. G., Steigerwald, M. L. & Brus, L. E. The quantum mechanics of larger semiconductor clusters ("quantum dots"). *Annu. Rev. Phys. Chem*. **41**, 477–496 (1990).
2. Billas, I. M., Châtelain, A. & de Heer, W. A. Magnetism from the atom to the bulk in iron, cobalt, and nickel clusters. *Science* **265**, 1682–1684 (1994).
3. Lee, S. C. & Holm, R. H. Nonmolecular metal chalcogenide/halide solids and their molecular cluster analogues. *Angew. Chem*. **29**, 840–856 (1990).
4. Gatteschi, D., Caneschi, A., Pardi, L. & Sessoli, R. Large clusters of metal ions: the transition from molecular to bulk magnets. *Science* **265**, 1054–1058 (1994).
5. Xia, Y., Xiong, Y., Lim, B. & Skrabalak, S. E. Shape-controlled synthesis of metal nanocrystals: Simple chemistry meets complex physics? *Angew. Chem*. **48**, 60–103 (2009).
6. Papatriantafyllopoulou, C., Moushi, E. E., Christou, G. & Tasiopoulos, A. J. Filling the gap between the quantum and classical worlds of nanoscale magnetism: giant molecular aggregates based on paramagnetic 3d metal ions. *Chem. Soc. Rev*. **45**, 1597–1628 (2016).
7. Kim, C. R., Uemura, T. & Kitagawa, S. Inorganic nanoparticles in porous coordination polymers. *Chem. Soc. Rev*. **45**, 3828–3845 (2016).
8. Meilikhov, M. et al. Metals@MOFs – Loading MOFs with metal nanoparticles for hybrid functions. *Eur. J. Inorg. Chem*. **2010**, 3701–3714 (2010).
9. Lin, H. et al. Bulk assembly of organic metal halide nanotubes. *Chem. Sci*. **8**, 8400–8404 (2017).
10. Chen, K.-J., Perry, J. J., Scott, H. S., Yang, Q.-Y. & Zaworotko, M. J. Double-walled pyr topology networks from a novel fluoride-bridged heptanuclear metal cluster. *Chem. Sci*. **6**, 4784–4789 (2015).
11. Gallington, L. C. et al. Regioselective atomic layer deposition in metal–organic frameworks directed by dispersion interactions. *J. Am. Chem. Soc*. **138**, 13513–13516 (2016).
12. Braglia, L. et al. Tuning Pt and Cu sites population inside functionalized UiO-67 MOF by controlling activation conditions. *Faraday Discuss*. **201**, 265–286 (2017).
13. An, B. et al. Confinement of ultrasmall Cu/ZnO_x nanoparticles in metal-organic frameworks for selective methanol synthesis from catalytic hydrogenation of CO_2. *J. Am. Chem. Soc*. **139**, 3834–3840 (2017).
14. Chen, L., Chen, H., Luque, R. & Li, Y. Metal–organic framework encapsulated Pd nanoparticles: towards advanced heterogeneous catalysts. *Chem. Sci*. **5**, 3708–3714 (2014).
15. Wang, X.-N. et al. Crystallographic visualization of postsynthetic nickel clusters into metal–organic framework. *J. Am. Chem. Soc*. **141**, 13654–13663 (2019).
16. Gonzalez, M. I., Bloch, E. D., Mason, J. A., Teat, S. J. & Long, J. R. Single-crystal-to-single-crystal metalation of a metal-organic framework: a route toward structurally well-defined catalysts. *Inorg. Chem*. **54**, 2995–3005 (2015).
17. Gonzalez, M. I., Oktawiec, J. & Long, J. R. Ethylene oligomerization in metal-organic frameworks bearing nickel(II) 2,2′-bipyridine complexes. *Faraday Discuss*. **201**, 351–367 (2017).
18. Ketelaar, J. A. A. Die Kristallstruktur des Nickelbromids und -jodids. *Z. Kristallogr. Cryst. Mater*. **88**, 26–34 (1934).
19. Ferrari, A., Braibanti, A. & Bigliardi, G. Refinement of the crystal structure of $NiCl_2$ and of unit-cell parameters of some anhydrous chlorides of divalent metals. *Acta Crystallogr*. **16**, 846–847 (1963).
20. George, P. & McClure, D. S. The effect of inner orbital splitting on the thermodynamic properties of transition metal compounds and coordination complexes. In *Progress in Inorganic Chemistry* Vol. 1 (ed. Cotton, F. A.) 381–463 (Interscience, 1959).
21. Wilkinson, M. K., Cable, J. W., Wollan, E. O. & Koehler, W. C. Neutron diffraction investigations of the magnetic ordering in $FeBr_2$, $CoBr_2$, $FeCl_2$, and $CoCl_2$. *Phys. Rev*. **113**, 497–507 (1959).
22. Tsubokawa, I. The magnetic properties of $NiBr_2$. *J. Phys. Soc. Jpn*. **15**, 2109 (1960).
23. Mydosh, J. A. *Spin Glasses* (Taylor & Francis, 1993).
24. Milios, C. J. & Winpenny, R. E. P. in *Molecular Nanomagnets and Related Phenomena* (ed. Gao, S.) 1–109 (Springer, 2014).
25. Huang, B. et al. Layer-dependent ferromagnetism in a van der Waals crystal down to the monolayer limit. *Nature* **546**, 270–273 (2017).
26. Gong, C. et al. Discovery of intrinsic ferromagnetism in two-dimensional van der Waals crystals. *Nature* **546**, 265–269 (2017).
27. Wang, Y. et al. Cryo-mediated exfoliation and fracturing of layered materials into 2D quantum dots. *Sci. Adv*. **3**, e1701500 (2017).
28. Lin, L. et al. Fabrication of luminescent monolayered tungsten dichalcogenides quantum dots with giant spin-valley coupling. *ACS Nano* **7**, 8214–8223 (2013).
29. Ritter, K. A. & Lyding, J. W. The influence of edge structure on the electronic properties of graphene quantum dots and nanoribbons. *Nat. Mater*. **8**, 235–242 (2009).
30. Wilcoxon, J. P. & Samara, G. A. Strong quantum-size effects in a layered semiconductor: MoS_2 nanoclusters. *Phys. Rev. B* **51**, 7299–7302 (1995).

Methods

General methods and materials

All manipulations were performed under a N_2 atmosphere in a Vacuum Atmospheres glovebox or under a N_2 or Ar atmosphere using standard Schlenk techniques. The solvent 1,2-difluorobenzene (DFB) was deoxygenated by purging with argon for 1 h and dried using a commercial solvent purification system designed by JC Meyer Solvent Systems. The solvents 1,2-dimethoxyethane (DME) and bis(2-methoxyethyl) ether (diglyme) were purchased from Sigma-Aldrich, dried over Na/benzophenone (DME) or 4 Å molecular sieves (diglyme), and degassed via three successive freeze-pump-thaw cycles. The compound 2,2′-bipyridine-5,5′-dicarboxylic acid (H_2bpydc) was synthesized using a previously published procedure[31]. The compounds $ZrCl_4$, Ni(DME)Br_2, Ni(DME)Cl_2, $NiBr_2$, $CoCl_2$ and $FeCl_2$ were purchased from commercial vendors (Sigma-Aldrich for $ZrCl_4$, Ni(DME)Br_2 and Ni(DME)Cl_2; Strem for $NiBr_2$, $CoCl_2$ and $FeCl_2$) and used as received. All other chemicals were purchased from commercial vendors and used as received unless otherwise noted. Inductively coupled plasma optical emission spectrometry (ICP-OES) analysis was performed on a Perkin Elmer Optima 7000 DV instrument at the University of California, Berkeley, microanalytical facility. UV-Vis diffuse reflectance spectra were collected using a CARY 5000 spectrophotometer interfaced with Varian Win UV software. The samples were contained in a Praying Mantis air-free diffuse reflectance cell and dispersed in non-absorbing $BaSO_4$ matrix. The Kubelka–Munk conversion ($F(R)$ versus wavenumber) of the raw diffuse reflectance spectrum (R versus wavenumber) was obtained by applying the formula $F(R) = (1 - R)^2/2R$.

Synthesis of $Zr_6O_4(OH)_4(bpydc)_6$ (1)

This material was synthesized as a microcrystalline powder using a previously published procedure[17]. Typically, a 2 l round bottom flask equipped with a Schlenk adaptor, glass stoppers and a magnetic stir bar was charged with H_2bpydc (6.11 g, 25.0 mmol), benzoic acid (224 g, 2.00 mol), and *N*,*N*-dimethylformamide (DMF; 1.00 l) from a newly opened bottle. The resulting mixture was purged with dry Ar for 30 min. Solid $ZrCl_4$ (5.83 g, 25.0 mmol) was then added, after which the mixture was purged with dry Ar for an additional 30 min. Deionized water (820 µl, 45.5 mmol) was added and the mixture was heated with magnetic stirring for 5 days at 120 °C under a N_2 atmosphere. After allowing the mixture to cool to room temperature, the solvent was decanted and the resulting white microcrystalline powder was washed by soaking three times in 1 l aliquots of fresh DMF for 24 h at 120 °C, followed by solvent exchange with tetrahydrofuran (THF) via Soxhlet extraction for 3 days. The THF-solvated powder was filtered under dry Ar, followed by heating at 120 °C under dynamic vacuum for 24 h to give fully desolvated **1**. The powder X-ray diffraction pattern and Langmuir surface area (2,700 $m^2\ g^{-1}$; N_2, 77 K) of the material were found to be consistent with those reported in the literature[17].

Single crystals of **1** were synthesized following a previously reported procedure[16] and characterized by single-crystal X-ray diffraction.

Note that refinement of the linker occupancies in the single-crystal and powder X-ray diffraction structures resulted in occupancies that range from 76.8% to 100%, consistent with previous reports of missing linker defects in $Zr_6O_4(OH)_4(bpydc)_6$[16] and other zirconium metal–organic frameworks[32].

General procedure for loading 1 with NiX_2 in diglyme

$X^- = Cl^-, Br^-$. Single crystals of **1** (<0.1 mg) suspended in diglyme were transferred into a 4 ml PTFE-capped vial. Most of the solvent was decanted, followed by addition of excess metal source (Ni(DME)Cl_2, Ni(DME)Br_2, or $NiBr_2$; 5–10 mg; >50 equiv) and diglyme (3 ml). The mixture was allowed to react for 1 month at 120 °C, resulting in a colour change of the crystals to pale yellow. The crystals were then characterized by single-crystal X-ray diffraction.

Stoichiometric reactions were performed on microcrystalline powder samples of **1** in the presence of single crystals that were later characterized by crystallography. Single crystals of **1** (<0.1 mg) suspended in diglyme were transferred into a 4 ml PTFE-capped vial. Most of the solvent was decanted, followed by addition of microcrystalline **1** (60 mg), metal source (1.0–3.25 equiv Ni(DME)Cl_2, Ni(DME)Br_2, or $NiBr_2$ per bpydc^{2-} in microcrystalline **1**) and diglyme. The mixture was allowed to react for 1 month at 120 °C, resulting in a colour change of both the crystals and the powder to pale yellow. Most of the solution was removed by pipette and the crystals were subsequently soaked three times in 3 ml of fresh DME at room temperature (~32 °C) for 24 h. In cases where unreacted metal halide solids were observed, these were removed by carefully transferring a slurry of the framework into a new vial before each wash. A slurry containing most of the microcrystalline powder was separated from the crystals and pipetted into a new vial, after which the solvent was removed under reduced pressure at 80 °C to give a microcrystalline powder sample of the NiX_2-loaded framework. The remaining single crystals were then used for single-crystal X-ray diffraction experiments.

General procedure for loading 1 with MX_2 in 10% (v/v) DME in DFB

$MX_2 = FeCl_2$, $CoCl_2$ and $NiBr_2$. Single crystals of **1** (<0.1 mg) suspended in diglyme were transferred into a thick-walled borosilicate tube. Most of the solvent was decanted, followed by addition of excess metal source ($FeCl_2$, $CoCl_2$ or Ni(DME)Br_2; 5–10 mg; >50 equiv), DME (0.30 ml) and DFB (2.70 ml). The reaction mixture was degassed by three freeze–pump–thaw cycles, after which the tube was flame-sealed and then placed in an oven preheated to 120 °C. The mixture was allowed to react for 1 month at this temperature, resulting in a colour change of the crystals (purple for $FeCl_2$, blue for $CoCl_2$, and pale yellow for Ni(DME)Br_2). The crystals were then characterized by single-crystal X-ray diffraction.

Stoichiometric reactions were performed on microcrystalline powder samples of **1** in the presence of single crystals that were later characterized by crystallography. Single crystals of **1** (<0.1 mg) suspended in diglyme were transferred into a thick-walled borosilicate tube. Most of the solvent was decanted, followed by addition of microcrystalline **1** (60 mg), metal source (3.25 equiv $FeCl_2$, $CoCl_2$, or Ni(DME)Br_2), DME (0.30 ml), and DFB (2.70 ml). The reaction mixture was degassed by three freeze–pump–thaw cycles, after which the tube was flame-sealed and then placed in an oven preheated to 120 °C. The mixture was allowed to react for 1 month at this temperature, resulting in a colour change of both the crystals and the powder (purple for $FeCl_2$, blue for $CoCl_2$, and pale yellow for Ni(DME)Br_2). Most of the solution was removed by pipette and the crystals were subsequently soaked three times in 3 ml of fresh DME at room temperature (~32 °C) for 24 h. In cases where unreacted metal halide solids were observed, these were removed by carefully transferring a slurry of the framework into a new vial before each wash. A slurry containing most of the microcrystalline powder was separated from the crystals and pipetted into a new vial, after which the solvent was removed under reduced pressure at 80 °C to give a microcrystalline powder sample of the MX_2-loaded framework. The remaining single crystals were then used for single-crystal X-ray diffraction experiments.

Single-crystal X-ray diffraction

X-ray diffraction analysis was performed on single crystals coated with Paratone-N oil and mounted on a MiTeGen loops. The crystals were frozen at 100 K by an Oxford Cryosystems Cryostream 700 Plus. Data were collected at beamline 11.3.1 at the Advanced Light Source at Lawrence Berkeley National Laboratory using synchrotron radiation ($\lambda = 0.8856$ and 0.9537 Å) on a Bruker D8 diffractometer equipped with either a Bruker PHOTON100 CMOS detector or a Bruker PHOTON II CMOS detector. Raw data were integrated and corrected for Lorentz

and polarization effects using Bruker AXS SAINT software[33]. Absorption corrections were applied using SADABS[34]. Initial evaluation of the diffraction data suggested that $Zr_6O_4(OH)_4(bpydc)_6$ undergoes a change of space group from $Fm\bar{3}m$ to $P2_13$ (no. 225 and 198, respectively) upon loading with $NiBr_2$, $NiCl_2$, $CoCl_2$, or $FeCl_2$. Based on previous work[16], attempts to solve and refine these structures in $P2_13$ resulted in unsatisfactory refinement, thus solution and refinement in the space group $Pa\bar{3}$ (no. 205) was instead attempted. In the end, the latter space group gave the most satisfactory refinement. The structure was solved using direct methods with SHELXS[35,36] and refined using SHELXL[37] operated in the OLEX2[38] interface. No significant crystal decay was observed during data collection. Thermal parameters were refined anisotropically for all non-hydrogen atoms. Hydrogen atoms were placed in ideal positions and refined using a riding model for all structures. Moving from $Fm\bar{3}m$ to $Pa\bar{3}$ results in two twin domains related by the lost mirror symmetry along the body diagonals of the unit cell. Consequently, a twin law (TWIN 0 1 0 1 0 0 0 0 −1 2; BASF ≈ 0.50) was required for the structural refinement.

The metal–organic framework $Zr_6O_4(OH)_4(bpydc)_6$ is derived from $Zr_6O_4(OH)_4(bdc)_6$ or UiO-66, which has been known to have structural defects where some of the linkers are absent[39]. Therefore, the linker occupancies in all structures were allowed to refine freely, resulting in occupancies that range from 76.8% to 100%. When the ligand is not present, water/hydroxide is known to replace it in the cluster[32]. These, however, could not be modelled in the structure due to their disorder and low occupancy. The oxygen atoms of the oxo and hydroxo groups on the zirconium clusters in the structure were disordered and, in cases where this disorder could be modelled, the site occupancy factors of these oxygen atoms were fixed to give a chemical occupancy of 50%. Hydrogen atoms on the hydroxo groups could neither be found nor placed and were omitted from the refinement but not from the formula. Disorder of the linkers and the metal halides in some of the structures required the use of geometric and displacement parameter restraints. Voids in the structures that result from disordered solvent that could not be modelled, large anisotropic displacement parameters that result from linker and solvent disorder, and, in some cases, low data resolution gave rise to several A and B level alerts from checkCIF. Responses addressing these alerts have been included in the crystallographic information files (CIFs) and can be read in reports generated by checkCIF. Extensive solvent disorder was found in the pores for most of the structures and could not be modelled. Consequently, the unassigned electron density in these structures was accounted for using SQUEEZE[40] as implemented in the PLATON[41] interface.

Powder X-ray diffraction

Powder X-ray diffraction patterns were collected on microcrystalline powder samples of **1**$(FeCl_2)_{19}$, **1**$(CoCl_2)_{18}$, **1**$(NiCl_2)_{15}$ and **1**$(NiBr_2)_{15}$, which were loaded into 1.0 mm boron-rich glass capillaries inside a N_2-filled glovebox and then flame-sealed. High-resolution synchrotron X-ray powder diffraction data were subsequently collected at 298 K with a wavelength of 0.45220 Å at beamline 17-BM-B at the Advanced Photon Source at Argonne National Laboratory. For all samples, a standard peak search, followed by indexing through the Single Value Decomposition approach[42], as implemented in TOPAS-Academic[43], allowed the determination of approximate unit cell parameters. Analysis of the patterns of all samples led to the assignment of the space group $Pa\bar{3}$ on the basis of systematic absences. The unit cells and space group were verified by structureless Pawley refinements. In **1**$(NiCl_2)_{15}$ and **1**$(NiBr_2)_{15}$ it was observed that there was broadening of the *hkl* reflections arising from the lowering of symmetry to $Pa\bar{3}$ from $Fm\bar{3}m$. Specifically, it was noted that the reflections corresponding to a mixture of even and odd *hkl* values were broadened, such as the (0 2 1) and (2 1 1) reflections at 2.2° and 2.4°. In the Pawley refinements, this broadening could be modelled by defining one Lorentzian function for the peaks corresponding to the $Fm\bar{3}m$ space group (all odd or all even *hkl* values) and another Lorentzian convolution for the broadened peaks. Doing so led to an excellent fit, and the parameters for the peak shapes were implemented in later Rietveld refinements using the data of **1**$(NiCl_2)_{15}$ and **1**$(NiBr_2)_{15}$, leading to improvements of ~8% and 4% in the weighted profile R-factor (R_{wp}), respectively, when compared to refinements performed without the broadening correction.

Subsequently, Rietveld refinements of all samples were attempted, using the structural models determined by single-crystal X-ray diffraction as starting points. The atomic positions were initially not refined. Occupancies of the metallated species (for example, Fe, Co, Ni, Cl and Br) were allowed to vary relative to the full occupancy of Zr. These atoms were also given isotropic atomic displacement parameters that were individually refined. A separate occupancy factor and an isotropic atomic displacement parameter were given to all atoms of the bipyridine ligand, consistent with practices done for the single-crystal structural model refinements. Finally, the cluster oxygen atoms were given separate atomic displacement parameters and their occupancies were refined relative to the Zr occupancy.

In the case of samples **1**$(FeCl_2)_{19}$ and **1**$(CoCl_2)_{18}$, it was found that when a Fourier difference map was generated from the single-crystal model relative to the observed pattern, disordered electron density near the extraneous Fe or Co species on the periphery of the sheet could be observed. This disorder is postulated to arise from the presence of a mixture of metal halide species and DME-solvated metal halide species being present in the material, and was modelled in the single-crystal model by reducing the occupancy of the chloride ligands of the peripheral species in order to accommodate partial oxygen occupancy. An improved fit in both iron and cobalt cases was obtained when a DME molecule was modelled as a rigid body and allowed to relax using a simulated annealing approach, while keeping the rest of the structural model constant. In both cases, a DME molecule could be found localized near the peripheral metal species, with one of the oxygen atoms of the DME molecule in bonding distance to the metal (~2.0 Å) and close to a chloride position, consistent with the differences in typical bond lengths between these ligands. Although disorder probably contributes to the high relative occupancies, the location is consistent with unresolved electron density observed in the single-crystal models.

In the course of all refinements, the atom positions could not be refined freely, as they resulted in chemically unreasonable positions for numerous components of the structural model (particularly the bipyridine linker). As a result, in the final stages of the refinement, soft constraints were placed on the atomic positions (with the exception of those for H, which were not refined). The thermal parameters, sample and instrument parameters were then fit together with the background parameters. The resulting calculated diffraction pattern for the final structural models of **1**$(FeCl_2)_{19}$, **1**$(CoCl_2)_{18}$, **1**$(NiCl_2)_{15}$ and **1**$(NiBr_2)_{15}$ are in excellent agreement with the experimental diffraction patterns (Rietveld plots shown in Supplementary Figs. 5–8 and further crystallographic details given in Supplementary Tables 10 and 11).

Finally, the refined occupancies of the metal(II) halide sheet atoms (Fe, Co, Ni, Cl, and Br) are within one standard error of the values obtained by single-crystal X-ray diffraction of closely related samples, confirming that the structural models used are reasonable and applicable to the bulk samples.

Low-pressure gas adsorption measurements

Gas adsorption isotherms for pressures in the range 0–1.2 bar were measured by a volumetric method using a Micromeritics ASAP2420 instrument. A typical sample, consisting of ~100 mg of material was transferred to a pre-weighed analysis tube, which was capped with a Micromeritics TranSeal and evacuated by heating at 120 °C for **1** or 80 °C for all samples loaded with metal(II) halides at a ramp rate of 1 °C per min under dynamic vacuum until an outgas rate of less than 3 μbar min^{-1} was achieved. The evacuated analysis tube containing the degassed sample was then carefully transferred to an electronic balance

and weighed again to determine the mass of sample. The tube was then transferred back to the analysis port of the gas adsorption instrument. The outgas rate was again confirmed to be less than 3 μbar min^{-1}. For all isotherms, warm and cold free space correction measurements were performed using ultra-high purity He gas (UHP, 99.999% purity); N_2 isotherms at 77 K were measured in liquid N_2 baths using UHP-grade gas sources. Oil-free vacuum pumps and oil-free pressure regulators were used for all measurements to prevent contamination of the samples during the evacuation process or of the feed gases during the isotherm measurements. Langmuir and Brunauer–Emmet–Teller (BET) surface areas were determined from N_2 adsorption data at 77 K.

Magnetic measurements

Samples were prepared by adding crystalline powder compound to a 5 mm I.D. (7 mm O.D.) quartz tube containing a raised quartz platform. Solid eicosane was added to cover the sample to prevent crystallite torqueing and provide good thermal contact between the sample and the cryostat. The tubes were fitted with Teflon sealable adapters, evacuated on a Schlenk line, and flame-sealed under static vacuum. Following flame sealing, the solid eicosane was melted in a water bath held at 40 °C. Magnetic susceptibility measurements were performed using a Quantum Design MPMS2-XL SQUID magnetometer. d.c. magnetic susceptibility measurements were collected in the temperature range 2–300 K under applied magnetic fields of 0.01 T, 0.1 T and 1 T. Magnetic hysteresis measurements were performed at a sweep rate of 9 mT s^{-1}. Diamagnetic corrections were applied to the data using Pascal's constant to give $\chi_D = -0.00177772$ emu/mol ($\mathbf{1}(NiCl_2)_{15}$), $\chi_D = -0.00207772$ emu/mol ($\mathbf{1}(NiBr_2)_{12}$), $\chi_D = -0.00205272$ emu/mol ($\mathbf{1}(FeCl_2)_{19}$), $\chi_D = -0.00196972$ emu/mol ($\mathbf{1}(CoCl_2)_{18}$), and $\chi_D = -0.00024306$ emu/mol (eicosane).

The Mydosh parameter was calculated by extracting the slope of the T_f vs $\log(\nu)$ plot, normalized against $T_f(0)$. The freezing temperature, T_f, is defined as the peak maximum in χ' at each frequency. The freezing temperature $T_f(0)$ is calculated by extrapolating the peak in χ' to $\log(\nu) = 0$ (ref. [23]).

Electron microscopy

Transmission electron microscopy (TEM) was performed on an FEI Titan 80–300 kV microscope operating at 300 kV at the National Center for Electron Microscopy. Annular dark field scanning TEM images and energy dispersive X-ray spectroscopy (EDS) maps were acquired using a beam current of 100–300 pA at room temperature. The four EDS silicon drift detectors had a collection solid angle of ~0.7 sr. Images were acquired before and after the EDS map to confirm that the sample did not damage visibly due to the electron beam.

Scanning electron microscopy (SEM) was performed on an FEI Quanta Dual Beam FIB 0.5–30 kV microscope operating at 20 kV at the Biomolecular Nanotechnology Center at UC Berkeley. Energy-dispersive X-ray spectroscopy (EDS) maps were obtained at room temperature using an Oxford EDS detector attached to the SEM.

Mössbauer spectral measurements

The Mössbauer spectra of $\mathbf{1}(FeCl_2)_{19}$ were obtained between 5 and 295 K with a SEE Mössbauer spectrometer equipped with a Co-57 in Rh source. The isomer shifts are given relative to α-iron at 295 K. The spectral absorbers were prepared in an N_2 atmosphere glove box by packing the powder sample into a 2.54 cm diameter polypropylene washer that was sealed with three layers of packing tape. The samples where then transferred to the spectrometer, where the absorber was maintained in a He atmosphere in order to prevent oxidation or decomposition.

General procedure for metal content analysis via ICP-OES

Roughly 10 mg of activated material was placed in a 20 ml plastic vial and digested with 10 μl of concentrated HF in 2 ml of dimethylsulfoxide and diluted with 18 ml of 5% HNO_3 in Millipore water. The resulting solution was transferred to a 100 ml volumetric flask and diluted to mark with 5% (v/v) aqueous HNO_3 in Millipore water to give a stock solution that contained roughly 25 ppm Zr from the sample. The stock sample solution (10.0 ml) and 2.50 ppm Y (1.00 ml) were added to a 25.0 ml volumetric flask and diluted to mark with 5% (v/v) aqueous HNO_3 to give sample solution that is ~10 ppm Zr with 0.100 ppm Y as an internal standard. Standard solutions with 0.100, 1.00, 5.00, 10.0 and 15.0 ppm Zr, Ni, Fe and Co with 0.100 ppm Y as an internal standard were prepared for the calibration curve.

Data availability

Additional crystallographic information, powder X-ray diffraction data, scanning electron microscopy and energy-dispersive X-ray spectroscopy data, gas-sorption data, magnetic data, Mössbauer spectroscopy data, diffuse reflectance UV–Vis spectra, and elemental analyses are available in the Supplementary Information. Metrical data for the solid-state structures are available from the Cambridge Crystallographic Data Centre under reference numbers CCDC 1901128 to 1901144.

31. Rama, G. et al. Stereoselective formation of chiral metallopeptides. *Chemistry* **18**, 7030–7035 (2012).
32. Trickett, C. A. et al. Definitive molecular level characterization of defects in UiO-66 crystals. *Angew. Chem.* **54**, 11162–11167 (2015).
33. Bruker Analytical X-ray Systems. *SAINT and APEX 2 Software for CCD Diffractometers* (2000).
34. Sheldrick, G. M. *SADABS* (Bruker Analytical X-ray Systems, 2014).
35. Sheldrick, G. M. *SHELXS* (Univ. Göttingen, 2014).
36. Sheldrick, G. M. A short history of SHELX. *Acta Crystallogr. A* **64**, 112–122 (2008).
37. Sheldrick, G. M. *SHELXL* (Univ. Göttingen, 2014).
38. Dolomanov, O. V., Bourhis, L. J., Gildea, R. J., Howard, J. A. K. & Puschmann, H. OLEX2: a complete structure solution, refinement and analysis program. *J. Appl. Cryst.* **42**, 339–341 (2009).
39. Shearer, G. C. et al. Tuned to perfection: ironing out the defects in metal–organic framework UiO-66. *Chem. Mater.* **26**, 4068–4071 (2014).
40. Spek, A. L. PLATON SQUEEZE: a tool for the calculation of the disordered solvent contribution to the calculated structure factors. *Acta Crystallogr. C* **71**, 9–18 (2015).
41. Spek, A. L. Single-crystal structure validation with the program PLATON. *J. Appl. Cryst.* **36**, 7–13 (2003).
42. Coelho, A. A. Indexing of powder diffraction patterns by iterative use of singular value decomposition. *J. Appl. Cryst.* **36**, 86–95 (2003).
43. Coelho, A. A. *TOPAS-Academic* v.4.1 (Coelho Software, 2007).

Acknowledgements This research was supported through a Multidisciplinary University Research Initiatives Program funded by the US Department of Defense, Office of Naval Research under award N00014-15-1-2681. Single-crystal X-ray diffraction experiments were performed at beamline 11.3.1 at the Advanced Light Source at Lawrence Berkeley National Laboratory. The Advanced Light Source is supported by the Director, Office of Science, Office of Basic Energy Sciences, of the US Department of Energy under contract no. DE-AC02-05CH11231. Powder X-ray diffraction data were collected at beamline 17-BM-B at the Advanced Photon Source, a US Department of Energy, Office of Science User Facility operated by the DOE Office of Science by Argonne National Laboratory under contract no. DE-AC02-06CH11357. Work at the Molecular Foundry was supported by the Office of Science, Office of Basic Energy Sciences, of the US Department of Energy under contract no. DE-AC02-05CH11231. We thank the US National Science Foundation for providing graduate fellowship support for A.B.T, L.E.D. and J.O. In addition, we thank S. J. Teat, K. Chakarawet, M. Jackson and N. Masciocchi for experimental assistance and helpful discussions. We also thank K. R. Meihaus for editorial assistance.

Author contributions M.I.G., A.B.T. and J.R.L. formulated the project. M.I.G. and A.B.T. synthesized the compounds. M.I.G. collected and analysed the single-crystal X-ray diffraction data, with the assistance of A.B.T. J.O. collected and analysed the powder X-ray diffraction data. A.B.T. and L.E.D. collected and analysed the magnetic susceptibility data. A.B.T. and K.B. collected and analysed the electron microscopy data. A.B.T. collected the Mössbauer spectra, and F.G. and G.J.L. analysed the spectra. M.I.G. collected and analysed the gas adsorption data. M.I.G., A.B.T. and J.R.L. wrote the paper, and all authors contributed to revising it.

Competing interests The authors declare no competing interests.

Additional information

Supplementary information is available for this paper at https://doi.org/10.1038/s41586-019-1776-0.

Correspondence and requests for materials should be addressed to J.R.L.

Peer review information *Nature* thanks Felipe Gándara, Mohamedally Kurmoo and the other, anonymous, reviewer(s) for their contribution to the peer review of this work.

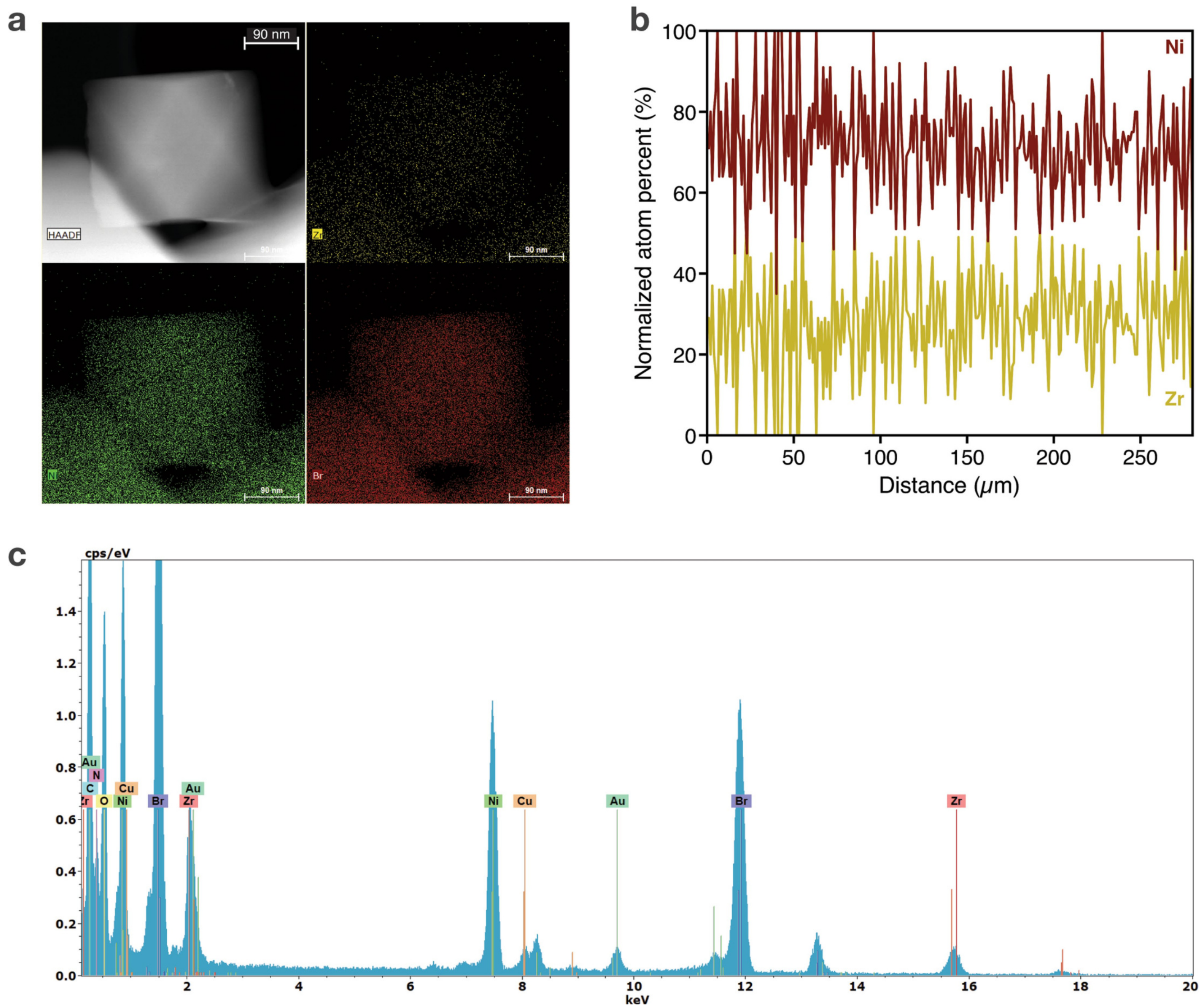

Extended Data Fig. 1 | High-angle annular dark field images and energy-dispersive spectroscopy data for 1($NiBr_2$)$_{15}$. **a**, High-angle annular dark field (HAADF) image (**a**, top left) and energy-dispersive X-ray spectroscopy (EDS) Zr (**a**, top right; yellow), Ni (**a**, bottom left; green) and Br (**a**, bottom right; red) mapping of a microcrystalline powder sample of **1**($NiBr_2$)$_{15}$. **b**, STEM-EDS line scan analysis for Ni (red) and Zr (yellow) across the length of the crystallite plotted as normalized atom per cent. The average amount for the two elements was determined to be 72 ± 12% for Ni and 28 ± 12% for Zr, corresponding to a Ni:Zr ratio of 2.6. **c**, EDS spectrum for the crystallite of **1**($NiBr_2$)$_{15}$. Signals for Cu and Au originate from the space-filling washer and sample grid, respectively.

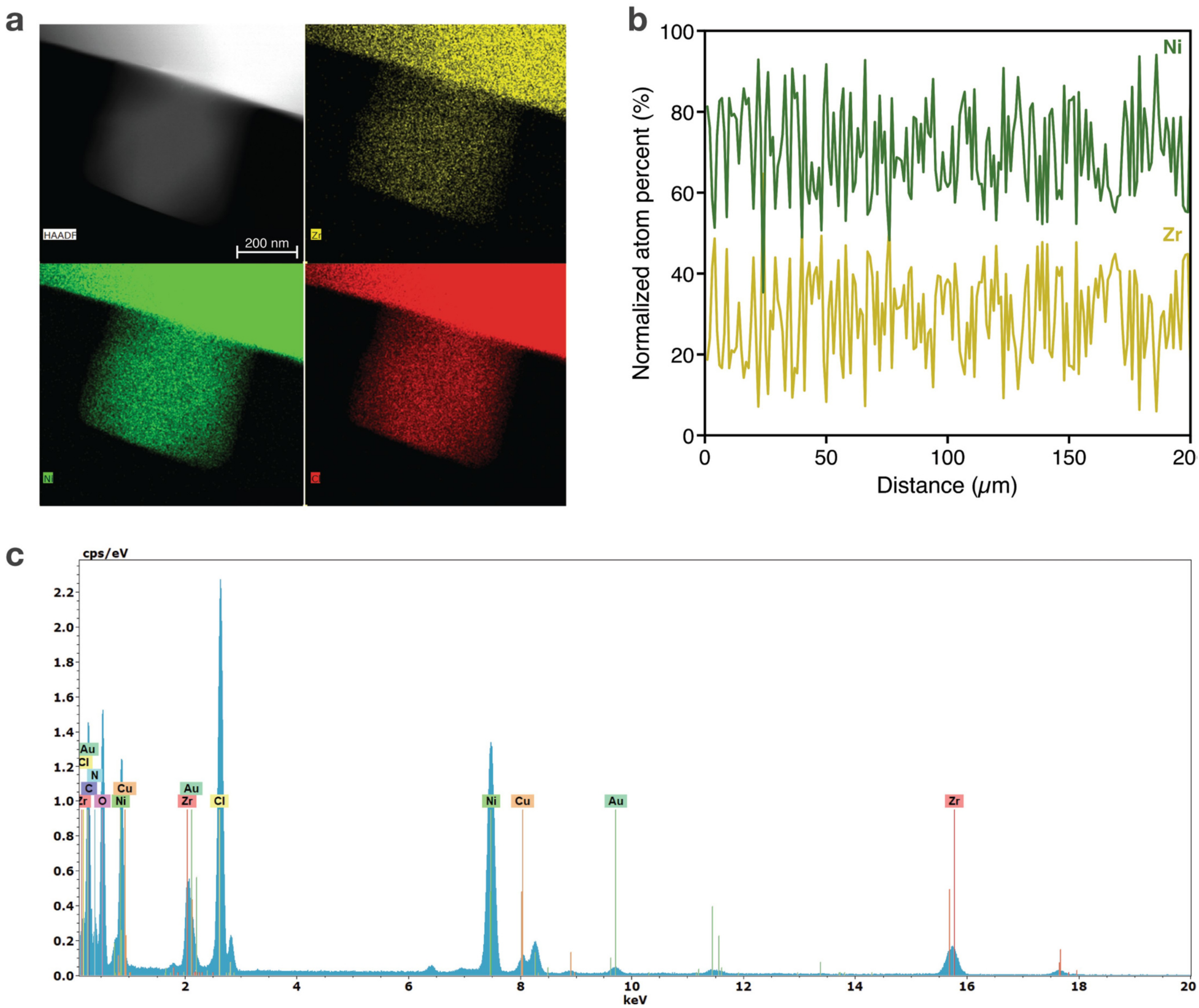

Extended Data Fig. 2 | High-angle annular dark field images and energy-dispersive spectroscopy data for 1($NiCl_2$)$_{15}$. **a**, High-angle annular dark field (HAADF) image (**a**, top left) and energy-dispersive X-ray spectroscopy (EDS) Zr (**a**, top right; yellow), Ni (**a**, bottom left; green) and Cl (**a**, bottom right; red) mapping of a microcrystalline powder sample of **1**($NiCl_2$)$_{15}$. **b**, STEM-EDS line scan analysis for Ni (green) and Zr (yellow) across the length of the crystallite plotted as normalized atom per cent. The average amount for the two elements was determined to be 70.7 ± 11% for Ni and 29 ± 11% for Zr, corresponding to a Ni:Zr ratio of 2.4. **c**, EDS spectrum for the crystallite of **1**($NiCl_2$)$_{15}$. Signals for Cu and Au originate from the space-filling washer and sample grid, respectively. cps, counts per second.

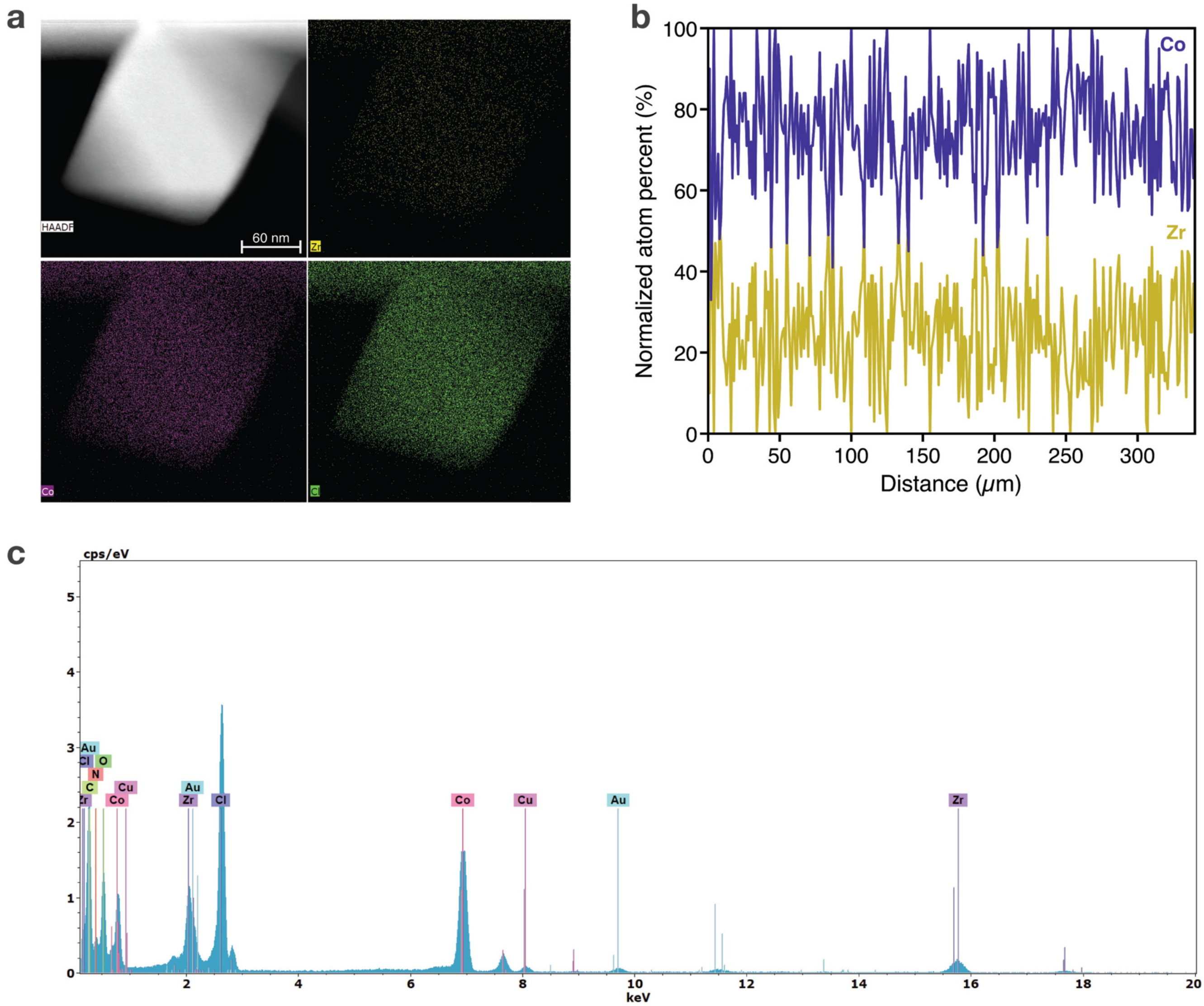

Extended Data Fig. 3 | High-angle annular dark field images and energy-dispersive spectroscopy data for 1($CoCl_2$)$_{18}$. **a**, High-angle annular dark field (HAADF) image (**a**, top left) and energy-dispersive X-ray spectroscopy (EDS) Zr (**a**, top right; yellow), Co (**a**, bottom left; violet) and Cl (**a**, bottom right; green) mapping of a microcrystalline powder sample of **1**($CoCl_2$)$_{18}$. **b**, STEM-EDS line scan analysis for Co (violet) and Zr (yellow) across the length of the crystallite plotted as normalized atom per cent. The average amount for the two elements was determined to be 75 ± 13% for Co and 25 ± 13% for Zr, corresponding to a Co:Zr ratio of 3.0. **c**, EDS spectrum for the crystallite of **1**($CoCl_2$)$_{18}$. Signals for Cu and Au originate from the space-filling washer and sample grid, respectively.

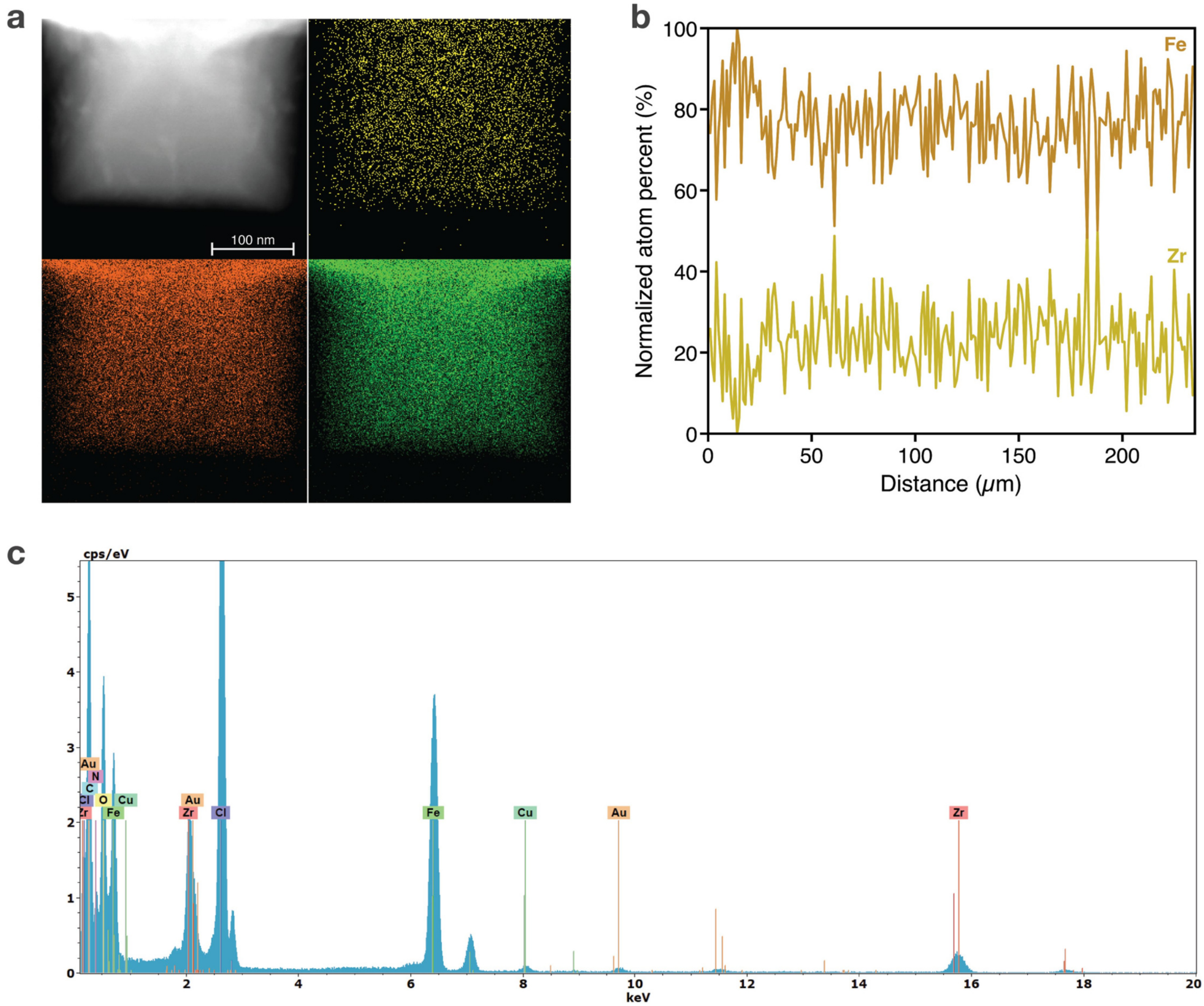

Extended Data Fig. 4 | High-angle annular dark field images and energy-dispersive spectroscopy data for 1($FeCl_2$)$_{19}$. **a**, High-angle annular dark field (HAADF) image (**a**, top left) and energy-dispersive X-ray spectroscopy (EDS) mapping Zr (**a**, top right; yellow), Fe (**a**, bottom left; orange) and Cl (**a**, bottom right; green of a microcrystalline powder sample of **1**($FeCl_2$)$_{19}$. **b**, STEM-EDS line scan analysis for Fe (orange) and Zr (yellow) across the length of the crystallite plotted as normalized atom per cent. The average amount for the two elements was determined to be 77 ± 9% for Fe and 23 ± 9% for Zr, corresponding to a Fe:Zr ratio of 3.3. **c**, EDS spectrum for the crystallite of **1**($FeCl_2$)$_{19}$. Signals for Cu and Au originate from the space-filling washer and sample grid, respectively.

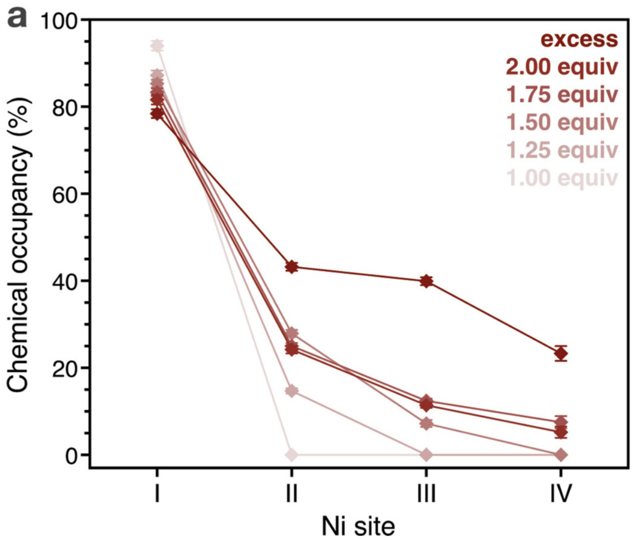

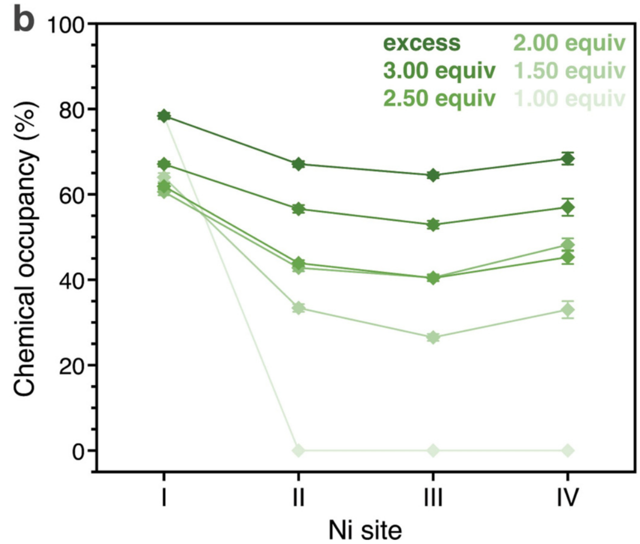

Extended Data Fig. 5 | Comparison of Ni(II) site occupancies. a, **b**, Nickel site occupancies for single-crystal structures of $NiBr_2$-loaded (**a**, light to dark red) and $NiCl_2$-loaded (**b**, light to dark green) **1** obtained by reaction of **1** with 1.00 equiv to excess (>50 equiv) NiX_2 (X = Br, Cl) in diglyme. Error bars represent the crystallographic standard uncertainties of the Ni(II) site occupancies. Lines are included to guide the eye.

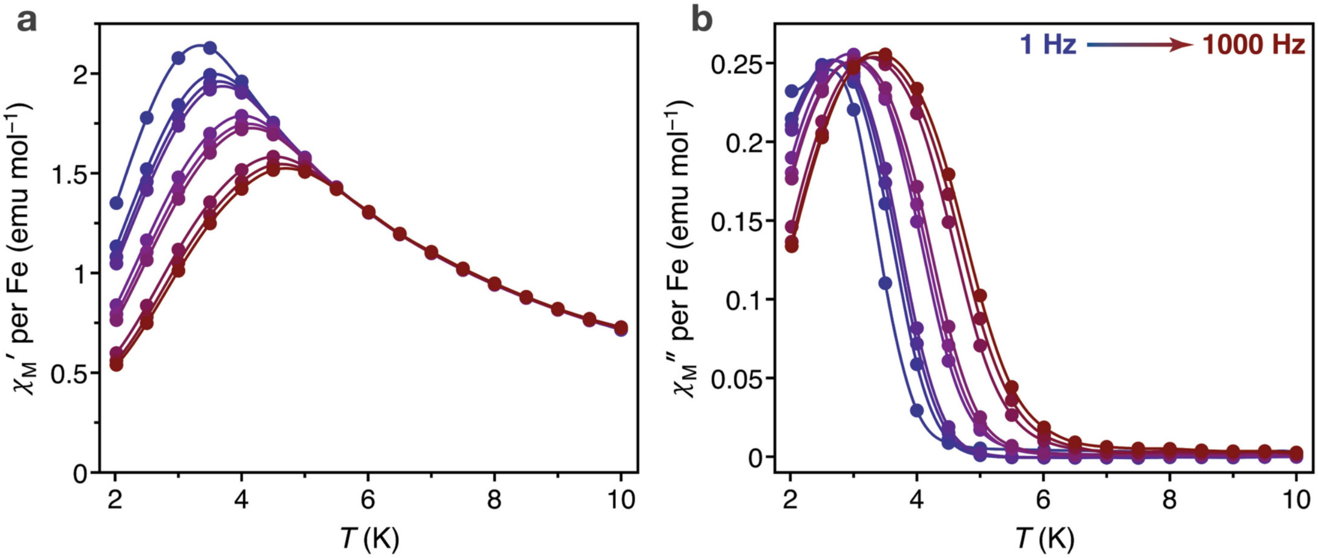

Extended Data Fig. 6 | a.c. magnetic susceptibility data. a, **b**, In-phase (**a**) and out-of-phase (**b**) variable-temperature a.c. magnetic susceptibility data from 2 to 10 K for **1**$(FeCl_2)_{19}$ under zero d.c. magnetic field and a 0.4 mT a.c. magnetic field oscillating at frequencies of 1, 5, 7.5, 10, 50, 75, 100, 500, 750 and 1,000 Hz (blue to red). Coloured lines are guides for the eye.

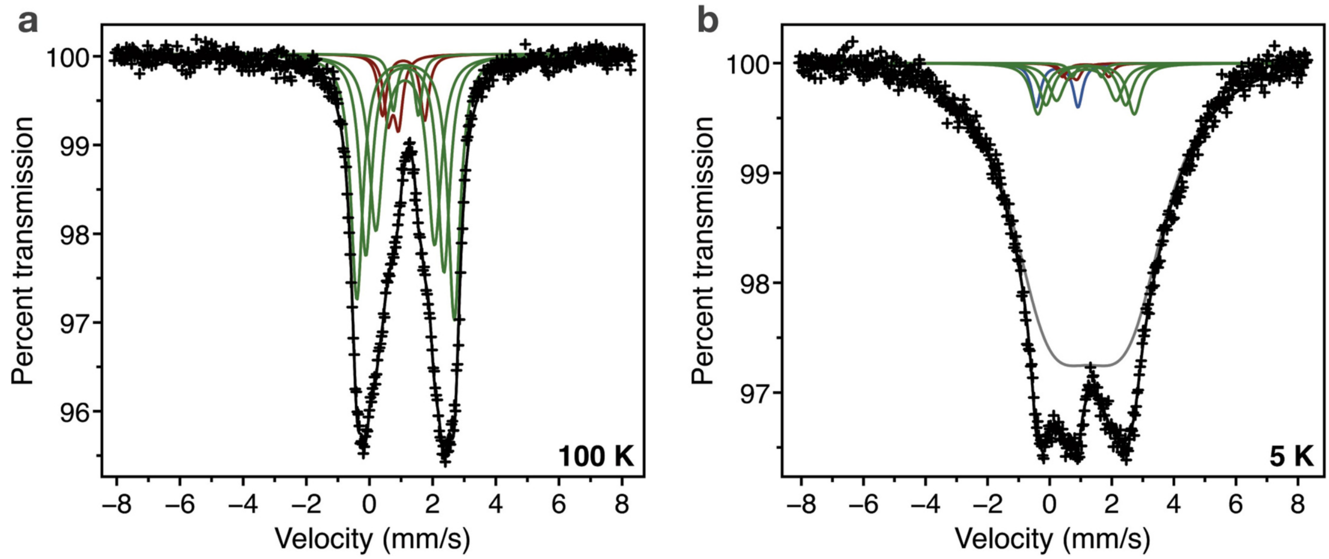

Extended Data Fig. 7 | Mössbauer spectra. a, **b**, ^{57}Fe Mössbauer spectra for **1**$(FeCl_2)_{19}$ at 100 K (**a**) and 5 K (**b**). The data were fit with four high-spin octahedral Fe(II) components (green), two high-spin four- and five-coordinate Fe(II) components (red), and a magnetic hyperfine component (grey). Spontaneous oxidation leads to a high-spin Fe(III) impurity (blue) visible at 5 K. Overall fits are depicted in black.

Article

The past and future of global river ice

https://doi.org/10.1038/s41586-019-1848-1

Received: 31 December 2018

Accepted: 16 October 2019

Published online: 1 January 2020

Xiao Yang[1*], Tamlin M. Pavelsky[1] & George H. Allen[2]

More than one-third of Earth's landmass is drained by rivers that seasonally freeze over. Ice transforms the hydrologic[1,2], ecologic[3,4], climatic[5] and socio-economic[6–8] functions of river corridors. Although river ice extent has been shown to be declining in many regions of the world[1], the seasonality, historical change and predicted future changes in river ice extent and duration have not yet been quantified globally. Previous studies of river ice, which suggested that declines in extent and duration could be attributed to warming temperatures[9,10], were based on data from sparse locations. Furthermore, existing projections of future ice extent are based solely on the location of the 0-°C isotherm[11]. Here, using satellite observations, we show that the global extent of river ice is declining, and we project a mean decrease in seasonal ice duration of 6.10 ± 0.08 days per 1-°C increase in global mean surface air temperature. We tracked the extent of river ice using over 400,000 clear-sky Landsat images spanning 1984–2018 and observed a mean decline of 2.5 percentage points globally in the past three decades. To project future changes in river ice extent, we developed an observationally calibrated and validated model, based on temperature and season, which reduced the mean bias by 87 per cent compared with the 0-degree-Celsius isotherm approach. We applied this model to future climate projections for 2080–2100: compared with 2009–2029, the average river ice duration declines by 16.7 days under Representative Concentration Pathway (RCP) 8.5, whereas under RCP 4.5 it declines on average by 7.3 days. Our results show that, globally, river ice is measurably declining and will continue to decline linearly with projected increases in surface air temperature towards the end of this century.

River ice, which is widespread at middle to high latitudes and elevations[12,13], regulates many aspects of river functions. For example, river ice contributes to the seasonal ice road network, which serves remote Arctic communities[14]. During the spring melt, ice-jam floods cost about US$300 million in 2017 in North America alone[7]. Although disruptive to humans, ice-jam flooding has an ecologically beneficial role, distributing fresh water, sediments and nutrients to riparian ecosystems[4]. River ice is also thought to regulate greenhouse gas emissions from rivers to the atmosphere by seasonally blocking an estimated 87,000 km^2 of stream surface[5].

Despite the wide-ranging importance of river ice, knowledge of its global extent and change is extremely limited. Three studies have investigated historical river ice extent in the Northern Hemisphere: the first[15] estimated changes in river ice phenology from 1979 to 2009 with a physically based model; the second[12] estimated that 56% of rivers were affected by ice cover, using the 0-°C surface air temperature (SAT) isotherm as a proxy for river ice; and the third study[10] found consistent trends of later surface water freeze-up (5.7 days later per 100 years) and earlier break-up (6.3 days earlier per 100 years) based on long-term records of ice occurrence from 5 rivers and 21 lakes. Various rates of changes have been observed from local to regional records[1,9,16,17], but extrapolating these observations globally is challenging because of poor spatial coverage and, more importantly, the spatially heterogeneous nature of ice dynamics revealed by evaluations of ice break-up dates along river profiles[18,19]. Moreover, trends from in situ observations are inconsistent owing to differences in the definitions of phenological dates, changes in instrumentation and the selection of study sites and analysis periods[9]. Of the few studies that have predicted future changes in river ice extent, most have been based on simple ice–SAT relationships derived from in situ records and conducted at regional scales[11,20]. To accurately project future changes in river ice extent at the global scale, a robust and comprehensive understanding of the relationship between climate and ice extent is required[21].

In this study, we present a global, multitemporal river ice extent dataset, based on 407,880 satellite images from 34 years of observations from the Landsat 5–8 missions (1984–2018). Analysis reveals patterns of change in global river ice cover and enables the development and validation of a simple, yet highly predictive, empirical model of river ice extent. Applying the model to future climate projections, we forecast end-of-century changes in the global extent and seasonal duration of river ice cover.

To construct a global multitemporal river ice extent dataset, we first identified 7.5 million river centreline locations observable by Landsat with a width ≥90 m and a water occurrence ≥90% (refs. [22,23]), largely corresponding to rivers with stream order ≥3 (ref. [24]). To calculate river ice extent, we then extracted snow/ice conditions from the quality band of Landsat images on the Google Earth Engine[25] platform. Snow/ice in the quality band was classified by the US Geological Survey using the Fmask

[1]Department of Geological Sciences, University of North Carolina at Chapel Hill, Chapel Hill, NC, USA. [2]Department of Geography, Texas A&M University, College Station, TX, USA. *e-mail: yangxiao@live.unc.edu

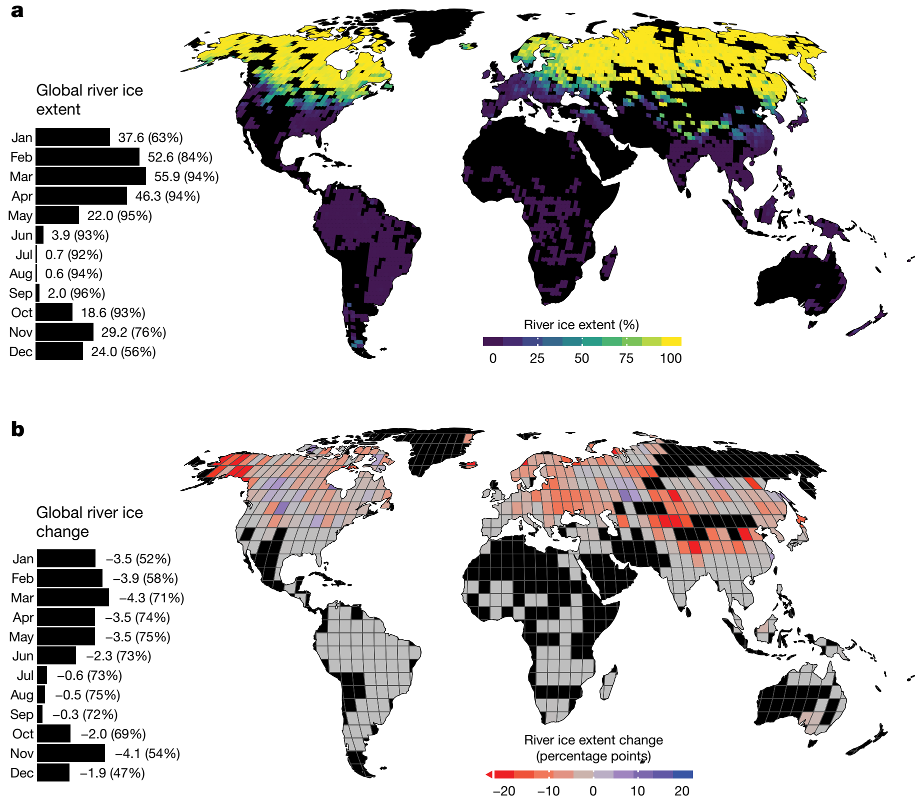

Fig. 1 | Extent of river ice from 1984 to 2018. a, Map of mean river ice extent (in terms of ice-covered length percentage) for the winter season—boreal winter (December, January and February) for the Northern Hemisphere and austral winter (June, July and August) for the Southern Hemisphere. The bar plot shows the monthly percentage of ice-covered rivers globally. The percentage of studied rivers observed successfully by Landsat is shown in parentheses. **b**, Map of changing river ice conditions between 1984–1994 and 2008–2018. Changes were calculated at a 5° × 5° tile scale instead of at the Landsat tile scale used in **a** to increase data availability. The bar plot shows the monthly river ice change with the percentage of studied rivers successfully observed by Landsat in parentheses. In both maps, the black area denotes either insufficient data or a lack of Landsat-observable rivers.

algorithm[26], which labels each pixel as clear, water, cloud, cloud shadow or snow/ice. To reduce the volume of data, we aggregated pixel-level snow/ice conditions into the percentage of total river length covered by ice, or river ice extent, for each Landsat image. To our knowledge, the result constitutes the first global multitemporal quantification of river ice extent.

The main source of uncertainty in the river ice extent dataset comes from the classification error of snow/ice in Fmask. Although the spectral method for classifying snow/ice was adapted from other optical sensors that have been validated[27], the snow/ice classification in Fmask has not previously been systematically evaluated for Landsat images. By comparing Fmask-derived river ice extent to in situ river ice records in Alaska (from the US National Weather Service) and Canada (from the Water Survey of Canada), we estimated the overall accuracy of the Fmask-derived river ice extent to be 0.94 ($P \leq 0.001$; see details in Methods).

Using the global river ice extent dataset, we calculated large-scale river ice coverage and estimated its recent changes. Globally, we estimated a maximum ice extent of 56% for the 94% of rivers that were successfully observed in March (Fig. 1a). The distribution of river ice was strongly asymmetric between hemispheres. In the Northern Hemisphere, where other studies have estimated the maximum extent of river ice, we found that 66% of the observed river length in March was ice-covered, about 18% higher than previous estimates[12] (note that 4% of the targeted rivers were not successfully observed in March owing to insufficient data). In the Southern Hemisphere, river ice was detected only in New Zealand, the southern tip of the Andes in South America and the southernmost part of Australia. River ice was found at the lowest latitudes in continental regions with high topographies, such as the Rocky Mountains in North America and the Tibetan Plateau in Asia. Conversely, less ice was detected over relatively high latitudes in Western Europe and the Pacific Northwest of the United States, probably because of the influence of nearby ice-free oceans.

Comparing observed river ice cover between 2008–2018 and 1984–1994, we detected a monthly global decline ranging from 0.3 to 4.3 percentage points (Fig. 1b; note that the percentage point change and the percentage change are different—that is, moving from 10% to 7.5% would be a 2.5 percentage point change, but a 25% change). The magnitude of decline was lower during July–September, when river ice is least prevalent. The majority of the changes in the northern mid- to high latitudes are towards less river ice cover, with the greatest declines around the Tibetan Plateau, eastern Europe and Alaska. The monthly river ice change was calculated wherever data were available for both decades (see Extended Data Figs. 1, 2), accounting for 47–75% of the global rivers successfully observed by Landsat, depending on the month.

The observed decline in river ice is likely to continue with predicted global warming. By matching the river ice extent dataset with a 30-day prior mean SAT from the ERA5 climate reanalysis dataset[28], we demonstrate that river ice extent can be accurately represented, based on temperature and season, by a logistic regression model (Fig. 2a; root-mean-square error, RMSE: 13.8 percentage points; mean bias (MBS), 0.6 percentage points). Within the critical temperature range (−10 °C to 10 °C) for ice–water transition, our model reduced the RMSE by 30% and MBS by 87% compared with the 0-°C-isotherm model (Fig. 2b). Using this model, we also found that, as suggested by a previous regional

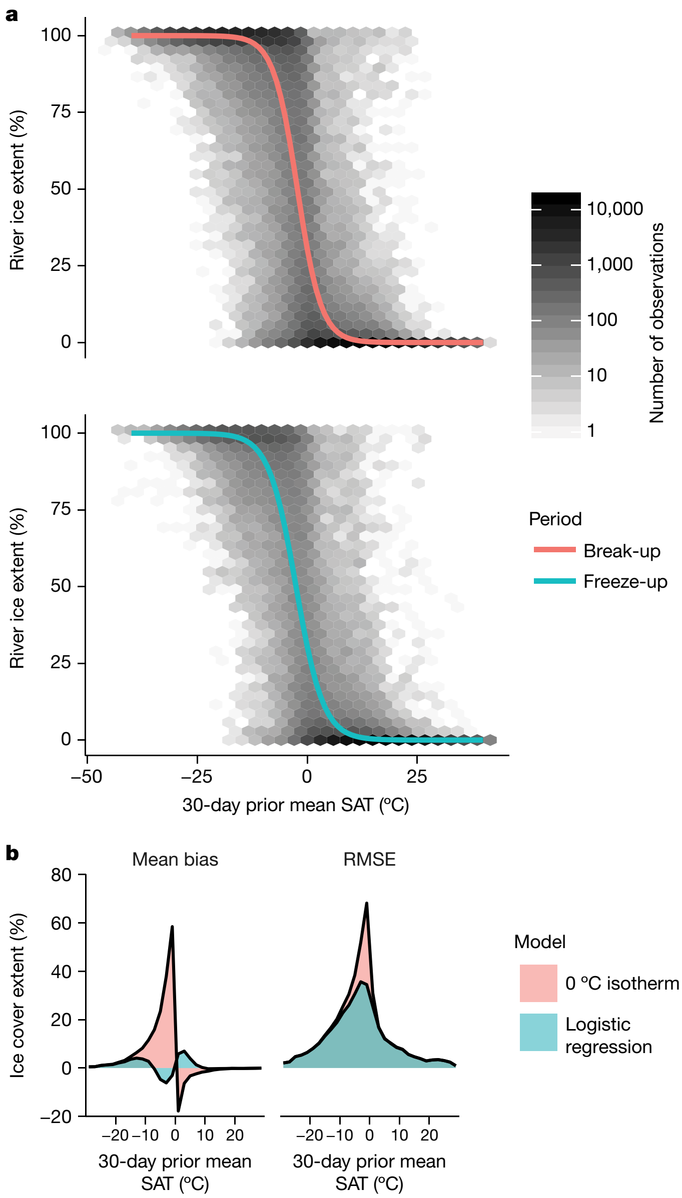

Fig. 2 | Modelling river ice extent. a, Logistic regression model (lines) constructed from the relationship between river ice extent and 30-day prior mean SAT, with the period encompassing break-up (August–January) and freeze-up (February–July) treated separately. **b**, Comparison of river ice models by mean bias and RMSE.

correlation analysis[29], SAT is a stronger control during break-up than during freeze-up.

Applying this river ice model to future SAT data for the end of the century (2080–2100) from the CESM climate model (under RCP 8.5)[30], we found that, compared with a 2009–2029 reference period (chosen to centre around the present year), monthly declines in global river ice extent ranged from 9 to 66% (0.4–9.3 percentage points) (Fig. 3 shows the changes for the Northern Hemisphere). We found a similar pattern for RCP 4.5, with a smaller magnitude of change (globally 0.2–3.2 percentage points, corresponding to a 4–35% decline, Extended Data Figs. 3, 4).

We divided the global landmass into zones defined by ice duration: ice-free (duration < 5 days), intermittent (5 days ≤ duration < 15 days), 0.5–3 months, 3–6 months and >6 months (Fig. 4a). We found substantial areal decline for regions with ice duration of >6 months and a general shift of zones with shorter ice duration to higher latitudes. Across

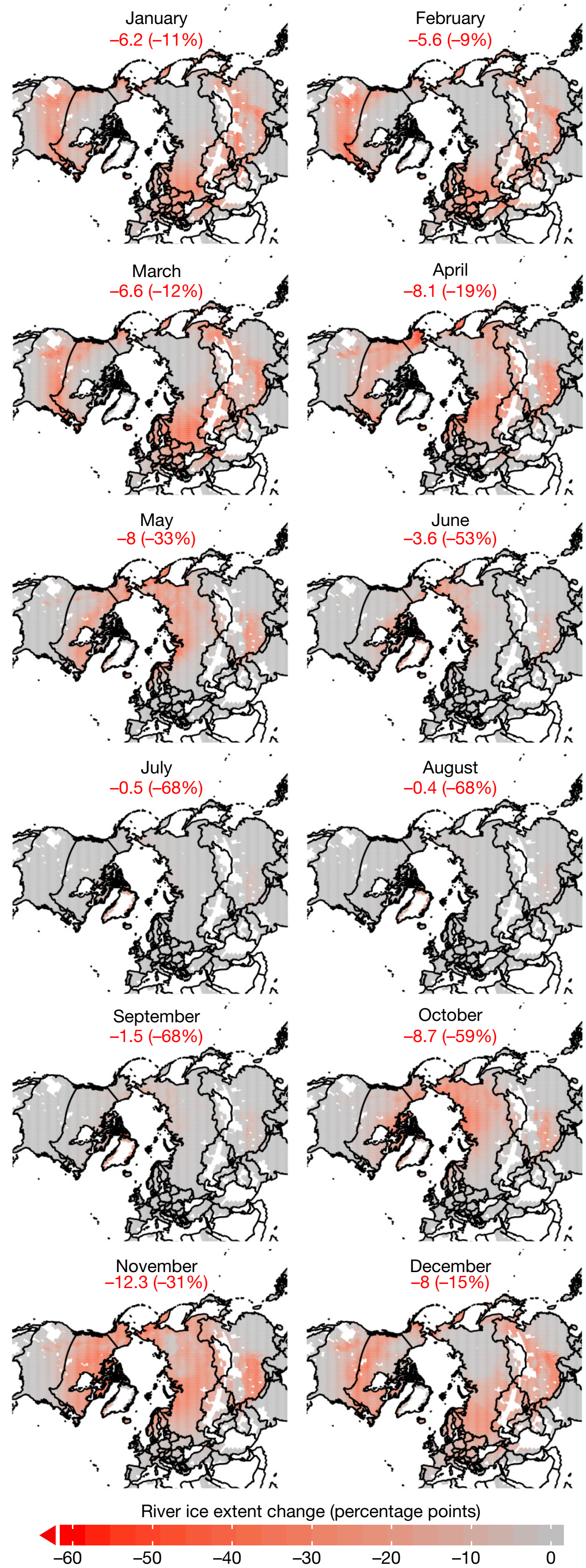

Fig. 3 | Modelled average monthly river ice difference between 2009–2029 and 2080–2100 using CESM SAT output (RCP 8.5). The percentage point change over Northern Hemisphere is shown in red, with the corresponding percentage change in parentheses. White land areas denote a lack of Landsat-observable rivers.

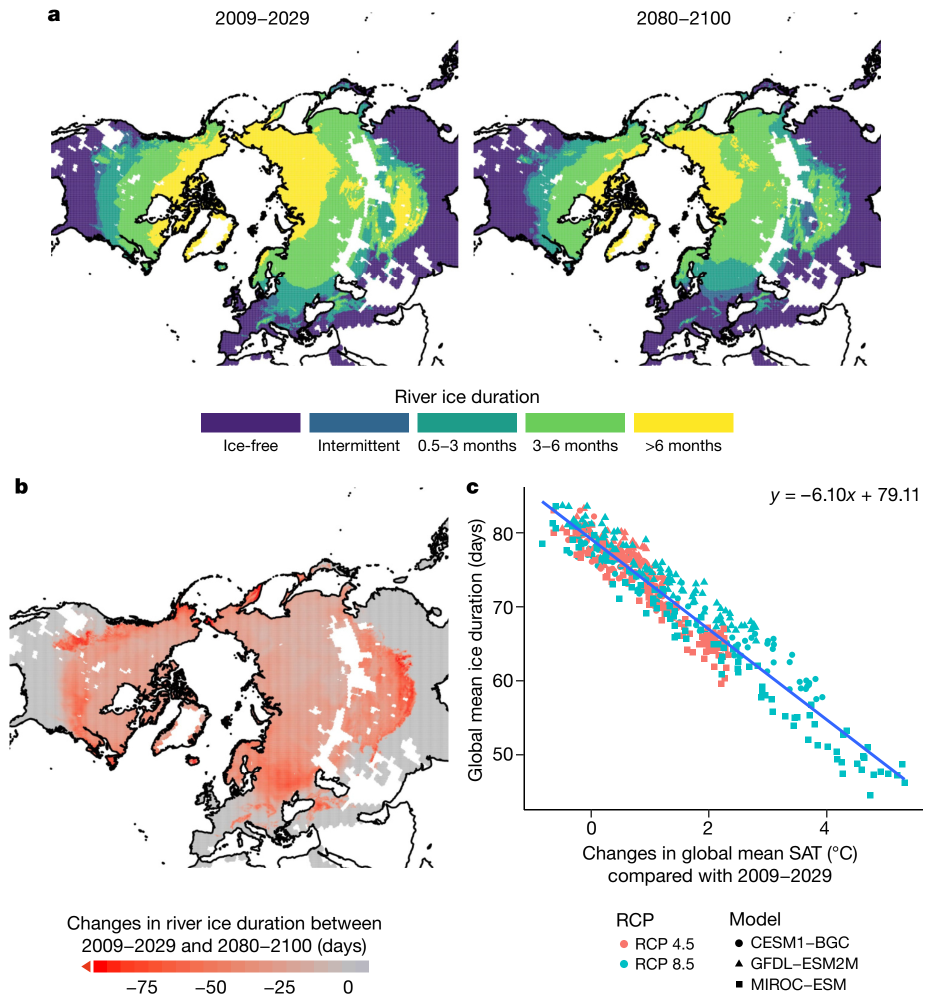

Fig. 4 | Future changes in river ice duration. **a**, Modelled northward shifts of ice duration zones between 2009–2029 and 2080–2100 using CESM SAT output (RCP 8.5) (see Extended Data Fig. 5 for an estimation for RCP 4.5 and for the Southern Hemisphere). White land areas denote a lack of Landsat-observable rivers. **b**, Map of changes in river ice duration between 2009–2029 and 2080–2100. **c**, The relationship between global mean river ice duration and the changes in global mean SAT.

the studied rivers, between 2009–2029 and 2080–2100, we estimated an average rate of decline in river ice duration of 23.5 days per century globally under RCP 8.5, with ice duration declining most severely in the Rocky Mountains, the northeastern United States, eastern Europe and the Tibetan Plateau (Fig. 4b). As expected, the decline in river ice duration under RCP 4.5 is less severe—the average decline in duration globally is 10.3 days per century, a rate slightly greater than that estimated for the twentieth-century Northern Hemisphere[10] (see Extended Data Fig. 5). Application of the river ice model to SAT from two other model simulations from the Coupled Model Intercomparison Project Phase 5 (CMIP5) shows a similar magnitude of change (see Methods). We also estimated the sensitivity of global river ice change to the increase in global mean SAT and found that for each 1 °C increase in global mean SAT, mean ice duration is projected to decrease by 6.10 ± 0.08 days (Fig. 4c), and the percentage of rivers affected by ice is projected to decrease by 1.48 ± 0.03 percentage points (Extended Data Fig. 6).

There are three primary implications of this study. First, our results reveal that more than half of Earth's rivers are covered by ice during the winter months, signifying a wider influence of river ice than previous estimates. As river ice is thought to impede the emission of greenhouse gases normally released by rivers[5], this upward revision implies a stronger seasonal signature in greenhouse gas emissions from the global river network. Second, projected future declines in river ice extent will transform the functions of Earth's ice-affected rivers. For example, shortening ice durations will force the transition from land-based winter transportation to waterways in the high latitudes, where a recent study suggests a 14% reduction in the land area accessible by winter roads by mid-century[6]. The loss of river ice will also substantially alter ways of living for residents of ice-affected regions in terms of the cultural ecosystem services that ice provides[8]. Finally, our results demonstrate that, globally, the mean duration and maximum extent of river ice vary approximately linearly with mean SAT for the studied range of warming. Knowing these linear rates of change enables us to quickly and accurately estimate the changes in river ice extent and duration caused by future climate change, allowing more accurate propagation of its influence on the socio-economic, hydrologic, biogeochemical and ecological processes of the global river system.

Online content

Any methods, additional references, Nature Research reporting summaries, source data, extended data, supplementary information, acknowledgements, peer review information; details of author contributions and competing interests; and statements of data and code availability are available at https://doi.org/10.1038/s41586-019-1848-1.

1. Beltaos, S. & Prowse, T. River-ice hydrology in a shrinking cryosphere. *Hydrol. Process.* **23**, 122–144 (2009).

2. Kämäri, M. et al. River ice cover influence on sediment transportation at present and under projected hydroclimatic conditions. *Hydrol. Process*. **29**, 4738–4755 (2015).
3. Prowse, T. D. River-ice ecology. I: hydrologic, geomorphic, and water-quality aspects. *J. Cold Reg. Eng*. **15**, 1–16 (2001).
4. Prowse, T. D. River-ice ecology. II: biological aspects. *J. Cold Reg. Eng*. **15**, 17–33 (2001).
5. Raymond, P. A. et al. Global carbon dioxide emissions from inland waters. *Nature* **503**, 355–359 (2013); erratum **507**, 387 (2014).
6. Stephenson, S. R., Smith, L. C. & Agnew, J. A. Divergent long-term trajectories of human access to the Arctic. *Nat. Clim. Change* **1**, 156–160 (2011).
7. Rokaya, P., Budhathoki, S. & Lindenschmidt, K.-E. Trends in the timing and magnitude of ice-jam floods in Canada. *Sci. Rep*. **8**, 5834 (2018).
8. Knoll, L. B. et al. Consequences of lake and river ice loss on cultural ecosystem services. *Limnol. Oceanogr. Lett*. **4**, 119–131 (2019).
9. Prowse, T. et al. Past and future changes in Arctic lake and river ice. *Ambio* **40**, 53–62 (2011).
10. Magnuson, J. J. et al. Historical trends in lake and river ice cover in the Northern Hemisphere. *Science* **289**, 1743–1746 (2000).
11. Prowse, T., Shrestha, R., Bonsal, B. & Dibike, Y. Changing spring air-temperature gradients along large northern rivers: implications for severity of river-ice floods. *Geophys. Res. Lett*. **37**, L19706 (2010).
12. Bennett, K. E. & Prowse, T. D. Northern Hemisphere geography of ice-covered rivers. *Hydrol. Process*. **24**, 235–240 (2010).
13. Brooks, R. N., Prowse, T. D. & O'Connell, I. J. Quantifying Northern Hemisphere freshwater ice. *Geophys. Res. Lett*. **40**, 1128–1131 (2013).
14. Brown, D. R. N. et al. Changing river ice seasonality and impacts on interior Alaskan communities. *Weather Clim. Soc*. **10**, 625–640 (2018).
15. Park, H. et al. Quantification of warming climate-induced changes in terrestrial Arctic river ice thickness and phenology. *J. Clim*. **29**, 1733–1754 (2016).
16. Ionita, M., Badaluta, C.-A., Scholz, P. & Chelcea, S. Vanishing river ice cover in the lower part of the Danube basin—signs of a changing climate. *Sci. Rep*. **8**, 7948 (2018).
17. Smith, L. C. Trends in Russian Arctic river-ice formation and breakup, 1917 to 1994. *Phys. Geogr*. **21**, 46–56 (2000).
18. Cooley, S. W. & Pavelsky, T. M. Spatial and temporal patterns in Arctic river ice breakup revealed by automated ice detection from MODIS imagery. *Remote Sens. Environ*. **175**, 310–322 (2016).
19. Pavelsky, T. M. & Smith, L. C. Spatial and temporal patterns in Arctic river ice breakup observed with MODIS and AVHRR time series. *Remote Sens. Environ*. **93**, 328–338 (2004).
20. Prowse, T., Bonsal, B. R., Duguay, C. R. & Lacroix, M. P. River-ice break-up/freeze-up: a review of climatic drivers, historical trends and future predictions. *Ann. Glaciol*. **46**, 443–451 (2007).
21. Collins, M. et al. in *Climate Change 2013: The Physical Science Basis* (eds Stocker, T. F. et al.) 1029–1136 (Cambridge Univ. Press, 2013).
22. Allen, G. H. & Pavelsky, T. M. Global extent of rivers and streams. *Science* **361**, 585–588 (2018).
23. Pekel, J.-F., Cottam, A., Gorelick, N. & Belward, A. S. High-resolution mapping of global surface water and its long-term changes. *Nature* **540**, 418–422 (2016).
24. Yamazaki, D. et al. MERIT Hydro: a high-resolution global hydrography map based on latest topography datasets. *Wat. Resour. Res*. **55**, 5053–5073 (2019).
25. Gorelick, N. et al. Google Earth Engine: planetary-scale geospatial analysis for everyone. *Remote Sens. Environ*. **202**, 18–27 (2017).
26. Zhu, Z. & Woodcock, C. E. Object-based cloud and cloud shadow detection in Landsat imagery. *Remote Sens. Environ*. **118**, 83–94 (2012).
27. Hall, D. K., Riggs, G. A. & Barton, J. S. *Algorithm Theoretical Basis Document (ATBD) for the MODIS Snow and Sea Ice-Mapping Algorithms* (NASA, 2001); https://eospso.gsfc.nasa.gov/sites/default/files/atbd/atbd_mod10.pdf
28. Copernicus Climate Change Service (C3S) *ERA5: Fifth Generation of ECMWF Atmospheric Reanalyses of the Global Climate* (C3S Climate Data Store, 2017); https://cds.climate.copernicus.eu/cdsapp#!/home
29. Lacroix, M. P., Prowse, T. D., Bonsal, B. R., Duguay, C. R. & Menard, P. River ice trends in Canada. In *13th Workshop on Ice Covered Rivers* 41–55 (Committee on River Ice Processes and the Environment, 2005).
30. Thrasher, B., Maurer, E. P., McKellar, C. & Duffy, P. B. Technical note: bias correcting climate model simulated daily temperature extremes with quantile mapping. *Hydrol. Earth Syst. Sci*. **16**, 3309–3314 (2012).

Publisher's note Springer Nature remains neutral with regard to jurisdictional claims in published maps and institutional affiliations.

Methods

Data

Multiple datasets have been used in this study, each of which is described in detail below:

1. Global River Widths from Landsat (GRWL)[22]
2. JRC surface water occurrence[23]
3. Quality band Fmask[26] classifications of the Landsat collection 1 tier 1 images
4. ECMWF ERA5[28] surface temperature
5. NEX-GDDP climate projection SAT data[30]

GRWL[22], or Global River Widths from Landsat, is a global river database that contains 58 million river centreline locations and widths. We used the GRWL Vector Product V01.01 (dataset link: https://zenodo.org/record/1297434#.W8JkshNKh24). Specifically, we used the following properties:

• Geometry (location): expressed as point geometry with latitude and longitude in EPSG:4326 projection.

• width_m: used to identify rivers with a width of more than 90 m.

• lake_flag: indicate whether or not a centreline belongs to a river or a lake or reservoir.

• nchannel: number of channels. GRWL tends to trace the overall river centre in multichannel or braided rivers, which sometimes overlaps with islands. We only used single channel rivers (by setting nchannel = 1) in our study to avoid extracting ice status over the non-water areas.

Global surface water occurrence map[23] contains a raster map at 30 m spatial resolution with pixel values ranging from 0 to 100, indicating the percentage of times when water was detected at its location in the Landsat record. The map layer was constructed by classifying water and non-water for each of the global monthly mosaic images from Landsat 5, 7 and 8 between March 1984 and October 2015 (inclusive).

Fmask[26] is a classification algorithm designed for Landsat images to classify each pixel into five different categories (clear, water, snow/ice, cloud, cloud shadow). It is competent at classifying cloud and cloud shadow, and its classification results have been incorporated into the quality band for all Landsat collection 1 tier 1 images.

ERA5[28] is a reanalysis product that incorporates historical records of land surface and atmospheric variables into the latest modelling framework to produce a global, gridded dataset at 31 km spatial resolution. So far, ERA5 is available from 1979 at hourly or monthly temporal steps. We accessed the dataset from the European Centre for Medium-Range Weather Forecasts (ECMWF) website. We first downloaded the hourly global SAT variable (t2m) from 1 March 1984 to 31 December 2018 at a 6 h intervals (0:00, 6:00, 12:00, 18:00). We then calculated the daily mean SAT by averaging these four hourly values. Finally, we calculated the time series of mean 30-day prior temperature and spatially joined it to each of the Landsat-derived river ice observations.

NEX-GDDP, or the NASA Earth Exchange Global Daily Downscaled Climate Projections[30], is spatially downscaled to 0.25° × 0.25° from a collection of lower-resolution climate projection results developed under the CMIP5 framework. The entire collection contains model output from 21 climate models, each with RCP 4.5 and RCP 8.5 for daily minimum SAT, maximum SAT and precipitation. We calculated the daily mean SAT separately for both RCPs by taking the mean of the minimum and maximum SAT for three models—CESM1-BGC, GFDL-ESM2M and MIROC-ESM. We then calculated the daily 30-day prior mean SAT, which was then used to predict future river ice extent.

Calculating the historical river ice cover dataset

Processing GRWL for river ice cover calculation. GRWL contains approximately 58 million river centreline points globally, each including a width value. In multichannel or braided rivers, GRWL computes an effective centreline, the total flow width, and the number of channels at each centreline point. As these effective centrelines do not necessarily trace the actual river channels, we only used single channel GRWL centreline points (nchannels = 1, around 80% of rivers are single channel). Moreover, lakes and reservoirs are part of many river networks in GRWL, and the centrelines over these features are flagged. We only used non-lake centerline points in GRWL to limit the calculation of ice conditions to rivers, as ice dynamics may be different over lakes and reservoirs. Finally, while GRWL represents our latest knowledge of global river location and width, it is a static dataset, making it suboptimal for capturing ice condition on rivers over the 34 year period, during which varying degrees of morphological changes could occur. To alleviate this problem, we used only GRWL centreline points where surface water occurrence based on a previous study[23] is 90% or above, ensuring that the detected ice conditions for these points were from water surfaces. After all three filters are applied, our final river ice cover dataset used approximately 7.5 million GRWL centreline points, constituting around 271,599 km of river length. This subset of GRWL largely corresponds to Strahler–Horton stream orders greater than 3.

Constructing the global river ice cover dataset. The acquisition of the Landsat Fmask classification (cloud, cloud shadow and snow/ice) was conducted on the Google Earth Engine platform[25] for all single-channel GRWL river centreline points with water occurrence ≥90%. Specifically, we extracted the total number of centreline pixels, as well as the number of pixels covered by snow/ice, cloud and cloud shadow, for all images from Landsat TM, ETM+ and OLI sensors, ranging from March 1984 to December 2018. Then the per-image river ice fraction ($P_{\mathrm{river\_ice}}$) and cloud fraction ($P_{\mathrm{cloud/shadow}}$) were calculated using the following formula:

$$P_{\mathrm{river\_ice}} = N_{\mathrm{snow/ice}}/(N_{\mathrm{total}} - N_{\mathrm{cloud}} - N_{\mathrm{shadow}})$$

$$P_{\mathrm{cloud/shadow}} = (N_{\mathrm{cloud}} + N_{\mathrm{shadow}})/N_{\mathrm{total}}$$

where N_{total}, N_{cloud}, N_{shadow} and $N_{\mathrm{snow/ice}}$ denote the number of the total, cloud, cloud shadow and snow or ice pixels from a particular image. In total, we processed 841,365 Landsat images, covering 1984–2018. Calculating the per-image ice extent directly on Google Earth Engine greatly reduces the size of the dataset at no observable cost in terms of the details of the river ice extent required for this study.

Cleaning the river ice dataset. We systematically excluded some river ice data before calculating and modelling historical changes. To increase the stability of the river ice fraction calculation, we excluded river ice data from images for which: (1) $P_{\mathrm{cloud/shadow}}$ is greater than 25%; (2) $N_{\mathrm{total}} \leq 333$ (around 10 km length of river); and (3) the percentage of river pixels affected by topographic shadow exceeds 5%. This filtering reduces the data volume from 841,365 to 407,880 images.

Calculating global historical monthly mean river ice extent. We estimated global monthly mean river ice extent through two levels of spatial aggregation. For each month, we first calculated mean river ice extent for each WRS-2 tile (WRS, Worldwide Reference System) using all available Landsat-derived river ice extent observations across 34 years. Then we estimated the mean global river ice extent by calculating the weighted mean of the tile-level data. We estimated the weight for this aggregation by multiplying the length of studied rivers in the tile by the extent of overlap between the current tile and its neighbouring tiles. Specifically, we estimated the percentage of studied rivers for each WRS-2 tile using the total number of river centreline points intersecting the corresponding tile; we then estimated the degree of tile overlap (denoted by r) by calculating the proportion of non-overlapping area out of the total tile area.

$$r = (A_{\mathrm{t}} - A_{\mathrm{i}})/A_{\mathrm{t}}$$

where A_{t} is the area of WRS-2 tile and A_{i} is the area of the intersection between two tiles.

The monthly weighted mean river ice extent is shown in the bar chart accompanying Fig. 1a. For each month, we also estimated the percentage of studied rivers actually captured by our satellite records. To estimate this monthly spatial coverage for each month, we divided the area of the union of all observed WRS-2 tiles for that month—representing the length of rivers observed—by the area of the union of all of the WRS-2 tiles intersecting our studied rivers. This coverage percentage was reported in the bar chart in Fig. 1a. Note that it is necessary to calculate the union of the tiles before the total covered area as there is overlap between neighbouring tiles.

Calculating historical changes in river ice extent

We assessed historical changes in river ice extent by calculating the difference in mean monthly river ice cover between two decades: March 1984–March 1994 and December 2008–December 2018—the starting and ending months were chosen to maximize the gap between the two decades. To compensate for the scarcity of Landsat records from the earlier decade and from high-latitude regions, the historical analysis—both the monthly statistics and the aggregated global map—was carried out by aggregating river ice data from the WRS-2 tile (roughly 1° × 1° at the Equator) to a 5° × 5° tile.

Calculating the global map of historical changes in river ice. To produce the map of the change in historical river ice extent for each month (Fig. 1b), we calculated the difference in mean river ice extent for each 5° × 5° tile. For each month, we kept only the tiles that contained at least five river ice observations for each of the two decades under comparison. The global map was then calculated by averaging all available monthly difference values for each tile. Monthly maps of the decadal difference in river ice extent can be found in Extended Data Fig. 2, which shows the temporal pattern of the change and the spatial coverage of the river ice record.

Calculating global historical changes in monthly mean river ice extent. To estimate the global monthly difference in river ice extent for each month, we calculated the difference in mean river ice extent for 5° × 5° tiles with at least five river ice observations for each decade. The monthly difference was then calculated by averaging the mean difference value from all available tiles, whereas the value of the observed percentage of rivers was estimated by taking the ratio between the total area of the available 5° × 5° tiles and the total area of all of the global 5° × 5° tiles that intersecting studied rivers. These statistics are shown in the bar chart in Fig. 1b.

Quantifying Landsat spatial and temporal sampling patterns. The aggregation done here to calculate historical changes in river ice could cause unintended systematic bias owing to the potential biases in the sampling time (within each month) and location (within each tile) between the two decades. We conducted the following two assessments to show that (1) both the sampling date for each month and sampling location for each 5° × 5° tile were small compared with their respective range of possible values (mean sampling time difference: −0.115 days and standard deviation: 3.4 days; mean sampling location difference: 0.012° and standard deviation: 0.41°) and (2) there was no correlation between the difference in sampling and the difference in the river ice extent, both in time and location (Pearson correlation coefficient $r_{\text{temporal}} = -0.04$ and $r_{\text{spatial}} = 0.07$). The results of these two assessments can be found in Extended Data Fig. 7.

Modelling river ice cover

Building the river ice cover model. After exploring the relationship between river ice extent and its corresponding 30-day prior mean SAT, we chose logistic regression to model their relationship. Logistic regression assumes a linear relationship between the logarithm of the odds of a phenomenon (ice) and the predictors (the 30-day prior mean SAT (SAT_{30}) and a categorical predictor we designated PERIOD), which our data follow. We used the following equations to model the river ice extent.

$$\text{odds(ice)} = N_{\text{snow/ice}}/N_{\text{water}} = P_{\text{river\_ice}}/(1 - P_{\text{river\_ice}})$$

$$\log(\text{odds(ice)}) = a\text{SAT}_{30} + b\text{SAT}_{30} \times \text{PERIOD} + c$$

The PERIOD predictor divides the data into two periods encompassing freeze-up (August–January = 0) and break-up (February–July = 1). The rationale for adding the PERIOD predictor is based on the different control strengths of temperature over ice processes between the freeze-up and breakup periods—a pattern suggested from analysis of in situ records in Canada[29].

We applied the regression model to the Landsat-derived river ice extent and ERA5-derived SAT_{30}. The parameters were estimated as $a = -0.32$, $b = -0.05$ and $c = -0.82$. Using the model, we were able to compare the strength of the control that SAT_{30} exerts on ice dynamics: we estimated that SAT_{30} control over break-up is stronger than that over freeze-up as b is negative. The entire dataset was used to assess the skill of the logistic model and the 0-°C-isotherm model (see Fig. 2b).

Projecting river ice cover at the end of the century. We projected future river ice extent by applying the river ice model to the future SAT data produced by CMIP5 climate projections. We used SAT_{30} outputs from CESM1-BGC, GFDL-ESM2M and MIROC-ESM climate simulations under both RCP 4.5 and RCP 8.5 to estimate future river ice extent and duration up to the end of the century. These models were chosen to account for potential trend biases in predicted temperature. In a similar way to evaluating the sensitivity of a model, which is common in the climate modelling community[31], we calculated the mean global SAT difference between the periods 2006–2036 and 2069–2099 for 21 models included in the CMIP5 ensemble and selected three models to represent the variabilities in relative temperature change (see Extended Data Fig. 8a). Projected future declines in river ice extent and duration are summarized in Extended Data Fig. 8b. To project future ice conditions, we calculated daily river ice extent throughout the periods 2009–2029 and 2080–2100, from which we then calculated, (1) monthly mean river ice extent and the difference between the two periods (Fig. 3, Extended Data Figs. 3, 4); (2) mean river ice duration (Fig. 4, Extended Data Fig. 5). The summary future changes in river ice extent and duration reported here were calculated by aggregating the values from the corresponding map of change at the locations of studied rivers.

Estimating the relationship between river ice condition and global mean surface temperature. For each year between 2009 and 2099, we estimated percentage of ice-affected rivers and the mean ice duration across the globe. The annual percentage of ice-affected rivers was derived by calculating the annual mean river ice extent for each studied river location, then flagging it as ice-affected if the mean value exceeded 0.041—15 days of effective ice cover over 365 days. The annual duration for each river location was estimated by counting the number of days when projected river ice extent exceeded 50%. The annual global mean surface temperature was then computed by averaging the daily mean SAT temperature across the year and then aggregating across the globe.

Sources of errors

Errors in a global dataset—especially one that quantifies highly dynamic Earth surface processes—are often unavoidable. Through building the historical river ice dataset, modelling the river ice processes and predicting future river ice conditions, we have identified three major sources of errors: errors from misclassifications in Fmask, errors in SAT values in the ERA5 dataset and errors in the projections of future river ice condition.

Qualitative evaluation of Fmask snow/ice classification. To qualitatively assess the accuracy of the Fmask snow/ice classification, we randomly selected—stratified sampling by temperature range and observed river ice cover—160 images for visual evaluation. We found that snow/ice classification is adversely affected in the following situations (from the most to the least frequent):

• Commission error in classifying turbid water as snow/ice—found mostly over the Yellow River in China and Amu Darya in Turkmenistan. Less frequently found over the Red River, Arkansas River and Missouri River in the United States.

• Commission error in classifying cloud as snow/ice—no strong spatial pattern found for this type of error.

• Omission error in classifying topographically shaded snow/ice as water.

• Omission error in classifying thin ice as water—this type of error is rare and mostly observed on still portions of rivers (such as reservoirs and lakes, which are not used in this analysis).

Evaluating Landsat-derived river ice extent. We use the US Geological Survey's quality band snow/ice classification to derived river ice extent. The snow/ice classification is calculated using Fmask[26]. Fmask classifies each pixel of the Landsat image into one of five classes. Although Fmask is considered the most accurate[31] cloud classification algorithm for Landsat images, its snow/ice classification has not been evaluated for accuracy. Here we used in situ reported river ice conditions to evaluate the accuracy of river ice extent calculated using Fmask.

Although direct in situ river ice records are scarce, we were able to obtain the river ice status for the state of Alaska, United States, from the archive of the National Weather Service (NWS). We also inferred river ice conditions using the backwater flag that accompanies the daily gauge flow records from Water Survey of Canada (WSC). The backwater flag was used in previous studies as strong indicator of ice conditions[32].

In the following, we first explain our approach to extracting and cleaning the in situ datasets. We then introduce our method for calculating the river ice extent from Landsat images and matching it to the in situ observations. Finally, we show the results of the evaluations.

NWS river ice observations. We obtained historical records for 485 stations in Alaska from S. Lindsey at the Alaska-Pacific River Forecast Center. We encountered two challenges in using this dataset for evaluation. First, the files we obtained, while containing ice observations and station descriptions, do not contain the geolocations of these stations. Fortunately, the station description often followed the 'river_name_at/near_location_name' naming convention (for example, 'Yukon River at Beaver'). We were able to manually identify 177 stations that have both freeze-up and break-up information for at least one water year, 115 of which we successfully georeferenced and 13 of which we eventually used for evaluation after excluding sites that either are close to a river that is too small for Landsat to observe or did not have records that temporally overlapped with the Landsat observation. Second, NWS reported multiple thresholds that indicate various ice conditions during both the freeze-up and break-up periods. However, there were varying amounts of missing data for these dates. For example, while the NWS directly reported freeze-up date, the majority of the values in this field were missing data, which rendered it of very limited value. Instead, we used the first ice date as the dates of ice onset and 'breakup' as the date of ice-off.

WSC flag. The WSC includes flags in its daily discharge data that indicate the state of flow conditions. Among these flags, the backwater flag or 'B' flag is used to indicate ice conditions[32]. In our evaluation, we followed existing practice, treating dates with B flags as dates of river ice cover.

Matching in situ ice coverage with Landsat-derived ice coverage. After merging the geolocations of the NWS stations and the WSC stations, we calculated the river ice conditions for these locations according to Fmask classifications. Specifically, for each in situ location, we calculated the Fmask-derived river ice extent for GRWL rivers (nchannel = 1; lake_flag = 0; width_mean ≥ 90 m) located within a 1,500-m radius of the gauge.

To evaluate the Landsat-derived ice coverage against the in situ records, we matched the datasets spatially (to the 1,500 m proximity of each station) and temporally (to the same day). The same-day temporal matching was straightforward for WSC records, as they reported daily ice conditions. However, as the NWS reported only dates of ice-on and ice-off, we treated dates that fell between an ice-on date and the following ice-off date as ice-covered dates, and those that fell between an ice-off and the following ice-on date as ice-free dates. In total, we matched 18,930 pairs (NWS-Alaska: 515 pairs over 13 sites; WSC: 18,415 pairs over 139 sites) of in situ and Landsat-derived river ice observation for our evaluation.

*Evaluating Landsat-derived river ice coverage***.** When comparing the Landsat-derived river ice coverage to that reported from the field, we first converted the continuous values (0–100%) to a binary ice condition using a threshold of 50%—ice coverage ≥50% is classified as 'ice-covered' and <50% is classified as 'ice-free'. The 50% threshold was chosen as we found that that threshold choice had little impact on the final evaluation. Then we calculated the accuracy, sensitivity and specificity by constructing a confusion matrix using the in situ reported ice condition as a reference and the Landsat-derived ice state as the observation. Overall, Landsat-derived river ice coverage was highly consistent with the in situ reports (accuracy = 0.94, sensitivity = 0.91, specificity = 0.96, Extended Data Fig. 9). When the analysis was broken down into monthly evaluations, accuracy was highest during summer months (June–August: mean accuracy: 0.98) and lower during the remaining months, with no particular seasonal pattern (accuracy: 0.8–1.0 with mean accuracy 0.91, Extended Data Fig. 9b). Reduced accuracy occurred during months when river ice was present and was attributed to: (1) complicated reflectance returns due to dynamic transition between ice and water; (2) increased turbidity accompanying ice break-up; (3) the difference in scale between the Landsat-derived ice condition (averaging across a 1,500-m radius) and the in situ records (scale unknown, see examples in Extended Data Fig. 9c); and (4) errors in the in situ records. Notably, the accuracy derived from the observation-based NWS ice conditions (overall accuracy: 0.97) was generally higher than that from the WSC (overall accuracy: 0.94) (see also Extended Data Fig. 9b). The fact that the ice condition from the WSC was inferred, instead of observed, could have contributed to this discrepancy.

Comparison with in situ river ice records also showed no systematic differences among Landsat sensors. Accuracy was similar across data from Landsat 5 (TM), Landsat 7 (ETM+) and Landsat 8 (OLI) (see Extended Data Table 1). It is worth noting that Landsat 8 has an extra flag for cirrus clouds, which could potentially improve the quality of ice data by better excluding cloud-affected observations. However, we decided not to use this flag, as its inclusion could potentially cause varying data quality between sensors, which then could compromise the detection of historical river ice change.

Human influence on river ice. Human activities that affect rivers—such as river engineering and water pollution—tend to systematically and permanently alter the river morphology, as well as the thermal and physical properties of the flow. River ice regimes affected by these influences cannot be explained by the changes in SAT alone. In one previous study, human activity was found to affect the river ice regime to a much greater degree than climate variation along two highly regulated river reaches in Europe[33]. While we acknowledge the contribution of these non-climatic factors, quantification of their effects globally exceeds the scope of this study. Nonetheless, interpretation of our results in rivers/regions that are known to be heavily engineered requires extra caution.

Although direct anthropogenic influence on river ice regimes should be considered when interpreting both in situ and remotely sensed data, interpreting remotely sensed data requires extra consideration

of the sensitivity of the classification algorithms to anthropogenic influence. Otherwise, there is a risk of falsely attributing changes in river ice to changing climate. For example, for the lower Yellow River, our detection of great historical river ice decline is likely to be largely due to the combined effect of changes in water turbidity—mostly owing to recent damming upstream—and the tendency for Fmask to falsely classify turbid water as snow/ice.

Uncertainties in ERA5 SAT. Because it was released very recently, there is no spatially comprehensive evaluation of SAT in ERA5, so its overall accuracy remains unknown. However, from studies that evaluated this parameter regionally, ERA5 has outperformed other reanalysis datasets and can accurately represent the magnitude and variability of near-surface air temperature over Antarctica[34].

Spatial scale mismatch between temperature dataset and river size. When attaching the ERA5 temperature data (spatial resolution of approximately 30 km) to our river ice extent dataset and modelling river ice based on the merged dataset, as well as predicting future river ice extent with temperature data from NEX-GDDP (spatial resolution 0.25°), we implicitly assumed that temperature for a grid cell is representative of that experienced by the river in it. This assumption could result in bias when mixing temperatures from land and water pixels, especially when large topographic variability exists in the grid cell, as rivers tend to flow along topographic low areas, and elevation greatly affects temperature. The degree of this inherent systematic bias may be reduced in the future with the development of more advanced reanalysis datasets.

Data availability

The global river ice dataset can be accessed at https://doi.org/10.5281/zenodo.3372709. The in situ and Landsat-derived river ice records for evaluating ice classification can be accessed at https://doi.org/10.5281/zenodo.3372754.

Code availability

The code used to acquire, analyse and visualize the dataset can be accessed online at the project's GitHub page (https://github.com/seanyx/global-river-ice-dataset-from-Landsat). The river ice model and all figures in the paper (including the extended data figures) were made using R statistical software (http://www.R-project.org/).

31. Foga, S. et al. Cloud detection algorithm comparison and validation for operational Landsat data products. *Remote Sens. Environ*. **194**, 379–390 (2017).
32. Beaton, A., Whaley, R., Corston, K. & Kenny, F. Identifying historic river ice breakup timing using MODIS and Google Earth Engine in support of operational flood monitoring in Northern Ontario. *Remote Sens. Environ*. **224**, 352–364 (2019).
33. Takács, K., Kern, Z. & Nagy, B. Impacts of anthropogenic effects on river ice regime: examples from Eastern Central Europe. *Quat. Int*. **293**, 275–282 (2013).
34. Gossart, A. et al. An evaluation of surface climatology in state-of-the-art reanalyses over the Antarctic Ice Sheet. *J. Clim*. **32**, 6899–6915 (2019).

Acknowledgements Funding was provided to T.M.P. by a subcontract from the SWOT Project Office at the NASA/Caltech Jet Propulsion Laboratory. We thank S. Lindsey at the Alaska-Pacific River Forecast Center for providing us with the NWS Alaska river break-up and freeze-up records, and W. Dolan for help with geolocating Alaskan river ice records.

Author contributions X.Y. developed the method, performed analysis and drafted the manuscript. T.M.P. conceptualized the study, assisted with analysis and reviewed and edited the manuscript. G.H.A. provided the GRWL dataset and reviewed and edited the manuscript.

Competing interests The authors declare no competing interests.

Additional information
Correspondence and requests for materials should be addressed to X.Y.
Peer review information *Nature* thanks John Kimball, Gerhard Krinner and Homa Kheyrollah Pour for their contribution to the peer review of this work.

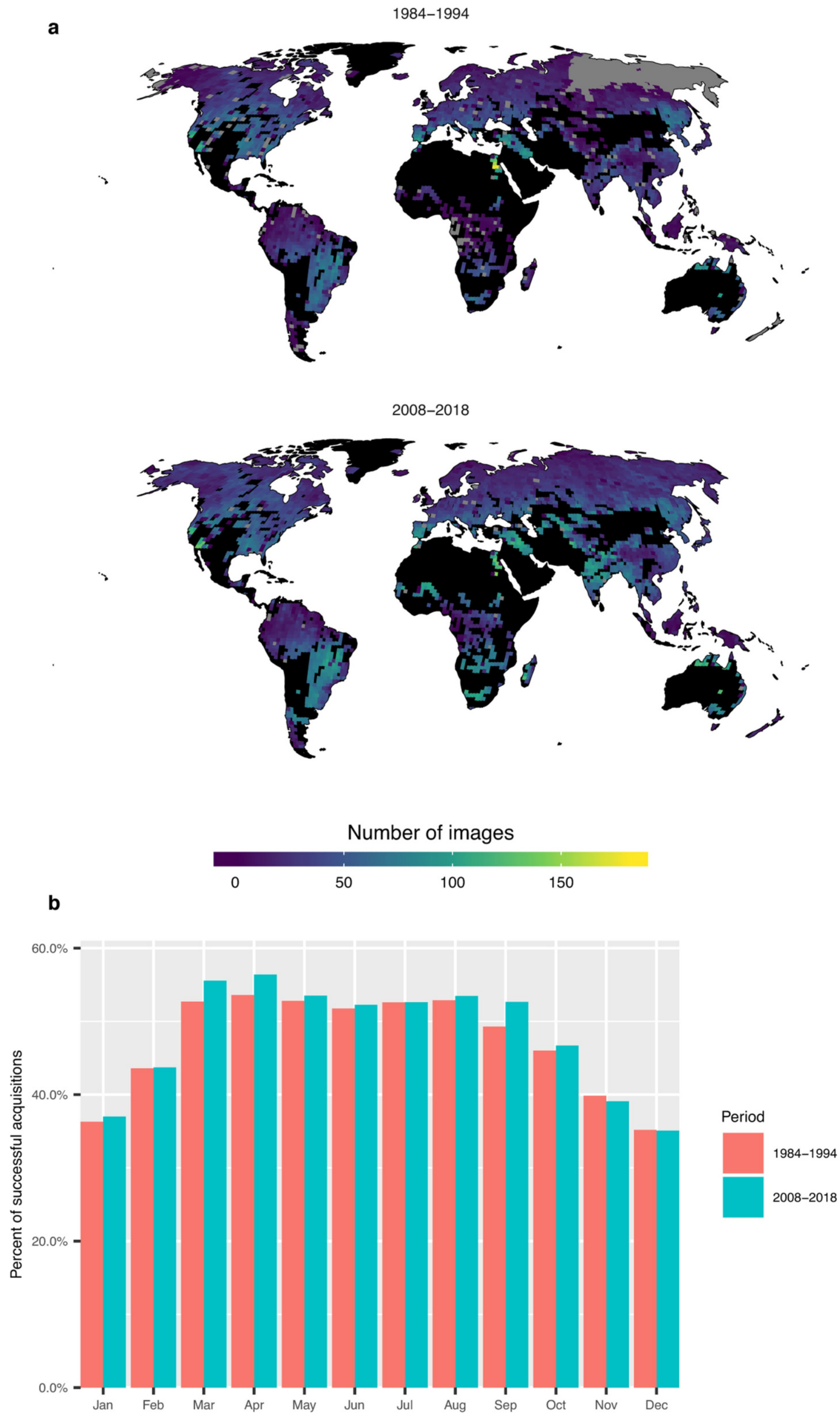

Extended Data Fig. 1 | Data availability between two historical decades. **a**, Data availability map for the decades 1984–1994 and 2008–2018 based on the river ice extent dataset. Black indicates no data or no studied river. **b**, Percentage of successful river ice observations for each month of each decade. The percentage was calculated by taking the ratio between the number of observations used in the historical analysis and the total number of Landsat river observations when no filters (cloud, topographic shadow and river length) were applied.

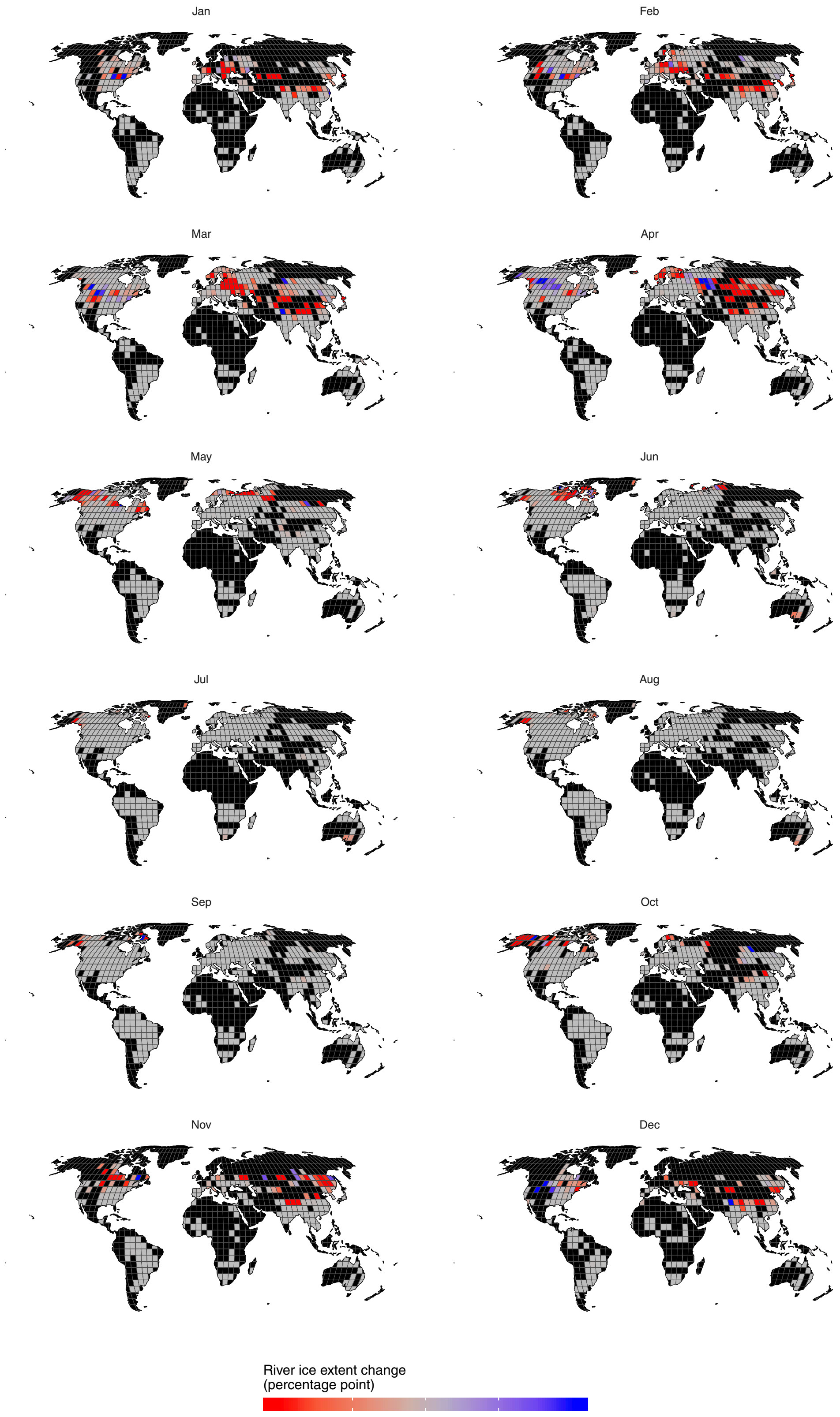

Extended Data Fig. 2 | Monthly maps of the changes in river ice extent between 1984–1994 and 2008–2018. Black indicates no data or no studied river.

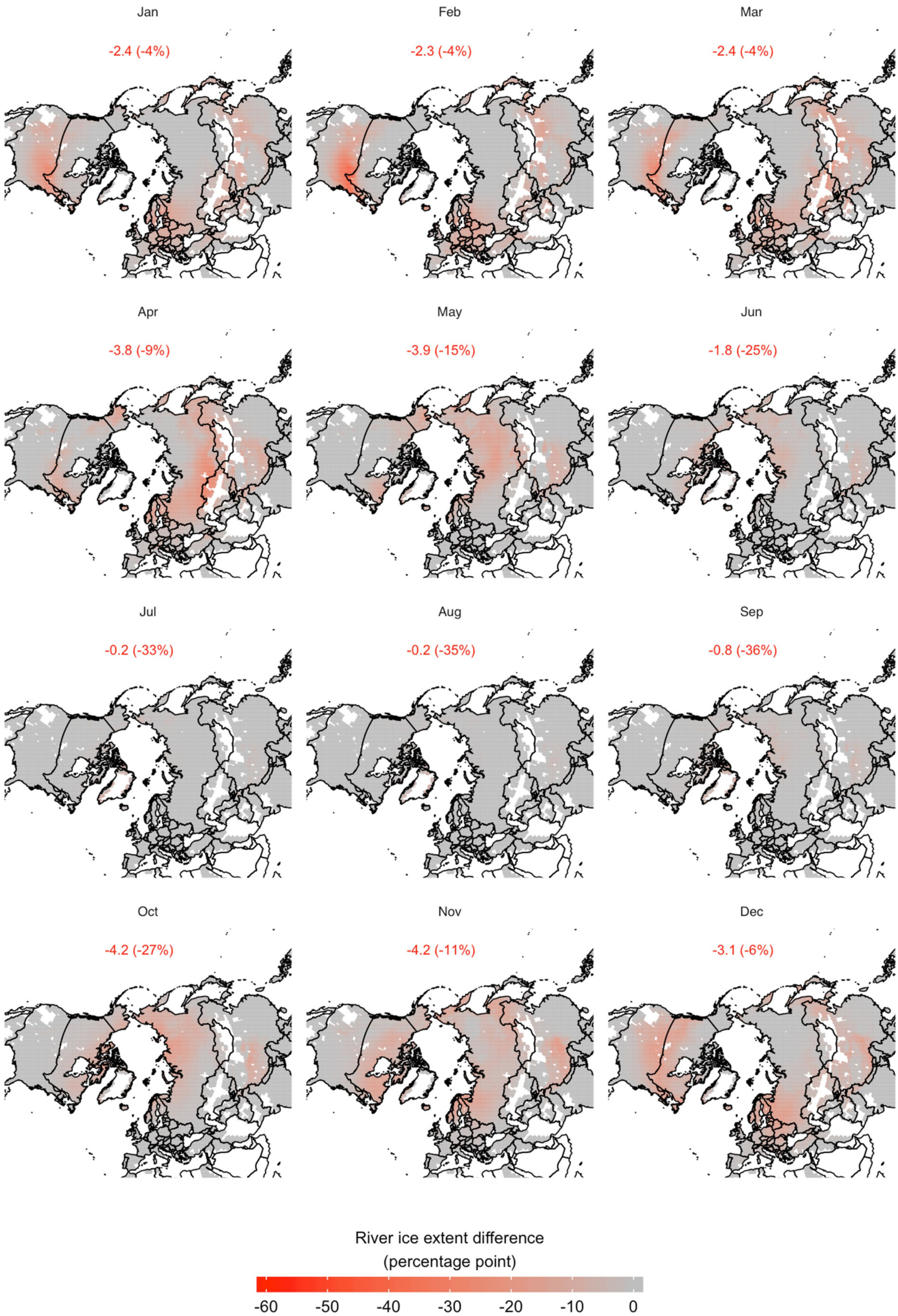

Extended Data Fig. 3 | Modelled average monthly river ice difference between 2009–2029 and 2080–2100 using CESM SAT output (RCP 4.5). The percentage point change over the Northern Hemisphere is listed under the month, with the percentage change in parentheses.

a

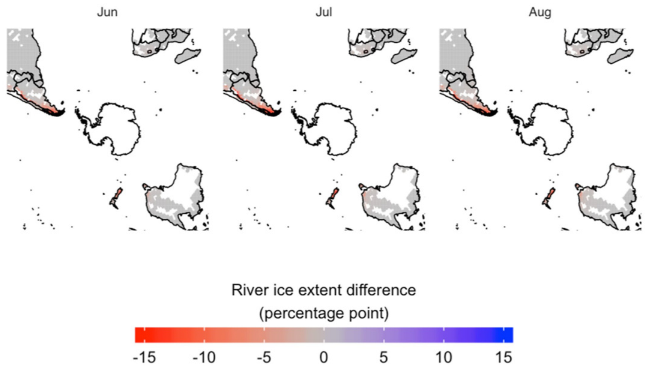

Month	Percentage point change	Percent change
Jan	-0.03	-61%
Feb	-0.02	-64%
Mar	-0.02	-65%
Apr	-0.05	-65%
May	-0.13	-61%
Jun	-0.3	-57%
Jul	-0.43	-55%
Aug	-0.39	-51%
Sep	-0.27	-50%
Oct	-0.16	-53%
Nov	-0.09	-58%
Dec	-0.05	-58%

b

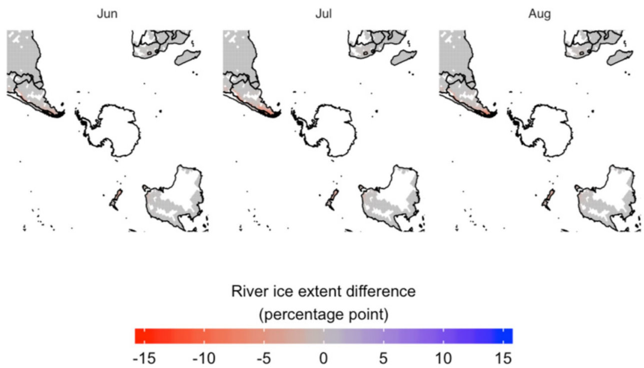

Month	Percentage point change	Percent change
Jan	-0.01	-25%
Feb	-0.01	-28%
Mar	-0.01	-31%
Apr	-0.02	-23%
May	-0.04	-22%
Jun	-0.09	-18%
Jul	-0.19	-24%
Aug	-0.15	-20%
Sep	-0.09	-17%
Oct	-0.07	-24%
Nov	-0.03	-23%
Dec	-0.02	-25%

Extended Data Fig. 4 | Modelled average monthly river ice difference between 2009–2029 and 2080–2100 using CESM SAT. a, Model output under RCP 8.5. **b**, Model output under RCP 4.5. Only the months that showed obvious changes in percentage points (June, July and and August) were mapped. The percentage point changes and percentage changes over the Southern Hemisphere are listed in the tables on the right.

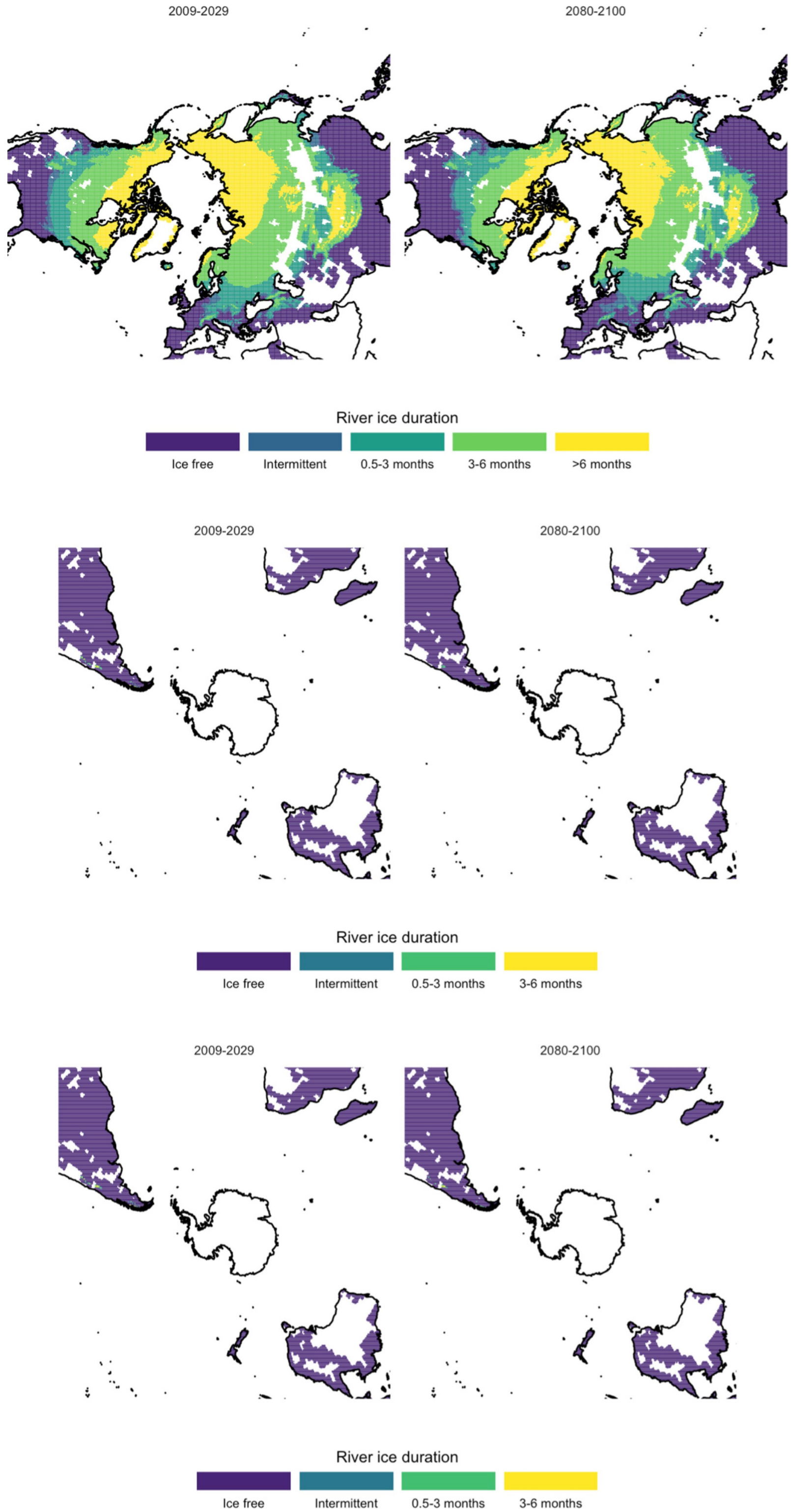

Extended Data Fig. 5 | Modelled ice duration zones between 2009–2029 and 2080–2100 using CESM modelled SAT. a, The Northern Hemisphere under RCP 4.5. **b**, **c**, The Southern Hemisphere under RCP 8.5 (**b**) and RCP 4.5 (**c**). Areas showing obvious changes are marked by red rectangles.

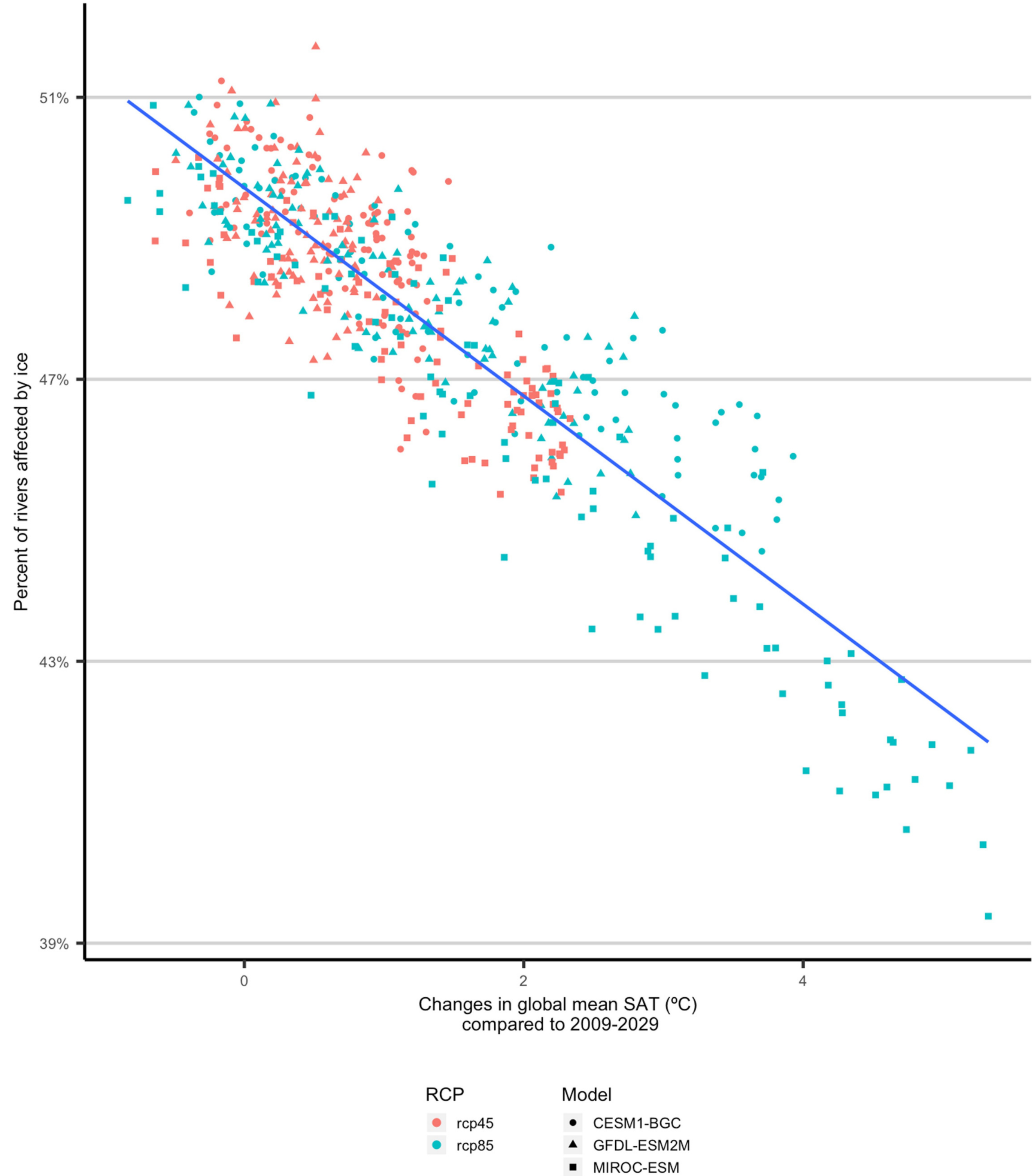

Extended Data Fig. 6 | Sensitivity of the changes in annual maximum river ice extent to the changes in global mean SAT. The sensitivity was assessed for three models (CESM1-BGC, GFDL-ESM2M and MIROC-ESM).

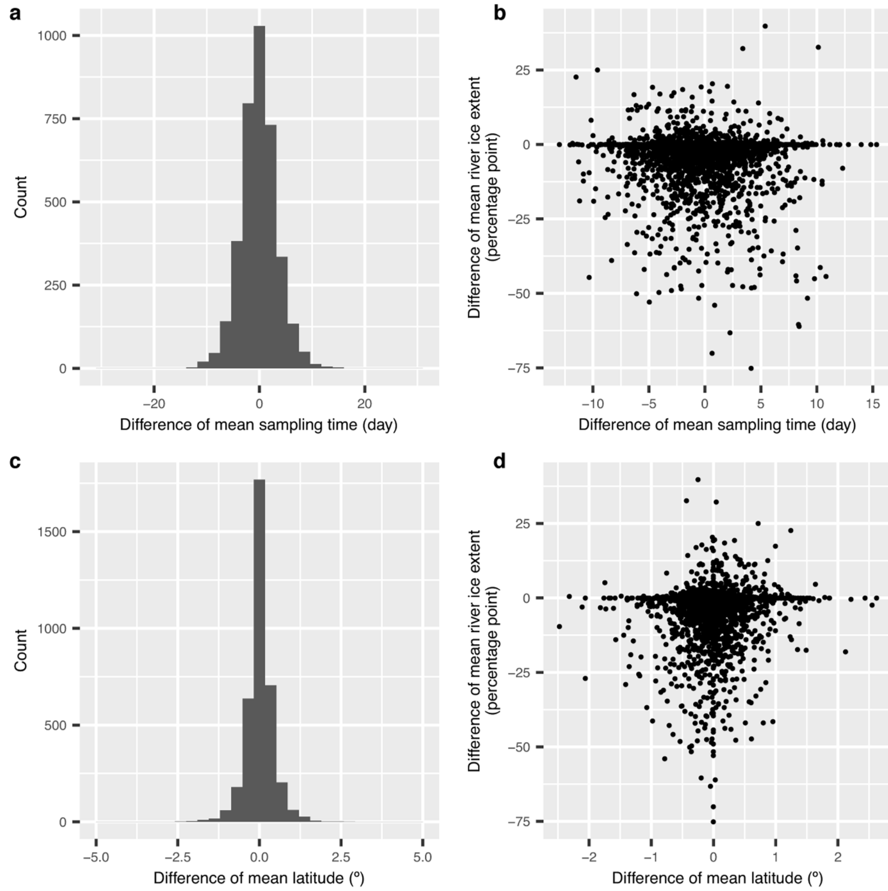

Extended Data Fig. 7 | Landsat sampling difference between the historical period 1984–1994 and 2008–2018. a, Distribution of the temporal sampling difference within each month. **b**, Temporal sampling difference and its relationship with the difference in the ice extent. **c**, Distribution of the spatial sampling difference within the 5° × 5° tiles. **d**, Spatial sampling difference and its relationship with the difference in the ice extent.

a

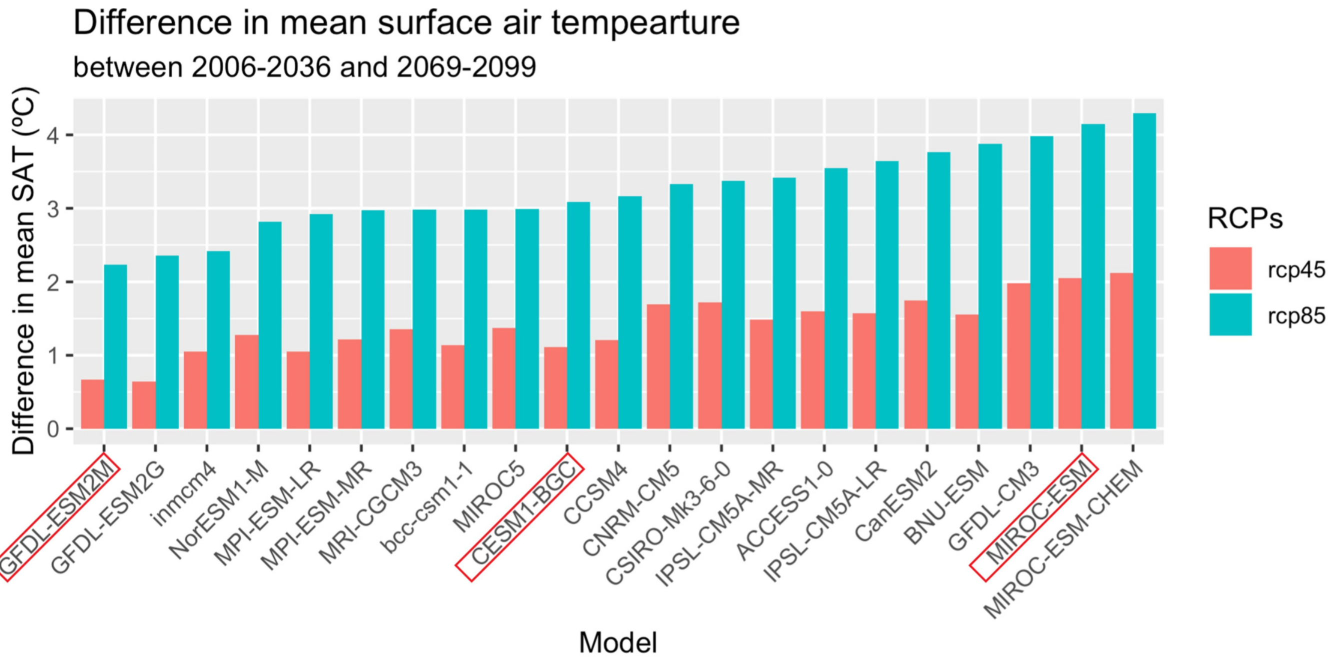

b

Model	**RCP**	**Duration Difference (days)**	**Global mean SAT difference (ºC)**
CESM1-BGC	8.5	-16.7	3.43
GFDL-ESM2M	8.5	-12.5	2.45
MIROC-ESM	8.5	-28.4	4.59
CESM1-BGC	4.5	-7.3	1.19
GFDL-ESM2M	4.5	-2.7	0.66
MIROC-ESM	4.5	-12.9	2.15

Extended Data Fig. 8 | Summary of river ice duration decline based on temperature outputs from three CMIP5 models. a, Difference in the global mean SAT across 21 CMIP5 models between 2006–2036 and 2069–2099. The three models used to assess future river ice change are marked with red rectangles. **b**, Decline in global mean river ice duration between 2009–2029 and 2080–2100 for the three selected models.

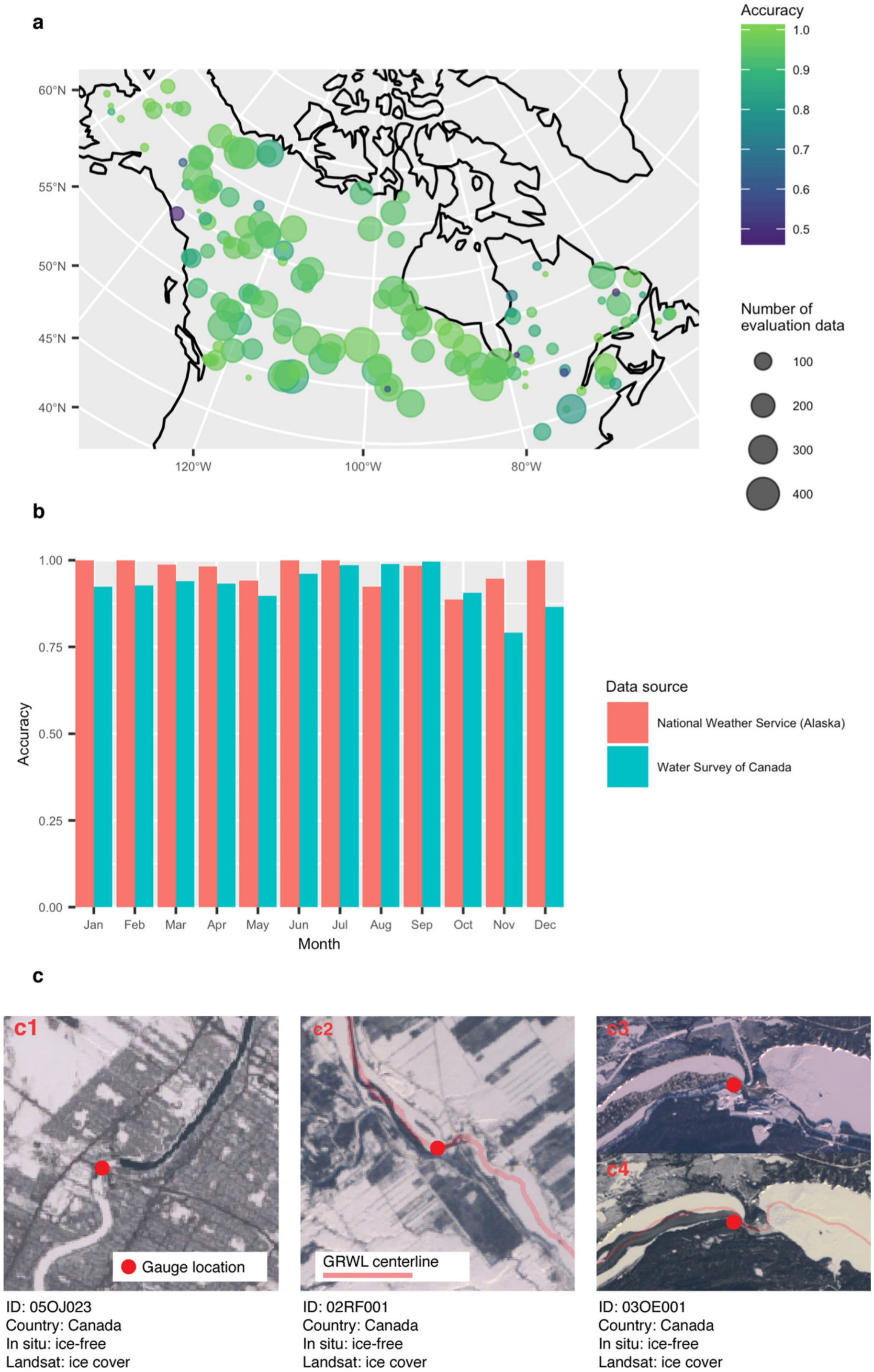

Extended Data Fig. 9 | Evaluating Landsat-derived river ice conditions against in situ river ice records. a, The accuracy of Landsat-derived river ice extents when evaluated against in situ reports of river ice condition. **b**, Monthly evaluation of Landsat-derived river ice estimates. **c**, Examples of differences in definition between remotely sensed and ground-based ice conditions. The GRWL centrelines are shown in images c2 and c4 to indicate the river. Satellite images courtesy of the US Geological Survey.

Extended Data Table 1 | Fmask-derived river ice evaluation across Landsat missions

Sensor	Accuracy	Specificity	Sensitivity	% of data
TM	0.943	0.957	0.919	72.3%
ETM+	0.933	0.943	0.922	12%
OLI	0.941	0.976	0.907	15.8%

Assessing progress towards sustainable development over space and time

https://doi.org/10.1038/s41586-019-1846-3

Received: 5 February 2018

Accepted: 6 November 2019

Published online: 1 January 2020

Zhenci Xu[1], Sophia N. Chau[1], Xiuzhi Chen[2], Jian Zhang[3], Yingjie Li[1], Thomas Dietz[1,4], Jinyan Wang[2], Julie A. Winkler[5], Fan Fan[6], Baorong Huang[7], Shuxin Li[1], Shaohua Wu[8], Anna Herzberger[1], Ying Tang[1,5], Dequ Hong[9], Yunkai Li[2]* & Jianguo Liu[1]*

To address global challenges[1–4], 193 countries have committed to the 17 United Nations Sustainable Development Goals (SDGs)[5]. Quantifying progress towards achieving the SDGs is essential to track global efforts towards sustainable development and guide policy development and implementation. However, systematic methods for assessing spatio-temporal progress towards achieving the SDGs are lacking. Here we develop and test systematic methods to quantify progress towards the 17 SDGs at national and subnational levels in China. Our analyses indicate that China's SDG Index score (an aggregate score representing the overall performance towards achieving all 17 SDGs) increased at the national level from 2000 to 2015. Every province also increased its SDG Index score over this period. There were large spatio-temporal variations across regions. For example, eastern China had a higher SDG Index score than western China in the 2000s, and southern China had a higher SDG Index score than northern China in 2015. At the national level, the scores of 13 of the 17 SDGs improved over time, but the scores of four SDGs declined. This study suggests the need to track the spatio-temporal dynamics of progress towards SDGs at the global level and in other nations.

To achieve these ambitious SDGs, the world needs to monitor progress towards all 17 SDGs by assessing past and current conditions at national and subnational levels[6]. However, no study has explored the spatio-temporal dynamics of progress towards the SDGs at both national and subnational levels. Such information is urgently needed, as many countries face the challenge of achieving sustainability in times of growing population, uneven development across regions within their borders and resource scarcity under rapidly developing economies. A spatio-temporal analysis of sustainable development can help countries to identify hotspot regions for targeted policy action and for tracking progress towards achieving the SDGs. Understanding the differences in sustainable development between developed and developing regions over time can help a nation to balance sustainable development across its regions.

In this study, we developed systematic methods to quantify the SDGs and provided a demonstration of quantification by performing a comprehensive spatio-temporal analysis of progress towards all 17 SDGs in China, the largest developing country both in areal extent and population. Over the past several decades, China has experienced rapid economic development, reflected in its exceptional growth in gross domestic product (GDP)[7] and becoming the world's second-largest economy. However, China also faces large socioeconomic challenges such as income and gender inequality[8], and environmental challenges such as water scarcity and pollution, energy shortages, and air and soil pollution[9]. These socioeconomic and environmental challenges within China vary substantially from region to region and have changed noticeably over time[10,11]. China is trying to achieve sustainability under complex environmental and socioeconomic challenges and policies[12]. To promote sustainable development, China has implemented a variety of policies such as the 'Western Development Strategy' and the 'Natural Forest Conservation Program'[11–13].

We tracked China's progress towards achieving the SDGs at the national and subnational (provincial) levels by quantifying (scoring) the SDGs over time (see details in the Methods). We addressed four major questions. First, how has sustainable development in China, as measured in terms of the SDGs, evolved at the national level? Second, how has sustainable development varied across China's provinces over time? Third, how have differences in sustainable development between more-developed and less-developed provinces in China evolved over time? Fourth, how has progress varied among the different SDGs?

To answer these questions, we used annual time series data relevant to the 17 SDGs from 2000 to 2015 at the national level and calculated the SDG Index score (0–100)[14], which consists of individual scores for the 17 SDGs and represents China's overall performance in achieving all 17 SDGs[14] (see details in the Methods). In total, 119 SDG indicators were used in this assessment (see data sources and indicator sources

[1]Center for Systems Integration and Sustainability, Department of Fisheries and Wildlife, Michigan State University, East Lansing, MI, USA. [2]College of Water Resources and Civil Engineering, China Agricultural University, Beijing, China. [3]School of Life Sciences, State Key Laboratory of Grassland Agro-ecosystems, Lanzhou University, Lanzhou, China. [4]Environmental Science and Policy Program, Department of Sociology and Animal Studies Program, Michigan State University, East Lansing, MI, USA. [5]Department of Geography, Environment, and Spatial Sciences, Michigan State University, East Lansing, MI, USA. [6]School of Economics, Renmin University of China, Beijing, China. [7]Institutes of Science and Development, Chinese Academy of Sciences, Beijing, China. [8]Institute of Land and Urban-Rural Development, Zhejiang University of Finance and Economics, Hangzhou, China. [9]Department of Humanities and Information, Zhejiang College of Construction, Hangzhou, China. *e-mail: yunkai@cau.edu.cn; liuji@msu.edu

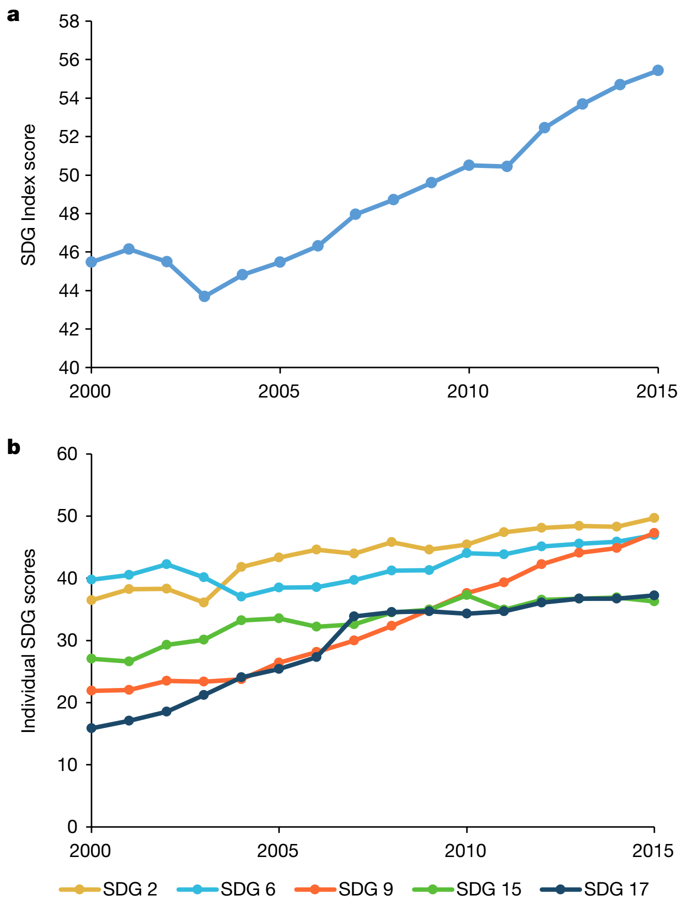

Fig. 1 | Change in China's SDG Index score and individual SDG scores. a, SDG Index score. **b**, Scores of selected SDGs (2, 6, 9, 15 and 17) at the national level from 2000 to 2015. For data sources, see Methods.

in Supplementary Table 1). We detected spatio-temporal changes in SDG Index scores across China's provinces based on data for the 17 SDGs at the provincial level in 2000, 2005, 2010 and 2015. We then compared the change in SDG Index scores over time between developed and developing provinces (determined by each province's average GDP per capita during 2000–2015; see details in the Methods) during the same period. Finally, by comparing scores for the individual SDGs we examined the relative progress toward achieving the different SDGs.

Results

Our results indicate that China has improved its SDG Index score at the national level over time (Fig. 1; Extended Data Fig. 1). Its national SDG Index score increased by approximately 21.9%, from a score of 45.5 in 2000 to 55.4 in 2015.

Notably, at the provincial level, eastern China had a higher SDG Index score than western China in the 2000s, while southern China had a higher SDG Index score than northern China in 2015, suggesting that substantial changes in sustainable development occurred across different regions (Fig. 2; see Supplementary Tables 2, 3). SDG Index scores at the provincial level ranged from 31.4 to 54.1 with a mean value of 42.2 in 2000, from 38.1 to 57.6 with a mean value of 45.2 in 2005, from 42.5 to 63.9 with a mean value of 49.8 in 2010, and from 47.0 to 66.1 with a mean value of 54.9 in 2015, reflecting a 30.0% increase in the mean value of the SDG Index score across provinces over time. The change in SDG Index score among provinces from 2000 to 2015 ranged from a 11.1% increase (Shanghai) to a 51.8% increase (Ningxia).

All provinces increased their SDG Index scores from 2000 to 2015 (Fig. 2; Supplementary Table 3). Developed provinces had higher SDG Index scores than developing provinces throughout our study period (Fig. 3; Supplementary Table 4). However, developing provinces experienced a greater growth rate in their average SDG Index scores than did developed provinces. These dynamics were also observed between the top five developed provinces and the bottom five developing provinces (Fig. 3; see details in the Methods).

At the national level, the scores of 13 of the 17 SDGs improved, while the scores of the remaining four SDGs decreased over time (Fig. 4). The four SDGs with declining scores, in order of greatest to least decline, were SDG 14 (life below water), SDG 12 (responsible consumption and production), SDG 5 (achieve gender equality) and SDG 13 (climate action) (Fig. 4). The three SDGs that improved the most, in order of greatest to least improvement, were SDG 9 (industry, innovation and infrastructure), SDG 10 (reduced inequalities), and SDG 17 (affordable and clean energy) . Generally, the changes in SDG scores at the provincial level showed similar dynamics as those at the national level (Supplementary Table 5). In terms of absolute SDG score, the bottom five SDGs, which lagged behind the other SDGs at the national level in 2015, included SDGs 15 (life on land), 14 (life below water), 17 (partnerships for the goals), 8 (decent work and economic growth) and 10 (reduced inequalities); see Supplementary Table 3.

Discussion

The spatio-temporal patterns of China's SDG Index scores may result from a number of factors, including the implementation of policies that have different regional impacts, geographical conditions, climate and infrastructure[13,15–17]. At the national level, factors such as governmental support for sustainability and investment in science and technology can strongly promote progress in national sustainable development (Supplementary Discussion). For the Chinese reform and opening-up policies that began in the late 1970s and early 1980s, the Chinese government focused on facilitating economic development more in eastern coastal regions than in inland regions, resulting in more advanced social services such as education and healthcare in eastern China[13]. Eastern China's relatively flat topography and favourable climate also make it more conducive for human habitation, as well as industrial and agricultural development[16]. Conversely, western China's rugged topography[11], combined with its distance from the coast, complicates transportation within the region and to and from other regions. As a result, in 2000, western China experienced limited urbanization and socioeconomic development and had the lowest industrialization level and highest poverty rate in China[16]. Western China's ecological assets have also historically limited its development (Supplementary Discussion). To alleviate this regional disparity, the Chinese government implemented the Western Development Strategy in 1999 to improve environmental and socioeconomic conditions in western China[13]. In 1999, only 29% of the Chinese government's fiscal transfers were allocated to western China, but this reached 39.4% in 2010[15]. Under the Western Development Strategy, both infrastructure development and ecological conservation in western China have greatly improved[17] (Supplementary Discussion). Meanwhile, after 2010 the growth rate of progress towards sustainable development (SDG Index score) in northeastern China fell behind other regions in socioeconomic development and environmental conservation because of low efficiency in resource use, unsustainable economic development and severe environmental pollution (Supplementary Discussion). Developed provinces experienced smaller increases in the SDG Index score than developing provinces mainly because they face problems associated with rapidly growing economies, such as a tendency for socioeconomic and gender inequality[18] to increase, as well as intensive resource consumption and severe environmental pollution (Supplementary Discussion).

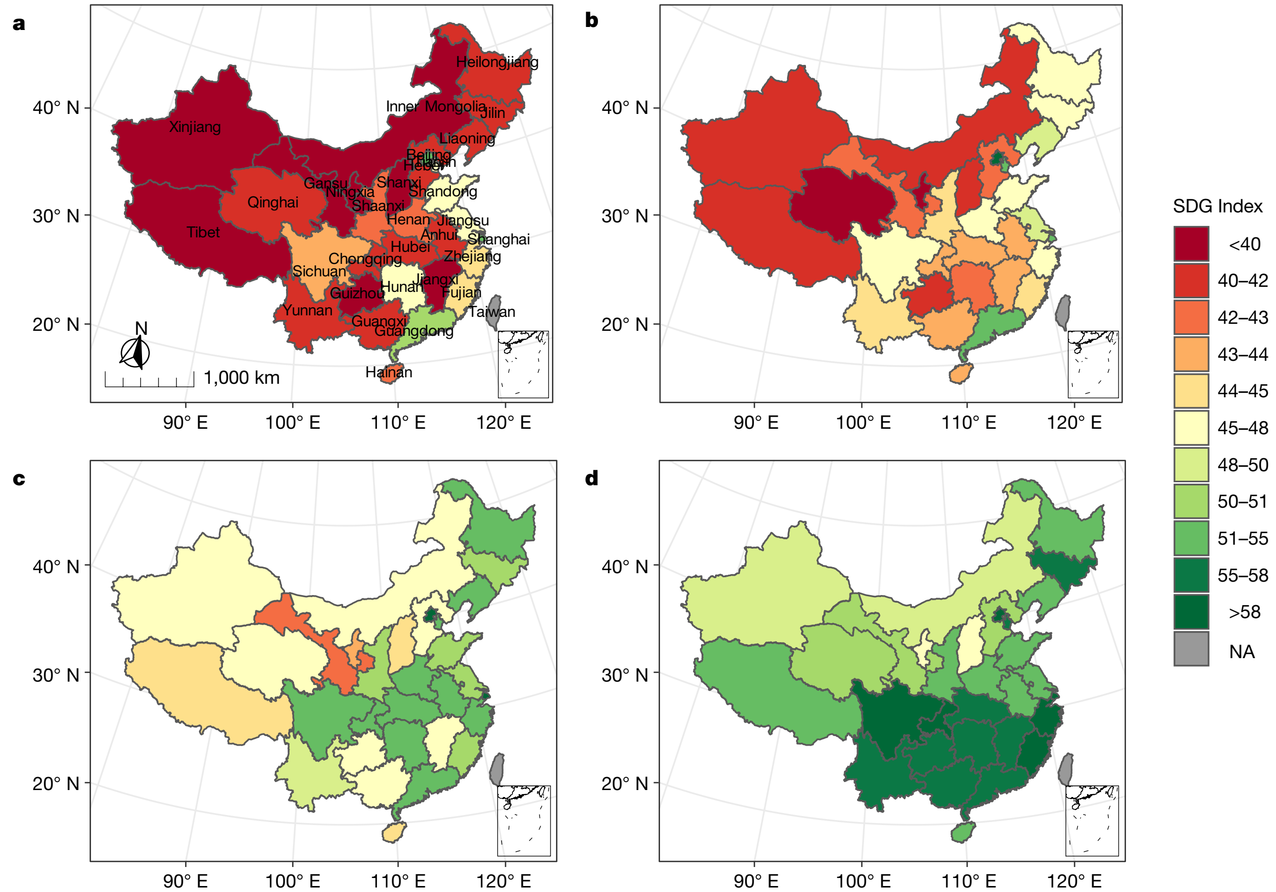

Fig. 2 | Spatial pattern of SDG Index scores in 2000, 2005, 2010 and 2015 for 31 Chinese provinces. a, 2000. **b**, 2005. **c**, 2010. **d**, 2015. The data for the base map was derived from the Resource and Environment Data Cloud Platform[39] and we generated the scores. For other data sources, see Methods. NA, not available.

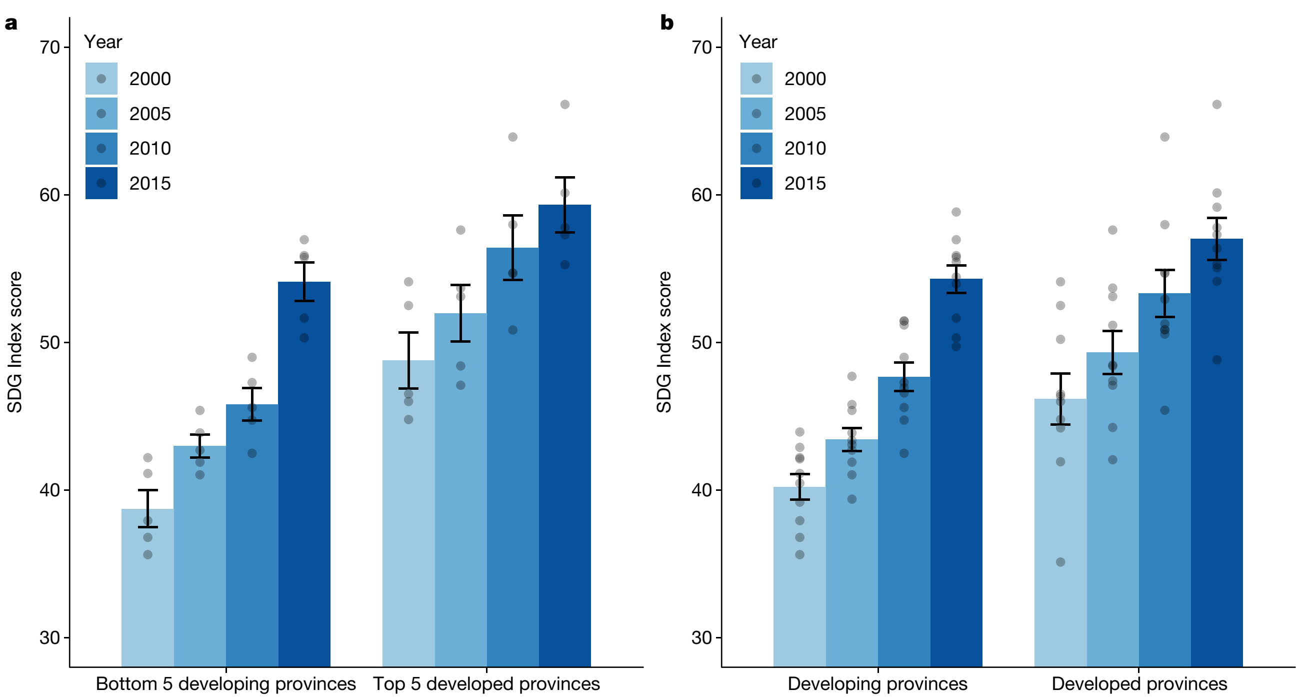

Fig. 3 | Comparison of average SDG Index scores for different groups of provinces in China. a, The top five developed (richest) provinces and the bottom five developing (poorest) provinces in China in 2000, 2005, 2010 and 2015 are compared. **b**, The developed provinces and developing provinces in China in 2000, 2005, 2010 and 2015 are compared. The vertical lines within the bar indicate the standard error in SDG Index scores ($n = 80$). For the data sources and a detailed definition for each category of province, see Methods.

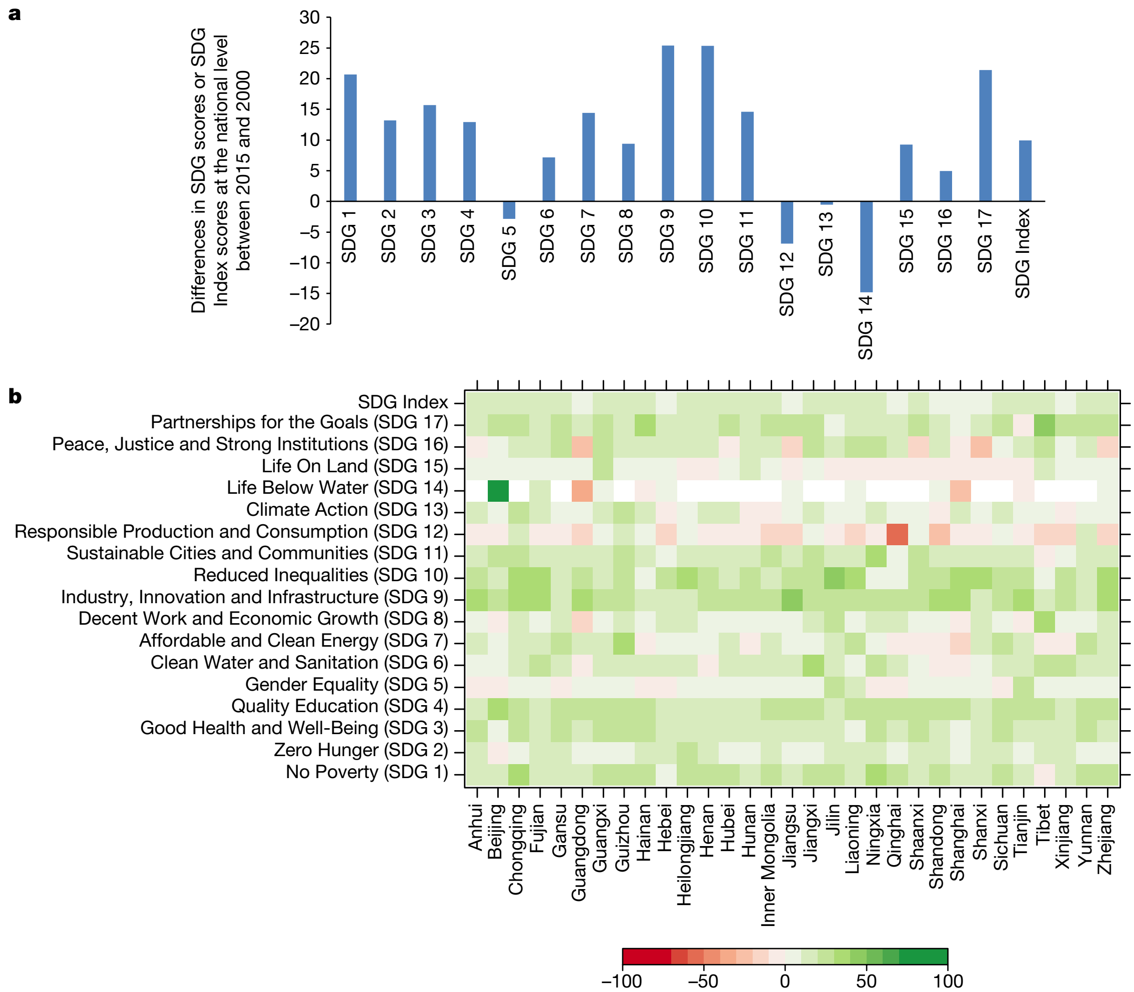

Fig. 4 | Differences in SDG scores or SDG Index scores between 2015 and 2000. a, At the national level. **b**, At the provincial level. The colour scale shows the change in the SDGs scores or SDG Index scores. A positive value (green) indicates an increase in the score from 2000 to 2015, while a negative value (red) indicates a decrease in the score from 2000 to 2015. For data sources, see Methods.

China's rapid technological advances, improved social services such as education and healthcare, and environmental conservation policies have all enhanced sustainability[10,11,13,19,20]. However, environmental problems such as water pollution and scarcity and land degradation still pose a great threat to China's sustainability because these burdens are often associated with other environmental problems such as biodiversity loss and severe droughts. Moreover, China's social problems, such as inequality, can be linked to other complex social problems (such as mental illness, violence, obesity, imprisonment, homicide, teen pregnancy, drug abuse and poor academic performance)[21] that make sustainability difficult to achieve. The Chinese government could therefore prioritize the SDGs that lag behind other SDGs, such as SDG 14 and SDG 15, while facilitating holistic sustainability through integrated policy action (Supplementary Discussion). In particular, for these SDGs more effective policies aimed at protecting life in water and on land are required. China can build on previous successes to deal with regional discrepancies. For example, policymakers could consider more strategies to promote development in northern China in order to reduce the gap in sustainable development between northern and southern China. Since the gap in sustainable development between western and eastern China has shrunk since the Western Development Strategy was implemented, lessons learned from the Western Development Strategy may help to close the gap in sustainable development between northern and southern China.

Future research could focus on the spillover effects of one region's actions on the sustainable development of other regions within China as well as on spillover effects across national borders[22] (Supplementary Discussion). Furthermore, exploring trade-offs and synergies between SDGs can help to reveal the complex mechanisms and consequences of sustainable development[23]. Research assessing the complex impacts of policies on sustainable development is also needed.

This study provides a temporal sustainability assessment of all 17 SDGs at national and subnational levels. China has mandated the monitoring of the progress toward the SDGs[24], but it has not developed systematic and comprehensive evaluation methods. Thus, the methods outlined in our paper are of value to China's monitoring efforts. Our approach might also lay a foundation for analysing spatio-temporal patterns of SDG progress for other countries and across local to global levels.

Online content

Any methods, additional references, Nature Research reporting summaries, source data, extended data, supplementary information, acknowledgements, peer review information; details of author contributions and competing interests; and statements of data and code availability are available at https://doi.org/10.1038/s41586-019-1846-3.

1. Liu, J. et al. Systems integration for global sustainability. *Science* **347**, 1258832 (2015).
2. Mekonnen, M. M. & Hoekstra, A. Y. Four billion people facing severe water scarcity. *Sci. Adv*. **2**, e1500323 (2016).
3. International Energy Agency. *World Energy Outlook 2015* (IEA, 2015).
4. Larivière, V., Ni, C., Gingras, Y., Cronin, B. & Sugimoto, C. R. Bibliometrics: global gender disparities in science. *Nature* **504**, 211–213 (2013).
5. United Nations. *Sustainable Development Goals: 17 Goals to Transform Our World* http://www.un.org/sustainabledevelopment/sustainable-development-goals/ (UN, 2015).
6. Schmidt-Traub, G., Kroll, C., Teksoz, K., Durand-Delacre, D. & Sachs, J. D. National baselines for the Sustainable Development Goals assessed in the SDG Index and Dashboards. *Nat. Geosci*. **10**, 547–555 (2017).
7. Rodrik, D. The past, present, and future of economic growth. *Challenge* **57**, 5–39 (2014).
8. Xie, Y. & Zhou, X. Income inequality in today's China. *Proc. Natl Acad. Sci. USA* **111**, 6928–6933 (2014).
9. Liu, J. G. et al. China's environment on a metacoupled planet. *Annu. Rev. Environ. Res*. **43**, 1–34 (2018).
10. Liu, J. & Diamond, J. China's environment in a globalizing world. *Nature* **435**, 1179–1186 (2005).
11. Ouyang, Z. et al. Improvements in ecosystem services from investments in natural capital. *Science* **352**, 1455–1459 (2016).
12. Bryan, B. A. et al. China's response to a national land-system sustainability emergency. *Nature* **559**, 193–204 (2018).
13. Ortuño-Padilla, A., Espinosa-Flor, A. & Cerdán-Aznar, L. Development strategies at station areas in Southwestern China: the case of Mianyang city. *Land Use Policy* **68**, 660–670 (2017).
14. Sachs, J., Schmidt-Traub, G., Kroll, C., Lafortune, G. & Fuller, G. *SDG Index and Dashboards Report 2018* https://www.sdgindex.org/reports/sdg-index-and-dashboards-2018 (Pica, 2018).
15. Lu, Z. & Deng, X. Regional policy and regional development: a case study of China's Western Development Strategy. *Ann. Univ. Apulensis Ser. Oeconomica* **15**, 250–264 (2013).
16. Gai, K. *Study on The Coordination between Ecological Environment and Economic Development in West China*. [in Chinese] https://www.sdgindex.org/reports/sdg-index-and-dashboards-2018, PhD thesis, Southwestern University of Finance and Economics (2008).
17. Yuan, N. *Study on the Sustainable Development of West China Economy.* [in Chinese] https://kns.cnki.net/KCMS/detail/detail.aspx?dbcode=CMFD&dbname=CMFD2008&filename=2008028325.nh&uid=WEEvREcwSlJHSldRa1FhdXNXaEhoOHRuWm1vU2REWU45b2ozL013SWRJTT0=$, Master's thesis, Sichuan University (2006).
18. Jayachandran, S. The roots of gender inequality in developing countries. *Ann. Rev. Econ*. **7**, 63 (2015).
19. Chen, Z. Launch of the health-care reform plan in China. *Lancet* **373**, 1322–1324 (2009).
20. Mok, K. H. & Wu, A. M. Higher education, changing labour market and social mobility in the era of massification in China. *J. Educ. Work* **29**, 77–97 (2016).
21. Wilkinson, R. G. & Pickett, K. E. Income inequality and social dysfunction. *Annu. Rev. Sociol*. **35**, 493–511 (2009).
22. Liu, J. An integrated framework for achieving Sustainable Development Goals around the world. *Ecol. Econ. Soc*. **1**, 11–17 (2018).
23. Nerini, F. F. et al. Mapping synergies and trade-offs between energy and the Sustainable Development Goals. *Nat. Energy* **3**, 10–15 (2018).
24. State Council of China. *China Implements the 2030 Agenda for Sustainable Development Country Programme* [in Chinese] https://www.fmprc.gov.cn/web/zyxw/t1405173.shtml (SSC, 2016).

Publisher's note Springer Nature remains neutral with regard to jurisdictional claims in published maps and institutional affiliations.

Methods

Six interrelated steps for calculating and comparing SDG scores

Step 1: indicator selection and data sources. We selected indicators from a combination of the United Nations' official list of global Sustainable Development Goal indicators[25], the 2018 SDG Index and Dashboards Report[14] and a report of the United Nations titled "Indicators and a Monitoring Framework for the Sustainable Development Goals"[26]. The 2018 SDG Index and Dashboards Report and the Monitoring Framework Report were published by the Sustainable Development Solutions Network, which operates under the auspices of the United Nations to promote the implementation of the SDGs and the Paris Climate Agreement. The 2018 SDG Index and Dashboards Report provides a robust, quantitative and transparent method of measuring SDG baselines at the country level that has been used in a subsequent peer-reviewed paper[6]. In addition to the above indicators, we also constructed additional indicators based on our understanding of the SDG targets.

For each SDG, we chose as many SDG indicators as was feasible from the list of recommended indicators, based on data availability both at the provincial and national levels and the availability of the indicators across organizational levels and temporal scales (see Supplementary Methods for an example of indicator selection for SDG 6). This approach follows that of previous studies[27,28]. Our list of indicators included a total of 119 SDG indicators at both the national level and provincial level over time, which is greater than the number of indicators in the 2018 SDG Index and Dashboards Report (which used 88 indicators to assess China's SDGs performances for a single year).

Data for the selected indicators in this study were obtained from the following authoritative sources: the National Bureau of Statistics of the People's Republic of China, the China Statistical Yearbook[29], the Finance Yearbook of China[30], the China Statistical Yearbook on the Environment[31], the Educational Statistics Yearbook of China[32], the China Health Statistics Yearbook[33], the China Energy Statistical Yearbook[34] and the China Population Statistics Yearbook[35]. See Supplementary Table 1 for a list of SDGs and their corresponding indicators and the data sources used in this paper.

Step 2: bound selection. To ensure comparability across different SDGs, the indicator values for each SDG were normalized to a standard scale ranging from 0 (worst-performing indicator value towards achieving SDGs, or worst performance) to 100 (best-performing indicator value towards achieving SDGs, or best performance). 'Performance' refers to the progress of a nation or subnational unit towards achieving a single SDG or all 17 SDGs as a whole, measured in terms of SDG indicator values. A higher normalized SDG score indicates better performance towards achieving an SDG. For the national level analysis, we pooled the annual values for 2000–2015 for the selected indicator metrics of each SDG. Thus, the data for each SDG indicator includes 16 indicator values (one per year) that reflect the temporal dynamics of China's overall performance towards that SDG indicator. At the provincial level, we pooled, again separately for each SDG indicator, the values of the indicator metric for the 31 provinces for four years (2000, 2005, 2010 and 2015). In this case, the data reflect the temporal dynamics for each province towards meeting the individual SDGs.

We followed the methods proposed by the 2018 SDG Index and Dashboards Report[14] to normalize the national and provincial data arrays for each SDG indicator. These methods of establishing an upper and a lower bound minimize the potential effects of skewed data because they offset the effects of extreme values on both tails of the data distribution.

Similarly, we identified upper and lower bounds for each SDG indicator in order to minimize the potential effects of skewed data distributions on the standardized values during normalization. Our method for setting the upper bound is similar to the approach used in the 2018 SDG Index and Dashboards report in order to make it easier to compare China with other countries. The upper bound for each indicator was determined using a five-step decision tree. If the condition for an earlier step is met, then all of the later steps are skipped. First, for all indicators that are also used in the 2018 SDG Index and Dashboards report, we adopted the bound used in the 2018 SDG Index and Dashboards report. Second, we used relevant absolute quantitative thresholds for SDGs and targets, such as 'no poverty' and 'absolute gender equality'. Third, if no explicit SDG target was stated, we adopted the principle of 'leave no one behind' to determine the upper bound of zero deprivation or universal access for the following types of indicators: (1) public service coverage, and disease and pollution control, (2) measures of ending hunger (consistent with the SDG purpose to remove extreme hunger in all forms), and (3) access to basic infrastructure (for example, mobile phone coverage). Fourth, where they exist, we used science-based targets set for 2030 or later. Fifth, we set the upper bound for all other indicators equal to the average of the top five performers across the provincial and national levels together.

In terms of lower bound, for all indicators that were used in the 2018 SDG Index and Dashboards report, we adopted the lower bound used in the 2018 SDG Index and Dashboards report. For other indicators, the lower bound was defined as the SDG indicator value (one data point) located close to the value of the bottom 2.5th-percentile performer (across all provinces over four time steps (2000, 2005, 2010 and 2015) and entire China over time (2000–2015 annually)) of the sorted arrays, which was also similar to criteria in the 2018 SDG Index and Dashboard report for selecting the lower bound[14]. If the place of the bottom 2.5th percentile was located between two consecutive integers, the larger or smaller interger was used as the place for the lower bound when a larger indicator data value represented better or worse performance. We specified 'top-performing SDG indicator values' and 'bottom-performing SDG indicator values' rather than referring to the data points as simply high or low values, because a low value may represent high performance in some SDGs (for example, zero poverty) but poor performance in others (for example, amount of protected areas).

Step 3: normalization of indicator values. After establishing the lower and upper bound for each indicator, we used the following formula to normalize SDG indicator values towards meeting a SDG target at the national and provincial levels on a scale of 0 to 100 (ref. [14]):

$$x' = \frac{x - \min(x)}{\max(x) - \min(x)} \times 100$$

where x is the original data value of each SDG indicator, max/min represents the upper/lower bounds for the best/worst performance, and x' is the normalized individual score for a given SDG indicator. All normalized values greater than the upper bound received a score of 100, and all normalized values less than the lower bound received a score of 0. Values between the upper and lower bounds were distributed along the spectrum from the worst performance (score 0) to the best performance (score 100). A province with a score of 50 is halfway towards achieving the best performance. The normalized scores can be used to evaluate relative performance over time and space towards achieving the SDGs. For example, if for a particular SDG indicator a province lagged behind all other provinces in both 2000 and 2015 but improved over time, its score for that SDG indicator in 2015 would be greater than its score in 2000, but in both years, its score would be lower than that of the other provinces. We normalized the data across provincial and national levels together, so that the SDG scores are comparable across China and its provinces.

Step 4: calculation of SDG Index scores. We calculated SDG Index scores at the national and provincial levels using arithmetic means, following the approach used in the 2018 SDG Index and Dashboards Report[14]. This is an aggregate score that consists of individual scores

for all 17 SDGs and represents China's overall performance in achieving all 17 SDGs over time[14]. All SDGs were weighted equally in the SDG Index score to convey the importance of integrated solutions that equally address all 17 SDGs[14]. Consistent with previous research[6,14], there is no a priori reason to give one measure greater weight than another[6,14]. The equal weighting is also consistent with the spirit that all countries need to achieve all 17 SDGs through integrated strategies[6,14]. Within each SDG each indicator is equally weighted, which means that every indicator is weighted inversely to the number of indicators available for that SDG[14].

Step 5: calculation of SDG Index scores and individual SDG score over time and between organization levels. At the national level, we aggregated China's 17 SDG scores into one national SDG Index score for each year from 2000 to 2015, yielding 16 SDG Index scores. At the provincial level, we aggregated each province's 17 SDG scores for 2000, 2005, 2010 and 2015, separately, yielding four SDG Index scores per province. In addition, we calculated the change in SDG scores separately for each of the 17 individual SDG scores and for China and its provinces, by subtracting the normalized score in 2000 from the score in 2015. The SDGs with the bottom five scores in 2015 were considered to be the bottom five SDGs, lagging behind other SDGs.

Step 6: comparison of SDG Index scores between developing and developed regions. Ten developing provinces and ten developed provinces in China were selected to compare SDG Index scores between relatively more- and less-developed regions, based on each province's average GDP per capita from 2000 to 2015[36]. Provinces with the highest ten GDP values per capita were considered to be developed provinces, whereas provinces with the lowest ten GDP values per capita were considered to be developing provinces. We also designated provinces with the highest five GDP values as the top five developed provinces and provinces with the lowest five GDPs as the bottom five developing provinces. Finally, we compared the average SDG Index scores, calculated across all SDGs, between developed and developing provinces.

Uncertainty and sensitivity analysis for SDG scores

To explore the uncertainty introduced by the number of SDG indicators, we ran uncertainty analyses. For each SDG, we analysed all possible combinations of SDG indicators for all possible numbers of SDG indicators, which yielded a distribution of SDG scores for China in 2015. This allowed us to determine the impact of different numbers of indicators and different combinations of indicators on the SDG score. We found that as the number of indicators increased, the uncertainty (variation) in the SDG score decreased. When the number of indicators per SDG is two or larger, the median SDG score was almost constant (Extended Data Fig. 2). We performed an uncertainty analysis for SDG 9 as an example using all combinations of SDG indicators, under all possible numbers of SDG indicators. Given that the total number of indicators for SDG 9 is 14, the possible number of indicators to be selected for an uncertainty analysis ranges from 1, 2,... to 14. The number of possible combinations of indicators can be calculated based on the theory of combinations.

When we choose m indicators from a total of n indicators, the number of possible combinations is:

$$C_n^m = \frac{n!}{m!^*(n-m)!}$$

For example, when selecting one indicator, there are only 14 possible combinations (that is, 1, 2, 3,..., 14).

When we choose 2 indicators from 14 indicators, the number of possible combinations is

$$C_{14}^2 = \frac{1\times 2\times \ldots \times 12\times 13\times 14}{(1\times 2)\times(1\times 2\times \ldots \times 10\times 11\times 12)} = 91$$

When selecting 3–13 indicators, the numbers of combinations are 364, 1,001, 2,002, 3,003, 3,432, 3,003, 2,002, 1,001, 364, 91 and 14, respectively. When selecting all 14 indicators for analysis, there is only one combination.

Next we calculated the scores of SDG 9 for all these combinations of SDG indicators under different possible numbers of selected indicators. We obtained the distribution of SDG 9 scores for China in 2015 to determine the effect of the number of indicators under all potential combinations of indicators on the SDG score. We found that as the number of indicators for SDG 9 increased, the uncertainty (variation) decreased. When the number of indicators for SDG 9 was two or larger, the median SDG score remained almost constant (Extended Data Fig. 2).

We also ran a sensitivity analysis[37] to assess the sensitivity of the SDG scores to different values of variables that affect the SDG scores. We employed a widely used sensitivity index to measure the degree of sensitivity[38]: $S_x = (\Delta X/X)/(\Delta P/P)$ where X is the SDG score under the original condition for a performer of interest, ΔX is the difference of the SDG score for the performer of interest (for example, one province in a specific year) between the original and modified conditions due to changes in the performer's data value of a certain SDG indicator. P represents the value of an SDG indicator of the performer of interest under the original condition and ΔP is the difference in the data value of the SDG indicator of the performer between the original and modified conditions. S_x refers to the change in the SDG score of the performer due to the change in the data value of the SDG indicator. We decreased and increased (separately) the value for each indicator by 10% for China at the national level as well as for three randomly chosen provinces (Beijing, Henan and Gansu) from provinces at three sustainable development levels (average SDG Index scores in years 2000, 2005, 2010 and 2015: 1st to 10th-highest as high level, 11th to 20th as middle level, 21st to 31st as low level) as examples and recalculated their SDG score and obtained the sensitivity index S_x. We found that the sensitivity of SDG scores to changes in an indicator's data value is very small (less than 0.2) (Extended Data Fig. 3).

To assess where China stands relative to the rest of the world, we recalculated China's SDG Index score using the indicators that overlapped between our paper and the 2018 SDG Index and Dashboards report. China's SDG Index score over time relative to the rest of world in one year is shown (Extended Data Fig. 4).

To examine the spatio-temporal heterogeneity of SDGs at the provincial level, we calculated the coefficient of variation for each SDG score across provinces over time (Extended Data Fig. 5).

Reporting summary

Further information on research design is available in the Nature Research Reporting Summary linked to this paper.

Data availability

All data are available from the corresponding authors upon reasonable request. Data that support the findings of this study are available within the paper and its Supplementary Information.

25. United Nations Statistics Division. *SDG Indicators* https://unstats.un.org/sdgs/indicators/indicators-list (UNSD, 2017).
26. Schmidt-Traub, G., De la Mothe Karoubi, E. & Espey, J. *Indicators and a Monitoring Framework for the Sustainable Development Goals: Launching a Data Revolution for the SDGs* https://ec.europa.eu/knowledge4policy/publication/indicators-monitoring-framework-sustainable-development-goals-launching-data-revolution_en (Sustainable Development Solutions Network, 2015).
27. Golding, N. et al. Mapping under-5 and neonatal mortality in Africa, 2000-15: a baseline analysis for the Sustainable Development Goals. *Lancet* **390**, 2171–2182 (2017).
28. Alia, D. Y. Progress toward the sustainable development goal on poverty: assessing the effect of income growth on the exit time from poverty in Benin. *Sustain. Dev.* **25**, 495–503 (2017).
29. National Bureau of Statistics of the People's Republic of China. *China Statistical Yearbook* [in Chinese] http://www.stats.gov.cn/tjsj/ndsj/ (China Statistics Press, 2001–2016).

30. Ministry of Finance of the People's Republic of China. *Finance Yearbook of China* [in Chinese] http://tongji.cnki.net/kns55/navi/HomePage.aspx?id=N2014020005&name=YZGCZ (China Financial & Economic Publishing House, 2001–2016).
31. National Bureau of Statistics & State Environmental Protection Administration of the People's Republic of China. *China Statistical Yearbook on Environment* [in Chinese] http://www.shujuku.org/china-environmental-statistics-yearbook.html (China Statistics Press, 2001-2016).
32. Ministry of Education of the People's Republic of China. *Educational Statistics Yearbook of China* [in Chinese] http://tongji.cnki.net/kns55/Navi/HomePage.aspx?id=N2012010030&name=YZKRM&floor=1 (People's Education Press, 2001-2016).
33. Ministry of Health of the People's Republic of China. *China Health Statistical Yearbook* [in Chinese] http://www.shujuku.org/china-health-statistical-yearbook.html (Peking Union Medical College Press, 2001-2016).
34. National Bureau of Statistics of the People's Republic of China. *China Energy Statistical Yearbook* [in Chinese] http://tongji.cnki.net/kns55/Navi/HomePage.aspx?id=N2016120537&name=YCXME&floor=1 (China Statistics Press, 2001–2016).
35. National Bureau of Statistics of the People's Republic of China. *China Population Statistics Yearbook* [in Chinese] http://tongji.cnki.net/kns55/navi/HomePage.aspx?id=N2007091124&name=YZGRL&floor=1 (China Statistics Press, 2001-2006).
36. Costa, L., Rybski, D. & Kropp, J. P. A human development framework for CO_2 reductions. *Plos One* **6**, e29262 (2011).
37. Turner, M. G., Wu, Y., Wallace, L. L., Romme, W. H. & Brenkert, A. Simulating winter interactions among ungulates, vegetation, and fire in northern Yellowstone Park. *Ecol. Appl*. **4**, 472–496 (1994).
38. Liu, J. & Ashton, P. S. FORMOSAIC: an individual-based spatially explicit model for simulating forest dynamics in landscape mosaics. *Ecol. Modell*. **106**, 177–200 (1998).
39. Institute of Geographic Sciences and Natural Resources Research of Chinese Academy of Sciences. *Resource and Environment Data Cloud Platform* [in Chinese] http://www.resdc.cn/data.aspx?DATAID=202 (2015).
40. Frigge, M., Hoaglin, D. C. & Iglewicz, B. Some implementations of the boxplot. *Am. Stat*. **43**, 50–54 (1989).
41. Krzywinski, M. & Altman, N. Visualizing samples with box plots. *Nat. Methods* **11**, 119–120 (2014).

Acknowledgements We acknowledge edits from S. Nichols and K. Kapsar, and data compilation from Y. Liu, Y. Wang, Z. Zhou and Y. Sun. We are grateful for financial support from the National Science Foundation, Michigan State University, Michigan AgBioResearch, the China Scholarship Council and the National Natural Science Foundation of China (grant numbers 51621061 and 51321001).

Author contributions Z.X. and J.L. designed the research. Yunkai Li and X.C. contributed and checked data. Z.X., S.N.C., J.L., T.D., Yunkai Li, Y.T., X.C., S.L., B.H., A.H., J.A.W. and D.H. provided comments on the manuscript. Z.X., J.Z., Yingjie Li and F.F. analysed the data. Yunkai Li and X.C. helped to analyse data related to SDGs 2 and 6. Z.X., S.N.C., J.Z., Yingjie Li and J.L. wrote the manuscript. All authors reviewed the manuscript.

Competing interests The authors declare no competing interests.

Additional information

Supplementary information is available for this paper at https://doi.org/10.1038/s41586-019-1846-3.

Correspondence and requests for materials should be addressed to Yunkai Li or J.L.

Peer review information *Nature* thanks Brett Bryan, Xiangzheng Deng, Lei Gao and Jürgen Kropp for their contribution to the peer review of this work.

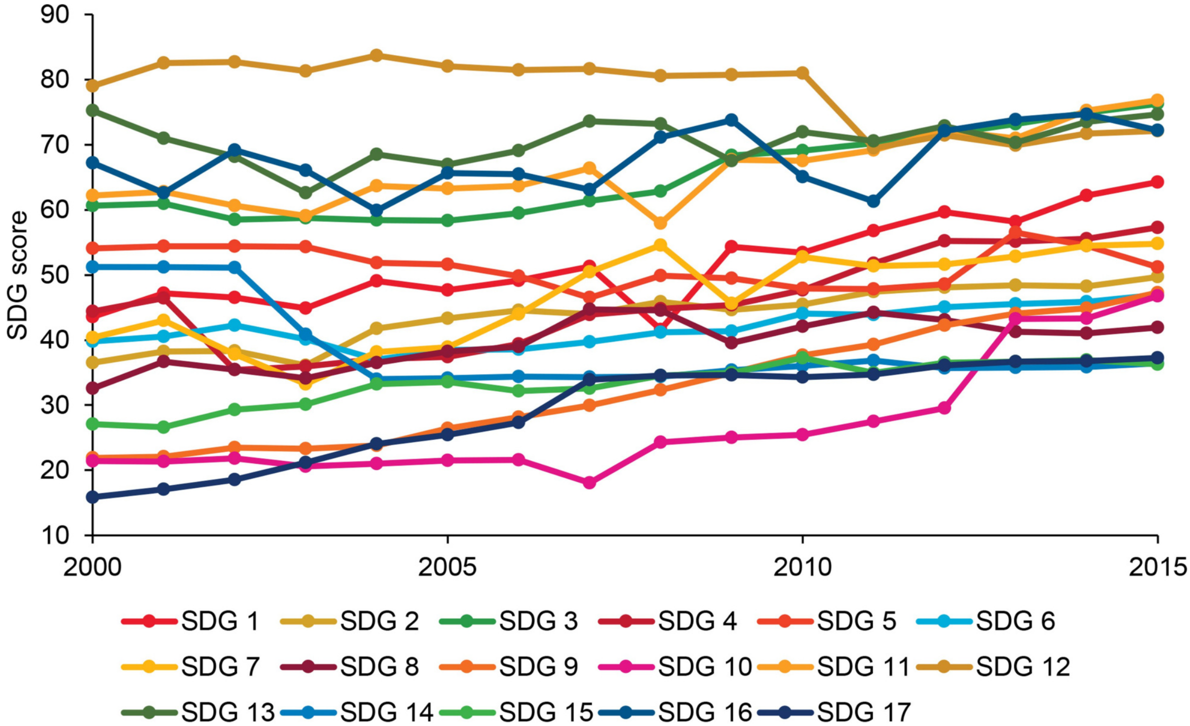

Extended Data Fig. 1 | Change in China's individual SDG scores at the national level from 2000 to 2015. For data sources, see Methods.

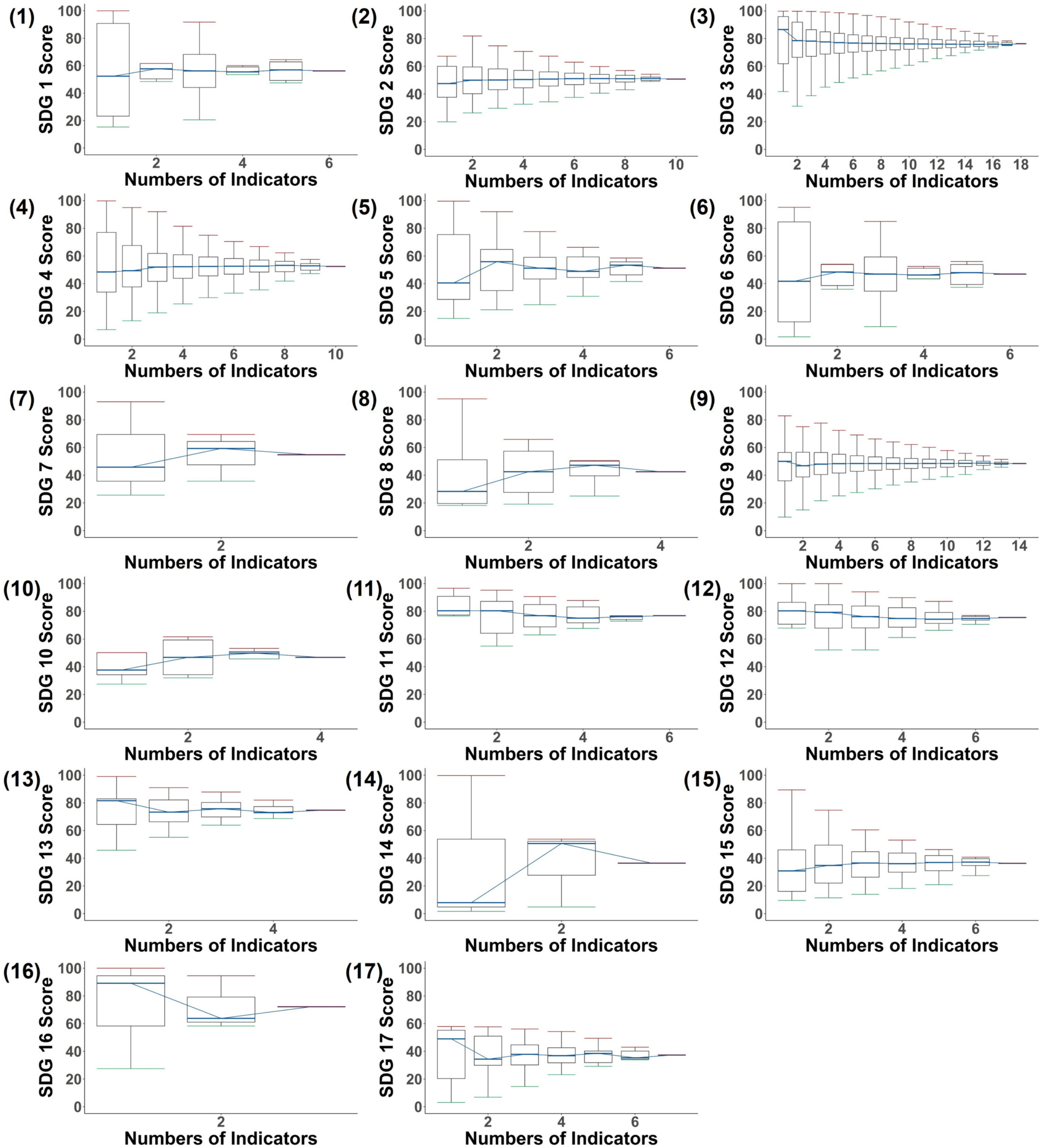

Extended Data Fig. 2 | Uncertainty analysis for SDG scores (n = 281,287) at the national level in 2015 for different numbers of selected indicators. 1–17 indicates uncertainty analysis for SDG 1–17. Sample sizes are 63, 1,023, 262,143, 1,023, 63, 63, 7, 15, 16,383, 15, 63, 127, 31, 7, 127, 7 and 127 for box plots of SDG 1–17. In each box plot, the central rectangle spans the first quartile Q1 to the third quartile Q3, which is the interquartile range (IQR)[40,41] (IQR = Q3 to Q1), while the line segment inside the rectangle shows the median. When the maximum observed SDG scores are greater than Q3 + 1.5 × IQR[40,41], the upper whisker (red) is Q3 + 1.5 × IQR[40,41]. Otherwise, the upper whisker is the maximum observed SDG score. When the minimum observed SDG scores are less than Q1 − 1.5 × IQR[40,41], the lower whisker (green) is Q1 − 1.5 × IQR. Otherwise, the lower whisker is the minimum observed SDG score[40,41].

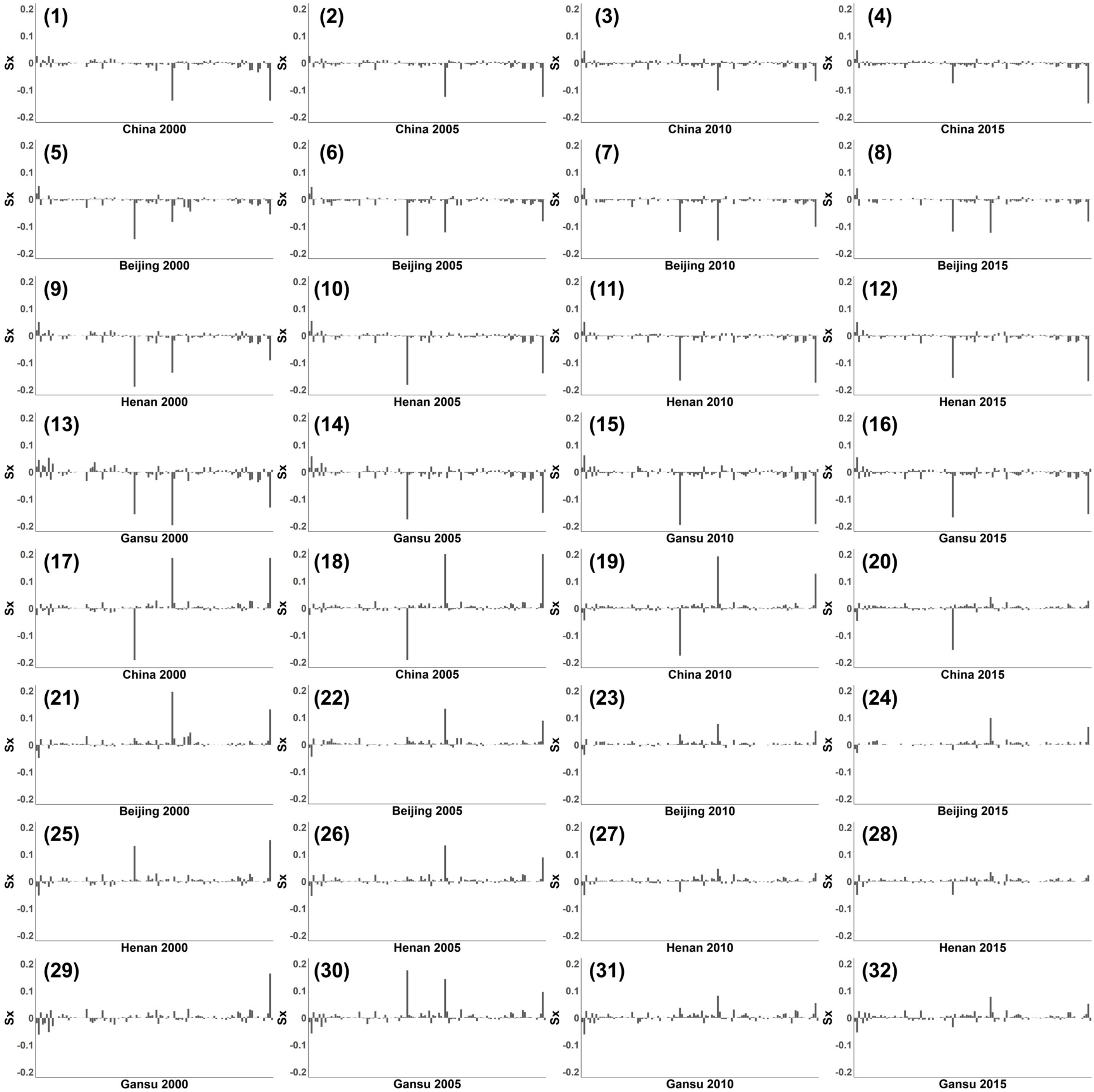

Extended Data Fig. 3 | Sensitivity of SDG scores to changes in each indicator. The sensitivity index S_x of SDG scores is shown when each SDG indicator's original data value decreased by 10%, (1)–(16), or increased by 10%, (17)–(32), for China and for three example provinces (Beijing, Henan and Gansu) at three levels (high, middle and low) of the average SDG scores in 2000, 2005, 2010 and 2015. The sample size *n* for each figure is 119 indicators. The *x* axes display the SDG indicators arranged from 1 to 119. The *y* axis is the sensitivity index S_x of SDG scores due to the 10% decrease or increase in the original value of each indicator.

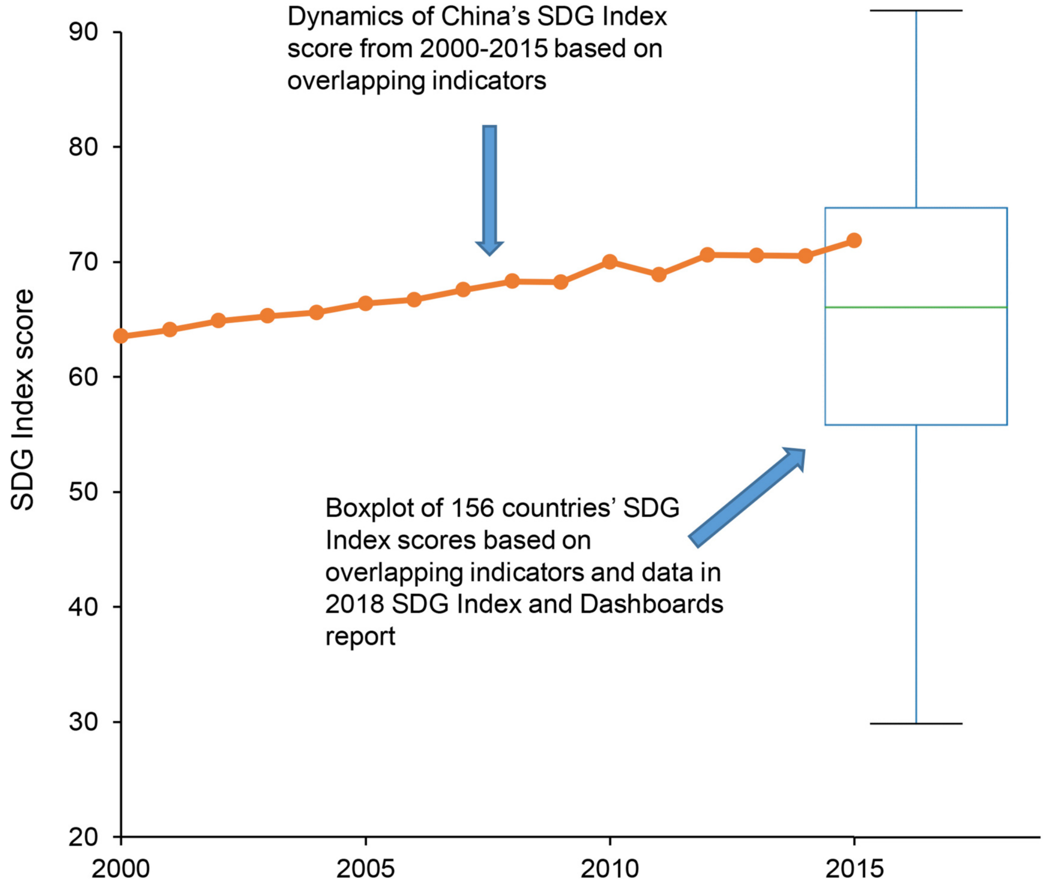

Extended Data Fig. 4 | China's SDG Index score compared with another 156 countries based on overlapping indicators. The box plot depicts the distribution of SDG Index scores ($n = 156$) for 156 countries in one year. The central rectangle spans the first quartile Q1 to the third quartile Q3, which is the IQR[40,41], while the line segment inside the rectangle shows the median. When the maximum observed SDG Index scores are greater than Q3 + 1.5 × IQR, the upper whisker is equal to Q3 + 1.5 × IQR[40,41]. Otherwise, the upper whisker is equal to the maximum observed SDG Index score. When the minimum observed SDG Index score is less than Q1 − 1.5 × IQR, the lower whisker is equal to Q1 − 1.5 × IQR[40,41]. Otherwise, the lower whisker is the minimum observed SDG Index score[40,41]. The green line segment within the box is the median value of SDG Index scores for the 156 countries.

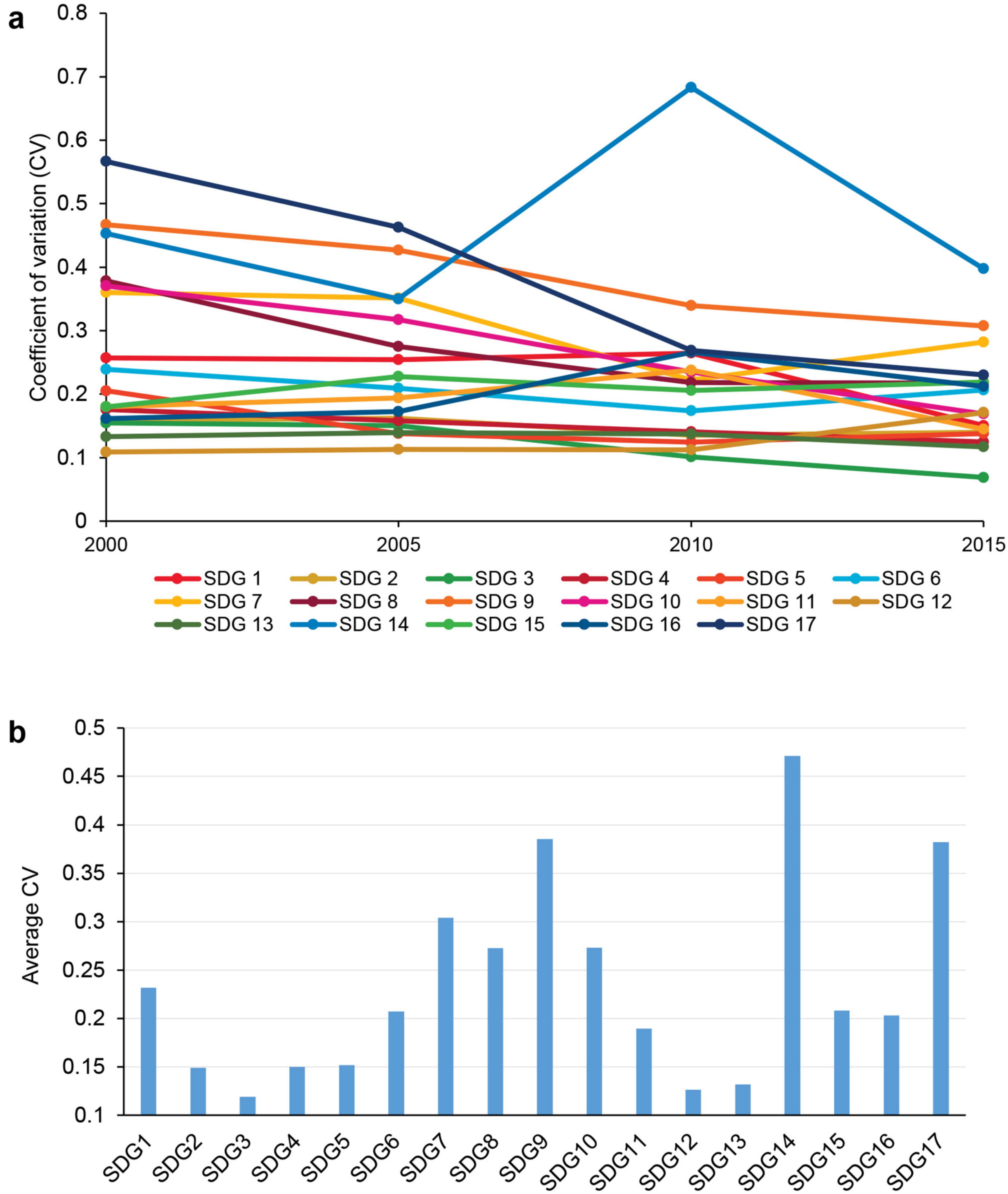

Extended Data Fig. 5 | Coefficient of variation for SDG scores. a, Coefficient of variation (CV) for SDG scores of provinces in 2000, 2005, 2010 and 2015. **b**, Average value of the coefficient of variation for SDG scores at the provincial level in 2000, 2005, 2010 and 2015.

nature research

Corresponding author(s): Jianguo (Jack) Liu

Reporting Summary

Nature Research wishes to improve the reproducibility of the work that we publish. This form provides structure for consistency and transparency in reporting. For further information on Nature Research policies, see Authors & Referees and the Editorial Policy Checklist.

Statistical parameters

When statistical analyses are reported, confirm that the following items are present in the relevant location (e.g. figure legend, table legend, main text, or Methods section).

n/a	Confirmed	
☐	☒	The exact sample size (n) for each experimental group/condition, given as a discrete number and unit of measurement
☐	☒	An indication of whether measurements were taken from distinct samples or whether the same sample was measured repeatedly
☒	☐	The statistical test(s) used AND whether they are one- or two-sided *Only common tests should be described solely by name; describe more complex techniques in the Methods section.*
☒	☐	A description of all covariates tested
☒	☐	A description of any assumptions or corrections, such as tests of normality and adjustment for multiple comparisons
☐	☒	A full description of the statistics including central tendency (e.g. means) or other basic estimates (e.g. regression coefficient) AND variation (e.g. standard deviation) or associated estimates of uncertainty (e.g. confidence intervals)
☒	☐	For null hypothesis testing, the test statistic (e.g. F, t, r) with confidence intervals, effect sizes, degrees of freedom and P value noted *Give P values as exact values whenever suitable.*
☒	☐	For Bayesian analysis, information on the choice of priors and Markov chain Monte Carlo settings
☒	☐	For hierarchical and complex designs, identification of the appropriate level for tests and full reporting of outcomes
☒	☐	Estimates of effect sizes (e.g. Cohen's d, Pearson's r), indicating how they were calculated
☐	☒	Clearly defined error bars *State explicitly what error bars represent (e.g. SD, SE, CI)*

Our web collection on statistics for biologists may be useful.

Software and code

Policy information about availability of computer code

Data collection	Data for the selected indicators in this study were obtained from the following authoritative sources: National Bureau of Statistics of the People’s Republic of China, China Statistical Yearbook Finance Yearbook of China, China Statistical Yearbook on the Environment, Educational Statistics Yearbook of China, China Health Statistics Yearbook, China Energy Statistical Yearbook, China Population Statistics Yearbook etc. See Table S1 for a list of SDGs and their corresponding indicators and data sources used in this paper.
Data analysis	I use Microsoft Excel 2013 and Matlab 2017b to analyze data.

For manuscripts utilizing custom algorithms or software that are central to the research but not yet described in published literature, software must be made available to editors/reviewers upon request. We strongly encourage code deposition in a community repository (e.g. GitHub). See the Nature Research guidelines for submitting code & software for further information.

Data

Policy information about availability of data

All manuscripts must include a data availability statement. This statement should provide the following information, where applicable:

- Accession codes, unique identifiers, or web links for publicly available datasets
- A list of figures that have associated raw data
- A description of any restrictions on data availability

Data for the selected indicators in this study were obtained from the following authoritative sources: National Bureau of Statistics of the People's Republic of China, China Statistical Yearbook Finance Yearbook of China, China Statistical Yearbook on the Environment, Educational Statistics Yearbook of China, China Health Statistics Yearbook, China Energy Statistical Yearbook, China Population Statistics Yearbook etc. See Table S1 for a list of SDGs and their corresponding indicators and data sources used in this paper.

Field-specific reporting

Please select the best fit for your research. If you are not sure, read the appropriate sections before making your selection.

☐ Life sciences ☐ Behavioural & social sciences ☒ Ecological, evolutionary & environmental sciences

For a reference copy of the document with all sections, see nature.com/authors/policies/ReportingSummary-flat.pdf

Ecological, evolutionary & environmental sciences study design

All studies must disclose on these points even when the disclosure is negative.

Study description	Global challenges such as hunger, water scarcity, energy shortage, environmental pollution, gender inequality and climate change pose threats to sustainability and human well-being worldwide. To address these and other challenges, nearly every country in the world has committed to the 17 United Nations Sustainable Development Goals (SDGs). Quantifying SDGs at the national and subnational levels can help track global progress towards sustainable development and identify priorities for policy-making and implementation, because nations and sub-nations are the basic units for implementing SDGs. However, there is no systematic spatio-temporal assessment of SDGs at national and subnational levels to guide policy development and implementation. To fill this gap, we used China, the largest developing country that increasingly shapes the world's future, as the first demonstration of examining the spatio-temporal dynamics of the 17 SDGs at both national and subnational levels. Our results indicate that China had an increasing SDG Index score (aggregated score representing China's overall performance in achieving all 17 SDGs) at the national level from 2000 to 2015. At the provincial level, east China had higher SDG Index score than west China in the 2000s, while south China had higher SDG Index score than north China in 2015. The SDG Index scores of all provinces increased over this period. Developed provinces had higher SDG index scores than developing provinces, but developing provinces experienced greater increases in SDG Index scores than did developed provinces. The Chinese government could consider prioritizing SDGs with low scores such as 15 (life on land), 14 (life below water) and 17 (partnerships for the goals). Also, since north China lags behind other areas it would warrant special attention. This study also suggests the need to track the spatio-temporal dynamics of progress toward SDGs in other nations to uncover significant shifts in sustainable development at national and subnational levels. Such insights can inform policy-making and implementation to achieve global sustainability.
Research sample	Data for the selected indicators in this study were obtained from the following authoritative sources: National Bureau of Statistics of the People's Republic of China, China Statistical Yearbook Finance Yearbook of China, China Statistical Yearbook on the Environment, Educational Statistics Yearbook of China, China Health Statistics Yearbook, China Energy Statistical Yearbook, China Population Statistics Yearbook etc. See Table S1 for a list of SDGs and their corresponding indicators and data sources used in this paper. At the national level, we aggregated China's 17 SDG scores into one national SDG Index score for each year from 2000 to 2015, yielding 16 SDG Index scores. At the provincial level, we aggregated each province's 17 SDG scores for 2000, 2005, 2010 and 2015 separately, yielding four SDG Index scores per province. In addition, we calculated the change in SDG scores separately for each of the 17 individual SDG scores and for China and its provinces, by subtracting the normalized score in 2000 from the score in 2015. The SDGs with bottom five scores in 2015 were considered as bottom five SDGs that lag behind other SDGs.
Sampling strategy	We study China and China's provinces over time, so the number of them is certain.
Data collection	Data for the selected indicators in this study were obtained from the following authoritative sources: National Bureau of Statistics of the People's Republic of China, China Statistical Yearbook Finance Yearbook of China, China Statistical Yearbook on the Environment, Educational Statistics Yearbook of China, China Health Statistics Yearbook, China Energy Statistical Yearbook, China Population Statistics Yearbook etc. See Table S1 for a list of SDGs and their corresponding indicators and data sources used in this paper.
Timing and spatial scale	We study China at national scale from 2000 to 2015, while study China's provinces in 2000, 2005, 2010 and 2015.
Data exclusions	No data was excluded
Reproducibility	We have followed the framework and guidelines in the 2019 report on reproducibility and replication by the National Science Foundation and the U.S. Department of Education (https://www.nsf.gov/pubs/2019/nsf19022/nsf19022.pdf). For instance, we have provided detailed, transparent, and clear descriptions of the methods (e.g., models, analysis procedures, data sources) that have led

to the findings. We are committed to making all data, models, code, etc. used in our research available to those interested individuals so that they can be used by others to exactly reproduce our findings.

Randomization	No allocation. We study China and China's provinces.
Blinding	No blinding. We study China and China's provinces.

Did the study involve field work? ☐ Yes ☒ No

Reporting for specific materials, systems and methods

Materials & experimental systems

n/a	Involved in the study
☒	☐ Unique biological materials
☒	☐ Antibodies
☒	☐ Eukaryotic cell lines
☒	☐ Palaeontology
☒	☐ Animals and other organisms
☒	☐ Human research participants

Methods

n/a	Involved in the study
☒	☐ ChIP-seq
☒	☐ Flow cytometry
☒	☐ MRI-based neuroimaging

Article

The water lily genome and the early evolution of flowering plants

https://doi.org/10.1038/s41586-019-1852-5

Received: 6 August 2019

Accepted: 31 October 2019

Published online: 18 December 2019

Open access

Liangsheng Zhang[1,23,24*], Fei Chen[1,2,23,24], Xingtan Zhang[1,23], Zhen Li[3,4,23], Yiyong Zhao[5,6,23], Rolf Lohaus[3,4,23], Xiaojun Chang[1,7,23], Wei Dong[1], Simon Y. W. Ho[8], Xing Liu[1], Aixia Song[1], Junhao Chen[9], Wenlei Guo[9], Zhengjia Wang[9], Yingyu Zhuang[1], Haifeng Wang[1], Xuequn Chen[1], Juan Hu[1], Yanhui Liu[1], Yuan Qin[1], Kai Wang[1], Shanshan Dong[7], Yang Liu[7,10], Shouzhou Zhang[7], Xianxian Yu[11], Qian Wu[12,13], Liangsheng Wang[12,13], Xueqing Yan[13,14], Yuannian Jiao[13,14], Hongzhi Kong[13,14], Xiaofan Zhou[15], Cuiwei Yu[16], Yuchu Chen[16], Fan Li[17], Jihua Wang[17], Wei Chen[18], Xinlu Chen[19], Qidong Jia[20], Chi Zhang[19], Yifan Jiang[2], Wanbo Zhang[2], Guanhua Liu[21], Jianyu Fu[21], Feng Chen[2,19,20,24], Hong Ma[6,24], Yves Van de Peer[3,4,22,24] & Haibao Tang[1,24]

Water lilies belong to the angiosperm order Nymphaeales. Amborellales, Nymphaeales and Austrobaileyales together form the so-called ANA-grade of angiosperms, which are extant representatives of lineages that diverged the earliest from the lineage leading to the extant mesangiosperms[1–3]. Here we report the 409-megabase genome sequence of the blue-petal water lily (*Nymphaea colorata*). Our phylogenomic analyses support Amborellales and Nymphaeales as successive sister lineages to all other extant angiosperms. The *N. colorata* genome and 19 other water lily transcriptomes reveal a Nymphaealean whole-genome duplication event, which is shared by Nymphaeaceae and possibly Cabombaceae. Among the genes retained from this whole-genome duplication are homologues of genes that regulate flowering transition and flower development. The broad expression of homologues of floral ABCE genes in *N. colorata* might support a similarly broadly active ancestral ABCE model of floral organ determination in early angiosperms. Water lilies have evolved attractive floral scents and colours, which are features shared with mesangiosperms, and we identified their putative biosynthetic genes in *N. colorata*. The chemical compounds and biosynthetic genes behind floral scents suggest that they have evolved in parallel to those in mesangiosperms. Because of its unique phylogenetic position, the *N. colorata* genome sheds light on the early evolution of angiosperms.

Many water lily species, particularly from *Nymphaea* (Nymphaeaceae), have large and showy flowers and belong to the angiosperms (also called flowering plants). Their aesthetic beauty has captivated notable artists such as the French impressionist Claude Monet. Water lily flowers have limited differentiation in perianths (outer floral organs), but they possess both male and female organs and have diverse scents and colours, similar to many mesangiosperms (core angiosperms, including eudicots, monocots, and magnoliids) (Supplementary Note 1). In addition, some water lilies have short life cycles and enormous numbers of seeds[4], which increase their potential as a model plant to represent the ANA-grade of angiosperms and to study early evolutionary events within the angiosperms. In particular, *N. colorata* Peter has a relatively small genome size ($2n = 28$ and approximately 400 Mb) and blue petals that make it popular in breeding programs (Supplementary Note 1).

We report here the genome sequence of *N. colorata*, obtained using PacBio RSII single-molecule real-time (SMRT) sequencing technology. The genome was assembled into 1,429 contigs (with a contig N50 of 2.1 Mb) and total length of 409 Mb with 804 scaffolds, 770 of which were anchored onto 14 pseudo-chromosomes (Extended Data Fig. 1 and Extended Data Table 1). Genome completeness was estimated to be 94.4% (Supplementary Note 2). We annotated 31,580 protein-coding genes and predicted repetitive elements with a collective length of 160.4 Mb, accounting for 39.2% of the genome (Supplementary Note 3).

The *N. colorata* genome provides an opportunity to resolve the relationships between Amborellales, Nymphaeales and all other extant angiosperms (Fig. 1a). Using six eudicots, six monocots, *N. colorata* and *Amborella*[5], and each of three gymnosperm species (*Ginkgo biloba*, *Picea abies* and *Pinus taeda*) as an outgroup in turn, we identified 2,169, 1,535 and 1,515 orthologous low-copy nuclear (LCN) genes, respectively (Fig. 1b). Among the LCN gene trees inferred from nucleotide sequences using *G. biloba* as an outgroup, 62% (294 out of 475 trees) place *Amborella* as the sister lineage to all other extant angiosperms with bootstrap support greater than 80% (type II, Fig. 1c). Using *P. abies* or *P. taeda* as the outgroup, *Amborella* is placed as the sister lineage to the remaining angiosperms in 57% and 54% of the LCN gene trees, respectively. LCN gene trees inferred using amino acid sequences show similar phylogenetic patterns (Supplementary Note 4.1).

A list of affiliations appears at the end of the paper.

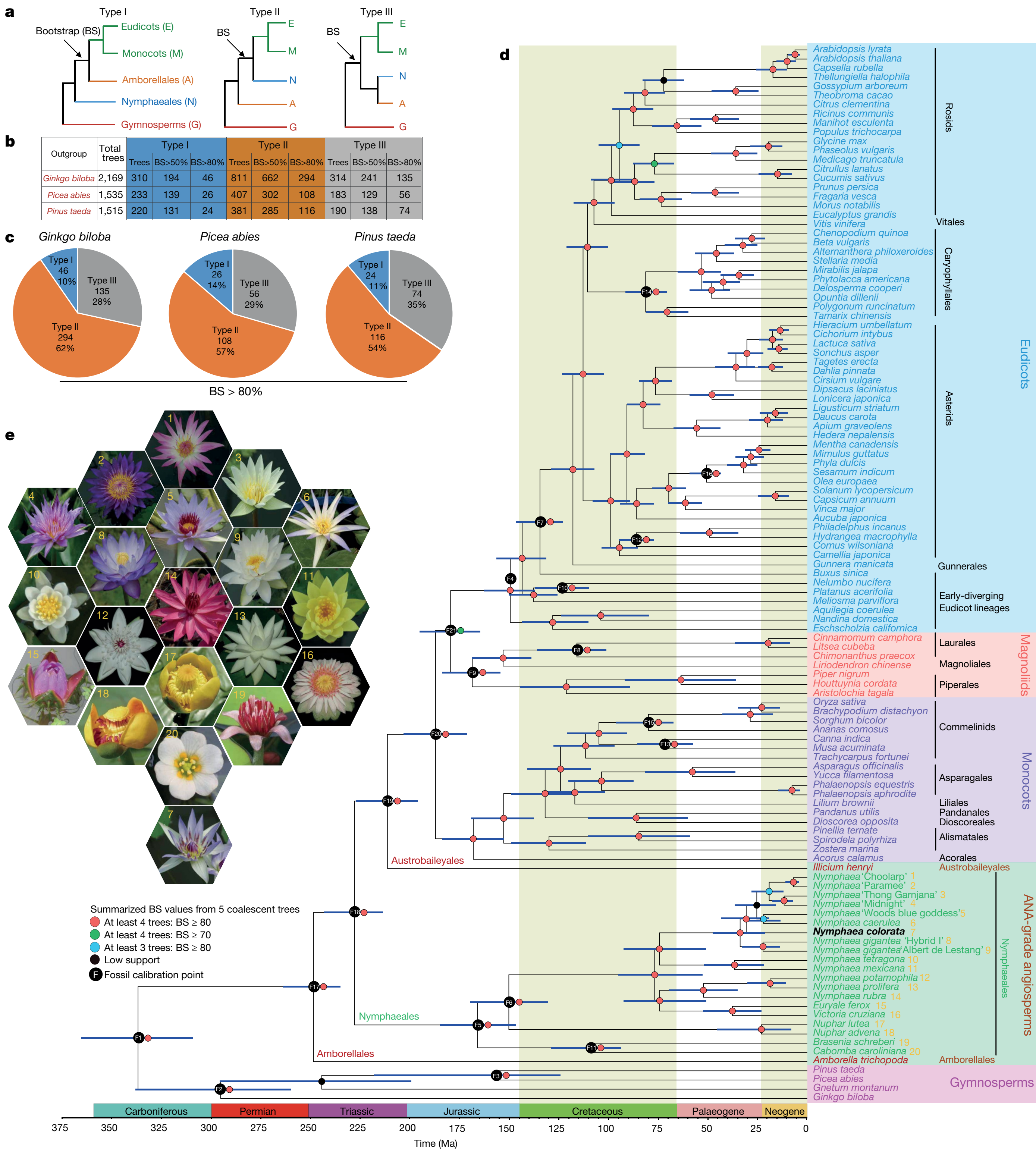

Fig. 1 | Phylogenomic relationships of angiosperms. a, Three different evolutionary relationships among major clades of angiosperms. **b**, Number of LCN gene trees with different bootstrap support (BS) values based on nucleotide sequences from six eudicots, six monocots, *N. colorata*, *Amborella* and three different gymnosperms. **c**, Comparison of gene trees supporting the three evolutionary relationships using each gymnosperm in turn as the outgroup. The percentage was calculated by dividing the number of type I, II or III trees (BS > 80%) by the total number of trees. **d**, Summary phylogeny and timescale of 115 plant species. Blue bars at nodes represent 95% credibility intervals of the estimated dates. **e**, The flowers of the 20 sampled water lilies in Nymphaeales used in **d**.

To minimize the potential shortcomings of sparse taxon sampling[6], we also inferred an angiosperm species tree using sequences from 44 genomes and 71 transcriptomes, including representatives of the ANA-grade, eudicots, magnoliids, monocots and a gymnosperm outgroup (*Gnetum montanum*, *G. biloba*, *P. abies* and *P. taeda*) (Methods). For further phylogenetic inference of these 115 species, we selected,

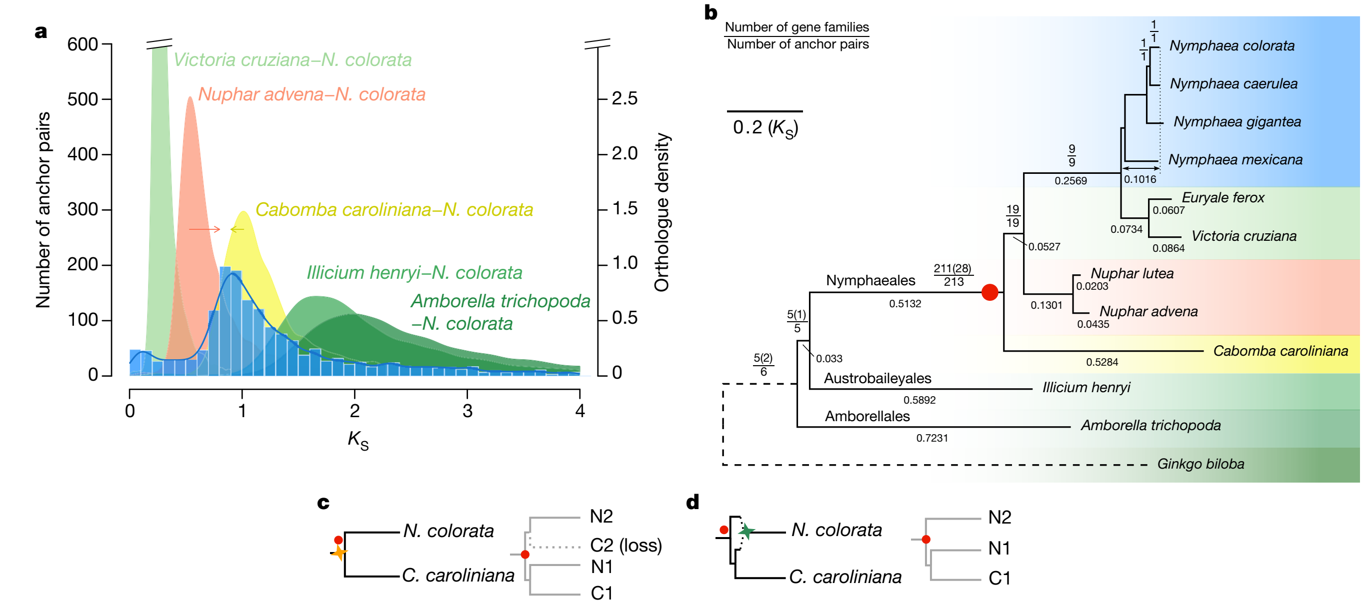

Fig. 2 | A Nymphaealean WGD shared by Nymphaeaceae and possibly Cabombaceae. **a**, K_S age distributions for paralogues found in collinear regions (anchor pairs) of *N. colorata* and for orthologues between *N. colorata* and selected Nymphaealean and angiosperm species. Red and yellow arrows indicate under- and overestimations of the *N. colorata*–*Nuphar advena* and *N. colorata*–*C. caroliniana* divergence, respectively. **b**, WGD phylogenomic analysis. Numbers in parentheses are the number of gene families with retained *C. caroliniana* duplicates supporting the duplication events. Numbers below branches show branch lengths in K_S units. The double-arrowed line denotes total K_S from the pointed node to *N. colorata*. We used *G. biloba* (dashed branch) as an outgroup. The red dot denotes the branch on which most of the anchor pairs in *N. colorata* coalesced. All mapped duplication events have BS ≥ 80% in the gene trees. **c**, Left, the scenario of a WGD (yellow four-pointed star) before the divergence between Nymphaeaceae and Cabombaceae. Right, a possible gene tree under this scenario, with loss of one duplicate in *C. caroliniana*. Two red dots show where the anchor pair of *N. colorata* would coalesce. **d**, Left, scenario of a WGD in the stem lineage of Nymphaeaceae involving an allotetraploid (green four-pointed star) that formed between two ancestral parents after the divergence of the lineages leading to *N. colorata* and *C. caroliniana*, with one of the parents being more closely related to *C. caroliniana*. Right, a gene tree under such a scenario. Red dots are as in **c**.

based on various criteria, five different LCN gene sets including 1,167, 834, 683, 602 and 445 genes. Analyses of these five datasets all yielded similar tree topologies with *Amborella* and Nymphaeales as successive sister lineages to all other extant angiosperms (Fig. 1d, e, Supplementary Note 4.2).

Molecular dating of angiosperm lineages, using a stringent set of 101 LCN genes and with age calibrations based on 21 fossils[7], inferred the crown age of angiosperms at 234–263 million years ago (Ma) (Fig. 1d). The split between monocots and eudicots was estimated at 171–203 Ma and that between Nymphaeaceae and Cabombaceae at 147–185 Ma.

Genomic collinearity unveiled evidence of a whole-genome duplication (WGD) event in *N. colorata* (Extended Data Figs. 1f, 2a and Supplementary Note 5.1). The number of synonymous substitutions per synonymous site (K_S) distributions for *N. colorata* paralogues further showed a signature peak at K_S of approximately 0.9 (Fig. 2a) and peaks at similar K_S values were identified in other Nymphaeaceae species (Supplementary Note 5.2), which suggests an ancient single WGD event that is probably shared among Nymphaeaceae members. Comparison of the *N. colorata* paralogue K_S distribution with K_S distributions of orthologues (representing speciation events) between *N. colorata* and other Nymphaeales lineages, *Illicium henryi*, and *Amborella* suggests that the WGD occurred just after the divergence between Nymphaeaceae and Cabombaceae (Fig. 2a). By contrast, phylogenomic analyses of gene families that contained at least one paralogue pair from collinear regions of *N. colorata* suggest that the WGD is shared between Nymphaeaceae and Cabombaceae (Fig. 2b, Supplementary Note 5.4). If true, *Cabomba caroliniana* seems to have retained few duplicates (Fig. 2b, c), which would explain the absence of a clear peak in the *C. caroliniana* paralogue K_S distribution (Supplementary Note 5.2). Absolute dating of the paralogues of *N. colorata* does suggest that the WGD could have occurred before or close to the divergence between Nymphaeaceae and Cabombaceae (Extended Data Fig. 2d, Supplementary Note 5.3), considering the variable substitution rates among Nymphaealean lineages (Fig. 2a, b, Extended Data Fig. 2c). An alternative interpretation of the above results could be that the WGD signatures were from an allopolyploidy event that occurred between ancestral Nymphaeaceae and Cabombaceae lineages shortly after their divergence and that gave rise to the Nymphaeaceae (but not Cabombaceae) stem lineage (Fig. 2d, Supplementary Note 5.4).

The water lily lineage descended from one of the early divergences among angiosperms, before the radiation of mesangiosperms. Thus, this group offers a unique window into the early evolution of angiosperms, particularly that of the flower. We identified 70 MADS-box genes, including homologues of the genes for the ABCE model of floral organ identities: *AP1* (and also *FUL*) and *AGL6* (A function for sepals and petals), *AP3* and *PI* (B function for petals and stamen), *AG* (C function for stamen and carpel), and *SEP1* (E function for interacting with ABC function proteins). Phylogenetic and collinearity analyses of the MADS-box genes and their genomic neighbourhood indicate that an ancient tandem duplication before the divergence of seed plants gave birth to the ancestors of A function (*FUL*) and E function genes (*SEP*) (Extended Data Fig. 3, Supplementary Note 6.1). Also, owing to the Nymphaealean WGD, *N. colorata* has two paralogues, *AGa* and *AGb* of the C-function gene *AG* (Extended Data Fig. 4). Similarly, the Nymphaealean WGD-derived duplicates are homologous to other genes associated with development of carpel and stamen[8], and to genes that regulate flowering time[9] and auxin-controlled circadian opening and closure of the flower[10] (Extended Data Figs. 4–6, Supplementary Note 6.2–6.4).

The expression profiles of *N. colorata* ABCE homologues largely agree with their putative ascribed roles in floral organ patterning (Fig. 3a).

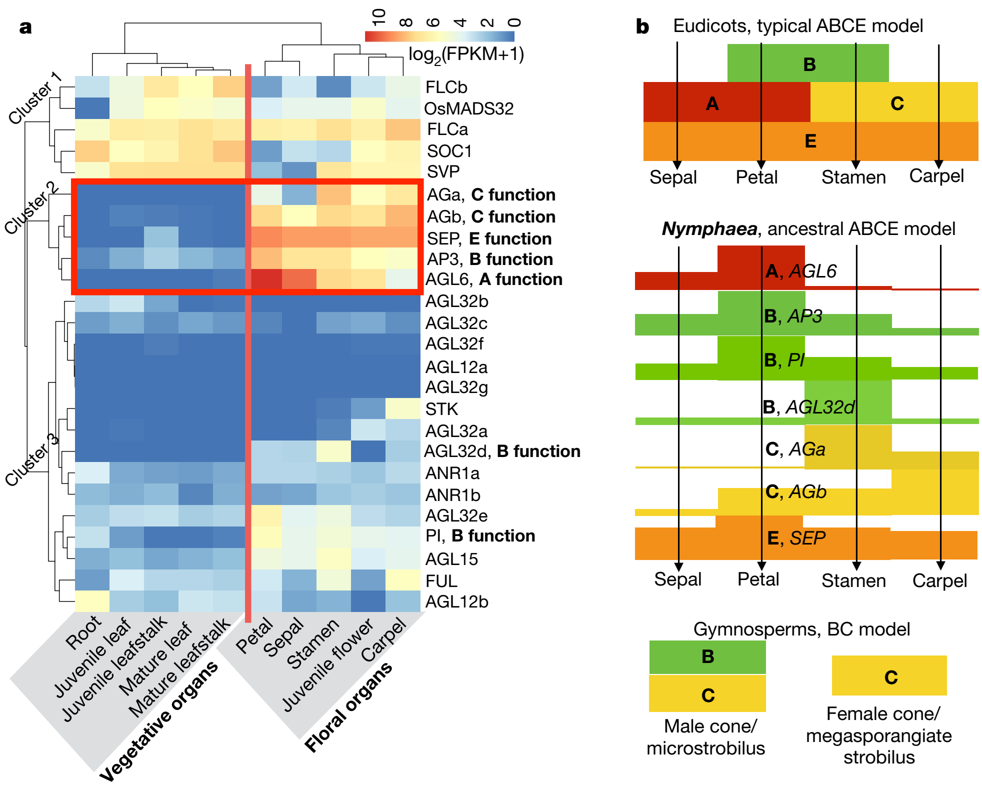

Fig. 3 | MADS-box genes in *N. colorata* and proposed floral ABCE model in early angiosperms. a, Gene expression patterns of MIKC^{c} from various organs of *N. colorata*. Three clusters of genes were classified according to the expression of type II MADS-box genes. The organ types (vegetative organs and floral organs) were matched to the expression patterns of type II MADS-box genes. Expression values were scaled by $\log_2$(FPKM + 1), in which FPKM is fragments per kilobase of exon per million mapped reads. **b**, The flowering ABCE model in *N. colorata* that specifies floral organs is proposed based on the gene expression values (bar heights) from **a**.

Notably, the *N. colorata AGL6* homologue is mainly expressed in sepals and petals, whereas the *FUL* homologue is mainly expressed in carpels, suggesting that *AGL6* acts as an A-function gene in *N. colorata*. The two C-function homologues *AGa* and *AGb* are highly expressed in stamens and carpels, respectively, whereas *AGb* is also expressed in sepals and petals, suggesting that they might have undergone subfunctionalization and possibly neofunctionalization for flower development after the Nymphaealean WGD. Furthermore, the ABCE homologues in *N. colorata* generally exhibit wider ranges of expression in floral organs than their counterparts in eudicot model systems (Fig. 3b). This wider expression pattern, in combination with broader expression of at least some ABCE genes in some eudicots representing an early-diverging lineage[11], some monocots[12] and magnoliids[13], suggest an ancient ABCE model for flower development, with subsequent canalization of gene expression and function regulated by the more specialized ABCE genes during the evolution of mesangiosperms, especially core eudicots[8]. This could also account for the limited differentiation between sepals and petals in Nymphaeales species, and is consistent with a single type of perianth organ proposed in an ancestral angiosperm flower[14].

Floral scent serves as olfactory cues for insect pollinators[15]. Whereas *Amborella* flowers are scentless[16], *N. colorata* flowers release 11 different volatile compounds, including terpenoids (sesquiterpenes), fatty-acid derivatives (methyl decanoate) and benzenoids (Fig. 4a). The *N. colorata* genome contains 92 putative terpene synthase (*TPS*) genes, which are ascribed to four previously recognized TPS subfamilies in angiosperms: TPS-b, TPS-c, TPS-e/f and TPS-g (Fig. 4b), but none was found for TPS-a, which is responsible for sesquiterpene biosynthesis in mesangiosperms[17]. Notably, TPS-b contains more than 80 genes in *N. colorata*; NC11G0123420 is highly expressed in flowers (Extended Data Fig. 7); this result suggests that it may be a candidate gene for sesquiterpene biosynthase in *N. colorata*. Also, methyl decanoate has not been detected as a volatile compound in monocots and eudicots[18] and is thought to be synthesized in *N. colorata* by the SABATH family of methyltransferases[19]. The *N. colorata* genome contains 13 *SABATH* homologues and 12 of them form a Nymphaeales-specific group (Supplementary Fig. 41). Among these 12 members, NC11G0120830 showed the highest expression in petals (Fig. 4c) and its corresponding recombinant protein was demonstrated to be a fatty acid methyltransferase that had the highest activity with decanoic acid as the substrate (Fig. 4d, Supplementary Note 7.1). These results suggest that the floral scent biosynthesis in *N. colorata* has been accomplished through enzymatic functions that have evolved independently from those in mesangiosperms (Fig. 4e).

Nymphaea colorata is valued for the aesthetically attractive blue colour of petals, which is a rare trait in ornamentals. To understand the molecular basis of the blue colour, we identified delphinidin 3′-*O*-(2″-*O*-galloyl-6″-*O*-acetyl-β-galactopyranoside) as the main blue anthocyanidin pigment (Extended Data Fig. 8a–c). By comparing the expression profiles between two *N. colorata* cultivars with white and blue petals for genes in a reconstructed anthocyanidin biosynthesis pathway, we found genes for an anthocyanidin synthase and a delphinidin-modification enzyme, the expression of which was significantly higher in blue petals than in white petals (Extended Data Fig. 8d, e). These two enzymes catalyse the last two steps of anthocyanidin biosynthesis and are therefore key enzymes specialized in blue pigment biosynthesis[20,21] (Supplementary Note 7.2).

Water lilies have a global distribution that includes cold regions (northern China and northern Canada), unlike the other ANA-grade angiosperms *Amborella* (Pacific Islands) and Austrobaileyales (temperate and tropical regions). We detected marked expansions of genes

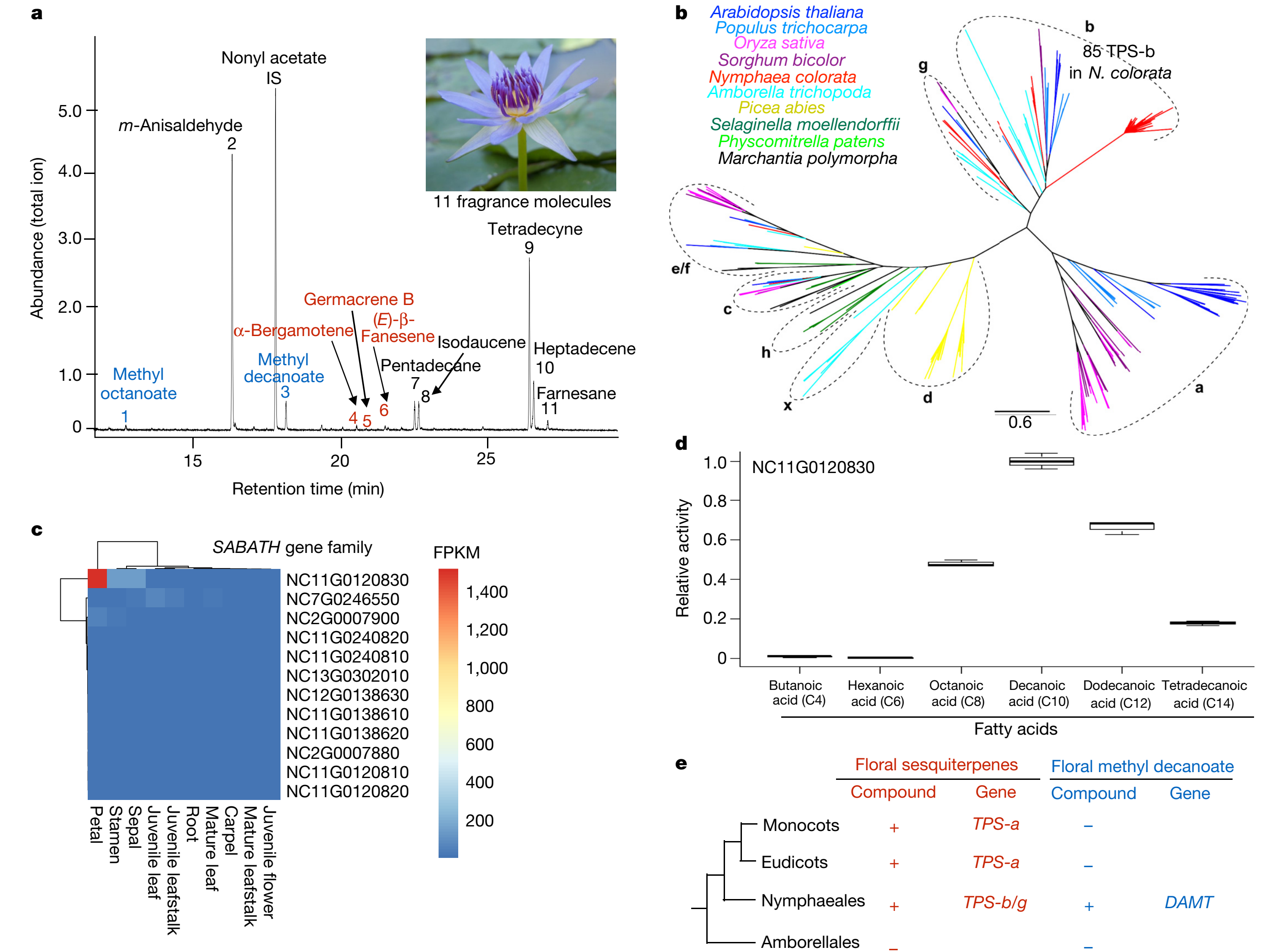

Fig. 4 | Floral scent and biosynthesis in *N. colorata*. a, Gas chromatogram of floral volatiles from the flower of *N. colorata*. The internal standard (IS) is nonyl acetate. Methyl esters are in blue; terpenes are in red. Floral scent was measured three times independently with similar results. **b**, Phylogenetic tree of terpene synthases from *N. colorata* and representative plants showing the subfamilies from a–h and x. **c**, Expression analysis of *SABATH* genes of *N. colorata* showed that NC11G0120830 had the highest expression level in petal. **d**, Relative activity of *Escherichia coli*-expressed NC11G0120830 with six fatty acids as substrates, with the activity on decanoic acid set at 1.0. Data are mean ± s.d. of three independent measurements. **e**, The presence (+) and absence (–) of sesquiterpenes and methyl decanoate as floral scent compounds and their respective biosynthetic genes in four major lineages of angiosperms when known. *DAMT*, decanoic acid methyltranferase.

related to immunity and stress responses in *N. colorata*, including genes encoding nucleotide-binding leucine-rich repeat (NLR) proteins, protein kinases and WRKY transcription factors, compared with those in *Amborella* and some mesangiosperms (Extended Data Fig. 9, Supplementary Note 8). It is possible that increased numbers of these genes enabled water lilies to adapt to various ecological habitats globally.

In conclusion, the *N. colorata* genome offers a reference for comparative genomics and for resolving the deep phylogenetic relationships among the ANA-grade and mesangiosperms. It has also revealed a WGD specific to Nymphaeales, and provides insights into the early evolution of angiosperms on key innovations such as flower development and floral scent and colour.

Online content

Any methods, additional references, Nature Research reporting summaries, source data, extended data, supplementary information, acknowledgements, peer review information; details of author contributions and competing interests; and statements of data and code availability are available at https://doi.org/10.1038/s41586-019-1852-5.

1. Byng, J. W. et al. An update of the Angiosperm Phylogeny Group classification for the orders and families of flowering plants: APG IV. *Bot. J. Linn. Soc.* **181**, 1–20 (2016).
2. Zeng, L. et al. Resolution of deep angiosperm phylogeny using conserved nuclear genes and estimates of early divergence times. *Nat. Commun*. **5**, 4956 (2014).
3. Qiu, Y. L. et al. The earliest angiosperms: evidence from mitochondrial, plastid and nuclear genomes. *Nature* **402**, 404–407 (1999).
4. Chen, F. et al. Water lilies as emerging models for Darwin's abominable mystery. *Hortic. Res*. **4**, 17051 (2017).
5. Amborella Genome Project. The *Amborella* genome and the evolution of flowering plants. *Science* **342**, 1241089 (2013).
6. Wiens, J. J. Missing data, incomplete taxa, and phylogenetic accuracy. *Syst. Biol*. **52**, 528–538 (2003).
7. Coiro, M., Doyle, J. A. & Hilton, J. How deep is the conflict between molecular and fossil evidence on the age of angiosperms? *New Phytol*. **223**, 83–99 (2019).
8. Alvarez-Buylla, E. R. et al. Flower development. *Arabidopsis Book* **8**, e0127 (2010).
9. Zhao, N. et al. Identification of flowering regulatory genes in allopolyploid *Brassica juncea*. *Hortic. Plant J*. **5**, 109–119 (2019).
10. Ke, M. et al. Auxin controls circadian flower opening and closure in the waterlily. *BMC Plant Biol*. **18**, 143 (2018).
11. Sharma, B. & Kramer, E. M. *Aquilegia* B gene homologs promote petaloidy of the sepals and maintenance of the C domain boundary. *Evodevo* **8**, 22 (2017).
12. Dodsworth, S. Petal, sepal, or tepal? B-genes and monocot flowers. *Trends Plant Sci*. **22**, 8–10 (2017).
13. Chanderbali, A. S. et al. Conservation and canalization of gene expression during angiosperm diversification accompany the origin and evolution of the flower. *Proc. Natl Acad. Sci. USA* **107**, 22570–22575 (2010).

14. Sauquet, H. et al. The ancestral flower of angiosperms and its early diversification. *Nat. Commun*. **8**, 16047 (2017).
15. Kessler, D. et al. How scent and nectar influence floral antagonists and mutualists. *eLife* **4**, e07641 (2015).
16. Thien, L. B. et al. The population structure and floral biology of *Amborella trichopoda* (Amborellaceae). *Ann. Mo. Bot. Gard*. **90**, 466–490 (2003).
17. Chen, F., Tholl, D., Bohlmann, J. & Pichersky, E. The family of terpene synthases in plants: a mid-size family of genes for specialized metabolism that is highly diversified throughout the kingdom. *Plant J*. **66**, 212–229 (2011).
18. Knudsen, J. T., Tollsten, L. & Bergstrom, L. G. Floral scents-a checklist of volatile compounds isolated by head-space techniques. *Phytochemistry* **33**, 253–280 (1993).
19. Zhao, N. et al. Structural, biochemical, and phylogenetic analyses suggest that indole-3-acetic acid methyltransferase is an evolutionarily ancient member of the SABATH family. *Plant Physiol*. **146**, 455–467 (2008).
20. Chen, W. H. et al. Downregulation of putative UDP-glucose: flavonoid 3-*O*-glucosyltransferase gene alters flower coloring in *Phalaenopsis*. *Plant Cell Rep*. **30**, 1007–1017 (2011).
21. Wu, Q. et al. Transcriptome sequencing and metabolite analysis for revealing the blue flower formation in waterlily. *BMC Genomics* **17**, 897 (2016).

[1]Fujian Provincial Key Laboratory of Haixia Applied Plant Systems Biology, Key Laboratory of Ministry of Education for Genetics, Breeding and Multiple Utilization of Crops, Key Laboratory of National Forestry and Grassland Administration for Orchid Conservation and Utilization, Fujian Agriculture and Forestry University, Fuzhou, China. [2]College of Horticulture, Nanjing Agricultural University, Nanjing, China. [3]Department of Plant Biotechnology and Bioinformatics, Ghent University, Ghent, Belgium. [4]VIB Center for Plant Systems Biology, Ghent, Belgium. [5]State Key Laboratory of Genetic Engineering, Ministry of Education Key Laboratory of Biodiversity Sciences and Ecological Engineering, School of Life Sciences, Fudan University, Shanghai, China. [6]Department of Biology, Huck Institutes of the Life Sciences, Pennsylvania State University, University Park, PA, USA. [7]Fairy Lake Botanical Garden, Shenzhen and Chinese Academy of Sciences, Shenzhen, China. [8]School of Life and Environmental Sciences, University of Sydney, Sydney, New South Wales, Australia. [9]State Key Laboratory of Subtropical Silviculture, School of Forestry and Biotechnology, Zhejiang A&F University, Hangzhou, China. [10]BGI-Shenzhen, Shenzhen, China. [11]School of Urban-Rural Planning and Landscape Architecture, Xuchang University, Xuchang, China. [12]Key Laboratory of Plant Resources/Beijing Botanical Garden, Institute of Botany, Chinese Academy of Sciences, Beijing, China. [13]University of the Chinese Academy of Sciences, Beijing, China. [14]State Key Laboratory of Systematic and Evolutionary Botany, Institute of Botany, Chinese Academy of Sciences, Beijing, China. [15]Guangdong Province Key Laboratory of Microbial Signals and Disease Control, Integrative Microbiology Research Centre, South China Agricultural University, Guangzhou, China. [16]Hangzhou Tianjing Aquatic Botanical Garden, Zhejiang Humanities Landscape Co. Ltd., Hangzhou, China. [17]National Engineering Research Center for Ornamental Horticulture, Key Laboratory for Flower Breeding of Yunnan Province, Floriculture Research Institute, Yunnan Academy of Agricultural Sciences, Kunming, China. [18]Innovative Institute of Chinese Medicine and Pharmacy, Chengdu University of Traditional Chinese Medicine, Chengdu, China. [19]Department of Plant Sciences, University of Tennessee, Knoxville, TN, USA. [20]Graduate School of Genome Science and Technology, University of Tennessee, Knoxville, TN, USA. [21]Key Laboratory of Tea Quality and Safety Control, Ministry of Agriculture and Rural Affairs, Tea Research Institute, Chinese Academy of Agricultural Sciences, Hangzhou, China. [22]Centre for Microbial Ecology and Genomics, Department of Biochemistry, Genetics and Microbiology, University of Pretoria, Pretoria, South Africa. [23]These authors contributed equally: Liangsheng Zhang, Fei Chen, Xingtan Zhang, Zhen Li, Yiyong Zhao, Rolf Lohaus, Xiaojun Chang. [24]These authors jointly supervised this work: Liangsheng Zhang, Fei Chen, Feng Chen, Hong Ma, Yves Van de Peer, Haibao Tang. *e-mail: fafuzhang@163.com

Methods

Genome and transcriptome sequencing

Total DNA for genome sequencing was extracted from young leaves. Leaf RNA was extracted from 18 water lily species: *N. colorata*, *Euryale ferox*, *Brasenia schreberi*, *Victoria cruziana*, *Nymphaea mexicana*, *Nymphaea prolifera*, *Nymphaea tetragona*, *Nymphaea potamophila*, *Nymphaea caerulea*, *Nymphaea rubra*, *Nymphaea* 'midnight', *Nymphaea* 'Choolarp', *Nymphaea* 'Paramee', *Nymphaea* 'Woods blue goddess', *Nymphaea gigantea* 'Albert de Lestang', *N. gigantea* 'Hybrid I', *Nymphaea* 'Thong Garnjana' and *Nuphar lutea*. In addition, for transcriptome sequencing we sampled several organs and tissues from *N. colorata* including mature leaf, mature leafstalk, juvenile flower, juvenile leaf, juvenile leafstalk, carpel, stamen, sepal, petal and root.

For PacBio sequencing, we prepared approximately 20-kb SMRTbell libraries. A total of 34 SMRT cells and 49.8 Gb data composed of 5.5 million reads were sequenced on PacBio RSII system with P6-C4 chemistry. All transcriptome libraries were sequenced using the Illumina platform, generating paired-end reads. For the Hi-C sequencing and scaffolding, a Hi-C library was created from tender leaves of *N. colorata*. In brief, the leaves were fixed with formaldehyde and lysed, and the cross-linked DNA was then digested with MboI overnight. Sticky ends were biotinylated and proximity-ligated to form chimeric junctions, which were physically sheared to and enriched for sizes of 500–700 bp. Chimeric fragments representing the original cross-linked long-distance physical interactions were then processed into paired-end sequencing libraries and 346 million 150-bp paired-end reads, which were sequenced on the Illumina platform.

Sequence assembly and gene annotation

To assemble the 49.8 Gb data composed of 5.5 million reads, we filtered the reads to remove organellar DNA, reads of poor quality or short length, and chimaeras. The contig-level assembly was performed on full PacBio long reads using the Canu package[22]. Canu v.1.3 was used for self-correction and assembly. We then polished the draft assembly using Arrow (https://github.com/PacificBiosciences/GenomicConsensus). To increase the accuracy of the assembly, Illumina short reads were recruited for further polishing with the Pilon program (https://github.com/broadinstitute/pilon). The genome assembly quality was measured using BUSCO (Benchmarking Universal Single-Copy Orthologues)[23] v.3.0. The paired-end reads from Hi-C were uniquely mapped onto the draft assembly contigs, which were grouped into chromosomes and scaffolded using the software Lachesis (https://github.com/shendurelab/LACHESIS).

Genscan (http://genes.mit.edu/GENSCAN.html) and Augustus[24] were used to carry out de novo predictions with gene model parameters trained from *Arabidopsis thaliana*. Furthermore, gene models were de novo predicted using MAKER[25]. We then evaluated the genes by comparing MAKER results with the corresponding transcript evidence to select gene models that were the most consistent on the basis of an AED metric.

The evolutionary position of water lily and divergence-time estimation

LCN genes were identified based on OrthoFinder[26] results. The orthologues were obtained from six monocots (*Spirodela polyrhiza*, *Zostera marina*, *Musa acuminata*, *Ananas comosus*, *Sorghum bicolor* and *Oryza sativa*) and six eudicots (*Nelumbo nucifera*, *Vitis vinifera*, *Populus trichocarpa*, *A. thaliana*, *Solanum lycopersicum* and *Beta vulgaris*), *N. colorata*, *Amborella*, and the gymnosperms *G. biloba*, *P. abies* and *P. taeda*. LCN genes needed to meet the following requirements: strictly single-copy in *N. colorata*, *Amborella*, *G. biloba*, *P. abies* or *P. taeda*, and single-copy in at least five of the 12 eudicots or monocots. With *G. biloba*, *P. abies* or *P. taeda* as the outgroup, we identified 2,169, 1,535 and 1,515 orthologous LCN genes, respectively. Furthermore, we trimmed the sites with less than 90% coverage. LCN gene trees were estimated from the remaining sites using RAxML v.7.7.8 using the GTR+G+I model for nucleotide sequences (Fig. 1c) and the JTT+G+I model for amino acid sequences (Supplementary Note 4.1). To account for incomplete lineage sorting and different substitution rates, we applied the multispecies coalescent model and a supermatrix method, respectively, to the LCN genes and found further support for the sister relationship between *Amborella* and all other extant flowering plants (Supplementary Note 4.2).

We further carefully selected five LCN gene sets (1,167, 834, 683, 602 and 445) from 115 species and applied both a supermatrix method[27–29] and the multi-species coalescent model to infer the phylogeny of angiosperms (Supplementary Note 4.2). The phylogeny inferred from 1,167 LCN genes is shown in Fig. 1d, with different support values from the multi-species coalescent analyses of the other four LCN gene sets.

To estimate the evolutionary timescale of angiosperms, we calibrated a relaxed molecular clock using 21 fossil-based age constraints[7] throughout the tree, including the earliest fossil tricoplate pollen (approximately 125 Ma) associated with eudicots[30]. We concatenated 101 selected genes (205,185 sites) and fixed the tree topology to that inferred from our coalescent-based analysis of 1,167 genes from 115 taxa. We performed a Bayesian phylogenomic dating analysis of the 101 selected genes in MCMCtree, part of the PAML package[31,32], and used approximate likelihood calculation for the branch lengths[33]. Molecular dating was performed using an auto-correlated model of among-lineage rate variation, the GTR substitution model, and a uniform prior on the relative node times. Posterior distributions of node ages were estimated using Markov chain Monte Carlo sampling, with samples drawn every 250 steps over 10 million steps following a burn-in of 500,000 steps. We checked for convergence by running the analysis in duplicate and checked for sufficient sampling.

We also implemented the penalized likelihood method under a variable substitution rate using TreePL[34] and r8s[35], as a constant substitution rate across the phylogenetic tree was rejected ($P < 0.01$) for all cases by likelihood-ratio tests in PAUP[36]. Three fossil calibrations, corresponding to the crown groups of Lamiales, Cornales and Laurales, were implemented as minimum age constraints in our penalized likelihood dating analysis, except that the earliest appearance of tricolpate pollen grains (about 125 Ma)[30] was used to fix the age of crown eudicots. We determined the best smoothing parameter value of the concatenated 101 LCN genes as 0.32 by performing cross-validations of a range of smooth parameters from 0.01 to 10,000 (algorithm = TN; crossv = yes; cvstart = −2; cvinc = 0.5; cvnum = 15). We used 100 bootstrap trees with branch lengths generated by RAxML[37] to infer the 95% confidence intervals of age estimates (Supplementary Note 4.2).

Identification of WGD

The *N. colorata* genome was compared with each of the other genomes by pairwise alignment using Large-Scale Genome Alignment Tool (LAST; http://last.cbrc.jp/). We defined syntenic blocks using LAST hits with a distance cut-off of 20 genes apart from the two retained homologous pairs, in which at least four consecutive retained homologous pairs were required. We then obtained the one-to-one blocks to exclude ancient duplication blocks with QUOTA-ALIGN[38].

K_S-based paralogue age distributions were constructed as previously described[39]. In brief, the paranome was constructed by performing an all-against-all protein sequence similarity search using BLASTP with an E-value cut-off of 10^{-10}, after which gene families were built with the mclblastline pipeline (v.10-201) (micans.org/mcl). Each gene family was aligned using MUSCLE (v.3.8.31)[40], and K_S estimates for all pairwise comparisons within a gene family were obtained using maximum likelihood in the CODEML program[41] of the PAML package (v.4.4c)[31]. We then subdivided gene families into subfamilies for which K_S estimates between members did not exceed a value of 5.

To correct for the redundancy of K_S values (a gene family of n members produces $n(n-1)/2$ pairwise K_S estimates for $n-1$ retained duplication events), we inferred a phylogenetic tree for each subfamily using PhyML[42] with the default settings. For each duplication node in the resulting phylogenetic tree, all m K_S estimates between the two child clades were added to the K_S distribution with a weight of $1/m$ (in which m is the number of K_S estimates for a duplication event), so that the weights of all K_S estimates for a single duplication event summed to one. Paralogous gene pairs found in duplicated collinear segments (anchor pairs) from *N. colorata* were detected using i-ADHoRe (v.3.0) with 'level_2_only = TRUE'[43,44]. The identified anchor pairs are assumed to correspond to the most recent WGD event.

The K_S-based orthologue age distributions were constructed by identifying one-to-one orthologues between species using InParanoid[45] with default settings, followed by K_S estimation using the CODEML program as above. K_S distributions for one-to-one orthologues between *N. colorata* and each of *V. cruziana*, *N. advena*, *C. caroliniana*, *I. henryi* and *Amborella* were used to compare the relative timing of the WGD in *N. colorata* with speciation events within Nymphaeales. K_S distributions for one-to-one orthologues between the outgroup species *I. henryi* and each of *N. lutea*, *N. advena*, *N. mexicana*, *Nymphaea* 'Woods blue goddess', *N. colorata*, and *C. caroliniana* were used to estimate and compare relative substitution rates among these Nymphaealean species. Additional comparisons using *V. vinifera* and *Amborella* as outgroup species instead of *I. henryi* gave similar results (data not shown).

Absolute dating of the identified WGD event in *N. colorata* was performed as previously described[46]. Briefly, paralogous gene pairs located in duplicated segments (anchor pairs) and duplicated pairs lying under the WGD peak (peak-based duplicates) were collected for phylogenetic dating. We selected anchor pairs and peak-based duplicates present under the *N. colorata* WGD peak and with K_S values between 0.7 and 1.2 (grey-shaded area in Extended Data Fig. 2b) for absolute dating. For each WGD paralogous pair, an orthogroup was created that included the two paralogues plus several orthologues from other plant species as identified by InParanoid[45] using a broad taxonomic sampling: one representative orthologue from the order Cucurbitales, two from Rosales, two from Fabales, two from Malpighiales, two from Brassicales, one from Malvales, one from Solanales, two from Poaceae (Poales), one from *A. comosus*[47] (Bromeliaceae, Poales), one from either *M. acuminata*[48] (Zingiberales) or *Phoenix dactylifera*[49] (Arecales), one from the Asparagales (from *Asparagus officinalis*[50], *Apostasia shenzhenica*[46], or *Phalaenopsis equestris*[51]), one from the Alismatales (either from *S. polyrhiza*[52] or *Z. marina*[53]), one from *Amborella*, and one from *G. biloba*[54]. In total, 217 orthogroups based on anchor pairs and 142 orthogroups based on peak-based duplicates were collected.

The node joining the two WGD paralogues of *N. colorata* was then dated using the BEAST v1.7 package[55] under an uncorrelated relaxed-clock model and an LG+G model with four site-rate categories. A starting tree with branch lengths satisfying all fossil prior constraints was created according to the consensus APG IV phylogeny[1]. Fossil calibrations were implemented using log-normal calibration priors on the following nodes: the node uniting the Malvidae based on the fossil *Dressiantha bicarpellata*[56] with prior offset = 82.8, mean = 3.8528, and s.d. = 0.5[57]; the node uniting the Fabidae based on the fossil *Paleoclusia chevalieri*[58] with prior offset = 82.8, mean = 3.9314, and s.d. = 0.5[59]; the node uniting the non-Alismatalean monocots based on fossil *Liliacidites*[60] with prior offset = 93.0, mean = 3.5458, and s.d. = 0.5[61]; the node uniting the *N. colorata* WGD paralogues with the eudicots and monocots based on the sudden abundant appearance of eudicot tricolpate pollen in the fossil record with prior offset = 124, mean = 4.8143 and s.d. = 0.5[62]; and the root uniting the above clades with *Amborella* and then *G. biloba* with prior offset = 307, mean = 3.8876, and s.d. = 0.5[63]. The offsets of these calibrations represent hard minimum boundaries, and their means represent locations for their respective peak mass probabilities in accordance with previous dating studies of these specific clades[63] (see Supplementary Note 5.3 for an alternative setting of orthogroups).

A run without data was performed to ensure proper placements of the marginal calibration priors, which do not necessarily correspond to the calibration priors specified above, because they interact with each other and the tree prior[64]. Indeed, a run without data indicated that the distribution of the marginal calibration prior for the root did not correspond to the specified calibration density, so we reduced the mean in the calibration prior of the node combining the *N. colorata* WGD paralogues with the eudicots and monocots with offset = 124, mean = 4.4397, s.d. = 0.5 to locate the marginal calibration prior at 220 Ma[62].

Markov chain Monte Carlo sampling for each orthogroup was run for 10 million steps, with sampling every 1,000 steps to produce a sample size of 10,000. The resulting trace files were inspected using Tracer v.1.5[55], with a burn-in of 1,000 samples, to check for convergence and sufficient sampling (minimum effective sample size of 200 for all parameters). In total, 263 orthogroups were accepted, and absolute age estimates of the node uniting the WGD paralogous pairs based on both anchor pairs and peak-based duplicates were grouped into one absolute age distribution, for which kernel density estimation and a bootstrapping procedure were used to find the peak consensus WGD age estimate and its 90% confidence interval boundaries, respectively. More detailed methods have been previously described[39].

To identify the duplication events that resulted in the 2,648 anchor pairs detected in the genome of *N. colorata*, we performed phylogenomic analyses to determine the timing of the duplication events relative to the lineage divergences in Nymphaeales as described previously[46]. Protein-coding genes from 12 species were used, including eight species from Nymphaeaceae and one species from Cabombaceae in Nymphaeales, one species (*I. henryi*) from Austrobaileyales, plus *Amborella* and *G. biloba*. The phylogeny of the 12 species was obtained from Fig. 1d, and the branch lengths in K_S units were estimated from 23 LCN genes (selected from the 101 LCN genes used in Fig. 1d, because only 23 are shared across all of the species studied) using PAML[31] under the free-ratio model. OrthoMCL (v.2.0.9)[65] was used with default parameters to identify gene families. Then, we removed 907 of the 2,648 anchor pairs with K_S values greater than five. If the remaining anchor pairs fell into different gene families, thus indicating incorrect assignment of gene families by OrthoMCL, we merged the corresponding gene families and finally obtained 53,243 multi-gene gene families. Next, phylogenetic trees were constructed for a subset of 881 gene families with no more than 200 genes that had at least one pair of anchors and one gene from *G. biloba*. Multiple sequence alignments were produced by MUSCLE (v3.8.31)[40] and were trimmed by trimAl (v.1.4)[66] to remove low-quality regions based on a heuristic approach (-automated1).

We then used RAxML (v.8.2.0)[67] with the GTR+G model to estimate a maximum-likelihood tree, starting with 200 rapid bootstraps followed by maximum-likelihood optimizations on every fifth bootstrap tree. Gene trees were rooted based on genes from *G. biloba* if these formed a monophyletic group in the tree; otherwise, mid-point rooting was applied. The timing of the duplication event for each anchor pair relative to the lineage divergence events was then inferred. In brief, internodes from a gene tree were first mapped to the species phylogeny according to the common ancestor of the genes in the gene tree. Each internode was then classified as a duplication node, a speciation node, or a node that has no paralogues and is inconsistent with divergence in the species phylogeny. The parental node(s) of a duplication node supported by an anchor pair were traced towards the root until reaching a speciation node in the gene tree. The duplication event that resulted in the anchor pair was hence circumscribed between the duplication node as the lower bound and the speciation node as the upper bound on the species tree. If the two nodes were directly connected by a single branch on the species tree, the duplication was thus considered to have occurred on the branch. To reduce biased estimations, we used

the bootstrap value on the branch leading to a duplication node as support for a duplication event. In total, 497 anchor pairs in 473 gene families coalesced as duplication events on the species phylogeny, and duplication events from 254 anchor pairs in 246 gene families (or from 380 anchor pairs in 364 gene families) had bootstrap values greater than or equal to 80% (or 50%).

Floral scent measurement, gene identification, and functional characterization

We collected floral volatiles of *N. colorata* using a dynamic headspace sampling system and analysed them using gas chromatography–mass spectrometry (GC–MS) as previously described[68]. After 2 h of collection from the headspace of detached open flowers of *N. colorata* in a glass chamber (10 cm diameter, 30 cm height), volatiles were eluted from the SuperQ volatile collection trap using 100 µl of methylene chloride containing nonyl acetate as an internal standard. We then analysed samples using an Agilent Intuvo 9000 GC system coupled with an Agilent 7000D Triple Quadrupole mass detector. Separation was performed on an Agilent HP 5 MS capillary column (30 m × 0.25 mm) with helium as carrier gas (flow rate of 1 ml min^{-1}). We applied splitless injections of 1 µl samples, injection temperature of 250 °C, an initial oven temperature of 40 °C (3-min hold) and a temperature gradient of 5 °C per min increase from 40 °C to 250 °C. Products were identified using the National Institute of Standards and Technology mass spectral database (https://chemdata.nist.gov).

A full-length cDNA of NC11G0120830 was amplified from the open flowers of *N. colorata* using reverse transcription PCR (RT–PCR), and cloned into pET-32a (MilliporeSigma). After confirmation by sequencing, NC11G0120830 was expressed in *E. coli* strain BL21 (DE3) (Stratagene) and the recombinant protein produced was purified using a modified nickel-nitrilotriacetic acid agarose (Invitrogen) protocol as previously reported[69]. For methyltransferase enzyme assays, we used both radiochemical and non-radiochemical reaction systems. The radiochemical reaction system (50 µl) was composed of 50 mM Tris-HCl, pH 7.8, 1 mM substrate, 1 µl ^{14}C-*S*-adenosyl-L-methionine, and 1 µl of purified NC11G0120830. After 30 min of incubation at room temperature, 150 µl of ethyl acetate was added to extract the ^{14}C-labelled reaction products. The extracts were counted using a scintillation counter (Beckman Coulter) to measure the activity of NC11G0120830. To determine the chemical identity of the reaction product, we performed non-radiochemical assays in which nonradioactive *S*-adenosyl-L-methionine was used as the methyl donor. The reaction product was collected by headspace solid-phase microextraction and analysed by GC–MS as previously described[70].

Reporting summary

Further information on research design is available in the Nature Research Reporting Summary linked to this paper.

Data availability

PacBio whole-genome sequencing data, Illumina data and genome assembly sequences have been deposited to the NCBI Sequence Read Archive (SRA) as Bioproject PRJNA565347, and were also deposited in the BIG Data Center (http://bigd.big.ac.cn) under project number PRJCA001283. The genome assembly sequences and gene annotations have been deposited in the Genome Warehouse in BIG Data Center under accession number GWHAAYW00000000. The genome assembly sequences, gene annotations, and the LCN genes used in this study, have been also deposited in the Waterlily Pond (http://waterlily.eplant.org). All other data are available from the corresponding author upon reasonable request.

22. Koren, S. et al. Canu: scalable and accurate long-read assembly via adaptive *k*-mer weighting and repeat separation. *Genome Res*. **27**, 722–736 (2017).
23. Simão, F. A., Waterhouse, R. M., Ioannidis, P., Kriventseva, E. V. & Zdobnov, E. M. BUSCO: assessing genome assembly and annotation completeness with single-copy orthologs. *Bioinformatics* **31**, 3210–3212 (2015).
24. Stanke, M. & Morgenstern, B. AUGUSTUS: a web server for gene prediction in eukaryotes that allows user-defined constraints. *Nucleic Acids Res*. **33**, W465–W467 (2005).
25. Cantarel, B. L. et al. MAKER: an easy-to-use annotation pipeline designed for emerging model organism genomes. *Genome Res*. **18**, 188–196 (2008).
26. Emms, D. M. & Kelly, S. OrthoFinder: solving fundamental biases in whole genome comparisons dramatically improves orthogroup inference accuracy. *Genome Biol*. **16**, 157 (2015).
27. Zeng, L. et al. Resolution of deep eudicot phylogeny and their temporal diversification using nuclear genes from transcriptomic and genomic datasets. *New Phytol*. **214**, 1338–1354 (2017).
28. Xiang, Y. et al. Evolution of Rosaceae fruit types based on nuclear phylogeny in the context of geological times and genome duplication. *Mol. Biol. Evol*. **34**, 262–281 (2017).
29. Huang, C. H. et al. Resolution of Brassicaceae phylogeny using nuclear genes uncovers nested radiations and supports convergent morphological evolution. *Mol. Biol. Evol*. **33**, 394–412 (2016).
30. Hickey, L. J. & Doyle, J. A. Early cretaceous fossil evidence for angisperm evolution. *Bot. Rev*. **43**, 3–104 (1977).
31. Yang, Z. PAML 4: phylogenetic analysis by maximum likelihood. *Mol. Biol. Evol*. **24**, 1586–1591 (2007).
32. Morris, J. L. et al. The timescale of early land plant evolution. *Proc. Natl Acad. Sci. USA* **115**, E2274–E2283 (2018).
33. dos Reis, M. & Yang, Z. Approximate likelihood calculation on a phylogeny for Bayesian estimation of divergence times. *Mol. Biol. Evol*. **28**, 2161–2172 (2011).
34. Smith, S. A. & O'Meara, B. C. treePL: divergence time estimation using penalized likelihood for large phylogenies. *Bioinformatics* **28**, 2689–2690 (2012).
35. Sanderson, M. J. r8s: inferring absolute rates of molecular evolution and divergence times in the absence of a molecular clock. *Bioinformatics* **19**, 301–302 (2003).
36. Wilgenbusch, J. C. & Swofford, D. Inferring evolutionary trees with PAUP*. *Curr. Prot. Bioinformatics* **6**, 6.4.1–6.4.28 (2003).
37. Stamatakis, A. RAxML-VI-HPC: maximum likelihood-based phylogenetic analyses with thousands of taxa and mixed models. *Bioinformatics* **22**, 2688–2690 (2006).
38. Tang, H. et al. Screening synteny blocks in pairwise genome comparisons through integer programming. *BMC Bioinformatics* **12**, 102 (2011).
39. Vanneste, K., Van de Peer, Y. & Maere, S. Inference of genome duplications from age distributions revisited. *Mol. Biol. Evol*. **30**, 177–190 (2013).
40. Edgar, R. C. MUSCLE: multiple sequence alignment with high accuracy and high throughput. *Nucleic Acids Res*. **32**, 1792–1797 (2004).
41. Goldman, N. & Yang, Z. A codon-based model of nucleotide substitution for protein-coding DNA sequences. *Mol. Biol. Evol*. **11**, 725–736 (1994).
42. Guindon, S. et al. New algorithms and methods to estimate maximum-likelihood phylogenies: assessing the performance of PhyML 3.0. *Syst. Biol*. **59**, 307–321 (2010).
43. Proost, S. et al. i-ADHoRe 3.0—fast and sensitive detection of genomic homology in extremely large data sets. *Nucleic Acids Res*. **40**, e11 (2012).
44. Fostier, J. et al. A greedy, graph-based algorithm for the alignment of multiple homologous gene lists. *Bioinformatics* **27**, 749–756 (2011).
45. Ostlund, G. et al. InParanoid 7: new algorithms and tools for eukaryotic orthology analysis. *Nucleic Acids Res*. **38**, D196–D203 (2010).
46. Zhang, G. Q. et al. The *Apostasia* genome and the evolution of orchids. *Nature* **549**, 379–383 (2017).
47. Ming, R. et al. The pineapple genome and the evolution of CAM photosynthesis. *Nat. Genet*. **47**, 1435–1442 (2015).
48. D'Hont, A. et al. The banana (*Musa acuminata*) genome and the evolution of monocotyledonous plants. *Nature* **488**, 213–217 (2012).
49. Al-Dous, E. K. et al. De novo genome sequencing and comparative genomics of date palm (*Phoenix dactylifera*). *Nat. Biotechnol*. **29**, 521–527 (2011).
50. Harkess, A. et al. The asparagus genome sheds light on the origin and evolution of a young Y chromosome. *Nat. Commun*. **8**, 1279 (2017).
51. Cai, J. et al. The genome sequence of the orchid *Phalaenopsis equestris*. *Nat. Genet*. **47**, 65–72 (2015).
52. Wang, W. et al. The *Spirodela polyrhiza* genome reveals insights into its neotenous reduction fast growth and aquatic lifestyle. *Nat. Commun*. **5**, 3311 (2014).
53. Olsen, J. L. et al. The genome of the seagrass *Zostera marina* reveals angiosperm adaptation to the sea. *Nature* **530**, 331–335 (2016).
54. Guan, R. et al. Draft genome of the living fossil *Ginkgo biloba*. *Gigascience* **5**, 49 (2016).
55. Drummond, A. J., Suchard, M. A., Xie, D. & Rambaut, A. Bayesian phylogenetics with BEAUti and the BEAST 1.7. *Mol. Biol. Evol*. **29**, 1969–1973 (2012).
56. Gandolfo, M., Nixon, K. & Crepet, W. A new fossil flower from the Turonian of New Jersey: *Dressiantha bicarpellata* gen. et sp. nov. (Capparales). *Am. J. Bot*. **85**, 964 (1998).
57. Beilstein, M. A., Nagalingum, N. S., Clements, M. D., Manchester, S. R. & Mathews, S. Dated molecular phylogenies indicate a Miocene origin for *Arabidopsis thaliana*. *Proc. Natl Acad. Sci. USA* **107**, 18724–18728 (2010).
58. Crepet, W. & Nixon, K. Fossil Clusiaceae from the late Cretaceous (Turonian) of New Jersey and implications regarding the history of bee pollination. *Am. J. Bot*. **85**, 1122–1133 (1998).
59. Xi, Z. et al. Phylogenomics and a posteriori data partitioning resolve the Cretaceous angiosperm radiation Malpighiales. *Proc. Natl Acad. Sci. USA* **109**, 17519–17524 (2012).
60. Ramírez, S. R., Gravendeel, B., Singer, R. B., Marshall, C. R. & Pierce, N. E. Dating the origin of the Orchidaceae from a fossil orchid with its pollinator. *Nature* **448**, 1042–1045 (2007).
61. Janssen, T. & Bremer, K. The age of major monocot groups inferred from 800+rbcL sequences. *Bot. J. Linn. Soc*. **146**, 385–398 (2004).
62. Smith, S. A., Beaulieu, J. M. & Donoghue, M. J. An uncorrelated relaxed-clock analysis suggests an earlier origin for flowering plants. *Proc. Natl Acad. Sci. USA* **107**, 5897–5902 (2010).

63. Clarke, J. T., Warnock, R. C. M. & Donoghue, P. C. J. Establishing a time-scale for plant evolution. *New Phytol*. **192**, 266–301 (2011).
64. Heled, J. & Drummond, A. J. Calibrated tree priors for relaxed phylogenetics and divergence time estimation. *Syst. Biol*. **61**, 138–149 (2012).
65. Li, L., Stoeckert, C. J., Jr & Roos, D. S. OrthoMCL: identification of ortholog groups for eukaryotic genomes. *Genome Res*. **13**, 2178–2189 (2003).
66. Capella-Gutiérrez, S., Silla-Martínez, J. M. & Gabaldón, T. trimAl: a tool for automated alignment trimming in large-scale phylogenetic analyses. *Bioinformatics* **25**, 1972–1973 (2009).
67. Stamatakis, A. RAxML version 8: a tool for phylogenetic analysis and post-analysis of large phylogenies. *Bioinformatics* **30**, 1312–1313 (2014).
68. Li, G. et al. Nonseed plant *Selaginella moellendorffi* has both seed plant and microbial types of terpene synthases. *Proc. Natl Acad. Sci. USA* **109**, 14711–14715 (2012).
69. Zhao, N., Guan, J., Lin, H. & Chen, F. Molecular cloning and biochemical characterization of indole-3-acetic acid methyltransferase from poplar. *Phytochemistry* **68**, 1537–1544 (2007).
70. Zhao, N. et al. Molecular and biochemical characterization of the jasmonic acid methyltransferase gene from black cottonwood (*Populus trichocarpa*). *Phytochemistry* **94**, 74–81 (2013).

Acknowledgements Fei Chen acknowledges funding from National Natural Science Foundation of China (31801898). L.Z. is partly supported by the open funds of the State Key Laboratory of Crop Genetics and Germplasm Enhancement (ZW201909) and State Key Laboratory of Tree Genetics and Breeding (TGB2018004). H.T. thanks the Fujian provincial government in China for a Fujian "100 Talent Plan". Y.V.d.P. acknowledges funding from the European Union Seventh Framework Programme (FP7/2007-2013) under European Research Council Advanced Grant Agreement 322739 – DOUBLEUP. Z.L. is funded by a postdoctoral fellowship from the Special Research Fund of Ghent University (BOFPDO2018001701).

Author contributions L.Z. led and managed the project. L.Z., Fei Chen and H.M. conceived the study. Fei Chen, L.Z., H.M., Feng Chen, Z.L., R.L. and Y.V.d.P. wrote the manuscript; L.Z., Fei Chen, X. Yu, X. Chang, C.Y., Y.C., Q.W., L.W. and H.K. collected and sequenced the plant material; L.Z., Y. Zhao, Fei Chen, S.Y.W.H., J.C., H.W., Xuequn Chen, J.H., A.S., X. Chang, W.D., X.L., Y. Zhuang, Y. Jiao, W.C., X. Yan, Y.Q., K.W. and H.M. performed gene family clustering and comparative phylogenomics. X. Zhang, L.Z., X. Zhou and Fei Chen assembled and annotated the genome. S.D., S.Z. and Yang Liu annotated the mitochondrial and chloroplast genomes. Yanhui Liu, L.Z. and Fei Chen conducted transcriptome sequencing and analysis. Z.L., R.L., Y.V.d.P., W.G., Fei Chen, H.T. and L.Z. conducted WGD analysis. Feng Chen, Q.J., Xinlu Chen, C.Z., Y. Jiang, W.Z., G.L., J.F. and Fei Chen conducted floral scent analysis. L.Z., Fei Chen, Q.W., L.W., Z.W., F.L. and J.W. conducted floral colour analysis. All authors read and approved the manuscript.

Competing interests The authors declare no competing interests.

Additional information
Supplementary information is available for this paper at https://doi.org/10.1038/s41586-019-1852-5.
Correspondence and requests for materials should be addressed to L.Z.
Peer review information *Nature* thanks Patrick Wincker and the other, anonymous, reviewer(s) for their contribution to the peer review of this work.

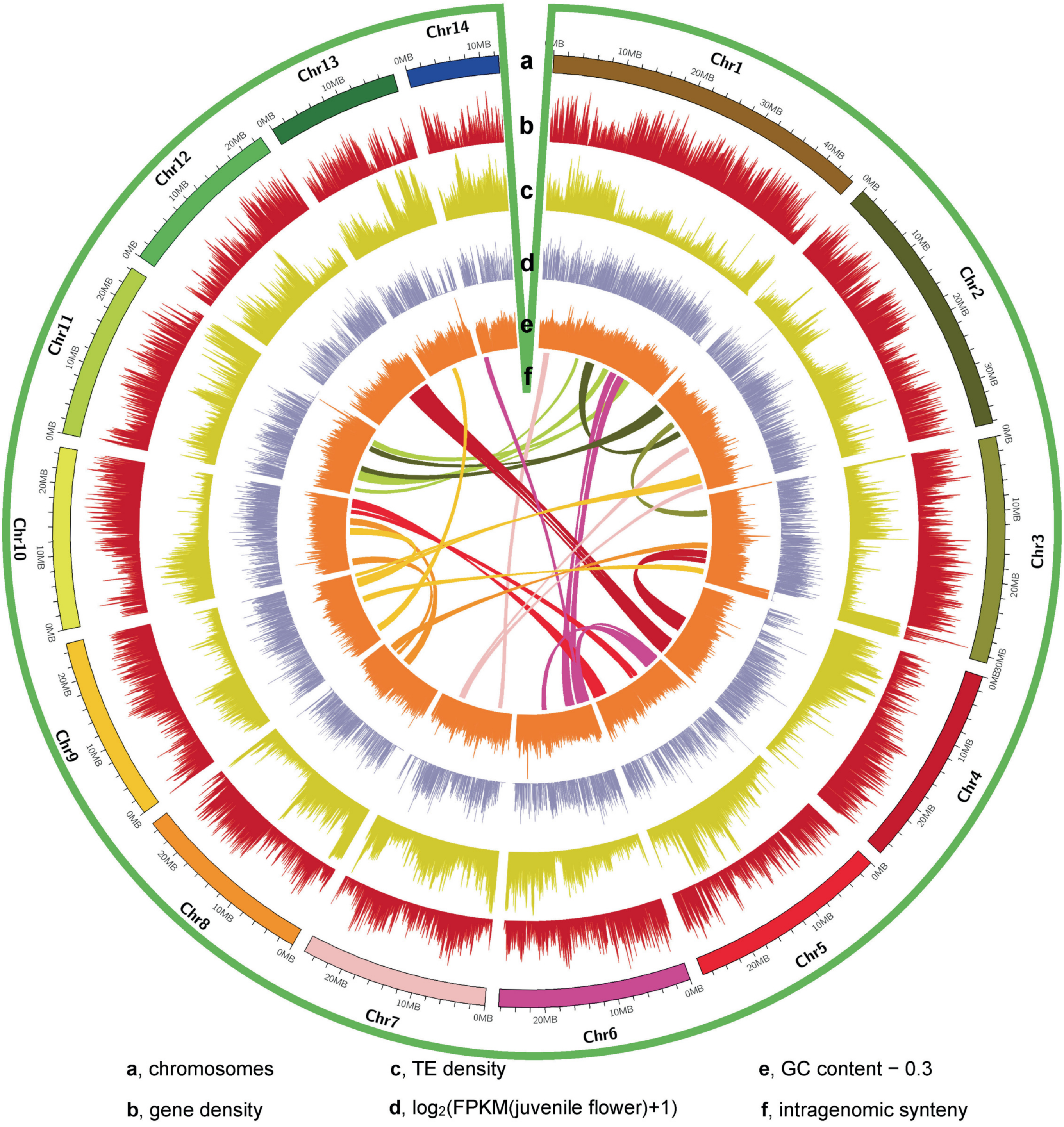

Extended Data Fig. 1 | High-quality genome of *N. colorata* allows integration of genetic and expression data. a, The assembled 14 chromosomes. **b**, Gene density plotted in a 100-kb sliding window. **c**, Transposable element (TE) density plotted in a 100-kb sliding window. **d**, Gene expression atlas of the juvenile flower, expression values were transformed with $\log_2(\mathrm{FPKM}+1)$. **e**, GC content plotted in a 100-kb sliding window. **f**, Intragenomic syntenic regions denoted by a single line represent a genomic syntenic region covering at least 20 paralogues.

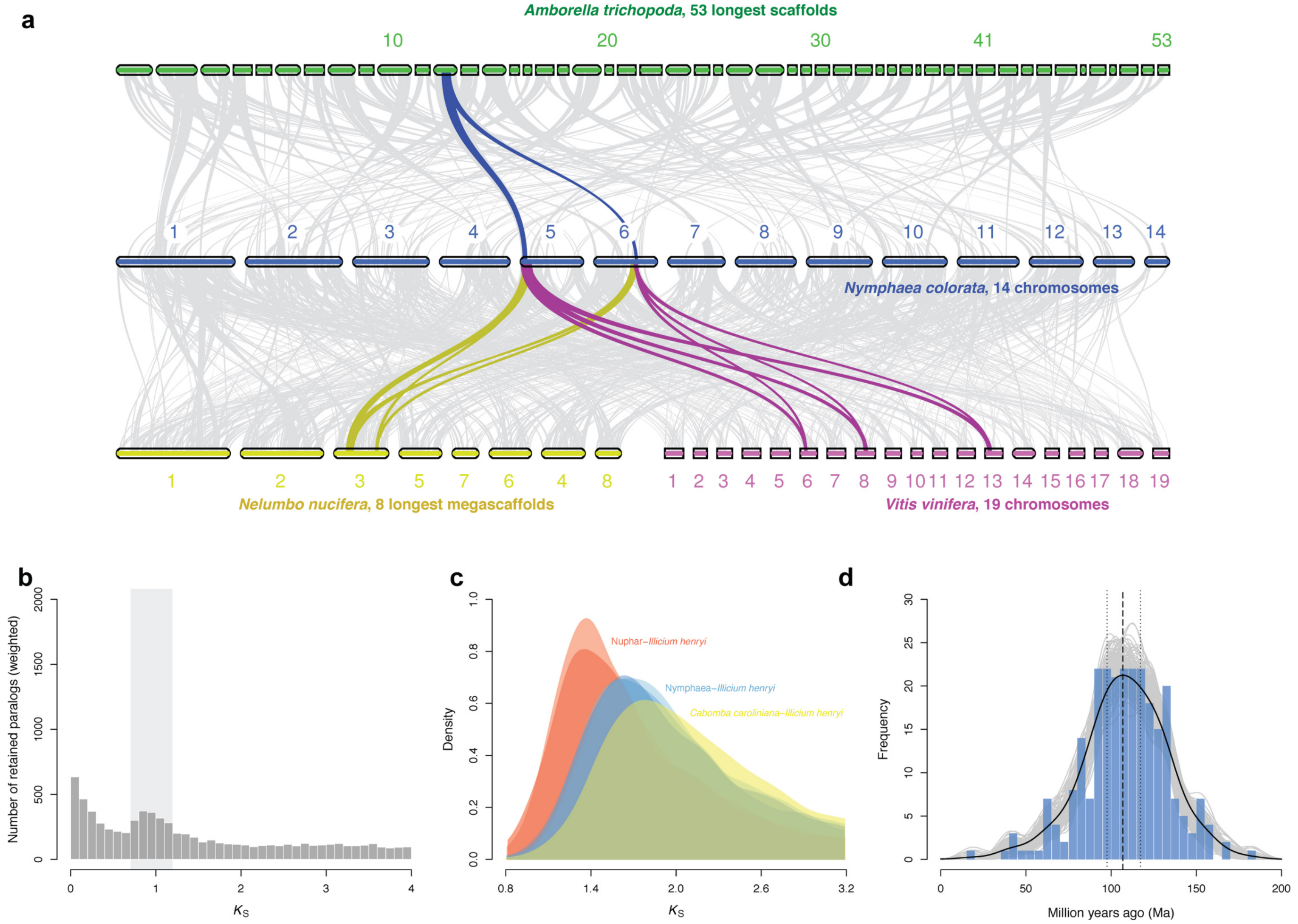

Extended Data Fig. 2 | WGD in Nymphaeales. a, Intergenomic synteny between *N. colorata* (14 chromosomes), *Amborella* (53 longest scaffolds), and the eudicots *N. nucifera* (8 longest megascaffolds) and *V. vinifera* (19 chromosomes). Five adjacent anchor pairs were plotted as one syntenic line. Coloured lines represent one example of syntenic genes found in other species that correspond to one copy in *Amborella*, two in *N. colorata*, two in *N. nucifera*, and three in *V. vinifera*. **b**, K_S distribution for the whole paranome of *N. colorata*. The light grey rectangle in the background indicates the K_S boundaries used to extract duplicate pairs for absolute phylogenomic dating of the WGD event, and also highlights the range in which WGD peaks can be identified in other species of Nymphaeaceae (Supplementary Note 5.2). **c**, Kernel-density estimates of K_S distributions for one-to-one orthologues between the outgroup species *I. henryi* and each of *N. lutea* and *N. advena* (red), *N. colorata*, *N. mexicana* and *Nymphaea* 'Woods blue goddess' (blue) and *C. caroliniana* (yellow). As each peak represents the same divergence event in the angiosperm phylogeny, the differences observed among the K_S values of the peaks indicate substantial substitution rate variation among these Nymphaealean lineages (see also Fig. 2b). **d**, Absolute age distribution obtained from phylogenomic dating of *N. colorata* WGD paralogues based on orthogroups with orthologues from *Amborella* and *G. biloba*. The solid black line represents the kernel density estimate of paralogue date estimates, and the vertical dashed black line represents its peak at 107 Ma. The grey lines represent density estimates from 2,500 bootstrap replicates and the vertical black dotted lines represent the corresponding 90% confidence interval for the WGD age estimate, 117–98 Ma (see Methods). The blue histogram shows the raw distribution of divergence date estimates for paralogues.

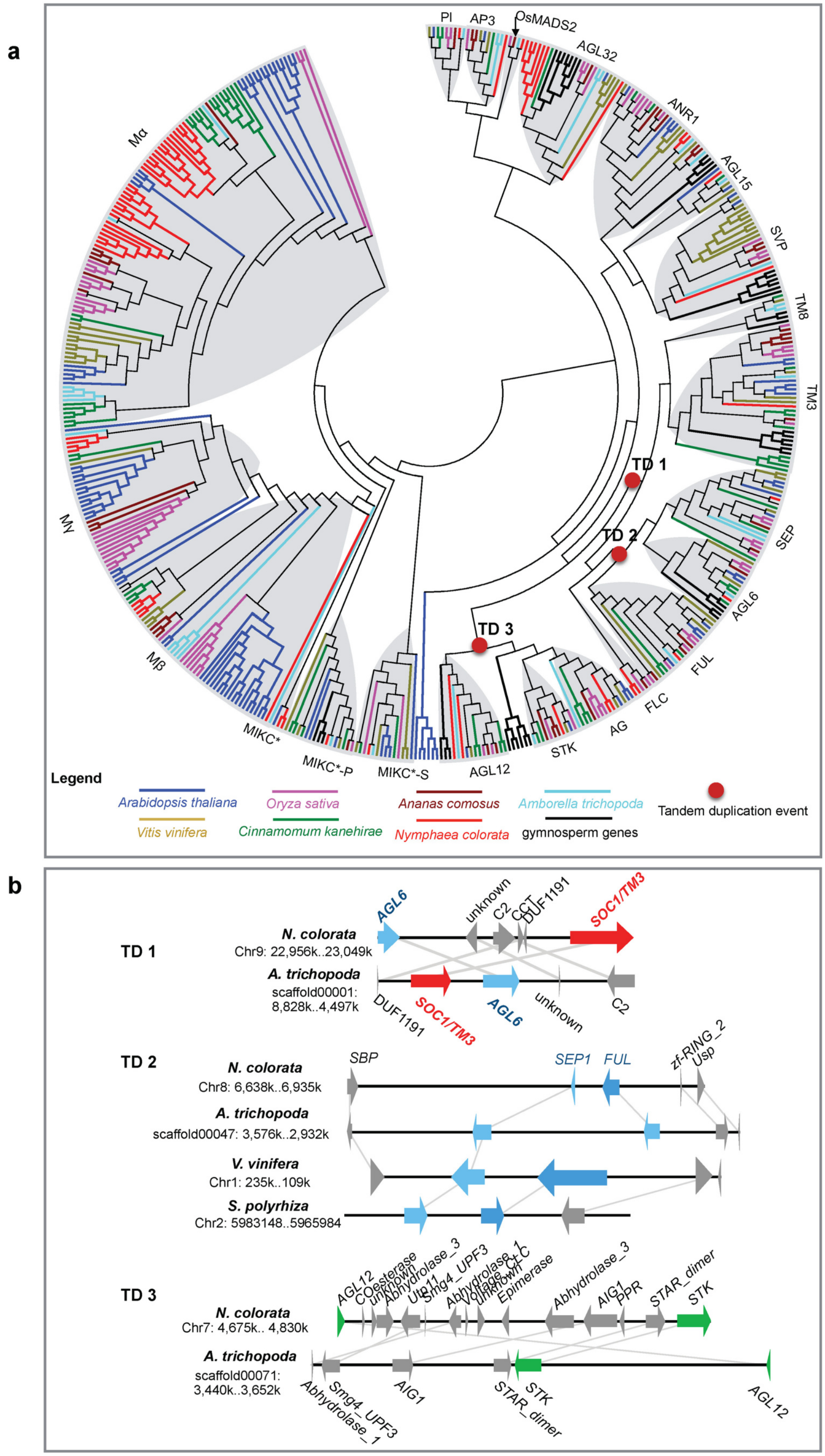

Extended Data Fig. 3 | The phylogenetic tree of MADS-box genes of *N. colorata*. **a**, The MADS-box genes are divided into type I and type II, and the latter was subdivided into MIKC^{c} and MIKC*. Branches of various species are shown in different colours, with the colour code below the tree. The nodes representing three tandem duplication events (TD1, TD2, and TD3 in **b**) are marked with red circles. **b**, Genomic regions with the duplicated genes derived from the three tandem duplication events (TD1, TD2 and TD3).

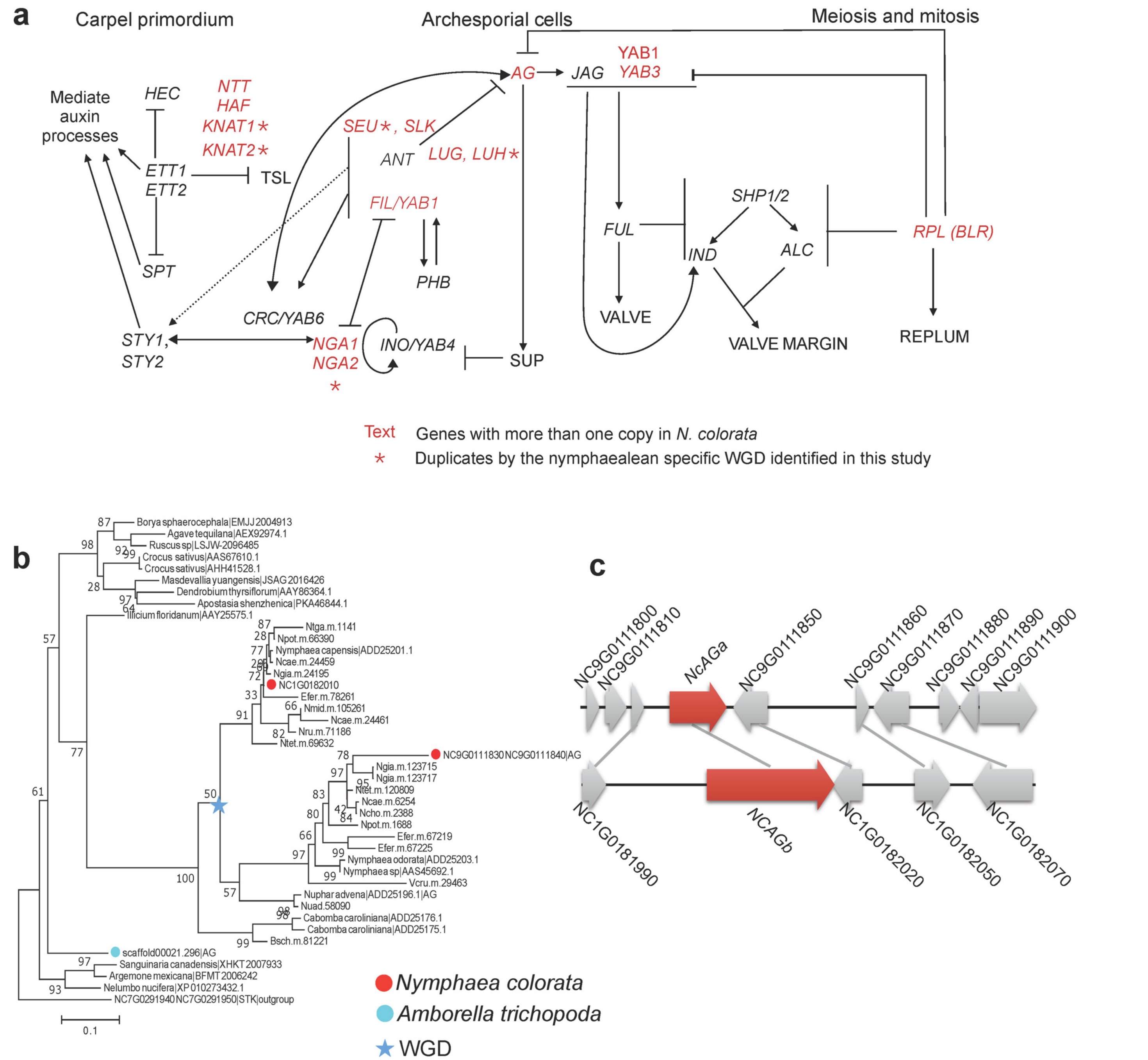

Extended Data Fig. 4 | Expansion of key genes regulating the carpel development by the Nymphaealean WGD. **a**, The reported pathway and genes that regulate carpel development. The red-labelled gene has two copies in *N. colorata*. The asterisk indicates that there is collinear support and is retained by the nymphaealean-specific WGD. **b**, Phylogenetic tree of *AG* genes, which specify floral meristem to determine the carpel and stamen identity. The star indicates the WGD specific to the water lily, as detected in this study. The duplicated *AG* genes in *N. colorata* are highlighted in red. **c**, Nc*AG* gene duplicates, Nc*AGa* and Nc*AGb*, are the result of the nymphaealean-specific WGD.

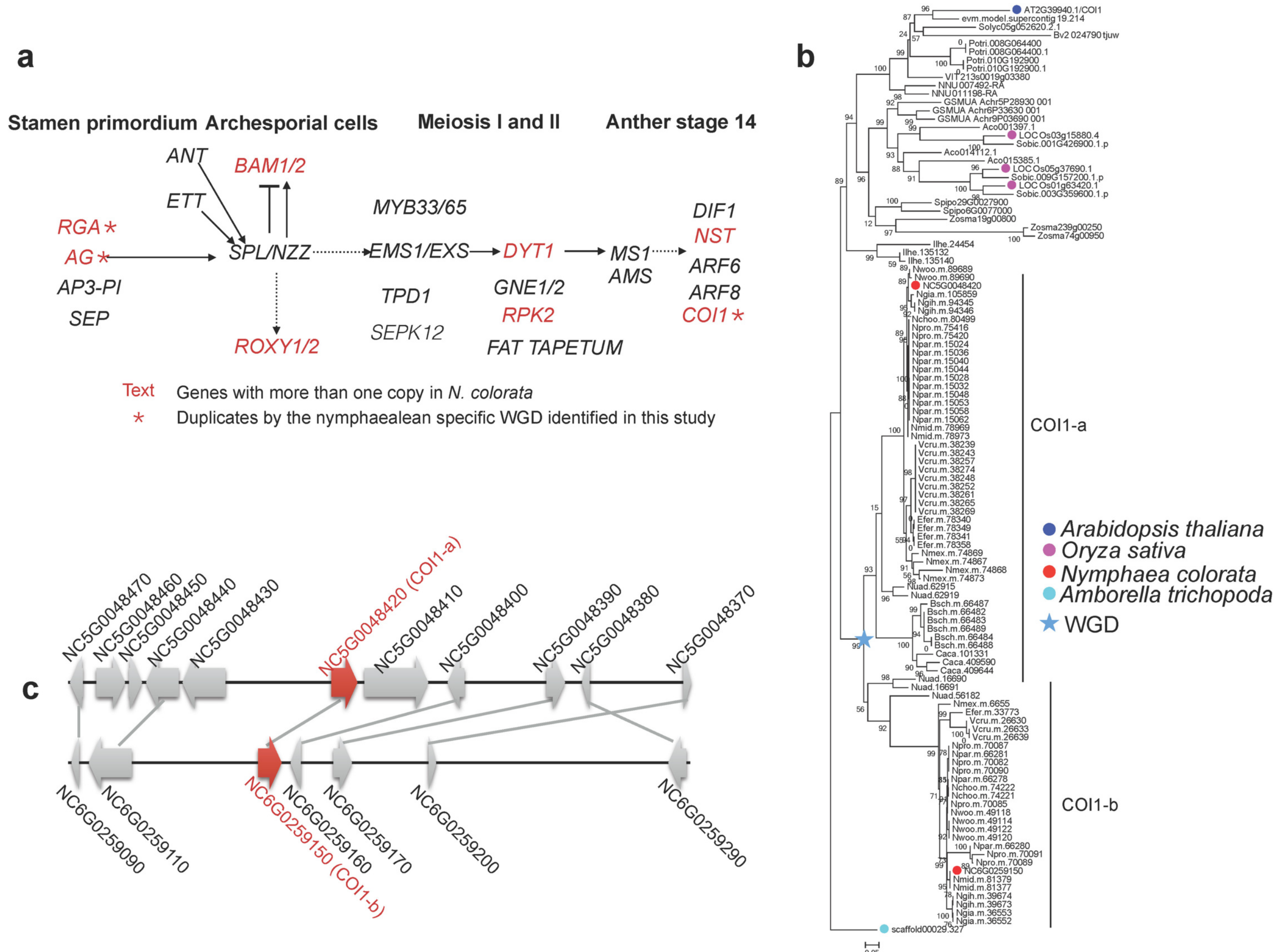

Extended Data Fig. 5 | Expansion of key genes regulating the development of the stamen by Nymphaealean WGD. a, The reported pathway and genes that regulate the stamen development. The red-labelled gene has two copies in *N. colorata*. The asterisk indicates that there is collinear support and is retained by the nymphaealean-specific WGD. **b**, Phylogenetic tree of *CORONATINE INSENSITIVE 1* (*COI1*), which recruits regulators of pollen development for modification by ubiquitination, needed in the JA response and regulating pollen fertility. **c**, Nc*COI1* gene duplicates have evolved through the WGD in Nymphaeales. The star indicates the nymphaealean-specific WGD.

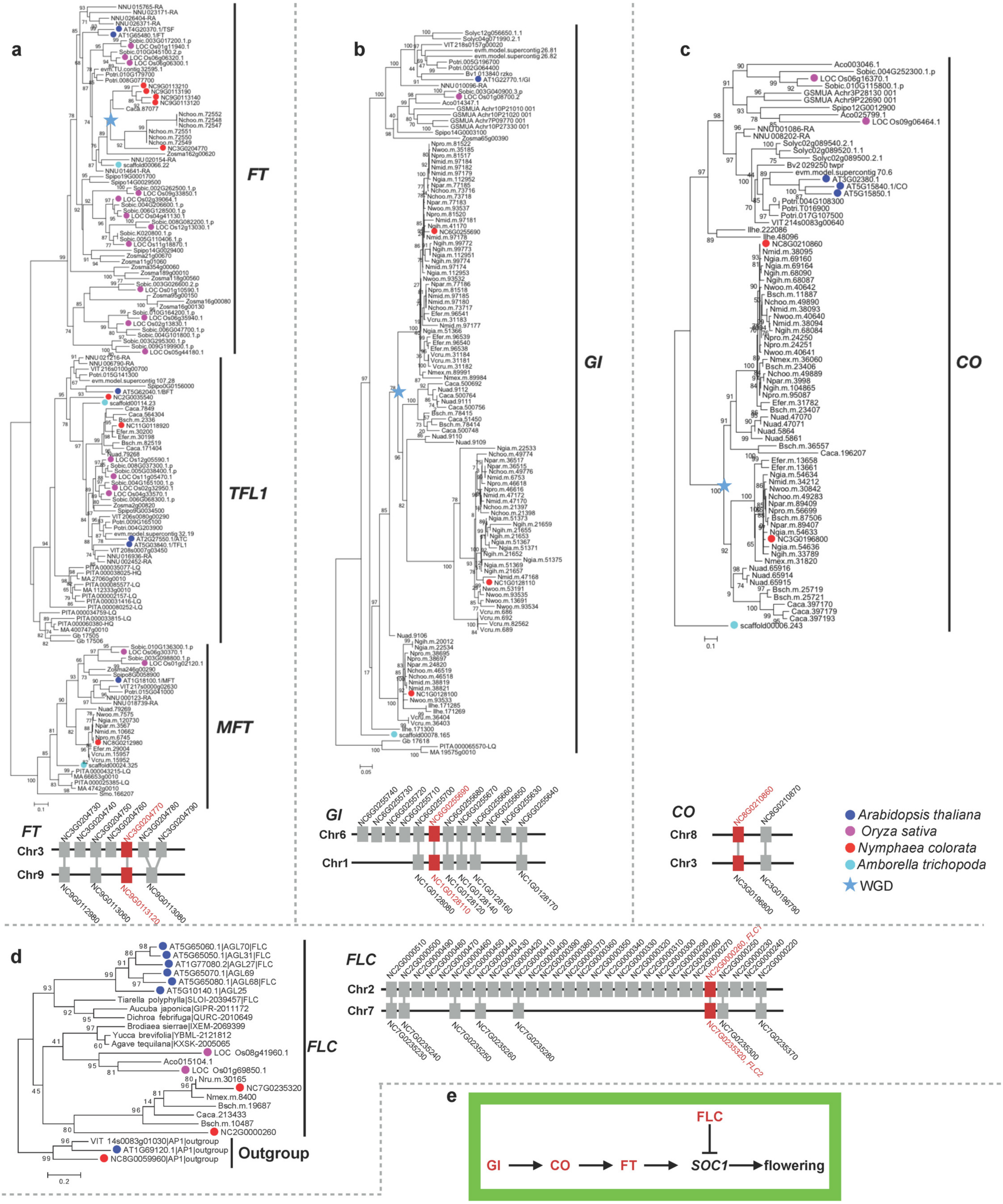

Extended Data Fig. 6 | Nymphaealean-specific duplication of the genes that control the initiation of flowering. a, Phylogenetic tree of the PEBP-domain containing gene family, including *FT*, *TFL1* and *MFT* subfamilies across various water lily species and other representative seed plants. **b**–**d**, Phylogenetic tree of the *GI* (**b**), *CO* (**c**) and *FLC* (**d**) gene family across various water lily species and other representative seed plants. **e**, The regulatory pathway for the flowering time control. The red-labelled gene has two copies in *N. colorata* and is retained by nymphaealean-specific WGD.

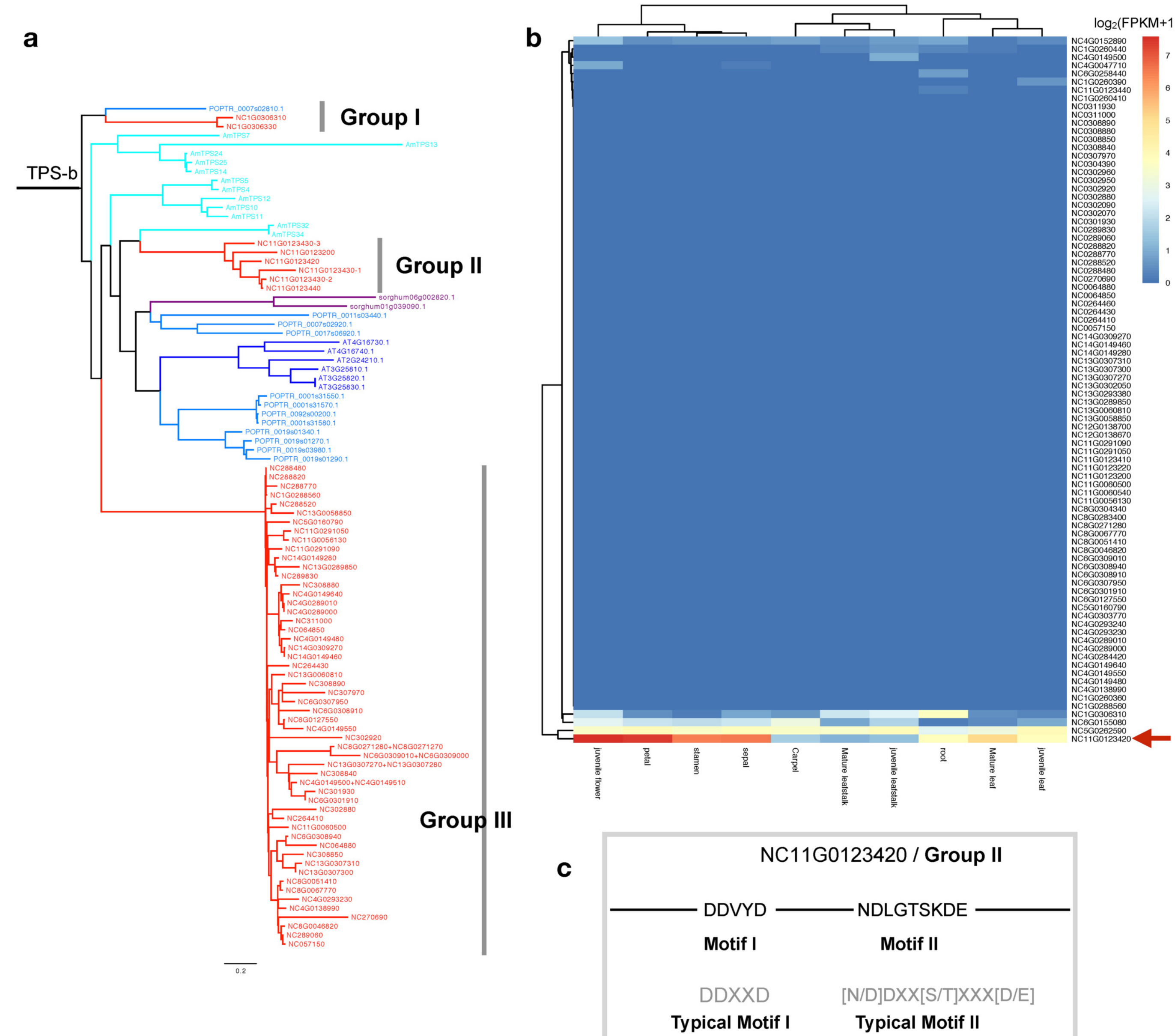

Extended Data Fig. 7 | Explosive expansion of the TPS-b subfamily and its implications. a, The phylogenetic classification of TPS-b subfamily into three groups. **b**, The group II member NC11G0123420 is the sole gene with high expression in the petal. **c**, Whereas most TPS-b members lack the two typical catalytic motifs, the NC11G0123420 retained both motifs, suggesting its potential role in producing sesquiterpene in *N. colorata*.

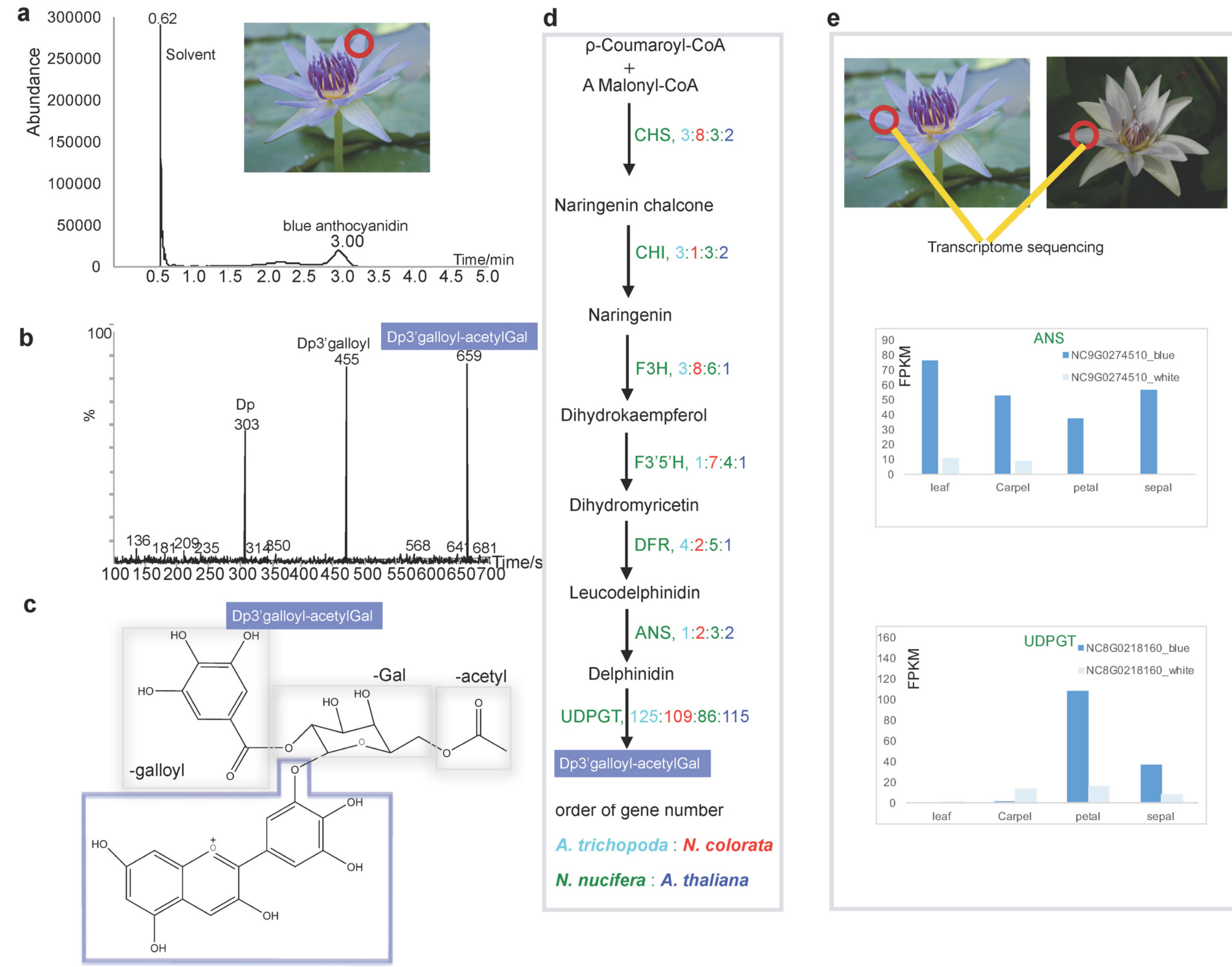

Extended Data Fig. 8 | The blue anthocyanidin and its potential biosynthesis pathway in *N. colorata*. a, The peak of the blue anthocyanidin appears at 3 min of the high-performance liquid chromatography (HPLC) detection. **b**, The three fragments of the blue anthocyanidin and their molecule mass. **c**, The molecule of the anthocyanidin was identified as delphinidin 3′-*O*-(2″-*O*-galloyl-6″-*O*-acetyl-β-galactopyranoside), abbreviated as Dp3′galloyl-acetylGal. **d**, The postulated pathway for the biosynthesis of Dp3′galloyl-acetylGal. Gene copy numbers are listed next to the enzymes. 3GGT, anthocyanidin 3-*O*-glucoside-2″-*O*-glucosyltransferase; 3′GT, 3′-*O*-beta-glucosyltranferase; 5AT, anthocyanin-5-aromatic acyltransferase; ANS, anthocyanidin synthase; CHI, chalcone isomerase; CHS, chalcone synthase; DFR, dihydroflavonol-4-reductase; F3H, flavanone-3-hydroxylase; F3′5′H, flavonoid-3′,5′-hydroxylase. **e**, Comparative transcriptomic analyses between the blue- and white-petal cultivars of *N. colorata* identified two genes, *ANS* and *UDPGT*, that are highly differentially expressed and might be potential regulators for blue coloration of the petals.

a

	Gene families	*Amborella trichopoda*	*Nymphaea colorata*	*Spirodela polyrhiza*	*Sorghum bicolor*	*Oryza sativa*	*Nelumbo nucifera*	*Vitis vinifera*	*Solanum lycopersicum*	*Arabidopsis thaliana*
Stress related	Gretchen Hagen3 (GH3)	6	36	13	13	14	16	9	31	20
	Auxin_inducible	30	62	55	76	62	88	93	106	78
	Salt stress response/antifungal (stress_antifung)	31	102	35	60	77	45	56	37	96
	Xylanase inhibitor (TAXi)	63	202	48	101	113	79	63	92	68
	NB-ARC (NLR)	105	416	52	326	498	134	442	248	165
	Terpene synthase	28	92	17	43	52	20	117	50	34
	Protein kinase	654	1176	784	1254	1468	1148	1320	1119	1022
	Cu oxidase	24	43	22	46	42	54	98	52	41
Transcription factors	WRKY	32	69	43	97	94	64	62	81	73
	MADS-box	34	70	44	78	75	39	81	105	108
	B3 DNA binding domain	32	57	39	89	87	68	73	102	93
	HSF_DNA-bind (Heat shock factor-type)	12	21	13	24	25	28	19	26	24
	NAC	44	68	53	128	136	86	83	96	111
	MYB	138	199	174	271	247	269	262	283	264
	AP2	73	102	81	173	157	124	140	165	141

b

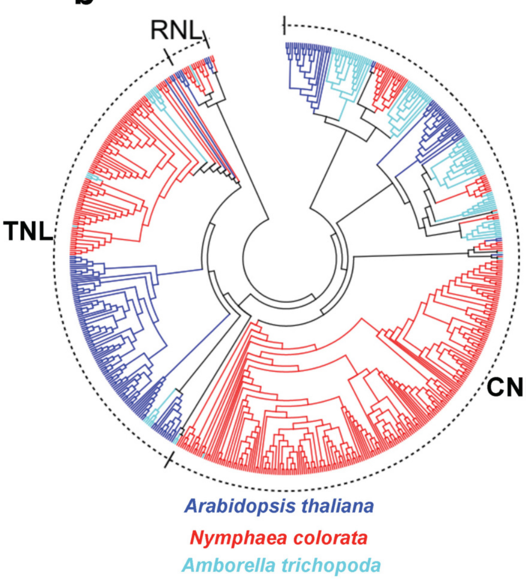

c

	TNL	CNL	RNL	Total R-genes	Total Protein Genes	Total R-genes/Total Protein Genes
Fragaria vesca	72	79	30	181	31,387	0.58%
Phaseolus vulgaris	103	224	10	337	32,720	1.03%
Glycine max	218	208	21	447	91,394	0.49%
Cajanus cajan	112	167	10	289	38,965	0.74%
Medicago truncatula	275	279	17	571	43,194	1.32%
Brassica rapa	127	68	9	204	47,942	0.43%
Brassica oleracea	132	10	5	147	56,687	0.26%
Arabidopsis thaliana	106	52	7	165	39,551	0.42%
Arabidopsis lyrata	138	55	5	198	39,161	0.51%
Capsella rubella	57	64	6	127	34,126	0.37%
Vitis vinifera	206	216	20	442	41,208	1.07%
Solanum lycopersicum	76	170	2	248	37,660	0.66%
Solanum tuberosum	68	376	3	447	37,966	1.18%
Beta vulgaris	34	134	18	186	32,874	0.57%
Nelumbo nucifera	26	103	5	134	38,191	0.35%
Aquilegia coerulea	94	99	10	203	41,063	0.49%
Brachypodium distachyon	0	252	1	253	37,892	0.67%
Oryza sativa	0	497	1	498	36,376	1.37%
Zea mays	0	137	2	139	52,470	0.26%
Sorghum bicolor	0	325	1	326	39,248	0.83%
Setaria italica	0	423	1	424	35,844	1.18%
Musa acuminata	0	110	1	111	47,707	0.23%
Phalaenopsis equestris	0	59	1	60	29,894	0.20%
Spirodela polyrhiza	0	51	1	52	19,623	0.26%
Zostera marina	0	20	0	20	20,648	0.10%
Nymphaea colorata	129	271	16	416	31,589	1.32%
Amborella trichopoda	15	89	1	105	31,494	0.33%
Gnetum montanum	127	98	10	235	27,491	0.85%
Pinus taeda	729	352	50	1,131	84,446	1.34%
Picea abies	370	170	45	585	66,632	0.88%
Ginkgo biloba	40	12	2	54	41,840	0.13%
Azolla filiculoides	1	0	1	2	33,800	0.01%
Salvinia cucullata	4	2	1	7	19,914	0.04%
Selaginella moellendorffii	13	1	3	17	45,247	0.04%
Physcomitrella patens	73	2	0	75	48,022	0.16%
Klebsormidium nitens	7	0	0	7	16,283	0.04%

d

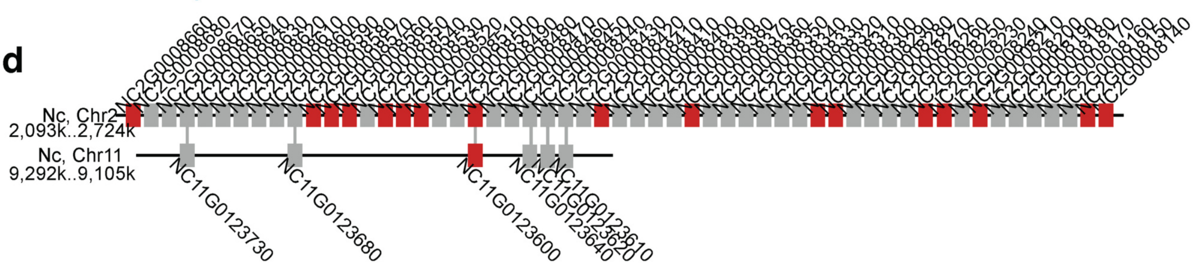

Extended Data Fig. 9 | Expanded stress-related and transcription factor gene families in the genome of *N. colorata*. **a**, Markedly expanded gene families for stress response and transcriptional regulation. NLR genes contain NB-ARC domains. Notably, *N. colorata* encodes the highest proportion of kinase genes compared with gymnosperms or other land plants. **b**, NLR genes expanded in all of its three subfamilies (*RNL*, *TNL* and *CNL*). **c**, Distribution of NLR genes across the representative algae and land plants. The background colours indicate the number variation in each species. **d**, An example showing how tandem duplication and WGD contributed to the expansion of R genes in *N. colorata*.

Extended Data Table 1 | Statistics of the sequenced and assembled genome of *N. colorata*

Statistic	Reads*	Contigs	Scaffolds	Chromosomes
Number	5,521,269	1,429	804	14
Longest Length	78 Kb	12.79 Mb	44.61 Mb	44.61 Mb
Total size	49.76 Gb	409.09 Mb	409.15 Mb	378.81 Mb
N50	12.59 Kb	2.14 Mb	25.52 Mb	27.06 Mb

*The reads only include sequencing by PacBio RS II SMRT sequencing technology.

nature research

Corresponding author(s): Liangsheng Zhang

Last updated by author(s): Sep 23, 2019

Reporting Summary

Nature Research wishes to improve the reproducibility of the work that we publish. This form provides structure for consistency and transparency in reporting. For further information on Nature Research policies, see Authors & Referees and the Editorial Policy Checklist.

Statistics

For all statistical analyses, confirm that the following items are present in the figure legend, table legend, main text, or Methods section.

n/a	Confirmed	
☒	☐	The exact sample size (*n*) for each experimental group/condition, given as a discrete number and unit of measurement
☒	☐	A statement on whether measurements were taken from distinct samples or whether the same sample was measured repeatedly
☒	☐	The statistical test(s) used AND whether they are one- or two-sided *Only common tests should be described solely by name; describe more complex techniques in the Methods section.*
☒	☐	A description of all covariates tested
☐	☒	A description of any assumptions or corrections, such as tests of normality and adjustment for multiple comparisons
☒	☐	A full description of the statistical parameters including central tendency (e.g. means) or other basic estimates (e.g. regression coefficient) AND variation (e.g. standard deviation) or associated estimates of uncertainty (e.g. confidence intervals)
☒	☐	For null hypothesis testing, the test statistic (e.g. *F*, *t*, *r*) with confidence intervals, effect sizes, degrees of freedom and *P* value noted *Give P values as exact values whenever suitable.*
☐	☒	For Bayesian analysis, information on the choice of priors and Markov chain Monte Carlo settings
☒	☐	For hierarchical and complex designs, identification of the appropriate level for tests and full reporting of outcomes
☒	☐	Estimates of effect sizes (e.g. Cohen's *d*, Pearson's *r*), indicating how they were calculated

Our web collection on statistics for biologists contains articles on many of the points above.

Software and code

Policy information about availability of computer code

Data collection	No software had been used for data collection
Data analysis	CANU (v1.3), Quiver, Arrow, Pilon (v1.20), bowtie2, Lachesis, HiC-Pro, Genscan, Augustus, Tandem Repeats Finder (v4.09), LTR_FINDER (v1.0.6), RepeatModeler (v1.0.5), RepeatMasker (v4.0.6), MAKER (v2.31.8), BUSCO software (v3.0.1), Tophat (v2.1.1), TRIMMOMATIC, Cufflink, TransDecoder, CD-HIT, Orthofinder (v1.1.8), Pfam (V31.0),MUSCLE(v3.8.31), TreePL, r8s, MCMCtree, ModelFinder, PAL2NAL (v14), trimAl (v1.4), RaxML (v8.0.19), PAML package (v4.4c), PhyML, ASTRAL(v5.5.12), PAUP(v4.0), InParanoid, LAST, BLAST, QUOTA-ALIGN, BEAST(v1.7), OrthoMCL (v2.0.9), Geneious (V.10.0.2), R, Python. Perl. Specific parameters used during run-time are provided in the methods. All softwares or scripts are available from official websites or GitHub as indicated in the methods.

For manuscripts utilizing custom algorithms or software that are central to the research but not yet described in published literature, software must be made available to editors/reviewers. We strongly encourage code deposition in a community repository (e.g. GitHub). See the Nature Research guidelines for submitting code & software for further information.

Data

Policy information about availability of data

All manuscripts must include a data availability statement. This statement should provide the following information, where applicable:

- Accession codes, unique identifiers, or web links for publicly available datasets
- A list of figures that have associated raw data
- A description of any restrictions on data availability

PacBio whole-genome sequencing data and Illumina data were deposited to the SRA at the NCBI under the BioProject ID PRJNA565347.
PacBio whole-genome sequencing data and Illumina data also were deposited in the BIG Data Center (http://bigd.big.ac.cn) under project number PRJCA001283. The genome assembly sequences and gene annotations have been deposited in the Genome Warehouse in BIG Data Center under accession number GWHAAYW00000000 and in ENA BioProject (PRJEB34452). The genome assembly sequences and gene annotations have been also deposited in the Waterlily Pond (http://waterlily.eplant.org). All these data are freely available to the public.

Field-specific reporting

Please select the one below that is the best fit for your research. If you are not sure, read the appropriate sections before making your selection.

☒ Life sciences ☐ Behavioural & social sciences ☐ Ecological, evolutionary & environmental sciences

For a reference copy of the document with all sections, see nature.com/documents/nr-reporting-summary-flat.pdf

Life sciences study design

All studies must disclose on these points even when the disclosure is negative.

Sample size	No statistical methods were used to predetermine sample size. Our samples were all from wild type and did not use processed samples and groups.
Data exclusions	No data were excluded.
Replication	The genome sequence was taken and sequenced with more than 120 fold coverage. No replication is needed our genome reports.
Randomization	No random sampling is required for genome sequencing, because the genome differences are very small within the wild population, thus any wild plant is allowed for genome sequencing.
Blinding	Blinding is not applicable in our study because it does not involve subjects which receive different treatments.

Reporting for specific materials, systems and methods

We require information from authors about some types of materials, experimental systems and methods used in many studies. Here, indicate whether each material, system or method listed is relevant to your study. If you are not sure if a list item applies to your research, read the appropriate section before selecting a response.

Materials & experimental systems

n/a	Involved in the study
☒	☐ Antibodies
☒	☐ Eukaryotic cell lines
☒	☐ Palaeontology
☒	☐ Animals and other organisms
☒	☐ Human research participants
☒	☐ Clinical data

Methods

n/a	Involved in the study
☒	☐ ChIP-seq
☐	☒ Flow cytometry
☒	☐ MRI-based neuroimaging

Flow Cytometry

Plots

Confirm that:

☒ The axis labels state the marker and fluorochrome used (e.g. CD4-FITC).

☒ The axis scales are clearly visible. Include numbers along axes only for bottom left plot of group (a 'group' is an analysis of identical markers).

☒ All plots are contour plots with outliers or pseudocolor plots.

☒ A numerical value for number of cells or percentage (with statistics) is provided.

Methodology

Sample preparation	Nuclei were isolated from young leaves in spring ,using PI staining for 15 minutes.
Instrument	Beckman Coulter COULTER EPICS XL™
Software	FACS data analyses were performed using CXP v2.2 Software
Cell population abundance	abundance >8000 cells were collected for each sample. Total nuclei populations were gated using relative fluorescence intensity: the proportions of nuclei with different ploidy levels were determined based on their relative fluorescence intensity: Pear is a diploid (2N) as a reference, according to the peak position (Supplementary Figure 5).

Gating strategy

Total nuclei populations were gated using PI intensity. In PI+ singles cells, the proportions of nuclei with different ploidy levels were determined based on their PI intensity (Supplementary Figure 5).

☒ Tick this box to confirm that a figure exemplifying the gating strategy is provided in the Supplementary Information.

Article

RGF1 controls root meristem size through ROS signalling

https://doi.org/10.1038/s41586-019-1819-6

Received: 30 November 2017

Accepted: 22 October 2019

Published online: 4 December 2019

Masashi Yamada[1,2,3], Xinwei Han[1,4] & Philip N. Benfey[1*]

The stem cell niche and the size of the root meristem in plants are maintained by intercellular interactions and signalling networks involving a peptide hormone, root meristem growth factor 1 (RGF1)[1]. Understanding how RGF1 regulates the development of the root meristem is essential for understanding stem cell function. Although five receptors for RGF1 have been identified[2–4], the downstream signalling mechanism remains unknown. Here we report a series of signalling events that follow RGF1 activity. We find that the RGF1-receptor pathway controls the distribution of reactive oxygen species (ROS) along the developmental zones of the *Arabidopsis* root. We identify a previously uncharacterized transcription factor, *RGF1-INDUCIBLE TRANSCRIPTION FACTOR 1* (*RITF1*), that has a central role in mediating RGF1 signalling. Manipulating *RITF1* expression leads to the redistribution of ROS along the root developmental zones. Changes in ROS distribution in turn enhance the stability of the PLETHORA2 protein, a master regulator of root stem cells. Our results thus clearly depict a signalling cascade that is initiated by RGF1, linking this peptide to mechanisms that regulate ROS.

Plant roots encounter varying environmental conditions and respond by altering their growth. Root growth arises through controlled cell division in the root's meristematic zone (equivalent to the transit amplifying zone in animals). After division, most cells increase their size in the elongation zone, and mature in the differentiation zone. The sizes of these developmental zones are determined by intrinsic and extrinsic signals. ROS are an intrinsic signal for establishing the size of the meristematic zone: superoxide (O_2^-) accumulates primarily in the meristematic zone, hydrogen peroxide (H_2O_2) accumulates mainly in the differentiation zone[5,6] and the balance between O_2^- and H_2O_2 modulates the transition from proliferation to differentiation[6].

The RGF1 peptide is essential in controlling the size of the meristematic zone, acting as both an intrinsic and an extrinsic signal[1,7,8]. Treating roots with RGF1 increases the size of the meristematic zone, and the *Arabidopsis rgf1/2/3* triple mutant has a smaller meristematic zone[1]. Quintuple mutants of the *rgf1 receptor* (*rgfr*) lack most cells in the root meristem and are insensitive to RGF1 (refs. [2–4]). RGF1 signalling controls the stability of the PLETHORA (PLT) 1/2 proteins[1], which are required for stem cell maintenance[9]. However, it is not known how RGF1 modulates the size of the meristematic zone and the stability of PLT1/2.

We began by treating *Arabidopsis* roots with RGF1, and detected green fluorescent protein (GFP)-labelled HIGH PLOIDY2 (HPY2)[10] (a marker protein specific to the meristematic zone) in an enlarged area that correlates with a larger meristematic zone (Extended Data Fig. 1a–c), suggesting that RGF1 controls gene expression primarily in this zone. Therefore, to identify target genes that are downstream of RGF1, we isolated the meristematic zone 1 h after RGF1 treatment (Extended Data Fig. 1d). Given that *HPY2-GFP* expression and the size of the meristematic zone were unchanged in this time period, we can exclude the possibility that an enlarged meristem is the reason for any changes in RNA levels. RNA-sequencing (RNA-seq) profiling found 583 genes that were differentially expressed between the RGF1-treatment and mock-treatment scenarios (Supplementary Table 1). Gene Ontology highly enriched categories included 'glutathione transferase activity' and 'oxidoreductase activity' (Extended Data Fig. 2 and Supplementary Table 2), suggesting that RGF1 might signal through an ROS intermediate.

To examine the relationship between RGF1 and ROS signalling, we analysed the distribution of O_2^- and H_2O_2 after RGF1 treatment. A specific indicator for H_2O_2—namely H_2O_2-3′-*O*-acetyl-6′-*O*-pentafluorobenzenesulfonyl-2′-7′-difluorofluorescein-Ac (H_2O_2-BES-Ac)[6]—exhibited lower fluorescence in the meristematic and elongation zones 24 h after RGF1 treatment (Fig. 1a, c). We detected O_2^- signals by nitro blue tetrazolium (NBT) staining[5] and observed these signals more broadly in the meristematic zone 24 h after RGF1 treatment (Fig. 1b, d). In the RGF1-receptor mutant *rgfr1/2/3*, the meristematic zone of which is unchanged after RGF1 treatment (Fig. 1e), levels of H_2O_2 and O_2^- were comparable between mock and RGF1 treatments (Fig. 1e–h).

To identify downstream factors in the RGF1 and ROS signalling pathway, we combined our RGF1 transcriptome data with developmental-zone-specific transcriptome data[11]. Among genes that are both meristematic-zone-specific and induced by RGF1, we identified *PLANT AT-RICH SEQUENCE AND ZINC-BINDING TRANSCRIPTION FACTOR* (*PLATZ*) *FAMILY PROTEIN* (AT2G12646), the expression of which increased approximately twofold after 1 h of RGF1 treatment (Fig. 2a). We named this gene *RGF1-INDUCIBLE TRANSCRIPTION FACTOR 1* (*RITF1*), and found that its expression occurs predominantly in the meristematic zone[11] (Fig. 2b). Quantitative reverse transcription with polymerase chain reaction (RT–PCR) showed that the abundance of the *RITF1* transcript increased approximately twofold in wild-type roots 1 h after RGF1 treatment, and was maintained at 6 h and 24 h (Fig. 2c). By contrast,

[1]Department of Biology and Howard Hughes Medical Institute, Duke University, Durham, NC, USA. [2]Agricultural Biotechnology Research Center, Academia Sinica, Taipei, Taiwan. [3]Biotechnology Center in Southern Taiwan, Academia Sinica, Tainan, Taiwan. [4]Present address: GlaxoSmithKline, Waltham, MA, USA. *e-mail: philip.benfey@duke.edu

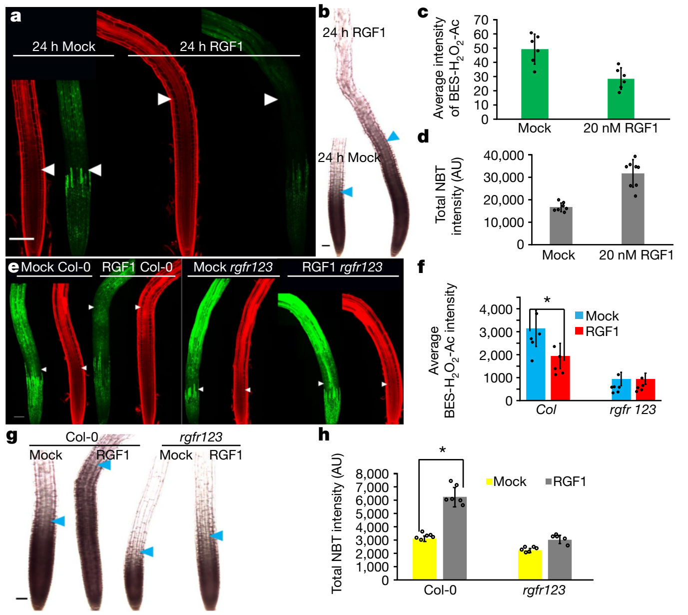

Fig. 1 | Distribution of ROS levels upon RGF1 treatment. a, Confocal images of roots 24 h after mock treatment or treatment with 20 nM RGF1. Propidium iodide (PI) staining is in red; H_2O_2-BES-Ac fluorescence is in green. **b**, Roots stained with NBT 24 h after mock treatment or treatment with 20 nM RGF1. **c**, Quantification of H_2O_2-BES-Ac intensity in the meristematic zone ($n = 6$ independent roots; $P < 0.003$). **d**, Quantification of NBT staining intensity (in arbitrary units, AU) in the meristematic zone ($n = 7$ independent roots; $P = 3.16 \times 10^{-5}$). **e**, Confocal images of roots 24 h after mock treatment or treatment with 20 nM RGF1 in wild-type roots (Columbia-0 (Col-0) background) or *rgfr1/2/3* mutants. Staining as in **a**. **f**, Quantification of H_2O_2-BES-Ac staining intensity in the meristematic zone in wild-type and *rgfr1/2/3* roots ($n = 5$ independent roots; $^*P < 0.025$). **g**, Wild-type or *rgfr1/2/3* roots stained with NBT 24 h after mock treatment or treatment with 20 nM RGF1. **h**, Quantification of NBT staining intensity in the meristematic zone of wild-type or *rgfr1/2/3* roots ($n = 5$ independent roots; $^*P = 1.65 \times 10^{-6}$). White and blue arrowheads indicate the junction between the meristematic and elongation zones. Scale bar, 50 µm. Bar graphs show means. Error bars show ± s.d. Dots indicate each data point. *P* values are calculated by two-sided Student's *t*-test.

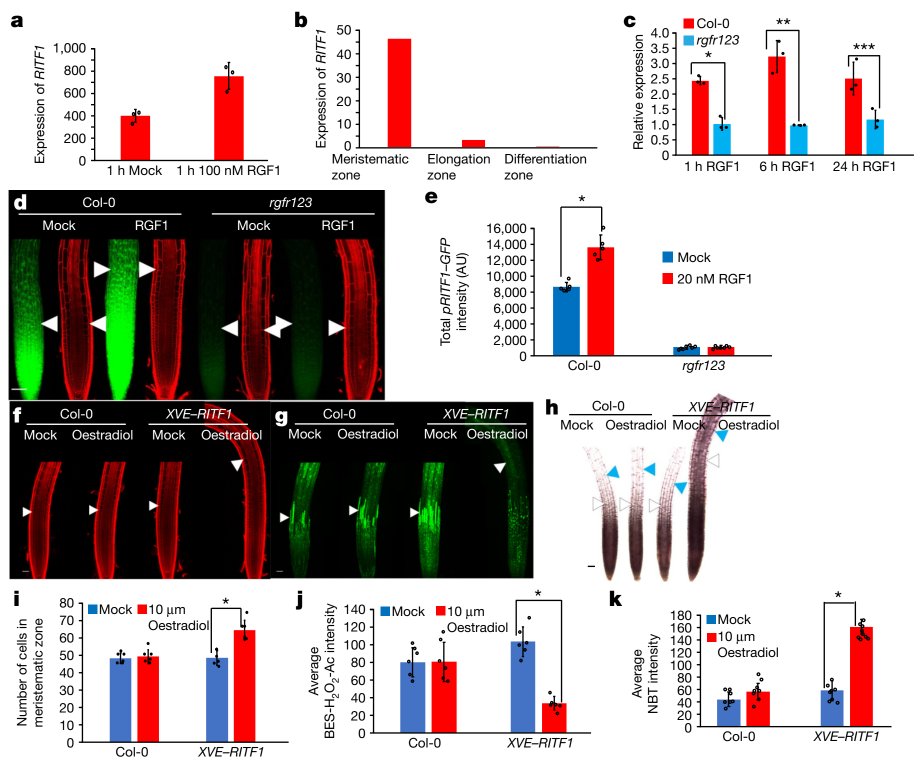

Fig. 2 | Expression of *RITF1* and phenotype of *RITF1* overexpression line. a, Expression of *RITF1* in the meristematic zone 1 h after treatment with 100 nM RGF1, measured by RNA-seq (CPM, counts per million mapped reads; $n = 3$ independent experiments; $P < 0.01$. **b**, Expression of *RITF1* in developmental zones as measured by RNA-seq (FPKM, fragments per kilobase of transcript per million mapped reads). **c**, Expression of *RITF1* in the meristematic zone of wild-type and *rgfr1/2/3* roots upon treatment with RGF1, measured by quantitative RT–PCR ($n = 3$ independent experiments; $^*P < 0.001$, $^{**}P < 0.002$, $^{***}P < 0.02$). **d**, Confocal images of *pRITF1-GFP* expression and PI staining in wild-type and *rgfr1/2/3* roots after RGF1 treatment. **e**, Total intensity of *pRITF1-GFP* expression in wild-type and *rgfr1/2/3* roots 24 h after RGF1 treatment ($n = 5$ independent roots; $^*P < 0.001$). **f**, **g**, Confocal images of roots stained with PI (**f**) and H_2O_2-BES-Ac (**g**) in Col-0 and *XVE–RITF1* roots after mock or oestradiol treatment. **h**, Light microscope images of NBT-stained roots after mock or oestradiol treatment. **i**, Number of cells in the meristematic zone in Col-0 and *XVE–RITF1* roots after mock or oestradiol treatment ($n = 6$ independent roots; $^*P < 0.001$). **j**, Average intensity of BES-H_2O_2-Ac in the differentiation zone after mock or oestradiol treatment ($n = 6$ independent roots; $^*P < 0.001$). **k**, Average intensity of NBT staining in the differentiation zone after mock or oestradiol treatment ($n = 7$ independent roots; $^*P < 0.001$). Scale bar, 50 µm. White and blue arrowheads throughout indicate the junctions between the meristematic and elongation zones and between the elongation and differentiation zones. Bar graphs show means. Error bars are ± s.d. Dots indicate each data point. *P* values are calculated by two-sided Student's *t*-test.

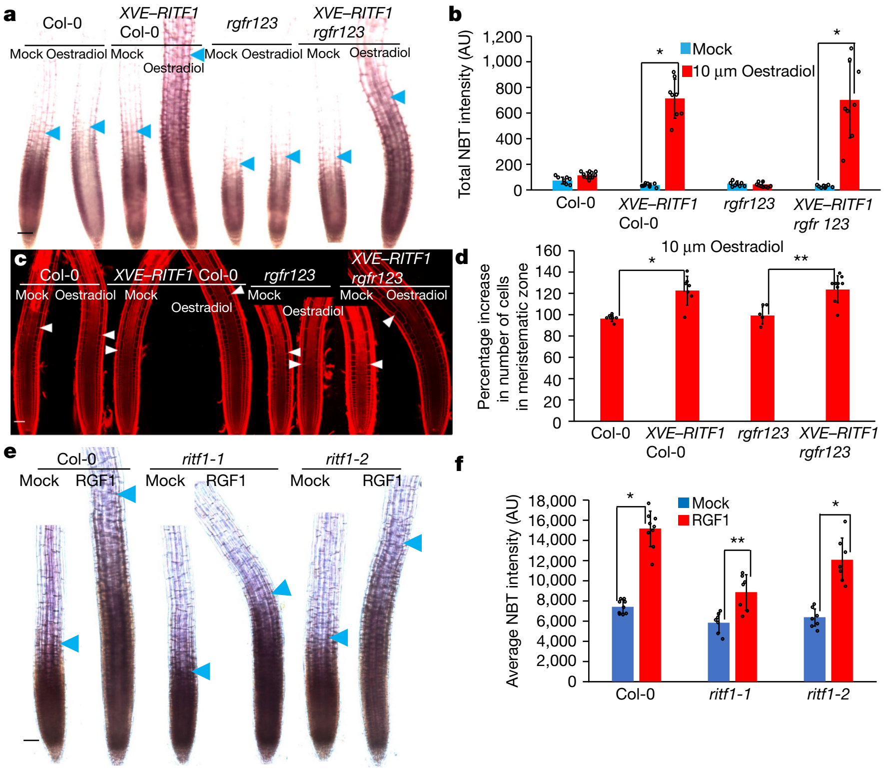

Fig. 3 | ROS signals and meristem size in *RITF1* overexpression lines in *rgfr1/2/3* roots. a, Light microscope images of NBT-stained roots with or without *XVE–RITF1* expression in Col-0 and *rfgr1/2/3* roots. **b**, Total intensity of NBT staining in the differentiation zone with or without *XVE–RITF1* expression, in Col-0 and *rgfr1/2/3* roots, 24 h after mock or oestradiol treatment ($n = 8$ independent roots; $*P < 2.0 \times 10^{-5}$). **c**, Confocal images of PI-stained roots with or without *XVE–RITF1* expression in Col-0 and *rfgr1/2/3* roots. **d**, Percentage increase in the number of cells in the meristematic zone (in which 100% is the number of cells in the mock treatment scenario) 24 h after oestradiol treatment compared with mock treatment in Col-0 roots, *rgfr1/2/3* roots, and *XVE–RITF1*-expressing Col-0 and *rgfr1/2/3* roots ($n = 6$ independent roots; $*P < 0.0002$, $**P < 0.0007$). **e**, Light microscope images of roots of Col-0, *ritf1-1* and *ritf1-2* roots stained with NBT 24 h after 5 nM RGF1 treatment. Scale bar, 50 μm. Blue arrowheads show the junction between the meristematic and elongation zones. **f**, Quantification of NBT staining intensity in the meristematic zone in Col-0, *ritf1-1* and *ritf1-2* roots after 5 nM RGF1 treatment ($n = 7$ independent roots; $*P \leq 2.4 \times 10^{-5}$, $**P < 0.021$). Bar graphs show means. Error bars represent ± s.d. Dots indicate each data point. *P* values are calculated by two-sided Student's *t*-test.

RITF1 expression in *rgfr1/2/3* roots was unchanged upon RGF1 treatment (Fig. 2c). Expression of a construct with the *RITF1* promoter driving the *GFP*-coding sequence (*pRITF1-GFP*) mirrored our transcriptome analysis and increased in the wild type following RGF1 treatment (Fig. 2b, d, e). By contrast, *pRITF1-GFP* expression was very low and exhibited no change following RGF1 treatment in *rgfr1/2/3* mutants (Fig. 2d, e). These data indicate that *RITF1* expression is regulated by the RGF1 pathway.

To understand its function, we inducibly overexpressed *RITF1* using the oestradiol-inducible promoter system[12,13]. After 24 h of β-oestradiol treatment, the meristematic zone became enlarged and the number of cells increased (Fig. 2f, i), similarly to RGF1-treated roots (Fig. 1a). We also found that H_2O_2 levels declined in all three developmental zones upon oestradiol treatment (Fig. 2g, j), and that enhanced O_2^- signals were observed in a broader area of the meristematic zone (Fig. 2h, k), with ectopic O_2^- signals in the elongation and differentiation zones (Fig. 2h). Altered ROS signals and an enlarged meristem suggest that *RITF1* can modulate ROS signalling and root meristem size downstream of the RGF1 pathway. We also observed an earlier response to the induction of *RITF1* than to RGF1 treatment. A decrease in the H_2O_2-BES-Ac signal was detected 4 h after oestradiol treatment (Extended Data Fig. 3a, b), in contrast to the lack of detectable change seen 4 h after RGF1 treatment in either the uninduced line or in the wild type (Extended Data Fig. 3a, b). Changes in ROS signals were first observed at approximately 6 h after RGF1 treatment in those lines (Extended Data Figs. 4i, j, o, p and 5b, c).

If *RITF1* functions downstream of the RGF1-receptor pathway, then overexpression of *RITF1* in *rgfr1/2/3* mutants should rescue root meristem defects and increase root meristem size. To test this hypothesis, we inducibly overexpressed *RITF1* in *rgfr1/2/3* mutants and in the wild type, and observed an enhanced O_2^- signal and increased root meristem size in both (Fig. 3a–d). Finally, we examined two *ritf1* mutant alleles. We generated the *ritf1-1* allele using CRISPR–Cas9; it contains a frameshift mutation early in the coding sequence, rendering it unlikely to produce a functional RITF1 protein. The *ritf1-2* allele has a transfer-DNA insertion in the intron, but still shows low expression of full-length *RITF1* and is likely to produce low levels of a functional protein. The *ritf1-1* mutant had a smaller meristem and lower root growth rate (Extended Data Fig. 6a, b) and was more resistant to RGF1 treatment than were wild-type plants or those with the weak allele, *ritf1-2* (Extended Data Fig. 6b, c). Further, there was lower induction of the O_2^- signal in *ritf1-1* mutants after RGF1 treatment than in the wild-type or *ritf1-2* background (Fig. 3e, f). Taken together, these results strongly suggest that *RITF1* is a primary regulator of ROS signalling and root meristem size in the RGF1 signalling pathway.

To confirm post-translational regulation of PLT2, we compared transcriptional (*pPLT2-CFP*)[14] and translational (*gPLT2-YFP*)[14] fusion lines (in which CFP and YFP are cyan and yellow fluorescent protein, respectively). At 24 h after RGF1 treatment, we observed broader localization of *gPLT2-YFP* (Extended Data Fig. 7b), and the localization and expression of *pPLT2-CFP* were comparable between mock and RGF1 treatments—even though RGF1-treated roots had a larger meristematic zone (Extended Data Fig. 7a). The *gPLT2-YFP* signal decreased more gradually and was broadly localized in the larger meristematic zone after RGF1 treatment (Extended Data Fig. 7a–c). These results confirm that RGF1 regulates PLT2 post-translationally.

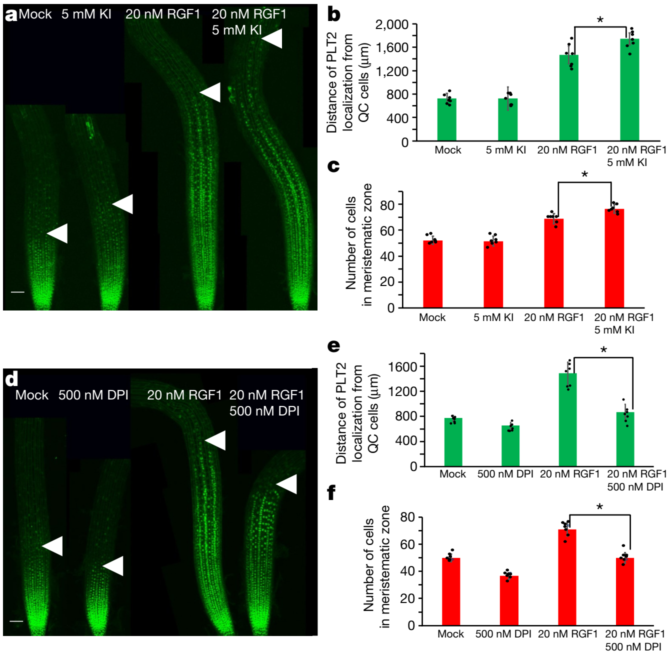

Fig. 4 | Stability of the PLT2 protein upon changes in oxidation conditions. **a**, **d**, Confocal images of gPLT2–YFP 24 h after treatment with RGF1, KI (a H_2O_2 scavenger) and DPI (an inhibitor of NADPH oxidase). **b**, **e**, Localization of gPLT2–YFP upon treatment with RGF1 and KI ($n = 7$ independent roots; $^*P < 0.015$) and RGF1 and DPI ($n = 7$ independent roots; $^*P < 1.5 \times 10^{-5}$). **c**, **f**, Meristem size upon treatment with RGF1 and KI ($n = 7$ independent roots, $^*P < 0.0017$) and RGF1 and DPI ($n = 7$ independent roots, $^*P < 2.6 \times 10^{-7}$). Bar graphs show means. Error bars show ± s.d. Dots indicate each data point. *P* values are calculated by two-sided Student's *t*-test. QC, quiescent centre.

PLT2 is a member of the APETALA2/ETHYLENE-RESPONSE FACTOR family of transcription factors, which has previously been reported to be regulated by oxidative post-translational modification[15–20]. To determine whether modifying the oxidative conditions can increase the stability of the PLT2 protein, we treated the *gPLT2-YFP* line with RGF1 and potassium iodide (KI), an H_2O_2 scavenger. We found that *gPLT2-YFP* was localized more broadly and that meristem size was larger than in roots treated only with RGF1 (Fig. 4a–c). By contrast, increased H_2O_2 levels inhibited the broad localization of *gPLT2-YFP* and reduced the increase in meristem size upon addition of RGF1 (Extended Data Fig. 8a–e). To decrease O_2^- levels, we used a low concentration (500 nM) of diphenyleneiodonium (DPI), an NADPH oxidase inhibitor (Fig. 4d–f), resulting in a slight inhibition of PLT2 stability and slight decrease in meristem size (Fig. 4d–f) with little effect on root meristem development. However, co-treatment using RGF1 and DPI markedly reduced PLT2 stability and meristem size as compared with RGF1 treatment alone (Fig. 4d–f). Finally, we measured *gPLT2-YFP*, O_2^- and H_2O_2 levels in a time course (4–10 h) after RGF1 treatment. Broader localization of *gPLT2-YFP* and increased superoxide levels along with lower H_2O_2 signals at the distal end of the meristematic zone appeared 6 h after treatment (Extended Data Figs. 4a–d, i, j, o, p and 5a–c). At 8 h and 10 h after treatment, expanded *gPLT2-YFP* expression and O_2^- signals correlated with declining H_2O_2 signals (Extended Data Figs. 4e–h, k–n, q–t and 5a–c). Taken together, these results indicate that ROS regulates PLT2 protein stability by modulating O_2^- and H_2O_2 levels.

To further test the hypothesis that the stability of the PLT2 protein is enhanced by ROS signalling produced by *RITF1*, we overexpressed *RITF1* in the *plt2* mutant. This produced an increase in the O_2^- signal (Extended Data Fig. 9a, b) but was unable to induce an increase in root meristem size (Extended Data Fig. 9c, d). Furthermore, we detected only a subtle change in root meristem size in *plt2* mutants as compared with wild-type roots upon RGF1 treatment (Extended Data Fig. 10a, b). However, we did observe an elevated O_2^- signal (Extended Data Fig. 10c, d). These results strongly suggest that ROS signals modulated by *RITF1* enhance PLT2 stability. In summary, we have identified a new transcription factor, RITF1, which is induced by RGF1 in the meristematic zone. This factor controls ROS levels, which in turn regulate PLT2 stability and meristem size. Overall, our data demonstrate a key role for the peptide hormone RGF1 in regulating root growth via modulation of ROS levels, which control the transition from proliferation to differentiation.

Online content

Any methods, additional references, Nature Research reporting summaries, source data, extended data, supplementary information, acknowledgements, peer review information; details of author contributions and competing interests; and statements of data and code availability are available at https://doi.org/10.1038/s41586-019-1819-6.

1. Matsuzaki, Y., Ogawa-Ohnishi, M., Mori, A. & Matsubayashi, Y. Secreted peptide signals required for maintenance of root stem cell niche in *Arabidopsis*. *Science* **329**, 1065–1067 (2010).
2. Ou, Y. et al. RGF1 INSENSITIVE 1 to 5, a group of LRR receptor-like kinases, are essential for the perception of root meristem growth factor 1 in *Arabidopsis thaliana*. *Cell Res*. **26**, 686–698 (2016).
3. Song, W. et al. Signature motif-guided identification of receptors for peptide hormones essential for root meristem growth. *Cell Res*. **26**, 674–685 (2016).
4. Shinohara, H., Mori, A., Yasue, N., Sumida, K. & Matsubayashi, Y. Identification of three LRR-RKs involved in perception of root meristem growth factor in *Arabidopsis*. *Proc. Natl Acad. Sci. USA* **113**, 3897–3902 (2016).
5. Dunand, C., Crèvecoeur, M. & Penel, C. Distribution of superoxide and hydrogen peroxide in *Arabidopsis* root and their influence on root development: possible interaction with peroxidases. *New Phytol*. **174**, 332–341 (2007).
6. Tsukagoshi, H., Busch, W. & Benfey, P. N. Transcriptional regulation of ROS controls transition from proliferation to differentiation in the root. *Cell* **143**, 606–616 (2010).
7. Whitford, R. et al. GOLVEN secretory peptides regulate auxin carrier turnover during plant gravitropic responses. *Dev. Cell* **22**, 678–685 (2012).
8. Meng, L., Buchanan, B. B., Feldman, L. J. & Luan, S. CLE-like (CLEL) peptides control the pattern of root growth and lateral root development in *Arabidopsis*. *Proc. Natl Acad. Sci. USA* **109**, 1760–1765 (2012).
9. Aida, M. et al. The PLETHORA genes mediate patterning of the *Arabidopsis* root stem cell niche. *Cell* **119**, 109–120 (2004).
10. Ishida, T. et al. SUMO E3 ligase HIGH PLOIDY2 regulates endocycle onset and meristem maintenance in *Arabidopsis*. *Plant Cell* **21**, 2284–2297 (2009).
11. Li, S., Yamada, M., Han, X., Ohler, U. & Benfey, P. N. High-resolution expression map of the *Arabidopsis* root reveals alternative splicing and lincRNA regulation. *Dev. Cell* **39**, 508–522 (2016).
12. Curtis, M. D. & Grossniklaus, U. A gateway cloning vector set for high-throughput functional analysis of genes in planta. *Plant Physiol*. **133**, 462–469 (2003).
13. Zuo, J., Niu, Q. W. & Chua, N. H. Technical advance: an estrogen receptor-based transactivator XVE mediates highly inducible gene expression in transgenic plants. *Plant J*. **24**, 265–273 (2000).
14. Galinha, C. et al. PLETHORA proteins as dose-dependent master regulators of *Arabidopsis* root development. *Nature* **449**, 1053–1057 (2007).
15. Waszczak, C. et al. Sulfenome mining in *Arabidopsis thaliana*. *Proc. Natl Acad. Sci. USA* **111**, 11545–11550 (2014).
16. Licausi, F., Ohme-Takagi, M. & Perata, P. APETALA2/ethylene responsive factor (AP2/ERF) transcription factors: mediators of stress responses and developmental programs. *New Phytol*. **199**, 639–649 (2013).
17. Shaikhali, J. et al. The redox-sensitive transcription factor Rap2.4a controls nuclear expression of 2-Cys peroxiredoxin A and other chloroplast antioxidant enzymes. *BMC Plant Biol*. **8**, 48 (2008).
18. Dietz, K. J., Vogel, M. O. & Viehhauser, A. AP2/EREBP transcription factors are part of gene regulatory networks and integrate metabolic, hormonal and environmental signals in stress acclimation and retrograde signalling. *Protoplasma* **245**, 3–14 (2010).
19. Licausi, F. et al. Oxygen sensing in plants is mediated by an N-end rule pathway for protein destabilization. *Nature* **479**, 419–422 (2011).
20. Welsch, R., Maass, D., Voegel, T., Dellapenna, D. & Beyer, P. Transcription factor RAP2.2 and its interacting partner SINAT2: stable elements in the carotenogenesis of *Arabidopsis* leaves. *Plant Physiol*. **145**, 1073–1085 (2007).
21. Wang, Z. P. et al. Egg cell-specific promoter-controlled CRISPR/Cas9 efficiently generates homozygous mutants for multiple target genes in *Arabidopsis* in a single generation. *Genome Biol*. **16**, 144 (2015).
22. Maeda, H. et al. Fluorescent probes for hydrogen peroxide based on a non-oxidative mechanism. *Angew. Chem. Int. Edn* **43**, 2389–2391 (2004).
23. Schindelin, J. et al. Fiji: an open-source platform for biological-image analysis. *Nat. Methods* **9**, 676–682 (2012).

Methods

Plant materials and growth conditions

All *Arabidopsis* mutants and marker lines used here are in the Columbia-0 (Col-0) background. The transfer (T)-DNA *plt2* insertion line (SALK_130119.20.25) was obtained from the *Arabidopsis* Biological Resource Center at Ohio State University. The T-DNA insertion was found to be 166 base pairs upstream of the transcription start site in the *plt2* mutant. Seeds were surface-sterilized using 50% (v/v) bleach and 0.1% Tween 20 (Sigma) for 15 min and then rinsed five times with sterile water. All seeds were plated on standard MS medium (1 × Murashige and Skoog salt mixture, Caisson Laboratories), 0.5 g l^{-1} MES, 1% sucrose and 1% agar (Difco) and adjusted to pH 5.7 with KOH. All plated seeds were stratified at 4 °C for 2 days before germination. Seedlings were grown on vertically positioned square plates in a Percival incubator with 16 h of daily illumination at 22 °C.

The *ritf1* mutants

The *ritf1-1* mutant was generated using the egg-cell-specific controlled CRISPR–Cas9 system[21].

sgRNA sequences are as follows: *RITF1* sgRNA1, GGGATGTCCA TACCATGAGA CGG; *RITF1* sgRNA2, CCGTCTACCACAGTTGATCG AGG; *RITF1* sgRNA3, GGCGAACTTGAAGGAGTCTA TGG; and *RITF1* sgRNA4, GACTTTCAGTTGAGTCCTCA TGG.

The CRISPR construct was transformed into the Col-0 background using the *Agrobacterium*-mediated floral dip method. The mutant was identified by direct sequencing of PCR products of the targets in the offspring in T1, T2 and T3 generations. The loss-of-function *ritf1-1* allele contains an insertion of a cytosine 74 bp after the transcription start site in the *RITF1* gene (771 bp). The additional insertion of a cytosine results in a frameshift and creates many premature stop codons after the insertion. To exclude issues related to off-target mutations, we confirmed the sequences of three potential off-target genes (At5g25170, At1g70110 and At3g20640) that include similar sequences of the target sites by direct sequencing of PCR products in the offspring in the T1, T2 and T3 generations. We did not find any mutations in these genes. Further, we identified another independent CRISPR allele (*ritf1-3*). This allele contains an insertion of an adenine 75 bp after the transcription start site in the *RITF1* gene. The additional insertion of an adenine results in a frameshift and creates many premature stop codons after the insertion. Similar to *ritf1-1* mutants, *ritf1-3* seedlings exhibited strong resistance to the RGF1 peptide and did not increase their O_2^- levels by comparison with wild-type seedlings or with the weak allele (*ritf1-2*) (Extended Data Fig. 6d, e). These results exclude the possibility that off-target mutations cause the RGF1-resistant phenotype.

In the *ritf1-2* allele (SALK_081503C), we identified the T-DNA insertion 787 bp downstream of the transcription start site (in the middle of the second intron) of *RITF1*. Even though the insertion disrupted an intron, a full-length transcript was weakly detected from this allele.

Detecting *gPLT2-YFP* and ROS signals

We grew wild-type and *rgfr1/2/3* mutant plants for seven days on MS agar plates, then transferred them to MS agar plates containing either water (mock treatment) or 20 nM synthetic sulfated RGF1 peptide (Invitrogen). After treatment with RGF1, seedlings were stained for 2 min in a solution of 200 μM NBT in 20 mM phosphate buffer (pH 6.1) in the dark and rinsed twice with distilled water. To detect hydrogen peroxide with BES-H_2O_2-Ac[22], we incubated seedlings in 50 μM BES-H_2O_2-Ac (WAKO) for 30 min in the dark, then mounted them in 10 mg ml^{-1} PI in water[6]. Roots were observed using a ×20 objective with a Zeiss LSM 880 laser scanning confocal microscope. Excitation and detection windows were set as follows: BES-H_2O_2-Ac, excitation at 488 nm and detection at 500–550 nm; PI staining, excitation at 561 nm and detection at 570–650 nm. Confocal images were processed, stitched and analysed using the Fiji package of ImageJ[23]. Maximum projection images were generated from about 30 *z*-section images of BES-H_2O_2-Ac staining. The average intensity of BES-H_2O_2-Ac in the meristematic zone was measured in five or six roots with three biological replicates. Images for NBT staining were obtained using a ×10 objective with a Leica DM 5000-B light microscope. The total intensities of NBT staining in the meristematic zone were measured in ten roots with three biological replicates using the Fiji software package[23].

For experiments with a shorter time course, we grew *gPLT2-YFP* seedlings[14] on MS agar plates for seven days, then transferred them to MS agar plates containing either water (mock) or 100 nM RGF1 peptide. At 4 h, 6 h, 8 h and 10 h after mock or RGF1 treatment, images were taken with a confocal or light microscope after PI, NBT and BES-H_2O_2-Ac staining, as above.

Total RNA extraction and library preparation

The *HYP2-GFP*[10] line was grown on MS plates for seven days. *HYP2-GFP* seedlings were then transferred into liquid MS medium and treated with water (mock) or 100 nM RGF1 peptide in 6-well plates for 1 h. After mock or RGF1 treatment, the seedlings were taken out of liquid MS medium and transferred onto a 2% agarose plate. Using an ophthalmic scalpel (Feather), the meristematic zone of the seedlings was precisely dissected on the basis of *HYP2-GFP* fluorescence as detected under a dissecting microscope (Axio Zoom, Zeiss). Using the RNeasy Micro Kit (Qiagen), we extracted total RNA from 20 root sections treated with water (mock) or 100 nM RGF1. For each treatment, three replicates of the RNA extractions were performed. All total RNA samples were treated with DNase I during RNA extraction. RNA quality was examined using a 2100 Bioanalyzer (Agilent). The RNA integrity number was more than 9.0 in all samples. The concentration of total RNA was measured by a Qubit (Invitrogen) instrument. For each replicate, we generated complementary DNA (cDNA) from 50 ng total RNA using the Ovation RNA-seq System V2 (NuGEN). We fragmented 3 μg of the cDNA using the Covaris S-Series System. We used 400 ng of the fragmented cDNA with an average size of 400 bp for library preparation with the Ovation Ultralow System V2 (NuGEN). Illumina sequencing was performed at the Duke Genome Sequencing Shared Resource. The libraries for three biological replicates of mock- and RGF1-treated meristematic zones were sequenced on an Illumina HiSeq 2000 (100 base paired end reads).

Differential expression analysis after RGF1 treatment

Illumina sequencing reads were mapped to the TAIR10 *Arabidopsis* genome using Tophat V2.1.1. The parameters used for mapping were: '-N 5–read-gap-length 5–read-edit-dist 5–b2-sensitive -r 100–mate-std-dev 150 -p 5 -i 5 -I 15000–min-segment-intron 5–max-segment-intron 15000–library-type fr-unstranded'. To select properly mapped reads with unique mapping positions, we kept for further analysis only those alignments with a flag of 83, 99, 147 or 163 and a mapping quality score of 50. Mapping positions of these reads were compared with the Araport11 genome annotation (https://www.araport.org/downloads/Araport11_Release_201606/annotation) using HTseq-count (v0.6.1) with parameters '–stranded=no–mode=intersection-nonempty', which generated a read count per gene. The raw read counts of microRNAs, long non-coding RNAs and protein-coding genes were then used as input into DESeq2 (v1.14.1) for differential gene expression analysis. Genes with a false discovery rate (FDR)-adjusted *P* value less than or equal to 0.1 were regarded as differentially expressed between the RGF and mock treatment scenarios. The enriched Gene Ontology (GO) groups among differentially expressed genes were identified using agriGO. The GO annotation downloaded from http://geneontology.org was used as input for agriGO. Enriched GO groups required an FDR-adjusted *P* value of 0.01 or less and a minimum mapping entry of 10.

qRT–PCR analysis of *RITF1* expression upon RGF1 treatment

To perform qRT-PCR, we dissected about 20 meristematic zones of wild-type and *rgfr1/2/3* mutant roots at 1 h, 6 h and 24 h after RGF1 treatment

as described above. We generated cDNA from 10 μg of total RNA using SuperScript IV Reverse Transcriptase (Invitrogen). Three biological replicates and technical replicates were used for each experiment. Standard curves were run for the primer pairs of: *RITF1*, 5′-CAAGCCATGCCACACTCTAA-3′ and 5′- TTATCCGAGGAAGCTGAGGA-3′; and (as reference) *PROTEIN PHOSPHATASE 2A SUBUNIT A3* (*PP2AA3*, AT1G13320), 5′-GGCCAAAATGATGCAATCTC-3′ and 5′- TGCGAAATACCGAACATCAA-3′. Expression of *RITF1* was assayed by qRT-PCR on a LightCycler 480 (Roche) with SYBR-based detection, normalized to *PP2AA3*, and analysed by the efficiency-corrected quantification model.

Plasmid constructs

To produce the overexpression line and the transcriptional reporter line of *RITF1*, we amplified the coding sequence (771 bp) or the promoter sequence (2,121 bp) of the *RITF1* gene (AT2G12646) using the Phusion High-Fidelity DNA polymerase (New England Biolabs) from a wild-type cDNA library and genomic DNA, respectively, then subcloned into the pENTR/D/TOPO vector (Invitrogen). We used the following primers to amplify the coding sequence: 5′-CACCATGGGAATTCAGAAACCGG-3′ and 5′- TTAACAGAGAGGAGATCGTTG-3′; and for the promoter, 5′- CACCGCATCATTTTATTATAACCCGA-3′ and 5′-GAGGACTCAACTGAAAGTCA-3′. We confirmed the sequences of the coding sequence and the promoter in the pENTR/D/TOPO vector using Sanger sequencing. The clones were recombined into the pMDC7 and pMDC204 vectors[12] using LR clonase II (Invitrogen) in order to fuse the oestradiol-inducible promoter (*XVE*)[13] with the coding region of *RITF1*, the *RITF1* promoter and GFP with a carboxy-terminus HDEL retention sequence.

Meristem size and ROS detection after *RITF1* overexpression

We transformed the *XVE–RITF1* construct into the wild-type (Col-0) background. To measure meristem size and detect ROS signals, we grew two independent *XVE–RITF1* and wild-type lines on MS medium for seven days, then transferred them to MS medium containing dimethylsulfoxide (DMSO, mock) or 10 μM β-oestradiol (Sigma). After 24 h with mock or oestradiol treatment, we measured meristem size and detected ROS signals in the wild-type and *XVE-RITF1* lines, as above.

Expression of *pRITF1-GFP* in roots

We introduced the *pRITF1-GFP* construct into wild-type (Col-0) and *rgfr1/2/3* plants. We grew two independent T3 lines of each background for seven days in MS medium and treated them with either water (mock) or 20 nM RGF1 peptide. As described above, 24 h after treatment, GFP signals were detected using a confocal laser scanning microscope.

Note

UPB1 is not required for the RGF1-receptor pathway. It has previously been reported that UPBEAT1 (UPB1) reduces H_2O_2 levels and controls meristem size by downregulating peroxidase genes in the elongation zone[6]. However, our present transcriptome analysis did not find substantial changes in *UPB1* expression upon RGF1 treatment (Supplementary Tables 1, 3). We did find elevated expression of five peroxidase genes (Supplementary Table 1), but these are not targets of *UPB1* (ref. [6]), suggesting that RGF1 regulates meristem size independently of *UPB1*. To determine whether the peroxidase genes upregulated by RGF1 play a part in controlling meristem size in the RGF1-signalling pathway, we overexpressed two of them (At5g39580 and At4g08780). In neither case did we observe a larger meristematic zone (data not shown).

Statistics and reproducibility

Experiments were independently repeated three times with similar results. No power analysis was done to estimate sample size. The experiments were not randomized and investigators were not blinded to allocation during experiments and outcome assessment.

Reporting summary

Further information on research design is available in the Nature Research Reporting Summary linked to this paper.

Data availability

All RNA-seq data from this study have been deposited in the National Center for Biotechnology Information (NCBI) Gene Expression Omnibus (GEO), with the accession number GSE108730. Source data for all graphs have been provided. A previous version of this work was deposited in the preprint depository server bioRxiv at https://doi.org/10.1101/244947. Source Data for Figs. 1–4 and Extended Data Figs. 1, 3, 5–10 are provided with the paper. All other data are available from the corresponding author upon reasonable request.

Code availability

All code from this study is available upon request.

Acknowledgements We thank I. Taylor, J. Dickinson, E. Pierre-Jerome, K. Lehner and C. Winter for comments on the manuscript; C. Wilson for help with generating overexpression lines; G. Yang for help in identifying CRISPR mutants; K. Sugimoto for *HYP2-GFP* seeds; Y. Matsubayashi for *rgfr1/2/3* seeds; R. Heidstra for *gPLT2-YFP* and *pPLT2-CFP* seeds; N.-H. Chua for the pMDC7 vector; The Duke Genome Sequencing Center for sequencing Illumina libraries; the Plant Tech Core Facility in the Agricultural Biotechnology Research Center for generating the CRISPR construct; and the Transgenic Plant Laboratory at Academia Sinica for transforming the CRISPR construct into plants. This work was funded by the Howard Hughes Medical Institute and the Gordon and Betty Moore Foundation (through grant GBMF3405), the US National Institutes of Health (MIRA 1R35GM131725) to P.N.B., and Academia Sinica, Taiwan, to M.Y.

Author contributions M.Y. and P.N.B. conceptualized the study; M.Y. performed all experiments; X.H. performed the computational analyses; all authors wrote the paper.

Competing interests The authors declare no competing interests.

Additional information
Supplementary information is available for this paper at https://doi.org/10.1038/s41586-019-1819-6.
Correspondence and requests for materials should be addressed to P.N.B.
Peer review information *Nature* thanks Yoshikatsu Matsubayashi and the other, anonymous, reviewer(s) for their contribution to the peer review of this work.

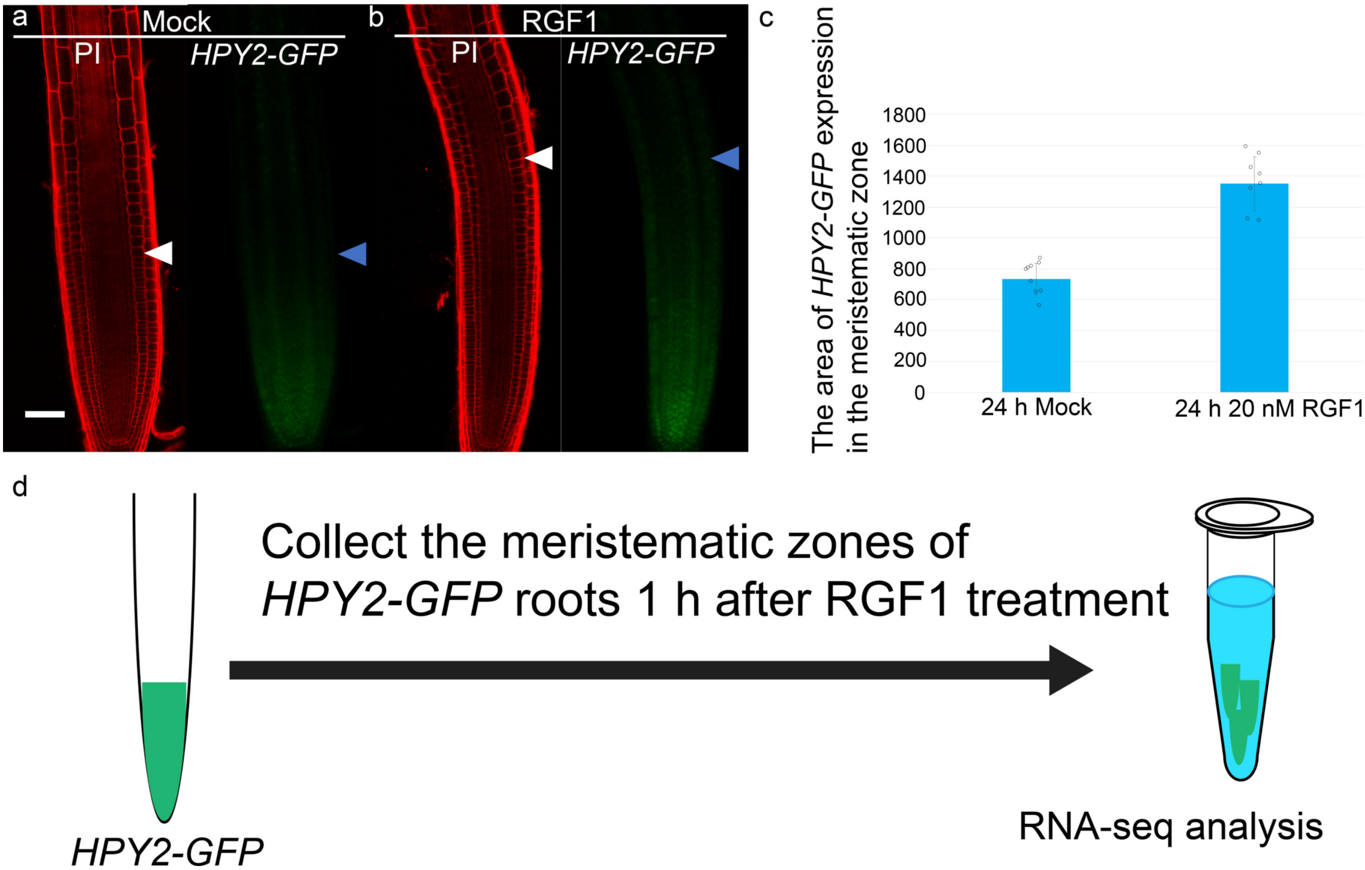

Extended Data Fig. 1 | Expression of meristematic-zone marker and transcriptome analysis upon RGF1 treatment. a, **b**, Confocal images of *HPY2-GFP* roots 24 h after treatment with water (mock; **a**) or 20 nM RGF1 (**b**). Seedlings were grown on MS plates for seven days before treatment. Left, PI-stained roots; right, GFP signals. White and blue arrowheads indicate the junction between the meristematic and elongation zones. Scale bar, 50 µm. **c**, Area of *HPY2-GFP* expression (in μm^2; $n = 8$ independent roots; $P < 2.1 \times 10^{-7}$). Bar graphs show means. Error bars are ± s.d. Dots indicate each data point. P values are calculated by two-sided Student's t-test. **d**, Method of RNA extraction following RGF1 treatment.

GO	Term	FDR
GO:0042221	response to chemical stimulus	5.10E-14
GO:0050896	response to stimulus	1.20E-12
GO:0042430	indole and derivative metabolic process	1.40E-12
GO:0005886	plasma membrane	1.90E-12
GO:0042434	indole derivative metabolic process	1.20E-11
GO:0051707	response to other organism	1.70E-11
GO:0010200	response to chitin	1.70E-11
GO:0051704	multi-organism process	7.50E-11
GO:0009617	response to bacterium	7.60E-11
GO:0009607	response to biotic stimulus	8.80E-11
GO:0006952	defense response	7.50E-10
GO:0006950	response to stress	2.80E-09
GO:0042435	indole derivative biosynthetic process	3.60E-09
GO:0042742	defense response to bacterium	8.00E-08
GO:0006790	sulfur metabolic process	1.00E-07
GO:0009743	response to carbohydrate stimulus	1.30E-07
GO:0009404	toxin metabolic process	1.70E-07
GO:0009407	toxin catabolic process	1.70E-07
GO:0010033	response to organic substance	2.50E-07
GO:0019748	secondary metabolic process	2.70E-07
GO:0005618	cell wall	3.10E-07
GO:0030312	external encapsulating structure	3.10E-07
GO:0004364	**glutathione transferase activity**	**4.10E-06**
GO:0003824	catalytic activity	4.10E-06
GO:0044272	sulfur compound biosynthetic process	5.90E-06
GO:0016137	glycoside metabolic process	5.90E-06
GO:0016020	membrane	9.50E-06
GO:0031224	intrinsic to membrane	9.90E-06
GO:0006725	cellular aromatic compound metabolic process	1.40E-05
GO:0009725	response to hormone stimulus	1.50E-05
GO:0009719	response to endogenous stimulus	6.20E-05
GO:0009636	response to toxin	6.20E-05
GO:0009505	plant-type cell wall	6.40E-05
GO:0030246	carbohydrate binding	7.10E-05
GO:0019760	glucosinolate metabolic process	0.00011
GO:0016143	S-glycoside metabolic process	0.00011
GO:0019757	glycosinolate metabolic process	0.00011
GO:0016021	integral to membrane	0.00011
GO:0023033	signaling pathway	0.00015
GO:0045087	innate immune response	0.00016
GO:0016740	transferase activity	0.00019
GO:0044425	membrane part	0.00021
GO:0010035	response to inorganic substance	0.00025
GO:0006955	immune response	0.00027
GO:0002376	immune system process	0.00027
GO:0009814	defense response, incompatible interaction	0.0003
GO:0031226	intrinsic to plasma membrane	0.00036
GO:0016491	**oxidoreductase activity**	**0.00039**
GO:0044271	cellular nitrogen compound biosynthetic process	0.00061
GO:0022804	active transmembrane transporter activity	0.00073
GO:0022857	transmembrane transporter activity	0.00073
GO:0016138	glycoside biosynthetic process	0.00076
GO:0023052	signaling	0.00078
GO:0022838	substrate-specific channel activity	0.0008
GO:0019438	aromatic compound biosynthetic process	0.00087
GO:0016765	transferase activity, transferring alkyl groups	0.00093
GO:0022892	substrate-specific transporter activity	0.00093
GO:0022891	substrate-specific transmembrane transporter activity	0.00093

FDR p<0.001

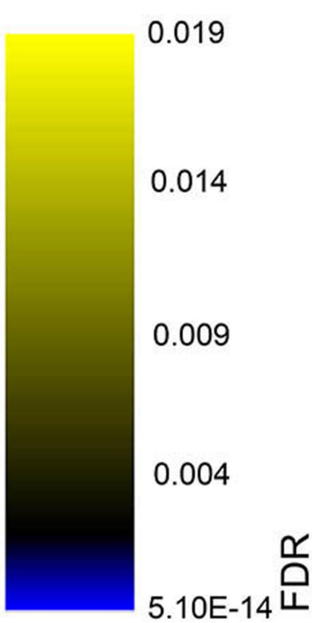

Extended Data Fig. 2 | GO categories that are enriched upon RGF1 treatment. These highly significantly enriched GO categories within lists of genes are regulated by RGF1 (FDR-adjusted $P < 0.001$), and include glutathione transferase activity (FDR-adjusted $P = 4.1 \times 10^{-6}$, red) and oxidoreductase activity (FDR-adjusted $P = 0.00039$, red). See Supplementary Table 2 (enriched GO categories upon RGF1 treatment). P values for GO enrichment analysis are based on Fisher's exact test, with the sample size being all genes in the genome and using a Benjamini–Yekutieli FDR for multiple testing correction.

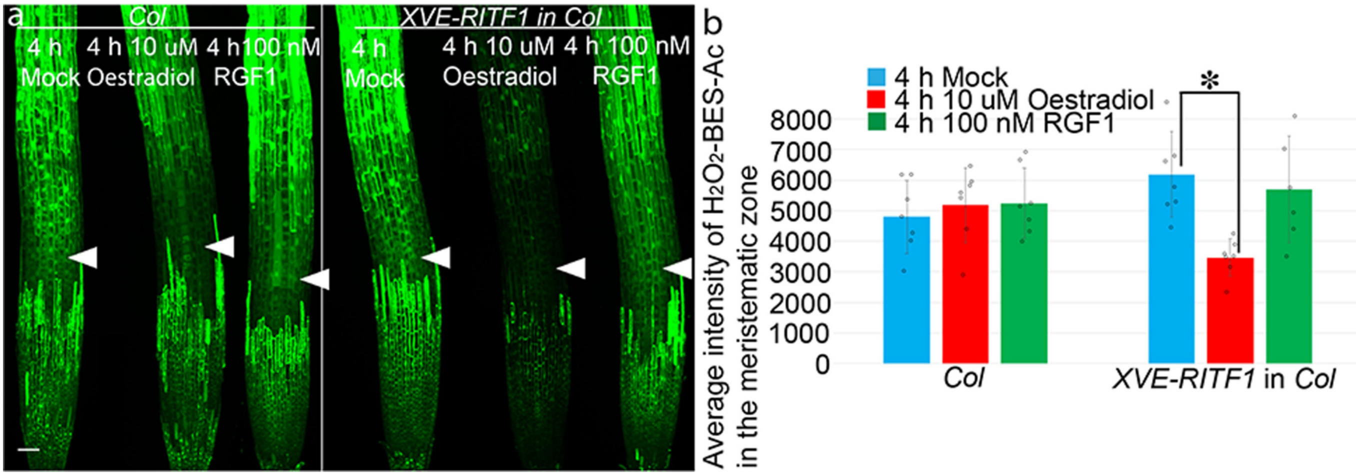

Extended Data Fig. 3 | H_2O_2 levels after inducible overexpression of *RITF1* and RGF1 treatment. a, Confocal images of H_2O_2-BES-Ac stained roots, with or without *XVE–RITF1* expression, in a wild-type (Col-0) background 4 h after treatment with water (mock), 10 μM oestradiol or 100 nM RGF1. **b**, Quantification of H_2O_2-BES-Ac intensity in the meristematic zone ($n = 6$ independent samples; $^*P < 0.0005$). Bar graphs show means. Error bars are ± s.d. Dots indicate each data point. P values are calculated by two-sided Student's t-test.

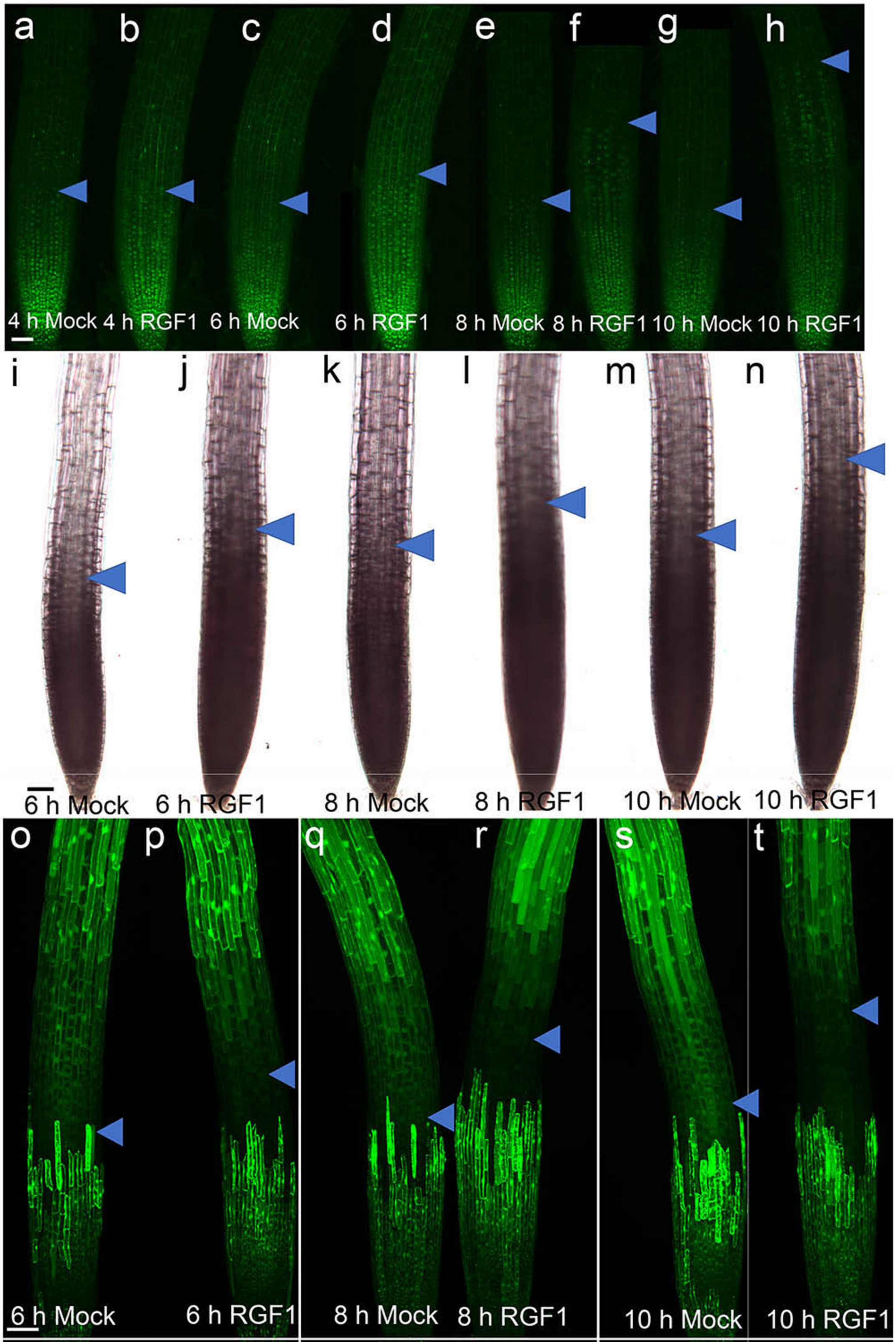

Extended Data Fig. 4 | Localization of gPLT2–YFP, NBT and H_2O_2-BES-Ac staining after RGF1 treatment. a–t, Localization of gPLT2–YFP (**a**–**h**), NBT staining (**i**–**n**) and H_2O_2-BES-Ac staining (**o**–**t**), 4 h after treatment with water (mock; **a**) or 100 nM RGF1 (**b**), 6 h after treatment with water (mock; **c**, **i**, **o**) or 100 nM RGF1 (**d**, **j**, **p**), 8 h after treatment with water (mock; **e**, **k**, **q**) or 100 nM RGF1 (**f**, **l**, **r**), or 10 h after treatment with water (mock; **g**, **m**, **s**) or 100 nM RGF1 (**h**, **n**, **t**). Blue arrowheads indicate the junction between the meristematic and elongation zones. Scale bar, 50 μm. Seedlings were grown on MS agar plates for seven days before treatment. Experiments were independently repeated three times with similar results.

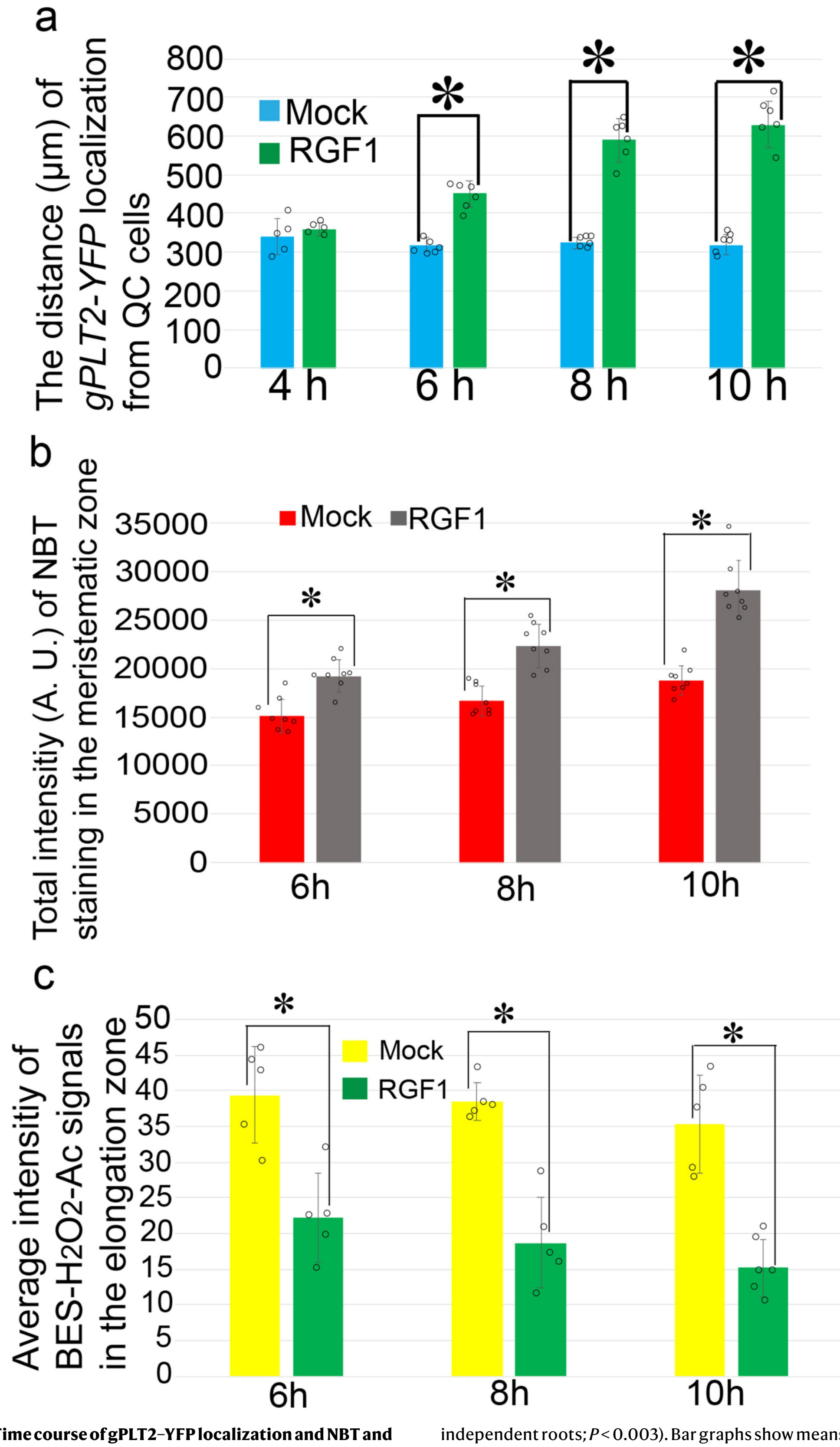

Extended Data Fig. 5 | Time course of gPLT2–YFP localization and NBT and H_2O_2-BES-Ac staining. a, Distance (in μm) of gPLT2–YFP localization from quiescent-centre cells ($n = 5$ independent roots; $P < 5.7 \times 10^{-6}$). **b**, Total intensity of NBT staining in the meristematic zone ($n = 8$ independent roots; $P < 0.0003$). **c**, Average intensity of H_2O_2-BES-Ac staining in the elongation zone ($n = 5$ independent roots; $P < 0.003$). Bar graphs show means. Error bars are ± s.d. Dots indicate each data point. P values are calculated by two-sided Student's t-test. Experiments were independently repeated three times with similar results.

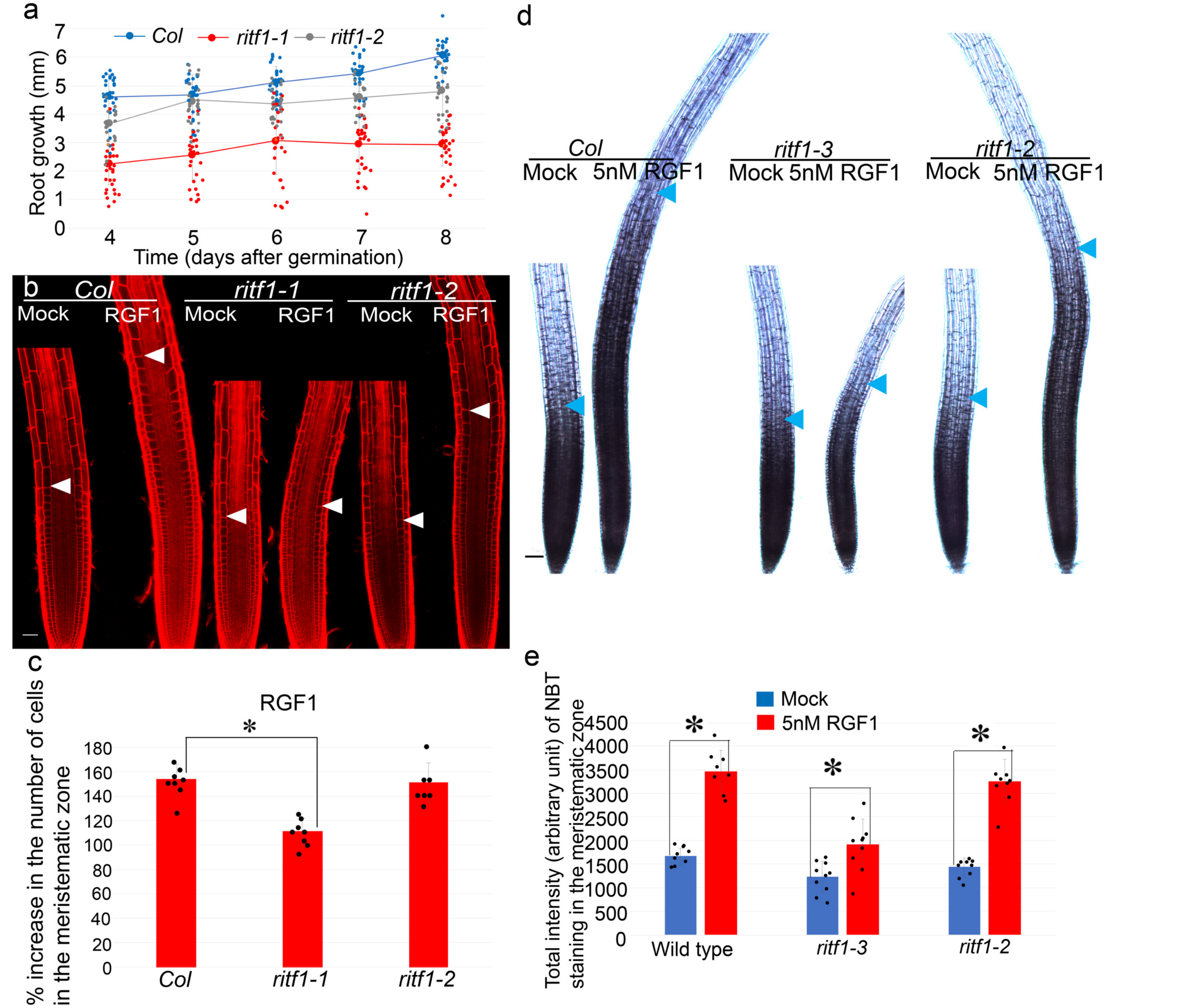

Extended Data Fig. 6 | Phenotype of *rift* mutants. a, Root growth (in mm) of wild-type (Col), *ritf1-1* (CRISPR mutant) and *ritf1-2* (SALK line) seedlings from 4 to 8 days after germination ($n = 21$ independent roots). **b**, Confocal images of wild-type, *ritf1-1* (CRISPR mutant) and *ritf1*-2 (Salk line) roots stained with PI. **c**, Percentage increase (in which 100% is the number of cells in the mock-treated case) in the number of cells in the meristematic zone of wild-type, *ritf1-1* and *ritf1-2* roots 24 h after mock treatment or 5 nM RGF1 treatment ($n = 7$ independent roots, $*P < 5.4 \times 10^{-6}$). **d**, Light microscope images of roots of wild-type, *ritf1-3* and *ritf1-2* roots stained with NBT 24 h after treatment with 5 nM RGF1. Scale bars, 50 µm. Blue arrowheads show the junction between the meristematic and elongation zones. **e**, Quantification of NBT staining intensity in the meristematic zone in wild-type, *ritf1-3* and *ritf1-2* roots after treatment with 5 nM RGF1 ($n = 8$ independent roots; $*P < 0.003$). Scale bars, 50 µm. Blue and white arrowheads show the junction between the meristematic and elongation zones. Bar and line graphs show means. Error bars are ± s.d. Dots indicate each data point. *P* values are calculated by two-sided Student's *t*-test.

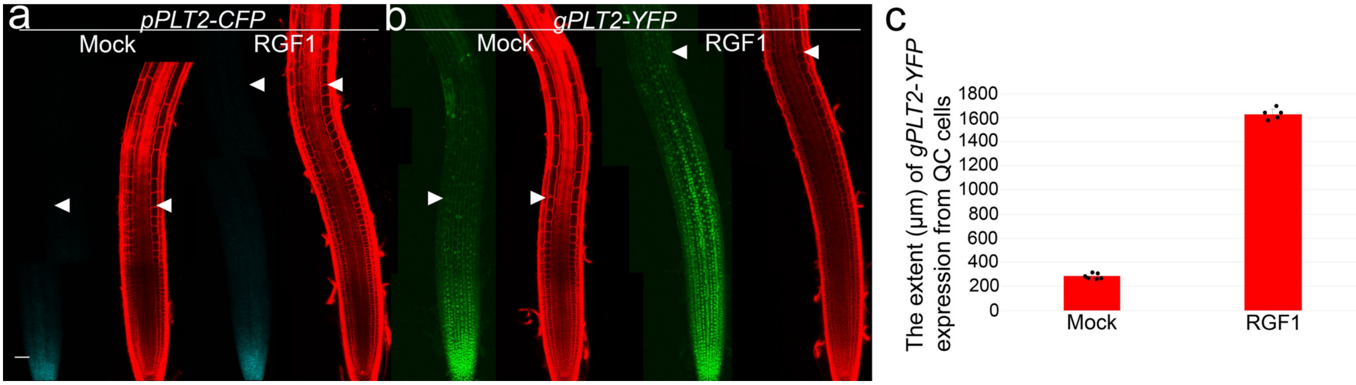

Extended Data Fig. 7 | Expression of *pPLT2-CFP* and *gPLT2-YFP* upon RGF1 treatment. **a**, **b**, Confocal images showing *pPLT2-CFP* expression (cyan; **a**) and *gPLT2-YFP* expression (green; **b**) 24 h after treatment with 20 nM RGF1. Red, PI staining. Scale bar, 50 μm. Arrow heads show the junction between the meristematic and elongation zones. **c**, Extent (in μm) of *gPLT2-YFP* expression from quiescent-centre cells ($n = 5$ independent roots; $P < 2.5 \times 10^{-13}$). Bar graphs show means. Error bars are ± s.d. Dots indicate each data point. *P* values are calculated by two-sided Student's *t*-test.

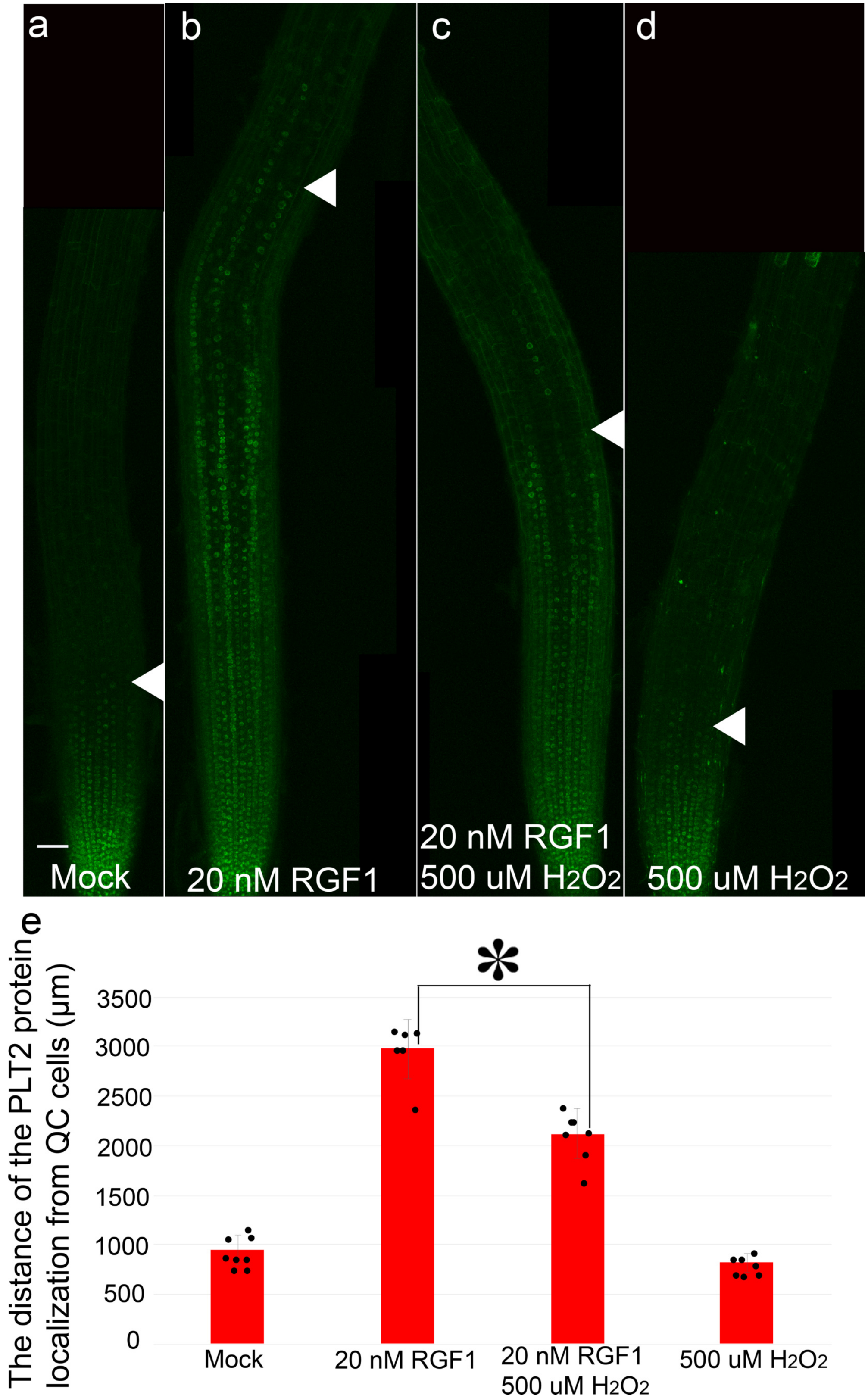

Extended Data Fig. 8 | Localization of PLT2 protein after RGF1 and/or H_2O_2 treatment. a–d, Confocal images showing gPLT2–YFP expression 24 h after treatment with water (mock), 20 nM RGF1, 20 nM RGF1 with 500 µM H_2O_2, or 500 µM H_2O_2. *gPLT2-YFP* seedlings were grown for seven days on MS agar plates before treatment. Scale bar, 50 µm. Arrowheads show the extent of *gPLT2-YFP* expression. **e**, Distance (in µm) of PLT2 localization as measured from quiescent-centre cells ($n = 6$, $^*P < 0.0002$). Bar graphs show means. Error bars are ± s.d. Dots indicate each data point. *P* values calculated by two-sided Student's *t*-test.

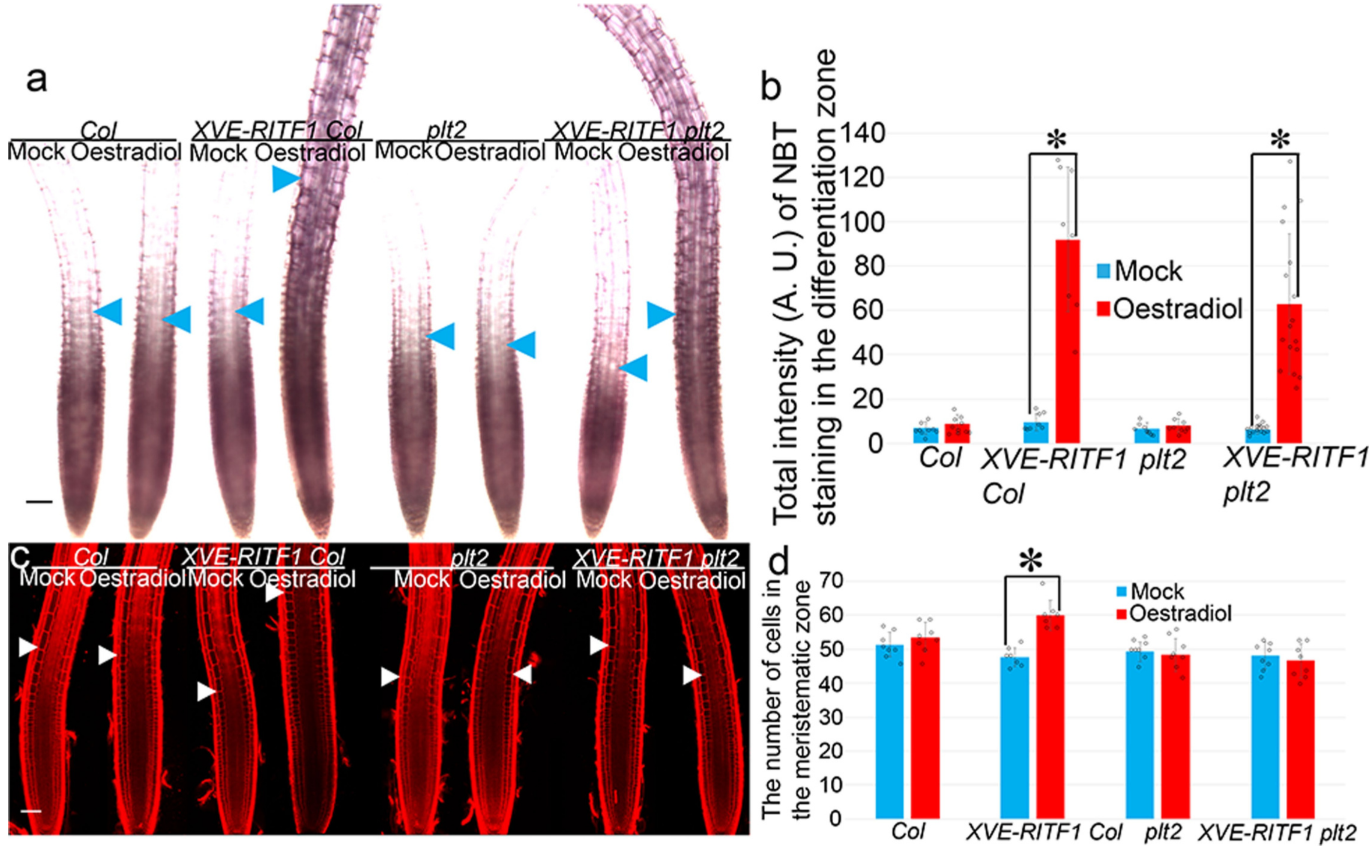

Extended Data Fig. 9 | Phenotypes resulting from *RITF1* overexpression in *plt2* mutants. a, NBT-stained roots, with or without *XVE–RITF1* expression, in a wild-type or *plt2* background 24 h after treatment with water (mock) or 10 μM oestradiol. **b**, Quantification of NBT staining intensity in the differentiation zone with or without *XVE–RITF1* in wild-type and *plt2* roots ($n = 8$ independent roots; $^*P < 5.4 \times 10^{-6}$). **c**, Confocal images of PI-stained roots with or without *XVE-RITF1*, in a wild-type or *plt2* background, 24 h after mock treatment or treatment with 10 μM oestradiol. **d**, Number of cells in the meristematic zone, with or without *XVE–RITF1*, in wild-type and *plt2* roots 24 h after mock or 10 μM oestradiol treatment ($n = 7$ independent roots; $^*P < 4.3 \times 10^{-5}$). Scale bars, 50 μm. White and blue arrowheads indicate the junction between the meristematic and elongation zones. Bar graphs show means. Error bars are ± s.d. Dots indicate each data point. *P* values are calculated by two-sided Student's *t*-test.

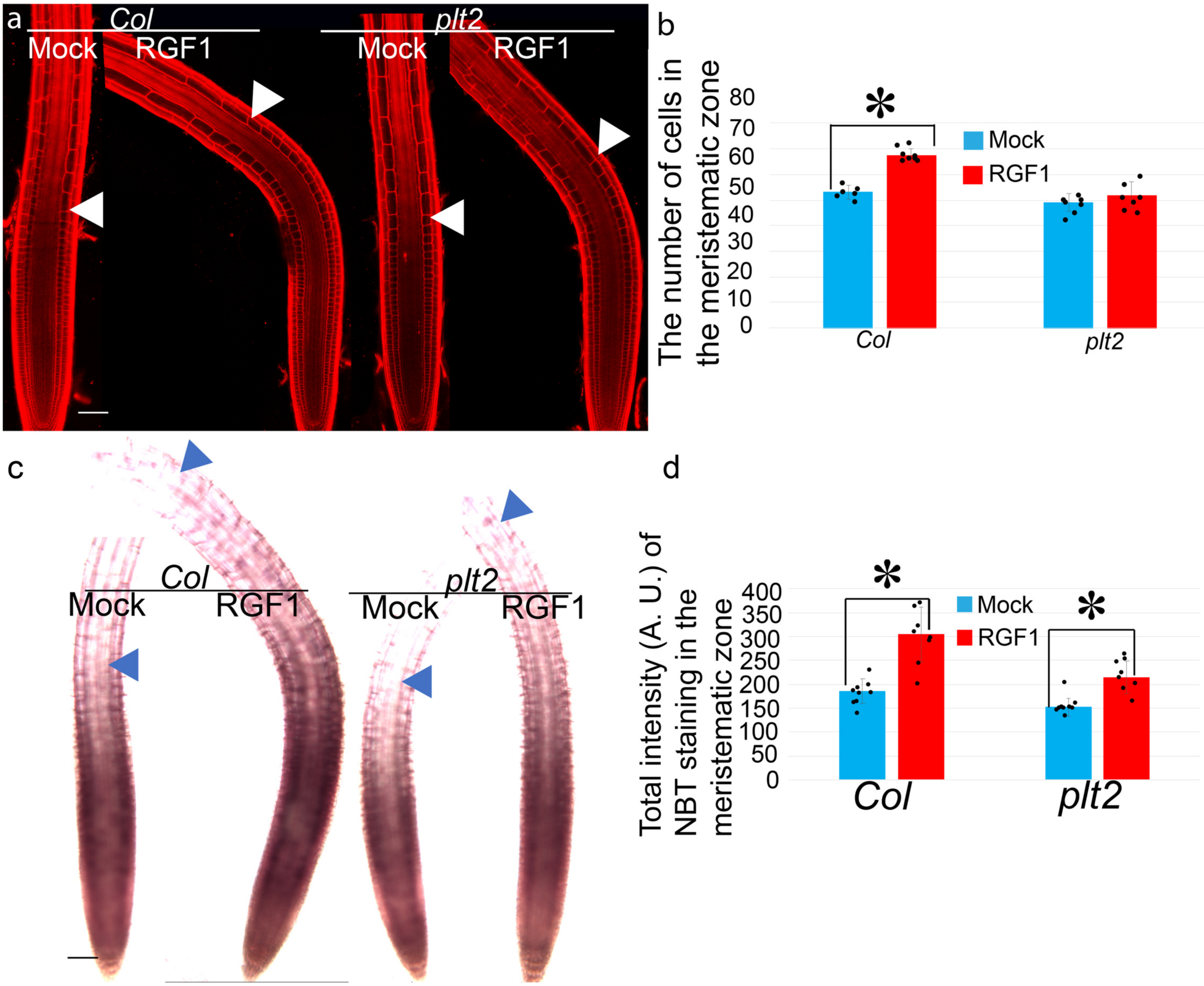

Extended Data Fig. 10 | Phenotype of *plt2* roots upon RGF1 treatment. **a**, Confocal images of PI-stained wild-type and *plt2* roots 24 h after treatment with water (mock) or 20 nM RGF1. Scale bar, 50 µm. White arrowheads show junctions between the meristematic and elongation zones. **b**, Number of cells in the meristematic zone 24 h after mock or 5 nM RGF1 treatment ($n = 6$ independent roots; $^*P < 4.9 \times 10^{-7}$). **c**, Light microscope images of roots from wild-type and *plt2* roots stained with NBT. Seedlings were grown on MS agar plates for 7 days before treatment with water (mock) or 20 nM RGF1. **d**, Total intensity of NBT staining in the differentiation zone of wild-type and *plt2* roots 24 h after treatment with water (mock) or 20 nM RGF1 ($n = 8$ independent roots; $^*P < 0.0003$). Scale bars, 50 µm. White arrowheads show the junction between the meristematic and elongation zones. Bar graphs show means. Error bars are ± s.d. Dots indicate each data point. *P* values are calculated by two-sided Student's *t*-test.

nature research

Corresponding author(s): Philip N. Benfey

Last updated by author(s): Oct 7, 2019

Reporting Summary

Nature Research wishes to improve the reproducibility of the work that we publish. This form provides structure for consistency and transparency in reporting. For further information on Nature Research policies, see Authors & Referees and the Editorial Policy Checklist .

Statistics

For all statistical analyses, confirm that the following items are present in the figure legend, table legend, main text, or Methods section.

n/a	Confirmed	
☐	☒	The exact sample size (*n*) for each experimental group/condition, given as a discrete number and unit of measurement
☐	☒	A statement on whether measurements were taken from distinct samples or whether the same sample was measured repeatedly
☐	☒	The statistical test(s) used AND whether they are one- or two-sided *Only common tests should be described solely by name; describe more complex techniques in the Methods section.*
☐	☒	A description of all covariates tested
☐	☒	A description of any assumptions or corrections, such as tests of normality and adjustment for multiple comparisons
☐	☒	A full description of the statistical parameters including central tendency (e.g. means) or other basic estimates (e.g. regression coefficient) AND variation (e.g. standard deviation) or associated estimates of uncertainty (e.g. confidence intervals)
☐	☒	For null hypothesis testing, the test statistic (e.g. *F*, *t*, *r*) with confidence intervals, effect sizes, degrees of freedom and *P* value noted *Give P values as exact values whenever suitable.*
☒	☐	For Bayesian analysis, information on the choice of priors and Markov chain Monte Carlo settings
☒	☐	For hierarchical and complex designs, identification of the appropriate level for tests and full reporting of outcomes
☒	☐	Estimates of effect sizes (e.g. Cohen's *d*, Pearson's *r*), indicating how they were calculated

Our web collection on statistics for biologists contains articles on many of the points above.

Software and code

Policy information about availability of computer code

Data collection	No software was used.
Data analysis	DESeq2 v1.14.1; Bowtie2 v2.2.7; TopHat v2.1.1; Samtools v1.2; HTSeq v0.6.1, Fiji v2.0.0

For manuscripts utilizing custom algorithms or software that are central to the research but not yet described in published literature, software must be made available to editors/reviewers. We strongly encourage code deposition in a community repository (e.g. GitHub). See the Nature Research guidelines for submitting code & software for further information.

Data

Policy information about availability of data

All manuscripts must include a data availability statement. This statement should provide the following information, where applicable:

- Accession codes, unique identifiers, or web links for publicly available datasets
- A list of figures that have associated raw data
- A description of any restrictions on data availability

All RNA-seq data in this study have been deposited in NCBI GEO with accession identifier GSE108730.

Field-specific reporting

Please select the one below that is the best fit for your research. If you are not sure, read the appropriate sections before making your selection.

☒ Life sciences ☐ Behavioural & social sciences ☐ Ecological, evolutionary & environmental sciences

For a reference copy of the document with all sections, see nature.com/documents/nr-reporting-summary-flat.pdf

Life sciences study design

All studies must disclose on these points even when the disclosure is negative.

Sample size	We used 3 biological replicates for RNA-seq, following the common practice in the field.
Data exclusions	No data were excluded.
Replication	We calculated gene-wise dispersion among biological replicates for RNA-seq data. The dispersion plot displayed typical pattern of RNA-seq.
Randomization	All samples for RNA-seq and measuring ROS and meristem size are randomly selected.
Blinding	For RNA-seq analysis, an investigator randomly collected samples and generated RNA-seq libraries. Another investigator did computational analysis. Our transcriptome analysis is completely blind.

Reporting for specific materials, systems and methods

We require information from authors about some types of materials, experimental systems and methods used in many studies. Here, indicate whether each material, system or method listed is relevant to your study. If you are not sure if a list item applies to your research, read the appropriate section before selecting a response.

Materials & experimental systems

n/a	Involved in the study	
☒	☐	Antibodies
☒	☐	Eukaryotic cell lines
☒	☐	Palaeontology
☒	☐	Animals and other organisms
☒	☐	Human research participants
☒	☐	Clinical data

Methods

n/a	Involved in the study	
☒	☐	ChIP-seq
☒	☐	Flow cytometry
☒	☐	MRI-based neuroimaging

International evaluation of an AI system for breast cancer screening

https://doi.org/10.1038/s41586-019-1799-6

Received: 27 July 2019

Accepted: 5 November 2019

Published online: 1 January 2020

Scott Mayer McKinney[1,14]*, Marcin Sieniek[1,14], Varun Godbole[1,14], Jonathan Godwin[2,14], Natasha Antropova[2], Hutan Ashrafian[3,4], Trevor Back[2], Mary Chesus[2], Greg C. Corrado[1], Ara Darzi[3,4,5], Mozziyar Etemadi[6], Florencia Garcia-Vicente[6], Fiona J. Gilbert[7], Mark Halling-Brown[8], Demis Hassabis[2], Sunny Jansen[9], Alan Karthikesalingam[10], Christopher J. Kelly[10], Dominic King[10], Joseph R. Ledsam[2], David Melnick[6], Hormuz Mostofi[1], Lily Peng[1], Joshua Jay Reicher[11], Bernardino Romera-Paredes[2], Richard Sidebottom[12,13], Mustafa Suleyman[2], Daniel Tse[1]*, Kenneth C. Young[8], Jeffrey De Fauw[2,15] & Shravya Shetty[1,15]*

Screening mammography aims to identify breast cancer at earlier stages of the disease, when treatment can be more successful[1]. Despite the existence of screening programmes worldwide, the interpretation of mammograms is affected by high rates of false positives and false negatives[2]. Here we present an artificial intelligence (AI) system that is capable of surpassing human experts in breast cancer prediction. To assess its performance in the clinical setting, we curated a large representative dataset from the UK and a large enriched dataset from the USA. We show an absolute reduction of 5.7% and 1.2% (USA and UK) in false positives and 9.4% and 2.7% in false negatives. We provide evidence of the ability of the system to generalize from the UK to the USA. In an independent study of six radiologists, the AI system outperformed all of the human readers: the area under the receiver operating characteristic curve (AUC-ROC) for the AI system was greater than the AUC-ROC for the average radiologist by an absolute margin of 11.5%. We ran a simulation in which the AI system participated in the double-reading process that is used in the UK, and found that the AI system maintained non-inferior performance and reduced the workload of the second reader by 88%. This robust assessment of the AI system paves the way for clinical trials to improve the accuracy and efficiency of breast cancer screening.

Breast cancer is the second leading cause of death from cancer in women[3], but early detection and treatment can considerably improve outcomes[1,4,5]. As a consequence, many developed nations have implemented large-scale mammography screening programmes. Major medical and governmental organizations recommend screening for all women starting between the ages of 40 and 50[6–8]. In the USA and UK combined, over 42 million exams are performed each year[9,10].

Despite the widespread adoption of mammography, interpretation of these images remains challenging. The accuracy achieved by experts in cancer detection varies widely, and the performance of even the best clinicians leaves room for improvement[11,12]. False positives can lead to patient anxiety[13], unnecessary follow-up and invasive diagnostic procedures. Cancers that are missed at screening may not be identified until they are more advanced and less amenable to treatment[14].

AI may be uniquely poised to help with this challenge. Studies have demonstrated the ability of AI to meet or exceed the performance of human experts on several tasks of medical-image analysis[15–19]. As a shortage of mammography professionals threatens the availability and adequacy of breast-screening services around the world[20–23], the scalability of AI could improve access to high-quality care for all.

Computer-aided detection (CAD) software for mammography was introduced in the 1990s, and several assistive tools have been approved for medical use[24]. Despite early promise[25,26], this generation of software failed to improve the performance of readers in real-world settings[12,27,28]. More recently, the field has seen a renaissance owing to the success of deep learning. A few studies have characterized systems for breast cancer prediction with stand-alone performance that approaches that of human experts[29,30]. However, the existing work has several limitations. Most studies are based on small, enriched datasets with limited follow-up, and few have compared performance to readers in actual clinical practice—instead relying on laboratory-based simulations of the reading environment. So far there has been little evidence of the ability of AI systems to translate between different screening populations and settings without additional training data[31]. Critically, the pervasive use of follow-up intervals that are no longer than 12 months[29,30,32,33]

[1]Google Health, Palo Alto, CA, USA. [2]DeepMind, London, UK. [3]Department of Surgery and Cancer, Imperial College London, London, UK. [4]Institute of Global Health Innovation, Imperial College London, London, UK. [5]Cancer Research UK Imperial Centre, Imperial College London, London, UK. [6]Northwestern Medicine, Chicago, IL, USA. [7]Department of Radiology, Cambridge Biomedical Research Centre, University of Cambridge, Cambridge, UK. [8]Royal Surrey County Hospital, Guildford, UK. [9]Verily Life Sciences, South San Francisco, CA, USA. [10]Google Health, London, UK. [11]Stanford Health Care and Palo Alto Veterans Affairs, Palo Alto, CA, USA. [12]The Royal Marsden Hospital, London, UK. [13]Thirlestaine Breast Centre, Cheltenham, UK. [14]These authors contributed equally: Scott Mayer McKinney, Marcin T. Sieniek, Varun Godbole, Jonathan Godwin. [15]These authors jointly supervised this work: Jeffrey De Fauw, Shravya Shetty. *e-mail: scottmayer@google.com; tsed@google.com; sshetty@google.com

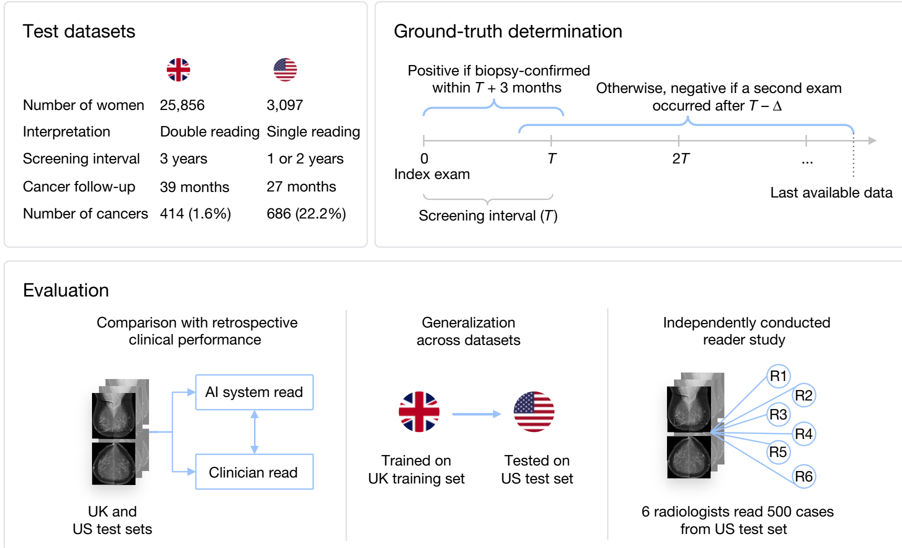

Fig. 1 | Development of an AI system to detect cancer in screening mammograms. Datasets representative of the UK and US breast cancer screening populations were curated from three screening centres in the UK and one centre in the USA. Outcomes were derived from the biopsy record and longitudinal follow-up. An AI system was trained to identify the presence of breast cancer from a set of screening mammograms, and was evaluated in three primary ways: first, AI predictions were compared with the historical decisions made in clinical practice; second, to evaluate the generalizability across populations, a version of the AI system was developed using only the UK data and retested on the US data; and finally, the performance of the AI system was compared to that of six independent radiologists using a subset of the US test set.

means that more subtle cancers that are not identified until the next screen may be ignored.

In this study, we evaluate the performance of a new AI system for breast cancer prediction using two large, clinically representative datasets from the UK and the USA. We compare the predictions of the system to those made by readers in routine clinical practice and show that performance exceeds that of individual radiologists. These observations are confirmed with an independently conducted reader study. Furthermore, we show how this system might be integrated into screening workflows, and provide evidence that the system can generalize across continents. Figure 1 shows an overview of the project.

Datasets from cancer screening programmes

A deep learning model for identifying breast cancer in screening mammograms was developed and evaluated using two large datasets from the UK and the USA. We report results on test sets that were not used to train or tune the AI system.

The UK test set consisted of screening mammograms that were collected between 2012 and 2015 from 25,856 women at two screening centres in England, where women are screened every three years. It included 785 women who had a biopsy, and 414 women with cancer that was diagnosed within 39 months of imaging. This was a random sample of 10% of all women with screening mammograms at these sites during this time period. The UK cohort resembled the broader screening population in age and disease characteristics (Extended Data Table 1a).

The test set from the USA, where women are screened every one to two years, consisted of screening mammograms that were collected between 2001 and 2018 from 3,097 women at one academic medical centre. We included images from all 1,511 women who were biopsied during this time period and a random subset of women who never underwent biopsy (Methods). Among the women who received a biopsy, 686 were diagnosed with cancer within 27 months of imaging.

Breast cancer outcome was determined on the basis of multiple years of follow-up (Fig. 1). We chose the follow-up duration on the basis of the screening interval in the country of origin for each dataset. In a similar manner to previous work[34], we augmented each interval with a three-month buffer to account for variability in scheduling and latency of follow-up. Cases that were designated as cancer-positive were accompanied by a biopsy-confirmed diagnosis within the follow-up period. Cases labelled as cancer-negative had at least one follow-up non-cancer screen; cases without this follow-up were excluded from the test set.

Retrospective clinical comparison

We used biopsy-confirmed breast cancer outcomes to evaluate the predictions of the AI system as well as the original decisions made by readers in the course of clinical practice. Human performance was computed on the basis of the clinician's decision to recall the patient for further diagnostic investigation. The receiver operating characteristic (ROC) curve of the AI system is shown in Fig. 2.

In the UK, each mammogram is interpreted by two readers, and in cases of disagreement, an arbitration process may invoke a third opinion. These interpretations occur serially, such that each reader has access to the opinions of previous readers. The records of these decisions yield three benchmarks of human performance for cancer prediction.

Compared to the first reader, the AI system demonstrated a statistically significant improvement in absolute specificity of 1.2% (95% confidence interval (CI) 0.29%, 2.1%; $P = 0.0096$ for superiority) and an improvement in absolute sensitivity of 2.7% (95% CI −3%, 8.5%; $P = 0.004$ for non-inferiority at a pre-specified 5% margin; Extended Data Table 2a).

Compared to the second reader, the AI system showed non-inferiority (at a 5% margin) for both specificity ($P < 0.001$) and sensitivity ($P = 0.02$). Likewise, the AI system showed non-inferiority (at a 5% margin) to the consensus judgment for specificity ($P < 0.001$) and sensitivity ($P = 0.0039$).

In the standard screening protocol in the USA, each mammogram is interpreted by a single radiologist. We used the BI-RADS[35] score that was assigned to each case in the original screening context as a proxy for human cancer prediction (see Methods section 'Interpreting clinical reads'). Compared to the typical reader, the AI system demonstrated statistically significant improvements in absolute specificity of 5.7%

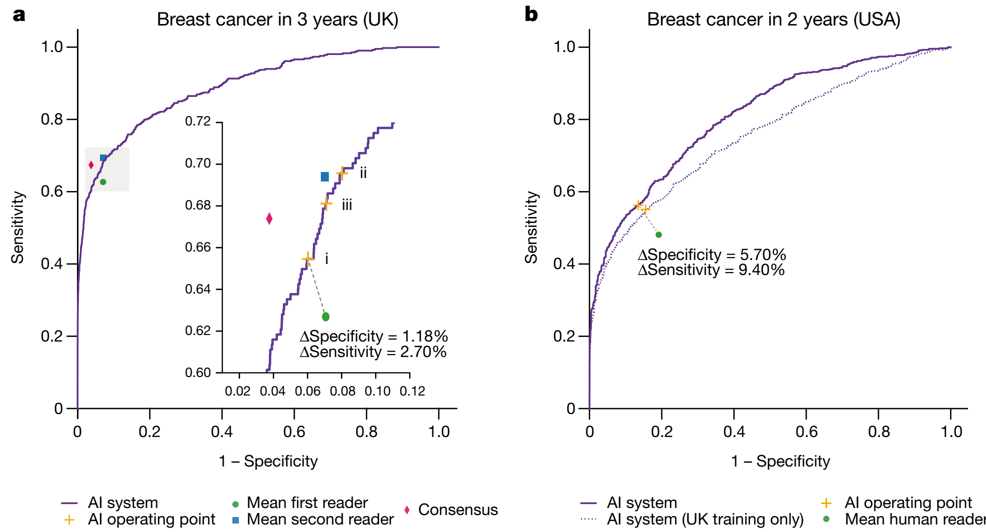

Fig. 2 | Performance of the AI system and clinical readers in breast cancer prediction. a, The ROC curve of the AI system on the UK screening data. The AUC is 0.889 (95% CI 0.871, 0.907; n = 25,856 patients). Also shown are the sensitivity and specificity pairs for the human decisions made in clinical practice. Cases were considered positive if they received a biopsy-confirmed diagnosis of cancer within 39 months of screening. The consensus decision represents the standard of care in the UK, and will involve input from between two and three expert readers. The inset shows a magnification of the grey shaded region. AI system operating points were selected on a separate validation dataset: point i was intended to match the sensitivity and exceed the specificity of the first reader; points ii and iii were selected to attain non-inferiority for both the sensitivity and specificity of the second reader and consensus opinion, respectively. **b**, The ROC curve of the AI system on the US screening data. When trained on both datasets (solid curve), the AUC is 0.8107 (95% CI 0.791, 0.831; n = 3,097 patients). When trained on only the UK dataset (dotted curve), the AUC is 0.757 (95% CI 0.732, 0.780). Also shown are the sensitivity and specificity achieved by radiologists in clinical practice using BI-RADS[35]. Cases were considered positive if they received a biopsy-confirmed diagnosis of cancer within 27 months of screening. AI system operating points were chosen, using a separate validation dataset, to exceed the sensitivity and specificity of the average reader. Negative cases were upweighted to account for the sampling protocol (see Methods section 'Inverse probability weighting'). Extended Data Figure 1 shows an unweighted analysis. See Extended Data Table 2a for statistical comparisons of sensitivity and specificity.

(95% CI 2.6%, 8.6%; P < 0.001) and in absolute sensitivity of 9.4% (95% CI 4.5%, 13.9%; P < 0.001; Extended Data Table 2a).

Generalization across populations

To evaluate the ability of the AI system to generalize across populations and screening settings, we trained the same architecture using only the UK dataset and applied it to the US test set (Fig. 2b). Even without exposure to the US training data, the ROC curve of the AI system encompasses the point that indicates the average performance of US radiologists. Again, the AI system showed improved specificity (+3.5%, P = 0.0212) and sensitivity (+8.1%, P = 0.0006; Extended Data Table 2b) compared with radiologists.

Comparison with a reader study

In a reader study that was conducted by an external clinical research organization, six US-board-certified radiologists who were compliant with the requirements of the Mammography Quality Standards Act (MQSA) interpreted 500 mammograms that were randomly sampled from the US test set. Where data were available, readers were equipped with contextual information typically available in the clinical setting, including the patient's age, breast cancer history, and previous screening mammograms.

Among the 500 cases selected for this study, 125 had biopsy-proven cancer within 27 months, 125 had a negative biopsy within 27 months and 250 were not biopsied (Extended Data Table 3). These proportions were chosen to increase the difficulty of the screening task and increase statistical power. (Such enrichment is typical in observer studies[36].)

Readers rated each case using the forced BI-RADS[35] scale, and BI-RADS scores were compared to ground-truth outcomes to fit an ROC curve for each reader. The scores of the AI system were treated in the same manner (Fig. 3).

The AI system exceeded the average performance of radiologists by a significant margin (change in area under curve (ΔAUC) = +0.115, 95% CI 0.055, 0.175; P = 0.0002). Similar results were observed when a follow-up period of one year was used instead of 27 months (Fig. 3c, Extended Data Fig. 2).

In addition to producing a classification decision for the entire case, the AI system was designed to highlight specific areas of suspicion for malignancy. Likewise, the readers in our study supplied rectangular region-of-interest (ROI) annotations surrounding concerning findings.

We used multi-localization receiver operating characteristic (mLROC) analysis[37] to compare the ability of the readers and the AI system to identify malignant lesions within each case (see Methods section 'Localization analysis').

We summarized each mLROC plot by computing the partial area under the curve (pAUC) in the false-positive fraction interval from 0 to 0.1[38] (Extended Data Fig. 3). The AI system exceeded human performance by a significant margin (ΔpAUC = +0.0192, 95% CI 0.0086, 0.0298; P = 0.0004).

Potential clinical applications

The classifications made by the AI system could be used to reduce the workload involved in the double-reading process that is used in the UK, while preserving the standard of care. We simulated this scenario by omitting the second reader and any ensuing arbitration when the decision of the AI system agreed with that of the first reader. In these cases, the opinion of the first reader was treated as final. In cases of disagreement, the second and consensus opinions were invoked as usual. This combination of human and machine results in performance equivalent to that of the traditional double-reading process, but saves 88% of the effort of the second reader (Extended Data Table 4a).

The AI system could also be used to provide automated, immediate feedback in the screening setting.

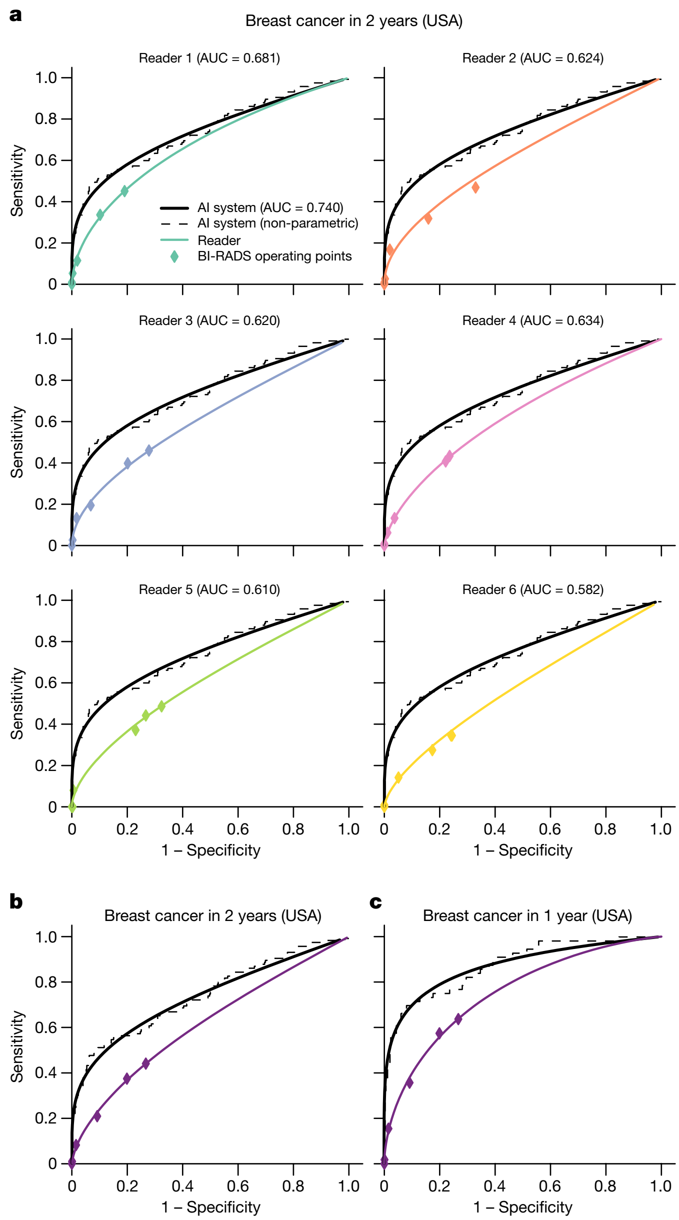

Fig. 3 | Performance of the AI system in breast cancer prediction compared to six independent readers. a, Six readers rated each case (*n* = 465) using the six-point BI-RADS scale. A fitted ROC curve for each of the readers is compared to the ROC curve of the AI system (see Methods section 'Statistical analysis'). For reference, a non-parametric ROC curve is presented in tandem. Cases were considered positive (*n* = 113) if they received a pathology-confirmed diagnosis of cancer within 27 months of the time of screening. Note that this sample of cases was enriched for patients who received a negative biopsy result (*n* = 119), making this a more-challenging population for screening. The mean reader AUC was 0.625 (s.d. 0.032), whereas the AUC for the AI system was 0.740 (95% CI 0.696, 0.794). The AI system exceeded human performance by a significant margin (ΔAUC = +0.115, 95% CI 0.055, 0.175; *P* = 0.0002 by two-sided ORH method (see Methods section 'Statistical analysis')). For results using a 12-month interval, see Extended Data Fig. 2. **b**, Pooled results from all six readers from **a**. **c**, Pooled results (*n* = 408) from all 6 readers using a 12-month interval for cancer definition. Cases were considered positive (*n* = 56) if they received a pathology-confirmed cancer diagnosis within one year (Extended Data Table 3).

To identify normal cases with high confidence, we used a very-low decision threshold. For the UK data, we achieved a negative predictive value (NPV) of 99.99% while retaining a specificity of 41.15%. Similarly, for the US data, we achieved a NPV of 99.90% while retaining a specificity of 34.79%. These data suggest that it may be feasible to dismiss 35–41% of normal cases if we allow for one cancer in every 1,000–10,000 negative predictions (NPV 99.90–99.99% in USA–UK). By comparison, consensus double reading in our UK dataset included one cancer in every 182 cases that were deemed normal.

To identify cancer cases with high confidence, we used a very-high decision threshold. For the UK data, we achieved a positive predictive value (PPV) of 85.6% while retaining a sensitivity of 41.2%. Similarly, for the US data, we achieved a PPV of 82.4% while retaining a sensitivity of 29.8%. These data suggest that it may be feasible to rapidly prioritize 30–40% of cancer cases, with approximately five out of six follow-ups leading to a diagnosis of cancer. By comparison, in our study only 22.8% of UK cases that were recalled by consensus double reading and 4.9% of US cases that were recalled by single reading were ultimately diagnosed with cancer.

Performance breakdown

Comparing the errors of the AI system with errors from clinical reads revealed many cases in which the AI system correctly identified cancer whereas the reader did not, and vice versa (Supplementary Table 1). Most of the cases in which only the AI system identified cancer were invasive (Extended Data Table 5). On the other hand, cases in which only the reader identified cancer were split more evenly between in situ and invasive. Further breakdowns by invasive cancer size, grade and molecular markers show no clear biases (Supplementary Table 2).

We also considered the disagreement between the AI system and the six radiologists that participated in the US reader study. Figure 4a shows a sample cancer case that was missed by all six radiologists, but correctly identified by the AI system. Figure 4b shows a sample cancer case that was caught by all six radiologists, but missed by the AI system. Although we were unable to determine clear patterns among these instances, the presence of such edge cases suggests potentially complementary roles for the AI system and human readers in reaching accurate conclusions.

We compared the performance of the 20 individual readers best represented in the UK clinical dataset with that of the AI system (Supplementary Table 3). The results of this analysis suggest that the aggregate comparison presented above is not unduly influenced by any particular readers. Breakdowns by cancer type, grade and lesion size suggest no apparent difference in the distribution of cancers detected by the AI system and human readers (Extended Data Table 6a).

On the US test set, a breakdown by cancer type (Extended Data Table 6b) shows that the sensitivity advantage of the AI system is concentrated on the identification of invasive cancers (for example, invasive lobular or ductal carcinoma) rather than in situ cancer (for example, ductal carcinoma in situ). A breakdown by BI-RADS[35] breast density category shows that performance gains apply equally across the spectrum of breast tissue types that is represented in this dataset (Extended Data Table 6c).

Discussion

In this study we present an AI system that outperforms radiologists on a clinically relevant task of breast cancer identification. These results held across two large datasets that are representative of different screening populations and practices.

In the UK, the AI system showed specificity superior to that of the first reader. Sensitivity at the same operating point was non-inferior. Consensus double reading has been shown to improve performance compared to single reading[39], and represents the current standard of care in the UK and many European countries[40]. Our system did not outperform this benchmark, but was statistically non-inferior to the second reader and consensus opinion.

a

b

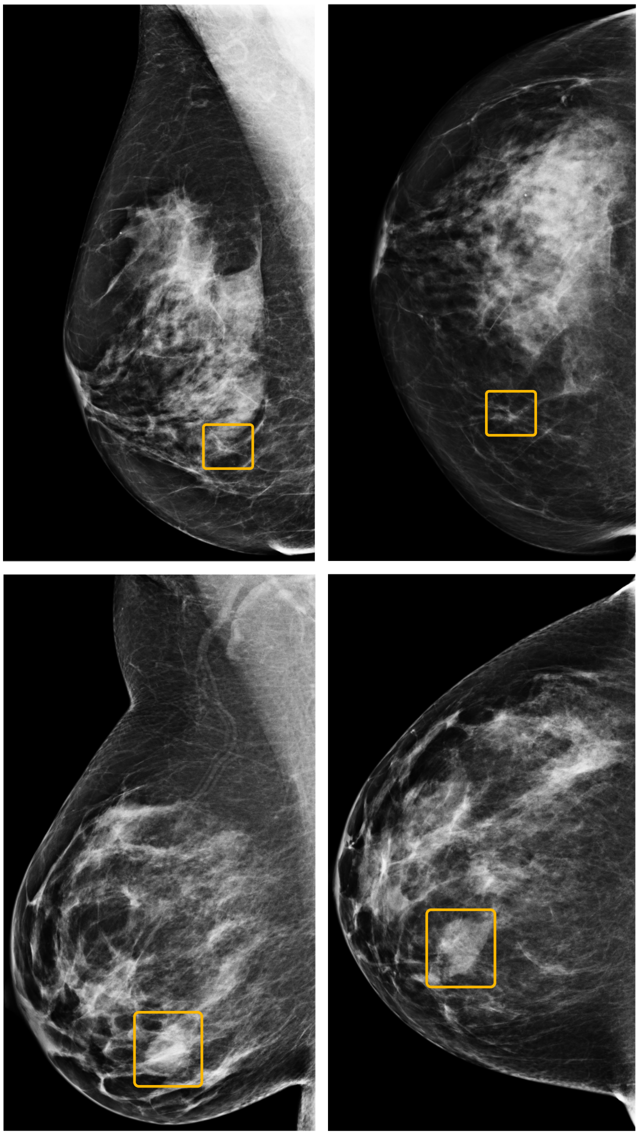

Fig. 4 | Discrepancies between the AI system and human readers. a, A sample cancer case that was missed by all six readers in the US reader study, but correctly identified by the AI system. The malignancy, outlined in yellow, is a small, irregular mass with associated microcalcifications in the lower inner right breast. **b**, A sample cancer case that was caught by all six readers in the US reader study, but missed by the AI system. The malignancy is a dense mass in the lower inner right breast. Left, mediolateral oblique view; right, craniocaudal view.

In the USA, the AI system exhibited specificity and sensitivity superior to that of radiologists practising in an academic medical centre. This trend was confirmed in an externally conducted reader study, which showed that the scores of the AI system stratified cases better than the BI-RADS ratings (the standard scale for mammography assessment in the USA) that were assigned by each of the six readers.

Notably, the human readers (both in the clinic and our reader study) had access to patient history and previous mammograms when making screening decisions. The US clinical readers may have also had access to breast tomosynthesis images. By contrast, the AI system only processed the most recent mammogram.

These comparisons are not without limitations. Although the UK dataset mirrored the nationwide screening population in age and cancer prevalence (Extended Data Table 1a), the same cannot be said of the US dataset, which was drawn from a single screening centre and enriched for cancer cases.

By chance, the vast majority of images used in this study were acquired on devices made by Hologic. Future research should assess the performance of the AI system across a variety of manufacturers in a more systematic way.

In our reader study, all of the radiologists were eligible to interpret screening mammograms in the USA, but did not uniformly receive fellowship training in breast imaging. It is possible that a higher benchmark for performance could have been obtained with readers who were more specialized[41].

To obtain high-quality ground-truth labels, we used extended follow-up intervals that were chosen to encompass a subsequent round of screening in each country. Although there is some precedent in clinical trials[34] and targeted cohort studies[42], this step is not usually taken during systematic evaluation of AI systems for breast cancer detection.

In retrospective datasets with shorter follow-up intervals, outcome labels tend to be skewed in favour of readers. As they are gatekeepers for biopsy, asymptomatic cases will only receive a cancer diagnosis if a mammogram raises the suspicions of a reader. A longer follow-up interval decouples the ground-truth labels from reader opinions (Extended Data Fig. 4) and includes cancers that may have been initially missed by human eyes.

The use of an extended interval makes cancer prediction a more challenging task. Cancers that are diagnosed years later may include new growths for which there could be no mammographic evidence in the original images. Consequently, the sensitivity values presented here are lower than what has been reported for 12-month intervals[2] (Extended Data Fig. 5).

We present early evidence of the ability of the AI system to generalize across populations and screening protocols. We retrained the system using exclusively UK data, and then measured performance on unseen US data. In this context, the system continued to outperform radiologists, albeit by a smaller margin. This suggests that in future clinical deployments, the system might offer strong baseline performance, but could benefit from fine-tuning with local data.

The optimal use of the AI system within clinical workflows remains to be determined. The specificity advantage exhibited by the system suggests that it could help to reduce recall rates and unnecessary biopsies. The improvement in sensitivity exhibited in the US data shows that the AI system may be capable of detecting cancers earlier than the standard of care. An analysis of the localization performance of the AI system suggests it holds early promise for flagging suspicious regions for review by experts. Notably, the additional cancers identified by the AI system tended to be invasive rather than in situ disease.

Beyond improving reader performance, the technology described here may have a number of other clinical applications. Through simulation, we suggest how the system could obviate the need for double reading in 88% of UK screening cases, while maintaining a similar level of accuracy to the standard protocol. We also explore how high-confidence operating points can be used to triage high-risk cases and dismiss low-risk cases. These analyses highlight the potential of this technology to deliver screening results in a sustainable manner despite workforce shortages in countries such as the UK[43]. Prospective clinical studies will be required to understand the full extent to which this technology can benefit patient care.

Online content

Any methods, additional references, Nature Research reporting summaries, source data, extended data, supplementary information, acknowledgements, peer review information; details of author contributions and competing interests; and statements of data and code availability are available at https://doi.org/10.1038/s41586-019-1799-6.

1. Tabár, L. et al. Swedish two-county trial: impact of mammographic screening on breast cancer mortality during 3 decades. *Radiology* **260**, 658–663 (2011).

2. Lehman, C. D. et al. National performance benchmarks for modern screening digital mammography: update from the Breast Cancer Surveillance Consortium. *Radiology* **283**, 49–58 (2017).
3. Bray, F. et al. Global cancer statistics 2018: GLOBOCAN estimates of incidence and mortality worldwide for 36 cancers in 185 countries. *CA Cancer J. Clin*. **68**, 394–424 (2018).
4. The Canadian Task Force on Preventive Health Care. Recommendations on screening for breast cancer in average-risk women aged 40–74 years. *CMAJ* **183**, 1991–2001 (2011).
5. Marmot, M. G. et al. The benefits and harms of breast cancer screening: an independent review. *Br. J. Cancer* **108**, 2205–2240 (2013).
6. Lee, C. H. et al. Breast cancer screening with imaging: recommendations from the Society of Breast Imaging and the ACR on the use of mammography, breast MRI, breast ultrasound, and other technologies for the detection of clinically occult breast cancer. *J. Am. Coll. Radiol*. **7**, 18–27 (2010).
7. Oeffinger, K. C. et al. Breast cancer screening for women at average risk: 2015 guideline update from the American Cancer *Society. J. Am. Med. Assoc*. **314**, 1599–1614 (2015).
8. Siu, A. L. Screening for breast cancer: U.S. Preventive Services Task Force recommendation statement. *Ann. Intern. Med*. **164**, 279–296 (2016).
9. Center for Devices & Radiological Health. *MQSA National Statistics* (US Food and Drug Administration, 2019; accessed 16 July 2019); http://www.fda.gov/radiation-emitting-products/mqsa-insights/mqsa-national-statistics
10. Cancer Research UK. *Breast Screening* (CRUK, 2017; accessed 26 July 2019); https://www.cancerresearchuk.org/about-cancer/breast-cancer/screening/breast-screening
11. Elmore, J. G. et al. Variability in interpretive performance at screening mammography and radiologists' characteristics associated with accuracy. *Radiology* **253**, 641–651 (2009).
12. Lehman, C. D. et al. Diagnostic accuracy of digital screening mammography with and without computer-aided detection. *JAMA Intern. Med*. **175**, 1828–1837 (2015).
13. Tosteson, A. N. A. et al. Consequences of false-positive screening mammograms. *JAMA Intern. Med*. **174**, 954–961 (2014).
14. Houssami, N. & Hunter, K. The epidemiology, radiology and biological characteristics of interval breast cancers in population mammography screening. *NPJ Breast Cancer* **3**, 12 (2017).
15. Gulshan, V. et al. Development and validation of a deep learning algorithm for detection of diabetic retinopathy in retinal fundus photographs. *J. Am. Med. Assoc*. **316**, 2402–2410 (2016).
16. Esteva, A. et al. Dermatologist-level classification of skin cancer with deep neural networks. *Nature* **542**, 115–118 (2017).
17. De Fauw, J. et al. Clinically applicable deep learning for diagnosis and referral in retinal disease. *Nat. Med*. **24**, 1342–1350 (2018).
18. Ardila, D. et al. End-to-end lung cancer screening with three-dimensional deep learning on low-dose chest computed tomography. *Nat. Med*. **25**, 954–961 (2019).
19. Topol, E. J. High-performance medicine: the convergence of human and artificial intelligence. *Nat. Med*. **25**, 44–56 (2019).
20. Moran, S. & Warren-Forward, H. The Australian BreastScreen workforce: a snapshot. *Radiographer* **59**, 26–30 (2012).
21. Wing, P. & Langelier, M. H. Workforce shortages in breast imaging: impact on mammography utilization. *AJR Am. J. Roentgenol*. **192**, 370–378 (2009).
22. Rimmer, A. Radiologist shortage leaves patient care at risk, warns royal college. *BMJ* **359**, j4683 (2017).
23. Nakajima, Y., Yamada, K., Imamura, K. & Kobayashi, K. Radiologist supply and workload: international comparison. *Radiat. Med*. **26**, 455–465 (2008).
24. Rao, V. M. et al. How widely is computer-aided detection used in screening and diagnostic mammography? *J. Am. Coll. Radiol*. **7**, 802–805 (2010).
25. Gilbert, F. J. et al. Single reading with computer-aided detection for screening mammography. *N. Engl. J. Med*. **359**, 1675–1684 (2008).
26. Giger, M. L., Chan, H.-P. & Boone, J. Anniversary paper: history and status of CAD and quantitative image analysis: the role of *Medical Physics* and AAPM. *Med. Phys*. **35**, 5799–5820 (2008).
27. Fenton, J. J. et al. Influence of computer-aided detection on performance of screening mammography. *N. Engl. J. Med*. **356**, 1399–1409 (2007).
28. Kohli, A. & Jha, S. Why CAD failed in mammography. *J. Am. Coll. Radiol*. **15**, 535–537 (2018).
29. Rodriguez-Ruiz, A. et al. Stand-alone artificial intelligence for breast cancer detection in mammography: comparison with 101 radiologists. *J. Natl. Cancer Inst*. **111**, 916–922 (2019).
30. Wu, N. et al. Deep neural networks improve radiologists' performance in breast cancer screening. *IEEE Trans. Med. Imaging* https://doi.org/10.1109/TMI.2019.2945514 (2019).
31. Zech, J. R. et al. Variable generalization performance of a deep learning model to detect pneumonia in chest radiographs: a cross-sectional study. *PLoS Med*. **15**, e1002683 (2018).
32. Becker, A. S. et al. Deep learning in mammography: diagnostic accuracy of a multipurpose image analysis software in the detection of breast cancer. *Invest. Radiol*. **52**, 434–440 (2017).
33. Ribli, D., Horváth, A., Unger, Z., Pollner, P. & Csabai, I. Detecting and classifying lesions in mammograms with deep learning. *Sci. Rep*. **8**, 4165 (2018).
34. Pisano, E. D. et al. Diagnostic performance of digital versus film mammography for breast-cancer screening. *N. Engl. J. Med*. **353**, 1773–1783 (2005).
35. D'Orsi, C. J. et al. *ACR BI-RADS Atlas: Breast Imaging Reporting and Data System* (American College of Radiology, 2013).
36. Gallas, B. D. et al. Evaluating imaging and computer-aided detection and diagnosis devices at the FDA. *Acad. Radiol*. **19**, 463–477 (2012).
37. Swensson, R. G. Unified measurement of observer performance in detecting and localizing target objects on images. *Med. Phys*. **23**, 1709–1725 (1996).
38. Samulski, M. et al. Using computer-aided detection in mammography as a decision support. *Eur. Radiol*. **20**, 2323–2330 (2010).
39. Brown, J., Bryan, S. & Warren, R. Mammography screening: an incremental cost effectiveness analysis of double versus single reading of mammograms. *BMJ* **312**, 809–812 (1996).
40. Giordano, L. et al. Mammographic screening programmes in Europe: organization, coverage and participation. *J. Med. Screen*. **19**, 72–82 (2012).
41. Sickles, E. A., Wolverton, D. E. & Dee, K. E. Performance parameters for screening and diagnostic mammography: specialist and general radiologists. *Radiology* **224**, 861–869 (2002).
42. Ikeda, D. M., Birdwell, R. L., O'Shaughnessy, K. F., Sickles, E. A. & Brenner, R. J. Computer-aided detection output on 172 subtle findings on normal mammograms previously obtained in women with breast cancer detected at follow-up screening mammography. *Radiology* **230**, 811–819 (2004).
43. Royal College of Radiologists. *The Breast Imaging and Diagnostic Workforce in the United Kingdom* (RCR, 2016; accessed 22 July 2019); https://www.rcr.ac.uk/publication/breast-imaging-and-diagnostic-workforce-united-kingdom

Publisher's note Springer Nature remains neutral with regard to jurisdictional claims in published maps and institutional affiliations.

Methods

Ethical approval

Use of the UK dataset for research collaborations by both commercial and non-commercial organizations received ethical approval (REC reference 14/SC/0258). The US data were fully de-identified and released only after an Institutional Review Board approval (STU00206925).

The UK dataset

The UK dataset was collected from three breast screening sites in the UK National Health Service Breast Screening Programme (NHSBSP). The NHSBSP invites women aged between 50 and 70 who are registered with a general practitioner (GP) for mammographic screening every three years. Women who are not registered with a GP, or who are older than 70, can self-refer to the screening programme. In the UK, the screening programme uses double reading: each mammogram is read by two radiologists, who are asked to decide whether to recall the woman for additional follow-up. When there is disagreement, an arbitration process takes place.

The data were initially compiled by OPTIMAM (Cancer Research UK) between 2010 and 2018, from St George's Hospital (London), Jarvis Breast Centre (Guildford) and Addenbrooke's Hospital (Cambridge). The collected data included screening and follow-up mammograms (comprising mediolateral oblique and craniocaudal views of the left and right breasts), all radiologist opinions (including the arbitration result, if applicable) and the metadata associated with follow-up treatment.

The mammograms and associated metadata of 137,291 women were considered for inclusion in the study. Of these, 123,964 women had screening images and uncorrupted metadata. Exams that were recalled for reasons other than radiographic evidence of malignancy, or episodes that were not part of routine screening, were excluded. In total, 121,850 women had at least one eligible exam. Women who were below the age of 47 at the time of the screen were excluded from validation and test sets, leaving 121,455 women. Finally, women for whom there was no exam with sufficient follow-up were excluded from validation and test sets. This last step resulted in the exclusion of 5,990 of 31,766 test-set cases (19%); see Supplementary Fig. 1.

The test set is a random sample of 10% of all women who were screened at two sites (St George's Hospital and Jarvis Breast Centre) between 2012 and 2015. Insufficient data were provided to apply the sampling procedure to the third site. In assembling the test set, we randomly selected a single eligible screening mammogram from the record of each woman. For women with a positive biopsy, eligible mammograms were those conducted in the 39 months before the date of biopsy. For women who never had a positive biopsy, eligible mammograms were accompanied by a non-suspicious mammogram at least 21 months later.

The final test set consisted of 25,856 women (see Supplementary Fig. 1). When compared to the UK national breast cancer screening service, we observed a very similar distribution of cancer prevalence, age and, cancer type (see Extended Data Table 1a). Digital mammograms were acquired predominantly on devices manufactured by Hologic (95%), followed by General Electric (4%) and Siemens (1%).

The US dataset

The US dataset was collected from Northwestern Memorial Hospital (Chicago) between 2001 and 2018. In the USA, each screening mammogram is typically read by a single radiologist, and screens are conducted annually or biannually. The breast radiologists at this hospital receive fellowship training and only interpret breast-imaging studies. Their experience levels ranged from 1 to 30 years. The American College of Radiology (ACR) recommends that women start routine screening at the age of 40; other organizations, including the United States Preventive Services Task Force (USPSTF), recommend that screening begins at the age of 50 for women with an average risk of breast cancer[6–8].

The US dataset included records from all women that underwent a breast biopsy between 2001 and 2018. It also included a random sample of approximately 5% of all women who participated in screening, but were never biopsied. This heuristic was used in order to capture all cancer cases (to enhance statistical power) and to curate a rich set of benign findings on which to train and test the AI system. The data-processing steps involved in constructing the dataset are summarized in Supplementary Fig. 2.

Among women with a completed mammogram order, we collected records from all women with a pathology report that contained the term 'breast'. Among women that lacked such a pathology report, those whose records bore an International Classification of Diseases (ICD) code indicative of breast cancer were excluded. Approximately 5% of this unbiopsied negative population was sampled. After de-identification and transfer, women were excluded if their metadata were unavailable or corrupted. The women in the dataset were split randomly among train (55%), validation (15%) and test (30%) sets. For testing, a single case was chosen for each woman, following a similar procedure as for the UK dataset. In women who underwent biopsy, we randomly chose a case from the 27 months preceding the date of biopsy. For women who did not undergo biopsy, one screening mammogram was randomly chosen from among those with a follow-up event at least 21 months later.

Cases were considered complete if they possessed the four standard screening views (mediolateral oblique and craniocaudal views of the left and right breasts), acquired for screening intent. Again, the vast majority of the studies were acquired using Hologic (including Lorad-branded) devices (99%); the other manufacturers (Siemens and General Electric) together constituted less than 1% of studies.

The radiology reports associated with cases in the test set were used to flag and exclude cases that involved breast implants or were recalled for technical reasons. To compare the AI system against the clinical reads performed at this site, we employed clinicians to manually extract BI-RADS scores from the original radiology reports. There were some cases for which the original radiology report could not be located, even if a subsequent cancer diagnosis was confirmed by biopsy. This might have happened, for example, if the screening case was imported from an outside institution. Such cases were excluded from the clinical reader comparison.

Randomization and blinding

Patients were randomized into training, validation, and test sets by applying a hash function to the de-identified medical record number. Set assignment was based on the value of the resulting integer modulo 100. For the UK data, values of 0–9 were reserved for the test set. For the US data, values of 0–29 were reserved for the test set. Test set sizes were chosen to produce, in expectation, a sufficient number of positives to power statistical comparisons on the metric of sensitivity.

The US and UK test sets were held back from AI system development, which only took place on the training and validation sets. Investigators did not access test set data until models, hyperparameters, and operating point thresholds were finalized. None of the readers who interpreted the images had knowledge of any aspect of the AI system.

Inverse probability weighting

The US test set includes images from all biopsied women, but only a random subset of women who never underwent biopsy. This enrichment allowed us to accrue more positives in light of the low baseline prevalence of breast cancer, but led to underrepresentation of normal cases. We accounted for this sampling process by using inverse probability weighting to obtain unbiased estimates of human and AI system performance in the screening population[44,45].

We acquired images from 7,522 of the 143,238 women who underwent mammography screening but had no cancer diagnosis or biopsy record. Accordingly, we upweighted cases from women who never underwent

biopsy by a factor of 19.04. Further sampling occurred when selecting one case per patient: to enrich for difficult cases, we preferentially chose cases from the timeframe preceding a biopsy (if one occurred). Although this sampling increases the diversity of benign findings, it again shifts the distribution from what would be observed in a typical screening interval. To better reflect the prevalence that results when negative cases are randomly selected, we estimated additional factors by Monte Carlo simulation. Choosing one case per patient with our preferential sampling mechanism yielded 872 cases that were biopsied within 27 months, and 1,662 cases that were not (Supplementary Fig. 2). However, 100 trials of pure random sampling yielded on average 557.54 and 2,056.46 cases, respectively. Accordingly, cases associated with negative biopsies were downweighted by 557.54/872 = 0.64. Cases that were not biopsied were upweighted by another 2,056.46/1,662 = 1.24, leading to a final weight of 19.04 × 1.24 = 23.61.Cancer-positive cases carried a weight of 1.0. The final sample weights were used in sensitivity, specificity and ROC calculations.

Histopathological outcomes

In the UK dataset, benign and malignant classifications (given directly in the metadata) followed NHSBSP definitions[46]. To derive the outcome labels for the US dataset, pathology reports were reviewed by US-board-certified pathologists and categorized according to the findings they contained. An effort was made to harmonize this categorization with UK definitions. Malignant pathologies included ductal carcinoma in situ, microinvasive carcinoma, invasive ductal carcinoma, invasive lobular carcinoma, special-type invasive carcinoma (including tubular, mucinous and cribriform carcinomas), intraductal papillary carcinoma, non-primary breast cancers (including lymphoma and phyllodes) and inflammatory carcinoma. Women who received a biopsy that found any of these malignant pathologies were considered to have a diagnosis of cancer.

Benign pathologies included lobular carcinoma in situ, radial scar, columnar cell changes, atypical lobular hyperplasia, atypical ductal hyperplasia, cyst, sclerosing adenosis, fibroadenoma, papilloma, periductal mastitis and usual ductal hyperplasia. None of these findings were considered to be cancerous.

Interpreting clinical reads

In the UK screening setting, readers categorize mammograms from asymptomatic women as normal or abnormal, with a third option for technical recall owing to inadequate image quality. An abnormal result at the conclusion of the double-reading process results in further diagnostic assessment. We treat mammograms deemed abnormal as a prediction of malignancy. Cases in which the consensus judgment recalled the patient for technical reasons were excluded from analysis, as the images were presumed to be incomplete or unreliable. Cases in which any single reader recommended technical recall were excluded from the corresponding reader comparison.

In the US screening setting, radiologists attach a BI-RADS[35] score to each mammogram. A score of 0 is deemed ‘incomplete’, and will later be refined on the basis of follow-up imaging or repeat mammography to address technical issues. For computation of sensitivity and specificity, we dichotomized the BI-RADS assessments in line with previous work[34]. Scores of 0, 4 and 5 were treated as positive predictions if the recommendation was based on mammographic findings, not on technical grounds or patient symptoms alone. Cases of technical recall were excluded from analysis, as the images were presumed to be incomplete or unreliable. BI-RADS scores were manually extracted from the free-text radiology reports. Cases for which the BI-RADS score was unavailable were excluded from the reader comparison.

In both datasets, the original readers had access to contextual information that is normally available in clinical practice. This includes the patient’s family history of cancer, prior screening and diagnostic imaging, and radiology or pathology notes from past examinations. By contrast, only the age of the patient was made available to the AI system.

Overview of the AI system

The AI system consisted of an ensemble of three deep learning models, each operating on a different level of analysis (individual lesions, individual breasts and the full case). Each model produces a cancer risk score between 0 and 1 for the entire mammography case. The final prediction of the system was the mean of the predictions from the three independent models. A detailed description of the AI system is available in the Supplementary Methods and Supplementary Fig. 3.

Selection of operating points

The AI system natively produces a continuous score that represents the likelihood of cancer being present. To support comparisons with the predictions of human readers, we thresholded this score to produce analogous binary screening decisions. For each clinical benchmark, we used the validation set to choose a distinct operating point; this amounts to a score threshold that separates positive and negative decisions. To better simulate prospective deployment, the test sets were never used in selecting operating points.

The UK dataset contains three clinical benchmarks—the first reader, second reader and consensus. This last decision is the outcome of the double-reading process and represents the standard of care in the UK. For the first reader, we chose an operating point aimed at demonstrating statistical superiority in specificity and non-inferiority for sensitivity. For the second reader and consensus reader, we chose an operating point aimed at demonstrating statistical non-inferiority for both sensitivity and specificity.

The US dataset contains a single operating point for comparison, which corresponds to the radiologist using the BI-RADS rubric for evaluation. In this case, we used the validation set to choose an operating point aimed at achieving superiority for both sensitivity and specificity.

Reader study

For the reader study, six US-board-certified radiologists interpreted a sample of 500 cases from 500 women in the test set. All radiologists were compliant with MQSA requirements for interpreting mammography and had an average of 10 years of clinical experience (Extended Data Table 7b). Two of them were fellowship-trained in breast imaging. The sample of cases was stratified to contain 50% normal cases, 25% biopsy-confirmed negative cases and 25% biopsy-confirmed positive cases. A detailed description of the case composition of the reader study can be found in Extended Data Table 3. Readers were not informed of the enrichment levels in the dataset.

Readers recorded their assessments on a 21CFR11-compliant electronic case report form within the Ambra Health (New York, NY) viewer v3.18.7.0R. They interpreted the images using 5MP MSQA-compliant displays. Each reader interpreted the cases in a unique randomized order.

For each study, readers were asked to first report a BI-RADS[35] 5th edition score using the values 0, 1 and 2, as if they were interpreting the screening mammogram in routine practice. They were then asked to render a forced diagnostic BI-RADS score using the values 1, 2, 3, 4A, 4B, 4C or 5. Readers also gave a finer-grained score between 0 and 100 that was indicative of their suspicion that the case contains a malignancy.

In addition to the four standard mammographic screening images, clinical context was provided to better simulate the screening setting. Readers were presented with the preamble of the de-identified radiology report that was produced by the radiologist who originally interpreted the study. This contained information such as the age of the patient and their family history of cancer. The information was manually reviewed to ensure that no impression or findings were included.

Where possible (in 43% of cases), previous imaging was made available to the readers. Readers could review up to four sets of previous

screening exams that were acquired between 1 and 4 years earlier, accompanied by de-identified radiologist reports. If prior imaging was available, the study was read twice by each reader—first without the prior information, and then immediately after, with the prior information present. The system ensured that readers could not update their initial assessment after the prior information was presented. For cases for which previous exams were available, the final reader assessment (given after having reviewed the prior exams) was used for the analysis.

Cases in which at least half of the readers indicated concerns with image quality were excluded from the analysis. Cases in which breast implants were noted were also excluded. The final analysis was performed on the remaining 465 cases.

Localization analysis

For this purpose, we considered all screening exams from the reader study for which cancer developed within 12 months. See Extended Data Table 3 for a detailed description of how the dataset was constructed. To collect ground-truth localizations, two board-certified radiologists inspected each case, using follow-up data to identify the location of malignant lesions. Instances of disagreement were resolved by one radiologist with fellowship training in breast imaging. To identify the precise location of the cancerous tissue, radiologists consulted subsequent diagnostic mammograms, radiology reports, biopsy notes, pathology reports and post-biopsy mammograms. Rectangular bounding boxes were drawn around the locations of subsequent positive biopsies in all views in which the finding was visible. In cases in which no mammographic finding was visible, the location where the lesion later appeared was highlighted. Of the 56 cancers considered for analysis, location information could be obtained with confidence in 53 cases; three cases were excluded owing to ambiguity in the index examination and the absence of follow-up images. On average, there were 2.018 ground-truth regions per cancer-positive case.

In the reader study, readers supplied rectangular ROI annotations surrounding suspicious findings in all cases to which they assigned a BI-RADS score of 3 or higher. A limit of six ROIs per case was enforced. On average, the readers supplied 2.04 annotations per suspicious case. In addition to an overall cancer likelihood score, the AI system produces a ranked list of rectangular bounding boxes for each case. To conduct a fair comparison, we allowed only the top two bounding boxes from the AI system to match the number of ROIs produced by the readers.

To compare the localization performance of the AI system with that of the readers, we used a method inspired by location receiver operating characteristic (LROC) analysis[37]. LROC analysis differs from traditional ROC analysis in that the ordinate is a sensitivity measure that factors in localization accuracy. Although LROC analysis traditionally involves a single finding per case[37,47], we permitted multiple unranked findings to match the format of our data. We use the term multi-localization ROC analysis (mLROC) to describe our approach. For each threshold, a cancer case was considered a true positive if its case-wide score exceeded this threshold and at least one culprit area was correctly localized in any of the four mammogram views. Correct localization required an intersection-over-union (IoU) of 0.1 with the ground-truth ROI. False positives were defined as usual.

CAD systems are often evaluated on the basis of whether the centre of their marking falls within the boundary of a ground-truth annotation[48]. This is potentially problematic as it does not properly penalize predicted bounding boxes that are so large as to be non-specific, but whose centre nevertheless happens to fall within the target region. Similarly, large ground-truth annotations associated with diffuse findings might be overly generous to the CAD system. We prefer the IoU metric because it balances these considerations. We chose a threshold of 0.1 to account for the fact that indistinct margins on mammography findings lead to ROI annotations of vastly different sizes depending on subjective factors of the annotator (see Supplementary Fig. 4). Similar work in three-dimensional chest computed tomography[18] used any pixel overlap to qualify for correct localization. Likewise, an FDA-approved software device for the detection of wrist fractures reports statistics in which true positives require at least one pixel of overlap[49]. An IoU value of 0.1 is strict by these standards.

Statistical analysis

To evaluate the stand-alone performance of the AI system, the AUC-ROC was estimated using the normalized Wilcoxon (Mann–Whitney) U statistic[50]. This is the standard non-parametric method used by most modern software libraries. For the UK dataset, non-parametric confidence intervals on the AUC were computed with DeLong's method[51,52]. For the US dataset, in which each sample carried a scalar weight, the bootstrap was used with 1,000 replications.

For both datasets, we compared the sensitivity and specificity of the readers with that of a thresholded score from the AI system. For the UK dataset, we knew the pseudo-identity of each reader, so statistics were adjusted for the clustered nature of the data using Obuchowski's method for paired binomial proportions[53,54]. Confidence intervals on the difference are Wald intervals[55] and a Wald test was used for non-inferiority[56]. Both used the Obuchowski variance estimate.

For the US dataset, in which each sample carried a scalar inverse probability weight[45], we used resampling methods[57] to compare the sensitivity and specificity of the AI system with those of the pool of radiologists. Confidence intervals on the difference were generated with the bootstrap method with 1,000 replications. A P value on the difference was generated through the use of a permutation test[58]. In each of 10,000 trials, the reader and AI system scores were randomly interchanged for each case, yielding a reader–AI system difference sampled from the null distribution. A two-sided P value was computed by comparing the observed statistic to the empirical quantiles of the randomization distribution.

In the reader study, each reader graded each case using a forced BI-RADS protocol (a score of 0 was not permitted), and the resulting values were treated as a 6-point index of suspicion for malignancy. Scores of 1 and 2 were collapsed into the lowest category of suspicion; scores 3, 4a, 4b, 4c and 5 were treated independently as increasing levels of suspicion. Because none of the BI-RADS operating points reached the high-sensitivity regime (see Fig. 3), to avoid bias from non-parametric analysis[59] we fitted parametric ROC curves to the data using the proper binormal model[60]. This issue was not alleviated by using the readers' ratings for their suspicion of malignancy, which showed very strong correspondence with the BI-RADS scores (Supplementary Fig. 5). As BI-RADS is used in actual screening practice, we chose to focus on these scores for their superior clinical relevance. In a similar fashion, we fitted a parametric ROC curve to discretized AI system scores on the same data.

The performance of the AI system was compared to that of the panel of radiologists using methods for the analysis of multi-reader multi-case (MRMC) studies that are standard in the radiology community[61]. More specifically, we compared the AUC-ROC and pAUC-mLROC for the AI system to those of the average radiologist using the ORH procedure[62,63]. Originally formulated for the comparison of multiple imaging modalities, this analysis has been adapted to the setting in which the population of radiologists operate on a single modality and interest lies in comparing their performance to that of a stand-alone algorithm[61]. The jackknife method was used to estimate the covariance terms in the model. Computation of P values and confidence intervals was conducted in Python using the numpy and scipy packages, and benchmarked against a reference implementation in the RJafroc library for the R computing language (https://cran.r-project.org/web/packages/RJafroc/index.html).

Our primary comparisons numbered seven in total: sensitivity and specificity for the UK first reader; sensitivity and specificity for the US clinical radiologist; sensitivity and specificity for the US clinical radiologist against a model trained using only UK data; and the AUC-ROC in

the reader study. For comparisons with the clinical reads, the choice of superiority or non-inferiority was based on what seemed attainable from simulations conducted on the validation set. For non-inferiority comparisons, a 5% absolute margin was pre-specified before the test set was inspected. We used a statistical significance threshold of 0.05. All seven *P* values survived correction for multiple comparisons using the Holm–Bonferroni method[64].

Reporting summary

Further information on research design is available in the Nature Research Reporting Summary linked to this paper.

Data availability

The dataset from Northwestern Medicine was used under license for the current study, and is not publicly available. Applications for access to the OPTIMAM database can be made at https://medphys.royalsurrey.nhs.uk/omidb/getting-access/.

Code availability

The code used for training the models has a large number of dependencies on internal tooling, infrastructure and hardware, and its release is therefore not feasible. However, all experiments and implementation details are described in sufficient detail in the Supplementary Methods section to support replication with non-proprietary libraries. Several major components of our work are available in open source repositories: Tensorflow (https://www.tensorflow.org); Tensorflow Object Detection API (https://github.com/tensorflow/models/tree/master/research/object_detection).

44. Pinsky, P. F. & Gallas, B. Enriched designs for assessing discriminatory performance—analysis of bias and variance. *Stat. Med.* **31**, 501–515 (2012).
45. Mansournia, M. A. & Altman, D. G. Inverse probability weighting. *BMJ* **352**, i189 (2016).
46. Ellis, I. O. et al. *Pathology Reporting of Breast Disease in Surgical Excision Specimens Incorporating the Dataset for Histological Reporting of Breast Cancer, June 2016* (Royal College of Pathologists, accessed 22 July 2019); https://www.rcpath.org/resourceLibrary/g148-breastdataset-hires-jun16-pdf.html
47. Chakraborty, D. P. & Yoon, H.-J. Operating characteristics predicted by models for diagnostic tasks involving lesion localization. *Med. Phys.* **35**, 435–445 (2008).
48. Ellis, R. L., Meade, A. A., Mathiason, M. A., Willison, K. M. & Logan-Young, W. Evaluation of computer-aided detection systems in the detection of small invasive breast carcinoma. *Radiology* **245**, 88–94 (2007).
49. US Food and Drug Administration. *Evaluation of Automatic Class III Designation for OsteoDetect* (FDA, 2018; accessed 2 October 2019); https://www.accessdata.fda.gov/cdrh_docs/reviews/DEN180005.pdf
50. Hanley, J. A. & McNeil, B. J. The meaning and use of the area under a receiver operating characteristic (ROC) curve. *Radiology* **143**, 29–36 (1982).
51. DeLong, E. R., DeLong, D. M. & Clarke-Pearson, D. L. Comparing the areas under two or more correlated receiver operating characteristic curves: a nonparametric approach. *Biometrics* **44**, 837–845 (1988).
52. Gengsheng Qin, & Hotilovac, L. Comparison of non-parametric confidence intervals for the area under the ROC curve of a continuous-scale diagnostic test. *Stat. Methods Med. Res.* **17**, 207–221 (2008).
53. Obuchowski, N. A. On the comparison of correlated proportions for clustered data. *Stat. Med.* **17**, 1495–1507 (1998).
54. Yang, Z., Sun, X. & Hardin, J. W. A note on the tests for clustered matched-pair binary data. *Biom. J.* **52**, 638–652 (2010).
55. Fagerland, M. W., Lydersen, S. & Laake, P. Recommended tests and confidence intervals for paired binomial proportions. *Stat. Med.* **33**, 2850–2875 (2014).
56. Liu, J.-P., Hsueh, H.-M., Hsieh, E. & Chen, J. J. Tests for equivalence or non-inferiority for paired binary data. *Stat. Med.* **21**, 231–245 (2002).
57. Efron, B. & Tibshirani, R. J. *An Introduction to the Bootstrap* (Springer, 1993).
58. Chihara, L. M., Hesterberg, T. C. & Dobrow, R. P. *Mathematical Statistics with Resampling and R & Probability with Applications and R Set* (Wiley, 2014).
59. Gur, D., Bandos, A. I. & Rockette, H. E. Comparing areas under receiver operating characteristic curves: potential impact of the "last" experimentally measured operating point. *Radiology* **247**, 12–15 (2008).
60. Metz, C. E. & Pan, X. "Proper" binormal ROC curves: theory and maximum-likelihood estimation. *J. Math. Psychol.* **43**, 1–33 (1999).
61. Chakraborty, D. P. *Observer Performance Methods for Diagnostic Imaging: Foundations, Modeling, and Applications with R-Based Examples* (CRC, 2017).
62. Obuchowski, N. A. & Rockette, H. E. Hypothesis testing of diagnostic accuracy for multiple readers and multiple tests an anova approach with dependent observations. *Commun. Stat. Simul. Comput.* **24**, 285–308 (1995).
63. Hillis, S. L. A comparison of denominator degrees of freedom methods for multiple observer ROC analysis. *Stat. Med.* **26**, 596–619 (2007).
64. Aickin, M. & Gensler, H. Adjusting for multiple testing when reporting research results: the Bonferroni vs Holm methods. *Am. J. Public Health* **86**, 726–728 (1996).
65. NHS Digital. *Breast Screening Programme* (NHS, accessed 17 July 2019); https://digital.nhs.uk/data-and-information/publications/statistical/breast-screening-programme

Acknowledgements We would like to acknowledge multiple contributors to this international project: Cancer Research UK, the OPTIMAM project team and staff at the Royal Surrey County Hospital who developed the UK mammography imaging database; S. Tymms and S. Steer for providing patient perspectives; R. Wilson for providing a clinical perspective; all members of the Etemadi Research Group for their efforts in data aggregation and de-identification; and members of the Northwestern Medicine leadership, without whom this work would not have been possible (M. Schumacher, C. Christensen, D. King and C. Hogue). We also thank everyone at NMIT for their efforts, including M. Lombardi, D. Fridi, P. Lendman, B. Slavicek, S. Xinos, B. Milfajt and others; V. Cornelius, who provided advice on statistical planning; R. West and T. Saensuksopa for assistance with data visualization; A. Eslami and O. Ronneberger for expertise in machine learning; H. Forbes and C. Zaleski for assistance with project management; J. Wong and F. Tan for coordinating labelling resources; R. Ahmed, R. Pilgrim, A. Phalen and M. Bawn for work on partnership formation; R. Eng, V. Dhir and R. Shah for data annotation and interpretation; C. Chen for critically reading the manuscript; D. Ardila for infrastructure development; C. Hughes and D. Moitinho de Almeida for early engineering work; and J. Yoshimi, X. Ji, W. Chen, T. Daly, H. Doan, E. Lindley and Q. Duong for development of the labelling infrastructure. A.D. and F.J.G. receive funding from the National Institute for Health Research (Senior Investigator award). Infrastructure support for this research was provided by the NIHR Imperial Biomedical Research Centre (BRC). The views expressed are those of the authors and not necessarily those of the NIHR or the Department of Health and Social Care.

Author contributions A.K., A.D., D.H., D.K., H.M., G.C.C., J.D.F., J.R.L., K.C.Y., L.P., M.H.-B., M. Sieniek, M. Suleyman, R.S., S.M.M., S.S. and T.B. contributed to the conception of the study; A.K., B.R.-P., C.J.K., D.H., D.T., F.J.G., J.D.F., J.R.L., K.C.Y., L.P., M.H.-B., M.C., M.E., M. Sieniek, M. Suleyman, N.A., R.S., S.J., S.M.M., S.S., T.B. and V.G. contributed to study design; D.M., D.T., F.G.-V., G.C.C., H.M., J.D.F., J.G., K.C.Y., L.P., M.H.-B., M.C., M.E., M. Sieniek, S.M.M., S.S. and V.G. contributed to acquisition of the data; A.K., A.D., B.R.-P., C.J.K., F.J.G., H.A., J.D.F., J.G., J.J.R., M. Suleyman, N.A., R.S., S.J., S.M.M., S.S. and V.G. contributed to analysis and interpretation of the data; A.K., C.J.K., D.T., F.J.G., J.D.F., J.G., J.J.R., M. Sieniek, N.A., R.S., S.J., S.M.M., S.S. and V.G. contributed to drafting and revising the manuscript.

Competing interests This study was funded by Google LLC and/or a subsidiary thereof ('Google'). S.M.M., M. Sieniek, V.G., J.G., N.A., T.B., M.C., G.C.C., D.H., S.J., A.K., C.J.K., D.K., J.R.L., H.M., B.R.-P., L.P., M. Suleyman, D.T., J.D.F. and S.S. are employees of Google and own stock as part of the standard compensation package. J.J.R., R.S., F.J.G. and A.D. are paid consultants of Google. M.E., F.G.-V., D.M., K.C.Y. and M.H.-B received funding from Google to support the research collaboration.

Additional information

Supplementary information is available for this paper at https://doi.org/10.1038/s41586-019-1799-6.

Correspondence and requests for materials should be addressed to S.M.M., D.T. or S.S.

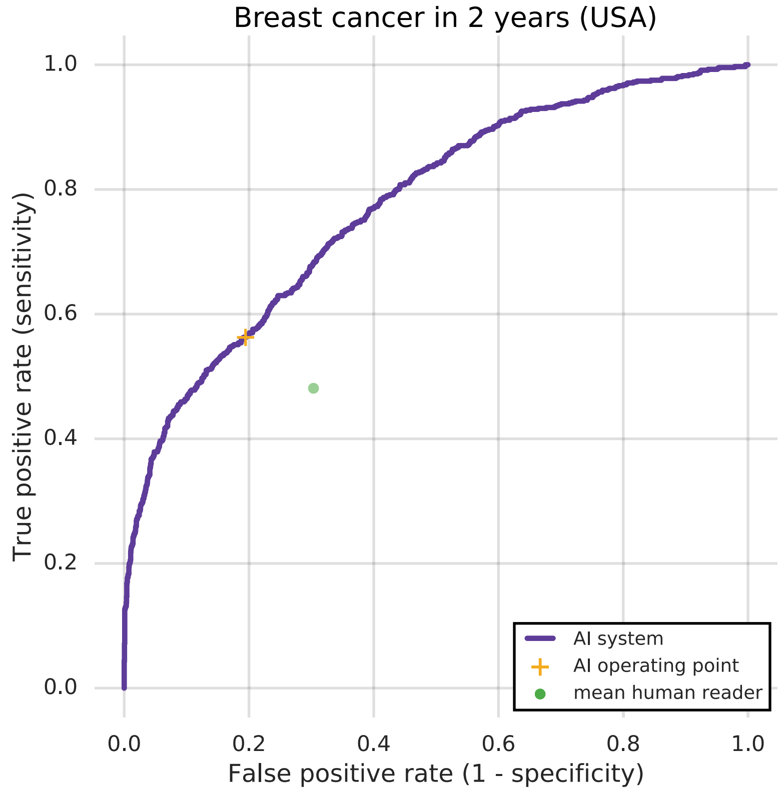

Extended Data Fig. 1 | Unweighted evaluation of breast cancer prediction on the US test set. In contrast to in Fig. 2b, the sensitivity and specificity were computed without the use of inverse probability weights to account for the spectrum enrichment of the study population. Because hard negatives are overrepresented, the specificity of both the AI system and the human readers is reduced. The unweighted human sensitivity and specificity are 48.10% ($n = 553$) and 69.65% ($n = 2,185$), respectively.

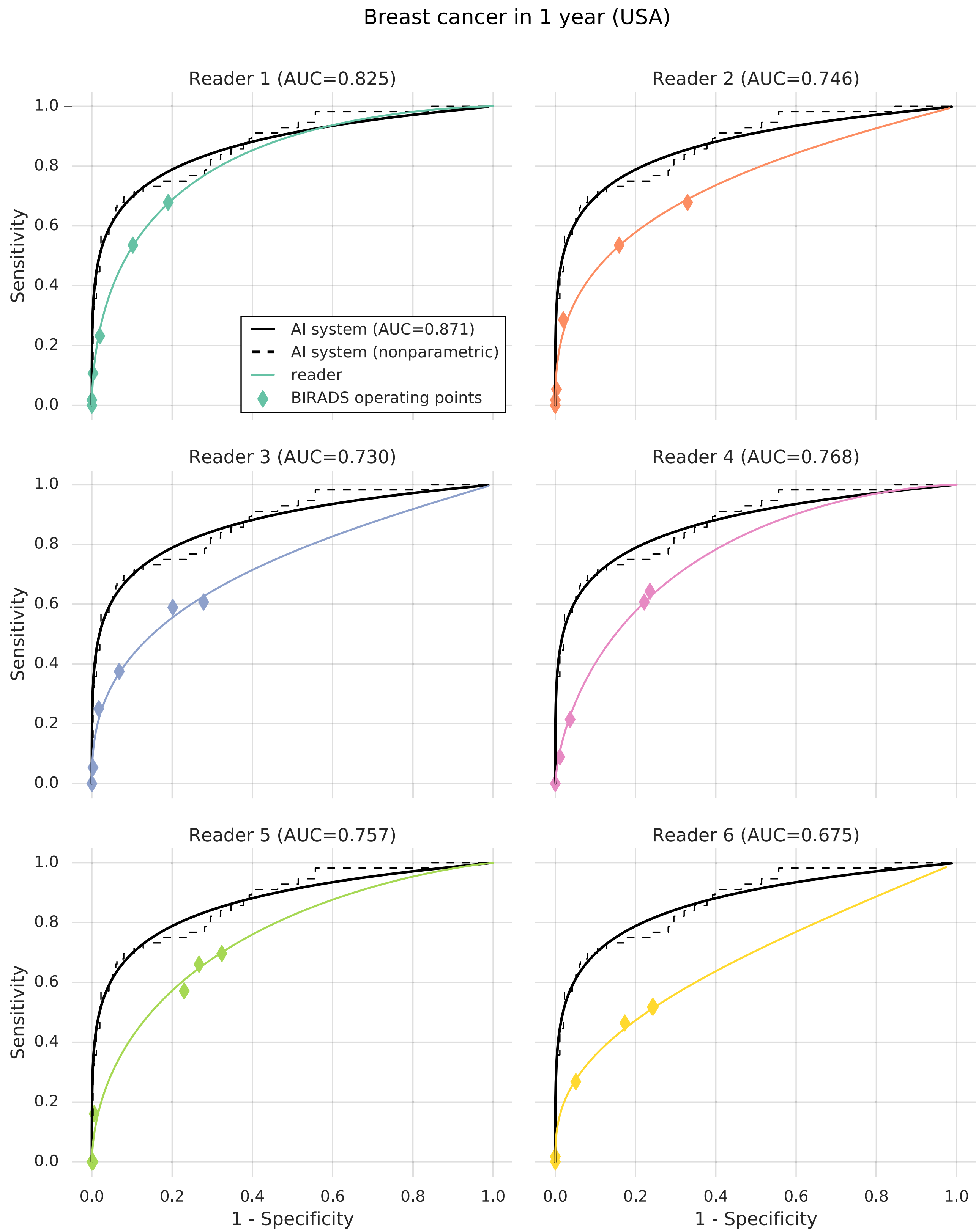

Extended Data Fig. 2 | Performance of the AI system in breast cancer prediction compared to six independent readers, with a 12-month follow-up interval for cancer-positive status. Whereas the mean reader AUC was 0.750 (s.d. 0.049), the AI system achieved an AUC of 0.871 (95% CI 0.785, 0.919). The AI system exceeded human performance by a significant margin (ΔAUC = +0.121, 95% CI 0.070, 0.173; $P = 0.0018$ by two-sided ORH method). In this analysis, there were 56 positives of 408 total cases; see Extended Data Table 3. Note that this sample of cases was enriched for patients who had received a negative biopsy result ($n = 119$), making it a more challenging population for screening. As these external readers were not gatekeepers for follow-up and eventual cancer diagnosis, there was no bias in favour of reader performance at this shorter time horizon. See Fig. 3a for a comparison with a time interval that was chosen to encompass a subsequent screening exam.

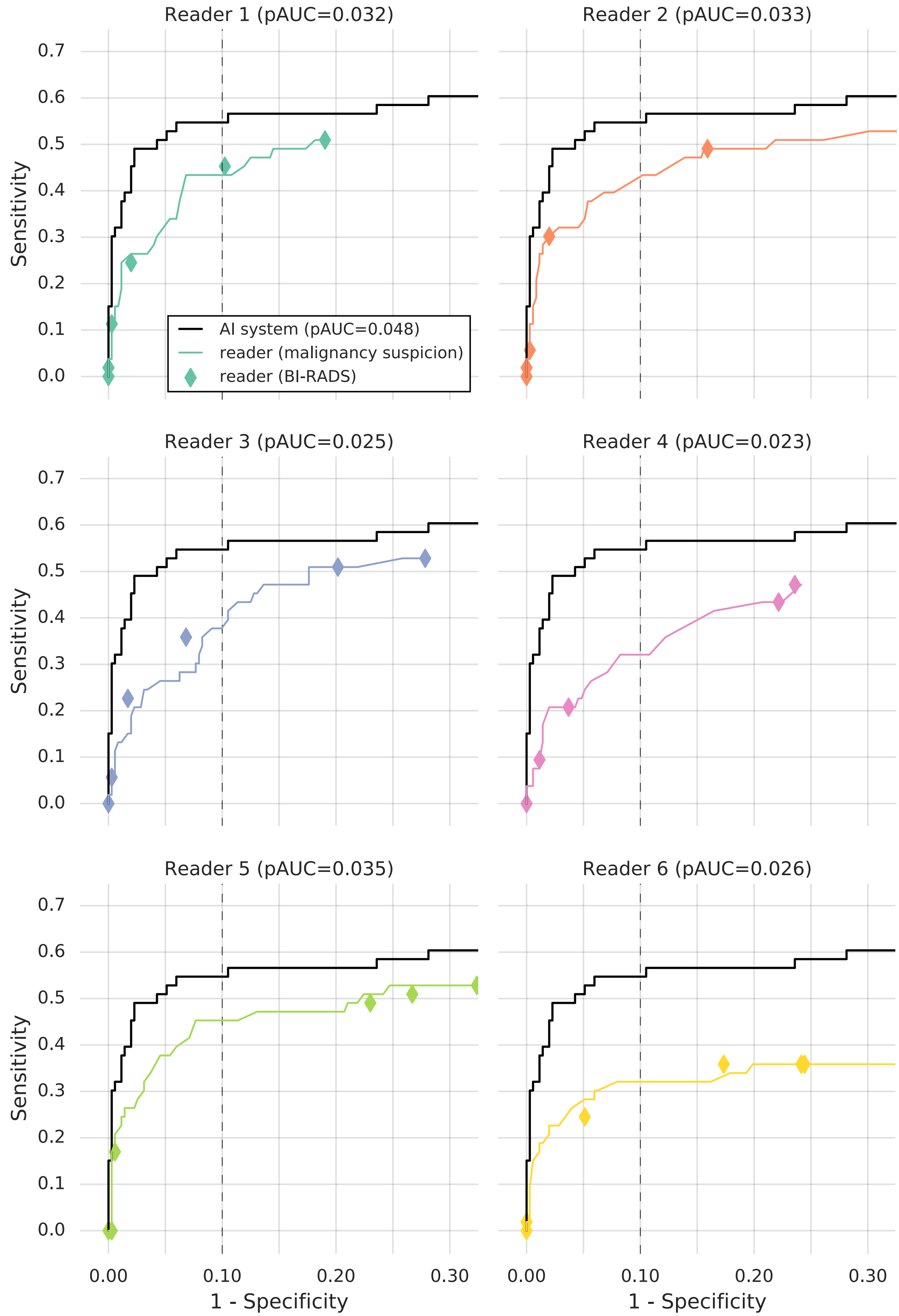

Extended Data Fig. 3 | Localization (mLROC) analysis. Similar to Extended Data Fig. 2, but true positives require localization of a malignancy in any of the four mammogram views (see Methods section 'Localization analysis'). Here, the cancer interval was 12 months ($n = 53$ positives of 405 cases; see Extended Data Table 3). The dotted line indicates a false-positive rate of 10%, which was used as the right-hand boundary for the pAUC calculation. The mean reader pAUC was 0.029 (s.d. 0.005), whereas that of the AI system was 0.048 (95% CI 0.035, 0.061). The AI system exceeded human performance by a significant margin (ΔpAUC = +0.0192, 95% CI 0.0086, 0.0298; $P = 0.0004$ by two-sided ORH method).

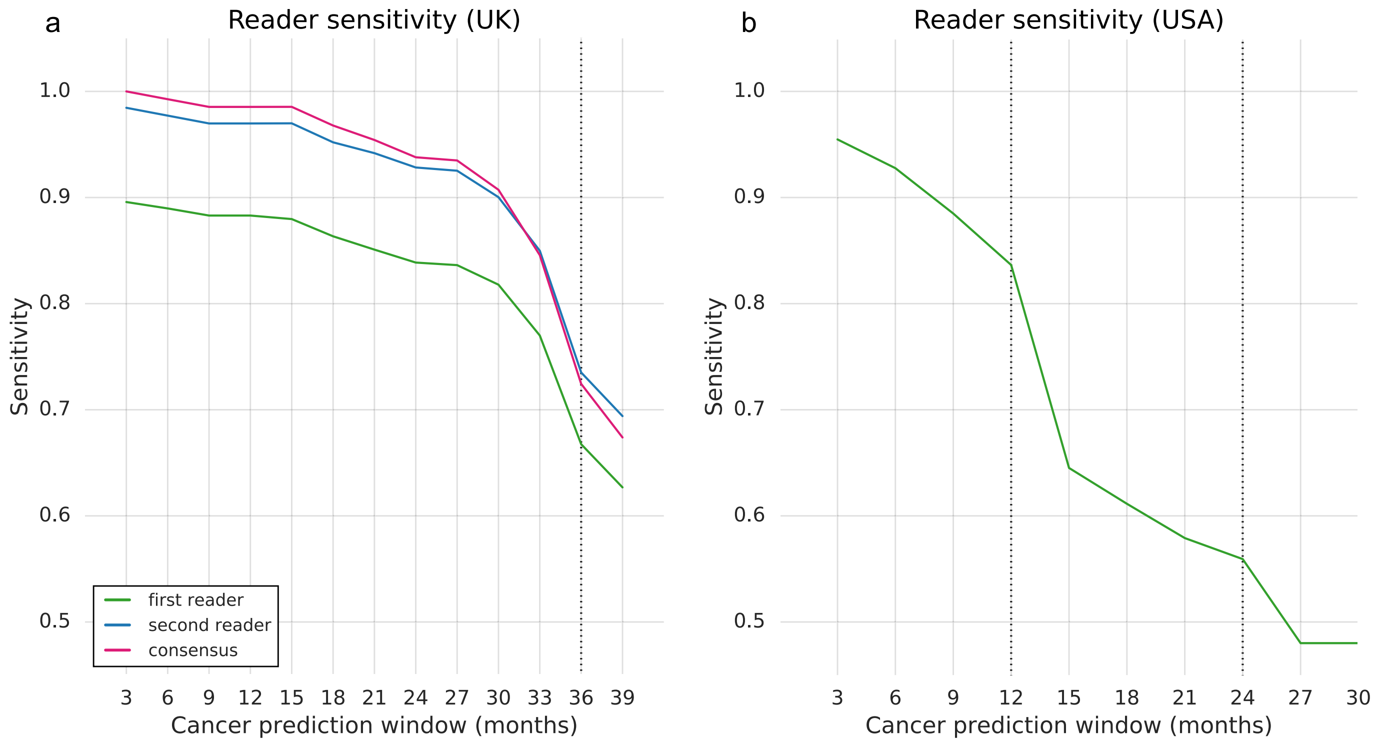

Extended Data Fig. 4 | Evidence for the gatekeeper effect in retrospective datasets. a, **b**, Graphs show the change in observed reader sensitivity in the UK (**a**) and the USA (**b**) as the cancer follow-up interval is extended. At short intervals, measured reader sensitivity is extremely high, owing to the fact that biopsies are only triggered based on radiological suspicion. As the time interval is extended, the task becomes more difficult and measured sensitivity declines. Part of this decline stems from the development of new cancers that were impossible to detect at the initial screening. However, steeper drops occur when the follow-up window encompasses the screening interval (36 months in the UK; 12 and 24 months in the USA). This is suggestive of what happens to reader metrics when gatekeeper bias is mitigated by another screening examination. In both graphs, the number of positives grows as the follow-up interval is extended. In the UK dataset (**a**), it increases from $n = 259$ within 3 months to $n = 402$ within 39 months. In the US dataset (**b**), it increases from $n = 221$ within $n = 3$ months to 553 within 39 months.

a b

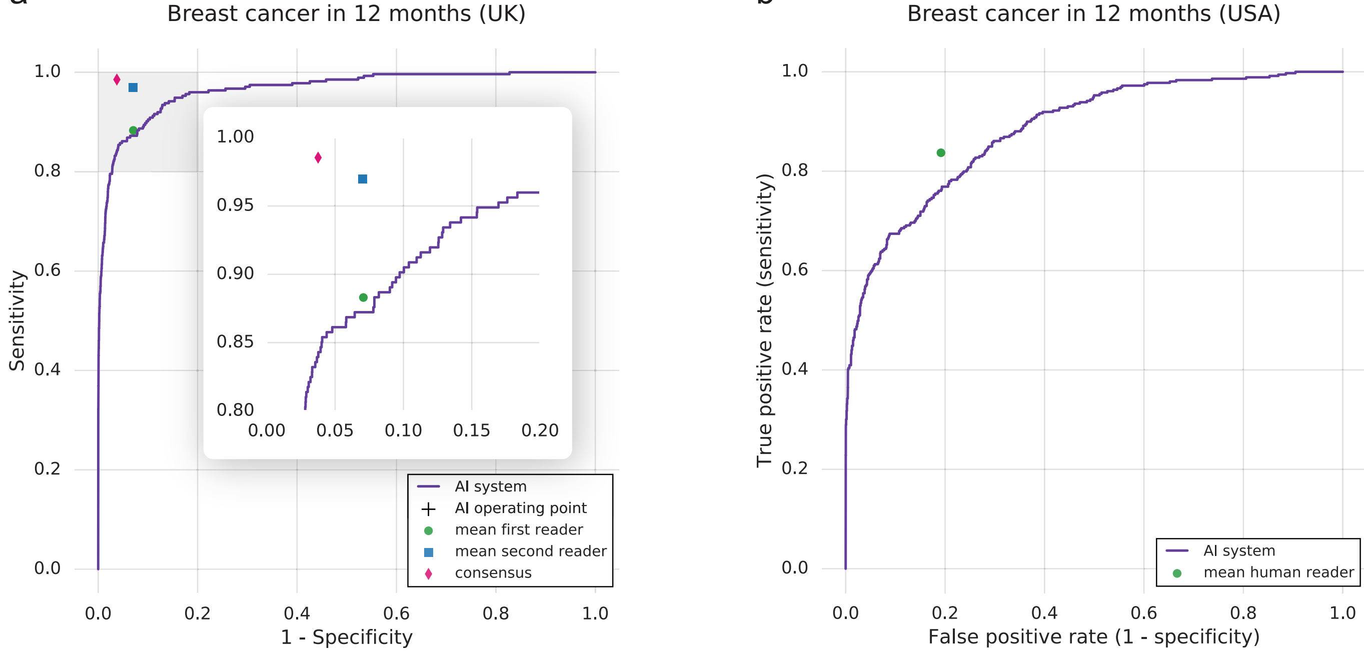

c

test dataset	human benchmark	metric	clinical decision (%)	*n*
UK	first reader	sensitivity	88.3	265
		specificity	92.9	25,116
	second reader	sensitivity	97.0	265
		specificity	93.0	25,114
	consensus	sensitivity	98.5	274
		specificity	96.2	25,443
USA	reader	sensitivity	83.7	359
		specificity	80.8	2,185

Extended Data Fig. 5 | Quantitative evaluation of reader and AI system performance with a 12-month follow-up interval for ground-truth cancer-positive status. Because a 12-month follow-up interval is unlikely to encompass a subsequent screening exam in either country, reader–model comparisons on retrospective clinical data may be skewed by the gatekeeper effect (Extended Data Fig. 4). See Fig. 2 for comparison with longer time intervals. **a**, Performance of the AI system on UK data. This plot was derived from a total of 25,717 eligible examples, including 274 positives. The AI system achieved an AUC of 0.966 (95% CI 0.954, 0.977). **b**, Performance of the AI system on US data. This plot was derived from a total of 2,770 eligible examples, including 359 positives. The AI system achieved an AUC of 0.883 (95% CI 0.859, 0.903). **c**, Reader performance. When computing reader metrics, we excluded cases for which the reader recommended repeat mammography to address technical issues. In the US data, the performance of radiologists could only be assessed on the subset of cases for which a BI-RADS grade was available.

Extended Data Table 1 | Characteristics of the UK and US test sets

a

		UK test set	CI at 95%	NHS BSP
	Years	2012 to 2015	-	2011 to 2016
	Sources	2 sites in the UK	-	All UK screening sites
	No. women	25,856	-	10,257,551
	No. normals	25,588 (99.0%)	(98.8, 99.1)	10,171,074 (99.1%)
	No. cancers	268 (1.0%)	(0.9, 1.2)	86,477 (0.8%)
	Recall rate	1,235 (4.8%)	(4.5, 5.1)	427,457 (4.2%)
Age	*45 – 49*	1,707 (6.6%)	(6.2, 7.1)	832,883 (8.1%)
	50 – 52	4,399 (17.1%)	(16.4, 17.7)	1,487,366 (14.5%)
	53 – 54	2,742 (10.6%)	(10.1, 11.1)	944,823 (9.2%)
	55 – 59	6,034 (23.3%)	(22.6, 24.0)	2,139,701 (20.9%)
	60 – 64	5,457 (21.1%)	(20.4, 21.8)	2,044,746 (19.9%)
	65 – 70	4,575 (17.7%)	(17.0, 18.3)	2,217,947 (21.6%)
	>= 70	942 (3.6%)	(3.3, 4.0)	590,085 (5.8%)
Cancer type	*Invasive*	204 (76.1%)	(69.5, 81.8)	68,006 (78.6%)
	Non-invasive	58 (21.6%)	(16.2, 28.1)	17,733 (20.5%)
	Micro-invasive	-	-	654 (0.8%)
	Unknown	6 (2.2%)	(0.9, 5.6)	84 (0.1%)
Cancer size (Invasive only)	*< 10mm*	41 (20.1%)	(13.7, 28.3)	17,242 (25.4%)
	10 – 15mm	44 (21.6%)	(15.3, 30.4)	17,745 (26.1%)
	15 – 20mm	39 (19.1%)	(12.9, 27.2)	12,864 (18.9%)
	20 – 50mm	61 (29.9%)	(22.1, 38.7)	16,316 (24.0%)
	>= 50mm	13 (6.4%)	(3.1, 12.4)	1,527 (2.3%)
	Unknown	6 (2.9%)	(1.0, 7.9)	2,312 (3.4%)

b

		US test set	CI at 95%	US BCSC
	Years	2001 to 2018	-	2007 to 2013
	Sources	1 US medical center	-	6 BCSC registries
	No. women	3,097	-	1,682,504
	No. normals	2,738 (88.4%)	(87.2, 89.8)	1,672,692 (99.4%)
	No. cancers	359 (11.6%)	(10.2, 12.8)	9,812 (0.6%)
	Recall rate	929 (30.0%)	(18.4, 21.5)	195,170 (11.6%)
Age	*< 40*	181 (5.9%)	(4.8, 7.1)	41,479 (2.5%)
	40 – 49	1,259 (40.8%)	(38.6, 43.0)	448,587 (26.7%)
	50 – 59	800 (26.1%)	(24.1, 28.1)	505,816 (30.1%)
	60 – 69	598 (19.0%)	(17.3, 20.9)	396,943 (23.6%)
	>= 70	259 (8.2%)	(7.0, 9.5)	289,679 (17.3%)
Cancer type	*Invasive*	240 (66.9%)	(60.5, 72.1)	5,885 (69.0%)
	DCIS	100 (27.9%)	(22.8, 33.9)	2,644 (31.0%)
	Other	19 (5.3%)	(3.2, 8.9)	-

For each feature, we constructed a joint 95% confidence interval on the proportions in each category. **a**, The UK test set was drawn from two sites in the UK over a four-year period. For reference, we present the corresponding statistics from the broader UK NHSBSP[65]. For comparison with national numbers, only cancers that were detected by screening are reported here. **b**, The US test set was drawn from one academic medical centre over an eighteen-year period. For reference, we present the corresponding statistics from the broader US screening population, as reported by the Breast Cancer Surveillance Consortium (BCSC)[2]. Cancers reported here occurred within 12 months of screening.
DCIS, ductal carcinoma in situ.

Extended Data Table 2 | Detailed comparison between human clinical decisions and AI predictions

a

test dataset	human benchmark	metric	clinical decision (%)	AI decision (%)	Δ (%)	95% CI (%)	p-value	comparison	N
UK	first reader	sensitivity	62.69	65.42	2.70	(-3.0, 8.5)	0.0043	noninferiority	402
		specificity	92.93	94.12	**1.18**	(0.29, 2.08)	0.0096	superiority	25,115
	second reader	sensitivity	69.40	69.40	0.00	(-4.89, 4.89)	0.0225	noninferiority	402
		specificity	92.97	92.13	-0.84	(-1.97, 0.282)	2e-13	noninferiority	25,113
	consensus	sensitivity	67.39	68.12	0.72	(-3.49, 4.94)	0.0039	noninferiority	414
		specificity	96.24	96.24	-3.35	(-4.06, -2.63)	3e-6	noninferiority	25,442
USA	reader	sensitivity	48.10	57.50	**9.40**	(4.45, 13.85)	0.0004	superiority	553
		specificity	80.83	86.53	**5.70**	(2.62, 8.64)	0.0002	superiority	2,185

b

USA	reader	sensitivity	48.10	56.24	**8.14**	(3.54, 12.5)	0.0006	superiority	553
		specificity	80.83	84.29	**3.47**	(0.6, 5.98)	0.0212	superiority	2,185

a, Comparison of sensitivity and specificity between human benchmarks (derived retrospectively from the clinical record) and the predictions of the AI system. Score thresholds were chosen, on the basis of separate validation data, to match or exceed the performance of each human benchmark (see Methods section 'Selection of operating points'). These points are depicted graphically in Fig. 2. Note that the number of cases (*N*) differs from Fig. 2 because the opinion of the radiologist was not available for all images. We also note that sensitivity and specificity metrics are not easily comparable to most previous publications in breast imaging (for example, the DMIST Trial[34]), given the differences in follow-up interval. Negative cases in the US dataset were upweighted to account for the sampling protocol (see Methods section 'Inverse probability weighting'). **b**, Same columns as **a**, but using a version of the AI system that was trained exclusively on the UK dataset. It was tested on the US dataset to show generalizability of the AI across populations and healthcare systems. Superiority comparisons on the UK data were conducted using Obuchowski's extension of the two-sided McNemar test for clustered data. Non-inferiority comparisons were Wald tests using the Obuchowski correction. Comparisons on the US data were performed with a two-sided permutation test. All *P* values survived correction for multiple comparisons (see Methods section 'Statistical analysis'). Quantities in bold represent estimated differences that are statistically significant for superiority; all others are statistically non-inferior at a pre-specified 5% margin.

Extended Data Table 3 | Detailed description of the case composition for the reader study

Row	Description	No. cancer cases	No. biopsied negative cases	No. normal cases	Total	Figure
1	inclusion based on 27-month outcome	125	125	250	500	-
2	manual quality review	113	119	233	465	Figure 3a,b
3	restrict to cancers in 12 months	56	119	233	408	Figure 3c Extended Data Figure 2
4	obtain ground truth localizations	53	119	233	405	Extended Data Figure 3

Row 1: 500 cases were selected for the reader study. The case mixture was enriched for positives as well as challenging negatives. Row 2: cases containing breast implants and those for which at least half of the readers indicated image-quality concerns were excluded from analysis. The remaining 465 cases are represented in Fig. 3a, b. Row 3: for further analysis, we restricted the cancers to those that developed within 12 months. Cases in which cancer developed later (but within 27 months) were excluded because they did not meet the follow-up criteria to be considered negative. The remaining 408 cases are represented in Fig. 3c and Extended Data Fig. 2. Row 4: to perform localization analysis, the areas of malignancy were determined using follow-up biopsy data. In three instances, ground truth could not reliably be determined. The remaining 405 cases are represented in Extended Data Fig. 3.

Extended Data Table 4 | Potential use of the AI system in two clinical applications

a

	Sensitivity (%) (n = 414)	Specificity (%) (n = 25,422)	Simulated reduction of second reader workload (%)
AI as second reader (UK)	66.66	96.26	87.98
Existing workflow (UK)	67.39	96.24	-
95% CI on the difference	(-2.68, 1.23)	(-0.13, 0.17)	-

b

Triage status	Dataset	Sensitivity (%) (95% CI)	Specificity (%) (95% CI)	Reliability of triage decision (%) (95% CI)
Negative	UK	99.63 (98.88, 100.0) n = 274	41.15 (40.57, 41.72) n = 25,443	99.99 (NPV) (99.97, 100.0) n = 10,471
	USA	98.05 (96.12, 99.16) n = 359	34.79 (31.97, 37.60) n = 2,411	99.90 (NPV) (99.83, 99.96) n = 720
Positive	UK	41.24 (35.63, 47.08) n = 274	99.92 (99.89, 99.95) n = 25,443	85.69 (PPV) (79.66, 90.98) n = 132
	USA	29.80 (25.21, 34.45) n = 359	99.90 (99.78, 99.97) n = 2,411	82.41 (PPV) (65.38, 94.71) n = 121

a, Simulation, using the UK test set, in which the AI system is used in place of the second reader when it concurs with the first reader. In cases of disagreement (12.02%) the consensus opinion was invoked. The high performance of this combination of human and machine suggests that approximately 88% of the effort of the second reader can be eliminated while maintaining the standard of care that is produced by double reading. The decision of the AI system was generated using the first reader operating point (i) shown in Fig. 2a. Confidence intervals are Wald intervals computed with the Obuchowski correction for clustered data. **b**, Evaluation of the AI system for low-latency triage. Operating points were set to perform with high NPV and PPV for detecting cancer in 12 months.

Extended Data Table 5 | Discrepancies between the AI system and human readers

Dataset	Cancer type	AI caught, reader missed	Reader caught, AI missed
UK	*Invasive*	31	20
	In situ	7	12
	Unknown	7	2
USA	*ILC or IDC*	83	37
	DCIS	31	27
	Other	7	5

Invasive cancer grade (UK only)	AI caught, reader missed	Reader caught, AI missed
Grade 1	10	4
Grade 2	15	13
Grade 3	6	3

Invasive primary tumour size (UK only)	AI caught, reader missed	Reader caught, AI missed
< 10mm	4	6
10 – 15mm	6	7
15 – 20mm	5	2
20 – 50mm	14	4
>= 50mm	2	1

For the UK comparison, we used the first reader operating point (i) shown in Fig. 2a. For the US comparison, we used the operating point shown in Fig. 2b. ILC, invasive lobular carcinoma; IDC, invasive ductal carcinoma; DCIS, ductal carcinoma in situ.

Extended Data Table 6 | Performance breakdown

a

Cancer type (UK first reader)			AI system	Reader	Delta (95% CI)	No. examples
Sensitivity	Invasive grade	Grade 1	81.94	73.61	8.33 (-4.71, 21.38)	72
		Grade 2	63.87	62.58	1.29 (-6.60, 9.15)	155
		Grade 4	69.36	64.52	4.84 (-3.66, 13.34)	62
		Grade unknown	25	25	-	8
	In situ grade	High grade	58.97	53.85	5.13 (-14.19, 24.45)	39
		Intermediate grade	25	75	-50.00 (-100.00, 14.82)	8
		Low grade	56	64	-8.00 (-24.194, 8.19)	25
		Grade unknown	69.23	76.92	-7.69 (-35.08, 19.70)	13
	Primary tumour size (invasive only)	< 10mm	61.81	65.46	-3.64 (-14.86, 7.59)	55
		10 – 15mm	72.73	74.55	-1.82 (-14.66, 11.02)	55
		15 – 20mm	71.42	66.07	5.36 (-3.80, 14.51)	56
		20 – 50mm	67.3	57.43	9.90 (1.90, 17.90)	101
		>= 50mm	88.24	82.35	5.88 (-13.89, 25.65)	17

b

Cancer type (US clinical radiologist)		AI system	Reader	Delta (95% CI)	No. examples
Sensitivity	ILC or IDC	57.97	45.33	12.63 (6.88, 18.39)	364
	DCIS	57.05	54.6	2.45 (-6.70, 11.60)	163
	Other	53.85	46.15	7.69 (-18.25, 33.64)	26

c

Breast density (US clinical radiologist)		AI system	Reader	Delta (95% CI)	No. examples
Sensitivity	Entirely fatty	53.84	48.71	5.12 (-12.21, 22.46)	39
	Scattered fibroglandular densities	60.41	49.58	10.8 (3.39, 18.28)	240
	Heterogeneously dense	56.11	48.1	8.01 (0.93, 15.11)	237
	Extremely dense	16.67	25	-8.33 (-44.55, 27.88)	12
	Unknown	66.67	66.67	0.00 (-92.39, 92.39)	5
Adjusted specificity	Entirely fatty	90.6	82.88	7.72 (-1.24, 17.40)	6
	Scattered fibroglandular densities	86.78	80.75	6.03 (1.57, 10.42)	149
	Heterogeneously dense	85.65	80.55	5.09 (0.76, 9.74)	831
	Extremely dense	92.18	77.1	15.07 (-1.90, 33.74)	1,061
	Unknown	95.34	93.01	2.33 (-25.36, 57.62)	73
Specificity	Entirely fatty	85.23	77.85	7.38 (-0.08, 14.85)	6
	Scattered fibroglandular densities	80.75	71	9.74 (5.92, 13.57)	149
	Heterogeneously dense	80.21	67.39	12.82 (9.38, 16.26)	831
	Extremely dense	86.3	75.34	10.96 (-2.50, 24.42)	1,061
	Unknown	66.67	50	16.67 (-38.32, 71.65)	73

The analysis excludes technical recalls and US cases for which BI-RADS scores were unavailable. **a**, Sensitivity across cancer subtypes in the UK data. We used the first reader operating point (i) shown in Fig. 2a. Also shown is the performance of the first reader on the same subset. **b**, Sensitivity across cancer subtypes in the US data. We used the operating point shown in Fig. 2b. Reader performance was derived from the clinical BI-RADS scores on the same subset. ILC, invasive lobular carcinoma; IDC, invasive ductal carcinoma; DCIS, ductal carcinoma in situ. **c**, Performance across breast density categories. BI-RADS breast density was extracted from the radiology report rendered at the time of screening, which was only available in the US dataset. We used the operating point shown in Fig. 2b. Adjusted specificities were computed using inverse probability weighting (Methods).

Extended Data Table 7 | Reader experience

a

UK	
Reads per year	**No. readers**
3,000-4,000	3
4,000-5,000	6
5,000-6,000	3
6,000-7,000	1
7,000-8,000	2
8,000+	3
Unknown	33

Years of experience	No. readers
5-10	4
10-15	5
15-20	4
20+	5
Unknown	33

Job title	No. readers
Consultant Radiologist	8
Consultant Radiographer	6
Advanced Practitioner Radiographer	4
Unknown	33

b

US reader study			
	Reads per year	**Years of experience**	**Fellowship trained**
Reader 1	5,500	12	Yes
Reader 2	4,000	7	No
Reader 3	2,000	4	No
Reader 4	3,000	12	No
Reader 5	3,500	15	Yes
Reader 6	2,500	10	No

a, Detailed information was available for 18 of the 51 readers represented in UK the test set. Reads were performed as part of routine practice and so reflect the standard of care in the UK screening programme. **b**, Experience levels of the six radiologists involved in the US reader study.

nature research

Corresponding author(s): Shravya Shetty

Last updated by author(s): Oct 23, 2019

Reporting Summary

Nature Research wishes to improve the reproducibility of the work that we publish. This form provides structure for consistency and transparency in reporting. For further information on Nature Research policies, see Authors & Referees and the Editorial Policy Checklist.

Statistics

For all statistical analyses, confirm that the following items are present in the figure legend, table legend, main text, or Methods section.

n/a	Confirmed	
☐	☒	The exact sample size (n) for each experimental group/condition, given as a discrete number and unit of measurement
☐	☒	A statement on whether measurements were taken from distinct samples or whether the same sample was measured repeatedly
☐	☒	The statistical test(s) used AND whether they are one- or two-sided *Only common tests should be described solely by name; describe more complex techniques in the Methods section.*
☐	☒	A description of all covariates tested
☐	☒	A description of any assumptions or corrections, such as tests of normality and adjustment for multiple comparisons
☐	☒	A full description of the statistical parameters including central tendency (e.g. means) or other basic estimates (e.g. regression coefficient) AND variation (e.g. standard deviation) or associated estimates of uncertainty (e.g. confidence intervals)
☐	☒	For null hypothesis testing, the test statistic (e.g. F, t, r) with confidence intervals, effect sizes, degrees of freedom and P value noted *Give P values as exact values whenever suitable.*
☒	☐	For Bayesian analysis, information on the choice of priors and Markov chain Monte Carlo settings
☒	☐	For hierarchical and complex designs, identification of the appropriate level for tests and full reporting of outcomes
☒	☐	Estimates of effect sizes (e.g. Cohen's d, Pearson's r), indicating how they were calculated

Our web collection on statistics for biologists contains articles on many of the points above.

Software and code

Policy information about availability of computer code

Data collection	Dicom files were handled with the open source libraries DCMTK (https://support.dcmtk.org/docs/, version 3.6.1_20160630) and Pydicom (https://pydicom.github.io/, version v1.2.0).
Data analysis	The code used for training deep learning models has a large number of dependencies on internal tooling, infrastructure and hardware, and its release is therefore not feasible. However, all experiments and implementation details are described in sufficient detail in the Methods section to allow independent replication with non-proprietary libraries. Several major components of our work are available in open source repositories including Tensorflow (https://www.tensorflow.org, version 1.14.0) and the Tensorflow Object Detection API (https://github.com/tensorflow/models/tree/master/research/object_detection; Oct 15th, 2019 release). Data analysis was conducted in Python using the numpy (version v1.16.4), scipy (version 1.2.1), and scikit-learn (version 0.20.4) packages.

For manuscripts utilizing custom algorithms or software that are central to the research but not yet described in published literature, software must be made available to editors/reviewers. We strongly encourage code deposition in a community repository (e.g. GitHub). See the Nature Research guidelines for submitting code & software for further information.

Data

Policy information about availability of data

All manuscripts must include a data availability statement. This statement should provide the following information, where applicable:
- Accession codes, unique identifiers, or web links for publicly available datasets
- A list of figures that have associated raw data
- A description of any restrictions on data availability

The dataset from Northwestern Medicine was used under license for the current study, and is not publicly available. Applications for access to the OPTIMAM database can be made at https://medphys.royalsurrey.nhs.uk/omidb/getting-access/.

Field-specific reporting

Please select the one below that is the best fit for your research. If you are not sure, read the appropriate sections before making your selection.

☒ Life sciences ☐ Behavioural & social sciences ☐ Ecological, evolutionary & environmental sciences

For a reference copy of the document with all sections, see nature.com/documents/nr-reporting-summary-flat.pdf

Life sciences study design

All studies must disclose on these points even when the disclosure is negative.

Sample size

The UK test set is a random sample of 10% of all women screened at two sites, St. George's and Jarvis, between the years 2012 and 2015. Women from the US cohort were split randomly between train (55%), validation (15%) and test (30%). This scheme follows machine learning convention, but errs on the side of a larger test set to power statistical comparisons and include a more representative population.

The size of the reader study was selected due to time and budgetary constraints. The case list was composed of 250 negative exams, 125 biopsy-confirmed negative exams and 125 biopsy-confirmed positive exams. We sought to include sufficient positives to power statistical comparisons on the metric of sensitivity, while avoiding undue enrichment of the case mixture. Biopsy-confirmed negatives were included to make the malignancy discrimination task more difficult.

Data exclusions

UK Dataset

The data was initially compiled by OPTIMAM, a Cancer Research UK effort, between the years of 2010 and 2018 from St. George's Hospital (London, UK), Jarvis Breast Centre (Guildford, UK) and Addenbrooke's Hospital (Cambridge, UK). The mammograms and associated metadata of 137,291 women were considered for inclusion in the study. Of these, 123,964 had both screening images and uncorrupted metadata. Exams that were recalled for reasons other than radiographic evidence of malignancy, or episodes that were not part of routine screening were excluded. In total, 121,850 women had at least one eligible exam. Women who were aged below 47 at the time of the screen were excluded from validation and test sets, leaving 121,455 women. Finally, women for whom there was no exam with sufficient follow-up were excluded from validation and test. This last step resulted in the exclusion of 5,990 of 31,766 test set cases (19%).

The test set is a random sample of 10% of all women screened at two sites, St. George's and Jarvis, between the years 2012 and 2015. Insufficient data was provided to apply the sampling procedure to the third site. In assembling the test set, we randomly selected a single eligible screening mammogram from each woman's record. For women with a positive biopsy, eligible mammograms were those conducted in the 39 months (3 years and 3 months) prior to the biopsy date. For women that never had a positive biopsy, eligible mammograms were those with a non-suspicious mammogram at least 21 months later. The final test set consisted of 25,856 women.
The US dataset included records from all women that underwent a breast biopsy between 2001 and 2018. It also included a random sample of approximately 5% of all women who participated in screening, but were never biopsied. This heuristic was employed in order to capture all cancer cases (to enhance statistical power) and to curate a rich set of benign findings on which to train and test the AI system.

US Dataset

Among women with a completed mammogram order, we collected the records from all women with a pathology report containing the term "breast". Among those that lacked such a pathology report, women whose records bore an International Classification of Diseases (ICD) code indicative of breast cancer were excluded. Approximately 5% of this population of unbiopsied negative women were sampled. After de-identification and transfer, women were excluded if their metadata was either unavailable or corrupted. The women in the dataset were split randomly among train (55%), validation (15%) and test (30%). For testing, a single case was chosen for each woman following a similar procedure as in the UK dataset. In women who underwent biopsy, we randomly chose a case from the 27 months preceding the date of biopsy. For women who did not undergo biopsy, one screening mammogram was randomly chosen from among those with a follow up event at least 21 months later.

The radiology reports associated with cases in the test set were used to flag and exclude cases in the test set which depicted breast implants or were recalled for technical reasons. To compare the AI system against the clinical reads performed at this site, we employed clinicians to manually extract BI-RADS scores from the original radiology reports. There were some cases for which the original radiology report could not be located, even if a subsequent cancer diagnosis was biopsy-confirmed. This might have happened, for example, if the screening case was imported from an outside institution. Such cases were excluded from the clinical reader comparison.

Replication

All attempts at replication were successful. Comparisons between AI system and human performance revealed consistent trends across three settings: a UK clinical environment, a US clinical environment, and an independent, laboratory-based reader study. Our findings persisted through numerous retrainings with random network initialization and training data iteration order. Remarkably, our findings on the US test set replicated even when we trained the AI system solely on UK data.

Randomization

Patients were randomized into training, validation, and test sets by applying a hash function to the deidentified medical record number. Assignment to each set was made based on the value of the resulting integer modulo 100. For the UK data, values of 0-9 were reserved for the test set. For the US data, values of 0-29 were reserved for the test set.

Blinding

The US and UK test sets were held back from AI system development, which only took place on the training and validation sets. Investigators did not access test set data until models, hyperparameters, and thresholds were finalized. None of the readers who interpreted the images (either in the course of clinical practice or in the context of the reader study) had knowledge of any aspect of the AI system.

Reporting for specific materials, systems and methods

We require information from authors about some types of materials, experimental systems and methods used in many studies. Here, indicate whether each material, system or method listed is relevant to your study. If you are not sure if a list item applies to your research, read the appropriate section before selecting a response.

Materials & experimental systems

n/a	Involved in the study
☒	☐ Antibodies
☒	☐ Eukaryotic cell lines
☒	☐ Palaeontology
☒	☐ Animals and other organisms
☐	☒ Human research participants
☒	☐ Clinical data

Methods

n/a	Involved in the study
☒	☐ ChIP-seq
☒	☐ Flow cytometry
☒	☐ MRI-based neuroimaging

Human research participants

Policy information about studies involving human research participants

Population characteristics

The focus of the paper is on breast cancer screening, so all individuals in the population were women from the screening populations in the US and UK.

The UK dataset was collected from three breast screening sites in the United Kingdom National Health Service Breast Screening Programme (NHSBSP). The NHSBSP invites women aged between 50 and 70 who are registered with a general practitioner (GP) for mammographic screening every 3 years. Women who are not registered with a GP, or who are older than 70, can self-refer to the screening programme. Specifically, there were 25,856 women in the test set, of which 268 (1%) had breast cancer detected during screening. For many cancers in the test set, additional metadata was available. There was a rich collection of both invasive (76.1%) and non-invasive cancers (21.6%). The invasiveness of 2.2% of cancers was unknown. These cancers had a lesion size of less than 10mm to lesions greater than 50mm.

The US dataset was collected from Northwestern Memorial Hospital (Chicago, IL) between the years of 2001 and 2018. In the US, each screening mammogram is typically read by a single radiologist, and screens are conducted annually or biannually. The breast radiologists at this hospital are fellowship-trained and only interpret breast imaging studies. Their experience levels ranged from 1-30 years. The American College of Radiology (ACR) recommends that women start routine screening at the age of 40, while other organizations including the US Preventive Services Task Force (USPSTF) recommend initiation at 50 for women with average breast cancer risk. For all the cancers in the test set, additional metadata was available. For example, 66.9% of the cancers were invasive, 27.9% were DCIS and the rest were of an other cancer subtype.

Recruitment

Patient data were gathered retrospectively from screening practices in the UK and US. As such, they reflect natural screening populations at the sites under study. Self-selection biases associated with the choice to enroll in screening may be present, but are likely to be representative of the real-world patient population.

In the UK, the NHSBSP invites women aged between 50 and 70 who are registered with a general practitioner (GP) for mammographic screening every 3 years. Women who are not registered with a GP, or who are older than 70, can self-refer to the screening programme. Specifically, for this paper, the data was initially compiled by OPTIMAM, a Cancer Research UK effort, from three between the years of 2010 and 2018: St. George's Hospital (London, UK), Jarvis Breast Centre (Guildford, UK) and Addenbrooke's Hospital (Cambridge, UK). The collected data included screening and follow-up mammograms (comprising mediolateral oblique "MLO" and craniocaudal "CC" views of the left and right breast), all radiologist opinions (including the arbitration result, if applicable) and metadata associated with follow-up treatment. The test set is a random sample of 10% of all women screened at two sites, St. George's and Jarvis, between the years 2012 and 2015. Insufficient data was provided to apply the sampling procedure to the third site.

In the US, the American College of Radiology, the American Cancer Society, and the US Preventive Services Task Force recommends screening every 1 or 2 years for women starting at age 40 or 50. The various US guidelines are summarized at https://www.acraccreditation.org/mammography-saves-lives/guidelines. Our US dataset was collected from Northwestern Memorial Hospital (Chicago, IL) between the years of 2001 and 2018. The US dataset included records from all women that underwent a breast biopsy between 2001 and 2018. It also included a random sample of approximately 5% of all women who participated in screening, but were never biopsied. This heuristic was employed in order to capture all cancer cases (to enhance statistical power) and to curate a rich set of benign findings on which to train and test the AI system.

Ethics oversight

Use of the UK dataset for research collaborations by both commercial and non-commercial organisations received ethical approval (Research Ethics Committee reference 14/SC/0258).

The US data was fully de-identified and released only after an Institutional Review Board approval (STU00206925).

Note that full information on the approval of the study protocol must also be provided in the manuscript.

Prevention of tuberculosis in macaques after intravenous BCG immunization

https://doi.org/10.1038/s41586-019-1817-8

Received: 11 June 2019

Accepted: 11 November 2019

Published online: 1 January 2020

Open access

Patricia A. Darrah[1], Joseph J. Zeppa[2], Pauline Maiello[2], Joshua A. Hackney[1], Marc H. Wadsworth II[3,4,5], Travis K. Hughes[3,4,5], Supriya Pokkali[1], Phillip A. Swanson II[1], Nicole L. Grant[6], Mark A. Rodgers[2], Megha Kamath[1], Chelsea M. Causgrove[2], Dominick J. Laddy[7], Aurelio Bonavia[7], Danilo Casimiro[7], Philana Ling Lin[8], Edwin Klein[9], Alexander G. White[2], Charles A. Scanga[2], Alex K. Shalek[3,4,5,10], Mario Roederer[1,11], JoAnne L. Flynn[2,11] & Robert A. Seder[1,11]*

Mycobacterium tuberculosis (Mtb) is the leading cause of death from infection worldwide[1]. The only available vaccine, BCG (Bacillus Calmette–Guérin), is given intradermally and has variable efficacy against pulmonary tuberculosis, the major cause of mortality and disease transmission[1,2]. Here we show that intravenous administration of BCG profoundly alters the protective outcome of Mtb challenge in non-human primates (*Macaca mulatta*). Compared with intradermal or aerosol delivery, intravenous immunization induced substantially more antigen-responsive CD4 and CD8 T cell responses in blood, spleen, bronchoalveolar lavage and lung lymph nodes. Moreover, intravenous immunization induced a high frequency of antigen-responsive T cells across all lung parenchymal tissues. Six months after BCG vaccination, macaques were challenged with virulent Mtb. Notably, nine out of ten macaques that received intravenous BCG vaccination were highly protected, with six macaques showing no detectable levels of infection, as determined by positron emission tomography–computed tomography imaging, mycobacterial growth, pathology and granuloma formation. The finding that intravenous BCG prevents or substantially limits Mtb infection in highly susceptible rhesus macaques has important implications for vaccine delivery and clinical development, and provides a model for defining immune correlates and mechanisms of vaccine-elicited protection against tuberculosis.

Two billion people worldwide are infected with Mtb, with 10 million new cases of active tuberculosis (TB) and 1.7 million deaths each year[1]. Prevention of pulmonary infection or disease in adolescents and adults would have the largest effect on the epidemic by controlling Mtb transmission[3]. The only licensed TB vaccine, BCG (live, attenuated *Mycobacterium bovis*), is administered intradermally at birth and provides protection against disseminated TB in infants but has variable efficacy against pulmonary disease in adolescents and adults[2].

T cell immunity is required to control Mtb infection and prevent clinical disease[4]. A major hurdle to developing an effective and durable T-cell-based vaccine against pulmonary TB is to induce and sustain T cell responses in the lung to immediately control infection while also eliciting a reservoir of systemic memory cells to replenish the lung tissue. Intradermal and intramuscular administration—the most common routes of vaccine administration—do not induce high frequencies of resident memory T (T_{RM}) cells in the lung. Studies performed 50 years ago suggested that administration of BCG by aerosol (AE) or intravenous (IV) routes enhanced protection in non-human primates (NHPs) challenged shortly after immunization[5–8]. However, there remains a limited understanding for mechanisms by which dose and route of BCG influence systemic and tissue-specific T cell immunity, and whether optimizing these variables would lead to high-level prevention of Mtb infection and disease. We hypothesized that a sufficiently high dose of IV BCG would elicit a high frequency of systemic and tissue resident T cells mediating durable protection against Mtb infection and disease in highly susceptible rhesus macaques.

Experimental design and safety

The central aim of this study was to assess how the route and dose of BCG vaccination influence systemic and tissue-resident T cell immunity, and protection after Mtb challenge. Rhesus macaques were vaccinated with 5×10^7 colony-forming units (CFUs) of BCG by intradermal (ID_{high}), AE or IV routes, or with a combination of both AE (5×10^7 CFUs) and ID

[1]Vaccine Research Center, National Institute of Allergy and Infectious Diseases (NIAID), National Institutes of Health (NIH), Bethesda, MD, USA. [2]Department of Microbiology and Molecular Genetics and Center for Vaccine Research, University of Pittsburgh School of Medicine, Pittsburgh, PA, USA. [3]Ragon Institute of MGH, Harvard, and MIT, Cambridge, MA, USA. [4]Department of Chemistry, Institute for Medical Engineering and Sciences (IMES), MIT, Cambridge, MA, USA. [5]Broad Institute of MIT and Harvard, Cambridge, MA, USA. [6]Department of Infectious Diseases and Microbiology, University of Pittsburgh School of Public Health, Pittsburgh, PA, USA. [7]Aeras, Rockville, MD, USA. [8]Department of Pediatrics, Children's Hospital of the University of Pittsburgh of UPMC, Pittsburgh, PA, USA. [9]Division of Animal Laboratory Resources, University of Pittsburgh School of Medicine, Pittsburgh, PA, USA. [10]Koch Institute for Integrative Cancer Research, MIT, Cambridge, MA, USA. [11]These authors contributed equally: Mario Roederer, JoAnne L. Flynn, Robert A. Seder. *e-mail: rseder@mail.nih.gov

(5×10^5 CFUs; AE/ID) (Extended Data Fig. 1a). Immune responses and protective efficacy of these regimens were compared to the standard human dose given ID (5×10^5 CFUs; ID_{low}). The dose of BCG selected for AE and IV vaccine groups was based on pilot dose-ranging studies (Supplementary Data 1). After BCG vaccination, immune responses in blood and bronchoalveolar lavage (BAL) were assessed over 24 weeks, after which NHPs were challenged with a low dose of Mtb (Extended Data Fig. 1b). Other macaques in each group were euthanized 1 or 6 months after vaccination for immune analysis of tissue responses (Extended Data Fig. 1c). To assess safety of BCG vaccinations, several clinical parameters were measured and found to be transiently affected by only IV BCG (Extended Data Fig. 2). A summary of all NHPs in this study and doses of BCG and Mtb administered are provided in Extended Data Fig. 1c and Supplementary Table 1.

Cellular composition of BAL and blood

Because generating immune responses in the lung was a major focus of the study, we first assessed whether the BCG vaccination regimen altered the number or composition of leukocytes in the BAL. Only IV BCG vaccination elicited significant changes in BAL cell numbers: a 5–10-fold increase in total cells, accounted for largely by conventional T cells (Fig. 1a and Supplementary Data 2a, b). This resulted in a sustained inversion of the alveolar macrophage:T-cell ratio up to 6 months after IV BCG vaccination (Extended Data Fig. 3a). Non-classical T cells (MAIT and $V\gamma9^+$ $\gamma\delta$) that can contribute to protection against TB[9–11] were transiently increased 2–4 weeks after IV BCG (Fig. 1a, Extended Data Fig. 3b and Supplementary Data 2b). A similar analysis performed on peripheral blood mononuclear cells (PBMCs) showed no significant changes in leukocyte composition (Extended Data Fig. 3c, d). Neither BAL nor PBMCs exhibited changes in the proportion of natural killer cells, which were recently suggested to correlate with protection[12,13] (Extended Data Fig. 3a, c). Finally, there were no increases in cytokines associated with trained innate immunity[14,15] in stimulated PBMCs after ID or IV BCG immunization (Supplementary Data 3). Overall, these data show that IV BCG immunization, in contrast to AE or ID, results in significant and sustained recruitment of T cells to the airways and substantially alters the ratio of T cells to macrophages.

Antigen-responsive adaptive immunity

We next evaluated how these regimens influenced the ability of T cells responsive to mycobacterial antigen (such as purified protein derivative (PPD)) to produce the canonical cytokines (IFNγ, IL-2, TNF or IL-17) that are important for protection against TB[4,16,17]. At the peak of the PBMC response (week 4), cytokine-producing CD4 T cells were higher in NHPs immunized with ID_{high} or IV BCG compared with those immunized with ID_{low} BCG; these responses declined over time but remained increased at week 24 (time of challenge; Fig. 1b and Extended Data Fig. 4a, g). PBMC CD8 responses in IV-immunized NHPs were greater than ID_{low} NHPs at both time points (Fig. 1c and Extended Data Fig. 4b, h). In BAL, antigen-responsive T cells peaked at 8 weeks and were largely maintained until time of challenge (Fig. 1d, e and Extended Data Fig. 4c, d). Compared with ID_{low} BCG, ID_{high} or AE BCG immunization elicited tenfold more PPD-responding CD4 T cells in BAL; IV BCG elicited 100-fold more PPD-responsive CD4 T cells, with approximately 40% of cells responding (Fig. 1d). Furthermore, only IV BCG induced an increase in antigen-responsive CD8 T cells (Fig. 1e). Central memory and transitional memory (T_{TM}) T cells[18] comprised the majority of CD4 T cell responses in PBMCs across all vaccine groups at the peak of the response, whereas T_{TM} cells predominated in the BAL (Extended Data Fig. 4e, f). IV-BCG-vaccinated NHPs had the largest proportion of T_{TM} cells in PBMCs and effector memory (T_{EM}) cells in BAL.

Despite differences in the magnitude of T cell responses among vaccine regimens, there were no differences in the quality of T cell responses (that is, the proportion of cells producing each combination of IFNγ, IL-2, TNF and IL-17)[19,20] in PBMCs (Extended Data Fig. 5a and Supplementary Data 4) or the BAL (Extended Data Fig. 5b and Supplementary Data 5). Of the CD4 T cell responses, 90% consisted of T helper 1 (T_H1) cytokines, with fewer than 10% also producing IL-17; most IL-17-producing CD4 T cells co-expressed T_H1 cytokines (Extended Data Fig. 5). Notably, approximately 10% of antigen-responsive CD4 T cells in PBMCs expressed CD154[21] but no T_H1 or T_H17 cytokines (Extended Data Fig. 5a and Supplementary Data 4), which suggests that there may be underlying qualitative differences among vaccine group responses that are not measured by the canonical T cell cytokines commonly used to assess BCG-elicited immunity[22,23].

To expand the qualitative analysis of BAL T cell responses using an orthogonal approach, we performed single-cell mRNA sequencing (scRNA-seq) with Seq-Well[24] to comprehensively assess phenotypic and transcriptional states among T cells that might underlie protective vaccine responses (Fig. 1f–h, Extended Data Fig. 6 and Supplementary Data 6). We examined correlated patterns of gene expression within unstimulated and PPD-stimulated T cells from BAL to identify groups of genes for which the coordinated activity differed by regimen (Extended Data Fig. 6b). A total of seven significant T cell modules were identified among in vitro-stimulated T cells 13 weeks after immunization (Supplementary Table 2) and used to generate expression scores across all T cells at weeks 13 and 25. Among these, we identified a stimulation-inducible module of gene expression, module 2, enriched for memory T cell functionality (Supplementary Table 3 and Methods), primarily expressed in a population of BAL CD4 T cells from IV-BCG-immunized NHPs at week 13, and maintained until week 25 (Fig. 1f, g, Extended Data Fig. 6c, d and Supplementary Table 2). Differential gene expression analysis, comparing T cells positive and negative for module 2 (Fig. 1h and Supplementary Table 4), showed enrichment of genes previously associated with protection against TB including *IFNG*, *TBX21*, *RORC*, *TNFSF8*[25] and *IL21R*[26].

To further analyse adaptive immunity, we found that IV BCG elicited higher antibody responses in the BAL and plasma than the other routes. Mtb-specific IgG, IgA and IgM peaked 4 weeks after IV BCG vaccination and returned to baseline by 24 weeks in the BAL (Extended Data Fig. 7).

M. tuberculosis challenge outcome

Six months after BCG immunization, NHPs were challenged in three separate cohorts with a nominal dose of 10 CFUs of the highly pathogenic Mtb Erdman strain, with a pre-defined study end point of 12 weeks after challenge (Extended Data Fig. 1b, c and Supplementary Table 1). Infection and disease were tracked serially using ^{18}F-fluorodeoxyglucose (FDG) positron emission tomography–computed tomography (PET–CT) imaging. Total FDG activity in lungs, a measure of cellular metabolism that correlates with total thoracic mycobacterial burden[27,28], was negative in all immunized macaques before Mtb challenge, but was increased throughout infection in unvaccinated NHPs (Fig. 2a). Three-dimensional reconstructions of pre-necropsy PET–CT scans are shown in Fig. 2b. All ID_{low}- and AE-BCG-immunized NHPs had increased FDG activity in lungs over 12 weeks. Two NHPs in the ID_{high} and AE/ID BCG groups had no lung FDG activity and two NHPs in the ID_{high} group had inflammation at 8 weeks that returned to baseline by 12 weeks, suggesting partial protection. By contrast, nine out of ten IV-BCG-immunized NHPs had no lung FDG activity throughout the challenge phase (Fisher's exact test, $P < 10^{-4}$ compared to ID_{low} BCG) (Fig. 2a–c).

PET–CT was used to track granuloma formation after Mtb infection as a correlate of active disease[27]. By 4 weeks and throughout infection, granulomas were detected in all unvaccinated as well as ID_{low}-, ID_{high}-, AE- and AE/ID-BCG-immunized NHPs (Fig. 2a). By contrast, IV-BCG-immunized NHPs had fewer granulomas compared with the benchmark ID_{low} BCG regimen ($P < 0.001$), with six out of ten NHPs having no granulomas throughout infection (Fig. 2a, d). Detailed necropsies

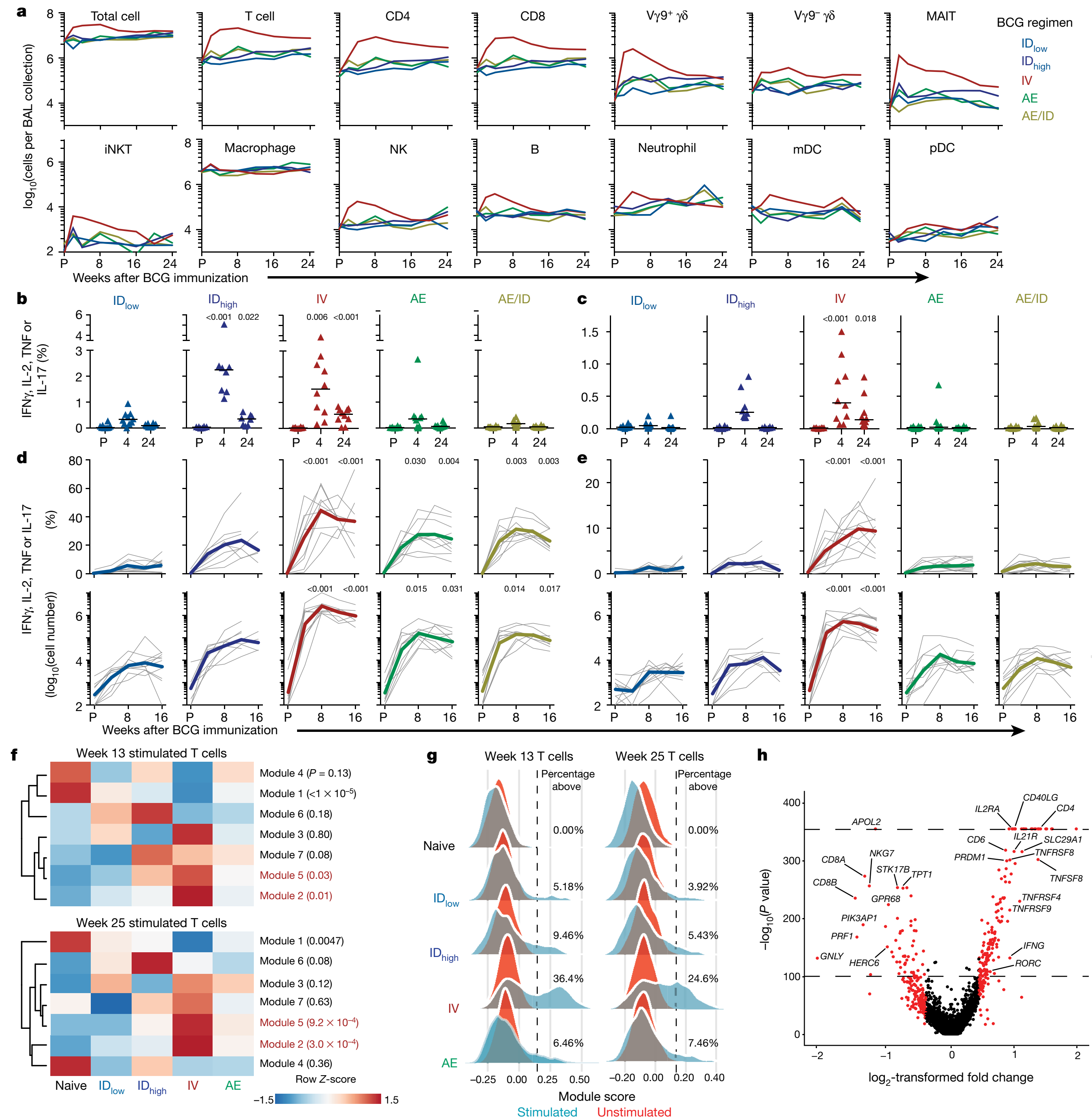

Fig. 1 | Cellular composition and immune analysis in blood and BAL after BCG vaccination. **a**, Number of cells (geometric mean) per BAL collection for leukocyte populations in each vaccine group before (pre, P) and up to 24 weeks after BCG; Supplementary Data 2 shows individual NHPs and statistical comparisons. Data are from cohorts 1–4 ($n = 11$–13 macaques per group as outlined in Extended Data Fig. 1) except at weeks 2, 20 and 24 (cohort 4 only, $n = 3$). Vγ9$^{+/-}$, Vγ9$^{+/-}$ γδ T cells; MAIT, mucosal-associated invariant T cells; mDC, myeloid dendritic cells; NK, natural killer cells; iNKT, invariant natural killer cells; pDC, plasmacytoid dendritic cells. **b**, **c**, Percentage of memory CD4 (**b**) or CD8 (**c**) T cells in PBMCs producing IFNγ, IL-2, TNF or IL-17 after PPD stimulation in vitro. Shown are individual and median (horizontal bar) responses for NHPs in challenge study (cohorts 1–3, $n = 8$–10 macaques) at weeks 4 (peak) and 24 (time of challenge) after BCG vaccination. **d**, **e**, Percentage (top) and number (bottom) of cytokine$^+$ memory CD4 (**d**) and CD8 (**e**) T cells in the BAL before and up to 16 weeks after BCG vaccination. Shown are individual (grey lines) and mean (coloured lines) responses for challenge cohorts ($n = 8$–10 macaques). Each group was compared to ID_{low} at weeks 4 and 24 for PBMCs (one-way ANOVA; P values are Dunnett's multiple comparison test) or weeks 8 and 16 for BAL (Kruskal–Wallis test; P values are Dunn's multiple comparison test). **f**–**h**, Single-cell transcriptional analysis of BAL cells at weeks 13 and 25 after BCG vaccination (cohort 4; $n = 3$ per group). **f**, Z-scored heat maps of the average cellular score for modules identified in week 13 PPD-stimulated T cells at weeks 13 and 25 after BCG vaccination. Red P values indicate modules uniquely elevated in the IV BCG group (one-way ANOVA). **g**, Distributions of module 2 expression in unstimulated and stimulated T cells at weeks 13 and 25 for each group. Percentage module 2-positive is shown; positivity (dashed line) defined as 2 s.d. above the mean score of the unvaccinated (Naive) NHPs. **h**, Volcano plot showing differentially expressed genes between T cells positive and negative for module 2 at week 13 (P values calculated using the likelihood ratio test with Bonferroni correction).

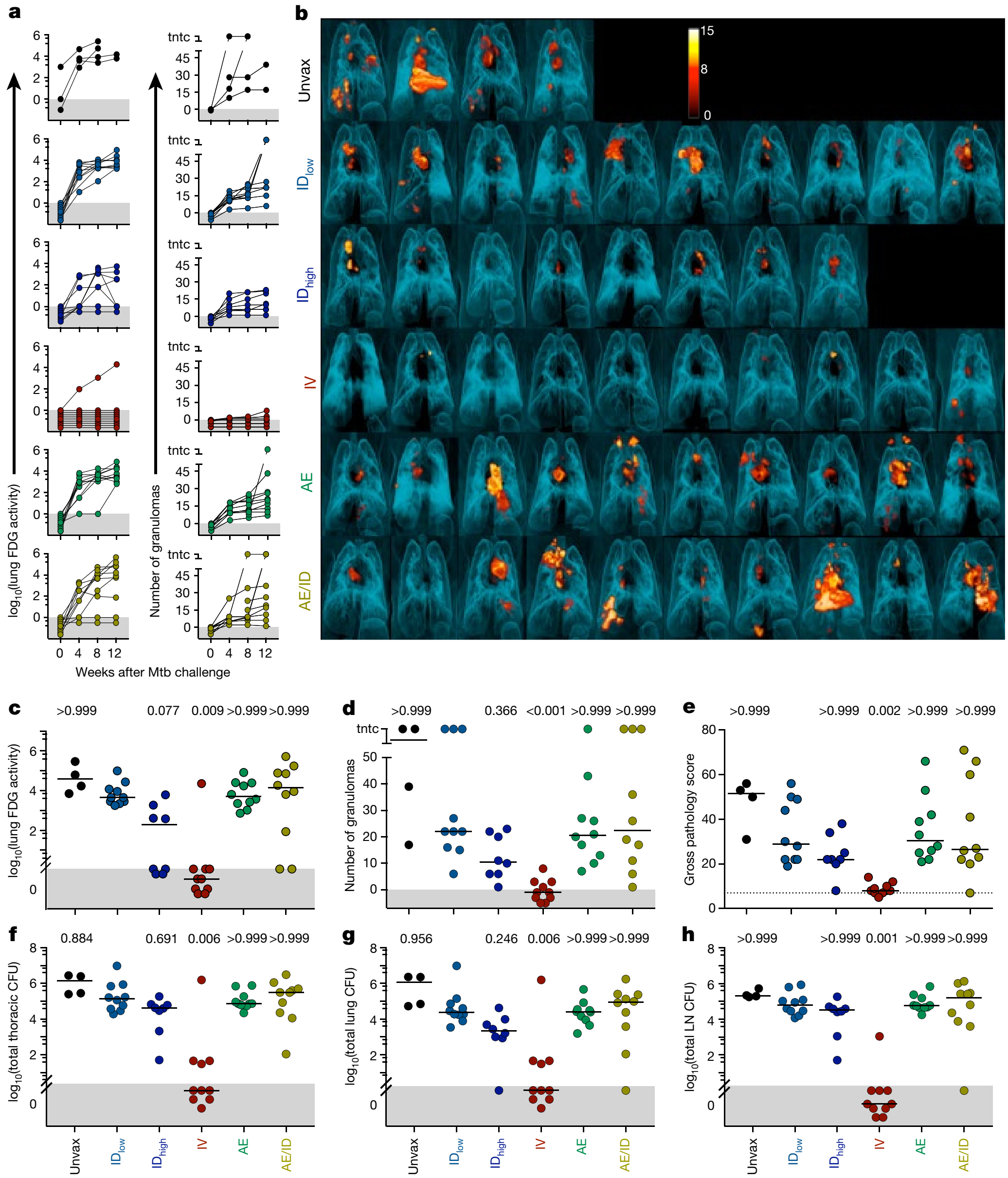

Fig. 2 | Protection against Mtb infection after IV BCG immunization. a, Lung inflammation (total FDG activity) and number of lung granulomas over the course of infection as measured by serial PET–CT scans. Each line shows one NHP over time; 3 NHPs (2 unvaccinated (unvax) and 1 ID_{low}) reached a humane end point before 12 weeks. tntc, too numerous to count. **b**, Three-dimensional volume renderings of PET–CT scans of each NHP at the time of necropsy. PET was limited to the thoracic cavity; the standardized uptake value colour bar is shown in the top right and indicates FDG retention, a surrogate for inflammation. **c**–**h**, Total lung FDG activity (**c**), number of lung granulomas (**d**), gross pathology score (**e**), total thoracic CFUs (mycobacterial burden) (**f**), total lung CFUs (**g**) and total thoracic LN CFUs (**h**) at time of necropsy. Dashed line in **e** is assumed normal pathology score accounting for variability in LN size in healthy rhesus macaques. **c**–**h**, Symbols represent individual challenged macaques (cohorts 1–3, $n = 8$–10 vaccinated NHPs; $n = 4$ unvaccinated NHPs) and horizontal bars represent the median; all data points within the grey areas are zero. Kruskal–Wallis tests were used and reported P values represent Dunn's multiple comparison test comparing each group to the ID_{low} group.

showed that the IV-BCG-immunized group had lower gross pathology scores[27] (Fig. 2e) compared with the ID_{low} BCG group ($P = 0.002$) and was the only group without detectable extrapulmonary disease (Extended Data Fig. 8a).

The primary measure of protection was a comprehensive quantification of Mtb burden (CFUs) at necropsy. The median total thoracic CFUs for ID_{low} BCG (5.1 ± 1.3, median ± interquartile range of $\log_{10}$-transformed total CFUs) was slightly lower than that of unvaccinated NHPs (5.9 ± 1.0 $\log_{10}$-transformed CFUs), consistent with ID_{low} BCG having a minimal protective effect in rhesus macaques (Fig. 2f). By contrast, the median total thoracic CFUs in IV-BCG-immunized NHPs was 0 (±16 CFUs)—a more than 100,000-fold reduction compared with ID_{low} BCG ($P = 0.006$). Six out of ten IV-BCG-immunized macaques had no detectable Mtb in any tissue measured, and another three macaques had ≤45 total CFUs, all contained within one granuloma. Only one of ten IV BCG NHPs was not protected, with CFU values similar to ID_{low} NHPs (Fig. 2f). The ID_{high}, AE and AE/ID groups had bacterial burdens similar to ID_{low} BCG.

Total thoracic bacterial burden can be separated into lung (Fig. 2g) and thoracic lymph node (LN) (Fig. 2h) CFUs. Only the IV BCG group was lower than the ID_{low} BCG group (lung, $P = 0.006$; LNs, $P = 0.001$), with nine of ten NHPs having no Mtb-positive LNs (Fig. 2h).

Protection can be defined as having less than a given number of total thoracic Mtb CFUs. By this criterion, protection was highly significant

(Fisher's exact test, $P < 10^{-4}$) at any given threshold less than 10,000 CFUs (Extended Data Fig. 8b), with the IV BCG group showing 90% protection (95% confidence interval: 60–98%) at a threshold as low as 50 CFUs. Thus, BCG IV confers an unprecedented degree of protection in a stringent NHP model of TB.

Immune responses after Mtb challenge

Measuring immune responses after challenge informs whether vaccine-elicited responses are boosted (anamnestic), and if de novo (primary) responses are generated to antigens expressed by the challenge microorganism (but not the vaccine). T cell responses to ESAT-6 and CFP-10—proteins expressed in Mtb but not BCG—are used to detect primary Mtb infection, even in BCG-immunized individuals. Peripheral T cell and antibody responses to these Mtb-specific antigens and those expressed by both BCG and Mtb (for example, PPD), were assessed after Mtb challenge (Extended Data Fig. 9). In contrast to all other groups, IV-BCG-immunized NHPs had low to undetectable primary or anamnestic T cell and antibody responses after TB infection, which suggests rapid elimination of Mtb after challenge.

BCG and immune responses in tissues

To provide insight into the potential mechanisms of IV-BCG-induced protection, we quantified BCG CFUs and T cell responses in tissues 1 month after vaccination. BCG was detected at the skin site(s) of injection and draining axillary LNs in ID-BCG-vaccinated NHPs, but not in lung lobes (Fig. 3a). In AE- or AE/ID-BCG-vaccinated NHPs, BCG was detected primarily in lung lobes and BAL. By contrast, BCG was detected in the spleen of all four IV-BCG-vaccinated NHPs, as well as in BAL, lung lobe, and peripheral and lung LNs (Fig. 3a). Indeed, PET–CT scans at 2 and 4 weeks after BCG vaccination showed increased metabolism localized to lung LNs, lung lobes and spleen elicited by the IV but not by other routes (Extended Data Fig. 10a).

CD4 T cell responses in IV-BCG-immunized NHPs were increased in spleen and lung compared to ID_{low} NHPs (Fig. 3b), consistent with detection of BCG at the same sites. Moreover, CD4 T cell responses were observed in systemic sites such as PBMCs, bone marrow and peripheral LNs. CD8 responses were highest in lung lobes, BAL and spleen after IV BCG (Fig. 3c). After ID_{high} BCG vaccination, CD4 T cell responses were detected in spleen, bone marrow and axillary LNs, but were limited in lung lobes and lung LNs, whereas responses in AE groups were confined to the lung and BAL. Collectively, these data indicate compartmentalization of BCG detection and T cell immunity by vaccine route, which highlights the systemic distribution of immune responses after IV BCG versus the more limited and localized responses following ID and AE delivery.

Further analysis of lung tissue one month after vaccination showed increased cell counts (Fig. 3d) after IV BCG with increased numbers of $CD3^+$ T cells and $CD11c^+$ antigen-presenting cells (Fig. 3e). These clustered into 'microgranulomas' that were histologically distinct from bronchus-associated lymphoid tissue (BALT) (Fig. 3f). IV-BCG-vaccinated macaques had transient splenomegaly as well as enlarged thoracic LNs that contained non-necrotizing granulomas and lymphoid follicular hyperplasia, often with active germinal centres (Extended Data Fig. 10b–e).

Six months after BCG vaccination (time of challenge), NHPs that received IV BCG maintained increased frequencies of antigen-responsive T cells in spleen, lung and BAL (Extended Data Fig. 11a, b). Notably, the numbers of total, $CD3^+$ or $CD11c^+$ cells in lung tissue had normalized, and lung histopathology, spleen size and FDG uptake in IV-BCG-vaccinated macaques were indistinguishable from ID_{low} BCG macaques (Extended Data Fig. 11c–g). Although BCG burden was not measured in these NHPs, no BCG (or Mtb) CFUs were detected in six out of ten IV-BCG-immunized, challenged macaques at 9 months after BCG. Collectively, these data suggest that BCG is cleared between 1 and 9 months after IV vaccination.

T cells in lung tissue after BCG

To substantiate whether T cells isolated from lung lobes one month after IV BCG were T_{RM} cells, labelled anti-CD45 antibody was injected IV into NHPs just before necropsy—a technique shown to delineate tissue-derived (ivCD45$^-$) from vasculature-derived (ivCD45$^+$) leukocytes[29,30]. Ex vivo phenotypic analysis of CD69 expression (a marker of T_{RM} and/or T cell activation) in combination with ivCD45 staining revealed that more than 80% of CD4 T cells isolated from all lung lobes of IV-BCG-immunized NHPs were derived from the lung parenchyma (CD69$^+$ivCD45$^-$) (Fig. 4a). Of note, more than 1,000 BCG CFUs were cultured from every lung lobe in this macaque. By contrast, ID_{high} and AE BCG vaccination resulted in 16–35% tissue-derived (CD69$^+$ivCD45$^-$) CD4 T cells in the lung lobes, with few or undetectable BCG CFUs. T cells from BAL in all NHPs were uniformly CD69$^+$ivCD45$^-$. Similar results were observed in the CD8 T cell compartment of the same macaques (Supplementary Data 7).

After in vitro antigen stimulation to assess antigen-responsive T cells in tissue, lung tissue-derived (ivCD45$^-$) IFNγ-producing CD4 T cells were observed in all lung lobes and lung LNs of IV-BCG-immunized NHPs (Fig. 4b and Extended Data Fig. 12). Antigen-responsive lung T cells were largely CD69$^+$ with a subset also expressing the tissue-homing marker CD103, which is expressed on some T_{RM} cells[31] (Fig. 4c). Thus, these cells may represent bona fide T_{RM} cells, or recently activated T cells owing to the presence of BCG (Fig. 4a). Overall, these data show that IV BCG vaccination provided the highest level of protection concomitant with increased antigen-responsive T cells throughout lung tissue.

The increased detection of T cell responses in tissues containing BCG suggests that alternative approaches to lung vaccine delivery may be crucial for generating T_{RM} cells. Indeed, direct endobronchial instillation of BCG into a single lung lobe protected two out of eight NHPs against Mtb challenge in the same lobe[32]. To determine how endobronchial BCG would affect T cells in the lung parenchyma, BCG was instilled directly into the left lung lobes of NHPs. Approximately 75% of CD4 and CD8 T cells isolated from the two left lung lobes were CD69$^+$ivCD45$^-$, compared with 7–45% in the right lobes (Fig. 4a and Supplementary Data 7a). Notably, BCG CFUs ($>10^4$) were detected in the left (but not right) lung lobes where the CD4 T cell response was highest (Extended Data Fig. 12). Collectively, these data suggest a general concordance between the presence of BCG in a given tissue after vaccination and the detection of antigen-responsive T cells.

Immune associations of bacterial control

Several multiple regressions were used to test whether peak antigen-responsive CD4 or CD8 T cells in the BAL or PBMCs after BCG immunization were associated with disease severity (Extended Data Fig. 13, Supplementary Tables 1 and 5). These analyses show that the route of BCG vaccination was the primary determinant of Mtb control with IV being the only regimen that afforded significant protection (Extended Data Fig. 8b).

Discussion

The data demonstrating that IV BCG immunization results in markedly increased antigen-responsive T cells, including T cells systemically and throughout the lung parenchyma, and unprecedented protection against Mtb challenge, represent a major step forward in the field of TB vaccine research.

The concept of alternative immunization routes rather than the standard ID approach was suggested 50 years ago in NHP studies comparing IV and AE immunization[5–8]. More recently, decreased lung pathology

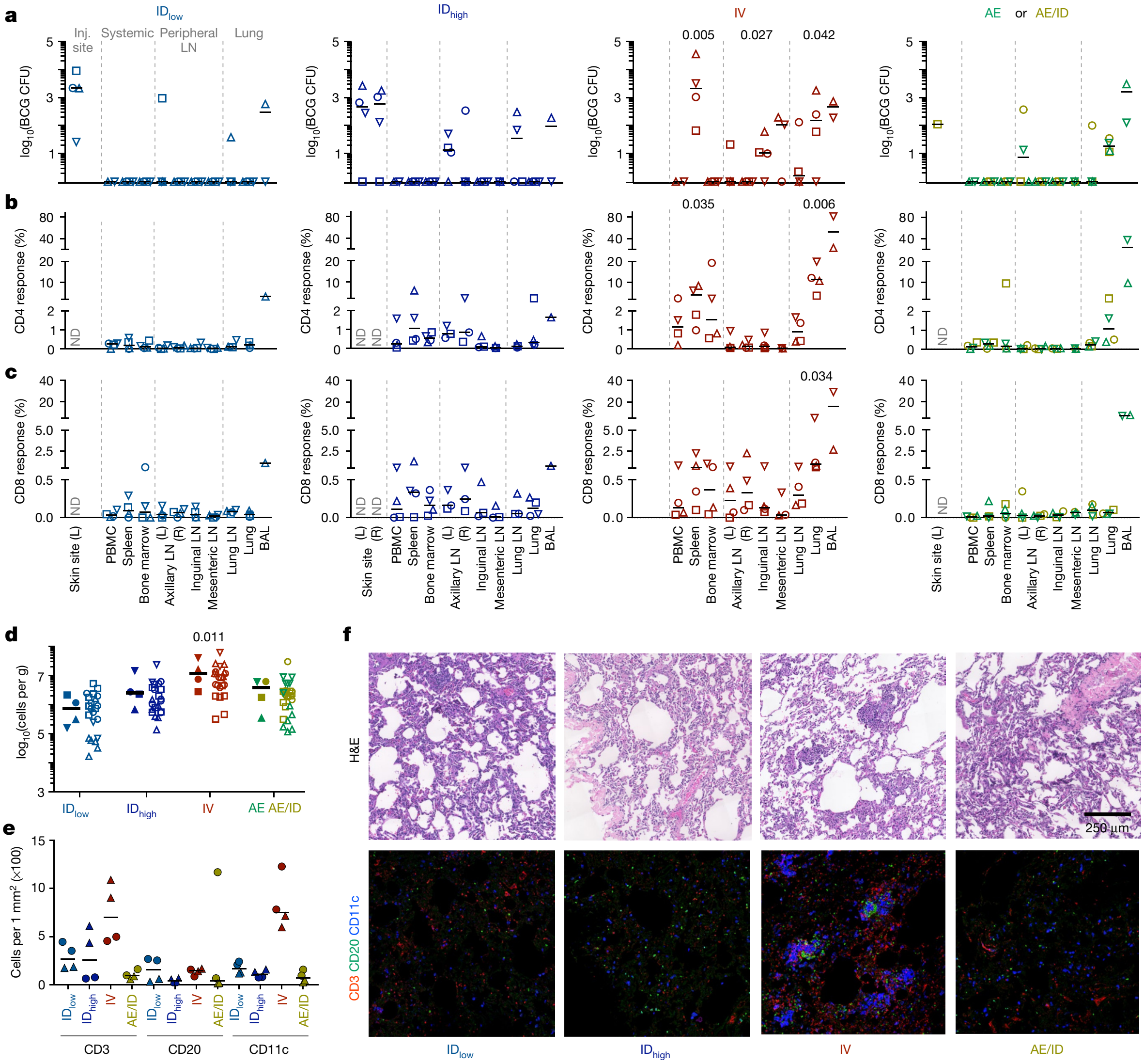

Fig. 3 | BCG CFUs and immune responses in tissues one month after BCG immunization. NHPs (cohorts 5a–c: ID$_{low}$, ID$_{high}$ and IV, $n = 4$ NHPs; AE and AE/ID, $n = 2$ NHPs) were euthanized one month after vaccination to quantify BCG and T cell responses in tissues. **a**, BCG CFUs at vaccination site(s) (skin, ID only) and in various tissues (per ml blood or bone marrow; per whole spleen, LN or lung lobe; or per total BAL collected). L, left; R, right; ND, not determined. **b**, **c**, Frequency of memory CD4 (**b**) and CD8 (**c**) T cells producing IFNγ, IL-2, TNF or IL-17 after PPD stimulation. Matched symbols within each vaccine group are the same macaque. Kruskal–Wallis tests were run and reported *P* values represent Dunn's multiple comparison test comparing each group to the ID$_{low}$ group. **d**, Total viable cells per gram of lung tissue for each vaccine regimen; data are shown as the median of four macaques per group (solid symbols, six lung lobes from each NHP are averaged) or as counts for each lung lobe ($n = 24$ lobes) from all NHPs (open symbols with lobes from same macaque matched). Kruskal–Wallis test was run on medians; Dunn's adjusted *P* values are from comparing each group to the ID$_{low}$ group. **e**, Quantification of CD3$^+$, CD20$^+$ and CD11c$^+$ cells from two lung sections per NHP (matched symbols, $n = 2$ macaques). **f**, Representative (one out of four) 1 mm^2 lung sections from each BCG regimen stained with haematoxylin and eosin (H&E; top) or with antibodies against CD3$^+$ T cells (red), CD20$^+$ B cells (green), and CD11c$^+$ macrophages or dendritic cells (blue).

and a trend towards increased survival was reported after IV BCG immunization compared with unvaccinated NHPs[33]. AE immunization with an attenuated Mtb strain enhanced cellular immunity in the BAL, and reduced lung pathology and bacterial burdens, after high-dose challenge 8 weeks later with a low virulence Mtb strain (CDC1551)[34]. In different method of pulmonary delivery, BCG instilled directly into the lower left lung lobe (that is, endobronchially), prevented infection and disease in two out of eight NHPs after repeated limiting-dose Mtb challenge in the same lung lobe, starting 13 weeks after vaccination[32]. The robust and localized T cell responses in lung tissue after direct BCG instillation (Fig. 4a and Extended Data Fig. 12d) provide a potential mechanistic difference between direct endobronchial and AE delivery that could influence protection. Finally, a cytomegalovirus (CMV) vector encoding Mtb antigens prevented TB disease in 14 out of 34 macaques across two studies, with 10 out of 14 being Mtb culture-negative[35]. In contrast to IV BCG immunization, all CMV-immunized macaques generated primary responses to Mtb antigens after challenge, suggesting that these vaccines elicit distinct mechanisms or kinetics of protection.

There are at least three immune mechanisms for how IV BCG may mediate protection. First, rapid elimination of Mtb may be due to the high magnitude of T cell responses in lung tissue. Our data are consistent with studies in mice that demonstrate the superior capacity of lung-localized T_{RM} cells to control TB disease[36,37], and studies in NHPs showing that depletion of lung interstitial CD4 T cells during SIV infection of Mtb latently infected NHPs is associated with reactivation and dissemination[38]. Second, there is some evidence that antibodies can

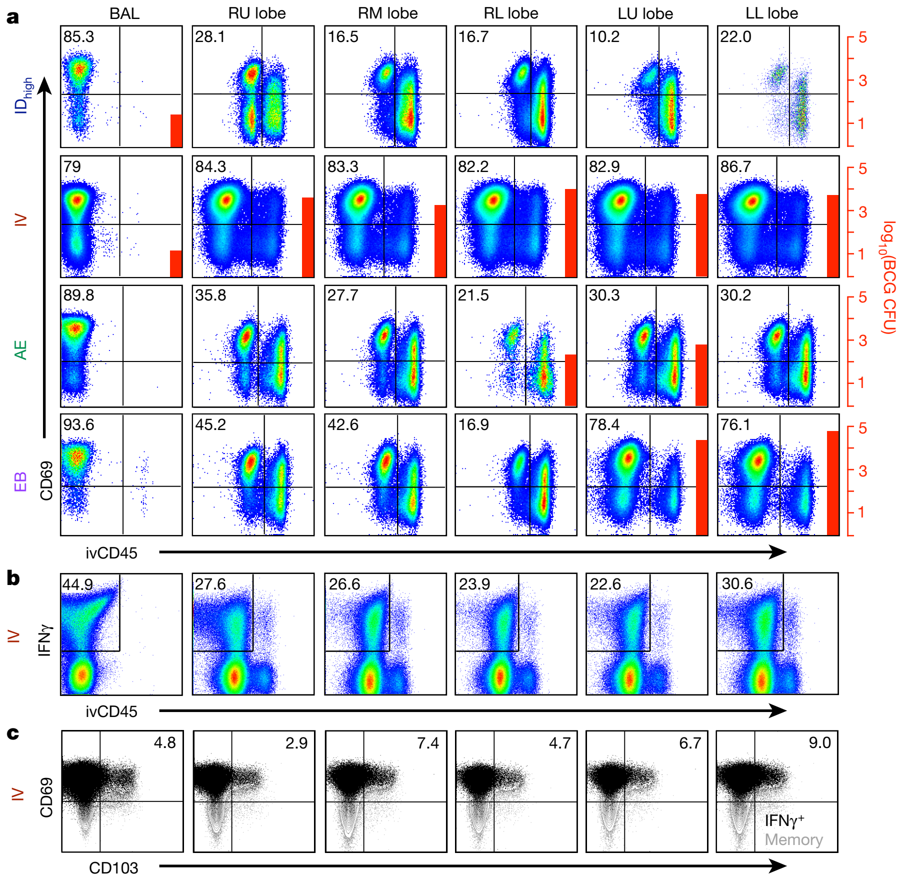

Fig. 4 | Detection of T cells in lung tissue after IV BCG immunization. a, One month after BCG vaccination, tissue-derived versus blood-derived cells in lung were delineated by injecting NHPs with a fluorochrome-conjugated anti-CD45 antibody (ivCD45) to label leukocytes in the vasculature. NHPs (cohort 6, $n = 2$ macaques) received 5×10^7 CFUs BCG ID, IV, AE or endobronchially (EB) into the left lung. At necropsy, BCG CFUs were quantified in tissues and cells were stained immediately ex vivo for surface marker expression (**a**) or stimulated with Mtb whole-cell lysate (WCL) and stained for cytokine production (**b**, **c**). Plots show CD4 T cells from the BAL and lung lobes (RU, right upper; RM, right middle; RL, right lower; LU, left upper; LL, left lower) from one of two macaques per BCG regimen. **a**, Percentage of ivCD45$^-$ (unstimulated) CD4 T cells expressing the tissue-resident/activation marker CD69; BCG CFUs (if detected) are indicated by red bars and right scale. **b**, Percentage of WCL-responsive (IFNγ$^+$) CD4 T cells in BAL and lung tissue (ivCD45$^-$) and (**c**) the percentage of IFNγ$^+$ CD4 memory T cells expressing CD69 and CD103 after IV BCG vaccination.

mediate control against Mtb in vivo or in vitro[39,40]. Antibody levels were higher in the BAL and plasma after IV BCG compared with other routes of vaccination, but declined to pre-vaccination levels in the BAL at the time of challenge (Extended Data Fig. 7). Third, IV BCG vaccination in mice induced epigenetically modified macrophages with enhanced capacity to protect against Mtb infection[41], a process termed 'trained immunity'[14,15]. Such an effect was dependent on BCG being detectable in the bone marrow; this was not observed one month after IV BCG vaccination in NHPs (Fig. 3a). Moreover, there was no increase in innate activation of PBMCs to non-Mtb antigens after IV BCG vaccination—a hallmark of trained immunity (Supplementary Data 3). Nonetheless, it is possible that any of these three mechanisms might act independently or together to mediate protection.

Because nine out of ten macaques were protected by IV BCG immunization (Fig. 2), we were unable to define an immune correlate of protection within this group (Extended Data Fig. 13); however, there were several unique quantitative and qualitative differences in the immune responses after IV BCG vaccination that may underlie protection. First, there were substantially higher numbers of Mtb antigen-responsive T cells in the BAL and PBMCs (Fig. 1b–e). Second, there was a unique CD4 T cell transcriptional profile in the BAL, which included upregulation of genes that have been associated with protection against TB (Fig. 1f–h). Third, and perhaps most noteworthy, was the large population of T cells in the tissue across all lung parenchyma lobes (Fig. 4, Extended Data Fig. 12 and Supplementary Data 7). Notably, although the BAL CD4 T cell responses were higher in ID$_{high}$-, AE- and AE/ID-BCG-immunized NHPs compared to the ID$_{low}$ BCG group, there was no increased protection. These data suggest that although measurement of BAL responses may provide greater insight into vaccine efficacy compared to blood, they may not fully reflect lung T_{RM} cell responses that might be the mechanism of protection.

In conclusion, this study provides a paradigm shift towards developing vaccines focused on preventing TB infection to prevent latency, active disease and transmission. The data support clinical development of IV delivery of BCG for use in adolescents or adults in whom modelling predicts the greatest effect on TB transmission[3], and suggest that the IV route may improve the protective capacity of other vaccine platforms. This study also provides a benchmark against which future vaccines will be tested and a new framework to understand the immune correlates and mechanisms of protection against TB.

Online content

Any methods, additional references, Nature Research reporting summaries, source data, extended data, supplementary information, acknowledgements, peer review information; details of author contributions and competing interests; and statements of data and code availability are available at https://doi.org/10.1038/s41586-019-1817-8.

1. World Health Organization. *Global Tuberculosis Report* https://www.who.int/tb/publications/global_report/en/ (2018).
2. Mangtani, P. et al. Protection by BCG vaccine against tuberculosis: a systematic review of randomized controlled trials. *Nephrol. Dial. Transplant*. **58**, 470–480 (2014).
3. Harris, R. C., Sumner, T., Knight, G. M. & White, R. G. Systematic review of mathematical models exploring the epidemiological impact of future TB vaccines. *Hum. Vaccin. Immunother*. **12**, 2813–2832 (2016).
4. Cooper, A. M. Cell-mediated immune responses in tuberculosis. *Annu. Rev. Immunol*. **27**, 393–422 (2009).
5. Barclay, W. R., Anacker, R. L., Brehmer, W., Leif, W. & Ribi, E. Aerosol-induced tuberculosis in subhuman primates and the course of the disease after intravenous BCG vaccination. *Infect. Immun*. **2**, 574–582 (1970).
6. Ribi, E. et al. Efficacy of mycobacterial cell walls as a vaccine against airborne tuberculosis in the rhesus monkey. *J. Infect. Dis*. **123**, 527–538 (1971).
7. Anacker, R. L. et al. Superiority of intravenously administered BCG and BCG cell walls in protecting rhesus monkeys (*Macaca mulatta*) against airborne tuberculosis. *Z. Immunitatsforsch. Exp. Klin. Immunol*. **143**, 363–376 (1972).
8. Barclay, W. R. et al. Protection of monkeys against airborne tuberculosis by aerosol vaccination with bacillus Calmette–Guerin. *Am. Rev. Respir. Dis*. **107**, 351–358 (1973).
9. Greene, J. M. et al. MR1-restricted mucosal-associated invariant T (MAIT) cells respond to mycobacterial vaccination and infection in nonhuman primates. *Mucosal Immunol*. **10**, 802–813 (2017).
10. Joosten, S. A. et al. Harnessing donor unrestricted T-cells for new vaccines against tuberculosis. *Vaccine* **37**, 3022–3030 (2019).
11. Qaqish, A. et al. Adoptive transfer of phosphoantigen-specific γδ T cell subset attenuates *Mycobacterium tuberculosis* infection in nonhuman primates. *J. Immunol*. **198**, 4753–4763 (2017).
12. Roy Chowdhury, R. et al. A multi-cohort study of the immune factors associated with *M. tuberculosis* infection outcomes. *Nature* **560**, 644–648 (2018).
13. Suliman, S. et al. Bacillus Calmette–Guerin (BCG) revaccination of adults with latent *Mycobacterium tuberculosis* infection induces long-lived BCG-reactive NK cell responses. *J. Immunol*. **197**, 1100–1110 (2016).
14. Joosten, S. A. et al. Mycobacterial growth inhibition is associated with trained innate immunity. *J. Clin. Invest*. **128**, 1837–1851 (2018).
15. Kleinnijenhuis, J. et al. Long-lasting effects of BCG vaccination on both heterologous Th1/Th17 responses and innate trained immunity. *J. Innate Immun*. **6**, 152–158 (2014).
16. Khader, S. A. et al. IL-23 and IL-17 in the establishment of protective pulmonary $CD4^+$ T cell responses after vaccination and during *Mycobacterium tuberculosis* challenge. *Nat. Immunol*. **8**, 369–377 (2007).
17. Gideon, H. P. et al. Variability in tuberculosis granuloma T cell responses exists, but a balance of pro- and anti-inflammatory cytokines is associated with sterilization. *PLoS Pathog*. **11**, e1004603 (2015).
18. Soares, A. P. et al. Longitudinal changes in $CD4^+$ T-cell memory responses induced by BCG vaccination of newborns. *J. Infect. Dis*. **207**, 1084–1094 (2013).
19. Darrah, P. A. et al. Multifunctional T_H1 cells define a correlate of vaccine-mediated protection against *Leishmania major*. *Nat. Med*. **13**, 843–850 (2007).
20. Lewinsohn, D. A., Lewinsohn, D. M. & Scriba, T. J. Polyfunctional $CD4^+$ T cells as targets for tuberculosis vaccination. *Front. Immunol*. **8**, 1262 (2017).
21. Chattopadhyay, P. K., Yu, J. & Roederer, M. Live-cell assay to detect antigen-specific $CD4^+$ T-cell responses by CD154 expression. *Nat. Protocols* **1**, 1–6 (2006).
22. Orr, M. T. et al. Interferon γ and tumor necrosis factor are not essential parameters of $CD4^+$ T-cell responses for vaccine control of tuberculosis. *J. Infect. Dis*. **212**, 495–504 (2015).
23. Sakai, S. et al. CD4 T cell-derived IFN-γ plays a minimal role in control of pulmonary *Mycobacterium tuberculosis* infection and must be actively repressed by PD-1 to prevent lethal disease. *PLoS Pathog*. **12**, e1005667 (2016).
24. Gierahn, T. M. et al. Seq-Well: portable, low-cost RNA sequencing of single cells at high throughput. *Nat. Methods* **14**, 395–398 (2017).
25. Sallin, M. A. et al. Host resistance to pulmonary *Mycobacterium tuberculosis* infection requires CD153 expression. *Nat. Microbiol*. **3**, 1198–1205 (2018).
26. Booty, M. G. et al. IL-21 signaling is essential for optimal host resistance against *Mycobacterium tuberculosis* infection. *Sci. Rep*. **6**, 36720 (2016).
27. Maiello, P. et al. Rhesus macaques are more susceptible to progressive tuberculosis than cynomolgus macaques: a quantitative comparison. *Infect. Immun*. **86**, e00505-17 (2018).
28. Darrah, P. A. et al. Boosting BCG with proteins or rAd5 does not enhance protection against tuberculosis in rhesus macaques. *Vaccines (Basel)* **4**, 21 (2019).
29. Anderson, K. G. et al. Intravascular staining for discrimination of vascular and tissue leukocytes. *Nat. Protocols* **9**, 209–222 (2014).
30. Kauffman, K. D. et al. Defective positioning in granulomas but not lung-homing limits CD4 T-cell interactions with *Mycobacterium tuberculosis*-infected macrophages in rhesus macaques. *Mucosal Immunol*. **11**, 462–473 (2018).
31. Masopust, D. & Soerens, A. G. Tissue-resident T cells and other resident leukocytes. *Annu. Rev. Immunol*. **37**, 521–546 (2019).
32. Dijkman, K. et al. Prevention of tuberculosis infection and disease by local BCG in repeatedly exposed rhesus macaques. *Nat. Med*. **25**, 255–262 (2019).
33. Sharpe, S. et al. Alternative BCG delivery strategies improve protection against *Mycobacterium tuberculosis* in non-human primates: protection associated with mycobacterial antigen-specific CD4 effector memory T-cell populations. *Tuberculosis (Edinb.)* **101**, 174–190 (2016).
34. Kaushal, D. et al. Mucosal vaccination with attenuated *Mycobacterium tuberculosis* induces strong central memory responses and protects against tuberculosis. *Nat. Commun*. **6**, 8533 (2015).
35. Hansen, S. G. et al. Prevention of tuberculosis in rhesus macaques by a cytomegalovirus-based vaccine. *Nat. Med*. **24**, 130–143 (2018).
36. Moguche, A. O. et al. ICOS and Bcl6-dependent pathways maintain a CD4 T cell population with memory-like properties during tuberculosis. *J. Exp. Med*. **212**, 715–728 (2015).
37. Sakai, S. et al. Cutting edge: control of *Mycobacterium tuberculosis* infection by a subset of lung parenchyma-homing CD4 T cells. *J. Immunol*. **192**, 2965–2969 (2014).
38. Corleis, B. et al. HIV-1 and SIV infection are associated with early loss of lung interstitial $CD4^+$ T cells and dissemination of pulmonary tuberculosis. *Cell Reports* **26**, 1409–1418 (2019).
39. Lu, L. L. et al. A functional role for antibodies in tuberculosis. *Cell* **167**, 433–443 (2016).
40. Li, H. & Javid, B. Antibodies and tuberculosis: finally coming of age? *Nat. Rev. Immunol*. **18**, 591–596 (2018).
41. Kaufmann, E. et al. BCG educates hematopoietic stem cells to generate protective innate immunity against tuberculosis. *Cell* **172**, 176–190 (2018).

Methods

Macaques and sample size

Indian-origin rhesus macaques (*Macaca mulatta*) used in these studies are outlined in Extended Data Fig. 1c and Supplementary Table 1. All experimentation complied with ethical regulations at the respective institutions (Animal Care and Use Committees of the Vaccine Research Center, NIAID, NIH and of Bioqual, Inc., and of the Institutional Animal Care and Use Committee of the University of Pittsburgh). Macaques were housed and cared for in accordance with local, state, federal, and institute policies in facilities accredited by the American Association for Accreditation of Laboratory Animal Care (AAALAC), under standards established in the Animal Welfare Act and the Guide for the Care and Use of Laboratory Animals. Macaques were monitored for physical health, food consumption, body weight, temperature, complete blood counts, and serum chemistries. All infections were performed at the University of Pittsburgh where animals were housed in a biosafety level 3 facility.

The sample size for this study was determined using bacterial burden (measured as $\log_{10}$-transformed total thoracic CFUs) as the primary outcome variable. Initially, we planned to test BCG route efficacy by comparing IV, AE and AE/ID routes to ID_{low} vaccination and found that ten macaques per group would be sufficient to obtain over 90% power and adjusted the type I error rate for three group comparisons ($\alpha = 0.0167$). After initiation of the first cohort of NHPs in this study, we elected to test the effect of dose on ID vaccination by adding an ID_{high} group ($n = 8$ macaques). The additional treatment group did not substantially reduce the power of the study. To detect a 1.5 difference in $\log_{10}$(total CFUs) with a pooled standard deviation of 0.8 (using previous data), we obtained over 90% (90.7%) power using 10 macaques per group with an adjusted type I error rate for 4 group comparisons ($\alpha = 0.0125$). The comparison made between the ID_{high} ($n = 8$ macaques) and ID_{low} ($n = 10$ macaques) groups achieved 85.6% power detecting the same difference ($\log_{10}(1.5)$) and with an $\alpha = 0.0125$.

BCG vaccination

For Mtb challenge studies (cohorts 1–3), 3–5-year-old male ($n = 32$) and female ($n = 20$) rhesus macaques were randomized into experimental groups based on gender, weight and pre-vaccination CD4 T cell responses to PPD in BAL. Macaques were vaccinated at Bioqual, Inc. under sedation and in successive cohorts as outlined in Extended Data Fig. 1c. BCG Danish Strain 1331 (Statens Serum Institute, Copenhagen, Denmark) was expanded[42], frozen at approximately 3×10^8 CFUs ml^{-1} in single-use aliquots and stored at −80 °C. Immediately before injection, BCG (for all vaccine routes) was thawed and diluted in cold PBS containing 0.05% tyloxapol (Sigma-Aldrich) and 0.002% antifoam Y-30 (Sigma-Aldrich) to prevent clumping of BCG and foaming during aerosolization[43]. For ID vaccinations, BCG was injected in the left upper arm (5×10^5 CFUs; ID_{low}) or split across both upper arms (5×10^7 CFUs; ID_{high}) in a volume of 100–200 µl per site. IV BCG (5×10^7 CFUs) was injected into the left saphenous vein in a volume of 2 ml; AE BCG (5×10^7 CFUs) was delivered in a 2 ml volume via paediatric mask attached to a Pari eFlow nebulizer (PARI Pharma GmgH) that delivered 4 µM particles into the lung, as previously described[28]; AE/ID macaques were immunized simultaneously (5×10^7 CFUs AE plus 5×10^5 CFUs ID in left arm); EB BCG (5×10^7 CFUs in 2 ml; cohort 6 only) was instilled into the left lung lobes using an endoscope. No loss of viability was observed for BCG after aerosolization. In pilot studies, lower doses of BCG were prepared and delivered as described above. Text refers to nominal BCG doses—actual BCG CFUs for vaccine regimens in every cohort were quantified immediately after vaccination and are reported in Extended Data Fig. 1c and Supplementary Table 1.

Mtb challenge

Macaques (cohorts 1–3) were challenged by bronchoscope with 4–36 CFUs barcoded Mtb Erdman 6–10 months after BCG vaccination (Extended Data Fig. 1c and Supplementary Table 1) in a 2 ml volume as previously described[44]. Infectious doses across this range result in similar levels of TB disease in unvaccinated rhesus in this and previous studies[28] (Supplementary Data 12). Clinical monitoring included regular monitoring of appetite, behaviour and activity, weight, erythrocyte sedimentation rate, Mtb growth from gastric aspirate and coughing. These signs, as well as PET–CT characteristics, were used as criteria in determining whether a macaque met the humane end point before the pre-determined study end point.

PET–CT scans and analysis

PET–CT scans were performed using a microPET Focus 220 preclinical PET scanner (Siemens Molecular Solutions) and a clinical eight-slice helical CT scanner (NeuroLogica Corporation) as previously described[27,45–47]. 2-deoxy-2-(^{18}F)fluorodeoxyglucose (FDG) was used as the PET probe. Serial scans were performed before, 4 and 8 weeks after Mtb, and before necropsy (cohorts 1–3) or at 2 and 4 weeks after BCG (cohorts 5a, b). OsiriX MD (v.10.0.1), a DICOM (Digital Imaging and Communications in Medicine) image viewer, was used for scan analyses, as described[47]. Lung inflammation was measured as total FDG activity within the lungs. A region of interest (ROI) was segmented which encompassed all lung tissue on CT and was then transferred to the co-registered PET scan. On the PET scan, all image voxels of FDG-avid pathology (Standard Uptake Value >2.3) were isolated and summated resulting in a cumulative standardized uptake value. To account for basal metabolic FDG uptake, total FDG activity was normalized to resting muscle resulting in a total lung inflammation value. Individual granulomas were counted on each CT scan. If granulomas were too small and numerous within a specific area to count individually or if they consolidated, quantification was considered to be too numerous to count. To measure the volume of the spleen, an ROI was drawn outlining the entire organ on each of the axial slices of the CT scan and the volume was computed across these ROIs (using a tool in OsiriX). Any scans for which visibility of the entire spleen was limited ($n = 2$ macaques) were excluded from this analysis.

Necropsy, pathology scoring and Mtb and BCG burden

For challenge studies (cohorts 1–3), NHPs were euthanized 11–15 weeks after Mtb or at humane endpoint by sodium pentobarbital injection, followed by gross examination for pathology. A published scoring system[27] was used to determine total pathology from each lung lobe (number and size of lesions), LN (size and extent of necrosis), and extrapulmonary compartments (number and size of lesions). All granulomas and other lung pathologies, all thoracic LNs, and peripheral LNs were matched to the final PET–CT scan and collected for quantification of Mtb. Each lesion (including granulomas, consolidations and clusters of granulomas) in the lung, all thoracic LNs, random sampling (50%) of each of the 7 lung lobes, 3–5 granulomas (if present) or random samples (30%) of spleen and liver, and any additional pathologies were processed to comprehensively quantify bacterial burdens. Suspensions were plated on 7H11 agar (Difco) and incubated at 37 °C with 5% CO_2 for 3 weeks for CFU enumeration or formalin-fixed and paraffin-embedded for histological examination. CFUs were counted and summed to calculate the total thoracic bacterial burden for the macaque[17,27,48]. Mtb CFUs for every challenged macaque are listed in Supplementary Table 1.

To determine BCG CFUs, BAL, bone marrow aspirates, and blood were collected from NHPs before euthanasia. Individual lung lobes and thoracic and peripheral LNs, spleen, liver, and the skin site(s) of injection (if applicable) were excised. 0.5 ml of blood and bone marrow and 10% of retrieved BAL wash fluid were plated; approximately 1 g of tissue (or one whole LN or skin biopsy) was processed in water in gentleMACS M Tubes (Miltenyi Biotec) using a gentleMACS Dissociator (Miltenyi Biotec). Samples were plated and counted as above. Data are reported as CFUs ml^{-1} of blood or bone marrow, CFUs per total BAL collected, CFUs per one LN or skin biopsy, CFUs per lung lobe or spleen. CFUs from individual lung lobes and LNs of the same category (for example, hilar) were averaged for each NHP.

Rhesus blood, BAL and tissue processing

Blood PBMCs were isolated using Ficoll-Paque PLUS gradient separation (GE Healthcare Biosciences) and standard procedures; BAL wash fluid (3 × 20 ml washes of PBS) was centrifuged and cells were combined before counting, as described[28]. LNs were mechanically disrupted and filtered through a 70-μm cell strainer. Lung and spleen tissues were processed using gentleMACS C Tubes and Dissociator in RPMI 1640 (ThermoFisher Scientific). Spleen mononuclear cells were further separated using Ficoll-Paque. Lung tissue was digested using collagenase, Type I (ThermoFisher Scientific) and DNase (Sigma-Aldrich) for 30–45 min at 37 °C with shaking, followed by passing through a cell strainer. Single-cell suspensions were resuspended in warm R10 (RPMI 1640 with 2 mM L-glutamine, 100 U ml^{-1} penicillin, 100 μg ml^{-1} streptomycin, and 10% heat-inactivated FBS; Atlantic Biologicals) or cryopreserved in FBS containing 10% DMSO in liquid nitrogen.

Multiparameter flow cytometry

Generally, longitudinal PBMC samples were batch-analysed for antigen-specific T cell responses or cellular composition at the end of the study from cryopreserved samples whereas BAL and tissue (necropsy) samples were analysed fresh. Cryopreserved PBMC were washed, thawed and rested overnight in R10 before stimulation, as described[28]. For T cell stimulation assays, 1–5 million viable cells were plated in 96-well V-bottom plates (Corning) in R10 and incubated with R10 alone (background), or with 20 μg ml^{-1} tuberculin PPD (Statens Serum Institut, Copenhagen, Denmark), 20 μg ml^{-1} H37Rv Mtb WCL (BEI Resources), or 1 μg ml^{-1} each of ESAT-6 and CFP-10 peptide pools (provided by Aeras, Rockville, MD) for 2 h before adding 10 μg ml^{-1} BD GolgiPlug (BD Biosciences). The concentrations of PPD and WCL were optimized to detect CD4 T cell responses; however, protein antigen stimulation may underestimate CD8 T cell responses. For logistical reasons, cells were stimulated overnight (14 h total) before intracellular cytokine staining. For cellular composition determination, cells were stained immediately ex vivo after processing or after thawing. Antibody and tetramer information for each flow cytometry panel is listed in Supplementary Data 8–11. Generally, cells were stained as follows (not all steps apply to all panels, all are at room temperature): Washed twice with PBS/BSA (0.1%); 20-min incubation with rhesus MR1 tetramer[49] (NIH Tetramer Core Facility) in PBS/BSA; washed twice with PBS; live/dead stain in PBS for 20 min; washed twice with PBS/BSA; 10-min incubation with human FcR blocking reagent (Miltenyi Biotec); incubation with surface marker antibody cocktail in PBS/BSA containing 1× Brilliant Stain Buffer Plus (BD Biosciences) for 20 min; washed three times with PBS/BSA (0.1%); 20 min incubation BD Cytofix/Cytoperm Solution (BD Biosciences); washed twice with Perm/Wash Buffer (BD Biosciences); 30 min incubation with intracellular antibody cocktail in Perm/Wash Buffer containing 1× Brilliant Stain Buffer Plus; washed thrice with Perm/Wash Buffer. For Ki-67 staining, samples were stained for surface markers and cytokines as described above, followed by nuclear permeabilization using eBioscience Foxp3/Transcription Factor Staining Buffer (ThermoFisher Scientific) and incubation with antibody against Ki-67 following kit instructions. Data were acquired on either a modified BD LSR II or modified BD FACSymphony and analysed using FlowJo software (v.9.9.6 BD Biosciences). Gating strategies can be found in Supplementary Data 8–11. All cytokine data presented graphically are background-subtracted.

Intravascular CD45 staining

One month after BCG vaccination, macaques in each cohort 6 (n = 2 macaques per group) received an IV injection of Alexa Fluor 647-conjugated anti-CD45 antibody (ivCD45; 60 μg kg^{-1}, clone MB4-6D6, Miltenyi Biotec) 5 min before euthanasia. Blood was collected before anti-CD45 injection as a negative control, and before euthanasia as a positive control. NHPs underwent whole body perfusion with cold saline before tissue collection. Tissues were processed for BCG CFU quantification and flow cytometric analysis as described above. Staining panels used were as in Supplementary Data 9, with the omission of the APC-conjugated antibodies.

Immunohistochemistry

Embedded tissue sections were deparaffinized (100% xylenes, 10 min; 100% ethanol, 5 min; 70% ethanol, 5 min), boiled under pressure for 6 min in antigen retrieval buffer (1× Tris EDTA, pH 9.0), and cooled. Sections were blocked in PBS (1% BSA) in a humidified chamber at room temperature for 30 min followed by staining for CD3 (CD3-12, Abcam), CD11c (5D11, Leica), and CD20 (Thermo Scientific, RB-9013-PO) for 18 h at 4 °C in a humidified chamber. After washing with PBS in coplin jars, sections were incubated for 1 h at room temperature with conjugated anti-rabbit IgG Alexa Fluor 488 (Life Technologies, A21206), anti-rat IgG Alexa Fluor 546 (Invitrogen, A11081), and anti-mouse IgG Alexa Fluor 647 (Jackson ImmunoResearch, 7 5606-150). After washing, coverslips were applied using Prolong Gold anti-fade with Dapi mounting media (Life Technologies). Slides were cured for 18–24 h before imaging on an Olympus FluoView FV1000 confocal microscope. Lung sections were imaged and two random representative 1 mm^2 ROIs from each macaque were analysed using CellProfiler v2.2.0. Pipelines were designed for analysis by adding modules for individual channel quantification based on pixel intensity and pixel size providing a numerical value for each cell type and total cells. Histological analyses were performed by a veterinary pathologist (E.K.) in a blinded fashion on H&E-stained sections from all tissues obtained.

ELISpot and Luminex

IFNγ ELISpots were performed at 0, 4, 6 and 8 weeks after Mtb and at necropsy. One day before use, hydrophobic high protein binding membranes 96-well plates (Millipore Sigma) were hydrated with 40% ethanol, washed with sterile water, and coated with anti-human/monkey IFNγ antibody (15 μg ml^{-1}, MT126L, MabTech) overnight at 4 °C. Plates were washed with HBSS and blocked with RPMI with 10% human AB serum for 2 h at 37 °C with 5% CO_2. Approximately 200,000 PBMCs per well were incubated in RPMI supplemented with L-glutamate, HEPES and 10% human AB serum containing 2 μg ml^{-1} ESAT-6 or CFP-10 peptide pools for 40–48 h at 37 °C with 5% CO_2. Medium alone or phorbol 12,13-dibutyrate (12.5 μg ml^{-1}) plus ionomycin (37.5 μg ml^{-1}) were added as negative (background) and positive controls, respectively. To develop, plates were washed with PBS and biotinylated anti-human IFNγ antibody (2.5 μg ml^{-1}, 7-B6-1, MabTech) was added for 2 h at 37 °C with 5% CO_2. After washing, streptavidin-horseradish peroxidase (1:100, MabTech) was added for 45 min at 37 °C with 5% CO_2. Spots were stained using AEC peroxidase (Vector Laboratories, Inc.) per the manufacturer's instructions and counted manually on an ELISpot plate reader. Data are reported as average ELISpots from duplicate background-subtracted wells. Wells with confluent spots were described as too numerous to count.

To measure innate cytokine production following BCG immunization, cryopreserved PBMC were batch-analysed. Cells were thawed and resuspended in warm R10. Then, 5×10^5 cells per well in 96-well V-bottom plates were rested overnight at 37 °C with 5% CO_2. Cells were resuspended in Trained Immunity Media[15] plus H37Rv Mtb whole cell lysate (BEI Resources, 20 μg ml^{-1}), heat-killed *Staphylococcus aureus* (InvivoGen, 1×10^6 per ml), *Escherichia coli* LPS (Sigma-Aldrich, 1 ng ml^{-1}), or RPMI and incubated for 24 h at 37 °C with 5% CO_2 before collecting supernatants. Cytokine and chemokine measurements were determined using a MILLIPLEX NHP cytokine multiplex kit per instructions (Millipore Sigma) and analysed on a Bio-Plex Magpix Multiplex Reader (Bio-Rad).

Antibody ELISAs

IgG, IgA and IgM titres to Mtb H37Rv WCL were assessed in plasma and tenfold concentrated BAL fluid. WCL was used based on greater sensitivity compared to PPD, culture filtrate protein, or lipoarabinomannan.

96-well MaxiSorp ELISA plates (Nunc) were coated overnight at 4 °C with 0.1 μg of WCL. Plates were blocked with PBS/FBS (10%) for 2 h at room temperature and washed with PBS/TWEEN 20 (0.05%). 1:5 serially diluted plasma or concentrated BAL fluid (8 dilutions per sample) was incubated at 37 °C for 2 h, followed by washing. Then, 100 μl of goat anti-monkey HRP-conjugated IgG h+l (50 ng ml^{-1}; Bethyl Laboratories, Inc.), IgA α chain (0.1 μg ml^{-1}, Rockland Immunochemicals Inc.), or IgM α chain (0.4 μg ml^{-1}, Sera Care) was added for 2 h at room temperature, followed by washing. Ultra TMB substrate (100 μl; Invitrogen) was added for 12 min followed by 100 μl 2 N sulfuric acid. Data were collected on a Spectramax i3X microplate reader (Molecular Devices) at 450 nm using Softmax Pro and presented either as endpoint titer (reciprocal of last dilution with an OD above the limit of detection or 2× the OD of an empty well) at 0.2 for IgG and IgA, or midpoint titer for IgM where samples did not titre to a cut off of 0.2.

Single-cell transcriptional profiling

High-throughput single-cell mRNA sequencing by Seq-Well was performed on single-cell suspensions obtained from NHP BAL, as previously described[24]. Approximately 15,000 viable cells per sample were applied directly to the surface of a Seq-Well device. At each time point after BCG, two arrays were run for each sample—one unstimulated and one stimulated overnight with 20 μg ml^{-1} of PPD in R10.

Sequencing and alignment. Sequencing for all samples was performed on an Illumina Nova-Seq. Reads were aligned to the *M. mulatta* genome using STAR[50], and the aligned reads were then collapsed by cell barcode and unique molecular identifier (UMI) sequences using DropSeq Tools v.1 to generate digital gene expression (DGE) matrices, as previously described[24,51]. To account for potential index swapping, we merged all cell barcodes from the same sequencing run that were within a hamming distance of 1.

Analysis of single-cell sequencing data. For each array, we assessed the quality of constructed libraries by examining the distribution of reads, genes and transcripts per cell. For each time point, we next performed dimensionality reduction (PCA) and clustering as previously described[52,53]. We visualized our results in a two-dimensional space using UMAP[54], and annotated each cluster based on the identity of highly expressed genes. To further characterize substructure within cell types (for example, T cells), we performed dimensionality reduction (PCA) and clustering over those cells alone as previously described[24]. We then visualized our results in two-dimensional space using *t*-distributed stochastic neighbour embedding (*t*-SNE)[24]. Clusters were further annotated (that is, as CD4 and CD8 T cells) by cross-referencing cluster-defining genes with curated gene lists and online databases (that is, SaVanT andGSEA/MsigDB)[55–57].

Module identification. Data from stimulated or unstimulated T cells at week 13 or 25 was subset on significant principal components as previously described[24] and, for those principal components, on genes with significant loadings as determined through a randomization approach ('JackStraw')[52]. These matrices were then used as the inputs for WGCNA[58]. Following the WGCNA tutorial (https://horvath.genetics.ucla.edu/html/CoexpressionNetwork/Rpackages/WGCNA/Tutorials/), we chose an appropriate soft power threshold to calculate the adjacency matrix. As scRNA-seq data is affected by transcript drop-out (failed capture events), adjacency matrices with high power further inflate the effect of this technical limitation, and yield few correlated modules. Therefore, when possible, we chose a power as suggested by the authors of WGCNA (that is, the first power with a scale free topology above 0.8); however, if this power yielded few modules (fewer than three), we decreased our power. We then generated an adjacency matrix using the selected soft power and transformed it into a topological overlap matrix (TOM). Subsequently, we hierarchically clustered this TOM, and used the cutreeDynamic function with method 'tree' to identify modules of correlated genes using a dissimilarity threshold of 0.5 (that is, a correlation of 0.5). To test the significance of the correlations observed in each module, we implemented a permutation test. Binning the genes in the true module by average gene expression (number of bins = 10), we randomly picked genes with the same distribution of average expression from the total list of genes used for module discovery 10,000 times. For each of these random modules, we performed a one-sided Mann–Whitney *U*-test between the distribution of dissimilarity values among the genes in the true module and the distribution among the genes in the random module. Correcting the resulting *P* values for multiple hypothesis testing by Benjamini–Hochberg false discovery rate correction, we considered the module significant if fewer than 500 tests ($P < 0.05$) had false discovery rate > 0.05.

Gene module enrichments. To characterize the seven significant gene modules identified among in vitro-stimulated T cells collected 13 weeks after vaccination, we performed an enrichment analysis using databases of gene expression signatures (SaVanT and GSEA/MsigDb). Specifically, the enrichments in the Savant database, which includes signatures from ImmGen, mouse body atlas and other datasets (http://newpathways.mcdb.ucla.edu/savant-dev/), were performed using genes included in significant modules with a background expression set of 32,681 genes detected across single cells using Piano (https://varemo.github.io/piano/).

Statistical methods

All reported *P* values are from two-sided comparisons. For continuous variables, vaccine routes were compared using a Kruskal–Wallis test with Dunn's multiple comparison adjustment or one-way ANOVA with Dunnett's multiple comparison adjustment (comparing all routes to ID_{low} BCG). Fisher's exact tests were run for multiple CFU thresholds (evaluating protection) to assess the association between vaccine route and protection from Mtb (Extended Data Fig. 8b). A permutation test[59] was used to compare fractional distributions (pie charts) of all vaccine groups to ID_{low} BCG. For clinical parameters, combined pre-vaccination measurements from all NHPs were compared against distributions from every vaccine group at every time point using Dunnett's test for multiple comparisons. To assess whether post-vaccination antigen-responsive CD4 or CD8 T cells in the BAL or PBMCs are associated with disease severity, we first calculated peak T cell responses for each NHP over the course of vaccine regimen. The $\log_{10}$-transformed CD4 and CD8 cell counts were calculated within BAL and frequencies of CD4 and CD8 cells were calculated within PBMCs. To assess the effects of vaccine route and T cells on $\log_{10}$-transformed total CFUs, several multiple linear regressions were run in JMP Pro (v.12.1.0). Peak T cell responses and CFUs for each macaque included in these analyses are provided in Supplementary Table 1; detailed regression output (including model fit, ANOVA results, effect tests and parameter estimates) is provided in Supplementary Table 5. Cytokine production for trained immunity assay was compared using a two-way ANOVA and Dunnett's multiple comparison test. Serial PBMC responses to CFP, ESAT-6 or CFP-10 by IFNγ ELISpot were analysed by using a Wilcoxon signed-rank test to compare pre-infection versus 12 weeks post-infection time points (within each vaccine route).

Reporting summary

Further information on research design is available in the Nature Research Reporting Summary linked to this paper.

Data availability

All relevant data are available from the corresponding author upon reasonable request. Supplementary Table 1 provides peak immune data and post-challenge data for individual NHPs and Supplementary Table 5

provides regression analyses that support Extended Data Fig. 13. Supplementary Tables 2–4 include stimulation-inducible module genes, gene enrichments for modules, and differentially expressed genes that support transcriptional profiling data. RNA-sequencing data that support this study have been deposited in the Gene Expression Omnibus (GEO) under accession number GSE139598. Source Data for Figs. 1–4 and Extended Data Figs. 2–13 are provided with the paper.

Code availability

All R code used for analysis of Seq-Well data is available upon request.

42. Fitzpatrick, M. et al. Comparison of pellicle and shake flask-grown BCG strains by quality control assays and protection studies. *Tuberculosis (Edinb.)* **114**, 47–53 (2019).
43. Saini, D. et al. Ultra-low dose of *Mycobacterium tuberculosis* aerosol creates partial infection in mice. *Tuberculosis (Edinb.)* **92**, 160–165 (2012).
44. Martin, C. J. et al. Digitally barcoding *Mycobacterium tuberculosis* reveals in vivo infection dynamics in the macaque model of tuberculosis. *mBio* **8**, e00312-17 (2017).
45. Coleman, M. T. et al. Early changes by ^{18}fluorodeoxyglucose positron emission tomography coregistered with computed tomography predict outcome after *Mycobacterium tuberculosis* infection in cynomolgus macaques. *Infect. Immun*. **82**, 2400–2404 (2014).
46. Lin, P. L. et al. Sterilization of granulomas is common in active and latent tuberculosis despite within-host variability in bacterial killing. *Nat. Med*. **20**, 75–79 (2014).
47. White, A. G. et al. Analysis of ^{18}FDG PET/CT imaging as a tool for studying *Mycobacterium tuberculosis* infection and treatment in non-human primates. *J. Vis. Exp*. **127**, e56375 (2017).
48. Phuah, J. et al. Effects of B cell depletion on early *Mycobacterium tuberculosis* infection in cynomolgus macaques. *Infect. Immun*. **84**, 1301–1311 (2016).
49. Corbett, A. J. et al. T-cell activation by transitory neo-antigens derived from distinct microbial pathways. *Nature* **509**, 361–365 (2014).
50. Dobin, A. et al. STAR: ultrafast universal RNA-seq aligner. *Bioinformatics* **29**, 15–21 (2013).
51. Macosko, E. Z. et al. Highly parallel genome-wide expression profiling of individual cells using nanoliter droplets. *Cell* **161**, 1202–1214 (2015).
52. Satija, R., Farrell, J. A., Gennert, D., Schier, A. F. & Regev, A. Spatial reconstruction of single-cell gene expression data. *Nat. Biotechnol*. **33**, 495–502 (2015).
53. Wolf, F. A., Angerer, P. & Theis, F. J. SCANPY: large-scale single-cell gene expression data analysis. *Genome Biol*. **19**, 15 (2018).
54. Becht, E. et al. Dimensionality reduction for visualizing single-cell data using UMAP. *Nat. Biotechnol*. **37**, 38–44 (2018).
55. Lopez, D. et al. SaVanT: a web-based tool for the sample-level visualization of molecular signatures in gene expression profiles. *BMC Genomics* **18**, 824 (2017).
56. Mootha, V. et al. PGC-1α-responsive genes involved in oxidative phosphorylation are coordinately downregulated in human diabetes. *Nat. Genet.* **34**, 267–273 (2003).
57. Subramanian, A. et al. Gene set enrichment analysis: a knowledge-based approach for interpreting genome-wide expression profiles. *Proc. Natl Acad. Sci. USA* **102**, 15545–15550 (2005).
58. Langfelder, P. & Horvath, S. WGCNA: an R package for weighted correlation network analysis. *BMC Bioinformatics* **9**, 559 (2008).
59. Roederer, M., Nozzi, J. L. & Nason, M. C. SPICE: exploration and analysis of post-cytometric complex multivariate datasets. *Cytometry A* **79**, 167–174 (2011).

Acknowledgements This project was funded by the Intramural Research Program of the VRC, NIAID, NIH and by the Bill and Melinda Gates Foundation (through Aeras to J.L.F. and to A.K.S.). A.K.S. was also supported, in part, by the Searle Scholars Program, the Beckman Young Investigator Program, the NIH (5U24AI118672, 2RM1HG006193), and a Sloan Fellowship in Chemistry. We acknowledge the outstanding work of veterinary and research technicians (J. Tomko, B. Stein, C. Ameel, A. Myers, N. Schindler, C. Cochran and C. Bigbee), and imaging personnel (L. J. Frye, J. Borish) at the University of Pittsburgh, as well as attending veterinarian D. Scorpio and animal program coordinators J. P. Todd, A. Taylor and H. Bao at the VRC, and BioQual, Inc. for expert animal care. We thank Flynn, Seder and Roederer laboratory members for discussions, Aeras members M. Fitzpatrick and J. Schaeffer for assistance with BCG, VRC NHP Immunogenicity Core for technical assistance, and VRC Flow Cytometry Core members for support. We are grateful to PARI Pharma GmbH for providing the eFlow nebulizer for use in this study.

Author contributions R.A.S., M.R. and J.L.F., conceived and designed experiments with P.A.D., D.J.L., A.K.S., C.A.S., D.C. and A.B. Pre-challenge data was generated at the NIH Vaccine Research Center under guidance of R.A.S. and M.R., who helped to write manuscript; P.A.D. wrote animal protocols, coordinated immunizations and NHP sampling, processed samples, designed flow cytometry panels (with M.R.), performed flow cytometry and analysis, created figures and helped write the manuscript. J.A.H. helped to develop staining panels, performed flow cytometry and analysis; M.H.W. and T.K.H. performed Seq-Well assays and transcriptional profiling analyses, and created figures with A.K.S., who helped to write the manuscript. S.P. performed antibody assays, BCG quantification in tissues, and flow cytometry with M.K.; P.A.S. performed PBMC adaptive and trained immunity assays and analysis. Post-challenge data were generated at the University of Pittsburgh under the oversight of J.L.F., who helped to write the manuscript; C.A.S. wrote animal protocols and coordinated all animal challenge experiments; J.J.Z. and M.A.R. processed samples and assessed immunology and microbiology post-challenge and performed data analysis; N.L.G. performed immunohistochemistry; C.M.C., P.L.L., E.K., J.L.F. and J.J.Z. performed animal procedures, necropsies and sample processing; P.M. and A.G.W. performed PET–CT scan, data and statistical analyses; J.J.Z. and P.M. generated figures from analysed data.

Competing interests Authors from University of Pittsburgh, NIH and MIT have no competing interests. A.B. is currently an employee of Vir Biotechnology, Inc., which is developing a CMV-based vaccine candidate for TB.

Additional information

Supplementary information is available for this paper at https://doi.org/10.1038/s41586-019-1817-8.

Correspondence and requests for materials should be addressed to R.A.S.

Peer review information *Nature* thanks Joel Ernst, Stefan Kaufmann and the other, anonymous, reviewer(s) for their contribution to the peer review of this work.

a

Group	Vaccine	BCG Route	Target Dose (CFU)	# of NHP Challenged
1	ID_{low}	Intradermal (1 site)	$5x10^5$	10
2	ID_{high}	Intradermal (2 sites)	$5x10^7$	8
3	IV	Intravenous	$5x10^7$	10
4	AE	Aerosol	$5x10^7$	10
5	AE/ID	Aerosol/Intradermal	$5x10^7$/ $5x10^5$	10
6	Unvax	Unvaccinated	N/A	4

b

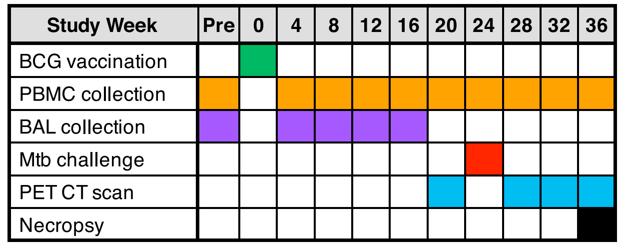

c

	Cohort	BCG Dose (CFU)			Duration	Challenge	Number of Macaques Per Arm							Total
		Low Dose ID	High Dose ID	High Dose IV, AE, EB	Time to Challenge (Weeks)	Mtb Dose (CFU)	ID low (n)	ID high (n)	IV (n)	AE (n)	AE/ID (n)	EB (n)	Unvax (n)	(n)
Immunology & Challenge	1	$3.5x10^5$	-	$5.2x10^7$	27	4	3	-	2	3	2	-	-	10
					29	16	2	-	3	2	3	-	-	10
	2	$3.1x10^5$	$2.9x10^7$	$3.7x10^7$	22/26	8	2	2	2	2	2	-	-	10
					24/28	11	2	2	2	2	2	-	-	10
	3	$3.1x10^5$	$2.9x10^7$	$3.7x10^7$	37/41	16	0	2	1	0	1	-	2	6
					38/42	36	1	2	0	1	0	-	2	6
Immunology Only	4	$2.1x10^6$	$4.7x10^7$	$3.7x10^7$	N/A	N/A	3	3	3	3	3	-	-	15
	5a	$1.6x10^5$	$1.9x10^7$	$2.5x10^7$	N/A	N/A	1	1	1	-	1	-	-	4
	5b	$2.2x10^6$	$2.2x10^7$	$1.2x10^7$	N/A	N/A	1	1	1	-	1	-	-	4
	5c	$1.5x10^6$	$4.3x10^7$	$2.4x10^7$	N/A	N/A	2	2	2	2	-	-	-	8
ivCD45	6	-	$7.4x10^7$	$3.6x10^7$	N/A	N/A	-	2	2	2	-	2	-	8
		BCG Dose (CFU)												
		Low Dose ID		High Dose IV or AE	Medium Dose IV or AE	Low Dose AE								
Immunology Pilot	Pilot a	$3.7x10^5$		$5.6x10^6$(AE)	$5.7x10^4$(AE)	$6.0x10^2$	3	-	-	-	9	-	-	12
	Pilot b	-		$2.1x10^7$(AE)	$2.7x10^5$(AE)	-		-	-	6	-	-	-	6
	Pilot c	-		$3.5x10^7$(IV)	$5.8x10^5$(IV)	-	-	-	6	-	-	-	-	6
	NHP (BCG or Unvax)						20	17	25	23	24	2	4	115
	NHP (TB Challenge)						10	8	10	10	10		4	52

Extended Data Fig. 1 | Study design, vaccine regimens, macaques and cohorts. a, Vaccine groups including route of BCG administration, target dose of BCG to be delivered (CFUs), and number of NHPs per BCG regimen ($n = 10$ macaques except ID_{high}, $n = 8$ macaques). Note that ID_{low} and ID_{high} groups received BCG in one or two sites, respectively, and AE/ID group received AE (high-dose) and ID (low-dose) BCG simultaneously. Unvaccinated macaques ($n = 4$) were used as Mtb challenge controls. **b**, Timeline for Mtb challenge cohorts including weeks relative to BCG vaccination for PBMC and BAL sample collection, Mtb challenge, PET–CT scanning, and scheduled necropsy after challenge. Macaques that met humane end-point criteria were euthanized earlier than 12 weeks post-challenge (Supplementary Table 1). **c**, Data are from a total of 115 rhesus macaques, 52 of which were challenged with Mtb. Owing to the ABSL-3 capacity constraints and logistical limits in the number of macaques that can be sampled, scanned by PET–CT, or necropsied at any given time point, studies were broken into sequentially immunized and/or challenged cohorts. A maximum of 20 NHPs were infected with Mtb in any challenge cohort with infections split over 2 days, staggered by 2 weeks. The actual doses of BCG administered, determined by subsequent culture, is noted for each vaccine group. The time interval between vaccination and challenge is noted in weeks and the challenge dose of Mtb (CFUs) is listed for each challenge cohort (BCG vaccine dose and Mtb challenge dose for individual NHPs, along with peak immune responses and detailed outcome data, is provided in Supplementary Table 1). Protection data are from 8–10 BCG-immunized NHPs per group and 4 unvaccinated controls in cohorts 1–3 ('Immunology & challenge'). Per protocol, BAL samples were not collected from animals 8 weeks before, or after, Mtb challenge. Three NHPs per vaccine group were immunized just as in cohorts 1–3 but were not challenged. Instead, these macaques (cohort 4; 'Immunology only') were sampled (BAL, PBMC) for 6 months after BCG immunization and then euthanized to perform extensive immune analysis in various tissues at what would have been the time of challenge. BAL samples from cohort 4 were transcriptionally profiled at weeks 13 and 25. Cohort 5 (a–c) includes 4 macaques per group (except AE and AE/ID groups, $n = 2$ NHPs each) that were immunized with BCG and were euthanized 1–3 months later to assess BCG CFUs and T cell responses in various tissues. NHPs in cohort 6 ('ivCD45', $n = 2$ macaques per group) received anti-CD45 injection before necropsy to distinguish blood- and tissue-derived cells. Pilot cohorts (a–c) include NHPs enrolled in the dose-finding pilot study ($n = 3$ macaques per dose and route; 'Immunology pilot').

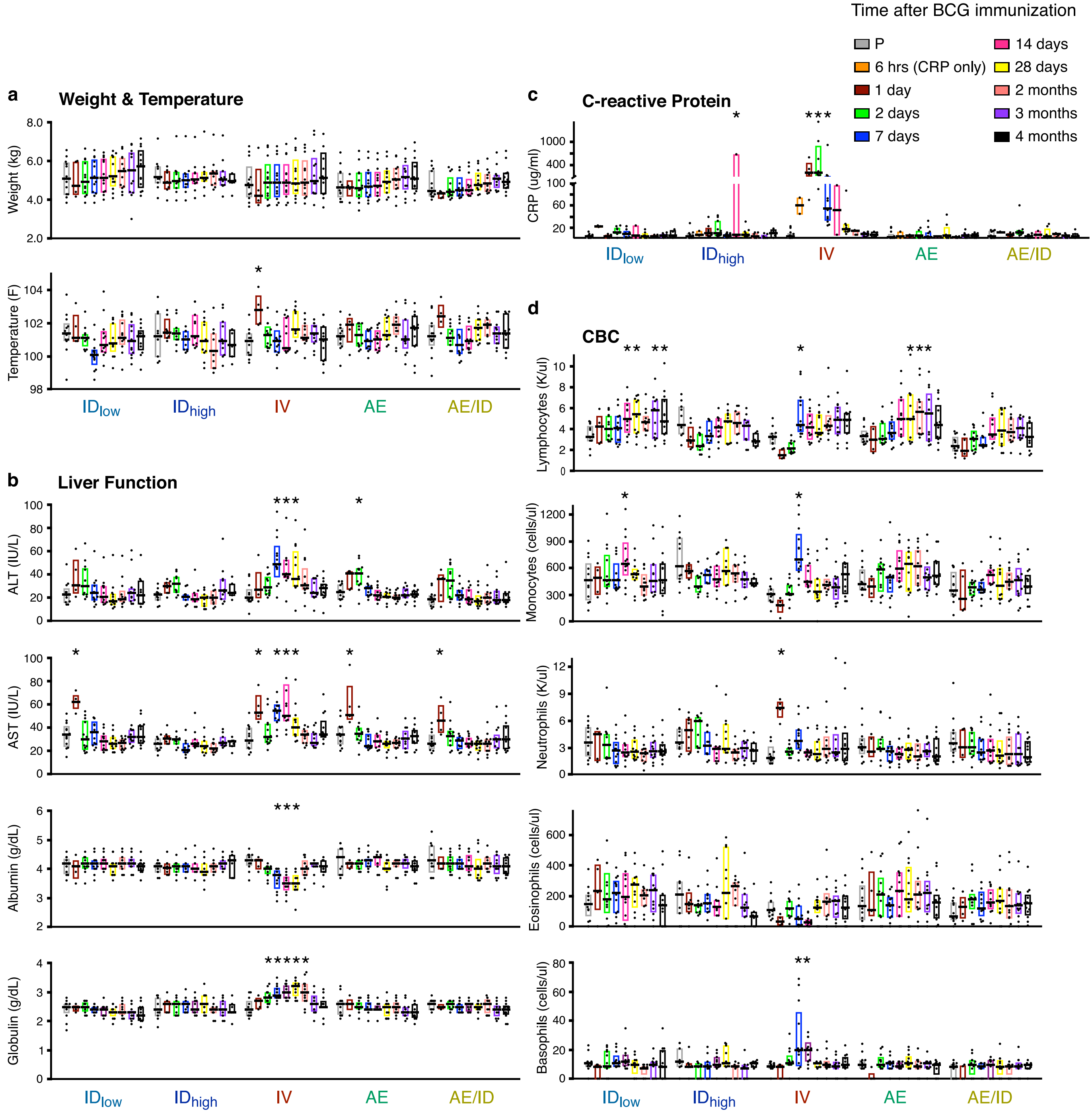

Extended Data Fig. 2 | Clinical parameters after BCG vaccination in NHPs. To assess safety of BCG vaccinations, all macaques (cohorts 1–4 excluding unvaccinated) were monitored for changes in several clinical parameters at various time points after BCG. After vaccination, changes were observed predominantly in IV BCG macaques; however, all were transient. **a**, Weight and temperature: there was a 0.9 °C increase in body temperature in the IV BCG group at day 1, which resolved by day 2; the average pre-vaccination temperature across all NHPs was 38.4 °C. **b**, Liver function tests (alanine aminotransferase (ALT), aspartate aminotransferase (AST), albumin and globulin): there was a twofold increase in ALT and AST above pre-vaccination levels (20–30 IU l^{-1}) in the IV BCG group, which resolved by day 28. **c**, C-reactive protein (CRP) in the IV BCG group increased up to a median of 400 μg ml^{-1} at day 2, which resolved by day 14; the average pre-vaccination CRP level in plasma across all NHPs ranged from 0 to 28 μg ml^{-1}. **d**, Complete blood counts (CBC). Transient increases in numbers of circulating neutrophils (day 1) and lymphocytes, monocytes and basophils (day 7) were observed in the IV BCG group. All tests were performed longitudinally on whole blood at time of collection except CRP, which was batch-analysed from frozen plasma samples; the 6-h time point was measured for CRP only. Data points shown are individual NHPs (n = 11–13 per group, n = 63 total) with interquartile range (box) and median (line). For each parameter, pre-vaccination (P) measurements for all NHPs were combined and compared against distributions from every vaccine group at every time point using Dunnett's test for multiple comparisons; $^*P < 0.05$. No clinical signals, such as lethargy, appetite suppression or weight loss, were observed up to time of Mtb challenge, 24 weeks later.

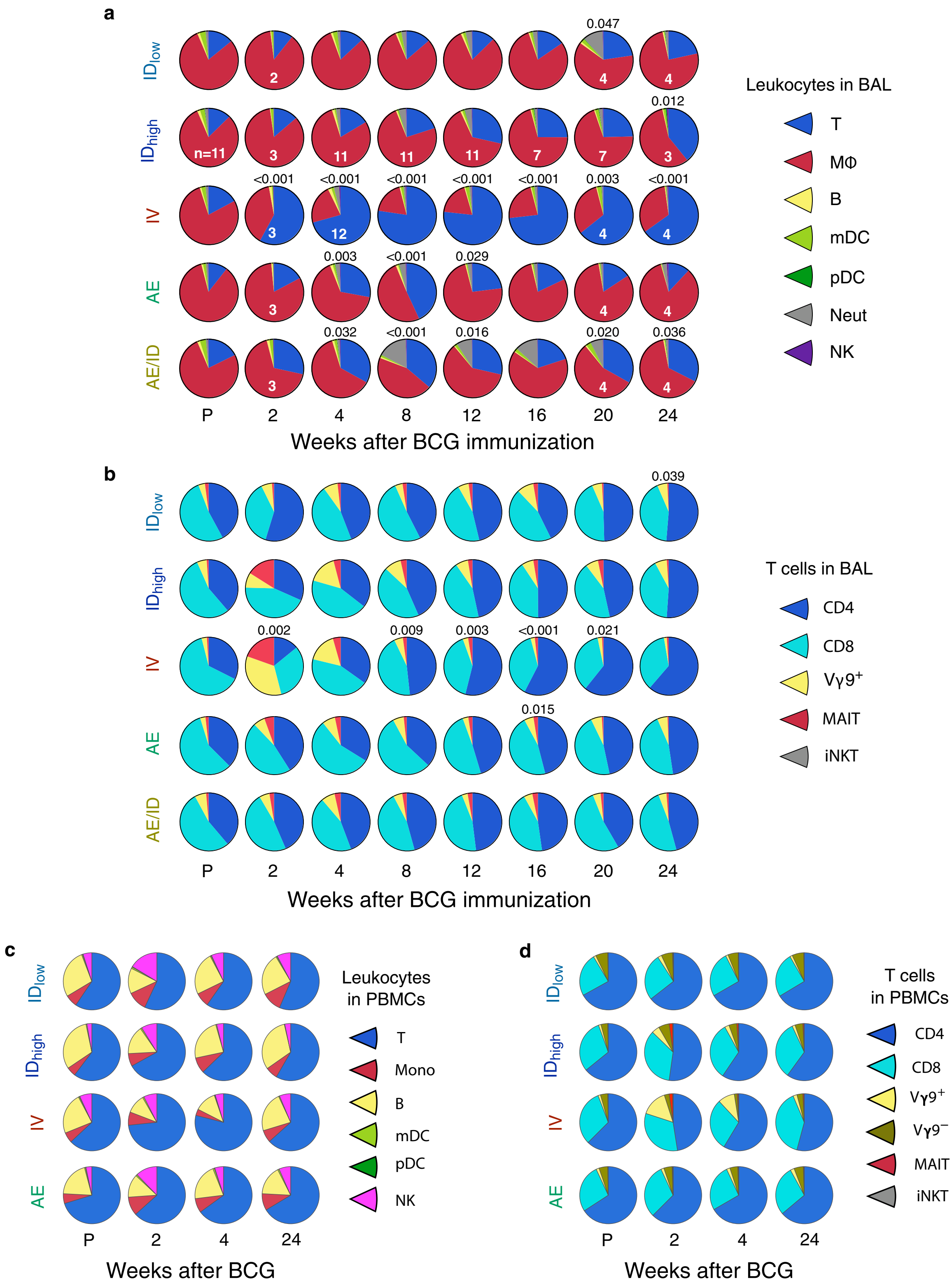

Extended Data Fig. 3 | See next page for caption.

Extended Data Fig. 3 | Proportions of leukocyte and T cell subsets in the BAL and PBMCs after BCG immunization. a–**d**, We assessed whether the composition of leukocytes in the BAL or PBMCs was altered after BCG vaccination. Shown are pie graphs comprising proportions of indicated leukocytes (**a**, **c**) or $CD3^+$ T cell subsets (**b**, **d**) in BAL (**a**, **b**) and PBMCs (**c**, **d**) for each BCG regimen from pre-vaccination up to 24 weeks post-BCG, identified using multi-parameter flow cytometry as in Supplementary Data 8. **a**, In the BAL, the rapid and sustained increase in T cell (but not macrophage) number (Fig. 1a and Supplementary Data 2b) altered the overall cellular composition of BAL from approximately 75% alveolar macrophages (red) and 15% T cells (blue) before vaccination to approximately 65% T cells and 30% macrophages, even 6 months after IV BCG. **b**, To delineate the composition of BAL T cells further, the proportions of CD4 and CD8 T cells, as well as non-classical T cells (γδ, MAIT and iNKT) that may also have a role in protection against TB[9–11] were assessed. Two weeks after vaccination, there was a substantial but transient increase in the proportion of $V\gamma9^+$ γδ T cells and MAIT cells after IV BCG, and a trend towards increased $V\gamma9^+$ γδ T cells and MAIT cells after BCG ID_{high}. However, by 8 weeks, the proportions of these non-classical T cells contracted to pre-vaccination levels. **c**, **d**, A similar analysis was performed to determine how the route of BCG immunization influenced the composition of leukocytes in PBMCs. Here, IV BCG induced a transient increase in $V\gamma9^+$ γδ T cells but not MAIT cells. BAL pie graphs represent the average proportions from 13 NHPs per BCG regimen (cohorts 1–4; Extended Data Fig. 1c) except where indicated (white numbers in **a** also apply to **b**). PBMC pie graphs represent the average proportions from three NHPs per BCG regimen (cohort 4). B, B cells; Mφ, macrophages; Mono, monocytes; T, T cells; Neut, neutrophils. *P* values indicate differences compared to pre-vaccination within the same vaccine group using a Permutation test.

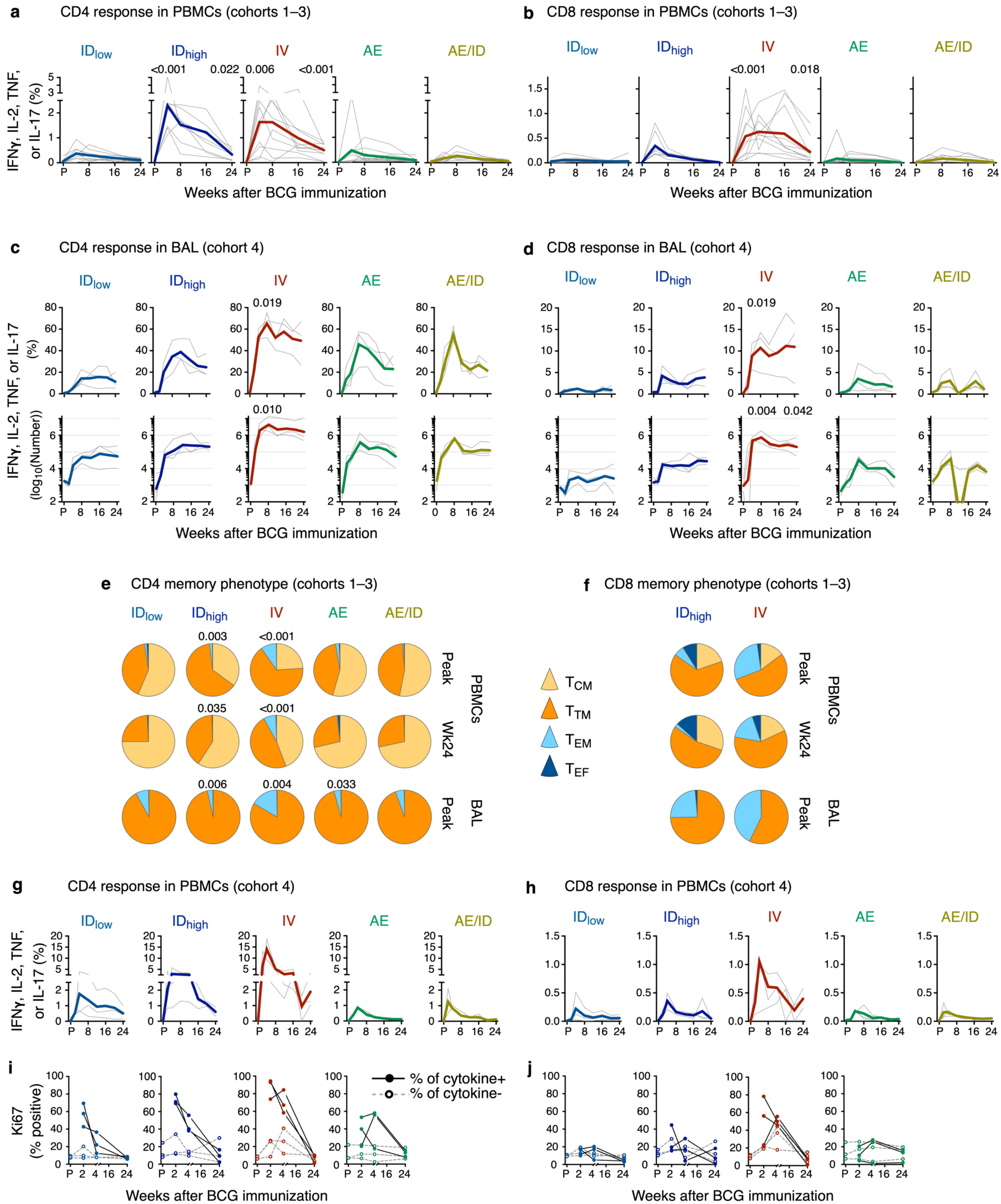

Extended Data Fig. 4 | See next page for caption.

Extended Data Fig. 4 | Extended immune data from challenge and immunology cohorts. a, **b**, Full kinetics of PBMC responses from NHPs in challenge cohorts (cohorts 1–3, $n = 8$–11 macaques) as in Fig. 1b, c. Shown is the frequency of memory CD4 (**a**) or CD8 (**b**) T cells producing any combination of IFNγ, IL-2, TNF or IL-17 in response to PPD stimulation at various time points before and up to 24 weeks after BCG. Grey lines are individual NHP responses; bold, coloured lines represent the median response. Each group was compared to ID_{low} at weeks 4 and 24 (one-way ANOVA; *P* values are Dunnett's multiple comparison test). **c**, **d**, T cell responses from a replicate cohort of similarly BCG-immunized rhesus macaques (cohort 4, $n = 3$ NHPs) from which BAL was collected for 24 weeks after BCG vaccination. Shown is the frequency (top) or absolute number ($\log_{10}$-transformed; bottom) of CD4 (**c**) or CD8 (**d**) memory T cells expressing any combination of IFNγ, IL-2, TNF or IL-17 in response to PPD stimulation, before and up to 24 weeks after BCG vaccination. Kruskal–Wallis test was used to compare each group to ID_{low} at weeks 8 (peak) and 24 (time of challenge); *P* values are Dunn's multiple comparison test. **e**, **f**, The memory phenotype of antigen-responsive CD4 (**e**) and CD8 (**f**) T cells in PBMCs and BAL at the peak of the response (week 4 for PBMC, week 8–12 for BAL; cohorts 1–3, $n = 8$–10 macaques) and time of challenge (week 24 collected for PBMC only) was assessed. Cytokine-positive T cells from PBMCs were categorized as central memory (T_{CM}), T_{TM}, effector memory (T_{EM}), or terminal effectors (T_{EF}) based on expression of CD45RA, CD28 and CCR7 as shown in Supplementary Data 10. Most responding cells in PBMCs were central memory and transitional memory T cells, with the proportion of transitional memory cells greater in ID_{high}- and IV-BCG-immunized NHPs compared with the ID_{low} group. In BAL, where T cells are CCR7-negative, most responding CD4 T cells were $CD45RA^{-}CD28^{+}$ T_{TM} cells (Supplementary Data 9). For CD8 memory phenotypes, pie graphs are shown only for groups that displayed measurable frequencies of cytokine^{+} CD8 T cells. IV-BCG-immunized NHPs had larger proportions of T_{EM} cells in PBMCs and BAL, which suggests a more diverse composition of memory and effector cells than other routes. *P* values indicate differences compared to ID_{low} using a permutation test (CD4 pie graphs only). **g**–**j**, PBMC T cell responses from a replicate cohort of similarly BCG-immunized rhesus macaques (cohort 4, $n = 3$ macaques). Shown is the frequency of CD4 (**g**) and CD8 (**h**) memory T cells producing any combination of IFNγ, IL-2, TNF or IL-17 in response to PPD stimulation before and up to 24 weeks after BCG. **i**, **j**, As an immunological indicator of recent antigen exposure and proliferation due to BCG persistence in vivo, Ki-67 expression in PBMCs over the course of immunization was assessed. Shown is the percentage of cytokine-positive (closed symbols, solid lines) or cytokine-negative (open symbols, dashed lines) memory CD4 or CD8 T cells expressing Ki-67 as identified in Supplementary Data 11. In IV-BCG-immunized NHPs, at least 60% of antigen-responsive CD4 T cells in blood were Ki-67^{+} at 2 and 4 weeks after BCG but were at baseline 6 months later.

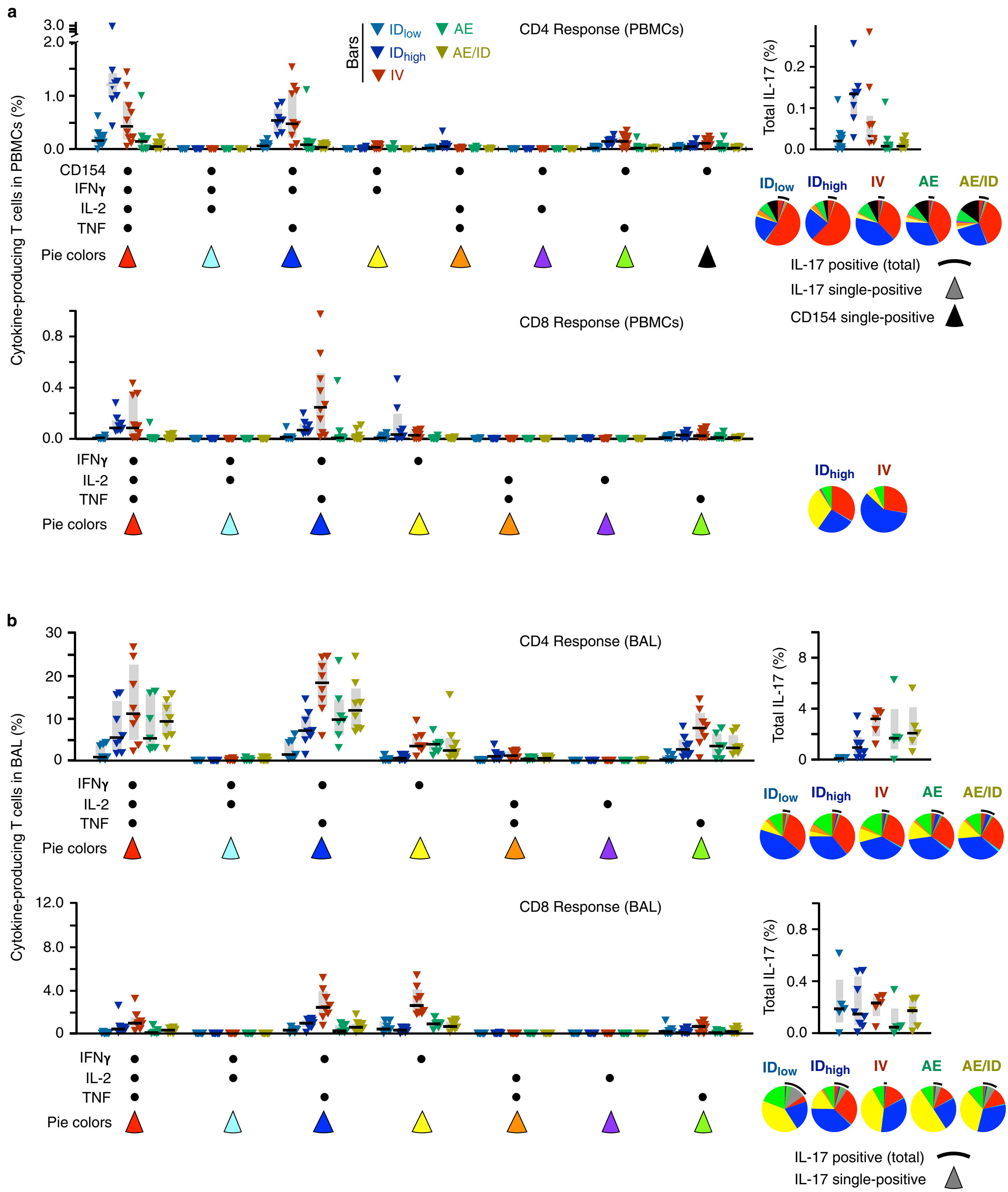

Extended Data Fig. 5 | See next page for caption.

Extended Data Fig. 5 | Quality of T cell responses in PBMCs and BAL after BCG immunization. The composition of the cytokine responses at the single-cell level, or 'quality' of the response, can reveal distinct functional differences that associate with protection against Mtb and other pathogens[19,20]. Here, the quality was defined by the relative proportion of antigen-stimulated cells producing every combination of IFNγ, IL-2 and TNF, with or without CD154 or IL-17. CD154 (also known as CD40L) expression in PBMCs was measured as a sensitive marker for detection of all antigen-stimulated CD4 T cells[21] based on evidence for CD4-dependent, IFNγ-independent mechanisms of protection against TB[22,23]. Shown are peak PPD-responsive memory CD4 and CD8 T cell responses in PBMCs (**a**, week 4) or BAL (**b**, week 12) after BCG vaccination for challenge cohorts 1–3 (n = 8–11 NHPs); analysis of all time points is shown in Supplementary Data 4 and 5. **a**, Bar graphs show the frequency of T cells in PBMCs expressing CD154 with IFNγ, IL-2, or TNF production, and total IL-17 production (CD4 response, top) or IFNγ, IL-2, or TNF for the CD8 response (bottom). Individual NHP responses are shown with interquartile range (bar) and median (horizontal line). Pie graphs represent the proportion of the total response comprising each cytokine combination, averaged for all NHPs, and are not shown for groups with low to undetectable responses. The proportion of the response producing IL-17 (with or without other cytokines) is indicated with a black arc and the proportion expressing CD154 alone is the black pie section. **b**, Bar graphs show the frequency of CD4 or CD8 T cells in BAL producing IFNγ, IL-2 or TNF, and total IL-17 production. Pie graphs represent the average proportion of total cytokine production comprising each cytokine combination; the proportion of the total response producing IL-17 (with or without other cytokines) is indicated with a black arc. Despite the notable differences in the magnitude of responses amongst BCG regimens, there were no differences in the quality of CD4 T cell responses nor CD8 T cell responses in PBMC or BAL. Of note, approximately 90% of the CD4 T cell responses were composed of T_H1 cytokines with fewer than 10% also producing IL-17; most IL-17 producing CD4 T cells co-expressed T_H1 cytokines.

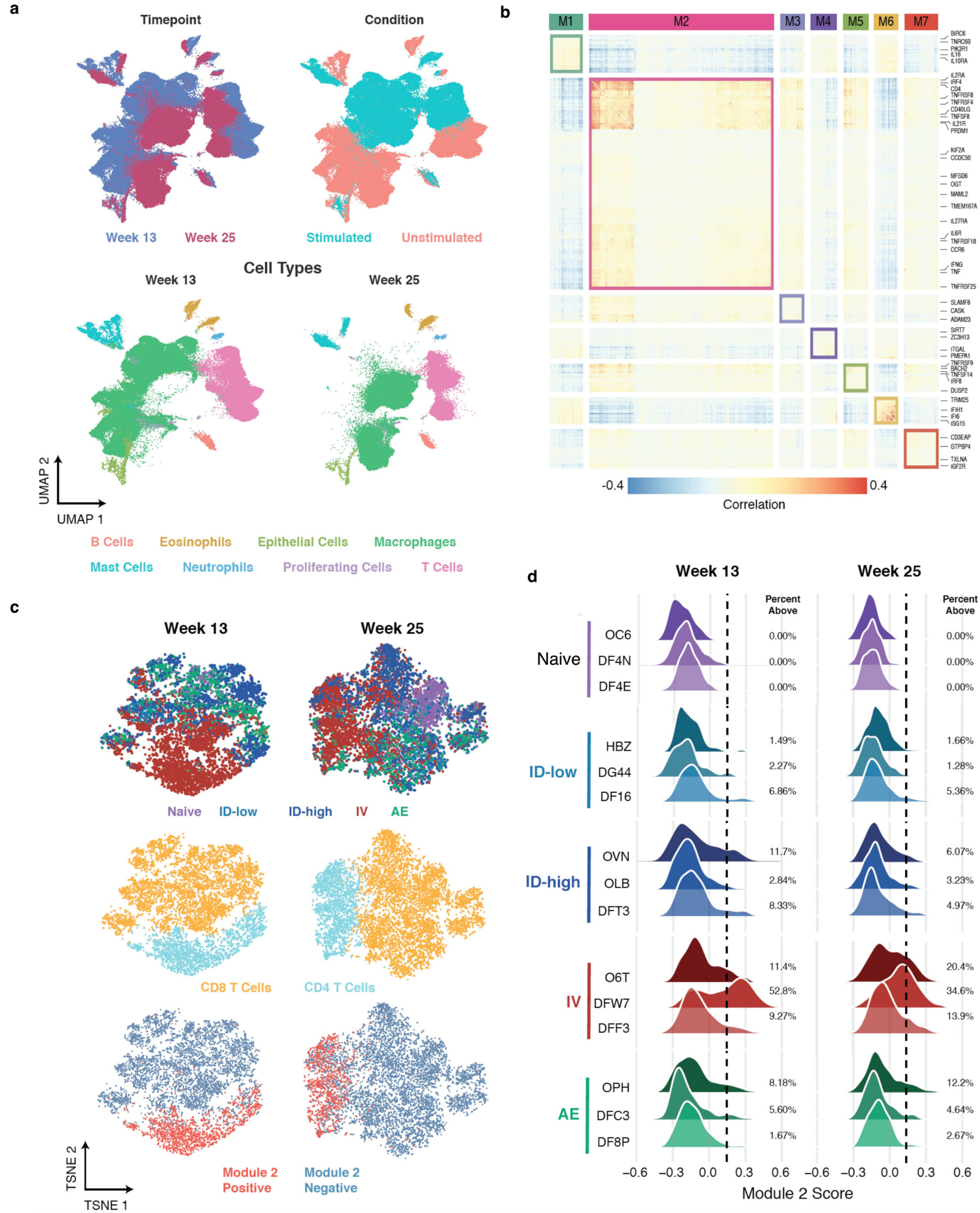

Extended Data Fig. 6 | See next page for caption.

Extended Data Fig. 6 | Identification of gene modules and distribution of module scores. A total of 162,490 single-cell transcriptomes derived from unstimulated and PPD-stimulated BAL cells from 15 NHPs (cohort 4, $n = 3$ per group) at weeks 13 (peak of BAL response) and 25 (time of challenge) were profiled. **a**, Uniform manifold approximation and projection (UMAP) plots of BAL cells at weeks 13 and 25 after BCG immunization, coloured by time point (top left), PPD stimulation condition (top right), and cell type (week 13, bottom left; week 25, bottom right). **b**, Gene–gene correlation heat map showing significant gene modules (M1–M7; top) identified among week 13 stimulated BAL T cells with select genes (right) highlighted. **c**, *t*-Distributed stochastic neighbour embedding (*t*-SNE) plots of stimulated BAL T cells from weeks 13 (left) and 25 (right), coloured by vaccine group (top), T cell subtypes (middle), and module 2-positivity (bottom). **d**, Histograms of the distribution of module 2 scores by vaccine group (colour) and macaque. Dashed line (placed at two s.d. above the mean score in the naive controls) indicates the threshold used to call cells as positive for the module. The percentage module 2-positive is shown for each NHP.

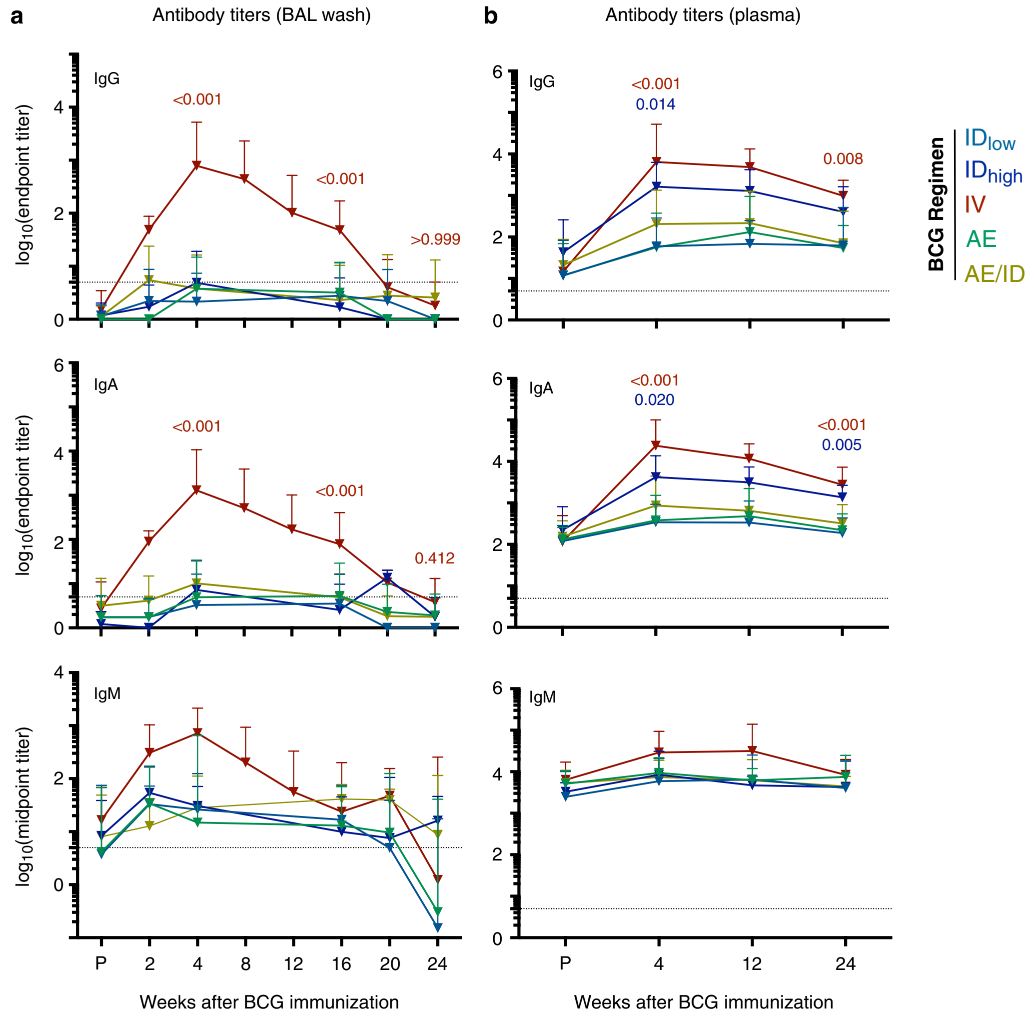

Extended Data Fig. 7 | Humoral immune response in BAL and plasma after BCG immunization. Mtb-responsive antibody responses were assessed in BAL and plasma after BCG immunization. Mtb WCL-specific IgG, IgA and IgM antibody titres were measured from individual NHPs at various time points before and after BCG immunization. Shown are end-point titres for IgG and IgA and mid-point titres for IgM (in which the end point was not reached) **a**, Antibody titres in tenfold-concentrated BAL fluid (cohorts 1–4, $n = 11$–13 macaques except at weeks 2, 20 and 24, cohort 4 only, $n = 3$ macaques). In concentrated BAL fluid, antigen-responsive IgG, IgA and IgM were detected only in IV-BCG-immunized NHPs and returned to pre-vaccination levels by the time of challenge. **b**, Antibody titres in plasma ($n = 11$–13 macaques). In plasma, both ID_{high} and IV BCG elicited increased IgG and IgA antibody responses compared to ID_{low} BCG. Data are geometric mean and s.d.; dashed line indicates assay limit of detection. A Kruskal–Wallis test was used to compare all vaccine groups to ID_{low} at weeks 4, 16 and 24 (BAL) or weeks 4 and 24 (plasma); *P* values are from Dunn's multiple comparison test (colour-coded to vaccine).

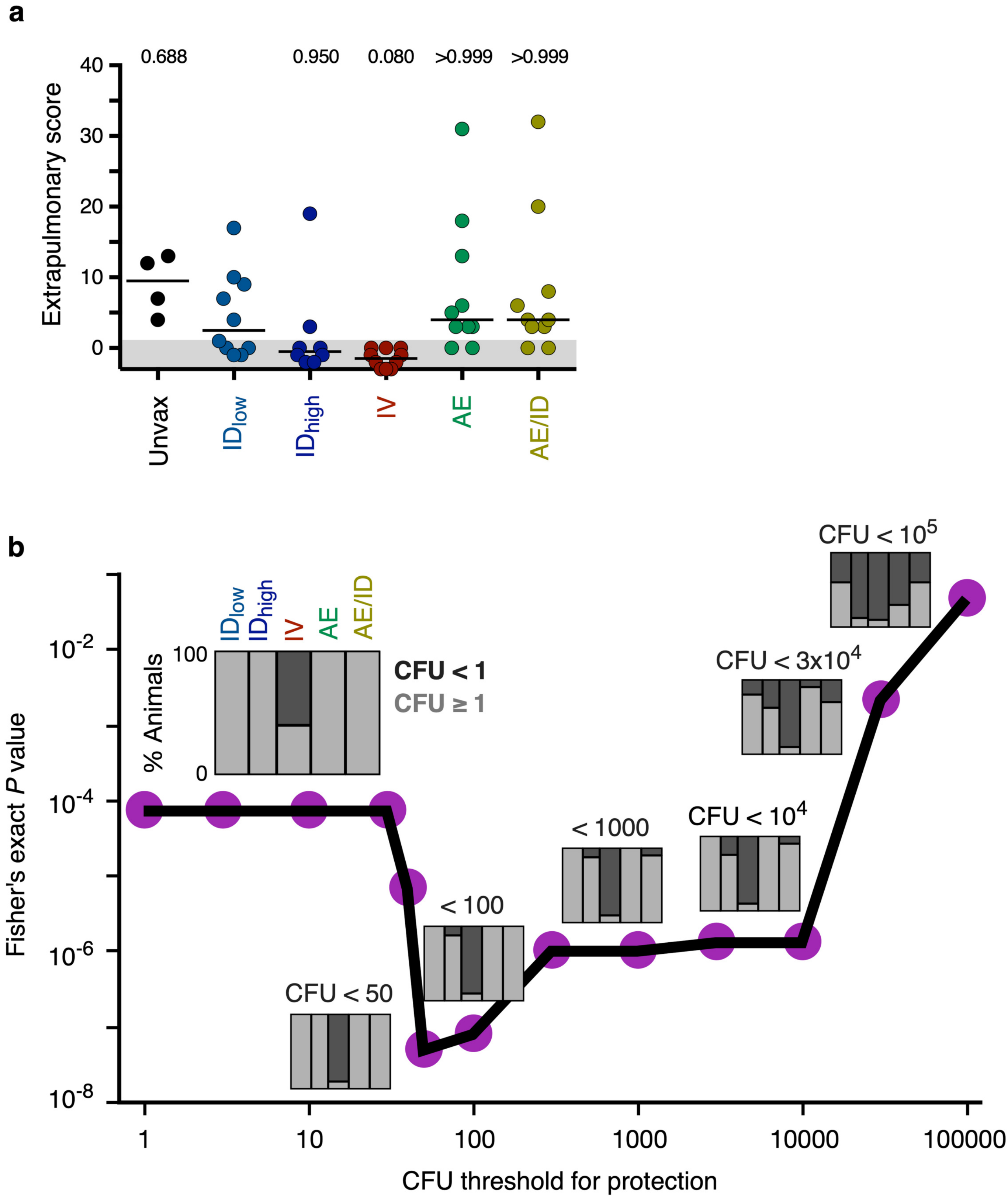

Extended Data Fig. 8 | IV BCG protects against extrapulmonary disease and lung infection across a wide range of thresholds of protection. **a**, Extrapulmonary disease was scored at necropsy based on a published system[27] taking into account the presence of Mtb-related pathology and Mtb growth from sites outside the thoracic cavity. Each symbol represents an animal and horizontal bars represent the median. Kruskal–Wallis tests were used and reported *P* values represent Dunn's multiple comparison test comparing each group to ID_{low}. All data points within the grey areas are zero. There was no extrapulmonary disease in any of the IV-BCG-vaccinated macaques, whereas the other groups had variable extrapulmonary involvement. **b**, Fisher's exact test *P* values are plotted for a range of CFU thresholds evaluating protection. For each threshold, a stacked bar plot indicates the percentage of NHPs with fewer CFUs than the threshold (that is, protected), in each vaccine group. Immunization route significantly ($P < 10^{-4}$) impacted protection at any given CFU threshold between <1 (sterile) and <10^4.

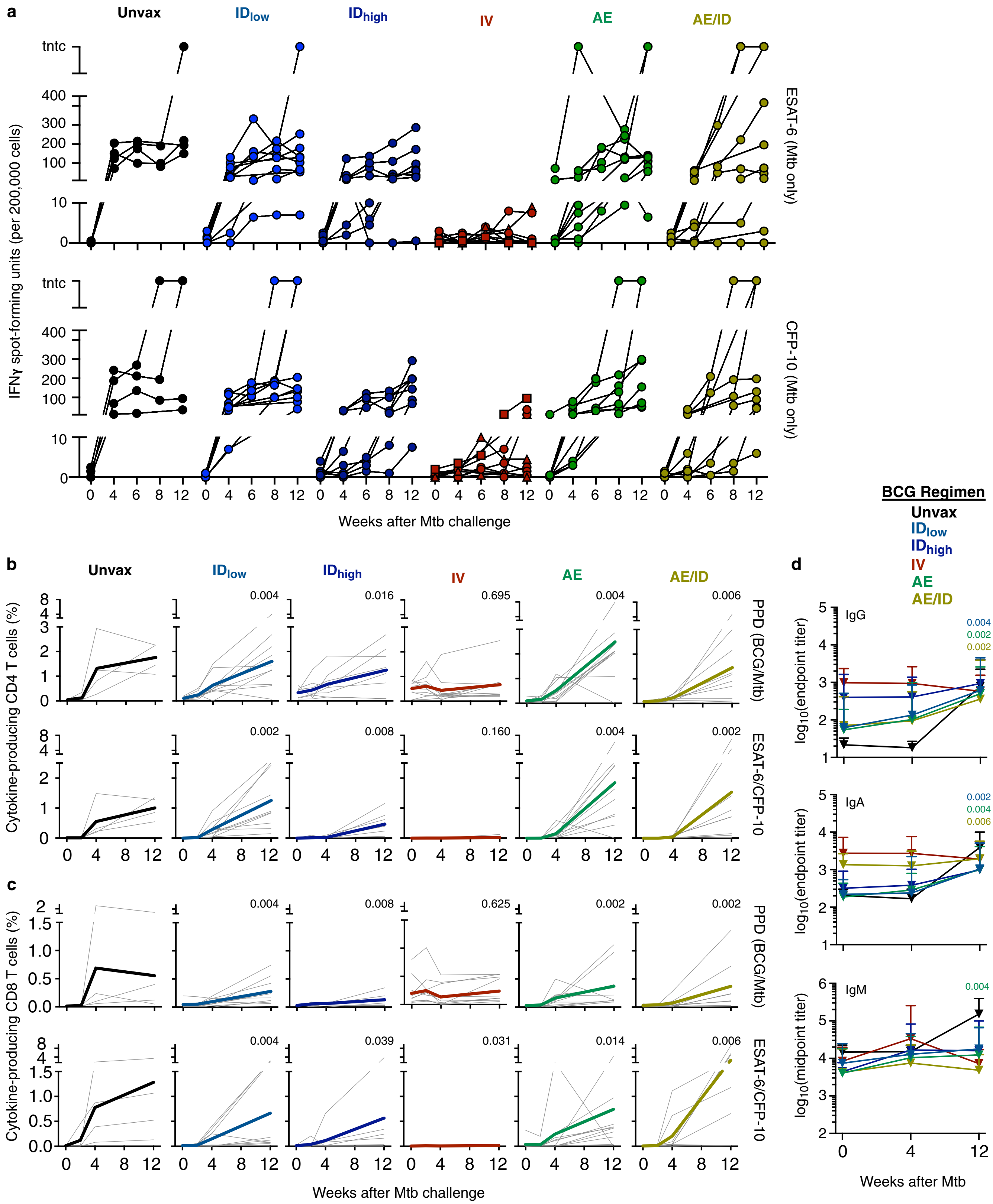

Extended Data Fig. 9 | See next page for caption.

Extended Data Fig. 9 | Post-challenge immune responses to mycobacterial antigens. a, PBMC response to ESAT-6 or CFP-10 peptides (antigens present in Mtb but not BCG) as determined by IFNγ ELISpot throughout Mtb infection. Each line is one NHP over time (*n* = 8–10 macaques; *n* = 4 unvaccinated); sterile animals are represented by a triangle, and non-sterile, protected animals (with 1 ≤ CFUs ≤ 50) denoted by squares. After infection, most animals in the AE or ID vaccine groups developed ESAT-6 or CFP10 ELISpot responses, which reflects a primary response to Mtb. By contrast, responses in the IV BCG group were lower than in the ID_{low} group at every time point after infection for ESAT-6 (4 weeks, $P = 0.001$; 6 weeks, $P = 0.045$; 8 weeks, $P = 0.025$; 12 weeks, $P = 0.006$) and CFP-10 (4 weeks, $P < 0.0001$; 6 weeks, $P = 0.035$; 8 weeks, $P = 0.001$; 12 weeks, $P = 0.004$). Kruskal–Wallis test was run at each time point with Dunn's adjusted *P* values reported accounting for comparisons of all groups against ID_{low}. **b**, **c**, The frequency of memory CD4 (**b**) and CD8 (**c**) T cells in PBMCs from BCG-immunized NHPs (*n* = 8–10) producing any combination of IFNγ, IL-2, TNF or IL-17 in response to stimulation with either PPD (antigen present in BCG and Mtb; top row) or pooled ESAT-6 and CFP-10 peptides (antigens present in Mtb only; bottom row) were measured at the time of challenge (0), and at 4, 8 and 12 weeks after Mtb challenge. Measurements from four unvaccinated, infected NHPs are included as controls (Unvax, black). Grey lines represent the responses of individual animals and bolded, coloured lines are the mean responses for each vaccine group. **d**, Antibody responses post-challenge. Mtb WCL-specific IgG, IgA and IgM antibody titres were measured in the plasma of unvaccinated (*n* = 4) and vaccinated (*n* = 8–10) NHPs at the time of challenge (0), and at 4 and 12 weeks after challenge. In **b**–**d**, Wilcoxon signed-rank unadjusted *P* values compare cytokine frequencies or antibody titres at week 12 after Mtb (or necropsy) to the time of challenge (week 0) within each vaccine group.

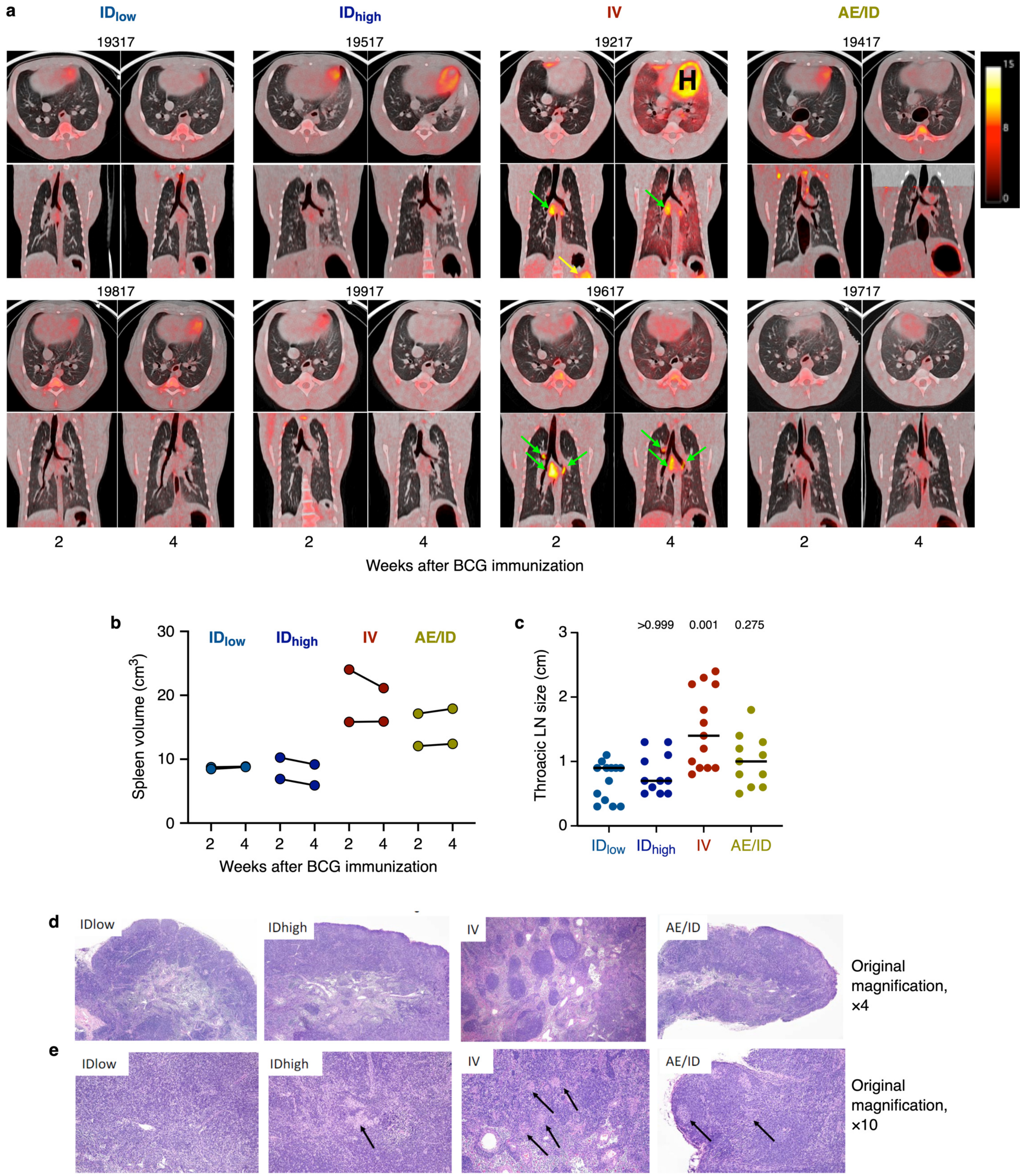

Extended Data Fig. 10 | See next page for caption.

Extended Data Fig. 10 | Inflammation and gross and histopathological assessment after BCG vaccination. **a**, Serial FDG PET–CT scans at 2 and 4 weeks after BCG vaccination showed increased metabolism (surrogate for inflammation) localized to the lung LNs (green arrows), lung lobes and spleen (yellow arrow) elicited by the IV but not by other routes (cohort 5a, b, $n = 2$ macaques). Warm colours indicate increased FDG retention; scale represents standardized uptake values. NHP ID numbers are listed above each scan; 'H' denotes the heart. **b**, Spleen volume was calculated from CT scans at 2 and 4 weeks after BCG vaccination ($n = 2$ macaques). At these time points, animals given IV BCG had approximately twofold larger spleens than those given ID BCG, with AE/ID BCG NHPs also displaying modestly enlarged spleens. **c**, Thoracic LNs were measured at necropsy, 4 weeks after BCG vaccination ($n = 2$ macaques); LNs from IV BCG NHPs were enlarged compared to those from ID_{low} NHPs. Kruskal–Wallis test was run; Dunn's adjusted P values are reported comparing each vaccine group to the ID_{low} group. **d**, **e**, H&E-stained sections of thoracic LNs from vaccinated NHPs ($n = 2$ macaques), 4 weeks after BCG vaccination. **d**, General structure with respect to cortical and medullary architecture and appearance was normal in LNs from ID_{low}, ID_{high} and AE/ID vaccinated NHPs. The thoracic LNs from the IV-vaccinated macaques demonstrated marked follicular lymphoid hyperplasia, with enlarged, prominent, variably sized follicles, often with active, expanded germinal centres. Original magnification, ×4. **e**, Small, non-necrotizing epithelioid histiocytic aggregates (non-necrotizing granulomas, black arrows) were abundantly disseminated within thoracic LNs from the IV BCG macaques. In the AE/ID NHPs, a wide nodal distribution of such lesions was also seen, although granuloma numbers and density were substantially less. The ID_{high} NHPs had only one observable granuloma in a single thoracic LN and in the ID_{low} NHPs, no such structures were evident. Original magnification, ×10.

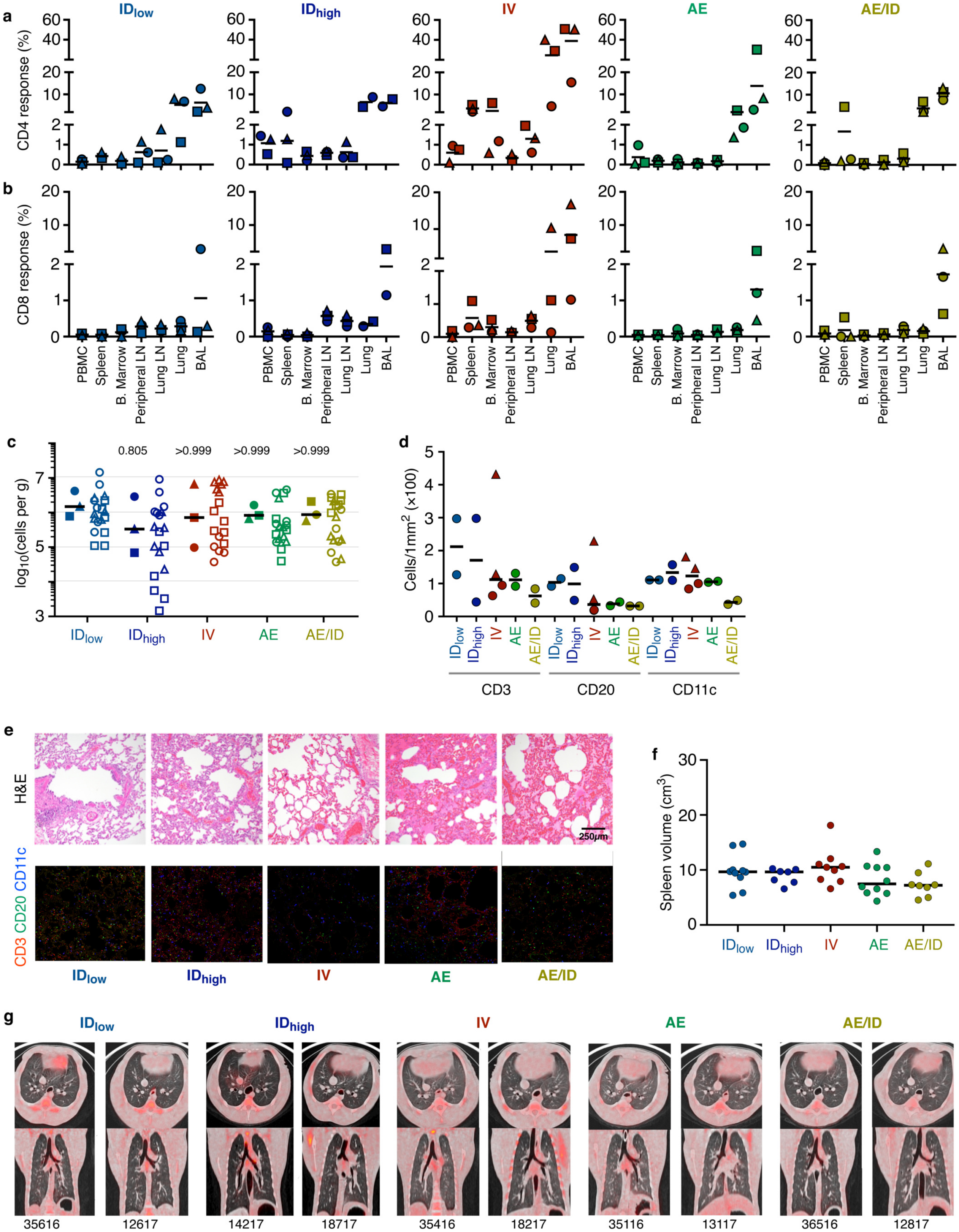

Extended Data Fig. 11 | See next page for caption.

Extended Data Fig. 11 | Immune response to BCG 6 months after vaccination. Analysis of tissue T cell responses, lung cell counts, immunohistochemistry, splenic volume and PET–CT scans was performed 6 months after BCG vaccination. **a**–**c**, A separate cohort (cohort 3, n = 3 macaques) was vaccinated with BCG in parallel to the challenge study with the purpose of assessing immune responses in various tissues 6 months after BCG (the time point at which macaques would be challenged). **a**, **b**, Frequency of memory CD4 (**a**) and CD8 (**b**) T cells producing any combination of IFNγ, IL-2, TNF, or IL-17 in response to Mtb WCL stimulation in the PBMC, spleen, bone marrow, peripheral LN, lung LN, lung tissue and BAL. Six months after IV BCG, immunized NHPs maintained increased frequencies of antigen-responsive T cells in spleen, BAL and lung lobes. Individual LN and lung lobe responses were averaged per macaque. Data points are individual macaques with symbols matched across tissues within a vaccine group; horizontal bar indicates the mean response. **c**, Number of cells recovered per gram of lung tissue for each NHP; the increased numbers of total cells observed at 1 month post-BCG (Fig. 3d) were not detected at 6 months post-BCG. Data are shown as the median of 3 macaques per group (solid symbols, counts from six lung lobes per animal are averaged) or as counts for individual lung lobes for each animal (open symbols; lobes from the same animal have matched symbols). Kruskal–Wallis test was used, and P values represent Dunn's multiple comparison test comparing each vaccine group to the ID_{low} group. **d**, Quantification of $CD3^+$, $CD20^+$, $CD11c^+$ cells from two lung sections (matched symbols) from 1–2 macaques per group using Cell Profiler. **e**, Representative 1-mm^2 lung sections from 1–2 macaques per vaccine group were stained with H&E or with antibodies against $CD3^+$ T cells (red), $CD20^+$ B cells (green), and $CD11c^+$ macrophages or dendritic cells (blue). Neither the increase in numbers of T cells and $CD11c^+$ cells nor the histopathological changes in lung sections from IV-BCG-immunized macaques observed at 1 month (Fig. 3e, f) were detected 6 months after BCG vaccination. **f**, Spleen volume was calculated from CT scans of 44 NHPs (cohorts 1–3) just before Mtb challenge (6 months after BCG vaccination) and was not significantly different among vaccine routes (Kruskal–Wallis test, P = 0.1643). Dots represent individual animals. **g**, Axial (top) and coronal (bottom) PET–CT scans of two representative macaques (n = 8–10) from each vaccine group 6 months after BCG, before Mtb infection. Animal ID numbers are shown below each set of scans. No detectable lung inflammation (FDG uptake) was observed in macaques from any vaccine group.

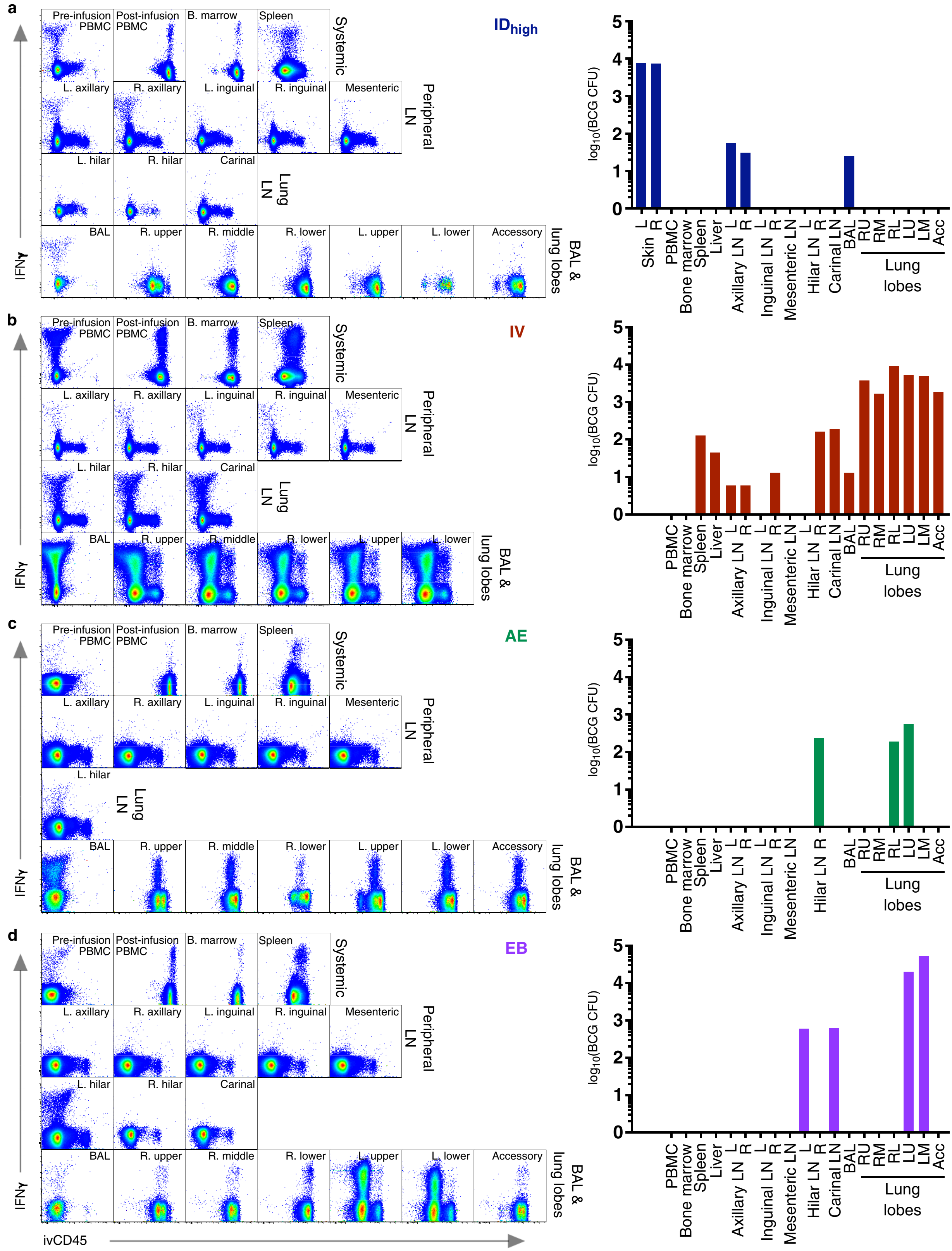

Extended Data Fig. 12 | See next page for caption.

Extended Data Fig. 12 | Determination of immune responses and BCG in tissues 1 month after immunization. NHPs (cohort 6, $n = 2$) were immunized with 5×10^7 BCG CFUs (ID_{high} (**a**), IV (**b**), AE (**c**), or EB (**d**)); BCG CFUs and antigen-responsive T cells were measured in various tissues 1 month later. Before euthanasia, a fluorochrome-conjugated anti-CD45 antibody was injected intravenously (ivCD45) such that circulating (intravascular) leukocytes were uniformly stained ($ivCD45^+$) while leukocytes in the tissue remained protected from staining ($ivCD45^-$). To investigate whether antigen-responsive ($IFN\gamma^+$) CD4 T cells were located in the $ivCD45^-$ lung tissue compartment, cells isolated from lung lobes were re-stimulated in vitro with Mtb WCL and analysed by intracellular cytokine staining. FACS plots show memory CD4 T cells in all tissues collected from one of two NHPs per BCG regimen, organized by type/location (systemic, peripheral LN, lung LN, BAL and lung lobes). The BAL and lung responses from the IV BCG NHPs, shown in the bottom row of **b**, is reproduced from Fig. 4b. Pre-infusion PBMC indicates PBMCs isolated from whole blood collected just before anti-CD45 injection. Bar graphs show the number of BCG CFUs in each respective tissue for each animal (colour-coded by vaccine), if detected.

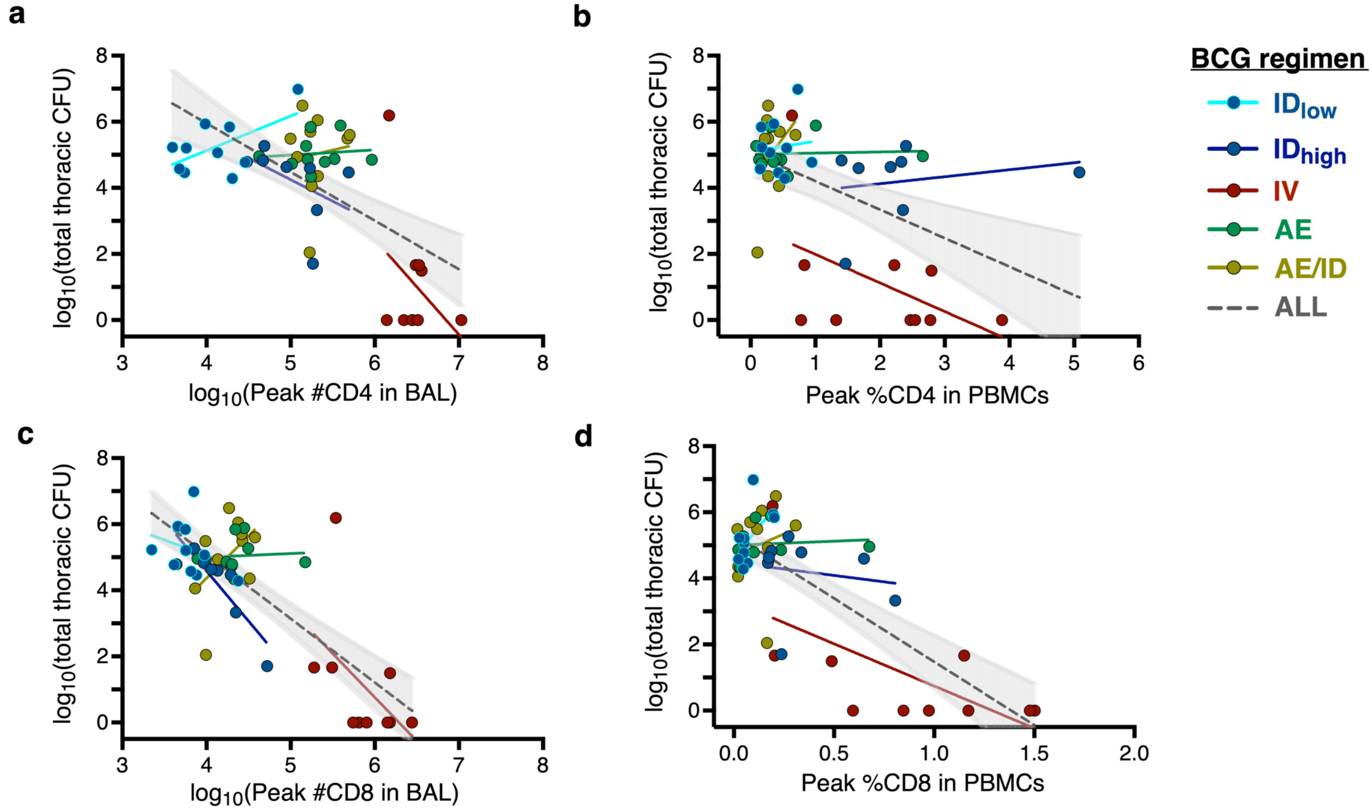

Extended Data Fig. 13 | Relationships between peak T cell responses in BAL or PBMCs and total CFUs at necropsy. a–d, Linear regressions were used to test whether antigen-responsive CD4 (**a**, **b**) or CD8 (**c**, **d**) T cell numbers (BAL; **a**, **c**) or frequencies (PBMC; **b**, **d**) after BCG immunization are associated with disease severity (total CFUs). Results indicate that when controlling for all vaccine routes, peak CD4 T cells in the BAL and PBMC, and peak CD8 T cells in the BAL do not have a significant association with total CFUs (Supplementary Table 5a–c). Of note, in PBMCs, higher peak CD8 frequencies are associated with lower total CFUs after controlling for route (Supplementary Table 5d). Each dot represents an individual animal; coloured lines represent linear fit for each vaccine route. Dotted black lines represent linear fit for all vaccine routes combined (with 95% confidence interval shaded in grey).

nature research

Corresponding author(s): Robert Seder

Last updated by author(s): Oct 25, 2019

Reporting Summary

Nature Research wishes to improve the reproducibility of the work that we publish. This form provides structure for consistency and transparency in reporting. For further information on Nature Research policies, see Authors & Referees and the Editorial Policy Checklist.

Statistics

For all statistical analyses, confirm that the following items are present in the figure legend, table legend, main text, or Methods section.

n/a	Confirmed	
☐	☒	The exact sample size (*n*) for each experimental group/condition, given as a discrete number and unit of measurement
☐	☒	A statement on whether measurements were taken from distinct samples or whether the same sample was measured repeatedly
☐	☒	The statistical test(s) used AND whether they are one- or two-sided *Only common tests should be described solely by name; describe more complex techniques in the Methods section.*
☐	☒	A description of all covariates tested
☐	☒	A description of any assumptions or corrections, such as tests of normality and adjustment for multiple comparisons
☐	☒	A full description of the statistical parameters including central tendency (e.g. means) or other basic estimates (e.g. regression coefficient) AND variation (e.g. standard deviation) or associated estimates of uncertainty (e.g. confidence intervals)
☐	☒	For null hypothesis testing, the test statistic (e.g. *F*, *t*, *r*) with confidence intervals, effect sizes, degrees of freedom and *P* value noted *Give P values as exact values whenever suitable.*
☒	☐	For Bayesian analysis, information on the choice of priors and Markov chain Monte Carlo settings
☒	☐	For hierarchical and complex designs, identification of the appropriate level for tests and full reporting of outcomes
☐	☒	Estimates of effect sizes (e.g. Cohen's *d*, Pearson's *r*), indicating how they were calculated

Our web collection on statistics for biologists contains articles on many of the points above.

Software and code

Policy information about availability of computer code

Data collection	DiVa v7; OsiriX MD v.10.0.1
Data analysis	FlowJo v9.9.6; JMP v13; Prism v6, Excel v16.25, Pestle v1.6; SPICE v5.0; R

For manuscripts utilizing custom algorithms or software that are central to the research but not yet described in published literature, software must be made available to editors/reviewers. We strongly encourage code deposition in a community repository (e.g. GitHub). See the Nature Research guidelines for submitting code & software for further information.

Data

Policy information about availability of data

All manuscripts must include a data availability statement. This statement should provide the following information, where applicable:

- Accession codes, unique identifiers, or web links for publicly available datasets
- A list of figures that have associated raw data
- A description of any restrictions on data availability

See Mss Lines 825-835

Field-specific reporting

Please select the one below that is the best fit for your research. If you are not sure, read the appropriate sections before making your selection.

☒ Life sciences ☐ Behavioural & social sciences ☐ Ecological, evolutionary & environmental sciences

For a reference copy of the document with all sections, see nature.com/documents/nr-reporting-summary-flat.pdf

Life sciences study design

All studies must disclose on these points even when the disclosure is negative.

Sample size	See Mss Lines 869-880 (M&M, "Animals")
Data exclusions	No data excluded
Replication	See Extended Data Figure 1
Randomization	See Mss Lines 883-885 (M&M "BCG Vaccination")
Blinding	Pathologists performing the necropsies, analysts reading PET-CT scans, and technicians processing tissues were blinded from treatment group

Reporting for specific materials, systems and methods

We require information from authors about some types of materials, experimental systems and methods used in many studies. Here, indicate whether each material, system or method listed is relevant to your study. If you are not sure if a list item applies to your research, read the appropriate section before selecting a response.

Materials & experimental systems

n/a	Involved in the study
☐	☒ Antibodies
☒	☐ Eukaryotic cell lines
☒	☐ Palaeontology
☐	☒ Animals and other organisms
☒	☐ Human research participants
☒	☐ Clinical data

Methods

n/a	Involved in the study
☒	☐ ChIP-seq
☐	☒ Flow cytometry
☒	☐ MRI-based neuroimaging

Antibodies

Antibodies used	See Suppl Data 8-11
Validation	All monoclonal antibodies used for flow cytometry were titrated to obtain optimal signal to noise, comparing the specific staining to a gold standard or previously published monoclonal antibody to ensure the staining is biologically appropriate.

Animals and other organisms

Policy information about studies involving animals; ARRIVE guidelines recommended for reporting animal research

Laboratory animals	See Mss Lines 857-867 (M&M, "Animals")
Wild animals	N/A
Field-collected samples	N/A
Ethics oversight	See Mss Lines 857-867 (M&M, "Animals")

Note that full information on the approval of the study protocol must also be provided in the manuscript.

Flow Cytometry

Plots

Confirm that:

☐ The axis labels state the marker and fluorochrome used (e.g. CD4-FITC).

☒ The axis scales are clearly visible. Include numbers along axes only for bottom left plot of group (a 'group' is an analysis of identical markers).

☒ All plots are contour plots with outliers or pseudocolor plots.

☒ A numerical value for number of cells or percentage (with statistics) is provided.

Methodology

Sample preparation	See mss Lines 972-1002 (M&M Multiparameter Flow Cytometry)
Instrument	BD LSR II and BD Symphony A5
Software	Diva v7 and FlowJo v9.9.6
Cell population abundance	N/A
Gating strategy	See Supplemental data 8-11

☒ Tick this box to confirm that a figure exemplifying the gating strategy is provided in the Supplementary Information.

Article

Mutations that prevent caspase cleavage of RIPK1 cause autoinflammatory disease

https://doi.org/10.1038/s41586-019-1828-5

Received: 5 March 2019

Accepted: 17 October 2019

Published online: 11 December 2019

Najoua Lalaoui[1,2,17]*, Steven E. Boyden[3,17]*, Hirotsugu Oda[3,17], Geryl M. Wood[3], Deborah L. Stone[3], Diep Chau[1], Lin Liu[1,2], Monique Stoffels[3], Tobias Kratina[1], Kate E. Lawlor[4,5], Kristien J. M. Zaal[6], Patrycja M. Hoffmann[3], Nima Etemadi[1,2], Kristy Shield-Artin[1,2], Christine Biben[1,2], Wanxia Li Tsai[7], Mary D. Blake[7], Hye Sun Kuehn[8], Dan Yang[9], Holly Anderton[1,2], Natasha Silke[1], Laurens Wachsmuth[10,11], Lixin Zheng[12], Natalia Sampaio Moura[3], David B. Beck[3], Gustavo Gutierrez-Cruz[13], Amanda K. Ombrello[3], Gineth P. Pinto-Patarroyo[3], Andrew J. Kueh[1,2], Marco J. Herold[1,2], Cathrine Hall[1], Hongying Wang[3], Jae Jin Chae[3], Natalia I. Dmitrieva[9], Mark McKenzie[1,2], Amanda Light[1], Beverly K. Barham[3], Anne Jones[3], Tina M. Romeo[3], Qing Zhou[3], Ivona Aksentijevich[3], James C. Mullikin[14], Andrew J. Gross[15], Anthony K. Shum[16], Edwin D. Hawkins[1,2], Seth L. Masters[1,2], Michael J. Lenardo[12], Manfred Boehm[9], Sergio D. Rosenzweig[8], Manolis Pasparakis[10,11], Anne K. Voss[1,2], Massimo Gadina[7], Daniel L. Kastner[3,18]* & John Silke[1,2,18]*

RIPK1 is a key regulator of innate immune signalling pathways. To ensure an optimal inflammatory response, RIPK1 is regulated post-translationally by well-characterized ubiquitylation and phosphorylation events, as well as by caspase-8-mediated cleavage[1–7]. The physiological relevance of this cleavage event remains unclear, although it is thought to inhibit activation of RIPK3 and necroptosis[8]. Here we show that the heterozygous missense mutations D324N, D324H and D324Y prevent caspase cleavage of RIPK1 in humans and result in an early-onset periodic fever syndrome and severe intermittent lymphadenopathy—a condition we term 'cleavage-resistant RIPK1-induced autoinflammatory syndrome'. To define the mechanism for this disease, we generated a cleavage-resistant *Ripk1*^{D325A} mutant mouse strain. Whereas *Ripk1*$^{-/-}$ mice died postnatally from systemic inflammation, *Ripk1*$^{D325A/D325A}$ mice died during embryogenesis. Embryonic lethality was completely prevented by the combined loss of *Casp8* and *Ripk3*, but not by loss of *Ripk3* or *Mlkl* alone. Loss of RIPK1 kinase activity also prevented *Ripk1*$^{D325A/D325A}$ embryonic lethality, although the mice died before weaning from multi-organ inflammation in a RIPK3-dependent manner. Consistently, *Ripk1*$^{D325A/D325A}$ and *Ripk1*$^{D325A/+}$ cells were hypersensitive to RIPK3-dependent TNF-induced apoptosis and necroptosis. Heterozygous *Ripk1*$^{D325A/+}$ mice were viable and grossly normal, but were hyper-responsive to inflammatory stimuli in vivo. Our results demonstrate the importance of caspase-mediated RIPK1 cleavage during embryonic development and show that caspase cleavage of RIPK1 not only inhibits necroptosis but also maintains inflammatory homeostasis throughout life.

Members of three families presented with a previously undescribed autoinflammatory disorder characterized by fevers and pronounced lymphadenopathy beginning in early childhood and continuing throughout adulthood (Fig. 1a) From birth or shortly thereafter, all affected individuals experienced fevers usually occurring approximately every 2–4 weeks, lasting 1–7 days, and reaching temperatures as high as 40–41 °C. Some individuals reported extreme chills, severe headaches, and/or hallucinations that coincided with their fevers. These flares were accompanied by intermittent episodes of cervical, axillary, inguinal and/or periaortic lymphadenopathy that often caused pain or discomfort (Fig. 1b, Table 1). Several individuals experienced splenomegaly and/or hepatomegaly, which were generally more prominent early in life, as well as oral ulcers, arthralgia or gastrointestinal symptoms such as abdominal pain, nausea, diarrhoea, constipation, loss of appetite or weight loss (Table 1). Patient 7 (P7) exhibited a more chronic inflammation with acute exacerbation. Study participants often had increased levels of inflammatory markers even during symptom-free periods. In contrast to some more severe autoinflammatory disorders, there were no signs of rash, arthritis, genital ulcers or end-stage organ damage and the condition was not life-threatening in any of the patients (Table 1).

Lymphocyte counts were normal between flares in the seven affected participants (Extended Data Table 1). However, pro-inflammatory cytokines were increased in the serum from P7 when inflamed but not

A list of affiliations appears at the end of the paper.

during a flare (Fig. 1c). Transcriptomic analysis from P7 whole-blood RNA revealed an enrichment of several inflammatory gene signatures (Fig. 1d, Extended Data Fig. 1a, b). Affected members of family 2 had all taken prednisone during flares, with varying degrees of acute relief but without long-term prevention of future episodes (Table 1). Participants P1, P6 and P7 had tonsillitis (Table 1), but tonsillectomy did not improve symptoms. Similarly, the IL-1 receptor antagonist, anakinra, and the TNF antagonist, etanercept, did not suppress inflammation in patients P1, P2, P4 or P7 (Table 1). However, treatment with the IL-6 receptor antagonist tocilizumab markedly, and in some cases severely, reduced the severity and frequency of the symptoms of P1, P2, P3, P6 and P7 (Fig. 1e, Table 1, Extended Data Table 2a). Tocilizumab also provided some initial relief to P4, but P4 reported aggravation of pre-existing oral ulcers, and P6 reported eventual onset of hand pain, and both participants elected to discontinue treatment (Table 1).

Identification of pathogenic mutations in *RIPK1*

Exome sequencing in P1 and her unaffected parents and all eight members of family 2 revealed that *RIPK1* was the only gene in which a variant from both families satisfied filtering criteria. A third mutation in *RIPK1* was later discovered in family 3. Affected individuals from the three families had different heterozygous missense mutations at the same crucial aspartate residue required for RIPK1 cleavage by caspase-8 (Fig. 1f). The D324N and D324Y mutations occurred de novo in families 1 (Extended Data Fig. 2) and 3, respectively, whereas D324H was inherited in an autosomal dominant pattern in family 2. These mutations are not reported in variant databases (Extended Data Table 2b), and none of the families had rare co-segregating coding or splice mutations in genes previously implicated in autoimmune lymphoproliferative syndrome (ALPS) or other monogenic autoinflammatory disorders. Mutations in the RIPK1 cleavage site were not found in an additional 554 individuals with sporadic unexplained fever, lymphadenopathy, ALPS or idiopathic Castleman disease that we screened by Sanger or targeted hybrid capture sequencing (Extended Data Table 2c). We therefore designated this condition as cleavage-resistant RIPK1-induced autoinflammatory (CRIA) syndrome.

The optimal caspase-8 cleavage motif is highly conserved in vertebrates (Fig. 1g, Extended Data Table 3). RIPK1 can be cleaved by both caspase-6 and caspase-8, yielding products of similar size, although the caspase-6 cleavage site has not been defined[9–11]. Consistent with these reports, RIPK1 mutants found in the patients—as well as the D324A mutant that has previously[6] been shown to prevent RIPK1 cleavage by caspase-8—were resistant to both caspase-6 and caspase-8 cleavage in vitro, which suggests that the cleavage sites of caspase-6 and caspase-8 are the same (Fig. 1h).

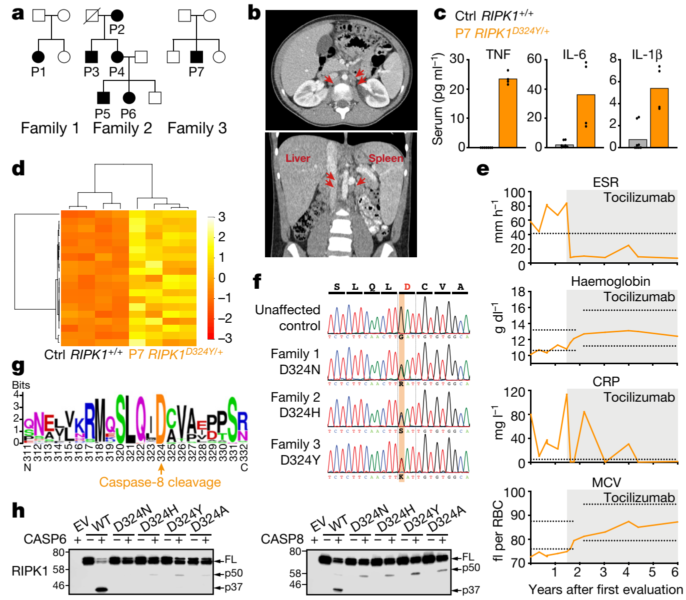

Fig. 1 | Heterozygous mutations of the RIPK1 caspase-8 cleavage site cause autoinflammatory disease. a, Affected individuals (filled symbols) in three families carried mutations in RIPK1 D324. Crossed symbol indicates a deceased individual. **b**, Axial (top) and coronal (bottom) planes of abdominal computerized tomography scans of participant P1 at age 11, after 2 months on tocilizumab but before substantial resolution of symptoms, revealing periaortic lymphadenopathy (arrows), splenomegaly (14 cm craniocaudal length), and liver at upper limit of normal (16 cm craniocaudal length). **c**, Serum cytokine levels of two P7 samples taken within 1 week, both during infliximab and before tocilizumab treatment, and four unrelated adolescent controls (ctrl). Dots are from technical duplicates for each time point. Graphs show mean. **d**, RNA sequencing of whole-blood RNA from P7 (two time points, as in **c**) and two unrelated adolescent unaffected controls, both with technical duplicates. Heat map shows differentially expressed inflammatory response genes (GO: 0006954). For gene names, see Supplementary Fig. 1. **e**, Response to tocilizumab infusion in P1. Erythrocyte sedimentation rate (ESR), C-reactive protein (CRP), haemoglobin and mean corpuscular volume (MCV) were measured serially before and after the start of tocilizumab treatment (grey shading). Time after the initial evaluation of this subject at age 10 years is depicted on the *x* axis. Horizontal lines indicate high values (ESR and CRP) or high and low values (haemoglobin and MCV) for the subject age-specific laboratory reference ranges for these markers. RBC, red blood cell count. **f**, *RIPK1* DNA sequence chromatograms show heterozygous single-base substitutions. **g**, WebLogo demonstrating conservation of the caspase-8 cleavage tetrapeptide motif in RIPK1 (human numbering) in 184 vertebrate species. **h**, In vitro caspase assays on wild-type (WT) and RIPK1 mutants. Western blots are representative of two independent experiments. For gel source data, see Supplementary Fig. 2.

Lack of RIPK1 cleavage causes embryonic lethality

To investigate the molecular mechanism for CRIA syndrome and characterize the role of RIPK1 cleavage in vivo, we generated RIPK1 cleavage-resistant mice. Rather than choosing one of the disease-associated variants, we mutated the aspartate to alanine. Although the heterozygous $Ripk1^{D325A/+}$ mice were viable and grossly normal, the homozygous $Ripk1^{D325A/D325A}$ mice died during mid-embryogenesis; much earlier than the postnatal lethality of the $Ripk1^{-/-}$ mice[12–15] (Fig. 2a, Extended Data Fig. 3a). $Ripk1^{D325A/D325A}$ lethality occurred between embryonic day 10.5 (E10.5) and E11.5, with the embryos showing several sites of mild-to-severe haemorrhage beginning in the cephalic vascular plexus, in the midbrain and hindbrain, but ultimately affecting the entire embryo including the pharyngeal arches and the pericardial space (Fig. 2a). At E11.5, all $Ripk1^{D325A/D325A}$ embryos were dead and displayed major haemorrhage in several locations (Fig. 2a, Extended Data Fig. 3a). E10.5 $Ripk1^{D325A/D325A}$ embryos had endocardial cushion hypoplasia, smaller limbs buds and a thinner neural retina (Fig. 2b). These developmental delays might be due to the defective vasculature, associated with extensive cell death observed in the yolk sac of these embryos (Fig. 2c). This phenotype was reminiscent of several strains of knockout mice with defects in TNF signalling, including $Casp8^{-/-}$ mice[8,16–22]. The E10.5 lethality of $Casp8^{-/-}$ mice is TNF-dependent[12], and can be prevented by loss of either *Ripk3* or *Mlkl*[8,22,23], which suggests that the lethality is due to TNF-induced activation of the necroptotic pathway that is normally inhibited by caspase-8. These findings led to the idea that cleavage of RIPK1 by caspase-8 inhibits necroptosis during embryogenesis[8,22]. However, $Ripk1^{D325A/D325A}Ripk3^{-/-}$ mice were not viable, consistent with a previous report[24]. Nevertheless, loss of RIPK3 extended survival more than loss of MLKL, which indicates that RIPK3 has a non-necroptotic role in the early embryonic lethality (Fig. 2d, Extended Data Fig. 3b). Combined loss of *Casp8* and *Ripk3* in these mice prevented the embryonic lethality, which suggests that caspase-8 does more than inhibiting RIPK1/RIPK3/MLKL-induced necroptosis

Table 1 | Clinical features of patients with CRIA syndrome

	Family 1	Family 2					Family 3
Mutation	**Asp324Asn**	**Asp324His**					**Asp324Tyr**
Patient number	**P1**	**P2**	**P3**	**P4**	**P5**	**P6**	**P7**
Gender	F	F	M	F	M	F	M
Age at evaluation (years)	10	82	55	54	22	20	13
Age at onset	2 months	Birth	2 weeks	Birth	Birth	Birth	6 months
Recurrent fevers	+	+	+	+	+	+	+
Fever maximum (°C/°F)	40.5/105	41/106	38.9/102	40.5/105	41/106	41/106	40.5/105
Fever frequency	1/2 week	1/month	1/3 weeks	1/2 weeks	1/3 weeks	1/2 weeks	1–3/2 weeks
Fever duration	3–7 days	3 days	3–5 days	2–5 days	2–5 days	3–5 days	1 day
Lymphadenopathy	+	+	+	+	+	+	+
Splenomegaly	+	–	–	–	+	+	+
Hepatomegaly	–	–	–	–	+	+	–
Tonsillitis	+	–	–	–	–	+	+
Abdominal pain	+	–	+	–	–	+	+
Rash	–	–	–	–	–	–	–
Oral ulcers	–	–	+	+	+	+	+
Genital ulcers	–	–	–	–	–	–	–
Arthritis	–	–	–	–	–	–	–
Arthralgia	–	–	+	–	–	+	+
Autoantibodies	+ ANA	+ RF	–	–	–	NA	–
Response to:							
Prednisone	+	+	+	+	+	+	+
Colchicine	NA	–	–	–	–	–	–
Anti-IL-1R	–	–	NA	–	NA	NA	–
Anti-TNF	–	–	NA	–	NA	NA	±
Anti-IL-6R	+	+	+	±D	NA	+D	+

Family 2 was first evaluated at the NIH in 1999 for unexplained periodic fever, but the data shown here are from their first return visit after identification of their *RIPK1* mutation. For fever frequency, '1/2 weeks' means once every 2 weeks.
±, partial or mixed response; ANA, antinuclear antibody; D, discontinued treatment after less than 1 year owing to reported side effects; NA, not applicable; RF, rheumatoid factor.

at this embryonic stage (Fig. 2d, Extended Data Fig. 3b). Although loss of *Ripk1* ameliorates the ALPS-like disorder observed in $Casp8^{-/-}Ripk3^{-/-}$ mice[8,12,13,15], lack of RIPK1 cleavage did not notably affect it (Extended Data Fig. 3c, d), consistent with observations in $Fadd^{-/-}Ripk3^{-/-}Ripk1^{D325A/D325A}$ mice[24]. Interestingly, inhibition of RIPK1 kinase activity also rescued the embryonic lethality of $Ripk1^{D325A/D325A}$ (Fig. 2d). However, $Ripk1^{D138N,D325A/D138N,D325A}$ mice were runty and did not survive past weaning (Fig. 2d, e). These mice had a multi-organ inflammation presenting with skin hyperplasia, infiltration of leukocytes in the liver and the lung, disorganized splenic architecture and scattered cleaved caspase-3-positive cells in these organs (Extended Data Fig. 3e). Loss of one allele of *Ripk3* or *Casp8* prolonged the survival of $Ripk1^{D138N,D325A/D138N,D325A}$ mice to 5 weeks of age, and complete loss of *Ripk3* rescued the inflammatory phenotype of $Ripk1^{D138N,D325A/D138N,D325A}$ mice (Fig. 2d, e).

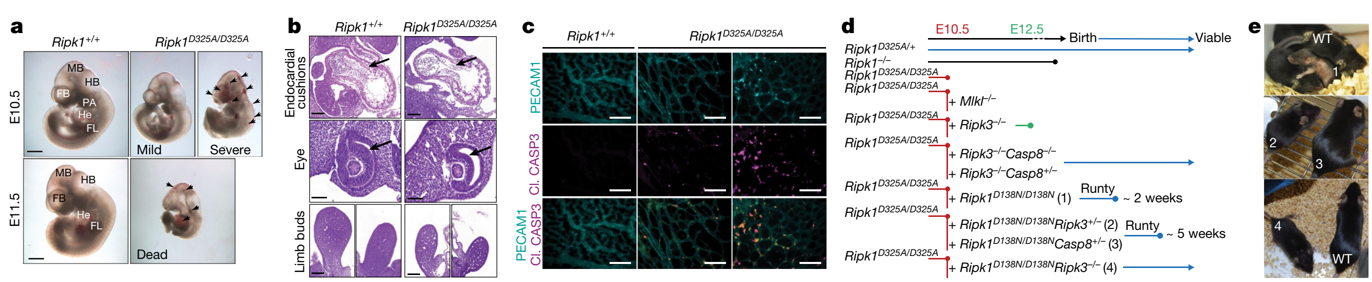

Fig. 2 | Homozygous mutation of the RIPK1 caspase-8 cleavage site in mice causes early embryonic lethality. a, E10.5 (top) and E11.5 (bottom) embryos, representative of four embryos per genotype. FB, forebrain; HB, hindbrain; He, heart; FL, forelimb; MB, midbrain; PA, pharyngeal arches. Arrows denote sites of haemorrhage. Scale bars, 900 µm (E10.5) and 1,400 µm (E11.5). **b**, Haematoxylin and eosin (H&E)-stained section of E10.5 embryos, representative of three embryos per genotype. Arrows denote endocardial cushions (top) and neural retina (middle). Scale bars, 200 µm. **c**, E10.5 yolk sacs stained with anti-PECAM1 (cyan) and anti-cleaved caspase-3 (Cl. CASP3; magenta) antibodies. Images with severely and less severely disrupted vasculature are shown. Scale bars, 50 µm. Images are representative of four embryos per genotype. **d**, Diagram depicting the extent of viability of different strains of $Ripk1^{D325A}$ mice. **e**, Representative pictures of three mice per genotype numbered in **d**.

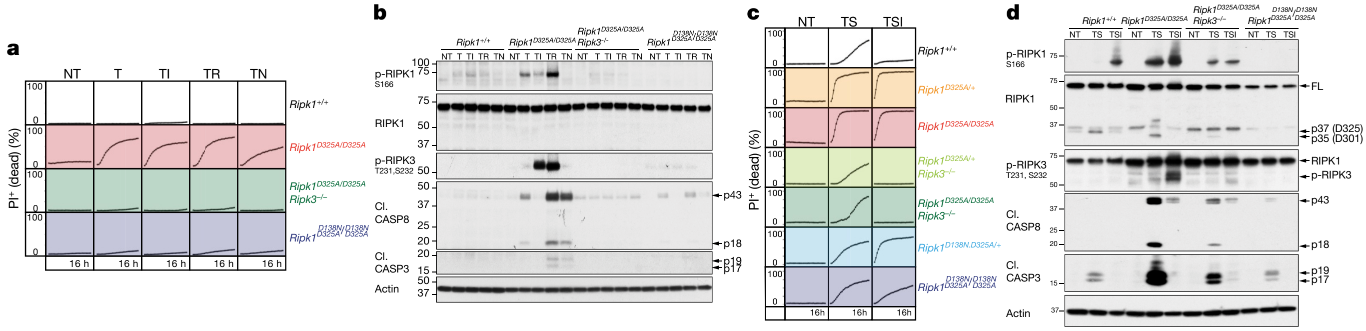

Fig. 3 | *Ripk1*$^{D325A/D325A}$ and *Ripk1*$^{D325A/+}$ cells are hypersensitive to TNF-induced death. a, **c**, Cell death of MEFs, monitored by time-lapse imaging of propidium iodide (PI) staining over 16 h. I denotes 5 μM caspase-8 inhibitor; N denotes 10 μM necrostatin; NT denotes untreated; R denotes 1 μM RIPK3 inhibitor; S denotes 100 nM SMAC mimetic; T denotes 100 ng ml^{-1} (**a**) or 10 ng ml^{-1} (**c**) TNF. Graphs are representative of four independent experiments performed with two biological repeats per genotype. **b**, **d**, Western blot of MEFs treated as in **a** for 2 h (**b**), and as in **c** for 2 h (**d**). Results are representative of two independent experiments. p-RIPK1, phosphorylated RIPK1. β-Actin was used as a loading control. For gel source data, see Supplementary Fig. 2.

RIPK1 cleavage limits TNF-induced cell death

To explore the function of RIPK1 cleavage in TNF signalling, we tested homozygous *Ripk1*$^{D325A/D325A}$ mouse embryonic fibroblasts (MEFs) for their response to TNF-induced cell death. Notably, even though TNF is not usually cytotoxic, we found that *Ripk1*$^{D325A/D325A}$ MEFs were sensitive to TNF alone and this induced increased phosphorylation of RIPK1, as well as activation of caspase-8 when compared to wild-type MEFs (Fig. 3a, b). Although inhibiting caspases or RIPK3 kinase activity did not affect cell death induced by TNF, genetic loss of RIPK3 or RIPK1 kinase activity significantly reduced TNF-induced cell death (Fig. 3a, b). Loss of RIPK3 not only completely abrogated death, but also blocked RIPK1 phosphorylation and caspase activation (Fig. 3a, b).

Given that the patients contain *RIPK1* mutations in only one allele, we tested the sensitivity of several *Ripk1*$^{D325A/+}$ heterozygous cell types to TNF. In contrast to homozygote *Ripk1*$^{D325A/D325A}$ MEFs, none of the tested *Ripk1*$^{D325A/+}$ cell types were sensitive to TNF alone (Extended Data Fig. 4a, b). However, inhibitors that directly activate the cytotoxic activity of RIPK1 (for example, SMAC mimetic, or TAK1, IKK or MK2 inhibitors)[1–4,6,25,26] rapidly sensitized *Ripk1*$^{D325A/+}$ MEFs and mouse dermal fibroblasts (MDFs) to low-dose TNF (Fig. 3c, Extended Data Fig. 4a, c). By contrast, only SMAC mimetic and TAK1 inhibitor sensitized *Ripk1*$^{D325A/+}$ bone-marrow-derived macrophages (BMDMs) to low-dose TNF (Extended Data Fig. 4b). In *Ripk1*$^{D325A/D325A}$ MEFs, TNF-induced cell death was more pronounced after the addition of IKK or TAK1 inhibitors or a combination of SMAC mimetic and MK2 inhibitor (Extended Data Fig. 4c). In addition, homozygote and heterozygote *Ripk1*^{D325A} MEFs and MDFs were slightly more sensitive to apoptosis induced by low-dose TNF and cycloheximide (Extended Data Fig. 4a, c).

Treatment with TNF plus SMAC mimetic induced a strong phosphorylation of RIPK1 and RIPK3, as well as activation of caspase-8 and caspase-3, in *Ripk1*$^{D325A/+}$ cells (Extended Data Fig. 4d–f), which was more pronounced in the *Ripk1*^{D325A} homozygote cells (Fig. 3d, Extended Data Fig. 4f). This increase in cell death induced by TNF plus SMAC mimetic correlated with increased formation of a RIPK1–caspase-8-containing complex 2 (Extended Data Fig. 4g).

Notably, given the increase in caspase-8 activation, loss of RIPK3 markedly delayed cell death induced by TNF plus SMAC mimetic or TAK1, IKK or MK2 inhibitors in both *Ripk1*^{D325A} homozygote and heterozygote fibroblasts (Fig. 3c, Extended Data Fig. 4a, c). In fibroblasts, loss of RIPK3 correlated with significantly reduced autophosphorylation of RIPK1 and caspase activation after TNF and SMAC mimetic treatment (Fig. 3d, Extended Data Fig. 4d, e). However, inhibition of RIPK3 kinase had little effect on the induction of cell death (Extended Data Fig. 4a–c), which suggests that RIPK3 contributes mostly in a structural capacity to the activation of caspase-8 in *Ripk1*^{D325A} cells.

We next analysed both *Ripk1*^{D138N,D325A} homozygote and heterozygote cells and, as expected, genetic loss of RIPK1 kinase activity prevented RIPK1 autophosphorylation (Fig. 3d, Extended Data Fig. 4d). It also provided some protection from cell death and this effect was mirrored by treatment with the RIPK1 inhibitor necrostatin (Fig. 3c, Extended Data Fig. 4a–c). Similar to RIPK3 loss, this correlated with reduced caspase-8 activation (Fig. 3d, Extended Data Fig. 4d). Together, these results indicate that in fibroblasts, RIPK3 promotes caspase-8 activation in a manner that is independent of its kinase activity and mostly independent of RIPK1 kinase activity (Fig. 3a, b), unless RIPK1 is further activated by an activating stimulus, such as SMAC mimetic (Fig. 3c, d).

One surprising observation was that the strong activation of caspase-8 in *Ripk1*^{D325A} cells led to RIPK1 cleavage (Fig. 3d, Extended Data Figs. 4d, f, 5a). In the case of the heterozygote cells, this was almost certainly due to cleavage of the wild-type protein; however, we also detected a slightly smaller RIPK1 cleavage product in homozygote cells (Fig. 3d, Extended Data Figs. 4f, 5a). This was the result of an alternative cleavage site (D301 in mouse) that is as well-conserved as the canonical site (Extended Data Fig. 5, Extended Data Table 2b). However, possibly owing to the unfavourable hydrophobic amino acid in the P1′ position[27], the D301 site was far less efficiently cleaved than the D325 site and only when the canonical site was mutated (Fig. 3d, Extended Data Figs. 4f, 5).

RIPK1 cleavage limits inflammatory responses

Patients with CRIA syndrome have recurrent fevers, so to understand how loss of RIPK1 cleavage might affect the response to inflammatory stimuli, we tested the responsiveness of the *Ripk1*$^{D325A/+}$ mice to Toll-like receptor (TLR) ligands. Although there was not a marked difference in levels of IL-6, the levels of TNF and IL-1β were higher in the *Ripk1*$^{D325A/+}$ sera after injection of a non-lethal dose of either lipopolysaccharide (LPS) or polyinosinic:polycytidylic acid (poly(I:C)) (Fig. 4a, Extended Data Fig. 6a). Similarly, PBMCs from P7 produced more TNF and IL-1β after LPS or poly(I:C) treatment (Fig. 4b, Extended Data Fig. 6b). Despite these increased levels of cytokines, hypothermia induced by LPS was not life-threatening (Extended Data Fig. 6c), which was also consistent with the symptoms of the patients with CRIA syndrome. BMDMs also produced more TNF after TLR activation (Fig. 4c), which correlated with the amount of cell death induced (Extended Data Fig. 6d).

To define the contribution of the haematopoietic compartment to the hyper-inflammatory phenotype, we generated bone marrow chimaeras. Notably, both wild-type mice transplanted with *Ripk1*$^{D325A/+}$ haematopoietic cells and *Ripk1*$^{D325A/+}$ mice transplanted with wild-type bone marrow were hyper-responsive to LPS compared with the controls (Fig. 4d). Although our data suggest that the increased inflammatory response in mice correlates with increased cell death in *Ripk1*$^{D325A/+}$

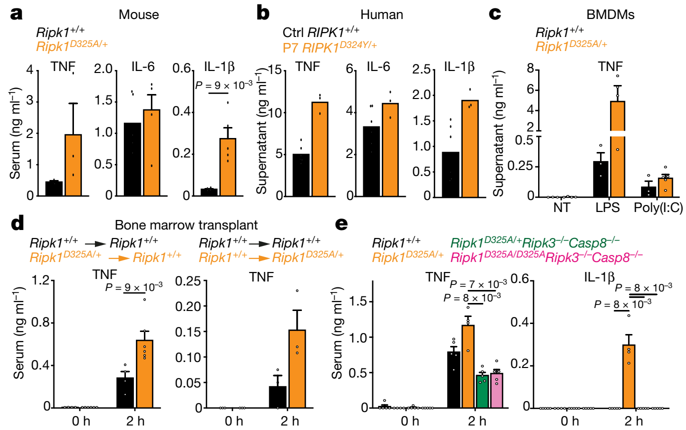

Fig. 4 | RIPK1 cleavage limits inflammation in vivo. a, Serum cytokine levels after 2 h treatment with 2 mg kg^{-1} LPS. Data are mean ± s.e.m., $n = 3$ mice for TNF and $n = 5$ mice for IL-6 and IL-1β. **b**, Cytokine levels in the supernatant of two unrelated adolescent controls (*RIPK1*$^{+/+}$) and P7 *RIPK1*$^{D324Y/+}$ PBMCs treated for 3 h with 10 ng ml^{-1} LPS. Data are mean of triplicates. **c**, TNF levels in the supernatant of BMDMs treated for 24 h with 25 ng ml^{-1} LPS or 2.5 μg ml^{-1} poly(I:C). Data are mean ± s.e.m., $n = 3$ for *Ripk1*$^{+/+}$ and $n = 3$–4 for *Ripk1*$^{D325A/+}$. **d**, Serum TNF levels in wild-type mice reconstituted with *Ripk1*$^{D325A/+}$ haematopoietic cells (left) or *Ripk1*$^{D325A/+}$ mice reconstituted with wild-type haematopoietic cells (right), treated for 2 h with 2 mg kg^{-1} LPS. Data are mean ± s.e.m., $n = 3$ and 4 *Ripk1*$^{+/+}$ → *Ripk1*$^{+/+}$, $n = 6$ *Ripk1*$^{D325A/+}$ → *Ripk1*$^{+/+}$, $n = 3$ for *Ripk1*$^{+/+}$ → *Ripk1*$^{D325A/+}$ mice per genotype. **e**, Serum cytokines levels after 2 h treatment with 2 mg kg^{-1} of LPS. Data are mean ± s.e.m., $n = 4$ for *Ripk1*$^{D325A/+}$, $n = 5$ for the other genotypes. Results in **a**, **c** and **e** are representative of two independent experiments. Each dot in **a** and **c**–**e** represents a mouse. All *P* values determined by unpaired, two-tailed *t*-test.

cells, RIPK1 also contributes to the activation of NF-κB and MAPK signalling pathways[14,28–30]. However, loss of RIPK1 cleavage did not affect TNF-induced NF-κB or MAPK activation in either mouse cells or patient-derived dermal fibroblasts (Extended Data Fig. 6e–g). Furthermore, the cytokine increases observed in the *Ripk1*$^{D325A/+}$ sera were dependent on RIPK3 and caspase-8, which suggests that cell death is the major contributor to cytokine induction in these mice (Fig. 4e).

RIPK1 has a role in activating NF-κB and MAPK inflammatory pathways, caspase-8-mediated apoptosis and RIPK3-dependent necroptosis. Each of these distinct responses can contribute to inflammatory signalling and it has been difficult to disentangle which pathway causes inflammation in any given physiological situation. We describe a human autoinflammatory disorder caused by heterozygous mutations in RIPK1 seemingly constrained to a single, evolutionarily conserved aspartate residue at the caspase-6/8 cleavage site. Mutation of this key aspartate prevents caspase-6/8 cleavage of RIPK1, sensitizes cells to TNF-induced cell death and causes embryonic lethality in homozygous mice. Several mechanisms inhibit cell death after TNF stimulation[1–7,26,31] and our data emphasize how important this is in limiting an inflammatory response. Pathogens may counter cell-death-mediated inflammation by expressing caspase-8 inhibitors and a cellular defensive mechanism that amplifies the cell death response in the absence of RIPK1 cleavage makes intuitive sense, and may explain why some pathogens also attempt to cleave RIPK1[32,33]. Previously, pathogen inhibition of caspase-8 was thought to unleash the necroptotic pathway; however, RIPK1 cleavage not only limits necroptosis, as previously assumed, but can also limit caspase-8-mediated apoptosis. Furthermore, the kinase activities of RIPK3 and RIPK1 have mainly been thought of as activators of necroptosis. However, the rescue of the postnatal lethal phenotype of the *Ripk1*^{D138N,D325A} mice by loss of *Casp8* or *Ripk3* reveals a far more complex interaction between these molecules than previously anticipated. Our data provide support for the concept of a hierarchy of preferred responses to TNF signalling: cell survival, then caspase-8-mediated apoptosis, with necroptosis as a last resort (Extended Data Fig. 7). Notably, despite the fact that most of our knowledge of RIPK1 function comes from analyses of TNF signalling, and that TNF has a pivotal role in many inflammatory diseases, patients with CRIA syndrome responded to the IL-6 inhibitor tocilizumab but did not respond to TNF inhibitors. It will be interesting therefore to determine what role RIPK1 has in IL-6-mediated inflammation.

Online content

Any methods, additional references, Nature Research reporting summaries, source data, extended data, supplementary information, acknowledgements, peer review information; details of author contributions and competing interests; and statements of data and code availability are available at https://doi.org/10.1038/s41586-019-1828-5.

1. Bertrand, M. J. M. et al. cIAP1 and cIAP2 facilitate cancer cell survival by functioning as E3 ligases that promote RIP1 ubiquitination. *Mol. Cell* **30**, 689–700 (2008).
2. Dondelinger, Y. et al. MK2 phosphorylation of RIPK1 regulates TNF-mediated cell death. *Nat. Cell Biol.* **19**, 1237–1247 (2017).
3. Dondelinger, Y. et al. NF-κB-independent role of IKKα/IKKβ in preventing RIPK1 kinase-dependent apoptotic and necroptotic cell death during TNF signaling. *Mol. Cell* **60**, 63–76 (2015).
4. Jaco, I. et al. MK2 phosphorylates RIPK1 to prevent TNF-induced cell death. *Mol. Cell* **66**, 698–710.e5 (2017).
5. Feltham, R. et al. Mind bomb regulates cell death during TNF signaling by suppressing RIPK1's cytotoxic potential. *Cell Reports* **23**, 470–484 (2018).
6. Menon, M. B. et al. p38^{MAPK}/MK2-dependent phosphorylation controls cytotoxic RIPK1 signalling in inflammation and infection. *Nat. Cell Biol.* **19**, 1248–1259 (2017).
7. Lafont, E. et al. TBK1 and IKKε prevent TNF-induced cell death by RIPK1 phosphorylation. *Nat. Cell Biol.* **20**, 1389–1399 (2018).
8. Oberst, A. et al. Catalytic activity of the caspase-8–FLIP$_L$ complex inhibits RIPK3-dependent necrosis. *Nature* **471**, 363–367 (2011).
9. Kim, J. W., Choi, E. J. & Joe, C. O. Activation of death-inducing signaling complex (DISC) by pro-apoptotic C-terminal fragment of RIP. *Oncogene* **19**, 4491–4499 (2000).
10. Lin, Y., Devin, A., Rodriguez, Y. & Liu, Z. G. Cleavage of the death domain kinase RIP by caspase-8 prompts TNF-induced apoptosis. *Genes Dev.* **13**, 2514–2526 (1999).
11. van Raam, B. J., Ehrnhoefer, D. E., Hayden, M. R. & Salvesen, G. S. Intrinsic cleavage of receptor-interacting protein kinase-1 by caspase-6. *Cell Death Differ.* **20**, 86–96 (2013).
12. Dillon, C. P. et al. RIPK1 blocks early postnatal lethality mediated by caspase-8 and RIPK3. *Cell* **157**, 1189–1202 (2014).
13. Kaiser, W. J. et al. RIP1 suppresses innate immune necrotic as well as apoptotic cell death during mammalian parturition. *Proc. Natl Acad. Sci. USA* **111**, 7753–7758 (2014).
14. Kelliher, M. A. et al. The death domain kinase RIP mediates the TNF-induced NF-κB signal. *Immunity* **8**, 297–303 (1998).
15. Rickard, J. A. et al. RIPK1 regulates RIPK3-MLKL-driven systemic inflammation and emergency hematopoiesis. *Cell* **157**, 1175–1188 (2014).
16. Moulin, M. et al. IAPs limit activation of RIP kinases by TNF receptor 1 during development. *EMBO J.* **31**, 1679–1691 (2012).
17. Peltzer, N. et al. LUBAC is essential for embryogenesis by preventing cell death and enabling haematopoiesis. *Nature* **557**, 112–117 (2018).
18. Peltzer, N. et al. HOIP deficiency causes embryonic lethality by aberrant TNFR1-mediated endothelial cell death. *Cell Reports* **9**, 153–165 (2014).
19. Varfolomeev, E. E. et al. Targeted disruption of the mouse *Caspase 8* gene ablates cell death induction by the TNF receptors, Fas/Apo1, and DR3 and is lethal prenatally. *Immunity* **9**, 267–276 (1998).
20. Yeh, W. C. et al. FADD: essential for embryo development and signaling from some, but not all, inducers of apoptosis. *Science* **279**, 1954–1958 (1998).
21. Yeh, W. C. et al. Requirement for Casper (c-FLIP) in regulation of death receptor-induced apoptosis and embryonic development. *Immunity* **12**, 633–642 (2000).
22. Kaiser, W. J. et al. RIP3 mediates the embryonic lethality of caspase-8-deficient mice. *Nature* **471**, 368–372 (2011).
23. Alvarez-Diaz, S. et al. The pseudokinase MLKL and the kinase RIPK3 have distinct roles in autoimmune disease caused by loss of death-receptor-induced apoptosis. *Immunity* **45**, 513–526 (2016).
24. Zhang, X., Dowling, J. P. & Zhang, J. RIPK1 can mediate apoptosis in addition to necroptosis during embryonic development. *Cell Death Dis.* **10**, 245 (2019).
25. Dondelinger, Y. et al. Serine 25 phosphorylation inhibits RIPK1 kinase-dependent cell death in models of infection and inflammation. *Nat. Commun.* **10**, 1729 (2019).
26. Geng, J. et al. Regulation of RIPK1 activation by TAK1-mediated phosphorylation dictates apoptosis and necroptosis. *Nat. Commun.* **8**, 359 (2017).
27. Stennicke, H. R. & Salvesen, G. S. Catalytic properties of the caspases. *Cell Death Differ.* **6**, 1054–1059 (1999).
28. Wong, W. W. et al. RIPK1 is not essential for TNFR1-induced activation of NF-κB. *Cell Death Differ.* **17**, 482–487 (2010).
29. Newton, K. et al. RIPK1 inhibits ZBP1-driven necroptosis during development. *Nature* **540**, 129–133 (2016).

30. Cuchet-Lourenço, D. et al. Biallelic *RIPK1* mutations in humans cause severe immunodeficiency, arthritis, and intestinal inflammation. *Science* **361**, 810–813 (2018).
31. Micheau, O., Lens, S., Gaide, O., Alevizopoulos, K. & Tschopp, J. NF-kappaB signals induce the expression of c-FLIP. *Mol. Cell. Biol.* **21**, 5299–5305 (2001).
32. Croft, S. N., Walker, E. J. & Ghildyal, R. Human Rhinovirus 3C protease cleaves RIPK1, concurrent with caspase 8 activation. *Sci. Rep.* **8**, 1569 (2018).
33. Pearson, J. S. et al. EspL is a bacterial cysteine protease effector that cleaves RHIM proteins to block necroptosis and inflammation. *Nat. Microbiol.* **2**, 16258 (2017).

[1]The Walter and Eliza Hall Institute, Parkville, Victoria, Australia. [2]Department of Medical Biology, University of Melbourne, Parkville, Victoria, Australia. [3]Inflammatory Disease Section, National Human Genome Research Institute, National Institutes of Health, Bethesda, MD, USA. [4]Centre for Innate Immunity and Infectious Diseases, Hudson Institute of Medical Research, Clayton, Victoria, Australia. [5]Department of Molecular and Translational Science, Monash University, Clayton, Victoria, Australia. [6]Light Imaging Section, Office of Science and Technology, National Institute of Arthritis and Musculoskeletal and Skin Diseases, National Institutes of Health, Bethesda, MD, USA. [7]Translational Immunology Section, National Institute of Arthritis and Musculoskeletal and Skin Diseases, National Institutes of Health, Bethesda, MD, USA. [8]Department of Laboratory Medicine, Clinical Center, National Institutes of Health, Bethesda, MD, USA. [9]Translational Vascular Medicine Branch, National Heart, Lung, and Blood Institute, National Institutes of Health, Bethesda, MD, USA. [10]Institute for Genetics & Cologne Excellence Cluster on Cellular Stress Responses in Aging-Associated Diseases (CECAD), University of Cologne, Cologne, Germany. [11]Center for Molecular Medicine (CMMC), University of Cologne, Cologne, Germany. [12]Molecular Development of the Immune System Section, Laboratory of Immune System Biology; Clinical Genomics Program, National Institute of Allergy and Infectious Diseases, National Institutes of Health, Bethesda, MD, USA. [13]Laboratory of Muscle Stem Cells and Gene Regulation, National Institute of Arthritis and Musculoskeletal and Skin Diseases, National Institutes of Health, Bethesda, MD, USA. [14]NIH Intramural Sequencing Center, National Human Genome Research Institute, National Institutes of Health, Bethesda, MD, USA. [15]Division of Rheumatology, Department of Medicine, University of California San Francisco, San Francisco, CA, USA. [16]Division of Pulmonary and Critical Care, Department of Medicine, University of California San Francisco, San Francisco, CA, USA. [17]These authors contributed equally: Najoua Lalaoui, Steven E. Boyden, Hirotsugu Oda. [18]These authors jointly supervised this work: Daniel L. Kastner, John Silke. *e-mail: lalaoui@wehi.edu.au; steven.boyden@genetics.utah.edu; kastnerd@mail.nih.gov; silke@wehi.edu.au

Methods

Participant enrolment

Families were enrolled and evaluated in the Clinical Center at the National Institutes of Health under a protocol approved by the Institutional Review Board of the National Institute of Diabetes and Digestive and Kidney Diseases and the National Institute of Arthritis and Musculoskeletal and Skin Diseases. Human studies complied with relevant ethical regulations and all participants provided written informed consent. No statistical methods were used to predetermine sample size.

Tocilizumab treatment

P1 was 11 years old at the time of her first intravenous infusion of tocilizumab at a dose of 8 mg kg^{-1}. She initially received medication every 3 weeks but later reduced the frequency to every 4 or 5 weeks because of a busy school schedule. On the less frequent dosing, P1 had more breakthrough symptoms, mainly tender lymphadenopathy. In 2018, when the US FDA approved the use of the injectable form in children with juvenile idiopathic arthritis, P1 was switched to 162 mg by subcutaneous injection every 2 weeks and did very well on this regimen. P2, P3, P4 and P6 received regular self-administered tocilizumab by 162 mg subcutaneous injections starting at every 2 weeks—the standard dose and route of administration for adults. The dose frequency for P3 was gradually increased to every 6 days. P7 received an initial infusion of tocilizumab at 8 mg kg^{-1} before being switched to the subcutaneous injectable form (162 mg every 2 weeks) for convenience. On this regimen, P7 noted prompt resolution of fevers, abdominal pain and joint pain, and gradual normalization of laboratory testing, including CRP, ESR, haemaglobin, haematological indices and serum iron.

Exome sequencing

Exome capture (Illumina TruSeq v2 for family 1, Roche SeqCap EZ Exome+UTR for family 2, and IDT xGen Exome Research Panel for family 3) and sequencing (Illumina HiSeq 2000, 2500 and NovaSeq 6000) was performed for all available family members at the National Institutes of Health (NIH) Intramural Sequencing Center (NISC) using 2 × 101-, 2 × 126-, and 2 × 151-base-pair (bp) paired-end reads. The data were analysed as follows: alignment with Novoalign; duplicate marking with Picard; re-alignment, re-calibration, and variant calling with GATK; and annotation with Annovar. Variants were filtered to select those that were nonsynonymous or in splice sites within 6 bp of an exon, had less than 1% mutant allele frequency in variant databases, and co-segregated with the phenotype. The mutations were validated by Sanger sequencing in all family members, and to rule out non-paternity, non-maternity or other sample identity errors, genders and relatedness were confirmed by examining heterozygous call rates on the X chromosome, Y chromosome call rates and Mendelian inheritance error rates in the exome data.

In vitro cleavage assays

Unlabelled in vitro transcription and translation of 1 µg of empty pCMV6-Entry control vector (Origene), wild-type *RIPK1* cDNA cloned into pCMV6-Entry vector (Origene), p.D324N, p.D324H, p.D324Y and p.D324A mutant *RIPK1* constructs (GENEART Site-Directed Mutagenesis System, Invitrogen) was performed in a 50-µl reaction using the TnT T7 Quick Coupled Transcription/Translation System (Promega). We incubated 2 µl of this reaction with either 12 U of purified recombinant caspase-8 (Calbiochem), 12 U of purified recombinant caspase-6 (Calbiochem), or an equal volume of re-suspension buffer, in caspase reaction buffer from the Caspase-8 Fluorometric Assay Kit (Enzo Life Sciences) and 10 mM dithiothreitol (DTT) in a 40 µl final volume at 37 °C for 3 h. These reactions were blotted for RIPK1 using an antibody recognizing a RIPK1 C-terminal antibody (610459, BD Transduction Laboratories).

RNA sequencing

Total RNA was isolated from whole blood collected in PAXgene Blood RNA Tubes using PAXgene Blood RNA Kit (PreAnalytiX) as per the manufacturer's instructions. Total RNA was used for cDNA library preparation using the TruSeq Stranded mRNA Library Preparation kit for NeoPrep (Illumina). Sequencing was performed on an Illumina HiSeq 3000 System in a 1 × 50-bp single-read mode. Sequenced reads were mapped against the human reference genome (GRCh38) using hisat v.2.2.1.0[34]. Reads mapped to haemoglobin genes were removed from further analysis. Mapped reads were quantified using HTSeq[35,36]. All the count data were normalized using TCC[37] and differentially expressed genes were detected using edgeR[38]. Gene Ontology enrichment analysis was performed using DAVID[36].

Mice

All mouse studies complied with relevant ethical regulations and approved by the Walter and Eliza Hall Institute Animal Ethics Committee. The *Ripk1*^{D325A} and *Ripk1*^{D138N,D325A} mice were generated by the MAGEC laboratory (WEHI) on a C57BL/6J background. To generate *Ripk1*^{D325A} mice, 20 ng μl^{-1} of *Cas9* mRNA, 10 ng μl^{-1} of sgRNA (ATTTGACCTGCTCGGAGGTA) and 40 ng μl^{-1} of the oligo donor (tgtcttctcattacagAAAGAGTATCCAGATCAAAGCCCAGTGCTGCAGAG AATGTTTTCACTGCAGCATGCCTGTGTACCATTACCTCCGAGCAGGTC AAATTCAGgtaactcacctattcgttcatttgcatactcgctca) (in which uppercase bases denote exons; lowercase bases denote intron sequences) were injected into the cytoplasm of fertilized one-cell stage embryos generated from wild-type C57BL/6J breeders. To generate *Ripk1*^{D138N,D325A} mice, 20 ng μl^{-1} of *Cas9* mRNA, 10 ng μl^{-1} of sgRNA (TGACAAAGGTGTGATACACA) and 40 ng μl^{-1} of oligo donor (GGATAATCGTGGAGGCCATAGAAGGCATGTGCTACTTACAT GACAAAGGTGTGATACACAAGAACCTGAAGCCTGAGAATATCCTCGTT GATCGTGACTTTCACATTAAGgtaatccacaatctg) were injected into the cytoplasm of fertilized one-cell stage embryos generated from *Ripk1*$^{D325A/D325A}$*Ripk3*$^{-/-}$*Casp8*$^{-/+}$ breeders. Twenty-four hours later, two-cell stage embryos were transferred into the uteri of pseudo-pregnant female mice. Viable offspring were genotyped by next-generation sequencing. Targeted animals were backcrossed twice to wild-type C57BL/6J to eliminate off-target mutations and to re-integrate *Ripk3* and *Casp8* genes into *Ripk1*^{D138N,D325A} mice. The *Ripk3*$^{-/-}$ mice[39], *Casp8*$^{-/-}$ mice[19] and *Mlkl*$^{-/-}$ mice[40] were all previously described. The *Ripk3*$^{-/-}$ mice were backcrossed to C57BL/6J mice for more than ten generations.

TLR challenge

Eight-to-twelve-week-old male mice received intraperitoneal injection of either 2 mg kg^{-1} LPS or 50 µg poly(I:C). Calculations to determine group sizes were not performed, mice were not randomized but were grouped according to genotype, and experiments were blinded.

Cells

MEFs were isolated from E10.5 embryos and MDFs were isolated from mouse tails. After SV40 transformation, MEFs and MDFs were tested for mycoplasma. 293T cells (ATCC) used to produce SV40 viruses and in Extended Data Fig. 5b were tested for mycoplasma but not authenticated.

Time-lapse imaging

Percentage cell death was assayed every 30–45 min by time-lapse imaging using the IncuCyte live cell analysis imaging (Essenbioscience) or the Opera Phenix High Content Screening System (PerkinElmer) for 16 h with 5% CO_2 and 37 °C climate control. For the IncuCyte and Opera Phenix imaging, dead cells were identified by propidium iodide (0.25 µg ml^{-1}) staining, and for the Opera Phenix imaging, all cells were stained with 250nM of SiR-DNA (Spirochrome). Dyes were added to the cells 2 h before imaging and compounds were added 10 min before the start

of imaging. For the Opera Phenix imaging, images were analysed using the server-based Columbus 2.8.0 software (PerkinElmer) to identify nuclei based on SiR-DNA staining and dead cells using propidium iodide staining. Results were exported as counts per well to be processed and graphed using R Studio (https://www.R-project.org/) with the tidyverse package (https://CRAN.R-project.org/package=tidyverse).

Human and mouse cytokines measurement

Human serum and PBMC supernatant cytokine content was measured by enzyme-linked immunosorbent assay (ELISA) (R&D: SLB50, STA00C and S6050) according to the manufacturer's instructions. The measurements were performed in technical duplicates. Student's *t*-test was performed for the statistical analysis. Mouse serum and BMDMs supernatant cytokine content was measured by ELISA (eBioscience for TNF and IL-6 and R&D for IL-1β) according to the manufacturer's instructions.

Human PBMC ex vivo stimulation

Ficoll-isolated human PBMCs were serum-starved for 20 min and stimulated for 3 h with LPS (Invivogen, tlrl-3pelps) or 6 h with poly(I:C) (Invivogen, tlrl-pic). Cytokines were measured by ELISA as described above.

Reagents

The SMAC mimetic compound A, the caspase inhibitor IDN-6556 (Idun Pharmaceuticals) and the RIPK1 inhibitor necrostatin were synthesized by TetraLogic Pharmaceuticals. The RIPK3 inhibitor GSK'872 was from Calbiochem. The TAK1 inhibitor (5Z)-7-oxozeaenol, the IKK inhibitor IKK-16 and the MK2 inhibitor PF-3644022 were from Tocris Bioscience. Cycloheximide was from Sigma. Recombinant Fc-TNF was produced in house. Ultrapure LPS-EB and poly(I:C) were purchased from Invivogen.

Immunostaining

Embryonic yolk sacs were fixed for 20 min at room temperature in 4% paraformaldehyde, blocked and permeabilized in PBS with 2% normal donkey serum (Jackson ImmunoResearch, 017-000-121) and 0.6% Triton X, probed with primary antibodies, cleaved caspase-3 (9661, CST) and PECAM1 (AF3628, R&D Systems) at 4 °C overnight, then secondary antibodies goat anti-rabbit AF488 (Invitrogen A-11008) and donkey anti-goat cy3 (705-165-147, Jackson ImmunoResearch) at room temperature for 1 h. Samples were cleared in a glycerol gradient (5–80%) overnight, whole-mounted in 80% glycerol and imaged using a DP72 microscope and cellSens Standard software (Olympus).

Immunoprecipitation

Ten million cells were seeded in 10-cm dishes. After the indicated treatments, cells were lysed in DISC lysis buffer (150 mM sodium chloride, 2 mM EDTA, 1% Triton X-100, 10% glycerol, 20 mM Tris, pH 7.5). Proteins were immunoprecipitated with 20 μl of protein G Sepharose plus 1.5 μg of FADD antibody (clone 7A2, in house) with rotation overnight at 4 °C. Beads were washed four times in DISC and samples eluted by boiling in 60 μl 1× SDS loading dye.

Western blotting

Cells lysates were separated on 4–12% gradient SDS–polyacrylamide gels (Biorad), transferred to polyvinylidene fluoride (Millipore) membranes and blotted with indicated antibodies purchased from CST except for phospho-RIPK3 (a gift from Genentech), actin (Sigma) and FADD (clone 7A2, in house). In vitro cleavage assays were blotted with a with an anti-RIPK1 antibody recognizing the C-terminal part (BD Transduction Laboratories, 610459). Cell lysates were blotted with an anti-RIPK1 antibody recognizing the N-terminal part (3493, Cell Signaling Technology).

NF-κB assay in patient-derived cells

NF-κB activation was assessed by measuring nuclear translocation of subunit p65 in fibroblasts derived from a single skin biopsy. Cells were grown overnight in 96-well plates seeded at 16,000 cells per well, and treated for 30 min with TNF (PeproTech) in PBS containing 1 mM $CaCl_2$ and 1 mM $MgCl_2$ (PBS-CM). Cells were pre-fixed for 5 min with 2% paraformaldehyde (PFA) in PBS-CM, then fixed for 10 min with 6% PFA in PBS-CM, and aldehyde groups were quenched with 50 mM NH_4Cl in PBS-CM for 15 min. After permeabilization with 0.3% SDS in PBS-CM for 5 min, cells were incubated with donkey serum dilution buffer (DSDB; 16% donkey serum, 0.3% Triton X-100, and 0.3 M NaCl in PBS) for 30 min, followed by overnight incubation at 4 °C with rabbit monoclonal NF-κB subunit p65 antibody (8242, Cell Signaling Technology) diluted at 1:500 in DSDB. Samples were then washed 3 times with permeabilization buffer (0.3% Triton X-100 and 0.1% BSA in PBS) and incubated with a 1:300 dilution of donkey anti-rabbit secondary antibody coupled to Alexa 488 (A21206, Molecular Probes) in DSDB for 1 h. Nuclei were counter-stained with a 1:2,000 dilution of SYTO 59 (Thermo Fisher) for 15 min. Automated field selection and plate imaging were performed with an IncuCyte Zoom incubator-microscopy system (Essen Bioscience) using a 20× objective. Nine fields per well of four wells per participant were pooled for analysis of nuclear p65 signal intensity. Nuclei were marked in red over a phase-contrast image, and p65 immunofluorescence was labelled in green. Overlaying a p65 mask on a nuclear mask showed both positive and negative nuclei, whereas a yellow co-staining mask showed positive nuclei only.

Reporting summary

Further information on research design is available in the Nature Research Reporting Summary linked to this paper.

Data availability

The original RNA sequencing data are uploaded and available at the Gene Expression Omnibus (GEO) under accession GSE127572. All other data are available from the corresponding authors upon reasonable request.

34. Kim, D., Langmead, B. & Salzberg, S. L. HISAT: a fast spliced aligner with low memory requirements. *Nat. Methods* **12**, 357–360 (2015).
35. Anders, S., Pyl, P. T. & Huber, W. HTSeq—a Python framework to work with high-throughput sequencing data. *Bioinformatics* **31**, 166–169 (2015).
36. Huang, W., Sherman, B. T. & Lempicki, R. A. Systematic and integrative analysis of large gene lists using DAVID bioinformatics resources. *Nat. Protocols* **4**, 44–57 (2009).
37. Sun, J., Nishiyama, T., Shimizu, K. & Kadota, K. TCC: an R package for comparing tag count data with robust normalization strategies. *BMC Bioinformatics* **14**, 219 (2013).
38. Robinson, M. D., McCarthy, D. J. & Smyth, G. K. edgeR: a Bioconductor package for differential expression analysis of digital gene expression data. *Bioinformatics* **26**, 139–140 (2010).
39. Newton, K., Sun, X. & Dixit, V. M. Kinase RIP3 is dispensable for normal NF-κBs, signaling by the B-cell and T-cell receptors, tumor necrosis factor receptor 1, and Toll-like receptors 2 and 4. *Mol. Cell. Biol.* **24**, 1464–1469 (2004).
40. Murphy, J. M. et al. The pseudokinase MLKL mediates necroptosis via a molecular switch mechanism. *Immunity* **39**, 443–453 (2013).
41. Conos, S. A., Lawlor, K. E., Vaux, D. L., Vince, J. E. & Lindqvist, L. M. Cell death is not essential for caspase-1-mediated interleukin-1β activation and secretion. *Cell Death Differ.* **23**, 1827–1838 (2016).
42. Mandal, P. et al. RIP3 induces apoptosis independent of pronecrotic kinase activity. *Mol. Cell* **56**, 481–495 (2014).
43. Newton, K. et al. Activity of protein kinase RIPK3 determines whether cells die by necroptosis or apoptosis. *Science* **343**, 1357–1360 (2014).

Acknowledgements This study was funded by the Intramural Research Programs of the National Human Genome Research Institute, the Intramural Research Program of NIH, NIH Clinical Center, National Institute of Arthritis and Musculoskeletal and Skin Diseases, National Institute of Allergy and Infectious Diseases, and National Heart, Lung, and Blood Institute, by European Research Council Advanced Grant 787826, by NHMRC grants 1025594, 1046984, 1145788, 1162765 and 1163581, NHMRC fellowships 1081421 and 1107149, by the Stafford Fox Foundation and was made possible through Victorian State Government Operational Infrastructure Support, Australian Government NHMRC IRIISS (9000433) and Australian Cancer Research Fund. N.L. is supported by project grant 1145588 from the Cancer Australia and Cure Cancer Australia Foundation and a Victorian Cancer Agency Mid-career Fellowship 17030. This work used the sequencing resources at the NIH Intramural Sequencing Center and the computational resources of the Biowulf Linux cluster at NIH (http://biowulf.nih.gov). We thank the families for their participation, D. Follmann for statistical advice, T. Uldrick and D. Fajgenbaum for assistance procuring samples, and D. Adams, A. Negro, A. Walts and Y. Yang

for clinical and technical assistance, C. Liegeois for IT assistance and the staff of the WEHI Bioservices facility for mouse husbandry. The generation of *Ripk1*^{D325A} and *Ripk1*^{D138N,D325A} mice used in this study was supported by the Australian Phenomics Network (APN) and the Australian Government through the National Collaborative Research Infrastructure Strategy (NCRIS) program.

Author contributions N.L., S.E.B. and H.O. designed and performed experiments and interpreted data. G.M.W., D.C., L.L., M.S., T.K., K.E.L., K.J.M.Z., N.E., K.S.-A., C.B., W.L.T., M.D.B., H.S.K., D.Y., H.A., N.S., L.W., L.Z., N.S.M., D.B.B., G.G.-C., C.H., H.W., J.J.C., N.I.D, M.M., A.L., Q.Z., I.A., J.C.M., A.K.V. and J.S. performed experiments. A.J.K., M.J.H., L.W. and M.P. generated the CRISPR mice. D.L.S., P.M.H., A.K.O., G.P.P.-P., B.K.B., A.J., T.M.R., A.J.G. and A.K.S. provided the clinical data. E.D.H., S.L.M., M.J.L., M.B., S.D.R. and M.G. contributed reagents, analysis and interpretation. N.L., S.E.B., D.L.K. and J.S. conceived the project and wrote the paper with input from all authors.

Competing interests The authors declare no competing interests.

Additional information
Supplementary information is available for this paper at https://doi.org/10.1038/s41586-019-1828-5.
Correspondence and requests for materials should be addressed to N.L., S.E.B., D.L.K. or J.S.

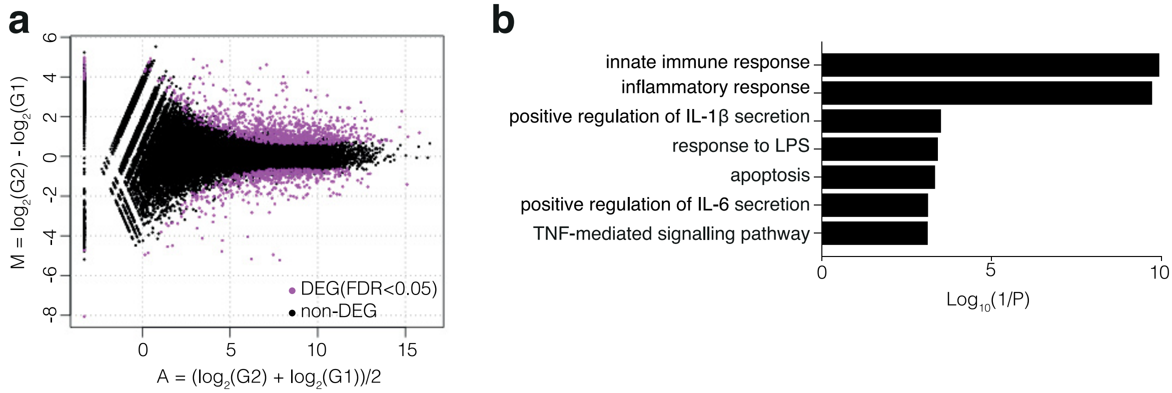

Extended Data Fig. 1 | Inflammatory gene signature in P7 whole-blood RNA. **a**, MA plot between two P7 samples and two unrelated adolescent healthy controls, both sequenced with technical duplicates. TCC-edgeR package of R followed by adjustment for multiple comparisons detected 1,394 differentially expressed genes (false discovery rate < 0.05), with 903 genes upregulated in P7, and 491 genes downregulated in P7. **b**, Representative Gene Ontology terms associated with immune signalling.

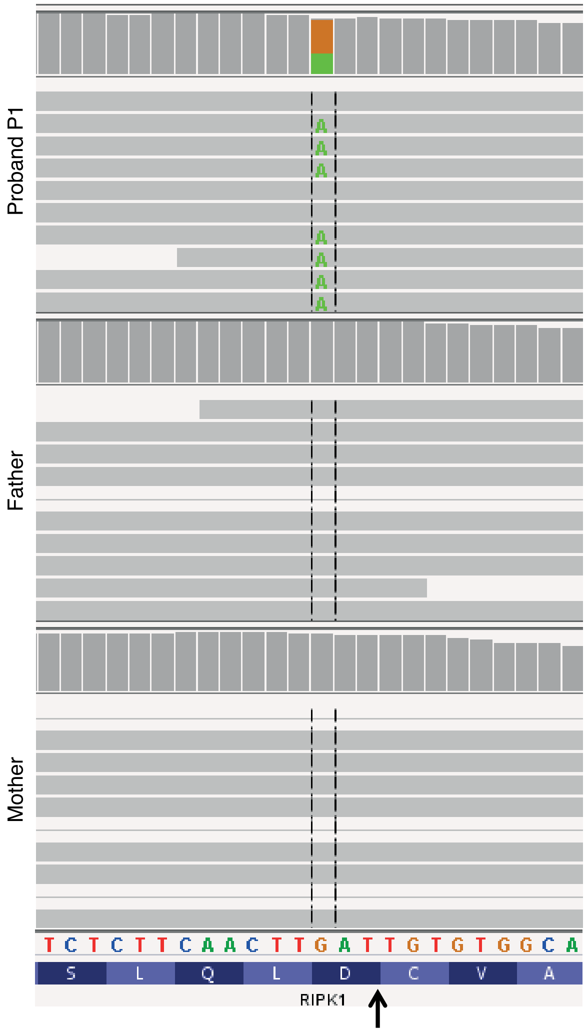

Extended Data Fig. 2 | Exome reads in family 1. Excerpts of coverage histograms and aligned exome sequence reads for the proband and her parents in family 1, displayed using the integrative genomics viewer, demonstrate de novo occurrence of the c.970G>A (p.D324N) missense mutation in the LXXD caspase-6/8 cleavage motif preceding the cleavage site (arrow). Paternity and maternity were confirmed using Mendelian inheritance error rates from the same exome data.

a

Stage		+/+	D325A/+	D325A/D325A
Weaned	Expected	45/180	90/180	45/180
	Observed	73/180	108/180	0/180
E14.5	Expected	3/12	6/12	3/12
	Observed	2/12	5/12	5/12
	Resorbed	**0/12**	**0/12**	**5/12**
E11.5	Expected	2/8	4/8	2/8
	Observed	1/8	5/8	2/8
	Dead	**0/8**	**0/5**	**2/8**
E10.5	Expected	11/44	22/44	11/44
	Observed	12/44	22/44	10/44
	Abnormal	**1/44**	**1/44**	**9/44**

b

		Ripk1$^{D325A/D325A}$					
Stage		*Ripk3*$^{-/-}$	*Mlkl*$^{-/-}$	*Casp8*$^{-/+}$	*Casp8*$^{-/-}$	*Ripk3*$^{-/-}$*Casp8*$^{-/-}$	*Ripk3*$^{-/-}$*Casp8*$^{-/+}$
Weaned	Expected	12/50	4/35	6/47	2/32	13/52	4/37
	Observed	0/50	0/35	0/47	0/32	13/52	5/37
E12.5	Expected	2/9	-	-	-	-	-
	Observed	2/9	-	-	-	-	-
	Abnormal	**1/9**	-	-	-	-	-
E11.5	Expected	-	2/10	-	-	-	-
	Observed	-	2/10	-	-	-	-
	Dead	-	**2/10**	-	-	-	-
E10.5	Expected	3/15	3/15	-	5/21	-	-
	Observed	2/15	1/15	-	1/21	-	-
	Abnormal	**0/15**	**1/15**	-	**1/21**	-	-

c

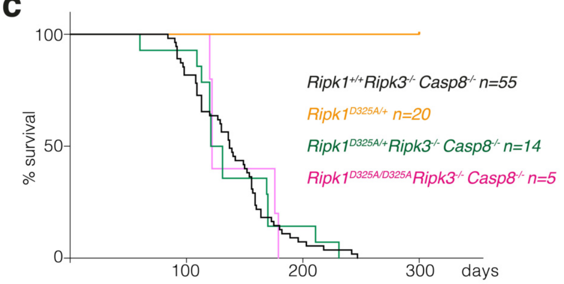

d

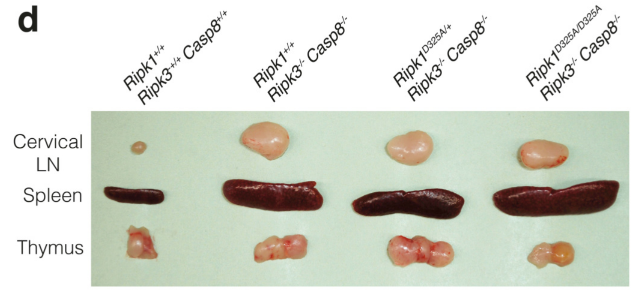

e

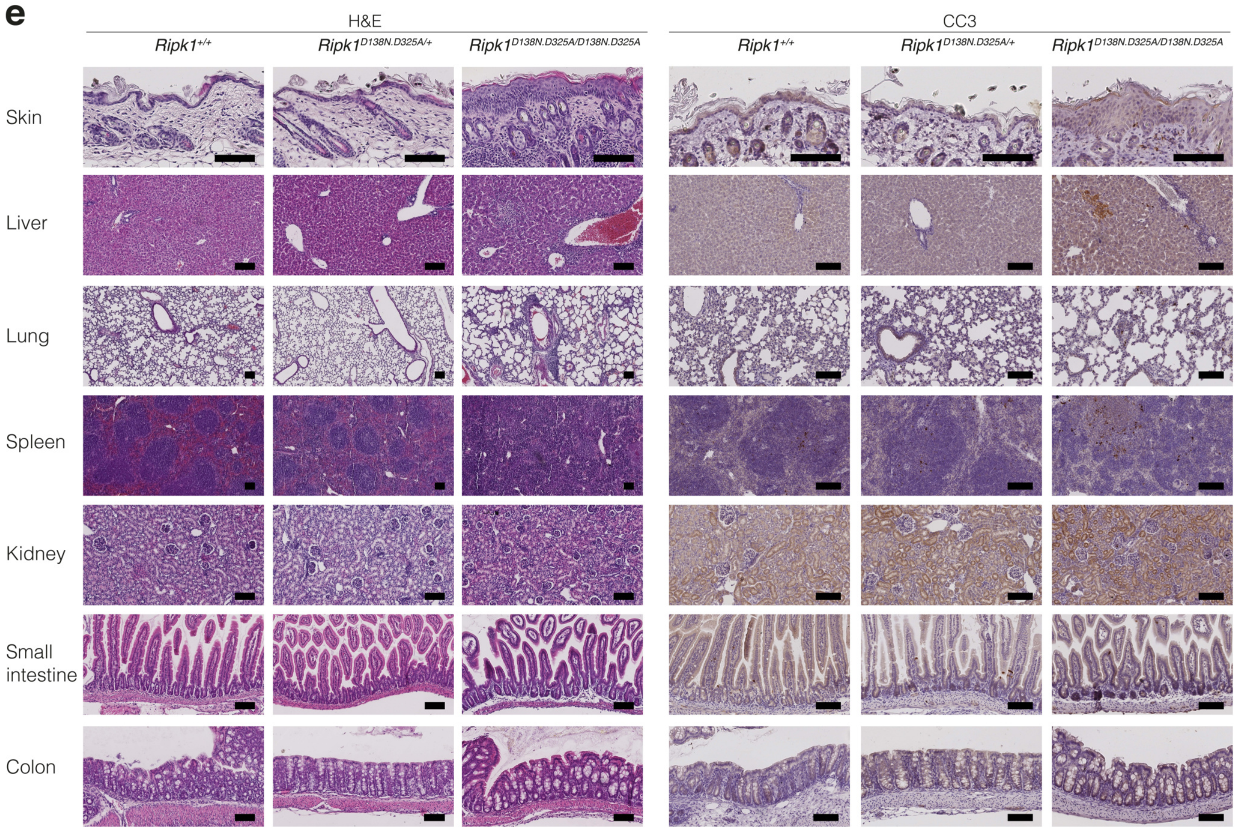

Extended Data Fig. 3 | 'Kinase-dead' RIPK1 or combined loss of *Ripk3* and *Casp8* rescue *Ripk1*$^{D325A/D325A}$ lethality. a, b, Observed numbers of offspring from *Ripk1*$^{D325A/+}$ intercrosses and numbers expected from Mendelian ratios at the indicated stage of development. *Ripk1*$^{D325A/D325A}$ mice are E10.5. All observed E11.5 *Ripk1*$^{D325A/D325A}$ embryos were dead and most of the E10.5 *Ripk1*$^{D325A/D325A}$ embryos were abnormal, as described in Fig. 2a, b. Loss of *Ripk3* rescued to E12.5; however, 50% of the embryos were abnormal. None of the *Ripk1*$^{D325A/D325A}$*Ripk3*$^{-/-}$ mice were born. All observed E11.5 *Ripk1*$^{D325A/D325A}$*Mlkl*$^{-/-}$ embryos were dead, showing that loss of *Mlkl* did not provide any protection. All *Ripk1*$^{D325A/D325A}$*Ripk3*$^{-/-}$*Casp8*$^{-/-}$ mice were born and developed ALPS owing to loss of *Casp8*. **c**, Kaplan–Meyer survival curves of the indicated genotypes. **d**, Cervical lymph nodes (LN), spleen and thymus of 17-week-old mice of the indicated genotypes. Pictures are representative of five mice per genotype. **e**, Tissue sections of 18-day-old *Ripk1*$^{D138N,D325A/+}$, *Ripk1*$^{D138N,D325A/D138N,D325A}$ and control mice stained with H&E (left) and anti-CC3 (brown; right). Pictures are representative of two mice per genotype.

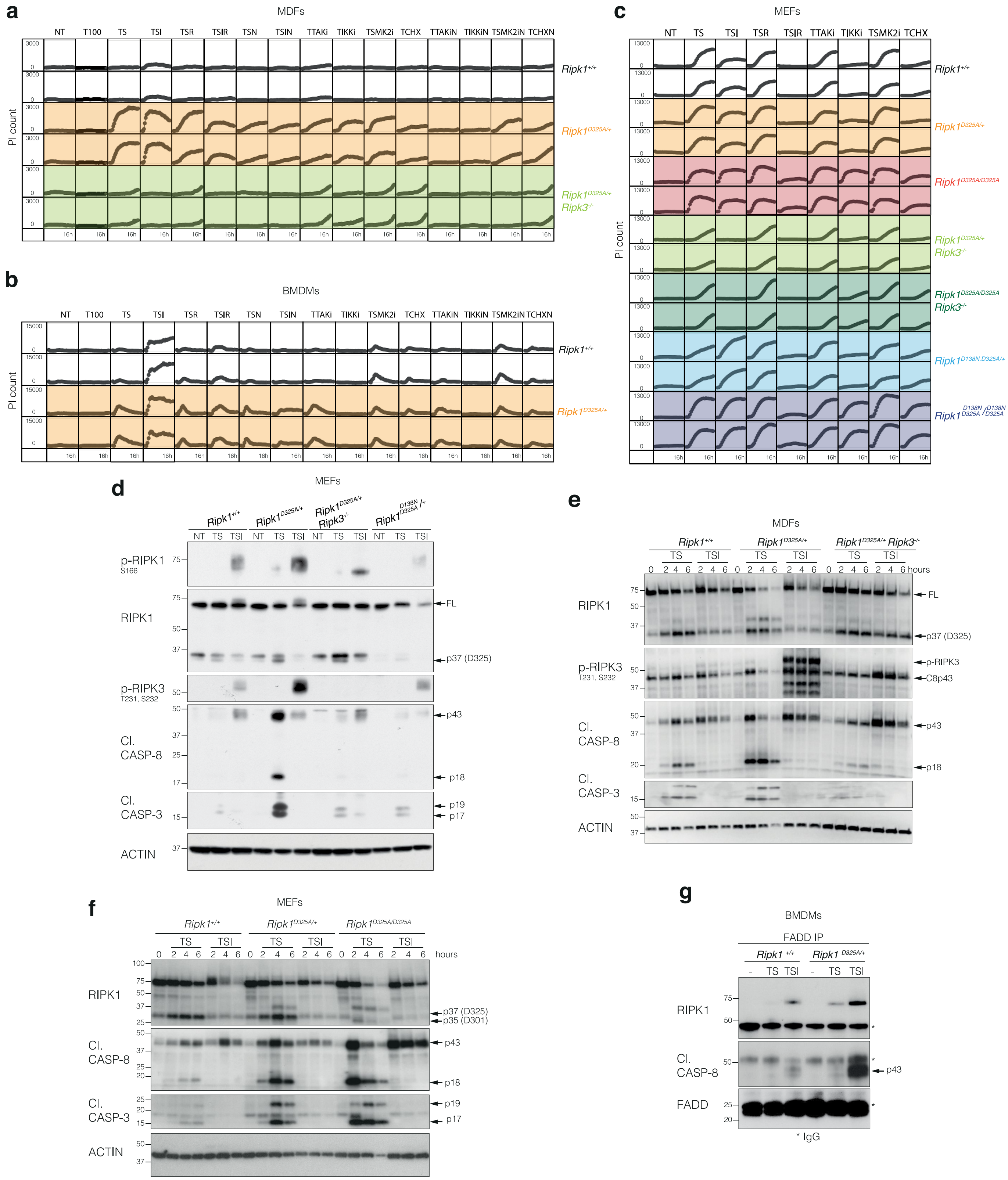

Extended Data Fig. 4 | *Ripk1*$^{D325A/+}$ cells are hypersensitive to TNF-induced death. a–c, MDFs (**a**), BMDMs (**b**) and MEFs (**c**) of the indicated genotypes were treated with either a high dose of TNF (T100; 100 ng ml^{-1}) or a low dose of TNF (T; 10 ng ml^{-1}) combined with SMAC mimetic (S; 100 nM), caspase inhibitor (I; 5 μM), RIPK3 inhibitor (R; 1 μM), necrostatin (N; 10 μM), TAK1 inhibitor (TAKi; 100 nM), IKK inhibitor (IKKi; 100 nM), MK2 inhibitor (MK2i; 2 μM) or cycloheximide (1 μg ml^{-1}) for 16 h. Cell death was quantified by propidium iodide uptake and time-lapse imaging every 30–45 min using IncuCyte. Duplicates are shown for each genotype. Graphs are representative of three (MEFs and MDFs) and two (BMDMs) biologically independent cell lines per genotype repeated independently. **d**, MEFs were treated as in Fig. 3d for 2 h. **e**, **f**, MDFs (**e**) and MEFs (**f**) were treated as in Fig. 3d for the indicated times. Results in **d**–**f** are representative of two independent experiments. β-Actin was used as a loading control. **g**, BMDMs were treated with TNF (100 ng ml^{-1}) combined with SMAC mimetic (500 nM) with or without caspase inhibitor (5 μM) for 90 min, and lysates were immunoprecipitated with anti-FADD. Results are representative of two independent experiments. For gel source data, see Supplementary Fig. 2.

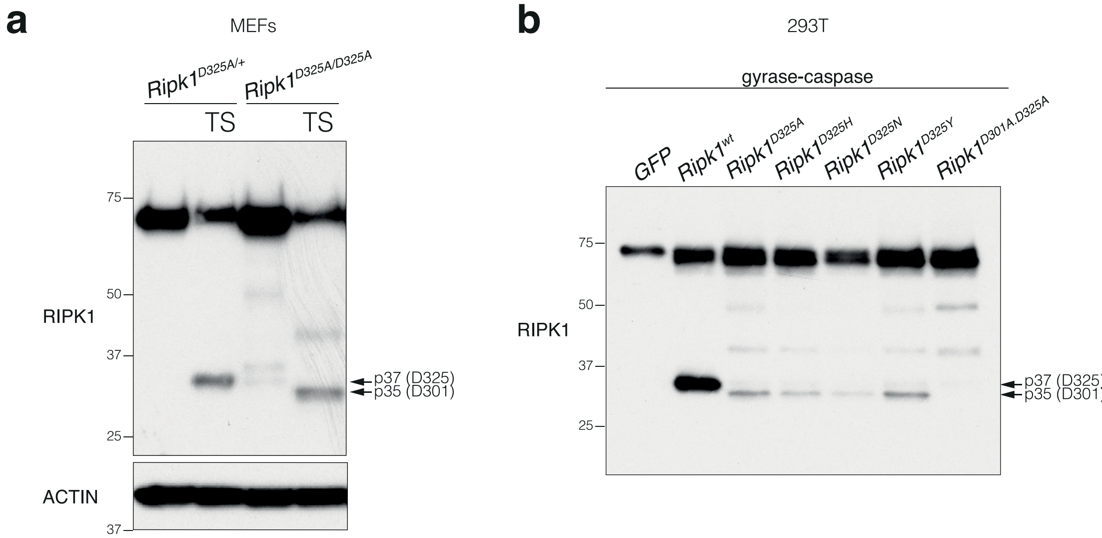

Extended Data Fig. 5 | Alternative cleavage of RIPK1. a, MEFs were treated with 10 ng ml^{-1} TNF combined with 500 nM SMAC mimetic for 2 h. **b**, Doxycycline-inducible caspase-8-gyrase[41], wild-type and mutant mouse RIPK1 constructs or GFP were co-expressed in 293T cells. Cells were treated for 2 h with 1 µg ml^{-1} doxycycline to induce caspase-8-gyrase expression and then for 2 h with 700 nM coumermycin to dimerize caspase-8-gyrase. Antibody recognizing the N-terminal end of RIPK1 was used. Results are representative of four (**a**) and two (**b**) independent experiments. For gel source data, see Supplementary Fig. 2.

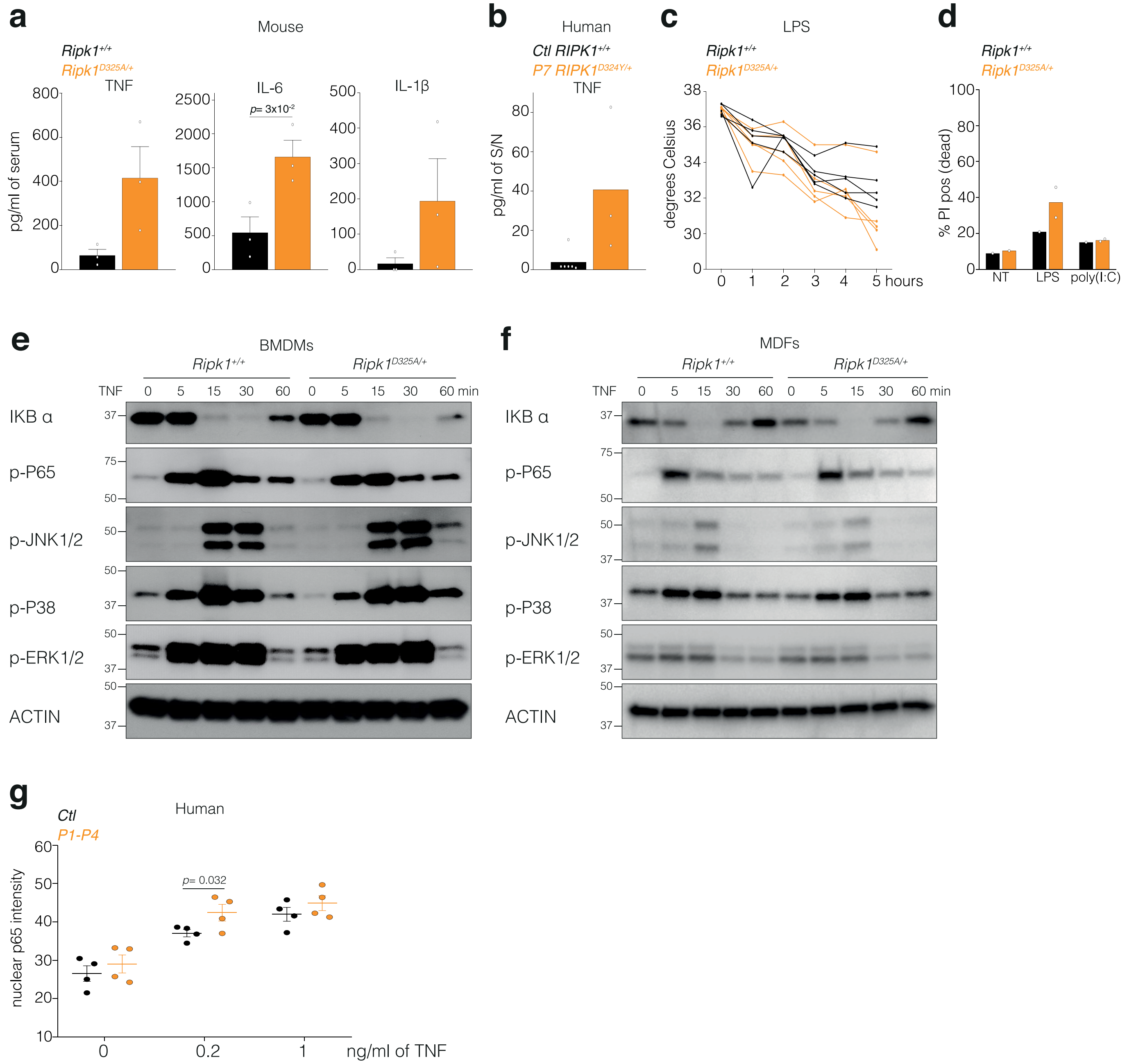

Extended Data Fig. 6 | RIPK1 cleavage limits inflammation in an NF-κB-independent manner. a, Serum cytokine levels in wild-type and *Ripk1*$^{D325A/+}$ mice treated for 3 h with 50 µg of poly(I:C). Each dot represents a mouse. Data are mean ± s.e.m., $n = 3$ mice. **b**, TNF levels in the supernatant (S/N) of two unrelated adolescent controls (Ctl *RIPK1*$^{+/+}$) and P7 *RIPK1*$^{D324Y/+}$ PBMCs treated for 3 h with 5 µg ml^{-1} poly(I:C). Data are mean of triplicates. **c**, Body temperature of mice of the indicated genotypes after injection of 2 mg kg^{-1} LPS. Each line represent a mouse; $n = 5$ mice per genotype. **d**, BMDMs of the indicated genotypes were treated for 24 h with 25 ng ml^{-1} LPS or with 2.5 µg ml^{-1} poly(I:C). Cell death was quantified by propidium iodide staining and flow cytometry. Each dot represents a biological repeat. Graph shows mean; $n = 1$ for *Ripk1*$^{+/+}$ and $n = 2$ for *Ripk1*$^{D325A/+}$. **e**, **f**, BMDMs (**e**) and MDFs (**f**) were treated with 100 ng ml^{-1} of TNF for the indicated times. Results are representative of two independent experiments. β-Actin was used as a loading control. For gel source data, see Supplementary Fig. 2. **g**, NF-κB activation in fibroblasts derived from patient skin biopsies was assessed by measuring nuclear translocation of subunit p65. Each dot represents the median of more than 1,000 single-cell measurements of nuclear mean p65 fluorescent intensities for one individual subject. Data are mean ± s.d., $n = 4$ patients and 4 controls. *P* values determined by unpaired one-tailed (**a**) or unpaired two-tailed (**g**) *t*-tests.

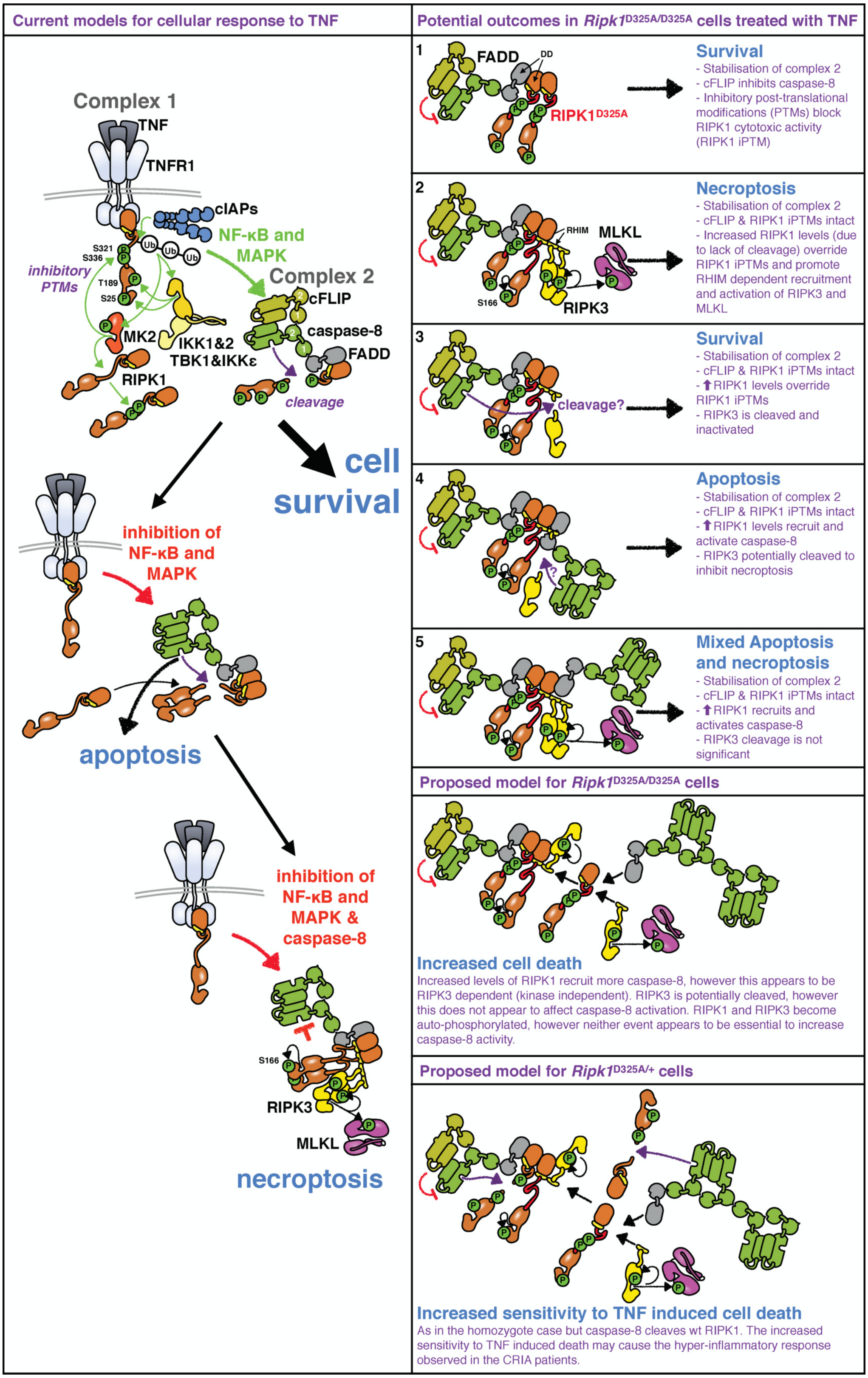

Extended Data Fig. 7 | See next page for caption.

Extended Data Fig. 7 | Proposed model for RIPK1(D325A)-induced cell death. Left, TNF binding to TNFR1 triggers the formation of complex I, and subsequent ubiquitylation and phosphorylation of RIPK1. These post-translational modifications (PTMs) inhibit the cytotoxic activity of RIPK1. Complex I formation activates NF-κB- and MAPK-dependent survival genes such as *CFLAR*, which encodes cFLIP. Subsequently, a cytosolic complex II containing FADD, caspase-8, RIPK1 and cFLIP is formed. In this complex, cFLIP inhibits caspase-8 activity so that a restricted number of substrates (such as RIPK1) are cleaved, but others (such as pro-caspase-3) are not. Cleavage of RIPK1 dismantles complex II. Activation of the NF-κB and MAPK signalling pathways PTM of RIPK1 prevent TNF from inducing cell death, resulting in cell survival (top left). Inhibition of the NF-κB or MAPK signalling pathways reduces levels of cFLIP and accelerates formation of complex II, resulting in cell death via apoptosis (middle left). When NF-κB or MAPK signalling is disrupted in caspase-8-deficient conditions, RIPK1 is not cleaved and autophosphorylates, which triggers the recruitment of RIPK3 and its autophosphorylation. RIPK3 phosphorylates MLKL and necroptosis occurs (bottom left). Right, according to this model, lack of RIPK1 cleavage could result in several distinct outcomes, as follows. (1) RIPK1 accumulation could stabilize complex II, and the presence of cFLIP and inhibitory PTMs to RIPK1 may prevent caspase-8 from killing, resulting in cell survival. (2) The accumulation of 'uncleavable' RIPK1 to complex II could override the inhibitory RIPK1 PTMs, resulting in autophosphorylation of RIPK1 and recruitment of RIPK3, leading to necroptosis. (3) RIPK1 accumulation could result in activated caspase-8 that cleaves RIPK3, resulting in cell survival. (4) Stabilization of complex II could result in recruitment and activation of caspase-8 that induces apoptosis and possibly prevents necroptosis by cleaving RIPK3. (5) Finally, the accumulation of RIPK1 could result in activation of both RIPK3 and caspase-8 and therefore induce both apoptotic and necroptotic cell death. In terms of how these potential outcomes match with our data, in homozygote *Ripk1*^{D325A} cells, both caspase-8 and RIPK3 are activated after TNF signalling, which suggests that apoptosis and necroptosis occur at the same time (Figs. 2d, 3a, b). However, according to these models, loss of RIPK3 limits caspase-8 activation (Fig. 3a, b). This suggests that the recruitment of RIPK3 to complex II increases the recruitment and activation of caspase-8. A precedent for this observation comes from experiments in which RIPK3 inhibitors promoted RIPK1-dependent caspase-8 activation[42,43], in a manner we term 'reverse activation'. In our experiments, however, RIPK3 activation occurs downstream of TNF signalling, which suggests that reverse activation might represent a physiological amplification loop that increases caspase-8 activation. Yet, this requirement for RIPK3 is not present in all cells, as the embryonic lethality of the RIPK1-cleavage mutant is only partially rescued by loss of *Ripk3*. In the heterozygote *Ripk1*^{D325A} cells, caspase-8 cleaves wild-type RIPK1, thus limiting TNF-induced cell death as compared to homozygote cells. However, reduction of cFLIP and/or RIPK1 PTMs by treatment with IAP, TAK1, IKK or translational inhibitors decreases the threshold of TNF sensitivity (Extended Data Fig. 4). This may cause the hyper-inflammatory response observed in patients with CRIA syndrome (Fig. 1).

Extended Data Table 1 | Leukocyte surface markers in patients with CRIA syndrome

			Controls		Affected subjects					
			Family 2		Family 2					Family 3
			P4 spouse	P4 son	P2	P3	P4	P5	P6	P7
		Gender	M	M	F	M	F	M	F	M
		Age at evaluation	57	22	82	55	54	22	20	12
	Percentage of leukocytes	**range**								
	Neutrophils	[34.0-67.9]	53.1	49.7	54.3	56.2	74.2^	61.9	71.5^	61.9
	Monocytes	[5.3-12.2]	9	4.5*	10.3	8.1	6.8	7.9	10.8	11.6
	Eosinophils	[0.8-7.0]	3.1	4	4.5	4.5	2.2	4	2.3	2.7
	Basophils	[0.2-1.2]	0.4	0.5	1.2	1	0.8	0.6	0.3	0.06
	Immature granulocytes	[0.0-0.4]	0.4	NA	0.4	0.3	0.3	0.7^	0.9^	0.3
	Total lymphocytes	[21.8-53.1]	34	41.2	29.3	29.9	15.7*	24.9	14.2*	22.9
Percentage of lymphocytes	**Surface markers**									
Total T	CD3+	[60.0-83.7]	79.5	81.3	83.3	62.6	82.3	83.9^	67	70
Total helper T	CD3+CD4+	[31.9-62.2]	44.6	34.5	24.2*	36.3	48.7	31.2*	30*	34.9
Helper T, naïve	CD3+CD4+CD62L+CD45RA+	[7.6-37.7]	18	22.4	2.4*	2.2*	10.2	6.7*	7.5*	18.1
Helper T, central memory	CD3+CD4+CD62L+CD45RA-	[10.4-30.7]	18.8	9.2*	17	25.1	28.4	17.6	16.7	13.2
Helper T, effector memory	CD3+CD4+CD62L-CD45RA-	[2.3-15.6]	7.1	2.8	4.8	9	7.4	6.9	5.8	3.5
Helper T, TEMRA	CD3+CD4+CD62L-CD45RA+	[0.0-1.5]	0.7	0.1	0	0	2.6^	0	0.1	3^
Total cytotoxic T	CD3+CD8+	[11.2-34.8]	32	37.5^	56.9^	20	30.2	37.9^	31.8	25.9
Cytotoxic T, naïve	CD3+CD8+CD62L+CD45RA+	[5.7-19.7]	14	26.6^	8.3	4.7*	8.5	14.2	11.4	15.8
Cytotoxic T, central memory	CD3+CD8+CD62L+CD45RA-	[1.5-10.3]	4.2	2.9	17.2^	7.9	4.6	13.8^	2.8	3.8
Cytotoxic T, effector memory	CD3+CD8+CD62L-CD45RA-	[1.1-9.2]	2.4	3.1	8.6	5.9	3.6	8.1	4.1	3.3
Cytotoxic T, TEMRA	CD3+CD8+CD62L-CD45RA+	[0.7-7.8]	11.4^	5	22.8^	1.5	13.4^	1.7	13.6^	3
Total double negative T	CD3+CD4-CD8-	[1.3-9.2]	1.6	9.2	1.8	5.5	2.1	13.9^	5	8.8
Double negative T, αβ	CD3+CD4-CD8-	[0.3-1.3]	0.3	1.4^	0.3	0.7	0.6	2.3^	1	NA
Double negative T, γδ	CD3+CD4-CD8-	[0.3-7.6]	0.9	7	0.8	4.1	1.1	10.7^	3.3	NA
Total B	CD20+	[3.0-19.0]	6.6	12.1	1.8*	10.8	11.4	3.3	12.6	12.9
Total B	CD19+	[3.3-19.3]	6.6	12.1	1.8*	10.8	11.4	3.3	12.6	12.9
Total NK	CD16+ or CD56+CD3-	[6.2-34.6]	13.6	7	15.3	26.3	6.6	13	20	17.1
Total NKT	CD16+ or CD56+CD3+	[2.2-12.4]	9.3	9	14.6^	5.8	8.4	26.7^	3.6	9.8

Percentages before tocilizumab treatment are shown. Values above or below reference ranges are marked by carets (^) or asterisks (*), respectively.
NA, not applicable; TEMRA, T effector memory re-expressing CD45RA.

Extended Data Table 2 | Effect of tocilizumab treatment and *RIPK1* caspase cleavage site mutations is absent in known autoinflammatory diseases

a

Affected subject	Months on tocilizumab	ESR (mm/hr) [0-42]	CRP (mg/L) [0-4.99]
P2	0	50	30.4
P2	12	7	0.6
P3	0	8	3.9
P3	10	2	<0.15
P3	10	1	<0.15
P3	34	2	<0.15

b

dbSNP v151
141,456 exomes and genomes from the Genome Aggregation Database (v2.1)
77,238 exomes and genomes from the Kaviar database (September 2015 release)
60,706 exomes from the Exome Aggregation Consortium (v0.3.1)
32,488 exomes from the Haplotype Reference Consortium
6,503 exomes from the NHLBI Exome Sequencing Project
2,577 genomes from the 1000 Genomes Project (August 2015 release)
662 exomes from the NHGRI ClinSeq project
95 exomes from the NIEHS Environmental Genome Project
69 genomes sequenced at Complete Genomics, Inc.

c

Phenotype	Number of subjects	RIPK1 cleavage site mutations
Unexplained recurrent fever	168	0
Lymphadenopathy	332	0
ALPS or ALPS-like	52	0
Idiopathic Castleman disease	2	0

a, Inflammatory markers in subjects treated with tocilizumab. The first time point for each subject is from 3 days before the first tocilizumab injection. P3 had two measurements from the same week at his 10-month post-tocilizumab evaluation. Reference ranges are given in brackets. **b**, Variant databases in which mutations in the *RIPK1* caspase cleavage site are absent. Variant databases are not independent.

c, Result of additional screening for mutations in the *RIPK1* caspase cleavage site.

ALPS, autoimmune lymphoproliferative syndrome; NHGRI, National Human Genome Research Institute; NHLBI, National Heart, Lung, and Blood Institute; NIEHS, National Institute of Environmental Health Sciences.

Extended Data Table 3 | Conservation of RIPK1 caspase-8 cleavage site

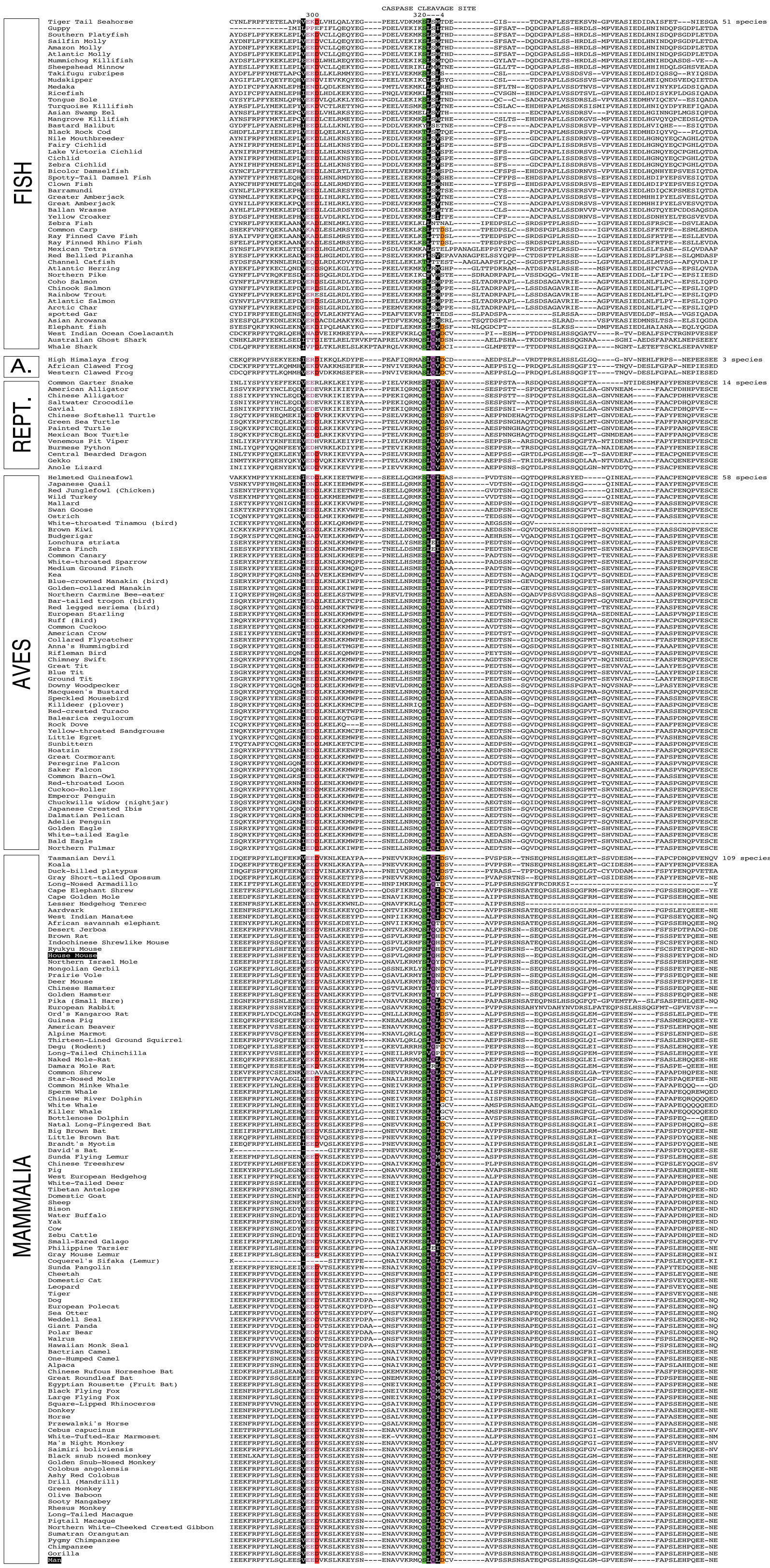

Protein sequences orthologous to human RIPK1 were aligned in 235 vertebrate species, using Multiz alignment in the UCSC Genome Browser. These include representative species from the major classes: 51 fish, 3 amphibians (A.), 14 reptiles (Rept.), 58 birds (Aves) and 109 mammals (Mammalia). Most species within these classes, except fish (7 out of 51), contain the very highly conserved D324 (human numbering) caspase cleavage site within this region. Notably, nearly all species (223) have a potential caspase cleavage site, D300; however, it is noteworthy that this Asp is in most cases succeeded by a large hydrophobic amino acid that is less favourable for caspase cleavage.

naturereserach

Corresponding author(s): Najoua Lalaoui

Last updated by author(s): Sep 22, 2019

Reporting Summary

Nature Research wishes to improve the reproducibility of the work that we publish. This form provides structure for consistency and transparency in reporting. For further information on Nature Research policies, see Authors & Referees and the Editorial Policy Checklist.

Statistics

For all statistical analyses, confirm that the following items are present in the figure legend, table legend, main text, or Methods section.

n/a	Confirmed	
☐	☒	The exact sample size (*n*) for each experimental group/condition, given as a discrete number and unit of measurement
☐	☒	A statement on whether measurements were taken from distinct samples or whether the same sample was measured repeatedly
☐	☒	The statistical test(s) used AND whether they are one- or two-sided *Only common tests should be described solely by name; describe more complex techniques in the Methods section.*
☒	☐	A description of all covariates tested
☒	☐	A description of any assumptions or corrections, such as tests of normality and adjustment for multiple comparisons
☐	☒	A full description of the statistical parameters including central tendency (e.g. means) or other basic estimates (e.g. regression coefficient) AND variation (e.g. standard deviation) or associated estimates of uncertainty (e.g. confidence intervals)
☒	☐	For null hypothesis testing, the test statistic (e.g. *F*, *t*, *r*) with confidence intervals, effect sizes, degrees of freedom and *P* value noted *Give P values as exact values whenever suitable.*
☒	☐	For Bayesian analysis, information on the choice of priors and Markov chain Monte Carlo settings
☒	☐	For hierarchical and complex designs, identification of the appropriate level for tests and full reporting of outcomes
☒	☐	Estimates of effect sizes (e.g. Cohen's *d*, Pearson's *r*), indicating how they were calculated

Our web collection on statistics for biologists contains articles on many of the points above.

Software and code

Policy information about availability of computer code

Data collection	Exome Sequencing was performed on an Illumina HiSeq 2000, 2500 and NovaSeq 6000). RNA Sequencing was performed on an Illumina HiSeq 3000 System. Cell death was monitored by time-lapse imaging using the IncuCyte⊡ live cell analysis imaging (Essenbioscience) and the Opera PhenixTM High Content Screening System (PerkinElmer, USA).
Data analysis	Exome Sequencing was analyzed as follows: alignment with Novoalign; duplicate marking with Picard; re-alignment, re-calibration, and variant calling with GATK; and annotation with Annovar. RNA Sequenced reads were mapped against the human reference genome (GRCh38) using hisat v2.2.1.035. Reads mapped to hemoglobin genes were removed from further analysis. Mapped reads were quantified using HTSeq36,37. All the count data were normalized using TCC38 and differentially expressed genes were detected using edgeR39. Gene ontology enrichment analysis was performed using DAVID37. The original RNA sequencing data is uploaded and available online (Gene Expression Omnibus: GSE127572). For the Opera PhenixTM, images were analysed using the server based Columbus 2.8.0 software (PerkinElmer, USA) to identify nuclei based on SiR-DNA staining and dead cells using PI staining. Results were exported as counts per well to be processed and graphed using R Studio (https://www.R-project.org/) with the tidyverse package (https://CRAN.R-project.org/package=tidyverse).

For manuscripts utilizing custom algorithms or software that are central to the research but not yet described in published literature, software must be made available to editors/reviewers. We strongly encourage code deposition in a community repository (e.g. GitHub). See the Nature Research guidelines for submitting code & software for further information.

Data

Policy information about availability of data

All manuscripts must include a data availability statement. This statement should provide the following information, where applicable:

- Accession codes, unique identifiers, or web links for publicly available datasets
- A list of figures that have associated raw data
- A description of any restrictions on data availability

The original RNA sequencing data is uploaded and available online (Gene Expression Omnibus: GSE127572).

Field-specific reporting

Please select the one below that is the best fit for your research. If you are not sure, read the appropriate sections before making your selection.

☒ Life sciences ☐ Behavioural & social sciences ☐ Ecological, evolutionary & environmental sciences

For a reference copy of the document with all sections, see nature.com/documents/nr-reporting-summary-flat.pdf

Life sciences study design

All studies must disclose on these points even when the disclosure is negative.

Sample size	No sample size calculations were performed. For the in vitro experiments the variability between biological repeats was very low, when possible at least 3 independent biological cell lines were analysed at least twice. For in vivo experiments, for each experiments at least 3 to 5 animals per genotype were used and experiments were performed twice to ensure reproducibility.
Data exclusions	No data were excluded from the study.
Replication	Experiments were reproduced at least twice and all attempts at replication were successful.
Randomization	Mice were grouped according to genotype and animals were age- and sex-matched.
Blinding	Animal technicians were blinded to treatment conditions and tempartures and body temperature measurements without any input from the experimental investigator.

Reporting for specific materials, systems and methods

We require information from authors about some types of materials, experimental systems and methods used in many studies. Here, indicate whether each material, system or method listed is relevant to your study. If you are not sure if a list item applies to your research, read the appropriate section before selecting a response.

Materials & experimental systems

n/a	Involved in the study	
☐	☒	Antibodies
☐	☒	Eukaryotic cell lines
☒	☐	Palaeontology
☐	☒	Animals and other organisms
☐	☒	Human research participants
☒	☐	Clinical data

Methods

n/a	Involved in the study	
☒	☐	ChIP-seq
☒	☐	Flow cytometry
☒	☐	MRI-based neuroimaging

Antibodies

Antibodies used

RIPK1 N-terminal antibody (clone D94C12, cat number 3493, Cell Signaling Technology)
RIPK1 C-terminal antibody (cat number 610459, BD Transduction Laboratories)
Phospho-RIPK1 (clone D1L3S, cat number 65746, Cell Signaling Technology)
Phospho -RIPK3 (Gift from Genetech)
Caspase-6 (clone EPR4405, cat number ab108335, Abcam)
Caspase-8 (clone E7, cat number ab32397, Abcam)
Cleaved caspase-3 (cat number 9661, Cell Signaling Technology)
Cleaved caspase-8 (clone D5B2, cat number 8592, Cell Signaling Technology)
PECAM1 (cat number AF3628, R&D Systems)
goat anti-rabbit AF488 (cat number A-11008, Invitrogen)
donkey anti-goat cy3 (cat number 705-165-147, Jackson ImmunoResearch)
FADD (clone 7A2, WEHI in house)

	IκBα (cat number 9242, Cell Signaling Technology) phospho-p65 (clone 93H1, cat number 3033, Cell Signaling Technology) p65 (clone D14E12, cat number 8242, Cell Signaling Technology) phospho-JNK1/2 (clone cat number 4668P, Cell Signaling Technology) phospho-p38 (clone D3F9, cat number 4511, Cell Signaling Technology) phospho ERK1/2 (cat number 9101 Cell Signaling Technology) β-actin (clone AC-15, cat number A-1978; Sigma-Aldrich)
Validation	Validation data for commercial antibodies are available on vendor websites. Validation of p-RIPK3 has been done on RIPK3 knock-out cells (Figure 3e). GEN135-35-9 anti-mouse phospho-RIPK3 T231, S232 is validated for WB and IHC in Newton et al (2016) Nature 540:129-133. Validation of anti FADD was with FADD knock-out cells in O'Reilly et al (2004) Cell Death Differ 11:724–736

Eukaryotic cell lines

Policy information about cell lines

Cell line source(s)	293T were from ATCC. All mouse cell line were generated from the different mice in this study.
Authentication	Mouse cell lines were sequenced to confirm the RIPK1 D325A genotyping. 293T were not authenticated.
Mycoplasma contamination	293T and most of mouse cell lines were tested and negative for mycoplasma
Commonly misidentified lines (See ICLAC register)	No commonly misidentified line was used

Animals and other organisms

Policy information about studies involving animals; ARRIVE guidelines recommended for reporting animal research

Laboratory animals	All mice are Mus musculus maintained on a C57BL/6 background. Litter-mates males of 8-12 weeks old were used for Fig 4a,e and Extended Data Fig6a. Litter-mates females of 8-12 weeks old were used for Fig 4d. Mice of both sexes of 8-12 weeks old were used for timed matings and to generate MDFs and BMDMs. Litter-mates mice of both sexes were monitor for enlarged lymph nodes and spleen until ethical point (extended data fig3c, d). Litter-mates mice of both sexes of 2 weeks old were used for HE and caspase-3 staining in Extended Data fig3e
Wild animals	The study did not involve wild animals.
Field-collected samples	The study did not involve samples collected from the field.
Ethics oversight	All mouse experiments were performed according to the guidelines of the animal ethics committee of WEHI

Note that full information on the approval of the study protocol must also be provided in the manuscript.

Human research participants

Policy information about studies involving human research participants

Population characteristics	Patient 1 Female 10 yrs Patient 2 Female 82 yrs Patient 3 Male 55 yrs Patient 4 Female 54 yrs Patient 5 Male 22 yrs Patient 6 Female 20 yrs. Patient 7 Male 13 yrs. All had Recurrent fevers. For more information please see Table 1.
Recruitment	Families were enrolled and evaluated in the Clinical Center at the National Institutes of Health under a protocol approved by the Institutional Review Board of the National Institute of Diabetes and Digestive and Kidney Diseases and the National Institute of Arthritis and Musculoskeletal and Skin Diseases. All subjects provided written informed consent. Patients with unexplained recurrent fevers were recruited.
Ethics oversight	All experiments in human samples were performed according to the guidelines of the human ethics committee of the NIH.

Note that full information on the approval of the study protocol must also be provided in the manuscript.

A dominant autoinflammatory disease caused by non-cleavable variants of RIPK1

https://doi.org/10.1038/s41586-019-1830-y

Received: 24 May 2019

Accepted: 21 October 2019

Published online: 11 December 2019

Panfeng Tao[1,16], Jinqiao Sun[2,16], Zheming Wu[3,16], Shihao Wang[1,16], Jun Wang[1,16], Wanjin Li[4,16], Heling Pan[3], Renkui Bai[5], Jiahui Zhang[1], Ying Wang[2], Pui Y. Lee[6], Wenjing Ying[2], Qinhua Zhou[2], Jia Hou[2], Wenjie Wang[2], Bijun Sun[2], Mi Yang[2], Danru Liu[2], Ran Fang[1], Huan Han[1], Zhaohui Yang[1], Xin Huang[3], Haibo Li[7], Natalie Deuitch[8], Yuan Zhang[9], Dilan Dissanayake[10], Katrina Haude[5], Kirsty McWalter[5], Chelsea Roadhouse[11], Jennifer J. MacKenzie[11,12], Ronald M. Laxer[13], Ivona Aksentijevich[14], Xiaomin Yu[1,17]*, Xiaochuan Wang[2,17]*, Junying Yuan[4,17]* & Qing Zhou[1,15,17]*

Activation of RIPK1 controls TNF-mediated apoptosis, necroptosis and inflammatory pathways[1]. Cleavage of human and mouse RIPK1 after residues D324 and D325, respectively, by caspase-8 separates the RIPK1 kinase domain from the intermediate and death domains. The D325A mutation in mouse RIPK1 leads to embryonic lethality during mouse development[2,3]. However, the functional importance of blocking caspase-8-mediated cleavage of RIPK1 on RIPK1 activation in humans is unknown. Here we identify two families with variants in RIPK1 (D324V and D324H) that lead to distinct symptoms of recurrent fevers and lymphadenopathy in an autosomal-dominant manner. Impaired cleavage of RIPK1 D324 variants by caspase-8 sensitized patients' peripheral blood mononuclear cells to RIPK1 activation, apoptosis and necroptosis induced by TNF. The patients showed strong RIPK1-dependent activation of inflammatory signalling pathways and overproduction of inflammatory cytokines and chemokines compared with unaffected controls. Furthermore, we show that expression of the RIPK1 mutants D325V or D325H in mouse embryonic fibroblasts confers not only increased sensitivity to RIPK1 activation-mediated apoptosis and necroptosis, but also induction of pro-inflammatory cytokines such as IL-6 and TNF. By contrast, patient-derived fibroblasts showed reduced expression of RIPK1 and downregulated production of reactive oxygen species, resulting in resistance to necroptosis and ferroptosis. Together, these data suggest that human non-cleavable RIPK1 variants promote activation of RIPK1, and lead to an autoinflammatory disease characterized by hypersensitivity to apoptosis and necroptosis and increased inflammatory response in peripheral blood mononuclear cells, as well as a compensatory mechanism to protect against several pro-death stimuli in fibroblasts.

RIPK1 is a key mediator of apoptotic and necrotic cell death as well as inflammatory pathways[1]. Activation of RIPK1 promotes several cell death responses, including apoptosis and necroptosis, downstream of TNFR1. Caspase-8-mediated cleavage after Asp324 in human RIPK1 (or Asp325 in mouse RIPK1) separates the kinase domain in the N-terminal part of RIPK1 from its intermediate and death domains. The death domain is involved in mediating the activation of the N-terminal kinase by dimerization[1,4,5]. The D324A variant in human RIPK1 blocks cleavage by caspase-8[6]. Homozygous D325A mutation in mouse RIPK1 sensitizes cells to both apoptosis and necroptosis induced by TNF and leads to embryonic lethality. The early demise of *Ripk1*$^{D325A/D325A}$ mice can be rescued by simultaneous deletion of *Ripk3* and *Fadd*[2], or *Mlkl* and *Fadd*[3], but not of either gene alone. However, the functional importance of caspase-8-mediated cleavage of RIPK1 in humans is unknown. Here, we identified a human autoinflammatory disease caused by non-cleavable RIPK1 variants with mutations at D324. We show that disrupted cleavage of RIPK1 by caspase-8 in humans leads to a dominantly inherited condition by promoting the activation of RIPK1.

[1]The MOE Key Laboratory of Biosystems Homeostasis & Protection, Life Sciences Institute, Zhejiang University, Hangzhou, China. [2]Department of Clinical Immunology, Children's Hospital of Fudan University, Shanghai, China. [3]Interdisciplinary Research Center on Biology and Chemistry, Shanghai Institute of Organic Chemistry, Chinese Academy of Sciences, Shanghai, China. [4]Department of Cell Biology, Harvard Medical School, Boston, MA, USA. [5]GeneDx, Gaithersburg, MD, USA. [6]Division of Immunology, Boston Children's Hospital, Boston, MA, USA. [7]Ningbo Women and Children's Hospital, Ningbo, China. [8]Department of Human Genetics, Stanford University School of Medicine, Stanford, CA, USA. [9]Laboratory of Allergic Diseases, National Institute of Allergy and Infectious Diseases, National Institutes of Health, Bethesda, MD, USA. [10]Division of Rheumatology, Department of Paediatrics, The Hospital for Sick Children and the University of Toronto, Toronto, Ontario, Canada. [11]Department of Pediatrics, McMaster Children's Hospital, Hamilton, Ontario, Canada. [12]McMaster University, Hamilton, Ontario, Canada. [13]Division of Rheumatology, Departments of Paediatrics and Medicine, The Hospital for Sick Children and the University of Toronto, Toronto, Ontario, Canada. [14]Inflammatory Disease Section, National Human Genome Research Institute, National Institutes of Health, Bethesda, MD, USA. [15]Women's Hospital, Zhejiang University School of Medicine, Hangzhou, China. [16]These authors contributed equally: Panfeng Tao, Jinqiao Sun, Zheming Wu, Shihao Wang, Jun Wang, Wanjin Li. [17]These authors jointly supervised this work: Xiaomin Yu, Xiaochuan Wang, Junying Yuan, Qing Zhou. *e-mail: yuxiaomin78@gmail.com; xchwang@shmu.edu.cn; junying_yuan@hms.harvard.edu; zhouq2@zju.edu.cn

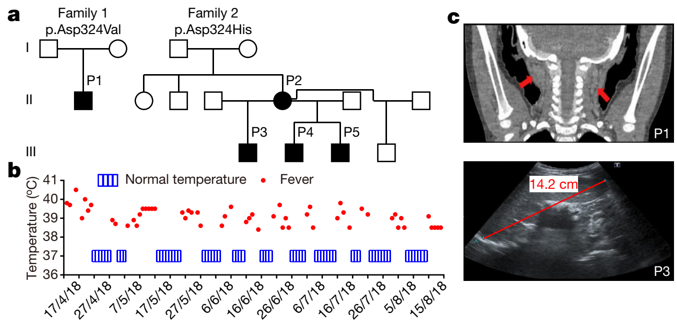

Fig. 1 | Heterozygous variants at the *RIPK1* cleavage site cause autoinflammatory disease in humans. a, Pedigrees of two families with variants in RIPK1 at the caspase-8 cleavage site. **b**, Timeline of recurrent fever episodes in P1 over 4 months. Red dots denote increased temperatures during fever episodes. Blue boxes denote normal temperatures between flares. **c**, Computerized tomography scans of P1 (top) and sonographic image of P3 (bottom) show lymphadenopathy (arrows) and splenomegaly, respectively.

Patients with RIPK1 non-cleavable variants

The first patient (P1) is a two-year-old Chinese boy. His symptoms began at two months of age with periodic fever episodes occurring every eight to ten days and lasting for three to five days (Fig. 1a, b, Extended Data Table 1). His fevers were associated with increased levels of C-reactive protein and white blood cell counts, but no other accompanying symptoms. He developed lymphadenopathy at two years of age (Fig. 1c). The patient did not have a skin rash, arthritis, arthralgia or hepatosplenomegaly. Lymphocyte phenotyping revealed increased counts of both double-negative T cells and naive B cells (Extended Data Table 2).

The second family is of European Canadian ancestry. The proband (P2) is a 35-year-old female who experienced recurrent fevers from six months of age, and developed intermittent lymphadenopathy, hepatosplenomegaly and microcytic anaemia. Three of her four sons are affected. Her eldest (P3, 14 years of age) and youngest (P5, 10 years of age) sons have a similar history of recurrent fevers, intermittent lymphadenopathy, splenomegaly and microcytic anaemia. Her second son (P4, 12 years of age) has microcytic anaemia but no history of recurrent fevers (Fig. 1a, c, Extended Data Table 1).

Whole-exome sequencing (WES) of P1 and his parents revealed that P1 has a heterozygous de novo D324V mutation in RIPK1 (Fig. 1a, Extended Data Fig. 1a–c). For the second family, WES identified a single variant, D324H in RIPK1, which is de novo in the mother and inherited by her three affected sons (Fig. 1a, Extended Data Fig. 1c). No other mutations—including rare variants of unknown importance in genes known to cause periodic fever or autoinflammatory syndromes—were found (Supplementary Tables 1, 2). Copy number variant analysis based on WES data for the first family, and microarray analysis for the second family, did not identify any copy number variants among affected individuals. Both variants affected the caspase-8 cleavage site, D324, which is highly conserved in RIPK1 across species (Extended Data Fig. 1d, e). These variants were not reported in any public database of human exomes and were predicted to be deleterious (combined annotation-dependent depletion (CADD) score > 20) for protein function by computational in silico modelling (Extended Data Fig. 1f).

Expression of wild-type and mutant RIPK1 in HEK293T cells indicated that variants at residue D324, including D324V and D324H, blocked the cleavage of RIPK1 by caspase-8 (Extended Data Fig. 1g). D325A mutation in mouse RIPK1 (the equivalent residue for D324 in human RIPK1) did not affect its turnover (Extended Data Fig. 1h), or block its interaction with other proteins such as binding with caspase-8 into the FADDosome complex (Extended Data Fig. 1i). The variants in D324 resulted in non-cleavable RIPK1, which was directly demonstrated by incubating mutant RIPK1 generated by TNT cell-free protein expression with recombinant caspase-8 (Extended Data Fig. 1j). The inhibitory effect of the D324V variant on the cleavage of RIPK1 by caspase-8 was further confirmed in patient P1 fibroblasts after stimulation by TNF and cycloheximide (CHX) (Extended Data Fig. 1k).

Activation of inflammatory signalling in the patients

We detected markedly increased production of pro-inflammatory cytokines and chemokines such as IL-6, TNF and IFNγ, and anti-inflammatory cytokines such as IL-10 in serum from patients by cytometric bead array (Fig. 2a) or enzyme-linked immunosorbent assay (ELISA) (Extended Data Table 3). Serial sampling from P1 showed that activation of inflammatory responses was even more notable during fever episodes (Fig. 2a). Increased expression of IL-6, TNF and IL-8 in monocytes and IL-6 in T cells from P1 after stimulation by lipopolysaccharide (LPS) was detected by intracellular cytokine staining (Extended Data Fig. 2a, b). Moreover, phosphorylation of STAT3, the downstream marker of IL-6 signalling, was upregulated during fever episodes in patient monocytes at basal level when compared with unaffected controls (Extended Data Fig. 2c). We also observed increased phosphorylation of MAPK p38 in patient monocytes, B cells and T cells after LPS stimulation (Extended Data Fig. 2c).

To study the transcriptional changes related to non-cleavable RIPK1 further, we performed single-cell RNA sequencing in patient peripheral blood mononuclear cells (PBMCs). The patient had a higher percentage of monocytes compared with an age- and sex-matched unaffected control (Fig. 2b, Extended Data Fig. 2d). We observed strong signals in both NF-κB and type-I IFN inflammatory pathways in the patient monocytes (Extended Data Fig. 2e, f). The patient monocytes highly expressed pro-inflammatory cytokines and chemokines, including *IL8*, *IL1B* and *CCL3* (Fig. 2c, Extended Data Figs. 2g, 3a, b). In addition, RNA sequencing in PBMCs implicated different gene expression patterns in cell death pathways that include increased expression of *RIPK3* and *MLKL*, suggesting increased levels of necroptosis machinery in the patient PBMCs (Fig. 2d). Quantitative PCR (qPCR) confirmed the increased expression of *IL6*, *TNF*, *IL8*, *IL1B*, *CXCL2* and *CXCL3* in patient PBMCs (Fig. 2e). Supporting a pathogenic role of excessive IL-6 production, P1 experienced clinical improvement and the PBMCs displayed normalized expression of inflammatory mediators after treatment with tocilizumab (monoclonal antibody against IL-6R) (Extended Data Fig. 4a).

Increased cell death and inflammatory response

We examined the response of patient PBMCs to TNF by measuring cell survival with the CellTiter-Glo assay, and quantified cell death by measuring the plasma membrane permeability with ToxiLight assay (Fig. 3a, Extended Data Fig. 4b). The PBMCs from patients P1, P2 and P3 showed increased sensitivity to both apoptosis induced by co-treatment with TNF and apoptosis-inducing SMAC mimetic SM-164, and necroptosis induced by co-treatment with SM-164 and the pan-caspase inhibitor Z-VAD-FMK (carbobenzoxy-valyl-alanyl-aspartyl-[*O*-methyl]-fluoromethylketone) compared with PBMCs from unaffected controls. Co-treatment was required as treatment with these compounds individually did not elicit cell death. Furthermore, both apoptosis and necroptosis of patient PBMCs were effectively suppressed by the RIPK1 inhibitor necrostatin-1s (Nec-1s) (Fig. 3a, Extended Data Fig. 4b). We found that levels of RIPK1 phosphorylated at S166 (p-S166-RIPK1)—a marker for the activation of RIPK1[7,8]—were increased in the patient PBMCs treated with various combinations of these compound known to activate apoptosis or necroptosis, compared to that of controls (Fig. 3b, Extended Data Fig. 4c), which suggests that blocking the cleavage of RIPK1 sensitizes the activation of its kinase activity. We also found increased levels of p-S358-MLKL—a biomarker for necroptosis[9]—in the patient PBMCs treated with SM-164 plus Z-VAD-FMK compared with that of control

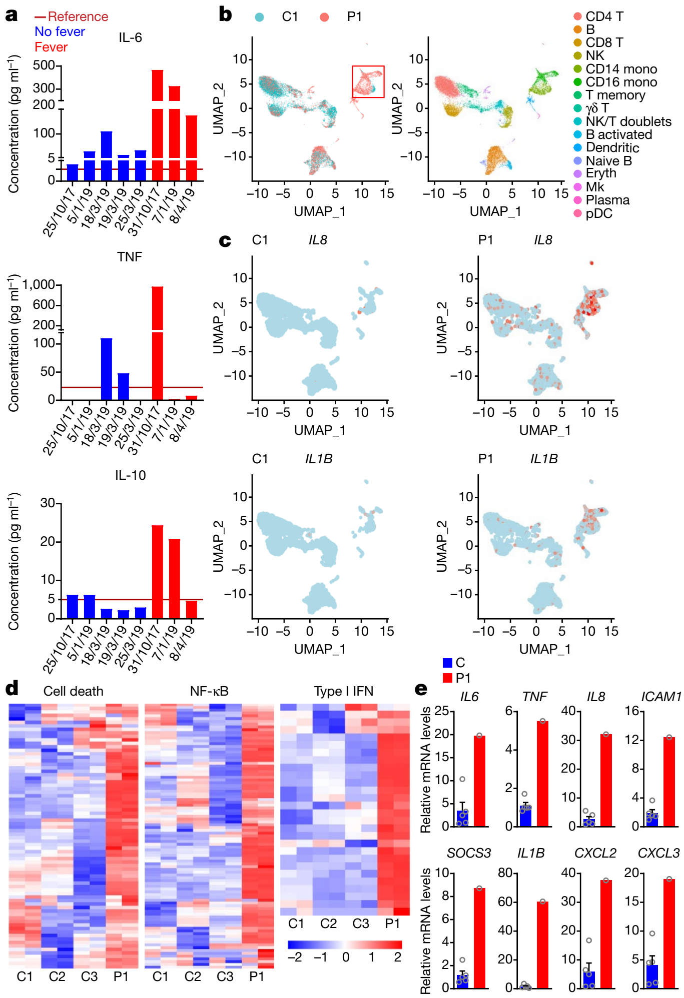

Fig. 2 | Strong activation of inflammatory signalling in patient P1. a, Serum levels of cytokines IL-6, TNF and IL-10 from patient P1 (red denotes serum during fever episodes; blue denotes serum during remission) determined by cytometric bead array. **b**, Left, uniform manifold approximation and projection (UMAP) of 18,928 cells, split between patient P1 and an age- and sex-matched unaffected control (C1) after alignment. Right, UMAP visualization and marker-based annotation of 16 cell subtypes, coloured by cluster identity. The patient P1 displayed higher percentage of monocytes (red frame). Eryth, erythrocytes; Mk, megakaryocyte; NK, natural killer cell; pDC, plasmacytoid dendritic cell. **c**, Visualization of expression of *IL8* and *IL1B* (coloured single cells) on UMAP plot projecting PBMCs from patient P1 (n = 7,936 cells) and an age- and sex-matched unaffected control (n = 10,992 cells). **d**, RNA-sequencing analysis of cell death, NF-κB and type I IFN pathways in patient PBMCs compared with three paediatric unaffected controls (C1–C3). Analysis of each sample was performed in duplicate. For gene names, see Supplementary Fig. 2. **e**, qPCR analysis of cytokine and chemokine-related genes in PBMCs from P1 compared with five paediatric unaffected controls (C). Data are mean ± s.e.m. Circles correspond to each tested individual. Analysis of each sample was performed in triplicate. The PBMCs from patient P1 in **b**–**e** were obtained during fever episodes.

cells (Fig. 3b). Notably, patient PBMCs treated with TNF and SM-164 showed increased levels of not only cleaved caspase-3, but also p-S358-MLKL, which were both effectively reduced by treatment with Nec-1s (Fig. 3b). These results suggest that the non-cleavable RIPK1 variant sensitized the patient PBMCs to both necroptosis and apoptosis in a RIPK1-dependent manner.

Release of cyclophilin A is a biomarker for necroptosis in cell-based assays and has also been implicated as a potential biomarker in human diseases[10,11]. We detected the presence of cyclophilin A in a urine sample from a patient during a fever episode but not in remission, which provides evidence for enhanced necrotic cell death in the setting of inflammation in vivo (Fig. 3c). These findings indicate that the non-cleavable RIPK1 variant may promote the activation of RIPK1, which leads to necrotic cell death in vivo.

Activation of necroptosis promotes a strong inflammatory response such as the production of pro-inflammatory cytokines[12]. Compared to that of control PBMCs, the patient PBMCs stimulated with TNF plus SM-164 showed an exacerbated inflammatory response, which was effectively inhibited by the RIPK1 inhibitor Nec-1s (Fig. 3d). Confirming the involvement of RIPK1 kinase activity in promoting the inflammatory responses, we found that the increased *IL6* expression owing to cell death induced by TNF plus SM-164 stimulation in patient PBMCs was suppressed by Nec-1s (Fig. 3e).

The patient data raised the possibility that non-cleavable RIPK1 variants function directly in promoting its own activation, which in turn mediates apoptosis and necroptosis in a signal-dependent manner. To test this possibility experimentally, we expressed the cleavage site D325V and D325H RIPK1 mutants in *Ripk1*-knockout mouse embryonic fibroblasts (MEFs). Compared to that of *Ripk1*-knockout MEFs and *Ripk1*-knockout MEFs complemented with wild-type RIPK1, MEFs expressing the D325V or D325H RIPK1 mutant were consistently hypersensitive to cell death induced by TNF, which was inhibited by the addition of Nec-1s. The enhanced cell death could also be blocked by introducing a RIPK1 kinase inactivation mutation, D138N, in *cis* with D325V or D325H, providing direct evidence for the role of RIPK1 kinase activity in promoting cell death (Fig. 3f, Extended Data Fig. 5a, b). Similar to patient PBMCs, MEFs expressing D325V or D325H mutant RIPK1 stimulated by TNF alone or TNF plus SM-164 showed increased levels of p-S166-RIPK1 (Fig. 3g). By contrast, stimulation of *Ripk1*-knockout MEFs complemented with wild-type RIPK1 with TNF alone was not sufficient to promote the activation of RIPK1 (Fig. 3g). These data support the hypothesis that the non-cleavable variants of RIPK1 directly promote the activation of RIPK1.

Similar to that of patient PBMCs, RIPK1(D325V)- or RIPK1(D325H)-complemented *Ripk1*-knockout MEFs stimulated by TNF or TNF plus SM-164 showed increased levels of cleaved caspase-3 compared to that of wild-type-complemented MEFs, which was inhibited by Nec-1s and by the kinase inactivation mutation D138N in *cis* with D325V or D325H construct (Fig. 3g, h, Extended Data Fig. 5c). Also similar to that of patient PBMCs, the stimulation of *Ripk1*-knockout MEFs expressing D325V or D325H RIPK1 mutant with TNF alone or TNF plus SM-164 induced increased levels of p-S345-MLKL (Fig. 3g, Extended Data Fig. 5c). By contrast and as expected, stimulation of *Ripk1*-knockout MEFs or *Ripk1*-knockout MEFs complemented with wild-type RIPK1 with TNF alone or TNF plus SM-164 was not sufficient to promote the activation of necroptosis and appearance of p-S345-MLKL. TNF-induced cell death and the appearance of p-S345-MLKL in D325V- or D325H-complemented *Ripk1*-knockout MEFs were both blocked by Nec-1s and by the inactivation D138N mutation in *cis* with D325V or D325H (Fig. 3f–h, Extended Data Fig. 5c). These results suggest that D325V and D325H are gain-of-function mutations in RIPK1 that promote the activation of its kinase, which in turn mediates apoptosis and necroptosis.

Because the expression of non-cleavable RIPK1 promotes both apoptosis and necroptosis, we next determined whether these two forms of cell death might be independent of each other by examining *Ripk1*$^{D325A/D325A}$*Ripk3*$^{-/-}$ MEFs from *Ripk1*$^{D325A/D325A}$ knock-in mice crossed with necroptosis-deficient *Ripk3*$^{-/-}$ mice[2]. Notably, we found that *Ripk1*$^{D325A/D325A}$*Ripk3*$^{-/-}$ MEFs remained sensitized to apoptosis induced by TNF alone and TNF plus SM-164 and showed increased levels of p-S166-RIPK1 and cleaved caspase-3, which are both inhibited by Nec-1s (Fig. 3i, j, Extended Data Fig. 5d, e). Thus, the activated RIPK1 in cells expressing non-cleavable RIPK1 is able to drive RIPK1-dependent apoptosis, independently of necroptosis.

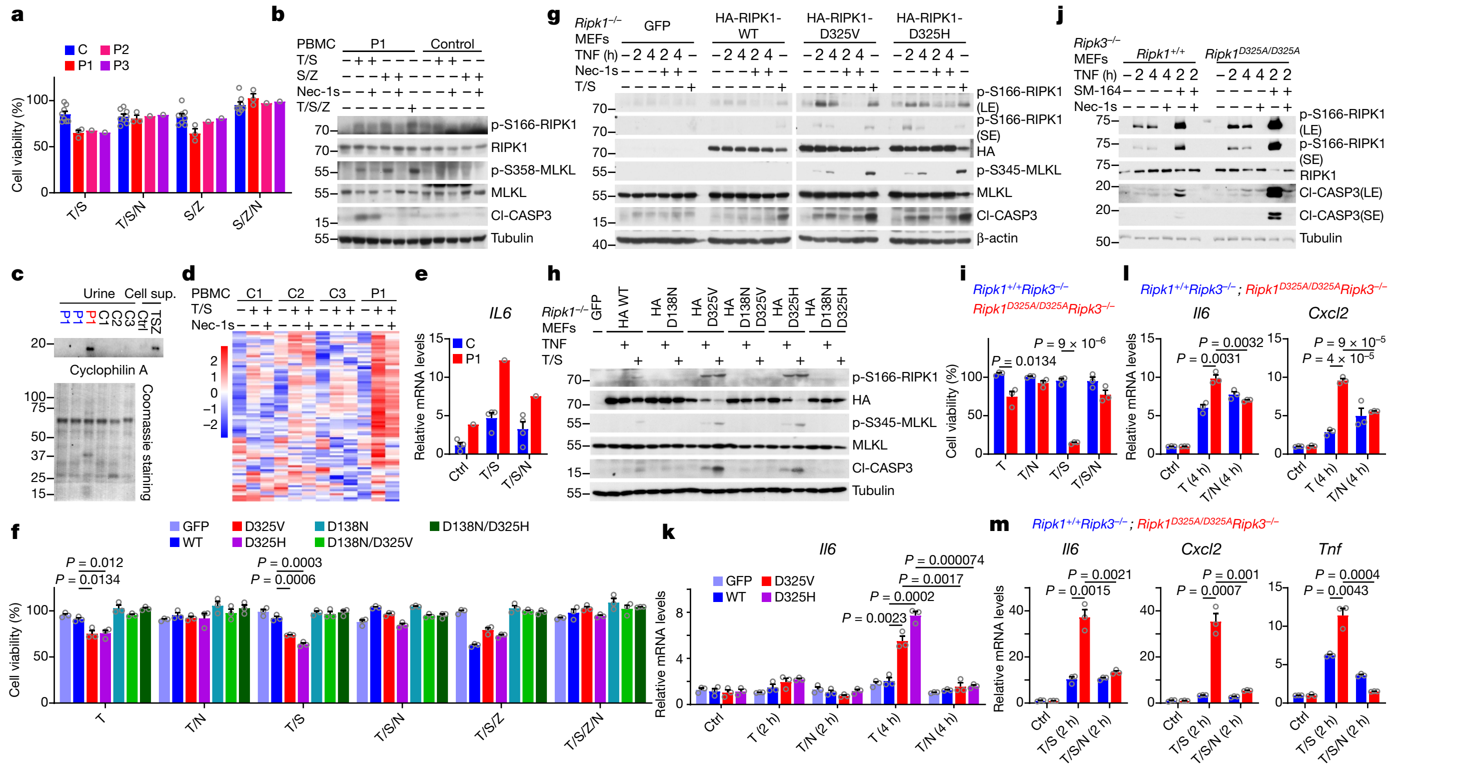

Fig. 3 | RIPK1 cleavage site variants promote cell death and inflammatory response induced by TNF in patient PBMCs and MEFs. a, Cell viability (as measured by CellTiter-Glo assay) of PBMCs from patients and eight paediatric unaffected controls after treatment as indicated for 24 h. N, Nec-1s; S, SM-164; T, TNF; Z, Z-VAD-FMK. Data are mean ± s.e.m. Circles indicate one sample from each individual (P1 was sampled three times). Analysis of each sample was performed in triplicate. **b**, Western blots of PBMCs from patient P1 and a paediatric unaffected control after treatment as indicated for 24 h. −, untreated; cl, cleaved. For gel source data, see Supplementary Fig. 1. Results are representative of two independent experiments. **c**, Western blots of urine samples from P1 during a fever episode (red) and remission (blue) and three paediatric unaffected controls. Supernatant (sup.) of fibroblasts from an unaffected control stimulated with TNF, SM-164 and Z-VAD-FMK (TSZ) served as a positive control. For gel source data, see Supplementary Fig. 1. Results are representative of three independent experiments. **d**, NanoString analysis of PBMCs from patient P1 and three paediatric unaffected controls after stimulation as indicated. For gene names, see Supplementary Fig. 2. **e**, qPCR analysis of *IL6* mRNA levels of PBMCs from patient P1 and four unaffected controls treated as indicated. Data are mean ± s.e.m. Circles correspond to each tested individual. Analysis of each sample was performed in triplicate. The PBMCs in **a**, **b**, **d** and **e** were obtained during remission. **f**, Cell viability of *Ripk1*-knockout MEFs complemented with: GFP; wild-type (WT) RIPK1; D325V, D325H or D138N mutant; or D138N/D325H or D138N/D325V double mutants, treated as indicated for 24 h. Data are mean ± s.e.m., $n = 3$. Circles correspond to each independent experiment. *P* values determined by unpaired two-tailed *t*-test (shown if $P < 0.05$). **g**, **h**, Western blots of *Ripk1*-knockout MEFs complemented with: GFP; wild-type RIPK1; D325V, D325H or D138N mutant; or D138N/D325H or D138N/D325V double mutants, treated as indicated. HA, haemagglutinin; LE, long exposure; SE, short exposure. For gel source data, see Supplementary Fig. 1. Results are representative of three independent experiments. **i**, Cell viability of $Ripk1^{D325A/D325A}Ripk3^{-/-}$ and $Ripk1^{+/+}Ripk3^{-/-}$ MEFs treated as indicated for 24 h. Data are mean ± s.e.m., $n = 3$. Circles correspond to each independent experiment. *P* values determined by unpaired two-tailed *t*-test. **j**, Western blots of $Ripk1^{D325A/D325A}Ripk3^{-/-}$ and $Ripk1^{+/+}Ripk3^{-/-}$ MEFs treated as indicated. For gel source data, see Supplementary Fig. 1. Results are representative of three independent experiments. **k**, *Il6* mRNA expression of *Ripk1*-knockout MEFs complemented with: GFP; wild-type RIPK1; or D325V or D325H mutant, treated as indicated. Data are mean ± s.e.m., $n = 3$. Circles correspond to each independent experiment. *P* values determined by unpaired two-tailed *t*-test. **l**, **m**, qPCR analysis of *Il6* and *Cxcl2* (**l**) or *Il6*, *Cxcl2* and *Tnf* (**m**) expression in $Ripk1^{D325A/D325A}Ripk3^{-/-}$ and $Ripk1^{+/+}Ripk3^{-/-}$ MEFs treated as indicated for 2 or 4 h. Data are mean ± s.e.m., $n = 3$. Circles correspond to each independent experiment. *P* values determined by unpaired two-tailed *t*-test.

We also examined the effect of non-cleavable RIPK1 on ligands of other death receptors such as TRAIL[13]. We found that the cells expressing the non-cleavable mutant RIPK1 also showed increased sensitivity to TRAIL-induced cell death, which could be rescued by the addition of Nec-1s (Extended Data Fig. 5f). Levels of p-S166-RIPK1 were also increased after TRAIL stimulation in mutant RIPK1-complemented MEFs compared to wild-type RIPK1-complemented MEFs (Extended Data Fig. 5g). These data further illustrated that the non-cleavable mutations in RIPK1 increase RIPK1 kinase activity and sensitize the cells to cell death after stimulation by several stimuli.

We next characterized the effect of non-cleavable RIPK1 on cytokine production. NanoString analysis of the patient PBMCs stimulated with TNF alone exhibited upregulated gene expression in the inflammatory pathway, including *IL6*, which was reduced by Nec-1s (Extended Data Fig. 4d). Because patient P1 responded well to IL-6 blockade, we also compared the effects of *Il6* expression in *Ripk1*-knockout MEFs expressing GFP alone, wild-type RIPK1 or mutant RIPK1 (D325V or D325H) (Fig. 3k). We found that MEFs expressing the D325V or D325H mutant showed distinctively enhanced transcription of *Il6* compared to that of wild-type-complemented *Ripk1*-knockout MEFs in response to TNF alone. In addition, the transcriptional production of *Il6*, *Cxcl2* and *Tnf* were also enhanced in $Ripk1^{D325A/D325A}$ $Ripk3^{-/-}$ MEFs after stimulation by TNF or both TNF and SM-164. The enhancement was inhibited by the addition of Nec-1s (Fig. 3l, m). Together, these results suggest that the augmented inflammatory signals associated with the non-cleavable variants were dependent on RIPK1 kinase activity. In keeping with the patient's therapeutic response to IL-6 blockade, these results demonstrate a pathogenic mechanism that relies on the activation of RIPK1 to mediate the production of IL-6.

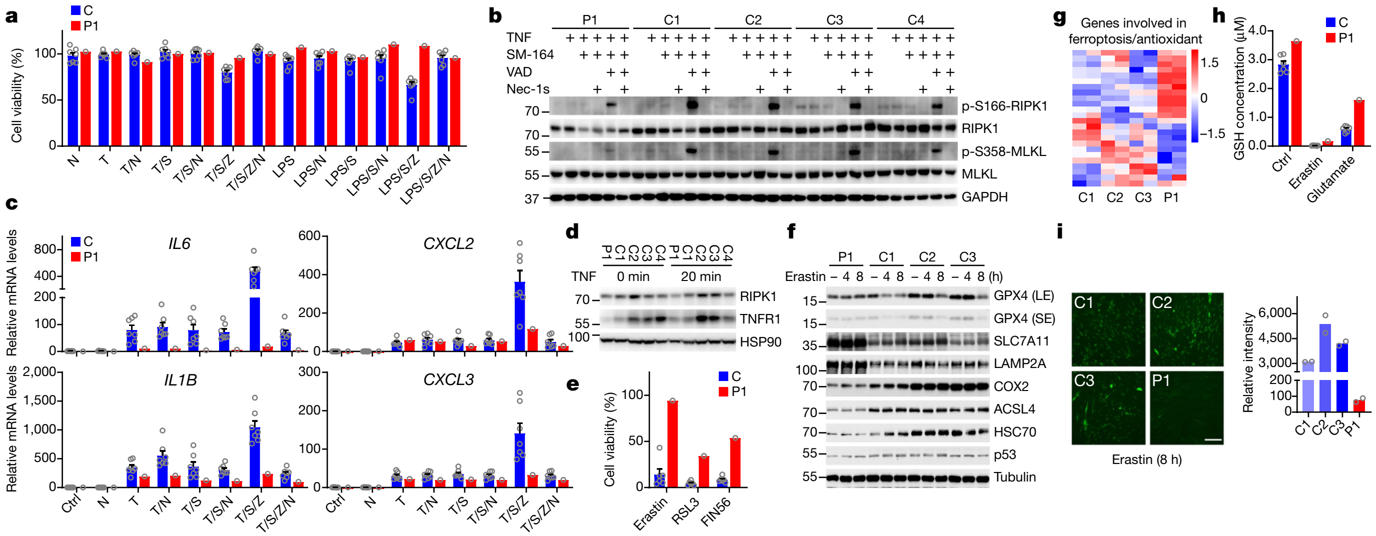

Fig. 4 | Necroptosis and ferroptosis are repressed in the patient fibroblasts. **a**, Cell viability of fibroblasts from P1 and seven paediatric unaffected controls after treatment with indicated stimulation for 24 h. N, Nec-1s; S, SM-164; T, TNF; Z, Z-VAD-FMK. Data are mean ± s.e.m. Circles correspond to each tested individual. Analysis of each sample was performed in triplicate. **b**, Western blots of fibroblasts from patient P1 and four paediatric unaffected controls after treatment with indicated stimulation for 6 h. For gel source data, see Supplementary Fig. 1. Results are representative of three independent experiments. VAD, Z-VAD-FMK. **c**, Patient and seven paediatric unaffected control fibroblasts were treated as indicated for 6 h. The mRNA levels of cytokines were measured by qPCR. Data are mean ± s.e.m. Circles correspond to each tested individual. Analysis of each sample was performed in triplicate. **d**, Western blots of RIPK1 and TNFR1 protein levels at basal state and after TNF stimulation in fibroblasts from P1 and four paediatric unaffected controls. For gel source data, see Supplementary Fig. 1. Results are representative of three independent experiments. **e**, Cell viability of patient fibroblasts treated with erastin, RSL3 or FIN56 compared with six paediatric unaffected controls. Data are mean ± s.e.m. Circles correspond to each tested individual. Analysis of each sample was performed in triplicate. **f**, Western blots of fibroblasts from P1 and three paediatric unaffected controls after treatment with erastin for 4 or 8 h. For gel source data, see Supplementary Fig. 1. Results are representative of three independent experiments. **g**, Expression patterns of genes involved in ferroptosis and antioxidant by RNA sequencing of fibroblasts from patient and three paediatric unaffected controls. Analysis of each sample was performed in duplicate. For gene names, see Supplementary Fig. 2. **h**, GSH concentrations in fibroblasts from P1 compared with six paediatric unaffected controls at baseline and after treatment with erastin or glutamate for 8 h. Data are mean ± s.e.m. Circles correspond to each tested individual. Analysis of each sample was performed in triplicate. **i**, Immunofluorescence (left) and relative fluorescent intensity (right) of cytosolic ROS (green foci) in patient fibroblasts after treatment with erastin for 8 h compared with that of three paediatric unaffected controls. Scale bar, 150 μm. Circles correspond to each tested individual sample. Analysis of each sample was performed in duplicate.

Necroptosis and ferroptosis resistance in fibroblasts

Notably, we observed the opposite response to inducers of cell death in fibroblasts from patient P1 compared with MEFs and patient PBMCs. The patient fibroblasts showed resistance to cell death after stimulation with TNF or LPS plus SM-164 and Z-VAD-FMK (Fig. 4a, Extended Data Fig. 6a). The cell death resistance was further demonstrated by reduced phosphorylation of RIPK1 and MLKL in the patient fibroblasts (Fig. 4b, Extended Data Fig. 6b, c). Patient fibroblasts also showed diminished gene expression of *IL6*, *IL1B* and pro-inflammatory chemokines *CXCL2* and *CXCL3* in response to TNF, SM-164 and Z-VAD-FMK stimulation (Fig. 4c). Levels of RIPK1 protein under basal and stimulated conditions were lower in patient fibroblasts than that of controls (Fig. 4d), and the reduction was rescued by the Nec-1s (Extended Data Fig. 6d). We observed reduction of *RIPK1* at the transcriptional level in fibroblasts (Extended Data Fig. 4e, Extended Data Fig. 6e). Together, these results suggest that decreased RIPK1 expression may compensate for the presence of the RIPK1-activating variant in patient fibroblasts. In addition, we found that patient fibroblasts exhibited reduced expression of TNFR1, which may provide a further mechanism for the decreased sensitivity to TNF (Fig. 4d, Extended Data Fig. 6f). Patient fibroblasts also showed decreased expression of genes involved in cell death pathways such as *RIPK1* and *RIPK3* and a different gene expression pattern (Extended Data Fig. 6g) compared to PBMCs (Fig. 2d). Together, these findings provide evidence of compensatory mechanisms to resist cell death in the patient fibroblasts.

We also characterized the sensitivity of patient fibroblasts to other cell death stimuli. Notably, we found that the patient fibroblasts were highly protected against ferroptosis induced by erastin, RSL3 or FIN56 (Fig. 4e)—an effect that was not found in patient PBMCs or MEFs expressing the RIPK1 D325V or D325H mutant (Extended Data Fig. 4f, Extended Data Fig. 5h). Consistent with these findings, erastin-induced degradation of GPX4[14] was blocked in patient fibroblasts (Fig. 4f), but not in *Ripk1*$^{-/-}$ MEFs expressing mutant RIPK1 (Extended Data Fig. 5i). To explore the mechanism of ferroptosis resistance, we analysed gene expression in patient fibroblasts by RNA sequencing. We found that the expression of several genes involved in inhibiting ferroptosis—such as *SLC7A11*, *CISD1* and *CD44*[15]—were upregulated in patient fibroblasts (Fig. 4g). This pattern was not observed in the patient PBMCs or MEFs (Extended Data Figs. 4g, h, 5j). Similarly, the concentration of the antioxidant glutathione (GSH) was much higher in patient fibroblasts than that of controls (Fig. 4h). By contrast, GSH levels were similar in PBMCs or MEFs expressing wild-type or mutant RIPK1 (Extended Data Figs. 4i, 5k). Consistent with increased levels of GSH, the amounts of reactive oxygen species (ROS) (as indicated by the cytosolic ROS sensor carboxy-H_2DCFDA) were lower after erastin stimulation in patient fibroblasts (Fig. 4i), but not in *Ripk1*-knockout MEFs complemented with mutant RIPK1 (Extended Data Fig. 5l). These data suggest that restricted release of ROS by the patient fibroblasts may help to protect against ferroptosis, as ROS is known to be crucial for mediating ferroptosis[16]. Similarly, because ROS production can promote RIPK1 activation and necroptosis[17,18], the high levels of antioxidant GSH in the patient fibroblasts may also contribute to the resistance to necroptosis.

Discussion

Our study identified a dominantly inherited autoinflammatory disease caused by impaired caspase-8 cleavage in RIPK1. This condition is distinct from the previously reported recessively inherited *RIPK1*-deficient condition that is characterized by immune deficiency[19,20]. By contrast, we show that patients with one copy of mutated RIPK1 in the caspase-8 cleavage site present with symptoms of immune dysfunction, including recurrent fevers and lymphadenopathy.

Our data highlight the role of RIPK1 kinase activity in promoting not only both apoptosis and necroptosis but also transcriptional production of pro-inflammatory cytokines, such as IL-6, which is a previously underappreciated aspect of RIPK1 biology. These results suggest that the periodic fevers of these patients may reflect the augmented production of cytokines such as IL-6 in response to what may be benign stimuli for normal individuals. Activated RIPK1 has been shown to mediate transcription of pro-inflammatory cytokines in myeloid lineages, independent of cell death, in neurodegenerative diseases[21,22]. In addition, cytokines such as TNF in turn can further promote cell death, thus establishing a vicious circle of inflammation that culminates in the development of an autoinflammatory disease.

We show that patient fibroblasts may have developed several compensatory mechanisms to protect against deleterious effects of activated RIPK1, including downregulating the expression of RIPK1 and TNFR1, as well as promoting anti-ROS mechanisms. These findings provide insights into the complex disease mechanisms behind non-cleavable RIPK1 variants in humans compared to that of the mouse models. Our study also linked an activating RIPK1 variant to ferroptosis, which sheds light on the diverse roles of RIPK1 in regulating several cell death pathways.

Online content

Any methods, additional references, Nature Research reporting summaries, source data, extended data, supplementary information, acknowledgements, peer review information; details of author contributions and competing interests; and statements of data and code availability are available at https://doi.org/10.1038/s41586-019-1830-y.

1. Yuan, J., Amin, P. & Ofengeim, D. Necroptosis and RIPK1-mediated neuroinflammation in CNS diseases. *Nat. Rev. Neurosci*. **20**, 19–33 (2019).
2. Zhang, X., Dowling, J. P. & Zhang, J. RIPK1 can mediate apoptosis in addition to necroptosis during embryonic development. *Cell Death Dis*. **10**, 245 (2019).
3. Newton, K. et al. Cleavage of RIPK1 by caspase-8 is crucial for limiting apoptosis and necroptosis. *Nature* **574**, 428–431 (2019).
4. Xu, D. et al. TBK1 suppresses RIPK1-driven apoptosis and inflammation during development and in aging. *Cell* **174**, 1477–1491 (2018).
5. Meng, H. et al. Death-domain dimerization-mediated activation of RIPK1 controls necroptosis and RIPK1-dependent apoptosis. *Proc. Natl Acad. Sci. USA* **115**, E2001–E2009 (2018).
6. Lin, Y., Devin, A., Rodriguez, Y. & Liu, Z. G. Cleavage of the death domain kinase RIP by caspase-8 prompts TNF-induced apoptosis. *Genes Dev*. **13**, 2514–2526 (1999).
7. Degterev, A. et al. Identification of RIP1 kinase as a specific cellular target of necrostatins. *Nat. Chem. Biol*. **4**, 313–321 (2008).
8. Ofengeim, D. et al. Activation of necroptosis in multiple sclerosis. *Cell Reports* **10**, 1836–1849 (2015).
9. Sun, L. et al. Mixed lineage kinase domain-like protein mediates necrosis signaling downstream of RIP3 kinase. *Cell* **148**, 213–227 (2012).
10. Nigro, P., Pompilio, G. & Capogrossi, M. C. Cyclophilin A: a key player for human disease. *Cell Death Dis*. **4**, e888 (2013).
11. Christofferson, D. E. & Yuan, J. Cyclophilin A release as a biomarker of necrotic cell death. *Cell Death Differ*. **17**, 1942–1943 (2010).
12. Zhu, K. et al. Necroptosis promotes cell-autonomous activation of proinflammatory cytokine gene expression. *Cell Death Dis*. **9**, 500 (2018).
13. Henry, C. M. & Martin, S. J. Caspase-8 acts in a non-enzymatic role as a SCAFFOLD for assembly of a pro-inflammatory "FADDosome" complex upon TRAIL Stimulation. *Mol. Cell* **65**, 715–729 (2017).
14. Ingold, I. et al. Selenium utilization by GPX4 Is required to prevent hydroperoxide-induced ferroptosis. *Cell* **172**, 409–422 (2018).
15. Stockwell, B. R. et al. Ferroptosis: a regulated cell death nexus linking metabolism, redox biology, and disease. *Cell* **171**, 273–285 (2017).
16. Dixon, S. J. & Stockwell, B. R. The role of iron and reactive oxygen species in cell death. *Nat. Chem. Biol*. **10**, 9–17 (2014).
17. Zhang, D.-W. et al. RIP3, an energy metabolism regulator that switches TNF-induced cell death from apoptosis to necrosis. *Science* **325**, 332–336 (2009).
18. Zhang, Y. et al. RIP1 autophosphorylation is promoted by mitochondrial ROS and is essential for RIP3 recruitment into necrosome. *Nat. Commun*. **8**, 14329 (2017).
19. Cuchet-Lourenço, D. et al. Biallelic *RIPK1* mutations in humans cause severe immunodeficiency, arthritis, and intestinal inflammation. *Science* **361**, 810–813 (2018).
20. Li, Y. et al. Human RIPK1 deficiency causes combined immunodeficiency and inflammatory bowel diseases. *Proc. Natl Acad. Sci. USA* **116**, 970–975 (2019).
21. Ito, Y. et al. RIPK1 mediates axonal degeneration by promoting inflammation and necroptosis in ALS. *Science* **353**, 603–608 (2016).
22. Ofengeim, D. et al. RIPK1 mediates a disease-associated microglial response in Alzheimer's disease. *Proc. Natl Acad. Sci. USA* **114**, E8788–E8797 (2017).

Publisher's note Springer Nature remains neutral with regard to jurisdictional claims in published maps and institutional affiliations.

Methods

Patients
Patient P1 was evaluated under protocols approved by the Institutional Review Board by Children's Hospital of Fudan University. Patients P2, P3, P4 and P5 and their unaffected family members were evaluated at McMaster Children's Hospital, and the Hospital for Sick Children. Signed consent for their clinical information to be shared and for research samples to be sent to Boston Children's Hospital was obtained. Ethics clearance was received from the Institutional Review Board at Boston Children's Hospital and from Western Institutional Review Board. All relevant ethical regulations were followed. All patients and/or substitute decision markers provided written informed consent.

Unaffected controls
We used unaffected controls for functional assays. Paediatric unaffected controls are less than 10 years old and had no symptoms of inflammation when sampling.

WES
DNA from whole blood was extracted using a Maxwell RSC Whole Blood DNA Kit (Promega, AS1520). One microgram of DNA was used for whole-exome sequencing. For the first family, WES and data analysis were performed as previously described[23–25]. Variants were annotated by ANNOVAR (2018Apr16). Candidate variants were filtered to remove those presenting in the gnomAD, Kaviar, dbSNP and an inhouse database. Variants were further filtered by de novo or dominant inheritance. For the second family, WES was performed and analysed concurrently for the proband, both parents and one affected son as previously described[26]. Other affected or unaffected family members were tested by Sanger sequencing for the presence or absence of the de novo variant identified in the proband.

Sanger sequencing
Sanger sequencing was used to confirm variants identified by exome sequencing as previously described[23–25].

Cell preparation, culture and stimulation
The HEK293T cell line was from the American Type Culture Collection. *Ripk1* gene knockout MEFs were established from *Ripk1*$^{-/-}$ mice. MEFs derived from D325A knock-in mice were provided by J. Zhang. PBMCs were separated by lymphocyte separation medium (LSM) and SepMate tubes (Stemcell) according to the manufacturer's instructions. Fibroblasts were derived from skin biopsies of patient and control donors. HEK293T cells, MEFs and fibroblasts were grown in DMEM (Gibco) supplemented with 10% fetal bovine serum (FBS) (ExCell Bio) and penicillin/streptomycin (HyClone). PBMCs were grown in RPMI-1640 (Gibco) supplemented with 10% FBS and penicillin/streptomycin. All cell lines tested negative for mycoplasma contamination.

Recombinant human TNF (Peprotech, 300-01A) was used to stimulate PBMCs (50 ng ml^{-1}, 100 ng ml^{-1}), fibroblasts (20 ng ml^{-1}, 50 ng ml^{-1}) and MEFs (50 ng ml^{-1}) for the indicated amount of time. LPS (Sigma, L6529) was used to stimulate PBMCs (1 μg ml^{-1}), MEFs (1 μg ml^{-1}) and fibroblasts (1 μg ml^{-1}) for the indicated amount of time. TRAIL (R&D, 1121-TL) was used to stimulate MEFs (100 ng ml^{-1}) for the indicated amount of time. Z-VAD-FMK (100 μM) and SM-164 (50 nM) (from Selleck) and Nec-1s (10 μM) (made by custom synthesis) were used to treat PBMCs, MEFs and fibroblasts. Erastin and RSL3 were used to induce cell ferroptosis in PBMCs (10 μM, 1 μM), MEFs (10 μM, 0.5 μM) and fibroblasts (10 μM, 0.5 μM).

RNA sequencing
One microgram of RNA was used for library preparation. Libraries were generated using NEBNext Ultra RNA Library Prep Kit for Illumina (NEB) following manufacturer's recommendations and index codes were added to attribute sequences to each sample. Library quality was assessed on the Agilent Bioanalyzer 2100 system. The libraries were sequenced on Illumina Novaseq and 150-bp paired-end reads were generated. Sequenced reads were mapped against the human reference genome (GRCh38) or mouse reference genome (GRCm38) using HISAT2. featureCounts was used to count the reads numbers mapped to each gene. Differential expression analysis was performed using the DESeq2 R package.

Single-cell RNA sequencing
10X Genomics Chromium machine was used for 8,000–10,000 single-cell capture and cDNA preparation. The machine divided thousands of cells into nanolitre-scale Gel Bead-In-EMulsions for barcoding followed by clean up using the silane magnetic beads and Solid Phase Reversible Immobilization beads. Barcoded cDNA was then amplified by PCR. The library was constructed according to the manufacturer's instruction. Sequencing was carried out on Illumina Novaseq. Sequence data were processed with Cell Ranger V3.0.1 (10X Genomics). The resulting count matrices followed the standard pipeline with default parameters. The UMAP plots were calculated based on the first 20 components of the CCA, and clusters were identified by Seurat R package (https://satijalab.org/seurat/).

NanoString assay
One-hundred nanograms of total RNA was used for NanoString assay and gene expression analysis was conducted using the nCounter Analysis System (NanoString Technologies) with a codeset designed to target 594 immunologically related genes. NanoString assay and data analysis were performed as previously described[25].

Quantitative RT–PCR assay
Total RNA from fibroblasts, MEFs and PBMCs was extracted using the RNeasy Mini kit (Qiagen, 74104). cDNA was generated by the PrimeScript RT reagent kit with gDNA Eraser (Perfect Real Time) (Takara, RR047A), and qPCR was performed using TB Green Premix Ex Taq II (Tli RNaseH Plus) (Takara, RR820A). The reactions were run on Applied Biosystems 7500 Real-Time PCR System (Life Technologies) and ROCHE 480II. Relative mRNA expression was normalized to *ACTB* or *GAPDH* and analysed by the $\Delta\Delta C_t$ method.

Antibodies and expression plasmids
The following antibodies were purchased from Cell Signaling Technology: β-actin (4970), β-tubulin (86298), GAPDH (5174), RIPK1 (3493), p-RIPK1 (Ser166) (65746), MLKL (14993), p-MLKL (Ser358) (91689), p-MLKL (Ser345) (37333), p65 (8242), p-p65 (Ser65) (3033), IKKα (11930), IKKβ (2370), p-IKKα/β (Ser176/180) (2697), IκBα (4814), p-IκBα (Ser32) (2859), p38 (8690), p-p38 (Thr180/Tyr182) (4511), TNFR1 (3736), caspase-8 (4790), cleaved-caspase-8 (8592), caspase-3 (9662), cleaved-caspase-3 (Asp175) (9661), HA-tag (3724), SLC7A11 (12691). Cyclophilin A (ab41684), GPX4 (ab125066), LAMP2A (ab125068), COX2 (ab15191) and p53 (ab32389) were purchased from Abcam. FADD (sc-6036) and ACSL4 (sc-365230) were purchased from Santa Cruz Biotechnology. p-RIPK1 (Ser166) (BX60008) was made by Biolyx. HSC70 (10654-1-AP) was purchased from Proteintech Group. HSP90 (BF9107) was purchased from Affinity. MLKL (reactivity for *Mus musculus*) was homemade[27].

Human wild-type RIPK1 plasmid (RC216024) was from Origene, and the mutant RIPK1 plasmids (D324V, D324H and D324K) were constructed by site-directed mutagenesis. Mouse wild-type RIPK1 plasmid was generated by PCR amplification from the cDNAs of MEFs, and then cloned into the pMSCV vector made in-house, and the mutant mouse RIPK1 plasmids (D325V and D325H) were constructed by site-directed mutagenesis.

Immunoprecipitation and western blotting
Cells were lysed in cold cell lysis buffer (20 mM Tris-HCl, pH 7.4, 150 mM NaCl, 0.5% NP-40, protease and phosphatase inhibitor mixture (Thermo

Fisher, 78442) and 10% glycerol) for 10 min and centrifuged at 20,000*g* for 10 min. Protein concentration was measured on the cleared lysates by BCA protein assay kit (Thermo Fisher, 23225). Immunoprecipitation and immunoblotting were conducted as described previously with specific antibodies[23,25].

In vitro RIPK1 cleavage assay
Unlabelled in vitro transcription and translation (IVTT) of 1 μg wild-type and mutant RIPK1 constructs were performed in 50 μl reactions using the TNT T7 Quick Coupled Transcription/Translation System (Promega, L1170). The reaction was incubated with purified recombinant caspase-8 protein (R&D, 705-C8/CF) and then immunoblotted with RIPK1 antibody.

Cytokine detection in serum
The concentrations of cytokines in serum were measured by BD Cytometric Bead Array. Cytokine concentrations for IL-6, TNF and IL-10 in the serum were determined by BD Cytometric bead arrays (BD Bioscience). All data were analysed by FCAPArray V3 software (BD Biosciences).

Flow cytometry analysis of phosphorylation
For phos-flow staining, isolated PBMCs were treated with or without LPS ($1\ \mu g\ ml^{-1}$) for 6 h at 37 °C, with 5% CO_2 and then permeabilized with Perm Buffer III according to the manufacturer's instructions (BD Biosciences). Surface marker CD3, CD14 and CD19 (BD Biosciences) were used to gate total T cells, monocytes and total B cells. The expression of p-STAT3, p-p65 and p-p38 were analysed by flow cytometry. For phos-flow analysis, the following antibodies were used: Alexa Fluor 647-conjugated antibody against STAT3 phosphorylated at Y705 (BD Biosciences), Alexa Fluor 488-conjugated antibody against NF-κB p65 phosphorylated at S529 (BD Biosciences) and Alexa Fluor 488-conjugated antibody against p38 phosphorylated at T180/Y182 (BD Biosciences). Isotype control antibodies were used to normalize the background signals for intracellular staining. All events were acquired on a FACS Canto II cytometer (BD Biosciences) and analysed with FlowJo (Tree Star). Blue lines in the Extended Data Fig. 2c indicate basal levels, orange lines indicate LPS stimulation for 6 h and red lines indicate an isotype control. The numbers mark the percentage of cells displaying phosphorylation of STAT3 or p38 based on comparison with isotype control staining for each cell type.

Intracellular cytokine staining
Intracellular cytokine staining for IL-6, TNF and IL-8 were measured in PBMCs at baseline and following LPS stimulation. Cells were washed twice with PBS, then treated with LPS ($1\ \mu g\ ml^{-1}$ per 1×10^6 PBMCs) and Golgi plug (BD Biosciences) for 6 h at 37 °C, with 5% CO_2 and then permeabilized with Perm/Fix for 30 min at 4 °C. Cells were stained by antibodies CD3-Percp-cy5.5 (BD Biosciences), CD14-PE-CY7 (BD Biosciences), CD4-FITC (BD Biosciences), CD19-APC (BD Biosciences), IL8-PE (Biolegend), IL10-BV421 (Biolegend), IL6-Percp-cy5.5 (Biolegend) and TNF-V450 (Biolegend). Isotype control antibodies were used to normalize the background signal for intracellular staining. All events were acquired on a FACS Canto II cytometer and analysed with FlowJo (Tree Star).

Cell viability assay
General cell survival was measured by the ATP luminescence assay CellTiter-Glo (Promega). The percentage of viability was normalized to readouts of untreated cells.

Cell death assay
Cell death was determined by ToxiLight Non-destructive Cytotoxicity BioAssay Kit (Lonza, LT07) or SYTOX Green Nucleic Acid Stain (Thermo Fisher, S7020). All experiments were conducted on 384-well plates with at least three biological replicates. Data were collected by the multimode plate reader (Bio Tek).

Intracellular ROS detection
Cells were seeded in 12-well plates and treated with the indicated stimuli for the indicated amount of time. After cell death induction, 5 μM carboxy-H_2DCFDA was added to cells for 30 min at room temperature. Cells were then returned to warm growth medium and incubated for 15 min, followed by replacement of growth medium with PBS. Images were taken using a Leica fluorescence microscope.

Intracellular GSH detection
The GSH concentration in cells was assessed by GSH-Glo Glutathione Assay Kit (Promega, V6911) according to the manufacturer's instructions.

Statistics
No statistical methods were used to predetermine sample size. For cell-based experiments, biological triplicates were performed in each single experiment in general, unless otherwise stated. All values were expressed as mean ± s.e.m. and calculated from the average of at least three independent biological replicates unless specifically stated. Statistical analysis was performed using GraphPad Prism 8 software (GraphPad Software). For comparisons between two groups, the Student's *t*-test (unpaired and two-tailed) was applied. In all tests, a 95% confidence interval was used, for which $P < 0.05$ was considered a significant difference. Statistical analysis of single-cell RNA sequencing and RNA sequencing was performed using R Software (R v.3.5.2).

URLs
ANNOVAR, http://annovar.openbioinformatics.org/en/latest/user-guide/download/; CADD, https://cadd.gs.washington.edu/; gnomAD, https://gnomad.broadinstitute.org/; Kaviar genomic variant database (Kaviar), http://db.systemsbiology.net/kaviar/; Sorting Intolerant from Tolerant (SIFT), https://sift.bii.a-star.edu.sg/; PolyPhen-2, http://genetics.bwh.harvard.edu/pph2/; likelihood ratio test (LRT), http://www.genetics.wustl.edu/jflab/lrt_query.html; MutationTaster, http://www.mutationtaster.org/.

Reporting summary
Further information on research design is available in the Nature Research Reporting Summary linked to this paper.

Data availability
Gel source data are shown in Supplementary Fig. 1. Source Data for Figs. 2–4 and Extended Data Figs. 1, 2, 4–6 are provided with the paper. All other data that support the findings of this study are available from the corresponding authors upon reasonable request.

23. Zhou, Q. et al. Loss-of-function mutations in *TNFAIP3* leading to A20 haploinsufficiency cause an early-onset autoinflammatory disease. *Nat. Genet*. **48**, 67–73 (2016).
24. Zhou, Q. et al. Early-onset stroke and vasculopathy associated with mutations in ADA2. *N. Engl. J. Med*. **370**, 911–920 (2014).
25. Zhou, Q. et al. Biallelic hypomorphic mutations in a linear deubiquitinase define otulipenia, an early-onset autoinflammatory disease. *Proc. Natl Acad. Sci. USA* **113**, 10127–10132 (2016).
26. Retterer, K. et al. Clinical application of whole-exome sequencing across clinical indications. *Genet. Med*. **18**, 696–704 (2016).
27. Wu, Z. et al. Chaperone-mediated autophagy is involved in the execution of ferroptosis. *Proc. Natl Acad. Sci. USA* **116**, 2996–3005 (2019).
28. Ding, Y. et al. Reference values for peripheral blood lymphocyte subsets of healthy children in China. *J. Allergy Clin. Immunol*. **142**, 970–973 (2018).

Acknowledgements We thank the patients, their families and the unaffected controls for their support during this research study. We thank J. Zhang for *Ripk1*$^{+/+}$*Ripk3*$^{-/-}$ *and Ripk1*$^{D325A/D325A}$ *Ripk3*$^{-/-}$ MEFs. We thank L. Shen, M. Shi, M. Yu and R. Wang for help. Q.Z. received the grants 2018YFC1004903 from National Key Research and Development Project, 31771548 and 81971528 from The National Natural Science Foundation of China, LR19H100001 from Zhejiang Provincial Natural Science Foundation of China and 2018QN81009 from the Fundamental Research Funds for the Central Universities. X.W. received the grant 81373221 from The National Natural Science Foundation of China. The work of Z.W., H.P. and X.H. was supported by the National Key R&D Program of China (2016YFA0501900) and the China National Natural

Science Foundation (31530041). The work of H.L. was supported by Ningbo Health Branding Subject Fund (PPXK2018-06).

Author contributions P.T., J.S., Z.W., S.W., J.W. and W.L. contributed equally. H.P., R.B., J.Z., Y.W. and P.Y.L. contributed equally. Q.Z., J.Y., X.W. and X.Y. designed the study, directed and supervised the research. P.T., J.S., Z.W., S.W., J.W., W.L. and H.P. performed experiments and analysed most of the data. J.Z., Y.W., P.Y.L., R.F., H.H., Z.Y., X.H. and Y.Z. performed experiments. J.S., R.B., W.Y., Q.Z., J.H., W.W., B.S., M.Y., D.L., H.L., D.D., K.H., K.M., C.R., J.M., R.M.L. and X.W. enrolled the patients, collected and interpreted clinical information. N.D. provided comments. Q.Z., J.Y., X.Y. and P.T. wrote the manuscript, with input from others. I.A. provided valuable advice and edited the manuscript. All authors contributed to the review and approval of the manuscript.

Competing interests J.Y. is a consultant of Denali Therapeutics. R.B., K.H. and K.M. are employees of GeneDx, Inc. The rest of authors declare no competing financial interests.

Additional information

Supplementary information is available for this paper at https://doi.org/10.1038/s41586-019-1830-y.

Correspondence and requests for materials should be addressed to X.Y., X.W., J.Y. or Q.Z.

Peer review information *Nature* thanks Min Ae Lee-Kirsch, Egil Lien and the other, anonymous, reviewer(s) for their contribution to the peer review of this work.

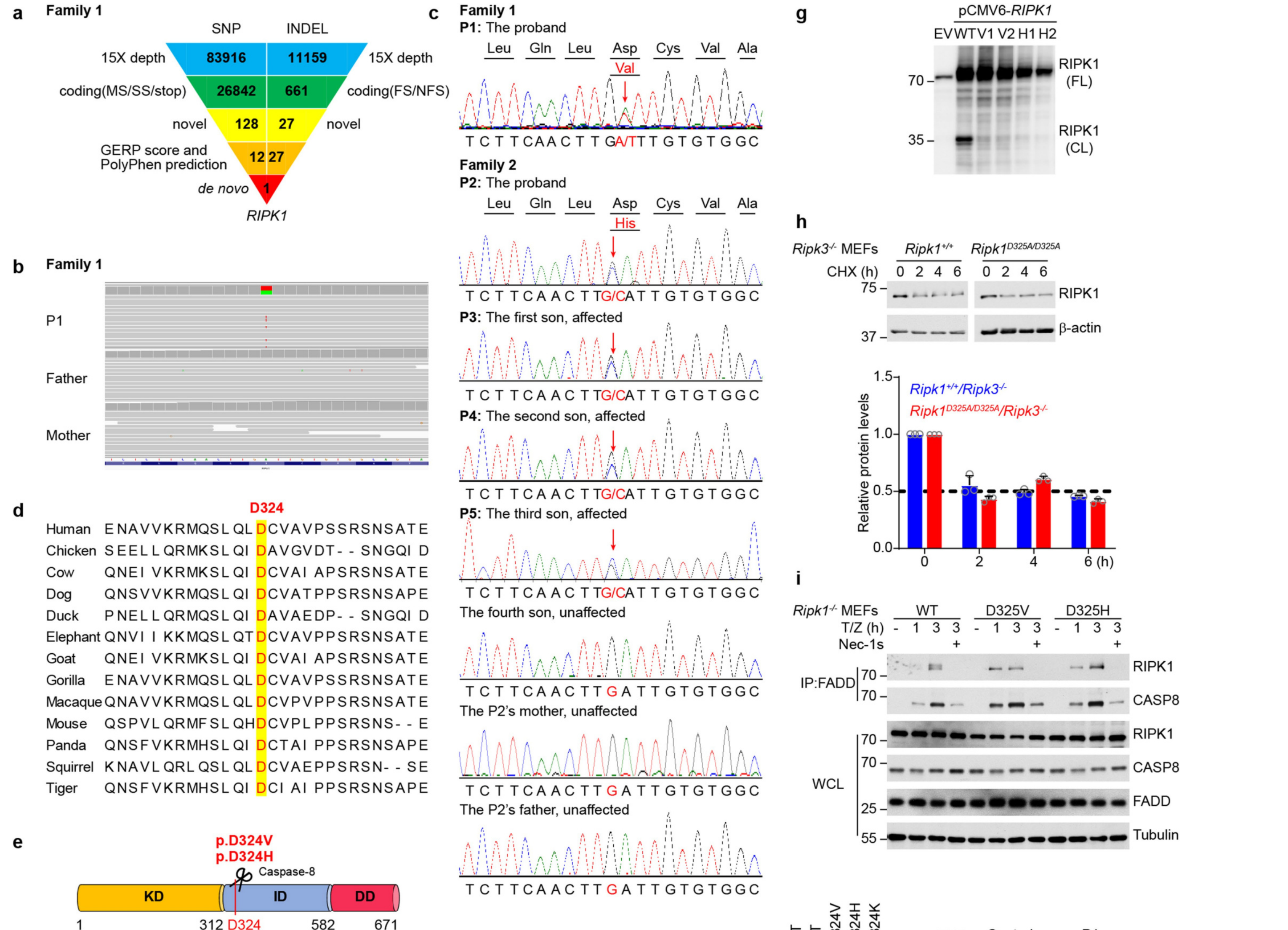

f

Family	Ancestry	Inheritance	Nucleotide alteration	cDNA alteration	Amino acid alteration	Prediction	CADD	gnomAD	Kaviar
1	Chinese	De novo	chr6:3104280A>T	c.971A>T	p.D324V	D, D, D, D	23.9	0	0
2	European Canadian	De novo Dominant	chr6:3104279G>C	c.970G>C	p.D324H	D, D, D, D	24.6	0	0

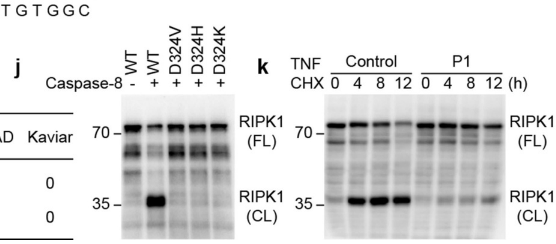

Extended Data Fig. 1 | See next page for caption.

Extended Data Fig. 1 | Identification of *RIPK1* variants and their effects. **a**, Schematic of the WES data-filtering approach under the assumption of de novo inheritance in family 1, leading to the identification of a novel *RIPK1* variant. INDEL, frameshift or non-frameshift insertions and deletions; SNP, single nucleotide polymorphisms including missense, splice-site and stop-codon variants. **b**, Exome sequencing reads covering the D324V variant in family 1, displayed by the integrative genomics viewer. **c**, Confirmation of RIPK1 variants at residue Asp324 for patients P1–P5 by Sanger sequencing. **d**, Evolutionary conservation of the caspase-8 cleavage site D324 in RIPK1. Amino acid sequence of RIPK1 flanking D324 was aligned by ClustalW across various species. **e**, Schematic domain structure of RIPK1. The position of identified variants leading to defective caspase-8 cleavage is indicated. **f**, In silico analysis of novel RIPK1 variants at D324. cDNA positions are determined according to the reference sequence NM_003804. Four predictions including SIFT, PolyPhen-2, LRT and Mutation Taster annotated by ANNOVAR were included in the analysis. D indicates damaging or deleterious variant. The gnomAD database includes 123,136 exomes and 15,496 genomes. The Kaviar database includes 77,238 exomes and genomes. **g**, RIPK1 cleavage site variants caused defective cleavage in vitro. HEK293T cells were transiently transfected with wild-type or mutant RIPK1 plasmids followed by immunoblotting of cell lysates. EV, empty vector; H1, H2, different cloning plasmids of RIPK1(D324H) variant; V1, V2, different cloning plasmids of RIPK1(D324V) variant; WT, wild-type RIPK1 plasmid. For gel source data, see Supplementary Fig. 1. Results are representative of three independent experiments. **h**, The degradation of wild-type and D325A mutant RIPK1 protein was analysed by CHX chase assay. Top, *Ripk1*$^{D325A/D325A}$*Ripk3*$^{-/-}$ and *Ripk1*$^{+/+}$*Ripk3*$^{-/-}$ MEFs were incubated with 50 μg ml^{-1} CHX for the indicated period of time and collected for western blot. Results are representative of three independent experiments. The western blot was quantified by Image J. Bottom, the relative RIPK1 protein level was normalized to CHX-untreated cells. Data are mean ± s.d., $n = 3$. Circles correspond to each independent experiment. For gel source data, see Supplementary Fig. 1. **i**, Neither mutant disrupted the recruitment of RIPK1 and caspase-8 into the FADDosome. *Ripk1*-knockout MEFs complemented with wild-type RIPK1, or D325V or D325H mutant were treated as indicated for 1 or 3 h. T/Z, 50 ng ml^{-1} TNF, 50 μM Z-VAD-FMK. '+' denotes 20 μM Nec-1s. Lysates were immunoprecipitated with anti-FADD, and analysed by immunoblotting using the indicated antibodies. For gel source data, see Supplementary Fig. 1. Results are representative of three independent experiments. **j**, Unlabelled in vitro transcription and translation of wild-type and mutant RIPK1 constructs (D324V, D324H and D324K) were performed in the TNT T7 Quick Coupled Transcription/Translation System followed by incubation with purified recombinant caspase-8 protein for 3 h and then analysed by immunoblotting of RIPK1. CL, cleaved RIPK1; FL, full-length RIPK1. For gel source data, see Supplementary Fig. 1. Results are representative of three independent experiments. **k**, The D324V variant disrupted the RIPK1 cleavage by caspase-8. Fibroblasts from patient P1 and an unaffected control were treated with TNF and CHX for the indicated amount of time followed by immunoblotting analysis. For gel source data, see Supplementary Fig. 1. Results are representative of three independent experiments.

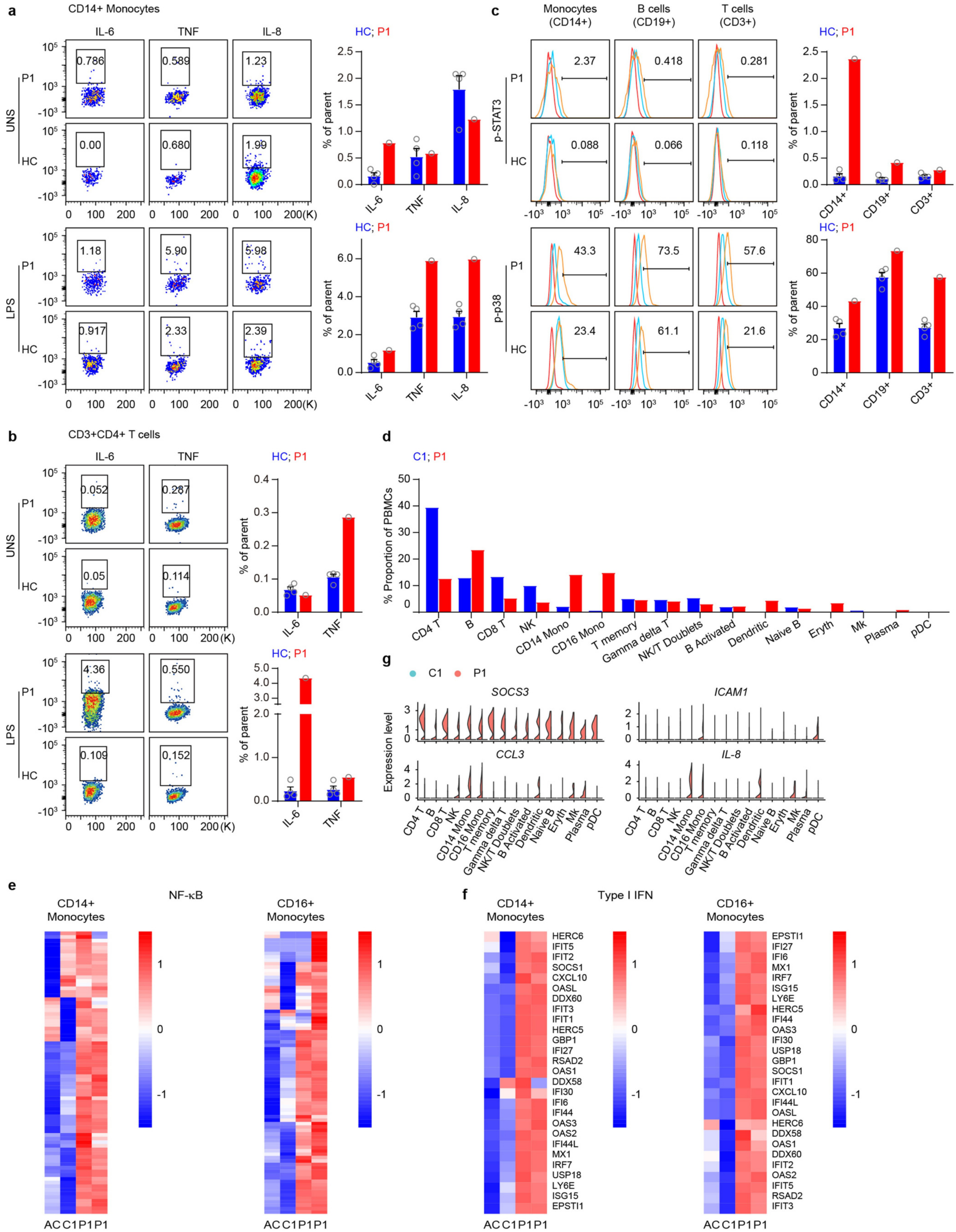

Extended Data Fig. 2 | See next page for caption.

Extended Data Fig. 2 | Increased pro-inflammatory signalling in patient PBMCs. a, Intracellular cytokine staining of patient PBMCs showed expression of IL-6, TNF and IL-8 in CD14$^+$ monocytes at baseline (unstimulated, UNS) (top) and after LPS stimulation for 6 h (bottom) compared to one representative (left) and four paediatric unaffected controls (right). Data are mean ± s.e.m. Circles correspond to each tested individual. **b**, Intracellular cytokine staining of patient PBMCs showed increased expression of IL-6 in patient CD3$^+$CD4$^+$ T cells after LPS stimulation (1 μg ml^{-1}) for 6 h compared to 1 representative (left) and 4 paediatric unaffected controls (right). Data are mean ± s.e.m. Circles correspond to each tested individual. **c**, Basal phosphorylation of STAT3 (top) and phosphorylation of p38 after LPS stimulation (bottom) of patient monocytes (CD14$^+$), B cells (CD19$^+$), and T cells (CD3$^+$) compared to one representative (left) and four paediatric unaffected controls (right) as determined by flow cytometry analysis. Data are mean ± s.e.m. Circles correspond to each tested individual. **d**, Single-cell RNA sequencing revealed a higher percentage of monocytes in P1 compared with an age- and sex-matched unaffected control (C1). **e**, **f**, Single-cell RNA sequencing revealed that the NF-κB (**e**) and type I IFN (**f**) signalling pathways were upregulated in patient CD14$^+$ and CD16$^+$ monocytes compared with an age- and sex-matched unaffected control (C1) and an adult control (AC). The adult control data were downloaded from 10X Genomics. Analysis of patient sample was performed in duplicate. For gene names, see Supplementary Fig. 2. **g**, Violin plots showing the distribution of gene expression of selected genes in different cell clusters for P1 and an age- and sex-matched unaffected control. n = 1,007 cells for patient and n = 4,340 cells for control CD4 T cell cluster. n = 1,868 cells for patient and n = 1,427 cells for control B cell cluster. n = 422 cells for patient and n = 1,478 cells for control CD8 T cell cluster. n = 302 cells for patient and n = 1,101 cells for control NK cell cluster. n = 1,125 cells for patient and n = 241 cells for control CD14 monocytes cluster. n = 1,184 cells for patient and n = 78 cells for control CD16 monocytes cluster. n = 371 cells for patient and n = 563 cells for control T memory cell cluster. n = 333 cells for patient and n = 524 cells for control γδ T cell cluster. n = 249 cells for patient and n = 597 cells for control NK cell/T doublets cluster. n = 182 cells for patient and n = 228 cells for control B activated cell cluster. n = 357 cells for patient and n = 20 cells for control dendritic cell cluster. n = 117 cells for patient and n = 217 cells for control naive B cell cluster. n = 279 cells for patient and n = 35 cells for control erythrocytes cluster. n = 29 cells for patient and n = 86 cells for control megakaryocyte cell cluster. n = 78 cells for patient and n = 23 cells for control plasma cell cluster. n = 33 cells for patient and n = 34 cells for control plasmacytoid dendritic cell cluster. The PBMCs from P1 for in **a**–**g** were obtained during a fever episode.

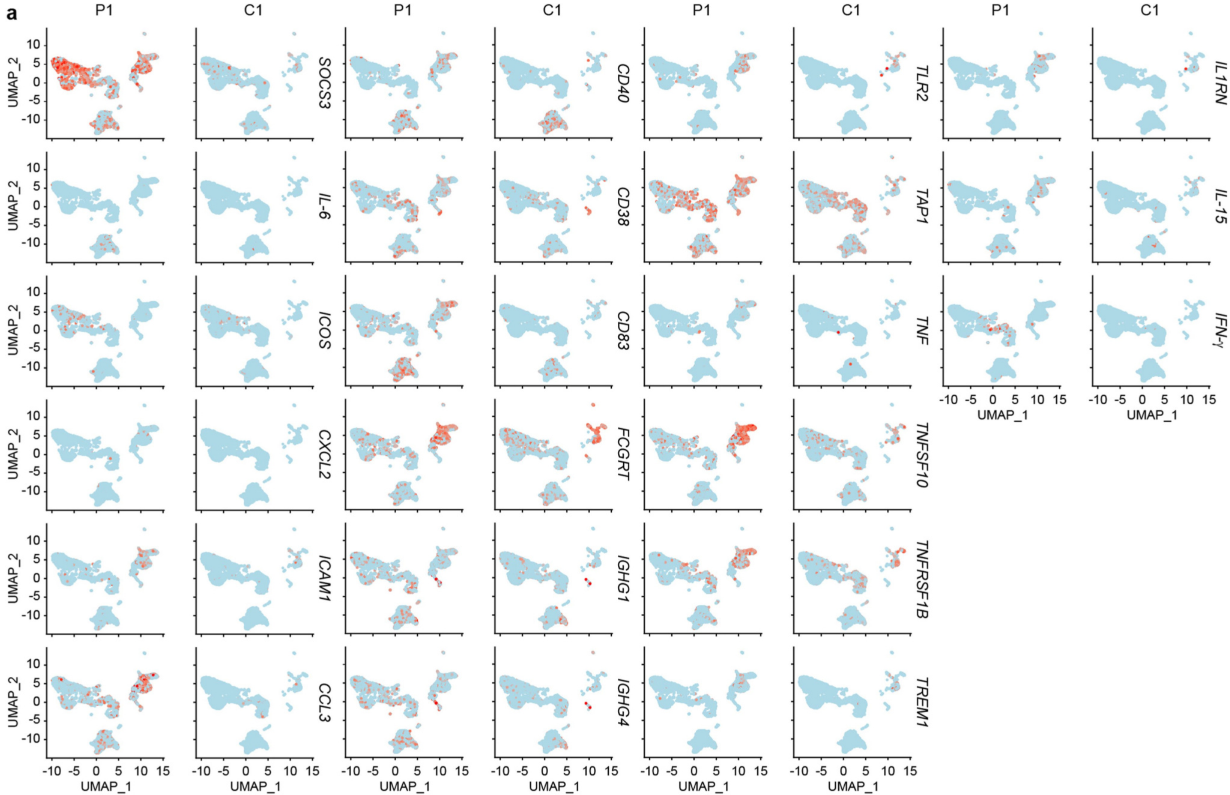

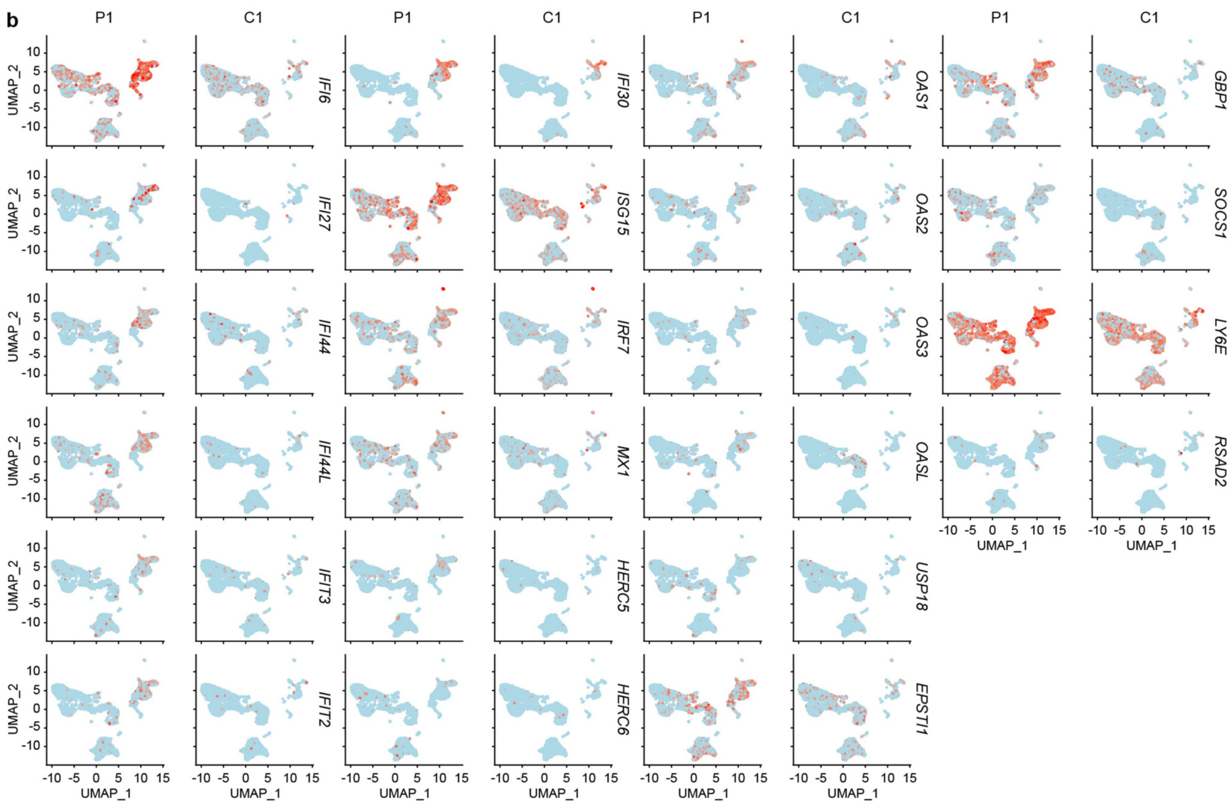

Extended Data Fig. 3 | Increased expression of genes in NF-κB and type-I IFN pathways in patient PBMCs. a, Visualization of expression of genes involved in NF-κB pathway (*SOCS3*, *CD40*, *TLR2*, *IL1RN*, *IL6*, *CD38*, *TAP1*, *IL15*, *ICOS*, *CD83*, *TNF*, *IFNG*, *CXCL2*, *FCGRT*, *TNFSF10*, *ICAM1*, *IGHG1*, *TNFRSF1B*, *CCL3*, *IGHG4* and *TREM1*) (coloured single cells) on UMAP plot projecting PBMCs from patient P1 (n = 7,936 cells) and an age- and sex-matched unaffected control (n = 10,992 cells). **b**, Visualization of expression of genes involved in type-I IFN signalling pathway (*IFI6*, *IFI30*, *OAS1*, *GBP1*, *IFI27*, *ISG15*, *OAS2*, *SOCS1*, *IFI44*, *IRF7*, *OAS3*, *LY6E*, *IFI44L*, *MX1*, *OASL*, *RSAD2*, *IFIT3*, *HERC5*, *USP18*, *IFIT2*, *HERC6* and *EPSTI1*) (coloured single cells) on UMAP plot projecting PBMCs from patient P1 (n = 7,936 cells) and an age- and sex-matched unaffected control (n = 10,992 cells). The PBMCs from P1 in **a** and **b** were obtained during a fever episode.

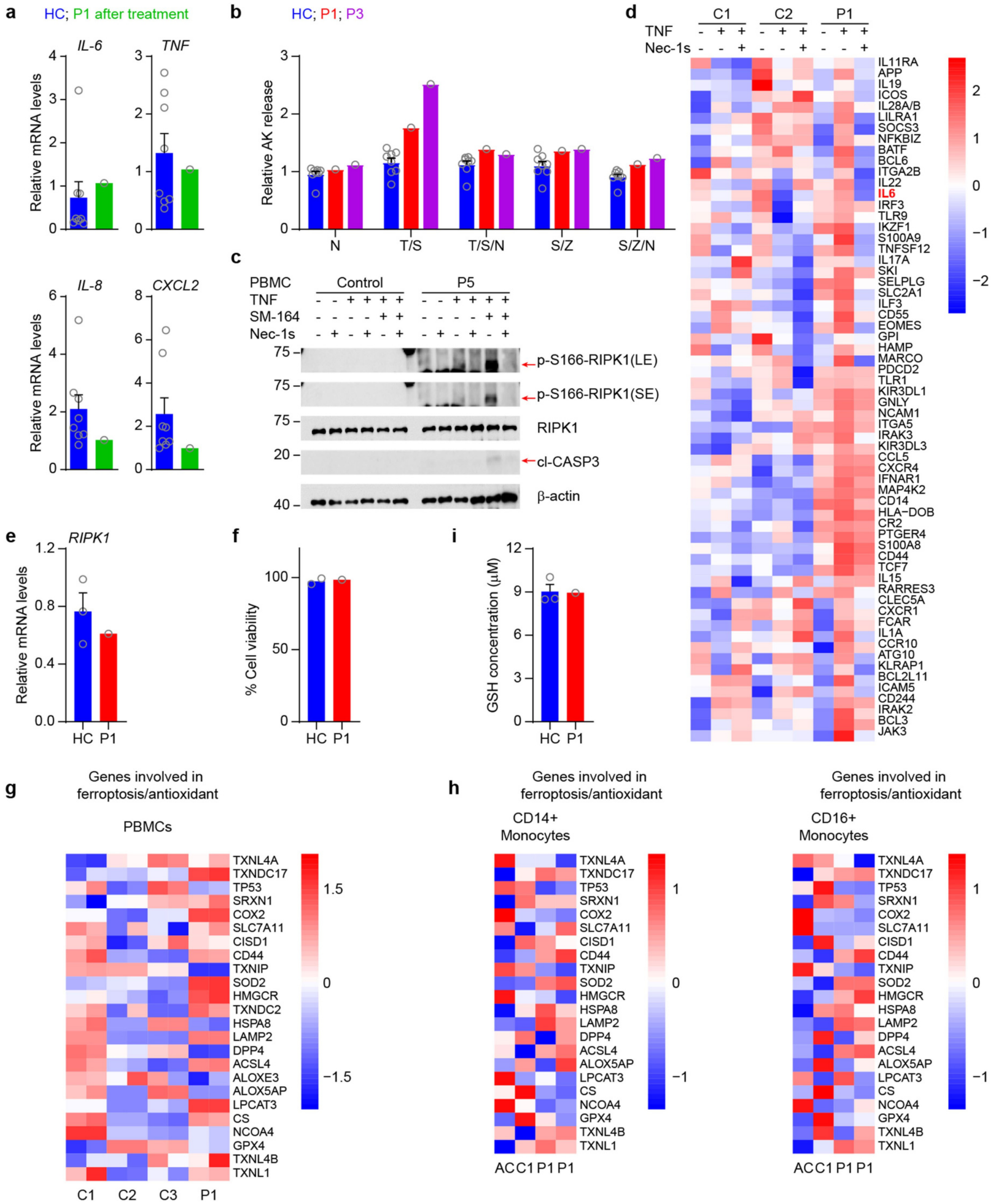

Extended Data Fig. 4 | Patient PBMCs are sensitive to TNF-induced cell death but not to ferroptosis. **a**, qPCR of PBMCs confirmed comparative expression levels of cytokine and chemokine-related genes in P1, after 4 months of tocilizumab treatment, compared to 8 paediatric unaffected controls. Data are mean ± s.e.m. Circles correspond to each tested individual. Analysis of each sample was performed in triplicate. **b**, Patient PBMCs were hypersensitive to TNF-induced cell death. PBMCs from 8 age-matched unaffected controls and patients P1 and P3 were treated as indicated for 24 h. N, 20 μM Nec-1s; S, 100 nM SM-164; T, 100 ng ml^{-1} TNF; Z, 100 μM Z-VAD-FMK. Cell death was measured by ToxiLight assay. Data are mean ± s.e.m. Circles correspond to each tested individual. Analysis of each sample was performed in triplicate. **c**, Induction of necroptosis and apoptosis by TNF in the patient PBMCs. PBMCs from patient P5 and a paediatric unaffected control were treated with indicated stimulation for 24 h before cell lysates were analysed by immunoblotting. For gel source data, see Supplementary Fig. 1. Results are representative of two independent experiments. **d**, Patient PBMCs stimulated with TNF alone exhibited upregulated gene expression of inflammatory signals, which was reduced by Nec-1s. PBMCs of patient and 2 unaffected controls were treated with 100 ng ml^{-1} TNF or TNF plus 20 μM Nec-1s for 24 h before being analysed by NanoString. **e**, The transcription levels of *RIPK1* in PBMCs from patient and unaffected controls measured by qPCR. Data are mean ± s.e.m. Circles correspond to each tested individual. Analysis of each sample was performed in triplicate. **f**, PBMCs of patient and two paediatric unaffected controls showed similar responses to RSL3-induced ferroptosis. Circles correspond to each tested individual. Analysis of each sample was performed in triplicate. **g**, RNA sequencing of patient PBMCs indicated no difference in expression patterns of genes involved in ferroptosis and antioxidant when compared to three paediatric unaffected controls. Analysis of each sample was performed in duplicate. **h**, Single-cell RNA sequencing did not reveal distinct expression patterns of genes involved in ferroptosis and antioxidant in patient CD14^{+} and CD16^{+} monocytes compared with an age- and sex-matched unaffected control (C1) and an adult control (AC). The adult control data were downloaded from 10X Genomics. **i**, GSH concentration in PBMCs from P1 was similar to three paediatric unaffected controls. Data are mean ± s.e.m. Circles correspond to each tested individual. Analysis of each sample was performed in triplicate. The PBMCs for **a**, **b**, **d**, **f** and **i** were obtained during remission. The PBMCs for **c**, **e**, **g** and **h** were obtained during a fever episode.

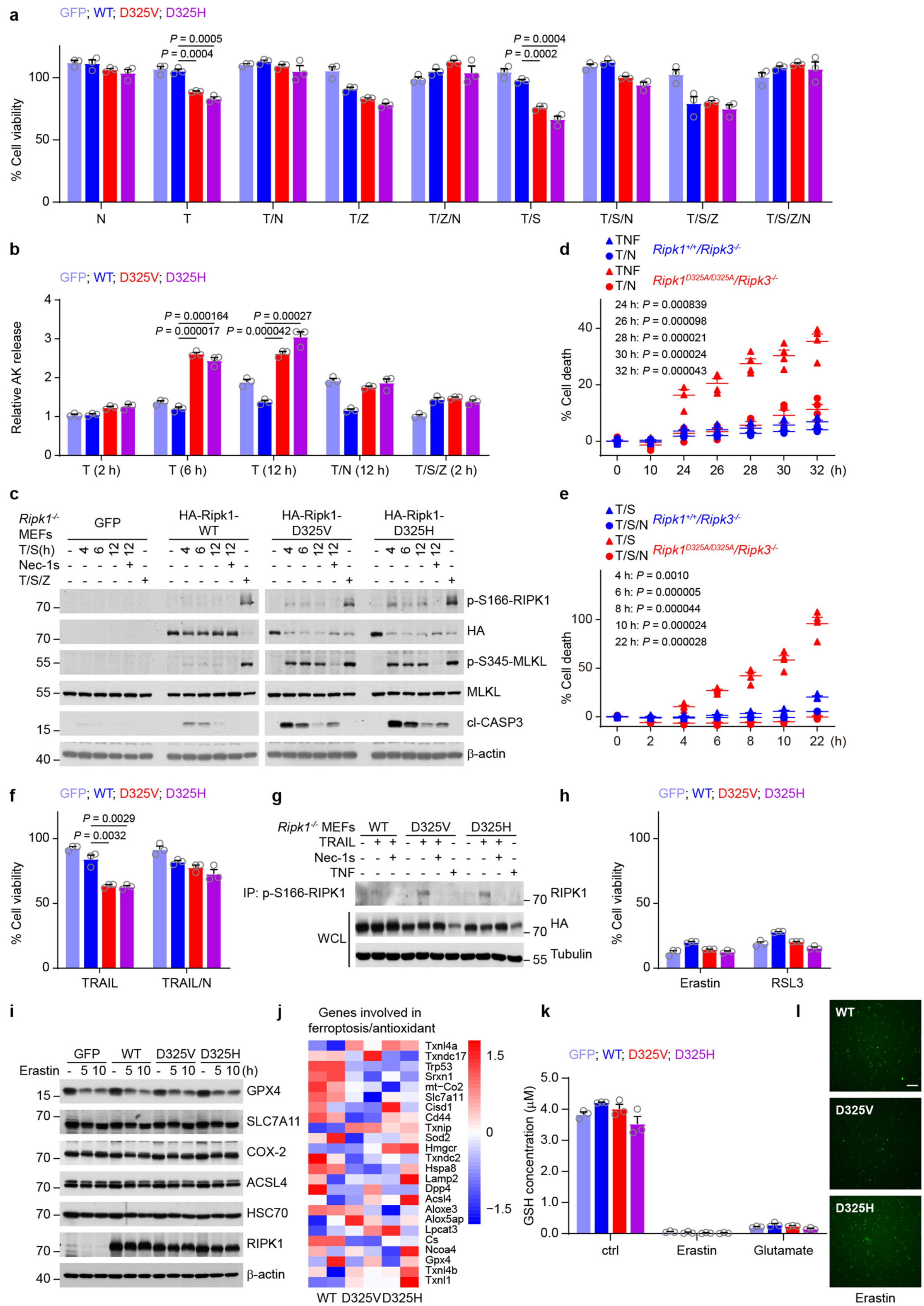

Extended Data Fig. 5 | See next page for caption.

Extended Data Fig. 5 | RIPK1 cleavage site variants in MEFs promote cell death and inflammatory response but have no protective effect against ferroptosis. a, **b**, RIPK1 cleavage site variants in MEFs promote cell death induced by TNF. *Ripk1*$^{-/-}$ MEFs were complemented with: GFP; wild-type RIPK1; or D325V or D325H mutant, and treated for 12 h (**a**) or as indicated (**b**). N, 20 μM Nec-1s; S, 20 nM SM-164; T, 50 ng ml^{-1} TNF; Z, 50 μM Z-VAD-FMK. Cell viability and cell death were measured by CellTiter-Glo assay (**a**) and ToxiLight assay (**b**), respectively. Data are mean ± s.e.m, $n = 3$. Circles correspond to each independent experiment. *P* values were determined by unpaired, two-tailed *t*-test (shown if $P < 0.05$). **c**, Western blots illustrating increased levels of p-S166-RIPK1, p-S345-MLKL and cleaved caspase-3 after stimulation with TNF and SM-164, which were inhibited by Nec-1s. *Ripk1*$^{-/-}$ MEFs complemented with: GFP; wild-type RIPK1; or D325V or D325H mutant, were treated as indicated. Cell lysates were analysed by immunoblotting using indicated antibodies. For gel source data, see Supplementary Fig. 1. Results are representative of three independent experiments. **d**, **e**, D325A knock-in *Ripk1* mutation sensitizes *Ripk3*$^{-/-}$ MEFs to TNF-induced RIPK1-dependent apoptosis. *Ripk1*$^{D325A/D325A}$ *Ripk3*$^{-/-}$ *and Ripk1*$^{+/+}$*Ripk3*$^{-/-}$ MEFs were simulated with TNF only, TNF plus Nec-1s (**d**) or a combination of TNF, SM-164 and Nec-1s (**e**) as indicated (concentrations as in **a**). Cell death was measured by the SYTOX Green Nucleic Acid Stain assay. Data are mean ± s.e.m., $n = 4$. Circles correspond to each independent experiment. *P* values determined by unpaired two-tailed *t*-test, and indicate the comparison between *Ripk1*$^{D325A/D325A}$*Ripk3*$^{-/-}$ *and Ripk1*$^{+/+}$*Ripk3*$^{-/-}$ MEFs after TNF or TNF plus SM-164 stimulation for indicated amount of time. **f**, RIPK1 cleavage site variants in MEFs sensitize TRAIL-induced cell death. *Ripk1*$^{-/-}$ MEFs complemented with: GFP, wild-type RIPK1, or D325V or D325H mutant were treated with TRAIL (100 ng ml^{-1}) or TRAIL plus Nec-1s (20 μM) for 36 h. Data are mean ± s.e.m., $n = 3$. Circles correspond to each independent experiment. *P* values determined by unpaired two-tailed *t*-test. **g**, TRAIL stimulation of *Ripk1*$^{-/-}$ MEFs complemented with D325V or D325H mutant promotes RIPK1 activation, which was inhibited by Nec-1s (20 μM). TRAIL (100 ng ml^{-1}); TNF (50 ng ml^{-1}) for 12 h. For gel source data, see Supplementary Fig. 1. Results are representative of three independent experiments. **h**, *Ripk1*-knockout MEFs complemented with wild-type RIPK1, or D325V or D325H mutant plasmid showed similar responses to erastin- or RSL3-induced ferroptosis. Data are mean ± s.e.m., $n = 3$. Circles correspond to each independent experiment. **i**, Western blots of proteins involved in ferroptosis in *Ripk1*$^{-/-}$ MEFs complemented with wild-type RIPK1, or D325V or D325H mutant. Cells were treated with erastin for 5 or 10 h, followed by immunoblotting of cell lysates. For gel source data, see Supplementary Fig. 1. Results are representative of three independent experiments. **j**, RNA sequencing of *Ripk1*$^{-/-}$ MEFs complemented with wild-type RIPK1, D325V or D325H mutant indicated no difference in expression patterns of genes involved in ferroptosis and antioxidant. Analysis of each sample was performed in duplicate. **k**, GSH concentration of *Ripk1*$^{-/-}$ MEFs complemented with wild-type RIPK1, D325V or D325H mutant was similar both at baseline and after erastin or glutamate stimulation for 8 h. Data are mean ± s.e.m., $n = 3$. Circles correspond to each independent experiment. **l**, Immunofluorescence showed similar levels of cytosolic ROS after erastin stimulation in *Ripk1*$^{-/-}$ MEFs complemented with wild-type RIPK1, D325V or D325H mutant. Cells were treated by erastin for 8 h before incubation with the cytosolic ROS sensor carboxy-H_2DCFDA. Green foci indicate cytosolic ROS. Scale bar, 150 μm. Results are representative of two independent experiments.

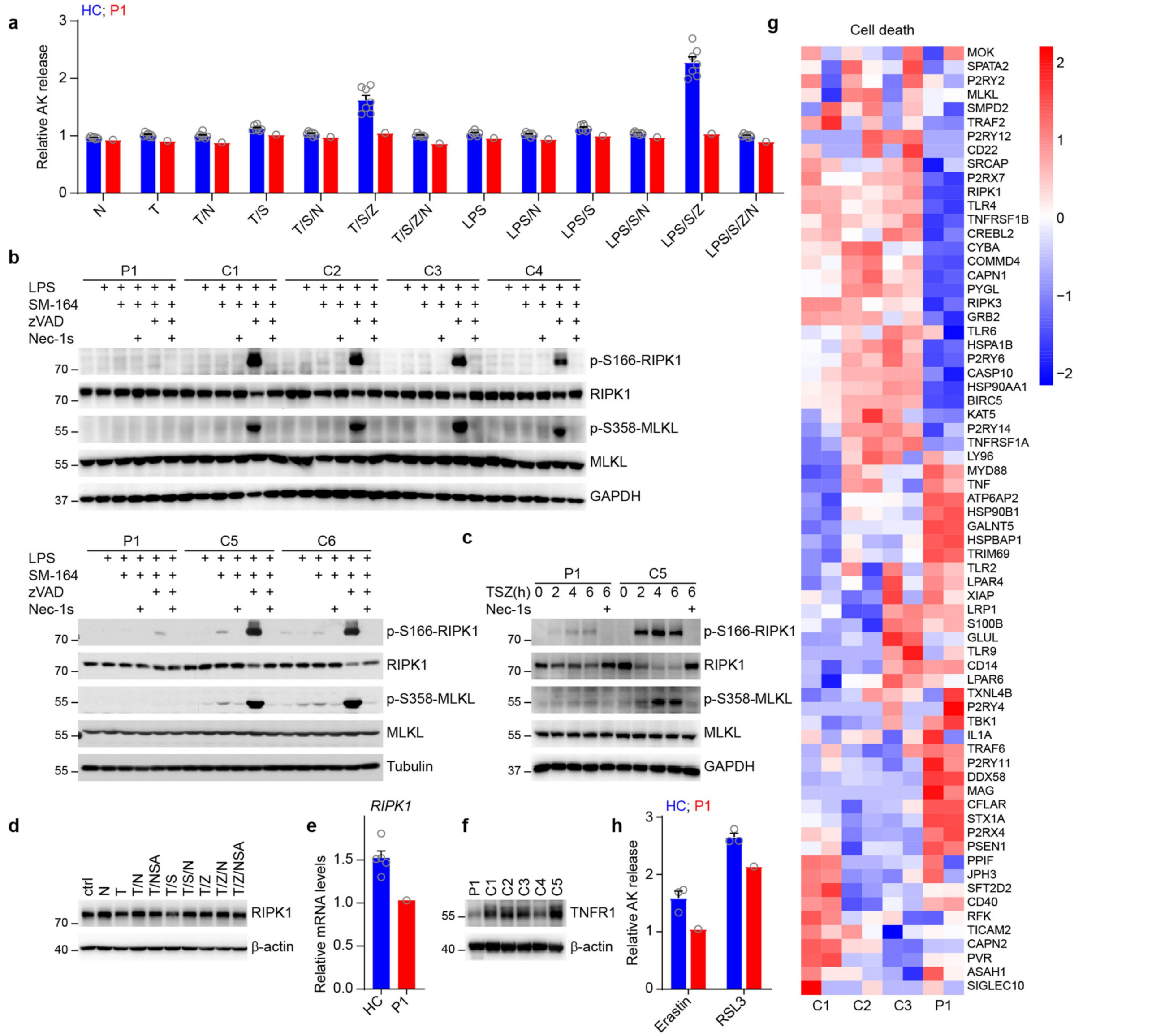

Extended Data Fig. 6 | Patient fibroblasts were resistant to both necroptosis and ferroptosis. a, Patient fibroblasts were resistant to necroptosis induced by SM-164, Z-VAD-FMK and TNF or LPS. Fibroblasts from P1 and seven paediatric unaffected controls were treated as indicated for 24 h. LPS, 1 μg ml^{-1}; N, 10 μM Nec-1s; S, 50 nM SM-164; T, 50 ng ml^{-1} TNF; Z, 50 μM Z-VAD-FMK. Cell death was measured by ToxiLight assay. Data are mean ± s.e.m. Circles correspond to each tested individual. Analysis of each sample was performed in triplicate. **b**, Patient fibroblasts showed reduced necroptosis signals after SM-164, Z-VAD-FMK and LPS stimulation compared to six paediatric unaffected controls. Patient and control fibroblasts were treated with indicated stimulation for 6 h (concentrations as in **a**). Cells were lysed and analysed by immunoblotting with indicated antibodies. For gel source data, see Supplementary Fig. 1. Results are representative of three independent experiments. **c**, Patient fibroblasts showed reduced necroptosis signals after SM-164, Z-VAD-FMK and TNF stimulation compared with a paediatric unaffected control. Patient and control fibroblasts were treated as indicated for 6 h (concentrations as in **a**). Cells were lysed and analysed by immunoblotting with indicated antibodies. For gel source data, see Supplementary Fig. 1. Results are representative of three independent experiments. **d**, The reduction of RIPK1 was rescued by Nec-1s in patient fibroblasts. Fibroblasts were treated as indicated for 24 h (concentrations as in **a**). NSA, 0.5 μM necrosulfonamide. Cell lysates were analysed by immunoblotting using indicated antibodies. For gel source data, see Supplementary Fig. 1. Results are representative of three independent experiments. **e**, Patient fibroblast showed reduced transcription levels of *RIPK1* compared to five paediatric unaffected controls. The mRNA levels of *RIPK1* were measured by qPCR. Data are mean ± s.e.m. Circles correspond to each tested individual. Analysis of each sample was performed in triplicate. **f**, Patient fibroblasts exhibited reduced TNFR1 expression at baseline compared to five paediatric unaffected controls. For gel source data, see Supplementary Fig. 1. Results are representative of three independent experiments. **g**, Patient fibroblasts displayed downregulation of genes involved in cell death compared with three paediatric unaffected controls. Analysis of each sample was performed in duplicate. **h**, Patient fibroblasts were resistant to erastin- or RSL3-induced ferroptosis compared with three paediatric unaffected controls. Cell death was measured by ToxiLight assay. Data are mean ± s.e.m. Circles correspond to each tested individual. Analysis of each sample was performed in triplicate.

Extended Data Table 1 | Clinical manifestations of patients with *RIPK1* variants

Patient	P1	P2	P3	P4	P5
Variant	p.D324V	p.D324H	p.D324H	p.D324H	p.D324H
Age	2 y	35 y	14 y	12 y	10 y
Gender	M	F	M	M	M
Age at onset	2 mo	6 mo	1 mo	-	1 mo
Recurrent fevers	+	+	+	-	+
Fever frequency	8-10 d	10-15 d	15 d	-	2-3 d
Fever duration	3-5 d	3 h-2 d	3 h-2 d	-	3 h-1 d
Lymphadenopathy	+	+	+	-	+
Splenomegaly	-	+	+	-	+
Hepatomegaly	-	+	-	-	-
Microcytic anemia	+	+	+	+	+
Abdominal pain	+	-	-	-	-

Extended Data Table 2 | The count and percentage of T and B cells in patient 1

	Controls	Patient 1
Gender		**M**
Age at evaluation	1-4 y (n = 289)	2 y
Counts (cells μl^{-1})		
CD4 Helper T, naive	472-1760	3887
CD4 Helper T, central memory	212-735	1570
CD4 Helper T, effector memory	15-87	145
CD4 TEMRA	0-22	16
CD8 Cytotoxic T, naive	356-1095	1912
CD8 Cytotoxic T, central memory	56-406	825
CD8 Cytotoxic T, effector memory	6-145	89
CD8 Cytotoxic T, TEMRA	9-440	434
DNT TCR αβ+	9-57	103 ↑
CD19 Naive B	323-1108	9216 ↑
CD19 Memory B	26-124	103
CD19 Transitional B	35-172	1504
CD19 Plasmablasts	4-63	61
Percentages (%)		
CD4 Helper T, naive	46.14-84.40	69.2
CD4 Helper T, central memory	13.88-48.12	27.9
CD4 Helper T, effector memory	0.94-6.46	2.6
CD4 TEMRA	0.00-1.36	0.3
CD8 Cytotoxic T, naive	36.80-83.16	58.7
CD8 Cytotoxic T, central memory	5.18-31.66	25.3
CD8 Cytotoxic T, effector memory	0.70-11.22	2.7
CD8 Cytotoxic T, TEMRA	0.84-33.02	13.3
DNT TCR αβ+	0.37-1.80	1.04
CD19 Naive B	65.54-86.62	95.4 ↑
CD19 Memory B	2.98-14.18	1.1
CD19 Transitional B	5.24-17.22	15.6
CD19 Plasmablasts	0.50-7.06	0.6

The relative and absolute numbers of lymphocyte subpopulations are determined by samples from 289 age-matched unaffected controls[28]. The whole blood sample from patient P1 was obtained during a fever episode.

Extended Data Table 3 | Cytokine levels in serum of patients from family 2

No.	Cytokine	P2	P3	P4	P5	C1	C2	C3	C4
1	IFN-γ	16.99	9.67	39.3	4.93	1.66	<0.97	<0.97	1.66
2	IL-6	1.62	1.79	9.83	1.24	<1.03	<1.03	<1.03	<1.03
3	IL-8	1.91	1.69	4.52	6.01	1.28	4.66	<1.07	1.11
4	IP10	89.31	19.95	52.18	30.3	20.37	16.59	18.21	12.87

C1 is the mother of P2; C2 is the fourth son of P2; C3 and C4 are adult unaffected controls. The serum samples were obtained when all of the patients were during remission. Cytokine concentrations are pg ml^{-1}.

nature research

Corresponding author(s): Xiaomin Yu, Xiaochuan Wang, Junying Yuan, Qing Zhou

Last updated by author(s): Oct 10, 2019

Reporting Summary

Nature Research wishes to improve the reproducibility of the work that we publish. This form provides structure for consistency and transparency in reporting. For further information on Nature Research policies, see Authors & Referees and the Editorial Policy Checklist.

Statistics

For all statistical analyses, confirm that the following items are present in the figure legend, table legend, main text, or Methods section.

n/a	Confirmed	
☐	☒	The exact sample size (*n*) for each experimental group/condition, given as a discrete number and unit of measurement
☐	☒	A statement on whether measurements were taken from distinct samples or whether the same sample was measured repeatedly
☐	☒	The statistical test(s) used AND whether they are one- or two-sided *Only common tests should be described solely by name; describe more complex techniques in the Methods section.*
☒	☐	A description of all covariates tested
☐	☒	A description of any assumptions or corrections, such as tests of normality and adjustment for multiple comparisons
☐	☒	A full description of the statistical parameters including central tendency (e.g. means) or other basic estimates (e.g. regression coefficient) AND variation (e.g. standard deviation) or associated estimates of uncertainty (e.g. confidence intervals)
☐	☒	For null hypothesis testing, the test statistic (e.g. *F*, *t*, *r*) with confidence intervals, effect sizes, degrees of freedom and *P* value noted *Give P values as exact values whenever suitable.*
☒	☐	For Bayesian analysis, information on the choice of priors and Markov chain Monte Carlo settings
☒	☐	For hierarchical and complex designs, identification of the appropriate level for tests and full reporting of outcomes
☒	☐	Estimates of effect sizes (e.g. Cohen's *d*, Pearson's *r*), indicating how they were calculated

Our web collection on statistics for biologists contains articles on many of the points above.

Software and code

Policy information about availability of computer code

Data collection	Flow cytometry, intracellular cytokine staining and BD™ Cytometric Bead Array data were acquired on a FACS Canto II cytometer (BD Biosciences). qPCR data were acquired on Applied Biosystems 7500 Real-Time PCR System (Life Technologies) and ROCHE 480II. Immunoblot images were scanned by FluorChem E (ProteinSimple) and scanner (Epson Perfection V700 Photo). Chemiluminiscence data were collected by the multimode plate reader (Bio Tek). Green fluorescent images were taken by a Leica fluorescence microscope (LEICA DMI 6000B). NanoString assay was conducted by the nCounter Analysis System (NanoString Technologies). RNA sequencing and Whole exome sequencing were carried out on an Illumina Novaseq system. Single cell RNA sequencing were carried out on 10x Genomics Chromium machine for single-cell capture and cDNA preparation and on an Illumina Novaseq system for sequencing.
Data analysis	FlowJo (Tree Star) (Flow cytometry and intracellular cytokine staining analysis); GraphPad Prism 8, IBM SPSS Statistics 25 and Microsoft Excel (Graphs, statistics); Image J (image analysis); nSolver 4.0 (NanoString assay); Cell Ranger V3.0.1 and Seurat R package (single cell RNA sequencing analysis); R 3.5.2 (data analysis and graph); DESeq2 R package (RNA sequencing analysis); FCAP Array V3.0 (BD Biosciences) (cytokines data measured by BD™ Cytometric Bead Array); ANNOVAR (2018Apr16) (mutation effect predictions).

For manuscripts utilizing custom algorithms or software that are central to the research but not yet described in published literature, software must be made available to editors/reviewers. We strongly encourage code deposition in a community repository (e.g. GitHub). See the Nature Research guidelines for submitting code & software for further information.

Data

Policy information about availability of data

All manuscripts must include a data availability statement. This statement should provide the following information, where applicable:

- Accession codes, unique identifiers, or web links for publicly available datasets
- A list of figures that have associated raw data
- A description of any restrictions on data availability

Source data for graphs are provided with the paper. Uncropped gels raw data are shown in Supplementary Fig. 1. Other source data that support the findings of this

study are available from the corresponding author upon reasonable request.

Field-specific reporting

Please select the one below that is the best fit for your research. If you are not sure, read the appropriate sections before making your selection.

☒ Life sciences ☐ Behavioural & social sciences ☐ Ecological, evolutionary & environmental sciences

For a reference copy of the document with all sections, see nature.com/documents/nr-reporting-summary-flat.pdf

Life sciences study design

All studies must disclose on these points even when the disclosure is negative.

Sample size	No statistical methods were used to predetermine the sample sizes.
Data exclusions	No data was excluded from analysis.
Replication	In Fig. 2d, Fig. 4g, Extended Data Fig. 4g, Extended Data Fig. 5j and Extended Data Fig. 6g, RNA sequencing analysis of each sample was performed in duplicate. In Fig. 2b, c, Extended Data Fig. 2d-g, Extended Data Fig. 3a, b, Extended Data Fig. 4h, Single cell RNA sequencing analysis of patient sample was performed in duplicate and healthy control (C1) was performed once. In Fig. 3d and Extended Data Fig. 4d, NanoString analysis of patient and healthy controls PBMCs were performed once. In Fig. 4i, the immunofluorescence of cytosolic ROS (green foci) in fibroblasts was performed in duplicate. The other data are representative of three independent biological replicates.
Randomization	Multiple age and gender matched healthy controls used in the experiment were randomly selected. Patient samples were taken multiple times and used for independent biological replicate experiments.
Blinding	Blinding was not possible as the authors who performed the experiment also analyzed the data.

Reporting for specific materials, systems and methods

We require information from authors about some types of materials, experimental systems and methods used in many studies. Here, indicate whether each material, system or method listed is relevant to your study. If you are not sure if a list item applies to your research, read the appropriate section before selecting a response.

Materials & experimental systems

n/a	Involved in the study	
☐	☒	Antibodies
☐	☒	Eukaryotic cell lines
☒	☐	Palaeontology
☒	☐	Animals and other organisms
☐	☒	Human research participants
☒	☐	Clinical data

Methods

n/a	Involved in the study	
☒	☐	ChIP-seq
☐	☒	Flow cytometry
☒	☐	MRI-based neuroimaging

Antibodies

Antibodies used	Western Blot: β-Actin (Cell Signaling Technology, 4970, clone 13E5, lot 15, 1:1000), β-Tubulin (Cell Signaling Technology, 86298, clone D3U1W, lot 1, 1:1000), GAPDH (Cell Signaling Technology, 5174, clone D16H11, lot 6, 1:1000), RIPK1 (Cell Signaling Technology, 3493, clone D94C12, lot 3, 1:1000), p-RIPK1 (Ser166) (Cell Signaling Technology, 65746, clone D1L3S, lot 02, 1:1000), MLKL (Cell Signaling Technology, 14993, clone D2I6N, lot 3, 1:1000), p-MLKL (Ser358) (Cell Signaling Technology, 91689, clone D6H3V, lot 3, 1:1000), p-MLKL (Ser345) (Cell Signaling Technology, 37333, clone D6E3G, lot 2, 1:1000), p65 (Cell Signaling Technology, 8242, clone D14E12, lot 9, 1:1000), p-p65 (Ser65) (Cell Signaling Technology, 3033, clone 93H1, lot 16, 1:1000), IKKα (Cell Signaling Technology, 11930, clone 3G12, lot 5, 1:1000), IKKβ (Cell Signaling Technology, 2370, clone D30C6, lot 4, 1:1000), p-IKKα/β (Ser176/180) (Cell Signaling Technology, 2697, clone 16A6, lot 19, 1:1000), IκBα (Cell Signaling Technology, 4814, clone L35A5, lot 17, 1:1000), p-IκBα (Ser32) (Cell Signaling Technology, 2859, clone 14D4, lot 18, 1:1000), p38 (Cell Signaling Technology, 8690, clone D13E1, lot 6, 1:1000), p-p38 (Thr180/Tyr182) (Cell Signaling Technology, 4511, clone D3F9, lot 13, 1:1000), TNFR1 (Cell Signaling Technology, 3736, clone C25C1, lot 2, 1:1000), caspase-8 (Cell Signaling Technology, 4790, clone D35G2, lot 2, 1:1000), cl-caspase-8 (Cell Signaling Technology, 8592, clone D5B2, lot 2, 1:1000), caspase-3 (Cell Signaling Technology, 9662, polyclonal, lot 18, 1:1000), cleaved-caspase-3 (Asp175) (Cell Signaling Technology, 9661, polyclonal, lot 18, 1:1000), HA-Tag (Cell Signaling Technology, 3724, clone C29F1, lot 8, 1:1000), SLC7A11 (Cell Signaling Technology, 12691, clone D2M7A, lot 1, 1:1000), Cyclophilin A (Abcam, ab41684, polyclonal, lot GR3201186-1, 1:1000), GPX4 (Abcam, ab125066, clone EPNCIR144, lot GR251529-29, 1:1000), Lamp-2A (Abcam, ab125068, clone EPR4207(2), lot GR7472-1, 1:1000), COX2 (Abcam, ab15191, polyclonal, 1:1000), p53 (Abcam, ab32389, clone E26, 1:1000), FADD (Santa Cruz Biotechnology, sc-6036, clone M-19, 1:1000), ACSL4 (Santa Cruz Biotechnology, sc-365230, clone F-4, lot G1116, 1:1000), HSC70 (Proteintech Group, 10654-1-AP, polyclonal, 1:1000), HSP90 (Affinity, BF9107, clone AFB5588, lot 55e0886, 1:1000), p-RIPK1 (Ser166) (Biolynx, BX60008, clone YJY-1-5,

1:1000), MLKL (Mus) (home made, 1:1000).

Flow cytometry and intracellular cytokine staining:
CD3-APC-H7 (BD Biosciences, 560176, clone SK7, lot 9022755, 1:20), CD14-PE-CY7 (BD Biosciences, 557742, clone M5E2, lot 3291733, 1:20), CD4-FITC (BD Biosciences, 555346, clone RPA-T4, lot 8037703, 1:20), CD19-BB700 (BD Biosciences, 566396, clone SJ25C, lot 8130761, 1:20), IL8-PE (Biolegend, 511408, clone E8N1, lot B230067,1:20), IL10-BV421 (Biolegend, 501421, clone JES3-9D7, lot B256252, 1:20), IL6-Percp-cy5.5 (Biolegend, 501118, clone MQ2-13A5, lot B267970, 1:20), TNF-V450 (BD Biosciences, 561311, clone Mab11, lot 7209966, 1:20).

Alexa Fluor® 647-conjugated antibody against STAT3 phosphorylated at Y705 (BD Biosciences, 557815, clone 4/P-STAT3, lot 7346960, 1:10), Alexa Fluor® 488-conjugated antibody against NF-κB p65 phosphorylated at S529 (BD Biosciences, 558421, clone K10-895.12.50, lot 8241506, 1:10), Alexa Fluor® 488-conjugated antibody against p38 phosphorylated at T180/Y182 (BD Biosciences, 612594, clone 36/p38 (pT180/pY182), lot 8032972, 1:10).

Isotype control antibodies:
Alexa Fluor® 647-conjugated mouse IgG1κ (BD Biosciences, 557714, clone MOPC-21, lot 7076782, 1:20), Alexa Fluor® 488-Mouse IgG1κ (BD Biosciences, 557782, clone MOPC-21, lot 7102576, 1:20), BV421-Rat IgG1κ (Biolegend, 400439, clone RTK2071, lot B272547, 1:20), PE- Mouse IgG1κ (Biolegend, 400140, clone MOPC-21, lot B272822, 1:20), Percp-cy5.5-Rat IgG1κ (Biolegend, 400426, clone RTK2071, lot B255186, 1:20), V450- Mouse IgG1κ (BD Biosciences, 560373, clone MOPC-21, lot 6021915, 1:20).

Validation

All antibodies except MLKL (Mus, home made) are commercially available and have been verified by the manufacturers according to the immunoblots and/or images on their websites.
β-Actin: https://www.cst-c.com.cn/products/primary-antibodies/b-tubulin-d3u1w-mouse-mab/86298,
β-Tubulin: https://www.cst-c.com.cn/products/primary-antibodies/b-tubulin-d3u1w-mouse-mab/86298,
GAPDH: https://www.cst-c.com.cn/products/primary-antibodies/gapdh-d16h11-xp-rabbit-mab/5174,
RIPK1: https://www.cst-c.com.cn/products/primary-antibodies/rip-d94c12-xp-rabbit-mab/3493,
p-RIPK1 (Ser166): https://www.cst-c.com.cn/products/primary-antibodies/phospho-rip-ser166-d1l3s-rabbit-mab/65746,
MLKL: https://www.cst-c.com.cn/products/primary-antibodies/mlkl-d2i6n-rabbit-mab/14993,
p-MLKL (Ser358): https://www.cst-c.com.cn/products/primary-antibodies/phospho-mlkl-ser358-d6h3v-rabbit-mab/91689,
p65: https://www.cst-c.com.cn/products/primary-antibodies/nf-kb-p65-d14e12-xp-rabbit-mab/8242,
p-p65 (Ser65): https://www.cst-c.com.cn/products/primary-antibodies/phospho-nf-kb-p65-ser536-93h1-rabbit-mab/3033,
IKKα: https://www.cst-c.com.cn/products/primary-antibodies/ikka-3g12-mouse-mab/11930,
IKKβ: https://www.cst-c.com.cn/products/primary-antibodies/ikkb-d30c6-rabbit-mab/8943,
p-IKKα/β (Ser176/180): https://www.cst-c.com.cn/products/primary-antibodies/phospho-ikka-b-ser176-180-16a6-rabbit-mab/2697,
IκBα: https://www.cst-c.com.cn/products/primary-antibodies/ikba-l35a5-mouse-mab-amino-terminal-antigen/4814,
p-IκBα (Ser32): https://www.cst-c.com.cn/products/primary-antibodies/phospho-ikba-ser32-14d4-rabbit-mab/2859,
p38: https://www.cst-c.com.cn/products/primary-antibodies/p38-mapk-d13e1-xp-rabbit-mab/8690,
p-p38 (Thr180/Tyr182): https://www.cst-c.com.cn/products/primary-antibodies/phospho-p38-mapk-thr180-tyr182-d3f9-xp-rabbit-mab/4511,
TNFR1: https://www.cst-c.com.cn/products/primary-antibodies/tnf-r1-c25c1-rabbit-mab/3736,
HA-Tag: https://www.cst-c.com.cn/products/primary-antibodies/ha-tag-c29f4-rabbit-mab/3724,
p-MLKL (Ser345): https://www.cst-c.com.cn/products/antibody-conjugates/phospho-mlkl-ser345-d6e3g-rabbit-mab/37333,
p-MLKL (Ser358): https://www.cst-c.com.cn/products/primary-antibodies/phospho-mlkl-ser358-d6h3v-rabbit-mab/91689,
caspase-8: https://www.cst-c.com.cn/products/primary-antibodies/caspase-8-1c12-mouse-mab/9746,
caspase-3:https://www.cst-c.com.cn/products/primary-antibodies/caspase-3-antibody/9662,
cleaved caspase-3 (Asp175): https://www.cst-c.com.cn/products/primary-antibodies/cleaved-caspase-3-asp175-antibody/9661,
SLC7A11: https://www.cst-c.com.cn/products/primary-antibodies/xct-slc7a11-d2m7a-rabbit-mab/12691,
HSP90: http://affbiotech.cn/goods-4354-BF9107-HSP90+beta+Antibody.html,
Cyclophilin A: https://www.abcam.com/cyclophilin-a-antibody-ab41684.html,
GPX4: https://www.abcam.com/glutathione-peroxidase-4-antibody-epncir144-ab125066.html,
Lamp-2A: https://www.abcam.com/lamp2a-antibody-epr42072-lysosome-marker-ab125068.html,
COX2: https://www.abcam.com/cox2--cyclooxygenase-2-antibody-ab15191.html,
p53: https://www.abcam.com/p53-antibody-e26-ab32389.html,
FADD: https://www.scbt.com/scbt/zh/product/fadd-antibody-m-19,
ACSL4: https://www.scbt.com/scbt/product/acsl4-antibody-a-5,
HSC70: https://www.ptglab.com/products/HSPA8-Antibody-10654-1-AP.html,
p-RIPK1 (Ser166) (Biolynx) : http://www.biolynx.cn/product/seDetail/722,
CD3-APC-H7: http://www.bdbiosciences.com/eu/applications/research/t-cell-immunology/th-1-cells/surface-markers/human/apc-h7-mouse-anti-human-cd3-sk7-also-known-as-leu-4/p/560176,
CD14-PE-CY7: http://www.bdbiosciences.com/eu/applications/research/stem-cell-research/hematopoietic-stem-cell-markers/human/negative-markers/pe-cy7-mouse-anti-human-cd14-m5e2/p/557742,
CD4-FITC: http://www.bdbiosciences.com/eu/applications/research/t-cell-immunology/th-1-cells/surface-markers/human/fitc-mouse-anti-human-cd4-rpa-t4/p/555346,
CD19-BB700: http://www.bdbiosciences.com/eu/reagents/research/antibodies-buffers/immunology-reagents/anti-human-antibodies/cell-surface-antigens/bb700-mouse-anti-human-cd19-sj25c1-also-known-as-sj25-c1/p/566396,
IL8-PE: https://www.biolegend.com/en-us/products/pe-anti-human-il-8-antibody-4131,
IL10-BV421: https://www.biolegend.com/en-us/products/brilliant-violet-421-anti-human-il-10-antibody-7156,
IL6-Percp-cy5.5: https://www.biolegend.com/en-us/products/percpcyanine55-anti-human-il-6-antibody-13095,
TNF-V450: http://www.bdbiosciences.com/eu/applications/research/t-cell-immunology/th-1-cells/intracellular-markers/cytokines-and-chemokines/human/v450-mouse-anti-human-tnf-mab11/p/561311,
Alexa Fluor® 647-conjugated antibody against STAT3 phosphorylated at Y705: http://www.bdbiosciences.com/eu/reagents/research/antibodies-buffers/cell-biology-reagents/cell-biology-antibodies/alexa-fluor-647-mouse-anti-stat3-py705-4p-stat3/

p/557815,
Alexa Fluor® 488-conjugated antibody against NF-κB p65 phosphorylated at S529: http://www.bdbiosciences.com/eu/applications/research/intracellular-flow/intracellular-antibodies-and-isotype-controls/anti-human-antibodies/alexa-fluor-488-mouse-anti-nf-b-p65-ps529-k10-8951250/p/558421,
Alexa Fluor® 488-conjugated antibody against p38 phosphorylated at T180/Y182: http://www.bdbiosciences.com/eu/applications/research/intracellular-flow/intracellular-antibodies-and-isotype-controls/anti-rat-antibodies/alexa-fluor-488-mouse-anti-p38-mapk-pt180py182-36p38-pt180py182/p/612594,
Alexa Fluor® 647-conjugated mouse IgG1κ: http://www.bdbiosciences.com/eu/reagents/research/antibodies-buffers/immunology-reagents/anti-human-antibodies/cell-surface-antigens/alexa-fluor-647-mouse-igg1-isotype-control-mopc-21/p/557714,
Alexa Fluor® 488- Mouse IgG1κ: http://www.bdbiosciences.com/eu/reagents/research/antibodies-buffers/cell-biology-reagents/isotype-controls/alexa-fluor-488-mouse-igg1-isotype-control-mopc-21/p/557782,
PE- Mouse IgG1κ: https://www.biolegend.com/en-us/products/pe-mouse-igg1--kappa-isotype-ctrl-icfc-3032,
Percp-cy5.5-Rat IgG1κ: https://www.biolegend.com/en-us/products/percp-cy5-5-rat-igg1--kappa-isotype-ctrl-4203,
V450- Mouse IgG1κ: http://www.bdbiosciences.com/eu/reagents/research/antibodies-buffers/immunology-reagents/anti-human-antibodies/cell-surface-antigens/v450-mouse-igg1-isotype-control-mopc-21/p/560373.
Data are provided per assurance by each supplier. The commercial antibodies are well used and reported in lots of previous publications.
The MLKL (Mus) (home made) has been validation by Wu, Z. et al. Chaperone-mediated autophagy is involved in the execution of ferroptosis. Proceedings of the National Academy of Sciences 116, 2996, doi:10.1073/pnas.1819728116 (2019).

Eukaryotic cell lines

Policy information about cell lines

Cell line source(s)	HEK293T cell line was from the American Type Culture Collection. Ripk1 gene knock-out MEFs were established from Ripk1-/- mice. MEFs derived from D325A knockin mice were kindly contributed by Jianke Zhang.
Authentication	Cell line from ATCC has been authenticated by ATCC. The primary lines are cultured for limited number of passages.
Mycoplasma contamination	Cell lines tested negative for Mycoplasma contamination.
Commonly misidentified lines (See ICLAC register)	No commonly misidentified cell lines were used.

Human research participants

Policy information about studies involving human research participants

Population characteristics	The patients characteristics have been described in Extended Data Table 1. Healthy controls are less than 10 years old and they had no symptoms of inflammation when sampling.
Recruitment	Patient samples were obtained from patients with early onset autoinflammatory disease but without clear genetic diagnosis. And multiple age and gender matched healthy controls used in the experiment were randomly selected.
Ethics oversight	Patient P1 was evaluated under protocols approved by the Institutional Review Board (IRB) by Children's Hospital of Fudan University (Shanghai, China). Patients P2, P3, P4 and P5 and their unaffected family members were evaluated at McMaster Children's Hospital (Ontario, Canada), and the Hospital for Sick Children (Toronto, Canada). Signed consent for their clinical information to be shared and for research samples to be sent to Boston Children's Hospital (Boston, USA) was obtained. Ethics clearance was received from the Institutional Review Board (IRB) at Boston Children's Hospital (Boston, USA) and from Western Institutional Review Board. All relevant ethical regulations were followed. All patients and/or substitute decision markers provided written informed consent.

Note that full information on the approval of the study protocol must also be provided in the manuscript.

Flow Cytometry

Plots

Confirm that:

☒ The axis labels state the marker and fluorochrome used (e.g. CD4-FITC).

☒ The axis scales are clearly visible. Include numbers along axes only for bottom left plot of group (a 'group' is an analysis of identical markers).

☒ All plots are contour plots with outliers or pseudocolor plots.

☒ A numerical value for number of cells or percentage (with statistics) is provided.

Methodology

Sample preparation	We used EDTA-anticoagulated peripheral whole blood from patients and health donors. PBMCs from patients and healthy donors were separated by lymphocyte separation medium (LSM) and SepMate tubes (Stemcell) according to the manufacturer's instructions.

Instrument	All events were acquired on a FACS Canto II cytometer.
Software	All events were analyzed with FlowJo (10.0).
Cell population abundance	1.0E6 of PBMCs were used for each test. Coutess II FL (Thermo Fisher) and 0.4% Typan Blue were used to determine the viability and number of cells. The viability of PBMCs is above 85% for each sample.
Gating strategy	Surface markers CD3, CD4, CD14 and CD19 were used to gate total T cells, CD4+T cells, monocytes and total B cells respectively. A figure exemplifying the gating strategy is provided in the Supplementary Information.

☐ Tick this box to confirm that a figure exemplifying the gating strategy is provided in the Supplementary Information.

Metabolic heterogeneity confers differences in melanoma metastatic potential

https://doi.org/10.1038/s41586-019-1847-2

Received: 3 December 2018

Accepted: 31 October 2019

Published online: 18 December 2019

Alpaslan Tasdogan[1], Brandon Faubert[1], Vijayashree Ramesh[1], Jessalyn M. Ubellacker[1], Bo Shen[1], Ashley Solmonson[1], Malea M. Murphy[1], Zhimin Gu[1], Wen Gu[1], Misty Martin[1], Stacy Y. Kasitinon[1], Travis Vandergriff[2], Thomas P. Mathews[1], Zhiyu Zhao[1], Dirk Schadendorf[3], Ralph J. DeBerardinis[1,4,5]* & Sean J. Morrison[1,4]*

Metastasis requires cancer cells to undergo metabolic changes that are poorly understood[1–3]. Here we show that metabolic differences among melanoma cells confer differences in metastatic potential as a result of differences in the function of the MCT1 transporter. In vivo isotope tracing analysis in patient-derived xenografts revealed differences in nutrient handling between efficiently and inefficiently metastasizing melanomas, with circulating lactate being a more prominent source of tumour lactate in efficient metastasizers. Efficient metastasizers had higher levels of MCT1, and inhibition of MCT1 reduced lactate uptake. MCT1 inhibition had little effect on the growth of primary subcutaneous tumours, but resulted in depletion of circulating melanoma cells and reduced the metastatic disease burden in patient-derived xenografts and in mouse melanomas. In addition, inhibition of MCT1 suppressed the oxidative pentose phosphate pathway and increased levels of reactive oxygen species. Antioxidants blocked the effects of MCT1 inhibition on metastasis. $MCT1^{high}$ and $MCT1^{-/low}$ cells from the same melanomas had similar capacities to form subcutaneous tumours, but $MCT1^{high}$ cells formed more metastases after intravenous injection. Metabolic differences among cancer cells thus confer differences in metastatic potential as metastasizing cells depend on MCT1 to manage oxidative stress.

Metastasis is a very inefficient process in which few disseminated cancer cells survive[1]. One factor that limits metastasis in some cancers, including melanoma, is oxidative stress[2–6]. Melanoma cells experience increased oxidative stress during metastasis, and must undergo metabolic changes to survive, including increased dependence on the folate pathway[3]—a major source of NADPH for oxidative stress resistance[7,8]. Cells use NADPH to regenerate glutathione (GSH), a buffer against oxidative stress. GSH and other antioxidants promote cancer initiation and progression[3,9–12]. This suggests that pro-oxidant therapies would inhibit the progression of some cancers, although they may promote the initiation or progression of others[13].

Lactate synthesis and export from highly glycolytic cells is necessary to remove excess acid and to sustain glycolysis[14]. Lactate was, thus, considered a waste product that must be eliminated by cancer cells despite the fact that some cancer cells take up and metabolize lactate in culture[15,16]. Lung cancers[17] and pancreatic cancers[18] use MCT1 to transport lactate from the circulation into the tumour, with some of the carbon from lactate supplying the tricarboxylic acid (TCA) cycle. Enhanced lactate transport correlates with worse outcomes[17], raising the question of whether lactate consumption is a biomarker of more aggressive cancers or whether it promotes cancer progression.

Lactate is transported across the cytoplasmic membrane mainly by MCT1 and MCT4[19]. These transporters enable bidirectional, passive transport of lactate and related monocarboxylates, including pyruvate[15,16,19,20]. Although MCT1 transports several carboxylates, its main physiological function in vivo is lactate import as lactate is at least tenfold more abundant than other carboxylates in the fed state[19]. Nonetheless, the directionality of transport by MCT transporters depends on lactate and proton concentration gradients. MCT1 inhibition can induce cell death by inhibiting glycolysis as a result of the failure to export lactate in culture[21], and can suppress xenograft growth in mice[15] and cancer cell migration in culture[22,23]. However, most studies of MCT function were performed in culture, in which cells tend to be more highly glycolytic than in vivo[17], raising the question of whether MCTs regulate cancer progression in vivo.

Efficient metastasizers take up more lactate

Efficient metastasizers give rise to circulating cancer cells and distant macrometastases in patients and after xenografting in NOD–SCID *Il2rg*$^{-/-}$ (NSG) mice, whereas inefficient metastasizers do not give rise to detectable cancer cells in the blood and metastasize more slowly in mice and in patients[24] (Extended Data Fig. 1a). We subcutaneously injected efficiently metastasizing (from patients M405, M481, M487 and UT10) and inefficiently metastasizing (from patients M715, UM17, UM22, UM43, UM47, M498, M528, M597 and M610) melanomas into NSG mice. We used established techniques[17] to infuse ^{13}C-labelled nutrients into these mice when the tumours reached approximately 2 cm in

[1]Children's Research Institute and Department of Pediatrics, University of Texas Southwestern Medical Center, Dallas, TX, USA. [2]Department of Dermatology, University of Texas Southwestern Medical Center, Dallas, TX, USA. [3]Department of Dermatology, University Hospital, University Duisburg-Essen, Essen and German Cancer Consortium (DKTK), Heidelberg, Germany. [4]Howard Hughes Medical Institute, University of Texas Southwestern Medical Center, Dallas, TX, USA. [5]Eugene McDermott Center for Human Growth and Development, University of Texas Southwestern Medical Center, Dallas, TX, USA. *e-mail: ralph.deberardinis@UTSouthwestern.edu; sean.morrison@UTSouthwestern.edu

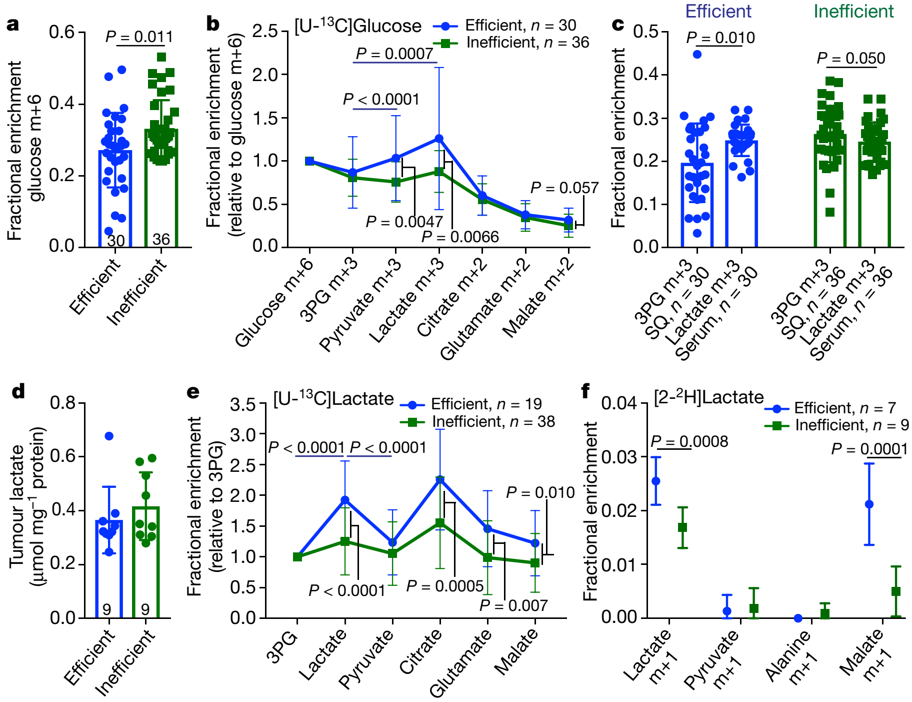

Fig. 1 | Efficiently metastasizing melanomas exhibit enhanced lactate uptake in vivo. Isotope tracing in primary subcutaneous tumours xenografted in NSG mice with efficiently (M405, M481, M487 and UT10) and inefficiently (M715, UM17, UM22, UM43, UM47, M498, M528, M597 and M610) metastasizing melanomas. The number of mice or tumours per treatment is indicated. **a**, **b**, Glucose m + 6 as a fraction of the glucose pool (**a**) and enrichment of other metabolites normalized to m + 6 glucose (**b**) in subcutaneous tumours after infusion of [U-^{13}C]glucose. **c**, The 3PG m + 3 fraction in subcutaneous tumours (SQ) and lactate m + 3 fraction in the plasma of mice infused with [U-^{13}C]glucose (20 experiments). **d**, Tumour lactate concentration (3 experiments). **e**, Enrichment of metabolites normalized to 3PG m + 3 in subcutaneous tumours after [U-^{13}C]lactate infusion (23 experiments). **f**, Isotope labelling after [2-^{2}H]lactate infusion (3 experiments). Data are mean ± s.d. Statistical significance was assessed using *t*-tests (**a**, **f**), paired *t*-tests (**c**), $\log_2$-transformed *t*-tests to compare efficient versus inefficient melanomas or Wilcoxon tests to compare metabolites (**b**, **e**). Multiple comparisons were adjusted using the Holm–Sidak's method (**b**, **c**, **e**, **f**).

diameter, then examined labelling in metabolites extracted from the blood and tumours. Infusion of uniformly labelled ^{13}C-glutamine ([U-^{13}C]glutamine) enriched the circulating glutamine pool and produced no differences in labelling between efficient and inefficient metastasizers (Extended Data Fig. 1b, c). Infusion of [U-^{13}C]glucose modestly but significantly increased glucose enrichments in inefficient metastasizers compared with efficient metastasizers (Fig. 1a), despite no differences in circulating glucose (Extended Data Fig. 1d, e). For this reason, we normalized glucose-derived metabolites in the tumour to glucose m + 6. After this normalization, the labelling of 3-phosphoglycerate (3PG) was similar between the tumour types, but the efficiently metastasizing tumours had increased labelling of lactate compared with 3PG (Fig. 1b). In efficient, but not inefficient, metastasizers, the absolute enrichment in circulating lactate also exceeded the enrichment in tumour 3PG (Fig. 1c). These labelling features in efficient metastasizers are similar to some human lung cancers, in which excess lactate labelling relative to 3PG was explained by the uptake of lactate derived from infused glucose[17].

Next, we infused [U-^{13}C]lactate using conditions that produced steady-state labelling and abundance in the blood (Extended Data Fig. 1e, f), and found no differences in the abundance of tumour lactate between efficient and inefficient metastasizers (Fig. 1d). To account for labelling resulting from the transfer of ^{13}C from lactate to glucose by gluconeogenesis, followed by glucose uptake and glycolysis in the tumour, we normalized metabolite labelling to 3PG, which presumably arises from glycolysis. Lactate enrichment was higher in efficient compared with inefficient metastasizers, and exceeded enrichment in 3PG or pyruvate (Fig. 1e). These data suggest that efficient metastasizers are better than inefficient metastasizers at taking up circulating lactate.

Efficient metastasizers also had higher enrichments in metabolites related to the TCA cycle (citrate, glutamate and malate) (Fig. 1e), which suggests that ^{13}C from lactate was transferred to the TCA cycle. Both efficiently and inefficiently metastasizing melanomas expressed lactate dehydrogenase (LDH) A and B, indicating their capacity to metabolize lactate (Extended Data Fig. 1i).

To verify lactate uptake directly, we infused [2-^{2}H]lactate. Exchanges between lactate and pyruvate transfer ^{2}H to NAD$^+$, resulting in unlabelled pyruvate (Extended Data Fig. 1h); thus, the appearance of label in the tumours indicates the uptake of lactate, not pyruvate[17]. As expected, we observed label in tumour lactate but not pyruvate or alanine (Fig. 1f). Lactate labelling was higher in efficient than in inefficient metastasizers (Fig. 1f), despite similar labelling in the blood (Extended Data Fig. 1g). Efficient metastasizers also contained labelled malate (Fig. 1f), which could arise from the transfer of ^{2}H from NAD^{2}H to malate[17,25] (Extended Data Fig. 1h).

Higher MCT1 in efficient metastasizers

We observed consistently higher levels of MCT1 in efficient metastasizers as compared to inefficient metastasizers by western blot analysis (Fig. 2a; see Extended Data Fig. 2a for quantification). We confirmed this difference using two other anti-MCT1 antibodies by immunofluorescence analysis (Extended Data Fig. 2e–j) and flow cytometry (Fig. 2d, e, Extended Data Fig. 2c; see Extended Data Fig. 2d for quantification). The difference in surface MCT1 staining between efficient and inefficient metastasizers by flow cytometry was particularly notable. Immunofluorescence analysis suggested that MCT1 staining tended to be associated with the cell surface in efficient metastasizers (Extended Data Fig. 2j),

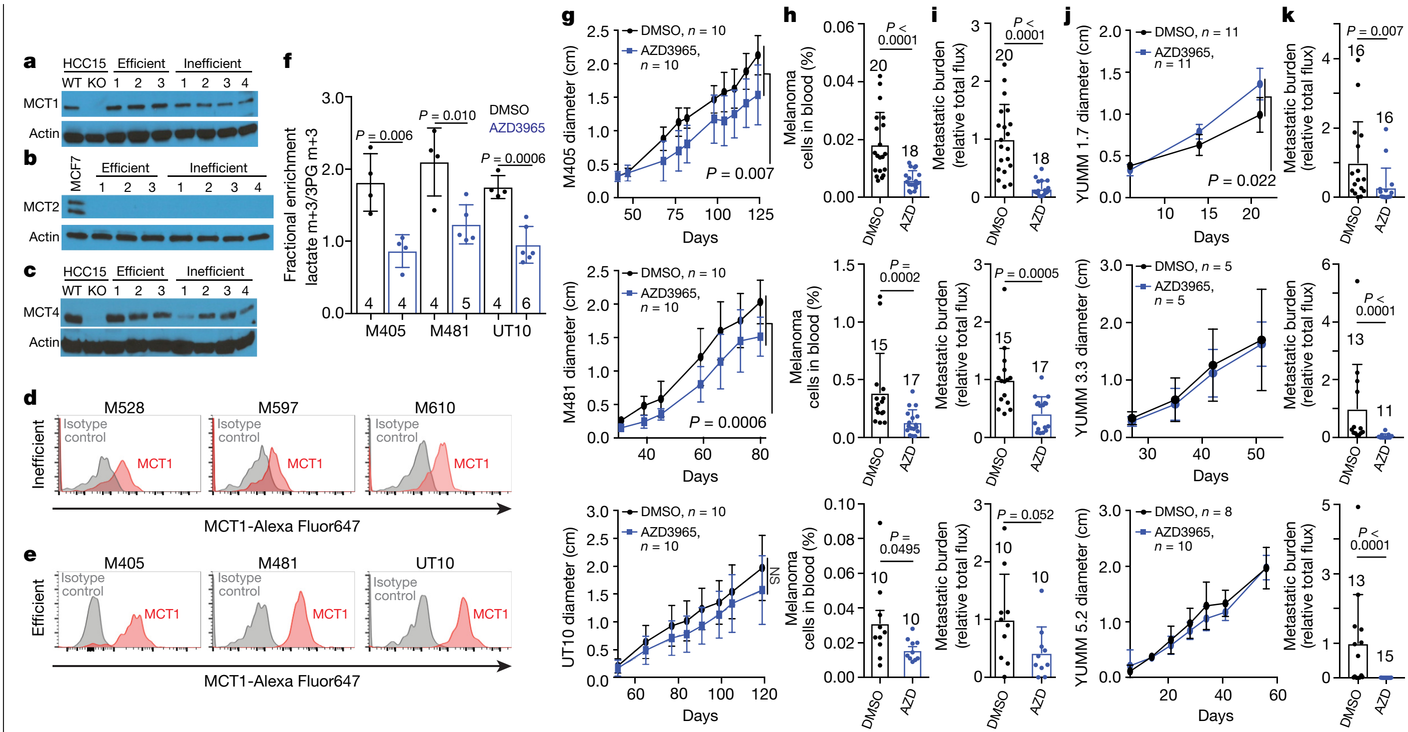

Fig. 2 | MCT1 inhibition selectively impairs metastasis in human and mouse melanomas. a–**c**, Western blot analysis of MCT1 (**a**), MCT2 (**b**) and MCT4 (**c**) in three efficiently (M405, M481 and UT10) and four inefficiently (M498, M528, M597 and M610) metastasizing xenografted melanomas. Wild-type (WT) HCC15 cells were positive controls for MCT1 and MCT4; MCT1- and MCT4-deficient (KO) HCC15 cells were negative controls for MCT1 and MCT4, respectively. MCF7 cells were a positive control for MCT2. The data are representative of four (**a**) or two (**b**, **c**) experiments. **d**, **e**, Flow cytometric analysis of MCT1 surface expression in inefficiently (**d**) and efficiently (**e**) metastasizing melanomas. **f**, Enrichment of lactate m + 3 normalized to 3PG m + 3 in xenografted tumours after treatment with the MCT1 inhibitor AZD3965 or DMSO control and infusion of [U-^{13}C]lactate (two experiments per melanoma). The number of mice per treatment is indicated. **g**–**i**, Growth of subcutaneous tumours (**g**) in mice treated with AZD3965 (AZD) or DMSO control; the frequency of circulating melanoma cells in the blood (**h**); and metastatic disease burden based on bioluminescence imaging (**i**). Data in **h** and **i** reflect one (UT10) or two experiments per melanoma, but only one representative experiment per melanoma is shown in **g**. **j**, **k**, Growth of subcutaneous tumours (**j**) and metastatic disease burden at end point by bioluminescence imaging (**k**) in mice transplanted with YUMM1.7, YUMM3.3 or YUMM5.2 mouse melanomas and treated with AZD3965 or DMSO control (two experiments per melanoma). Data are mean ± s.d. Statistical significance was assessed using *t*-tests (**f**), nparLD (**g**), mixed-effects analysis (**j**) or Mann–Whitney tests (**h**, **i**, **k**). NS, not significant.

but more diffusely cytoplasmic in inefficient metastasizers (Extended Data Fig. 2i).

The expression of MCT1 and CD147 (a co-chaperone of MCT1[26]) did not differ between primary and metastatic tumours (Extended Data Fig. 3a–g), consistent with a previous study[27]. We did not detect MCT2 in any of the melanomas we studied (Fig. 2b). MCT4 was expressed (Fig. 2c; see Extended Data Fig. 2b for quantification), but did not consistently differ between primary and metastatic tumours (Extended Data Fig. 3b).

MCT1 is required during metastasis

To test whether MCT1 mediates lactate uptake by melanoma cells, we transplanted efficiently metastasizing melanomas from three patients subcutaneously into NSG mice, and then treated half of the mice for 7 days with the selective MCT1 inhibitor AZD3965 (30 mg kg^{-1} day^{-1}), which does not have activity against MCT4[28]. We infused [U-^{13}C]lactate and measured the fractional enrichment in lactate relative to 3PG in the tumours. In all three melanomas, AZD3965 treatment significantly reduced lactate labelling, to the point that lactate and 3PG were equivalently labelled, consistent with the labelled lactate arising from glycolysis rather than lactate uptake (Fig. 2f). Therefore, MCT1 mediates lactate uptake in efficient metastasizers.

AZD3965 treatment did not significantly alter the levels of MCT1 (Extended Data Fig. 3h, i), CD147 (Extended Data Fig. 3j, k), β_1 integrin (Extended Data Fig. 3n, o) or CD98 (Extended Data Fig. 3l, m) on the surface of melanoma cells. In addition, AZD3965 treatment did not significantly alter the levels of IKKα (Extended Data Fig. 3p–r) or IKKβ (Extended Data Fig. 3s–u), or the epithelial–mesenchymal transition markers E-cadherin (Extended Data Fig. 4a), N-cadherin (Extended Data Fig. 4b) or vimentin (Extended Data Fig. 4c).

To test whether MCT1 inhibition affected primary tumour growth or metastasis, we subcutaneously transplanted efficiently metastasizing melanoma cells from three patients into NSG mice. Once tumours were palpable, we treated every other day with AZD3965[29]. AZD3965 had little effect on the growth of subcutaneous tumours (Fig. 2g) but substantially reduced the frequency of circulating melanoma cells in the blood (Fig. 2h), and metastatic disease burden in the same mice (Fig. 2i, Extended Data Fig. 5).

We also infected melanoma cells from three patients with scrambled control short hairpin RNA (shRNA) or with shRNAs against *MCT1* (also known as *SLC16A1*) (Extended Data Fig. 6a, b; these shRNAs did not affect MCT4 expression) and then transplanted the cells subcutaneously into NSG mice. MCT1 knockdown had little effect on the growth of the subcutaneous tumours (Extended Data Fig. 6c), but significantly reduced the frequency of circulating melanoma cells in the blood (Extended Data Fig. 6d), and metastatic disease burden in all three melanomas (Extended Data Fig. 6e). The overexpression of an shRNA-insensitive *MCT1* cDNA (Extended Data Fig. 6f) rescued these effects (Extended Data Fig. 6h) without affecting subcutaneous tumour growth (Extended Data Fig. 6g).

MCT1 overexpression in inefficiently metastasizing melanoma cells significantly increased metastatic burden in vivo without affecting

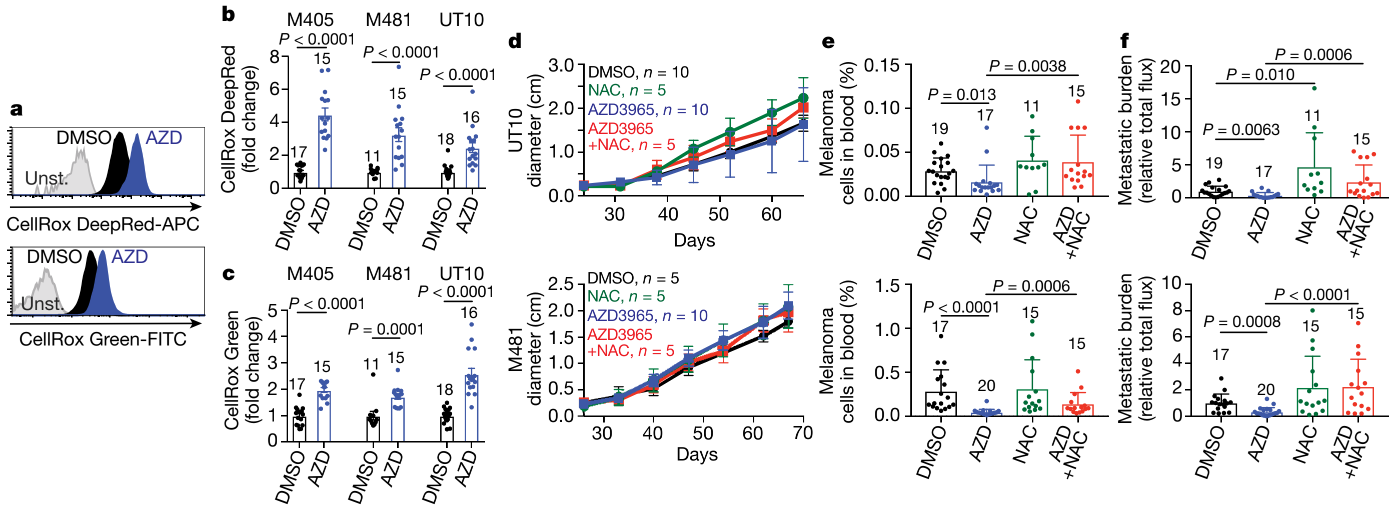

Fig. 3 | MCT1 inhibition causes oxidative stress in melanoma cells. a–c, Representative flow cytometry histograms of ROS levels (**a**) and fold change in mean fluorescence intensity (**b**, **c**) in melanoma cells from mice treated with AZD3965 (blue) or DMSO control (black) (two experiments per melanoma). The number of tumours or mice analysed per treatment is indicated. Unst., unstained. **d–f**, Growth of subcutaneous tumours (**d**) in xenografted mice treated with DMSO, AZD3965, *N*-acetyl cysteine (NAC), or AZD3965 plus NAC, as well as the frequency of circulating melanoma cells in the blood (**e**) and metastatic disease burden based on bioluminescence imaging at end point (**f**). Data in **e** and **f** reflect three experiments per melanoma, but only one representative experiment per melanoma is shown in **d**. Data are mean ± s.d. Statistical significance was assessed using $\log_2$-transformed *t*-tests (**b**), Mann–Whitney tests (**c**), nparLD followed by Benjamini–Hochberg's multiple comparisons adjustment (**d**) and $\log_2$-transformed one-way ANOVA with Holm–Sidak's multiple comparisons adjustment (**e**, **f**).

subcutaneous tumour growth (Extended Data Fig. 7e–g). MCT1 is thus able to increase metastasis in at least some melanomas.

We also inhibited MCT1 in mouse melanomas[30] in immunocompetent C57BL mice (AZD3965 also has activity against mouse MCT1[31]). MCT1 inhibition by treatment with AZD3965 (Fig. 2j, k) or CRISPR-mediated deletion (Extended Data Fig. 7a–c) reduced metastatic disease burden without significantly affecting the growth of subcutaneous tumours. Human and mouse melanomas thus became more dependent on MCT1 function during metastasis in both immunocompromised and immunocompetent environments.

MCT1 promotes cell survival during metastasis

Inhibition of MCT1 with AZD3965 did not impair the migration or invasion of melanoma cells in culture (Extended Data Fig. 8a). Acute treatment with AZD3965 for 7 days in mice with established subcutaneous and metastatic tumours did not significantly affect the growth of subcutaneous or metastatic tumours, but did reduce the frequency of melanoma cells in the blood (Extended Data Fig. 8b, c). This suggests that MCT1 inhibition reduced the survival of melanoma cells during metastasis.

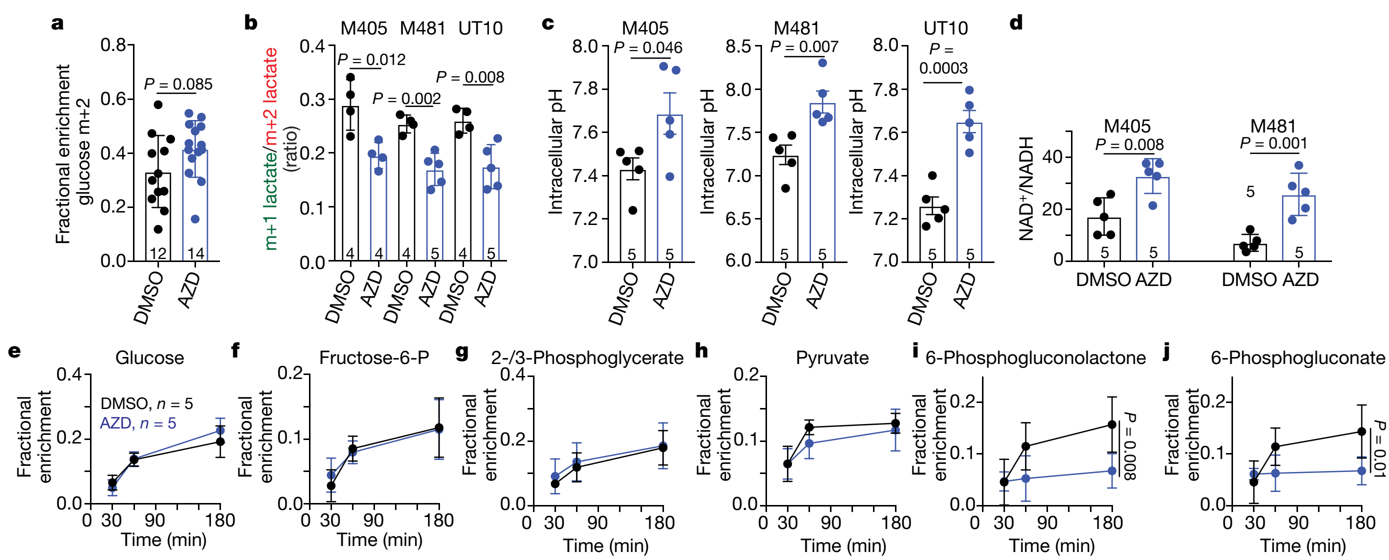

Fig. 4 | MCT1 inhibition reduces flux through the oxidative branch of the PPP relative to glycolysis. a, Glucose m + 2 as a fraction of total glucose in xenografted tumours after infusion of [1,2-^{13}C]glucose (six experiments). The number of tumours or mice per treatment is indicated. **b**, The lactate m + 1/lactate m+2 ratio in subcutaneous tumours from the same mice (two experiments per melanoma). **c**, **d**, Intracellular pH (**c**) and NAD^+/NADH ratio (**d**) in dissociated melanoma cells from subcutaneous tumours (one experiment per melanoma). **e–j**, Fractional enrichment in glycolytic (**e–h**) and PPP (**i**, **j**) metabolites, 30, 60 or 180 min after [U-^{13}C]glucose infusion (two experiments). Fructose-6-P, fructose-6-phosphate. Data are mean ± s.d. Statistical significance was assessed using *t*-tests (**a**, **b** and **d**), nparLD (**c**) or repeated measures two-way ANOVA (**e–j**).

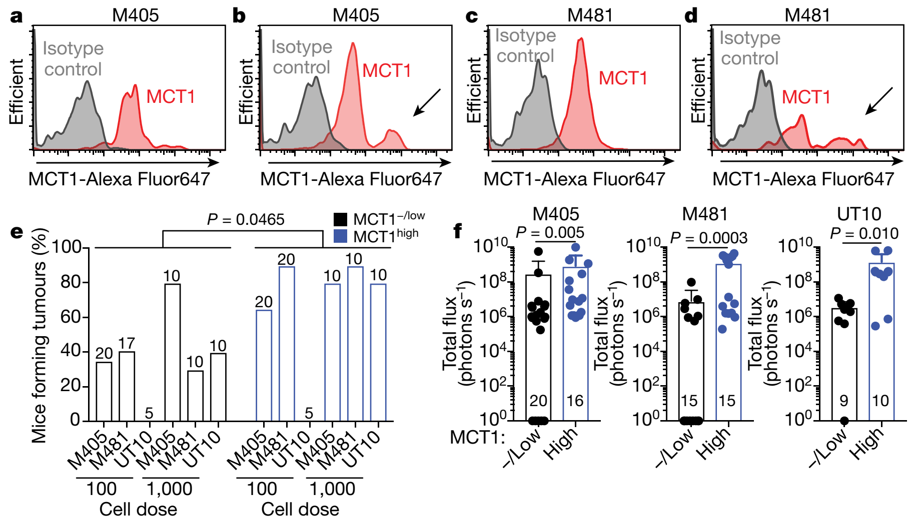

Fig. 5 | Heterogeneous MCT1 expression among melanoma cells from the same tumour. a–**d**, Flow cytometric analysis of anti-MCT1 staining in melanoma cells from subcutaneous tumours (**a**, **c**) or circulating melanoma cells (**b**, **d**) from the same mice xenografted with M405 (**a**, **b**) or M481 (**c**, **d**) (the gating strategies to identify human melanoma cells is in Extended Data Fig. 9e, f; data are representative of two experiments). **e**, Flow cytometrically isolated MCT1^{high} or MCT1$^{-/low}$ melanoma cells were intravenously transplanted into NSG mice, using 100 or 1,000 cells per injection. The percentage of injections that formed metastatic tumours is shown (one or two experiments per melanoma). The number of mice analysed per treatment is indicated. **f**, Metastatic disease burden in the visceral organs of mice that survived to end point after injection with 100 (M405 and M481) or 1,000 (UT10) cells based on bioluminescence signal intensity. Data are mean ± s.d. Statistical significance was assessed using multiple linear regression (**e**) or Mann–Whitney tests (**f**).

To test this further, we resected the primary tumours to extend mouse survival (see schematic in Extended Data Fig. 8d). Treatment with AZD3965 before primary tumour resection, when cells were spontaneously metastasizing, significantly reduced metastatic tumour burden (Extended Data Fig. 8e). By contrast, treatment with AZD3965 only after primary tumour resection—after metastatic tumours were established—did not reduce metastatic tumour burden (Extended Data Fig. 8e). Melanoma cells are, therefore, particularly dependent on MCT1 during metastasis.

Analyses of clinical data[27] and TCGA data showed that higher expression of *MCT1* is associated with significantly worse overall survival (Extended Data Fig. 9a). Differences in *MCT2* (also known as *SLC16A7*) or *MCT4* (*SLC16A3*) expression did not significantly affect survival (Extended Data Fig. 9b, c). Consistent with the correlation between CD147 and MCT1 expression[26], higher *CD147* expression was also associated with significantly worse survival (Extended Data Fig. 9d).

Inhibition of MCT1 induces oxidative stress

Inhibition of MCT1 or MCT4 in cancer cells in culture promotes oxidative stress by inhibiting lactate export, leading to reduced glycolysis[21,32]. AZD3965 treatment increased levels of reactive oxygen species (ROS) in all three melanomas (Fig. 3a–c; see Extended Data Fig. 9e, f for the gating strategy to identify melanoma cells), as did deletion of *MCT1* from YUMM cells (Extended Data Fig. 7d). AZD3965 did not increase ROS levels in melanomas after shRNA-mediated knockdown of *MCT1*, which suggests an on-target effect (Extended Data Fig. 6i). AZD3965 also reduced the ratios of GSH to oxidized glutathione (GSSG) (Extended Data Fig. 10a) and levels of NADPH (Extended Data Fig. 10b). Moreover, treatment with the antioxidant *N*-acetyl cysteine (NAC) rescued the effects of AZD3965 on circulating melanoma cells and metastatic disease burden (Fig. 3d–f). MCT1 inhibition thus impairs metastasis at least partly by increasing oxidative stress.

To test whether MCT1 inhibition affected the pentose phosphate pathway (PPP), we infused [1,2-^{13}C]glucose into xenografted mice and compared the relative flux of labelled glucose through glycolysis versus the oxidative PPP by comparing the ratio of m + 1 lactate (derived from the oxidative PPP) to m + 2 lactate (derived from glycolysis)[33] (Extended Data Fig. 10c). We observed a trend towards increased glucose enrichment in tumours treated with AZD3965 (Fig. 4a). We consistently observed a lower m + 1 lactate/m + 2 lactate ratio in AZD3965-treated as compared to control tumours for all three melanomas (Fig. 4b, Extended Data Fig. 10d). This suggests that MCT1 inhibition reduced flux through the oxidative PPP relative to glycolysis.

After infusion of [U-^{13}C]glucose into xenografted mice (Extended Data Fig. 10e), AZD3965 treatment did not alter isotope enrichment in glucose or glycolytic intermediates (Fig. 4e–h), but reduced isotope enrichment in the oxidative PPP (Fig. 4i, j). AZD3965 treatment did not generally reduce the levels of glycolytic intermediates (Extended Data Fig. 10f, h) but did reduce the levels of oxidative PPP intermediates (Extended Data Fig. 10g, i). Therefore, the effect of MCT1 inhibition in melanoma cells in vivo (inhibition of lactate import, favouring glycolysis over the PPP) was quite different from MCT1 inhibition in culture (inhibition of lactate export, reducing glycolysis[21,32]). In lung cancer, *MCT1* deletion also reduced lactate export and glycolysis in culture, but reduced lactate uptake and enhanced glucose metabolism in vivo[17].

Lactate import can alter intracellular pH and the NAD$^+$/NADH ratio because lactate is co-transported with a proton and converted to pyruvate intracellularly, converting NAD$^+$ to NADH[19]. Consistent with this, in all three melanomas, AZD3965 treatment significantly increased intracellular pH (Fig. 4c), strongly suggesting substantial MCT1-dependent lactate and proton import in these tumours. The increase in pH after MCT1 inhibition could reduce flux through the PPP relative to glycolysis as increased pH activates the activity of phosphofructokinase and suppresses the activity of glucose-6-phosphate dehydrogenase[34,35]—rate-limiting enzymes in glycolysis and the PPP, respectively. AZD3965 treatment also significantly increased the NAD$^+$/NADH ratios (Fig. 4d), which has the potential to enhance glycolysis at the expense of the PPP.

Heterogeneity in MCT1 expression

Flow cytometry revealed a more prominent MCT1^{high} cell population among melanoma cells in the blood (see arrows in Fig. 5b, d) as compared with subcutaneous tumours in the same mice (Fig. 5a, c).

This suggests that surface MCT1 was upregulated in circulating cells to increase PPP function, or that MCT1^{high} cells preferentially survived during metastasis.

To test whether differences in MCT1 expression conferred differences in metastatic potential, we isolated MCT1^{high} and MCT1$^{-/low}$ melanoma cells by flow cytometry from subcutaneously growing M405, M481 and UT10 xenografts and then transplanted the cells either subcutaneously (where oxidative stress does not appear to be limiting for tumour formation) or intravenously (where oxidative stress is limiting for tumour formation)[3]. MCT1^{high} and MCT1$^{-/low}$ cells did not differ in their ability to form subcutaneous tumours or the rates at which the subcutaneous tumours grew (Extended Data Fig. 10j). By contrast, after intravenous injection, MCT1^{high} cells formed significantly more metastatic tumours than MCT1$^{-/low}$ cells (Fig. 5e) and the metastatic disease burden in visceral organs was significantly greater (Fig. 5f). This suggests that differences in MCT1 expression confer differences in the ability to survive during metastasis.

The ability of MCT1 to export lactate and to transport other monocarboxylates bidirectionally[15,19,20] may contribute to its ability to promote metastasis. Other MCT transporters, such as MCT4, may also influence the survival of melanoma cells during metastasis. Lactate taken up by melanoma cells via MCT1 probably has several metabolic fates. Some of the lactate, or pyruvate generated from the lactate, might be exported from the cell[20]. The conversion of imported lactate to pyruvate generates NADH and a proton and could therefore stimulate PPP flux by reducing both intracellular pH and the NAD$^+$/NADH ratio, even if the resulting pyruvate is exported from the cell.

Online content

Any methods, additional references, Nature Research reporting summaries, source data, extended data, supplementary information, acknowledgements, peer review information; details of author contributions and competing interests; and statements of data and code availability are available at https://doi.org/10.1038/s41586-019-1847-2.

1. Vanharanta, S. & Massagué, J. Origins of metastatic traits. *Cancer Cell* **24**, 410–421 (2013).
2. Le Gal, K. et al. Antioxidants can increase melanoma metastasis in mice. *Sci. Transl. Med*. **7**, 308re8 (2015).
3. Piskounova, E. et al. Oxidative stress inhibits distant metastasis by human melanoma cells. *Nature* **527**, 186–191 (2015).
4. Luo, M. et al. Targeting breast cancer stem cell state equilibrium through modulation of redox signaling. *Cell Metab*. **28**, 69–86 (2018).
5. Kfoury, A. et al. AMPK promotes survival of c-Myc-positive melanoma cells by suppressing oxidative stress. *EMBO J*. **37**, e97673 (2018).
6. Xu, I. M. et al. Transketolase counteracts oxidative stress to drive cancer development. *Proc. Natl Acad. Sci. USA* **113**, E725–E734 (2016).
7. Fan, J. et al. Quantitative flux analysis reveals folate-dependent NADPH production. *Nature* **510**, 298–302 (2014).
8. Lewis, C. A. et al. Tracing compartmentalized NADPH metabolism in the cytosol and mitochondria of mammalian cells. *Mol. Cell* **55**, 253–263 (2014).
9. Harris, I. S. et al. Glutathione and thioredoxin antioxidant pathways synergize to drive cancer initiation and progression. *Cancer Cell* **27**, 211–222 (2015).
10. Sayin, V. I. et al. Antioxidants accelerate lung cancer progression in mice. *Sci. Transl. Med*. **6**, 221ra15 (2014).
11. DeNicola, G. M. et al. Oncogene-induced Nrf2 transcription promotes ROS detoxification and tumorigenesis. *Nature* **475**, 106–109 (2011).
12. Schafer, Z. T. et al. Antioxidant and oncogene rescue of metabolic defects caused by loss of matrix attachment. *Nature* **461**, 109–113 (2009).
13. Reczek, C. R. & Chandel, N. S. The two faces of reactive oxygen species in cancer. *Ann. Rev. Cancer Biol*. **1**, 79–98 (2017).
14. Vander Heiden, M. G. & DeBerardinis, R. J. Understanding the intersections between metabolism and cancer biology. *Cell* **168**, 657–669 (2017).
15. Sonveaux, P. et al. Targeting lactate-fueled respiration selectively kills hypoxic tumor cells in mice. *J. Clin. Invest*. **118**, 3930–3942 (2008).
16. Feron, O. Pyruvate into lactate and back: from the Warburg effect to symbiotic energy fuel exchange in cancer cells. *Radiother. Oncol*. **92**, 329–333 (2009).
17. Faubert, B. et al. Lactate metabolism in human lung tumors. *Cell* **171**, 358–371.e9 (2017).
18. Hui, S. et al. Glucose feeds the TCA cycle via circulating lactate. *Nature* **551**, 115–118 (2017).
19. Halestrap, A. P. Monocarboxylic acid transport. *Compr. Physiol*. **3**, 1611–1643 (2013).
20. Hong, C. S. et al. MCT1 modulates cancer cell pyruvate export and growth of tumors that co-express MCT1 and MCT4. *Cell Reports* **14**, 1590–1601 (2016).
21. Doherty, J. R. et al. Blocking lactate export by inhibiting the Myc target MCT1 disables glycolysis and glutathione synthesis. *Cancer Res*. **74**, 908–920 (2014).
22. Izumi, H. et al. Monocarboxylate transporters 1 and 4 are involved in the invasion activity of human lung cancer cells. *Cancer Sci*. **102**, 1007–1013 (2011).
23. Payen, V. L. et al. Monocarboxylate transporter MCT1 promotes tumor metastasis independently of its activity as a lactate transporter. *Cancer Res*. **77**, 5591–5601 (2017).
24. Quintana, E. et al. Human melanoma metastasis in NSG mice correlates with clinical outcome in patients. *Sci. Transl. Med*. **4**, 159ra149 (2012).
25. Chen, Y. J. et al. Lactate metabolism is associated with mammalian mitochondria. *Nat. Chem. Biol*. **12**, 937–943 (2016).
26. Kirk, P. et al. CD147 is tightly associated with lactate transporters MCT1 and MCT4 and facilitates their cell surface expression. *EMBO J*. **19**, 3896–3904 (2000).
27. Pinheiro, C. et al. The metabolic microenvironment of melanomas: prognostic value of MCT1 and MCT4. *Cell Cycle* **15**, 1462–1470 (2016).
28. Curtis, N. J. et al. Pre-clinical pharmacology of AZD3965, a selective inhibitor of MCT1: DLBCL, NHL and Burkitt's lymphoma anti-tumor activity. *Oncotarget* **8**, 69219–69236 (2017).
29. Polański, R. et al. Activity of the monocarboxylate transporter 1 inhibitor AZD3965 in small cell lung cancer. *Clin. Cancer Res*. **20**, 926–937 (2014).
30. Meeth, K., Wang, J. X., Micevic, G., Damsky, W. & Bosenberg, M. W. The YUMM lines: a series of congenic mouse melanoma cell lines with defined genetic alterations. *Pigment Cell Melanoma Res*. **29**, 590–597 (2016).
31. Guan, X., Rodriguez-Cruz, V. & Morris, M. E. Cellular uptake of MCT1 inhibitors AR-C155858 and AZD3965 and their effects on MCT-mediated transport of L-lactate in murine 4T1 breast tumor cancer cells. *AAPS J*. **21**, 13 (2019).
32. Baek, G. et al. MCT4 defines a glycolytic subtype of pancreatic cancer with poor prognosis and unique metabolic dependencies. *Cell Reports* **9**, 2233–2249 (2014).
33. Jang, C., Chen, L. & Rabinowitz, J. D. Metabolomics and isotope tracing. *Cell* **173**, 822–837 (2018).
34. Kirkman, H. N. & Hendrickson, E. M. Glucose 6-phosphate dehydrogenase from human erythrocytes. II. Subactive states of the enzyme from normal persons. *J. Biol. Chem*. **237**, 2371–2376 (1962).
35. Andrés, V., Carreras, J. & Cussó, R. Regulation of muscle phosphofructokinase by physiological concentrations of bisphosphorylated hexoses: effect of alkalinization. *Biochem. Biophys. Res. Commun*. **172**, 328–334 (1990).

Publisher's note Springer Nature remains neutral with regard to jurisdictional claims in published maps and institutional affiliations.

Methods

Melanoma specimen collection and enzymatic tumour disaggregation

Melanoma specimens were obtained with informed consent from patients according to protocols approved by the Institutional Review Board of the University of Michigan Medical School (IRBMED approvals HUM00050754 and HUM00050085)[24] and the University of Texas Southwestern Medical Center (IRB approval 102010-051). Materials used in the manuscript are available, either commercially or from the authors, though there are restrictions imposed by Institutional Review Board requirements and institutional policy on the sharing of materials from patients. Single-cell suspensions were obtained by dissociating tumours in Kontes tubes with disposable pestles (VWR) followed by enzymatic digestion in 200 U ml^{-1} collagenase IV (Worthington), DNase (50 U ml^{-1}) and 5 mM $CaCl_2$ for 20 min at 37 °C. Cells were filtered through a 40-µm cell strainer to remove clumps.

Mouse studies and xenograft assays

All mouse experiments complied with all relevant ethical regulations and were performed according to protocols approved by the Institutional Animal Care and Use Committee at the University of Texas Southwestern Medical Center (protocol 2016-101360). Melanoma cell suspensions were prepared for injection in staining medium (L15 medium containing bovine serum albumin (1 mg ml^{-1}), 1% penicillin/streptomycin and 10 mM HEPES (pH 7.4) with 25% high-protein Matrigel (product 354248; BD Biosciences)). Subcutaneous injections were performed in the right flank of NOD.CB17-*Prkdc*^{scid} *Il2rg*^{tm1Wjl}/SzJ (NSG) mice in a final volume of 50 µl. Four-to-eight-week-old male and female NSG mice were transplanted with 100 melanoma cells subcutaneously unless otherwise specified. Mouse cages were randomized between treatments (mice within the same cage had to be part of the same treatment). Both male and female mice were used. Subcutaneous tumour diameters were measured weekly with callipers until any tumour in the mouse cohort reached 2.5 cm in its largest diameter, in agreement with the approved animal protocol. At that point, all mice in the cohort were euthanized and spontaneous metastasis was evaluated by gross inspection of visceral organs for macrometastases and bioluminescence imaging of visceral organs to quantify metastatic disease burden (see details below).

YUMM1.7 (*Braf*$^{V600E/+}$;*Pten*$^{-/-}$;*Cdkn2*$^{-/-}$), YUMM3.3 (*Braf*$^{V600E/+}$;*Cdkn2a*$^{-/-}$), and YUMM5.2 (*Braf*$^{V600E/+}$;*p53*$^{-/-}$) (*p53* is also known as *Trp53*) cell lines[30] were obtained from and authenticated by ATCC and cell lines were confirmed to be mycoplasma free using the MycoAlert detection kit (Lonza). YUMM1.7, YUMM3.3 and YUMM5.2 were transfected with dsRed2 and luciferase (dsRed2-P2A-Luc) for bioluminescence imaging. Subcutaneous injections of 20,000–50,000 cells were performed in the right flank of 6-to-8-week-old male and female C57BL/6 mice in 50 µl.

For studies that involved treatment with the MCT1 inhibitor (AZD3965, Selleckchem), when subcutaneous tumours became palpable, the mice were administered AZD3965 by oral gavage every second day in xenografted mice and every day for mice transplanted with YUMM cells (30 mg kg^{-1} body mass in 200 µl of 0.5% promethylcellulose, 0.2% Tween80 and 5% DMSO). Tumour growth was monitored weekly with a calliper. Mice were euthanized when the primary tumour reached 2.5 cm in its largest diameter. In addition to measuring subcutaneous tumour diameters, the frequency of circulating melanoma cells in the blood (obtained by cardiac puncture) was measured by flow cytometry, and metastatic disease burden was measured by total bioluminescence levels in dissected visceral organs.

Bioluminescence imaging

Metastatic disease burden was monitored using bioluminescence imaging (all melanomas were tagged with stable expression of luciferase). Five minutes before performing luminescence imaging, mice were injected intraperitoneally with 100 µl of PBS containing D-luciferin monopotassium salt (40 mg ml^{-1}) (Biosynth) and mice were anaesthetized with isoflurane 2 min before imaging. All mice were imaged using an IVIS Imaging System 200 Series (Caliper Life Sciences) with Living Image software. After completion of whole-body imaging, mice were euthanized and individual organs were surgically removed and imaged. The exposure time ranged from 10 to 60 s, depending on the maximum signal intensity, to avoid saturation of the luminescence signal. To measure the background luminescence, a negative control mouse not transplanted with melanoma cells was imaged. The bioluminescence signal (total photon flux) was quantified with 'region of interest' measurement tools in Living Image (Perkin Elmer) software. Metastatic disease burden was calculated as observed total photon flux across all organs in xenografted mice minus background total photon flux in negative control mice. Negative values were set to 1 for purposes of presentation and statistical analysis.

Cell labelling and flow cytometry

Melanoma cells were identified and sorted by flow cytometry as previously described[3]. All antibody staining was performed for 20 min on ice, followed by washing with HBBS and centrifugation at 200*g* for 5 min. Cells were stained with directly conjugated antibodies against mouse CD45 (violetFluor 450, eBiosciences), mouse CD31 (390-eFluor450, Biolegend), mouse Ter119 (eFluor450, eBiosciences) and human HLA-ABC (G46-2.6-FITC, BD Biosciences). Human melanoma cells were isolated as cells that were positive for HLA and negative for mouse endothelial and haematopoietic markers. Cells were washed with staining medium and re-suspended in 4′,6-diamidino-2-phenylindole (DAPI; 1 µg ml^{-1}; Sigma) to eliminate dead cells from sorts and analyses. To analyse other markers, cells were stained with Alexa Fluor647-conjugated anti-human MCT1 (Bioss antibodies), Alexa Fluor488-conjugated anti-human CD147, PE-Vio770-conjugated anti-human CD98, Alexa Fluor700-conjugated anti-human β_1-integrin, FITC-conjugated anti-E-cadherin (CD324) or PE/Cy7-conjugated anti-N-cadherin (CD325). Cells were examined on an LSRFortessa cell analyser (Becton Dickinson) or sorted on a FACS Fusion Cell Sorter (Becton Dickinson). For analysis of circulating melanoma cells, blood was collected from mice by cardiac puncture with a syringe pretreated with citrate-dextrose solution (Sigma) when subcutaneous tumours reached 2.5 cm in diameter. Red blood cells were sedimented using Ficoll, according to the manufacturer's instructions (Ficoll Paque Plus, GE Healthcare). Remaining cells were washed with HBSS (Invitrogen) before antibody staining and flow cytometry.

Lentiviral/shRNA transduction of human melanoma cells

All melanomas expressed DsRed and luciferase as previously described[3,24]. All shRNAs were expressed from a pGFP-C-shLenti vector (Origene). For knockdown of *MCT1*, Origene shRNA clones TL309405A (5′-GAGGAAGAGACCAGTATAGATGTTGCTGG-3′) and TL309405B (5′-ATCCAGCTCTGACCATGATTGGCAAGTAT-3′) were used. For overexpression of *MCT1*, the human open reading frame was obtained from the Precision LentiORF collection (Dharmacon) in a bicistronic lentiviral construct that co-expressed turbo green fluorescent protein (pLOC-MCT1-IRES-tGFP). As a control, turbo red fluorescent protein (tRFP) was expressed in place of *MCT1* in the same construct (pLOC-tRFP-IRES-tGFP). In rescue experiments, the *MCT1* cDNA was mutated to change wobble bases in 10 consecutive codons to render the *MCT1* cDNA insensitive to the anti-MCT1 shRNAs we used without affecting the amino acid sequence (5′-GAGGAAGAGACCAGTATAGATGTTGCTGGG-3′ to 5′-GAAGAGGAAACTAGCATTGACGTCGCAGGC-3′ for shRNA #1 and 5′-AATCCAGCTCTGACCATGATTGGCAAGTAT-3′ to 5′-AACCCGGCCCTAACGATGATAGGGAAATAC-3′ for shRNA #2). The shRNA-resistant *MCT1* sequence was cloned into the pLVX-EF1a-IRES-mCherry lentiviral vector to infect melanoma cells.

For virus production, 0.9 μg of the appropriate plasmid together with 1 μg of helper plasmids (0.4 μg pMD2G and 0.6 μg of psPAX2) were transfected into 293T cells using PolyJet (SignaGen) according to the manufacturer's instructions. The resulting replication-incompetent viral supernatants were collected at 48 h after transfection and filtered through a 45-μm filter. Then, 300,000 freshly dissociated melanoma cells were infected with viral supernatants supplemented with 10 μg ml^{-1} polybrene (Sigma) for 4 h. Cells were then washed twice with staining medium (L15 medium containing bovine serum albumin (1 mg ml^{-1}), 1% penicillin/streptomycin and 10 mM HEPES (pH 7.4)), and approximately 25,000 cells (a mixture of infected and non-infected cells) were suspended in staining medium with 25% high-protein Matrigel (product 354248; BD Biosciences) and then injected subcutaneously into NSG mice. After growing to 1–2 cm in diameter, the tumours were excised and dissociated into single-cell suspensions as described above. DsRed and GFP double-positive cells were sorted and transplanted into NSG mice for in vivo studies to assess the effect of each shRNA construct on tumour growth and metastasis.

CRISPR editing of *MCT1* in mouse melanoma cells

Single-guide RNAs (sgRNAs) targeting exon 2 of mouse *Mct1* were designed using publicly available tools (http://crispr.mit.edu): *Mct1* sgRNA #1, 5′– AAATGCCACCTGCGATTGGA–3′; *Mct1* sgRNA #2, 5′–ATGGATATCATCTATAATGT–3′. The sgRNAs were cloned into the U6-driven Cas9 expression vector (pX458-pSpCas9(BB)-2AGFP; 48318, Addgene)[36]. Approximately 100,000 YUMM1.7 mouse melanoma cells were plated in tissue-culture-treated 6-well plates in DMEM low glucose plus 10% fetal bovine serum (FBS) and 1% penicillin/streptomycin. One microgram of each of the two sgRNA constructs was co-transfected into the melanoma cells using PolyJet (SignaGen) according to the manufacturer's instructions. After 48 h, GFP^+ cells were sorted into 96-well plates with DMEM low glucose plus 10% FBS and 1% penicillin/streptomycin at clonal density, then clones were expanded and genomic DNA was isolated to screen for *MCT1* exon 2 deletions.

Cell invasion

Transwell invasion assays were carried out using Corning BioCoat Tumour Invasion Systems (354165, Corning) as previously described[37]. In brief, 5×10^5 cells were seeded in the upper chamber of each well in serum-free culture medium. FBS (10%) in DMEM in the lower chamber was used as the chemoattractant. The invasive cells that migrated across the insert towards the lower chamber were stained with crystal violet solution after 24 h of incubation at 37 °C in 5% CO_2. Images were captured using an Olympus microscope with a DP71 high-resolution digital camera and cells were counted using ImageJ.

In vivo isotope tracing

All in vivo isotope tracing experiments were performed when subcutaneous tumours reached 2 cm in diameter. Before infusions, mice were fasted for 16 h, then a 27-gauge catheter was placed in the lateral tail vein under anaesthesia. We intravenously infused [U-^{13}C]glutamine (CLM-1822, Cambridge Isotope Laboratories) as a bolus of 0.1725 mg g^{-1} body mass over 1 min in 150 μl of saline, followed by continuous infusion of 0.00288 mg g^{-1} body mass per min for 5 h (in a volume of 150 μl h^{-1})[38]. For infusions of [U-^{13}C]glucose (CLM-1396, Cambridge Isotope Laboratories) and [1,2-^{13}C]glucose (CLM-504, Cambridge Isotope Laboratories), we intravenously infused a bolus of 0.4125 mg g^{-1} body mass over 1 min in 125 μl of saline, followed by continuous infusion of 0.008 mg g^{-1} body mass per min for 3 h (in a volume of 150 μl h^{-1})[17]. At the end of the infusion, mice were killed and tumours were collected and immediately frozen in liquid nitrogen. To assess the fractional enrichments in plasma, 20 μl of blood was obtained after 30, 60, 120 and 180 min of infusion. For [U-^{13}C]lactate (CLM-1579, Cambridge Isotope Laboratories) and [2-^{2}H] lactate (693987, Sigma-Aldrich) infusion, we intravenously infused a bolus of 0.24 mg g^{-1} body mass over 10 min in 15 μl of saline, followed by continuous infusion of 0.0048 mg g^{-1} body mass per min for 3 h (in 120 μl h^{-1})[17]. Care was taken during infusions not to increase blood glucose or lactate concentrations over pre-infusion levels.

Gas chromatography mass spectrometry

For gas chromatography–tandem mass spectrometry (GC–MS), subcutaneous tumour fragments weighing 5–15 mg were homogenized using an electronic tissue disruptor (Qiagen) in ice-cold 80:20 methanol:water (v/v) followed by three freeze–thaw cycles in liquid nitrogen. The supernatant was collected after a 10-min centrifugation at 13,000*g* at 4 °C then lyophilized. To analyse isotope enrichment in the plasma, whole blood was chilled on ice then centrifuged for 1 min at 13,000*g* at 4 °C to separate the plasma. Aliquots of 20–40 μl of plasma were added to 80:20 methanol:water to extract the metabolites, then lyophilized using a SpeedVac (Thermo), and re-suspended in 40 μl anhydrous pyridine. This solution was added to pre-prepared GC–MS autoinjector vials containing 80 μl *N*-(tert-butyldimethylsilyl)-*N*-methyltrifluoroacetamide (MTBSTFA) to derivatize polar metabolites. The samples were incubated at 70 °C for 1 h, then aliquots of 1 μl were injected for analysis. Samples were analysed using either an Agilent 6890 or an Agilent 7890 gas chromatograph coupled to an Agilent 5973N or 5975C Mass Selective Detector, respectively. The observed distributions of mass isotopologues were corrected for natural abundance[39].

Metabolomic analysis

HILIC chromatographic separation of metabolites was achieved using a Millipore ZIC-pHILIC column (5 μm, 2.1 × 150 mm) with a binary solvent system of 10 mM ammonium acetate in water, pH 9.8 (solvent A) and acetonitrile (solvent B) with a constant flow rate of 0.25 ml min^{-1}. For gradient separation, the column was equilibrated with 90% solvent B. After injection, the gradient proceeded as follows: 0–15 min linear ramp from 90% B to 30% B; 15–18 min isocratic flow of 30% B; 18–19 min linear ramp from 30% B to 90% B; 19–27 column regeneration with isocratic flow of 90% B. Metabolites were measured with a Thermo Scientific QExactive HF-X hybrid quadrupole orbitrap high-resolution mass spectrometer (HRMS) coupled to a Vanquish UHPLC. HRMS data were acquired with two separate acquisition methods. Individual samples were acquired with an HRMS full scan (precursor ion only) method switching between positive and negative polarities. For data-dependent, high-resolution tandem mass spectrometry (ddHRMS/MS) methods, precursor ion scans were acquired at a resolving power of 60,000 full width at half-maximum (FWHM) with a mass range of 80–1,200 Da. The AGC target value was set to 1×10^6 with a maximum injection time of 100 ms. Pooled samples were generated from an equal mixture of all individual samples and analysed using individual positive- and negative-polarity spectrometry ddHRMS/MS acquisition methods for high-confidence metabolite ID. Product ion spectra were acquired at a resolving power of 15,000 FWHM without a fixed mass range. The AGC target value was set to 2×10^5 with a maximum injection time of 150 ms. Data-dependent parameters were set to acquire the top 10 ions with a dynamic exclusion of 30 s and a mass tolerance of 5 ppm. Isotope exclusion was turned on and a stepped normalized collision energy applied with values of 30, 50 and 70. Settings remained the same in both polarities.

Metabolite identities were confirmed in three ways: (1) precursor ion m/z was matched within 5 ppm of theoretical mass predicted by the chemical formula; (2) fragment ion spectra were matched within a 5 ppm tolerance to known metabolite fragments; and (3) the retention time of metabolites was within 5% of the retention time of a purified standard run with the same chromatographic method. Metabolites were relatively quantitated by integrating the chromatographic peak area of the precursor ion searched within a 5 ppm tolerance.

GSH/GSSG analysis by LC–MS/MS

For analysis of the GSH to GSSG ratio by liquid chromatography–tandem mass spectrometry (LC–MS/MS), subcutaneous tumour

fragments weighing 5–15 mg were homogenized using an electronic tissue disruptor (Qiagen) in ice-cold 80:20 methanol:water (v/v), with 0.1% formic acid to prevent spontaneous oxidation[40], followed by three freeze-thaw cycles in liquid nitrogen. The supernatant was collected after a 10-min centrifugation at 13,000*g* at 4 °C then lyophilized. Lyophilized samples were reconstituted in 100 µl of 0.1% formic acid in water, vortexed and analysed by LC–MS/MS. GSH/GSSG analysis was performed using a SCIEX 6500+ Q-Trap mass spectrometer coupled to a Shimadzu LC-20A UHPLC system. Chromatographic separation was carried out with a Waters HSS T3 column and a binary solvent gradient of water with 0.1% formic acid (solvent A) and acetonitrile with 0.1% formic acid (solvent B). The following gradient was used for separation: 0–3 min, isocratic flow of 0% B; 3–8 min, 0–100% B; 8–13 min, isocratic flow of 100% B; 13–13.1 min, 100–0% B; 13.1–18 min, isocratic flow of 0% B. The flow rate was held constant at 0.2 ml min^{-1}. The mass spectrometry analysis was operated in MRM mode monitoring the following transitions for GSH, GSSH and their respective internal standards in positive mode: GSH 308/162; GSSG 613/355; GSH internal standard (ISTD) 311/165; GSSG ISTD 619/165. Transitions and source parameters were optimized by infusion before analysis. GSH/GSSG ratios were calculated by first determining the molar values of GSH and GSSG individually using a standard curve and the addition of internal standards. Data are reported as the ratio of calculated molar values.

^{13}C tracing analysis for glycolytic and PPP metabolites

The theoretical masses of ^{13}C isotopes of glycolytic and PPP metabolites were calculated and added to a library of predicted isotopes. These masses were then searched with a 5 ppm tolerance and integrated only if the peak apex showed less than 1% difference in retention time from the [U-^{12}C] monoisotopic mass in the same chromatogram. After analysis of the raw data, theoretical natural abundance was calculated. Natural isotope abundances were corrected using a customized R script, which can be found at the GitHub repository (https://github.com/wencgu/nac). The script was written by adapting the AccuCor algorithm[41].

NAD^+/NADH analysis by LC–MS/MS

Analysis of NAD^+/NADH levels was performed on 5–15 mg tumour specimens. Tissues were homogenized manually with a pestle in ice-cold 80:20 methanol:water (v/v). After thorough homogenization, samples were spun at 13,000*g* for 15 min at 4 °C. Samples were then transferred to a fresh conical tube and spun for an additional 10 min at 13,000*g* at 4 °C. The supernatant was placed directly into autosampler vials for analysis by LC/MS.

NAD^+/NADH measurements were carried out on a Thermo Scientific QExactive HF-X hybrid quadrupole orbitrap HRMS coupled to a Vanquish UHPLC. Chromatographic separation of metabolites was achieved using a Millipore ZIC-pHILIC column (5 µm, 2.1 × 150 mm) with a binary solvent system of 10 mM ammonium acetate in water, pH 9.8 (solvent A) and acetonitrile (solvent B) with a constant flow rate of 0.25 ml min^{-1}. For gradient separation, the column was equilibrated with 90% solvent B. After injection, the gradient proceeded as follows: 0–15 min linear ramp from 90% B to 30% B; 15–18 min isocratic flow of 30% B; 18–19 min linear ramp from 30% B to 90% B; 19–27 min of column regeneration with isocratic flow of 90% B.

HRMS data were acquired with two different methods. Pooled samples were generated from an equal mixture of all individual samples and were analysed using individual positive- and negative-polarity ddHRMS/MS for high-confidence metabolite ID. Individual conditions were acquired with an HRMS full scan (precursor ion only) switching between positive and negative polarities. For ddHRMS/MS methods, precursor ion scans were acquired at a resolving power of 60,000 FWHM, with a mass range of 80–1,200 Da. The automated gate control (AGC) target value was set to 10^6, with a maximum injection time of 100 ms. Product ion spectra were acquired at a resolving power of 15,000 FWHM without a fixed mass range. The AGC target value was set to 2×10^5 with a maximum injection time of 150 ms. Data-dependent parameters were set to acquire the top 10 ions with a dynamic exclusion of 30 s and a mass tolerance of 5 ppm. Isotope exclusion was turned on and the normalized collision energy was set to a constant value of 30. Settings remained the same in both polarities. Polarity-switching HRMS full scan data were acquired with a resolving power of 60,000 FWHM and a mass range of 80–1,200 Da; the AGC target was set to 10^6 and a maximum injection time of 100 ms. NAD^+/NADH ratios were determined by integrating the extracted ion chromatograms for NAD^+ in positive mode (m/z = 664.1164) and NADH in negative mode (m/z = 664.1175). Fragmentation spectra from pooled samples were used for structural confirmation of NAD^+ and NADH.

NADPH/$NADP^+$ measurement

Subcutaneous tumours were surgically excised as quickly as possible after killing the mice, then melanoma cells were mechanically dissociated and NADPH and $NADP^+$ were measured using the NADPH/NADP Glo-Assay (Promega) following the manufacturer's instructions. Standard curves were generated using purified $NADP^+$ (N-5755, Sigma-Aldrich) and NADPH (N-6705, Sigma-Aldrich) prepared in the same buffers used for the experimental samples. The absolute amounts of NADP+ and NADPH in each sample were then determined using these standard curves. Luminescence was measured using a using a FLUOstar Omega plate reader (BMG Labtech). Values were normalized to tissue mass.

Assays for ROS levels and intracellular pH

Subcutaneous tumours were surgically excised as quickly as possible after euthanizing the mice, and then melanoma cells were mechanically dissociated in 700 µl of staining medium. Single-cell suspensions were obtained by passing the dissociated cell suspensions through a 40-µm cell strainer. To analyse ROS levels, equal numbers of dissociated cells from each treatment were stained for 30 min at 37 °C with 5 mM CellROX Green or CellROX DeepRed (Life Technologies) in HBSS-free (Ca^{2+} and Mg^{2+}-free) and DAPI (to distinguish live from dead cells). The cells were then washed and analysed by flow cytometry using either a FACS Fusion or a FACS Fortessa (BD Biosciences) to assess ROS levels in live human melanoma cells (positive for human HLA and dsRed and negative for DAPI and mouse CD45/CD31/Ter119).

To assess intracellular pH, equal numbers of dissociated cells from each treatment were stained with a pH-dependent ratiometric dye, Seminaphthorhodaflouor-1 (Acetoxymethyl Ester) (SNARF1)[42] in HBSS-free, and DAPI. We generated standard curves by incubating dissociated melanoma cells with pH 5.5, pH 6.5 or pH 7.5 buffers in the presence of 10 mM valinomycin and nigercin (ionophores that allowed the cytoplasm to equilibrate with extracellular pH; Intracellular pH Calibration Buffer Kit, Life Technologies). SNARF1 fluorescence was measured by flow cytometry as described above and then converted to pH values using the standard curves.

Western blot analysis

We used HCC15 cell lines as positive and negative controls for MCT1 and MCT4 expression (previously described[17]). The identity of the HCC15 cells was confirmed using DNA fingerprinting and they were confirmed to be mycoplasma free using the e-Myco kit (Bulldog bio).

MCF7 cell lines were used as a positive control for MCT2. MCF7 cell lines were obtained from, and authenticated by, ATCC and confirmed to be mycoplasma free using the e-Myco kit (Bulldog bio). Melanomas were excised and quickly snap-frozen in liquid nitrogen. Tumour lysates were prepared in Kontes tubes with disposable pestles using RIPA Buffer (Cell Signaling Technology) supplemented with phenylmethylsulphonyl fluoride (Sigma), and protease and phosphatase inhibitor cocktail (Roche). The bicinchoninic acid protein assay (Thermo) was used to quantify protein concentrations. Equal amounts of protein (10–20 µg) were loaded into each lane and separated on 4–20% polyacrylamide tris glycine SDS gels (BioRad), then transferred to polyvinylidene

difluoride membranes (BioRad). The membranes were blocked for 1 h at room temperature with 5% milk in TBS supplemented with 0.1% Tween-20 (TBST) and then incubated with primary antibodies overnight at 4 °C. After washing, then incubating with horseradish peroxidase conjugated secondary antibody (Cell Signaling Technology), signals were developed using SuperSignal West (Thermo Fisher). Blots were sometimes stripped using Restore stripping buffer (Thermo Fisher) and re-stained with other primary antibodies. The following antibodies were used for western blots: anti-MCT1 (AB3538P, Millipore), anti-MCT2 (LN2021159, LabNed), anti-MCT4 (AB3316P, Millipore), anti-CD147 (ab64616, Abcam), anti-LDHA (C4B5, Cell Signaling Technologies), anti-LDHB (ab53292, Abcam), anti-IKKα (D3W6N, Cell Signaling Technology), anti-IKKβ (D30C6, Cell Signaling Technology), anti-vimentin (D21H3, Cell Signaling Technology), anti-tubulin (ab52866, Abcam) and anti-β-actin (D6A8, Cell Signaling Technologies).

Immunofluorescence staining of frozen tissue sections

Tissues were fixed in 4% paraformaldehyde overnight at 4 °C, washed in PBS and cryoprotected in 30% sucrose overnight. Tissues were then frozen in OCT (Fisher). Sections (10 μm) were cut using a cryostat, washed three times in PBS for 5 min each, and blocked in 5% donkey serum (JacksonImmuno) in PBS for 1 h at room temperature. Sections were then stained with primary antibodies overnight: anti-MCT1 (HPA003324, Sigma, 1:500) and anti-S100 (Z0311, Dako, 1:500). The next day, sections were washed three times in PBS for 5 min each and stained with secondary antibodies: Alexa Fluor488-AffiniPure F(ab')2 Fragment Donkey anti-Rabbit IgG, Cy3-AffiniPure F(ab')2 Fragment Donkey anti-Rat IgG (JacksonImmuno) at 1:250 for 1 h in the dark at room temperature. Sections were washed three times in PBS for 5 min each then stained with DAPI (1:1,000) and mounted with Flouromount-G (SouthernBiotech) for confocal imaging.

Statistical methods

Generally, several melanomas from different patients were tested in multiple independent experiments performed on different days. Mice were allocated to experiments randomly and samples processed in an arbitrary order, but formal randomization techniques were not used. Before analysing the statistical significance of differences among treatments, we tested whether data were normally distributed and whether variance was similar among treatments. To test for normality, we performed the Shapiro–Wilk tests when $3 \leq n < 20$ or D'Agostino omnibus tests when $n \geq 20$. To test whether variability significantly differed among treatments we performed F-tests (for experiments with two treatments) or Levene's median tests (for experiments with more than two treatments). When the data significantly deviated from normality ($P < 0.01$) or variability significantly differed among treatments ($P < 0.05$), we $\log_2$-transformed the data and tested again for normality and variability. If the transformed data no longer significantly deviated from normality and equal variability, we performed parametric tests on the transformed data. If $\log_2$-transformation was not possible or the transformed data still significantly deviated from normality or equal variability, we performed non-parametric tests on the non-transformed data.

All of the statistical tests we used were two-sided, where applicable. To assess the statistical significance of a difference between two treatments, we used Student's t-tests or paired t-tests (when a parametric test was appropriate), Welch's t-tests (when data were normally distributed but not equally variable) or Mann–Whitney or Wilcoxon tests (when a non-parametric test was appropriate). When it was possible to perform a one-sided or a two-sided statistical test we always performed two-sided tests. Multiple t-tests (parametric or non-parametric) were followed by Holm–Sidak's multiple comparisons adjustment. To assess the statistical significance of differences between more than two treatments, we used one-way or two-way ANOVAs (when a parametric test was appropriate) followed by Holm–Sidak's multiple comparisons adjustment or Kruskal–Wallis tests (when a non-parametric test was appropriate) followed by Dunn's multiple comparisons adjustment. To assess the statistical significance of differences between time-course data, we used repeated-measures two-way ANOVAs (when a parametric test was appropriate and there were no missing data points) or mixed-effects analyses (when a parametric test was appropriate and there were missing data points) followed by Dunnett's multiple comparisons adjustment, or nparLD[43]— a statistical tool for the analysis of non-parametric longitudinal data, followed by the Benjamini–Hochberg method for multiple comparisons adjustment. To assess the statistical significance of overall differences between percentages of tumours formed by different treatments and cell doses in all melanomas, we used multiple linear regressions. To assess the statistical significance of differences in overall survival of TCGA SKCM patients, we used Mantel–Cox's log-rank tests. All statistical analyses were performed with Graphpad Prism 8.1 or R 3.5.1 with the stats, fBasics, car and nparLD packages. All data are mean ± s.d.

Sample sizes were not predetermined based on statistical power calculations but were based on our experience with these assays. For assays in which variability is commonly high, we typically used $n > 10$. For assays in which variability is commonly low, we typically used $n < 10$. No data were excluded; however, mice sometimes died during experiments, presumably owing to the growth of metastatic tumours. In those instances, data that had already been collected on the mice in interim analyses were included (such as subcutaneous tumour growth measurements over time) even if it was not possible to perform the end-point analysis of metastatic disease burden (due to the premature death of the mice).

During all isotope tracing experiments, the data were analysed in a manner blinded to sample identity or treatment. A.T. performed all of the infusions, collected tumour specimens and performed mass spectrometry, then passed the de-identified data files to B.F. and A.S., who analysed the isotope tracing patterns. After the patterns had been analysed for individual mice, the samples were re-identified so the results could be interpreted.

Reporting summary

Further information on research design is available in the Nature Research Reporting Summary linked to this paper.

Data availability

Source Data for Figs. 1–5 and Extended Data Figs. 1–10 are provided with the paper. All other data are available from the corresponding authors upon request.

36. Ran, F. A. et al. Genome engineering using the CRISPR–Cas9 system. *Nat. Protocols* **8**, 2281–2308 (2013).
37. Shi, X. et al. The abundance of metabolites related to protein methylation correlates with the metastatic capacity of human melanoma xenografts. *Sci. Adv*. **3**, eaao5268 (2017).
38. Marin-Valencia, I. et al. Analysis of tumor metabolism reveals mitochondrial glucose oxidation in genetically diverse human glioblastomas in the mouse brain in vivo. *Cell Metab*. **15**, 827–837 (2012).
39. Yang, C. et al. Glutamine oxidation maintains the TCA cycle and cell survival during impaired mitochondrial pyruvate transport. *Mol. Cell* **56**, 414–424 (2014).
40. Tu, B. P. et al. Cyclic changes in metabolic state during the life of a yeast cell. *Proc. Natl Acad. Sci. USA* **104**, 16886–16891 (2007).
41. Su, X., Lu, W. & Rabinowitz, J. D. Metabolite spectral accuracy on Orbitraps. *Anal. Chem*. **89**, 5940–5948 (2017).
42. Matsuyama, S., Llopis, J., Deveraux, Q. L., Tsien, R. Y. & Reed, J. C. Changes in intramitochondrial and cytosolic pH: early events that modulate caspase activation during apoptosis. *Nat. Cell Biol*. **2**, 318–325 (2000).
43. Noguchi, K., Gel, Y., Brunner, E. & Konietschke, F. nparLD: an R software package for the nonparametric analysis of longitudinal data in factorial experiments. *J. Stat. Softw*. **50**, 1–23 (2012).

Acknowledgements S.J.M. is a Howard Hughes Medical Institute (HHMI) Investigator, the Mary McDermott Cook Chair in Pediatric Genetics, the Kathryn and Gene Bishop Distinguished Chair in Pediatric Research, the director of the Hamon Laboratory for Stem Cells and Cancer, and a Cancer Prevention and Research Institute of Texas Scholar. R.J.D. is an HHMI Investigator, the Robert L. Moody, Sr. Faculty Scholar at UT Southwestern and Joel B. Steinberg, M.D. Chair in

Pediatrics. The research was supported by the Cancer Prevention and Research Institute of Texas (RP170114 and RP180778), the National Institutes of Health (R35 CA220449; U01 CA228608) and the Robert A. Welch Foundation (I-1733). A.T. was supported by the Else Kröner-Forschungskolleg and the Leopoldina Fellowship Program (LPDS 2016-16) of the German National Academy of Sciences. B.F. was supported by a postdoctoral fellowship from the Canadian Institutes of Health Research (MFE 140911). B.S. and A.S. were supported by Ruth L. Kirschstein National Research Service Award Postdoctoral Fellowships from the National Heart, Lung, and Blood Institute (F32 HL139016-01) and the National Institute of Child Health and Human Development (F32 HD096786-01). We thank A. Gross for mouse colony management as well as N. Loof and the Moody Foundation Flow Cytometry Facility.

Author contributions A.T., R.J.D. and S.J.M. conceived the project, and designed and interpreted experiments. A.T. performed most of the experiments. B.F., A.S., W.G. and R.J.D. participated in the design, analysis and interpretation of isotope tracing and metabolomics experiments. B.F., T.P.M. and R.J.D. developed methods for metabolomics and isotope tracing in vivo. V.R. and J.M.U. helped A.T. to perform the in vivo tumorigenesis assays. J.M.U. performed the melanoma cell migration experiments in culture. B.S., Z.G. and S.Y.K. helped to design the CRISPR gene-targeting and MCT1 overexpression constructs, and generated the constructs. D.S. and T.V. helped with the assessment and interpretation of MCT1 expression patterns in patient specimens. T.P.M. and M.M. performed all of the mass spectrometric analysis of metabolomic and isotope tracing specimens. M.M.M. performed the immunofluorescence analysis of MCT1 expression. Z.Z. performed statistical analyses. A.T., B.F., R.J.D. and S.J.M. wrote the manuscript.

Competing interests R.J.D. is an advisor for Agios Pharmaceuticals. S.J.M. is an advisor for Frequency Therapeutics and Protein Fluidics

Additional information
Supplementary information is available for this paper at https://doi.org/10.1038/s41586-019-1847-2.
Correspondence and requests for materials should be addressed to R.J.D. or S.J.M.
Peer review information *Nature* thanks John Cleveland, Markus Ralser and the other, anonymous, reviewer(s) for their contribution to the peer review of this work.
Reprints and permissions information is available at http://www.nature.com/reprints.

a

Metastatic potential in mice	Melanoma ID	Age/ sex	AJCC clinical stage	Tumor site	Known BRAF / NRAS driver mutations	% of mice with macromets	% of mice with micrometastasis only in the lung (BLI)	% of mice with micrometastasis in organs other than the lung (BLI)
Inefficient	M597	61/M	IIIA	Primary cutaneous	None	0% (0/22)	10% (1/10)	30% (3/10)
Inefficient	UM17	72/F	IIA	Lymph node	None	0% (0/10)	50% (5/10)	0% (0/10)
Inefficient	UM43	64/M	IIIB	Lymph node	BRAF V600E BRAF V600M	0% (0/17)	0% (0/17)	0% (0/17)
Inefficient	UM47	Unk./M	IV	Lymph node	None	0% (0/19)	0% (0/19)	0% (0/19)
Inefficient	UM22	67/M	Unk.	Lymph node	BRAF V600E	6% (1/18)	94% (17/18)	0% (0/18)
Inefficient	M715	Unk.	IV	Primary cutaneous	None	0% (0/19)	0% (0/19)	5% (1/19)
Inefficient	M498	83/M	IIIB	Primary cutaneous	None	0% (0/17)	0% (0/8)	0% (0/8)
Inefficient	M528	72/M	IIIB	Lymph node	BRAF V600E	0% (0/61)	42% (7/17)	0% (0/17)
Inefficient	M610	76/F	IIA	Primary cutaneous	BRAF V600E	0% (0/27)	43% (3/7)	0% (0/7)
Efficient	M405	29/M	IIIB	Lymph node	NRAS Q61R	70% (52/74)	0% (0/23)	96% (22/23)
Efficient	M481	67/M	IIIB	Primary cutaneous	BRAF V600E	56% (75/135)	22% (4/18)	78% (14/18)
Efficient	UT10	65/M	IIIC	Lymph node	NRAS Q61K	28% (15/54)	76% (41/54)	61% (33/54)
Efficient	M487	54/M	IV	Primary cutaneous	BRAF V600E	37% (15/41)	18% (5/28)	79% (22/28)

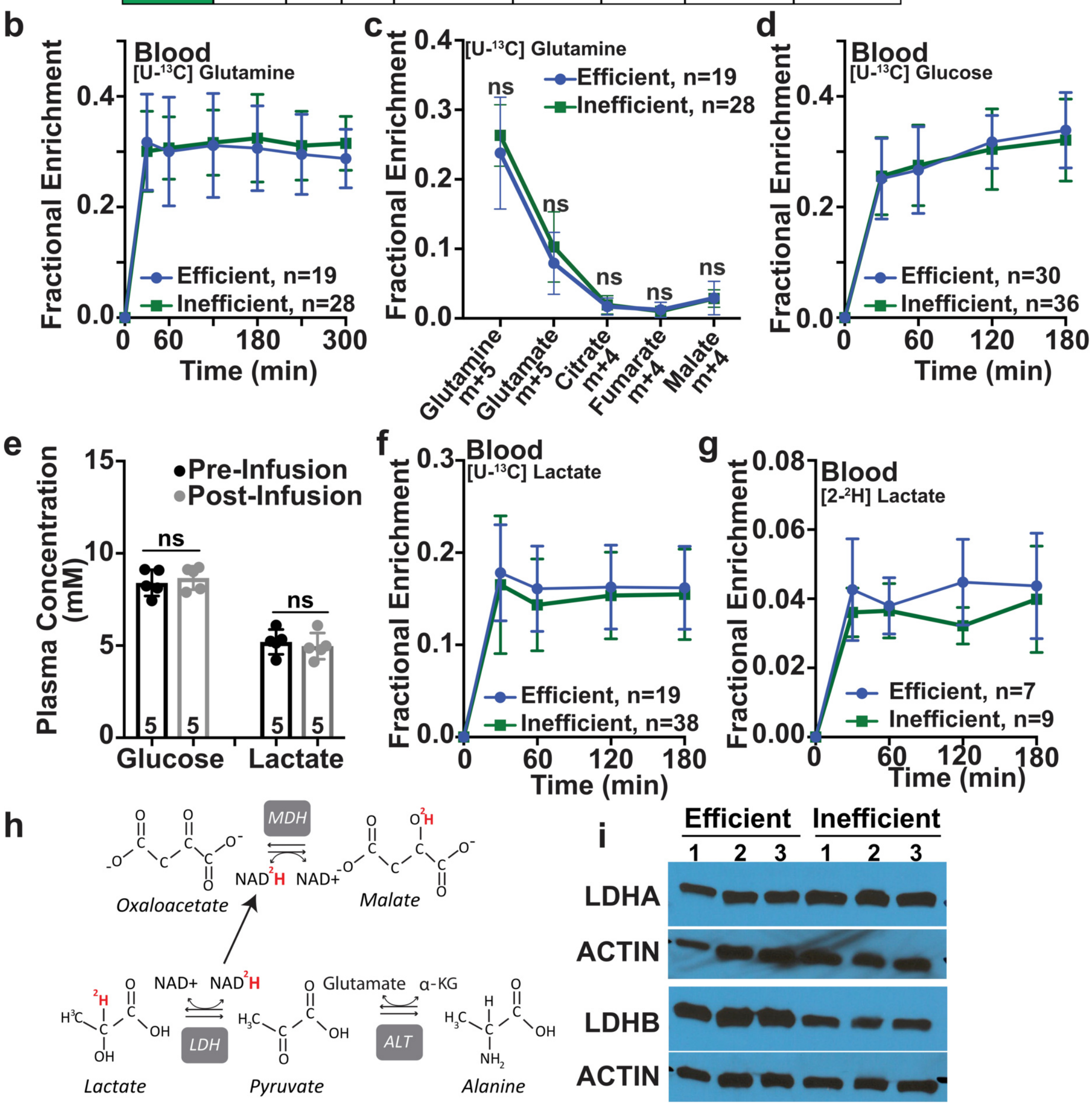

Extended Data Fig. 1 | See next page for caption.

Extended Data Fig. 1 | Plasma enrichment of isotopically labelled metabolites after infusion into xenografted mice. Related to Fig. 1. **a**, Summary of the melanomas used in this study and their spontaneous metastatic behaviour after subcutaneous transplantation into NSG mice. Melanomas were characterized as inefficient or efficient metastasizers. Before subcutaneous tumours grew to 2.5 cm in diameter (when the mice were killed per approved protocol), inefficient metastasizers rarely formed macrometastases or micrometastases beyond the lung, whereas efficient metastasizers commonly formed macrometastases as well as micrometastases in several organs (data reflect results from one to five independent experiments per melanoma). Some of these data have been published previously[24]. **b**–**g**, Isotope tracing was performed in NSG mice subcutaneously xenografted with efficiently metastasizing melanomas from four patients (M405, M481, M487 and UT10) and inefficiently metastasizing melanomas from nine patients (M715, UM17, UM22, UM43, UM47, M498, M528, M597 and M610). The number of tumours or mice analysed per treatment is indicated. **b**, Glutamine m + 5 as a fraction of total plasma glutamine in mice infused with [U-^{13}C]glutamine (14 independent experiments). **c**, Isotope enrichment in subcutaneous tumours after [U-^{13}C]glutamine infusion (14 independent experiments). **d**, Glucose m + 6 as a fraction of total plasma glucose in mice infused with [U-^{13}C]glucose (20 independent experiments). **e**, Plasma glucose and lactate concentrations before and after infusion. **f**, Lactate m + 3 as a fraction of total plasma lactate in mice infused with [U-^{13}C]lactate (23 independent experiments). **g**, Lactate m + 1 as a fraction of total plasma lactate in mice infused with [2-^{2}H]lactate (three independent experiments). **h**, Expected isotope labelling after [2-^{2}H]lactate infusion. **i**, Western blot analysis of LDHA and LDHB in subcutaneous tumours from NSG mice xenografted with efficiently (M405, M481 and UT10) or inefficiently (UM17, UM43 and UM47) metastasizing melanomas (representative of four independent experiments). Data are mean ± s.d. Statistical significance was assessed using Mann–Whitney tests (**c**) and *t*-tests at 180 or 300 min when tumours were obtained for analysis (**b**, **d**, **f**, **g**) or paired *t*-tests (**e**).

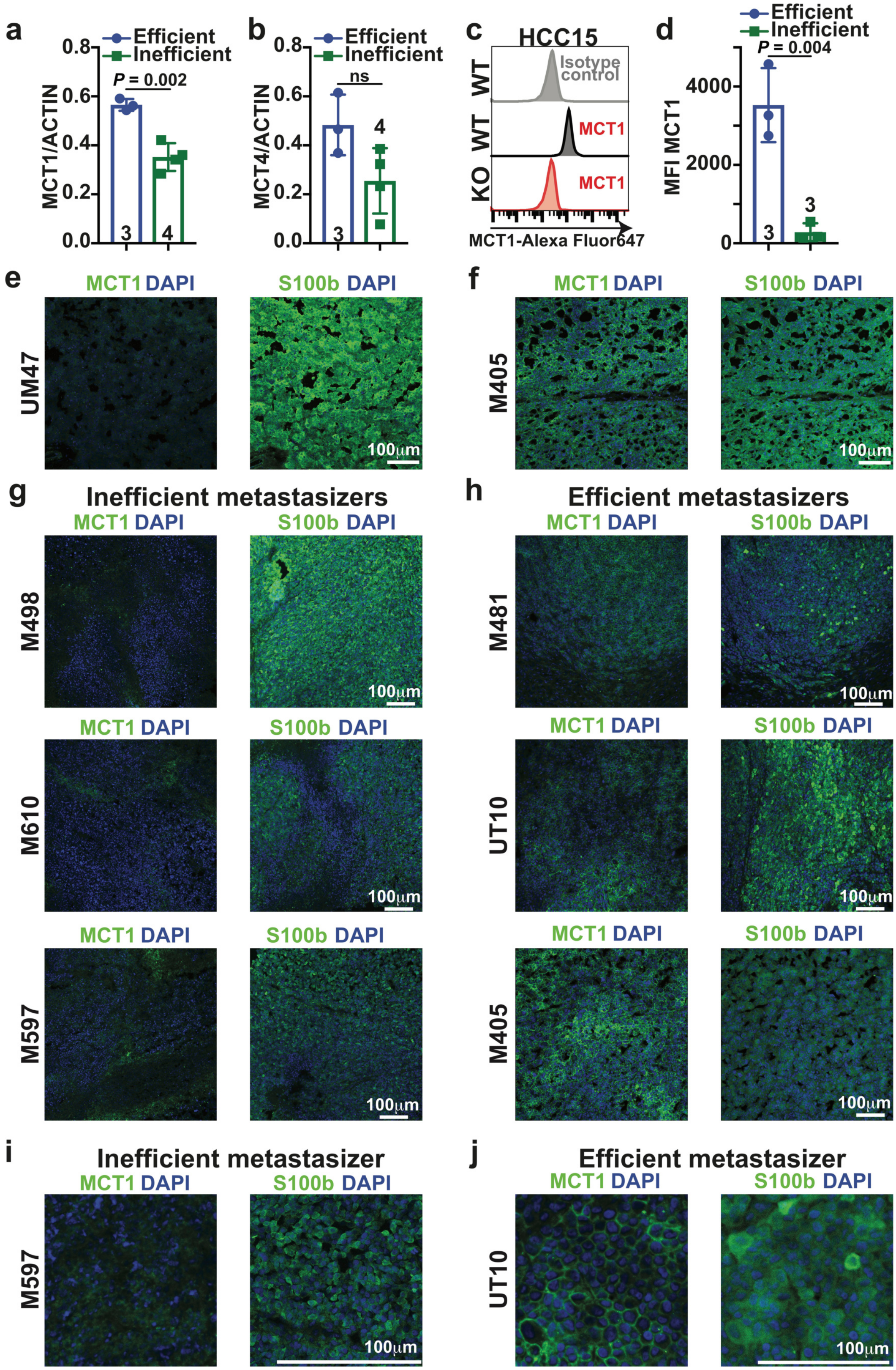

Extended Data Fig. 2 | See next page for caption.

Extended Data Fig. 2 | Efficient metastasizers express higher levels of MCT1 than inefficient metastasizers. Related to Fig. 2. **a**, Quantification of MCT1 relative to actin bands from the western blot in Fig. 2a comparing efficient and inefficient metastasizers. **b**, Quantification of MCT4 relative to actin bands from the western blot in Fig. 2c comparing efficient and inefficient metastasizers. **c**, **d**, Quantification of mean fluorescence intensities for MCT1 staining in the flow cytometry plots comparing efficient (Fig. 2e) and inefficient (Fig. 2d) metastasizers. HCC15 cells and *MCT1*-deficient HCC15 cells were positive and negative controls (**c**). **e**, **f**, Immunofluorescence staining for MCT1 (green) in sections from subcutaneous tumours from inefficiently (**e**, UM47) or efficiently (**f**, M405) metastasizing melanomas. An adjacent section was stained with an antibody against the melanoma marker S100b (green). Images are representative of three independent experiments per melanoma. **g**, **h**, Immunofluorescence staining for MCT1 (green) in sections from subcutaneous tumours from inefficient (**g**; M498, M610 and M597) and efficient (**h**; M481, UT10 and M405) metastasizers. In each case, an adjacent section was stained with an antibody against S100b (green). Images are representative of results from two independent experiments per melanoma. **i**, **j**, Although efficient metastasizers often exhibited cell-surface staining (**j**), inefficient metastasizers typically exhibited diffuse cytoplasmic staining (**i**). Images are representative of results from two independent experiments per melanoma. Data are mean ± s.d. Statistical significance was assessed using Student's *t*-tests (**a**, **b**, **d**).

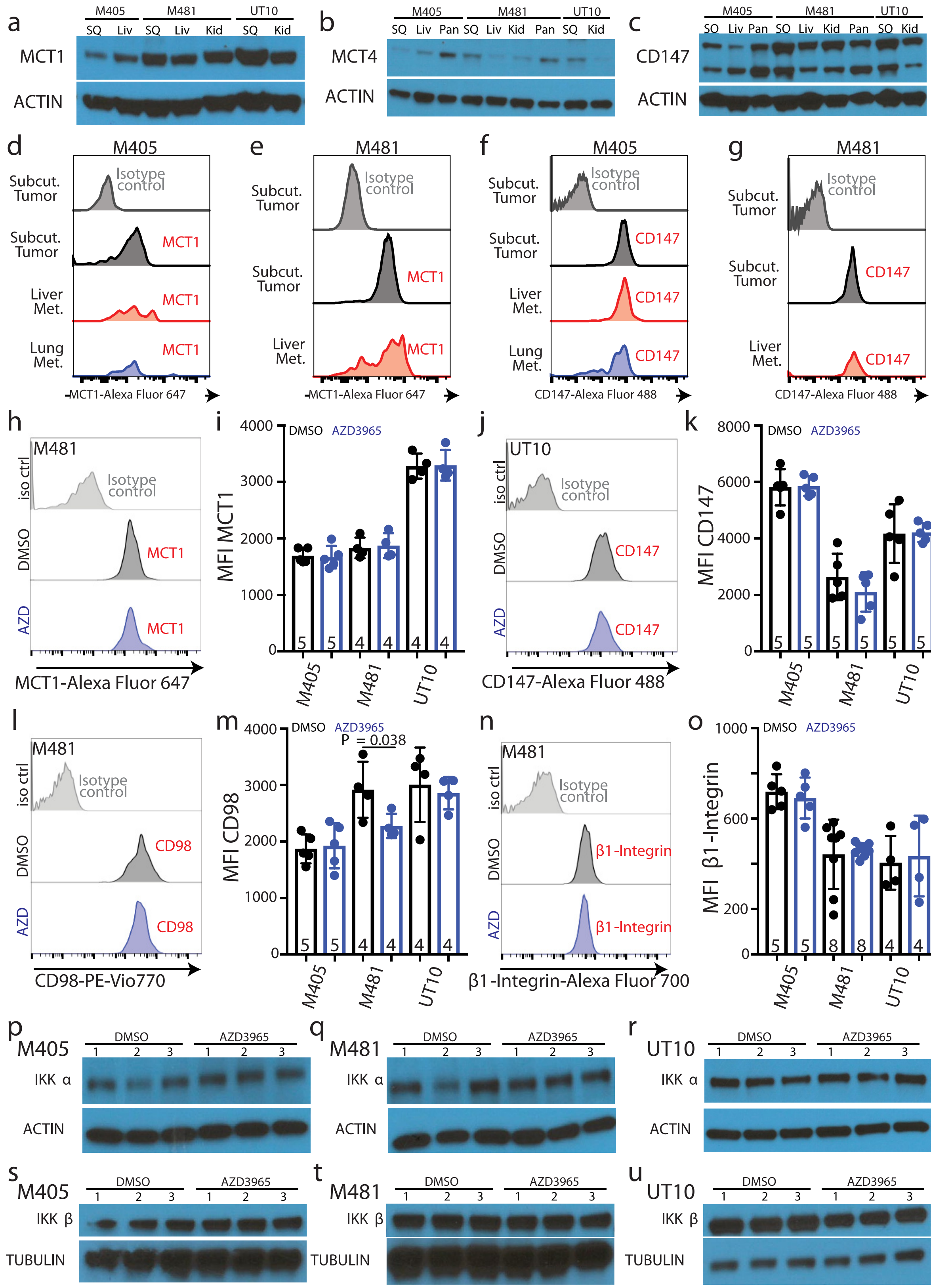

Extended Data Fig. 3 | See next page for caption.

Extended Data Fig. 3 | MCT1 inhibition impairs metastasis without altering MCT1, CD147, CD98 or β_1-integrin expression levels. Related to Fig. 2. **a**–**c**, Western blot analysis of MCT1 (**a**), MCT4 (**b**) and CD147 (**c**) in subcutaneous tumours versus metastatic liver, kidney and pancreas nodules from NSG mice transplanted with three melanomas. **d**–**g**, Flow cytometry histograms of anti-MCT1 (**d**, **e**) or anti-CD147 (**f**, **g**) staining in melanoma cells from subcutaneous tumours or metastatic nodules from mice transplanted with M405 (**d**, **f**) or M481 (**e**, **g**) melanomas. **h**–**o**, Flow cytometry histograms and mean fluorescence intensities of anti-MCT1 (**h**, **i**), anti-CD147 (**j**, **k**), anti-CD98 (**l**, **m**) or anti-β_1-integrin (**n**, **o**) staining in melanoma cells from subcutaneous tumours treated with DMSO (control; black) or AZD3965 (MCT1 inhibitor; blue). The number of tumours or mice analysed in each treatment is indicated (two to three experiments). In all flow cytometric analyses, human melanoma cells were distinguished from mouse cells based on positivity for HLA-ABC and DsRed and negativity for mouse CD31, CD45 and Ter119 staining (see Extended Data Fig. 9e, f for gating strategy). **p**–**u**, Western blot analysis of IKKα (**p**–**r**) and IKKβ (**s**–**u**) in subcutaneous tumours from NSG mice treated with DMSO or AZD3965. Data are mean ± s.d. Statistical significance was assessed with two-way ANOVA (**i**, **k**, **m**, **o**).

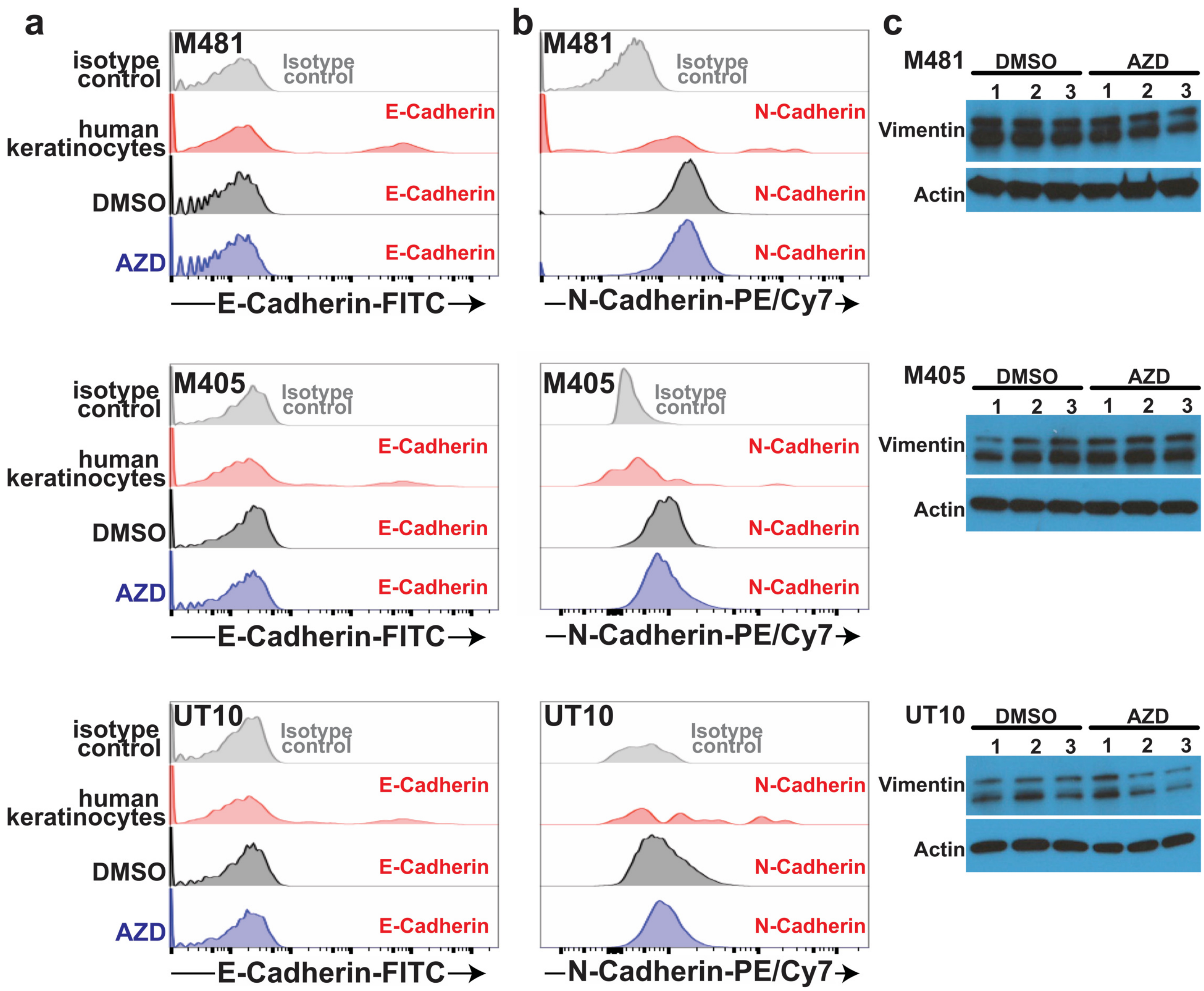

Extended Data Fig. 4 | MCT1 inhibition with AZD3965 impairs metastasis without altering markers of epithelial-to-mesenchymal transition. Related to Fig. 2. **a**, **b**, Flow cytometry histograms of anti-E-cadherin (**a**) and anti-N-cadherin (**b**) staining in melanoma cells from subcutaneous tumours of mice treated with DMSO (control) or AZD3965. Human keratinocytes were included as a control in each case as they are known to include subpopulations of E-cadherin- and N-cadherin-positive cells. In xenografts, human melanoma cells were distinguished from mouse cells based on positivity for HLA-ABC and DsRed and negativity for mouse CD31, CD45 and Ter119 staining (see Extended Data Fig. 9e, f for gating strategy). Data are representative of two to three mice analysed in two independent experiments. **c**, Western blot analysis of vimentin in subcutaneous tumours from NSG mice treated with DMSO or AZD3965.

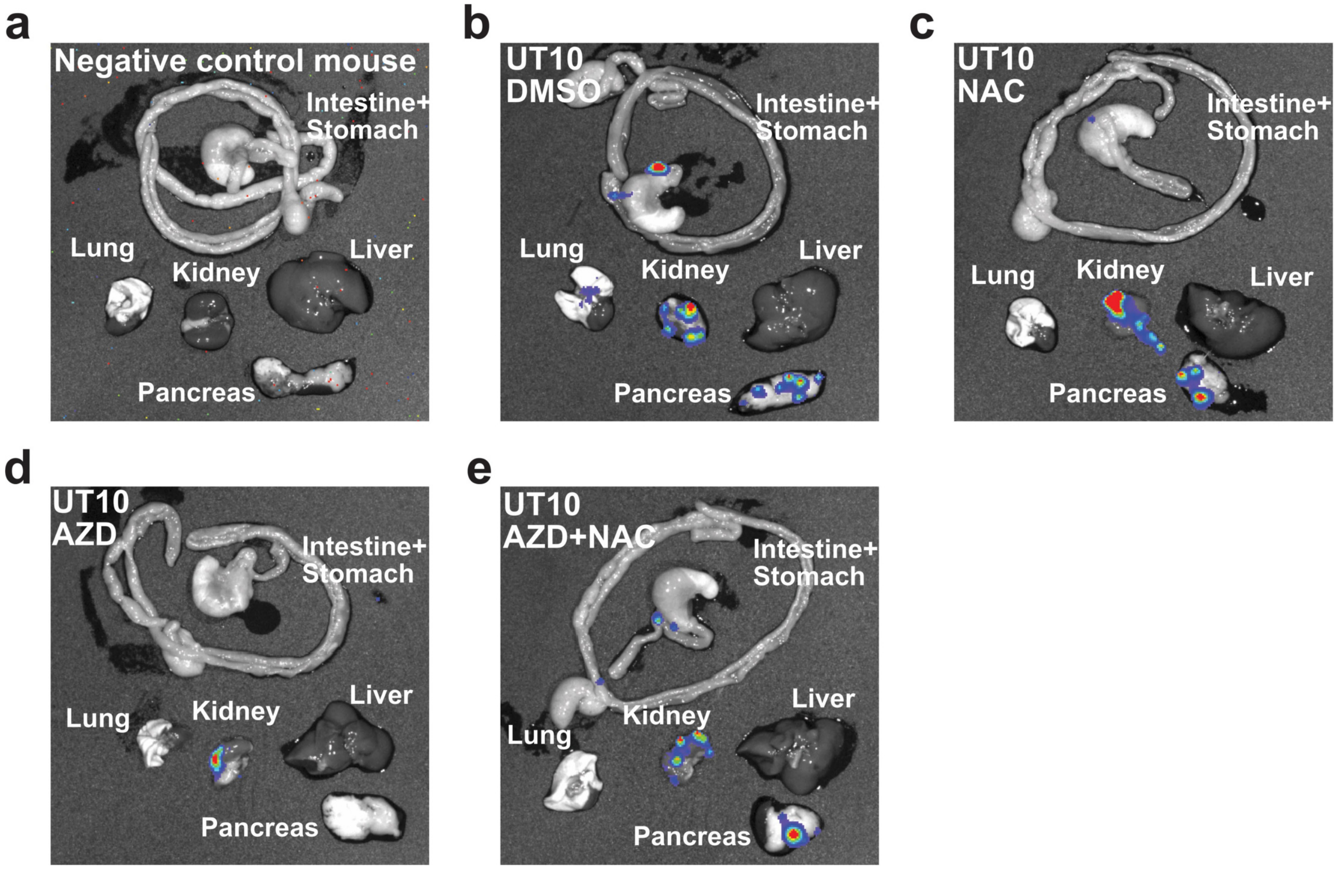

Extended Data Fig. 5 | Representative images of the bioluminescence analysis of visceral organs to determine metastatic disease burden at end point. Related to Figs. 2, 3 and 5. **a**–**e**, Visceral organs were surgically removed from each mouse at end point and imaged to identify macrometastases and micrometastases and to determine bioluminescence signal intensity. Each melanoma was tagged with constitutive luciferase expression.

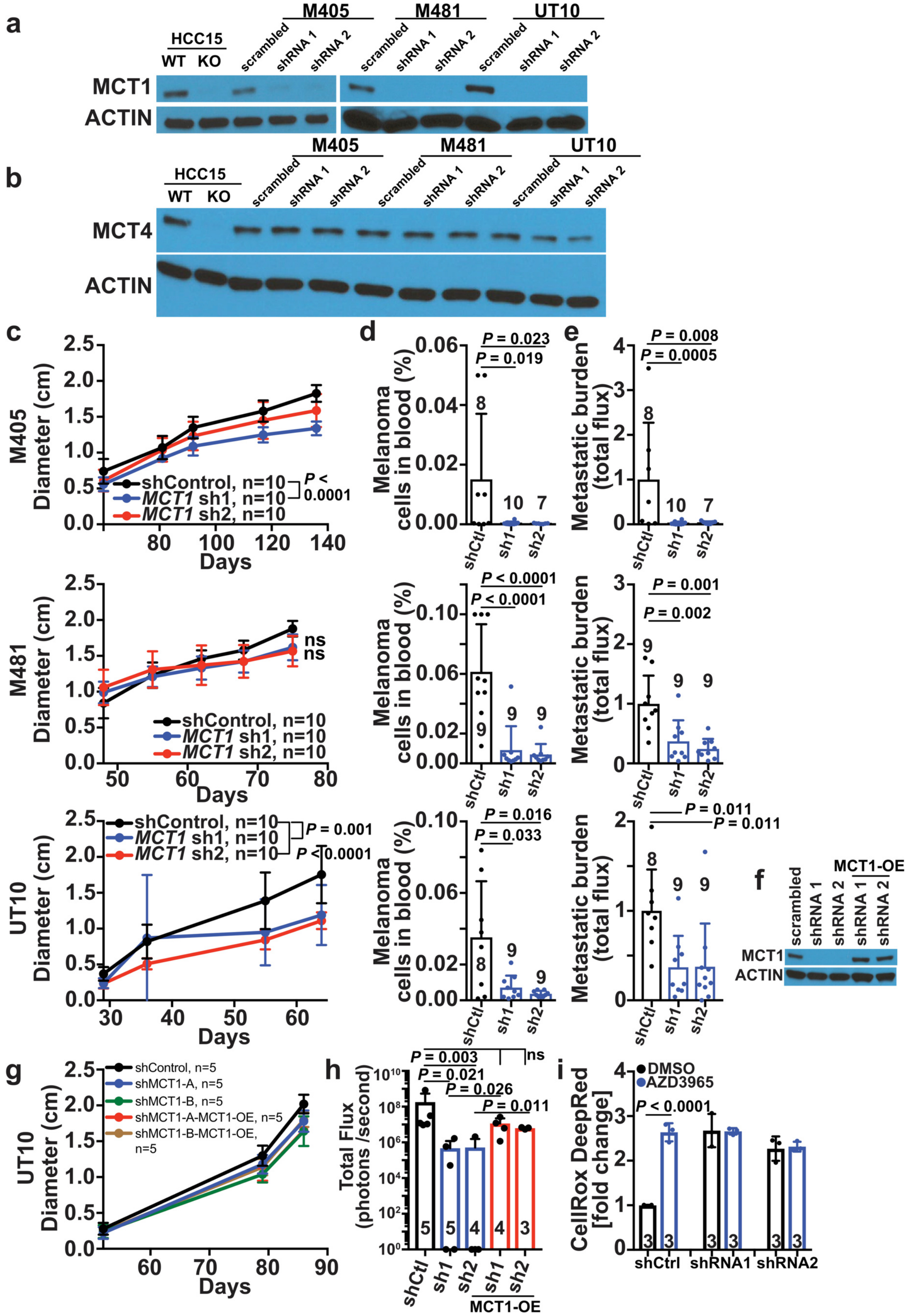

Extended Data Fig. 6 | See next page for caption.

Extended Data Fig. 6 | shRNA-mediated knockdown of MCT1 inhibits melanoma metastasis in vivo. Related to Fig. 2. **a**, **b**, Western blot analysis of MCT1 (**a**) or MCT4 (**b**) in subcutaneous tumours from mice xenografted with efficiently metastasizing melanomas transfected with scrambled control shRNA or with two different shRNAs (1 and 2) against *MCT1* (**a**) or *MCT4* (**b**). Wild-type HCC15 cells were used as a positive control for MCT1 (WT, **a**) and MCT4 (WT, **b**) and *MCT1*-deficient (KO, **a**) or *MCT4*-deficient (KO, **b**) HCC15 cells were used as a negative control (representative of two independent experiments). **c**–**e**, Growth of subcutaneous tumours (**c**) in mice transplanted with melanomas transfected with scrambled control shRNA or shRNAs (sh1 and sh2) against *MCT1*. The number of mice analysed in each treatment is indicated in (one experiment per melanoma). The frequency of circulating melanoma cells in the blood (**d**) and metastatic disease burden based on bioluminescence imaging (**e**) in the same mice were determined. **f**, Western blot analysis of MCT1 in subcutaneous tumours transfected with scrambled control shRNA or shRNAs against *MCT1*, with (MCT1-OE) or without an shRNA-insensitive *MCT1* cDNA. **g**, **h**, Growth of subcutaneous tumours (**g**) and metastatic disease burden at end point (**h**) in mice transplanted with melanomas transfected with scrambled control shRNA or shRNAs against *MCT1* and an shRNA-insensitive *MCT1* cDNA. **i**, Fold change in mean fluorescence intensity for CellRox DeepRed staining (ROS) in xenografted melanoma cells with scrambled control shRNA or shRNAs against *MCT1* treated with AZD3965 or DMSO. Data are mean ± s.d.. Statistical significance was assessed using nparLD followed by Benjamini–Hochberg's multiple comparisons adjustment (**c**), $\log_2$-transformed one-way ANOVAs with Holm–Sidak's multiple comparisons adjustment (**d**, **e**, **h**), mixed-effects analysis followed by Dunnett's multiple comparisons adjustment (**g**) or $\log_2$-transformed two-way ANOVA with Sidak's multiple comparisons adjustment (**i**).

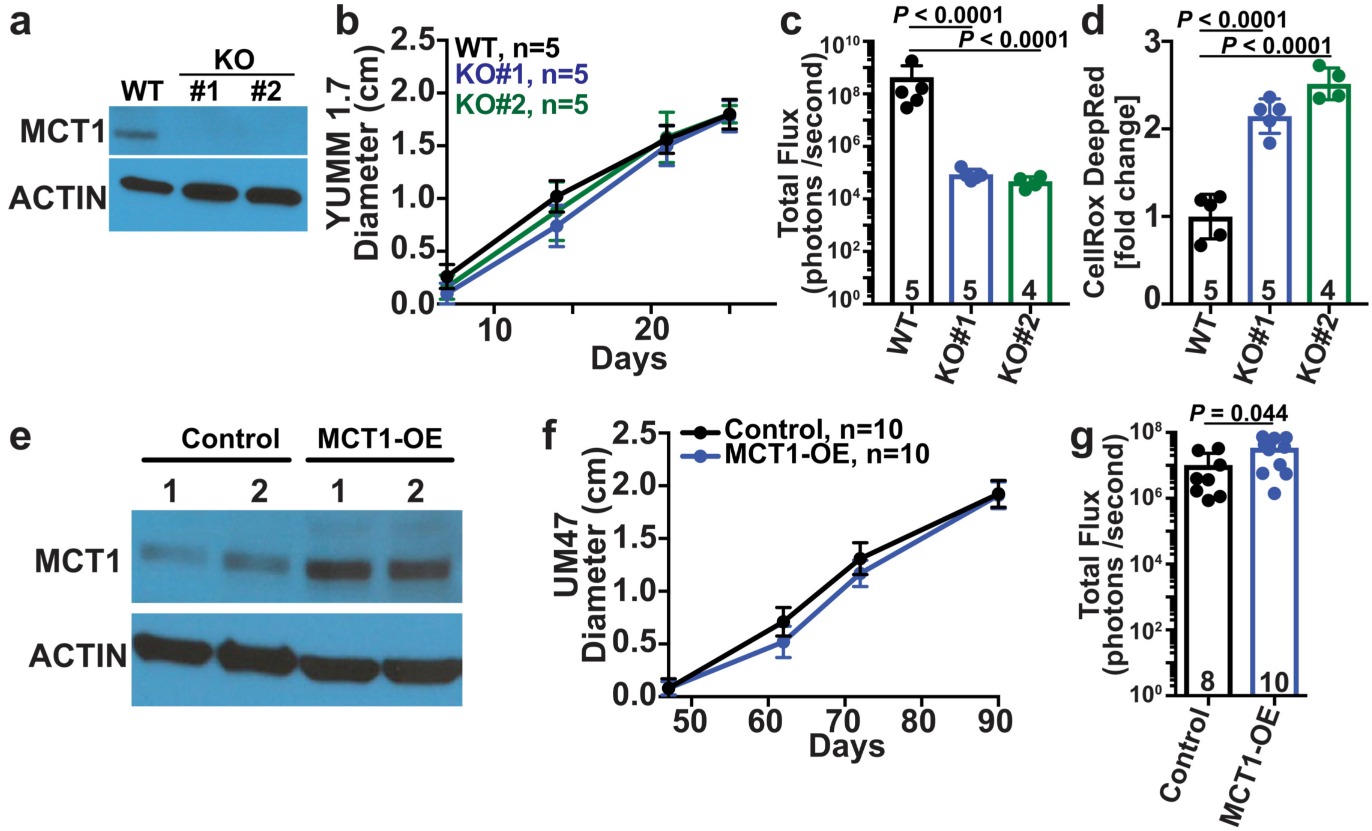

Extended Data Fig. 7 | CRISPR deletion of *MCT1* from mouse melanoma cells impairs metastasis, whereas MCT1 overexpression in patient-derived xenografts increases metastasis. Related to Fig. 2. **a**, Western blot analysis of MCT1 in wild-type parental YUMM1.7 melanoma cells as well as two lines from which *MCT1* had been deleted using CRISPR (KO #1 and #2). **b**–**d**, Growth of subcutaneous tumours (**b**), total metastatic disease burden at end point by bioluminescence imaging of visceral organs (**c**) and CellRox DeepRed staining of subcutaneous tumour cells (**d**). The number of mice analysed in each treatment is indicated (one experiment; note that one mouse died in the KO #2 treatment before end-point analysis). **e**, Western blot analysis of MCT1 in an inefficiently metastasizing melanoma (UM47) expressing *MCT1* cDNA. **f**, **g**, Growth of subcutaneous tumours (**f**) and total metastatic disease burden at end point by bioluminescence imaging of visceral organs (**g**) from mice transplanted with these melanomas (one experiment; note that two mice died in the control treatment before end-point analysis). Data are mean ± s.d. Statistical significance was assessed using one-way ANOVA followed by Dunnett's multiple comparison adjustment (**b**, day 25) or $\log_2$-transformed one-way ANOVAs followed by Dunnett's multiple comparisons adjustment (**c**, **d**), *t*-test (**f**, day 90) or $\log_2$-transformed *t*-test (**g**).

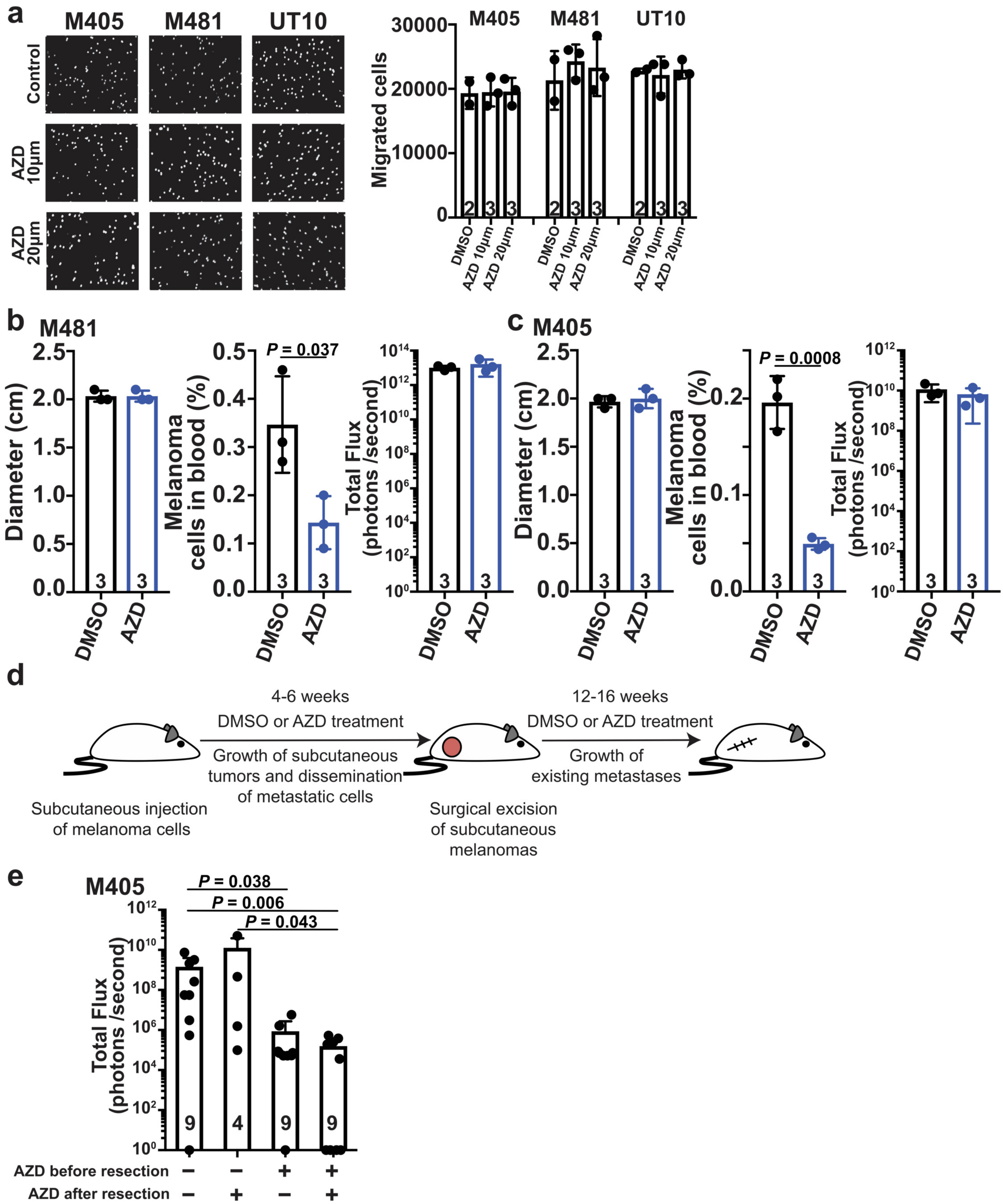

Extended Data Fig. 8 | See next page for caption.

Extended Data Fig. 8 | MCT1 inhibition does not impair the migration of melanoma cells in culture but appears to reduce metastatic disease burden by killing metastasizing melanoma cells in vivo. Related to Fig. 2. **a**, Migration in transwell invasion assays of three melanomas treated with DMSO (control) or AZD3965 (MCT1 inhibitor), including representative images (left) and counts (right) of the cells that migrated across the insert after 24 h (one experiment with two to three replicate cultures per melanoma). **b**, **c**, Effect of acute treatment with AZD3965 (7 days) on the diameter of subcutaneous tumours, the frequency of circulating melanoma cells in the blood and metastatic disease burden in mice with established M481 (**b**) or M405 (**c**) melanomas. Treatment was initiated when the subcutaneous tumours reached 2 cm in diameter (one experiment per melanoma with three mice per treatment). **d**, Efficiently metastasizing melanoma cells (M405) were subcutaneously transplanted into mice and allowed to spontaneously metastasize; then the primary tumours were resected to prolong survival and to allow the metastatic tumours that had formed before primary tumour resection to grow larger. Mice were treated with AZD3965 for the duration of the experiment, only before primary tumour resection, or only after primary tumour resection. **e**, Analysis of total metastatic disease burden at end point showing that metastatic disease burden was reduced when AZD3965 treatment was performed before primary tumour resection, during the time when melanoma cells were spontaneously metastasizing, but before metastatic tumours were established. The number of mice per treatment is shown (two independent experiments). Data are mean ± s.d. Statistical significance was assessed using two-way ANOVA followed by Dunnett's multiple comparison's adjustment (**a**), *t*-tests (**b**, **c**) or Kruskal–Wallis test followed by Dunn's multiple comparison's adjustment (**e**).

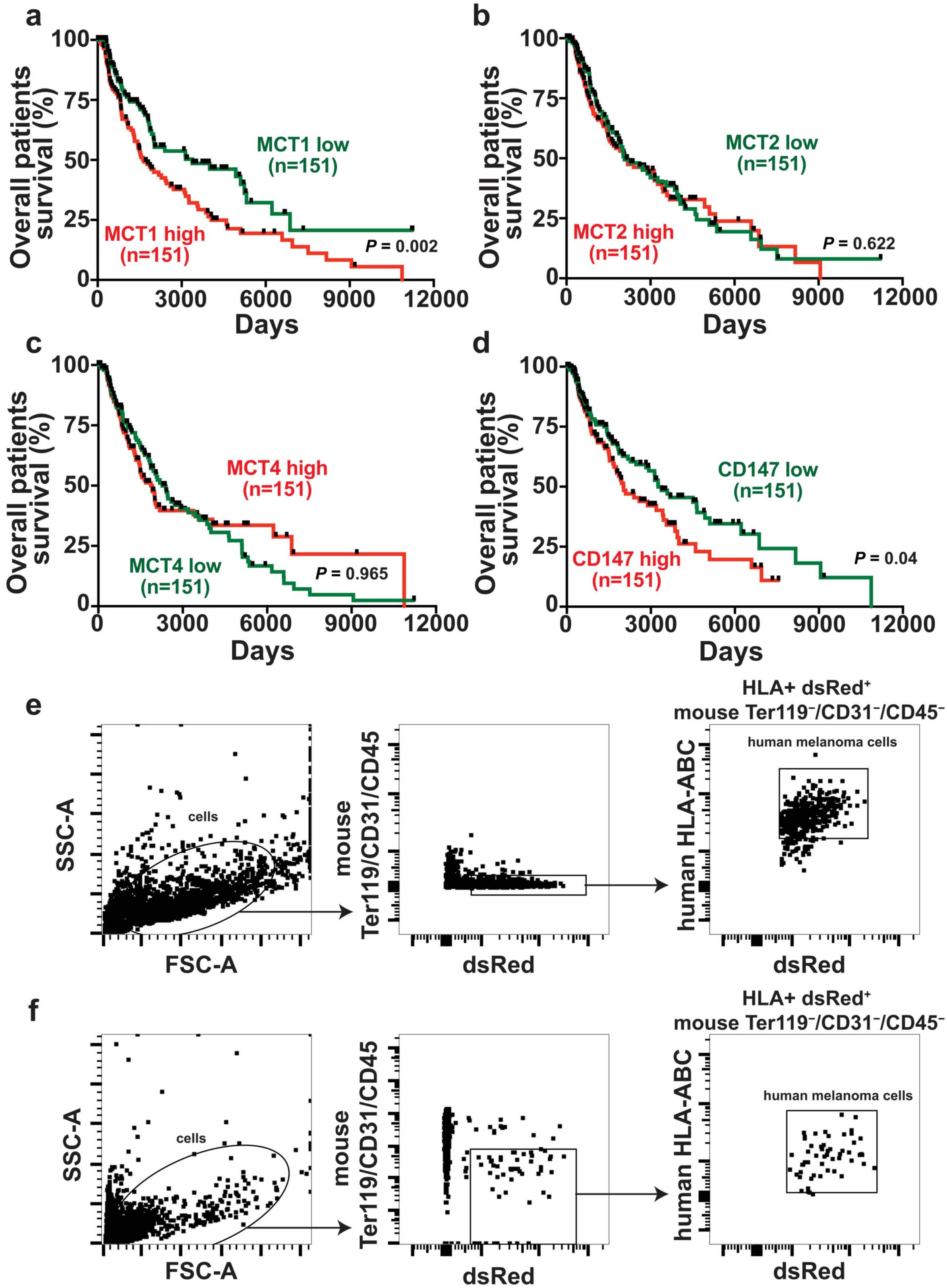

Extended Data Fig. 9 | See next page for caption.

Extended Data Fig. 9 | Increased MCT1 expression in melanomas is associated with significantly worse patient survival. Related to Fig. 2. **a**–**d**, Kaplan–Meier overall survival curves of patients with melanoma stratified based on expression levels of *MCT1* (**a**), *MCT2* (**b**), *MCT4* (**c**) and *CD147* (**d**) within tumour specimens. Data are from the SKCM cohort in TCGA (https://portal.gdc.cancer.gov/projects/TCGA-SKCM). Each panel compares the top third of patients with the highest expression levels versus the bottom third of patients with the lowest expression levels. Ticks represent censored values. **e**, **f**, Flow cytometry plots showing the gating strategies used to identify human melanoma cells in subcutaneous tumours (**e**) or the blood (**f**) of xenografted mice. Cells were gated on forward versus side scatter (FSC-A versus SSC-A) to exclude red blood cells and clumps of cells. Human melanoma cells were selected by including cells that stained positively for DsRed (stably expressed in all melanoma lines) and HLA and excluding cells that stained positively for the mouse haematopoietic and endothelial markers CD45, CD31 or Ter119. Statistical significance of the differences in overall survival (**a**–**d**) was assessed using the Mantel–Cox log-rank test.

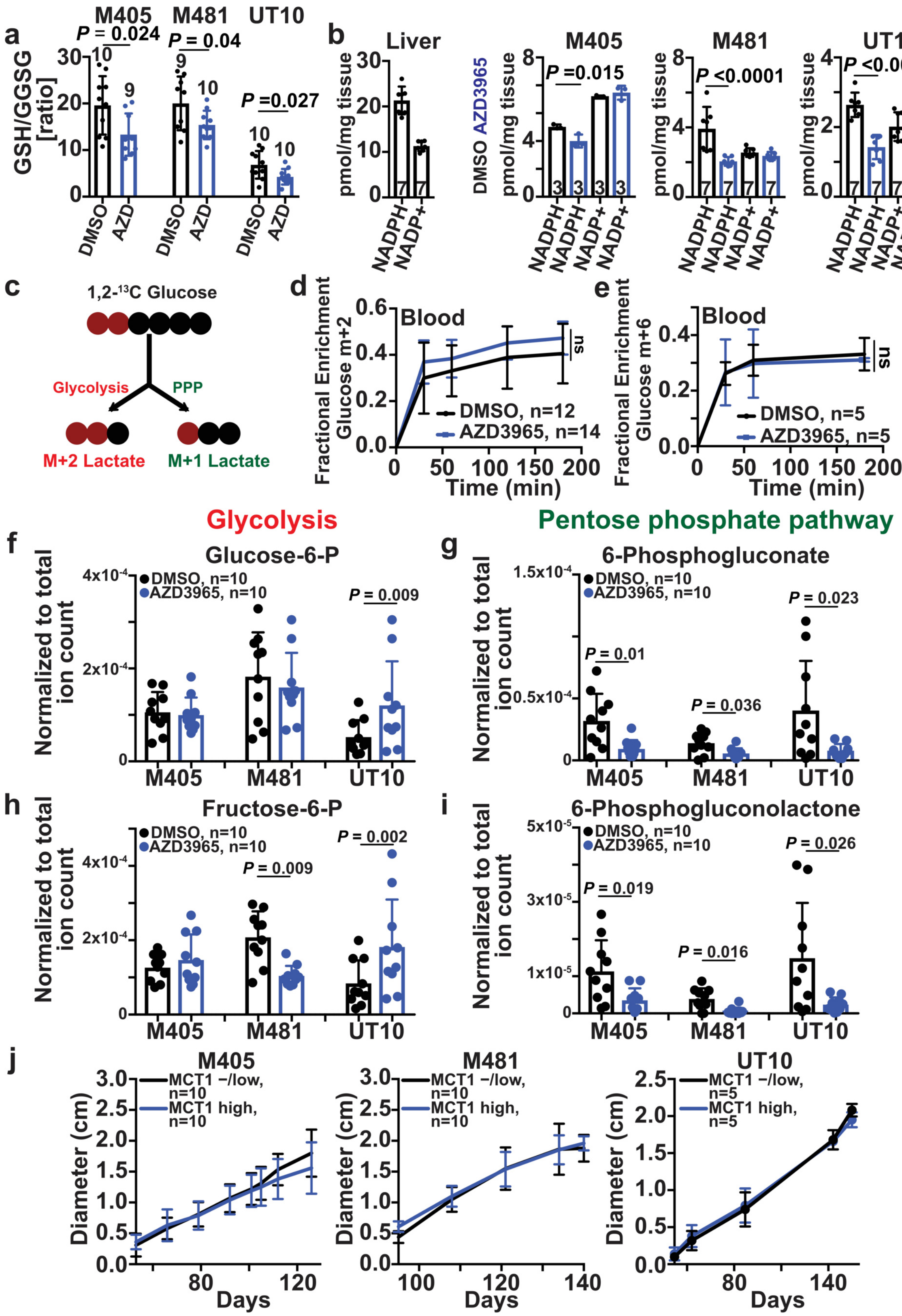

Extended Data Fig. 10 | See next page for caption.

Extended Data Fig. 10 | MCT1 inhibition reduces the levels of PPP, but not glycolytic, metabolites. Related to Figs. 3–5. **a**, The GSH to GSSG ratios in melanoma cells from mice treated with AZD3965 or DMSO (two independent experiments per melanoma). **b**, Quantitative analysis of NADPH and $NADP^+$ in melanoma cells from mice treated with AZD3965 or DMSO (one or two experiments per melanoma). Liver cells were included as a control, with a high NADPH/$NADP^+$ ratio. **c**, Expected isotope-labelled species after infusion of [1,2-^{13}C]glucose. **d**, Glucose m + 2 as a fraction of total plasma glucose in mice xenografted with efficiently metastasizing melanomas (M405, M481 and UT10), treated with DMSO or AZD3965 and infused with [1,2-^{13}C]glucose. **e**, Glucose m + 6 as a fraction of total plasma glucose in mice infused with [U-^{13}C] glucose. The number of mice per treatment is indicated (two independent experiments). **f**–**i**, LC–MS measurement of the levels of glycolytic (**f**, **h**) and oxidative PPP (**g**, **i**) metabolites in subcutaneous tumour cells from mice xenografted with melanomas treated with DMSO (control) or AZD3965 (MCT1 inhibitor) for 7 days. **j**, Flow cytometrically isolated $MCT1^{high}$ or $MCT1^{-/low}$ melanoma cells were subcutaneously transplanted into NSG mice, using 10 or 100 cells per injection. All injections formed tumours. Rate of growth of the tumours initiated with 10-cell injections. Data are mean ± s.d. Statistical significance was assessed using *t*-tests (**a**), repeated-measures two-way ANOVAs (**b**), *t*-test (**e**, 180 min), log_2-transformed two-way ANOVAs (**f**, **h**), log_2-transformed *t*-tests (**g**, M405 and UT10), Mann–Whitney test (**g**, M481 and **i**, M481), Welch's *t*-tests (**i**, M405 and UT10) or using nparLD test (**d**, **j**).

nature research

Corresponding author(s): Sean J. Morrison

Reporting Summary

Nature Research wishes to improve the reproducibility of the work that we publish. This form provides structure for consistency and transparency in reporting. For further information on Nature Research policies, see Authors & Referees and the Editorial Policy Checklist.

Statistical parameters

When statistical analyses are reported, confirm that the following items are present in the relevant location (e.g. figure legend, table legend, main text, or Methods section).

n/a	Confirmed	
☐	☒	The exact sample size (n) for each experimental group/condition, given as a discrete number and unit of measurement
☐	☒	An indication of whether measurements were taken from distinct samples or whether the same sample was measured repeatedly
☐	☒	The statistical test(s) used AND whether they are one- or two-sided *Only common tests should be described solely by name; describe more complex techniques in the Methods section.*
☒	☐	A description of all covariates tested
☐	☒	A description of any assumptions or corrections, such as tests of normality and adjustment for multiple comparisons
☐	☒	A full description of the statistics including central tendency (e.g. means) or other basic estimates (e.g. regression coefficient) AND variation (e.g. standard deviation) or associated estimates of uncertainty (e.g. confidence intervals)
☐	☒	For null hypothesis testing, the test statistic (e.g. F, t, r) with confidence intervals, effect sizes, degrees of freedom and P value noted *Give P values as exact values whenever suitable.*
☒	☐	For Bayesian analysis, information on the choice of priors and Markov chain Monte Carlo settings
☒	☐	For hierarchical and complex designs, identification of the appropriate level for tests and full reporting of outcomes
☒	☐	Estimates of effect sizes (e.g. Cohen's d, Pearson's r), indicating how they were calculated
☐	☒	Clearly defined error bars *State explicitly what error bars represent (e.g. SD, SE, CI)*

Our web collection on statistics for biologists may be useful.

Software and code

Policy information about availability of computer code

Data collection	Flow cytometry data were collected using BD FACSDiva 8.0, Bioluminescence data were collected using Living Image software V4.3.1, GC-MS data were collected using Agilent ChemStation E02.02.1431, LC-MS/MS data were collected using SCIEX Analyst v1.6.3 and Thermo Scientific XCalibur 4.1.50. Immunofluorescence data were collected using Zeiss ZEN 2.3 software.
Data analysis	Graphpad Prism 8 and R 3.5.1 with the stats, fBasics, car, and nparLD packages, Flow cytometry data analysis using BD FACSDiva 8.0, and FlowJo V10 (Treestar), Bioluminescence data were analyzed using Living Image software V4.3.1. GC-MS data analysis using Agilent ChemStation E02.02.1431. LC-MS/MS data analysis using SCIEX Multiquant v2.1.1, Thermo Scientific Compound Discoverer 3.0 and Thermo Scientific Trace Finder 4.1, Immunofluorescence data were analyzed using Bitplane Imaris V9.2.1 software, Western blot densities were quantified using ImageJ 1.52k.

For manuscripts utilizing custom algorithms or software that are central to the research but not yet described in published literature, software must be made available to editors/reviewers upon request. We strongly encourage code deposition in a community repository (e.g. GitHub). See the Nature Research guidelines for submitting code & software for further information.

Data

Policy information about availability of data

All manuscripts must include a data availability statement. This statement should provide the following information, where applicable:

- Accession codes, unique identifiers, or web links for publicly available datasets
- A list of figures that have associated raw data
- A description of any restrictions on data availability

Data supporting the findings of this study are available within the article and its Supplementary Information files ore from the corresponding author on request.

Field-specific reporting

Please select the best fit for your research. If you are not sure, read the appropriate sections before making your selection.

☒ Life sciences ☐ Behavioural & social sciences ☐ Ecological, evolutionary & environmental sciences

For a reference copy of the document with all sections, see nature.com/authors/policies/ReportingSummary-flat.pdf

Life sciences study design

All studies must disclose on these points even when the disclosure is negative.

Sample size	Samples sizes were not pre-determined based on statistical power calculations but were based on our experience with these assays. For assays in which variability is commonly high, we typically used n>10. For assays in which variability is commonly low, we typically used n<10.
Data exclusions	No data were excluded; however, mice sometimes died during experiments, presumably due to the growth of metastatic tumors. In those instances, data that had already been collected on the mice in interim analyses were included (such as subcutaneous tumor growth measurements over time) even if it was not possible to perform the end-point analysis of metastatic disease burden (due to the premature death of the mice).
Replication	The experimental findings were reproduced in multiple independent experiments. The number of independent experiments and biological replicates for each data panel is indicated in the figure panel itself, in the figure legends, and in the source data files. Data shown in the figures represent the aggregate of all independent experiments in most cases. Data shown in a minority of panels are from a representative experiment (e.g. for western blots) and in those cases the number of independent experiments that reproduced the finding is also indicated in the figure legends. Tumor growth curves also show representative experiments because it is difficult to combine together tumor growth curve data from multiple different experiments.
Randomization	No formal randomization techniques were used; however, samples were allocated randomly to experiments and processed in an arbitrary order.
Blinding	During all isotope tracing experiments, the data were analyzed in a manner blinded to sample identity or treatment. A.T. performed all of the infusions, collected tumor specimens, and performed mass spectrometry, then passed the de-identified data files to B.F. and A.S., who analyzed the isotope tracing patterns. After the patterns had been analyzed for individual mice, the samples were re-identified so the results could be interpreted.

Reporting for specific materials, systems and methods

Materials & experimental systems

n/a	Involved in the study	
☒	☐	Unique biological materials
☐	☒	Antibodies
☐	☒	Eukaryotic cell lines
☒	☐	Palaeontology
☐	☒	Animals and other organisms
☐	☒	Human research participants

Methods

n/a	Involved in the study	
☒	☐	ChIP-seq
☐	☒	Flow cytometry
☒	☐	MRI-based neuroimaging

Antibodies

Antibodies used	The following antibodies have been used in this study:

Anti-Mouse CD31 (PECAM-1) eFlour 450, clone:390, Cat. #48-0311-82, LOT:1982691
ebioscience, 1:100, Flow

Anti-Mouse TER-119, VioletFluor450, clone:TER-119, Cat. #75-5921-U100, LOT:C5921081018753
Tonbo, 1:100, Flow

Anti-Mouse CD45, VioletFluor450, clone:30-F11, Cat. #75-0451-U100, LOT:C0451033117753
Tonbo, 1:100, Flow

Mouse Anti-Human HLA-ABC, FITC, clone:G46-2.6, Cat. #555552, LOT:8183993
BD Pharmingen, 1:20, Flow

Anti-Human MCT1, Alexa Fluor 647, clone:bs-10249R, Cat. #bs-10249R-A647, LOT:AE112116
Bioss antibodies, 1:100, Flow

Anti-Human CD147, Alexa Fluor 488, clone:HIM6, Cat. #306207, LOT:B213982, BioLegend, 1:100, Flow

Anti-Human CD98, PE-Vio 770, clone:REA387, Cat. #130-105-710, LOT:5170207052, Miltenyi Biotec, 1:200, Flow

Anti-Human beta 1-Integrin, Alexa Fluor 700, clone:P5D2, Cat. #FAB17781N-100UG, LOT:1529055, R&D systems, 1:100, Flow

Anti-Human CD324 (E-Cadherin), FITC, clone:67A4, Cat. #324104, LOT:B203125, BioLegend, 1:100, Flow

Anti-Human CD325 (N-Cadherin), PE/Cy7, clone:8C11, Cat. #350811, LOT:B272631, BioLegend, 1:100, Flow

Anti-Rabbit IgG, isotype control, Alexa Fluor 647, Cat. #bs-0295P-A647, LOT:AG0726809, Bioss antibodies,1:100, Flow

Anti-Mouse IgG1, k, isotype control, Alexa Fluor 488, clone:MOPC-21, Cat. #400129, LOT:B220820, BioLegend, 1:100, Flow

Anti-Human IgG1, isotype control, PE-Vio 770, clone:REA293, Cat. #130-113-452, LOT:5190329516, Miltenyi Biotec,1:100, Flow

anti-Mouse IgG1,k, isotype control, Alexa Fluor 700, clone:11711, Cat. #IC002N, LOT:ACIJ0418111, R&D systems, 1:100, Flow

Anti-MCT1, clone:HPA003324, Cat. #HPA003324-100UL, LOT:C75340, Sigma, 1:500, IF

Anti-Rabbit IgG, biotinylated, Cat. #PK-6104, Vector Laboratories, 1:250, IF

Anti-Rabbit IgG, peroxidase conjugated, Cat. #PK-6101, Vector Laboratories, 1:250, IF

Anti-S100, Cat. #Z0311, polyclonal, LOT:00060051, Dako, 1:500, IF

Donkey anti-Rabbit-IgG, Alexa Fluor 488 AffiniPure F(ab')2 fragment, Cat. #711-545-152, JacksonImmuno, 1:250, IF

Donkey anti-rat IgG, Cy3-AffiniPure F(ab')2 fragment, Cat. #712-166-150, JacksonImmuno, 1:250, IF

Anti-MCT1, Cat. #AB3538P, LOT:3190916, EMD Millipore, 1:5000, WB

Anti-MCT2, Cat. #LN2021159, LOT:5653586301013, LabNed, 1:5000, WB

Anti-MCT4, Cat. #AB3316P, LOT:2972442, EMD Millipore, 1:5000, WB

Ant-CD147, Cat. #ab64616, LOT:GR205454-1, Abcam, 1:10000, WB

Anti-Vimentin, clone:D21H3, Cat. #5741T, LOT:6 , Cell Signaling, 1:10000, WB

Anti-IKK-alpha, clone:D3W6N, Cat. #61294S, LOT:1, Cell Signaling, 1:5000, WB

Anti-IKK-beta, clone:D30C6, Cat. # 8943S, LOT:4, Cell Signaling, 1:5000, WB

Anti-LDHA, clone:C4B5, Cat. #3582 LOT:9, Cell Signaling, 1:10000, WB

Anti-LDHB, clone:EP1565Y, Cat. #ab53292, LOT:GR103088-10, Abcam, 1:10000, WB

Anti-alpha Tubulin, clone:EP1332Y, Cat. #ab52866, LOT:GR3241238-1, Abcam, 1:10000, WB

Anti-beta-Actin, clone:D6A8, Cat. #12620S, LOT:6, Cell Signaling, 1:10000, WB

Validation

All antibodies are commercially available and have been validated in previously published studies (e.g. Nature 527:186). Antibodies that were central to our conclusions, such as the anti-MCT1 antibodies, were validated with control lines (that were positive or deficient for MCT1) and similar results were obtained using multiple independent antibodies.

Anti-Mouse CD31 (Cat. #48-0311-82, ebioscience). This monoclonal antibody recognizes mouse CD31. https://

www.thermofisher.com/antibody/product/CD31-PECAM-1-Antibody-clone-390-Monoclonal/48-0311-82

Anti-Mouse TER-119 (Cat. #75-5921-U100, Tonbo). This monoclonal antibody recognizes mouse TER-119. https://www.tonbobio.com/violetfluortm-450-anti-mouse-ter-119-ter-119.html

Anti-Mouse CD45 (Cat.#75-0451-U100, Tonbo). This monoclonal antibody recognizes mouse CD45. https://www.tonbobio.com/violetfluor-mouse-cd45-30-f11.html

Mouse Anti-Human HLA-ABC (Cat. #555552, BD Pharmingen). This monoclonal antibody binds to a monomorphic epitope on the human alpha chain of HLA-A, HLA-B and HLA-C. www.bdbiosciences.com/us/applications/research/stem-cell-research/mesenchymal-stem-cell-markers-adipose/human/positive-markers/fitc-mouse-anti-human-hla-abc-g46-26/p/555552

Anti-Human MCT1 (Cat. #bs-10249R-A647, Bioss antibodies). This polyclonal antibody recognizes extracellular epitopes of MCT1. Species reactivity - Human, Mouse and Rat. We tested this antibody on MCT1-deficient cells (Fig. 2f) and found it to be specific for MCT1. https://www.biossusa.com/products/bs-10249R-A647

Anti-Human CD147 (Cat. #306207, BioLegend). This monoclonal antibody recognizes human CD147. Species reactivity - Human. https://www.biolegend.com/en-us/products/alexa-fluor-488-anti-human-cd147-antibody-3367

Anti-Human CD98 (Cat. #130-105-710, Miltenyi Biotec). This monoclonal antibody recognizes the human CD98 antigen. https://www.miltenyibiotec.com/US-en/products/macs-flow-cytometry/antibodies/primary-antibodies/cd98-antibodies-human-rea387-1-11.html?utm_source=3rd_labome%20&utm_medium=product_listing&utm_term=flow-cytometry&utm_campaign=reafinity

Anti-Human beta 1-Integrin (Cat. #FAB17781N-100UG, R&D systems). This monoclonal antibody recognizes human Integrin beta 1/CD29. Species reactivity - Human. https://www.rndsystems.com/products/human-integrin-beta-1-cd29-alexa-fluor-700-conjugated-antibody-p5d2_fab17781n

Anti-Human CD324 (E-Cadherin) (Cat. # 324104, BioLegend). This monoclonal antibody recognizes human CD324 also known as E-cadherin. Species reactivity - human. https://www.biolegend.com/en-us/products/fitc-anti-human-cd324-e-cadherin-antibody-3750

Anti-Human CD325 (N-Cadherin) (Cat. #350811, BioLegend). This monoclonal antibody recognizes human CD325, also known as N-cadherin. Species reactivity - human. https://www.biolegend.com/en-us/products/pe-cy7-anti-human-cd325-n-cadherin-antibody-9041

Rabbit IgG, isotype control (Cat. #bs-0295P-A647, Bioss antibodies). This polyclonal antibody is designed to serve as a control to account for non-specific staining by primary antibodies that is caused by Fc Receptor-mediated binding or other isotype-specific mechanisms. It was conjugated with Alexa Fluor 647. https://www.biossusa.com/products/bs-0295p-a647

Mouse IgG1k, isotype control (Cat. # 400129, BioLegend). This monoclonal antibody is designed to serve as a control to account for non-specific staining by primary antibodies that is caused by Fc Receptor-mediated binding or other isotype-specific mechanisms. It was conjugated with Alexa Fluor 488. https://www.biolegend.com/en-us/products/alexa-fluor-488-mouse-igg1--kappa-isotype-ctrl-fc-2687

Human IgG1, isotype control (Cat. # 130-113-452, Miltenyi Biotec). This monoclonal antibody is designed to serve as a control to account for non-specific staining by primary antibodies that is caused by Fc Receptor-mediated binding or other isotype-specific mechanisms. It was conjugated with PE-Vio 770. https://www.miltenyibiotec.com/US-en/products/macs-flow-cytometry/antibodies/isotype-control-antibodies/rea-control-antibodies-rea293-1-50.html

Mouse IgG1k, isotype control (Cat. # IC002N, R&D systems). This monoclonal antibody is designed to serve as a control to account for non-specific staining by primary antibodies that is caused by Fc Receptor-mediated binding or other isotype-specific mechanisms. It was conjugated to Alexa Fluor 700. https://www.rndsystems.com/products/mouse-igg-1-alexa-fluor-700-conjugated-antibody_ic002n

Anti-human MCT1 (Cat. #HPA003324-100UL, Sigma). This polyclonal antibody recognizes human MCT1. This antibody has been used previously to identify MCT1 in human cells (Cell Stem Cell. 20:635). This antibody was validated by the Human Protein Atlas (HPA) project. https://www.proteinatlas.org/ENSG00000155380-SLC16A1.
https://www.sigmaaldrich.com/catalog/product/sigma/hpa003324?lang=en&region=US

Anti-Rabbit IgG, biotinylated (Cat. #PK-6104, Vector Laboratories).
The biotinylated anti-rabbit IgG recognizes specifically rabbit IgG primary antibodies.
https://vectorlabs.com/vectastain-elite-abc-kit-rat-igg.html

Anti-Rabbit IgG, peroxidase conjugated (Cat. #PK-6101, Vector Laboratories).
The peroxidase anti-rabbit IgG recognizes specifically rabbit IgG primary antibodies. https://vectorlabs.com/vectastain-elite-abc-kit-rabbit-igg.html

Anti-S100 (Cat. #Z0311, Dako). This polyclonal antibody strongly reacts with human S100B, and weakly or very weakly with S100A1 and S100A6, respectively. This antibody has been used previously to identify S100 expression in melanoma cells (Nature 527:186). https://www.agilent.com/en/product/immunohistochemistry/antibodies-controls/primary-antibodies/s100-(dako-omnis)-76198

Donkey anti-Rabbit-IgG, Alexa Fluor 488 AffiniPure F(ab')2 fragment (Cat. #711-545-152, JacksonImmuno). This polyclonal antibody binds to rabbit IgG heavy and light chains. It also reacts with the light chains of other rabbit immunoglobulins. https://

www.jacksonimmuno.com/catalog/products/711-545-152

Donkey anti-rat IgG, Cy3-AffiniPure F(ab')2 fragment (Cat. #712-166-150, JacksonImmuno). This polyclonal antibody binds to rabbit IgG heavy and light chains. It also reacts with the light chains of other rat immunoglobulins. https://www.jacksonimmuno.com/catalog/products/712-166-150

Anti-MCT1 (Cat. #AB3538P, EMD Millipore).
This antibody recognizes human MCT1. This polyclonal antibody has been used previously to identify MCT1 expression in cancer cells by western blotting (Cancer Res. 77:5591). We tested the specificity of this antibody by staining MCT1-deficient cells in Fig. 2a and ED Fig. 5a by western blot. http://www.emdmillipore.com/US/en/product/Anti-Monocarboxylate-Transporter-1-Antibody,MM_NF-AB3538P

Anti-MCT2 (Cat. #LN2021159, LabNed). This polyclonal antibody recognizes epitopes of human MCT2. This antibody was tested with a known positive control (MCF7 protein, Nat Chem Biol. 14:1032, Fig.1e) in Fig. 2b of this manuscript. https://labned.com/slc16a7-human-unlb-antibody-ln2021159

Anti-MCT4 (Cat. #AB3316P, EMD Millipore). This polyclonal antibody recognizes human MCT4. This antibody has been used previously to identify MCT4 staining in human cancer cells by western blotting (Cancer Res. 77:5591). We independently tested the specificity of this antibody by staining positive and negative control cells in Fig. 2c and ED Fig. 5b of this manuscript by western blot. https://www.emdmillipore.com/US/en/product/Anti-Monocarboxylate-Transporter-4-Antibody,MM_NF-AB3316P

Anti-CD147 (Cat. #ab64616, Abcam). This polyclonal antibody recognizes human and mouse CD147. The manufacturer validated the antibody in western blots using synthetic peptides. https://www.abcam.com/cd147-antibody-ab64616.html

Anti-Vimentin (Cat. #5741T, Cell Signaling). This monoclonal antibody recognizes human, mouse, rat, and monkey vimentin proteins. https://www.cellsignal.com/products/primary-antibodies/vimentin-d21h3-xp-rabbit-mab/5741

Anti-IKK-alpha (Cat. #61294S, Cell Signaling). This monoclonal antibody recognizes human, mouse, and rat IKKα proteins. https://www.cellsignal.com/products/primary-antibodies/ikka-d3w6n-rabbit-mab/61294?site-search type=Products&N=4294956287&Ntt=61294s&fromPage=plp&_requestid=3523507

Anti-IKK-beta(Cat. #8943S, Cell Signaling)..
This monoclonal antibody recognizes total IKKβ protein from human, mouse, rat, and monkey but does not cross-react with other IKK family members. https://www.cellsignal.com/products/primary-antibodies/ikkb-d30c6-rabbit-mab/8943

Anti-LDHA (Cat. #3582, Cell Signaling). This monoclonal antibody recognizes endogenous levels of total LDHA protein. Species Reactivity- Human, Monkey. https://www.cellsignal.com/products/primary-antibodies/ldha-c4b5-rabbit-mab/3582

Anti-LDHB (Cat. #ab53292, Abcam). This monoclonal antibody recognizes total human LDHB protein and the specificity was validated by the manufacturer using LDHB-deficient HAP1 cells.
https://www.abcam.com/lactate-dehydrogenase-bldh-b-antibody-ep1565y-ab53292.html?productWallTab=ShowAll

Anti-Alpha Tubulin (Cat. #ab52866, Abcam). This monoclonal antibody recognizes mouse, rat, human, pig, and drosophila alpha Tubulin. https://www.abcam.com/alpha-tubulin-antibody-ep1332y-microtubule-marker-ab52866.html

Anti-beta-Actin (Cat. #12620S, Cell Signaling). This monoclonal antibody
recognizes total β-actin protein in human, mouse, rat, monkey, drosophila, and zebrafish cells.
https://www.cellsignal.com/products/antibody-conjugates/b-actin-d6a8-rabbit-mab-hrp-conjugate/12620?site-search type=Products&N=4294956287&Ntt=12620s&fromPage=plp&_requestid=3526589

Eukaryotic cell lines

Policy information about cell lines

Cell line source(s)	YUMM1.7, YUMM3.3 and YUMM5.2 cell lines were purchased from ATCC.
Authentication	YUMM1.7, YUMM3.3 and YUMM5.2 cell lines were authenticated by ATCC.
Mycoplasma contamination	All cell lines were confirmed to be mycoplasma free by MycoAlert detection kit (Lonza).
Commonly misidentified lines (See ICLAC register)	No commonly misidentified cell lines were used.

Animals and other organisms

Policy information about studies involving animals; ARRIVE guidelines recommended for reporting animal research

Laboratory animals	Four to 8-week-old NOD.CB17-Prkdcscid Il2rgtm1Wjl/SzJ (NSG) and four to-8-week old C57/BL6 mice were used. Both male and female mice were used.
Wild animals	No wild animals were used.

Field-collected samples | No field-collected samples were used.

Human research participants

Policy information about studies involving human research participants

Population characteristics: Our research did not involve human subjects, but relied upon patient melanoma specimens that had been collected and described in prior studies cited in the paper. The melanoma specimens were obtained with approval by the Institutional Review Board of the University of Michigan Medical School (IRBMED approvals HUM00050754 and HUM00050085) and the University of Texas Southwestern Medical Center (IRB approval 102010-051). They were shared with us as de-identified specimens.

Recruitment: We did not recruit any patients.

Flow Cytometry

Plots

Confirm that:

☒ The axis labels state the marker and fluorochrome used (e.g. CD4-FITC).

☒ The axis scales are clearly visible. Include numbers along axes only for bottom left plot of group (a 'group' is an analysis of identical markers).

☒ All plots are contour plots with outliers or pseudocolor plots.

☒ A numerical value for number of cells or percentage (with statistics) is provided.

Methodology

Sample preparation: Tumors were dissociated in Kontes tubes with disposable pestles (VWR) followed by enzymatic digestion for 20 min with 200 U/ml collagenase IV (Worthington), 5mM CaCl2 and 50 U/ml DNase. To obtain a single-cell suspension, cells were filtered through a 40 um cell strainer.

Instrument: BD FACS Aria Fusion (for cell sorting or analysis), BD Fortessa (for analysis).

Software: BD FACSDiva 8.0, FlowJo V10

Cell population abundance: The abundance of the relevant cell populations within post-sort fractions was 90-100% in experiments.

Gating strategy: Human melanoma cells were isolated as cells that were positive for human HLA and negative for mouse endothelial and hematopoietic markers (mouse CD31 , mouse CD45 and mouse TER119). To eliminate dead cells from sorts and analyses, cells were stained with 4’,6-diamidino-2-phenylindole (DAPI).

☒ Tick this box to confirm that a figure exemplifying the gating strategy is provided in the Supplementary Information.

Article

Impaired cell fate through gain-of-function mutations in a chromatin reader

https://doi.org/10.1038/s41586-019-1842-7

Received: 13 December 2018

Accepted: 22 October 2019

Published online: 18 December 2019

Liling Wan[1,15]*, Shasha Chong[2,3,16], Fan Xuan[4,16], Angela Liang[1,16], Xiaodong Cui[5], Leah Gates[1], Thomas S. Carroll[6], Yuanyuan Li[7], Lijuan Feng[1], Guochao Chen[7], Shu-Ping Wang[8,9], Michael V. Ortiz[10], Sara K. Daley[11], Xiaolu Wang[4], Hongwen Xuan[4], Alex Kentsis[10,12], Tom W. Muir[11], Robert G. Roeder[8], Haitao Li[7], Wei Li[5,13], Robert Tjian[2,3,14], Hong Wen[4]* & C. David Allis[1]*

Modifications of histone proteins have essential roles in normal development and human disease. Recognition of modified histones by 'reader' proteins is a key mechanism that mediates the function of histone modifications, but how the dysregulation of these readers might contribute to disease remains poorly understood. We previously identified the ENL protein as a reader of histone acetylation via its YEATS domain, linking it to the expression of cancer-driving genes in acute leukaemia[1]. Recurrent hotspot mutations have been found in the ENL YEATS domain in Wilms tumour[2,3], the most common type of paediatric kidney cancer. Here we show, using human and mouse cells, that these mutations impair cell-fate regulation by conferring gain-of-function in chromatin recruitment and transcriptional control. ENL mutants induce gene-expression changes that favour a premalignant cell fate, and, in an assay for nephrogenesis using murine cells, result in undifferentiated structures resembling those observed in human Wilms tumour. Mechanistically, although bound to largely similar genomic loci as the wild-type protein, ENL mutants exhibit increased occupancy at a subset of targets, leading to a marked increase in the recruitment and activity of transcription elongation machinery that enforces active transcription from target loci. Furthermore, ectopically expressed ENL mutants exhibit greater self-association and form discrete and dynamic nuclear puncta that are characteristic of biomolecular hubs consisting of local high concentrations of regulatory factors. Such mutation-driven ENL self-association is functionally linked to enhanced chromatin occupancy and gene activation. Collectively, our findings show that hotspot mutations in a chromatin-reader domain drive self-reinforced recruitment, derailing normal cell-fate control during development and leading to an oncogenic outcome.

The eleven-nineteen-leukaemia protein (ENL) is a chromatin reader that maintains the oncogenic state in leukaemia[1,4]. ENL interacts with acetylated histone proteins via its well conserved YEATS (Yaf9, ENL, AF9, Taf14, Sas5) domain, and, in so doing, helps to recruit and stabilize its associated transcriptional machinery to drive the transcription of target genes. Recently, somatic mutations in the *ENL* gene (also known as *MLLT1*) were found in about 5% of people with Wilms tumour, making *ENL* one of the most frequently mutated genes in this cancer type. These mutations are recurrent, heterozygous and highly clustered in the ENL YEATS domain. Interestingly, these 'hotspot' mutations all involve small in-frame insertions or deletions (Fig. 1a and Extended Data Fig. 1a). Whether and how such ENL mutations promote the formation of Wilms tumour was unclear and is the focus of our study.

Impaired cell fate with ENL mutants

To investigate the functional relevance of these ENL mutations, we created isogenic HEK293 (human embryonic kidney 293) and HK-2

[1]Laboratory of Chromatin Biology and Epigenetics, The Rockefeller University, New York, NY, USA. [2]Department of Molecular and Cell Biology, University of California, Berkeley, CA, USA. [3]Howard Hughes Medical Institute, University of California, Berkeley, CA, USA. [4]Center for Epigenetics, Van Andel Institute, Grand Rapids, MI, USA. [5]Division of Biostatistics, Dan L. Duncan Cancer Center and Department of Molecular and Cellular Biology, Baylor College of Medicine, Houston, TX, USA. [6]Bioinformatics Core, The Rockefeller University, New York, NY, USA. [7]Beijing Advanced Innovation Center for Structural Biology, MOE Key Laboratory of Protein Sciences, Department of Basic Medical Sciences, School of Medicine, Tsinghua University, Beijing, China. [8]Laboratory of Biochemistry and Molecular Biology, The Rockefeller University, New York, NY, USA. [9]Institute of Biomedical Sciences, Academia Sinica, Taipei, Taiwan. [10]Department of Pediatrics, Memorial Sloan Kettering Cancer Center, New York, NY, USA. [11]Department of Chemistry, Princeton University, Princeton, NJ, USA. [12]Molecular Pharmacology Program, Sloan Kettering Institute, Memorial Sloan Kettering Cancer Center, New York, NY, USA. [13]Department of Biological Chemistry, University of California Irvine, Irvine, CA, USA. [14]CIRM Center of Excellence, University of California, Berkeley, CA, USA. [15]Present address: Department of Cancer Biology, University of Pennsylvania Perelman School of Medicine, Philadelphia, PA, USA. [16]These authors contributed equally: Shasha Chong, Fan Xuan, Angela Liang. *e-mail: Liling.Wan@Pennmedicine.upenn.edu; Hong.Wen@vai.org; alliscd@rockefeller.edu

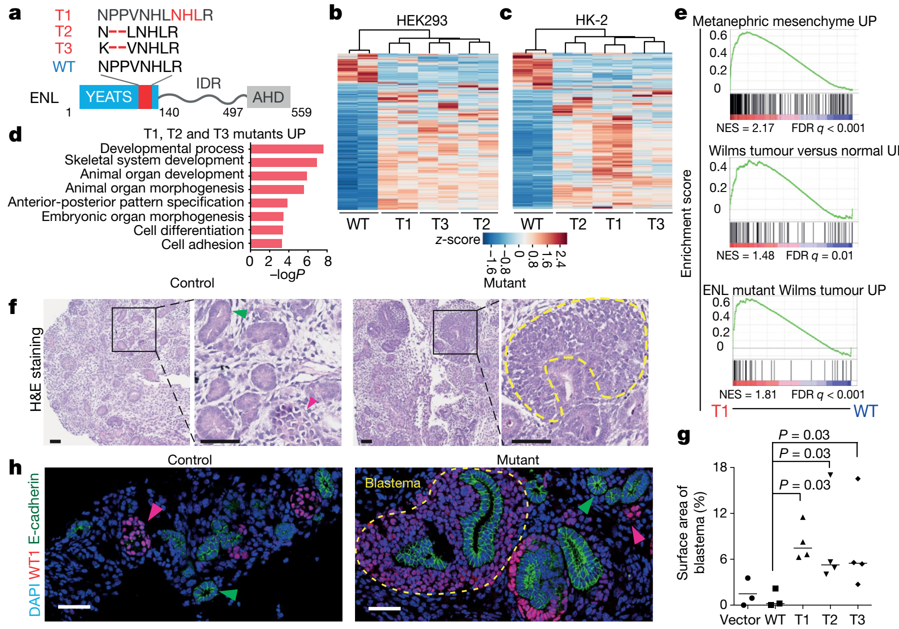

Fig. 1 | ENL mutations drive aberrant developmental programs and impair nephron differentiation. a, Bottom, the domain structure of the ENL protein. Top, the mutations found in the tumour mutants (T1 to T3) compared with the wild-type (WT) protein sequence (in single-letter amino-acid code). The mutated regions are in red. IDR, intrinsically disorderedregion; AHD, ANC1 homologue domain. **b**, **c**, Heat map representation of genes that are differentially expressed in HEK293 (**b**) and HK-2 (**c**) cells expressing WT or mutant ENL (with a fold change of 1.5 or more, and false discovery rate (FDR) of 0.01 or less). Red and blue indicate relative high and low expression, respectively (Supplementary Tables 1, 2). **d**, Gene ontology (GO) analyses of upregulated genes ('UP') that are common to T1, T2 and T3 mutant in HEK293 cells (n = 219 genes; Supplementary Table 3). P-values ($-\log_{10}P$) were obtained by two-tailed Fisher exact test, adjusted by Bonferroni correction. **e**, Gene-set-enrichment analysis (GSEA) plots evaluating the changes in the indicated gene signatures (n = 366, 80, 95 genes from top to bottom; Supplementary Table 10) induced by the T1 mutant in HEK293 cells. NES, normalized enrichment score. **f**, Representative haematoxylin and eosin (H&E) staining of mESC-derived kidney structures. Green and red arrowheads point to nephric tubule and glomerulus, respectively. The yellow dashed line outlines a region of blastema. Control group, empty vector or WT ENL; mutant group, T1, T2 or T3. **g**, Quantification of the surface area of blastema components. Mean ± s.e.m., one-sided Mann–Whitney ranked test; from left to right, n = 3, 3, 4, 4, 4 independent experiments. **h**, Representative immunofluorescence staining of induced kidney structures, labelling the nephric-tubule marker E-cadherin (green arrow) and the glomerular marker WT1 (pink arrow). The yellow dashed line outlines a region of blastema. DAPI, 4′,6-diamidino-2-phenylindole, a nuclear marker. Scale bars in **f**, **h** represent 50 μm. Data in **f**, **h** represent four independent experiments.

(human kidney-2) cells that stably expressed wild-type ENL or one of three distinct mutants (hereafter referred to tumour mutants, or T mutants) at equal levels (Fig. 1a and Extended Data Fig. 1b, c). The selected mutations include those that are most frequently observed in patients (T1)[3], and represent both insertion (T1) and deletion (T2 and T3) mutational patterns (Fig. 1a). By comparison with the transcription induced by wild-type ENL, the transcriptional changes induced by all three mutants were remarkably similar and were highly enriched for pathways involved in developmental processes (Fig. 1b–d and Extended Data Fig. 1d, e). Notably, upon introduction of ENL mutants, there was a marked upregulation of genes that are enriched in embryonic kidney progenitors and Wilms tumour (Fig. 1e and Extended Data Fig. 1f, g). These genes include developmentally critical genes such as *HOXA* genes[3] (Extended Data Fig. 1h, i). We observed a robust increase in the expression of *HOXA* genes when a mutant transgene was expressed at levels close to those of the endogenous ENL protein (Extended Data Fig. 1j, k). We next expanded the analysis to other ENL YEATS mutations (Extended Data Fig. 1a) that have been found so far in Wilms tumour and leukaemia (T4). All eight ENL mutations tested (T1–T8) were capable of inducing the expression of key target genes (Extended Data Fig. 1l, m), suggesting that they probably act through convergent mechanisms. Taken together, these results indicate that ENL YEATS mutations confer gain-of-function in transcription control and cause gene-expression changes that are involved in kidney differentiation and Wilms tumour.

Wilms tumour is characterized by persistent embryonic kidney tissues and arrested cellular differentiation[5]. This, coupled with the transcriptional changes induced by ENL mutations, prompted us to examine the impact of ENL mutations on embryonic kidney differentiation. To this end, we adopted a well established three-dimensional nephrogenesis assay[6]. In this assay, nephron progenitors are first derived from mouse embryonic stem cells (mESCs), and then induced to undergo robust tubulogenesis upon co-culture with embryonic spinal cord (Extended Data Fig. 2a). We observed signature gene-expression changes[6] at each step of the differentiation process (Extended Data Fig. 2b). These included *Hoxa* genes (for example, *Hoxa11*) peaking at the induced metanephric mesenchyme, which contains nephron progenitors. We also identified differentiated nephron structures, including proximal tubules, distal tubules and glomeruli (Extended Data Fig. 2c–e). In the presence of ENL mutants (Extended Data Fig. 2f), there was a marked increase in the presentation of structures that pathologically resemble undifferentiated blastema components in human Wilms tumour (Fig. 1f–h). Unlike the well differentiated epithelium, these undifferentiated components were highly proliferative, and expressed the mesenchymal marker protein vimentin (Extended Data Fig. 3a–i). They also retained the expression of the Wilms tumour-1 protein (encoded by the *WT1* gene) (Fig. 1h)—a transcription factor that is normally expressed in nephron progenitors and glomerular podocytes[7]. Collectively, these results show that ENL mutations impair kidney cell differentiation and give rise to tumour-like structures, suggesting a role in the development of Wilms tumour.

Enhanced chromatin occupancy by mutant ENL

Next, we investigated the mechanisms by which ENL mutations drive aberrant gene expression. Given that these mutations are clustered in

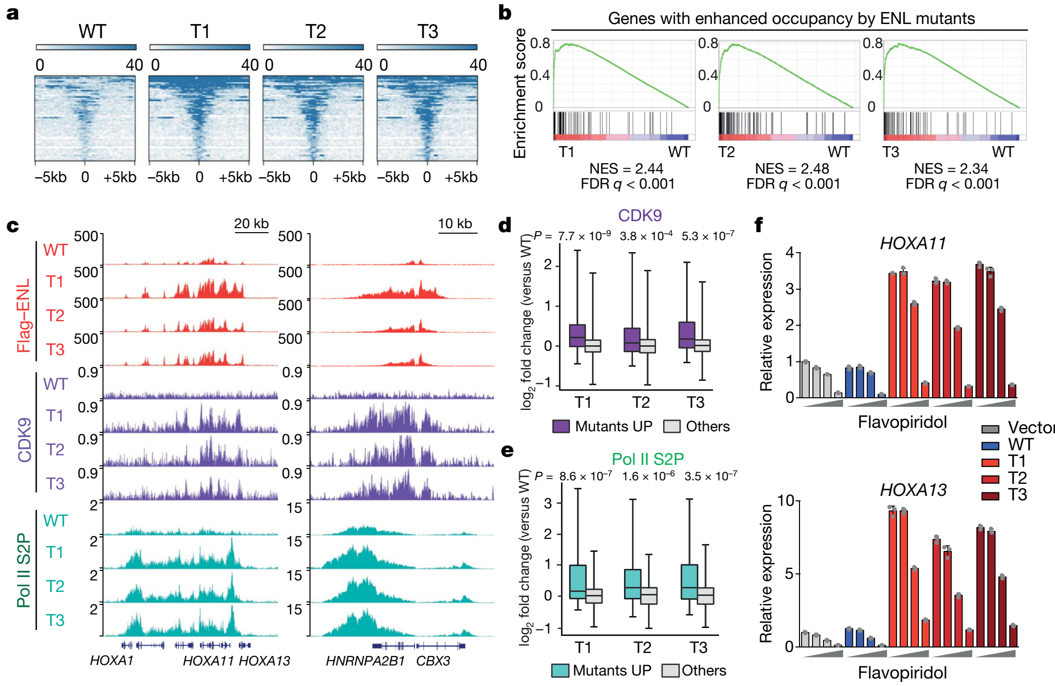

Fig. 2 | ENL mutations enhance chromatin occupancy by ENL and associated SEC complex to enforce active transcription. a, Heat map representation of ENL-bound chromatin peaks that show increased occupancy by T1, T2 and T3 mutants compared with WT ENL ($n = 54$; Supplementary Table 6) in HEK293 cells. These heat maps are centred on ENL-bound peaks across a ±5-kb window. The colour key represents the signal density, with darker colour representing a more intense signal. **b**, GSEA plots showing that genes ($n = 87$; Supplementary Table 10) with enhanced occupancy by ENL mutants are upregulated in mutant-expressing HEK293 cells. **c**, Genome browser view of Flag–ENL, CDK9 and Pol II phosphorylated serine 2 (S2P) ChIP–seq signals at selected ENL target genes in HEK293 cells. **d**, **e**, Box plots showing $\log_2$ fold changes (T mutants versus WT) in CDK9 (**d**) or Pol II S2P (**e**) ChIP–seq signals at genes that have enhanced binding of ENL mutants (mutants_up, $n = 87$; Supplementary Table 10) and at the other genes in the genome (others) in HEK293 cells. The indicated *P*-values were obtained by one-sided Wilcoxon signed-rank tests. For box plots, the centre lines represent the median; the box limits are the 25th and 75th percentiles; and the whiskers show the minimum to maximum values. **f**, Analysis of messenger RNA expression (normalized to *GAPDH* expression) from the indicated ENL-target genes in HEK293 cells that express the indicated ENL or vector constructs upon treatment with flavopiridol for 3 h. Increasing dosages (0, 10 nM, 100 nM and 1,000 nM) are depicted by grey wedge. Means ± s.e.m., $n = 3$ technical replicates. Data represent two independent experiments.

the YEATS domain, which is important for ENL to localize to chromatin[1,4], we first investigated whether the genomic distribution of ENL is altered by the mutations. We performed chromatin immunoprecipitation followed by high-throughput DNA sequencing (ChIP–seq) experiments to map Flag-tagged wild-type or mutant ENL in HEK293 and HK-2 cells. We found that all three mutant ENL proteins occupied largely similar genomic loci to wild-type ENL (Extended Data Fig. 4a–f), indicating that the mutations largely do not redistribute ENL to new target sites. Instead, each mutant exhibited enhanced occupancy at a subset of ENL target genes, and there was substantial overlap between the subsets occupied by each mutant, including the *HOXA* cluster (Fig. 2a and Extended Data Fig. 5a–e). Notably, increased occupancy of ENL mutants at these target genes correlated strongly with gene activation (Fig. 2b and Extended Data Fig. 5f).

We next investigated how increased occupancy of ENL mutants leads to aberrant gene activation. ENL resides in large protein complexes that are involved in transcription activation, notably the super elongation complex (SEC), elongation-assisting proteins (EAPs), and AFF1–ENL–P-TEFb complex (AEP), which contain overlapping subunits[8–10] (for simplicity, we refer only to 'SEC' hereafter), as well as the DOT1L complex[11]. The interaction of ENL with these complexes is mediated by ENL's ANC1 homologue domain (AHD) (Fig. 1a), and such interactions are not greatly affected by tumour mutations (Extended Data Fig. 6a). We then investigated whether the chromatin occupancy of these complexes is affected by ENL mutations. We first carried out ChIP–seq analyses to compare the binding of cyclin-dependent kinase 9 (CDK9)—a component of the SEC complex that phosphorylates RNA polymerase II (Pol II) at the serine 2 site on its carboxy-terminal tail[12]. We observed a marked increase in CDK9 occupancy, preferentially at genomic loci that exhibit enhanced binding of ENL mutants (Fig. 2c, d and Extended Data Fig. 6b, d). We also detected increased levels of elongation-specific phosphorylation of Pol II serine 2 at these same sites (Fig. 2c, e and Extended Data Fig. 6c, e). In agreement with this mechanism of gene activation, we found that ENL-mutant-induced gene activation was abolished by treatment with flavopiridol (Fig. 2f and Extended Data Fig. 6g), which inhibits kinase activity of CDK9[13].

By contrast, we did not observe a substantial change in DOT1L-mediated dimethylation of lysine 79 on histone H3 proteins at the same ENL-target genes (Extended Data Fig. 6f). A recent study[14] proposed that increased interaction of ENL with PAF1 underlies the effects of the ENL mutations found in Wilms tumour. However, contrary to this proposed model, we did not observe changes in PAF1 binding as a result of ENL mutations (Extended Data Fig. 7a). Moreover, depletion of *PAF1* (Extended Data Fig. 7b, c) had minimal effects on the chromatin occupancy of ENL mutants and the activation of target genes (Extended Data Fig. 7d–f). Together, these results suggest that ENL YEATS mutations drive aberrant gene expression mainly by increasing chromatin occupancy by ENL and associated SEC proteins. This observation prompted us to further investigate the mechanisms underlying the enhanced ENL chromatin occupancy driven by the mutations.

Acylation binding required by ENL mutants

Using the structure of the ENL YEATS domain[1], we mapped the tumour mutations to a region that is distant from the acetyl-lysine-binding

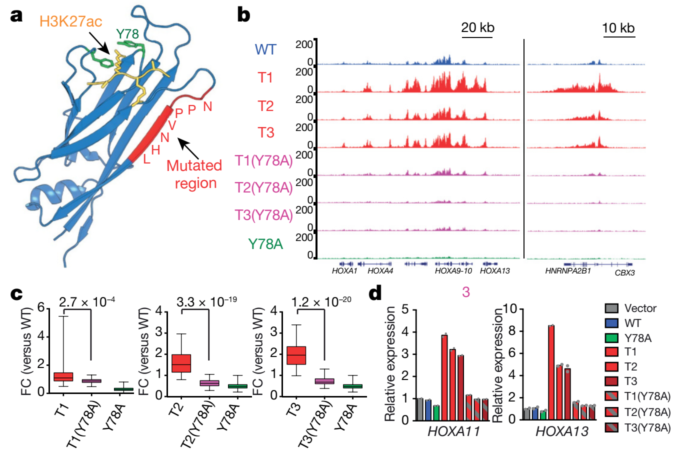

Fig. 3 | Acylation-reading activity is required for enhanced chromatin occupancy by ENL T mutants. a, Structure (Protein DataBank code 5J9S) of the ENL YEATS domain (blue ribbon) bound to a histone H3 peptide comprising an acetylated lysine 27 residue (H3K27ac, yellow), showing a key ENL residue (Y78, green) that mediates recognition of histone acetylation and the region that is mutated in cancer (red). **b**, Genome browser view of the ChIP–seq signals from different Flag–ENL proteins at the genes indicated at the bottom in HEK293 cells. **c**, Box plots showing the fold change (FC) in Flag–ENL ChIP–seq signals (relative to wild-type ENL) at peak regions that bear enhanced occupancy of ENL T mutants ($n = 54$) in HEK293 cells. Centre lines represent medians, the box limits are the 25th and 75th percentiles and the whiskers show the range of values. *P*-values were obtained using paired two-tailed *t*-tests. **d**, mRNA expression analysis (normalized to *GAPDH*) of selected genes in HEK293 cells expressing the indicated constructs. Data represent means from $n = 2$ technical replicates, and results are representative of three independent experiments.

pocket (Fig. 3a). As such, we wondered whether ENL T mutants could bypass the acetyl-lysine-binding activity that is ordinarily required for chromatin targeting. To this end, we introduced a point mutation (Y78A, referred to as a 'pocket mutation' hereafter) that is known to abolish the acetyl-lysine-binding activity of the YEATS domain[1] into either wild-type or T-mutant ENL (Extended Data Fig. 8a). As expected, this pocket mutation severely reduced the chromatin occupancy of the otherwise wild-type ENL. Moreover, the chromatin occupancy of T mutants was also diminished upon introduction of the pocket mutation (Fig. 3b, c and Extended Data Fig. 8b–f). Consequently, tumour-mutation-induced activation of target genes was blunted (Fig. 3d). These results indicate that, like wild-type ENL, T-mutant ENL still requires its reader function for proper genomic localization.

We then considered the possibility that ENL tumour mutations might drive enhanced chromatin occupancy by increasing the acetyl-lysine-binding affinity albeit at a distance from the defined binding pocket. To test this hypothesis, we performed quantitative isothermal titration calorimetry (ITC) assays using the purified wild-type or mutant ENL YEATS domain and a histone H3 peptide comprising acetylated lysine 27. We found that although each T mutant showed variable degrees of interaction with the acetylated histone peptide, none of them exhibited an increase in acetyl-lysine binding compared with the wild type (Extended Data Fig. 8g, h). In addition, these tumour mutations did not increase the binding to other, longer acylations, such as crotonylation (Extended Data Fig. 8i)—another histone modification that the YEATS domain recognizes[15]. Together, these results strongly suggest that, although mutant ENL still depends on its reader function for chromatin targeting, tumour mutations enhance ENL accumulation at target sites through a mechanism that is distinct from the reading of histone acylation.

Increased self-association of ENL mutants

Given the similar genomic localization of wild-type and mutant ENL proteins (Extended Data Fig. 4a–f), we next speculated that tumour mutations might drive the self-mediated recruitment of ENL to chromatin. To test this possibility, we co-expressed enhanced yellow fluorescent protein (eYFP)-labelled ENL fused with LacI and mCherry–ENL without LacI (Fig. 4a) in cells that contain a synthetic Lac operator (LacO) array in the genome[16], and examined the recruitment of ENL to the LacO locus. As expected, the LacO array recruited a large number of eYFP–ENL–LacI molecules via targeted DNA binding, forming a concentrated local interaction hub on the chromatin (Fig. 4b). We predicted that mCherry–ENL becomes enriched at the array only when it can associate with the co-expressed eYFP–ENL–LacI through ENL self-association. We observed a modest self-association of wild-type ENL at the array, while all three T mutants showed much stronger self-mediated recruitment (Fig. 4b, c). These results suggest that tumour mutations promote self-reinforced recruitment of ENL, and that this can occur independently of the initial recruitment mechanism (for example, histone acylation binding) and the underlying genomic target sequences.

We also noticed that mutant, but not wild-type, ENL formed many smaller puncta outside of the LacO array (Fig. 4b), further supporting the idea of stronger self-association driven by the mutations. Consistently, we observed the formation of discrete puncta throughout the nucleus by T mutants over a wide range of expression levels (Fig. 4d, e and Extended Data Fig. 9a) when we expressed mutant mCherry–ENL alone. By contrast, wild-type mCherry–ENL was largely diffused throughout the nucleus when expressed at the same levels as the mutants. Of note, the puncta formed by T1 mutants were noticeably larger than those formed by T2 and T3 mutants (Extended Data Fig. 9b), correlating with the highest self-mediated recruitment of T1 to the LacO array (Fig. 4b, c). Notably, T1 exhibits a mutational pattern (an insertion) that is distinct from that of T2 and T3 mutants (deletion). Introduction of the Y78A mutation into all three T mutants had minimal impacts on puncta formation (Extended Data Fig. 9c, d). These results further support the conclusion that tumour mutations promote ENL self-association through a mechanism that is decoupled from the acylation-reading function of ENL.

Further characterization of the puncta formed by ENL mutants revealed that they are spherical in shape (Fig. 4d), undergo fusion on contact (Supplementary Video S1) and are highly dynamic (Extended Data Fig. 9e, f). These features are characteristics of phase-separation-driven biomolecular condensates in other biological contexts[17–19]—an extreme form of local high-concentration hubs mediated by weak and dynamic multivalent molecular interactions. These results suggest that the self-association of mutant ENL involves multivalent interactions, which could be achieved by proteins composed of modular interaction domains or intrinsically disordered regions[17]. ENL contains a well structured YEATS domain, a predicted intrinsically disordered region (IDR), and an AHD region that mediates ENL's interaction with binding partners such as SEC (Fig. 4f). To determine which regions of ENL are required for mutation-driven self-association and function, we generated a series of truncated ENL proteins harbouring the T1 mutation (Fig. 4f). A YEATS domain alone with the T1 mutation was not sufficient to drive the formation of nuclear puncta (Fig. 4g and Extended Data Fig. 9g), suggesting that regions outside of the YEATS domain are also involved. Supporting this, deletion of the IDR, and to a lesser extent of the AHD, compromised T1-driven ENL self-association and reduced puncta formation (Fig. 4g and Extended Data Fig. 9g). Enhanced chromatin occupancy driven by the T1 mutation was also attenuated to varying degrees by deletion of the IDR or AHD (Fig. 4h and Extended Data Fig. 9h). Lastly, we observed a substantial decrease in T1-induced gene activation upon deletion of the IDR or AHD (Fig. 4i). Of note, despite retaining partial self-association and chromatin targeting, deletion of the AHD in T1 mutant ENL resulted in a profound defect

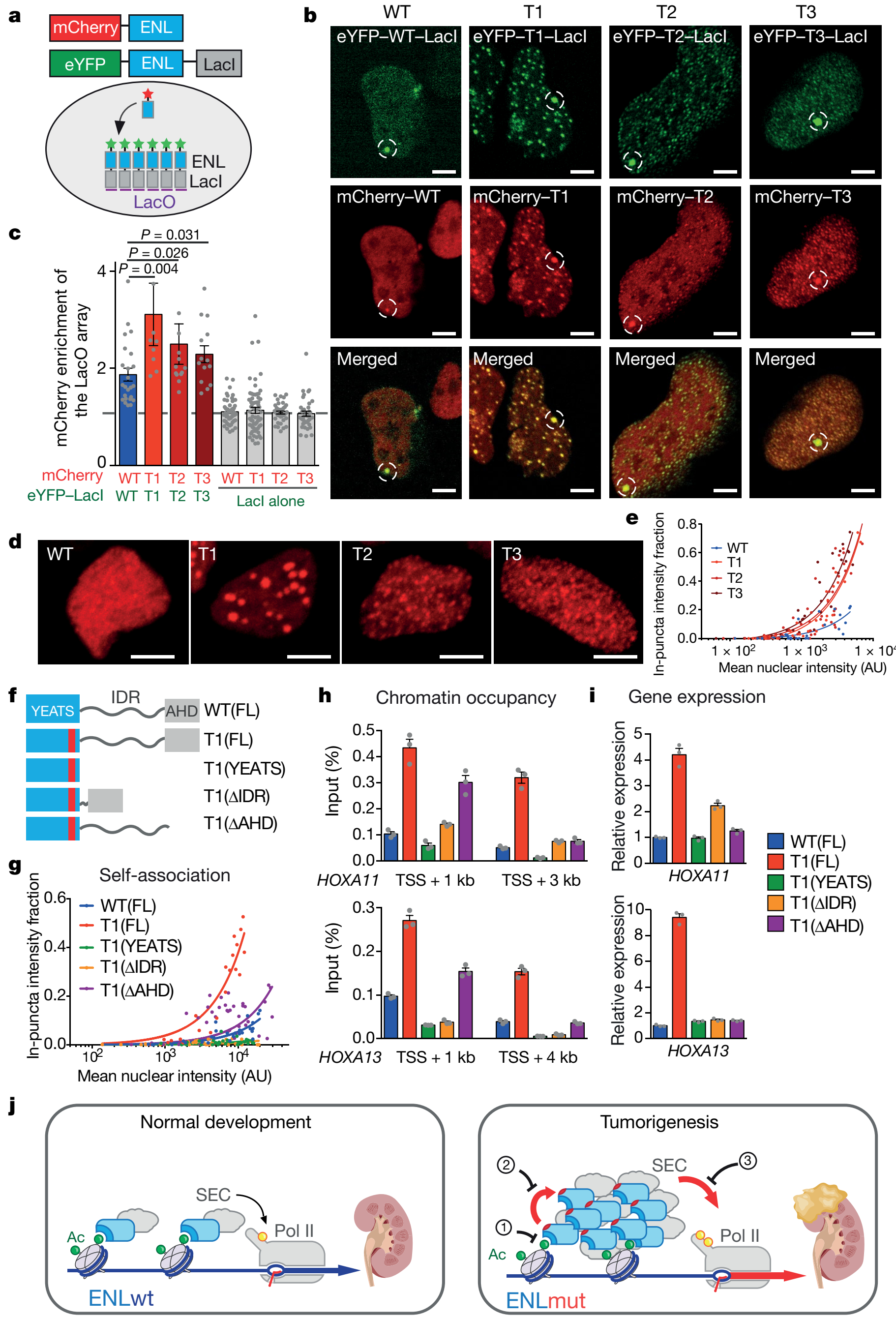

Fig. 4 | Tumour mutations enhance ENL self-association to drive reinforced recruitment and gene activation. a, Testing of ENL self-mediated recruitment to the LacO array. mCherry–ENL can be recruited to the array only through self-association with eYFP–ENL–LacI proteins that have already been recruited. **b**, Fluorescence images of LacO-containing U2OS cells that have co-expressed various combinations of mCherry–ENL and eYFP–ENL–LacI. White dashed circles indicate the LacO array. Scale bar, 5 μm. **c**, Quantification of mCherry–ENL enrichment at the LacO array bound by various eYFP–ENL–LacI proteins. Enrichment of mCherry above an expression level of 1 suggests ENL–ENL self-association. Shown are means ± s.e.m.; n = 24, 9, 13, 14, 51, 62, 39, 38 cells from left to right; one-tailed unpaired t-test. **d**, Fluorescence images of HEK293 cells that express similar levels of WT or mutant mCherry–ENL. Scale bar, 5 μm. **e**, **g**, Fraction of in-puncta fluorescence intensity in the nucleus of HEK293 cells that express the indicated mCherry–ENL constructs as a function of mean nuclear intensity. Each dot represents one cell. **f**, Schematics of full-length (FL) or different deletion forms of ENL. AU, arbitrary units. **h**, ChIP with quantitative PCR (ChIP–qPCR) analysis of the indicated Flag–ENL constructs at *HOXA* genes in HEK293 cells. TSS, transcription start site. **i**, mRNA expression analysis (normalized to *GAPDH*) of *HOXA* genes in HEK293 cells expressing equal levels of the indicated ENL constructs. The data in panels **h**, **i** represent means ± s.e.m. from n = 3 technical replicates; independent experiments were repeated three times with similar results. **j**, During normal kidney development, wild-type ENL (ENLwt), a component of the SEC, binds to acetylated histone proteins in chromatin. The CDK9 component of the SEC phosphorylates RNA polymerase II (yellow circle on pol II), resulting in transcription appropriate to normal development. By contrast, mutant ENL (ENLmut) shows increased self-association and increased phosphorylation of pol II, resulting in aberrant gene activation that contributes to the development of Wilms tumour. Potential strategies to inhibit the oncogenic effects of ENL mutations are indicated by numbers 1–3.

in gene activation, further strengthening the conclusion that AHD-mediated interaction with SEC proteins is critical for ENL mutation-driven transcriptional control. These results suggest that, in addition to the YEATS domain, the IDR and, to a lesser extent, the AHD domain are also involved in mutation-driven ENL self-association, and provide further evidence that functionally links the enhanced self-association propensity to chromatin occupancy and gene activation.

Discussion

In this study, we have shown that cancer-associated hotspot mutations in a chromatin reader drive enhanced self-association (Fig. 4j). This gain-of-function property, coupled with its acylation-reading activity, is functionally required for mutant ENL to be recruited to chromatin and to control gene expression, thus providing a previously unrecognized mechanism for driving developmentally critical genes into an extended active state to restrict cellular differentiation (Fig. 4j). These findings shed new light on how the dysregulation of chromatin-mediated mechanisms derails normal cell-fate control towards an oncogenic path, and unveil potential mechanism-guided strategies for inhibiting the oncogenic function of ENL mutations. These strategies include disrupting the interaction between the ENL YEATS domain and acylated histones, blocking the self-association of mutant ENL and inhibiting the activity of ENL-associated SEC (Fig. 4j). Notably, the enhanced self-association conferred by tumour mutations enables overexpressed ENL protein to form local hubs that involve weak and dynamic multivalent interactions and harbour characteristics of phase separation. Future studies are needed to probe the dynamics and regulation of mutant-ENL-driven interaction hubs at target chromatin, and to evaluate the extent to which these interaction hubs resemble recently described transcriptional clusters[16,18,19]. It remains to be seen whether other chromatin-associated proteins are hijacked in cancer in a similar fashion, but these gain-of-function mutations involving the acylation reader ENL in Wilms tumour and leukaemia expand our knowledge of the types of diseases that are caused by 'misinterpreting' histone modifications. These pathologies, together with the rapidly growing list of those that arise from 'mis-writing' or 'mis-erasing' histone marks[20], highlight important roles of histone modifications in human health and disease that warrant further investigation.

Online content

Any methods, additional references, Nature Research reporting summaries, source data, supplementary information, acknowledgements, peer review information; details of author contributions and competing interests; and statements of data and code availability are available at https://doi.org/10.1038/s41586-019-1842-7.

1. Wan, L. et al. ENL links histone acetylation to oncogenic gene expression in acute myeloid leukaemia. *Nature* **543**, 265–269 (2017).
2. Gadd, S. et al. A children's oncology group and TARGET initiative exploring the genetic landscape of Wilms tumor. *Nat. Genet*. **49**, 1487–1494 (2017).
3. Perlman, E. J. et al. MLLT1 YEATS domain mutations in clinically distinctive Favourable Histology Wilms tumours. *Nat. Commun*. **6**, 10013 (2015).
4. Erb, M. A. et al. Transcription control by the ENL YEATS domain in acute leukaemia. *Nature* **543**, 270–274 (2017).
5. Rivera, M. N. & Haber, D. A. Wilms' tumour: connecting tumorigenesis and organ development in the kidney. *Nat. Rev. Cancer* **5**, 699–712 (2005).
6. Taguchi, A. et al. Redefining the in vivo origin of metanephric nephron progenitors enables generation of complex kidney structures from pluripotent stem cells. *Stem Cells* **14**, 53–67 (2014).
7. Ozdemir, D. D. & Hohenstein, P. Wt1 in the kidney—a tale in mouse models. *Pediatr. Nephrol*. **29**, 687–693 (2014).
8. Lin, C. et al. AFF4, a component of the ELL/P-TEFb elongation complex and a shared subunit of MLL chimeras, can link transcription elongation to leukemia. *Mol. Cell* **37**, 429–437 (2010).
9. He, N. et al. HIV-1 Tat and host AFF4 recruit two transcription elongation factors into a bifunctional complex for coordinated activation of HIV-1 transcription. *Mol. Cell* **38**, 428–438 (2010).
10. Yokoyama, A., Lin, M., Naresh, A., Kitabayashi, I. & Cleary, M. L. A higher-order complex containing AF4 and ENL family proteins with P-TEFb facilitates oncogenic and physiologic MLL-dependent transcription. *Cancer Cell* **17**, 198–212 (2010).
11. Bitoun, E., Oliver, P. L. & Davies, K. E. The mixed-lineage leukemia fusion partner AF4 stimulates RNA polymerase II transcriptional elongation and mediates coordinated chromatin remodeling. *Hum. Mol. Genet*. **16** ʃ92–106 (2007).
12. Peterlin, B. M. & Price, D. H. Controlling the elongation phase of transcription with P-TEFb. *Mol. Cell* **23**, 297–305 (2006).
13. Chao, S. H. & Price, D. H. Flavopiridol inactivates P-TEFb and blocks most RNA polymerase II transcription in vivo. *J. Biol. Chem*. **276**, 31793–31799 (2001).
14. Hetzner, K., Garcia-Cuellar, M.-P., Büttner, C. & Slany, R. K. The interaction of ENL with PAF1 mitigates polycomb silencing and facilitates murine leukemogenesis. *Blood* **131**, 662–673 (2018).
15. Li, Y. et al. Molecular coupling of histone crotonylation and active transcription by AF9 YEATS domain. *Mol. Cell* **62**, 181–193 (2016).
16. Chong, S. et al. Imaging dynamic and selective low-complexity domain interactions that control gene transcription. *Science* **361**, eaar2555 (2018).
17. Banani, S. F., Lee, H. O., Hyman, A. A. & Rosen, M. K. Biomolecular condensates: organizers of cellular biochemistry. *Nat. Rev. Mol. Cell Biol*. **18**, 285–298 (2017).
18. Sabari, B. R. et al. Coactivator condensation at super-enhancers links phase separation and gene control. *Science* **361**, eaar3958 (2018).
19. Cho, W.-K. et al. Mediator and RNA polymerase II clusters associate in transcription-dependent condensates. *Science* **361**, 412–415 (2018).
20. Chi, P., Allis, C. D. & Wang, G. G. Covalent histone modifications—miswritten, misinterpreted and mis-erased in human cancers. *Nat. Rev. Cancer* **10**, 457–469 (2010).

Reporting summary

Further information on research design is available in the Nature Research Reporting Summary linked to this paper.

Data availability

The ChIP–seq and RNA-seq data have been deposited in the Gene Expression Omnibus database under accession number GSE125186. All other raw data generated or analysed during this study are included in this paper, the Extended Data figures, and the Supplementary Information.

Acknowledgements We thank R. Nishinakamura, A. Taguchi and Z. Li for providing reagents and discussions related to kidney differentiation assays; M. Leboeuf for technical assistance; A. Soshnev for help with figure preparation; and members of the Allis and Wen laboratories for scientific input throughout the study. We thank the Rockefeller University Genomic Resource Center, the Bio-Imaging Resource Center, the Flow Cytometry Resource Center and the MD Anderson Science Park Next-Generation Sequencing Facility (Cancer Prevention and Research Institute of Texas (CPRIT), grant RP120348). The research was supported by funds from the National Cancer Institute (grant 5R01CA204639-03), the Leukaemia and Lymphoma Society (LLS-SCOR 7006-13), and the Rockefeller University and St Jude Children's Research Hospital Collaborative on Chromatin Regulation in Pediatric Cancer (to C.D.A.); from CPRIT (grant RP160237) and the Van Andel Institute (to H.W.); and from the National Institutes of Health (NIH grants R01HG007538, R01CA193466 and R01CA228140, to W.L.). L.W. is supported by the Jane Coffin Childs Memorial Fund and an NIH Pathway to Independence Award (1K99CA226399-01). M.V.O. is supported by a K12 Award from the National Cancer Institute (K12CA184746).

Author contributions L.W. and H.W. conceived and designed the study. L.W., H.W., A.L. and F.X. performed most of the molecular and genomic studies. L.W. and A.L. performed kidney differentiation studies. S.C. and L.W. performed imaging studies with assistance from L.F. X.C., T.S.C., H.X. and W.L. performed bioinformatics analyses. Y.L., G.C. and H.L. performed the calorimetric studies. X.W. provided technical assistance. L.G., S.-P.W., S.K.D., R.G.R. and T.W.M. generated unpublished data. M.V.O. and A.K. provided discussion and assistance with pathology analysis. L.W. wrote the paper with critical input and edits from C.D.A., H.W., R.T., L.G., X.C., A.L. and S.C. C.D.A. and H.W. jointly supervised the research.

Competing interests C.D.A. is a co-founder of Chroma Therapeutics and Constellation Pharmaceuticals and a Scientific Advisory Board member of EpiCypher.

Additional information

Supplementary information is available for this paper at https://doi.org/10.1038/s41586-019-1842-7.

Correspondence and requests for materials should be addressed to L.W., H.W. or C.D.A.

Peer review information *Nature* thanks Tanja Mittag and the other, anonymous, reviewer(s) for their contribution to the peer review of this work.

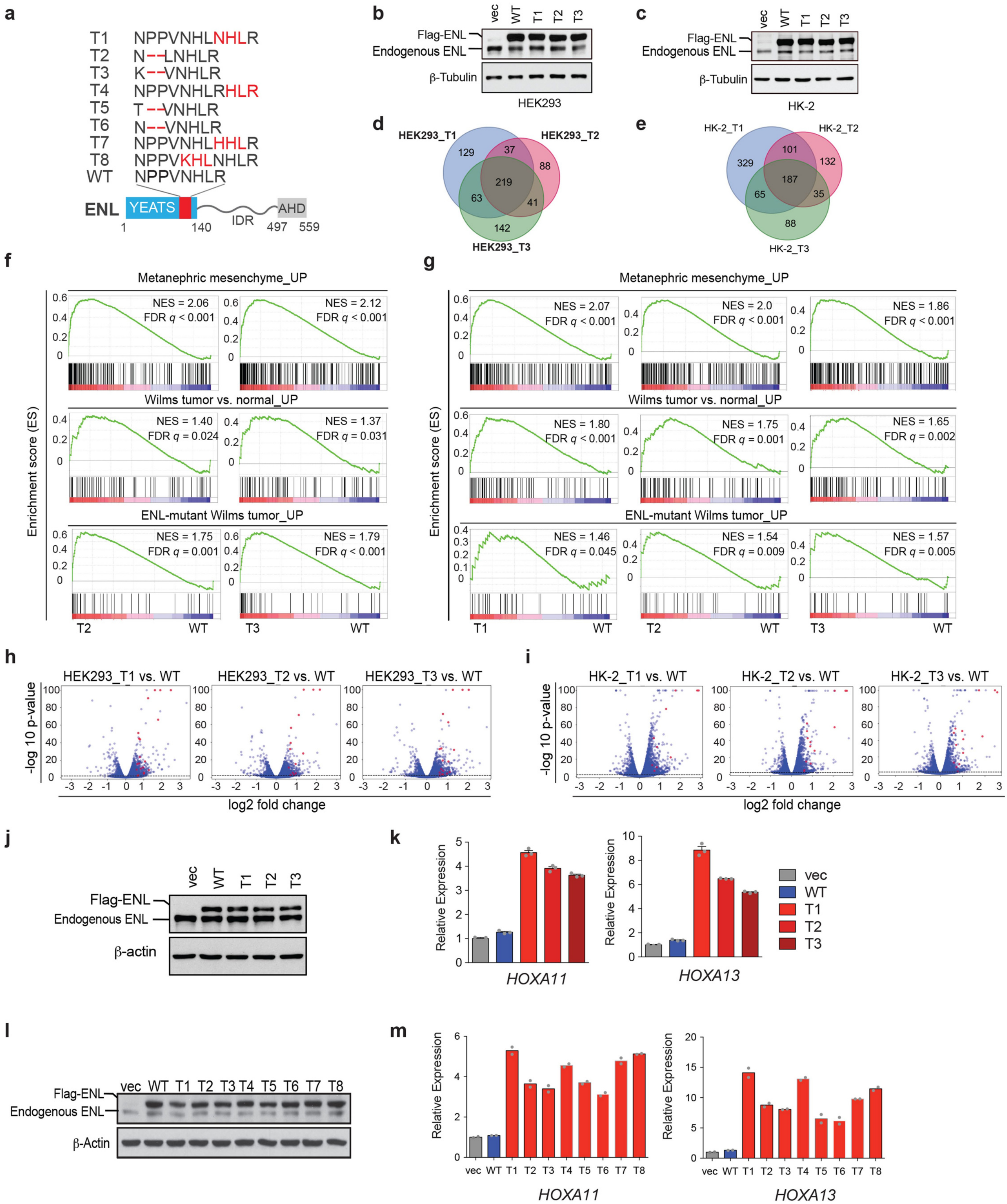

Extended Data Fig. 1 | See next page for caption.

Extended Data Fig. 1 | ENL mutations induce transcriptional changes that are implicated in developmental programs and in Wilms tumour. a, Bottom, ENL protein structure, with the region that is mutated in cancer shown in red. Above, amino-acid sequences of the T1 to T8 tumour-associated mutations and the corresponding WT region. **b**, **c**, Western blots showing the levels of ectopically expressed WT or mutant Flag–ENL proteins in HEK293 (**b**) and HK-2 (**c**) cells. Independent experiments were repeated four times with similar results. β-Tubulin is used as a loading control. **d**, **e**, Venn diagrams showing the number and overlap of genes for which expression is significantly upregulated upon expression of mutant ENL as compared with WT ENL in HEK293 (**d**) and HK-2 (**e**) cells. Genes with a fold change of 1.5 or more and a false discovery rate (FDR) of 0.01 or less are considered to be significantly upregulated. **f**, **g**, GSEA plots evaluating the changes in the indicated gene signatures upon expression of the indicated ENL mutants compared with WT in HEK293 (**f**) and HK-2 (**g**) cells. **h**, **i**, Volcano plots of RNA-sequencing data demonstrating the $-\log_{10}$ P-values versus $\log_2$ fold changes in HEK293 (**h**) and HK-2 (**i**) cells. *HOXA* genes are highlighted in red. P-values were determined by two-tailed exact test, adjusted by FDR. **j**, Western blot showing the close-to-endogenous levels of ectopically expressed WT or mutant Flag–ENL in HEK293 cells. Independent experiments were repeated three times with similar results. **k**, mRNA expression analysis (normalized to *GAPDH*) of selected ENL target genes in HEK293 cells (from panel **j**) expressing the indicated constructs. vec, vector control. Data represent mean ± s.e.m., $n = 3$ technical replicates, independent experiments were repeated three times with similar results. **l**, western blot showing the protein levels of ectopically expressed wildtype or indicated mutants (as illustrated in a) Flag-ENL in HEK293 cells. Experiment repeated three times independently with similar results. **m**, mRNA expression analysis (normalized to *GAPDH*) of selected ENL target genes in HEK293 cells (from panel **l**) expressing the indicated constructs. Vec, vector control. Data represent means from $n = 2$ technical replicates; results are representative of three independent experiments. For gel source data (**b**, **c**, **j**, **l**), see Supplementary Fig. 1.

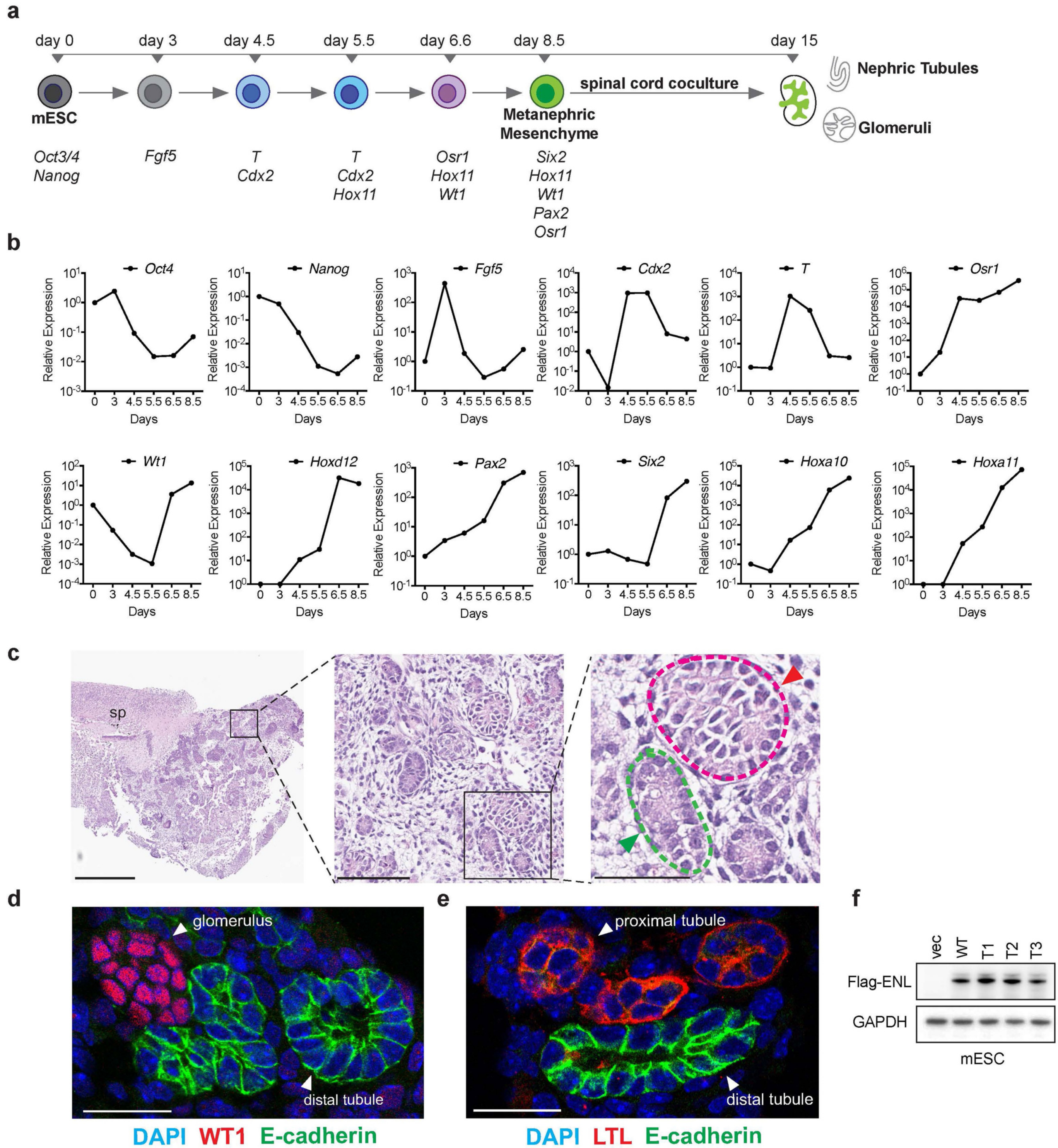

Extended Data Fig. 2 | Three-dimensional nephron structures derived from mESCs. **a**, Diagram showing the in vitro directed differentiation assay. Signature genes expressed at each step are shown at the bottom. *T*, the *Brachyury* gene. **b**, mRNA expression analysis (normalized to *Gapdh)* of the indicated genes at different time points during the assay. Data shown are representative of two independent experiments. **c**, Haematoxylin and eosin staining shows the induced embryoid body co-cultured with the spinal cord (sp). Green and red arrowheads point to nephric tubule and glomerulus, respectively. Scale bars: left, 500 µm; middle, 100 µm; right, 50 µm. **d**, Representative immunofluorescence staining of induced kidney structures for the nephric distal-tubule marker E-cadherin (green) and the glomerular marker WT1 (red). DNA is stained with DAPI (blue). Scale bar, 25 µm. **e**, Representative immunofluorescence staining of induced kidney structures for E-cadherin (green) and the proximal-tubule marker lotus tetragonolobus lectin (LTL, red). DNA was stained with DAPI (blue). Scale bar, 25 µm. **f**, Western blot showing the protein levels of ectopically expressed WT or mutant Flag-tagged ENL in mESCs. For gel source data, see Supplementary Fig. 1. For panels **c**–**f**, independent experiments were repeated three times with similar results.

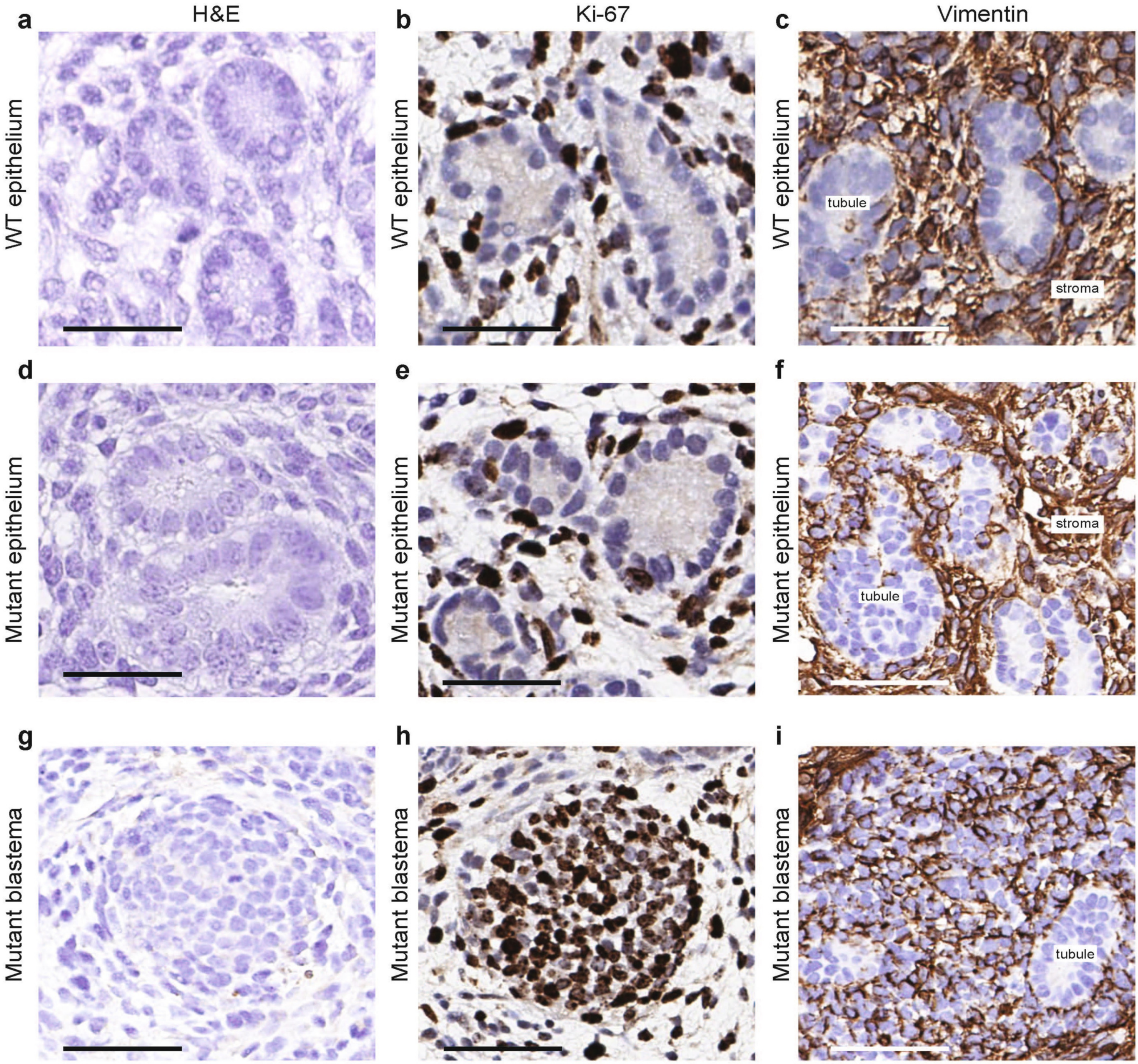

Extended Data Fig. 3 | Characterization of ENL-mutant kidney structures. **a**, **d**, **g**, Representative haematoxylin and eosin staining of the indicated kidney structures. **b**, **e**, **h**, Representative immunohistochemistry staining of the indicated kidney structures for the proliferation marker Ki-67. **c**, **f**, **i**, Representative immunohistochemistry staining of the indicated kidney structures for the mesenchymal marker vimentin. In panels **c**, **f**, the vimentin-positive cells shown are stroma cells. In panel **i**, the vimentin-positive cells shown are mostly blastema components. **a**–**c**, WT epithelium; **d**–**f**, mutant epithelium; **g**–**i**, mutant blastema. All experiments were repeated twice with similar results. Scale bars, 50 μm.

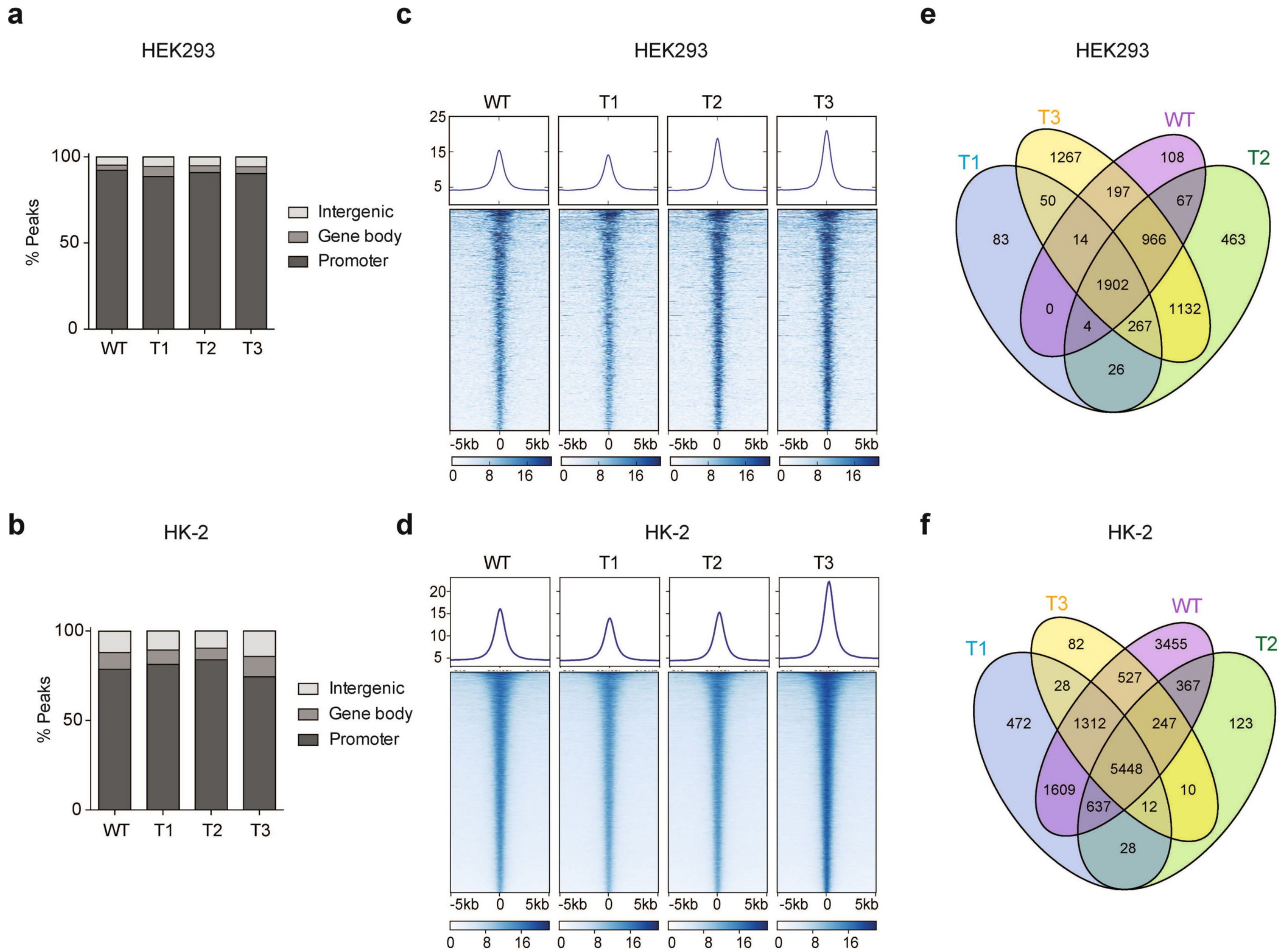

Extended Data Fig. 4 | ENL mutants occupy largely the same genomic loci as the wild-type protein. a, **b**, Bar graphs showing the genomic distribution of Flag–ENL-bound peaks in HEK293 (**a**) and HK-2 (**b**) cells. **c**, **d**, Heat maps of normalized WT or mutant Flag–ENL ChIP–seq signals in HEK293 (**c**) and HK-2 (**d**) cells, centred on ENL-bound peaks across a ±5-kb window. The colour key represents the signal density, with darker colour representing more signal. More details are in Supplementary Tables 4, 5. **e**, **f**, Venn diagrams showing the overlap of WT or mutant ENL-bound peaks in HEK293 (**e**) and HK-2 (**f**) cells.

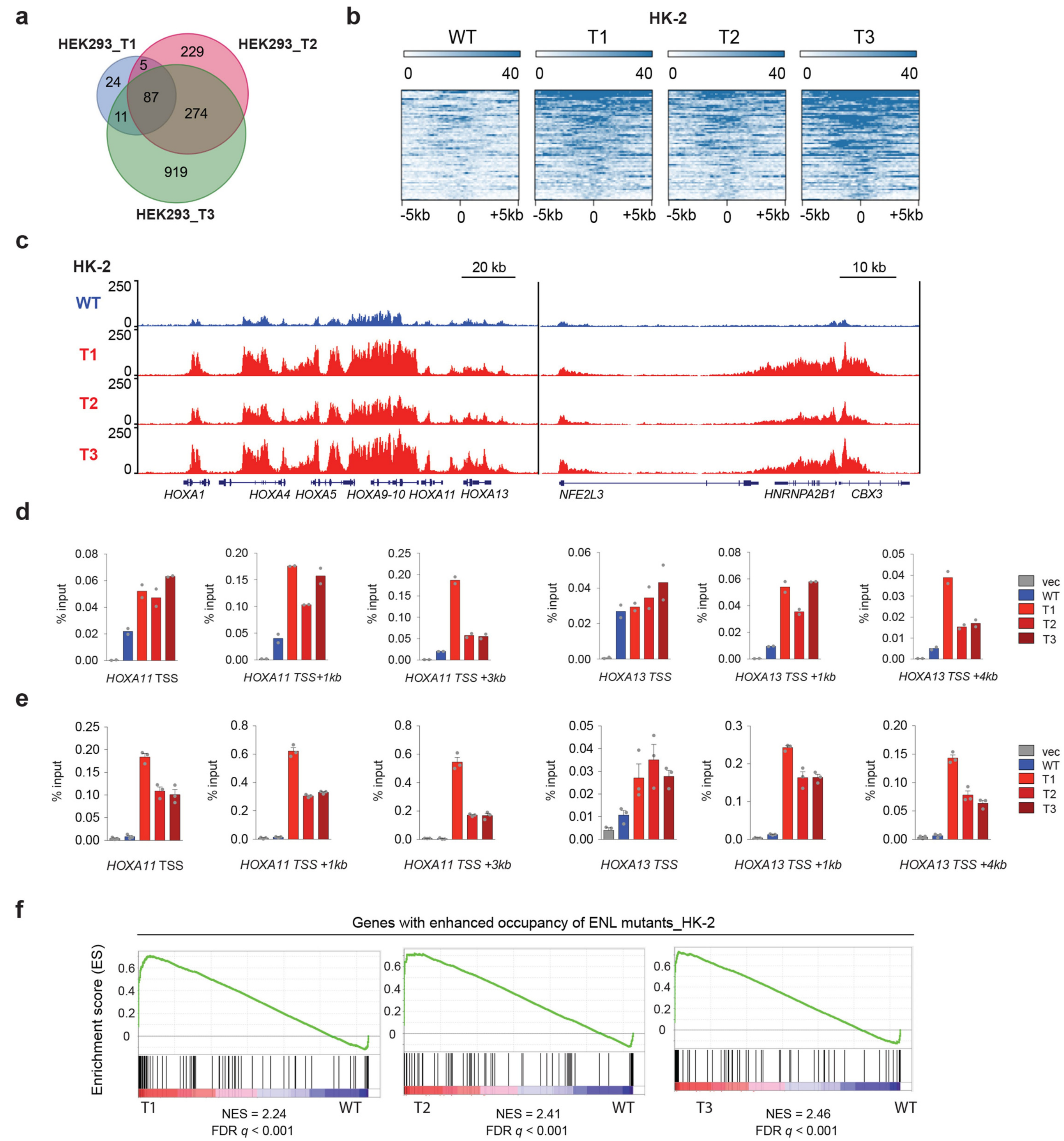

Extended Data Fig. 5 | Enhanced occupancy of ENL mutants at a shared subset of target genes correlates with gene activation. a, Venn diagram showing the number and the overlap of peaks with enhanced binding of individual mutant ENLs as compared with WT ENL in HEK293 cells. **b**, Heat maps of normalized WT or mutant Flag–ENL ChIP–seq signals in HK-2 cells, centred on mutant-enhanced peaks (fold change greater than 1.5) across a ± 5-kb window. More details are in Supplementary Table 7. **c**, Genome browser view of Flag–ENL ChIP–seq signals at selected target genes in HK-2 cells expressing indicated Flag–ENL transgenes. **d**, **e**, ChIP–qPCR of Flag–ENL at selected ENL target genes in two batches of HEK293 cells that are expressing the indicated ENL transgenes at levels higher than those of the endogenous ENL protein (**d**; see Extended Data Fig. 1b) or close to endogenous levels (**e**; see Extended Data Fig. 1j). Data in **d** represent means from $n = 2$ technical replicates, and are representative of three independent experiments. Data in **e** represent means ± s.e.m. from $n = 3$ technical replicates; independent experiments were repeated twice with similar results. **f**, GSEA plots showing that genes ($n = 91$; Supplementary Table 10) with enhanced occupancy of ENL mutants are upregulated in mutant-expressing HK-2 cells.

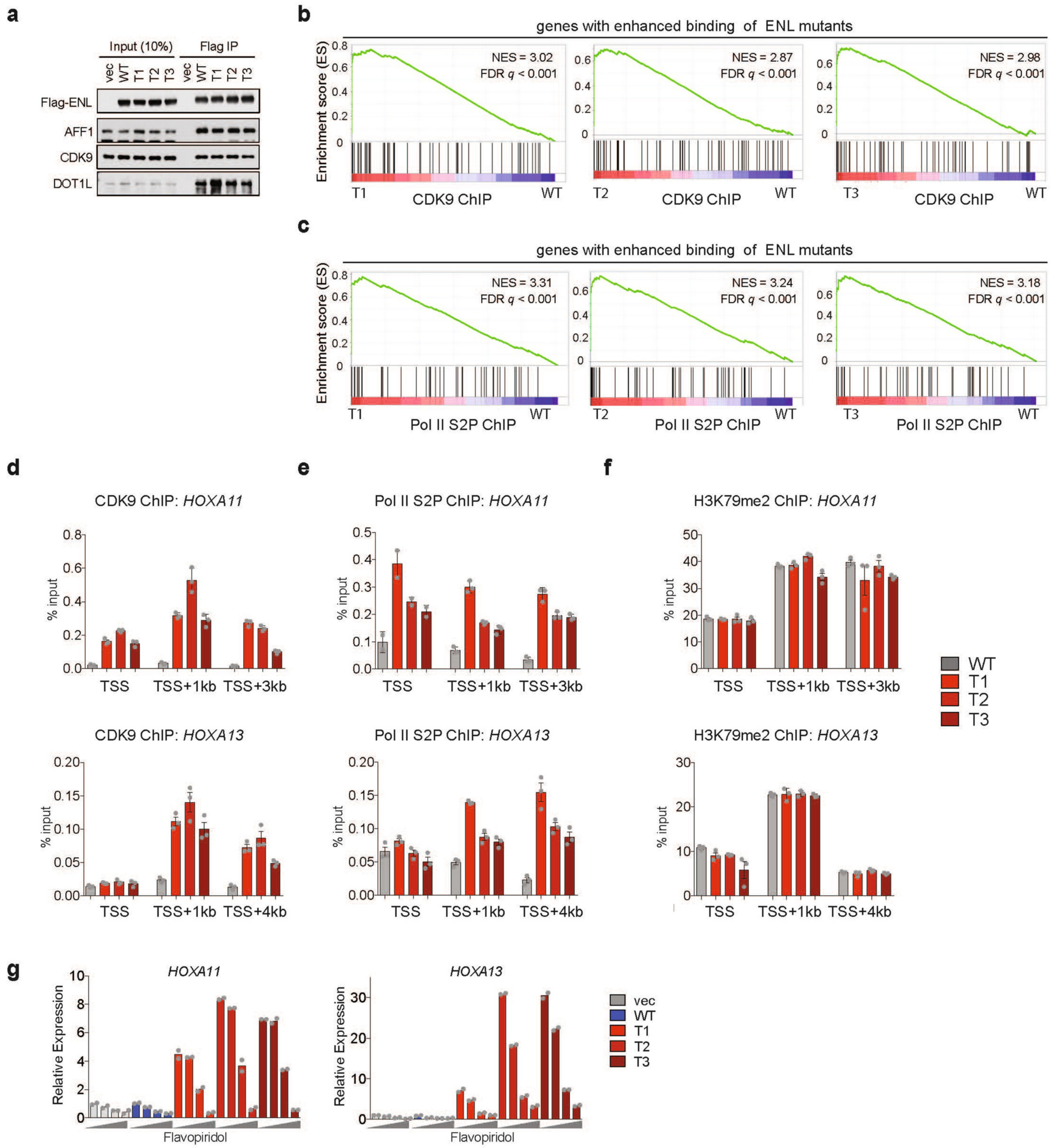

Extended Data Fig. 6 | Enhanced binding of ENL mutants at target genes leads to increased SEC recruitment and activity. a, Western blot analysis of co-immunoprecipitation (IP) using the M2 anti-Flag antibody with lysates from HEK293T cells that are expressing the indicated Flag–ENL constructs. The experiment was repeated twice with similar results. For source data, see Supplementary Fig. 1. **b**, **c**, GSEA plots of genes ranked by their fold-change (mutant over WT) of CDK9 (**b**) or Pol II S2P (**c**) ChIP–seq signals in HEK293 cells, annotated against the set of genes ($n = 87$) that show increased occupancy of ENL mutants compared with WT. **d**–**f**, ChIP–qPCR analysis of CDK9 (**d**), Pol II S2P (**e**) and H3K79me2 (**f**; dimethylation of lysine 79 of histone H3) at selected ENL target genes in HEK293 cells that are expressing the indicated Flag–ENL constructs. Data represent means ± s.e.m.; $n = 3$ technical replicates. Experiments were repeated twice with similar results. **g**, mRNA expression analysis (normalized to *GAPDH*) of selected ENL target genes in HK-2 cells expressing the indicated constructs upon treatment with flavopiridol for 3 h. Increasing dosages (0, 125 nM, 250 nM and 1,000 nM) are depicted by grey wedges. Data represent means from $n = 2$ technical replicates. Experiments were repeated twice with similar results.

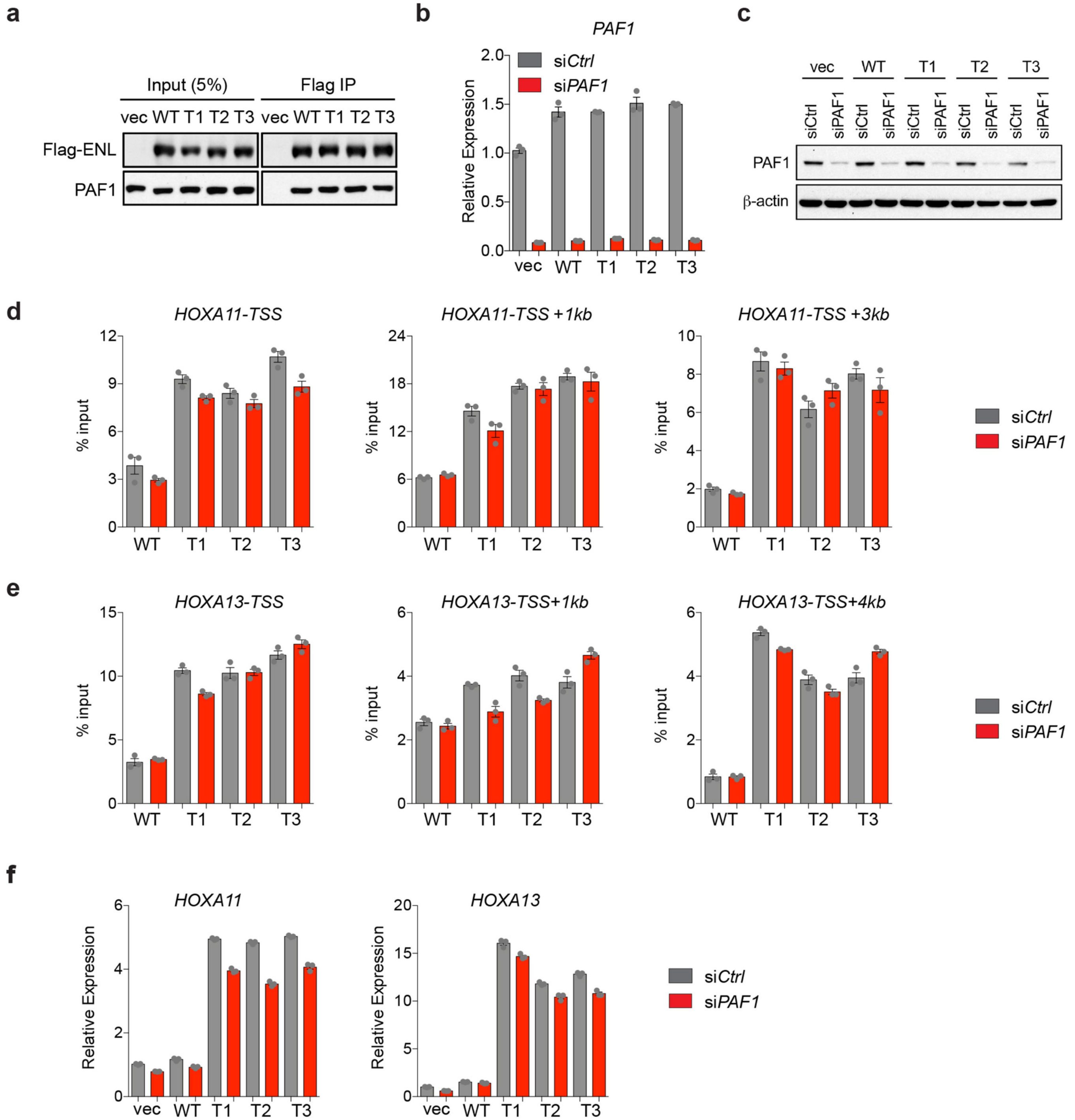

Extended Data Fig. 7 | Loss of PAF1 has minimal effect on the functionality of cancer-associated ENL mutants. **a**, Western blot analysis of co-immunoprecipitation using the M2 anti-Flag antibody in lysates from HEK293T cells expressing the indicated Flag–ENL constructs. Results are representative of three independent experiments. **b**, **c**, mRNA expression (**b**) and western blot (**c**) analysis showing the knockdown efficiency of short interfering (si)RNAs that target *PAF1* in HEK293 cells. Independent experiments were repeated twice with similar results. **d**, **e**, ChIP–qPCR analysis of Flag–ENL at selected ENL target genes in control (si*Ctrl*) or *PAF1* knockdown (si*PAF1*) HEK293 cells. **f**, mRNA expression analysis (normalized to *GAPDH*) of selected ENL target genes in control (si*Ctrl*) or *PAF1* knockdown (si*PAF1*) HEK293 cells. Data in **d**–**f** represent means ± s.e.m.; $n = 3$ technical replicates. For gel source data in panels **a**, **c**, see Supplementary Fig. 1.

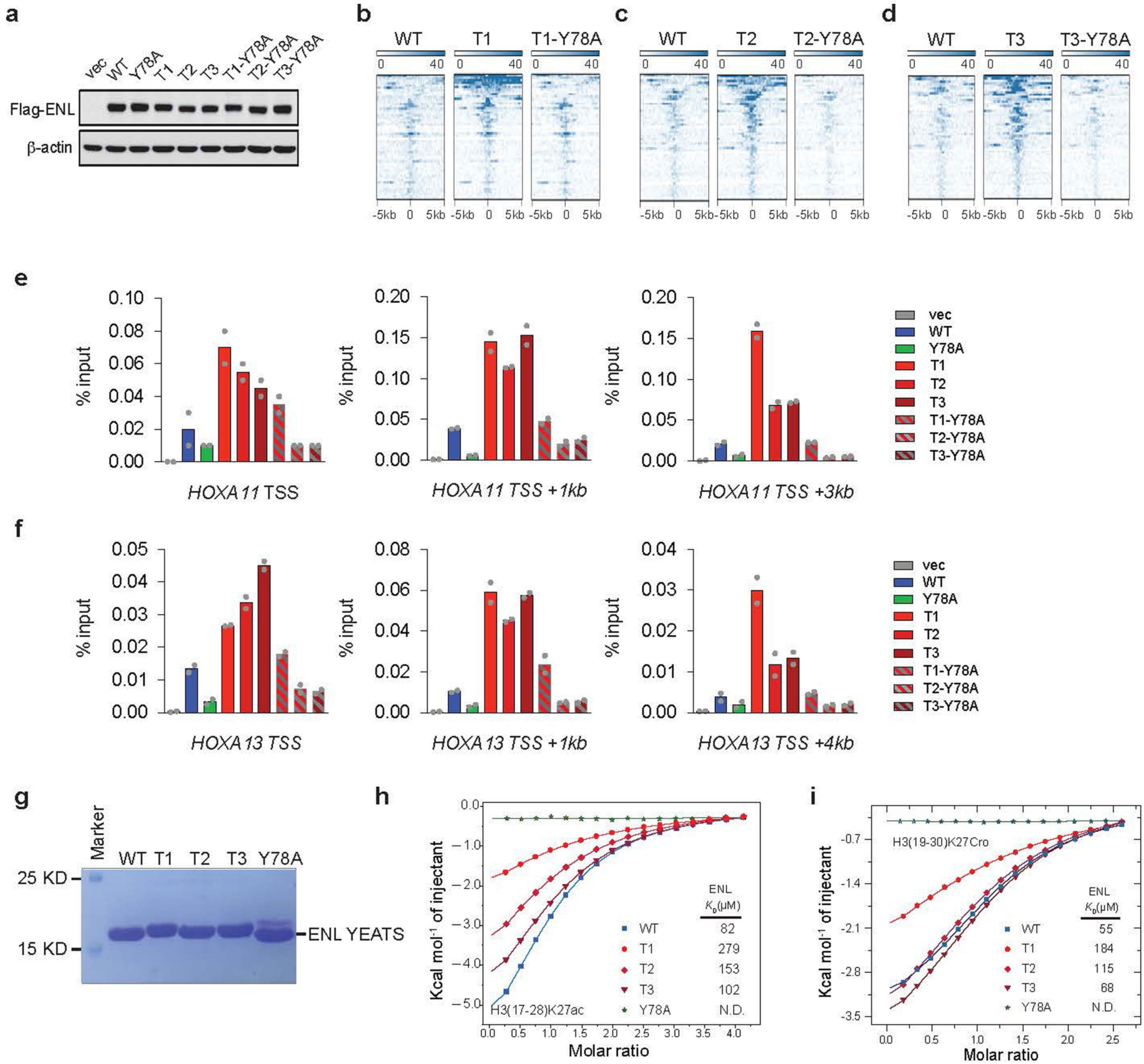

Extended Data Fig. 8 | Interaction with histone acylation is essential but not sufficient for chromatin occupancy by cancer-associated ENL mutants. **a**, Western blot showing the protein levels of ectopically expressed WT or mutant Flag–ENL in HEK293 cells. Experiments were repeated twice with similar results. For source data, see Supplementary Fig. 1. **b**–**d**, Heat maps of normalized WT or mutant Flag–ENL ChIP–seq signals in HEK293 cells, centred on peaks that are enhanced in all three T mutants (as in Fig. 2a; $n = 54$) across a ± 5-kb window. **e**, **f**, ChIP–qPCR analysis of Flag–ENL at selected ENL target genes in HEK293 cells expressing the indicated constructs. Data represent means of $n = 2$ technical replicates. Independent experiments were repeated twice with similar results. **g**, Coomassie staining of purified WT ENL YEATS domain, and of YEATS domains with the indicated T mutations or a Y78A mutation. Data represent two independent experiments. **h**, **i**, ITC titration fitting curves for the indicated ENL YEATS domains (as in panel **g**), using a histone H3 peptide that is either acetylated at lysine 27 (H3(17-28)K27ac; **h**) or crotonylated at lysine 27 (H3(19-30)K27Cro; **i**).

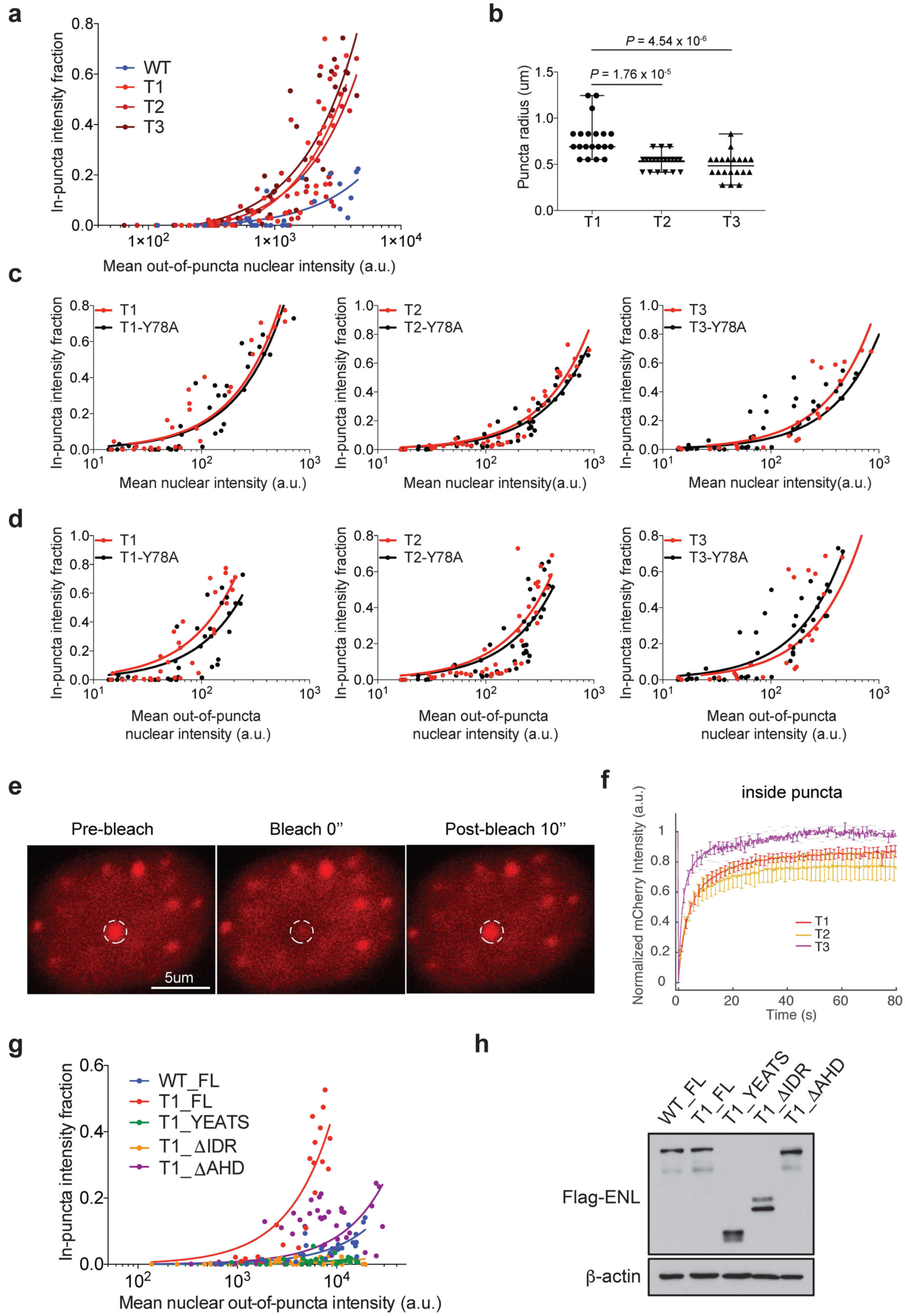

Extended Data Fig. 9 | See next page for caption.

Extended Data Fig. 9 | Characterization of nuclear puncta formed by ectopically expressed ENL tumour mutants. a, Fraction of in-puncta fluorescence intensity in the nucleus of HEK293 cells that express WT or mutant mCherry–ENL, as a function of mean out-of-puncta nuclear intensity. Each dot represents one cell (the same experiment as in Fig. 4e). **b**, Dot plots showing the radius of puncta in HEK293 cells that are expressing similar levels of the indicated mCherry–ENL proteins. $n = 20$ independent puncta, randomly selected from four different cells per group. *P*-values were obtained using two-tailed unpaired Student's *t*-test. Centre lines represent medians; whiskers indicate the minimum to maximum range. **c**, **d**, Fraction of in-puncta mCherry–ENL intensity in the nucleus as a function of mean nuclear intensity (**c**) or mean out-of-puncta nuclear intensity (**d**) in HEK293 cells that express the indicated mCherry–ENL proteins. Each dot represents one cell. **e**, Representative images from fluorescence recovery after photobleaching (FRAP) analysis in HEK293 cells expressing T3 mutant mCherry–ENL. The white dashed circles indicate the punctum undergoing targeted bleaching. Images represent 14 FRAP experiments in total with T1/2/3 mCherry–ENL. **f**, Averaged FRAP curves from areas inside the mCherry–ENL puncta formed by the indicated ENL mutants. Bleaching occurs at $t = 0$ s. Data represent means ± s.e.m.; $n = 6$ (T1), 5 (T2) and 3 (T3) distinct puncta from multiple cells. **g**, Fraction of in-puncta fluorescence intensity in the nucleus of HEK293 cells that express the indicated mCherry–ENL constructs as a function of mean nuclear out-of-puncta intensity. Each dot represents one cell (same experiment as in Fig. 4g). **h**, Western blot showing the protein levels of ectopically expressed Flag–ENL in HEK293 cells. Experiments were repeated three times with similar results. For gel source data, see Supplementary Fig. 1.

nature research

Corresponding author(s): Liling Wan, Hong Wen, C. David Allis

Last updated by author(s): 10/8/2019

Reporting Summary

Nature Research wishes to improve the reproducibility of the work that we publish. This form provides structure for consistency and transparency in reporting. For further information on Nature Research policies, see Authors & Referees and the Editorial Policy Checklist.

Statistics

For all statistical analyses, confirm that the following items are present in the figure legend, table legend, main text, or Methods section.

n/a	Confirmed	
☐	☒	The exact sample size (*n*) for each experimental group/condition, given as a discrete number and unit of measurement
☐	☒	A statement on whether measurements were taken from distinct samples or whether the same sample was measured repeatedly
☐	☒	The statistical test(s) used AND whether they are one- or two-sided *Only common tests should be described solely by name; describe more complex techniques in the Methods section.*
☐	☒	A description of all covariates tested
☒	☐	A description of any assumptions or corrections, such as tests of normality and adjustment for multiple comparisons
☐	☒	A full description of the statistical parameters including central tendency (e.g. means) or other basic estimates (e.g. regression coefficient) AND variation (e.g. standard deviation) or associated estimates of uncertainty (e.g. confidence intervals)
☒	☐	For null hypothesis testing, the test statistic (e.g. *F*, *t*, *r*) with confidence intervals, effect sizes, degrees of freedom and *P* value noted *Give P values as exact values whenever suitable.*
☒	☐	For Bayesian analysis, information on the choice of priors and Markov chain Monte Carlo settings
☒	☐	For hierarchical and complex designs, identification of the appropriate level for tests and full reporting of outcomes
☒	☐	Estimates of effect sizes (e.g. Cohen's *d*, Pearson's *r*), indicating how they were calculated

Our web collection on statistics for biologists contains articles on many of the points above.

Software and code

Policy information about availability of computer code

Data collection	Zeiss Zen was used to collect imaging data
Data analysis	GSEA v2.2.2, MACS v1.4.2, TopHat v2.0.10, HTSeq v0.6.0, edgeR v3.8.6, VennDiagram v1.6, Panther Classification System, and python matplotlib package were used for data analysis

For manuscripts utilizing custom algorithms or software that are central to the research but not yet described in published literature, software must be made available to editors/reviewers. We strongly encourage code deposition in a community repository (e.g. GitHub). See the Nature Research guidelines for submitting code & software for further information.

Data

Policy information about availability of data

All manuscripts must include a data availability statement. This statement should provide the following information, where applicable:

- Accession codes, unique identifiers, or web links for publicly available datasets
- A list of figures that have associated raw data
- A description of any restrictions on data availability

The ChIP-seq and RNA-seq data have been deposited in the Gene Expression Omnibus database under accession number GSE125186.

Field-specific reporting

Please select the one below that is the best fit for your research. If you are not sure, read the appropriate sections before making your selection.

☒ Life sciences ☐ Behavioural & social sciences ☐ Ecological, evolutionary & environmental sciences

Life sciences study design

All studies must disclose on these points even when the disclosure is negative.

Sample size	For most high-throughput sequencing experiments, two independent biological replicates were used (e.g. RNA-seq, and most of ChIP-seq). Additional independent experiments were repeated and ChIP-qPCR and RT-qPCR were used to validate key results obtained from high-throughput sequencing. Sample sizes for other assays were not predetermined and were chosen based on our prior experience and common standards in the field for detecting statistically significant differences between conditions.
Data exclusions	No data was excluded from the analysis.
Replication	Each experiment was repeated (See Figure Legends) and all findings were reproducible. In most assays, the conclusions about functional difference between wild-type and mutant ENL were drawn from comparing wild-type and multiple distinct mutants (T1, T2, T3), which further strengthens the conclusions.
Randomization	Samples were allocated to groups according to genotype or treatment. No randomization was required as the starting materials (e.g. parental cell lines before generation of sub-lines with different genotypes) are identical.
Blinding	The investigators were not blinded to allocation during experiments and outcome assessment except for pathological analysis in Figure. 1g.

Reporting for specific materials, systems and methods

We require information from authors about some types of materials, experimental systems and methods used in many studies. Here, indicate whether each material, system or method listed is relevant to your study. If you are not sure if a list item applies to your research, read the appropriate section before selecting a response.

Materials & experimental systems

n/a	Involved in the study	
☐	☒	Antibodies
☐	☒	Eukaryotic cell lines
☒	☐	Palaeontology
☐	☒	Animals and other organisms
☒	☐	Human research participants
☒	☐	Clinical data

Methods

n/a	Involved in the study	
☐	☒	ChIP-seq
☒	☐	Flow cytometry
☒	☐	MRI-based neuroimaging

Antibodies

Antibodies used	All antibodies used have been provided in Supplementary Tables with details (e.g. supplier name, catalog number, application and dilution)
Validation	For Immunoblot, the correct size of the detected bands was assessed based on the protein marker. 1. Flag: Manufacturer indicates reactivity by immunoblot to detect Flag epitope-tagged proteins. We have demonstrated in prior work (Wan et al. 2017) that this antibody can be used for ChIP-seq and confirmed its specificity using cells without Flagged transgenes. 2. ENL: Manufacturer indicates human reactivity by immunoblot. We have demonstrated its specificity in prior work (Wan et al. 2017) using ENL KD cells. 3. b-actin: Manufacturer indicates human and mouse reactivity by immunoblot. It is widely used in western blot as a loading control. 4. GAPDH: Manufacturer indicates human and mouse reactivity by immunoblot. It is widely used in western blot as a loading control. 5. b-tubulin: Manufacturer indicates human and mouse reactivity by immunoblot. It is widely used in western blot as a loading control. 6. AFF1: Manufacturer indicates human reactivity by immunoblot. We have demonstrated its specificity in prior work (Wan et al. 2017) using AFF1 KD cells. 7. PAF1: Manufacturer indicates human reactivity by immunoblot. We have demonstrated its specificity using PAF1 KD cells. 8. DOT1L: Manufacturer indicates human reactivity by immunoblot. We showed it can be used for western blot in current study. 9. Myc: Manufacturer indicates reactivity by immunoblot to detect Myc epitope-tagged proteins. We have demonstrated its specificity in prior work (Wan et al. 2017) in co-immunoprecipitation assays. 10. CDK9: Manufacturer indicates human and mouse reactivity by immunoblot. We showed that it can be used for ChIP-seq in current study. 11. Pol II (ser-2p): Manufacturer indicates human and mouse reactivity by immunoplot. We have demonstrated in prior work (Wan et al. 2017) that this antibody can be used for ChIP-seq.

12. H3K79me2: Manufacturer indicates human and mouse reactivity by immunoplot. We have demonstrated in prior work (Wan et al. 2017) that this antibody can be used for ChIP-seq.
13. E-cadherin: Manufacturer indicates human and mouse reactivity by IF.
14. WT-1: Manufacturer indicates human and mouse reactivity by IF.
15. Biotinylated Lotus Tetragonolobus Lectin (LTL): Manufacturer indicates application for IF staining.

Eukaryotic cell lines

Policy information about cell lines

Cell line source(s)	HEK293, HK-2 lines purchased from ATCC; mESCs cells derived in house
Authentication	For cells purchased directly from ATCC, cells are authenticated by sequencing at ATCC. During culture, parental lines were authenticated based on the testing and monitoring of phenotypic features (morphology, differentiation potential, growth conditions, etc.) characteristic of each line that were previously reported by manufacturers and other groups. Immunoblot analysis was performed to confirm the genotypes after transgene/siRNA expression.
Mycoplasma contamination	All cell lines tested negative for mycoplasma contamination.
Commonly misidentified lines (See ICLAC register)	No commonly misidentified lines were used in this study.

Animals and other organisms

Policy information about studies involving animals; ARRIVE guidelines recommended for reporting animal research

Laboratory animals	*For laboratory animals, report species, strain, sex and age OR state that the study did not involve laboratory animals.*
Wild animals	*Provide details on animals observed in or captured in the field; report species, sex and age where possible. Describe how animals were caught and transported and what happened to captive animals after the study (if killed, explain why and describe method; if released, say where and when) OR state that the study did not involve wild animals.*
Field-collected samples	*For laboratory work with field-collected samples, describe all relevant parameters such as housing, maintenance, temperature, photoperiod and end-of-experiment protocol OR state that the study did not involve samples collected from the field.*
Ethics oversight	*Identify the organization(s) that approved or provided guidance on the study protocol, OR state that no ethical approval or guidance was required and explain why not.*

Note that full information on the approval of the study protocol must also be provided in the manuscript.

ChIP-seq

Data deposition

☒ Confirm that both raw and final processed data have been deposited in a public database such as GEO.

☒ Confirm that you have deposited or provided access to graph files (e.g. BED files) for the called peaks.

Data access links *May remain private before publication.*	https://www.ncbi.nlm.nih.gov/geo/query/acc.cgi?acc=GSE125186 Token: gdwbimyqlhyxlar
Files in database submission	GSM3564782 ChIPSeq.PolII_S2P_T1_mut GSM3564783 ChIPSeq.PolII_S2P_T2_mut GSM3564784 ChIPSeq.PolII_S2P_T3_mut GSM3564785 ChIPSeq.PolII_S2P_WT_ENL GSM3564786 ChIPSeq.CDK9_T1_mut GSM3564787 ChIPSeq.CDK9_T2_mut GSM3564788 ChIPSeq.CDK9_T3_mut GSM3564789 ChIPSeq.CDK9_WT_ENL GSM3564790 ChIPSeq.HEK293_WT_ENL_B GSM3564791 ChIPSeq.HEK293_T1_mut_C GSM3564792 ChIPSeq.HEK293_T1_Y78A_mut GSM3564793 ChIPSeq.HEK293_T2_B_mut GSM3564794 ChIPSeq.HEK293_T2_Y78A_mut GSM3564795 ChIPSeq.HEK293_T3_B_mut GSM3564796 ChIPSeq.HEK293_T3_Y78A_mut GSM3564797 ChIPSeq.HEK293_vec GSM3564798 ChIPSeq.HEK293_Y78A_B_mut GSM3564799 ChIPSeq.HEK293_F_ENL GSM3564800 ChIPSeq.HEK293_F_T1_mut GSM3564801 ChIPSeq.HEK293_F_T2_mut

GSM3564802 ChIPSeq.HEK293_F_T3_mut
GSM3564803 ChIPSeq.HEK293_input
GSM3564804 ChIPSeq.HK2_F_ENL
GSM3564805 ChIPSeq.HK2_F_T1_mut
GSM3564806 ChIPSeq.HK2_F_T2_mut
GSM3564807 ChIPSeq.HK2_F_T3_mut
GSM3564808 ChIPSeq.HK2_input_S31
GSM3564809 RNASeq.HEK293_WT_ENL_A
GSM3564810 RNASeq.HEK293_WT_ENL_B
GSM3564811 RNASeq.HEK293_ENL_T1_mut_A
GSM3564812 RNASeq.HEK293_ENL_T1_mut_B
GSM3564813 RNASeq.HEK293_ENL_T2_mut_A
GSM3564814 RNASeq.HEK293_ENL_T2_mut_B
GSM3564815 RNASeq.HEK293_ENL_T3_mut_A
GSM3564816 RNASeq.HEK293_ENL_T3_mut_B
GSM3564817 RNASeq.HK2_WT_ENL_A
GSM3564818 RNASeq.HK2_WT_ENL_B
GSM3564819 RNASeq.HK2_ENL_T1_mut_A
GSM3564820 RNASeq.HK2_ENL_T1_mut_B
GSM3564821 RNASeq.HK2_ENL_T2_mut_A
GSM3564822 RNASeq.HK2_ENL_T2_mut_B
GSM3564823 RNASeq.HK2_ENL_T3_mut_A
GSM3564824 RNASeq.HK2_ENL_T3_mut_C

Genome browser session
(e.g. UCSC)

```
track type=bigWig name=293_F_ENL db=hg19 windowingFunction=maximum viewLimits=0:500 autoScale=off visibility=full
bigDataUrl=http://dldcc-web.brc.bcm.edu/lilab/xc3/ENL2/ChIP/bw/293_F_ENL.sp.bw
track type=bigWig name=293_F_T1 db=hg19 windowingFunction=maximum viewLimits=0:500 autoScale=off visibility=full
bigDataUrl=http://dldcc-web.brc.bcm.edu/lilab/xc3/ENL2/ChIP/bw/293_F_T1.sp.bw
track type=bigWig name=293_F_T2 db=hg19 windowingFunction=maximum viewLimits=0:500 autoScale=off visibility=full
bigDataUrl=http://dldcc-web.brc.bcm.edu/lilab/xc3/ENL2/ChIP/bw/293_F_T2.sp.bw
track type=bigWig name=293_F_T3 db=hg19 windowingFunction=maximum viewLimits=0:500 autoScale=off visibility=full
bigDataUrl=http://dldcc-web.brc.bcm.edu/lilab/xc3/ENL2/ChIP/bw/293_F_T3.sp.bw
track type=bigWig name=293_F_Y78A db=hg19 windowingFunction=maximum viewLimits=0:500 autoScale=off visibility=full
bigDataUrl=http://dldcc-web.brc.bcm.edu/lilab/xc3/ENL2/ChIP/bw/293_F_Y78A.sp.bw
track type=bigWig name=293_input db=hg19 windowingFunction=maximum viewLimits=0:500 autoScale=off visibility=full
bigDataUrl=http://dldcc-web.brc.bcm.edu/lilab/xc3/ENL2/ChIP/bw/293_input.sp.bw
track type=bigWig name=HK2_F_ENL db=hg19 windowingFunction=maximum viewLimits=0:500 autoScale=off visibility=full
bigDataUrl=http://dldcc-web.brc.bcm.edu/lilab/xc3/ENL2/ChIP/bw/HK2_F_ENL.sp.bw
track type=bigWig name=HK2_F_T1 db=hg19 windowingFunction=maximum viewLimits=0:500 autoScale=off visibility=full
bigDataUrl=http://dldcc-web.brc.bcm.edu/lilab/xc3/ENL2/ChIP/bw/HK2_F_T1.sp.bw
track type=bigWig name=HK2_F_T2 db=hg19 windowingFunction=maximum viewLimits=0:500 autoScale=off visibility=full
bigDataUrl=http://dldcc-web.brc.bcm.edu/lilab/xc3/ENL2/ChIP/bw/HK2_F_T2.sp.bw
track type=bigWig name=HK2_F_T3 db=hg19 windowingFunction=maximum viewLimits=0:500 autoScale=off visibility=full
bigDataUrl=http://dldcc-web.brc.bcm.edu/lilab/xc3/ENL2/ChIP/bw/HK2_F_T3.sp.bw
track type=bigWig name=HK2_F_Y78A db=hg19 windowingFunction=maximum viewLimits=0:500 autoScale=off visibility=full
bigDataUrl=http://dldcc-web.brc.bcm.edu/lilab/xc3/ENL2/ChIP/bw/HK2_F_Y78A.sp.bw
track type=bigWig name=HK2_input db=hg19 windowingFunction=maximum viewLimits=0:500 autoScale=off visibility=full
bigDataUrl=http://dldcc-web.brc.bcm.edu/lilab/xc3/ENL2/ChIP/bw/HK2_input.sp.bw
track type=bigWig name=293_ENL_B db=hg19 windowingFunction=maximum viewLimits=0:500 autoScale=off visibility=full
bigDataUrl=http://dldcc-web.brc.bcm.edu/lilab/xc3/ENL2/ChIP/second_batch/sp/bw/293_ENL_B_treat.sp.bw
track type=bigWig name=293_ENL_C db=hg19 windowingFunction=maximum viewLimits=0:500 autoScale=off visibility=full
bigDataUrl=http://dldcc-web.brc.bcm.edu/lilab/xc3/ENL2/ChIP/second_batch/sp/bw/293_ENL_C_treat.sp.bw
track type=bigWig name=293_T1_B db=hg19 windowingFunction=maximum viewLimits=0:500 autoScale=off visibility=full
bigDataUrl=http://dldcc-web.brc.bcm.edu/lilab/xc3/ENL2/ChIP/second_batch/sp/bw/293_T1_B_treat.sp.bw
track type=bigWig name=293_T1_C db=hg19 windowingFunction=maximum viewLimits=0:500 autoScale=off visibility=full
bigDataUrl=http://dldcc-web.brc.bcm.edu/lilab/xc3/ENL2/ChIP/second_batch/sp/bw/293_T1_C_treat.sp.bw
track type=bigWig name=293_T1_Y78A db=hg19 windowingFunction=maximum viewLimits=0:500 autoScale=off
visibility=full bigDataUrl=http://dldcc-web.brc.bcm.edu/lilab/xc3/ENL2/ChIP/second_batch/sp/
bw/293_T1_Y78A_treat.sp.bw
track type=bigWig name=293_T2_B db=hg19 windowingFunction=maximum viewLimits=0:500 autoScale=off visibility=full
bigDataUrl=http://dldcc-web.brc.bcm.edu/lilab/xc3/ENL2/ChIP/second_batch/sp/bw/293_T2_B_treat.sp.bw
track type=bigWig name=293_T2_C db=hg19 windowingFunction=maximum viewLimits=0:500 autoScale=off visibility=full
bigDataUrl=http://dldcc-web.brc.bcm.edu/lilab/xc3/ENL2/ChIP/second_batch/sp/bw/293_T2_C_treat.sp.bw
track type=bigWig name=293_T2_Y78A db=hg19 windowingFunction=maximum viewLimits=0:500 autoScale=off
visibility=full bigDataUrl=http://dldcc-web.brc.bcm.edu/lilab/xc3/ENL2/ChIP/second_batch/sp/
bw/293_T2_Y78A_treat.sp.bw
track type=bigWig name=293_T3_B db=hg19 windowingFunction=maximum viewLimits=0:500 autoScale=off visibility=full
bigDataUrl=http://dldcc-web.brc.bcm.edu/lilab/xc3/ENL2/ChIP/second_batch/sp/bw/293_T3_B_treat.sp.bw
track type=bigWig name=293_T3_C db=hg19 windowingFunction=maximum viewLimits=0:500 autoScale=off visibility=full
bigDataUrl=http://dldcc-web.brc.bcm.edu/lilab/xc3/ENL2/ChIP/second_batch/sp/bw/293_T3_C_treat.sp.bw
track type=bigWig name=293_T3_Y78A db=hg19 windowingFunction=maximum viewLimits=0:500 autoScale=off
visibility=full bigDataUrl=http://dldcc-web.brc.bcm.edu/lilab/xc3/ENL2/ChIP/second_batch/sp/
bw/293_T3_Y78A_treat.sp.bw
track type=bigWig name=293_Y78A_B db=hg19 windowingFunction=maximum viewLimits=0:500 autoScale=off visibility=full
bigDataUrl=http://dldcc-web.brc.bcm.edu/lilab/xc3/ENL2/ChIP/second_batch/sp/bw/293_Y78A_B_treat.sp.bw
track type=bigWig name=293_Y78A_C db=hg19 windowingFunction=maximum viewLimits=0:500 autoScale=off visibility=full
bigDataUrl=http://dldcc-web.brc.bcm.edu/lilab/xc3/ENL2/ChIP/second_batch/sp/bw/293_Y78A_C_treat.sp.bw
track type=bigWig name=293_vec db=hg19 windowingFunction=maximum viewLimits=0:500 autoScale=off visibility=full
bigDataUrl=http://dldcc-web.brc.bcm.edu/lilab/xc3/ENL2/ChIP/second_batch/sp/bw/293_vec_B_C_treat.sp.bw
track type=bigWig name="CDK9 WT" db=hg19 windowingFunction=maximum viewLimits=0:1 autoScale=off visibility=full
bigDataUrl=http://dldcc-web.brc.bcm.edu/lilab/jlyu/ENL2/bw/Sorted_ChIP18_WT_CDK9Normalised.bw
track type=bigWig name="CDK9 T1" db=hg19 windowingFunction=maximum viewLimits=0:1 autoScale=off visibility=full
bigDataUrl=http://dldcc-web.brc.bcm.edu/lilab/jlyu/ENL2/bw/Sorted_ChIP18_T1_CDK9Normalised.bw
track type=bigWig name="CDK9 T2" db=hg19 windowingFunction=maximum viewLimits=0:1 autoScale=off visibility=full
bigDataUrl=http://dldcc-web.brc.bcm.edu/lilab/jlyu/ENL2/bw/Sorted_ChIP18_T2_CDK9Normalised.bw
track type=bigWig name="CDK9 T3" db=hg19 windowingFunction=maximum viewLimits=0:1 autoScale=off visibility=full
bigDataUrl=http://dldcc-web.brc.bcm.edu/lilab/jlyu/ENL2/bw/Sorted_ChIP18_T3_CDK9Normalised.bw
track type=bigWig name="PolII S2P WT" db=hg19 windowingFunction=maximum viewLimits=0:2 autoScale=off visibility=full
bigDataUrl=http://dldcc-web.brc.bcm.edu/lilab/jlyu/ENL2/bw/Sorted_ChIP15_WT_Pol_II_S2PNormalised.bw
track type=bigWig name="PolII S2P T1" db=hg19 windowingFunction=maximum viewLimits=0:2 autoScale=off visibility=full
bigDataUrl=http://dldcc-web.brc.bcm.edu/lilab/jlyu/ENL2/bw/Sorted_ChIP15_T1_Pol_II_S2PNormalised.bw
track type=bigWig name="PolII S2P T2" db=hg19 windowingFunction=maximum viewLimits=0:2 autoScale=off visibility=full
bigDataUrl=http://dldcc-web.brc.bcm.edu/lilab/jlyu/ENL2/bw/Sorted_ChIP15_T2_Pol_II_S2PNormalised.bw
track type=bigWig name="PolII S2P T3" db=hg19 windowingFunction=maximum viewLimits=0:2 autoScale=off visibility=full
bigDataUrl=http://dldcc-web.brc.bcm.edu/lilab/jlyu/ENL2/bw/Sorted_ChIP15_T3_Pol_II_S2PNormalised.bw
```

Methodology

Replicates	HEK293 Flag ChIP-seq: wt, T1 ,T2, T3 and control: 2 replicates HEK293 Flag-ENL wt, T1, T2 and T3 RNA-seq: 2 replicates HK-2 Flag-ENL wt, T1, T2 and T3 RNA-seq: 2 replicates all others: 1 replicate Note: Key target genes were validated by ChIP-qPCR and gene expression qPCR analyses for all conditions in additional, independent repeated experiments (n>3).
Sequencing depth	Sample Sequencing depth GSM3564782 ChIPSeq.PolII_S2P_T1_mut 74852492 GSM3564783 ChIPSeq.PolII_S2P_T2_mut 86431056 GSM3564784 ChIPSeq.PolII_S2P_T3_mut 82360591 GSM3564785 ChIPSeq.PolII_S2P_WT_ENL 67652603 GSM3564786 ChIPSeq.CDK9_T1_mut 66925666 GSM3564787 ChIPSeq.CDK9_T2_mut 76629800 GSM3564788 ChIPSeq.CDK9_T3_mut 94390261 GSM3564789 ChIPSeq.CDK9_WT_ENL 84910393 GSM3564790 ChIPSeq.HEK293_WT_ENL_B 68322465 GSM3564791 ChIPSeq.HEK293_T1_mut_C 93069874 GSM3564792 ChIPSeq.HEK293_T1_Y78A_mut 75093254 GSM3564793 ChIPSeq.HEK293_T2_B_mut 61175503 GSM3564794 ChIPSeq.HEK293_T2_Y78A_mut 68255927 GSM3564795 ChIPSeq.HEK293_T3_B_mut 68788471 GSM3564796 ChIPSeq.HEK293_T3_Y78A_mut 69951070 GSM3564797 ChIPSeq.HEK293_vec 61797238 GSM3564798 ChIPSeq.HEK293_Y78A_B_mut 68043038 GSM3564799 ChIPSeq.HEK293_F_ENL 71607516 GSM3564800 ChIPSeq.HEK293_F_T1_mut 72912339 GSM3564801 ChIPSeq.HEK293_F_T2_mut 82750115 GSM3564802 ChIPSeq.HEK293_F_T3_mut 79967093 GSM3564803 ChIPSeq.HEK293_input 82872696 GSM3564804 ChIPSeq.HK2_F_ENL 80396084 GSM3564805 ChIPSeq.HK2_F_T1_mut 62880686 GSM3564806 ChIPSeq.HK2_F_T2_mut 59955976 GSM3564807 ChIPSeq.HK2_F_T3_mut 62638629 GSM3564808 ChIPSeq.HK2_input_S31 63931469
Antibodies	Antibodies used in ChIP-seq in this study: Flag (Sigma, F1804), CDK9 (Santa Cruz, sc-13130), Pol II S2P (Abcam, ab5095), and H3K79me2 (Abcam, ab3594), and more detailed in Supplementary Method and Supplementary Tables
Peak calling parameters	bowtie hg19 -v 1 -r --best --strata -m 1 -p 8 *.seq *.bowtie macs14 -t *.bed -c Input.bed -g hs --tsize=* --wig
Data quality	FASTQC 0.11.8 is run to check the sequencing quality.
Software	FASTQC 0.11.8;Bowtie1 v1.1.0; MACS (version 1.4.2); R package VennDiagram v1.6;deepTools v2.0 edgeR 3.26.0.

Article

Regulation of α-synuclein by chaperones in mammalian cells

https://doi.org/10.1038/s41586-019-1808-9

Received: 9 July 2017

Accepted: 21 October 2019

Published online: 4 December 2019

Björn M. Burmann[1,2,3,9]*, Juan A. Gerez[4,9], Irena Matečko-Burmann[1,3,5], Silvia Campioni[4,7], Pratibha Kumari[4], Dhiman Ghosh[4], Adam Mazur[1], Emelie E. Aspholm[2,3], Darius Šulskis[2,3], Magdalena Wawrzyniuk[6,8], Thomas Bock[1], Alexander Schmidt[1], Stefan G. D. Rüdiger[6], Roland Riek[4]* & Sebastian Hiller[1]*

Neurodegeneration in patients with Parkinson's disease is correlated with the occurrence of Lewy bodies—intracellular inclusions that contain aggregates of the intrinsically disordered protein α-synuclein[1]. The aggregation propensity of α-synuclein in cells is modulated by specific factors that include post-translational modifications[2,3], Abelson-kinase-mediated phosphorylation[4,5] and interactions with intracellular machineries such as molecular chaperones, although the underlying mechanisms are unclear[6–8]. Here we systematically characterize the interaction of molecular chaperones with α-synuclein in vitro as well as in cells at the atomic level. We find that six highly divergent molecular chaperones commonly recognize a canonical motif in α-synuclein, consisting of the N terminus and a segment around Tyr39, and hinder the aggregation of α-synuclein. NMR experiments[9] in cells show that the same transient interaction pattern is preserved inside living mammalian cells. Specific inhibition of the interactions between α-synuclein and the chaperone HSC70 and members of the HSP90 family, including HSP90β, results in transient membrane binding and triggers a remarkable re-localization of α-synuclein to the mitochondria and concomitant formation of aggregates. Phosphorylation of α-synuclein at Tyr39 directly impairs the interaction of α-synuclein with chaperones, thus providing a functional explanation for the role of Abelson kinase in Parkinson's disease. Our results establish a master regulatory mechanism of α-synuclein function and aggregation in mammalian cells, extending the functional repertoire of molecular chaperones and highlighting new perspectives for therapeutic interventions for Parkinson's disease.

We characterized the interactions of an array of molecular chaperones with α-synuclein on the basis of previous findings that have shown that molecular chaperones share common patterns of client recognition[10,11]. The array included human HSC70 and HSP90β, and bacterial chaperones SecB, Skp, SurA and Trigger Factor, all of which have strongly diverse architectures[10]. All of these chaperones interfered functionally with the aggregation of α-synuclein in a thioflavin T assay[6,8,12], showing effects already at a stoichiometry of 1:20 (chaperone:α-synuclein) and even stronger effects at 1:10 ratios (Fig. 1a–c). The known HSP90 inhibitors geldanamycin and radicicol (referred to hereafter as drugs) decreased the chaperoning effect of HSP90β (Fig. 1c), consistent with the known mechanism of these drugs[13,14]. We determined the segments of α-synuclein that interact with the individual chaperones at the atomic level by measuring the attenuation of the NMR signal intensity and chemical-shift perturbations using two-dimensional [^{15}N, ^{1}H]-NMR spectroscopy. For all 6 chaperones, the effects were most pronounced for 12 amino acid residues at the N terminus and for 6 residues around Tyr39, indicating that a direct—albeit transient—intermolecular interaction occurs via these 2 segments, which are therefore identified as the canonical chaperone-interaction motif of α-synuclein (Fig. 1d–g and Extended Data Figs. 1, 2). Inhibition of HSP90β using drugs partially impaired the interaction with α-synuclein. For HSC70, the interaction was observed in the ADP-bound ($HSC70_{ADP}$) and the ATP-bound ($HSC70_{ATP}$), but not the apo, state (Fig. 1g and Extended Data Fig. 3), consistent with previous reports[6,15,16] (Supplementary Discussion). Notably, for all six chaperones, the interactions were observed at protein concentrations of 100 μM, which suggests that these interactions are unlikely to arise from nonspecific effects of macromolecular crowding. We investigated such nonspecific effects using high concentrations of either bovine serum albumin (BSA) or ubiquitin. The

[1]Biozentrum, University of Basel, Basel, Switzerland. [2]Department of Chemistry and Molecular Biology, University of Gothenburg, Gothenburg, Sweden. [3]Wallenberg Centre for Molecular and Translational Medicine, University of Gothenburg, Gothenburg, Sweden. [4]Laboratory of Physical Chemistry, Department of Chemistry and Applied Biosciences, Eidgenössische Technische Hochschule Zürich, Zurich, Switzerland. [5]Department of Psychiatry and Neurochemistry, University of Gothenburg, Gothenburg, Sweden. [6]Cellular Protein Chemistry, Bijvoet Center for Biomolecular Research and Science for Life, Utrecht University, Utrecht, The Netherlands. [7]Present address: Cellulose and Wood Materials Laboratory, Department of Functional Materials, Empa, Dübendorf, Switzerland. [8]Present address: Department of Infectious Diseases and Immunology, Utrecht University, Utrecht, The Netherlands. [9]These authors contributed equally: Björn M. Burmann, Juan A. Gerez. *e-mail: bjorn.marcus.burmann@gu.se; roland.riek@phys.chem.ethz.ch; sebastian.hiller@unibas.ch

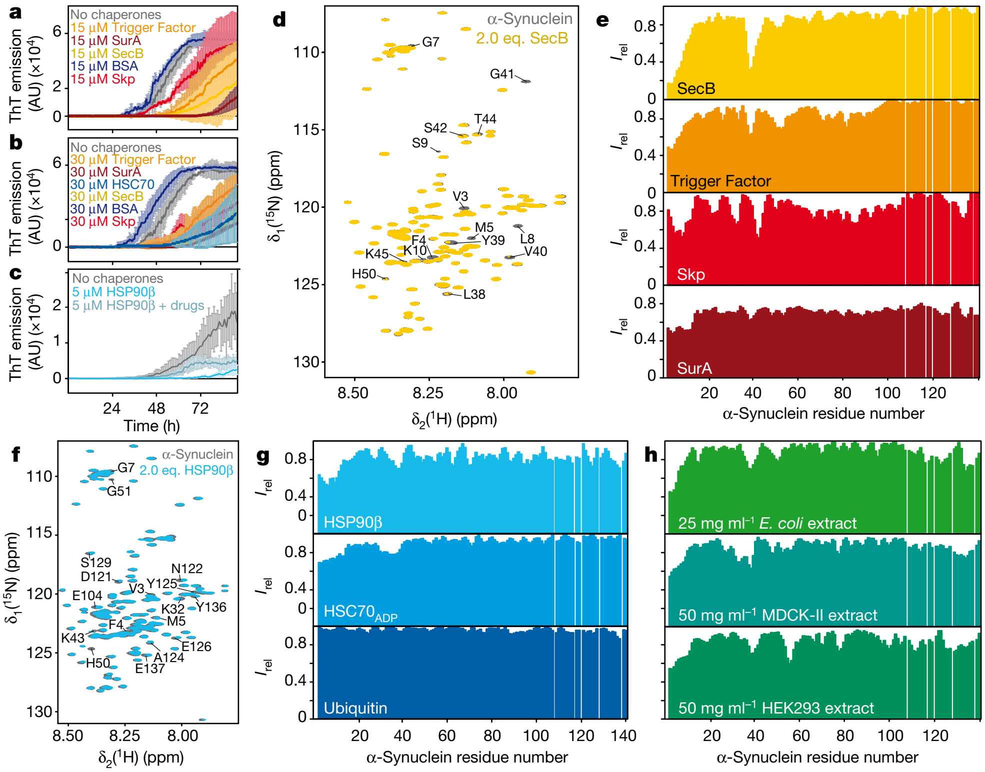

Fig. 1 | Molecular chaperones prevent aggregation through the interaction with the N terminus of α-synuclein. a, b, Thioflavin T (ThT) emission curves of 300 μM α-synuclein in the presence or absence of chaperones (15 μM (**a**) or 30 μM (**b**)). **c**, Thioflavin T emission curves of 100 μM α-synuclein in the presence of 5 μM HSP90β with and without the addition of 1 μM of drugs. **a**–**c**, Data are mean ± s.d. ($n = 3$). AU, arbitrary units. **d**, Overlay of two-dimensional [^{15}N, ^{1}H]-NMR spectra of 250 μM [*U*-^{15}N]-α-synuclein in the absence (grey) and presence (yellow) of 500 μM of SecB tetramer ($n = 3$, with similar results). **e**, Residue-resolved backbone amide NMR signal attenuation ($I_{rel} = I/I_0$) of α-synuclein upon addition of two equivalents (eq.) of SecB tetramer (yellow), Trigger Factor dimer (orange), Skp trimer (red) or SurA dimer (dark red). **f**, Overlay of two-dimensional [^{15}N, ^{1}H]-NMR spectra of [*U*-^{15}N]-α-synuclein in the absence (grey) and presence (cyan) of two equivalents HSP90β dimer ($n = 2$, with similar results). **g**, **h**, Residue-resolved backbone amide NMR signal attenuation ($I_{rel} = I/I_0$) of α-synuclein upon addition of two equivalents of HSP90β dimer (cyan), HSC70$_{ADP}$ (light blue), and ubiquitin (dark blue) as well as *E. coli* cell extract (green), mammalian MDCK-II cell extract (blue) and mammalian HEK293 cell extract (green). **e**, **g**, **h**, Values that are less than 1.0 indicate intermolecular interactions.

signal was not attenuated after addition of 150–310 mg ml^{-1} ubiquitin, thus excluding the possibility that these interactions arose because of macromolecular crowding effects. For high concentrations of BSA the canonical chaperone-interaction signature is observed (Fig. 1g and Extended Data Fig. 3d–j), owing to the weak molecular chaperone function of BSA[17]. Taken together, these experiments using six chaperones and two control proteins revealed that there is a canonical chaperone interaction with α-synuclein at the N terminus and around Tyr39 that is transient in nature. Notably, it comprises the two segments of α-synuclein that are locally the most hydrophobic (Extended Data Fig. 3k, l), indicating an importance of hydrophobic residues for the interaction with chaperones.

To characterize the physiological role of chaperone–α-synuclein interactions, we determined the affinity of α-synuclein for HSC70$_{ADP}$, SecB and Skp using bio-layer interferometry. α-Synuclein binds to each of these chaperones with affinities ranging from 1 to 2 μM (Extended Data Fig. 4 and Supplementary Table 1). The ΔN-α-synuclein variant, which lacks 10 N-terminal residues, shows a decrease in affinity of two orders of magnitude, validating that this segment is part of the interaction site. At the reported cellular concentrations of α-synuclein in neuronal synapses of approximately 50 μM combined with a concentration of around 70 μM of the chaperones HSP70 and HSP90[18], about 90% of cellular α-synuclein can therefore be bound to chaperones.

We then analysed published data on the NMR intensity profiles of α-synuclein inside living mammalian cells, and found that these data feature the canonical chaperone-interaction signature[9]. Because this pattern has been suggested to arise from interactions with cellular membranes, we first characterized α-synuclein in soluble cellular extracts, which were devoid of membranes, from *Escherichia coli* cells or mammalian HEK293 and MDCK-II cells. Notably, in each case we observed the canonical chaperone-interaction pattern (Fig. 1h and Extended Data Fig. 5a–d), indicating that this pattern does not result from the interaction with membranes. Second, we characterized the interaction pattern of α-synuclein with lipid bilayer membranes in vitro. Titrating large unilamellar vesicles (LUVs) with α-synuclein in a 125:1 lipid:protein ratio leads to a uniform decrease in the NMR signal for amino acid residues 1–90 of α-synuclein (Extended Data Fig. 6a), in agreement with previously published reports[9,19]. Adding 2–6 equivalents of SecB to solutions containing α-synuclein and LUV restored the chaperone signature, whereas the reverse experiment—that is, the addition of LUVs to an existing SecB–α-synuclein complex—led to attenuation of the NMR signal for amino acid residues 1–90 of α-synuclein, indicating that LUVs and SecB mutually compete for binding to α-synuclein (Extended Data Fig. 6). Overall, the data suggest that α-synuclein is in an equilibrium between its free state, its membrane-bound state and its chaperone-bound state, of which the last two states are mutually exclusive. The emerging hypothesis that, in mammalian cells, α-synuclein is predominantly in contact with chaperones rather than with the lipid bilayer was supported by the experimental determination of the interactome of the N terminus of α-synuclein in mammalian cells using chemical cross-linking and mass spectrometry. The interactome consists of a large number of molecular chaperones

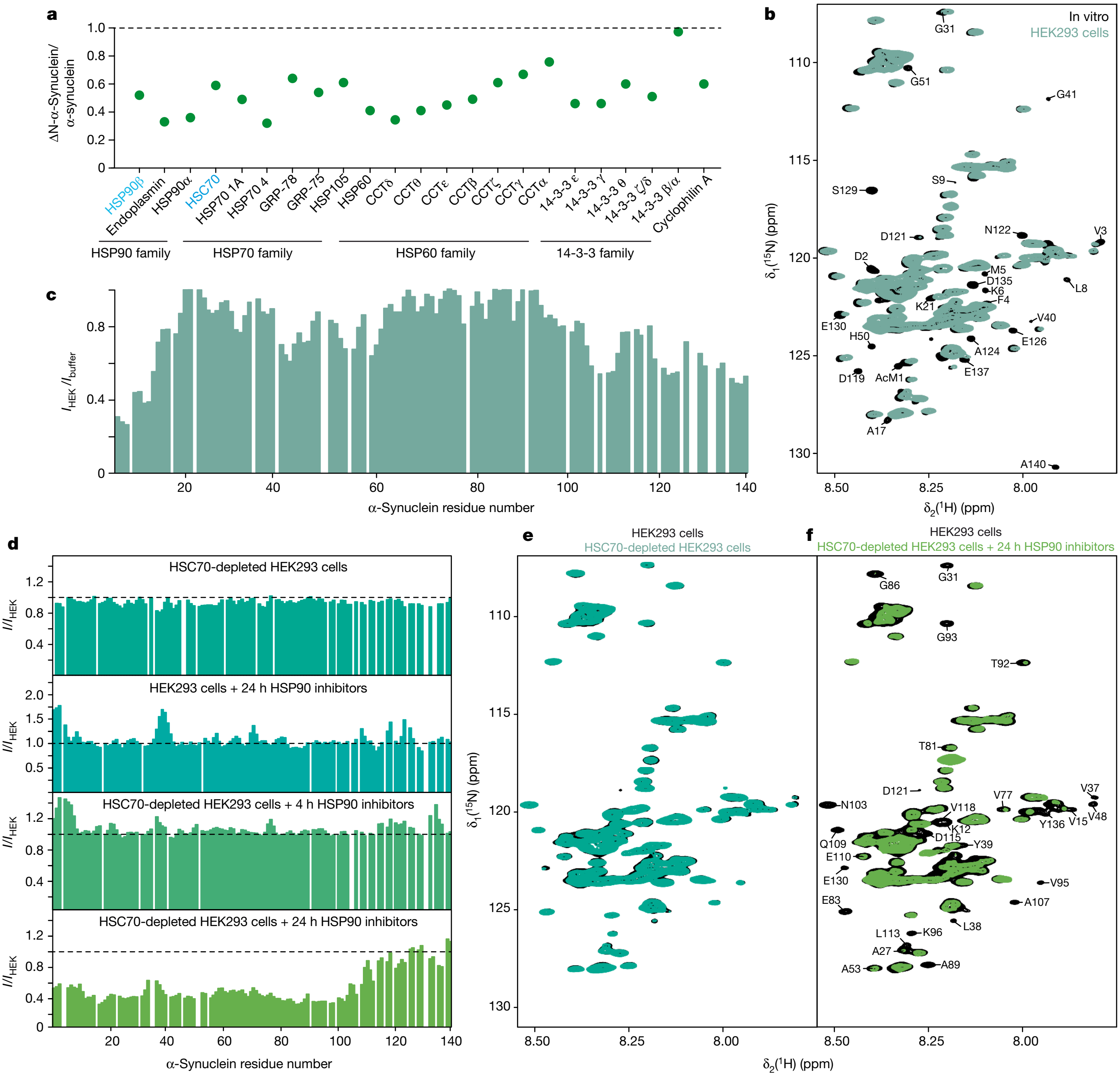

Fig. 2 | The interaction between α-synuclein and chaperones is dominant in living cells. a, Abundance ratios of proteins bound to ΔN-α-synuclein versus wild-type full-length α-synuclein determined by relative quantitative mass spectrometry (mean values, $n = 2$). **b**, Overlay of two-dimensional [^{15}N, ^{1}H]-NMR spectra of [U-^{15}N]-α-synuclein in NMR buffer (black) and inside living HEK293 cells (blue-green). Representative spectrum from $n > 5$. **c**, Residue-resolved backbone amide NMR signal attenuation (I_{HEK}/I_{buffer}) of α-synuclein in mammalian cells. **d**, NMR signal attenuation in treated cells, relative to untreated cells (I/I_{HEK}). Different combinations of HSC70 depletion and HSP90 inhibition were applied, as indicated. **e**, **f**, Overlay of two-dimensional [^{15}N, ^{1}H]-NMR spectra of [U-^{15}N]-α-synuclein in untreated HEK293 cells (black) and in HSC70-depleted HEK293 cells (green) (**e**) or in HSC70-depleted HEK293 cells after 24 h of HSP90 inhibition (green) (**f**). Representative data (**d**–**f**) for three technical replicates, with similar results.

that had abundances ranging between 30 and 75%, including several isoforms of HSP90 and six HSP70 isoforms (Fig. 2a; see Supplementary Information for details).

NMR spectroscopy in cells

Next, we carried out NMR experiments in cells to study the interaction between α-synuclein and chaperones inside living mammalian cells at atomic resolution. [U-^{15}N]-α-Synuclein was delivered into HEK293 cells at concentrations of 3–10 μM, yielding intensity patterns that are characteristic for mammalian cell lines[9] (Fig. 2b, c), such as the canonical chaperone-interaction signature. Multiple molecular chaperones are present in the cell that have mutually overlapping functions and 'clientomes'[20]. To complement the in vitro chaperone analyses, we investigated two of the most abundant chaperones found in mammalian cells, HSC70 and HSP90β. When [U-^{15}N]-α-synuclein was delivered into HEK293 cells with reduced HSC70 levels (Extended Data Fig. 7c, d), the NMR intensity profile resembled the one observed for untreated cells, suggesting that there is functional redundancy between HSC70 and other chaperones in these cells (Fig. 2d, e). Next, we treated HEK293

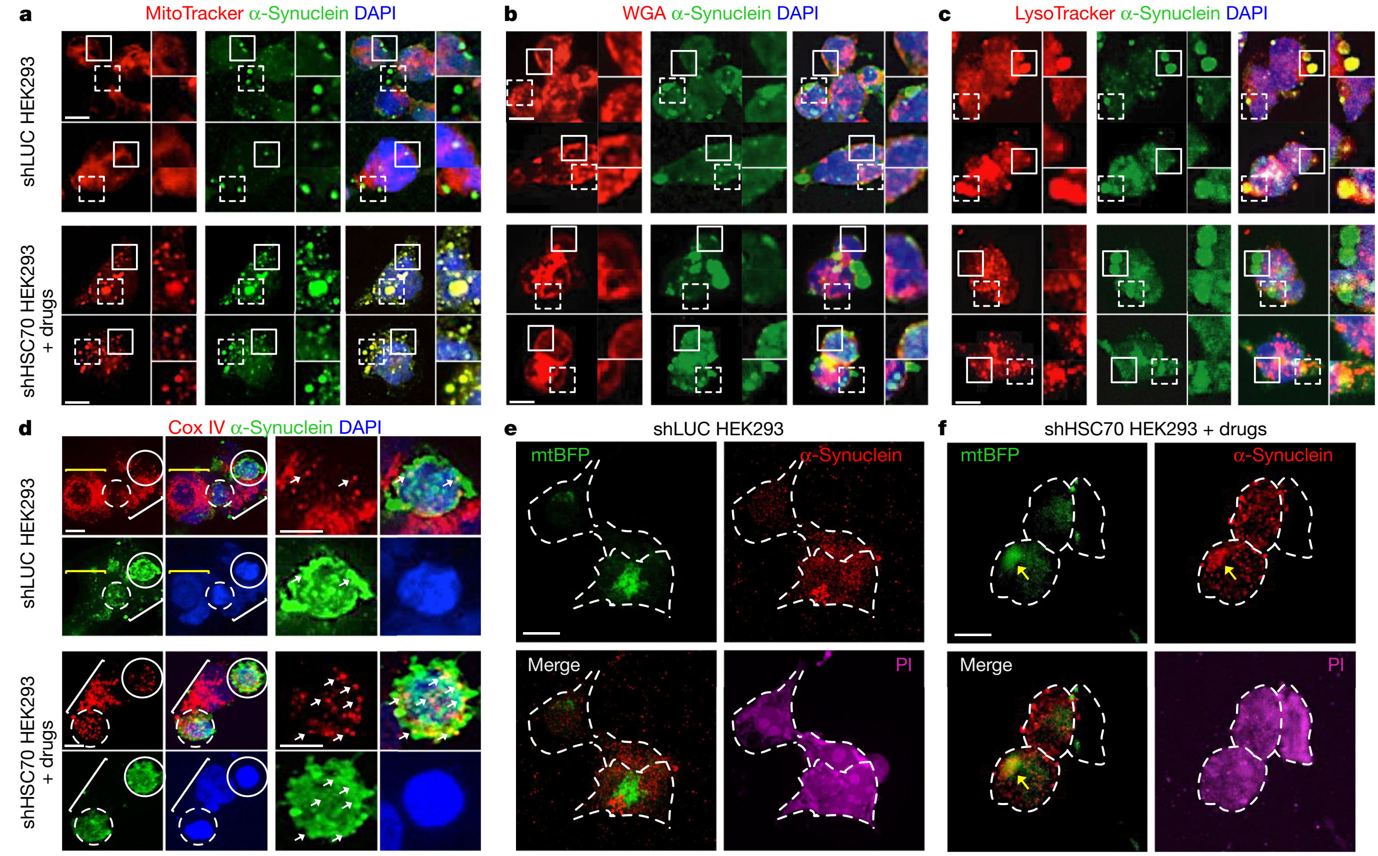

Fig. 3 | Co-localization of α-synuclein and cellular organelles assessed using immunofluorescence. a–**f**, Immunofluorescence analysis of α-synuclein electroporated into HEK293 cells. Cells were treated with either a control short hairpin RNA (shRNA) targeting Firefly luciferase (shLUC) or a combination of an shRNA targeting *HSC70* (shHSC70) and inhibitors of HSP90 (shHSC70 + drugs). Cells were stained with MitoTracker (red; **a**) to stain mitochondria, DAPI (blue) to stain cell nuclei, an α-synuclein-specific antibody (green) and either wheat germ agglutinin (WGA; red in **b**) to stain the plasma membrane and the endoplasmatic reticulum or LysoTracker (red in **c**) to stain acidic vesicles such as lysosomes. Outlines indicate areas of intense signal for MitoTracker and α-synuclein. Solid outlines, top magnifications; dashed outlines, bottom magnifications. **d**, Cox IV (red, mitochondrial marker) and α-synuclein (green) were visualized by specific antibodies, nuclei were stained with DAPI (blue). Circles indicate cells with high α-synuclein content, brackets indicate cells with low α-synuclein content. Solid outlines, magnified on the right. Arrows indicate the positions of selected colocalization spots. **e**, **f**, Control HEK293 cells (shLUC; **e**) or HEK293 cells treated for the combined knockdown of HSC70 and inhibition of HSP90 (shHSC70 + drugs; **f**) were stably transfected with an expression plasmid containing the mitochondrial marker mtBFP. Cells were fixed and subjected to immunofluorescence analyses using an anti-α-synuclein antibody. Propidium iodide (PI) was used to stain cells to enable the visualization of cell morphology. Note, the blue colour of mtBFP was changed to green to better visualize the co-localization of mtBFP and α-synuclein. Scale bars, 10 μm. Experiments were performed twice, with similar results.

cells with the HSP90-inhibiting drugs, and found that the canonical chaperone-interaction motif showed increased intensities compared to untreated cells (Fig. 2d). This suggests that HSP90 chaperones physically and transiently interact with α-synuclein in cells, and that this interaction is lost upon drug treatment. Immunoprecipitation assays confirmed that this interaction is almost completely lost 24 h after treatment (Extended Data Fig. 7e). Finally, we simultaneously inhibited both HSC70 and HSP90, and observed a moderate effect on the canonical chaperone-interaction motif 4 h after treatment, at which point a substantial fraction of HSP90 still remains bound to α-synuclein (Extended Data Fig. 7e). At this time point, a low but measurable amount of free intracellular α-synuclein was observed (Fig. 2d). At 24 h after treatment, a marked global reduction in the signal of amino acid residues 1–90 of α-synuclein was observed, which was essentially identical to the LUV interaction pattern and to the profile that has previously been reported in which α-synuclein was bound to bacterial membranes[19,21] (Fig. 2d, f). The combined inhibition of the two types of chaperone (HSC70 and HSP90) therefore leads to a transient membrane interaction of α-synuclein, which is absent in the basal state of cells. Furthermore, in these experiments, we observed the formation of stable high-molecular-mass aggregates that contained α-synuclein (Extended Data Fig. 7f). Overall, these in-cell NMR and in vitro experiments show that, in cells, α-synuclein transiently interacts with a pool of constitutively expressed chaperones and that this interaction predominates over the transient interaction of α-synuclein with lipid bilayer membranes. In cells such as neurons[18,22], as well as in our experiments using HEK293 cells, the concentration of chaperones is substantially larger than the concentrations of α-synuclein, highlighting the physiological relevance of these observations (Extended Data Fig. 7g, h).

Intracellular membrane localization

The interactions between α-synuclein and cellular membranes after inhibition of HSC70 and HSP90 may be a key mechanism for disease pathogenesis and we thus aimed to identify the membranous organelle that is involved using co-localization analyses. To this end, control cells and HEK293 cells depleted of HSC70 and treated with drugs for 24 h were first stained with MitoTracker (which stains mitochondria), LysoTracker (which stains acidic vesicles such as lysosomes) or Alexa-Fluor-labelled wheat germ agglutinin (which stains the plasma membrane and endoplasmic reticulum) and subsequently immunostained with anti-α-synuclein antibodies. These experiments revealed a strong colocalization of α-synuclein with mitochondria after the chaperones were depleted (Fig. 3a–c). To further confirm this association, we

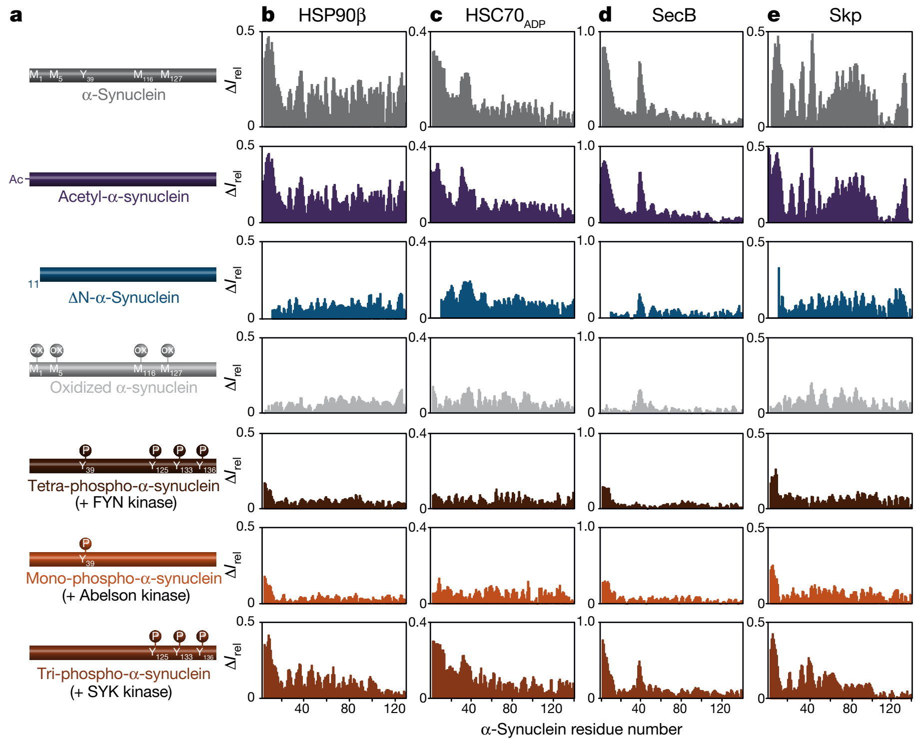

Fig. 4 | Effect of post-translational modifications on the chaperone–α-synuclein interaction. a, Modified α-synuclein variants. **b**–**e**, Residue-resolved backbone amide NMR signal attenuation ($\Delta I_{rel} = 1 - I/I_0$) of the α-synuclein variants upon interaction with two equivalents of HSP90β dimer (**b**), $HSC70_{ADP}$ (**c**), SecB tetramer (**d**) or Skp trimer (**e**). Increased ΔI_{rel} values are indicative of an interaction.

carried out immunofluorescence analyses using antibodies that were specific to the mitochondrial marker CoxIV and α-synuclein (Fig. 3d). In a complementary experiment, we expressed the marker mitochondrial blue-fluorescent protein (mtBFP) in control and HSC70- and HSP90-deficient HEK293 cells and stained α-synuclein with antibodies (Fig. 3e, f). Both approaches confirmed the localization of α-synuclein to mitochondria after HSC70 and HSP90 inhibition.

Effect of post-translational modifications

After establishing the canonical chaperone-interaction signature and validating its presence in living mammalian cells, we investigated the effect of chemical modifications on the α-synuclein–chaperone interaction. Using the chaperones HSP90β, $HSC70_{ADP}$, SecB and Skp, we analysed the effects of N-terminal acetylation of α-synuclein, the predominant form in mammalian cells[9,19]. N-terminal acetylation does not interfere with the interaction between α-synuclein and chaperones (Fig. 4 and Extended Data Fig. 8a–g). By contrast, ΔN-α-synuclein has a greatly reduced interaction with all chaperones, in agreement with the bio-layer interferometry experiments, and showing a synergistic effect between the N terminus and the amino acid region around Tyr39 (Fig. 4b–e). Cellular oxidative stress and an imbalance in reactive oxygen species are known hallmarks of the onset of Parkinson's disease, leading to the oxidative modification of α-synuclein[2]. Titrating of HSP90β, $HSC70_{ADP}$, SecB or Skp with methionine-oxidized α-synuclein[23] showed that oxidation of Met1 and Met5 abolish the N-terminal chaperone interaction (Fig. 4 and Extended Data Fig. 9). Next, we explored the effects of phosphorylation on the interaction with chaperones, using in vitro tyrosine phosphorylation by different kinases[5,24] (Fig. 4 and Extended Data Fig. 9). Titration of SecB, Skp, HSP90β or $HSC70_{ADP}$ with either tetra-phosphorylated or Tyr39-mono-phosphorylated α-synuclein resulted in the elimination of the chaperone interaction, whereas Tyr125-Tyr133-Tyr136-tri-phosphorylated α-synuclein showed the chaperone-interaction pattern of unmodified α-synuclein (Fig. 4). Tyr39 phosphorylation therefore has a specific inhibitory effect on the interaction with chaperones, providing a direct rationale for in vivo studies that have shown that upregulation of Abelson kinase (c-Abl) correlates strongly with Tyr39 phosphorylation and disease progression in Parkinson's disease[5,25].

Conclusion

In summary, we have identified a functional mechanism for the regulation of α-synuclein by chaperones in mammalian cells through transient binding (Extended Data Fig. 10). Molecular chaperones bind to α-synuclein through a canonical motif, by recognizing intrinsic biophysical features at the N terminus and around Tyr39. The interaction is abrogated after inhibition of two major chaperones, and results in transient interactions of α-synuclein with cellular membranes and relocalization of α-synuclein to mitochondria. Aggregates of α-synuclein, as well as mitochondria, have been identified as major components of Lewy bodies[26,27]. We propose a model in which α-synuclein is predominantly found in a transient chaperone-interacting state in healthy cells, indicating that chaperones are a master regulator of the cellular states of α-synuclein. The model also predicts that changes in the activity or cellular levels of chaperones or α-synuclein—or the modulation of their interaction—will disturb the homeostatic balance, eventually causing or promoting Parkinson's disease. Notably, this model is in agreement with a multitude of reported experimental observations (Supplementary Discussion), including studies that have shown that the ratio of α-synuclein to chaperone is deteriorated in familial parkinsonism and that oxidative stress can lead to an increase in the phosphorylation of Tyr39 of α-synuclein[5,25], which interferes with chaperone binding. The model further shows how modulation of chaperone activity might prevent the formation of oligomeric α-synuclein, the aggregation of which leads to the disruption of the mitochondrial membrane[28], and

also accounts for recent reports that impairment of mitochondria may constitute an important factor in Parkinson's disease[29–31].

Reporting summary

Further information on research design is available in the Nature Research Reporting Summary linked to this paper.

Data availability

The data that support the findings of this study are available from the corresponding authors upon request.

Online content

Any methods, additional references, Nature Research reporting summaries, source data, extended data, supplementary information, acknowledgements, peer review information; details of author contributions and competing interests; and statements of data and code availability are available at https://doi.org/10.1038/s41586-019-1808-9.

1. Goedert, M., Spillantini, M. G., Del Tredici, K. & Braak, H. 100 years of Lewy pathology. *Nat. Rev. Neurol*. **9**, 13–24 (2013).
2. Barnham, K. J., Masters, C. L. & Bush, A. I. Neurodegenerative diseases and oxidative stress. *Nat. Rev. Drug Discov*. **3**, 205–214 (2004).
3. Lashuel, H. A., Overk, C. R., Oueslati, A. & Masliah, E. The many faces of α-synuclein: from structure and toxicity to therapeutic target. *Nat. Rev. Neurosci*. **14**, 38–48 (2013).
4. Hantschel, O. & Superti-Furga, G. Regulation of the c-Abl and Bcr–Abl tyrosine kinases. *Nat. Rev. Mol. Cell Biol*. **5**, 33–44 (2004).
5. Mahul-Mellier, A. L. et al. c-Abl phosphorylates α-synuclein and regulates its degradation: implication for α-synuclein clearance and contribution to the pathogenesis of Parkinson's disease. *Hum. Mol. Genet*. **23**, 2858–2879 (2014).
6. Dedmon, M. M., Christodoulou, J., Wilson, M. R. & Dobson, C. M. Heat shock protein 70 inhibits α-synuclein fibril formation via preferential binding to prefibrillar species. *J. Biol. Chem*. **280**, 14733–14740 (2005).
7. Dimant, H., Ebrahimi-Fakhari, D. & McLean, P. J. Molecular chaperones and co-chaperones in Parkinson disease. *Neuroscientist* **18**, 589–601 (2012).
8. Pemberton, S. et al. Hsc70 protein interaction with soluble and fibrillar α-synuclein. *J. Biol. Chem*. **286**, 34690–34699 (2011).
9. Theillet, F. X. et al. Structural disorder of monomeric α-synuclein persists in mammalian cells. *Nature* **530**, 45–50 (2016).
10. Burmann, B. M., Wang, C. & Hiller, S. Conformation and dynamics of the periplasmic membrane-protein–chaperone complexes OmpX–Skp and tOmpA–Skp. *Nat. Struct. Mol. Biol*. **20**, 1265–1272 (2013).
11. He, L., Sharpe, T., Mazur, A. & Hiller, S. A molecular mechanism of chaperone–client recognition. *Sci. Adv*. **2**, e1601625 (2016).
12. Falsone, S. F., Kungl, A. J., Rek, A., Cappai, R. & Zangger, K. The molecular chaperone Hsp90 modulates intermediate steps of amyloid assembly of the Parkinson-related protein α-synuclein. *J. Biol. Chem*. **284**, 31190–31199 (2009).
13. Karagöz, G. E. et al. Hsp90–Tau complex reveals molecular basis for specificity in chaperone action. *Cell* **156**, 963–974 (2014).
14. Schopf, F. H., Biebl, M. M. & Buchner, J. The HSP90 chaperone machinery. *Nat. Rev. Mol. Cell Biol*. **18**, 345–360 (2017).
15. Roodveldt, C. et al. Chaperone proteostasis in Parkinson's disease: stabilization of the Hsp70/α-synuclein complex by Hip. *EMBO J*. **28**, 3758–3770 (2009).
16. Gao, X. et al. Human Hsp70 disaggregase reverses Parkinson's-linked α-synuclein amyloid fibrils. *Mol. Cell* **59**, 781–793 (2015).
17. Finn, T. E., Nunez, A. C., Sunde, M. & Easterbrook-Smith, S. B. Serum albumin prevents protein aggregation and amyloid formation and retains chaperone-like activity in the presence of physiological ligands. *J. Biol. Chem*. **287**, 21530–21540 (2012).
18. Wilhelm, B. G. et al. Composition of isolated synaptic boutons reveals the amounts of vesicle trafficking proteins. *Science* **344**, 1023–1028 (2014).
19. Maltsev, A. S., Ying, J. & Bax, A. Impact of N-terminal acetylation of α-synuclein on its random coil and lipid binding properties. *Biochemistry* **51**, 5004–5013 (2012).
20. Kim, Y. E., Hipp, M. S., Bracher, A., Hayer-Hartl, M. & Hartl, F. U. Molecular chaperone functions in protein folding and proteostasis. *Annu. Rev. Biochem*. **82**, 323–355 (2013).
21. McNulty, B. C., Young, G. B. & Pielak, G. J. Macromolecular crowding in the *Escherichia coli* periplasm maintains α-synuclein disorder. *J. Mol. Biol*. **355**, 893–897 (2006).
22. Cremades, N. et al. Direct observation of the interconversion of normal and toxic forms of α-synuclein. *Cell* **149**, 1048–1059 (2012).
23. Binolfi, A. et al. Intracellular repair of oxidation-damaged α-synuclein fails to target C-terminal modification sites. *Nat. Commun*. **7**, 10251 (2016).
24. Kosten, J. et al. Efficient modification of α-synuclein serine 129 by protein kinase CK1 requires phosphorylation of tyrosine 125 as a priming event. *ACS Chem. Neurosci*. **5**, 1203–1208 (2014).
25. Brahmachari, S. et al. Activation of tyrosine kinase c-Abl contributes to α-synuclein-induced neurodegeneration. *J. Clin. Invest*. **126**, 2970–2988 (2016).
26. Shahmoradian, S. H. et al. Lewy pathology in Parkinson's disease consists of crowded organelles and lipid membranes. *Nat. Neurosci*. **22**, 1099–1109 (2019).
27. Mahul-Mellier, A.-L. et al. The making of a Lewy body: the role of α-synuclein post-fibrillization modifications in regulating the formation and the maturation of pathological inclusions. Preprint at https://www.biorxiv.org/content/10.1101/500058v1 (2018).
28. Fusco, G. et al. Structural basis of membrane disruption and cellular toxicity by α-synuclein oligomers. *Science* **358**, 1440–1443 (2017).
29. Guardia-Laguarta, C., Area-Gomez, E., Schon, E. A. & Przedborski, S. Novel subcellular localization for α-synuclein: possible functional consequences. *Front. Neuroanat*. **9**, 17 (2015).
30. Park, J. S., Davis, R. L. & Sue, C. M. Mitochondrial dysfunction in Parkinson's disease: new mechanistic insights and therapeutic perspectives. *Curr. Neurol. Neurosci. Rep*. **18**, 21 (2018).
31. Reeve, A. K. et al. Mitochondrial dysfunction within the synapses of substantia nigra neurons in Parkinson's disease. *NPJ Parkinsons Dis*. **4**, 9 (2018).
32. Korndörfer, I. P., Dommel, M. K. & Skerra, A. Structure of the periplasmic chaperone Skp suggests functional similarity with cytosolic chaperones despite differing architecture. *Nat. Struct. Mol. Biol*. **11**, 1015–1020 (2004).
33. Ferbitz, L. et al. Trigger factor in complex with the ribosome forms a molecular cradle for nascent proteins. *Nature* **431**, 590–596 (2004).
34. Saio, T., Guan, X., Rossi, P., Economou, A. & Kalodimos, C. G. Structural basis for protein antiaggregation activity of the trigger factor chaperone. *Science* **344**, 1250494 (2014).
35. Bull, H. B. & Breese, K. Surface tension of amino acid solutions: a hydrophobicity scale of the amino acid residues. *Arch. Biochem. Biophys*. **161**, 665–670 (1974).
36. Rüdiger, S., Germeroth, L., Schneider-Mergener, J. & Bukau, B. Substrate specificity of the DnaK chaperone determined by screening cellulose-bound peptide libraries. *EMBO J*. **16**, 1501–1507 (1997).
37. Banerjee, P. R., Moosa, M. M. & Deniz, A. A. Two-dimensional crowding uncovers a hidden conformation of α-synuclein. *Angew. Chem. Int. Edn* **55**, 12789–12792 (2016).

Acknowledgements We thank S. Grzesiek, D. Otzen, M. Goedert, B. Bukau, D. P. Mulvihill and D. Kahne for providing plasmids; T. Maier and M. Plodinec for providing mammalian cell lines; E. Stuttfeld and D. Asgeirsson for technical help with cell-culture experiments; V. Juvin for help with graphic design; and the Swedish NMR Centre of the University of Gothenburg for spectrometer time. This work was supported by the Swiss National Science Foundation (PP00P3_128419 to S.H., Ambizione Fellowship PZ00P3_148238 to B.M.B. and Marie Heim-Vögtlin PMPDP3_164425 to S.C.) as well as the European Research Council (FP7 contract MOMP 281764 to S.H.). B.M.B. also acknowledges funding from the Swedish Research Council and the Knut and Alice Wallenberg Foundation through a Wallenberg Academy Fellowship as well as through the Wallenberg Centre for Molecular and Translational Medicine, University of Gothenburg, Sweden. S.G.D.R. was supported by a ZonMW TOP grant (91215084) and Marie-Curie Actions of the 7th Framework programme of the EU (608180).

Author contributions B.M.B. expressed and purified chaperones, and performed NMR experiments. B.M.B. and S.C. expressed and purified α-synuclein variants with help of P.K. E.E.A. and D.Š. supported protein purification of chaperones as well as α-synuclein variants. J.A.G. prepared and performed in-cell NMR experiments as well as chaperone knockdown experiments and immunofluorescence experiments. S.C. and D.G. performed the aggregation assays. I.M.-B. performed cell-culture experiments, prepared lipid vesicles, performed and analysed mass spectrometry experiments together with T.B. and A.S. A.M. performed model calculations. M.W. and S.G.D.R. provided purified HSP90β for interaction studies. B.M.B., S.C., R.R. and S.H. designed the study, analysed the data and wrote the manuscript with input from all co-authors.

Competing interests The authors declare no competing interests.

Additional information

Supplementary information is available for this paper at https://doi.org/10.1038/s41586-019-1808-9.

Correspondence and requests for materials should be addressed to B.M.B., R.R. or S.H.

Peer review information *Nature* thanks Gary J. Pielak and the other, anonymous, reviewer(s) for their contribution to the peer review of this work.

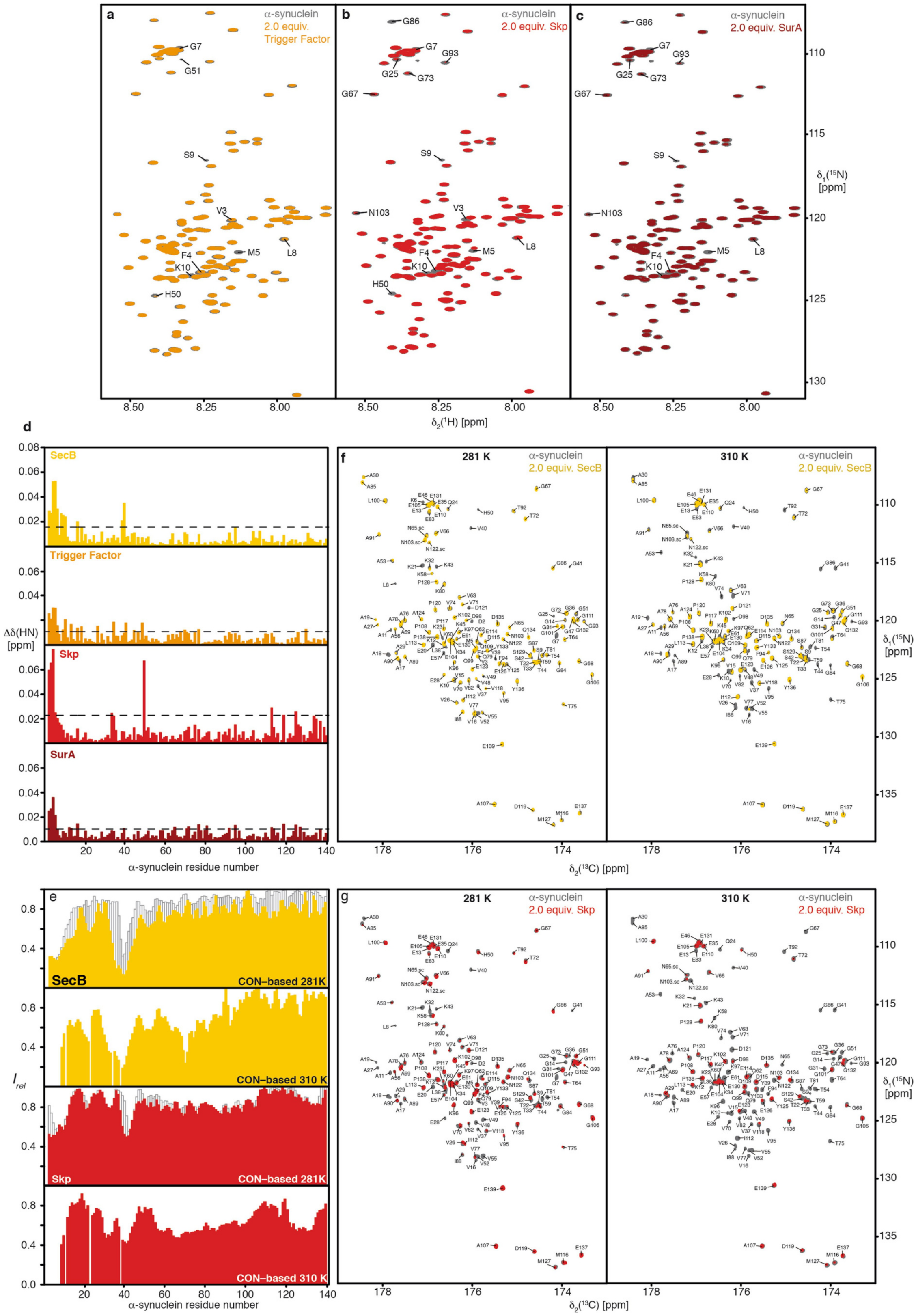

Extended Data Fig. 1 | See next page for caption.

Extended Data Fig. 1 | Interaction between α-synuclein and bacterial chaperones. **a**–**c**, Overlay of two-dimensional [^{15}N, ^{1}H]-NMR spectra of 250 μM [U-^{15}N]-α-synuclein in the absence (grey) and presence (orange, red or dark red) of 500 μM chaperones. The sequence-specific assignments for significantly affected resonances are indicated. **d**, Residue-resolved chemical-shift perturbations of α-synuclein caused by the addition of two equivalents of SecB tetramer (yellow), Trigger Factor dimer (orange), Skp trimer (red) or SurA dimer (dark red). Broken lines indicate a significance level of two s.d. from the mean. **e**, Temperature dependence of the α-synuclein interaction with either SecB (yellow) or Skp (red) monitored by residue-resolved intensity ratios ($I_{rel} = I/I_0$) of ^{13}C-direct-detected two-dimensional [^{15}N, ^{13}C]-NMR spectra. The intensity ratios of two-dimensional [^{15}N, ^{1}H]-NMR spectra at 281 K (Fig. 1c) are shown as an outline (grey). **f**, **g**, Overlay of two-dimensional [^{13}C, ^{15}N]-NMR spectra of 500 μM [U-^{13}C, ^{15}N]-α-synuclein in the absence (grey) and presence of 1 mM of SecB tetramer (**f**; yellow) or 1 mM of Skp trimer (**g**; red). Experiments were performed at 281 K and 310 K as indicated. The sequence-specific resonance assignment is shown. Experiments in **a**–**c**, **f**, **g** were done in duplicates, with similar results.

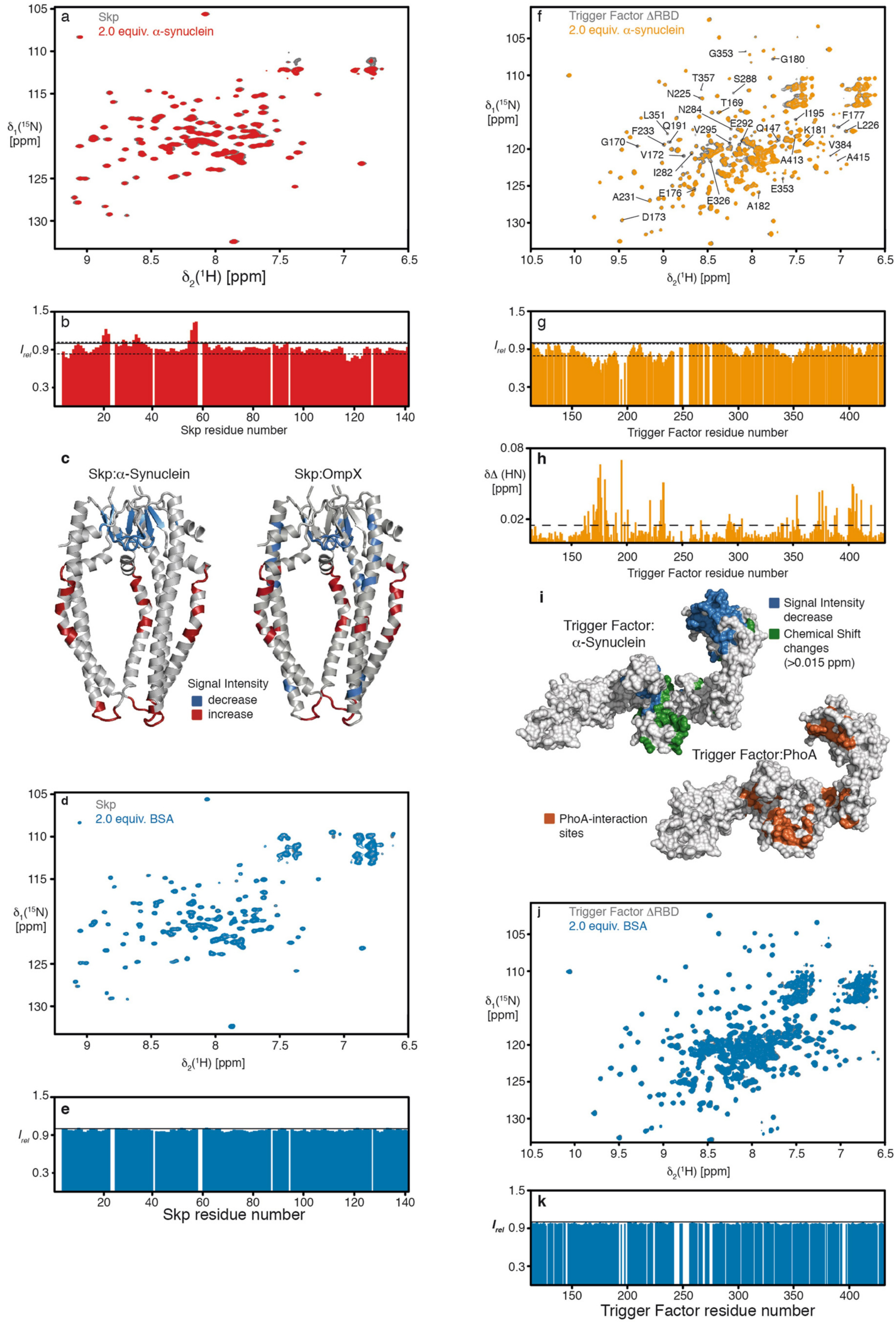

Extended Data Fig. 2 | See next page for caption.

Extended Data Fig. 2 | Chaperones Skp and Trigger Factor bind α-synuclein at their native client sites. a, Overlay of two-dimensional [^{15}N, ^{1}H]-NMR spectra of 250 μM [U-^{2}H, ^{15}N]-Skp in the absence (grey) and presence (red) of 750 μM α-synuclein. **b**, Residue-resolved NMR signal intensity ratios ($I_{rel} = I/I_0$) of Skp (250 μM) in the presence of three equivalents of α-synuclein measured at 310 K. The thin dashed lines indicate a significance level of one s.d. from the mean. The solid line represents an intensity ratio of 1. **c**, α-Synuclein induced intensity changes plotted on the Skp crystal structure (RCSB Protein Data Bank code (PDB) 1SG2)[32] and previously reported effects upon binding of its native client OmpX[10]. A decrease in the signal intensity of more than one s.d. is highlighted in blue, whereas an increase in signal intensity is highlighted in red. **d**, Overlay of two-dimensional [^{15}N, ^{1}H]-NMR spectra of 250 μM [U-^{2}H, ^{15}N]-Skp in the absence (grey) and presence (blue) of 500 μM BSA. **e**, Residue-resolved NMR signal intensity ratios ($I_{rel} = I/I_0$) of Skp (250 μM) in the presence of two equivalents of BSA measured at 310 K. The solid line represents an intensity ratio of 1. **f**, Overlay of two-dimensional [^{15}N, ^{1}H]-NMR spectra of 250 μM [U-^{2}H, ^{15}N]-TF(ΔRBD), a monomeric Trigger Factor (TF) variant that lacks its ribosome-binding and main dimerization domain (RBD), in the absence (grey) and presence (orange) of 750 μM α-synuclein. **g**, Residue-resolved NMR signal intensity ratios ($I_{rel} = I/I_0$) of 250 μM TF(ΔRBD) in the presence of three equivalents of α-synuclein measured at 298 K. The thin broken lines indicate a significance level of one s.d. from the mean. The thick line represents an intensity quotient of 1. **h**, Residue-resolved combined chemical-shift differences of the amide moieties. The broken line indicates a significance level of two s.d. from the mean. **i**, Significant chemical-shift changes (green) and intensity decrease (blue) plotted on the Trigger Factor structure (PDB 1W26)[33]. Comparison with the published Trigger Factor interaction sites of PhoA (orange)[34]. **j**, Overlay of two-dimensional [^{15}N, ^{1}H]-NMR spectra of 250 μM [U-^{2}H, ^{15}N]-TF(ΔRBD) in the absence (grey) and presence (blue) of 500 μM BSA. **k**, Residue-resolved NMR signal intensity ratios ($I_{rel} = I/I_0$) of TF(ΔRBD) (250 μM) in the presence of two equivalents of BSA measured at 298 K. The solid line represents an intensity ratio of 1. Experiments with α-synuclein (**a**, **f**) were done as duplicates yielding similar results, whereas control experiments with BSA (**d**, **j**) were performed once.

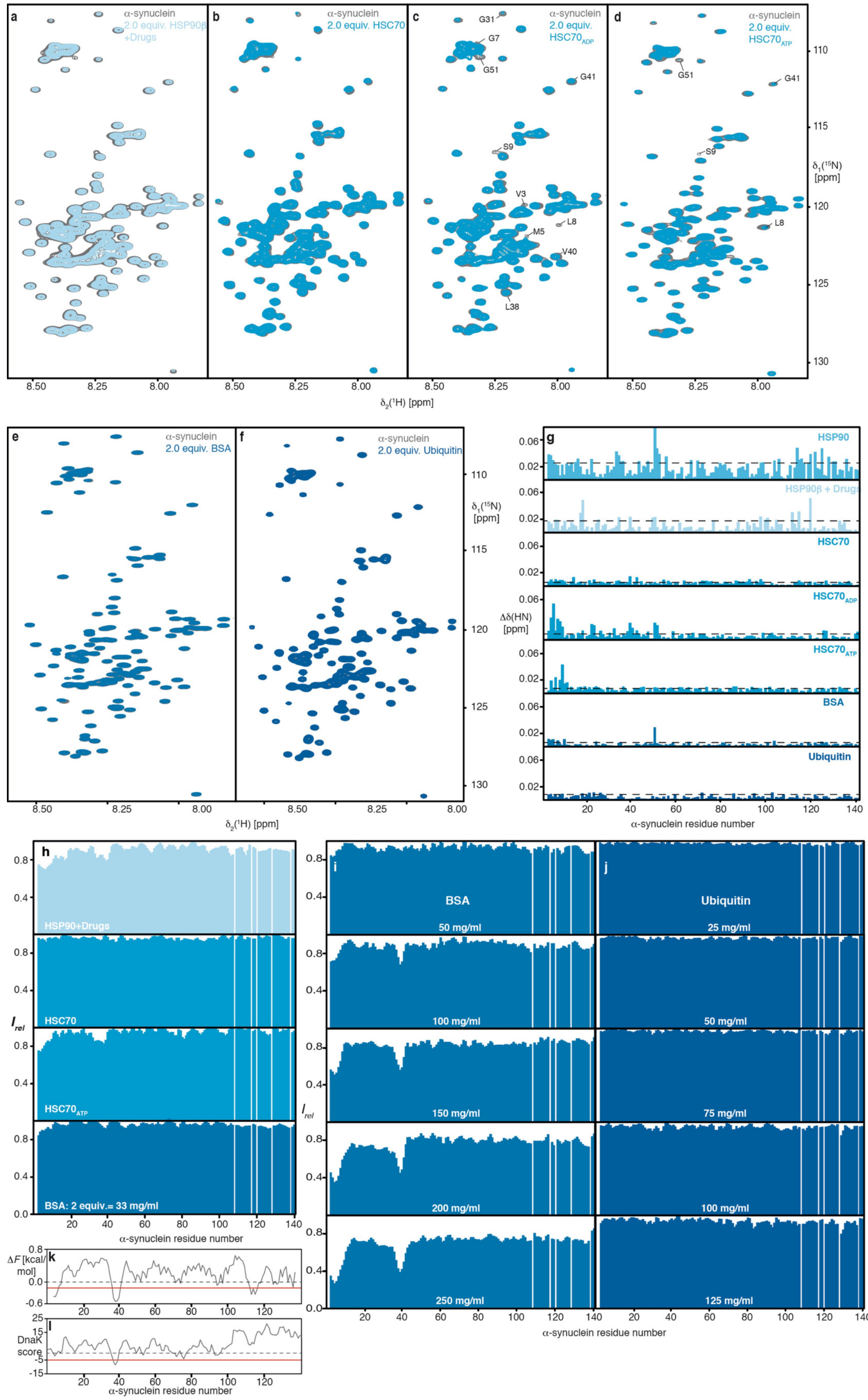

Extended Data Fig. 3 | See next page for caption.

Extended Data Fig. 3 | Interaction between α-synuclein and mammalian proteins. a, Overlay of two-dimensional [^{15}N, ^{1}H]-NMR spectra of 25 μM [U-^{15}N]-α-synuclein in the absence (grey) and presence (light blue) of 50 μM inhibited HSP90β dimer. Measured in NMR buffer plus 5 mM $MgCl_2$, 5 mM ATP, 1 μM radicicol and 1 μM geldanamycin. **b**, Overlay of two-dimensional [^{15}N, ^{1}H]-NMR spectra of 100 μM [U-^{15}N]-α-synuclein in the absence (grey) and presence (light blue) of 200 μM HSC70. **c**, Overlay of two-dimensional [^{15}N, ^{1}H]-NMR spectra of 100 μM [U-^{15}N]-α-synuclein in the absence (grey) and presence (light blue) of 200 μM $HSC70_{ADP}$. Measured in NMR buffer plus 5 mM $MgCl_2$ and 5 mM ADP. **d**, Overlay of two-dimensional [^{15}N, ^{1}H]-NMR spectra of 100 μM [U-^{15}N]-α-synuclein in the absence (grey) and presence (light blue) of 200 μM $HSC70_{ATP}$. Measured in NMR buffer plus 5 mM $MgCl_2$ and 5 mM ATP. **e**, Overlay of two-dimensional [^{15}N, ^{1}H]-NMR spectra of 250 μM [U-^{15}N]-α-synuclein in the absence (grey) and presence (blue) of 500 μM (33 mg ml^{-1}) BSA. **f**, Overlay of two-dimensional [^{15}N, ^{1}H]-NMR spectra of 250 μM [U-^{15}N]-α-synuclein in the absence (grey) and presence (dark blue) of 500 μM of ubiquitin. **g**, Residue-resolved combined chemical-shift perturbations of amide moieties upon addition of HSP90β (cyan), inhibited HSP90β (light cyan), HSC70 (light blue), $HSC70_{ADP}$ (light blue), $HSC70_{ATP}$ (light blue), BSA (blue) and ubiquitin (dark blue). Broken lines indicate a significance level of two s.d. from the mean. **h**, Residue-resolved backbone amide NMR signal attenuation ($I_{rel} = I/I_0$) of α-synuclein caused by the addition of two equivalents of inhibited HSP90β (light cyan), HSC70 (light blue), $HSC70_{ATP}$ (light blue) and BSA (blue). **i**, Residue-resolved NMR signal attenuation ($I_{rel} = I/I_0$) of 100 μM [U-^{15}N]-α-synuclein upon addition of increasing BSA concentrations (50–250 mg ml^{-1}). **j**, Residue-resolved NMR signal attenuation ($I_{rel} = I/I_0$) of 50 μM [U-^{15}N]-α-synuclein upon addition of increasing ubiquitin concentrations (25–125 mg ml^{-1}). **k**, Local hydrophobicity of α-synuclein plotted against the amino acid sequence. ΔF are the free energies of transfer of the individual amino acids from an aqueous solution to its surface[35]. Hydrophobicity corresponds to negative ΔF values. An exponentially weighted seven-window average was applied to the raw data, with the edges contributing 50%. The red line indicates the average value of 1.5 s.d. from the mean, the chosen threshold for the identification of the most hydrophilic segments. **l**, Sequence-dependent DnaK score for α-synuclein derived from a computational DnaK prediction algorithm[36]. Regions of the primary sequence with scores less than −5 (red line) are predicted to bind DnaK, a bacterial homologue of HSC70. Experiments in **a**–**f** were done in duplicates with similar results.

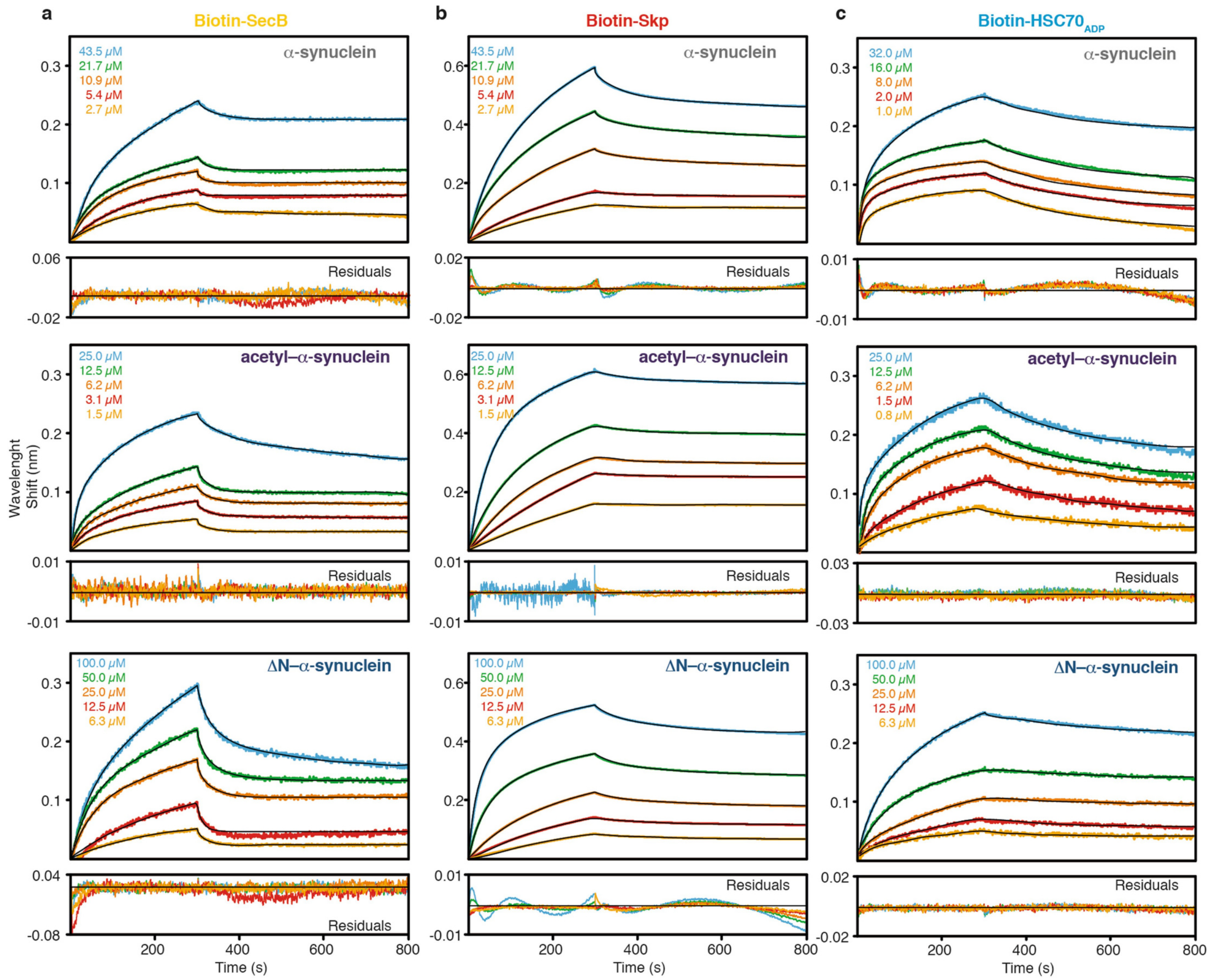

Extended Data Fig. 4 | Kinetic analysis of the interaction of the chaperones with α-synuclein variants. a–c, Kinetic analysis by bio-layer interferometry of biotinylated Skp (**a**), SecB (**b**) and HSC70$_{ADP}$ (**c**) to different α-synuclein variants (α-synuclein (top), acetyl-α-synuclein (middle) and ΔN-α-synuclein (bottom). Black lines represent least-square fits to the data. The residuals of the fits are shown below each set of bio-layer interferometry curves. Each individual kinetic experiment was run twice in triplicates with similar results.

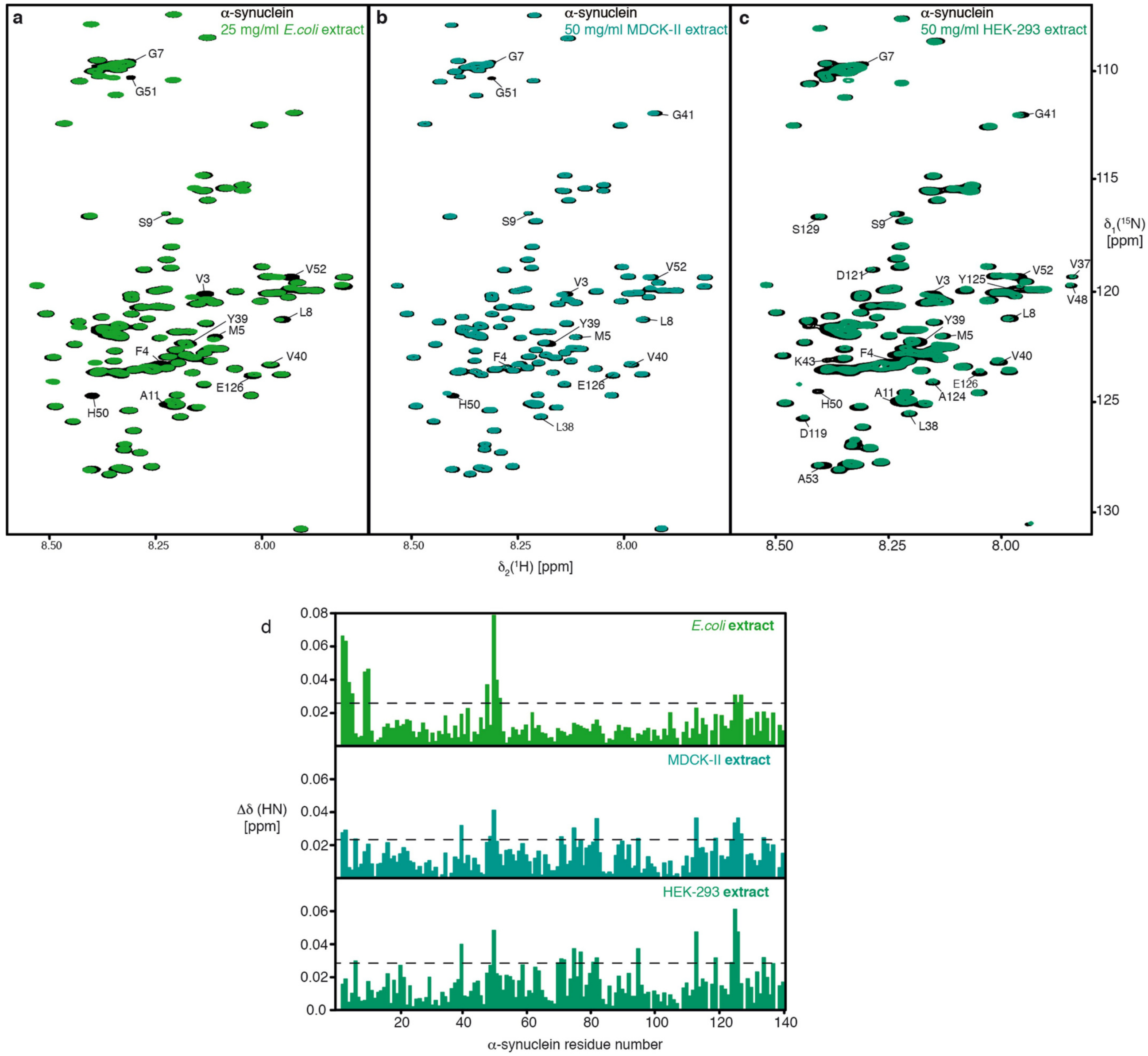

Extended Data Fig. 5 | Interaction between α-synuclein and cellular extracts. **a**, Overlay of two-dimensional [^{15}N, ^{1}H]-NMR spectra of 50 μM [*U*-^{15}N]-α-synuclein in the absence (black) and presence (green) of 25 mg ml^{-1} of *E. coli* cell extract. **b**, Overlay of two-dimensional [^{15}N, ^{1}H]-NMR spectra of 50 μM [*U*-^{15}N]-α-synuclein in the absence (black) and presence of 50 mg ml^{-1} mammalian MDCK-II cell extract (blue-green). **c**, Overlay of two-dimensional [^{15}N, ^{1}H]-NMR spectra of 50 μM [*U*-^{15}N]-α-synuclein in the absence (black) and presence (green) of 50 mg ml^{-1} mammalian HEK293 cell extract. **d**, Residue-resolved combined chemical-shift perturbations of the α-synuclein amide moieties in *E. coli* cell extract (green), mammalian MDCK-II cell extract (blue) and mammalian HEK293 cell extract (green), all relative to aqueous buffer. Broken lines indicate a significance level of two s.d. from the mean. Experiments in **a**–**c** were done in duplicates with similar results.

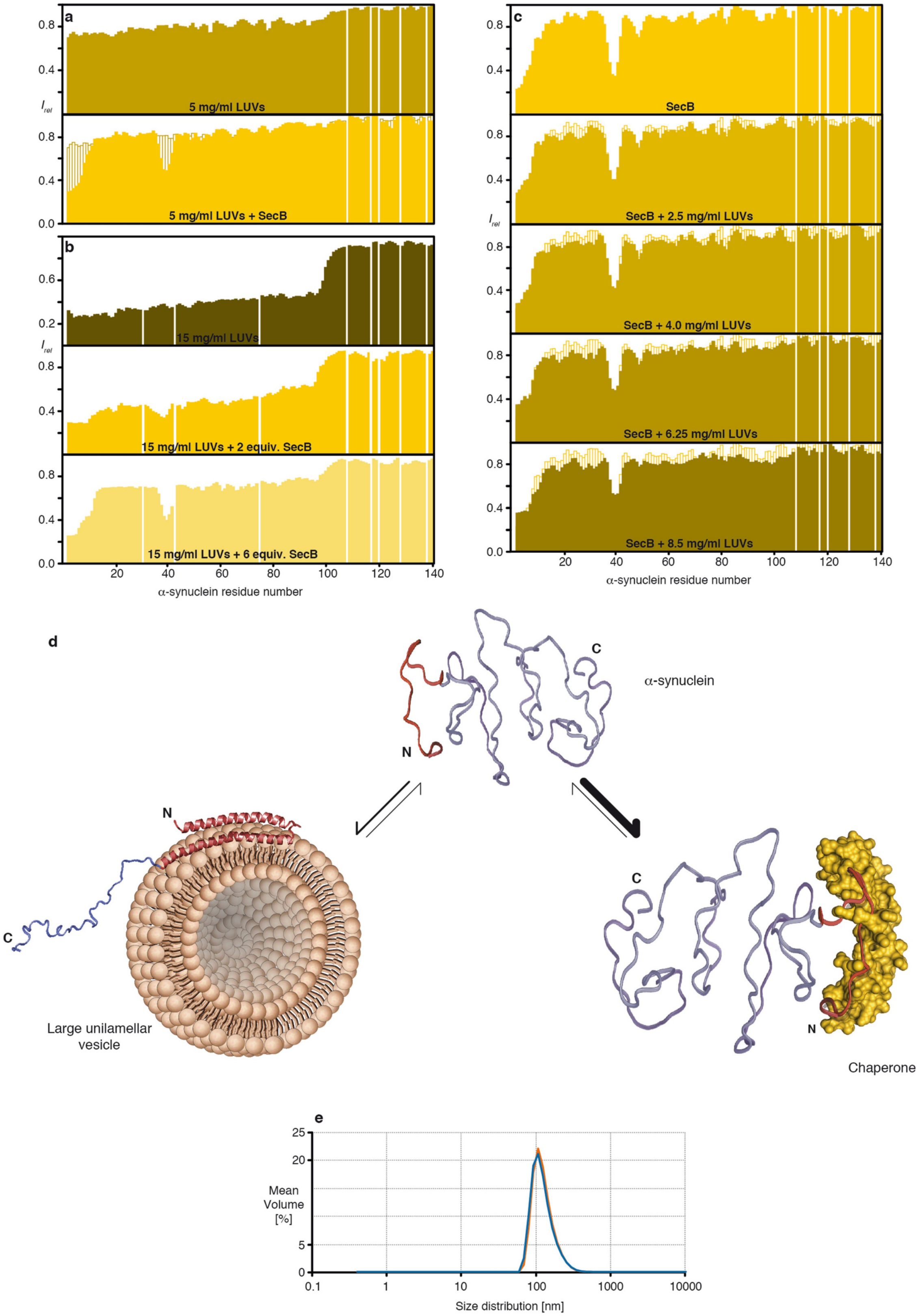

Extended Data Fig. 6 | See next page for caption.

Extended Data Fig. 6 | LUVs and the chaperone SecB compete for α-synuclein binding. a, Residue-resolved backbone amide NMR signal attenuation ($I_{rel} = I/I_0$) of α-synuclein caused by the addition of 5 mg ml^{-1} LUVs (125:1 molar ratio of lipid:protein; dark yellow) and after further addition of 2 equivalents of SecB (yellow). **b**, Residue-resolved backbone amide NMR signal attenuation ($I_{rel} = I/I_0$) of α-synuclein caused by the addition of 15 mg ml^{-1} LUVs (375:1 molar ratio lipid:protein; dark yellow) and after further addition of 2 and 6 equivalents of SecB, respectively (yellow), measured at 298 K. **c**, Residue-resolved backbone amide NMR signal attenuation ($I_{rel} = I/I_0$) of α-synuclein caused by the addition of 2 equivalents of SecB (yellow) and increasing amounts of LUVs with the following ratios: 2.5 mg ml^{-1}, 62.5:1; 4.0 mg ml^{-1}, 100:1; 6.25 mg ml^{-1}, 156:1; 8.5 mg ml^{-1}, 212.5:1. **d**, Schematic showing the conformational equilibrium of free α-synuclein, its chaperone-bound state and one possible conformation of its LUV-bound state (PDB 1XQ8)[19]. Notably, these observations are also in full agreement with related studies for HSP90[12] and HSP27[37]. **e**, Dynamic light scattering (DLS) measurements of LUVs prepared from pig brain polar lipids. Two independent preparations are shown in blue and orange, respectively, with an average diameter of 110 nm.

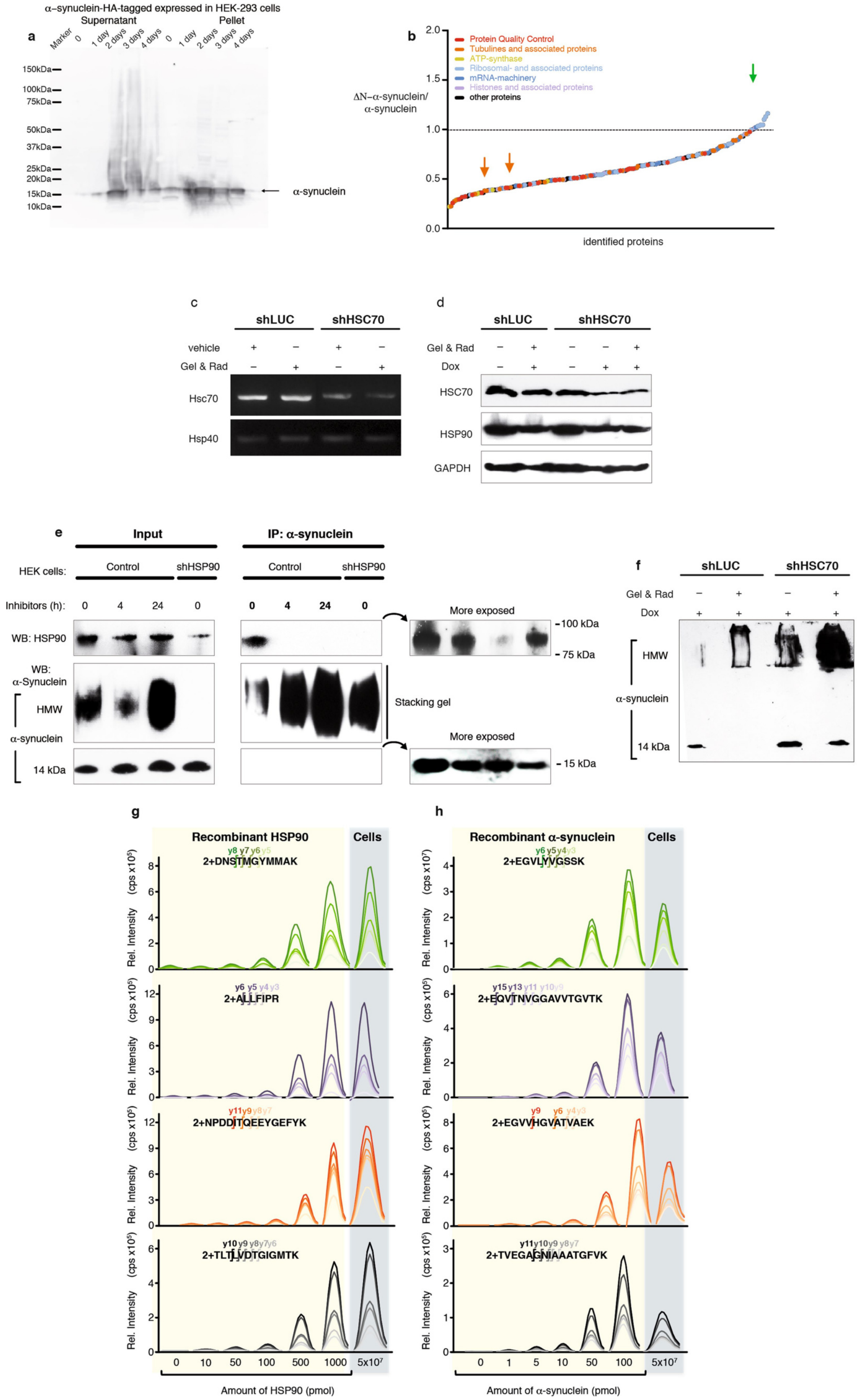

Extended Data Fig. 7 | See next page for caption.

Extended Data Fig. 7 | Interaction of α-synuclein and chaperones in cells. **a**, Western blot analysis of the expression of α-synuclein fused to a C-terminal haemagglutinin (HA)-tag in HEK293 cells. The molecular mass marker and the band corresponding to α-synuclein–HA are indicated. With these samples, immunoprecipitation and subsequent mass-spectrometry analysis was performed (**b** and Fig. 2a). **b**, Intensity ratios of carboxy-terminally HA-tagged ΔN-α-synuclein and α-synuclein immunoprecipitation determined by relative quantitative mass-spectrometry analysis. Experiments were performed as duplicates in HEK293 cells. Identification of at least five peptides per protein was required for quantification. Data are mean. The dotted line represents an intensity ratio of 1. Proteins that belong to specific groups are highlighted in colours. The values for α-synuclein (green) as well as tubulin β4 and tubulin α1B (orange arrows from left to right) are indicated by coloured arrows. **c**, Efficiency of HSC70 knockdown in HEK293 cells (constitutively expressing the T-Rex repressor) stably transfected with an inducible shRNA targeting *HSC70* mRNA (shHSC70). The image shows a representative semiquantitative reverse-transcription (RT)–PCR of *HSC70* mRNA in cells treated with doxycycline to induce shHSC70 and geldanamycin (Gel) and radicicol (Rad) for 24 h (+). Cells transfected with a control shRNA targeting firefly luciferase (shLUC) as well as semiquantification of an unrelated chaperone (HSP40) were included as negative and loading controls. **d**, Semiquantification of HSC70 and HSP90 protein levels by western blot. HEK293 cells (constitutively expressing the T-Rex repressor) stably transfected with shHSC70 and shLUC were grown in normal (−) or doxycycline-containing (+) medium for HSC70 knockdown. The cells were subsequently treated with vehicle (−) or geldanamycin and radicicol for HSP90 inhibition. The constitutively expressed protein GAPDH was assayed as loading control. **e**, Efficiency of the combined treatment of geldanamycin and radicicol in disrupting the α-synuclein–HSP90 interaction. HEK293 cells were treated with geldanamycin and radicicol for 4 or 24 h and then electroporated with recombinant α-synuclein using the protocol for in-cell NMR experiments. Whole-cell lysates were collected and used in immunoprecipitation assays with anti-α-synuclein antibodies. The obtained precipitates were then resolved by SDS–PAGE and analysed by western blot using the indicated antibodies. In addition to HEK293 cells with normal levels of HSP90 (control cells), cells with reduced levels of HSP90 (shHSP90) were used to validate the HSP90 band. **f**, Inhibition of both HSP90 and HSC70 promotes aggregation of α-synuclein. The image shows a representative semiquantitative western blot of HSC70-depleted HEK293 cells treated with geldanamycin and radicicol. After 24 h of treatment, the cells were subjected to electroporation with recombinant α-synuclein and 4 h after electroporation the cells were collected and analysed by western blot. HMW and 14 kDa refer to high-molecular weight and monomeric α-synuclein species, respectively. **g**, **h**, Quantification of intracellular levels of HSP90 and electroporated α-synuclein in HEK293 cells by parallel reaction monitoring mass spectrometry. A standard curve (contained in the yellow boxes) using increasing amounts of recombinant HSP90 (**g**) or α-synuclein (**h**) enables the relative quantification of the intracellular protein levels. As surrogates for intracellular protein levels, at least four tryptic peptides of HSP90 (**g**) or human α-synuclein (**h**) were quantified. Targeted peptides are shown at the top of each plot, and at least four transitions of the *y*-series of the product ions were monitored over the chromatographic separation of the peptides (different colours). The determined cellular concentrations of HSP90 and α-synuclein were 30 μM and 2.5 μM, respectively (see Supplementary Methods for details of this calculation). cps, counts per second. The original and uncropped gels of **a**, **c**–**f** can be found in Supplementary Fig. 1. Western blot and PCR experiments (**a**, **c**–**f**) were done in duplicates, with in similar results.

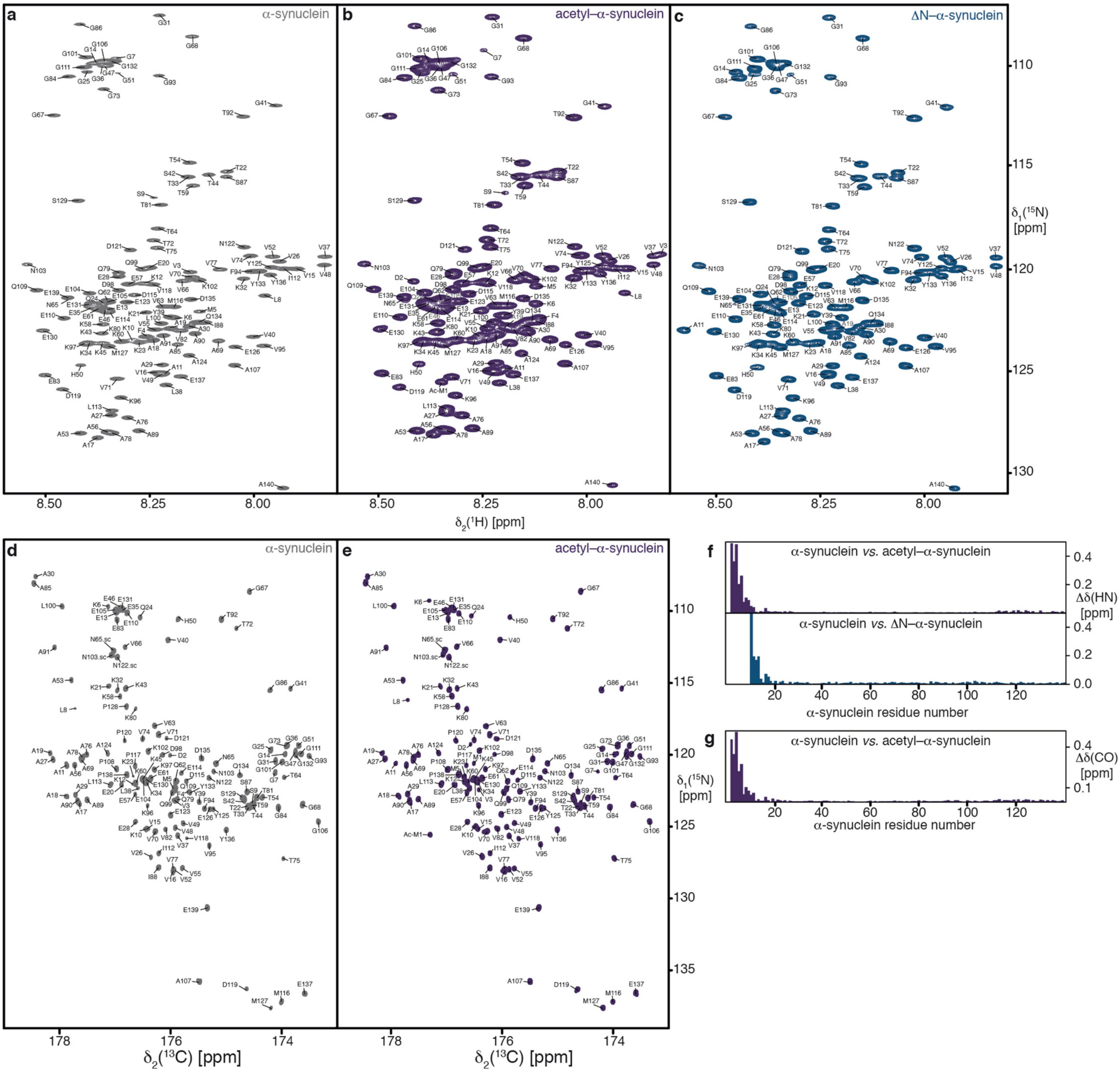

Extended Data Fig. 8 | Sequence-specific NMR-resonance assignments of α-synuclein variants. a–**c**, Two-dimensional [^{15}N, ^{1}H]-NMR spectra of 500 µM [*U*-^{13}C, ^{15}N]-α-synuclein (grey), 450 µM [*U*-^{13}C, ^{15}N]-acetyl-α-synuclein (dark violet) and 100 µM [*U*-^{15}N]-ΔN-α-synuclein (dark blue). The sequence-specific resonance assignments for wild-type as well as acetylated α-synuclein obtained from three-dimensional triple resonance experiments and from chemical-shift mapping of ΔN-α-synuclein are indicated. **d**, **e**, Two-dimensional [^{13}C, ^{15}N]-NMR spectra of 500 µM [*U*-^{13}C, ^{15}N]-α-synuclein (grey) and 450 µM [*U*-^{13}C, ^{15}N]-acetyl-α-synuclein (dark violet). The sequence-specific resonance assignments for wild-type and acetylated α-synuclein obtained from three-dimensional triple resonance experiments are indicated. **f**, Residue-resolved combined chemical-shift perturbations of the amide moieties for acetyl-α-synuclein (dark violet) and ΔN-α-synuclein (dark blue) versus wild-type α-synuclein. **g**, Residue-resolved combined chemical-shift difference of the carbonyl-amide moieties for acetyl-α-synuclein (dark violet) versus wild-type α-synuclein. [^{15}N, ^{1}H]-NMR spectra in **a**–**c** were measured five times and [^{13}C, ^{15}N]-NMR spectra (**d**, **e**) were measured in duplicates, all yielding similar results.

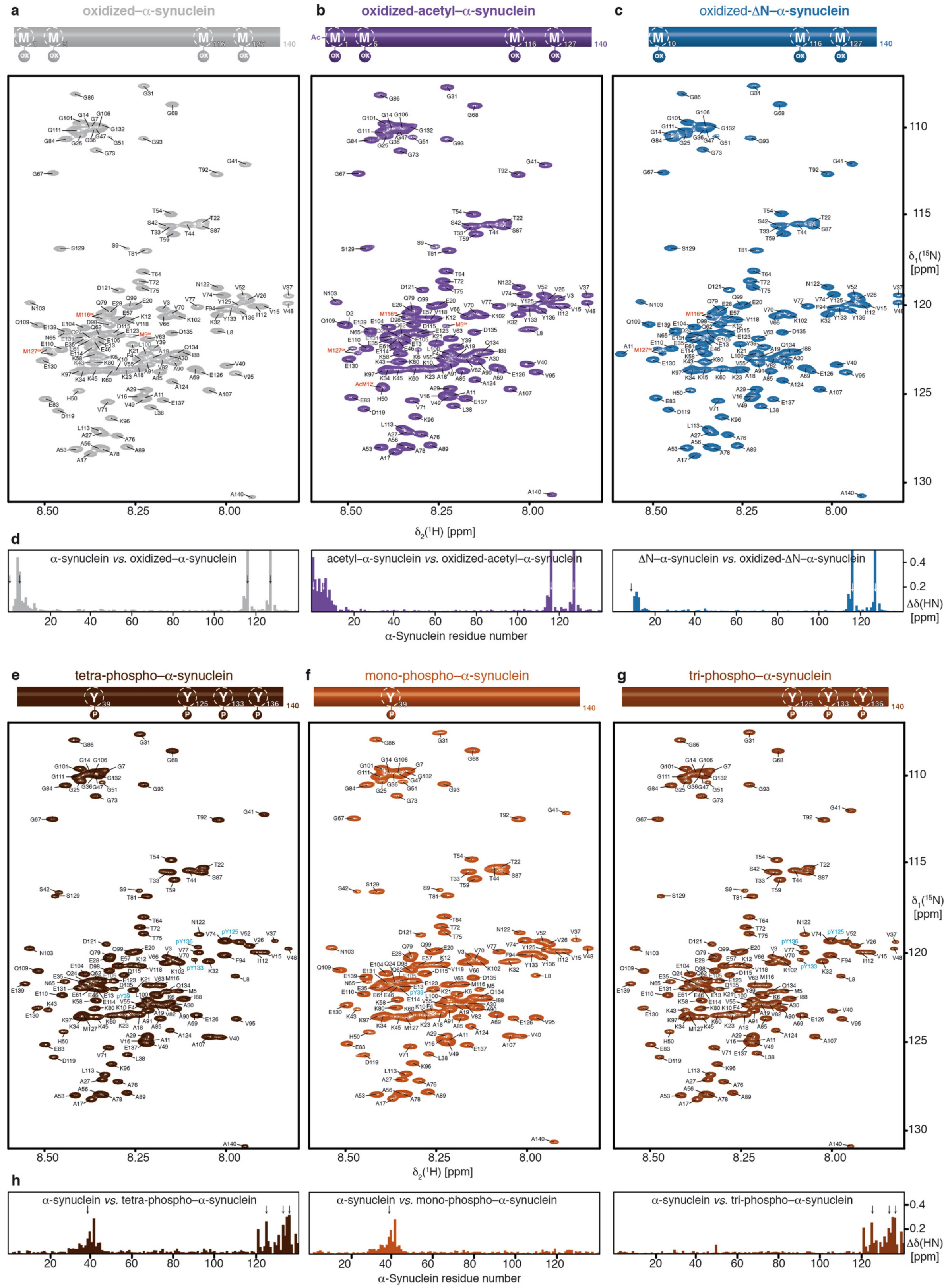

Extended Data Fig. 9 | See next page for caption.

Extended Data Fig. 9 | Sequence-specific NMR-resonance assignments of methionine-oxidized and tyrosine-phosphorylated α-synuclein variants. **a**–**c**, Two-dimensional [^{15}N, ^{1}H]-NMR spectra of 100 μM oxidized [*U*-^{15}N]-α-synuclein (light grey), 100 μM oxidized [*U*-^{15}N]-acetyl-α-synuclein (violet) and 100 μM oxidized [*U*-^{15}N]-ΔN-α-synuclein (blue). The sequence-specific resonance assignments from chemical-shift mapping and published assignments of the oxidized state[23] are indicated. Oxidized methionines are highlighted in red. **d**, Residue-resolved combined chemical-shift differences of the amide moieties for oxidized α-synuclein (light grey), oxidized acetyl-α-synuclein (violet) and oxidized-ΔN-α-synuclein (blue) relative to their respective reduced states. Colours as in **a**–**c**. Arrows indicate the positions of the oxidized methionines. **e**–**g**, Two-dimensional [^{15}N, ^{1}H]-NMR spectra of 50 μM [*U*-^{15}N]-mono-phospho-α-synuclein (red-brown), 50 μM [*U*-^{15}N]-tri-phospho-α-synuclein (brown) and 50 μM [*U*-^{15}N]-tetra-phospho-α-synuclein (dark brown). The sequence-specific resonance assignments based on published assignments for phosphorylated α-synuclein are indicated[24]. Phosphorylated residues are highlighted in cyan. **h**, Residue-resolved combined chemical-shift differences of the amide moieties for the phosphorylated α-synuclein variants relative to wild-type α-synuclein. Colours as in **e**–**g**. Arrows indicate the positions of the phosphorylated tyrosines. [^{15}N, ^{1}H]-NMR spectra of the different modified α-synuclein variants were measured several times ($n = 4$) yielding similar results.

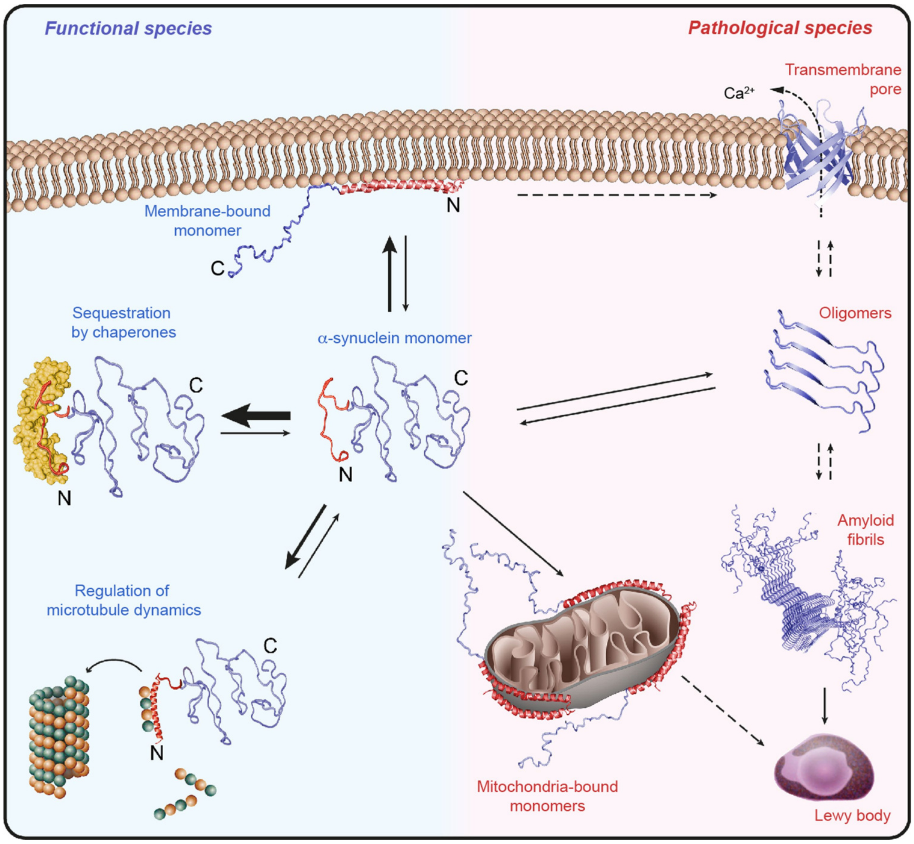

Extended Data Fig. 10 | Mechanism of chaperone-controlled regulation of α-synuclein function, conformation and localization in mammalian cells. Cellular chaperones (yellow) interact with the N-terminal segment of α-synuclein (red), thus actively regulating its functional species by shifting conformational equilibria. Impairment of the natural α-synuclein–chaperone ratio or abrogation of the α-synuclein–chaperone interaction by post-translational modifications can lead to the formation of pathological species, including the accumulation of α-synuclein at mitochondria.

nature research

Corresponding author(s): Sebastian Hiller, Björn M. Burmann, Roland Riek

Last updated by author(s): Sep 22, 2019

Reporting Summary

Nature Research wishes to improve the reproducibility of the work that we publish. This form provides structure for consistency and transparency in reporting. For further information on Nature Research policies, see Authors & Referees and the Editorial Policy Checklist.

Statistics

For all statistical analyses, confirm that the following items are present in the figure legend, table legend, main text, or Methods section.

n/a	Confirmed	
☐	☒	The exact sample size (*n*) for each experimental group/condition, given as a discrete number and unit of measurement
☐	☒	A statement on whether measurements were taken from distinct samples or whether the same sample was measured repeatedly
☒	☐	The statistical test(s) used AND whether they are one- or two-sided *Only common tests should be described solely by name; describe more complex techniques in the Methods section.*
☒	☐	A description of all covariates tested
☒	☐	A description of any assumptions or corrections, such as tests of normality and adjustment for multiple comparisons
☒	☐	A full description of the statistical parameters including central tendency (e.g. means) or other basic estimates (e.g. regression coefficient) AND variation (e.g. standard deviation) or associated estimates of uncertainty (e.g. confidence intervals)
☒	☐	For null hypothesis testing, the test statistic (e.g. *F*, *t*, *r*) with confidence intervals, effect sizes, degrees of freedom and *P* value noted *Give P values as exact values whenever suitable.*
☒	☐	For Bayesian analysis, information on the choice of priors and Markov chain Monte Carlo settings
☒	☐	For hierarchical and complex designs, identification of the appropriate level for tests and full reporting of outcomes
☒	☐	Estimates of effect sizes (e.g. Cohen's *d*, Pearson's *r*), indicating how they were calculated

Our web collection on statistics for biologists contains articles on many of the points above.

Software and code

Policy information about availability of computer code

Data collection	NMR data were collected on Bruker spectrometers operated with TOPSPIN 3.0-3.5.
Data analysis	NMR data were processed with PROSA and analyzed with CARA. MS data were analyzed with Skyline (MacCoss, Version 3.7).

For manuscripts utilizing custom algorithms or software that are central to the research but not yet described in published literature, software must be made available to editors/reviewers. We strongly encourage code deposition in a community repository (e.g. GitHub). See the Nature Research guidelines for submitting code & software for further information.

Data

Policy information about availability of data

All manuscripts must include a data availability statement. This statement should provide the following information, where applicable:

- Accession codes, unique identifiers, or web links for publicly available datasets
- A list of figures that have associated raw data
- A description of any restrictions on data availability

The data that support the findings of this study are available from the corresponding authors upon request.

Field-specific reporting

Please select the one below that is the best fit for your research. If you are not sure, read the appropriate sections before making your selection.

☒ Life sciences ☐ Behavioural & social sciences ☐ Ecological, evolutionary & environmental sciences

For a reference copy of the document with all sections, see nature.com/documents/nr-reporting-summary-flat.pdf

Life sciences study design

All studies must disclose on these points even when the disclosure is negative.

Sample size	No statistical methods were used to predetermine sample size. Sample sizes were chosen in agreement with established procedures in the field.
Data exclusions	No data was excluded from the analyses
Replication	Experiments were replicated to ensure reproducibility of the findings. The number of independent replicates for each experiment are specified in the respective Figure captions. All attempts at replication were successful.
Randomization	The experiments were not randomized, in agreement with established procedures in the field.
Blinding	The investigators were not blinded to allocation during experiments and outcome assessment, in agreement with established procedures in the field.

Reporting for specific materials, systems and methods

We require information from authors about some types of materials, experimental systems and methods used in many studies. Here, indicate whether each material, system or method listed is relevant to your study. If you are not sure if a list item applies to your research, read the appropriate section before selecting a response.

Materials & experimental systems

n/a	Involved in the study	
☐	☒	Antibodies
☐	☒	Eukaryotic cell lines
☒	☐	Palaeontology
☒	☐	Animals and other organisms
☒	☐	Human research participants
☒	☐	Clinical data

Methods

n/a	Involved in the study	
☒	☐	ChIP-seq
☒	☐	Flow cytometry
☒	☐	MRI-based neuroimaging

Antibodies

Antibodies used	Mouse anti-alpha-Synuclein Abcam Cat#: ab27766, RRID: AB_727020, 1:1000 for Western blot and Immunofluorescence Rabbit anti-alpha-Synuclein CellSignaling Cat#: 2642, RRID: AB_10695412, 1:1000 for Western blot and Immunofluorescence Mouse anti-Hsc70 Abcam Cat#: ab2788, RRID: AB_303301, 1:1000 for Western blot Mouse anti-Hsp90 Beta Abcam Cat#: ab53497, RRID: AB_881097, 1:3000 for Western blot Rabbit anti-COX IV ProteinTech Cat#: 11242-1-AP, RRID: AB_2085278, 1:500 for Immunofluorescence Rabbit anti-COX IV Abcam Cat#: ab16056, RRID: AB_443304, 1:1000 for Immunofluorescence Mouse anti-GAPDH Thermo Fischer Scientific Cat#: GA1R, RRID: AB_10751612, 1:5000 for Western blot
Validation	Mouse anti-alpha-Synuclein Abcam Cat#: ab27766, validated by Abcam Rabbit anti-alpha-Synuclein CellSignaling Cat#: 2642, validated by CellSignaling and by our lab Mouse anti-Hsc70 Abcam Cat#: ab2788, validated by Abcam Mouse anti-Hsp90 Beta Abcam Cat#: ab53497, validated by Abcam Rabbit anti-COX IV ProteinTech Cat#: 11242-1-AP, validated by Proteintech Rabbit anti-COX IV Abcam Cat#: ab16056, validated by Abcam Mouse anti-GAPDH Thermo Fischer Scientific Cat#: GA1R, validated by Thermo Fischer Scientific

Eukaryotic cell lines

Policy information about cell lines

Cell line source(s)	Flp-In™ 293 cells were purchased from Thermo Fisher Scientific (R75007), HEK-293 were purchased from the American Type Culture Collection (CRL-1573).
Authentication	The authenticity of the cells was provided by Thermo Fisher Scientific and the American Type Culture Collection upon purchase. We have not authenticated these cell lines.
Mycoplasma contamination	The cells were tested for mycoplasma contamination every four weeks. Only mycoplasma-free cultures were used for the experiments.
Commonly misidentified lines (See ICLAC register)	No commonly misidentified cells were used.

Work

Your story

Send your careers story to: naturecareerseditor @nature.com

TRISTAN BRAND

Conservation scientist Aerin Jacob (right) conducts field work with a colleague in British Columbia, Canada, in 2018.

SECRETS TO WRITING A WINNING GRANT

Experienced scientists reveal how to avoid application pitfalls to submit successful proposals. **By Emily Sohn**

When Kylie Ball begins a grant-writing workshop, she often alludes to the funding successes and failures that she has experienced in her career. "I say, 'I've attracted more than $25 million in grant funding and have had more than 60 competitive grants funded. But I've also had probably twice as many rejected.' A lot of early-career researchers often find those rejections really tough to take. But I actually think you learn so much from the rejected grants."

Grant writing is a job requirement for research scientists who need to fund projects year after year. Most proposals end in rejection, but missteps give researchers a chance to learn how to find other opportunities, write better proposals and navigate the system. Taking time to learn from the setbacks and successes of others can help to increase the chances of securing funds, says Ball, who runs workshops alongside her role as a behavioural scientist at Deakin University in Melbourne, Australia.

Do your research

Competition for grants has never been more intense. The European Commission's Horizon 2020 programme is the European Union's largest-ever research and innovation programme, with nearly €80 billion (US$89 billion) in funding set aside between 2014 and 2020. It reported a 14% success rate for its first 100 calls for proposals, although submissions to some categories had lower success rates. The commission has published its proposal for Horizon Europe, the €100-billion programme that will succeed Horizon 2020. In Australia, since 2017, the National Health and Medical Research Council has been funding less than 20% of proposals it receives. And the US National Science Foundation (NSF) received 49,415 proposals and funded 11,447 of them in 2017 – less than 25%. That's tens of thousands of rejections in a single year from the NSF alone.

Being a renowned scientist doesn't ensure success. On the same day that molecular biologist Carol Greider won a Nobel prize in 2009, she learnt that her recently submitted grant proposal had been rejected. "Even on the day when you win the Nobel prize," she said in a 2017 graduation speech at Cold Spring Harbor Laboratory in New York, "sceptics may question whether you really know what you're doing."

To increase the likelihood of funding success, scientists suggest doing an extensive search of available grants and noting differences in the types of project financed by various funding bodies. Government agencies such as the NSF tend to be interested in basic science that addresses big, conceptual questions, says Leslie Rissler, programme director at the NSF's Division of Environmental Biology in Alexandria, Virginia. A private foundation, however, might prioritize projects that inform social change or that have practical implications that fit into one of its specific missions.

Pitching a proposal

Before beginning an application, you should read descriptions and directions carefully, advises Ball, who recently pored over 200 pages of online material before starting a proposal. That effort can save time in the end, helping researchers to work out which awards are a good fit and which aren't. "If you're not absolutely spot on with what they're looking for, it may not be worth your time in writing that grant," she says.

Experienced scientists suggest studying successful proposals, which can often be acquired from trusted colleagues and supervisors, university libraries or online databases. A website called Open Grants, for example, includes more than 200 grants, both successful and unsuccessful, that are free to peruse.

Grant writers shouldn't fear e-mailing or calling a grants agency to talk through their potential interest in a project, advises Amanda Stanley, executive director at COMPASS, a non-profit organization based in Portland, Oregon, that supports environmental scientists. For six years, she worked as a programme officer for the Wilburforce Foundation in Seattle, Washington, which supports conservation science. At this and other private foundations, the application process often begins with a 'soft pitch' that presents a brief case for the project. Those pitches should cover several main points, Stanley says: "'Here's what I'm trying to do. Here's why it's important. Here's a little bit about me and the people I'm collaborating with. Would you like to talk further?'" She notes that a successful proposal must closely align with a foundation's strategic goals.

Each organization has its own process, but next steps typically include a phone conversation, a written summary and, finally, an invitation to submit a formal application. "Once you've gotten that invitation to submit a proposal from the programme officer, your chances of getting funded are really, really high," Stanley says.

The write stuff

Applicants should put themselves in the shoes of grant reviewers, who might need to read dozens of applications about complicated subjects that lie outside their own fields of expertise, often while juggling their own research.

"Imagine you're tired, grumpy and hungry. You've got 50 applications to get through," says Cheryl Smythe, international grants manager at the Babraham Institute, a life-sciences research institution in Cambridge, UK. "Think about how you as an applicant can make it as easy as possible for them."

Formatting is an important consideration, says Aerin Jacob, a conservation scientist at the Yellowstone to Yukon Conservation Initiative in Canmore, Canada. White space and bold headings can make proposals easier to read, as can illustrations. "Students are tempted and sometimes encouraged to squeeze in as much information as possible, so there are all kinds of tricks to fiddle with the margin size, or to make the font a little bit smaller so that you can squeeze in that one last sentence," Jacob says. "For a reviewer, that's exhausting to read."

Ball advises avoiding basic deal-breakers, such as spelling errors, grammatical slips and lengthy proposals that exceed word limits. Those kinds of mistake can cast doubt on how rigorous applicants will be in their research, she says. A list of key words, crucial for indexes and search engines, should be more than an afterthought, Ball adds. On a proposal for a project on promoting physical activity among women, she tagged her proposal with the word 'women'. The descriptor was too broad, and her application ended up with a reviewer whose expertise appeared to be in sociology and gender studies instead of in exercise or nutrition. The grant didn't score well in that round of review.

To prevent a reviewer's eyes from glazing over, Jacob says, use clear language instead of multisyllabic jargon. When technical details are necessary, follow up a complex sentence with one that sums up the big picture. Thinking back to her early proposals, Jacob remembers cramming in words instead of getting to the point. "It was probably something like, 'I propose to study the heterogeneity of forest landscapes in spatial and temporal recovery after multiple disturbances,' rather than, 'I want to see what happens when a forest has been logged, burnt and farmed, and grows back,'" she says.

Grants can be more speculative and more self-promotional than papers are, Rissler adds. "A grant is about convincing a jury that your ideas are worthy and exciting," she says. "You can make some pretty sweeping generalizations about what your proposed ideas might do for science and society in the long run. A paper is much more rigid in terms of what you can say and in what you must say."

Getting some science communication training can be a worthwhile strategy for strengthening grant-writing skills, Stanley says. When she was reviewing pitch letters for a private foundation, she recalls that lots of scientists couldn't fully explain why their work mattered. But when she received pitches that were clear and compelling, she was more willing to help those scientists brainstorm other

LOUISA WOOD

Grants manager Cheryl Smythe (left) allows for IT glitches when submitting grant proposals.

possible funding agencies if her foundation wasn't the right fit. Scientists who sent strong – albeit unsuccessful – applications were also more likely to get funding from the foundation for later projects.

Science storytelling

To refine project pitches and proposals, Stanley recommends that scientists use a free communication tool from COMPASS called the Message Box Workbook, which can help to identify key points and answer the crucial question for every audience: 'So what?' Scientific conferences often provide symposia or sessions that include funders and offer helpful tips for writing grants. And development officers at institutions can help scientists to connect with funders. "A good development officer is worth their weight in gold," Stanley says. "Make friends with them."

Jacob has taken science-communication training through COMPASS, The Story Collider (a science-storytelling organization) and from other such organizations. She has learnt how to talk about her work in the manner of a storyteller. In proposals and interviews, she now includes personal details, when relevant, that explain the problems she wants to address and why she decided to speak out about conservation – an example of the kind of conflict and resolution that builds a good story. Jacob senses that the approach strikes a chord. "As a reviewer, you remember somebody's proposal just that little bit more," she says. "If you have a stack of proposals, you want to find the one that you connect with."

A clear focus can help to boost a grant to the top of a reviewer's pile, Ball adds. In one of the first large grants that she applied for, she proposed collecting information on the key factors that prevent weight gain as well as designing and implementing an obesity-intervention programme. In retrospect, it was too much within the grant's two-year time frame. She didn't get the funding, and the feedback she received was that it would have worked better as two separate proposals. "While it's tempting to want to claim that you can solve these enormous, challenging and complex problems in a single project," Ball says, "realistically, that's usually not the case."

Teaming up with collaborators can also increase the chance of success. Earlier this year, Ball was funded by the Diabetes Australia Research Program for a study that she proposed in collaboration with hospital clinicians, helping disadvantaged people with type 2 diabetes to eat healthy diets. Earlier in her career, she had written grants based on her own ideas, rather than on suggestions from clinicians or other non-academic partners. This time, she says, she focused on a real-world need rather than on her own ideas for a study. Instead of overreaching, she kept the study small and preliminary, allowing her to test the approach before trying to get funding for larger trials.

It is acceptable – even advisable – to admit a study's limitations instead of trying to meet preconceived expectations, Jacob adds. In 2016, she had a proposal rejected for a study on spatial planning on the west coast of Canada that would, crucially, be informed by knowledge from Indigenous communities. She resubmitted the same proposal the next year to the same reviewers, but with a more confident and transparent approach: she was straightforward about her desire to take a different tack from the type of research that had been tried before. This time, she made it clear that she wanted to listen to Indigenous peoples and use their priorities to guide her work. She got the funding. "I saw that if I tried to change it to meet what I thought funders wanted, I might not be accurately representing what I was doing," she says. "I just wanted to be really clear with myself and really clear with the interviewers that this is who I am, and this is what I want to do."

> **"Grant writers shouldn't fear e-mailing or calling a grants agency."**

What not to do

Writing is hard, and experienced grant writers recommend devoting plenty of time to the task. Smythe recommends setting aside a week for each page of a proposal, noting that some applications require only a few pages while major collaborative proposals for multi-year projects can run to more than 100 pages. "It can take months to get one of these together," she says.

Scheduling should include time for rewrites, proofreads and secondary reads by friends, colleagues and family members, experts say. Working right up to the deadline can undo weeks to months of hard work. At the last minute, Jacob once accidentally submitted an earlier draft instead of the final version. It included sections that were bolded and highlighted, with comments such as, "NOTE TO SELF: MAKE THIS PART SOUND BETTER." She didn't get that one, and has never made the same mistake again.

Add an extra buffer for technology malfunctions, adds Smythe, who once got a call from a scientist at another organization who was in a panic because his computer had stopped working while he was trying to submit a grant proposal half an hour before the deadline. She submitted it for him with 23 seconds to spare. "My hand was shaking," she says. That proposal was not successful, although the scientist sent her a nice bottle of champagne afterwards.

Grant writing doesn't necessarily end with a proposal's submission. Applicants might receive requests for rewrites or more information. Rejections can also come with feedback, and if they don't, applicants can request it.

Luiz Nunes de Oliveira, a physicist at the University of São Paulo, Brazil, also works as a programme coordinator at the São Paulo Research Foundation. In this role, he sometimes meets with applicants who want to follow up on rejected proposals. "We sit down and go through their résumé, and then you find out that they had lots of interesting stuff to say about themselves and they missed the opportunity," he says. "All it takes is to write an e-mail message asking [the funder] for an interview."

Jacob recommends paying attention to such feedback to strengthen future proposals. To fund her master's programme, she applied for a grant from the Natural Sciences and Engineering Research Council of Canada (NSERC), but didn't get it on her first try. After requesting feedback by e-mail (to an address she found buried on NSERC's website), she was able to see her scores by category, which revealed that a few bad grades early in her undergraduate programme were her limiting factor.

There was nothing she could do about her past, but the information pushed her to work harder on other parts of her application. After gaining more research and field experience, co-authoring a paper and establishing relationships with senior colleagues who would vouch for her as referees, she finally secured funding from NSERC on her third try, two years after her first rejection.

Negative feedback can be one of the best learning experiences, Rissler adds. She kept the worst review she ever received, a scathing response to a grant proposal she submitted to the NSF in 2003, when she was a postdoc studying comparative phylogeography. The feedback, she says, was painful to read. It included comments that her application was incomprehensible and filled with platitudes.

After she received that letter, which is now crinkled up in her desk for posterity, Rissler called a programme officer to ask why they let her see such a negative review. She was told that the critical commenter was an outlier and that the panel had gone on to recommend her project for the grant, which she ultimately received. "I learnt that you do need to be tough," says Rissler, who now helps to make final decisions on funding for other scientists. She emphasizes that whereas reviewers' opinions can vary, all proposals undergo multiple independent expert reviews, followed by panel discussions and additional oversight by programme directors.

Grant writing tends to provoke anxiety among early-career scientists, but opportunities exist for people who are willing to take the time to develop ideas and push past rejections and negative feedback, she says. "We can't review proposals that we don't get."

Emily Sohn is a freelance journalist in Minneapolis, Minnesota.

Where I work
Paul Nurse

Photographed for *Nature* by Leonora Saunders.

I don't like thinking alone. I like the bustle and energy of other people. So I do my thinking in a glass-covered, grand atrium with gigantic windows, where I'm surrounded by people. I like to be able to think and write, then look up and see people talking, thinking and writing. We're all trying to wrestle with some problem.

I oversee everything that happens at the Francis Crick Institute: from our discovery research to our engagement with schools, the local community and the public.

I work with colleagues to develop the Crick's strategy for delivering high-quality research that unlocks deeper understanding of the biology underlying human health and disease. That strategy includes bringing in the best scientific talent, and supporting the UK biomedical research endeavour.

The Crick is a grand building shaped a bit like a cathedral. We have glass walls at the four ends of the central atrium.

At the east end, some glass is treated with a special refractive film, so the colour changes depending on the angle between the light source and the viewer. It's very beautiful.

I quite often live in my head, and my mind wanders over a range of things.

In my laboratory, I study cells to find out how they work as the fundamental unit of life. This is difficult and complex, and I like an environment that I find both stimulating and restful at the same time.

Sometimes I'm really disciplined, focused and wrestling with the problem in hand. Sometimes I'm daydreaming, looking at the rest of the world and allowing my mind to wander into a wider environment. So I vacillate between those two types of thinking.

What I like about the glass in this atrium is that you don't feel constrained. If you sit in a little office, then you're physically cramped and your brain is cramped, too.

Here, looking up through the windows and to the sky, my mind can expand beyond its normal confines.

Paul Nurse, geneticist and cell biologist, is director of the Francis Crick Institute in London, UK. **Interview by Josie Glausiusz.**